

Woodhead Publishing in Materials

The Science of Armour Materials

Edited by

Ian G. Crouch



AMSTERDAM • BOSTON • CAMBRIDGE • HEIDELBERG
LONDON • NEW YORK • OXFORD • PARIS • SAN DIEGO
SAN FRANCISCO • SINGAPORE • SYDNEY • TOKYO

Woodhead Publishing is an imprint of Elsevier



List of contributors

- L. Arnold** RMIT University, Brunswick, Victoria, Australia
- H. Billon** Defence Science and Technology Group, Fishermans Bend, Victoria, Australia
- S.J. Cimpoeu** Defence Science and Technology Group, Fishermans Bend, Victoria, Australia
- I.G. Crouch** RMIT University, Brunswick, Victoria, Australia; Armour Solutions Pty Ltd, Trentham, Victoria, Australia
- D.P. Edwards** Defence Science and Technology Group, Fishermans Bend, Victoria, Australia
- L. Edwards** ANSTO, Lucas Heights, NSW, Australia
- B. Eu** Ballistic and Mechanical Testing, Port Melbourne, Victoria, Australia
- G.V. Franks** The University of Melbourne, Victoria, Australia
- M.A. Kariem** Bandung Institute of Technology, Bandung, West Java, Indonesia
- H. Li** University of Wollongong, NSW, Australia
- M. Naebe** Deakin University, Waurn Ponds, Victoria, Australia
- A. Pierlot** CSIRO, Waurn Ponds, Victoria, Australia
- D. Ruan** Swinburne University of Technology, Hawthorn, Victoria, Australia
- S. Ryan** Defence Science and Technology Group, Fishermans Bend, Victoria, Australia
- M. Saleh** ANSTO, Lucas Heights, NSW, Australia
- J. Sandlin** DMTC, Hawthorn, Victoria, Australia
- D. Shanmugam** Thales, Bendigo, Victoria, Australia
- C. Tallon** Virginia Tech, Blacksburg, VA, United States
- S. Thomas** Defendtex, Dandenong South, Victoria, Australia

Introduction

In 2009, the Defence Materials Technology Centre (DMTC) was in its establishment phase. Founded by a leading group of Australian research and industry sector players, DMTC represented — and represents — a significant initiative on the part of the sector to consolidate a broad range of high-technology activities and focus outcomes on improving Australian defence capability. The organization had an established programme aimed at the protection of land vehicles and the beginnings of a programme aimed at protection of dismounted personnel.

My diary is always close to full.

In a good week, there might be two or three blocks of a couple of hours unfilled by meetings and appointments and I have an excellent EA who diligently works to keep things moving. It can be a challenge to fit everything in and appointments with some people often needing to give way some or all of the time to pressing schedules. Not so for Ian Crouch, who I had known for several years and who was always consistent in his passion and belief that we could do things better. His ‘we can do this’ attitude has always been so important and I very much looked forward to our meetings. We met as planned. I’m so glad we did.

As an engineer myself and the leader of the centre, I was of course aware of some of the nascent and established capabilities in the Australian armour and protective technologies arena, but Ian who had been a leading light for some years, was able to outline the true extent of the environment with great authority and his usual wit, passion and charm. The story of Australian armour and protective technologies both before and since the advent of the DMTC encompasses a narrative of persistence and excellence. Characterised by largely self-contained, short supply-chains with low production runs and a liberal helping of uncertainty, life can be challenging for industrialists in this sector. Ian and many of his colleagues from industry and research were significant drivers of the effort to stand up a programme of technologies that brought together a suite of armour and protective technologies in the mounted/vehicles and dismounted/personnel domains, and deliver these to a very demanding customer with, appropriately, little tolerance for second best.

These efforts and successes arising therefrom have been lauded in many fora, and most importantly have been acknowledged as saving lives by the Australian Army. Surely there can be no more worthy pursuit for innovators.

Success is, of course, a very confused being with regard to claims against its true parentage, but as one who has been close to the action for the past decade, I can attest to the central role Ian played in developing and championing the technologies and capabilities presented herewith. Many others have also made significant contributions to

this body of knowledge, experience and expertise, that have given Australian and allied personnel the confidence in their protective equipment ensembles. Some of the authors in this publication have the passing privilege of youth...others (who I'm confident will not mind me pointing out) bring experience to the table.

Ian Crouch manages both qualities, and has spearheaded the development of this significant body of work in, by and for the benefit of Australia and its allies. This has been — in the spirit embodied by the DMTC and its many partner organisations — a true collaborative effort and a proudly all-Australian initiative which we present for your consideration.

Dr Mark Hodge
Chief Executive Officer
Defence Materials Technology Centre
Australia

Foreword

For the first half of 2009 I was responsible for the effective employment and protection of all Australians in Afghanistan. The men and women under my command had a mixture of body armour, none of which in my opinion was entirely suitable for the work they were doing and most of it was most certainly inferior to that which many of our coalition partners' soldiers were wearing. In my view the Australian 'modular combat body armour system' did little more than turn a soldier into a 'pillbox'. There appeared to be a lack of appreciation in its development that a significant component of a soldier's protection was the ability to fire a weapon and to move quickly, in addition to physical protection. If a soldier did nothing more than wear all the issued body armour, he or she was carrying almost as much weight as any Australian soldier in history before even considering the weight of ammunition, water and rations. It was at this point I became fascinated with the technologies and functionality of body armour.

My chance came to do something about it when I returned from Afghanistan. I returned to Army Headquarters on promotion as the inaugural Head of Modernisation and Strategic Planning. Then, to make my mission of fixing the situation more urgent, in the Senate Estimates hearing after I returned in 2009, the Chief of Army was asked to explain the very significant number of complaints by soldiers and their concerned parents about the lack of utility of the personal load carrying and protective equipment issued to soldiers, especially the weight and physical restriction imposed by the body armour.

In late 2009, I met Dr Ian Crouch and found in him someone able to answer all of my questions about the weight versus protection dilemma; and someone who would be a great help to me to do something about it. Together, after a meeting at Australian Defence Apparel (ADA) in Bendigo, we started the journey to get our soldiers better protection on combat operations. He had the technical expertise and I had the authority. Before we had left the factory floor we had established what was feasible, acceptable and suitable, how long that would take and what the major issues were.

Almost two years to the day after that meeting with Ian, I was very proud to visit the battle group training in Townsville, which was readying for deployment to Afghanistan. The commanding officer was ecstatic with the result and we could not find one soldier who was not likewise impressed with his new equipment issue. What became known as T-BAS (Tiered Body Armour System) incorporated the new body armour and an innovative combat load-carrying equipment solution. All of this was pursued and coordinated by 'Diggerworks', an organisation raised as a collaboration in Defence to lead and stay at the front of developments in soldier personal

equipment. The Defence personnel who became the engine room of Diggerworks were the architects of the first TBAS design and drivers of its user-centred iteration that made TBAS the truly fit-for-purpose system of which we are all justifiably proud.

Every soldier, their families and their commanders on combat operations owe a debt of gratitude to Ian and his team for their work in fixing this problem in quick order. There is no doubt we saved lives as a consequence. We achieved this through Ian's intimate knowledge of armour materials combined with a shared understanding of an infantryman's approach to the optimal balance between weight, fit and protection that enabled effective fire and movement. The current design is a significant step change from MCBAS.

This book is a testament to the knowledge and enthusiasm of Dr Ian Crouch. It is people like him and those who will gain from this book that can have a significant impact on the lives of our service personnel. I am eternally grateful for what Dr Ian Crouch has done for us already and what he continues to do in publications such as this.

Lt Gen John Caligari, AO, DSC (Rtd),
Chief of Capability Development Group to August 2015



Ministers Warren Snowden and Jason Clare, together with Lt Gen John Caligari, at the official opening of the DMTC's Boron Carbide Pilot Plant in March 2011.

Preface

I am proud to present this new work on armour materials for I believe that it is the first truly materials-focused book on armour in more than 40 years. It is comprehensive in its treatment of the international literature and its coverage of recent technological advances. To its credit, it is also coherent in its treatment of the interdependence of the various material groups, with numerous cross-references between individual chapters.

The idea of compiling such a book came to me during 2010, as I was finishing up my career with Australian Defence Apparel, supplier of body armour systems to the Australian Defence Force. I realised then what a charmed working life I had been fortunate to experience; one that started in the UK, within the defence research organisations, followed by 20 years in Australia with a number of defence industrial companies. Throughout this time, since 1980, I have been intimately involved in the international armour community, either as a researcher, armour technologist, or as someone pushing to commercialise new armour materials and systems. This book contains many extracts, incidents and armour materials downloaded from those various experiences. It also reflects the collaborative nature of my most recent activities, working as a Project Leader within the Defence Materials Technology Centre (DMTC) in Australia, since all of my fellow coauthors are participating researchers within that centre. The Australian armour community has certainly expanded during the past 10 years or so.

The book itself has been written primarily for the early practitioner since I had no such textbook back in the 1980s when I was learning my craft. It is structured along the lines of a conventional materials engineering textbook, covering all major families of materials. Each chapter covers one group of armour materials, treating each group as a specialised subset of the broader set of engineering materials, from the well-established armour steels, through the families of light alloys, to the designer armours involving ceramics, textiles and composites. The material science behind each family of armour material is treated in great detail: energy-absorbing mechanisms are well covered, as are the various penetration modes, since understanding these failure mechanisms is at the heart of developing new armour materials. As mentioned at the beginning of Chapter 1, the science of armour materials is not a codified branch of engineering – it is a science in its own right – a science based around the high-strain-rate properties of materials and localised deformation behaviour. Each of the chapters contains summary tables of key properties providing an excellent source of reference material and ballistic data. One of the major themes running through the book is the design of real armour systems: the principles and guidelines used to design

not only simple, elemental systems but also multilayered structures, like the ceramic-faced composite armours. Many examples of real-life case studies are provided.

Chapter 1 commences by considering the operational environment as well as detailing the threat, since this is always the first thing to consider when designing or developing an armour system. For a number of reasons, the threat spectrum has been limited to small arms ammunition, high-velocity fragments, knife and spike attacks, and various blast loadings. The introductory chapter also includes essential background reading for the nonmaterial scientist and some revision notes for the more experienced researcher. Two chapters follow it on traditional armour materials, namely the family of armour steels in Chapter 2, and the group of light alloys, covered in Chapter 3. Both chapters provide sound metallurgical background information and key points about these traditional armours, their engineering properties and comparable joining techniques. Most of them are structural in nature and, whilst the steels are close to the end of their research and development phase, after more than 100 years, they are still the material of choice for most armoured military platforms. They may also still have a role to play in future body armour systems. Titanium alloys certainly have a role to play in protection against small arms ammunition, as do the high-strength grades of aluminium alloys.

Chapter 4 is very much a transition chapter between the traditional, monolithic, metallic armours in Chapter 2 (Steels) and Chapter 3 (Light Alloys) and the 'designer armours' covered in later chapters. It provides an insightful review of laminated materials and layered structures, recognising that the most efficient armour materials have a lamellar, laminated or layered structure. Key properties of a laminate are elucidated: their crack-arresting behaviour, as well as the essential role of interfaces and interlayer materials. The chapter makes essential reading before considering the laminated fibre-reinforced structures in Chapter 5 (Polymers and Fibre-Reinforced Plastics), the layered, textile structures of Chapter 6 (Fires, Textiles and Protective Apparel) and the ceramic-composite armours covered in Chapter 7 (Glasses and Ceramics).

Chapter 5 introduces the range of both reinforced and unreinforced polymers and includes a comprehensive review of the many methods of manufacturing armour-quality, composite components. This is an important topic since each approach results in an armour product with very different properties. The chapter also introduces the new wave of spliceless technologies that enable fully formed combat helmet shells to be manufactured in one step from a flat, lay-up of composite materials, especially those based upon advanced materials like the ultrahigh-molecular-weight polyethylene (UHMWPE) fibres.

In Chapter 6, the theme of layered armour materials is continued by introducing the reader to the science behind soft armour vests that can stop not only handgun bullets but also knife and spike threats. Each constituent of the vest is considered in turn, from the constitution of the fibres, and the structures of both woven and nonwoven fabrics, to the stitched layers of dry fabrics and finally to the shaping of the vest itself. The variables within each element are detailed, as well as the various energy-absorbing mechanisms, and, as stated above, many tables of relevant properties and characteristics accompany these. Stopping a knife from penetrating the human body is as challenging as defeating a handgun bullet.

Glasses and ceramics are, in my opinion, the most important family of armour materials, and Chapter 7 covers this highly developed group in some detail. The transparent ceramics, evolving steadily to replace the poorer-performing float glasses are

reviewed, and manufacturing methods compared. However, most attention is given to the high-performance opaque ceramics, like the aluminas and the carbides of both silicon and boron, which have the highest ballistic merit ratings, certainly in terms of weight. Regularly used as key elements of a body armour system, particular attention is given to describing reaction sintered/bonded products and a newly developed process based upon viscous ceramic processing which, in combination with pressureless sintering, has been developed by the DMTC to produce thin, shapeable, armour-grade, boron carbide products.

Whilst computers, or numerical modellers, do not design armour systems per se, their role within the science of armour materials is well established. Two, standalone chapters are dedicated to these mathematical approaches. Chapter 8 presents a very comprehensive review of analytical techniques. Written by one of Australia's leading defence scientists, Dr Shannon Ryan, it covers various formulations to calculate critical penetration limits of armour materials and systems. From simple models based upon quasistatic work done to sophisticated algorithms based upon either semiempirical or fundamental physical relationships, these mathematical tools enable the armour technologist to estimate/predict ballistic performance without having to carry out expensive and/or time-consuming ballistic experiments. Chapter 9, on numerical modelling techniques, is equally comprehensive. The largest chapter in the book, it introduces the basic physics behind these nonlinear, finite element computer codes, by covering most armour materials and including many worked examples. A gamut of armour/antiarmour interactions is focused upon impacts from either small arms ammunition or high-velocity fragments. However, the real power of computer simulations is their ability to simulate a specific failure mode or defeat mechanism, and thereby raise our understanding of the science involved. Chapter 9 also includes a very useful collation of standard input parameters for the various strength models or underpinning equations of state — essential data when starting out in numerical modelling.

Input data for the above-mentioned mathematical formulae are normally generated via dedicated high-strain-rate tests, such as the well-known split Hopkinson pressure bar (SHPB). Chapter 10 describes these test procedures in detail, as well as a number of selected, quasistatic tests that have been used to simulate a particular failure mechanism. For example, armour materials can absorb a considerable amount of impact energy in the through-thickness (TT) direction. But, rather than carrying out a standard TT compression test on a simple cylinder of test material, it is preferable, and far more relevant to an armour impact, to perform the test using a constrained compression test (CCT). Chapter 10 provides details of this test, as well as the standard range of high-strain-rate methods including plate impact, fragmentation, and spallation tests.

The lay reader may find that one of the most useful chapters in this book is Chapter 11 on Ballistic Testing Methodologies. It provides a brief overview of the scientific principles and engineering objectives behind a ballistic test. Written by two authors who, between them, have more than 40 years experience in ballistic testing, it presents a broad suite of tests which can be adopted by researchers at the outset of an armour program, or by engineers when accurately validating their preferred armour system, or by ballistic testing staff when carrying out certification tests. Commentary about the well-known, but poorly understood, 'V-50' test is particularly insightful.

The book concludes by taking a visionary look at the future of armour materials. Whilst research into steels may have run its course, exciting new developments in transparent ceramics, 3D printed structures, and graphene-reinforced interlayers, for example, ensure that even better armour materials are yet to be developed. However, driving down the manufacturing costs of these specialist materials is just as important as continuing to improve their ballistic properties. In Chapter 12, therefore, a new approach to selecting targeted groups is proposed, based upon a quantitative cost-benefit analysis.

Finally, I need to thank all of those people who have contributed not only to this work but also to my career. To my fellow coauthors, I am indebted to you for all of your dedicated efforts — without you this book would not have been the same. I am particularly grateful to Dr Stephen Cimpoeru, Dr Shannon Ryan and Horace Billon, from the Defence Science and Technology Group, as well as James Sandlin from the DMTC. To my sponsors, Armour Solutions Pty Ltd and the Defence Materials Technology Centre, I thank them for their financial support. I am especially grateful to Dr Mark Hodge, CEO of the DMTC, who has always shared the same vision, on many topics. Across my long career, there are three people who have inspired me and supported me: Dr Neill Griffiths, Head of the Armour/Anti-Armour Group at DRA, in the 1980s; Dr Bill Carson, Head of the Armour Physics division at DERA, in the 1990s, and finally Brian Rush (pictured below), owner of Australian Defence Apparel (1995–2011), whose visionary outlook, and willingness to spend the R&D dollar, ensured that Australia developed a new suite of armour technologies during the past 20 years.



Defence Minister Joel Fitzgibbon (c.2008), with Brian Rush, Managing Director of ADA, and Dr Ian Crouch, during a visit to ADA, Bendigo, during the production of the Modular Combat Body Armour System, supplied to the Australian Defence Forces.

Success, in any field, is about understanding, and overcoming, failure, and in the field of armour materials it is about understanding the penetration failure mechanisms associated with different forms of attack. Following this Preface is a poignant piece of poetry for the professional engineer responsible for ensuring that material failures do not occur. Enjoy the poem, and the book!

Dr Ian G. Crouch, Managing Director (Armour Solutions Pty Ltd), Adjunct Professor (RMIT University, Melbourne), and Project Leader (Defence Materials Technology Centre, Australia)

Forethought

Hymn of Breaking Strain (1935) by Rudyard Kipling (AD 1865–1936)

The careful text-books measure
 (Let all who build beware!)
The load, the shock, the pressure
 Material can bear.

So, when the buckled girder
Lays down the grinding span,
The blame of loss, or murder,
 Is laid upon the man.

Not of the Stuff — the Man!

But, in our daily dealing
With stone and steel, we find
The Gods have no such feeling
 Of justice toward mankind.

To no set gauge they make us, —
For no laid course prepare —
And presently o’ertake us
With loads we cannot bear:
 Too merciless to bear.

The prudent text-books give it
 In tables at the end —
The stress that shears a rivet
 Or makes a tie-bar bend —

What traffic wrecks macadam —
What concrete should endure —

But we, poor Sons of Adam,
 Have no such literature,
 To warn us or make sure!

We hold all Earth to plunder —
All Time and Space as well —
Too wonder-stale to wonder

At each new miracle;
Till in the mid-illusion

Of Godhead 'neath our hand,
Falls multiple confusion
On all we did or planned —
The mighty works we planned.

We only of Creation
(Oh, luckier bridge and rail!)
Abide the twin-damnation —
To fail and know we fail.
Yet we — by which sole token
We know we once were Gods —
Take shame in being broken
However great the odds —
The Burden or the Odds.

Oh, veiled and secret Power
Whose paths we seek in vain,
Be with us in our hour
Of overthrow and pain;
That we — by which sure token
We know Thy ways are true —
In spite of being broken,
Because of being broken,
May rise and build anew.
Stand up and build anew!



Introduction to armour materials

1

I.G. Crouch

Armour Solutions Pty Ltd, Trentham, Victoria, Australia

The design and application of armour is a science rather than a codified branch of engineering. Whilst all professional engineers follow sound engineering principles and practice, I suspect that some might mistakenly believe that the application of the engineering process is all that is required for optimised, risk-free armour solutions, like choosing the optimum tyre for a car based upon the conduct of standardised tyre testing. The science of armour materials is a specialised, cross-disciplinary subject not taught within the educational system and most armour technologists, like me, learn on the job. To begin to understand the underpinning science we must first consider the operational environment and then, most importantly, the threat.

1.1 The operational environment

Imagine yourself in the middle of a war zone or, as the military like to call it, a theatre of operation, somewhere in the Middle East. Whether it is a location like Iraq, or Afghanistan, during the period 2003–14, these battlefields are dangerous, chaotic environments where many random explosions, or high-energy impact events, occur on a regular basis. This is the environment that armour materials have to function in, and function reliably, as there is minimal margin for error (Fig. 1.1).

For the Australian Defence Force (ADF), fighting these ground-based wars has proven to be very costly, with 41 Australian fatalities occurring during the 10-year conflict in Afghanistan; not forgetting, of course, the many thousands of civilian and military lives lost from other nations. As Chris Masters reports in his recent account of the life of a serving soldier on active duty in Uruzgan province (Masters, 2012), from bases like Tarin Kowt, this environment is dusty, hot (during the day), cold (at night), even snowy (during the winter) and very rugged. Extremely harsh conditions for the soldier: extremely harsh conditions for the equipment, and therefore very challenging for the engineering materials. For example, the rapidly rotating blades of the Blackhawk helicopter, constructed from relatively soft, carbon-fibre reinforced plastic, need to withstand the grinding action of the dusty, sandy conditions. The pilots need to feel protected from small-arms fire coming up from the ground. Troopers in their armoured vehicles like the Bushmaster, an Australian protected mobility vehicle, need to feel protected from random explosions coming from improvised explosive devices (IEDs) and landmines, and survive. The combatants on the ground, chasing the Taliban across the open plains, need to feel fully protected wearing their latest body armour, as well as comfortable and mobile.



Figure 1.1 Range of materiel and armour materials in active service, 2012.
 Anon, 2012. Australian Department of Defence Website. www.defence.gov.au.

Consider for a moment the armour materials that are also present on these same battlefields. Lightweight, aluminium alloys, forming the helicopter structures, with ultra-lightweight ceramic armour on the underside of the pilot's seat. A range of weldable, high-strength steels act as structural armours in the Bushmaster vehicles. However, which grades of steel are being used, and why? Thick-sectioned, weldable, aluminium alloys which form the box-like structures of the fleet of up-armoured M113s (an armoured personnel carrier, APC); vehicles which have remained in active service for the past 50 years. What about the range of materials that make up the modern-day body armour system (BAS)? These can be the most complex passive armour systems on the battlefield and traditionally include a Kevlar vest, as well as a hard armour plate (HAP) to provide additional protection against high-velocity rifle rounds, like the AK47 bullets, fired from Kalashnikov rifles.

Such BASs do save lives! Take the case of Lance Sergeant Collins of the 1st Battalion of the Welsh Guards who was on a tour of duty in Afghanistan during 2009. He and his company had been under sporadic fire during a day's clearance operation (Anon, 2009). 'I knelt down in an irrigation ditch in partial cover when I was hit in the back by a single shot. It must have been from about 200 to 300 metres away', he said. In describing his near-death experience, Collins said, 'The round knocked me down in an instant. It felt like being hit by a sledge-hammer at full swing. I slammed into the dirt, face down'. Fig. 1.2 not only shows the damage to his body armour but also to his back — the HAP had done its job and Collins survived to fight another day.



Figure 1.2 Survivor, Lance Sergeant Collins (1st Battalion, Welsh Guards) with his damaged body armour system and bruised back.

Anon, 2009. Shot Soldier's Body Armour Praise. <http://www.dailymail.co.uk/news/article-1191872/Soldier-snipers-bullet-pulled-comrade-shot-Taliban.html>.

These HAPs are highly engineered products, finely tuned to offer maximum protection for minimum weight, but which grade of ceramic is best to use in this application? Fig. 1.3 shows a schematic of a section through such a BAS and the full range of armour materials that are considered when designing such systems, especially the HAP.

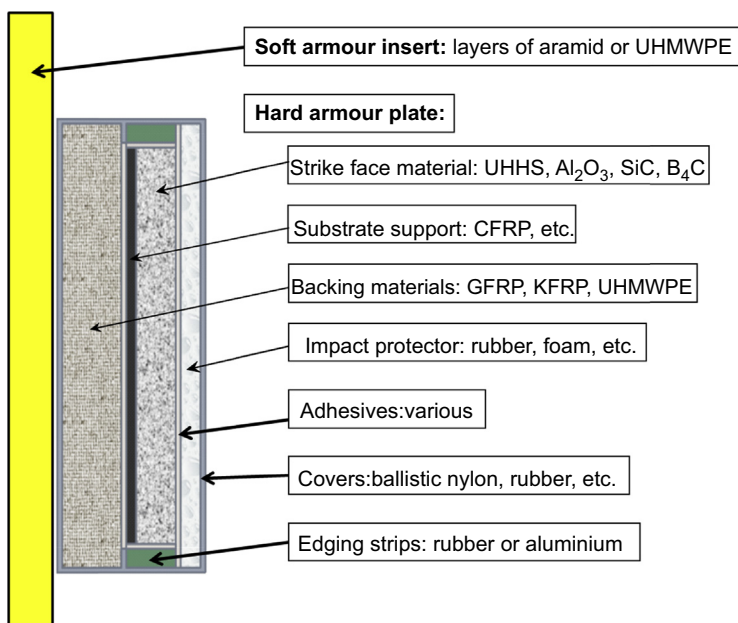


Figure 1.3 Cross-section through a typical body armour system.

Crouch, I.G., 2009. Threat defeating mechanisms in body armour systems. Paper Presented at the Next Generation Body Armour, London, September 2009.

How do all of these armour materials (the steels, the aluminium alloys, as well as the ceramic materials in the HAPs) get qualified for use in such demanding roles? Imagine the training, history and the processes that armour designers and engineers have had to go through in order to develop, produce and approve the use of such materials in these hostile environments. Like any other field of science, or engineering, the armour technologist needs to simplify the real situation and design for the worst-case scenarios. In this case, this means developing an armour system, which can stop the prescribed threat (eg, a steel-cored bullet) at a specified velocity and obliquity. Designing, and/or selecting, the most appropriate material to best suit an engineering application is, of course, what practicing material scientists and design engineers do, as a conventional part of their profession. So, what makes working with armour materials so different and the science of armour materials so exciting?

From a material science perspective, imagine a typical impact event: the impact of a steel-cored bullet, travelling at many hundreds of metres a second, striking the steel armour on the side of an armoured vehicle. Consider the step-by-step series of physical events that follow. Do not forget that the entire impact event will be completed within 100 μ s or so.

- Upon impact, a series of stress waves are induced within the material, and travel throughout the structure. These waves travel at the speed of sound, within the material, which, in the case of steel structures, is almost 6,000 m/s. Since these waves are travelling much faster than the bullet, do they cause any changes in the material, ahead of the bullet, which might affect the subsequent behaviour of that material?
- If the armour system has been designed correctly, there will be a period of dwell, where the bullet is deformed at, or near, the surface of the steel, without penetrating the armour. How much deformation occurs to the bullet? Will it be eroded or plastically deformed? Will it simply ricochet off?
- Once the bullet starts to penetrate the armour, the material needs to flow, as it would in a hardness test, where a diamond tip is forced into the surface of the material. However, unlike a hardness test, this penetration process occurs dynamically. How does the material flow under these extreme conditions of high strain rates, high temperatures and high local pressures? How will the material resist this momentous force, and how can a material scientist best describe this complex flow behaviour? Can analytical or numerical modelling help?
- As the bullet is arrested, and the strain-rate decreases, the rear side of the armour will start to experience the full force of the impact event and be stretched to the limit. Literally, in some cases. How might the material fail? Locally? Globally? Will the steel structure be deformed?

These questions, and many others, will be analysed in the coming sections and chapters. The rest of this introductory chapter focuses upon the fundamentals of armour materials and the design principles behind the development of lightweight armour systems.

1.2 The threat

The most challenging task in developing a particular armour material, or system, is analysis of the real, or perceived, threat and the generation of incident data that are

both accurate and current. This approach is vital because there is not a single armour system available that is the best armour for all types of threat. This is especially true for soft armours where different sets of high-performance fabrics (eg, Kevlar) are required for stab and spike threats compared with, say, handgun bullets. Both [Brady \(2003\)](#) and [Horsfall \(2009\)](#) have compiled lists of military casualties by war and by threat type. For example, in the Gulf War, like WW2, many more casualties occurred as a result of impacts from high-velocity fragments compared with bullets. However, in Borneo, 90% of casualties arose from bullet strikes. In recent conflicts, like those theatres of operation in Afghanistan and Iraq, the major cause of fatalities and casualties has been from the IED, not small arms ammunition ([Kelly et al., 2008](#)). In fact, Kelly reported a significant change in the threat spectrum, with IED threats becoming dominant in the 2 years from 2004 to 2006. Since then, in military campaigns involving terrorist activities, IEDs have become the major threat.

In Australia, the Department of Defence has taken a direct approach in relaying the real demands of the dismounted soldier by forming an organisation called Diggerworks in 2010 ([Cebon and Samson, 2010](#)). Its purpose is to steer research and rapid development, based upon first-hand military experience – its first Director was Colonel Jason Blain who had led an Australian battalion in Afghanistan the previous year. Diggerworks, DSTO (now the DST Group) and the Defence Materials Technology Centre (DMTC), have been working in closer collaboration ever since.

In the civilian world, handguns and rifles are still the weapon of choice in the Americas, whilst in Europe, and especially the major cities like London, knife and spike attacks dominate. Paul Fenne, from the technical department of the London Metropolitan Police reported ([Fenne, 2008, 2009](#)) that the total number of violent crimes in London had reached 13,000 per annum and that, in 2009, armed response units responded to 11,725 calls. Of these, 2232 calls required specific deployment of armed police wearing body armour.

In general, textbooks that cover armour/antiarmour interactions normally divide these events into two categories: those in which material properties do not play a strong part (the hydrodynamic regime, where density dominates) and those impacts in which material properties do have a strong influence. The latter group of impact scenarios normally occurs at ordnance velocities or less. For many reasons, this book focuses predominantly upon this latter group, since these are not only of prime interest to the material scientist but are also those events of greatest interest to the Australian defence community in which small arms ammunition, high-velocity fragmentation and knife attack dominate the thinking of those who set the Statements of Requirements (SoRs). Protection from blast, as well as high-velocity fragmentation, is not only important but also very current, and has therefore been included within the threat spectrum covered by this book.

As a corollary to this introductory section, I have personally carried out a number of ballistic experiments in the “hydrodynamic regime” that have shown quite a dependence upon material strength. So, even for armour systems designed to function against long-rod penetrators and/or chemical energy weapons, understanding the dynamic properties of the armour materials can still be very applicable. For further reading on kinetic energy

(KE) threats (up to very long rods, etc.) the reader is referred to [Hameed et al. \(2004\)](#) and [Ogorkiewicz \(2015\)](#).

1.2.1 Small arms ammunition

These range in calibre from the 5.56 and 7.62 mm rifle rounds, through the 9 mm handgun bullets, up to 12.7 and 14.5 mm calibre, armour-piercing rounds. The latter two calibres are approaching the class of medium arms (>20 mm) and so have been excluded from this short overview – however, details of their construction and the principles of penetration, as well as the opportunities for defeat, are exactly the same across all calibres of KE projectiles. The armour technologist needs to understand what provides these rounds with their penetrative power since this differs in all cases. The important aspect is the core of the projectile, the internal penetrator, especially its nose shape and material type, since this will govern possible defeat mechanisms – see [Section 1.4](#). The following subsections therefore describe the constructional details of the most common small arms ammunition, details which are also extremely valuable to the numerical modeller – see Chapter 9.

1.2.1.1 Handgun bullets

As can be seen from [Table 1.1](#), the nature, shape and geometry of the conventional, lead-filled handgun rounds has not significantly changed in 150 years. In fact the 0.44" Colt round from the 1860s is very similar to the current '44 Magnum' bullet – the lead-cores are much the same weight – the latter simply has a copper jacket. The 0.44" SJHP round from Remington was originally designed as a dual-purpose cartridge for use in both handguns and rifles. In armour testing, this bullet is one of two used for certification of soft body armour and is typically chosen for evaluation of behind-armour blunt trauma. It has been banned from private ownership in Australia and has been excluded from the current version of the ballistic test standard, NIJ0101.06. On the

Table 1.1 Conventional handgun ammunition, past and present





Ammunition	0.44" colt (US 1860s)	0.52" sharps (US 1860s)	9 mm FMJ Remington	0.44" SJHP Remington
Bullet and deformed core				
Bullet weight (g)	14.0	27.1	8.0	15.6
Core material	Lead-based	Lead-based	Lead-based	Lead-based

Table 1.2 Special handgun ammunition

Ammunition	7.62 × 25 mm Tokarev	5.7 × 28 mm SS195LF
Bullet and core		
Bullet weight (g)	5.5	1.8
Core material	Mild steel	Aluminium

other hand, the 9-mm FMJ is probably the most widely used military and law enforcement calibre in the world so it is with good reason that the 9-mm “Luger” is used to evaluate the performance of body armour across many national test standards. The lead filling in these conventional handgun rounds is easily deformed and can be arrested by a layered pack of woven fabric, made from a high-performance fibre like Kevlar — see Chapter 6.

Two nonconventional handgun rounds need to be mentioned here, as shown in Table 1.2. The 7.62 × 25 mm (the first number is the calibre of the round in mm and the second number is the length of the cartridge in mm) Tokarev is a steel-cored round of unusual geometry. It is particularly effective against soft targets. The 5.7 × 28 mm SS195LF is also of current interest. It was developed to replace the 9 mm Parabellum but, unlike the 9 mm, is totally lead-free. The lightweight, aluminium core greatly reduces the risk of collateral damage but still requires special attention from the soft armour designer, compared with traditional lead-filled handgun rounds.





1.2.1.2 Rifle bullets

High-velocity, lead-filled rounds

Details of these high-velocity, lead-filled, rifle rounds are shown in Table 1.3. The first two types are extremely common. Quite a few different countries manufacture the 7.62 × 51 mm NATO Ball L2A2 and users actually specify the required manufacturer. For this reason, ballistic ranges usually stock a range of ammunition from different manufacturers. The M80 NATO ball round was first adopted by NATO in 1954 but is still commonly used for testing both body armour components and lightly protected vehicles. Even though they are lead-filled, they are a heavy round, at ~9.5 g, and pack quite a punch when travelling at over 800 m/s. These two rounds are classically described as “Level 3” threats.

The smaller-calibre variants, the 5.45 × 39 mm AK74 ball and the 5.56 × 45 mm NATO M193 round, are lighter weight versions of the same. Lead-filled, but weighing only ~3.5 g, they were developed so that the combatant could carry more rounds.

Table 1.3 Common lead-filled, ball ammunition

Ammunition	7.62 mm L2A2 NATO ball	7.62 mm M80 NATO ball	5.45 × 39 mm AK74 ball	5.56 × 45 mm M193
Bullet and core				
Bullet weight (g)	9.3	9.5	3.5	3.6
Core material	Lead-based	Lead-based	Lead-based	Lead-based

High-velocity, cored rounds






This selection of high-velocity, cored rounds (see [Table 1.4](#)) is classically described as belonging to the Level 3+ group of small arms ammunition. Of these, the 5.56 × 45 mm NATO SS109 round has become well established since 1979, following a review by NATO of candidate rounds. It contains a small steel conoidal core, near its tip, which is less likely to fragment in soft targets compared with the lead-filled M193. Military users commonly specify it. Two variants of this round need mention: the APHC variant which replaces the steel core with a tungsten carbide one, giving the round more penetrative power; the M855A1 variant is relatively new and is an interesting development – the core is manufactured from steel but it has been designed to weigh the same as the tungsten carbide core of the APHC round. Variations such as this are actively pursued all of the time.

The 7.62 variants in this family of Level 3+ bullets contain a mild steel core. Commonly known as the AK47, it is fired from the infamous Kalashnikov rifle still very common in conflict zones around the world. The mild steel core was adopted for its low cost and ease of manufacture. Whilst not intended as an armour-piercing bullet, the M43’s construction gives it armour-penetrating properties against both BASs and lightweight military platforms. Its construction has been well documented – see [Fig. 1.4](#) – and well used in the R&D sector ([Crouch et al., 2015a](#)). The 7.62 × 54R LPS is similar in nature but a much heavier round. Even though it is classed as a ball round, because of its high lead content, the round is used in a number of test standards alongside conventional, armour-piercing rounds.

Armour-piercing rounds

[Table 1.5](#) shows a selection of hard-cored, armour-piercing ammunition employed across the various ballistic testing standards. The most common is the US 30-06” Springfield M2 AP round, fondly referred to as the APM2. It has actually been out

Table 1.4 Selection of cored, high-velocity ammunition

Ammunition	5.56 × 45 mm SS109 (M855)	5.56 × 45 mm M855A1 enhanced	5.56 × 45 mm APHC	7.62 × 39 mm AK47	7.62 × 54R LPS
Bullet and core					
Bullet weight (g)	4.0	4.0	4.6	7.9	10.0
Core material	Steel cone	Steel	WC cone	Mild steel	Mild steel

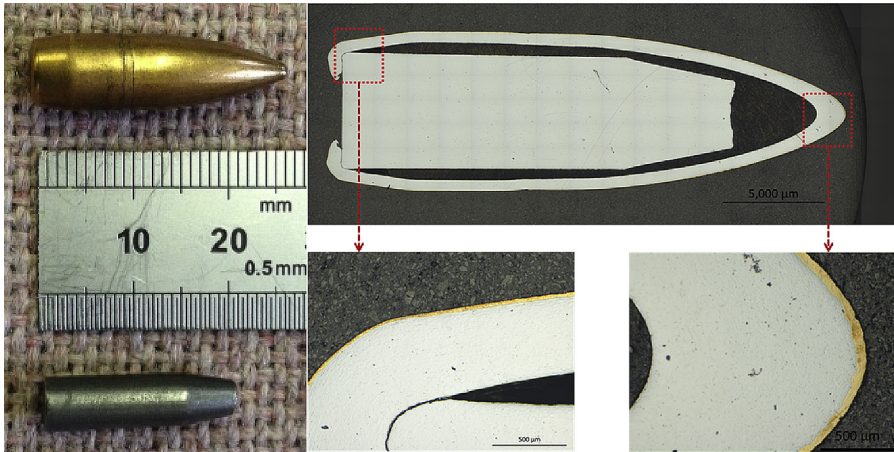


Figure 1.4 Cross-section of the 7.62 × 39 mm AK47 round showing the mild steel core, lead-filling and copper-coated steel jacket.

After Crouch, I.G., Appleby-Thomas, G., Hazell, P., 2015a. A study of the penetration behaviour of mild-steel-cored ammunition against boron carbide ceramic armours. *International Journal of Impact Engineering* 80, 203–211.






of production for some time now, with supplies only available through military surplus from WW2 and the Korean War. It remains the bullet of choice, however, for many armour test standards and, of course, because it has been used for more than 50 years there is an enormous stockpile of ballistic data — there is therefore great reluctance to stop using it. Because it is not seen as a current battlefield round, it is also very popular with researchers and armour technologists. It is still a very penetrating round with a hardened steel, ogival-shaped core.

A similar round is the 7.62 × 54R API B-32, which has had the longest in-use military service life of them all. It is, however, unpredictable, as a test round, due to some irregularity on the quality of its steel core manufacturing. The actual core illustrated in [Table 1.5](#) shows slight asymmetry in the ogival portion of the core, for example.

The 7.62 × 51 mm P80 round is again similar to the APM2 but the shape of the core is a lot more like the head of an arrow. This shape prevents this particular core from being fragmented, as is often experienced with the cores of both the APM2 and the B32 rounds. The P80 is therefore considered to have a similar penetrative power, even though the core is significantly lighter. The shorter 7.62 × 39 mm API-BZ is equally surprising in its ballistic performance.

Lastly, but by no means least, is the 7.62 × 51 mm, tungsten-carbide-cored, “FFV round”, as supplied by NAMMO. FFV refers to the original supplier, Bofors AB, in Sweden. Both it and its smaller sister, the 5.56 × 45 mm M995 round, were under development during the late 1990s and, since 2000, have been available in niche quantities. The core, with a sharp conical tip, is more penetrative than steel cores. Many researchers have used it for the past two decades but its high price has limited its availability.

Table 1.5 Selection of cored, high-velocity ammunition

Ammunition	US 30-06" (AP M2)	7.62 mm × 54 R (B32)	7.62 mm × 51 (P80)	7.62 mm × 39 (API-BZ)	7.62 mm × 51 (FFV)
Bullet and core					
Bullet weight (g)	10.7	10.0	9.8	7.7	8.4
Core material	Hardened steel	Hardened steel	Hardened steel	Hardened steel	Tungsten carbide

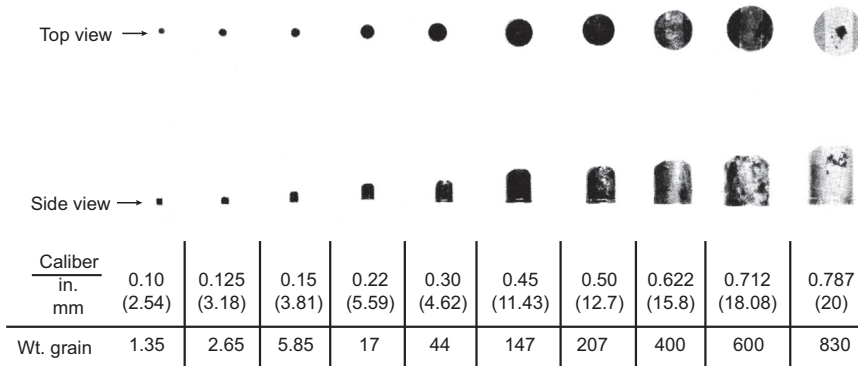


Figure 1.5 Copy of original series of fragment-simulating projectiles.

Mascianica, F.S., 1980. Ballistic testing methodology. In: Laible, R. (Ed), *Ballistic Materials and Penetration Mechanics*. Elsevier Scientific Publishing Co., Amsterdam.

1.2.2 High-velocity fragmentation

Protection from fragmenting munitions like high-explosive shells and, more recently, IEDs is an extremely challenging task because such weapons eject multiple steel fragments with a very broad, and varied, distribution of fragment sizes. This was first recognised by scientists and engineers working at the Watertown Arsenal Laboratories in the 1950s. [Fig. 1.5](#) is a copy of the original set of chisel-nosed projectiles forming an homologous series from 2.54 to 20 mm in diameter ([Mascianica, 1980](#)). These fragment-simulating projectiles (FSPs), as schematically shown in [Fig. 1.6](#), are precision-manufactured from a medium-strength steel to a military specification ([Specification, 2006](#)), and are heat-treated into a very specific hardness range of 28–32 Rockwell C — this was chosen to represent the hardness of typical munitions like the shell of the 105 mm HE round, a common overhead threat since the 1960s.

Since that time, these FSPs have been universally adopted not only to test steel structures against overhead blast threats but also as a standard part of acceptance testing for aluminium armours and armour steels, as well as combat helmets and soft body armour components — see Chapter 11. When used, they do undergo plastic deformation but in a controlled and reproducible fashion (see [Fig. 1.7](#)) and they have become totally accepted by the global armour community as a design tool. With the aid of a sabotaged launching system, they can be fired at velocities of up to 2000 m/s. Similar series of simulating fragments are also available with different shapes, right circular cylinders, spheres and cubes, but these are nowhere near as popular as the chisel-nosed FSPs for mainstream armour work.

1.2.3 Stab and spike threats

The majority of stabbing incidents happen with the use of domestic knives (kitchen knives, utility knives, sheath knives, lock knives, combat knives, penknives and other

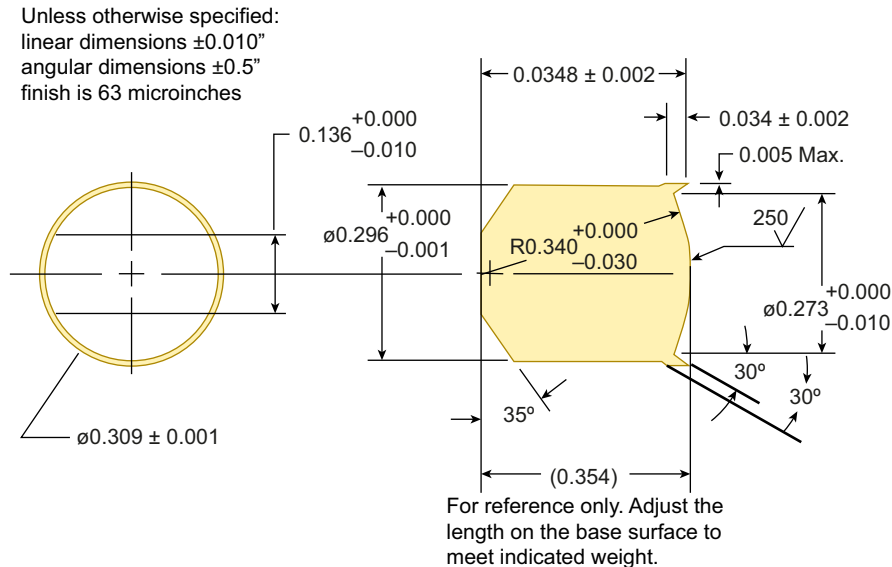


Figure 1.6 Extract from MIL-DTL-46593B (MR) showing precise geometry of the 0.3" FSP. Specification, 2006. MIL-DTL-46593B (MR), Projectile, Calibers 22, 30, 50 and 20 mm Fragment Simulating Projectiles.

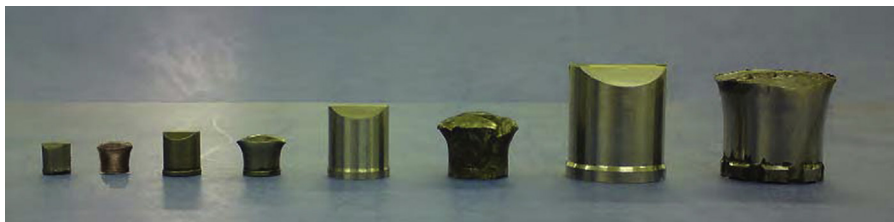


Figure 1.7 Pairs of fragment-simulating projectiles (FSPs), untested and impacted, with diameters of 5.6, 7.6, 12.5 and 20 mm. The impacted FSPs were tested against polymer ceramic targets — see Section 7.7.

Naebe, M., Sandlin, J., Crouch, I.G., Fox, B., 2011. Novel lightweight polymer ceramic composites for ballistic protection. Paper Presented at the ICCS 16, Porto, Portugal, 2011.

variations) (Hainsworth et al., 2008). Other weapons include scissors, bayonets, samurai swords, screwdrivers and broken glass bottles (Nolan et al., 2012). Different types of weapons which may be used for stab, puncture and slash attacks are shown in Fig. 1.8, and recent reviews by Horsfall (2000), as well as Paul Fenne, from the London Metropolitan Police (Fenne, 2009), and the DMTC (Crouch et al., 2014), show that this threat is difficult to define and standardise.

As stated in the NIJ standard 0115.00, dated September 2000, 'The threat posed by a knife depends, amongst others things, on sharpness, pointedness, style, handle and blade design, attacking angle, the physical condition of the attacker, and the skill of the attacker.'



Figure 1.8 Typical array of knives used in civilian crimes.

Fenne, P., 2009. Can the key design aims for body armour for police officers be achieved? Paper Presented at the Next Generation Body Armour, London, UK.

All the stabbing weapons shown in [Fig. 1.8](#) can be classified as either edged or pointed. Hence, the act of stabbing can be described in terms of cutting or puncturing of materials. Weapons such as knives, tools, swords and other implements designed to perforate or cut materials have a long continuous cutting edge and are classified as ‘edged’ weapons. Stabbing describes the cutting action where an edged weapon travels primarily in a direction normal to the surface of the material being penetrated, and a slash describes the cutting action where the edged weapon travels parallel to the material surface during an attack, using the knife-edge with a swinging motion. Preventing stab attacks is significantly more difficult than preventing slash attacks because, during a stabbing event, the force is concentrated over a very small area at the tip of the blade and the long cutting edge contributes a continuous source of damage. In contrast, slashing by a knife-edge is easier to stop because the force of a blow is distributed along the cutting edge resulting in continuous damage to a larger area of the target. Today, blade materials used for stab and slash attacks may include modern materials such as ceramics, synthetic sapphire, zirconium dioxide and even very hard plastics. Other pointed weapons may have a slender rod with a pointed tip and these include objects such as awls, ice axes, and ice picks, which can easily puncture materials. In fact, because of the small area of impact, they deliver a much larger kinetic energy per unit area than handgun bullets.

Law enforcement centres around the globe have developed test methods that standardise both the attack weapon and how it is projected. [Fig. 1.9](#) shows the range of weapons used by the UK Home Office to assess the stab and spike resistance of armour materials. Impacts are normally restricted to 33 or 50 J and the pass/fail criteria stipulated in terms of residual perforation: the length of weapon extending into the ‘body’.



Figure 1.9 Various test blades, from top PSDB #5, PSDB #1, Metropolitan police spike, American ice-pick and a double-sided dagger of the type used in Swiss and German tests. After Horsfall, I., 2000. Stab Resistant Body Armour (Ph.D. thesis). Cranfield University, Shrivenham, UK.

Do not forget that body armour is designed to limit injury as well as save lives, so a minimal depth of penetration is acceptable, albeit not very desirable. Users tend to define their own requirements within the general framework of these global standards.

1.2.4 Blast events and blast loadings

Explosive munitions, particularly landmines, are a challenging threat for armoured vehicles. The rise in the number of buried IED attacks in the last decade (Kelly et al., 2008) and the resultant number of casualties (Anon, 2014) has led defence forces to increase vehicle protection and field new vehicles to counter blast threats, specifically underbelly blast threats.

Vehicle blast response, and occupant protection, is complex and vehicle system-dependent, and is discussed elsewhere (eg, Cimpoeu et al., 2015). Key issues for armour materials subjected to blast are their resistance to deformation and whether or not this results in rupture (or even brittle fracture) that would allow blast ingress into a vehicle. This is predominantly a near-field rather than far-field blast problem. Whilst a complete description of blast loading is well beyond the scope of this book, key aspects are summarised here to illustrate the complexity of a unique and dynamically changing loading condition.

1.2.4.1 Air blast loading

The following discussion relates to the case of an idealised blast from a bare spherical high-explosive charge in air. Fig. 1.10 gives an illustration of a far-field event where an exploding vehicle, outside of a compound, exerts far-field blast pressures

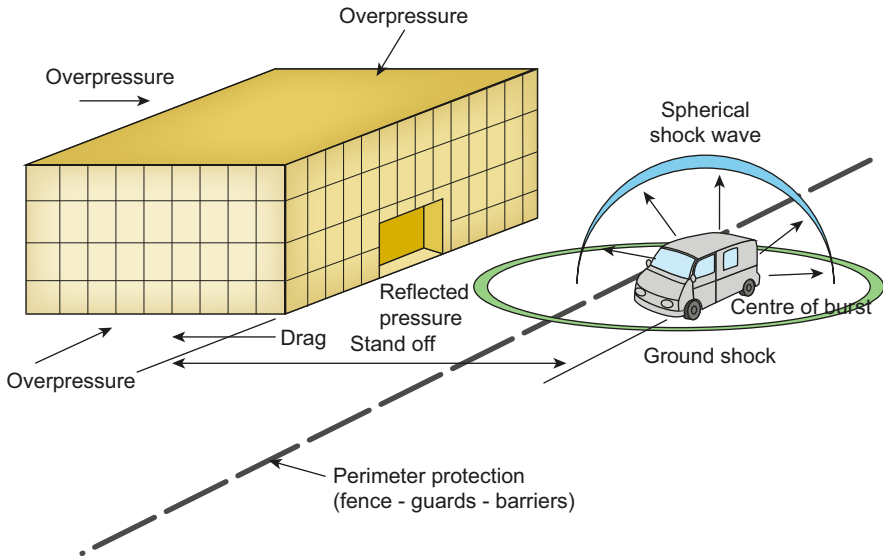


Figure 1.10 Far-field blast loads on a building.

After Lane, R., Craig, B., Babcock, W., 2002. Materials for blast and penetration resistance. The AMPTIAC Quarterly, 6(4), 39–45.

on a building. In reality, actual blast events are mostly nonideal and strongly affected by explosive type and many other factors, including interactions with the ground.

Following initiation of an explosive, a detonation wave sweeps through the unreacted explosive material at very high speed, effectively converting solid explosive into hot and extremely high-pressure gases. Due to their extreme pressure, the gaseous detonation products expand rapidly to about 4000-fold the original charge volume and are visible as a radiant fireball; it is the hydrodynamics of this expansion process which generates the blast-wave flow.

The rapid expansion of this fireball of combustion products drives a shock wave into the surrounding air, ahead of the fireball. The passage of an air shock wave results in a transient, nearly instantaneous, step change in all gas-dynamic conditions of the air including static pressure, density, flow velocity, and temperature. (Static pressure is the pressure experienced by a point, which does not obstruct the air-blast wave, ie, as would be measured on a surface parallel to the flow.) The combined violent expansion of detonation-product gases and the resultant propagated air shock wave constitutes the ‘blast flow field’ loading condition, and it is important to recognise the dual nature of these flow conditions. That is, close to the charge within the region of the fireball expansion not only is the amplitude of the blast forces more extreme as would be expected, but the flow field consists primarily of the expanding explosion product gases as distinct from air. Compared to blast at greater distance, there is proportionately much higher kinetic energy in near-field blast (Sternberg and Hurwitz, 1976) as well as dramatically variant spatial and temporal energy partitions.

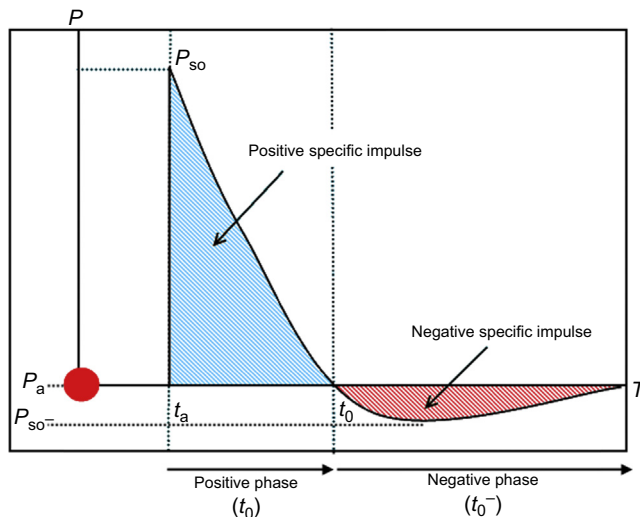


Figure 1.11 Static blast pressure parameters and terminology used for analyses of far-field blast.

These aspects of the near-field blast conditions have significant implications regarding consequent loading and damage processes which should be distinguished from classical understandings of static overpressure loading and damage in the far-field (Baker, 1973) (see Fig. 1.11). The very strong near-field flow forces due to dynamic pressure, especially from the impingement of the expanding detonation products, are directional and interact with structures quite differently than the static pressure component. (Dynamic pressure is a measure of the specific kinetic energy of the flow, ie, $\frac{1}{2} \rho v^2$, where ρ and v are the density and velocity of the flow.) In comparison, targets beyond the fireball expansion are subjected not only to reduced blast loading because of the greater distance, but a rapidly decreasing proportion of effects from dynamic pressure forces. The energy from the latter is transferred to the propagating air-blast shock wave as the fireball expands and weakens.

It is important to consider that air shock waves exhibit distinctly different behaviour with respect to propagation and interactions at interfaces than waves considered in electromagnetics or radiology, for example. Although some aspects of acoustic (sound) wave theory can be applied to exceedingly weak air shock waves, this regime is of little relevance for vehicle blast loading. Even when the blast flow is entirely an air shock wave in the far-field (as distinct from combined air shock and detonation-product flow in the near-field), at the surface of most structures of practical interest, the air shock wave loading condition is fully reflected (imparting loading) or diffracted (potentially imparting loading) as distinct from being transmitted.

1.2.4.2 Underbelly blast loading

The detonation of a shallow buried charge results in a cone-shaped ejecta plume being thrown upwards by the blast, as illustrated in Fig. 1.12. The multiphase plume consists



Figure 1.12 A controlled detonation of an improvised explosive device (IED), exploding in front of an Australian Bushmaster during a move down one of the most dangerous IED routes in Northern Kandahar.

Photo: Sgt Neil Ruskin; Anon, 2012. Australian Department of Defence Website. www.defence.gov.au.

of overburden material augmented by detonation product gases from the expanding fireball as well as casing fragmentation. The detonation products and ejecta are channelled or vented upwards by the confinement of the surrounding ground and will inflict most of the damage to a vehicle in its path. The blast conditions away from the ejecta cone are relatively weak with only an air-blast shock wave diffracting into this region.

An air shock wave will be driven ahead of the multiphase contact surface of the ejecta plume. Over distance, the solid and gaseous phases of the plume will begin to separate with the momentum of the larger clumps or solid particles causing them to be thrown ahead of the decelerating gas-dynamic contact surface of the fireball. However, in the blast flow regimes of relevance for vehicle damage, the air shock wave and the dense high-speed multiphase ejecta plume will be closely coupled. Although the solid particulate does not technically exhibit ‘pressure’, the ‘specific kinetic energy’ of the particulate phase will inflict the equivalent of a dynamic pressure loading on any obstruction in the flow, noting that the mechanical properties of the ground conditions can significantly affect the explosive loading condition (Cimpoeru et al., 2015).

A substantial proportion of the blast energy from buried charges is ‘given up’ to accelerate the solid particulate forming the ejecta plume; the kinetic energy of this particulate is highly directional across the span of the ejecta cone (see [Fig. 1.12](#)). The loading process and consequent damage from buried charges will therefore be somewhat analogous to the effect of a shotgun blast heavily laden with shot that imparts momentum transfer directly to targets by impact, unlike classical air-blast effects (air-blast acts as a hydrodynamic wave, whose energy can reflect and diffract around an obstacle). Underbelly blast is near-field blast and will therefore involve a distributed zone of impinging high-density multiphase flow combined with high static pressures.

1.2.4.3 *Armour response*

Near-field blast conditions have significant implications regarding loading and damage processes. The very strong near-field flow forces due to dynamic pressure are directional and interact with structures quite differently than the static pressure component, which dominates damage from an air-shock wave in the far-field. The intense and localised very dense, high-pressure and (for underbelly blast) multiphase high-speed flow of material will result in stretching and bending deformation of the armour which, in some cases, can result in rupture (or even brittle fracture). Preventing rupture, and the ingress of a blast wave, is the number one objective when designing against blast attacks. There are, however, a number of methods and materials used to mitigate the effects of blast loadings and these can be found throughout the rest of this book.

1.3 **Terminal ballistics, impact dynamics and armour physics**

Ballistics is divided into three subject areas: internal, which is concerned with the science of launching a projectile; external, which is concerned with the flight dynamics of the projectile; and terminal, which is concerned with the interaction between the projectile and its target. So, terminal ballistics covers all impacts, whether from kinetic energy rounds, chemical energy rounds like shaped-charge weapons, or explosive events, against the entire range of targets; buildings, tanks, helicopters, as well as ground troops, of course. The full gamut of these various armour/antiarmour interactions is well covered in a recent publication by [Rosenberg and Dekel \(2012\)](#). Here, we shall simply focus upon the armour’s response to the terminal ballistic effects associated with ordnance KE threats and explosive events, since KE threats tend to drive the design of the hull armour of most armoured vehicles, whilst blast loadings drive the design of their underbellies.

Understanding the physics involved in armour/antiarmour interactions is the key to comprehending the complete threat spectrum. The first major work to pull this cross-disciplinary subject together was by Roy Laible, in 1980, who gathered a distinguished team of coauthors, including legendary names like Mark Wilkins (ceramics and numerical modelling), Henry Kolsky (stress waves), Francis Mascianica (ballistic testing) and

David Roylance (textiles), to name but a very few. It makes excellent reading and is still one of the very few materials-orientated textbooks on armour (Laible, 1980). Of course, as in many disciplines, there is a wealth of essential background reading – the following list recommends just a few of them:

Brings together the various analytical and experimental aspects of impact dynamics, presenting a broad overview of the response of material and structures subjected to intense short-duration loading under conditions varying from low-speed to hypervelocity.

Zukas (1982)

This compendium of mathematical techniques for the modeling and simulation of high-velocity impacts presents the various analytical and experimental aspects of impact dynamics and describes the responses of a variety of materials and structures under impact.

Zukas (1990)

Addresses fundamentals and advanced topics relevant to the behavior of materials under in-service conditions such as impact, shock, stress and high-strain rate deformations. Deals extensively with materials from a microstructure perspective which is the future direction of research today.

Meyers (1994)

This book develops several different methodologies for analysing collisions between structures. These range from rigid body theory for structures that are stiff and compact, to vibration and wave analyses for flexible structures. The emphasis is on low-speed impact where damage is local to the small region of contact between the colliding bodies.

Stronge (2000)

One particular aspect of impact deserves a little more attention – the generation, transmission and role of stress waves during a ballistic impact event. As schematically shown in Fig. 1.13, when a projectile strikes the front face of an armour material/

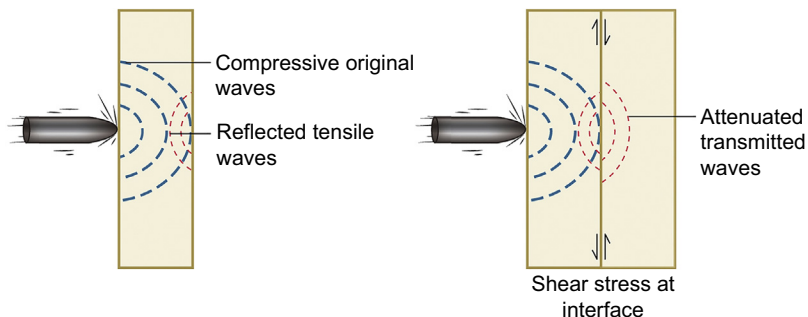


Figure 1.13 Schematic of stress waves being generated within an armour material and the creation of both reflected tensile waves and initiation of shear stresses at any interfaces.

system the first thing to occur, within the armour, is the generation of stress waves. Depending upon the stress level involved, these will be elastic, plastic or shock waves. When in the elastic regime, elastic waves travel through the armour material at a velocity, V , dictated by the material's bulk density, ρ , and elastic modulus, E , according to the expression, $V = [E/\rho]^{1/2}$. So, the wave velocity increases with an increase in elastic modulus and a decrease in bulk density. This means that for most armour materials, the generated stress waves move much faster than the projectile and therefore move ahead of the projectile as it penetrates the armour. This is significant because of the possibility of the material being changed ahead of the projectile, and therefore changing the material's penetration resistance.

Stress wave management is important, as is discussed in Chapter 4, but consideration of high-pressure shock waves is not so important when considering impacts from kinetic energy weapons travelling at ordnance velocities (up to 1200 m/s). The treatment of stress waves, including shock waves, in terminal ballistic events, is introduced extremely well in a recent publication by [Paul Hazell \(2015\)](#). He pointed out that whilst shock physics is important in extremely high-velocity/direct explosive detonations, it is not overly important when considering terminal ballistic events with small arms ammunition. Shock physics is therefore not covered in this book. Nevertheless, it should be recognised that some materials do undergo solid-state phase changes when subjected to intense shocks. For example, under extremely high pressures, ~ 13 GPa, mild steels do undergo a transition ([De'ath et al., 2011](#)).

One characteristic of materials that is fundamentally important to the science of armour materials is strain-rate sensitivity. In other words, many materials have time-dependent properties. That is, a material's elastic modulus or flow strength may depend upon the rate at which the material is tested/loaded/impacted. At one end of the scale, some materials, like lead, creep at near quasistatic loading rates (self-loading when it comes to a heavyweight material, like lead) — at the other end of the scale, at ballistic loading rates, the material may 'lock-up' or 'freeze' and not have sufficient time to respond to the rapid rise in applied stress. [Table 1.6](#) shows the various categories of strain-rate events, indicating the type of physical response, material response and the importance of inertial forces, as a function of strain rate. Explosive events can induce strain rates of up to 10^6 , whilst most impacts from small arms ammunition will peak at around 10^4 . In contrast, knife attacks, with speeds up to ~ 5 m/s, will only generate strain rates of $\sim 10^1$. So, when generating mechanical property data, as a function of strain rate (see Chapter 10), in order to understand or model armour materials, the strain-rate range of interest is from 10^{-2} to 10^4 .

1.4 Defeat mechanisms

Defeating a threat, in a safe and secure manner, is the one single driver in the design of an armour system. For bullets and high-velocity fragments, the defeat mechanisms include:

- Deflection of the bullet, as in ricochets from angled plates;

Table 1.6 Categories of strain-rate events

Strain rate (s^{-1})	10^{-8} to 10^{-6}	10^{-4} to 10^{-2}	10^0	10^2 to 10^4	10^5 to 10^6
Characteristic time (s)	10^6 to 10^4	10^2 to 10^0	10^{-2}	10^{-4} to 10^{-6}	10^{-6} to 10^{-8}
Type of test	Creep	Quasistatic	Intermediate strain rate	Bar impact	High-velocity plate impact
Type of physical response			Mechanical resonance in machines and specimen	Elastic-plastic wave propagation	Shock wave propagation
Type of material response	Isothermal			Adiabatic	
Importance of inertial forces	Inertia forces neglected			Inertia forces important	
Stress state	Plane stress				Plane strain
Level of stress	————— Increasing stress levels —————>				

Table 1.7 Ballistic damage code, based upon WW2 documentation

Damage code	Description of damage
A	No evidence of damage to front or rear of target
B	Some evidence of impact damage to the front of the target but no evidence of damage to the rear
C	Development of a smooth bulge on rear of target
D	Development of a cracked bulge on rear of target
E	Development of a cracked bulge, with light shining through target
P	Development of a pinhole, through the target, caused by the partial penetration of the nose of the round
W	Full penetration of the round through the target

- Defeating the round at the surface of the armour, during the so-called dwell period: damage code A in [Table 1.7](#). This is the ultimate defeat mechanism;
- Plastic deformation of the round/core, as with most lead-filled, handgun bullets;
- Erosion of the core, as with hardened steel-cored rounds;
- Shattering of the core, as with extremely hard, brittle cores, like tungsten carbide.

[Fig. 1.14](#) shows examples of these defeat mechanisms. Note that in some instances this involves loss of mass of the projectile/core but, in some cases, it is simply modifying the shape of the penetrator, normally through plastic deformation.

For stab and spike events, defeat mechanisms can include:

- Elastic and plastic deformation of the armour — see Chapter 6;
- Blunting the tip of a spike or cutting edge of the knife;
- Deflecting the weapon itself.

For blast events, the defeat mechanisms are more systems-orientated, as discussed by [Cimpoeru et al. \(2015\)](#). Preventing hull rupture under blast loading is the number one priority for an armour technologist. See Chapter 2, for blast loading of steels, and Chapter 10, for blast loading techniques and measurements.

1.5 Penetration mechanics and failure modes

Defeating the threat is one thing — preventing the armour from failing is another! The key message/ethos of this book is that understanding the possible failure modes in armour materials is absolutely essential when designing improved armour materials and armour systems. So, before describing in great detail the structure and properties of all of the different families of armour materials (Chapters 2–7), it is fundamentally important to understand each possible penetration/perforation mode, and the associated energy-absorbing mechanism(s).



The soft, lead-filled, 9 mm HG round which becomes highly deformed upon impact. The copper jacket splits but there is no overall loss of mass



Blunt mild steel cores of AK47 round mushrooming at surface of target, without loss of mass



High hardness steel cores of the 7.62 mm APM2 round, showing varying extent of tip erosion, with corresponding loss of mass



Tungsten carbide cores of 7.62 mm FFV round showing tip erosion and/or fracturing of core body

Figure 1.14 Examples of defeat mechanisms for small arms ammunition.

1.5.1 Ductile hole formation

This is observed in monolithic structural armours or armour elements against pointed KE projectiles, and is considered to be an efficient energy-absorbing mechanism.

Whether fully arrested or not, the pointed, or ogival-shaped, round creates a clean hole-like impression in the armour through plastic deformation, and displacement, of the material (see [Fig. 1.15](#)). No target material is lost. No, or little, round deformation occurs. The armour material, whether it is a low-strength steel, or a ductile aluminium or titanium alloy, flows outward (especially radially) from the nose of the round. Because of the physical displacement of material, excess quantities of

material get pushed ahead of the round (to form a bulge in the rear of the armour) as well as rearwards to form petals of fractured metal around the entry point. Because this arresting mechanism is totally associated with plastic flow, most of the resistance offered by the target comes from its plastic yield characteristics. Since most of the flow is radial, then the amount of resistance will be proportional to the in-plane compressive yield strength of the material. As one can imagine though, frictional heating occurs and the material (both target and bullet material), close to the newly formed 'hole', will increase in temperature. It is not unusual to see temper colours on these surfaces in steel targets, for example. However, most energy is absorbed through the work of plastic deformation. So, strictly speaking, the penetration resistance of a ductile metal target that fails solely by ductile hole formation (DHF) will be proportional to the dynamic, in-plane, compressive strength under varying conditions of temperature and pressure. This is why complex yield strength models are required in order to best describe even a simple penetration failure mode like DHF. However, [Woodward \(1978\)](#), and more recent work, have shown that a strength measure as simple as flow stress at a true strain of 1.0 is often sufficient to predict the performance of materials that fail by DHF. Chapter 2 provides more detail.

Of all the possible failure modes, DHF maximises penetration resistance, and minimises behind-armour effects, since there is no loss of material, at any stage in the penetration or perforation process.

In the UK, c.1940, a standardised ballistic damage code was developed to describe the damage caused by a single impact against monolithic steel armour plate. This enabled accurate descriptive records to be kept of the resultant stage of penetration into ductile targets, as a function of impact velocity, thus providing a much more informative guide to impact behaviour than simply quoting a single V_{50} value based upon averaging a number of 'wins' and 'defeats'. The author believes that such a damage code, as reproduced in [Table 1.7](#), should be used more frequently in the present day.

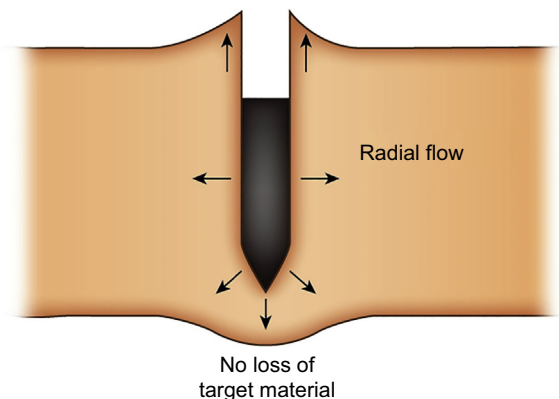


Figure 1.15 Schematic of ductile hole formation.

1.5.2 Plugging

This is observed in monolithic structural armours, or armour elements, subjected to attack from blunt objects and is usually associated with a low-energy absorption process. It is therefore one mechanism to prevent, or suppress.

When a blunt projectile strikes a target, the material ahead of the projectile accelerates, whilst the rest of the target remains relatively stationary. This leads to local compression of the material ahead of the projectile, and shear deformation in narrow shear bands under adiabatic conditions where the shear strain, strain rate and temperature may be locally very high.

The perforation mechanism known as plugging is an event controlled by the transverse shear properties of the target material. As illustrated in Fig. 1.16, it occurs when a blunt, or blunted, projectile imposes an intense, cylindrical shear stress on the target which, by some means or another, initiates a shear failure in the target. Because the shearing event is localised, very little actual plastic deformation occurs, even on the impact side where very little is extruded rearwards. Plugging occurs under conditions which favour transverse shearing — the most well-known being a geometrical relationship between the calibre of the round (or core) and the thickness of the target: if this is close to a 1:1 ratio, then plugging is often initiated. Since most of the cores of small arms ammunition are sub-7.62 mm, thin steels in the range of 5–8 mm can be quite susceptible to this type of failure event. Some steels are even more susceptible because some grades of steel suffer from adiabatic shear failure. This is a special, low-energy absorbing form of plugging in which the deformation concentrates within a narrow, adiabatic shear band, with decreased shearing resistance even further (see Chapters 2 and 3). Even after 40 years of research, there is still no agreement of the precise cause of adiabatic shear bands, although phase transformation is still a popular hypothesis.

In general, plugging absorbs a lot less kinetic energy compared to DHF. It also forms a very dangerous secondary projectile, namely the plug itself. If this is ejected ahead of the bullet, even though the bullet itself might be arrested, the ballistic limit of the target will be seriously compromised.

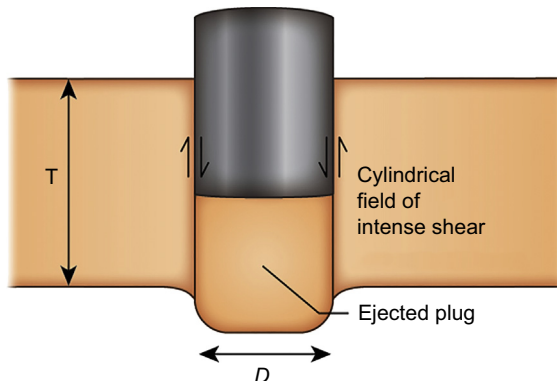


Figure 1.16 Schematic of plugging failure, a through-thickness failure event.

For the armour technologist, this is one particular failure mode, which has to be designed around. Preventing this unacceptable mode of failure has been one of the drivers for laminated targets, whether it is through an adhesively bonded laminate (to prevent through-thickness shearing) or even a steel/GFRP laminate (to alter the t/D ratio). These design approaches are described in more detail in Chapter 4.

Because the initial impact causes through-thickness compression, the thickness of the plug is normally measurably less than the thickness of armour plate, as can be seen in Fig. 1.17, from the work of Borvik et al. (2003).

1.5.3 Delamination

This is observed in highly orthotropic solids, laminated armours and layered structures, as described in Chapter 4.

It can occur in the armour material irrespective of projectile nose shape, although it is exacerbated by penetration from blunt projectiles. Two main energy-absorbing processes accompany delamination: membrane stretching, which involves out-of-plane plastic deformation of the rear elements, and interlaminar fracture, which involves either translaminar tensile failure, as shown in Fig. 1.18, and/or interlaminar shear failure of the interlaminar bond, if one exists. Chapter 4 addresses this particular failure mode in some detail.

The amount of energy absorbed in this process is difficult to quantify, although some researchers have tried to do this with an adhesively bonded set of laminates — see the paper by Simmons et al. (1989), as well as delamination of fibre-reinforced plastics (FRPs) in Chapter 5, adhesively bonded laminates in Chapter 4, and simulation of delamination events in Chapter 10. Fig. 1.19 presents an example of excessive delamination in an adhesively bonded aluminium laminate.

1.5.4 Discing

This is observed in highly orthotropic solids and laminated armour materials and is a special case of rear-face spalling in targets subjected to high-velocity impact from solid projectiles (Fig. 1.20). Its occurrence can dramatically reduce the ballistic limit of an armour system and is very common in ballistic failure of the light alloys (see Chapter 3). The premature failure event occurs as a result of intense bending stresses created in the target. Some degree of delamination is a natural precursor. It occurs on all types of targets: thick steel targets, as above, and thick aluminium or titanium targets, as well as some grades of laminated materials. In all cases, it is caused by a mechanical fracture event, late in the penetration process, and is *not* caused by a shock-wave interaction. It is *not* to be confused with classical spallation (see later mode).

Early work by Woodward (1979), based upon the penetration behaviour of high-strength aluminium alloy, 7001-T6 (see Chapter 3), and a tempered steel to SAE 4130 (see Chapter 2), described the failure mode with elegance and simplicity, and developed an early analytical model. More recently, Crouch has described this premature failure event in great detail (Crouch, 1992) and, after carrying out a forensic examination of typical steel discs (see Fig. 1.21), reported three stages in the failure

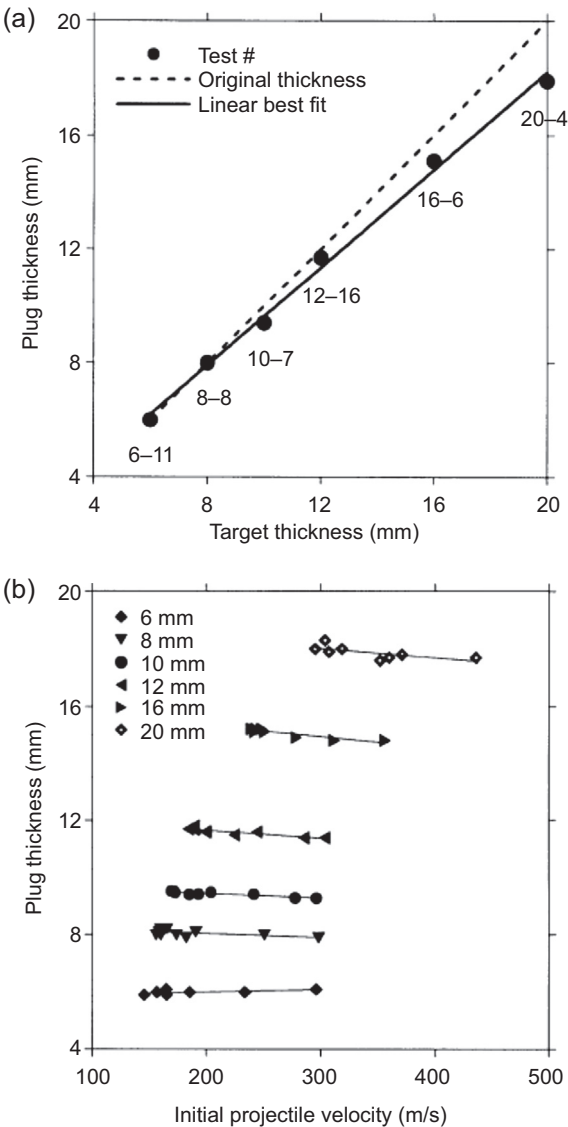


Figure 1.17 Plug thickness as a function of (a) target thickness and (b) projectile impact velocity.
After Borvik, T., et al., 2003. Effect of target thickness in blunt projectile penetration of Weldox 460E steel plates. *International Journal of Impact Engineering*, 28, 413–464.

event: (1) creation of intense bending moments and initiation of interlaminar shear cracks; (2) rapid propagation of the delamination crack, along the major spall plane and (3) final formation and separation of the disc via an in-plane, tensile-tearing fracture event.

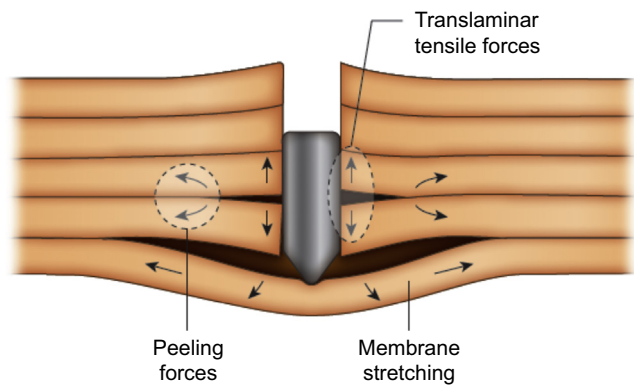


Figure 1.18 Schematic of delamination event in a lamellar, laminated or layered structure.



Figure 1.19 Cross-section through an adhesively bonded aluminium laminate, subjected to impact from a high-velocity, fragment-simulating projectile.
After Crouch, I.G., 1993. Penetration and perforation mechanisms in composite armour materials. Paper Presented at the Euromech Colloquium 299, Oxford University, March 1993.

In summary, the following material parameters are thought to be critical in controlling the behaviour of a target at each stage in this, low-energy absorbing, failure event:

Stage 1:	(a) In-plane elastic modulus (b) Through-thickness, strain-to-failure (for laminated materials) (c) Interlaminar shear strain-to-failure (for wrought monolithics)
Stage 2:	(d) In-plane elastic modulus of rear portion of target (e) Interlaminar fracture toughness
Stage 3:	(f) Fracture toughness in LT and LS orientation (see Fig. 4.2)

1.5.5 Conoidal fracture

This type of through-thickness failure is observed in glasses, ceramics, ultra-high hardness steels as well as hard polymers such as the polycarbonates, which are described in Chapter 5.

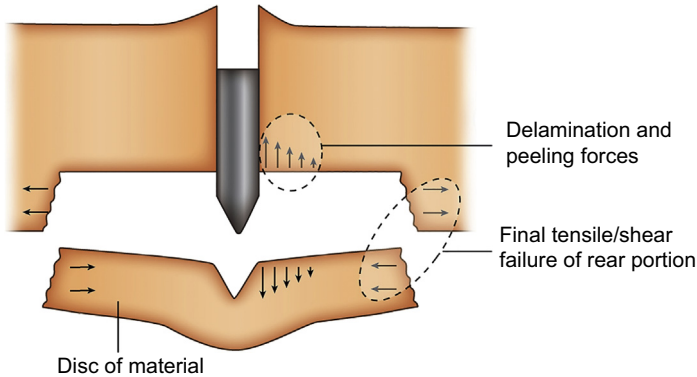


Figure 1.20 Schematic of discing event in a lamellar, laminated or layered structure.

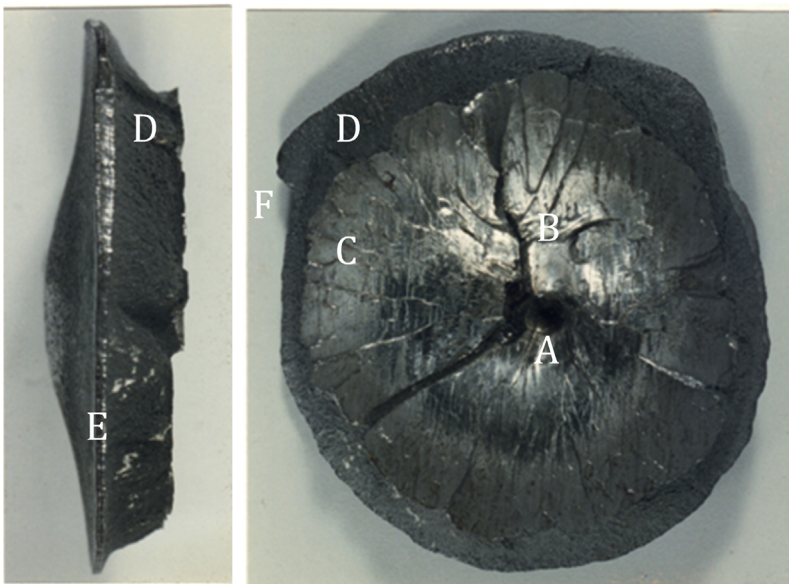


Figure 1.21 Forensic examination of a disc from a thick RHA steel plate impacted by a 20 mm AP round showing: (A) an impression of the tip of the projectile in the centre of the fracture, and corresponding bulge on the rear of the disc, shown on the left-hand image; (B) a central area which is very smooth and reflective, indicating sliding wear damage; (C) evidence of multiple crack initiation near the periphery of the spall plane, and river patterns indicating inward crack growth; (D) a ductile fracture conoid linking the spall plane with the rear surface; (E) a thin, but significant, shear lip around the perimeter of the disc, and; (F) evidence of the propagation of a single, spiraling crack around the disc, indicative of a slow fracture event. Crouch, I.G., 1992. Discing failures in both traditional and composite armour materials. Paper Presented at the International Symposium on Ballistics, Stockholm, June 1992.

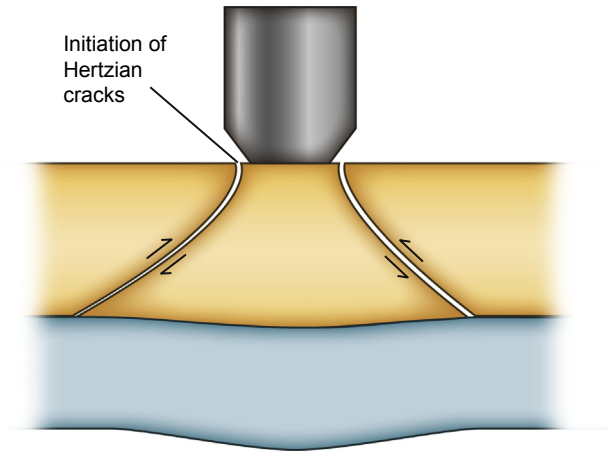


Figure 1.22 Schematic of conoidal fracture in brittle solids, following initiation of Hertzian cracks on the impact surface.

As originally identified by Hertz in 1881, when the surface of a brittle material is impacted by a blunt, or blunted, projectile, an incipient flaw in the surface, under the influence of a localised tensile stress, develops a cone crack that initially runs around the contact surface and then, driven by the forward momentum of the projectile, rapidly spreads downward through the material, shearing out a complete cone of separated material (Fig. 1.22). Examples of such cones are shown in Fig. 1.23. Note the change in shape of the conical cracks as they propagate through the material.

A classic review of the principles and applications of this indentation fracture phenomenon was carried out by Lawn and Wilshaw (1975) and many others since, especially those working with the family of glasses like Ball and McKenzie (1994). The

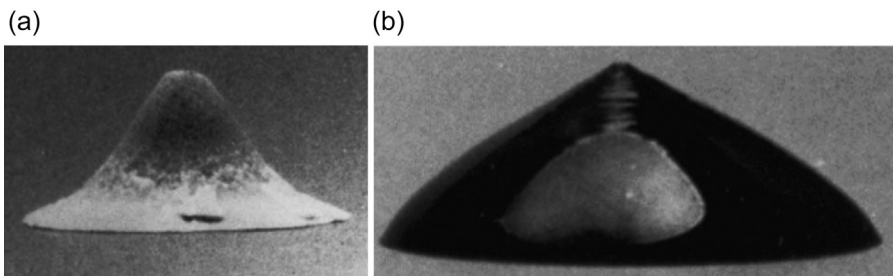


Figure 1.23 Examples of cones formed by normal impact of a 5-mm diameter steel sphere onto (a) alumina tile and (b) a glass-ceramic material.

After Field, J.E., Sun, Q., Townsend, D., 1989. Ballistic impact of ceramics. Institute of Physics Conference Series, 102, 387e393 and Walley, S.M., Field, J.E., 2005. The contribution of the Cavendish Laboratory to the understanding of solid particle erosion mechanisms. *Wear* 258, 552e566.

work of John Field and his team at the Cavendish Laboratory in Cambridge, especially through utilisation of visual measurement techniques, was well reviewed by [Walley and Field \(2005\)](#).

Conoidal fracture is an essential failure mechanism for brittle materials to be ballistically efficient ([Crouch et al., 2015b](#)), but what material characteristics affect the shape and size of the cone? [Zeng et al. \(1992\)](#) pointed out that Poisson's ratio affects the entire stress field beneath the impactor and hence affects the cone angle, θ . This is defined as the half-cone angle, measured between the cone crack and the normal. According to [Kocer \(2003\)](#), researchers have found that the cone angle increases with Poisson's ratio such that materials with a high value of Poisson's ratio should provide the largest-diameter cones and therefore have the highest ballistic efficiencies. Cone angles between 60° and 70° have been reported, or calculated, for materials with Poisson's ratio between 0.1 and 0.3. However, other factors do influence cone angle such as impact velocity ([Fellows and Barton, 1999](#)), where higher velocities result in larger cone angles, confinement and stiff support conditions, result in larger cone angles, as reported by [Sherman \(2000\)](#).

1.5.6 Comminution

In general, the term comminution means the reduction of solid materials from one average particle size to a smaller average particle size, by crushing, grinding, cutting, vibrating or other processes. In terminal ballistics, this fracture phenomenon is observed in brittle, defective solids like glasses, ceramics and concrete agglomerates.

In certain impact scenarios, as illustrated in [Fig. 1.24](#), a region of comminuted material occurs ahead of the projectile, but remains confined within the boundary of the conoidal fracture. This is often referred to as the Mescall zone, after John Mescall, a US researcher working at the Army Materials and Mechanics Center in the 1980s, who predicted its presence from carrying out numerical modelling studies. This is normally associated with hypervelocity impact from long rod penetrators but can certainly

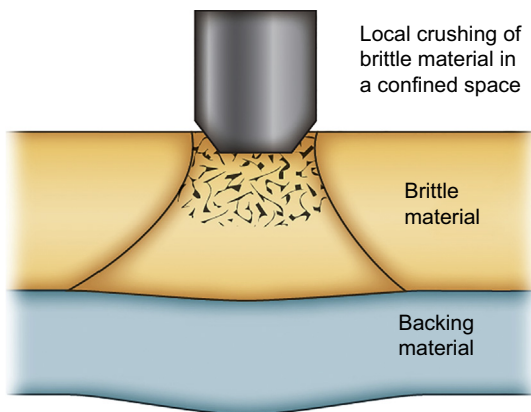


Figure 1.24 Schematic of conoidal fracture in brittle solids, following initiation of Hertzian cracks on the impacted surface.

occur at high velocities with small arms ammunition. The comminuted material is the source of spall, ejected frontwards out of the impact site. [Meyers \(1994\)](#) describes other scenarios and suggests that the ballistic efficiency of a ceramic-based armour can be enhanced by ensuring that this comminuted material is not ejected by placing a confining plate on top of the ceramic. This is discussed more in Chapter 4. More recently, [Carton et al. \(2014\)](#) at TNO suggested that the submicron and nanosized particles collected from the impact of small arms against alumina tiles probably originated from the Mescall zone. Having religiously collected all of the particles, including what they describe as the ‘aerosol’ fraction, the submicron-sized particles, they concluded that there must be considerable transcrystalline fracturing occurring within the comminuted area. Their work also confirmed the original findings of [Woodward et al. \(1989\)](#), who found that the creation of fresh fracture surfaces does not, in itself, absorb much kinetic energy.

1.5.7 Radial cracking

When brittle solids are impacted by a single projectile many fracture events occur, as shown in [Fig. 1.25](#): the formation of a conoidal fracture zone, as described in [Section](#)

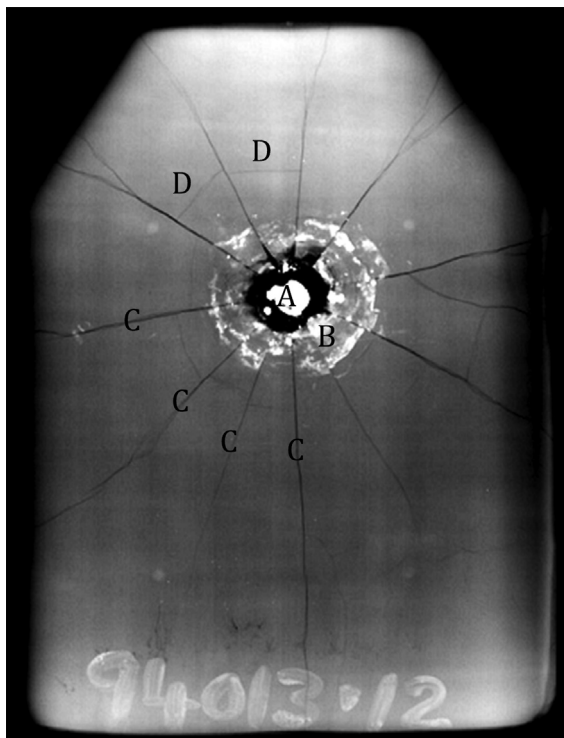


Figure 1.25 High resolution X-ray image of a ceramic-based hard armour plate showing arrest of the projectile (a), the conoidal fracture zone (b), radial cracks (c), and circumferential cracks (d).

1.5.5, as well as a series of radial cracks emanating from the point of impact. These are invariably accompanied by the formation of circumferential cracks which are described in [Section 1.5.8](#). In monolithic ceramic tiles, like those used in the HAP of a BAS, these radial cracks rapidly propagate to the extremities of the product. This is certainly so in very brittle materials like glass. However, in tougher materials like ultrahigh-strength steels (see Chapter 2) and hard plastics (see Chapter 5) whilst these radial cracks still form, they can be arrested within the body of the material.

However, what drives their formation, and what parameters dictate how many radial cracks actually form? In a recent presentation, Crouch summarised current thinking on the step-wise evolution of radial cracks ([Crouch, 2014](#)), based upon earlier work of [Sherman \(2000\)](#) who stated that ‘the radial cracks are driven by the generation of a hoop stress which is developed around the Point of Impact, during localised dishing...’. [Fig. 1.26](#) schematically illustrates these steps more clearly: (1) initiation of multiple cracks near impact zone, (2) development of a field of tensile hoop stress as the ceramic plate momentarily dishes elastically and finally (3) relief of that hoop stress through the propagation of a finite number of radial cracks. The magnitude of the tensile hoop stress and the fracture mechanics associated with the material will dictate the number of radial cracks. Whilst [Sherman \(2000\)](#) demonstrated a strong relationship between the number of radial cracks and the support condition given to ceramic targets, Crouch and Elder, in a recent DMTC piece of research ([Elder, 2012](#)) analysed Sherman’s alumina data and found that, on average, one radial crack is propagated for every ~ 150 MPa of developed hoop stress.

In an analogous situation, even the number of star cracks in ductile failure of RHA when attacked by a pointed projectile, does vary depending upon the degree of over-match. Star cracks are those radial cracks that appear on the rear surface of a ductile armour material when failing by DHF. If the arrest is early in the penetration process, the number of cracks will be few (maybe two or three) but if the round is arrested late (just catching the projectile) the number of star cracks (radial cracks) could be as high as seven or eight. As with ceramics, this cracking phenomenon is also a result of selective propagation of just a few cracks from the myriad of cracks that will have been initiated as the RHA begins to perforate.

1.5.8 Circumferential cracking

This secondary form of cracking always follows the development of radial cracks and reflects the amount of flexing that occurs in a hard-faced armour system. As can be seen in [Fig. 1.27](#), they often form as families of concentric circles around the impact site. Forensic examination tells us that they form after the radial cracks have formed and therefore occur independently but for some common reason.

That reason is thought to be due to the local dishing of the target and the backing material in particular. Do not forget that, invariably, the ceramic is bonded to the backing material (see Chapters 4 and 7). So, in a typical impact event in which the projectile is arrested by the backing material, the support material immediately in front of the projectile gets pushed rearwards — see [Fig. 1.28](#). This immediately creates a bending moment along the radial axis of each of the segments. The presence of surface

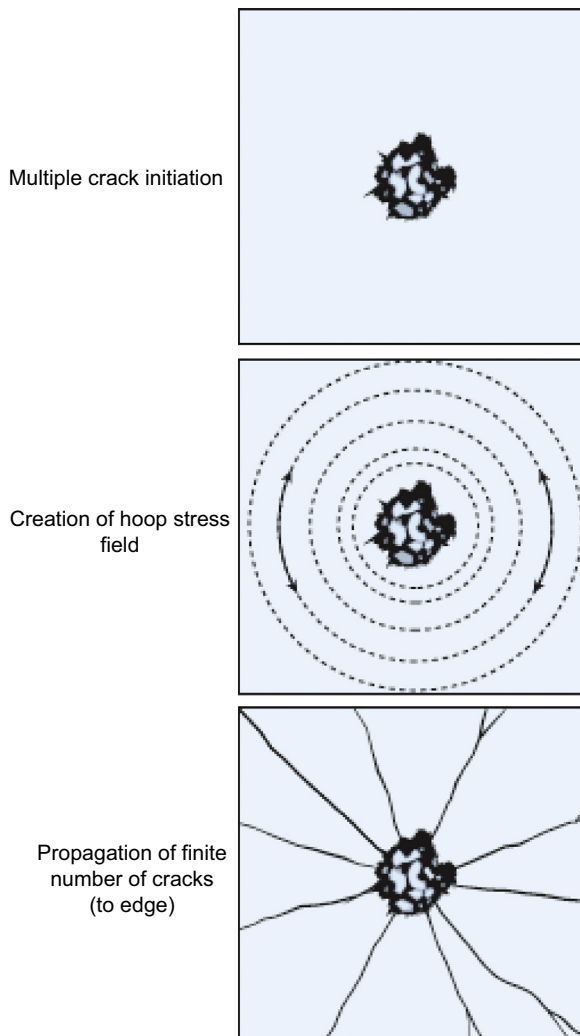


Figure 1.26 Schematic of step-wise formation of radial cracks.

After Sherman, D., 2000. Impact failure mechanisms in alumina tiles on finite thickness support and the effect of confinement. *International Journal of Impact Engineering*, 24, 313–328 and Crouch, I.G., 2014. Effects of cladding ceramic and its influence on ballistic performance. Paper Presented at the International Symposium on Ballistics, Atlanta, GA, USA, September 2014.

defects and the fracture toughness of the ceramic will then dictate the location and number of times each segment is broken. However, because the support conditions are normally symmetrical, these fractures will occur at similar locations in each segment giving the impression that they are behaving sympathetically. Circumferential cracking can therefore be limited by providing greater support to the brittle material in a multilayered armour system.



Figure 1.27 High-resolution X-ray image of the impact site of a ceramic tile showing series of circumferential cracks circling the point of impact, forming a spider-web pattern.

Limiting the amount of circumferential cracking and especially the number of radial cracks is very important since this will limit the collateral damage from a ballistic strike and improve the ballistic performance of second and subsequent strikes (Crouch, 2014).

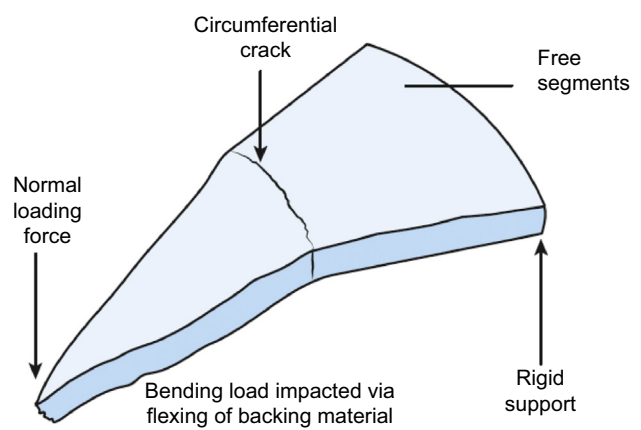


Figure 1.28 Schematic of the formation of a circumferential crack in a ceramic segment.

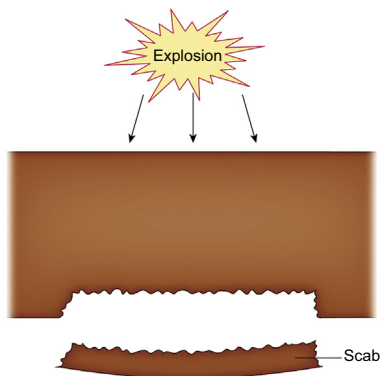


Figure 1.29 Schematic of a spallation event which forms a scab of material, ejected from the rear of the armour.

1.5.9 Spallation (including scabbing)

This is a noninvasive, highly destructive failure of thick, monolithic, structural armours when attacked by high-explosive squash head rounds that detonate in contact with the armour. [Fig. 1.29](#) shows a thick steel plate that has been impacted on several occasions and, on each occasion, a scab of armour material has been ejected from the back of the plate. This occurs as a result of strong compressive stress waves (elastic, plastic and/or shock) generated at the point of impact. The waves are reflected from any discontinuity, or free surface, as tensile waves, which interact with the original compressive waves. If the magnitude of this interaction is greater than the through-thickness tensile fracture strength of the material, spallation occurs. See [Meyers \(1994\)](#) for more detailed treatment of spalling. A high, dynamic, through-thickness, tensile strength, commonly termed spall strength, is therefore required for a material not to spall.

Scabbing is a classic defeat mechanism for the thick-walled, monocoque military vehicles of the 1940–1970s but is easily countered by having spaced armours and the use of the new generation of advanced armour systems (see Chapter 2). However, research still continues in some quarters ([Deshpande et al., 2003](#)) to fully understand and model this classic phenomenon.

Of course, internal spallation can create growth of cavities within an armour material, as a precursor to discing, as described in [Section 1.5.4](#). It can also account for the ejection of front spall, and rear spall, in brittle systems like those based upon ceramics. In fact, [Fig. 1.30](#) shows the formation of a region of intermittent spall around the periphery of a HAP. This occurred as a result of intense stress waves radiating outwards from the point of strike and reflecting off the internal edges of the plate – an unusual and rarely seen phenomenon in HAPs, since they are not normally impacted by a 20 mm FSP!

Spallation, and the associated material parameter, spall strength, is an important armour material characteristic and methods of measuring spall strength are duly covered in Chapter 10 on high strain-rate testing.

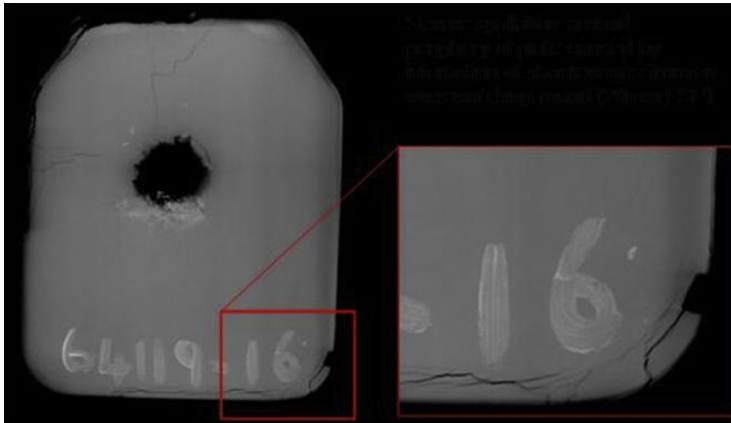


Figure 1.30 High resolution X-ray image of spalling around the periphery of an HAP which has been impacted with an overmatching 20 mm FSP round.

Crouch, I.G., 2009. Threat defeating mechanisms in body armour systems. Paper Presented at the Next Generation Body Armour, London, September 2009.

1.5.10 Fragmentation

Fragmentation describes the process of generating many fragments simultaneously from an original solid, stable body, as defined by [Meyers \(1994\)](#). Three scenarios are envisaged here: (1) the fragmentation of the steel shell of a bomb casing, (2) the fragmentation of a hand grenade casing, and (3) the catastrophic disintegration of concrete columns under blast loading from nearby explosive events.

In the first case, [Mott \(1947\)](#) considered the rapid expansion of a ring of steel (see Chapter 10) and proposed that this fragmented into a finite number of discrete fragments because the fracture strains around the ring actually varied about an average value. In the second case, that of the hand grenade, the size of the fragments is predetermined by designing-in hatched ridges into the casing. The third case, that of the disintegrating concrete column, is more materials-orientated. Consider the following range of brittle materials: ceramics, which contain small pre-existing cracks or pores; cast irons, which contain large, isolated islands of graphite nodules, and metal matrix composites, which might contain small, isolated reinforcing particles. In each of these families of materials, discontinuities exist within the microstructure, just like in the complex structure of a concrete aggregate. When such materials are dynamically loaded, [Louro and Meyers \(1988\)](#) suggested a sequence of microstructural events that leads to fragmentation (see [Fig. 1.31](#)): (1) the presence of pre-existing flaws or particles, (2) the activation of these discontinuities by the passage of a compression pulse, (3) dynamic growth of the activated flaws by the passage of a tensile pulse, and (4) intersection of the cracks and fragmentation. [Louro and Meyers \(1989\)](#) also developed mathematical expressions to describe this step-wise fragmentation process and demonstrated that final fragment size depends upon original grain size of the material, the amplitude and duration of both the compressive and tensile pulses, as well as the

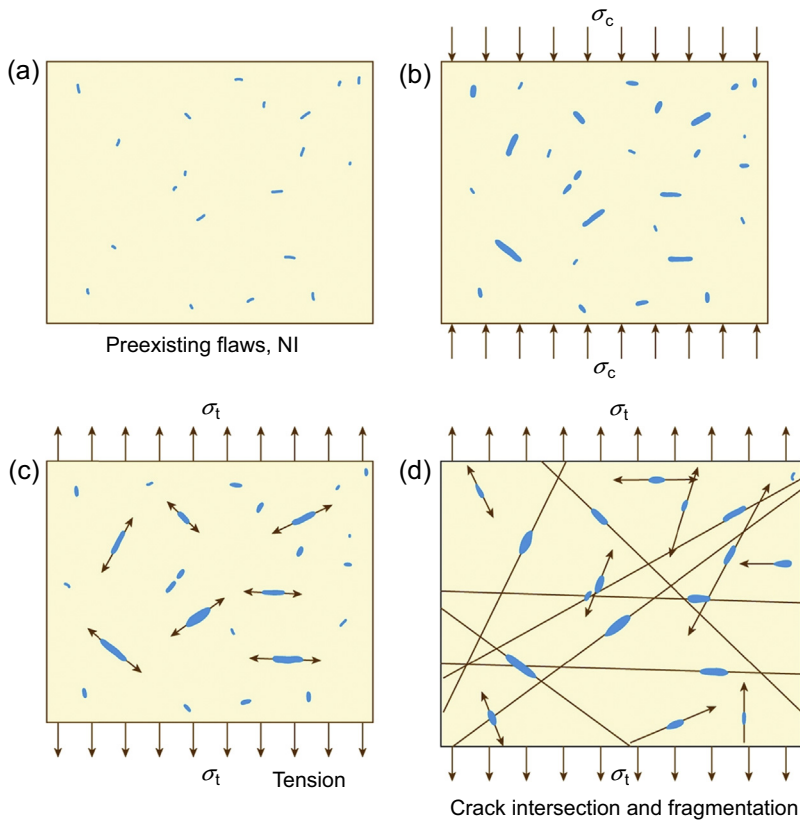


Figure 1.31 Proposed sequence of events in the fragmentation of ceramics.

After Louro, L.H.L., Meyers, M.A., 1988. Stress waves induced damage in alumina. Paper Presented at the DYMAT 88, Ajaccio, France.

maximum crack velocity. Using such mathematical expressions, numerical models can now simulate this event (see Chapter 9).

1.6 Design of armour systems

By way of example, the following sections describe the evolutionary design of an armour system. In [Section 1.6.1](#), a simple case of a steel plate is considered. However, more often than not, the threat changes and the existing armour system requires improvement — this reflects the leapfrogging nature of the armour/antiarmour profession. [Section 1.6.2](#) therefore considers possible up-armouring scenarios. [Section 1.6.3](#) covers the role of mathematical modelling in this design process to allay a number of misconceptions in this area. Finally, in [Section 1.6.4](#), alternative systems are considered and methods of comparing different armour systems are introduced.

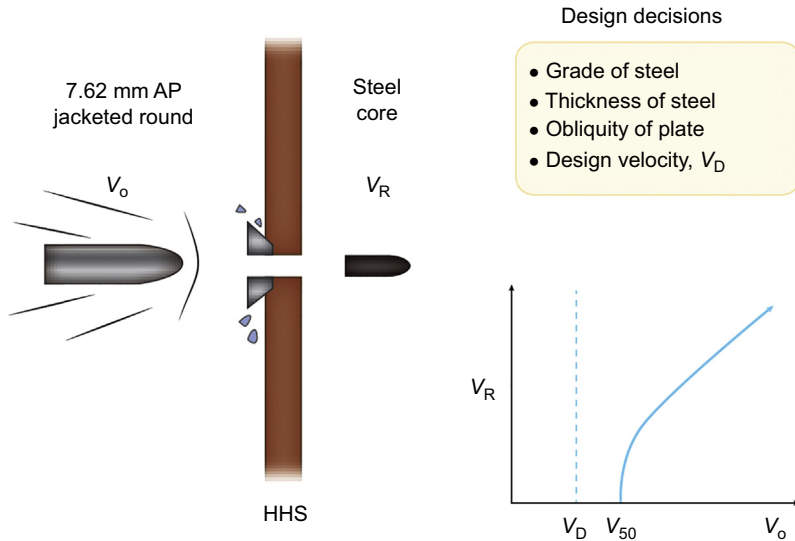


Figure 1.32 The design of a simple, one-plate armour system.

1.6.1 Design of simple, elemental systems

How can designers of an armour system guarantee that a specified bullet will never perforate their armour? In other words, how can an armour technologist or materials engineer reach a situation where they can guarantee that their armour material will offer full protection to its user (wearer or occupant)? In order to answer these questions, we need to understand how an armour system is tested.

Consider the simple armour system shown in Fig. 1.32, involving nothing more than a single plate of steel. If this is to offer full protection against a 7.62 mm AP round, for example, the armour technologist needs to consider the four variables listed. If the chosen steel is a high hardness steel (HHS) and the obliquity is normal, then it is simply a case of determining the thickness of steel that will possess a V_{50} value that exceeds the design velocity, V_D . So, how is the V_{50} determined and how much should it exceed V_D by?

Consider a simple series of impacts involving the normal attack of an armour-piercing bullet against a single plate of HHS. At low velocities of V_o , the bullet will simply be stopped, but as one gradually increases the impact velocity there will come a time when some of the bullets start to perforate the steel plate, with a residual velocity V_R . Increasing the impact velocity still further will reach a situation in which all rounds perforate the steel plate, with higher and higher residual velocities. This is represented by the simple schematic in Fig. 1.32.

However, if one was to plot the probability of a perforation, as a function of impact velocity, then the curve would look something like that shown in Fig. 1.33. This can be considered to be very similar to the bell curve for normal distribution of a random set of events or measures. So, associated with this curve will be a mean point and a

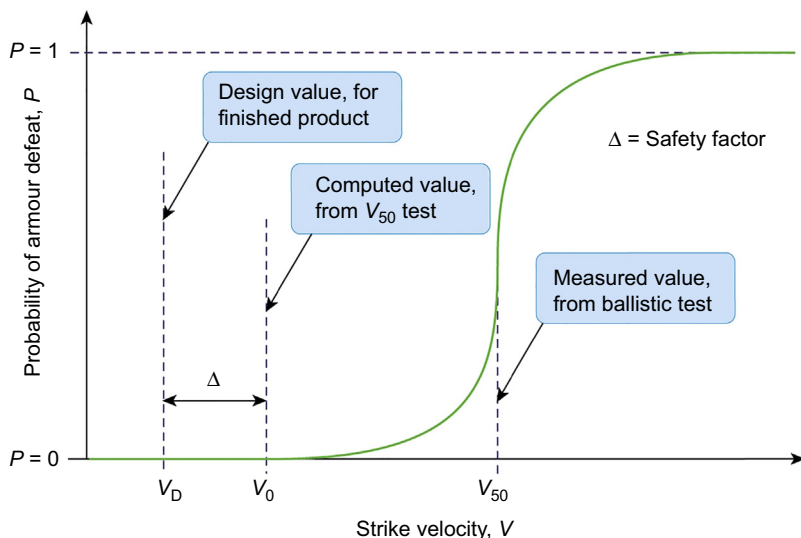


Figure 1.33 A schematic plot of the probability of perforation of the armour as a function of the strike velocity of the projectile.

standard deviation. The mean point is called the V_{50} , the velocity at which 50% of impacting rounds will result in a perforation. The standard deviation, sigma (σ), like in all normal distributions, is a measure of how wide ‘the zone of mixed results’ is. The lower and upper bounds of this zone of uncertainty (or grey zone) can be separated by about six standard deviations, ie, six sigmas. Most importantly, with ballistic probability curves, the lower bound is known as V_O , the velocity at which most (if not all) rounds will not perforate the armour.

So, when designing a safe, conservative armour material, or system, the design velocity, V_D , is well below V_O so that the designer can guarantee that no perforations will occur. The degree of safety employed, and the associated safety margin (Δ) selected, will depend upon the level of confidence to be applied versus the desirability of achieving the lowest weight solution.

This process is covered in more detail in Chapter 11. It should be noted here that ballistic test standards, like the NIJ Standard 0101.04, covering the testing of BASs, give, very precisely, the minimum test velocity at which zero rounds are permitted to penetrate the armour. In a well-designed armour system this specified test velocity would correspond to the value of V_D . This is the worst-case scenario, of course: maximum velocity, normal attack, zero yaw. On the battlefield, it is presumed that real impact events will be less penetrating since they are likely to be oblique and probably yawing.

In terminal ballistics, the width of the grey zone, as defined by six-sigma, is an excellent measure of how complex the armour system is and/or how consistent the armour material is. For simple armour systems, consisting of, say, a single plate of steel, the grey zone can be very narrow (less than 5 m/s in most cases) but with complex, multilayered systems the grey zone can be as wide as 50 m/s. In soft armour systems

(see Chapter 6) involving layers of woven fabrics, the width of the grey zone can be used as a measure of how well the material has been manufactured, in terms of consistency of stitching, weave pattern, and fibre strength (for example). With ceramics, six-sigma may also depend upon the number of defects embedded within the micro-structure. In this sense, the width of the grey zone may well be related to the Weibull Modulus of the ceramic material (see Chapter 7 and [Section 1.7.3](#)).

1.6.2 Design of multilayered systems

Consider the same example as in the previous section but now consider a situation in which the threat level has been increased and the armour technologist has to up-armour the existing steel structure. The designer could consider installing a spall liner, made from a FRP, behind the main armour, for example, as shown in [Fig. 1.34](#). Recognise, however, that the number of variables, and therefore the number of engineering decisions, increase. These are considered further in Chapters 4 and 5. Might the steel perform better if the air gap, d_1 , was zero?

Now consider what might be required if this same upgraded system needed further enhancing because the perceived threat had significantly increased, say to a 14.5 mm AP round. One common solution is to consider a lightweight, ceramic-based armour system attached to the outside of the existing steel structure, as shown in [Fig. 1.35](#) but, once again, note how rapidly the number of variables, and the number of engineering decisions, increase.

1.6.3 The design process, design drivers and the role of mathematical modelling

The design of an armour system is a holistic process and one not only based upon current engineering decisions, and conventional design and development processes, but one that may involve consideration of either analytical approaches and/or computer

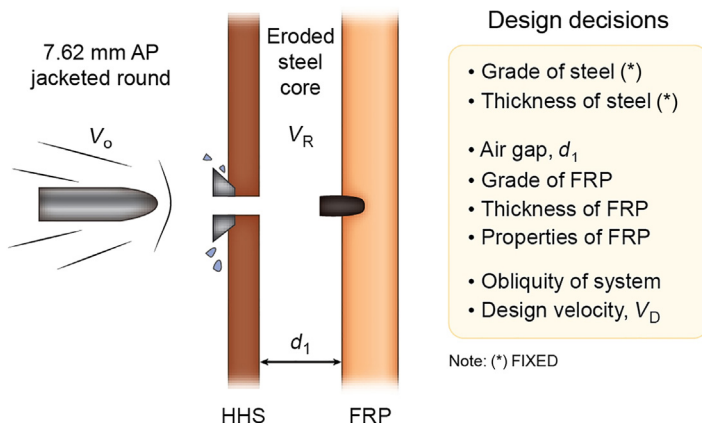


Figure 1.34 The addition of a spall liner to a simple, one plate armour system.

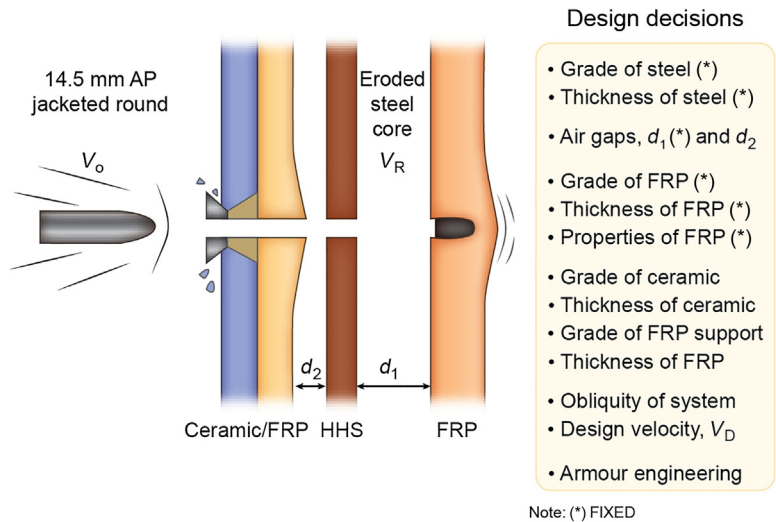


Figure 1.35 The addition of a ceramic appliqué armour system to enhance protection.

simulations. Fig. 1.36 illustrates this holistic approach. The conventional design and development process is represented by the tasks listed in the left-hand column. Once the threat has been designed, an initial design is conceived and tested, and there are a number of fairly quick, semiquantitative methods of doing this, as described in

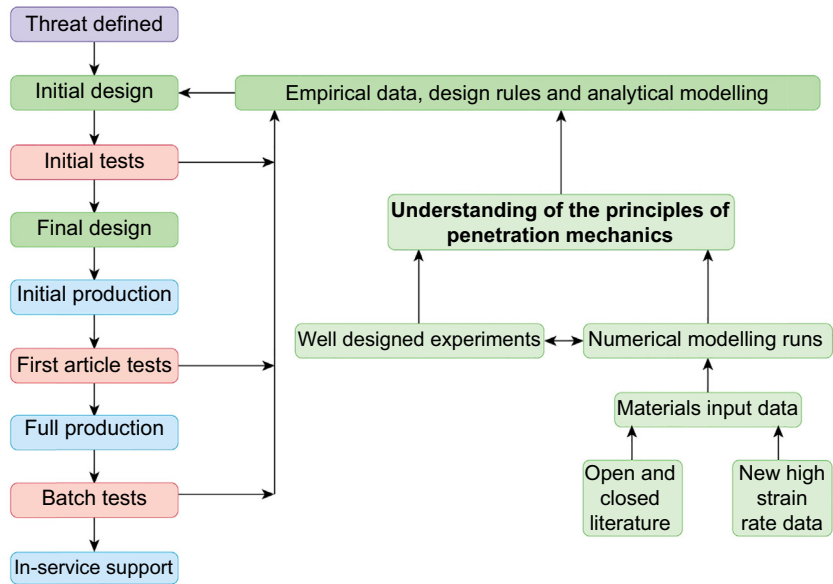


Figure 1.36 A schematic of the armour design process, showing both the standard design and development tasks, as shown in the left-hand column, and the role of analytical modelling and computer simulations, and related materials input data.

Chapter 11. This initial design might be refined, of course, through a number of iterative steps but eventually a final design is fixed. At this stage initial production commences but only up to the production of a set of ‘first articles’, which are then presented to the customer for comprehensive ballistic testing. If these first article tests (FATs) are satisfactory, the customer will then give authority to proceed with full production, during which an agreed set of batch tests is carried out to check that the armour product is maintaining the requisite performance levels. For BASs, it is not untypical for ~ 25 items to be batch tested for every 1000 items produced. For a large armoured structure, like a cast steel turret (see Chapter 2), it might be one in every 25 that are batch tested (often called proof testing).

Let us return to the start of the design process — creation of the initial design. This early part of the process is aided by consideration of databanks of empirical results (from similar impact scenarios), a few general design principles, all supported by some analytical modelling (see Chapter 8) and on occasions, numerical simulations (see Chapter 9). However, computers are not used to design real armour systems!

Two other points need to be made about Fig. 1.36. First, that numerical modelling can only be useful if the material data that are required are available, accurate and relevant — Chapter 9 deals with this point, in depth, and also provides a compendium of useful material input parameters. Second, and most importantly, numerical models have to be validated against some well-designed experiments with accurate predictions highly dependent on replicating a priori experimental ballistic test results — the literature is awash with this type of research activity. But, in so doing, they simply increase our common understanding of the principles of penetration mechanics. It is this fundamental understanding that assists with the design process, not computer simulations per se.

1.6.4 Different armour systems for different applications


There are several ways to classify armour materials and systems. There are the structural armours which have to perform the dual role of being both the engineering structure as well as the armour (see Chapter 2 for armour steels, and Chapter 3 for the light alloys). These mainly rely upon the grade of material and the obliquity of the armour to resist penetration. Then there are the nonstructural armours, like ceramic and composite-based examples, that cannot carry any engineering load but behave as very effective armour systems (see Chapter 5 for FRPs, Chapter 6 for fibres and textiles, and Chapter 7 for the glasses and ceramics).

Alternatively, in order to consider *all* possible armour systems, one can group them according to the nature of their system: passive, reactive, active and electric. Table 1.8 lays out these alternatives and independently lists the main material and geometrical variables that are available. At this point the reader should refer to the overview given by Gooch (2002) and to others, like Yaziv (2008), who have presented work on appliqué armour systems. This is an extremely broad and complex subject, reflecting the imaginative and innovative thinking that has gone into developing protective systems.


For completeness, the following examples are given, with due reference to the images in Table 1.8:

Table 1.8 An overview of the different categories of armour systems and materials


System	Materials	Geometry	Application
Passive	Steels	Obliquity	Tank (MBTs)
Reactive	Aluminium alloys	Laminated	Naval vessels
Active/smart	Titanium alloys	Spaced	Helicopters
Electro-magnetic	Ceramics	Perforated	Personnel
	Composites (FRPs)	Elemental	Armoured personnel carriers
	Explosives		Logistic vehicles




(A)




(B)




(C)




(D)



(E)



(F)



(G)

- A: Main battle tank armours using a passive system including steel plates at oblique angles;
- B: Bar armour, consisting of elements of steel, designed to protect a vehicle against antitank rocket-propelled grenades by forming a rigid cage which disrupts the shaped charge of the warhead;
- C: A passive, composite armour system used to protect RAN minehunters (see Chapter 5);
- D: A well-known passive system of ceramics and composites protecting military helicopters;
- E: A set of SAPI plates — another example of a passive system consisting of ceramics, composites and textiles to protect armed service personnel (see Chapter 7);
- F: An example of a reactive system: a reactive armour consisting of laminates of steel and explosive, designed by the US Army, developed by Rafael in Israel, and attached to a US M2 Bradley APC;
- G: An example of a smart, active armour system fielded by the Israel Defense Forces, which involves sensors, to detect incoming projectiles, as well a suite of defensive aids to defeat the projectile. The image is of the Trophy system fitted to Merkava Mk 4 tank;
- Electromagnetic armour systems have been researched for decades and, according to [James \(2009\)](#), have now reached the stage of full-scale testing and development, although battery power and weight still remain a challenge.

The main message in this very brief section is that, irrespective of the armour system, armour materials are always involved and therefore engineering decisions need to be made as to their construction and method of manufacture. The information contained in Chapters 2 through 7 is therefore relevant whatever system is being designed, or developed, or researched.

Finally, how are these very different systems compared in an attempt to select the most suitable system for a particular application? Well, apart from cost, availability

and strategic reasons, there are two standard figures of merit ratings, mass efficiency, E_m , and space efficiency, E_s , as defined below:

E_m = areal density of RHA/areal density of candidate system

E_s = total path length for RHA system/total path length for candidate system

For example, the E_m value for lightweight ceramic systems can be as high as 5–10, whereas E_s values are normally less than 1, since most advanced systems are thicker than a standard, monolithic plate of armour steel. Space is not always a concern, whereas weight always is, so the most common comparison is mass per unit area.

In a global sense, use is still made of a somewhat dated plot, based upon the Milne-de-Marre graph as reproduced in Fig. 1.37 (Doig, 1998). This is a plot of projectile kinetic energy to just penetrate a target versus the logarithm of the areal density of that target material. The graph is of a very general nature and not overly useful when designing real armour systems. However, from a broad perspective, general trends can be observed. For example, it is clear that for lightweight vehicles designed against KE ammunition with an impact energy of $\sim 10^4$ J, aluminium-based solutions are lighter than steel-based solutions.

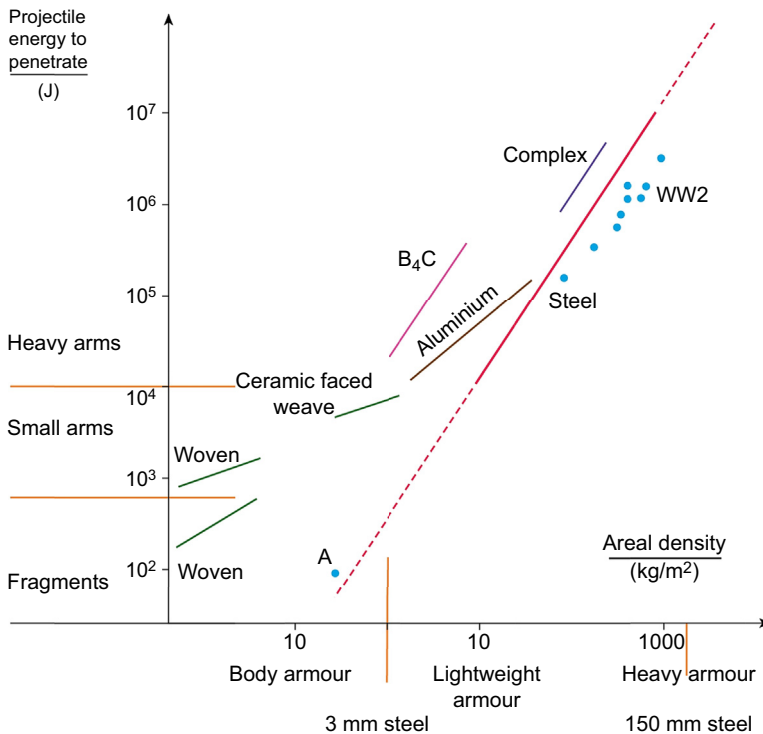


Figure 1.37 The Milne-de-Marre graph for the entire family of armour materials against a range of KE projectiles. Point A represents attack by arrows against chain mail and the family of blue dots represents specific data from WW2 tanks.

After Doig, A., 1998. Military Metallurgy. Maney Publishing, London.

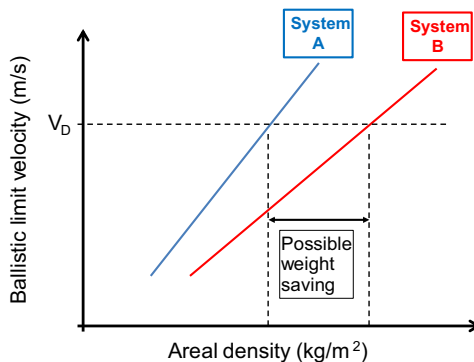


Figure 1.38 Ballistic limit velocity versus areal density for two armour systems, (A and B) indicating the possible weight saving/advantage achieved if System A was selected.

In a more refined, and useful, manner it is very conventional, and strictly necessary, to compare armour systems using the term “areal density”. This is nothing more than weight per unit area (kg/m^2) but the layperson does grapple with the concept. Plotting some measure of ballistic performance against areal density is extremely generic to the science of armour materials and is used throughout this book. Fig. 1.38 illustrates its function. It should be noted that this relationship is not normally linear, except over a small range of areal density. However, in this generic example, when designing a system to defeat a specific threat, and knowing the total surface area of the armour system, Fig. 1.38 shows the weight saving that could be achieved at the desired impact velocity, V_D , the design velocity (refer back to Fig. 1.33) if System A was selected rather than System B.

1.7 Revision of essential materials science

This final section is included to ensure that the reader is aware of the required level of understanding of the underpinning material science running through the rest of the chapters. It might seem a little basic to start with the Periodic Table of the Elements but the lay-reader should be aware that most lightweight armour materials are constructed using the lightest chemical elements available (Fig. 1.39). It might also be useful for the long-serving researcher to remind themselves of its fundamental importance.

One fundamental characteristic of all materials is how they respond to an external force. For example, Fig. 1.40 illustrates the different ways in which both idealised and real-world materials behave when mechanically tested in tension. The idealised forms are often used in mathematical analyses. Elastic moduli, yield stress, the stress–strain curve and strain-to-failure are important armour material properties, both in tension and compression. Note that these stress–strain curves are affected by temperature and strain rate, as will be appreciated throughout the rest of the chapters.

The following bullet points are considered essential facts about the various families of armour materials, and are offered as a checklist of requisite background knowledge.

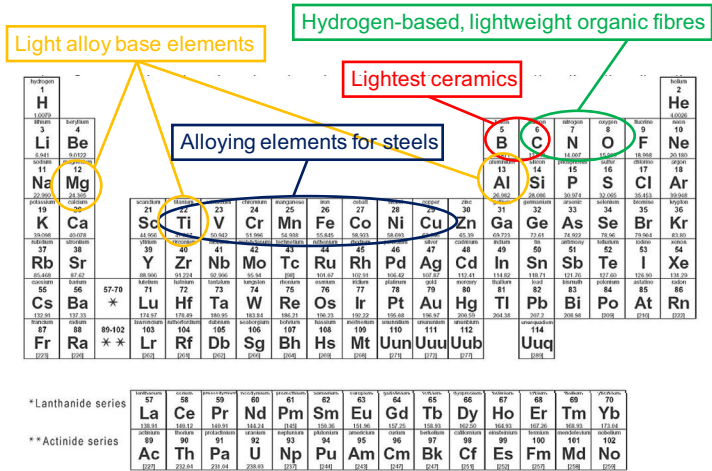


Figure 1.39 Periodic table of the elements, indicating use of lightest elements in armour materials.

1.7.1 Metals

- These are continuous, homogeneous materials with negligible microdefects, ductile in nature, with a high level of fracture toughness (see Chapters 2 and 3);
- Their basic crystal structure dictates their properties, especially the degree of ductility: body-centred cubic (BCC), face-centred cubic (FCC) and hexagonal close packed (HCP) are the most common crystal structures;
- The movement of dislocations (line defects within the metallic crystals) provides a mechanism for plastic deformation;
- Grain size has a strong influence on flow properties, as given by the Hall–Petch relationship where flow stress is inversely proportional to the square root of the mean grain diameter;

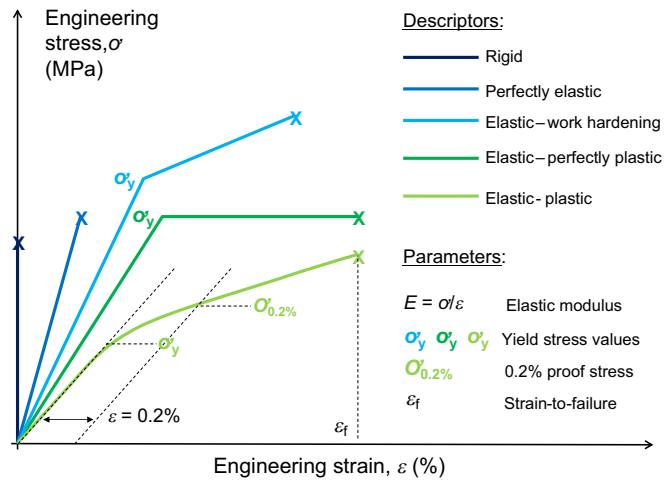


Figure 1.40 Schematic stress–strain curves for a range of idealised material types.

- The microstructural grain structure can range from equi-axed grains to pancake-shaped grains with a variety of aspect ratios;
- Heavily worked alloys, with extreme pancake-shaped grains have an anisotropic nature and display orthotropic properties (see Chapter 4);
- Some metals, like some BCC steels, will have time—temperature, stress—state, dependent properties which can result in a transition from ductile to brittle behaviour.

1.7.2 Polymers

- These are continuous, heterogeneous materials with low moduli, high ductility and low strength (see Chapter 5);
- They are formed by the polymerisation of simple organic molecules called monomers;
- They form a chain of polymer of varying molecular weight and structure, such that every polymeric material will contain polymer chains with a normal distribution of lengths;
- They will not normally be fully crystalline and usually contain areas of amorphous polymers chains;
- The polymer chains can be crosslinked to produce an interlocking, 3D structure;
- They are grouped into two classes: thermoplastics, which soften/melt when heat is applied and resolidify upon cooling; and thermosets, which do not soften/melt with the application of heat;
- Most polymers have time—temperature-dependent properties because the polymer chains ‘need time to move’ — ie, they are normally strain-rate-dependent.

1.7.3 Ceramics

- These are continuous, homogeneous materials with measurable microdefects, high compressive strength, but very low strain-to-failure, especially in tension (see Chapter 7);
- They normally have an isotropic microstructure and therefore display isotropic properties;
- Their bulk density is normally expressed as a percentage of theoretical density, since some porosity is invariably present;
- They are normally formed from dry ceramic powders with different morphologies and a range of powder size to assist the packing density;
- The processing of the material will determine the size and number of flaws within a material. The aim of good ceramic processing is to produce ceramics with a small number of small flaws in order to increase the reliability of the ceramic objects produced (see Chapter 7);
- Since defects will be present, ceramic objects with larger-size flaws will have lower strength than objects with small flaws for the same ceramic material;
- Weibull statistics are useful in describing the probability of failure of brittle materials. The Weibull modulus is the slope of a plot of $\ln \left[\ln \left(\frac{1}{1-PF} \right) \right]$ versus the natural logarithm of the applied stress and is indicative of the distribution of flaws in a material. A higher Weibull modulus means a more reliable material.

1.7.4 Fibres and textiles

- These are discontinuous, heterogeneous materials, manufactured from bundles of fibres (see Chapters 5 and 6);

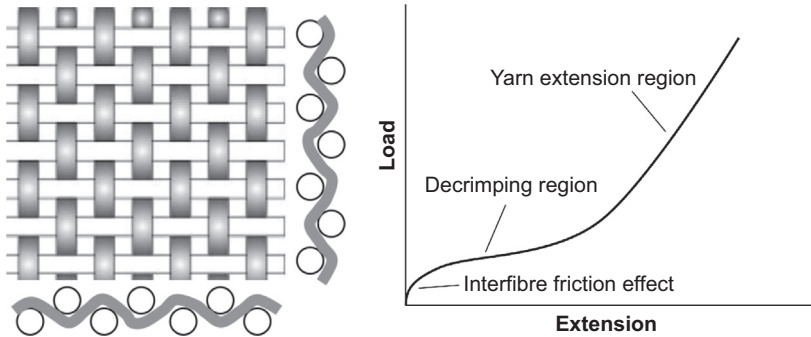


Figure 1.41 Typical form of a load–extension curve for a woven fabric.

- Tenacity is the term used to describe the tensile strength of fibres or yarns;
- An infinite variety of fabric types exist and they are normally described by weave style: woven, nonwoven, unidirectional, etc.;
- The fabrics are produced to a set width, and are characterised by weight (expressed in grams per square metre) and thickness;
- Drapeability is a global property of the fabric and an important parameter when working with fabrics, either as reinforcement (see Chapter 5) or as textiles (see Chapter 6);
- Their mechanical properties are very orientation-specific and strain-rate-sensitive. [Fig. 1.41](#) shows how different the stress–strain curves are compared with continuous materials (as shown in [Fig. 1.40](#)). In applying a tensile load the wavy fibres in a crimped woven fabric will want to straighten giving the characteristic shape to the early part of the stress–strain curve.

1.7.5 Structure–property–performance relationships

And finally, if there is one golden rule in material science, this is it: the material’s structure dictates its physical properties which, in turn, controls the way the material performs in a particular function. This is true whether the material is a fine-grained, orthotropic aluminium alloy or a multilayered, fibre-reinforced polymer. The alloying, or heat treatment, of metals, and the firing of ceramics are examples of techniques that can significantly change the properties of materials. Material scientists continually strive to understand the relationship between microstructure and mechanical properties. Hall and Petch, for example, developed the firm relationship between grain size and yield strength. Civil engineers use tables of physical and mechanical properties to design buildings and bridges, and aero-engineers base their aircraft designs upon a well-characterised set of physical and mechanical properties of carbon-fibre reinforced epoxy laminates. Composites in particular have an infinite range of properties dependent upon their processing route. So, processing of materials has a key influence over the structure–property relationship.

This triangular relationship is also true for all armour materials and systems. As [Fig. 1.42](#) shows, in the case of armour, the structure can be a simple plate of armour steel or a complex, ceramic-based armour system. Both microstructures and macrostructures obey this golden rule. Critical properties of those structures, such as section

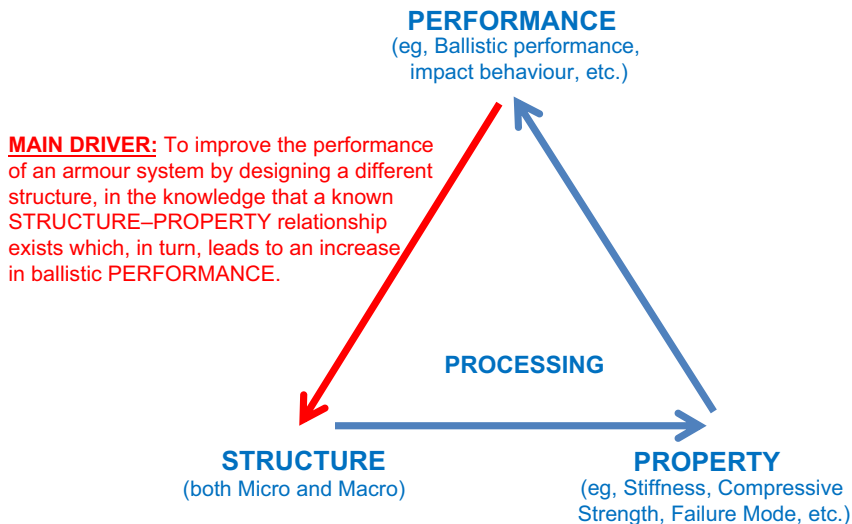


Figure 1.42 The golden triangle of material science, as applied to the design of improved armour systems.

modulus, through-thickness compressive strength and even mode of failure, will be dictated by the armour's structure but will also be affected by the environmental conditions, such as ambient temperature, relative humidity, UV radiation, as well as strain rate. In turn, this generic set of properties will govern performance: in this case, both ballistic performance and the behaviour of the material under ballistic impact. This underpinning, fundamental, triangular relationship, therefore, provides a pathway to drive innovation and performance improvement. As shown in Fig. 1.42 therefore, the main drive in the development of armour materials is to change the structure of the armour, in the full knowledge that the structural change will bring about a positive change in a relevant physical property of the system, which, in turn, will lead to an improvement in ballistic performance or impact behaviour. Of course, the prevailing environmental conditions will also affect the outcome. For example, the type of impact (namely, the type of weapon used) and the structural support conditions, operational at the time (for example, whether the armour is being simply or globally supported) will affect the ballistic performance of the system — these detailed, second-order relationships will be discussed in the following chapters.

It should not be forgotten that these armour materials also need to be well-proven engineering materials: not only do all armour materials have to function as an armour but they also have to perform, perhaps primarily, as an engineering material. For example, aluminium alloys need to be resistant to stress corrosion cracking, welded steels need to be resistant to fatigue failure, and ceramic materials need to be sufficiently rugged to withstand the vibrational loads of a military vehicle running across rough terrain. However, this textbook is *not* going to cover the engineering properties of all materials, per se, but will focus exclusively upon their abilities to function as an armour material.

Acknowledgements

The author is indebted to Dr Stephen Cimpoeru, of the Defence Science and Technology Group, Australia, and David Ritzel of Dyn-FX Consulting, for kindly offering precise wording for [Section 1.2.4](#) on blast and to Ben Eu, General Manager, Ballistic and Mechanical Testing, Melbourne, for providing some of data on small arms ammunition.

References

- Anon, 2009. Shot Soldier's Body Armour Praise. http://news.bbc.co.uk/2/hi/uk_news/wales/mid_/8089181.stm.
- Anon, 2012. Australian Department of Defence Website. images.defence.gov.au.
- Anon, 2014. Iraq Coalition Casualty Count. <http://icasualties.org>.
- Baker, W.E., 1973. Explosions in Air. University of Texas Press, Texas, USA.
- Ball, A., McKenzie, H.W., September 1994. On the low velocity impact behaviour of glass plates. *Journal de Physique IV; Colloque C3*, 4, 783–788.
- Borvik, T., et al., 2003. Effect of target thickness in blunt projectile penetration of Weldox 460E steel plates. *International Journal of Impact Engineering* 28, 413–464.
- Brady, C.G., 2003. An Analysis of Wound Statistics in Relation to Personal Ballistic Protection. DSTO Technical Note #0510, August 2003.
- Carton, E.P., Weerheijm, J., Ditzhuijzen, C., Tuinman, I., 2014. Fragment and particle size distribution of impacted ceramic tiles. In: Paper Presented at the 28th International Symposium on Ballistics, Atlanta, GA, USA, September 2014.
- Cebon, P., Samson, D., 2010. DSTO-GD-0738: Diggerworks - Driving Innovation and Effectiveness in the Defence Sector; a Study of Success Factors. Department of Defence, Canberra, Australia.
- Cimpoeru, S.J., Phillips, P., Ritzel, D.V., 2015. A systems view of vehicle landmine survivability. *International Journal of Protective Structures* 6, 137–153.
- Crouch, I.G., 1992. Discing failures in both traditional and composite armour materials. In: Paper Presented at the International Symposium on Ballistics, Stockholm, June 1992.
- Crouch, I.G., 1993. Penetration and perforation mechanisms in composite armour materials. In: Paper Presented at the Euromech Colloquium 299, Oxford University, March 1993.
- Crouch, I.G., 2009. Threat defeating mechanisms in body armour systems. In: Paper Presented at the Next Generation Body Armour, London, September 2009.
- Crouch, I.G., 2014. Effects of cladding ceramic and its influence on ballistic performance. In: Paper Presented at the International Symposium on Ballistics, Atlanta, GA, USA, September 2014.
- Crouch, I.G., Appleby-Thomas, G., Hazell, P., 2015a. A study of the penetration behaviour of mild-steel-cored ammunition against boron carbide ceramic armours. *International Journal of Impact Engineering* 80, 203–211.
- Crouch, I.G., et al., 2014. Stab and Spike Armour Materials - a Review of the Scientific Literature and Commercially Available Materials. DMTC internal report, dated December 2014.
- Crouch, I.G., Kesharaju, M., Nagarajah, R., 2015b. Characterisation, significance and detection of defects in Reaction Sintered Silicon Carbide armour materials. *Ceramics International* 41, 11581–11591.

- De'ath, J.M., Proud, W.G., Millet, J.C.F., Appleby-Thomas, G.J., 2011. Phase change in 080M40 plain carbon steel. *Shock Compression of Dense Matter* 2011, 1537–1540.
- Deshpande, P.U., Prabhu, V.D., Prabhakaran, K.V., 2003. Impulsive loading of armour by high explosive squash head munition. *Defence Science Journal* 53 (4), 357–365.
- Doig, A., 1998. *Military Metallurgy*. Maney Publishing, London.
- Elder, D., 2012. The DMTC KBE-based, Analytical Model for Predicting Second Round Impact Behaviour and Ballistic Performance. DMTC internal report, dated August 2012.
- Fellows, N.A., Barton, P.C., 1999. Development of impact model for ceramic faced, semi-infinite armour. *International Journal of Impact Engineering* 22, 793–811.
- Fenne, P., 2008. Police body armour: the problem and the solution. In: Paper Presented at the Materials in Armour Systems, London, UK.
- Fenne, P., 2009. Can the key design aims for body armour for police officers be achieved?. In: Paper Presented at the Next Generation Body Armour, London, UK.
- Field, J.E., Sun, Q., Townsend, D., 1989. Ballistic impact of ceramics. *Institute of Physics Conference Series* 102, 387–393.
- Gooch, W.A., 2002. An overview of protection technology for ground and space applications. In: Paper Presented at the NATO Applied Vehicle Technology Panel, Aalborg, Denmark, September 2002.
- Hainsworth, S.V., Delaney, R., Rutty, G., 2008. How sharp is sharp? Towards quantification of the sharpness and penetration ability of kitchen knives used in stabbings. *International Journal of Legal Medicine* 122 (4), 281–291.
- Hameed, A., Hetherington, J.G., Brown, R.D., 2004. Design trends in the development of large-calibre kinetic energy rounds. *Journal of Battlefield Technology* 7 (3), 9–16.
- Hazell, P.J., 2015. Stress waves. In: Hazell, P.J. (Ed.), *Armour: Materials, Theory and Design*. CRC Press, Florida, pp. 137–175.
- Horsfall, I., 2000. *Stab Resistant Body Armour* (Ph.D. thesis). Cranfield University, Shrivenham, UK.
- Horsfall, I., 2009. Human vulnerability. In: Paper Presented at the Next Generation Body Armour, London, UK.
- James, B.J., 2009. Armour and protection: science and technology centre. In: DSTL Presentation, October 2009.
- Kelly, J.F., et al., 2008. Injury severity and causes of death from Operation Iraqi Freedom and Operation Enduring Freedom: 2003–2004 versus 2006. *The Journal of Trauma* 64 (2), 21–27.
- Kocer, C., 2003. Using the Hertzian fracture system to measure crack growth data: a review. *International Journal of Fracture* 121, 111–132.
- Laible, R., 1980. *Ballistic Materials and Penetration Mechanics*. Elsevier Scientific Publishing Company, Amsterdam.
- Lane, R., Craig, B., Babcock, W., 2002. Materials for blast and penetration resistance. *The AMPTIAC Quarterly* 6 (4), 39–45.
- Lawn, B., Wilshaw, R., 1975. Review: indentation fracture - principles and applications. *Journal of Materials Science* 10, 1049–1081.
- Louro, L.H.L., Meyers, M.A., 1988. Stress waves induced damage in alumina. In: Paper Presented at the DYMAT 88, Ajaccio, France.
- Louro, L.H.L., Meyers, M.A., 1989. Shock-induced fracture and fragmentation in alumina. In: Paper Presented at the Shock Waves in Condensed Matter 1989.
- Mascianica, F.S., 1980. Ballistic testing methodology. In: Laible, R. (Ed.), *Ballistic Materials and Penetration Mechanics*. Elsevier Scientific Publishing Co., Amsterdam.

- Masters, C., 2012. *Uncommon Soldier: Brave, Compassionate and Tough; the Making of Australia's Modern Diggers*. Allen and Unwin, Sydney, Australia.
- Meyers, M.A., 1994. *Dynamic Behavior of Materials*. John Wiley & Sons, Inc., New York.
- Mott, N.F., 1947. *Proceedings of the Royal Society of London* 300, 300.
- Naebe, M., Sandlin, J., Crouch, I.G., Fox, B., 2011. Novel lightweight polymer ceramic composites for ballistic protection. In: Paper Presented at the ICCS 16, Porto, Portugal, 2011.
- Nolan, G., et al., 2012. A study considering the force required for broken glass bottles to penetrate a skin simulant. *International Journal of Legal Medicine* 126 (1), 19–25.
- Ogorkiewicz, R., 2015. *Tanks: 100 Years of Evolution*. Osprey Publishing, Oxford, UK.
- Rosenberg, Z., Dekel, E., 2012. *Terminal Ballistics*. Springer-Verlag, Berlin.
- Sherman, D., 2000. Impact failure mechanisms in alumina tiles on finite thickness support and the effect of confinement. *International Journal of Impact Engineering* 24, 313–328.
- Simmons, M.J., Smith, T.F., Crouch, I.G., 1989. Delamination of metallic composites subjected to ballistic impact. In: Paper Presented at the 11th International Symposium on Ballistics, Brussels, Belgium, May 1989.
- Specification, 2006. MIL-DTL-46593B (MR), Projectile, Calibers 22, 30, 50 and 20 mm Fragment Simulating Projectiles.
- Sternberg, H.M., Hurwitz, H., 1976. Calculated spherical shock waves produced by condensed explosives in air and water. In: Paper Presented at the 6th Symposium on Detonation, ONR, Arlington, 1976, pp. 528–539.
- Stronge, W.J., 2000. *Impact Mechanics*. Cambridge University Press, Cambridge.
- Walley, S.M., Field, J.E., 2005. The contribution of the Cavendish Laboratory to the understanding of solid particle erosion mechanisms. *Wear* 258, 552–566.
- Woodward, R.L., 1978. The penetration of metal targets by conical projectiles. *International Journal of Mechanical Sciences* 20, 349–359.
- Woodward, R.L., March 1979. Penetration behaviour of a high strength aluminium alloy. *Metals Technology*.
- Woodward, R.L., O'Donnell, R.G., Baxter, B.J., Nicol, B., Pattie, S.D., 1989. Energy absorption in the failure of ceramic composite armours. *Materials Forum* 13, 174–181.
- Yaziv, D., 2008. Advanced add-on armour systems for combat vehicles. In: Paper Presented at the Land Warfare Conference, Brisbane, Australia, October 2008.
- Zeng, K., Breder, K., Rowcliffe, D.J., 1992. The Hertzian stress field and formation of cone cracks - 1: theoretical approach. *Acta Metallurgica and Materials* 40 (10), 2595–2600.
- Zukas, J.A., 1982. *Impact Dynamics*. Wiley, New York.
- Zukas, J.A., 1990. *High Velocity Impact Dynamics*. Wiley, New York.

I.G. Crouch¹, S.J. Cimpoeu², H. Li³, D. Shanmugam⁴

¹Armour Solutions Pty Ltd, Trentham, Victoria, Australia; ²Defence Science and Technology Group, Fishermans Bend, Victoria, Australia; ³University of Wollongong, NSW, Australia; ⁴Thales, Bendigo, Victoria, Australia

2.1 Introduction

2.1.1 Brief history: from ‘Little Willie’ to ‘Bushmaster’

Both the selection and development of suitable armour to protect the fighting armies of the world have always been highly specialised areas for metallurgists to exercise their technical skill and judgement (Crouch, 1988). Since the early days of ‘Little Willie’, the 18-tonne, all-steel vehicle recognised as being the world’s first military tank built in 1915, the design and constitution of a vehicle’s armour have played a significant role in attaining that highly desirable competitive edge which is sought by both users and manufacturers of armoured fighting vehicles.

In response to the numerous casualties in the early years of the First World War (WW1), Winston Churchill, then First Lord of the Admiralty, created a Landships Committee in 1915 to tackle the problems of trench warfare — this led to the evolution of Little Willie (see Fig. 2.1) which, by today’s standards, was a very lightly clad, box-like structure, with no main gun, and simply constructed of riveted steel plates. It was designed to house six personnel (two crew and four gunners), and was built by William



Figure 2.1 Little Willie, being trialed at Burton Park, 3 December 1915. Reproduced from: Anon., 2014. Bovington Tank Museum database.

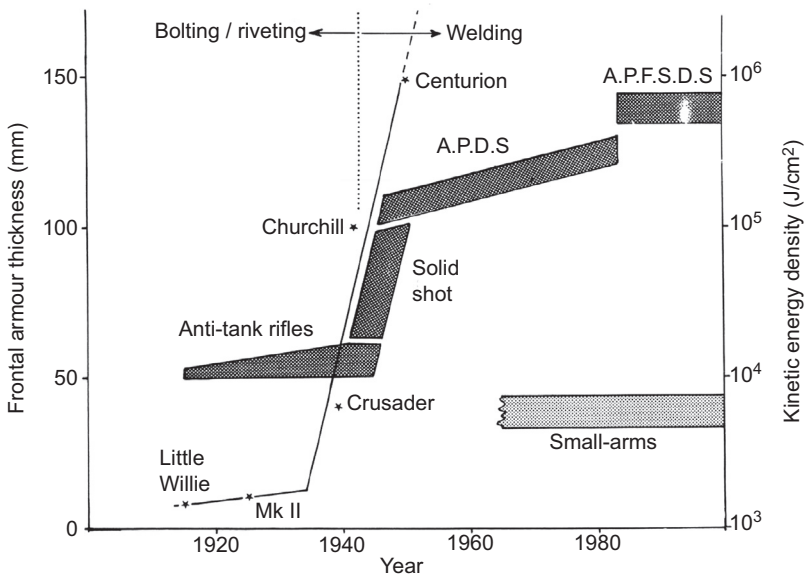


Figure 2.2 History of tank armour and kinetic energy (KE) penetrators.

After Crouch, I.G., 1988. Metallic armour — from cast aluminium alloys to high strength steels. *Materials Forum* 12, 31–37; Jones, P.N., 1984. *The Metallurgist and Materials Technologist* 16, 465.

Foster and Co., a small agricultural firm in Lincolnshire, England. However, it never actually saw active duty: it was quickly superseded by other more superior designs and currently resides, undamaged (without a bullet hole in sight), at the Bovington Tank Museum, Dorset, UK. From data compiled by Jones (1984), its frontal armour was no more than about 10 mm in thickness. The grade of steel used was certainly not chosen primarily for its bullet resistance, but more because of its availability. It was described as ‘0.39 in. of Boiler Plate’ (Anon, 2014) and, although the actual grade is not known, it was probably supplied to one of the early ASME codes, like SA516, and therefore of high quality.

Fig. 2.2 shows the impact that the Second World War (WW2) had on the accelerated development of steel armour, at least in terms of thickness. This rapid increase in frontal armour thickness was necessary to meet (and defeat!) the rapid development in large-calibre, solid steel projectiles of the early 1940s (eg, the 2-, 6- and 17-pounder shots). WW2 also spawned the introduction of the first fusion-welded tank, the Churchill Mk7 (Wilson, 1978). From that vehicle to the streamlined, high-performance Challenger, the UK’s most recent main battle tank (MBT), armoured fighting vehicles, designed for the front line, have been heavy, welded, steel constructions.

The Chieftain MBT, designed and built in the early 1960s, was the last UK tank to be constructed using thick monolithic grades of armour steel. The highly curved, turret castings, each weighing approximately 6 tonnes, were large, thick-walled structures.



Figure 2.3 UK Challenger II tank on a firing exercise in Wales in 2014.

Yet, 20 years later, during a conflict between Iran and Iraq, even this thickness was found to be inadequate and an up-armouring kit had to be quickly developed. This requirement was met by the addition of the Stillbrew appliqué system (Anon, 1986).

By the 1980s, and with the advancement in kinetic energy weapons, with the development of Fin Stabilised Armour Piercing Discarding Sabot (FSAPDS) rounds, a more advanced concept of tank was required. The UK's Challenger tank, shown in Fig. 2.3, was the first of this new generation: weighing 62 tonnes, and capable of speeds of up to 50 km/h, it was fitted with a 120 mm L11A5 rifled gun, suitable for firing both APDS and FSAPDS ammunition. The quantum jump in energy density (see Fig. 2.2) brought about by the development of the subcalibre, long-rod rounds (eg, FSAPDS rounds), with their highly dense cores of tungsten or depleted uranium, took the level of protection, then required, beyond the practical capabilities of thick, monolithic materials. Armour, for the heavy main battle tanks, moved into the realms of sophisticated, special armours, like Chobham Armour, which gives the Challenger its high level of protection.

Whether special armours are used or not, the basic structure of any armoured fighting vehicle needs to be engineered from monolithic, armour-grade materials (normally steel) that will operate in service, without any metallurgical problems, for perhaps 30 years or more. These structural armour steels selected and developed to operate within such a hostile environment are typically medium-carbon grades of high-quality, reasonable hardenability and are normally represented by the Mn–Mo, Cr–Mo or Ni–Cr–Mo–(V) low-alloy steels (Doig, 1979). The additional need for these structural grades to be weldable restricts their total alloy content to a carbon equivalent (CE) of less than 1, typically around 0.8. The steels are produced by approved manufacturers under conditions of strict quality control to very tight specifications. Product forms are typically sand castings, as used for most shaped items like turrets, mantlets and hatch-covers, or rolled plate, known as rolled homogeneous armour (RHA). Most hull constructions are welded fabrications. The RHA plate,



Figure 2.4 The Bushmaster from Australia operating in Iraq (2005).
Photo: Cpl Cameron Jamieson (Thales, Bendigo).

required in sections of up to 100 mm or more, is usually heat-treated to give a tempered martensitic microstructure, which is optimised for strength and toughness.

At the other end of the scale, many armoured personnel carriers (APCs) are designed and built using relatively thin plates of weldable structural steels, since these are only designed to protect the occupants from small arms ammunition, which has a much lower kinetic energy density (see Fig. 2.2). One such vehicle is the Australian Bushmaster (Fig. 2.4); designed during the early 1990s, early prototypes were deployed into East Timor in 1999 and eventually accepted into Australian Defence Force (ADF) service in 2006. Thales at Bendigo in Victoria has built more than 1000 vehicles. Designed with a V-shaped undercarriage to better withstand the blasts from mines, the vehicle utilises two grades of steel: one grade for the underbelly, which needs to optimise blast performance; one grade for the sides, which needs to be optimised for bullet resistance.

Strangely enough, these vehicles use similar steels to those used in Little Willie — however, the ballistic protection of today's armour steels are far superior to the boilerplate used in 1915!

The on-going conflict in the Middle East between Israel and Palestine over the past few decades has driven the Israelis, in particular, to develop extremely novel and inventive armour solutions, especially in the area of up-armouring kits. Typically, these kits are used to clad the M113 series of lightweight, aluminium-based, box-like vehicles and include systems such as Toga and varieties of bar-armour (see Section 1.7). Toga was an interesting system that was fielded on the IDF's M113 Zelda (see Fig. 2.5). It utilised perforated steel plates for the very first time. As discussed in Chapter 1 (Section 1.7) these plates are perforated with holes that are actually larger than the calibre of typical small arms ammunition. However, the appliqué is designed to deflect bullets, not stop them. Of course, the plates are lighter in weight, but what grade of armour steel would be best to use for this application, and how might the holes have been manufactured?



Figure 2.5 Israeli M113 fitted with Toga perforated armour system.

The most recent developments in ultrahigh-hardness (UHH) steel armours, especially for appliqué systems, have also been driven by demand from the most recent conflicts in Iraq and Afghanistan. For example, the latest version of the US specification, MIL-DTL-32332, was released in 2009, as a result of considerable research carried out by both manufacturers, like SSAB, and research laboratories, like ARL in the US (Showalter et al., 2008), during the early 2000s.

Because weight is such a critical factor in many vehicle projects, whether it is for structural or appliqué applications, the aim for researchers and steel developers alike is to offer the highest possible mass efficiency. This is what drives the need for steels with higher and higher hardness values. However, this drive needs to be tempered by serious consideration for application and associated, overriding, engineering requirements.

In summary, the following schematic (Fig. 2.6) illustrates the wide range of steels that have been developed for the whole gamut of applications to a military vehicle. Note the different hardness ranges for the different applications.

2.1.2 Ferrous alloys generally (mild steels to cast irons)

Most people will have observed (not firsthand!) how the thin, mild steel bodies of saloon cars are peppered with holes from typical shotgun or handgun rounds, like the 9 mm Parabellum. Cold-rolled, mild steel sheets, in thicknesses around 1–2 mm, offer very little ballistic protection and the resulting perforations are nothing more than witnesses to an attack, as was aptly demonstrated in recent work by Durmas et al. (2011) (Fig. 2.7).

The steel sheet simply gets punctured, with a limited amount of local deformation (dishing — see Chapter 1), and a cap of steel which gets sheared out, ahead of the bullet — there is also very little deformation to the bullet itself!

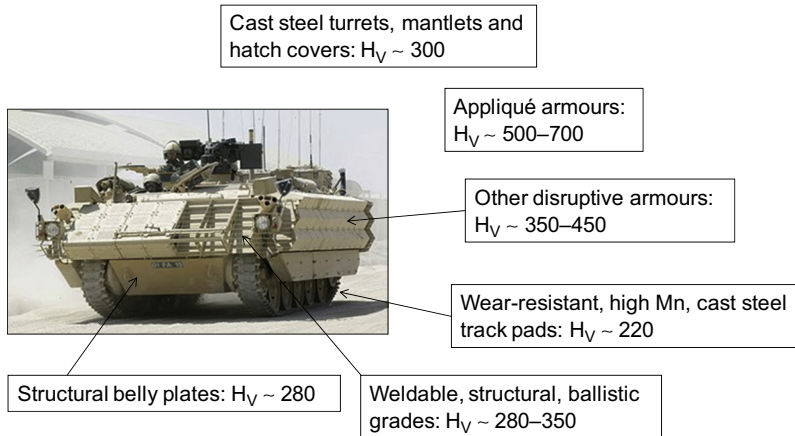


Figure 2.6 Family of armour steels. Image is of a UK FV432 fitted with various appliqué systems over a welded structural steel hull. Note: not all families of armour steels were employed on this vehicle.



Figure 2.7 Images extracted from Durmas' work, showing perforation of a 1 mm thick mild steel sheet (front, rear and side views) as well as the undeformed 9 mm round and the sheared caps.

Reproduced from: Durmas, A., Guden, M., Gulcimen, B., Ulku, S., Musa, E., 2011.

Experimental investigations on the ballistic impact performances of cold rolled sheet metals. Materials and Design 32 (2011), 1356–1366.

So, what grade of steel does make a good armour material? In general, this will be a grade of steel with a high flow stress and high stiffness (either by section or through elastic modulus). Since all steels have a very similar value for elastic modulus (around 210 GPa), an increase in stiffness must come about through increased thickness. A high flow stress means higher carbon content and, with reference to the classical Fe–C phase diagram (Fig. 2.8), contents up to $\sim 2\%$ might be considered.

At the very low carbon content end of the spectrum (less than 0.3%), the plain carbon steels have a ferritic microstructure, which is relatively soft and of low yield strength. At the high end, is the family of cast irons, which are too brittle to be used as armour materials, although certain grades could potentially be suitable as appliqué armours. Of course, cast irons are more suited to penetrators like cannon balls or fragmenting shells, as in High Explosive Squash Head (HESH) rounds and hand-grenade cases.

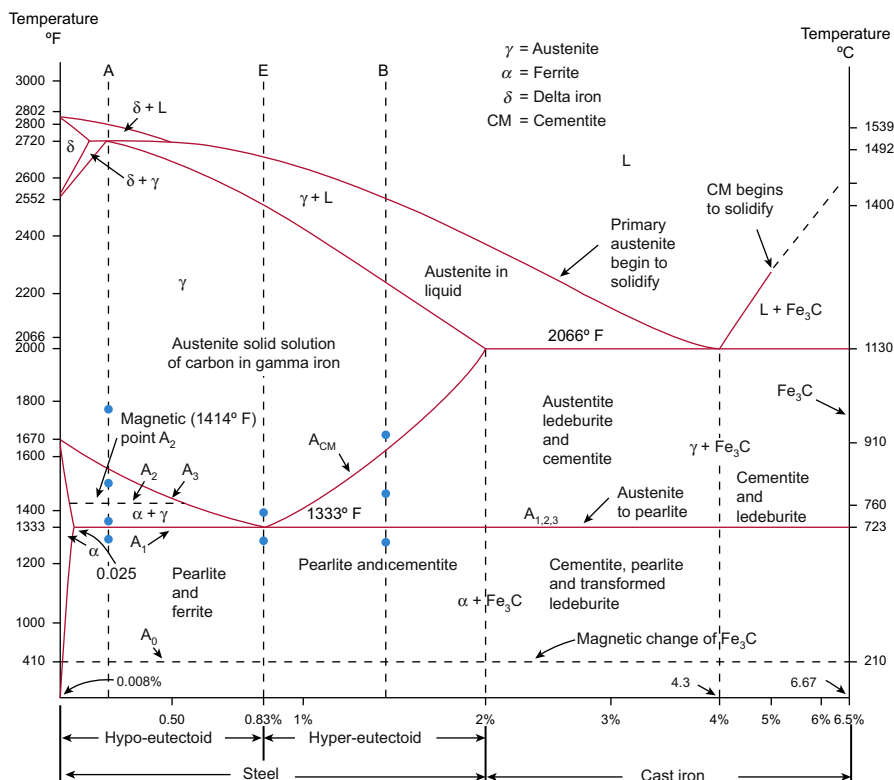


Figure 2.8 Typical Fe–C phase diagram.

The earliest monolithic armours were derived from naval steels of the late 19th century as reported by [Jones \(1907\)](#). These naval armour steels were based upon 0.25% C, Ni–Cr steels that were suitable for face-hardening, using a cementation process. Such dual-hardness steels are discussed further in [Section 2.4.3](#). The steels possessed a tempered martensitic structure.

As reported by [Edwards and Mathewson \(1997\)](#), a broad-based review of alloys for armour, carried out by the UK Ministry of Supply in 1941, emphasised the need for careful processing, using electric arc manufacture, in order to prevent cracking and spallation of the armour at hardnesses greater than about 300 HB for thick armour. In their own work on tool steels, with a carbon content of 0.95%, Edwards identified the classic limitations in UHH steels, namely cracking and discing failures. In the fully hardened condition, with hardnesses between 510 and 710 HV, all targets suffered from gross cracking, whereas when tempered back to 380 HV, the tool steels had similar ballistic performance to conventional RHA (see [Table 2.1](#)).

But, why are the martensitic steels so popular, and effective, as armour materials? Is it simply because they represent the strongest grades with the highest yield stress? In a

Table 2.1 Results from a study of tool steels (0.95% C) as candidate grades of steel armour

ID	Grade of steel	Hardness (Hv)	AD (kg/m ²)	Threat	V-50 (m/s)	Failure mode
1	Tool steel (Q&T)	386	39	7.62 × 39 mm MSC (AK47)	707	Petalling/ discing
2	Tool steel (annealed)	200	39	7.62 × 39 mm MSC (AK47)	578	Petalling
3	Mild steel	133	39	7.62 × 39 mm MSC (AK47)	466	Petalling
4	Tool steel (Q&T)	364	78	7.62 mm FFV	588	Petalling/ discing
5	Tool steel (annealed)	200	78	7.62 mm FFV	502	Petalling
6	RHA	340	78	7.62 mm FFV	520	Petalling

MSC, mid steel cored.
Reproduced from: Edwards, M.R., Mathewson, A., 1997. The ballistic properties of tool steel as a potential improvised armour plate. *International Journal of Impact Engineering* 19 (4), 297–309.

detailed study by [Kasonde \(2006\)](#), he investigated a number of metallurgical variables thought to influence ballistic performance:

- Alloying content, and its affect upon hardenability;
- Type of martensite, and both transformation start (M_s) and finish (M_f) temperatures;
- Levels of retained austenite.

[Table 2.2](#) lists the typical alloying elements added to steels and summarises the effect that their presence has on properties, some of which may affect ballistic behaviour or ballistic performance. In addition, [Atapek \(2013\)](#) investigated a different compositional variation, using cobalt additions of ~2.4%, compared to conventional Ni additions (only 0.04%), based on a 0.23% C steel and showed that the V-50 against 7.62 mm APM2 rounds was ~780 m/s for a 12.7 mm thick steel plate. Adiabatic shear bands (ASB) were observed and the steel appeared to perform in an expected manner.

Hardenability is a very important aspect when designing an armour steel. Whilst hardness is by far the most important and, as we will learn in [Section 2.2.2](#), especially dynamic compressive yield strength, it is critically important that the steel has high strength throughout its thickness. If achieved, this will maximise penetration resistance and, in turn, enhance the ballistic performance of the steel.

Of course, hardenability is related to section size: the thicker the steel, the more hardenability is required to guarantee through hardening. So, a different balance of alloying elements is used for steels of different thicknesses — see [Sections 2.4 and 2.5](#). This is especially true for very thick sections. It is also sometimes

Table 2.2 Summary of effects of alloying additions upon the properties of steel that may affect ballistic performance

Element	Metallurgical effect
C	<ul style="list-style-type: none"> Increases microhardness of martensite Increases volume fraction of retained austenite, after quenching Affects weldability
Mn	<ul style="list-style-type: none"> Improves hardenability Weak carbide former
Mo	<ul style="list-style-type: none"> Metastable formation of Mo_2C which dissolves at 700°C and above Possible effect upon hardenability
Ni	<ul style="list-style-type: none"> Solid solution hardening Increases the precipitate/matrix misfit by modifying the lattice spacing Grain refiner Decreases Ductile Brittle Transition Temperature (DBTT) Strongly decreases A_{C1} temperature
Cr	<ul style="list-style-type: none"> Retards softening from Fe_3C, by forming M_3C Increases hardenability, especially with $>5\%$
V	<ul style="list-style-type: none"> Promotes fine grain size Increases hardenability
Cu	<ul style="list-style-type: none"> Increases matrix precipitation
Si	<ul style="list-style-type: none"> Delays the decomposition of martensite Reduces the lattice spacing of the ferritic matrix
N	<ul style="list-style-type: none"> Increases hardenability Decreases M_s Forms carbonitrides
S	<ul style="list-style-type: none"> Segregates to grain boundaries Forms deleterious MnS particles/stringers
P	<ul style="list-style-type: none"> Segregates to grain boundaries and encourages intergranular fracture

Based upon Kasonde, M., 2006. Optimizing the Mechanical Properties and Microstructure of Armoured Steel Plate in Quenched and Tempered Condition (M.Sc. thesis). University of Pretoria, South Africa.

desirable to develop a martensitic microstructure simply through air-cooling an austenitised structure, to avoid excessive distortion or to minimise residual stress content. Quantifying the hardenability of a candidate armour alloy steel is therefore critically important.

Hardenability curves, like that in [Fig. 2.9](#), can be derived using the standard Jominy End–Quench test method ([Jominy and Boegehold, 1938](#)) and a hardenability index (DI) assigned to all grades of steel. For every thickness of armour steel plate, the DI needs to be high enough to guarantee complete through hardening.

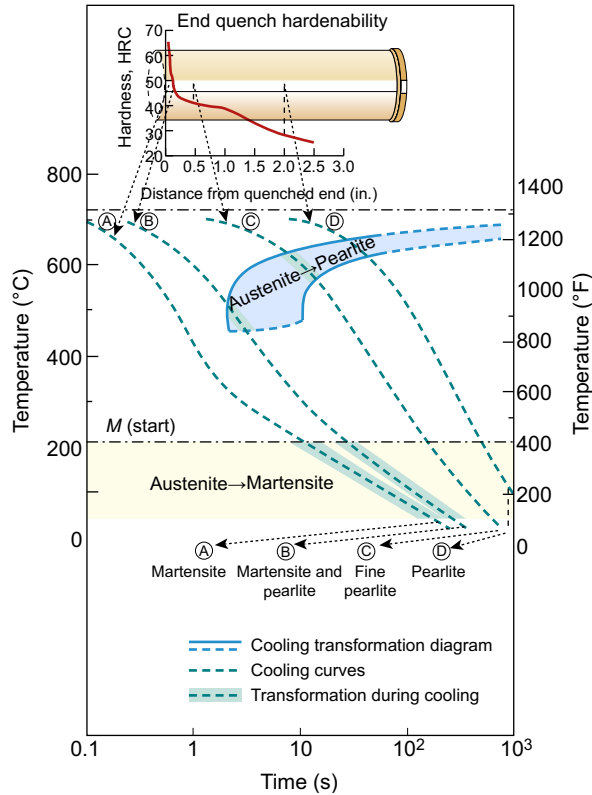


Figure 2.9 Typical hardenability curve.

2.2 Beneficial properties of armour steels

2.2.1 Microstructural aspects

It is now duly recognised that a tempered martensitic structure throughout the entire thickness of a plate of armour steel is fundamentally important. But, what about second-order effects, especially microstructural features?

In Chapter 1, we learnt that preventing premature through-thickness failure modes like delamination and discing was important in order to maximise ballistic protection. So, at a microstructural level, what metallurgical features can be designed-in to minimise these unacceptable failure modes?

2.2.1.1 Grain size and shape

Grain size is important, as the traditional Hall–Petch equation (Hall, 1951; Petch, 1953) tells us: yield strength is inversely proportional to the square root of grain

size. So, a very small grain size is required since grain size affects hardenability as well as key plastic flow characteristics.

However, wrought steels, just like laminated composites, are also orthotropic materials, because their rolled or forged microstructure leads to flat, pancake-shaped grains running parallel to the forming direction. Rolling practices can also generate texture within the grains, such that specific crystallographic orientations are preferred. Grain shape, in turn, gives rise to this variation in mechanical properties as a function of direction. For example, tensile properties, in rolled plates, are normally significantly better in the longitudinal and transverse direction than in the short transverse (ST) direction. In fact, the fracture toughness in the ST orientation can be quite poor as a result of these grain shape effects. Small, equiaxed grains are therefore highly desirable in an armour steel.

2.2.1.2 *Microsegregation of alloying elements*

In Fig. 2.10, of the microstructure of a 3% low alloy steel, microsegregation banding of alloying elements is very clear. There are alternate bands of rich and poor alloying content, which are remnants of dendritic and interdendritic regions from the original cast ingot: still evident, even after extensive thermomechanical reduction via hot-rolling. This type of banding needs to be avoided through better steelmaking practices since it can lead to much lower Charpy V-notch data, particularly in the ST direction.

2.2.1.3 *Size and distribution of carbides*

In general, since a transgranular fracture path is more energy-absorbing than an intergranular fracture, it is more desirable for inherent carbide particles to be located within the grains rather than along grain boundaries. A fine dispersion of small carbides is also more attractive than a coarse distribution of large carbides. The same applies to other precipitates, as well.

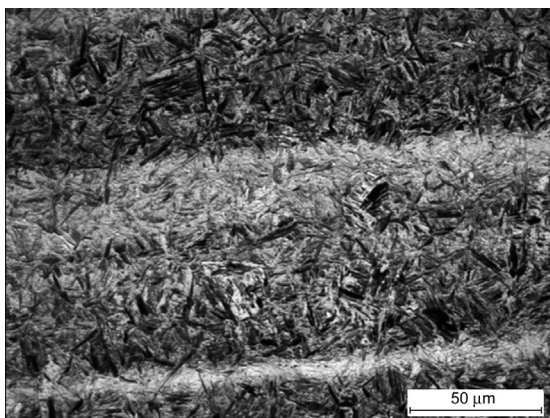


Figure 2.10 Micrograph of armour steel showing microsegregation.

2.2.1.4 Size and shape of manganese sulphide stringers

Nonmetallic inclusions are, in general, undesirable. However, if inclusions like manganese sulphide (MnS) stringers are present, the ST properties can be extremely poor and the propensity for discing and delamination failures increases.

These MnS stringers form during the steelmaking process but can be significantly reduced by remelting the steel, under a reducing slag in an electric arc furnace – the electroslag refining (ESR) process (see Section 2.4.4). This reduces the sulphur (and phosphorus) levels in the steel ingot that, in turn, reduces the volume fraction of MnS particles. ST properties are improved and, in summary, premature discing, scabbing and delamination events can be avoided. According to Doig (1998), ballistic trials showed that ESR steel plates would not scab, making them proof against HESH rounds. To achieve very low sulphur levels, expensive metallurgical techniques have to be introduced, together with measures for sulphide shape control. Lower levels of Mn allow higher sulphur content without extensive formation of MnS. A low Mn approach (0.20–0.50 wt% Mn) has been developed mainly to reduce centreline segregation and improve the mechanical properties, through lowering the volume of MnS inclusions present in the material.

2.2.1.5 Characteristics of martensite

From recent work by Kasonde (2006) it has been demonstrated that steels with high martensitic transformation start temperatures, M_s , performed poorly in ballistic tests (see Table 2.3). M_s values are affected by composition, magnetic character of the

Table 2.3 Summary of ballistic data for a range of high-strength steels, based upon 0.4% C, 4% Ni, 2% Mn, 1% Cr, against 5.56 mm soft-cored ammunition

Steel	Thickness (mm)	Hardness (VPN)	Measured M_s value	Retained austenite (V_f)		Ballistic limit (m/s)
				Before	After	
P	4.7	580	115	6.0	<0.5	>955
Q	4.9	615	178	4.0	<0.5	>948
R	5.1	610	170	5.0	<0.5	>947
S	5.2	578	182	3.0	<0.5	>947
T	5.4	610	184	0.6	<0.5	<935
U	4.9	578	170	2.0	<0.5	>961
V	5.1	595	145	5.3	<0.5	>952
W	4.8	565	130	6.0	<0.5	>942

After Kasonde, M., 2006. Optimizing the Mechanical Properties and Microstructure of Armoured Steel Plate in Quenched and Tempered Condition (M.Sc. thesis). University of Pretoria, South Africa.

austenite, quench rate, stacking fault energy and shear strength of the austenite. Furthermore, the range of low-alloy steels, as given in Table 2.3, also illustrated transformation-induced plasticity (TRIP) of the retained austenite to martensite upon impact together with a transition from twinned plates of martensite to slipped lath martensite. This TRIP effect is thought to consume a significant amount of kinetic energy but optimum performance is achieved with only a small volume fraction of retained austenite in the microstructure. TRIP steels are described in more detail in Section 2.4.5.4.

2.2.1.6 Retained austenite

It would appear from results in Table 2.3 that a finite amount of retained austenite in a martensitic structure is beneficial in terms of the ballistic performance of thin steels (~ 5 mm in thickness) against small arms ammunition.

In summary, the latest evidence suggests that, for a steel to confer maximum ballistic protection, it should possess the following qualities:

- A through-hardened steel of uniform high hardness;
- A fine, equiaxed grain size, free from any microsegregation;
- An absence of MnS stringers;
- A martensite start temperature of less than 210°C ;
- A volume fraction of retained austenite of $>1\%$, in a bed of plate martensite.

2.2.2 Hardness, strength and toughness

Since the 1970s (Manganello and Abbott, 1972) and summarised by Dino Papetti in 1980 (Laible, 1980), a general relationship has been identified between hardness, as a crude measure of a steel's flow properties, and ballistic performance, against small arms, armour-piercing ammunition. Fig. 2.11, from Crouch (1988), shows an upwardly trending relationship but one which is very dependent upon the prevailing failure mode. These have been described, in depth, in Chapter 1.

At low values of hardness, plastic flow controls performance and the steel fails through ductile hole formation (DHF) – Mode A in Fig. 2.11. As target strength increases, localised failure by through-thickness shearing becomes more likely and the steel eventually fails by soft-plugging (Mode B) with the core of the AP round still intact. The point at which this transition occurs, and the magnitude of the degradation, will depend not only on the quality and grade of steel but also on the geometry of both target and projectile. Plugging failures are quite common when t/D ratios are close to one. Cleaner steels, manufactured by electro slag refining, or more recently through advanced ladle metallurgical practices, have been shown to delay this transition (Rawson and Dawson, 1972). As hardness is increased even further, there comes a time when the steel core will begin to erode, and/or fracture, and the shape of its ogival nose will be blunted. The blunted nose shape strongly encourages plugging failure – a failure mode called hard-plugging (Mode C). Little plastic deformation of the target occurs and most of the impact energy will be dissipated as the projectile erodes. Generally speaking, in this hardness regime, the harder the target, the greater the erosion, the

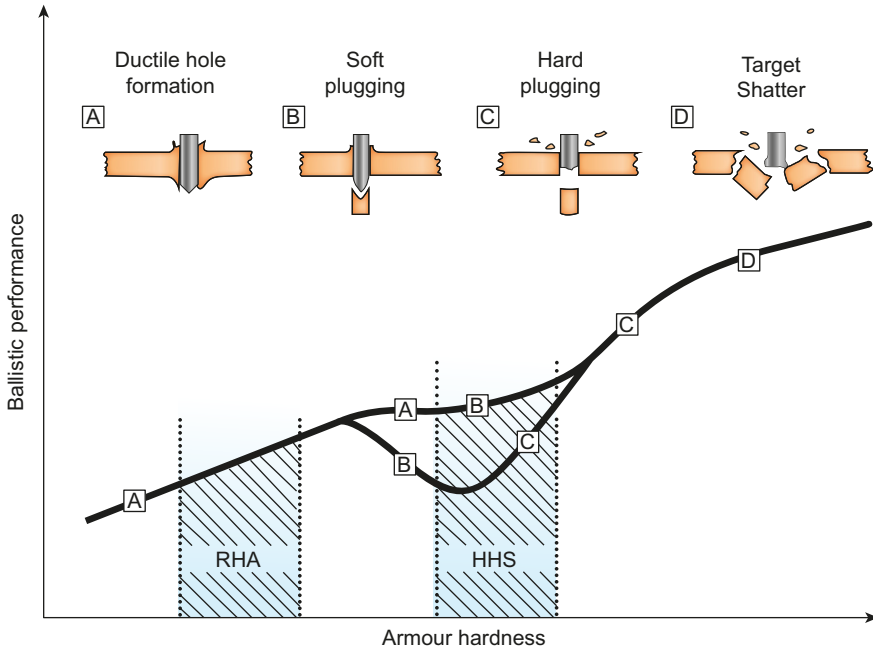


Figure 2.11 A schematic illustration of the general relationship between target hardness and ballistic performance for the family of armour steels. Performance is very much related to the failure mode(s) which are operative within a particular hardness range. The relative ranges are shown for the rolled homogenous armours (RHA) and the high-hardness steels (HHA). After Crouch, I.G., 1988. *Metallic armour – from cast aluminium alloys to high strength steels*. Materials Forum 12, 31–37.

better the ballistic performance will be. Still further up the hardness scale there is a natural ceiling to this relationship for, when toughness has diminished to such a low level, the target itself simply shatters in a very brittle manner and offers no structural support. Whilst ballistic performance may theoretically still continue to increase, its value as a structural armour has ceased.

Whilst all of these failure modes absorb a different amount of impact energy, and produce different types of shrapnel, *all* of the failure modes can be put to good use when designing an armour system...even the 'poorly-performing' shattering grades! (See [Section 2.4.5.5](#).)

For DHF perforations, the ballistic resistance of the steel will be governed by the dynamic plastic flow characteristics of the steel. While ballistic performance can sometimes be correlated to a hardness measurement, hardness is a quasistatic measure of yield pressure for a specific indenter geometry that can be related to a compressive yield stress and thus quasistatic plastic flow (see Chapter 1). However, hardness is not a measure of dynamic yield or flow stress that accounts for strain rate hardening, work hardening or thermal softening (as discussed in [Section 2.2.3](#)) as would be required to define the armour material resistance to plastic flow under dynamic projectile impact conditions.

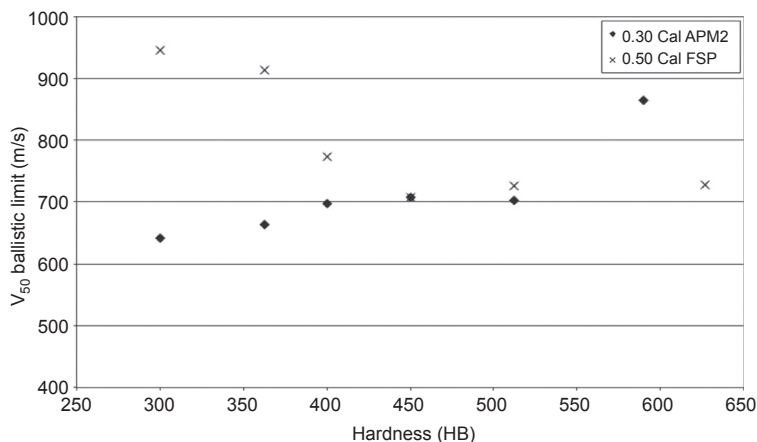


Figure 2.12 The effect on the V_{50} ballistic limit as the hardness increases for 10 mm Bisalloy armour steel plates against 0.30 Cal APM2 and 0.50 Cal FSPs.

After Gooch, W.A., Showalter, D.D., Burkins, M.S., Thorn, V., Cimpoeu, S.J., Barnett, R., 2007. Ballistic testing of Australian Bisalloy steel for armor applications. In: Paper Presented at the 23rd International Symposium on Ballistics, Tarragona, Spain; Ryan, S., Li, H., Edgerton, M., Gallardy, D., and Cimpoeu, S.J., 2016. The Ballistic Performance of an Ultra-High Hardness Armour Steel: an experimental investigation, *International Journal of Impact Engineering*, 94, 60-73.

Fig. 2.12 shows how the ballistic limit varies for a wide range of practical armour steel hardness values (Gooch et al., 2007; Ryan, 2016) from RHA (Specification, 2013) through to ultra-high-hardness armour (UHHA) (Specification, 2009). The improved ballistic resistance of steel as a function of increasing hardness is well established in the ballistic community, particularly by Rapacki (1995), and for this reason armour designers are more often incorporating higher-strength armour steels in their appliqué and structural armour solutions.

Fig. 2.12 also shows that there is no difference between the ballistic performance of 450 HB steel and HHA (512 HB) and this is also seen for other plate thicknesses (Gooch et al., 2007). The 450 HB grade has a leaner chemistry, providing improved toughness and weldability compared to HHA and would be a better choice for structural applications and the more consistent ballistic performance may allow a weight saving for some protection levels.

Whilst increasing hardness increases projectile protection, this does not apply for fragmentation protection, as demonstrated by the fragment-simulating projectile (FSP) ballistic limits in Fig. 2.12. Fragmentation protection decreases significantly with increasing hardness, making the high-hardness armour (HHA) grades (Specification, 2008) a poor choice for such applications. This is because impacts of blunt fragments cause high-strength steels to fail by adiabatic shear plugging, a low-energy failure mechanism (Woodward, 1984). Adiabatic shear is responsible for the fall-off in FSP performance shown in Fig. 2.12.

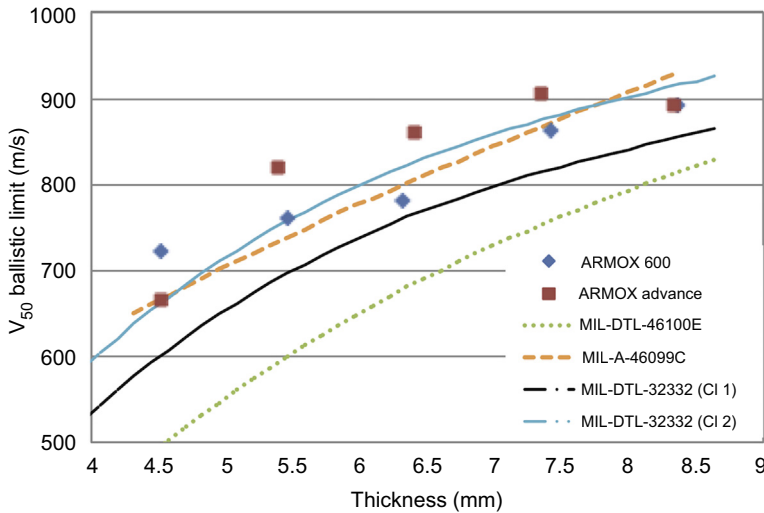


Figure 2.13 The V_{50} ballistic limit for ARMOX 600 and ARMOX Advance UHHA grades, HHA (MIL-DTL-46100E), dual-hardness armour (MIL-A-46099C) and UHHA Class 1 and Class 2 (MIL-DTL-32332) against 0.30 Cal APM2 at 30° obliquity.

Based upon Showalter, D.D., Gooch, W.A., Burkins, M.S., Koch, R.S., 2008. Ballistic testing of SSAB ultra-high hardness steel for armor applications. In: Paper Presented at the 24th International Symposium on Ballistics, New Orleans, LA.

More recently (c.2008), UHHA steels have been produced that have been assessed and applied as practical armour materials (Gooch et al., 2004; Showalter et al., 2008). Fig. 2.13 shows how they can offer considerable performance improvements over HHA (also seen in Fig. 2.12) and also fulfil an equivalent ballistic role to dual-hardness armour but as an homogeneous plate (Specification, 1987). The fact that ballistic performance increases at very high steel hardness values has been known for many years but it is only recently that armour steels have been produced that consistently meet ballistic requirements without shattering upon impact (refer Section 2.3.2).

In summary, Fig. 2.12 demonstrates that ballistic performance relates to steel armour hardness, though over specific hardness ranges there can be an increasing or decreasing relationship between ballistic performance and hardness, depending on the projectile and the armour failure mechanism adopted. Another important influence of armour hardness is whether or not it is sufficient to significantly deform or shatter a projectile, both of which will strongly affect ballistic performance. In practical terms hardness is a measurement of strength that can be easily measured on a plate-by-plate basis, particularly for quality assurance purposes.

2.2.3 High strain rate effects

Extensive studies have found that the ballistic performance of the structural and armour-grade steels correlates to hardness and tensile strength (but not yield strength, per se) (Manganello and Abbott, 1972). Interestingly, the classic work of Borvik et al.

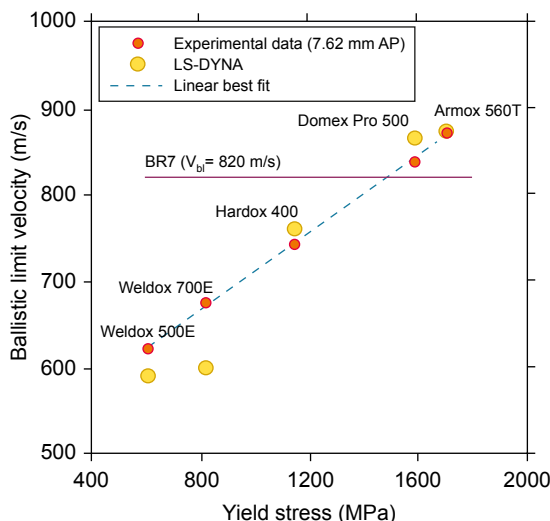


Figure 2.14 Linear relationship between quasistatic tensile yield stress and ballistic limit. From Borvik, T., Dey, S., Clausen, A.H., 2009. Perforation resistance of five different high strength steel plates subjected to small arms fire. *International Journal of Impact Engineering* 36, 948–964.

(2009) in Fig. 2.14 shows a quite linear relationship between measured quasistatic tensile yield stress values of 600–1700 MPa for a range of quenched and tempered steels.

Woodward (1978a) demonstrated a strong correlation between predicted and measured ballistic performance for a range of materials impacted by nondeforming projectiles when the quasistatic compressive flow stress at high strains, ie, the uniaxial flow stress at a true strain of 1.0 (Fig. 2.15), was used as a measure of material strength. Such a measure of flow stress is reasonable when considering the large strains involved

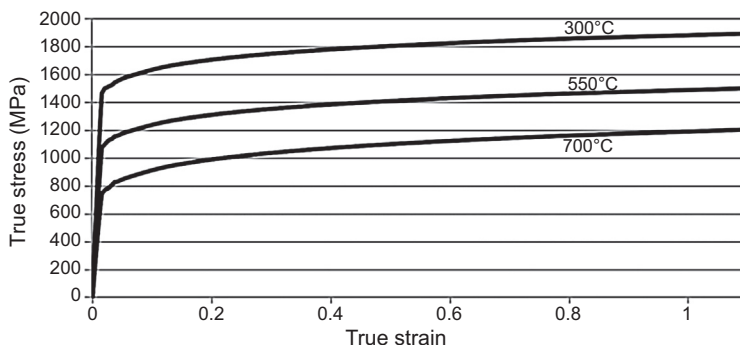


Figure 2.15 Compressive quasistatic true stress–strain curves for a 4130 steel that has been quenched and tempered at 300°C (480 HV), 550°C (370 HV) and 700°C (260 HV) with flow stresses described by $\sigma = \sigma_0 \varepsilon^n$.

After Cimpoeru, S.J., and Woodward, R.L. Unpublished research.

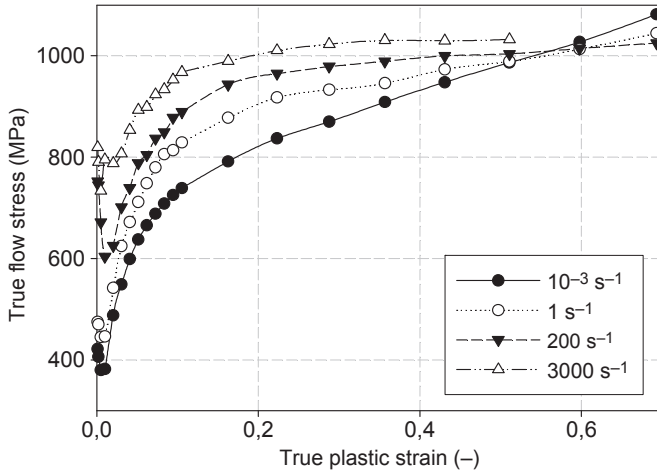


Figure 2.16 Compressive true stress–strain curves for a 1045 steel.

From Meyer, L.W., Halle, T., Herzig, N., Krüger, L., Razorenov, S.V., 2006. Experimental investigations and modelling of strain rate and temperature effects on the flow behaviour of 1045 steel. *Journal de Physique IV France* 134, 75–80.

in a ballistic impact event, especially through ductile hole formation and many other failure mechanisms.

High-rate uniaxial compression testing is most often used to measure dynamic material properties because it allows the large strains of ballistic impact to be achieved at the highest strain rates. The effect of strain rate on the stress–strain performance of mild steel (Meyer et al., 2006; Cimpoeu, 1990) and representative armour steels (Nahme and Lach, 1997) is shown in Figs 2.16 and 2.17. The increase in

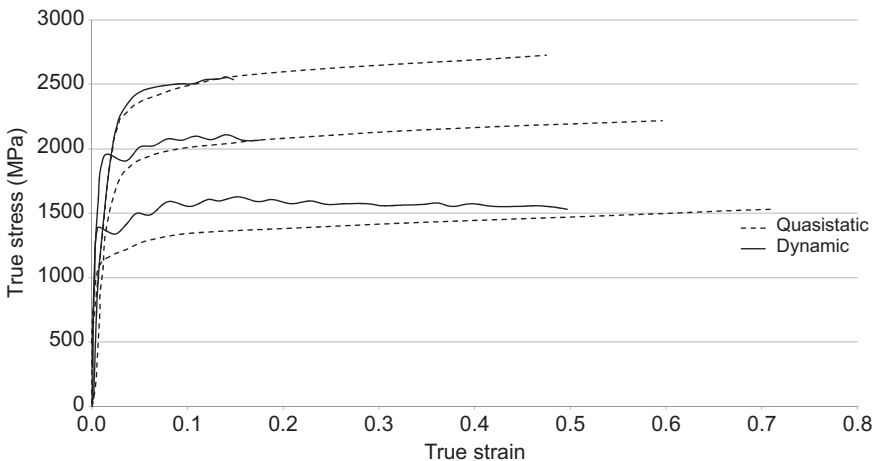


Figure 2.17 Compressive true stress–strain curves for MARS armour steels.

From Nahme, H., Lach, N., 1997. Dynamic behavior of high strength armour steels. *Journal de Physique IV France* 7, C373–C377.

flow stress is known as strain rate hardening or a strain rate effect. Dynamic loading is shown to considerably enhance the flow stress of steels in the vicinity of the yield and initial flow stresses. These two figures show that the flow stress at large plastic strains appears to not be affected by the loading rate with the initial flow stresses at high loading rates tending to approach the value of the quasistatic flow stress at large plastic strains. Strain rate hardening is still occurring, but the overall shape of the stress–strain curve is modified as a result of thermal softening due to adiabatic heating associated with the large, high-rate plastic deformations. In other words, the flow curve is a combination of a flow stress increase due to strain rate hardening as well as a decrease due to thermal softening, which together can lead to flattened stress–strain curves.

Considering the loading rates relevant for ballistic impact and the effect of loading rate on the stress–strain performance of steels (Figs 2.16 and 2.17) an assumption of rigid–plastic stress–strain behaviour can be a reasonable approximation for the material behaviour in some instances, eg, for use in one-dimensional analytical models (Woodward, 1978a). However, high strain rate testing is normally used to provide greater fidelity and understanding of material behaviour and to populate material models employed for numerical modelling (see Chapter 9).

What is the reason for the enhancement in the initial flow stress of steel at high strain rates? In the vicinity of the initial flow stress, flow stress is affected by both temperature and strain rate, and strain rate enhancement can be explained by a thermal activation model of dislocation movement which assumes that at temperatures lower than a critical temperature (dependent on strain rate), the flow stress depends on both an athermal component and a thermally activated component (Schulze and Vöhringer, 2000). The athermal component of flow stress is determined by the effect of long-range dislocation obstacles (eg, grain boundaries, precipitates, etc.) and is largely strain rate independent, but still dependent on temperature. The thermally activated component of flow stress is related to short-range glide obstacles (eg, dislocations), which can be overcome by thermally activated glide of mobile slip dislocations due to thermal fluctuations and thus is more strongly affected by temperature and strain rate; it is increased by either decreasing temperature or increasing strain rate (Schulze and Vöhringer, 2000). Decreasing temperature leads to reduced thermal energy while increasing strain rate reduces the time available for dislocation movement. Both circumstances result in a reduced ability of mobile dislocations to overcome short-range obstacles and hence lead to strain rate hardening.

Fig. 2.18 shows a thermal activation model (Schulze and Vöhringer, 2000) successfully describing stress–strain behaviour at initial flow stresses from low to very high strain rates, ie, from strain rates of 10^{-3} to 10^5 s^{-1} . Other models do not effectively account for the observed behaviour (Meyer et al., 2006). However, the thermal activation model was originally established for initial flow stresses. While this model can also be applied to larger strains, this is seldom done, as there are no closed form solutions available that describe the stress–strain behaviour as a function of plastic strain, strain rate and temperature. At larger strains, empirical models such as those of Johnston and Cook (1983) or the semiempirical model of

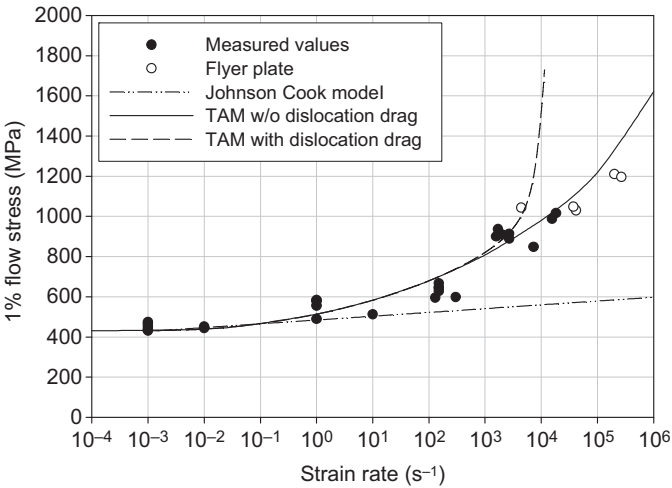


Figure 2.18 True compressive flow stress at 1% true plastic strain for 1045 steel at strain rates from 10^{-3} to 10^5 s^{-1} , compared to the thermal activation model (TAM), TAM with dislocation drag and the Johnson Cook model.

From Meyer, L.W., Halle, T., Herzig, N., Krüger, L., Razorenov, S.V., 2006. Experimental investigations and modelling of strain rate and temperature effects on the flow behaviour of 1045 steel. *Journal de Physique IV France* 134, 75–80.

Zerilli and Armstrong (1987) are often used to describe flow stress behaviour as a function of strain, strain rate and temperature.

Dynamic tensile properties have also been measured. Fig. 2.19 compares quasistatic tensile and dynamic tensile properties for a range of quenched and tempered steels.

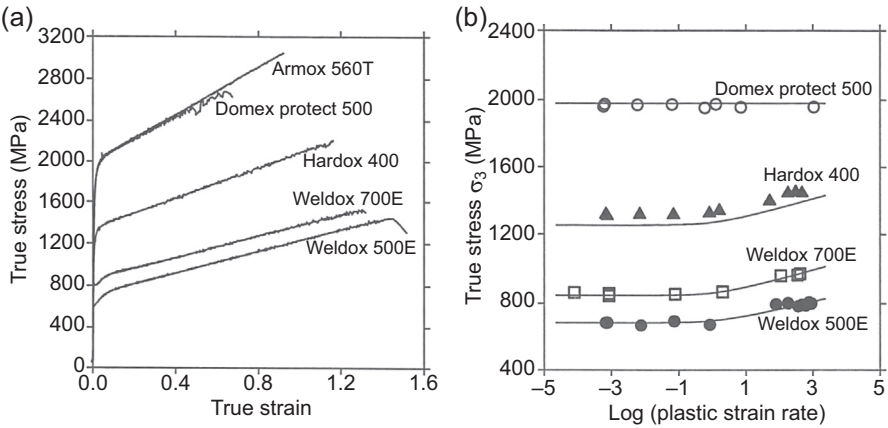


Figure 2.19 Tensile quasistatic true stress–strain (A), and true stress–strain rate curves (B) for a range of quenched and tempered steels.

From Borvik, T., Dey, S., Clausen, A.H., 2009. Perforation resistance of five different high strength steel plates subjected to small arms fire. *International Journal of Impact Engineering* 36, 948–964.

The difference between quasistatic compressive and tensile properties of quenched and tempered steels is the strength differential (Spitzig et al., 1975). This also applies under dynamic loading (Meyer and Abdel-Malek, 2000). The strength differential arises because of different material responses between compressive and tensile loading and has a number of potential causes such as: microscopic cracks and quench cracks arising from hardening; dislocation movements against grain boundaries or inclusions; and texture effects and anisotropy, arising from prior plastic deformation. Under tensile loading, cracks propagate, thus increasing material volume, resulting in greater plastic strains. Under compressive loading, cracks are closed, resulting in lower measured plastic strains. Any retained austenite left over from quenching will also have different behaviour under tension compared to compression (Meyer and Abdel-Malek, 2000).

Fig. 2.20 shows that the differences in stress–strain behaviour between compression and tension can be quite significant for quenched and tempered steels and demonstrates the ability of the Johnson–Cook and Zerilli–Armstrong models to represent the material behaviour at a strain rate of interest.

Armour steels are available in a range of thicknesses, and as a consequence material properties vary due to the difficulty in achieving sufficient quench rates with thicker sections. This is particularly the case for RHA, which is available in a wide range of thicknesses (2.5–150 mm). The alloys used for the thicker sections have higher alloying contents to increase their hardenability but changes in composition cannot always fully compensate for such significant changes in thickness, resulting in reduced hardnesses in the middle of the cross-section for thicker plates. Fig. 2.21 clearly shows how the dynamic properties of RHA are affected by hardness (a consequence of plate thickness) (Weerasooriya and Moy, 2004). Note the tendency for these steels to effectively exhibit rigid–plastic behaviour with increasing strain rate, due to strain rate enhancement at the initial flow stresses and a flattened stress–strain curve due to thermal softening at larger plastic strains.

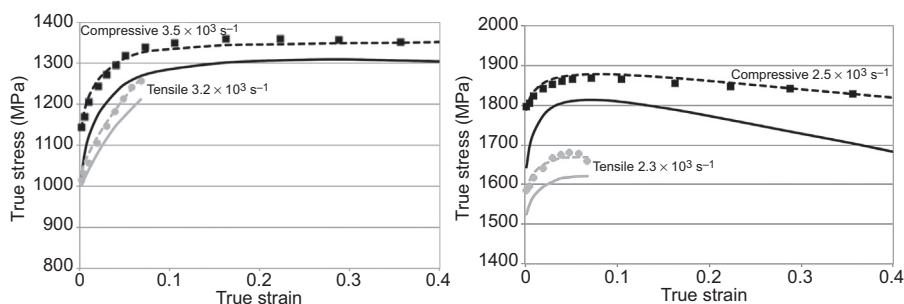


Figure 2.20 Compressive and tensile flow stresses for two quenched and tempered steels at nominal identical strain rates: left, 290 HV30 (tensile $3.2 \times 10^3 \text{ s}^{-1}$ and compressive $3.5 \times 10^3 \text{ s}^{-1}$) and right, 410 HV30 (tensile $2.3 \times 10^3 \text{ s}^{-1}$ and compressive $2.5 \times 10^3 \text{ s}^{-1}$). Associated Zerilli–Armstrong and Johnson–Cook predictions are also shown. After Meyer, L.W., Abdel-Malek, S., 2000. Strain rate dependence of strength-differential effect in two steels. *Journal de Physique IV France* 10, PR9, 63–68.

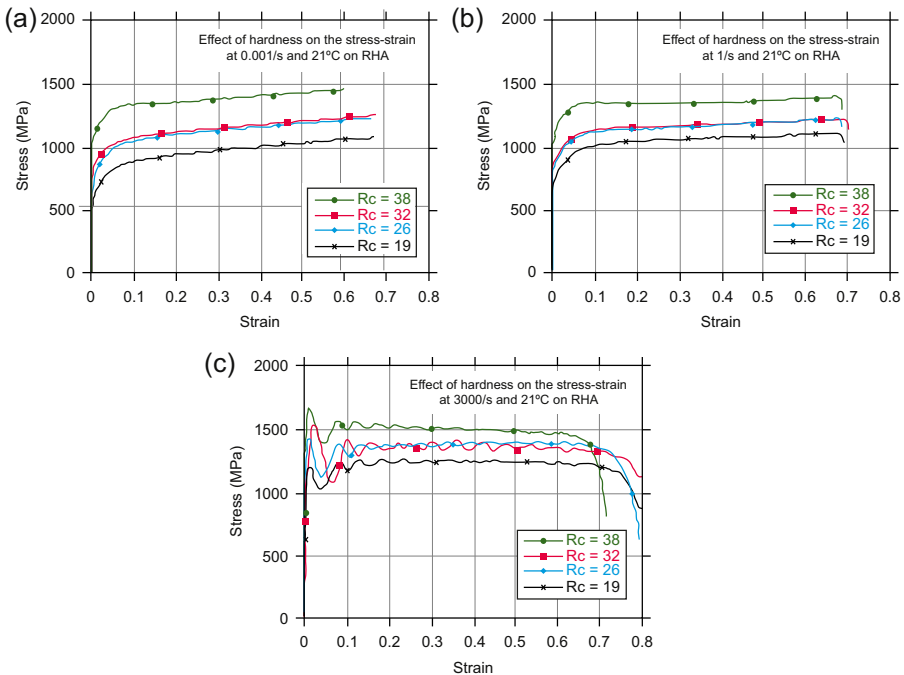


Figure 2.21 Compressive stress–strain curves at different hardnesses ($R_c\ 38 \cong 353\text{ HB}$, $R_c\ 32 \cong 301\text{ HB}$, $R_c\ 26 \cong 258\text{ HB}$ and $R_c\ 19 \cong 223$) for RHA at strain rates of: (A) 0.001 s^{-1} , (B) 1 s^{-1} and (C) 3000 s^{-1} .

From Weerasooriya, T., Moy, P., 2004. Effect of strain rate on the deformation behaviour of rolled-homogenous armour (RHA) steel at different hardnesses. In: Paper Presented at the SEM Congress and Exposition on Experimental Mechanics, CostaMesa, CA.

2.2.4 Fabricability

This is the main advantage of utilising steel as the base material in any military vehicle. As stated by Bill Gooch and co-workers in 2008, ‘the ability to fabricate armor components in both commercial and military operational areas, with available equipment and personnel, is a major advantage of steel solutions’ (Showalter et al., 2008). However, quenched and tempered, martensitic steels are affected by any form of reheating and therefore hot-rolling, hot-forming, cutting and welding will affect the microstructure and local properties of the steel, and therefore the ballistic performance.

2.2.4.1 Effects of hot- and cold-rolling

Hot working is a process where the steel is plastically deformed into a different shape above its recrystallisation temperature. Recrystallisation is most likely to lower the yield strength and hardness and increase the ductility, thereby resisting the strain hardening. Where ballistic integrity cannot be compromised, hot working must be avoided. If needed, a secondary heat-treatment process is recommended to re-establish an

acceptable level of hardness. On the other hand, cold working is a process where the steel is plastically deformed into a different shape below the recrystallisation temperature and is generally performed at room temperature. Some benefits of cold working are:

- No heating is required;
- Better surface finish and superior dimensional control are achieved;
- Strength, fatigue and wear properties are improved;
- Directional properties can be imparted;

and some of the disadvantages are:

- Heavier forces are required;
- Strain hardening occurs (may require intermediate annealing treatment to relieve internal stresses);
- Residual stresses may be produced.

Typical scanning electron microscopy and electron backscatter diffraction images of a hot and cold rolled steel are shown in Figs 2.22 and 2.23 (Peranio et al., 2010). Note how the cold-rolled microstructure is much finer and the grains have experienced much more plastic deformation.

2.2.4.2 Effects of welding

Welding is a common joining technique used for armoured steels. Welding produces heat-affected zones (HAZ) between the parent and weld metal, which includes

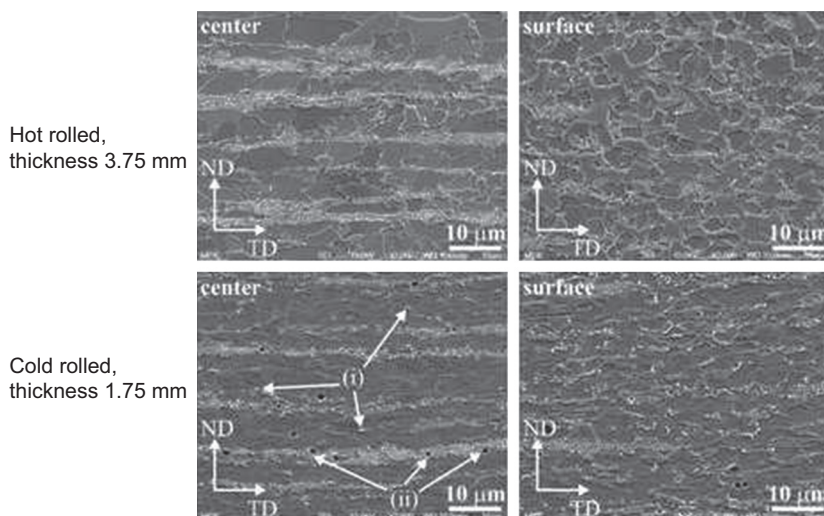


Figure 2.22 Scanning electron microscopy on transverse sections of hot- and cold-rolled sheets. From Peranio, N., Li, J.Y., Roters, F., Raabe, D., 2010. Microstructure and texture evolution in dual-phase steels: competition between recovery, recrystallisation and phase transformation Materials Science and Engineering: A 527, 4161–4167.

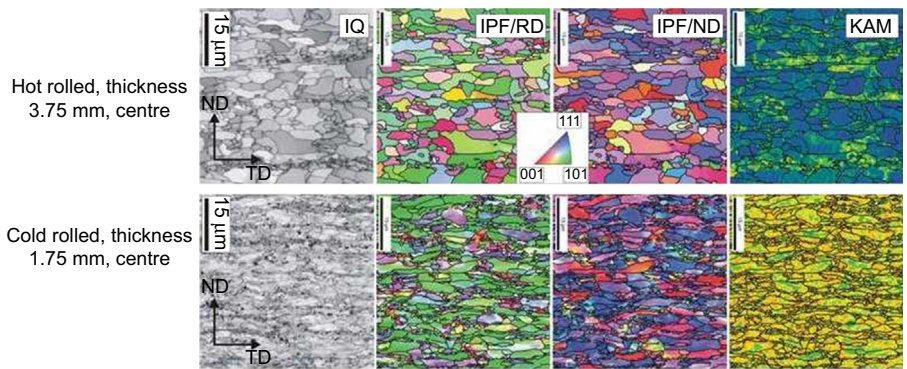


Figure 2.23 Electron backscatter diffraction carried out in the centre of transverse sections of hot- and cold-rolled sheets.

From Peranio, N., Li, J.Y., Roters, F., Raabe, D., 2010. Microstructure and texture evolution in dual-phase steels: competition between recovery, recrystallisation and phase transformation Materials Science and Engineering: A 527, 4161–4167.

subzones of various hardness (rehardened, softened/tempered) (as shown in Fig. 2.24) and could affect the structural, ballistic and fatigue performances.

Ferritic steels suffer from two issues that may affect armour performance. These phenomena are hydrogen-assisted cold cracking (HACC) and the HAZ softening indicated in Fig. 2.24. The welding procedures required for avoidance of HACC are well established for ferritic structural steels and are incorporated in international standards (Ref AS/NZS 1554, ISO EN 1011). Since the cause of HACC is the combined effect of a susceptible microstructure, stress and the presence of hydrogen, it may be eliminated by removing any one of these factors. In typical welding procedures the microstructure

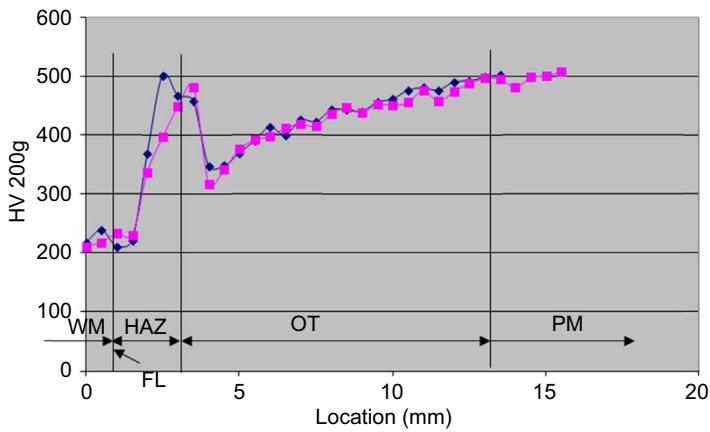


Figure 2.24 Typical weldment hardness profile.
After Kuzmikova, L., 2012. An Investigation of the Weldability of High Hardness Armour Steels (Ph.D. thesis). University of Wollongong.

is made less susceptible by reducing the cooling rate by increasing heat input and applying preheat. Low hydrogen practices, which involve careful control of consumables and parent material, are adopted and again increased heat input, increased preheat and even additional post heat or controlled cooling are used to aid hydrogen diffusion. The use of high heat input and preheat does, however, have an adverse effect on heat-affected zone softening. For this reason the operating window for welding procedures is relatively narrow for ferritic steels in general and thermomechanically treated or quench and tempered steels in particular. The most effective measure that can be used to ensure an adequate operating window is probably hydrogen management. This is acknowledged in EN 1011-2 where the use of austenitic filler material is also suggested as an alternative to high preheat. Recent work by the Defence Materials Technology Centre (DMTC) in Australia (Kuzmnikova, 2012) has demonstrated the effectiveness of this approach and its role in controlling hydrogen diffusion to prevent a build-up in the heat-affected zone.

The magnitude to which HAZ softens depends on factors such as chemical composition, weld thermal cycle (welding method) and kinetics of the phase transformation (Magudeeswaran et al., 2008). The likelihood of HACC occurrence depends on various factors such as hardness (influenced by the steel's microstructure, CE and weld cooling rate), type and magnitude of residual stresses and importantly the level of diffusible hydrogen which is trapped in the heat-affected zone (Alkemade, 1996).

A stress-relieving heat treatment is often used to reduce the stresses that remain locked into a structure as a result of manufacturing processes. Uniformly heating the structure to a sufficiently high temperature below the lower transformation temperature range, and then uniformly cooling it can relax the stresses. By stress-relieving, a greater dimensional stability is maintained, the potential for stress corrosion cracking (ie, HACC) is reduced and the metallurgical structure can be improved.

2.2.4.3 Effects of cutting

Plate cutting and machining procedures used during vehicle manufacture play an important role in determining vehicle integrity. A study was undertaken to determine the cause of cracking in HHA steel plates used in the manufacture of light armoured vehicles (LAVs) (Wells et al., 1992). Cracks in several components from fielded vehicles were analysed. In many cases the cracking was caused by improper edge preparation in cutting the steel that resulted in environmental-assisted cracking. Microscopic examination of the edge of the plate at the crack origin revealed a layer of untempered martensite, that is a result of plate cutting operation and was not completely removed during subsequent grinding. This layer of untempered martensite is quite brittle and can be a crack initiation site.

Table 2.4 illustrates the effect of various methods of edge preparation on the thicknesses of untempered martensite and the heat-affected zone. It shows that more edge material must be removed (and consequently more time spent on its removal) when, for example, oxyacetylene cutting is used instead of plasma-arc cutting. It should be

Table 2.4 Thickness of untempered martensite surface layer and HAZ

Edge preparation	Thickness of untempered martensite (mm)	Thickness of HAZ (mm)
Water-jet cut	Not detectable	Not detectable
Abrasive wheel cut	Not detectable	2.5
Plasma-arc cut (air, high speed)	0.5	2.5
Plasma-arc cut (water)	0.5	2.5
Air carbon-arc cut (multipass)	1.0	3.8
Oxyacetylene cut	3.0	15.0
Laser cut	0.1	0.5

After Wells, M., Weiss, R., Montgomery, J., 1992. LAV Armour Plate Study. MTL TR 92-96.

noted that laser cutting produces by far the thinnest layer of untempered martensite and HAZ. The water-jet process has no untempered martensite thickness and HAZ since it is done cold and has comparable surface finish. Since plate edge cutting is so important it is recommended that laser or water-jet cutting be considered. This procedure would reduce or eliminate the thickness of the HAZ of cutting to a level that would obviate edge grinding.

To circumvent all of these disadvantages of reheating armour steels, an armoured structure can be constructed simply by bolting the armour plates together, and this approach is gaining some traction, especially for lightweight vehicles. Table 2.5 summarises the major differences between welded and bolted structures. It should also be pointed out that bolted structures, involving overlapping plates, will be slightly heavier, although if replacement, refurbishment and/or upgrades are envisaged, bolted structures are attractive. The possible formation of secondary projectiles, from ejected bolts, is considered to be an issue, as well as corrosion in the joints. However, if these inherent disadvantages can be designed-out then mechanical fastening becomes a real option for joining armour materials together.

2.2.5 Cost and availability

Normal market forces apply but grades of armour steel have been plentiful since the early-1900s. So, compared with other materials, the low price of steel makes it a very attractive material for mass production of large quantities of military vehicles. Local, in-field repairability of welded steel structures is also a huge driver when most armies around the world still use steel-based vehicles.

Globalisation of the steel industry has meant that countries do not have to rely upon purchasing armour steels from their own country, as was certainly the case up to the 1980s. Crouch recalls the momentous decision taken by UK MoD, around 1984, to widen the source of armour steels to European suppliers – up till then all

Table 2.5 A comparison between welded and bolted structures for an armoured platform

Engineering aspect	Welded structures	Bolted structures
Fabricability	Conventional joining practices. Preheat required. Hands-down welding modes favoured	Ease of assembly and disassembly. Tightness of joints? Jigs and fixtures required to achieve the set tolerance. Bolt torque needs to be checked periodically
Normal application	Water-tight, air-tight, monocoque structures	Sealing required between joints, eg. water fording. Appliqué systems and secondary structures
Electro-magnetic shielding and earthing	Continuous connectivity as the hull will act as a Faraday's cage	Needs stitch welding between joints or electrical connectivity straps or conductive sealants
Nature of joints	HAZs and environmental cracking associated with weld line	Overlapping joints leading to excessive material and weight penalty
Field repairs	Limited to minor repairs as it needs specialised equipment, technique and trained personnel	Individual panels could be disassembled and reassembled with standard field service equipments
Choice of armour grades	Limited to weldable grades with minimal carbon equivalent	Unlimited, therefore higher hardness grades can be selected and successfully integrated into/onto a structure
Ballistic performance	Small, narrow ballistic windows present around weld lines	Ballistic windows, only under oblique strike, but potential for secondary projectiles (nuts and bolts!)

armour steels for UK-built armoured vehicles, had been produced in the UK, under strictly controlled, highly secure manufacturing conditions. The Cold War was still raging!

Table 2.6 shows the cost of a steel-based armour system compared to some alternative material systems. Even today, with many exotic armour materials now available, steel is still extremely competitive in terms of cost, even though it is invariably the heaviest solution. Against the 0.3" APM2 threat, the composite armour

Table 2.6 A trade-off between weight and cost of alternative armour systems for a given threat (in this case, the 7.62 mm APM2 rounds was selected)

ID	Type and description	Reference for AD	AD (kg/m ²)	Cost (\$/kg)	Cost (\$/m ²)
1	Monolithic steel (RHA)	IDR#4, 1991, p349	114	4	456
2	Monolithic steel (HHS)	IDR#4, 1991, p349	98	4	392
3	Monolithic aluminium alloy (5083)	IDR#4, 1991, p349	128	9	1152
4	Monolithic aluminium alloy (7039)	IDR#4, 1991, p349	106	15	1590
5	Monolithic titanium alloy (Ti-6Al-4V)	Timet, 2015	86	113	9718
6	Monolithic magnesium alloy (ZK60A)	ISB22, 2005, Van de Voorde	135	120	16,200
7	Glass Fibre Reinforced Plastic (GFRP) (S-glass)	IDR#4, 1991, p349	93	30	2790
8	Alumina/Aluminium	IDR#4, 1991, p349	50	35	1750
9	Boron carbide/Ultra High Molecular Weight PolyEthylene (UHMWPE)	Armour Solutions, 2014	32	220	7040

solution (represented by a laminate of boron carbide and high-density polyethylene) is about a third of the weight of an RHA solution. In personnel armour applications this weight saving is very important. However, for heavy armoured vehicles in particular, the weight of the structural armour is only a fraction of the total vehicle weight. These trade-offs will be examined again, in depth, in Chapter 12, when future armour materials are considered.

2.3 Failure mechanisms and modes

2.3.1 Adiabatic shear

Heat, generated from the work of plastic deformation during impact, is usually contained within the deforming material, as there is often not enough time for the heat to escape to the surrounding material. These conditions are considered adiabatic for practical purposes, and under such conditions the rate of material softening, due to the temperature rise, can be greater than the rate of work hardening. This can lead

to an instability, within the microstructure of the material, and a subsequent, sometimes significant, fall-off in material strength. This has important implications for a number of armour materials, particularly high-strength steels, where increases in static material strength properties are sometimes accompanied by a reduction in penetration resistance over certain hardness ranges (Manganello and Abbott, 1972; Wingrove and Wulf, 1973) (Fig. 2.25).

This is because of the phenomenon of adiabatic shear. Under a particular set of conditions, there is a significant fall in the shear yield stress, and the formation and ejection of a plug of armour and thus reduced ballistic resistance. Fig. 2.11 introduced this potential drop-off. This can also be seen in Fig. 2.25, where a fall-off in ballistic resistance against fragments is associated with adiabatic shear plugging. In general, the fall-off in ballistic resistance is expected at about 350 HV (~ 330 HB) (Wingrove and Wulf, 1973; Woodward, 1978b), but this will also be affected by the obliquity of the impact (Woodward and Baldwin, 1979).

The general theory of adiabatic shear was developed by Zener and Hollomon (1944) and further refined by Recht (1964) to allow a relative ranking of materials in terms of their susceptibility to adiabatic shear by determining a critical shear strain rate from their thermomechanical material properties. Low values of specific heat, thermal conductivity, density and work hardening rate were favourable to adiabatic shear along with high values of shear yield stress and the rate of thermal softening.

The fall-off in shear yield stress associated with adiabatic shear will cause deformation to concentrate, resulting in bands of intense shear deformation (Fig. 2.26). The presence of adiabatic shear bands (ASB) in steel can be detected in metallographic specimens as they resist etching and appear as a white band that contrasts with the rest of the steel microstructure, which more readily etches.

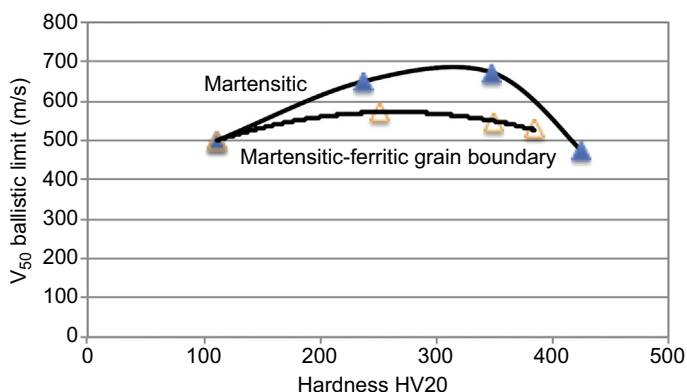


Figure 2.25 Relationship between ballistic limit and hardness for quenched and tempered steels with a martensitic microstructure and martensitic-grain boundary ferrite microstructure. From Wingrove, A.L., Wulf, G.L., 1973. Some aspects of target and projectile properties on penetration behaviour. *Journal of the Australian Institute of Metals* 18, 167–172.

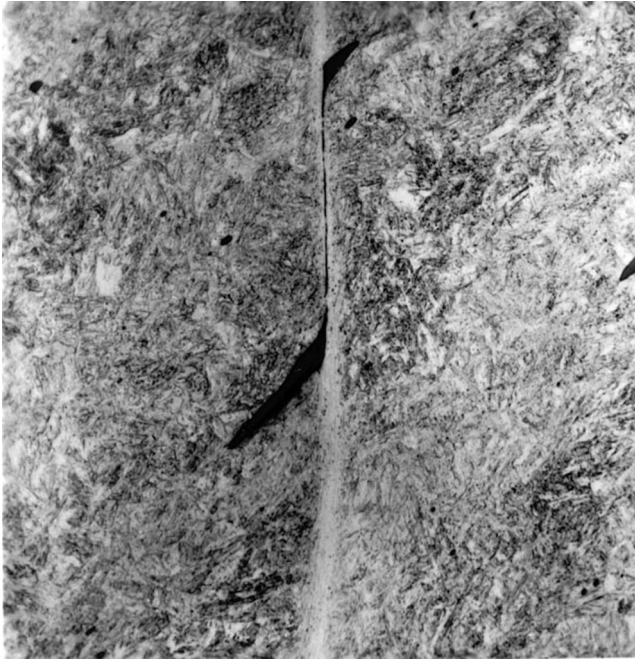


Figure 2.26 Adiabatic shear band. Significant shear strains are evident from the deformation of the inclusion.

From Woodward, R.L., 1984. The interrelation of failure modes observed in the penetration of metallic targets. *International Journal of Impact Engineering* 23, 121–129.

ASB have a very fine grain size, high hardness and exhibit anomalous tempering characteristics (Bedford et al., 1974).

Material susceptibility to adiabatic shear alone does not necessarily result in adiabatic failure. Adiabatic shear failure consists of narrow, white etching bands of intense shear strain, where the shears are generally of a much greater magnitude than the material would normally sustain in conventional shear failure. The latter normally involves the exhaustion of ductility through a failure mechanism involving void nucleation, growth and coalescence and thus by comparison requires greater plastic deformation and work (Woodward, 1984; Flockhart et al., 1991).

The conditions for adiabatic shear failure to occur are complex and not just related to material properties. Adiabatic shear failure will also depend upon the geometry of the penetrator, being more likely to occur in less susceptible materials when they are impacted by blunt projectiles. Such projectiles tend to produce plugging failures, even when adiabatic shear is not involved.

Reduced strain rate-dependent behaviour is known to encourage adiabatic shear failure (Dorneval, 1988; Wang, 2007). The simple target geometry of a cylindrical specimen in a high strain rate compression test allows some of the key requirements

for adiabatic shear failure to be identified. In such circumstances, the following conditions are required for adiabatic shear failure:

1. A negative slope on a material stress–strain curve;
2. A suitable specimen geometry so that intense shears can develop (O'Donnell and Woodward, 1988);
3. Conditions, eg, friction, that ensure that material deformation/flow can continue in a stable manner over time (Cimpoeru and Woodward, 1990).

Some ASB will only develop within a material, whereas other shear bands will intersect free surfaces, allowing material separation and thus adiabatic shear failure to be achieved. These observations are consistent with the changing direction of material flow over time in many circumstances (Flockhart et al., 1991). ASB have been correlated with slip lines associated with plastic deformation problems and in particular in those slip lines that are also velocity discontinuities (Backman and Finnegan, 1973). Flockhart numerically modelled a range of impact problems to demonstrate a correlation between adiabatic shear failure and slip-line field velocity discontinuities. It was shown in finite element simulations that such velocity discontinuities can be identified by maxima in shear strain rate.

Meyer and Pursche (2012) provide an up-to-date and comprehensive account of the material properties that have the strongest influence on the adiabatic shear failure of high-strength low-alloy (HSLA) steels. They also systematically examined the importance of various material properties for the initiation of adiabatic shear failure in quenched and tempered HSLA steels. The most important material property, from both qualitative and quantitative analysis of the adiabatic failure, was found to be dynamic thermal softening behaviour (Table 2.7).

Adiabatic shear is a very important failure mechanism for steels because it results in low-energy failure mechanisms over a range of hardness values where reduced ballistic performance is normally found. While much work has been conducted in the past, adiabatic shear will continue to be an important research topic for many years to come.

2.3.2 Brittle failure

Shattering of armour plate upon ballistic impact can be described as occurring when the ductility of an armour plate is insufficient to withstand the strains associated with bending arising from an impact and bending is the preferred failure mechanism (Woodward and Baldwin, 1979). It is evidenced when a plate is fractured with little discernible deformation and can also be combined with other failure mechanisms (Fig. 2.27). Armour plate shattering is clearly a catastrophic event.

In a uniaxial tensile test, ductility is measured by the fracture strain that accounts for both homogeneous strain and the necking strain after the ultimate tensile strength has been reached. For a ductile material, ductility is normally a uniaxial measure of the total elastic and plastic strain before void growth and coalescence leads to final fracture.

Table 2.7 A ranking of material properties in accordance with their propensity to fail by adiabatic shearing

No.	Property	Qualitative consideration	Quantitative consideration	Assessment rating
		Threshold value	R^2 value	
1	Temperature instability from dynamic stress–temperature behaviour	Yes	0.95	Very good
2	Shear failure from dynamic hat-shaped test	Yes	0.95	Very good
3	Stress instability from dynamic stress–temperature behaviour	Yes	0.94	Very good
4	Area under the dynamic stress–temperature curve	Yes	0.94	Very good
5	Hardness	Yes	0.91	Good
6	Failure energy, according to Grady	Yes	0.87	Good
7	Dynamic compression flow stress at room temperature	Yes	0.86	Good
8	Dynamic tensile strength at room temperature	Yes	0.84	Good
9	Decline behaviour from dynamic compression–stress–temperature behaviour	Yes	0.79	Good
10	Decline behaviour from dynamic stress–compression behaviour of compression/shear test	Yes	0.61	Insufficient
11	Uniform elongation under dynamic loading	Yes	0.47	Insufficient
12	Simplified Culver equation	Yes	0.02	—

From Meyer, L.W., Pursche, F., 2012. Adiabatic shear localization. In: Dodd, B. (Ed.), *Adiabatic Shear Localization*, Frontiers and Advances, second ed. Elsevier, London, p. 85.

The shattering failure mechanism is of course an example of a brittle fracture. Such fractures typically involve rapid crack propagation, exhibit little plastic deformation and can occur in a range of circumstances, even for steels that normally exhibit ductile behaviour!

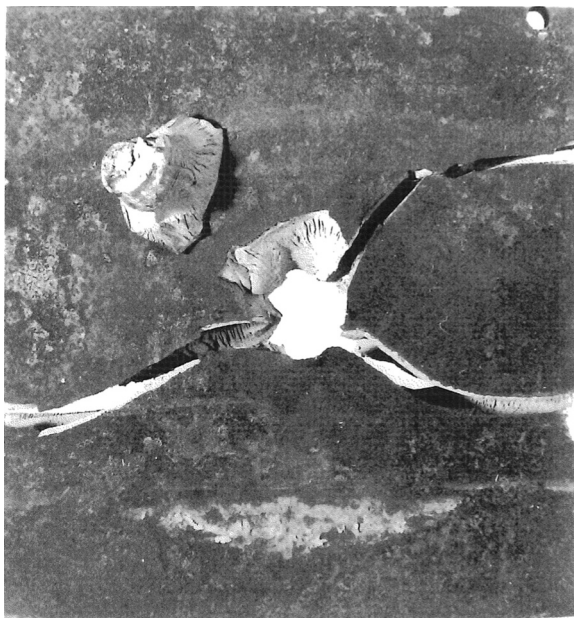


Figure 2.27 Armour steel failure evidenced by a combination of discing and shattering. Note that the disc is associated with a partially formed plug.

From Woodward, R.L., Baldwin, N.J., 1979. Oblique perforation of steel targets by 0.30 Cal. APM2 projectiles. *International Journal of Mechanical Sciences* 21, 85–91.

In practical terms, the utility of a material for demanding applications such as resisting ballistic or blast loading depends on how it responds in the presence of notches or cracks. Notches will produce high local stresses and a high local magnification of the strain rate at the root of a notch (Dieter, 1981). Importantly, notches will also lead to a three-dimensional multiaxial stress state that is particularly severe directly in front of a notch and even more so in front of a crack. Here the ability for local dislocation gliding controls the ductility, defined as ‘toughness’ in these circumstances. Toughness is always related to and specific to a three-dimensional stress field, which is preventing or hindering global plastic flow, ie, dislocation movement. Yielding, and thus plastic flow, takes place in only a small volume of material because it is only locally in front of the notch or crack that the stress exceeds the yield stress.

High-strength materials, including some armour steels (where the ductility, even in a uniaxial case, is often very low), often have small local plastic zones (and thus very high local stresses) in front of cracks (Dieter, 1981). Even with low external forces, a high local stress can be produced which can result in crack propagation and fracture. Steels with high work hardening and high fracture strains are preferred as they can produce a large plastic zone in front of any incipient cracks that provides greater resistance to crack propagation. The advantage of such steels is that the size of the plastic zone at the root of a notch pushes the elastically loaded zone into an area where the stresses will be much, much less. Hence such steels have much greater resistance to fracture.

Toughness also becomes an increasingly important issue for thick armour plates because of the triaxial stress state caused by the higher constraint of the thicker sections (Manganello and Abbott, 1972). In such circumstances, the stress state due to a notch approaches plane strain rather than plane stress, the former state having a lesser stress for fracture (Dieter, 1981). Thicker armour steels will generally need to have higher alloy content to increase their toughness to better manage triaxial stress states (Manganello and Abbott, 1972).

MacKenzie et al. (1977) showed that fracture strain is sensitive to stress state (ie, degree of triaxiality) in a range of high-strength steels and, as would be expected, there were significant differences between in-plane and through-thickness fracture strains. Sato et al. (2015) showed that there was not a significant influence of strain rate on the fracture strain for a range of steels above 600 MPa tensile strength, at least for strain rates up to 10^2 s^{-1} .

Other factors such as temperature and the rate of loading or strain rate (Dieter, 1981) can also strongly reduce toughness. Whittington (2014), for instance, examined the ductile fracture morphology of an RHA armour steel and found that an increase in strain rate resulted in smaller ductile void growth to the point at which fracture occurred. Conversely, an increase in test temperature resulted in larger ductile void growth to the point of fracture and thus greater failure strains.

Charpy impact testing is used to assess whether steels meet certain minimum levels of toughness (measured in Joules) for different armour applications (Standard, 2008). Testing is conducted at -40°C as this temperature is usually sufficient to enable brittle behaviour to be distinguished (Fig. 2.28), and allows a relative measure of toughness under such circumstances. The Charpy test (see Chapter 10) can help distinguish low-toughness steels on a comparative basis and hence help define what armour applications they are best suited for.

The Charpy transition temperature is the temperature at which material behaviour changes from ductile to brittle behaviour in the Charpy test. Low test temperatures, such as -40°C , impede dislocation movement and thus encourage brittle behaviour. However, ductile to brittle transition temperatures are unique to specific test configurations, stress states and loading rates and thus results from laboratory Charpy tests cannot be used to make definitive predictions of the behaviour of real armoured structures at field temperatures.

While the Charpy test is a useful means to rank the toughness of different armour steels, fundamentally it is an empirical test with an ill-defined triaxial condition at the notch and this is why it cannot be used to predict the onset of brittle fracture. Impacts or blasts produce very high local stresses that can easily produce cracks. Whether or not such cracks propagate and lead to brittle fracture relates to material-specific crack propagation properties that are not measured by the Charpy test (Herzig et al., 2010). Herzig et al. conducted Charpy tests as well as blast tests that measured crack propagation for a range of steels and have shown that the rankings from such tests vary with test temperature (-40°C versus ambient temperature). Importantly it was shown that there was a good correlation between material toughness properties and their resistance to crack propagation under high rate (explosive) loading.

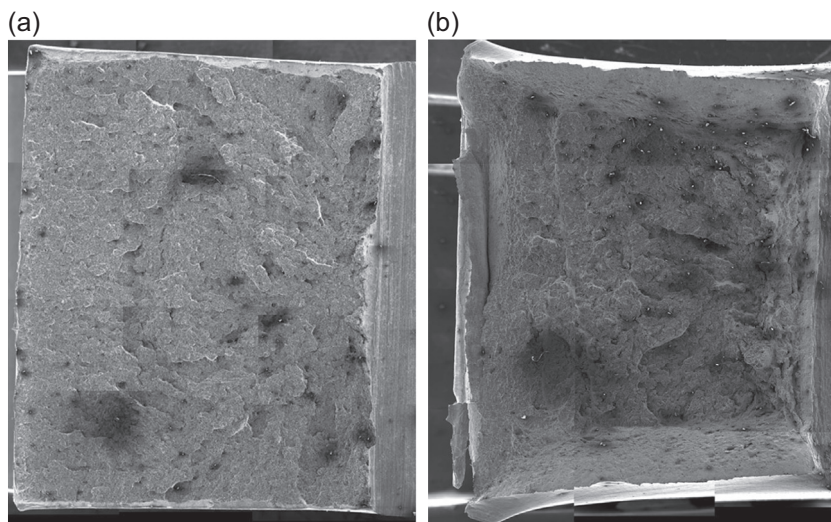


Figure 2.28 Brittle (95% brittle behaviour), left, and ductile/brittle (46% brittle behaviour), right, fracture surfaces exhibited after Charpy impact tests at -40°C (18 J measured) and ambient temperature (84 J measured), respectively. Samples were taken in the T–L (transverse–longitudinal) direction from a quenched and tempered steel (Shah Khan, M.Z., Unpublished DST Group research).

Armour toughness has been increased from the relatively lean steel compositions that were designed for low-cost volume production in WW2, when there were also shortages of critical alloying elements. Increasing the nickel content, for instance, has increased toughness and reduced the likelihood of shattering with increasing hardness, also providing more consistent ballistic perforations and thus tighter ballistic limits. While this will increase armour cost and reduce weldability, increasing toughness, particularly in high- and ultrahigh-hardness grades, has been a significant theme in armour steel development over the last 15 years and this trend is expected to continue.

2.3.3 Structural engineering failures

An armoured structure is considered to fail structurally when cracking, either progressively or rapidly, propagates through an armour plate to an extent that the local structure is unable to withstand further structural or impact loads. The key for maintaining structural integrity is to avoid such cracking, termed structural cracking here because of its severe nature in armour steels and possible effect upon ballistic integrity. Appropriate armour steel selection and fabrication will avoid, or at least minimise, the initiation or growth of structural cracking and thus expensive structural remedial actions.

Structural cracking in armour steels results from the precise metallurgical details produced by fabrication and as such cannot be predicted with any fidelity, eg,

numerically. Tiny cracks, often less than a millimetre and below a practical size for crack detection, are all that are required for free crack propagation but it is important to understand that these cracks are not caused by, or necessarily propagated by, fatigue. Tensile residual stresses play a dominant role in structural cracking, as they can be as high as the yield stress, which is considerable for many armour steels. The dynamic loads from vehicle operation are very small by comparison!

2.3.3.1 Cracking associated with welding

The welding processes can cause a host of defects and cracks (Fig. 2.29), many of which can lead to structural cracking problems. The avoidance of weld defects and particularly cracking is the reason why armour steel welding processes are carefully controlled through various welding standards, and have allowed rolled homogeneous armour (Specification, 2013), a much higher-strength steel than normal quenched and tempered steels, to be successfully welded into a range of armoured vehicle structures over many decades.

However, much harder armour steels are now also required to be welded. While HHA (Specification, 2008) was originally developed as a nonstructural armour, it is now also used as a welded structural armour, eg, for wheeled LAVs. Such steels must be carefully selected and fabrication must be performed according to specific procedures to minimise the risks of structural cracking.

Hydrogen assisted cold cracking, HACC, most commonly occurs in the HAZ of armour steels where it is sometimes known as weld-toe or underbead cracking. It is a significant risk when welding ferritic steels and can result in cracks that are detected sometimes long after welding has been completed. A number of welding procedures have been developed to avoid cracking in both RHA (Ritter et al., 1989) and HHA (Alkemade, 1996) steels. Cracking can also be found after repair welding. The repair of welded armour steel can be particularly difficult due to the high level of constraint in some weldments and the presence of high residual stresses.

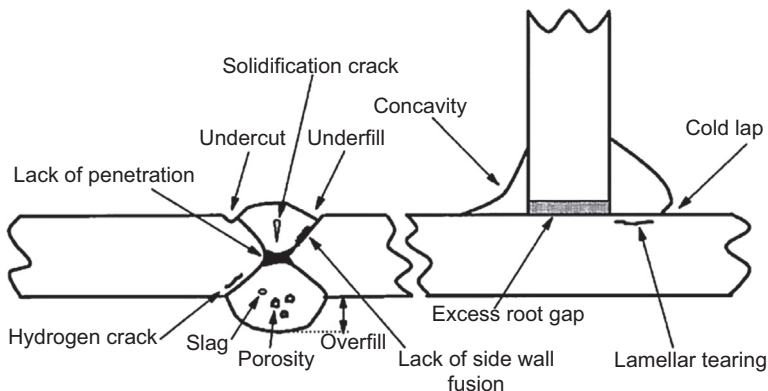


Figure 2.29 Schematic of weld defects and discontinuities (Source unknown).

2.3.3.2 Fatigue cracking

While fatigue cracking is possible in armour steels, in practical terms it is a rare occurrence since armoured structures, by definition, are normally overdesigned from a fatigue point of view. When found, fatigue is normally associated with poor weld joint design resulting in complex residual stresses with dynamic loads that are either, (1) unforeseen nondesign loads, or (2) occur over an extended period beyond a sensible service life.

2.3.3.3 Stress corrosion cracking

Stress corrosion (and corrosion fatigue when dynamic loading is significant) is an environmentally assisted form of cracking. For instance, high-strength armour steels have been shown to be much more susceptible to cracking in saltwater than when exposed to other environments, even tropical environments (Shah Khan et al., 1998). Stress corrosion cracking occurs, following crack initiation, when all three of the following conditions are present:

1. An applied or residual stress;
2. A susceptible microstructure;
3. A corrosive environment.

If any one of these three conditions is removed, then stress corrosion cracking will be prevented. As high-strength armour steels will have a susceptible microstructure, it is important to maintain protective coatings and use procedures that minimise the build-up of residual stresses during fabrication.

2.3.3.4 Delayed cracking

‘Delayed cracking’ can be a serious structural issue. Such cracking is known to occur either during, or after, completion of the fabrication of an armoured vehicle and can be quite widespread. Cracks with a length measured in decimetres rather than millimetres can be discovered long after fabrication has been completed, but are not considered to extend by fatigue, though stress corrosion can sometimes play a role. Fig. 2.30 shows a typical structural crack caused by delayed cracking.

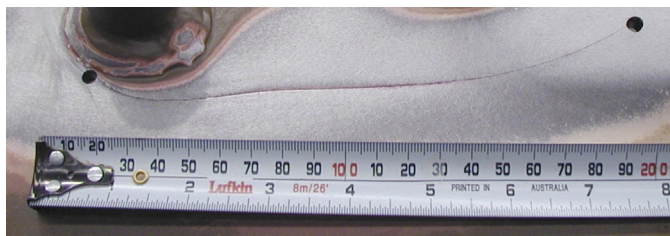


Figure 2.30 Structural crack in highhardness armour caused by delayed cracking. This crack is over 200 mm in length.

After Alkemade, S.J., 2015 unpublished research.

Sometimes armour plates even crack prior to welding, with such cracking sometimes being termed ‘picture frame cracking’ because the cracking occurs around the periphery of a freestanding plate, often around two or more sides. Even after fabrication, delayed cracking is often found to originate from free plate edges. The four main causes of delayed cracking are:

1. A susceptible microstructure of sufficient hardness that allows cracks of a critical length to freely propagate;
2. A tensile residual stress field;
3. Hydrogen-induced cold cracking in the plate HAZ adjacent to welds ([Ritter et al., 1989](#); [Alkemade, 1996](#));
4. Insufficiently controlled material specifications leading to microstructures with reduced toughness and greater susceptibility to crack propagation ([Wells et al., 1992](#)).

Crack starters are often associated with the presence of untempered martensite on the free edges of armour plates after cutting. The untempered martensite can be of a size that allows cracks of a critical length to form and thus freely propagate into the rest of the plate. Delayed cracking is prevented or reduced by:

1. Adopting low hydrogen welding procedures;
2. Exercising an armour steel specification with tight compositional limits and higher toughness requirements;
3. Using laser cutting to reduce the size of untempered martensite at the free edges of plates or even the use of water-jet cutting to eliminate untempered martensite entirely.

2.4 Grades of armour steels

2.4.1 *Wrought homogeneous armours*

RHA, as conventional, wrought, armour-grade steels, is loosely referred to, evolved during WW1 and the alloy grades were covered by early specifications like IT80 and IT100. IT stands for Inspectorate of Tanks and was the regulatory authority, which emerged in the 1930s. These UK specifications were still being used in the 1980s, before being superseded by the various Defence Standards (eg, DEF STAN 95-24), which are described in more detail in [Section 2.5](#).

RHA grades are low-alloy, quenched and tempered, martensitic steels, based upon a carbon content of $\sim 0.25\%$ with the additions of Ni, Cr, Mo and/or Mn. [Table 2.8](#) lists some of the approved alloy compositions, along with minimum values for some basic mechanical properties. A maximum value for the CE is normally quoted (typically less than 0.8) in order to achieve adequate weldability, expressed as a weight percent:

$$CE = C + [Mn/6] + [(Cr + Mo + V)/5] + [(Ni + Cu)/15]$$

Only approved suppliers, working to tightly controlled quality standards with metallurgical precision, manufacture the rolled plates. The ballistic properties of

Table 2.8 Compositional ranges, and basic minimum properties, of approved armour steels

Element	Wrought armour steels		Cast armour steels	
	DEF(AUST) 8030 Class 2: typical RHA	DEF(AUST) 8030 Class 6: typical HHS	DEF STAN 95-25 (2004): water- quenched grades	DEF STAN 95-26/4 (2011): air-hardening grades
Carbon	<0.30	<0.32	0.25–0.35	0.20–0.28
Silicon	0.20–0.60 (b)	0.60–1.00 (a)	0.20–0.60	0.30–0.50
Manganese	0.70–1.00 (b)	<1.00 (a)	1.20–1.70	0.70–1.10
Sulphur	<0.015	<0.005	0.020 max	0.015 max
Phosphorus	<0.025	<0.020	0.020 max	0.020 max
Nickel	NR (b)	NR (a)	0.50–1.00	3.20–3.50
Chromium	0.95–1.25 (b)	<1.25 (a)	0.40–0.80	1.20–1.60
Molybdenum	0.13–0.20 (b)	<0.20 (a)	0.30–0.50	0.40–0.50
Vanadium	0.10 max (b)	None	None	0.07–0.10
Copper	<0.25 (b)	<0.25 (a)	0.30 max	0.20 max
Property				
Hardness (HB)	260–310	477–534	241–285	260–310
Ultimate tensile strength (MPa)	n/a	n/a	770 min	850–1050
0.2%PS (MPa)	n/a	n/a	600 min	700 min
% Elongation	n/a	n/a	14 min	12 min
Charpy V-notch Impact (CVI) at –40 (J)	40 min	16 min	40 min	30 min

Notes: (a) as specified in MIL-A-46100E (MR), dated February 2009.

(b) Typical ranges, as indicated in MIL-A-12560H, dated November 1990.

(c) DEF STAN 95-25 is now classified as obsolete (ie, not used for purchasing; only maintenance).

these plates are controlled through production sampling and rigorous proof testing regimes. However, the ballistic tests are only quality control tests and, even to this day, are carried out using old WW2 ammunition. In the UK, the 2, 6 and 17 pounders (pdr) are regularly used for thicker plate with an homologous 20 mm APP round used for thinner plate. It is then up to the design authority to determine the ballistic properties of these plates against the specified threats of the day.

Approved suppliers range from SSAB, in Sweden, Thyssen, in Germany, and Biralloy, in Australia, to the many steel producers spread across the US states. In the UK, approved suppliers faded away with the rest of the steel industry. Crouch recollects the time in the mid-1980s when the UK MoD made the momentous decision to widen its approved suppliers outside of the UK, to the rest of Europe — a momentous, political and business decision of the day!

In the US, military specification, MIL-A-46100E (MR), dated 2008, is used for production of high-hardness steels, like DEF STAN 8030 Class 6 (Standard, 2008), and provides detailed guidance to steelmaking practices and quality control procedures. Hot-rolling and cold-rolling practices also include an amount of cross-rolling in order to achieve suitable texture and grain structure.

2.4.2 Cast steel armours

Armour-grade steel castings evolved during WW1 and early UK specifications were covered by grades like IT90, as issued by the Inspectorate of Tanks. Section thicknesses rose sharply during WW2 (see Fig. 2.2) and this required water-quenching treatments in order to achieve a reasonable through-thickness, hardness profile. Alloy grades were very lean and relied upon low carbon contents and the use of manganese as the principal alloying element. The last version was IT90G, written in the early 1960s to cover procurement of turret castings, glacis plates, and other components, for the UK MBT Chieftain. This document was upgraded to a Defence Standard (DEF STAN 95-25, 2004) and Table 2.8 gives typical compositional ranges. It is now classed as obsolete and is only available for upkeep of existing products, not for acquisition of new products.

During the 1980s, the design of turrets needed to change and the use of water-quenching alloys proved troublesome in manufacturing the newer designs. The need arose for an air-hardening grade. Crouch, Luck and others, at RARDE (Chobham), worked in the early 1980s to develop, and prove, such a new grade of cast steel armour. A draft specification for a new alloy was the outcome (Crouch, 1985), and even though the MBT80 project did not proceed, a new air-hardening grade had been successfully developed, based upon a clean, Ni—Cr—Mo—V composition, rather than a plain C—Mn steel.

By chance, and quite serendipitously, during this same period, an operational emergency arose: the turrets of the Chieftain MBT needed to be up-armoured. The Iran—Iraq conflict of the early 1980s had identified that the Chieftain tanks were not performing very well on the battlefield. Enhanced frontal protection was required. The use of thick-sectioned castings was the chosen engineering solution, since they had to be contoured to comply with the external shape of the existing turrets. Each of a number of thick-sectioned castings was produced in the new air-hardening alloy. For this project, the driver was through hardening, not suppression of distortion. Following a series of full-scale ballistic trials using Main Battle Tank rounds the Stillbrew up-armouring kit was born (see Fig. 2.31), and with it, a new cast steel armour specification, RARDE 823 (Specification, 1985). Since then, the



Figure 2.31 Images of the Stillbrew Crew Protection Package as fitted to the UK Chieftain MBT in the 1980s. The kit first saw service as part of the Chieftain Mk 10. Reproduced from: Anon., 2014. Bovington Tank Museum Database.

specification has been upgraded to a UK defence standard, DEF STAN 95-26: Specialised Armour Quality Castings, 2011, and was still current at the time of writing (2015).

When using this high-performance casting alloy, due care, and good foundry practices, need to be put in place to avoid ‘rock candy’ fractures and craze-cracking phenomena, as originally discovered by the US Navy during development of HY130 casting in the 1970s. ‘Rock Candy’ fractures are caused by AlN intergranular embrittlement and craze cracking is thought to be related to sulphur and/or phosphorus segregation to the prior-austenite grain boundaries.

Other nations have continued to use sophisticated designs of cast product, especially for turret castings. The Russians, in particular, have been past masters at taking full advantage of the cost-effectiveness and design freedoms that clever foundry practices provide.

However, whilst the Russians and others, like the UK, still retain an interest in development and use of cast steel armours (the latest version of DEF STAN 95-26 is dated 2011), the US have chosen not to — indicating, perhaps, that US designers may prefer to use welded RHA plate for their steel-based military vehicles. Nevertheless, US specification MIL-A-11356F (MR), dated May 1987, is still current and covers castings from a quarter of an inch up to 8 in. in thickness. It also provides a lot of manufacturing detail.

2.4.3 Dual-hardness grades

Very high armour hardnesses are required to shatter hard armour-piercing projectiles. Homogeneous armour of such hardnesses would normally be brittle and prone to shatter. This led to the concept of dual-hardness armour steels where a hard front face defeats a projectile by breaking it and the more ductile rear layer prevents penetration by the residual projectile, arrests any cracks and also maintains the structural integrity of the laminate.

A great deal of development work in the 1960s led to the specification of roll-bonded dual hard plate in MIL-A-46099C (Specification, 1987) which had a front layer hardness of 601–712 HB with a rear layer hardness of 461–534 HB. These materials are both Ni–Mo–Cr steels with a higher carbon content in the front layer to achieve the required hardness (Gooch et al., 2005). A strong metallurgical bond between the layers is required for high ballistic resistance (Manganello and Abbott, 1972) and for good multihit capability and is achieved by hot-rolling. The ballistic performance of such materials can be problematic unless a strong metallurgical bond can be produced reliably.

ESR (refer to Section 2.4.4) was used to produce dual-hardness armour with front and rear face hardnesses (500–560 HB front, 340–370 HB rear) better optimised for improved fragmentation protection (Gooch et al., 2005). In this case, a reliable metallurgical bond between the two steel layers was achieved as the ESR process welds one of the layers (which is molten) to the other, which is in a solid or partially molten state. While this steel was not fully optimised for projectile protection, Fig. 2.32 shows the increase in ballistic performance that can be achieved over both RHA and HHA.

Explosive bonding is also used commercially to produce dual-hardness steel armour plate, where two Ni–Cr–Mo armour steel layers are bonded explosively together to form a strong metallurgical and mechanical bond. The explosive bonding process produces a stronger metallurgical bond than roll bonding. This is because correct operation of the explosive bonding process (Blazynski, 1983) cleans metal oxides from the two bonding surfaces immediately before they are bonded and produces a

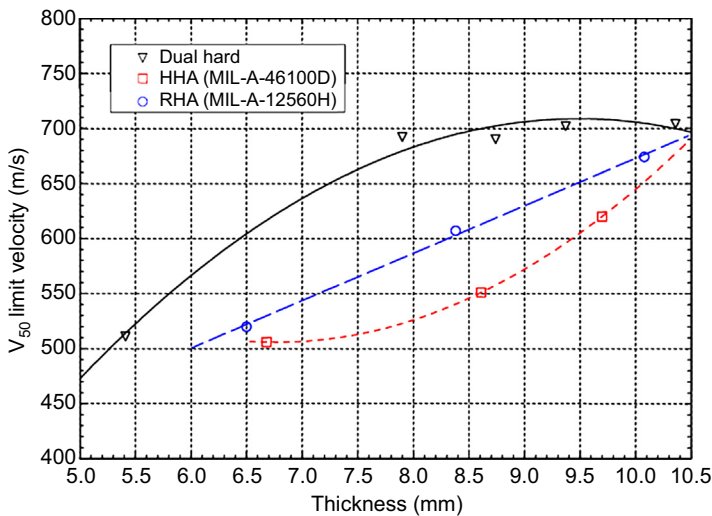


Figure 2.32 The V_{50} ballistic limit for Bulgarian dual-hardness armour, HHA and RHA against 0.30 Cal APM2 at 0° obliquity.

After Gooch, W.A., Burkins, M.S., MacKenzie, D., Vodenicharov, S., 2005. Ballistic analysis of Bulgarian electroslag remelted dual hard steel armor plate. In: Paper Presented at the 22nd International Symposium on Ballistics, Vancouver, BC, Canada.

wavy interface between the two bonding layers, which also has a finer grain size. This and the mechanical interlock between the two wavy layers maximises the shear strength of the interface between the layers so that it better withstands shear from bending deformations, better maintaining the integrity of the laminate, particularly when it is impacted multiple times. Fig. 2.33 shows an example of the mechanical interlock that can be achieved between a quenched and tempered martensitic steel and a soft austenitic steel.

An important advantage of some Ni–Mo–Cr dual-hardness armour steels is that they can be softened by a solution annealing heat treatment to allow easy fabrication (forming, cutting, drilling, welding, etc.). Such steels are then easily rehardened by a lower aging heat treatment, followed by air-cooling to the final design hardnesses. This offers considerable flexibility for fabrication. While such steels will be more expensive than conventional quenched and tempered steels, they offer the ability to form large structures or complex shapes prior to any final hardening heat treatment.

Homogeneous Ni–Cr–Mo steels are also now available which meet Class 2 MIL-DTL-46100E. These steels include additional Ni, Cr and Mo compared to conventional quenched and tempered HHA to increase hardenability and toughness and allow an aging heat treatment, followed by air-cooling (Gooch et al., 2009). Such steels are a logical development from the Ni–Cr–Mo maraging dual-hardness steel compositions discussed above and allow easier fabrication, including forming, cutting and drilling as well as any post fabrication heat treatments to recover ballistic properties. The slower air-cooling also results in significantly higher dimensional stability.

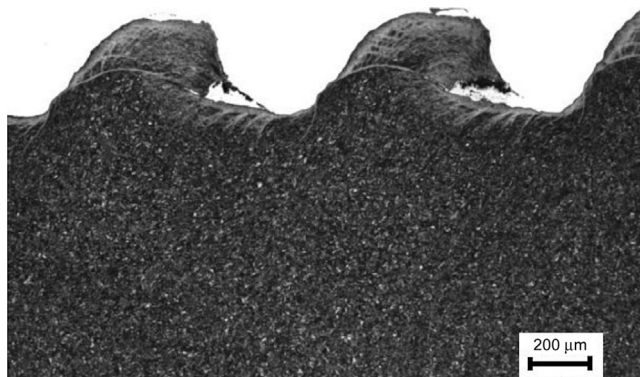


Figure 2.33 Microstructure of explosively welded steels demonstrating the wavy mechanical interlock between a 440-HV martensitic steel (lower part of the image) and a 215-HV austenitic steel. Note the shear bands in the quenched and tempered martensitic steel. Scale bar is 200 μm.

From Choi, C., Callaghan, M., van der Schaaf, P.L.H., Dixon, B., 2014. DSTO Technical Report, DSTO-TR-2960, Modification of the Gurney Equation for Explosive Bonding by Slanted Elevation Angle.

2.4.4 Electroslag refining (ESR) grades

Electroslag refining (or remelting) (ESR) has been used to produce cleaner steels with more uniform composition than conventional, even existing high-quality, steels. This process significantly reduces the sulphur content and the size of nonmetallic inclusions. ESR steels therefore have better ductility and toughness, particularly in the through-thickness direction, than equivalent conventional steels that are more anisotropic (MacKenzie et al., 1977).

Fig. 2.34 shows how ESR processed steels can achieve much greater through-thickness (short transverse) toughness than the same steel which has been vacuum arc remelted, even though both steels have similar toughness in the plane of the plate. This correlates to observations that ESR steels show improved spallation resistance against through-thickness stress waves arising from contact detonations of explosives (Doig, 1979). ESR steels have improved ballistic resistance over a hardness range where adiabatic shear occurs (Rawson and Dawson, 1972) and thus are best suited for applications that require such steel hardnesses. Any enhancement of ballistic resistance against small arms projectiles would be due to the greater work of plug tear out once asymmetric deformation occurs (Woodward, 1984).

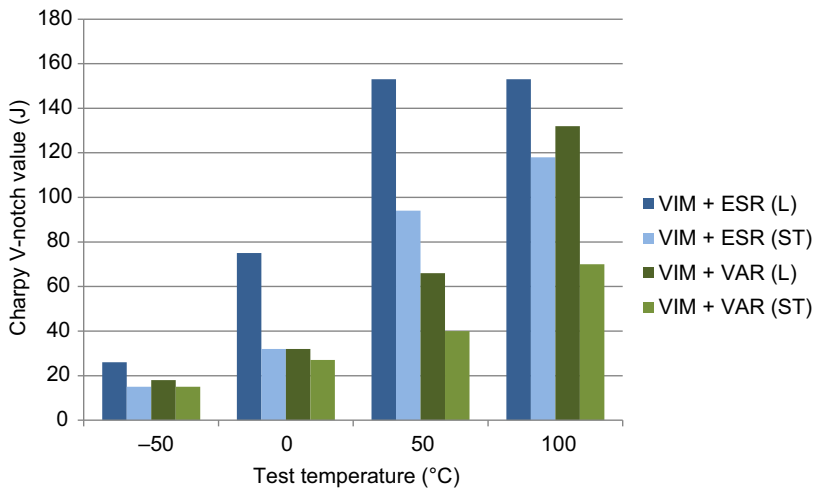


Figure 2.34 Longitudinal and short transverse Charpy values for vacuum induction melted (VIM) steel that is followed by either ESR or vacuum arc remelting (VAR).

After Doig, A., 1979. Comparative anisotropy of quenched and tempered alloy steel plates made by high quality air melting, ESR, VIM & VAR, and VIM & ESR processes. In: Paper Presented at the Sixth International Vacuum Metallurgy Conference on Special Melting, San Diego, CA.

The overall move by steel makers to continuous casting processes and improved ladle metallurgical practices, as well as the cost of the ESR process and its complexity, has led to it not being widely applied for armour applications in the Western world.

2.4.5 Research grades

Conventional RHA and HHA have been used for many years as preferred armour materials. However, as metallurgical, and mechanical, developments increase, so too does the penetrating ability of the kinetic energy projectiles. Therefore, the need for research and development into improved steel armour, to defend against such threats during combat, is paramount in order for armoured vehicles to maintain survivability and combat effectiveness. In recent years, the steels that have been procured for further investigation include super bainitic steel, flash bainitic steel, twinning-induced plasticity (TWIP) steel, TRIP steel and dual-phase steel, all of which may be considered as potential candidates for 'next-generation' ferrous armour systems, especially for blast protection, since their yield strengths are normally low and their ductility high.

2.4.5.1 Super bainitic steels

Martensitic armour steels rely on fine martensitic structures generated through rapid cooling (quenching) for strength and hardness. The heat-treatment process limits the size, or complexity, of the component that can be produced with homogeneous properties. However, bainitic steels can possess extremely attractive properties as a candidate material for armour systems. Indeed, a press release by DSTL (Defence Science and Technology Laboratory, UK) in 2008 ([Anon, 2008](#)) entitled 'The story of the best armour steel ever made', has described the current collaborative research by DSTL and the University of Cambridge into super bainitic armour, where the achievement of ultrahigh-hardness levels were obtained in the material by employing low-temperature isothermal hardening.

Currently, much research has been conducted into super bainitic steels by the University of Cambridge. It has been reported ([Bhadeshia, 2006](#)) that super bainitic steels can be designed to have an extraordinary combination of strength, hardness and toughness, without the use of expensive alloying elements or mechanical processing. Moreover, super bainitic steels have a number of other attractive features: lower production costs and more shapeability for large components ([Bhadeshia, 2006, 2005](#)).

Super bainite may be described as steel transformed into carbide-free bainite, with the particular microstructure of bainitic plates. This type of material has produced hardness of approximately 600 VHN ([Garcia-Mateo et al., 2003](#)), ultimate tensile strengths of 2500 MPa, toughness of 30–40 MPa m^{1/2}, at room temperature, and ductility between 5% and 30%. The microstructure is also reported to contain thin bainite plates ([Bhadeshia, 2006](#)). [Fig. 2.35](#) shows the typical Transmission Electron Microscopy (TEM) micrograph of super bainite. The thickness of these bainitic plates in the microstructure is normally 20–50 nm. The strength of the steel is derived from

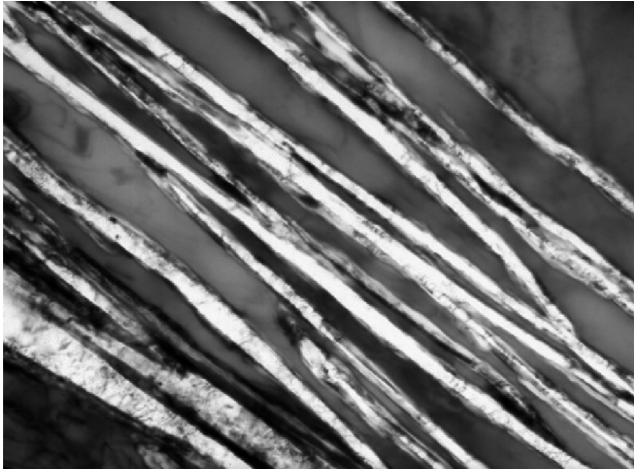


Figure 2.35 Fe-0.98C-1.46Si-1.89Mn-0.26Mo-1.26Cr-0.09V (wt%), transformed at 200°C for 5 days.

the bainite plate thickness and as the transformation temperature is reduced the thickness of the plates decreases. Therefore, it can be understood that the aim of the heat-treatment process is to reduce the transformation temperature in order to promote thin plate formation. However, this reduction in transformation temperature results in a reduction in the rate at which bainite forms (in the order of hours to years depending on the carbon concentration). For 1 wt% carbon it is predicted to take approximately a year (Garcia-Mateo et al., 2003). This is the key disadvantage of super bainitic steels. However, alloying with cobalt or aluminium accelerated transformation and in future research the possibility of rapid transformation could be produced by controlling manganese content (Caballero and Bhadeshia, 2004).

2.4.5.2 Flash bainitic steels

A US company (SFP Works, LLC) developed an evolutionary steel thermo-processing technique, called the flash bainitic process, in 2007. It is claimed to possess tensile strengths from 1100 to 1900 MPa, with 8–9% elongation. Commercial off-the-shelf steel sheet, plate (up to 61 mm wide and 6.6 mm thick), and tubing (12–63 mm in diameter) can be transformed to flash bainite. Through rapid heating and water quenching, a bainitic microstructure is produced very rapidly in a continuous rolling process (Fig. 2.36).

Work conducted in the US showed that flash bainitic armour (FBA) is superior to RHA and conventional HHA (Lolla et al., 2011). FBA4130, for example, appears to offer a 40% mass reduction over RHA for armour piercing threats (Fig. 2.37) and 34% less areal density than conventional HHA against FSP threats (see Fig. 2.38). However, because of the processing limitations, the thicknesses of useable steels are restricted to less than 6.6 mm.

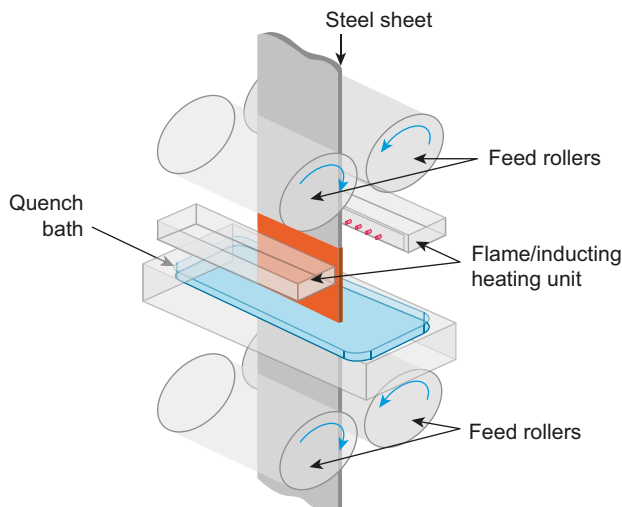


Figure 2.36 Schematic illustration of the experimental set-up of the flash processing technique. After Lolla, T., Cola, G., Narayanan, B., Alexandrov, Babu, B., 2011. Development of rapid heating and cooling (flash processing) process to produce advanced high strength steel microstructures. *Material Science and Technology* 27 (5), 863–875.

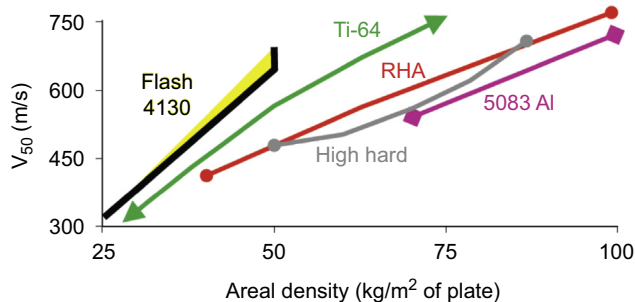


Figure 2.37 Ballistic testing of FBA 4130 against 0.3" APM2 rounds at normal. After Lolla, T., Cola, G., Narayanan, B., Alexandrov, Babu, B., 2011. Development of rapid heating and cooling (flash processing) process to produce advanced high strength steel microstructures. *Material Science and Technology* 27 (5), 863–875.

2.4.5.3 Twinning-induced plasticity steels

The development of TWIP steels has been mainly driven by the automotive industry. TWIP steels have an excellent combination of high strength and formability (ductility), which is particularly attractive for structural reinforcements and energy absorption parts.

TWIP steels, which were developed from the late 1990s, have excellent ductility, high work hardening rate, and a significantly enhanced capability to absorb energy

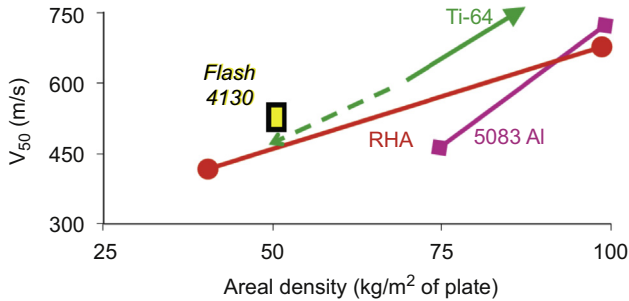


Figure 2.38 Ballistic testing of FBA 4130 against 20 mm FSP rounds at normal. After Lolla, T., Cola, G., Narayanan, B., Alexandrov, Babu, B., 2011. Development of rapid heating and cooling (flash processing) process to produce advanced high strength steel microstructures. *Material Science and Technology* 27 (5), 863–875.

upon impact, while maintaining stability and strength of components. TWIP steels normally comprise 20–30% manganese and small quantities of carbon, aluminium and silicon, which causes the steels to be fully austenitic at room temperature. The principal deformation mode is twinning inside the grains and the tensile elongation can be as high as 100%, while the ultimate strength can be above 1000 MPa (Bouaziz and Guelton, 2001; Zhen-li et al., 2009).

Compared with TRIP steels, which have been on the market since the 1980s, TWIP steels have greater reserve ductility and a higher work hardening rate. Their ductility stems from stacking faults in its face-centred crystal lattice. If an extra two stacks of atomic planes are introduced to the lattice from above, it disturbs the regular sequencing of the atomic planes, forming a stacking fault on a mirror plane and creating regularly mirrored sections of crystal. The effect is called twinning, which causes a high value of the instantaneous hardening rate as the microstructure becomes finer and finer. The resultant twin boundaries act like grain boundaries and strengthen the steel. Therefore, once a particular volume of steel has started to deform, its yield strength rises such that deformation spreads out to neighbouring volumes. The full material participates in deformation and hence energy absorption.

However, whilst their energy-absorbing capacity is attractive to the automotive industry, their relatively low yield strength limits their application as an armour material.

2.4.5.4 Transformation-induced plasticity steels

TRIP-assisted steels have a microstructure that is a mixture of allotriomorphic ferrite, bainite (~20%) and retained austenite (~10%). During plastic deformation and straining, the metastable austenite phase is transformed into martensite. This transformation enables enhanced strength and ductility, with typical ranges of 500–1000 MPa for tensile strength, and 15–30% for elongation. A typical TRIP steel would have a composition based upon 0.1–0.4% C with 1–2% of each of

silicon and manganese: the high silicon concentration ensures that cementite is not precipitated during the growth of upper bainite. The carbon that is partitioned from the bainitic ferrite stabilises the residual austenite, enabling it to be retained at ambient temperature. TRIP steels are produced by various combinations of thermomechanical processes and heat treatments related to their chemical composition (Zrník et al., 2008).

This transformation process has also been observed by Kasonde (2006) during ballistic impact. His results, published in 2006, even showed a relationship between the amount of transformation (in the impact zone) and the steel's ballistic performance. His main research finding has been reproduced in Fig. 2.39, where the volume fraction of retained austenite appears to be related to ballistic performance. The optimum ballistic parameter obtained from this research was between 0.018 and 0.06. This is an interesting observation that requires deeper investigation.

2.4.5.5 High-alloy, high-carbon steels

For nonstructural applications, especially those that can tolerate poor toughness, the development of a grade of UHHS is extremely attractive because such steels may be able to compete with some of the ceramic grades (see Chapter 7). For example, thin steels have been used in body armour applications (eg, AR500 steel) to provide protection against small arms ammunition. However, in order to compete on a weight basis, these UHHSs need to be very thin; between 2 and 4 mm. At that thickness they also possess another attractive quality: the finished product will only be ~50% of the thickness of a ceramic-based hard armour plate (see Chapter 7). In recent research

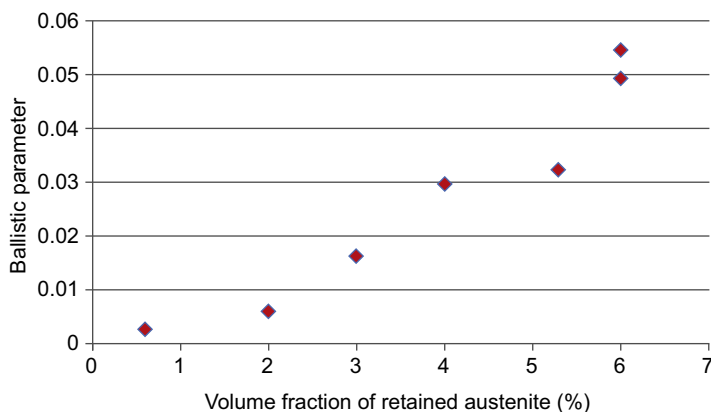


Figure 2.39 Relationship between retained austenite and ballistic performance. Derived from Kasonde, M., 2006. Optimizing the Mechanical Properties and Microstructure of Armoured Steel Plate in Quenched and Tempered Condition (M.Sc. thesis). University of Pretoria, South Africa.

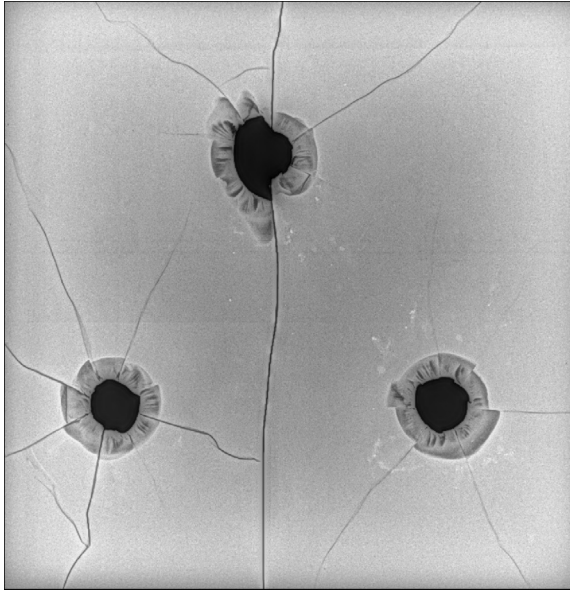


Figure 2.40 X-radiograph of a UHHS target struck on three occasions using an AK47 bullet at ~ 650 m/s. The steel target was tested as part of a body armour system. Note the conoidal fracture and radial cracking, as typically observed in a ceramic-based system (Crouch, 2014).

work, carried out by the Defence Materials Technology Centre, in Australia (Li, 2013), this low-profile body armour concept has been researched. However, in order to really compete with ceramic-based systems, the steel also needs to be extremely hard – to the point where it will shatter. In this application, that will not matter, since designers of Hard Armour Plates (HAPs) are used to designing with brittle materials and using cladding layers of aramid, for example (Crouch, 2014). Early results from initial ballistic impacts have already demonstrated that high-alloy, high-carbon steels do behave like a ceramic and fail in a conoidal manner (see Fig. 2.40). The composition of the steel was selected in order to achieve maximum attainable hardness, in excess of 700 VPN. With a carbon content of $\sim 0.9\%$ and based upon a 13% chromium, ‘razor blade’ steel, the researchers have demonstrated that both conoidal fracture and radial cracking occur, and the target remains intact because it had been clad as a brittle ceramic would have been. Current objectives are to match the ballistic performance of an alumina-based HAP system, at half the thickness.

2.5 Armour specifications and standards

In practical terms, armour is required to deliver optimised performance against a range of battlefield threats, including armour piercing and fragmentation threats. Such protection has to be provided at realistic areal densities for an affordable price. Quenched and tempered martensitic steel has continued to be highly competitive as an armour material

for many ballistic applications. Defence specifications are used to control the quality assurance of the minimum required material properties for particular applications.

2.5.1 Wrought armour steels

Two of the most common armour steel grades in use are MIL-DTL-12560K Class 1 RHA with a hardness range of 250–410 HB ([Specification, 2013](#)) and MIL-DTL-46100E HHA with a hardness range of 477–534 HB ([Specification, 2008](#)). Both of these specifications had their origins in WW2 and have not changed markedly since ([Gooch et al., 2007](#)), though the former was modified after many years to incorporate a new class of wrought armour plate, Class 4, which is heat-treatable to higher hardness ranges than Class 1 as well as other improvements. MIL-DTL-32332 ([Specification, 2009](#)) is a new specification that specifies ultra high hardness steels with hardnesses in excess of 570 HB. There has been development and application of unified armour steel specifications that control armour steel properties over a wide range of steel hardness. DEF(AUST) 8030 ([Standard, 2008](#)) and UK DEF STAN 95-24 ([Standard, 2004](#)) are examples of such specifications. [Tables 2.9 and 2.10](#) compare these specifications with US Military Specifications.

DEF(AUST) 8030 is a unified armour steel specification, which controls the mechanical and chemical properties over a full range of functional rolled homogeneous armour steel classes. It is a performance-based specification, allowing a designer the freedom to choose an armour steel that best meets their needs while defining ballistic performance quality assurance requirements and, importantly, ensuring that the structural integrity of the resulting armoured structure will also meet a minimum standard ([Cimpoeru and Alkemade, 2002](#)).

Increasing the hardness of armour steels will usually reduce their toughness. Hardness limits ([Table 2.9](#)) are therefore set for specific steel armour classes to control toughness during production ([Table 2.10](#)), and reduce the risk of shattering or other brittle failures for specific steel compositions and applications. For example, HHA is highly susceptible to stress-corrosion cracking in marine (saltwater) environments.

While ballistic performance will generally increase with hardness, this will depend on the threat projectile and armour thickness and toughness. It is also the case that the optimum armour choice will depend on whether the armour is to be applied as a stand-alone structural armour or appliqué armour. The armour designers are to ensure that they have selected the armour class that offers the best combination of ballistic performance and structural properties appropriate for the intended application (ie, [Table 2.11](#)). It is the responsibility of the armour designer to choose the grade and thus armour properties (strength/hardness/toughness) that both maximise protection and minimise through-life costs for any specific armour application.

2.5.2 Cast steel armours

[Section 2.4.2](#) described the typical alloys used for cast steel armours and the corresponding military specifications.

Table 2.9 Hardness of armour steel grades, less than 35 mm

Armour class according to DEF(AUST) 8030	Hardness equivalences (HB)		
	DEF(AUST) 8030 ^a	US specification approx. nominal equivalent grade	DEF STAN 95-24 approx. nominal equivalent grade
Class 1	Not explicitly specified	No equivalent	No equivalent
Class 2	260–310	MIL-DTL-12560K: Class 2 260–310	Class 1 262–311
Class 3	340–390	MIL-DTL-12560K: Class 1 6.35 to ≤15.8 mm: 340–390 15.9 to <28.6 mm: 330–380 28.6 to ≤50.8 mm: 310–360	Class 2 <9 mm: ≥341 9 to <15 mm: ≥311 15 to <35 mm: ≥285
Class 4	370–430	MIL-DTL-12560K: Class 1 ≤6.3 mm: 360–410	No equivalent
Class 5	420–470	MIL-DTL-12560K: Class 4 420–470	Class 3A 5 to <50 mm: 420–480
Class 6	477–534	MIL-DTL-46100E 477–534	Class 3 <15 mm: 470–540 15 to <35 mm: 470–535
Class 7	≥570	MIL-DTL-32332: Class 1 <16mm: ≥570	Class 5 560–655
Class 8	≥570	MIL-DTL-32332: Class 2 <16mm: ≥570	No equivalent

^aEach hardness range in DEF STAN 8030 applies for all thicknesses from 3 to 35 mm, unless otherwise specified. After Standard, 2008. Australian Defence Standard, DEF(AUST) 8030, Rolled Armour Plate, Steel (3–35 mm).

In the UK, two defence standards apply: DEF STAN 95-25 (2004) for plain C–Mn, water quenching, grades, and DEF STAN 95-26 (2011) for cleaner, air-hardening grades. No Australian specification exists for cast steel armours and, in the US, an old version of the US Specification MIL-A-11356F (MR), dated May 1987, still remains open and active.

These are all production specifications, which detail compositional and mechanical property requirements, and inspection standards, as well as other quality control

**Table 2.10 Charpy toughness of armour steels less than 35 mm.
Charpy toughness measured according to AS 1544.2 (DEF(AUST) 8030) or BS EN 10045-1 (DEF(AUST) 8030 and DEF STAN 95-24) or ASTM E23 and ASTM A370 (US Specification)**

Armour class according to DEF(AUST) 8030	Minimum Charpy toughness (J)		
	DEF(AUST) 8030	US specification approx. nominal equivalent grade	DEF STAN 95-24 approx. nominal equivalent grade
Class 1	Not explicitly specified	No equivalent	No equivalent
Class 2	260–310 HB 40	MIL-DTL-12560K: Class 2 260–270 HB: 75.9 270–280 HB: 69.1 280–290 HB: 62.4 290–300 HB: 55.6 300–310 HB: 48.8	Class 1 260–310 HB: 40
Class 3	340–390 HB 20	MIL-DTL-12560K: Class 1 340–350 HB: 29.8 350–360 HB: 25.7 360–370 HB: 24.4 370–380 HB: 23.0 380–470 HB: 21.7	Class 2 <9 mm: ≥ 341 HB: 20 9 to <15 mm: ≥ 311 HB: 20 15 to <35 mm: ≥ 285 HB: 25 35 to <50 mm: ≥ 262 HB: 30
Class 4	370–430 HB 18	MIL-DTL-12560K: Class 1 370–380 HB: 23.0 380–470 HB: 21.7	No equivalent
Class 5	420–470 HB 16	MIL-DTL-12560K: Class 4 420–470 HB: 21.7	Class 3A 5 to <50 mm: 420–480 HB: 16
Class 6	477–534 HB 16	MIL-DTL-46100E 477–534 HB: 16.3	Class 3 <15 mm: 470–540 HB: 16 15 to <35 mm: 470–535 HB: 29
Class 7	≥ 570 HB 12	MIL-DTL-32332: Class 1 ≥ 570 HB: 8.1	Class 5 560–655 HB: 5
Class 8	≥ 570 HB 8.1	MIL-DTL-32332: Class 2 ≥ 570 HB: 8.1	No equivalent

Table 2.11 Intended use for each armour class in DEF(AUST) 8030

Class	Hardness (HB)	Intended use
Class 1	Not explicitly specified	<p>Class 1 armour grade allows the application of structural grades of quenched and tempered steels for specialised armour applications, for example, naval applications. Class 1 armour has excellent toughness and good weldability and formability</p> <p>Steels nominated as Class 1 armour shall meet the requirements of a nominated structural steel specification. AS 3597, ASTM A514 or MIL-S-24645A are examples of typical structural steel specifications that would meet the requirements of this class of armour, ie, they have a minimum 0.2% proof stress of 550 MPa and also meet the additional requirements of Sections 3.4–3.9 of this specification. Class 1 armour is not equivalent to Class 1 armour in MIL-A-12560K</p>
Class 2	260–310	<p>Class 2 armour is intended for use in those areas where maximum resistance to failure under conditions of blast loading and fragmentation protection is required and where resistance to penetration by armour-piercing ammunition is of secondary importance to resistance. Class 2 armour is intended for use for protection against landmines and other blast-producing weapons. Class 2 armour can be cold-worked and is weldable</p>
Class 3	340–390	<p>Class 3 armour is intended for use in applications where very good resistance to penetration is combined with excellent structural properties. Class 3 armour can be cold-worked and is weldable</p>
Class 4	370–430	<p>Class 4 armour is heat-treated to higher hardness levels than Class 3 armour to further increase resistance to penetration whilst maintaining similar structural properties to Class 3 armour. Class 4 armour can offer an advantage over Class 3 and Class 5 armours for certain applications</p>
Class 5	420–470	<p>Class 5 armour is heat-treated to higher hardness levels than Class 4 armour to further increase resistance to penetration. Class 5 armour is intended as a tougher alternative for Class 6 armour and can ballistically outperform it</p>
Class 6	477–534	<p>Class 6 armour was originally created for appliqué armour only and can be used with care for welded structural applications</p>
Class 7	≥570	<p>Class 7 armour is intended for use as a nonstructural standalone or appliqué armour that is designed for better resistance to penetration than Class 6 armour</p>
Class 8	≥570	<p>Class 8 armour is intended for use as a nonstructural standalone or appliqué armour that is designed for better resistance to penetration than Class 7 armour</p>

procedures, including numerous casting defects. Ballistic testing is carried out simply as part of the QC procedures, using standard, old ammunition like the 2 and 6 pdr in the UK and WW2 ammunition like the 0.3" APM2, 0.5" APM2 and 75 mm AP (M72) rounds in the US.

Specified ranges of chemical composition and typical minimum mechanical property levels are given in [Table 2.8](#).

2.5.3 Perforated steel armours

Perforated steel armour involves steel armour that is in effect perforated with a grid of holes perpendicular to the face of the armour ([Fig. 2.41](#)). The holes are generally no bigger than half the expected diameter of the expected penetrator. In 2007, a specification for 'Perforated homogeneous steel armour' was approved for use by the Department of the Army and was available for use by all Departments and Agencies of the Department of Defense ([Specification, 2007](#)). To reduce the weight and the overall areal density of the plate or casting, the perforations need to be made according to the requirements specified in the contract or purchase order.

Attempts have been made in the past to improve the performance of perforated armour steel by introducing different hole configurations. For example, perforated armour steel plates using circular ([Trasi et al., 1987](#)), triangular ([Auyer et al., 1989](#)) and other types of holes ([Moshe and Hirschberg, 2006](#)) have been employed as the front panel of the armour assembly to defeat the projectiles. The deflection of projectiles and generation of higher stresses on the projectile during such interaction are the



Figure 2.41 Typical example of perforated steel armour plates.
See www.mtladv.com.

primary reasons for breaking the projectile, thereby, decreasing the depth of penetration. In addition, perforated plates are also attractive for passive mitigation systems against explosive blast (Langdon et al., 2008). A recent investigation on effect of geometry, mechanical properties, thickness, obliquity and gap on ballistic resistance of perforated plates against 12.7 mm M-8 API ammunition has shown mass effectiveness as high as 5.91 (Balos and Sidjanin, 2011). In this study, perforated plates were made of two types of steel, 50CrV4 and Hardox 450. 50CrV4 was used, 50CrV4 plates were quenched at 840°C in oil and subsequently tempered at 170°C (C170) and 450°C (C450), for achieving two levels of tensile properties, hardness and impact strength. Hardox 450 was used as supplied by the manufacturer. Mechanical properties of these materials were tested at room temperature (20°C) and are given in Table 2.12.

Test steel plate thickness was 6 mm (all tested materials) and 4 mm (only Hardox 450). The holes in the perforated plates were machined by water-jet technology, operating at 3500 bar pressure. Perforated plates with two diameters were tested, 7 and 9 mm, with distance between centres of holes 10.5 and 13.5 mm, respectively. Therefore, the ligament between the holes is 3.5 and 4.5 mm, which means that the ratio between hole diameter and the ligament is constant. The distance between the perforated plate and the base plate was typically 400 mm. The optimal sample was shown to have 9 mm diameter holes. Its resistance is sufficient to induce bending stresses in penetrating core to frequently fracture it in more than two parts. Therefore, the debris cannot sufficiently affect the basic plate, enabling it to have a very high multihit resistance.

Research continues in this area, including work at the DMTC (Li, 2013) which is aimed at personnel armour systems, and a range of fully commercialised products for vehicular applications, as supplied by Sleeman Engineering, for example. Recently, the UK Ministry of Defence has signed a licensing agreement with Tata Steel to manufacture super bainitic steel in the UK. Under the agreement the steel will be turned into seven different items, including perforated armour plates that could be used on future frontline armoured vehicles. Tata Steel has since produced ultrahigh-hardness perforated

Table 2.12 Composition of steels used in perforated armour trials

	50CrV4 Tempered at 170°C	50CrV4 Tempered at 450°C	Hardox 450
Hardness BHN (kgf/mm ²)	598 ± 5	465 ± 4	445 ± 3
Ultimate tensile strength (MPa)	1885 ± 10	1470 ± 14	1450 ± 8
Yield strength (MPa)	1845 ± 15	1410 ± 13	1255 ± 7
Elongation (%)	3 ± 1	6 ± 1	11 ± 2
Contraction in radial direction (%)	14 ± 2	21 ± 3	45 ± 5
Impact strength (J)	5 ± 2	14 ± 2	60 ± 3

kgf, kilogram force.

Reproduced from Balos, S., Sidjanin, L., 2011. Metallographic study of non-homogenous armour impacted by armour-piercing incendiary ammunition. *Materials and Design* 32, 4022–4029.

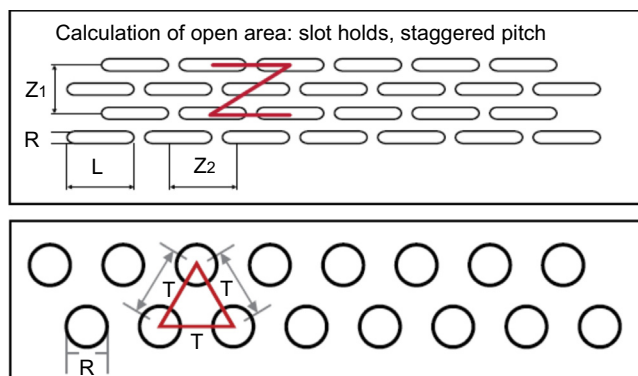


Figure 2.42 Tata Steel's Pavise ultrahigh-hardness perforated armour steel has been specifically developed for demanding military applications.

Reproduced from www.mtladv.com; Ministry of Defence, 2011. New Armour Steel Showcased at DSEi. (Retrieved from U.K.).

armour steel with the brand name 'PAVISE SBS 600P' (Ministry of Defence, 2011). Fig. 2.42 shows the typical hole design of super bainitic steel armour plates. The ballistic performance of PAVISE is at least twice that of conventional rolled homogeneous steel armour. The perforated design of the steel creates a large number of edges, which disrupt the path of incoming projectiles, significantly reducing their potency.

Acknowledgements

The authors would like to thank all of their colleagues within the DMTC who contributed in some way to this chapter, in particular Stewart Alkemade, from the Defence Science and Technology Group, and Dr John Norrish, Emeritus Professor at the University of Wollongong. Dr Norman Herzig and Professor Lothar Meyer of Nordmetall are also gratefully thanked for their careful reviews and suggestions on the topics of High Strain Rate Effects and Failure.

References

- Alkemade, S.J., 1996. DSTO Technical Report DSTO-TR-0320, the Weld Cracking Susceptibility of High Hardness Armour Steel.
- Alkemade, S.J., 2015. Unpublished DST Group research.
- Anon., 1986. Low-cost add-on Chobham at last. *Defence Attache* 6 (1986), 4.
- Anon., 2008. Super Armor – The Story of the Best Armour Steel Ever Made. Made in the U.K. Defence Science and Technology Laboratory, p. 1.
- Anon., 2014. Bovington Tank Museum Database.
- Atapek, S.H., 2013. Development of a new armor steel and its ballistic performance. *Defence Science Journal* 63 (3), 271–277.
- Auyer, R.A., Buccellato, R.J., Gidynski, A.J., Ingersol, R.M., Sridharan, S., 1989. Perforated Plate Armor. International Patent No. WO89/08233.

- Backman, M.E., Finnegan, S.A., 1973. The propagation of adiabatic shear. In: Rohde, R.W., Butcher, B.M., Karnes, C.H. (Eds.), *The Propagation of Adiabatic Shear in Metallurgical Effects at High Strain Rates*. Plenum, New York.
- Balos, S., Sidjanin, L., 2011. Metallographic study of non-homogenous armour impacted by armour-piercing incendiary ammunition. *Materials and Design* 32, 4022–4029.
- Bedford, A.J., Wingrove, A.L., Thompson, K.R., 1974. The phenomenon of adiabatic shear. *Journal of the Australian Institute of Metals* 19, 61–73.
- Bhadeshia, H.K., 2005. Large chunks of very strong steel. *Materials Science and Technology* 21 (11), 1293–1302.
- Bhadeshia, H.K., 2006. Bainitic bulk-nanocrystalline steel. In: Paper Presented at the 3rd International Conference on Advanced Structural Steels. Korean Institute for Metals, Korea.
- Blazynski, T.Z., 1983. Explosive Welding, Forming and Compaction Barking. Applied Science Publishing, England.
- Borvik, T., Dey, S., Clausen, A.H., 2009. Perforation resistance of five different high strength steel plates subjected to small arms fire. *International Journal of Impact Engineering* 36, 948–964.
- Bouaziz, O., Guelton, N., 2001. Modelling of TWIP effect on work-hardening. *Materials Science and Engineering A* 319–321, 246–249.
- Caballero, F.G., Bhadeshia, H.K., 2004. Very strong bainite. *Current Opinion in Solid State and Materials Science* 8, 251–257.
- Choi, C., Callaghan, M., van der Schaaf, P.L.H., Dixon, B., 2014. DSTO Technical Report, DSTO-TR-2960, Modification of the Gurney Equation for Explosive Bonding by Slanted Elevation Angle.
- Cimpoeru, S.J., Alkemade, S., 2002. Guidelines for effective armour material specifications for defence applications. In: Paper Presented at the Technological and Research Developments in Welded Defence Equipment. WTIA.
- Cimpoeru, S.J., Woodward, R.L. Unpublished DST Group research.
- Cimpoeru, S.J., Woodward, R.L., 1990. High strain rate properties of three liquid phase sintered tungsten alloys. *Journal of Materials Science Letters* 9, 187–191.
- Cimpoeru, S.J., 1990. The flow stress of a 0.21% C mild steel from strain rates of 10^{-3} to $2 \times 10^4 \text{ sec}^{-1}$. *Journal of Materials Science Letters* 9, 198–199.
- Crouch, I.G., 1985. Final Development Phase of a New Air-Hardenable, Cast Steel, Armour Alloy – Part 1. Technical Report, MVEE, Chertsey.
- Crouch, I.G., 1988. Metallic armour – from cast aluminium alloys to high strength steels. *Materials Forum* 12, 31–37.
- Crouch, I.G., 2014. Effects of cladding ceramic and its influence on ballistic performance. In: Paper Presented at the International Symposium on Ballistics, Atlanta, GA, USA, September 2014.
- Dieter, G.E., 1981. *Mechanical Metallurgy*, second ed. McGraw-Hill.
- Doig, A., 1979. Comparative anisotropy of quenched and tempered alloy steel plates made by high quality air melting, ESR, VIM & VAR, and VIM & ESR processes. In: Paper Presented at the Sixth International Vacuum Metallurgy Conference on Special Melting, San Diego, CA.
- Doig, A., 1998. *Military Metallurgy*. Maney Publishing, London.
- Dormeval, R., 1988. The adiabatic shear phenomena. In: Chiem, C.Y., Kunze, H.D., Meyer, L.W. (Eds.), *Impact Loading and Dynamic Behavior of Materials*, vol. 1. DGM Informationsgesellschaft, Oberursel, pp. 43–56.
- Durmas, A., Guden, M., Gulcimen, B., Ulku, S., Musa, E., 2011. Experimental investigations on the ballistic impact performances of cold rolled sheet metals. *Materials and Design* 32 (2011), 1356–1366.

- Edwards, M.R., Mathewson, A., 1997. The ballistic properties of tool steel as a potential improvised armour plate. *International Journal of Impact Engineering* 19 (4), 297–309.
- Flockhart, C.J., Woodward, R.L., Lam, Y.C., O'Donnell, R.G., 1991. The use of velocity discontinuities to define shear failure trajectories in dynamic plastic deformation. *International Journal of Impact Engineering* 11, 93–106.
- Garcia-Mateo, C., Caballero, F.G., Bhadeshia, H.K., 2003. Development of hard bainite. *ISI International* 43 (8), 1238–1243.
- Gooch, W.A., Burkins, M.S., Squillacioti, R., Koch, R.M.S., Oscarsson, H., Nash, C., 2004. Ballistic testing of Swedish steel for U.S. Armor applications. In: Paper Presented at the 21st International Symposium on Ballistics.
- Gooch, W.A., Burkins, M.S., MacKenzie, D., Vodenicharov, S., 2005. Ballistic analysis of Bulgarian electroslag remelted dual hard steel armor plate. In: Paper Presented at the 22nd International Symposium on Ballistics, Vancouver, BC, Canada.
- Gooch, W.A., Showalter, D.D., Burkins, M.S., Thorn, V., Cimpoeu, S.J., Barnett, R., 2007. Ballistic testing of Australian Bisalloy steel for armor applications. In: Paper Presented at the 23rd International Symposium on Ballistics, Tarragona, Spain.
- Gooch, W.A., et al., 2009. Development and Ballistic Testing of a New Class Auto-tempered, High Hard Steels Under Military Specification MIL-DTL-46100. TMS (Retrieved from San Francisco, CA).
- Hall, E.O., 1951. *Proceedings of the Physical Society of London* B64, 747.
- Herzig, N., Meyer, L.W., Pursche, F., Hüsing, K., 2010. Relation between dynamic strength and toughness properties and the behavior under blast conditions of high strength steels. In: Paper Presented at the 7th International Symposium on Impact Engineering, ISIE, Warsaw, Poland.
- Johnston, G.R., Cook, W.H., 1983. A constitutive model and data for metals subjected to large strains. In: Paper Presented at the 7th International Symposium on Ballistics the Hague, Netherlands.
- Jominy, W.E., Boegehold, A.L., 1938. A hardenability test for carburising steel. *Transactions of the American Society for Metals* 26 (1938), 574–606.
- Jones, H.J., 1907. Modern armor and armor-piercing projectiles. *Journal of American Society of Naval Engineers* 19 (3), 726–760.
- Jones, P.N., 1984. *The Metallurgist and Materials Technologist* 16, 465.
- Kasonde, M., 2006. Optimizing the Mechanical Properties and Microstructure of Armoured Steel Plate in Quenched and Tempered Condition (M.Sc. thesis). University of Pretoria, South Africa.
- Kuzmikova, L., 2012. An Investigation of the Weldability of High Hardness Armour Steels (Ph.D. thesis). University of Wollongong.
- Laible, R.C., 1980. *Ballistic Materials and Penetration Mechanics*. Elsevier, Amsterdam.
- Langdon, G.S., Nurick, G.N., Balden, V.H., Timmis, R.B., 2008. Perforated plates as passive mitigation systems. *Defence Science Journal* 58, 238–247.
- Li, H., 2013. DMTC Project P7.1.3, Low Profile Body Armour.
- Lolla, T., Cola, G., Narayanan, B., Alexandrov, Babu, B., 2011. Development of rapid heating and cooling (flash processing) process to produce advanced high strength steel microstructures. *Material Science and Technology* 27 (5), 863–875.
- MacKenzie, A.C., Hancock, J.W., Brown, D.K., 1977. On the influence of state of stress on ductile failure initiation in high strength steels. *Engineering Fracture Mechanics* 9, 168–188.
- Magudeeswaran, G., Balasubramanian, V., Madhusudhan Reddy, G., 2008. Hydrogen induced cold cracking studies on armour grade high strength, quenched and tempered steel weldments. *International Journal of Hydrogen Energy* 33 (7), 1897–1908.

- Manganello, S.J., Abbott, K.H., 1972. Metallurgical affecting the ballistic behaviour of steel targets. *Journal of Materials* 7, 231–239.
- Meyer, L.W., Abdel-Malek, S., 2000. Strain rate dependence of strength-differential effect in two steels. *Journal de Physique IV France* 10. PR9, 63–68.
- Meyer, L.W., Pursche, F., 2012. Adiabatic shear localization. In: Dodd, B. (Ed.), *Adiabatic Shear Localization, Frontiers and Advances*, second ed. Elsevier, London, p. 85.
- Meyer, L.W., Halle, T., Herzig, N., Krüger, L., Razorenov, S.V., 2006. Experimental investigations and modelling of strain rate and temperature effects on the flow behaviour of 1045 steel. *Journal de Physique IV France* 134, 75–80.
- Ministry of Defence, 2011. New Armour Steel Showcased at DSEi (Retrieved from U.K.).
- Moshe, R., Hirschberg, Y., 2006. European Patent No. EP 1 705452 A1, Perforated Armor Plates.
- Nahme, H., Lach, N., 1997. Dynamic behavior of high strength armour steels. *Journal de Physique IV France* 7, C373–C377.
- O'Donnell, R.G., Woodward, R.L., 1988. Instability during high strain rate compression of 2024 T351 aluminium. *Journal of Materials Science* 23, 3578–3587.
- Peranio, N., Li, J.Y., Roters, F., Raabe, D., 2010. Microstructure and texture evolution in dual-phase steels: competition between recovery, recrystallisation and phase transformation. *Materials Science and Engineering: A* 527, 4161–4167.
- Petch, N.J., 1953. *The Journal of the Iron and Steel Institute* 174, 25.
- Rapacki, E.J., 1995. Armor steel hardness influence on kinetic energy penetration. In: Paper Presented at the 15th International Symposium on Ballistics, Jerusalem, Israel.
- Rawson, J.D., Dawson, D.I., 1972. British Steel Corporation Corporate Laboratories Report MG/34/72.
- Recht, R.F., 1964. Catastrophic thermoplastic shear. *Journal of Applied Mechanics* 31E, 189–193.
- Ritter, J.C., Dixon, B.F., Baldwin, N.J., 1989. Deformation and weld repair of armour steel. *Materials Forum* 13, 216–224.
- Ryan, S., Li, H., Edgerton, M., Gallardy, D., Cimpoeu, S.J., 2016. The Ballistic Performance of an Ultra-High Hardness Armour Steel: an experimental investigation. *International Journal of Impact Engineering* 94, 60–73.
- Sato, K., Yu, Q., Hiramato, J., Urabe, T., Yoshitake, A., 2015. A method to investigate strain rate effects on necking and fracture behaviours of advanced high-strength steels using digital imaging strain analysis. *International Journal of Impact Engineering* 75, 11–26.
- Schulze, V., Vöhringer, O., 2000. Influences of alloying elements on the strain rate and temperature dependence of the flow stress of steels. *Metallurgical and Materials Transactions, Physical Metallurgy and Materials Science* 31, 825–830.
- Shah Khan, M.Z., Alkemade, S.J., Weston, G.M., 1998. DSTO Technical Report, DSTO-TR-0320, Fracture Studies on High Hardness Bisalloy 500 steel.
- Shah Khan, M.Z. Unpublished DST Group research.
- Showalter, D.D., Gooch, W.A., Burkins, M.S., Koch, R.S., 2008. Ballistic testing of SSAB ultra-high hardness steel for armor applications. In: Paper Presented at the 24th International Symposium on Ballistics, New Orleans, LA.
- Spec, US Specification MIL-DTL-46100E High Hardness Armor, 2008
- Spec, US Specification MIL-DTL-12560K Class 1 Rolled Homogeneous Armor, 2013
- Specification, March 1985. RARDE 823, Specialised Armour Quality Steel Castings (UK Restricted).
- Specification, September 14, 1987. MIL-A-46099C, Armor Plate, Steel, Roll-Bonded, Dual Hardness (0.187 inches to 0.700 inches Inclusive).
- Specification, October 18, 2007. MIL-PRF-32269(MR).

- Specification, July 9, 2008. MIL-DTL-46100E(MR), Armor Plate, Steel, Wrought, High Hardness.
- Specification, July 24, 2009. MIL-DTL-32332(MR), Armor Plate, Steel, Wrought, Ultra-High Hardness.
- Specification, December 7, 2013. MIL-DTL-12560K(MR), Armor Plate, Steel, Wrought, Homogeneous (For Use in Combat-Vehicles and for Ammunition Testing).
- Spitzig, W.A., Sober, R.J., Richmond, O., 1975. Pressure dependence of yielding and associated volume expansion for tempered martensite. *Acta Metallurgica* 23, 885–893.
- Standard, 2004. UK Defence Standard, DEF STAN 95-24, Armour Plate, Steel (3–160 mm). Issue 3.
- Standard, 2008. Australian Defence Standard, DEF(AUST) 8030, Rolled Armour Plate, Steel (3–35 mm).
- Trasi, Y., Ben-Moshe, D., Rosenberg, G., 1987. An Armor Assembly for Armored Vehicles. EP 0209221 A1.
- Wang, X.B., 2007. Adiabatic shear localization for steels based on Johnson-Cook-Model and second- and fourth-order gradient plasticity models. *Journal of Iron and Steel Research, International* 14, 56–61.
- Weerasooriya, T., Moy, P., 2004. Effect of strain rate on the deformation of behaviour of rolled-homogenous armour (RHA) steel at different hardnesses. In: Paper Presented at the SEM Congress and Exposition on Experimental Mechanics, CostaMesa, CA.
- Wells, M.G., Weiss, R.K., Montgomery, J.S., Melvin, T.G., 1992. LAV Armor Plate Study. U.S. Army Materials Technology Laboratory Report, MTL TR 92-26.
- Whittington, 2014. Capturing the effect of temperature, strain rate and stress state on the plasticity and fracture of rolled homogenous armour (RHA) steel. *Materials Science and Engineering: A* 594, 82–88.
- Wilson, J.P., 1978. In: Paper Presented at the Int. Conf. on Trends in Steels and Consumables for Welding, London, UK.
- Wingrove, A.L., Wulf, G.L., 1973. Some aspects of target and projectile properties on penetration behaviour. *Journal of the Australian Institute of Metals* 18, 167–172.
- Woodward, R.L., Baldwin, N.J., 1979. Oblique perforation of steel targets by 0.30 Cal. APM2 projectiles. *International Journal of Mechanical Sciences* 21, 85–91.
- Woodward, R.L., 1978a. The penetration of metal targets by conical projectiles. *International Journal of Mechanical Sciences* 20, 349–359.
- Woodward, R.L., 1978b. The penetration of metal targets which fail by adiabatic shear plugging. *International Journal of Mechanical Sciences* 20, 599–607.
- Woodward, R.L., 1984. The interrelation of failure modes observed in the penetration of metallic targets. *International Journal of Impact Engineering* 23, 121–129.
- Zener, C., Hollomon, J.H., 1944. Effect of strain rate upon plastic flow of steel. *Journal of Applied Physics* 15, 22–32.
- Zerilli, F.J., Armstrong, R.W., 1987. *Journal of Applied Physics* 61, 1816–1825.
- Zhen-li, M., et al., 2009. Effects of annealing temperature on the microstructure and properties of the 25Mn-3Si-3Al-TWIP steel. *International Journal of Minerals, Metallurgy, and Materials* 16 (2), 154.
- Zrník, J., Muransky, O., Stejskal, O., Lukas, P., Hornak, P., 2008. Structural materials: properties, microstructures and processing. *Materials Science and Engineering: A* 483–484, 71–75.

Light alloys

3

D.P. Edwards¹, I.G. Crouch²

¹Defence Science and Technology Group, Fishermans Bend, Victoria, Australia; ²Armour Solutions Pty Ltd, Trentham, Victoria, Australia

3.1 General introduction

The family of light engineering alloys consists of those based upon aluminium, titanium and magnesium, as can be appreciated from a review of the Periodic Table covered in Chapter 1. All three alloy systems have been used as an armour material but by far the most prolific has been the use of aluminium alloys, mainly because of its availability, fabricability and forgiving nature (ductile, malleable, tough and durable).

3.1.1 Brief history of the light alloys

Since the early 1960s, aluminium alloys have been part of the suite of armour materials available to the armour technologist designing armoured military structures. Because the bulk density of aluminium alloys is about one-third that of steel, section sizes (thicknesses of plate) are much greater for the same weight. This brings an automatic advantage in terms of structural stiffness, which is very attractive when designing box-like, lightweight structures. The first, and most formidable, application of this principle was the structural shell of the US M113 armoured personnel carrier. Why formidable? Because more than 80,000 (see Figs 3.1 and 3.2) of these vehicles have been built and



Figure 3.1 An early version of the M113, circa 1975.

From <https://upload.wikimedia.org/wikipedia/commons/c/cf/M113.jpg>



Figure 3.2 Australian troops storming out of the rear door of an M113. Reproduced from Anon., 2015d. <http://www.army.gov.au/Our-work/Equipment-and-clothing/Vehicles/M113AS4>.

the majority have lasted for more than 50 years! That exemplifies a very successful engineering feat ... or may be a very conservative one!

It was first fielded by the US Army in April 1962, during the Vietnam War, and, at that time, had an aggressive role in overrunning enemy positions, under fire, through dense undergrowth. The Viet Cong nicknamed it ‘The Green Dragon’. As a front-line, armoured vehicle, it has been superseded by vehicles like the Bradley, a US armoured personnel carrier (APC), but many of them still remain in support roles, and, even today, they represent ~50% of the US Army’s fleet of armoured vehicles. The US Army plans to retire the M113 family of vehicles by 2018, seeking replacement through the Armored Multi-Purpose Vehicle program. We shall see!

In Australia, the Department of Defence has recently delivered a new variant, the M113AS4, under Project LAND 106. Upgrades to the M113 include an electrically powered turret, day/night weapon sights, a new engine, steering controls, drive train, electrical and fuel systems as well as a newly designed internal layout to accommodate safe storage in a variety of situations (Anon, 2015d).

The main aluminium alloy used to fabricate the armoured shell of the M113 was a work-hardening grade, designated 5083, based upon an Al–5%Mg–Mn composition and cold-rolled into the H115 or H131 condition (see Tables 3.2 and 3.3). This alloy variant has excellent ductility, formability and good corrosion resistance - it also has good weldability and geometrically, strong corner joints. Alloy 5083 has remained the standard, reference alloy to this day, and, like rolled homogeneous armour (RHA) in the ferrous armour field, is used to baseline all other aluminium armour alloys, as we shall do here. More significantly, the 1960s saw the birth of lightweight, structural armours, when the structure of a vehicle was also the protective shroud (the armour). As we shall see below, the ductility and forgiving nature of this

engineering alloy enabled the structure to evolve into an excellent backing system, for higher-performing external appliqué armours. This was the secret to the success of the M113 series of armoured vehicles — the ability of the engineering box-like structure to transition from being the structural armour into an ever-evolving part of an appliqué armour system.

As a base material, these work-hardening alloys were soon found to be limited in strength and, as we shall see later in this chapter, the ballistic resistance of an alloy generally increases with hardness so, during the 1970s, considerable effort was put into finding a heat-treatable alloy. Many alloys were investigated, but the optimum composition was found to be an aluminium–zinc–magnesium alloy, designated 7039 (see Table 3.3), which offered a much greater resistance to armour-piercing ammunition. This was mass-produced in the US to conform to MIL-A-46063A MR (see Section 3.5) and vehicles like the US Bradley (see Fig. 3.3) were constructed from this high-strength alloy.

In the UK, research had also been undertaken into the military uses of the heat-treatable 7000 series alloys. An Al–4Zn–2Mg alloy was being used in the construction of military bridging components for the UK Medium Girder Bridge, and higher alloy variants were being considered for armoured vehicles in the 1970s. UK military specification MVEE 1318B, preceding alloy specification 7017, evolved from in-depth R&D work carried out at MVEE (Chobham); the UK's 'Tank Factory', as the locals used to call it! One of the early applications was the armoured hulls of the combat vehicle reconnaissance tracked (CVRT) family of vehicles (see Fig. 3.4). Scorpions and Scimitars were the only fighting vehicles that the UK used during the Falklands War of 1982, and, by 1986, the United Kingdom had taken delivery of 1863 CVRTs, including 313 Scorpions and 334 Scimitars. High-strength, weldable, structural armours had therefore become the lightweight armour material of choice in the 1970s and 1980s.

In the UK, it was not until the late 1980s that an armoured vehicle emerged that had been designed in such a way that the engineering structure of the vehicle



Figure 3.3 US army soldiers take cover behind a Bradley fighting vehicle in Iraq in 2003.



Figure 3.4 Image of up-graded UK Scimitar circa 2011.

was, in the main, decoupled from the armour. Protection systems for the Warrior evolved as the threat levels increased without the baseline, engineering structure changing, or the alloys used (MVEE 1318B, similar to 7017 and 7020). More than 750 Warriors were successfully delivered to the British Army between 1987 and 1995 (Fig. 3.5).

What Warrior did make use of was the squeeze-casting process — certainly in the early variants. As a process, this was fully commercialised by GKN, in conjunction with staff at MVEE, in the late 1970s. The road-wheels, all 24 of them, were manufactured from a new squeeze-cast alloy based upon 7039 (Crouch, 1987). The rims of the road-wheels even incorporated bicycle chains as wear-resistant elements! The final drive covers, welded to the toe-plate, were also produced via the squeeze-casting route, albeit in a leaner Al–4Zn–2Mg alloy (designated SF1), much like the bridging alloy DGFVE 232A.



Figure 3.5 UK Warrior variants, with (right) and without (left) appliqué armour systems.
<http://www.defenceimagery.mod.uk/fotoweb/LandingPage.fwx>.

Aluminium alloys do have many attractive properties, including general corrosion resistance — unfortunately some can suffer from stress corrosion cracking. This has been well documented since the 1970s and a huge amount of in-depth, material science research has been carried out ever since. Palliative treatments abound (see Section 3.2.4.2) and strict tests for stress corrosion cracking (SCC) resistance are regularly included in aluminium armour procurement specifications. The majority of alloy development over the past 40 years has, however, been seriously impacted by this Achilles heel. Of course, a high SCC resistance is a prerequisite for alloys used for amphibious and naval applications. In the US, aluminium alloy 2519, an Al–Cu–Mg, precipitation-hardening alloy was developed for this purpose: to eliminate problems associated with SCC. Early prototypes of the Advanced Amphibious Assault Vehicle (AAAV), c.2000, used 2519 in several critical extrusions.

In fact, the construction of modern aluminium naval vessels has rapidly grown (from the 1990s) since its early use by the US Navy in the 1930s in ship superstructures and deckhouses of vessels such as the USS Sims and USS Gleaves (Crum et al., 2012). The myth, raised after the Falklands War, about ‘aluminium burning’ was officially refuted in a UK Defence White Paper, dated 14th December 1982. The increase in aluminium shipbuilding can be linked to improvements in aluminium fabrication techniques, alloy development and a broader acceptance of aluminium as a maritime material due to decades of usage in commercial shipping and passenger vessels. The use of aluminium in naval ship structures is highly attractive as it offers a significant weight saving over steel ($\sim 56\%$ by mass for equivalent stress) that can be readily translated into higher ship speeds, fuel savings (up to 21%) and the potential to up-load vessels with additional equipment or personnel (Ferraris and Volpone, 2005).

In addition to the high strength-to-weight ratio, Al-alloys selected for ship-building applications are required to be readily weldable, possess good formability and high corrosion resistance. The 5xxx series aluminium alloys (eg, 5059, 5383 and 5083) have been shown to fulfil these prerequisite performance criteria. With a magnesium content between 2.5% and 5%, corrosion rates, in seawater, are approximately 1/20th those of mild steel. Applicable 6xxx series marine-grade alloys 6082, 6063 and 6061 possess corrosion rates of $\sim 1/10$ th those of mild steel, according to Austal Ships (Anon, 2015a).

Aluminium naval vessels, such as the Australian Navy’s 56m Armidale class patrol boats, the 127m Littoral Combat Ship and the Joint High Speed Vessel, for the US Army and Navy, as seen in Fig. 3.6, have been fabricated by Austal from extruded and rolled 5xxx and 6xxx series aluminium alloys. However, because these alloys attain their specific mechanical properties through work-hardening and age-hardening heat treatments, respectively, significant structural integrity design consideration is required to account for the reduction in tensile mechanical properties that occurs within the heat-affected zone upon welding such alloys. A failure to acknowledge the influence of additional thermal input from various fabrication processes on the mechanical properties of wrought aluminium and fabricated structures is likely to result in reduced ship service due to excessive loading and structural fatigue issues.

None of the aluminium alloys used for marine and maritime applications have been selected because of their ballistic performance. The overriding requirement for

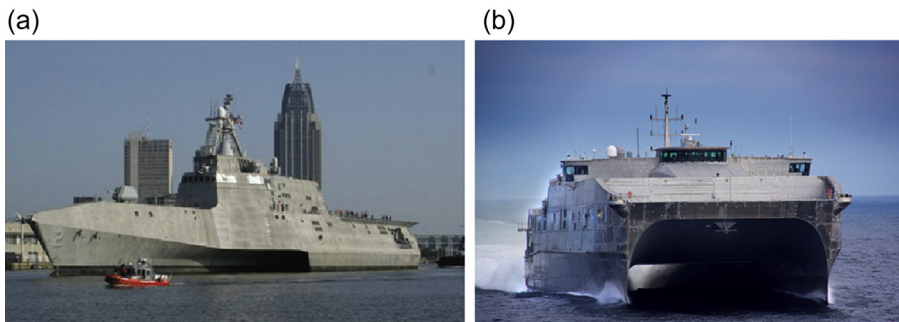


Figure 3.6 Examples of naval ships built by Austal Ships (a) the Littoral Combat Ship and (b) Joint High Speed Vessel, as supplied to the US Navy.

Reproduced from Anon., 2015a. Aluminium — Hull Structures in Naval Applications. www.austal.com.

weldability and (stress) corrosion resistance demands this. However, as will be appreciated in later sections, their high strength and ductility do give them some inherent penetration resistance.

In terms of specific aluminium armour development, the new century has seen an increase in the use of ultrahigh-strength aluminium alloys being used as appliqué armours. In a stroke, this totally negates the issue of SCC, of course, because of the absence of any tensile stress. This is also true for both titanium and, more recently, magnesium alloys which have seen only a small increase in their use as appliqué armour materials. For example, a high-strength titanium alloy has been used in up-armouring kits applied to the turrets of the US Bradley, with much saving in weight (Gooch, 2012).

3.1.2 Ballistic properties and specific failure modes

Aluminium armours are used in thick sections and because of this the dominant energy-absorbing mechanism is by ductile hole formation (see Chapter 1), especially against pointed projectiles like the 0.3 cal APM2 round. Because of this single fact, the penetration resistance of these alloys is directly proportional to their dynamic yield properties. So, as the schematic diagram in Fig. 3.7 shows, for the medium-to-high-strength alloys, the ballistic performance increases with hardness (in its simplest form). However, as all metallurgists know, as strength increases, toughness decreases and lack of toughness starts to affect ballistic performance at the higher-strength levels. The aluminium alloys fail prematurely by discing (see Chapter 1). This does not reduce the inherent penetration resistance of the alloy: it simply reduces the effective thickness of the material resisting the final penetration. It also gives rise to damaging spall. This effect is also a reflection of the way ballistic performance is measured — see Chapters 1 and 11: if any part of the projectile or target material (eg, a disc) is able to penetrate a witness sheet placed behind the target, then the target is deemed to have failed. Its ballistic limit has been reduced and its protective qualities, especially for personnel and equipment inside a vehicle, will have been seriously compromised.

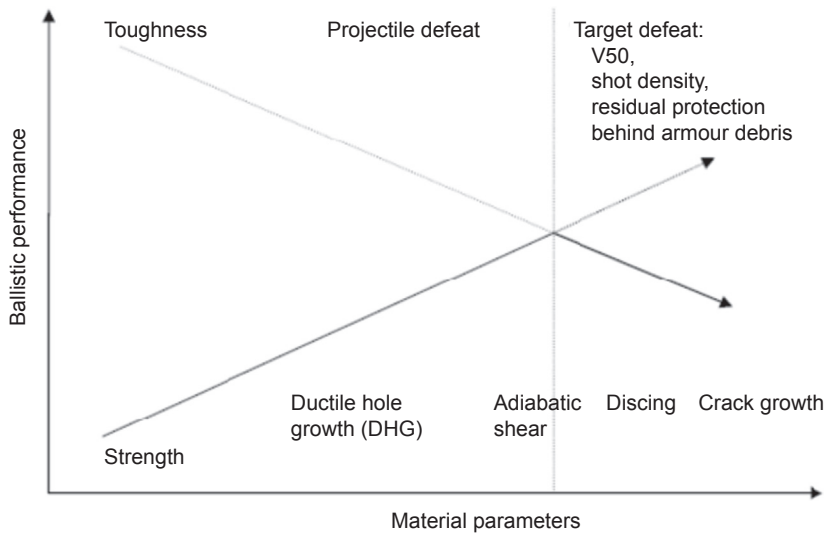


Figure 3.7 Schematic showing how ballistic performance is strongly dependent upon material parameters (strength and toughness).

Reproduced from Chinella, J.F., 2004. ARL-TR-3185: High Strength Al-Cu-Li and Al-Zn Alloys: Mechanical Properties and Statistical Analysis of Ballistic Performance. US Army Research Laboratory.

This phenomenon is the Achilles heel of the entire family of light-alloy armour materials: not only do high-strength aluminium alloys fail by discing but also titanium and magnesium alloys do too, as will be described later. Discing, as defined in some detail by Crouch (1992) occurs via delamination of the material in the short-transverse (ST) direction. More precisely, this delamination occurs because ST cracks, which get initiated during penetration in areas of high transverse shear stress, are able to propagate due to the material's poor resistance to crack propagation (ie, low fracture toughness). This, in turn, may be due to poor grain structure and/or the presence of intergranular impurities like iron- or silicon-based compounds. Alloys, with different K_{Ic} values, will disc to differing extents — Figs 3.8 and 3.9 show discing failure in two different alloys, 7075-T6 and 2024-T351, from work carried out by the DST Group, Australia c.2014. The extent of discing (ie, diameter and thickness of the disc) is also related to the nose shape of the penetrator: the more blunt the penetrator, the larger the disc. It should also be noted that, although the spall on the front of the 7075 target is also a discing phenomenon, its formation does not cause loss of penetration resistance nor does it contribute to a reduction in ballistic resistance. It is a secondary effect.

More recently, in 2015, Frasier et al. reported a comprehensive set of experiments, and numerical analyses, of 40-mm thick 7020-T651 against 20 mm fragmentation simulator projectiles (FSPs), which also resulted in low-energy, discing and plugging failures. Against blunt projectiles these alloys do fail by plugging (as described in Chapter 1) — this low-energy-absorbing, shearing process can be accentuated through the formation of adiabatic shear bands (ASBs), which form in regions of high shear stress.



Figure 3.8 Entry and exit holes from a 0.3 cal APM2 round against 7075-T6 (left) and 2024-T351 strike-face (top) and back-face (below) for 30 mm targets (Edwards, 2014).

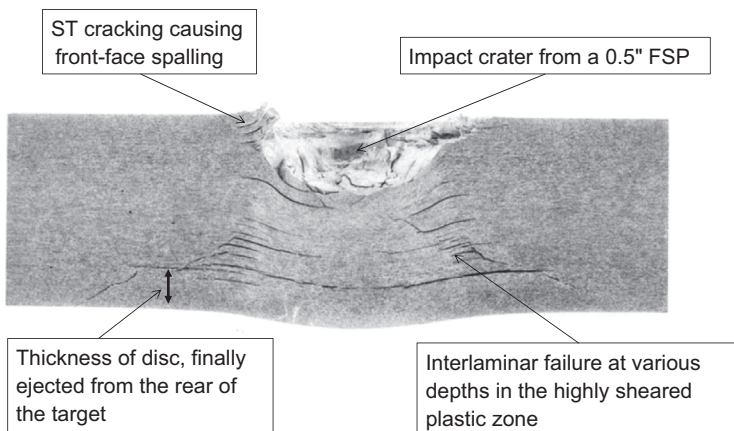


Figure 3.9 Formation of ST cracking and discing failure in a 25-mm plate of 7075-T6 alloy impacted by a 0.5 cal FSP round. Reproduced from Crouch, I.G., 1992. Discing failures in both traditional and composite armour materials. In: Paper Presented at the International Symposium on Ballistics, Stockholm, Sweden.

This loss of material, through discing, is more likely to happen in thinner sections where the grain structure has been well developed, the grains are more pancake-shaped and the properties far more anisotropic. In a technical report by [Cheeseman et al. \(2008\)](#), K_{Ic} data, for a number of different alloy grades, have been summarised: in the worst case, that of alloy 8090-T8771, the K_{Ic} value for the ST orientation is less than half that for the Transverse Longitudinal (TL) and Longitudinal Transverse (LT) orientations.

This impact phenomenon, discing, contributed to the need for composite spall liners to be fitted inside aluminium-based vehicles. Their presence not only reduced the level of internal damage (due to spallation from overmatching rounds) but also the cone angle from shaped-charge weapons. Fibre-reinforced polymer spall liners are discussed in Chapter 5. Discing behaviour has also been one of the drivers for development of improved alloys, for ballistic application, through better control of the final microstructure.

3.2 Aluminium alloys

Recent reviews of the metallurgy of the aluminium alloys include those of [Polmear \(2006\)](#) and [Lumley \(2011\)](#). The wide industrial use of aluminium can primarily be attributed to its low specific gravity (one-third that of steel) and good corrosion resistance (derived from the rapid formation of a strong adherent oxide film). In its purest form, aluminium possesses relatively low strength and high ductility, making it of limited engineering use. Hence, in order to take advantage of aluminium for lightweight practical engineering applications, notably in the aerospace, automotive and building industries, significant improvements in material strength are required. This is achieved either by alloying and/or strain hardening, via mechanical deformation. Alloying elements increase strength through solid solution hardening (interstitial and/or atomic substitution), or through the formation of secondary intermetallic phases by precipitation hardening via tailored heat treatment ([ASM, 2000](#)). In practice, the desired strength level is often achieved by a combination of alloying, heat treatment and mechanical strain hardening processes such as forging, extrusion and rolling of plate material. They can be grouped into two distinct classes in addition to their specific alloy designation ([Table 3.1](#); [ASM, 2000](#)): non-heat-treatable and heat-treatable alloys.

The aluminium industry often applies a range of proprietary work-hardening and heat-treatment temper conditions to each alloy to meet specific mechanical property requirements for engineering applications (especially in aerospace and defence). To enable a quick indication of an alloy's relative mechanical properties, and the sequence of treatments applied, a standardised designation system has been developed. For a detailed explanation and guide to the alloy designation system the reader is referred to the ASM Metals Handbook Vol. 2 ([ASM, 2000](#)). In summary, a specific alloy designation is typically followed by the letters H or T and up to three digits, for example 5xxx-H14 or 2xxx-T351. The strain hardening (H) level and precipitation aging heat treatment (T) condition of an alloy are described by the preceding digits ([Table 3.2](#)).

Table 3.1 Aluminium alloy designation system

Series number	Major alloying element(s)	Heat treatable ^a	Strengthening method ^b
1xxx	Aluminium purity $\geq 99.00\%$	No	Cold work
2xxx	Copper (with magnesium)	Yes	Precipitation — aging
3xxx	Manganese	No	Cold work
4xxx	Silicon	No	Cold work
5xxx	Magnesium	No	Cold work
6xxx	Magnesium and silicon	Yes	Precipitation — aging
7xxx	Zinc (with magnesium)	Yes	Precipitation — aging

^aGeneral rule, although some specific alloys may deviate.

^bIn addition to alloy hardening.

Adapted from ASM, 2000. Hand Book Vol. 2. Properties and Selection: Nonferrous Alloys and Special-Purpose Materials, tenth ed. USA.

Table 3.2 Summary of temper designations for aluminium alloys (ASM, 2000; Benedyk, 2010)

Work-hardened alloys (H)	Heat-treated alloys (T)	
H1 strain-hardened only	T1 cooled from an elevated temperature forming process and naturally aged	T6 solution heat-treated, quenched and artificially aged
H2 strain-hardened and partially annealed	T2 cooled from elevated temperature forming process, cold-worked and naturally aged	T7 solution heat-treated, quenched and artificially over-aged
H3 strain-hardened and stabilised by low-temperature heat treatment	T3 solution heat-treated, quenched, cold-worked and naturally aged	T8 solution heat-treated, quenched, cold-worked and artificially aged
H1x, x = 1–9 level of strain hardening and ultimate tensile strength increase, eg, x = 4: 35% cold work, 6: 55% cold work, 8: 75% cold work	T4 solution heat-treated, quenched and naturally aged T5 cooled from an elevated temperature forming process and artificially aged	T9 solution heat-treated, quenched, artificially aged and cold-worked T10 cooled from an elevated temperature forming process, cold-worked, and artificially aged

Naturally aged, natural increase in properties at ambient temperatures; *Artificially aged*, heat treatment at temperatures 100–200°C to promote precipitation.

Table 3.3 summarises the chemical composition and basic mechanical properties of the full range of aluminium alloys which have been used in armour applications. This table of data has been based upon the work of [Doherty et al. \(2012\)](#), but divides the alloys into three main categories:

1. Structural alloy grades, used in welded structures;
2. Appliqué grades, as used in standalone, nonstructural applications;
3. Other grades, like the many high-strength grades that have been researched.

Note how the appliqué grades and the R&D grades are much stronger than the structural grades (see bottom rows) and the wide differences in bulk densities (last row). This is particularly important when designing lightweight armour systems.

The need for a high specific strength is one of the key drivers in the development of aluminium armour alloys.

3.2.1 Work-hardening grades

Non-heat-treatable alloys, typically the 3xxx, 4xxx and 5xxx series, contain the major alloying elements of manganese up to 2% and/or magnesium 3.5–5%, together with impurity levels of chromium, silicon and iron. Strength improvements in such alloys are predominantly derived through work-hardening ([Van Horn, 1967](#)). Heat treatment procedures applied to such alloys will have no positive influence on the material strength properties. Specific ballistic grades include 5083, 5456 and 5059. The non-armour grade alloys of 3xxx series find application as materials for storage tanks, roofing and architectural products and the Al–Silicon 4xxxx series alloys are widely used as weld filler wire for joining other Al-alloys due to their reduced melting point and also as anodized architectural products.

The requisite mechanical and concomitant ballistic properties of 5083 are achieved primarily through the application of strain-hardening by heavy rolling of plate forms or via extrusion processes, in addition to the strengthening provided by the presence of the major solute alloying element magnesium. The tensile yield strength achieved for the 5xxx series alloys can be increased with cold rolling and the addition of magnesium up to the series maximum of 6 wt% (see [Fig. 3.10](#)). In the annealed condition (O-temper) the yield strength of the Al–Mg alloy 5xxx series is shown to exhibit a near linear relationship with Mg-solute concentration according to $\sigma_Y \propto B$ (wt% Mg) where $B = 15$ MPa, whilst the alloy grain size (d) will influence the yield strength according to the well-known Hall–Petch relationship $\sigma_Y \propto kd^{-1/2}$, where k is a constant for the material ([Lloyd, 2004](#)) and noting that the ballistic performance of metals is strongly governed by the flow properties, as measured by yield and tensile strength (see Chapter 8).

To increase the range of available armour-grade alloys beyond 5083 and the need to overcome ever-increasing lethal ballistic and blast threats, in particular armour-piercing (AP) projectiles, the requirement existed to develop aluminium alloys with higher strengths to field on the next generation of armoured vehicles whilst maintaining the desirable corrosion resistance of the 5083 alloy. In response to these needs, the ALUSTAR Al-alloy 5059 in tempers H131 and H136 was

Table 3.3 Summary of aluminium armour alloys

	Structural grades							Appliqué grades			Other grades		
Element	6061	5083	5456	5059	7020	7039	2519	2139	2195	7085A	2090	7075	7449
Silicon	0.40–0.80	0.4	0.25	0.45	0–0.35	0.3	0.25	0.1	0.12	0.06	≤0.10	≤0.4	≤0.12
Iron	0.7	0.4	0.4	0.5	0–0.4	0.4	0.3	0.15	0.15	0.08	≤0.12	≤0.5	≤0.15
Copper	0.15–0.40	0.1	0.1	0.25	0–0.2	0.1	5.3–6.4	4.5–5.5	3.7–4.3	1.3–2.0	2.4–3.0	1.2–2	1.4–2.1
Manganese	0.15	0.40–1.0	0.50–1.0	0.60–1.2	0.05–0.5	0.10–0.40	0.10–0.50	0.20–0.60	0.25	0.04	≤0.05	≤0.3	≤0.2
Magnesium	0.8–1.2	4.0–4.9	4.7–5.5	5.0–6.0	1.0–1.4	2.3–3.3	0.05–0.40	0.20–0.80	0.25–0.80	1.2–1.8	≤0.25	2.1–2.9	1.8–2.7
Chromium	0.04–0.35	0.05–0.25	0.05–0.20	0.25	0.10–0.35	0.15–0.25		0.005		0.04	≤0.05	0.18–0.28	
Zinc	0.25	0.25	0.25	0.40–0.90	4.0–5.0	3.5–4.5	0.1	0.25	0.25	7.0–8.0	≤0.10	5.1–6.1	7.5–8.7
Titanium	0.15	0.15	0.2	0.2	0–0.17	0.1	0.02–0.10	0.15	0.1	0.06	≤0.15	≤0.2	
Zirconium					0.08–0.20		0.10–0.25		0.08–0.16	0.08–0.15	0.08–0.15		
Zr + Ti													≤0.25
Vanadium							0.05–0.15	0.05					
Lithium									0.8–1.2		1.9–2.6		
Silver								0.15–0.60	0.25–0.60				
Other, max. each	0.05	0.05	0.05	0.05	0.05	0.05	0.05	0.05	0.05	≤0.05	0.05	≤0.05	
Other, max. total	0.15	0.15	0.15	0.15	0–0.15	0.15	0.15	0.15	0.15	0.15	≤0.15	0.15	≤0.15
Property					T651						T83	T6	
Yield Strength (YS) (MPa)	255	255	255	269	310	352	407	441	434	510	520	503	585
Ultimate Tensile Strength (UTS) (MPa)	262	310	310	359	380	414	455	462	490	552	550	572	625
%EL	10	8	8	7	12	9	10	9	9	11	6	11	12
Density (kg/m ³)	2700	2660	2660	2660	2780	2740	2820	2810	2710	2850	2590	2810	2850

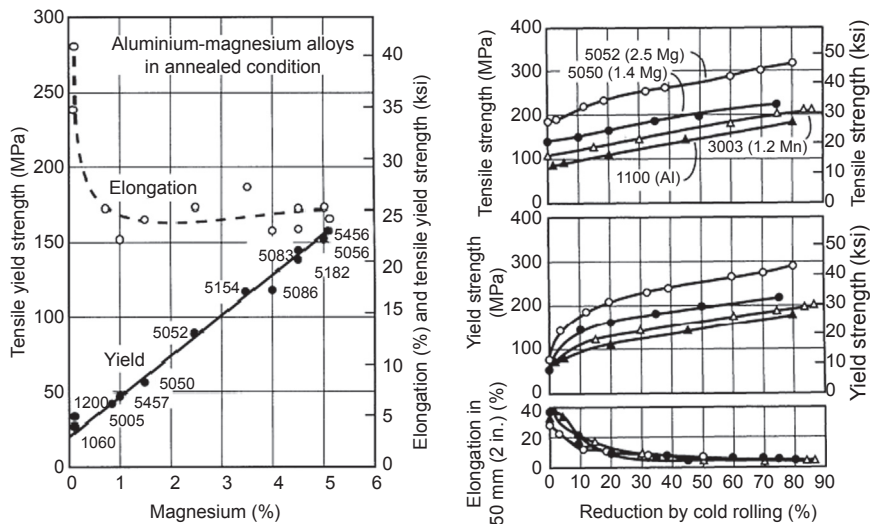


Figure 3.10 Influence of Mg-solute concentration and cold work via rolling on the tensile yield strength of 5xxx series Al-alloys.

Reproduced from ASM, 2000. Hand Book Vol. 2. Properties and Selection: Nonferrous Alloys and Special-Purpose Materials, tenth ed. USA.

produced by Aleris Aluminium Koblenz, Germany, as an improved strain-hardening alloy (Anon, 2015b). The 5059 alloy composition contains a higher maximum magnesium content, more than twice that of zinc and copper. More zirconium is added, compared to the 5083 alloy, providing a 15–20% increase in both tensile yield and ultimate strength with similar ductility. Corrosion studies on the effect of Zn in welded 5xxx series alloys have found higher Zn contents to cause increased localized corrosion attack in weld heat-affected zones (Sanders et al., 2004). However, long-term seawater corrosion tests carried out by Aleris indicate the current 5059 to be resistant to such localised weld attack for immersion periods of up to 14 months.

As a potential repair material for the hulls of the M2 Bradley, the US Army Research Laboratory (ARL) undertook ballistic performance testing of 5059 against 0.3 and 0.5 cal. AP (armour-piercing) and 20 mm FSP to compare with the structural alloy 7039. The high-strength 5059 alloy proved ballistically superior for both AP projectiles and FSP to 5083 and possessed the desirable ductile and plugging failure mode similar to 5083. The 5059 AP performance was somewhat inferior to the much higher-strength age-hardened 7039, although achieving an equivalent or slightly improved FSP performance (see Fig. 3.11). Nonetheless the ready weldability and superior corrosion performance of 5059, lower susceptibility to stress corrosion cracking, compared to the higher-strength 7039 and the potential longer-term costs associated with repair make 5059 a viable alternative to 5083 and 7039, as covered in report ARL-TR-4427 (Showalter et al., 2008).

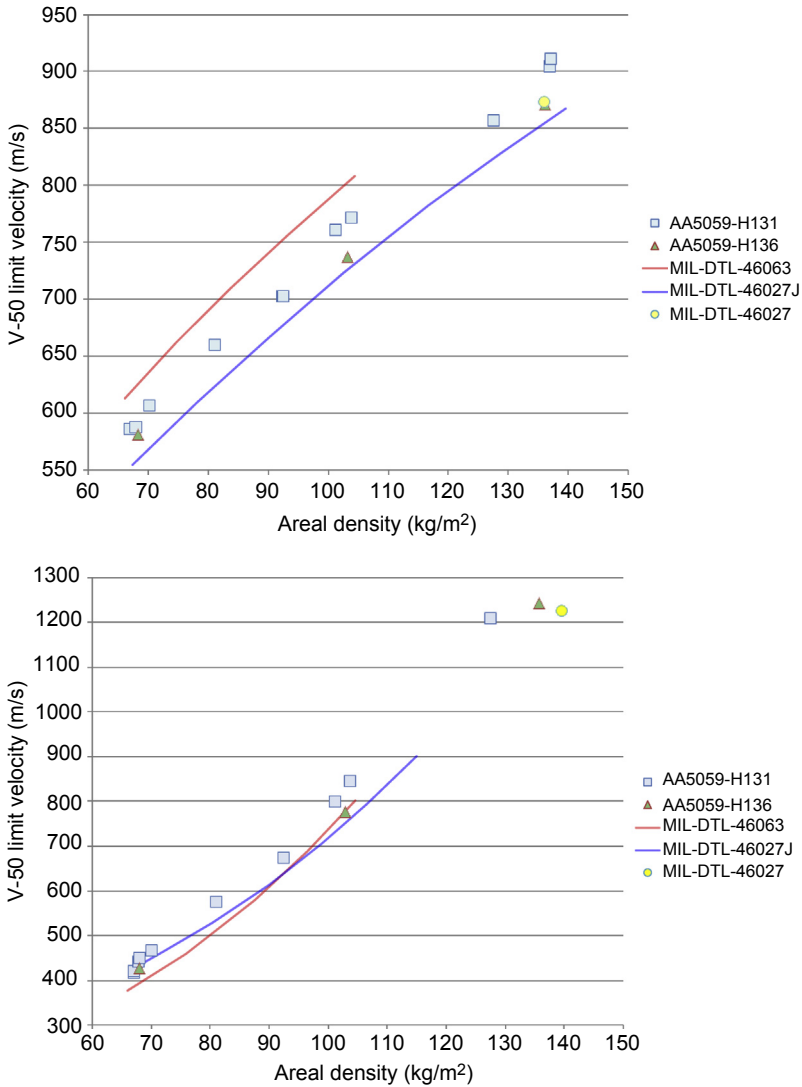


Figure 3.11 0.30 cal APM2 and 20 mm FSP data for 5059. Note: MIL-DTL-46063 covers 7039; MIL-DTL 46027 covers 5083/5456.

Reproduced from Showalter, D.D., Placzankis, B.E., Burkins, M.S., 2008. Ballistic Performance Testing of Aluminum Alloy 5059-H131 and 5059-H136 for Armor Applications. ARL-TR-4427.

3.2.2 Age-hardening grades

Heat-treatable aluminium alloys, designated 2xxx, 6xxx and 7xxx, contain the major alloying elements copper, magnesium, silicon, zinc and combinations thereof. They readily form a single-phase solid solution at elevated temperature (eg, 500°C) and also upon rapidly cooling to ambient temperatures. Strengthening occurs through

the controlled heat treatment of the rapidly cooled solid solution at a relatively low temperature ($<180^{\circ}\text{C}$) for a specified period of time (ie, conventional age-hardening). The aging process promotes atomic ordering and subsequent precipitation of submicron intermetallic compounds that are distributed throughout the microstructure and of a composition determined by the alloy composition equilibrium phase diagram (Schlenker, 1970; Van Horn, 1967). The presence of such fine-scale precipitates, observable only by electron microscopy, increases both the strength and hardness of the aluminium by affecting the local lattice strain and hindering dislocation movement through the atomic lattice (Higgins, 1968) (Fig. 3.12).

Peak mechanical strength properties are achieved by aging conditions that result in a microstructure that consists of a high concentration of uniformly distributed precipitates of an optimum size and coherent, possessing atomic registry within the alloy matrix. Extended aging times and high heat-treatment temperatures promote the growth and coarsening of precipitates by over-aging (such that they may be observed via optical microscopy), precipitate incoherency (with the matrix lattice) and a concomitant decrease in the alloy tensile strength towards the equilibrium microstructure properties. A schematic representation of the influence of aging on the microstructure and tensile properties of a heat-treatable Al–Cu alloy is shown in Figs 3.13 and 3.14.

High-strength heat-treatable aluminium alloys that have been used as vehicle ballistic armour include the 7xxx series alloys 7017 and 7039 (Specification, 1992). The UK Scimitar CVRT was first produced in the 1970s and fabricated with 7017 base armour, whilst the United States M2/3 Bradley Fighting Vehicle and M551

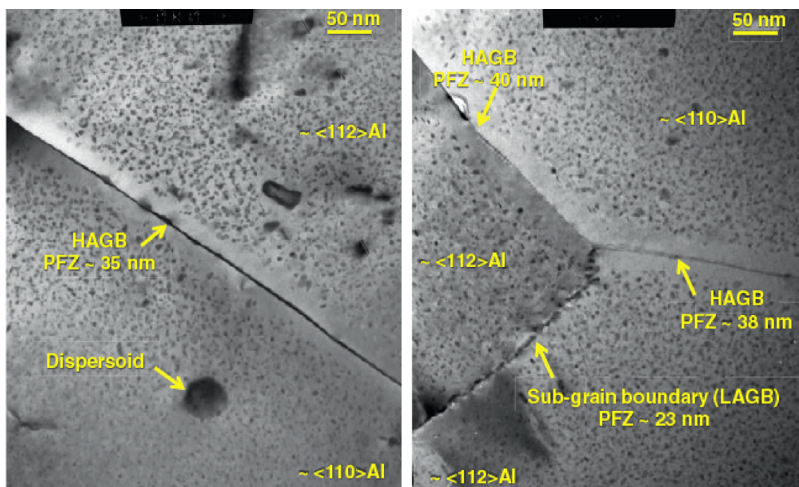


Figure 3.12 Bright-field transmission electron micrographs from peak-strength aged 7075-T651 alloy showing a high density of fine-scale hardening precipitates adjacent to both high- and low-angle grain boundaries (HAGB, LAGB) and the presence of a precipitation-free zone (PFZ).

Reproduced from Hopperstad, O.S., Børvik, T., Fourmeau, M., Pedersen, K.O., Benallal, A., 2014. Quasi-static and dynamic fracture of high-strength aluminium alloy. *Procedia Materials Science* 3, 51–56.

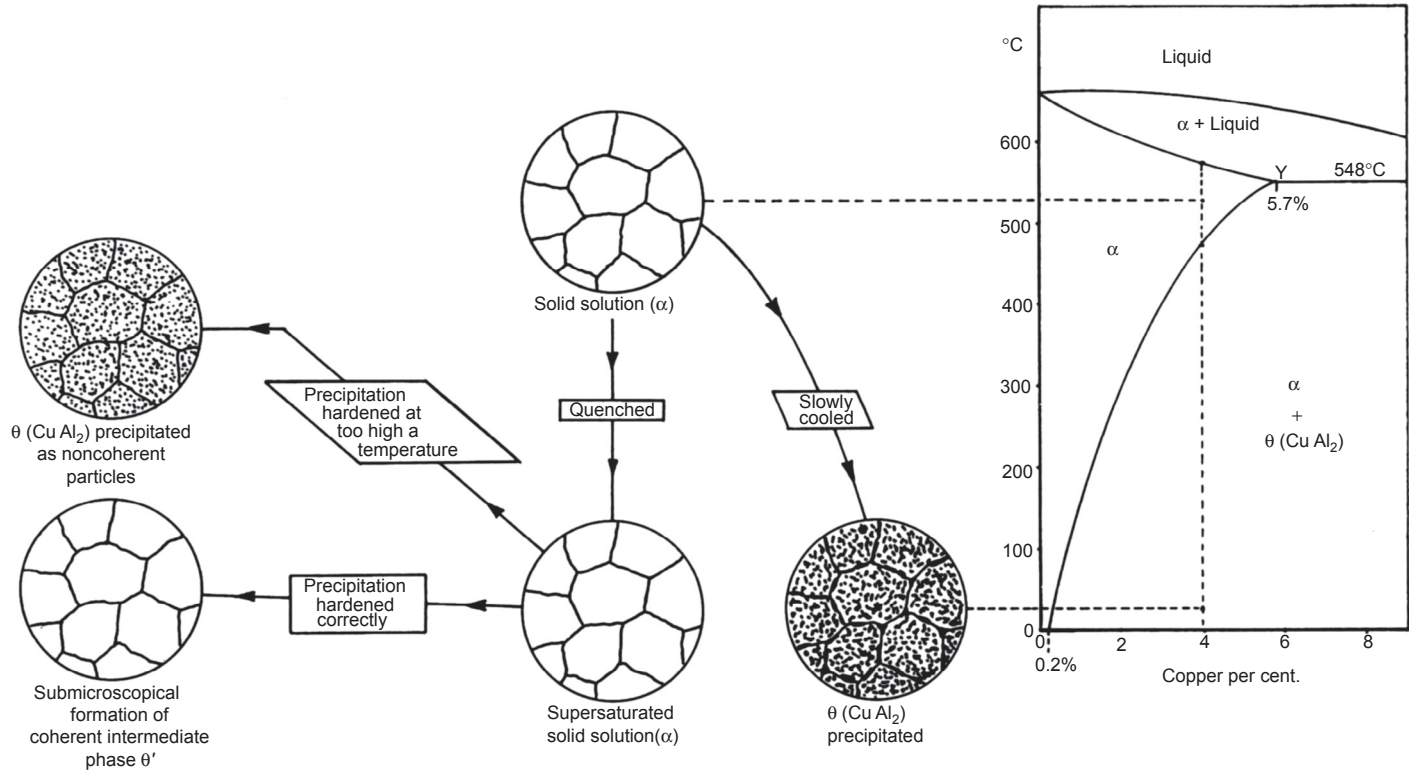


Figure 3.13 Schematic of the aluminium-rich section of the Al–Cu alloy equilibrium phase diagram illustrating the microstructural relationship of the precipitation hardening heat treatment process.

Adapted from Higgins, R.A., 1968. *Engineering Metallurgy: Part I Applied Physical Metallurgy*, second ed. The English Universities Press Ltd, London.

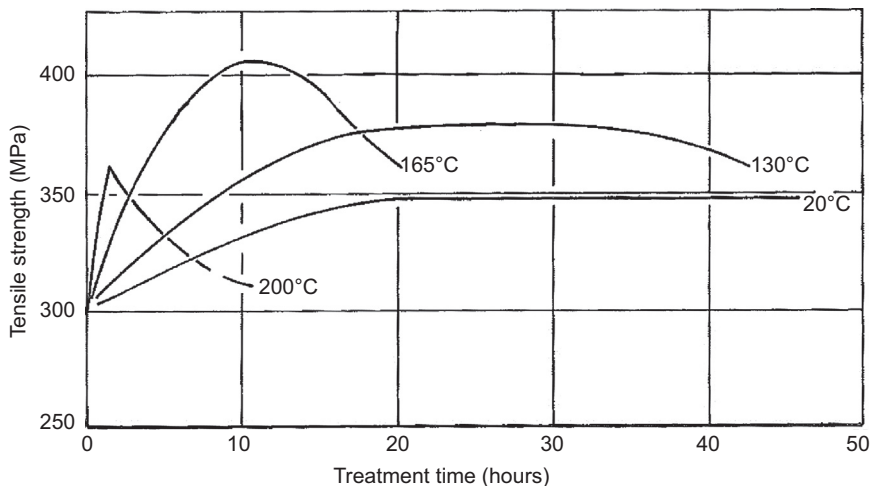


Figure 3.14 Graphical representation showing the relationship between the precipitation hardening heat-treatment time–temperature and tensile strength for an Al–Cu alloy. Adapted from Higgins, R.A., 1968. *Engineering Metallurgy: Part I Applied Physical Metallurgy*, second ed. The English Universities Press Ltd, London.

both contained 7039-T64 aluminium hull armour (see Fig. 3.3) (Crum et al., 2012; Ogorkiewicz, 2005; Perez-Bergquist et al., 2011; Showalter et al., 2008). Although the high-strength properties of such alloys offer improved ballistic protection in comparison to the traditional work-hardened armour alloy 5083-H131 against armour-piercing projectiles, the 7xxx series alloys were revealed to be much more susceptible to SCC, an issue of particular concern with regard to weld repairs and the propensity for weld heat-affected zone cracking. The tendency for the high-strength 7039 to exhibit significant back-face spallation (see Fig. 3.15) was also seen as an area for improvement, the result being a concerted move away from 7039 for proposed future US armoured vehicles, eg. AAHV.

Extensive academic research (Borvik et al., 2010; Demir et al., 2008; Flores-Johnson et al., 2011; Forrestal et al., 2010; Pedersen et al., 2011) has been undertaken and continues on the ballistic behaviour of the 7xxx series alloy 7075-T651 due to its benchmark high-tensile-strength properties. Nonetheless, this alloy has also found limited practical application as an armour material for applications subject to environmental exposure due also to its susceptibility to SCC.

In response to the shortcomings in corrosion properties of the 7039 alloy, effort has been dedicated to the development of other Al-alloys with an equivalent ballistic performance to the high-strength 7xxx series alloys, although with lower or no susceptibility to stress corrosion cracking (vis-à-vis 5083). To this end, a range of 2xxx series lithium- and silver-containing heat-treatable aerospace alloys such as 2090-T8E48 (Al–Li), 2195 (Al–Cu–Li–Mg–Mn–Ag–Zr), 2139-T8 (Al–Cu–Mg–Mn–Ag), Al–Cu–Mg alloys 2519-T87 and 2219-T851 were evaluated as potential

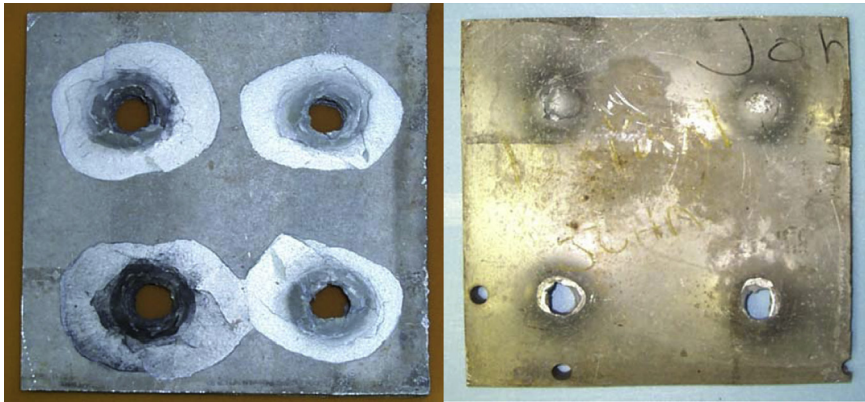


Figure 3.15 Photographs showing comparison of alloy 5083 (right) and 7039 back-face failure against 20 mm FSPs.

Reproduced from Gooch, W.A., Burkins, M.S, Squillaciotti R.J., 2007. Ballistic testing of commercial aluminium alloys and alternative processing techniques to increase the availability of aluminium armor. In: Paper Presented at the International Symposium on Ballistics, Tarragona, Spain.

armour materials. Typical mechanical properties of some of these alloys are shown in [Table 3.3](#). However, from this family, only alloy 2519 has been approved as a structural armour material.

In terms of strain-rate sensitivity, recent studies ([Chen et al., 2009](#)) have shown that the 6xxx series alloys are only mildly strain-rate-dependent, compared with the 7xxx series alloys which showed some dependency, in all three orientations (LT, TL and ST).

3.2.3 Ballistic properties of different grades

It is now recognised that aluminium armours are very forgiving in their nature, absorbing most of the kinetic energy from the penetrator through ductile hole formation but that some variants do suffer from premature discing. This section consolidates available ballistic performance data, measured in a number of different ways. For example, [Fig. 3.16](#), based upon the work of [Gasqueres and Nussbaum \(2011\)](#), shows how the residual velocity of a standard AP round, the P80 (see Chapter 1), with an impact velocity of 840 m/s, decreases as the measured UTS of the alloy increases. Over this large range of strength levels this relationship appears quite linear. The figure also shows that the experimental alloy 7449-T651 has performed best against this AP threat.

However, because this alloy performed badly against the 20 mm FSP (due to excessive discing), it was alloy 2139-T8 which had the best combination of performance against both rounds. Significantly, this was attributed to an optimum balance of strength and fracture toughness. It is not coincidental that the shape of this curve ([Fig. 3.16\(b\)](#)) looks very similar to [Fig. 3.7](#). The performance indices were calculated as follows:

$$\text{Performance index (\%)} = (V_o - V_r)/V_o$$

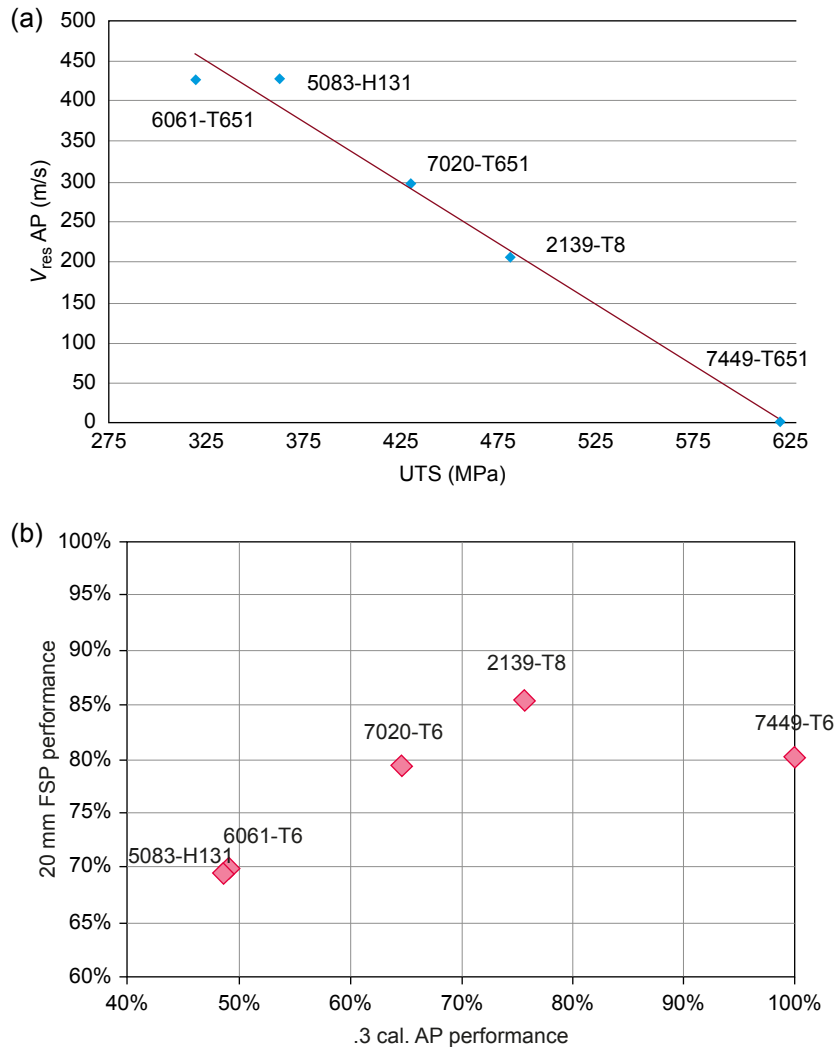


Figure 3.16 (a) Residual velocity values, V_{res} , for different aluminium armour alloys, and (b) performance indices against both AP and FSP. Based upon Gasqueres, C., Nussbaum, J., 2011. Ballistic performance and failure mode of high performance 2139-T8 and 7449-T6 aluminium alloys. In: Paper Presented at the International Symposium on Ballistics, Miami, FL.

By now, the reader will appreciate that the entire armour-grade alloys are wrought alloys — no casting grades have been approved for use in ballistic applications, principally because of their poor mechanical properties and the lack of adequate ductility. However, squeeze-cast alloys have been used (Crouch, 1987) — this is because the squeeze-casting process enables the traditional wrought alloys to be precision cast into near-net shapes, like the wheels of the UK’s Warrior APC (see Fig. 3.5). The rapid

solidification produces a fine, equiaxed grain structure, and whilst some alloy segregation does occur, it is usually contained within the centre of the section.

The use of new high-strength Al-alloys also offers the opportunity to further reduce the weight burden of armour on vehicles. Alcoa's 2090 alloy was found to outperform 2519-T87 and 7039-T67 against the 0.30 cal APM2 projectiles, as anticipated from the higher tensile mechanical properties, although it showed a reduced ballistic performance for 20 mm FSP and exhibited severe target discing and delamination, thereby preventing it from being considered as an armour material. Corrosion studies also revealed the 2090 to have a high propensity for pitting, with preferential attack in high-stress regions, and a lower resistance to SCC than 5083. Evidence of intergranular SCC on fracture surfaces was most likely due to the presence of Al_6CuLi_3 or Al_2CuLi grain boundary precipitates (Chin et al., 1989).

Alloy 2519-T87, a variant of 2219, with a reduced copper and higher magnesium content, was especially developed by Alcoa and the US Army as a potential alternative to 7039 (Kackley and Bethoney, 1986). The alloy possesses ballistic properties superior to 2219 and equivalent to, or better than, alloy 7039 for AP and FSP. It also has good SCC resistance, although it is still susceptible to general corrosion and pitting. Weldability studies on 2519 found that using appropriate procedures and filler material (eg, 2319 or 4145) that welding to itself or 5083-H131 could be accomplished with good tensile strengths and weldment failure occurring in a desirable ductile manner. Weldments passed the necessary ballistic shock qualification standard tests (Devletian et al., 1988).

In search of future combat vehicle ballistic materials, high-strength aluminium alloys developed through the research efforts of NASA and the aerospace industry were evaluated by the US Army to determine the potential for direct transfer into new armour materials (Nickodemus et al., 2002). Tests performed on the Al–Li alloy 2195, a structural alloy used for the space shuttle external fuel tanks, were undertaken on the off-the-shelf commercial T8 and an experimental TE1B temper. The 2195-T8 temper developed for high toughness at cryogenic temperatures provides high strength (twice that of 5083) and good ductility at ambient conditions. Both the T8 and lower-strength TE1B temper proved to possess superior AP and FSP ballistic properties over conventional 5083. The T8 temper provided a 25% and 11% improvement over 5083 against 0.5 cal AP and 20 mm FSP, respectively, and a 22% and 17% increase for the TE1B temper.

Another aerospace alloy developed by NASA to possess high tensile strength and high fracture toughness, alloy 2139, was assessed by the US Army Research Laboratory to determine its ballistic performance in comparison to 2519, 7039 and 5083 due to its potential as a light armour material with good blast properties (Cheeseman et al., 2008). Ballistic tests revealed the 2139-T8 alloy to significantly outperform 7039 and 5083 for both the 0.3 and 0.5 cal APM2 and 20 mm FSP. In comparison to alloy 2519 the high-strength 2139 alloy showed slight improvement against 0.3 cal APM2 with much greater ballistic performance for 0.5 cal APM2 and 20 mm FSP. Fig. 3.17 shows the front and rear failure zones, whilst Fig. 3.18 illustrates the ballistic performance of a range of new alloys compared with the standard armour alloys (Cheeseman et al., 2008).

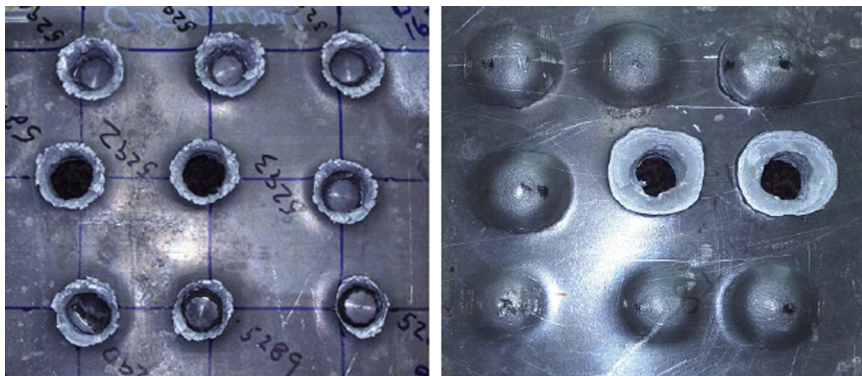


Figure 3.17 Front and back of 50-mm thick 2139 aluminium against 20 mm FSP showing ductile bulging and discing.

Reproduced from Cheeseman, B., Gooch, W., Burkins, R.S., 2008. Ballistic evaluation of aluminium 2139-T8. In: Paper Presented at the International Symposium on Ballistics, New Orleans, LA.

In the late 2000s, ARL researchers assessed the high-strength alloy, 7085, based upon a 7.5% Zn, 1.5% Mg, 1.5% Cu composition, in two temper conditions (T7E01 and T7E02) and found that it represents an excellent appliqué armour grade (Gallardy, 2011). In fact, MIL-DTL-32375 (Specification, 2012) was developed to cover procurement of this new grade of armour alloy. It out performs 7039 by $\sim 15\%$, especially in the T7E01 temper. The properties of this attractive, new alloy are given in Table 3.3 and referenced in Section 3.5.1 (Specifications).

In recent work by Ryan and Cimpoeru (2015), they presented (see Fig. 3.19) a summary of ballistic data for a range of alloys and showed that these results appeared to obey a scaling law based upon the Forrestal Cavity Expansion Law (see Chapter 8). Whilst these data ignore any effects due to discing failures, the trend is very clear, as it has been for 30 years, but predicting performance to within $\pm 5\%$ is impressive.

Research directions have, over the years, invariably been to increase the specific flow strength of useable grades (ie, those that can be formed and welded). Unfortunately, most of the drive, and sponsorship, for such developments have come from outside the armour community. Since the late 1980s, there has been active interest to explore the usefulness of the ultralightweight alloys like those based upon Al–Li (eg, 8090), with a bulk density 2.55, some 8% less than most armour-grade alloys. The drive for this alloy development was, again, for aerospace applications, not armour, due to the large difference in market sizes (and pull). In 1992, Holmes et al., from ARL, published work that showed that Al–Li alloys had great potential as an armour material. Alas, since those times, very little progress has been made. Their abstract states, ‘Aluminium-lithium (Al–Li) alloys with their high strength, high stiffness, and low density continue to be of great interest to the aerospace industry. The microstructure, properties and fracture of 8090-T8771 and Weldalite TM 049-T8 Al–Li alloys were studied at MTL in participation with a cooperative round robin sponsored by the Air Force Advanced Aluminium Alloy Test Program. Both 8090 and Weldalite Al–Li alloys

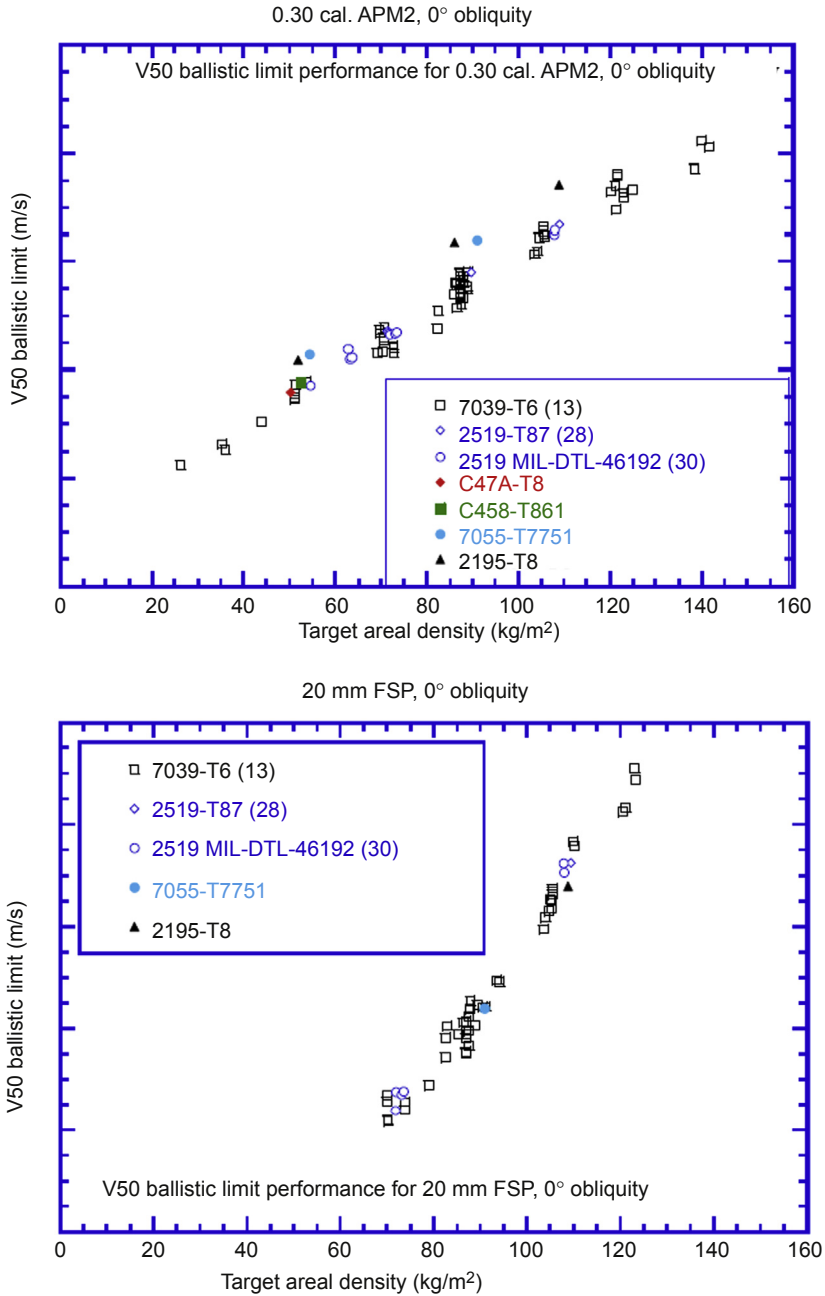


Figure 3.18 Ballistic curves for a range of aluminium armour alloys.

Reproduced from Chinella, J.F., 2004. ARL-TR-3185: High Strength Al-Cu-Li and Al-Zn Alloys: Mechanical Properties and Statistical Analysis of Ballistic Performance. US Army Research Laboratory.

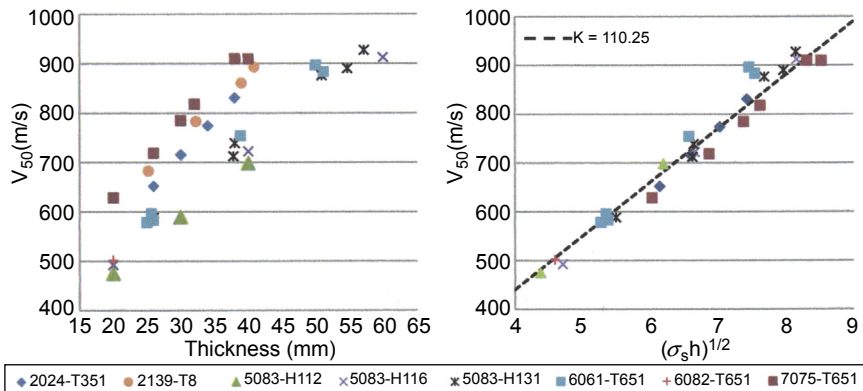


Figure 3.19 Ballistic limit test results for impact of 7.62 mm APM2 projectiles on aluminium alloys: Left — in terms of target material and thickness; Right — in terms of Forrestal's scaling law.

demonstrate superior strength to weight ratios compared to the 2519 and 5083 aluminium armor alloys. The 8090 alloy possesses comparable mechanical and ballistic properties to 2519, while providing an 8% reduction in density. The Weldalite has a comparable density to 2519 but demonstrates improvements of over 25% in yield strength, ultimate tensile strength and fracture toughness. Both Al-Li alloys display significantly improved axial fatigue properties over 2519. Under static loading, both materials display mixed modes of transgranular shear, micro-ductility and inter-subgranular failure. Under ballistic testing, both alloys display mixed modes of dynamic failure by plugging, spalling and delamination. Whether the goal is to reduce weight or to improve strength, Al-Li alloys offer significant potential for replacing alloys such as 2519 and 5083 as lightweight, high-strength structural armor materials.

More recently, Tolga Durson has reviewed the latest developments in advanced aircraft aluminium alloys (Durson and Soutis, 2014), including the Al–Li alloys. He cites many EH101 applications but, to date, there appears not to be a ballistic grade — still lacking real application except in laminates perhaps (see Chapter 4).

3.2.4 Engineering issues

3.2.4.1 Stress corrosion cracking

SCC is an insidious failure mechanism and compromises the structural and ballistic integrity of a military platform. An enormous amount of research has been undertaken in this subject area over many decades to understand, and more importantly, to develop SCC-resistant alloys. Of the nine PhD students under Dr John Scully, Leeds University, during the 1970s, eight were studying SCC (Crouch was studying oxidation!). From an engineer's perspective, SCC has three concurrent requirements for an SCC event to occur:

1. A susceptible microstructure in a susceptible alloy (chemical and physical state);
2. An applied stress (normally a residual tensile stress from welding or cutting);
3. A corrosive environment (giving rise to free H_2).

By removing just one of these three determinants will totally prevent SCC!

SCC in aluminium alloys, most particular the heat-treatable alloys, is linked with the presence of intergranular cracking within the microstructure that arises due to the selective precipitation of phases along the grain boundaries. The development of such precipitates upon aging, the compositional differences between precipitate composition, grain matrix and the adjacent alloy-depleted zone leads to the formation of electrochemical differences that in an appropriate aqueous environment promote intergranular corrosion and crack growth that follows the grain structure (Hatch, 1984). The extent of grain boundaries (directionality and continuity) is strongly dependent upon the fabrication processes applied to the material. For example, heavy rolling of plate produces continuous grain structures lying parallel to the rolling direction.

Non-heat-treatable alloys may become susceptible to stress corrosion cracking over many years of the alloy in service at ambient conditions or through periods at elevated temperatures, leading to the development of precipitate networks within the microstructure and in particular along the grain boundaries. For example, in heavily work-hardened 5xxx aluminium–magnesium alloys exposed to slightly elevated temperatures the precipitation of the beta-phase Mg_2Al_3 , a process often referred to as sensitisation, may occur and lead to initiation of microstructural cracking due to the lower corrosion resistance, more anodic characteristics of the precipitate phase compared with the adjacent Al–Mg matrix.

3.2.4.2 *Palliative treatments for SCC*

The occurrence of SCC in welded structures of aluminium armour alloys has brought about many palliative treatments, since very little has been achieved over the years to develop armour alloys that are inherently SCC-resistant. These practical engineering solutions include:

1. Weld-buttering exposed edges of thick alloy plate, to seal the susceptible structure from the environment;
2. Needle-peening of susceptible regions (weld toes, exposed edges), to induce compressive residual stresses in the surface;
3. Burnishing the surface, with a shallow “roller bearing”, to create a layer of heavily plastic-worked material;
4. Coating susceptible regions, with metal sprays or nonmetallic resins, to seal the susceptible structure from the environment;
5. Radically changing welding practice, to remove or reduce the level of tensile residual stress in the welded structure.

3.2.4.3 *Weldability*

Conventional welding of work-hardened, or aged, aluminium alloys using Metal Inert Gas (MIG) or Tungsten Inert Gas (TIG) processes give rise to heat-affected zones (HAZs), which include regions which are thermally softened, below the hardness level of the parent material. This gives rise to ‘ballistic windows’ in a welded structure – ie, areas that are ballistically inferior to the parent material and which could perform in a

substandard manner. Such windows need to be kept to a minimum size and preferably avoided in any ballistically sound structure, even though recent studies (Holmen et al., 2015) of welded joints in 6082-T6 alloys have shown that the decrease in ballistic performance is less than 10%. When a prototype military vehicle is being proof tested, as part of its acceptance trials, these areas receive a great deal of attention from inspectors. Suffice it to say that finding a ballistic window, through accurate shooting, is not always an easy task — far better to design them out in the first place!

The successful joining of aluminium alloy plate by fusion welding techniques and the retention of mechanical properties that are derived either through strain-hardening processes (non-heat-treatable alloys) or precipitation aging heat treatments has been a cause of concern for design engineers for many years. Fusion welding involves the melting of material at the interface between two materials and the introduction of a filler material, thereby giving rise to the possibility of the introduction of defects such as porosity, inclusions and the development of solidification cracks. In addition the thermal input drastically changes the base alloy microstructure within the weld bead region and adjacent HAZ, leading to dramatic changes in mechanical properties.

These microstructural changes lead to a significant reduction in mechanical properties, which, in turn, reduces ballistic performance. To overcome these effects the joining of Al-alloys via a friction stir welding (FSW) process has been extensively studied. For detailed information of FSW the reader is directed to the review papers by Mishra and Ma on FSW, processing, welding parameters and mechanical properties (Mishra and Ma, 2005; Ma, 2008). FSW is a solid-state joining technique that was first invented in 1991 at The Welding Institute in the UK. It is an attractive joining technique for metals in comparison to traditional fusion welding as the solid-state process enables joining of materials at temperatures below the metal melting point and no consumable filler metals are required. FSW is carried out by plunging a rotating hard metal, or ceramic, tool into the weld joint surface and slowly traversing the length of the workpiece. Sufficient frictional heat is generated at the tool shoulder in contact with the workpiece surface that metal flow and plastic deformation occur across the joint to eliminate the interface and create a sound defect-free weld region (Figs 3.20 and 3.21).

Texture development in FSW materials results in anisotropic properties in both the transverse and longitudinal directions. Property variations are noted in tensile strength, ductility and fracture toughness with respect to orientation to the FSW zone. The mechanical properties in the direction transverse to the FSW weld are typically reduced compared to the longitudinal. Dissolution of precipitates in age-hardened Al-alloys can result in a decrease in properties in the nugget zone — alternatively thermal cycling of undeformed material adjacent to the HAZ can cause precipitate growth in heat-treatable alloys and a deleterious increase in width of precipitate-free zones.

In general a reduction in tensile and yield strength in as-FSW age-hardened aluminium alloys occur, this decrease is due to the reduction in precipitates within the nugget zone of the FSW. UTS values in alloys are typically observed to be 80–90% of the base material. Aging treatments on postweld material to recover the lost strength in the nugget zone were found to improve the yield strength with no effect

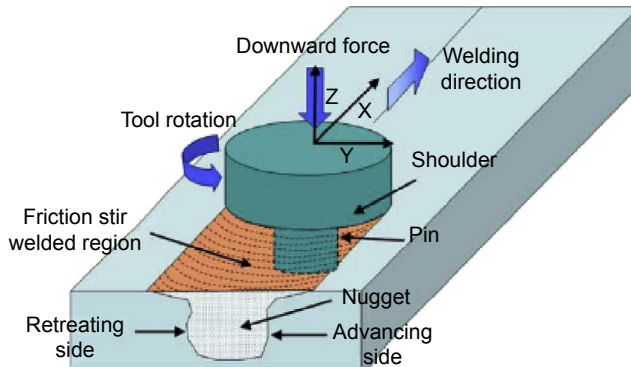


Figure 3.20 Schematic representation of the friction stir welding process, features of the weld tool and weld region.

Reproduced from Mishra, R.S., Ma, Z.Y., 2005. Friction stir welding and processing. Materials Science and Engineering: R: Reports 50 (1–2), 1–78. Retrieved from: <http://www.sciencedirect.com/science/article/B6TXH-4GX0C6S-1/2/cd3adba839cb56524581ff3c074f3b45>.

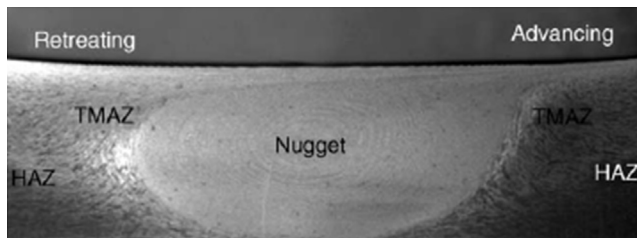


Figure 3.21 Example of the various microstructural zones in FSP aluminium alloy: heat-affected zone (HAZ), thermomechanically affect zone (TMAZ) and the stirred nugget zone. Reproduced from Mishra, R.S., Ma, Z.Y., 2005. Friction stir welding and processing. Materials Science and Engineering: R: Reports 50 (1–2), 1–78. Retrieved from: <http://www.sciencedirect.com/science/article/B6TXH-4GX0C6S-1/2/cd3adba839cb56524581ff3c074f3b45>.

on UTS, although at a drastic cost to the ductility, eg, 14% down to 3.5% due to the increase in precipitates and precipitate-free zones at grain boundaries (Mahoney et al., 1998).

Al-alloys that after FSW were subsequently solution heat-treated, quenched and aged showed a significant increase in tensile strength, yield strength and elongation over the as-FSW material and a return in properties equivalent or superior to the base material. It should be noted that specimens removed from FSW material will in general contain heat-affected, thermomechanical and nugget zone regions, therefore properties are expected to vary widely across these zones due to variations in grain size and structure, hence large test specimens represent average properties and material behaviour.

3.3 Titanium alloys

Titanium alloys offer a lightweight alternative to traditional armour steels for ballistic protection because its density is $\sim 60\%$ that of steel (see Fig. 3.22) and tensile strength properties equivalent to or better than RHA steel. In addition, titanium possesses excellent corrosion resistance in marine environments, a high melting point (1680°C) and superior high-temperature mechanical properties that have historically favoured its use in aerospace applications.

The metallurgy of titanium alloys was reviewed by Polmear (2006). In its pure form, titanium undergoes a phase transformation upon heating at the so-called β -transus temperature, whereby the room temperature stable α -phase (α) is transformed to β -phase (β) at 882°C . The α -phase is characterised by a hexagonal close-packed crystal structure whilst the β -phase possesses a body-centred cubic crystal structure. With the addition of specific alloying elements that have varying solid solubility in the α and β -phases, the transus temperature may be influenced such that the β -phase may exist at ambient temperatures. As a result, mixed $\alpha+\beta$ phase titanium alloys may be realised and the microstructure and mechanical properties of such alloys tailored via heat treatment and precipitation (strengthening) processes. Typical β -phase stabilising elements that lower the transus temperature include copper, vanadium, chromium, iron, nickel, molybdenum and, as an interstitial element, hydrogen. The α -phase stabilising elements include aluminium and the interstitial elements oxygen, nitrogen and carbon, together with tin, zirconium and silicon which have a neutral to weak influence on the transus temperature (see Fig. 3.23). To prevent the deleterious loss of ductility and toughness strict concentration limits are typically maintained for iron and especially the interstitial elements hydrogen, carbon and oxygen. The pioneering work of Chris Hammond and Jack Nutting, at Leeds University in the 1970s, is duly recognised (Hammond and Nutting, 1977), as well as more recent work by Wasz et al. in 1996.

Titanium is one of the most abundant elements in the earth's crust, naturally occurring as ilmenite (FeTiO_2) and rutile (TiO_2). However the historically high cost of extraction

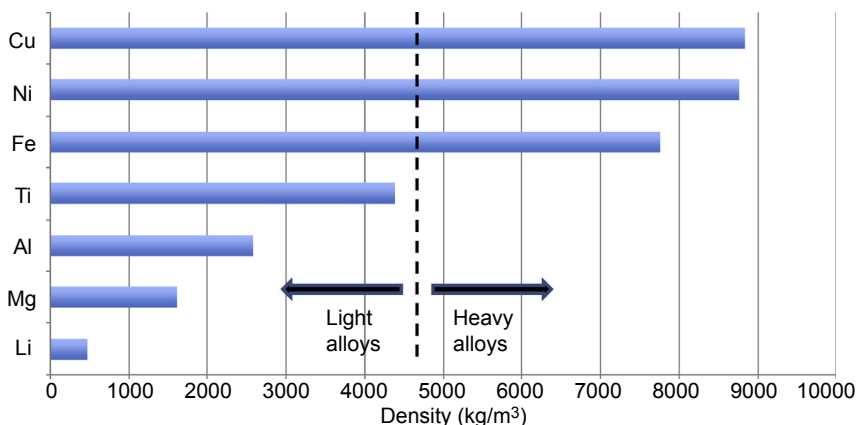


Figure 3.22 Relative bulk densities of metallic alloys.

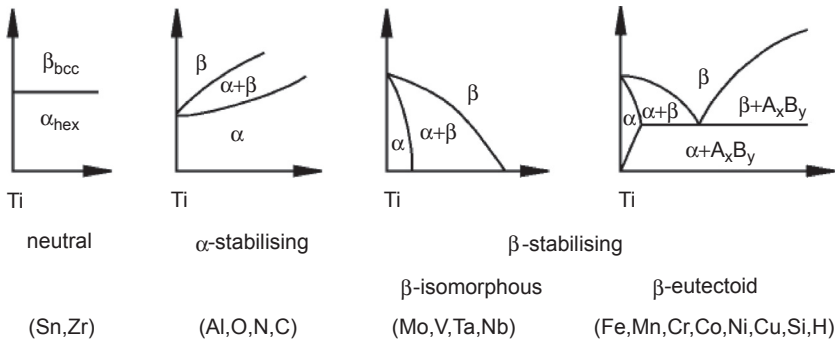


Figure 3.23 Influence of alloying elements on phase transformations in titanium alloys. Peters, M., et al., 2003. *Titanium and Titanium Alloys*, Wiley-VCH.

and processing, from the ore, has limited its broad application as a military material despite its attractive ballistic performance. New processing methodologies such as plasma and electron beam melting have reduced material costs, although no technologies have yet been developed that decrease cost such that titanium alloys are selected based solely on ballistic performance.

The titanium alloy of most significance for military armour applications is the $\alpha+\beta$ phase alloy Ti-6Al-4V which is weldable, has good formability and through heat treatment can attain tensile strengths in excess of 900 MPa. Due to the ballistic mass efficiency of armour grade Ti-6Al-4V alloy (typically ~ 1.5 compared with RHA) weight reductions of 30–40% have been anticipated when used to replace RHA steel (Montgomery et al., 1997). Within the US military, effort is on-going to incorporate Ti-6Al-4V, and other Ti-alloys, into armoured platforms and alike.

For example, a weight reduction of ~ 600 kg has been demonstrated for the M1A2 Abrams battle tank through replacement of select armour and various cover plates, and the development of a 3175 kg lighter M777A1 field howitzer compared to the M198 by utilising cast Ti-alloys and for the M2A2 Bradley vehicle lower weight commander's hatch fabricated from a titanium forging (Gooch, 2012) (see Fig. 3.24). The M1A2 Abrams tank is an excellent example of the use of titanium armour. The vehicle weighs ~ 62 tonnes. The hull armour represents $\sim 28\%$ of that weight, of which $\sim 85\%$ is RHA steel. The turret armour represents $\sim 23\%$ of the total weight, of which $\sim 60\%$ is RHA steel. Hence, substitution of the RHA by a titanium armour alloy, with its 30% weight-saving, has the potential to significantly reduce the overall weight of the vehicle. Furthermore, rather than retrofitting Ti-alloys to the M1A2 platform, it is envisaged that for a fresh build, with titanium alloys designed-in from the outset, and used in the turret, appendages (skirts, hatches, grilles), hull and support structures, could save up to 7300 kg (Lewis, 1994).

3.3.1 Ti-6Al-4V grades

Due to the deleterious influence of minor concentrations of carbon, oxygen, nitrogen and hydrogen on the ductility and ballistic performance of Ti-alloys such as Ti-6Al-4V,



Figure 3.24 The M1A2 Abrams and the M777A1 field howitzer.

From Montgomery, J.S., Wells, M., Roopchand, B., Ogilvy, J., 1997. Low-cost titanium armors for combat vehicles. *Journal of Materials* 49 (5), 45–47; Gooch, W.A., 2012. Processing and fabrication technologies for current and potential titanium military applications. In: Paper Presented at the Titanium 2012, Atlanta, Georgia, USA.

these armour materials are classified in accordance with defined interstitial concentration limits and impurity elements. The armour plate class composition limits and mechanical properties for the Ti-6Al-4V alloy are shown in [Table 3.4 \(Specification, 2006\)](#). Alloys that satisfy Class 1 composition limits are often referred to as extra low interstitial grades (ELI). Owing to the cost associated with production of the ELI, Class 1 alloy, this grade may be substituted where lower ductility and toughness can be afforded without influencing the minimum ballistic performance requirements. Class 4 alloys may possess Al, V and Fe compositions that vary from the conventional Ti-6Al-4V alloy in addition to increased interstitial element levels.

Research scientists at ARL have contributed a great deal to our understanding of the metallurgy of these alloys and its influence upon ballistic performance ([Burkins et al., 1997, 2000, 2001](#)). For example, various annealing heat treatments applied to the ELI Ti-6Al-4V alloy have been studied and shown to influence the ballistic performance, due to changes in the relative α and β -phase structure and content.

Armour plates annealed for a period of 30 min at a range of temperatures up to and beyond the β -transus temperature and air-cooled were evaluated with 20 mm FSPs. The ballistic limit velocity (V_{50}) remained constant over the temperature range of 732 to 954°C, whilst plate annealed above the β -transus exhibited a dramatic reduction in V_{50} value (815 m/s, compared to 1100 m/s). Plates annealed below the β -transus contained equiaxed α -phase with a propensity for increased intergranular β -phase at higher annealing temperatures. Tested plates exhibited ductile bulging and development of multiple delamination cracks parallel to the plate-rolling plane and perpendicular adiabatic shear cracks that were partially deflected by the presence of the delamination cracks. Plates annealed above the β -transus exhibited a microstructure of coarse prior β -phase grains transformed to a α + β phase lamellar or Widmanstatten structure (see [Fig. 3.25](#)). Ballistically tested plates showed limited deformation (reduced ductility), an absence of planar delamination cracks, and increased through-thickness ASBs,

Table 3.4 Specification data for Ti-6Al-4V alloys, based upon [Specification \(2006\)](#)

Class	Al	V	C	O	N	H ^a	Fe	Ti ^b	Others ^c
1	5.50–6.50	3.50–4.50	0.04 max	0.14 max	0.02 max	0.0125 max	0.25 max	Rem	0.10 max
2	5.50–6.75	3.50–4.50	0.08 max	0.20 max	0.05 max	0.0150 max	0.30 max	Rem	0.10 max
3	5.50–6.75	3.50–4.50	0.08 max	0.30 max	0.05 max	0.0150 max	0.30 max	Rem	0.10 max
4			0.08 max	0.30 max	0.05 max	0.0150 max		Rem	
Class		Yield strength 0.2% offset (MPa)			Tensile strength (MPa)			Elongation (%)	
1		758			827			10	
2		758			827			6	
3		758			827			6	
4		758			827			6	

^aHydrogen determined on each lot of product as shipped.

^bTitanium is determined by differences.

^cOther elements need not be analyzed nor reported unless otherwise specified but total content must not exceed 0.40.

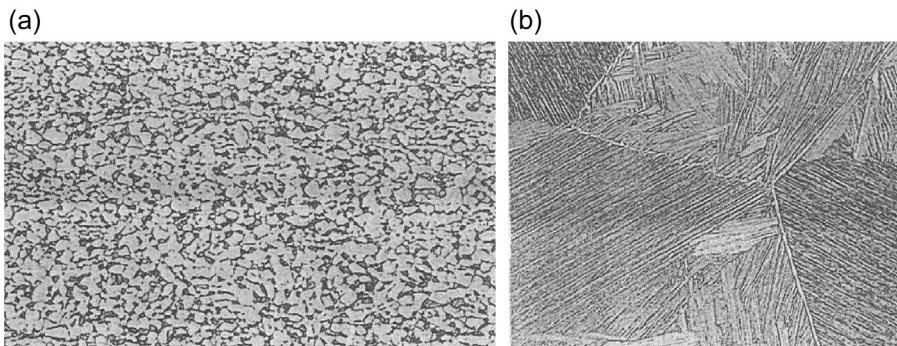


Figure 3.25 Metallographic sections showing the resultant microstructures of a Ti-6Al-4V ELI alloy annealed for 30 min at temperature (a) 900°C — fine α -phase matrix with intergranular β -phase (b) 1038°C — Widmanstätten α - β microstructure in a coarse-grained prior β -phase. Reproduced from Burkins, M.S., Love, W.W., Wood, J.R., 1997. ARL-MR-359, Effect of Annealing Temperature on the Ballistic Limit of Ti-6Al-4V ELI.

indicative of the low-energy failure (see Figs 3.26 and 3.27). Mechanical property tests from annealed plates showed that the tensile properties all met the required armour plate standard minimum (Specification, 2006), although those annealed above the β -transus failed to meet the elongation and reduction in area requirements (Burkins et al., 1997).

Similarly, Ti-6Al-4V ELI alloy plates subjected to mechanical rolling at temperatures above and below the β -transus temperature, followed by annealing treatments, exhibited reduced ballistic performance against 20 mm FSP when rolling is undertaken in the β -phase field, above the transus temperature (see Figs 3.28 and 3.29). A reduction in the V_{50} ballistic of up to 200 m/s was measured for plates processed in the β -phase field. The failure mode for materials processed in the β -phase field exhibits low-energy

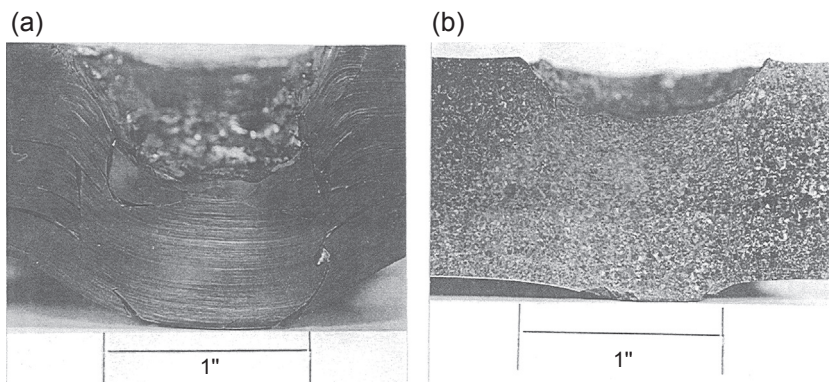


Figure 3.26 Photographs of annealed Ti-6Al-4V alloy targets after 20 mm FSP ballistic tests showing (a) 900°C annealed target with extensive delamination cracks, ductile bulging and shear plug formation, (b) 1038°C annealed target with limited back-face bulging and absence of energy-absorbing delamination cracks.

Reproduced from Burkins, M.S., Love, W.W., Wood, J.R., 1997. ARL-MR-359, Effect of Annealing Temperature on the Ballistic Limit of Ti-6Al-4V ELI.

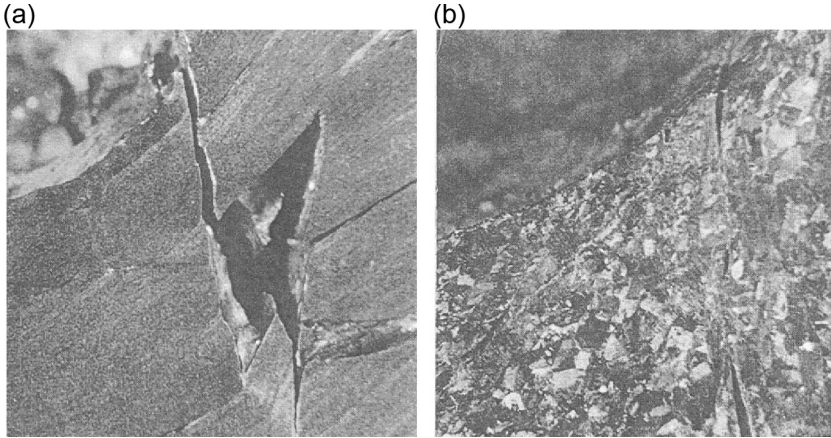


Figure 3.27 Photographs showing (a) adiabatic shear crack deflection by planar delamination cracks, (b) shear cracking and absence of delamination cracks.
 Reproduced from Burkins, M.S., Love, W.W., Wood, J.R., 1997. ARL-MR-359, Effect of Annealing Temperature on the Ballistic Limit of Ti-6Al-4V ELI.

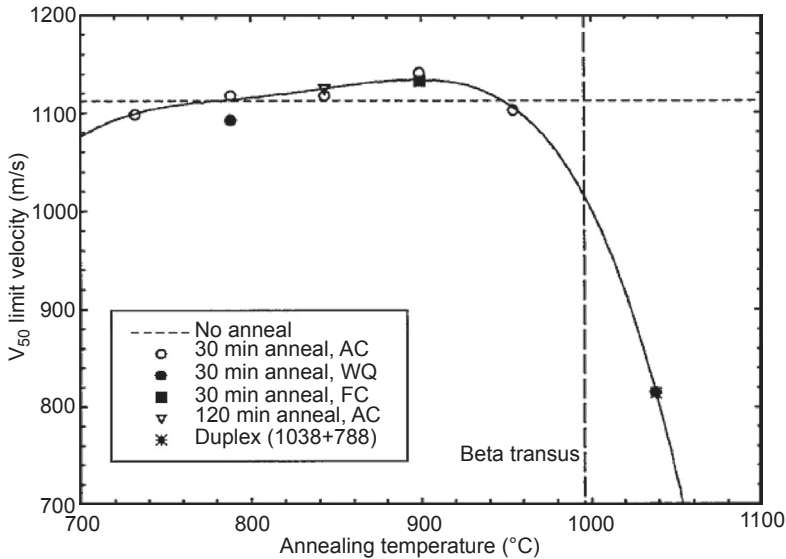


Figure 3.28 Normalised V_{50} ballistic limit velocity for Ti-6Al-4V plate annealed at various temperatures showing the influence of annealing above the β -transus temperature.
 Reproduced from Burkins, M.S., Love, W.W., Wood, J.R., 1997. ARL-MR-359, Effect of Annealing Temperature on the Ballistic Limit of Ti-6Al-4V ELI.

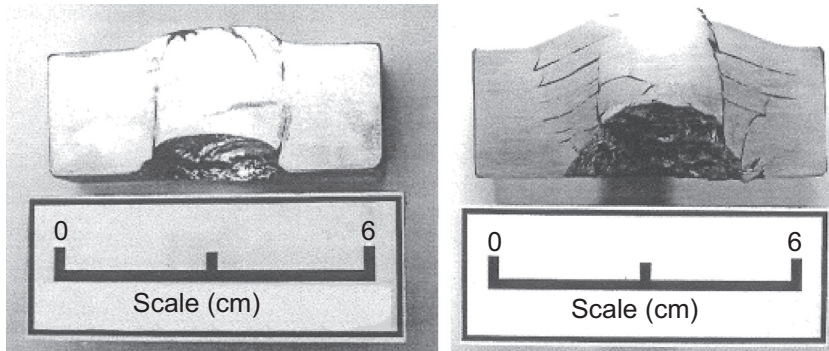


Figure 3.29 Photographs of Ti-6Al-4V alloy targets after 20 mm FSP ballistic tests for plate subjected to mechanical roll processing at a temperature (a) above the β -transus showing predominance of plugging failure by adiabatic shear (b) in the β -phase field showing additional cracking in the form of planar delamination. Reproduced from Burkins, M.S., Hansen, J.S., Paige, J.I., Turner, P.C., 2000. ARL-MR-486, The Effect of Thermo-Mechanical Processing on the Ballistic Limit Velocity of Ti-6Al-4V ELI.

adiabatic shear plugging, whilst $\alpha+\beta$ phase processed plates possessed enhance bulging, planar delamination cracks, adiabatic shearing and spalling. In addition, it is revealed that plate processed in the $\alpha+\beta$ phase region and followed by an anneal heat treatment in the β -phase region also exhibits an equivalent reduction in ballistic performance against the 20 mm FSP projectile (cf, V_{50} 978 to 775 m/s). The microstructure of such plates consisting of coarse grain prior β -phase transformed to lamellar $\alpha+\beta$ phase is shown in Fig. 3.30.

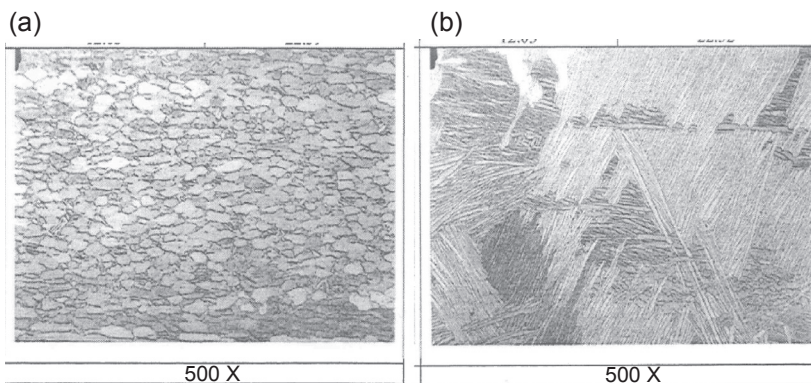


Figure 3.30 Micrographs showing microstructural changes in a Ti-6Al-4V alloy plate roll processed at 954°C followed by an anneal heat treatment at temperature (a) 788°C – $\alpha+\beta$ -phase region (20 mm FSP V_{50} 978 m/s) and (b) 1038°C – β -phase field (20 mm FSP V_{50} 775 m/s).

Reproduced from Burkins, M.S., Hansen, J.S., Paige, J.I., Turner, P.C., 2000. ARL-MR-486, The Effect of Thermo-Mechanical Processing on the Ballistic Limit Velocity of Ti-6Al-4V ELI.

For the 12.7 mm APM2 armour-piercing projectile the difference in ballistic limit was not so pronounced (~ 25 m/s) and a similar failure mode observed between α + β phase and β -phase field processed plate as compared to the 20 mm FSP.

Sukumar et al. (2013) compared the 0.3 cal APM2 ballistic performance of high-strength meta-stable β -phase titanium alloy β -CEZ to solution-treated and aged Ti-6Al-4V. A range of solution plus ageing heat treatments were applied to the β -CEZ alloy plates to achieve tensile properties up to 200 MPa higher than those of the Ti-6Al-4V alloy. The various β -CEZ alloy plates failed to show any significant ballistic improvement over the Ti-6Al-4V alloy, noting that the β -CEZ alloy measured Charpy impact properties were more than halved in some instances. Examination metallographic sections of penetrated plates revealed the β -CEZ to have a greater propensity for the nucleation of ASBs and shear band-induced cracking, and therefore decreased energy dissipation.

Due to the high strength and low thermal conductivity of Ti-6Al-4V alloys there is a propensity to fail via an adiabatic shear plugging mode upon impact. The shear failure arises due to the high rate of deformation derived from the perforating projectile and the inability of the surrounding material to dissipate the heat generated by plastic flow. When the thermal softening of material exceeds the process of work hardening, formation of distinct thin layers of thermally softened material, known as shear bands, occur and failure proceeds. Evidence of metal particles on shear boundary surfaces and ejected shear plugs suggests temperatures may be raised as high as the melting temperature. The adiabatic shear and plugging failure mode occurs only when a critical projectile velocity (high strain rate) is achieved, above which the ballistic performance of the Ti-alloy deteriorates (Woodward, 1979; Holt et al., 1993). As shown by Zheng et al. (2015), very recently, the formation of ASBs in this alloy has a very strong influence over local failure modes and can lead to very brittle behaviour.

In order to expand the usage of titanium alloys for military vehicle ballistic armour applications a range of strategies have been undertaken by industry and aided by defence organisations to develop low-cost titanium alloys. The term low-cost titanium has been defined as: useful titanium alloy products whose production path involves processing that lowers costs, including reduction processes, electron beam and plasma arc, optimised thermomechanical processing, and near-net shape fabrication (Pickens, 2004).

One approach that has been investigated is the influence of different methods of melt processing of Ti-6Al-4V alloys, so to move away from the expensive processing requirements of aircraft-grade materials. This has included evaluation of alloys from a low-cost single melt electron beam cold hearth melting (EBCHM) process, to eliminate the costly multiple vacuum arc melts necessary for critical aircraft components in order to meet strict impurity limit specifications. The US Army Research Laboratory undertook a study on Ti-6Al-4V (Class 2) plates produced by EBCHM. It was found that the Ti-6Al-4V material exceeded the minimum required mechanical properties and also met the ballistic performance specification for titanium armour against the 20 mm FSP (Burkins et al., 2001).

In summary, Figs 3.31 and 3.32 show how the ballistic performance of standard Ti-6Al-4V alloys, compared to 5083 and RHA standards, are far superior, across a wide range of areal density values, as given by Timet, suppliers of Ti-alloys, in 2010

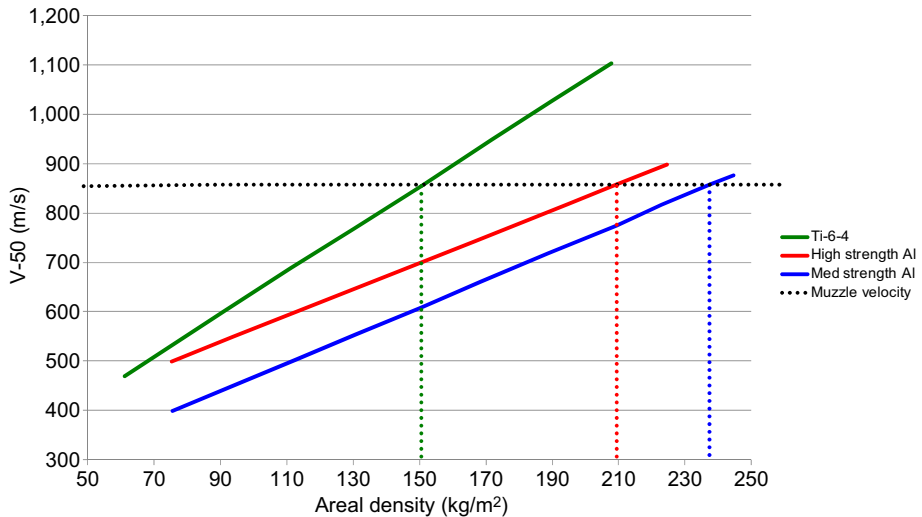


Figure 3.31 Ballistic performance of Ti-6V-4Al alloy compared to general aluminium alloys, against the 0.5 cal APM2 round.

After Fanning, J.C., 1999. Ballistic evaluation of TIMETAL 6-4 plate for protection against armor piercing projectiles. In: Paper Presented at the Titanium 99, Science and Technology, St. Petersburg, Russia.

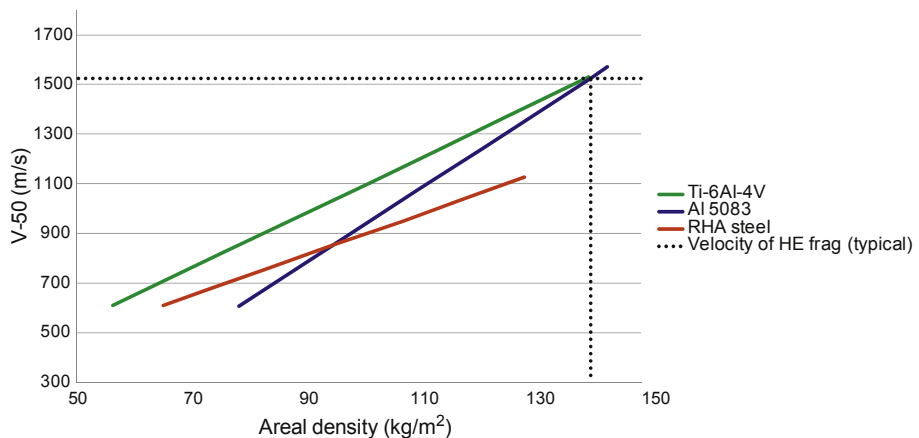


Figure 3.32 Ballistic performance of Ti-6V-4Al alloy compared to both 5083 and RHA steel, against the 20 mm FSP round.

After Fanning, J.C., 1999. Ballistic evaluation of TIMETAL 6-4 plate for protection against armor piercing projectiles. In: Paper Presented at the Titanium 99, Science and Technology, St. Petersburg, Russia.

(Fanning, 1999). If this is so, then why are these alloys not used more prolifically in armour systems? The answer is cost and availability (see Table 2.6). For a titanium-based solution, against the 0.3 cal APM2 round, it is estimated to cost about 20 times that of an equivalent RHA solution, albeit saving $\sim 28 \text{ kg/m}^2$ in weight. So, unless a large area of armour was required, one might rightfully challenge the cost-effectiveness of using titanium alloys.

The excellent ballistic properties of these titanium alloys, against armour-piercing rounds, are reported to be consistently high across all calibres up to the 20 mm M602 projectile (see Fig. 3.33) so the behaviour is universal. But why are the titanium alloys so fundamentally superior to the aluminium alloys, and steels for that matter, against the AP threats (see Figs 3.31 and 3.32)? Perhaps a frictional term or a heat conduction term needs to be considered alongside the conventional DHF calculations. This will be considered in Chapter 12.

Reductions in cost have also been sought through a decrease in the use of expensive alloying additions such as vanadium, for example in the $\alpha+\beta$ alloy ATI-425-Mil that possesses a higher iron (β -stabiliser substitute) and oxygen content than standard Ti-6Al-4V Class 1 to infer the necessary tensile strength and satisfy MIL-DTL-46077G as a Class 4 alloy. The ATI-425 alloy (Anon, 2008), based upon Ti-4V-2.5V-1.5Fe, is also reported to be easily cold-worked, compared to Ti-6Al-4V, which is unworkable at cold temperatures. The titanium alloy TIMET 62S, based upon Ti-6Al-1.5Fe, similarly replaces expensive alloying elements to reduce costs, whilst aiming to retain the properties of typical Ti-6Al-4V alloys for potential application as an alternative armour material. Ballistic performance tests performed on low-cost armour plate have shown such alloys to possess ballistic properties (see Fig. 3.34) that enable them to fulfil the

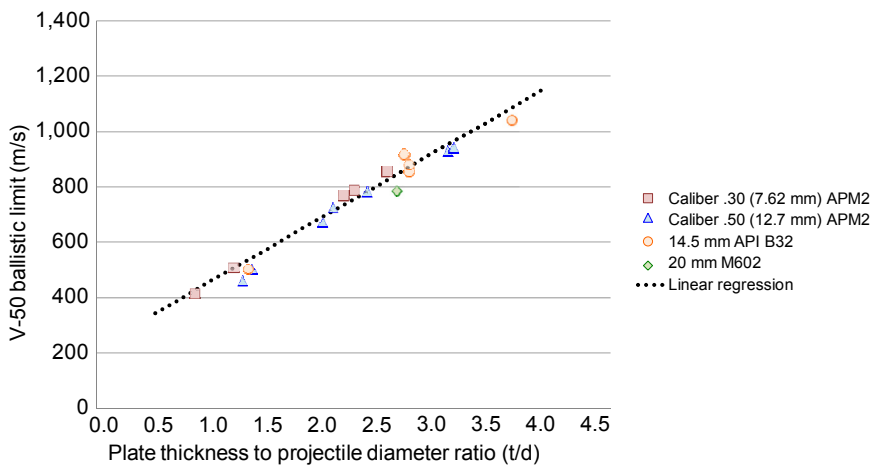


Figure 3.33 Combined plot for AP projectiles against Ti-6V-4Al alloys.

After Fanning, J.C., 1999. Ballistic evaluation of TIMETAL 6-4 plate for protection against armor piercing projectiles. In: Paper Presented at the Titanium 99, Science and Technology, St. Petersburg, Russia.

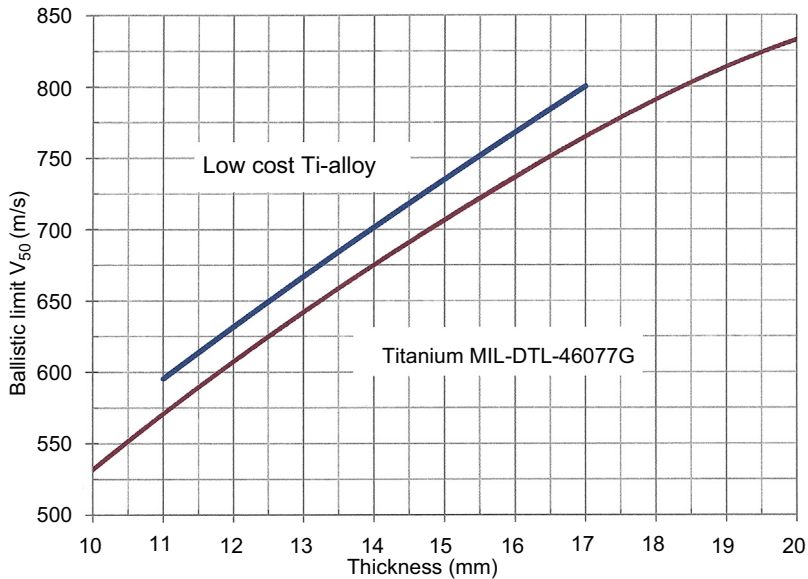


Figure 3.34 Ballistic data for a low-cost titanium alloy against 0.3 cal APM2 projectile compared to the titanium armour plate specification.

Reproduced from Edwards, D., 2014. Private Communication. DST Group, Australia.

titanium armour specification (Specification, 2006), therefore suggesting that low-cost titanium alloys are a viable alternative to the more costly standard aerospace Ti-6Al-4V alloy armour grade.

3.3.2 Future titanium alloy armours

Lightweight armour in the future is likely to be processed and fabricated in ballistic panels as appliqué or vehicle structural elements via very different methodologies. As touched upon in Section 3.2.4.3, friction stir welding, or variations of, may become the preferred approach to joining high-strength alloys, where heat input needs to be carefully controlled and the HAZ ideally all but eliminated. In recent years additive manufacturing has enabled 3D printing of bulk materials, via laser or electron beam consolidation of fine powder Ti-6Al-4V, to become a reality (Vega, 2014) with the necessary industrial-scale equipment readily available and now being widely investigated in academic facilities. The compositional range of powder feedstock is rapidly increasing and the characterisation of the bulk materials produced being the focus of significant research and industrial efforts to enable the certification of additive manufactured materials for applications currently satisfied by materials fabricated by traditional means.

The additive manufacture methodology is widely considered as the next industrial revolution with the ability to enable rapid and short production runs of unique components — new geometries and material properties. Research into the properties of additive manufactured Ti-6Al-4V aerospace and armour has already begun (Anon, 2015c) at the Oakridge National Laboratory on functionally graded and geometrically ordered materials. Industry and research organisations have appropriately responded to the potential future of additive manufacture by investing in research into new methods of powder manufacture and bulk consolidation, in particular to further reduce the cost of high-grade titanium alloys (Grainger, 2014).

3.4 Magnesium alloys

With a bulk density of only 1740 kg/m^3 , based on pure magnesium, these alloys represent the lightest structural engineering alloy. A useful review of the metallurgy of magnesium alloys was published by Nie (2012). Favoured by some automotive designers (for its excellent damping properties) and aerospace engineers (eg, for transmission housings in helicopters) it has established itself in small, niche markets. However, as a ballistic material, it has not done so. This is for two main reasons: firstly, it is not easy to process economically, at large scale, because of its reactive nature; secondly, it has a high propensity to spall, much like titanium alloys and some of the aluminium alloys, since very large thicknesses are required and the through-thickness ductility is poor. The alloys are so relatively soft that, in some cases (eg, against 0.5 cal APM2 rounds), the material is not even strong enough to strip the copper jacket from an impacting bullet (Van de Voorde et al., 2005)!

Nevertheless, some research effort has been expended on this family, especially in the US, and this has resulted in the issuing of a military standard for appliqué applications. MIL-DTL-32333 (Specification, 2009) was issued only relatively recently, in 2009, so this family is still in its infancy. The question is, has it real potential to become a mainstream armour material?

The metallurgy of magnesium alloys has been thoroughly reviewed by Pekguleryuz et al. (2013), and is highly recommended background reading for this section. Because of its extremely low density, magnesium alloys compare quite favourably to other armour materials (see Fig. 3.35) when normalised for density. However, in reality, its low density goes against it because such thick sections are required (even for the same areal density of armour) which, in turn, leads to poorly worked microstructures, inherently stiff structures, and therefore a high propensity for discing failures (see Chapter 1). Nevertheless, specific alloy grades have become established and research continues with the objective to overcome these two limitations.

The properties of magnesium alloys are governed by its close-packed hexagonal crystal structure (limiting available slip systems) and by its atomic size (favouring solid solubility). Deformation twinning, especially at high strain rates, enables larger strains to be accommodated, rather than normal dislocation movement. The alloys are heat-treatable, and so most alloy development has been through solute additions and precipitation hardening (see Table 3.5).

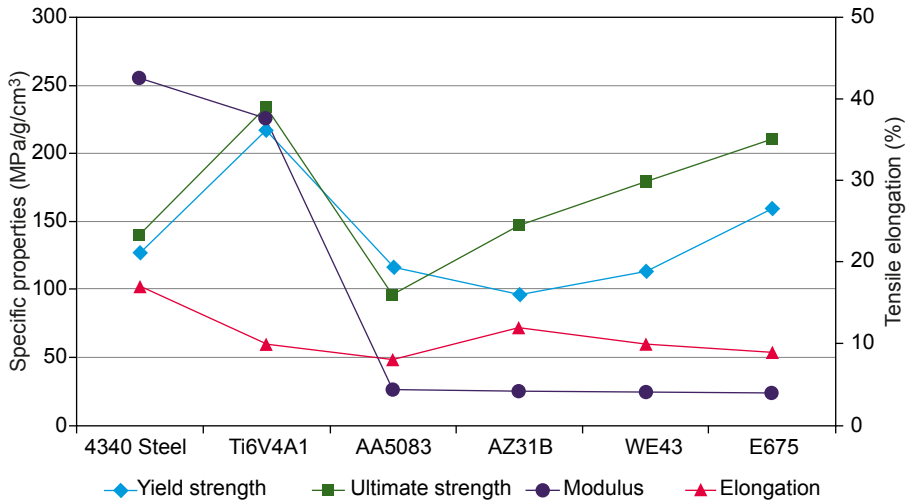


Figure 3.35 Comparison of light-alloy properties compared with 4340 steel. Reproduced from Cho, K., et al., 2009. ARL-RP-236, Magnesium Technology and Manufacturing for Ultra Lightweight Armored Ground Vehicles.

The Army Research Laboratory, in the US, carried out an intense R&D program in the early 2000s, and published a plethora of technical reports and conference papers around 2008–2010. One in particular, entitled ‘Magnesium Technology and Manufacturing for Ultra Lightweight Armored Ground Vehicles’ (Cho et al., 2009) is especially relevant to this section, and covers important topics such as deformation mechanisms, corrosion behaviour, joining and flammability.

3.4.1 Mg-3Al-1Zn alloys

This is the primary alloy approved for armour applications. It is based upon a 3–4% aluminium, 0.5–1.5% zinc, composition and is manufactured to strict operating procedures, standardised in ASTM-B90 (Specification, 2007) and/or AMS-4377. The standard embraces three temper conditions, covering a range of minimum mechanical properties (see Table 3.6) for thicknesses up to 80 mm. Because of the alloy’s poor corrosion resistance, the standard (Specification, 2007) recommends a chrome pickle or oil finish as a protective measure against tarnish and general corrosion during transit.

Key performance indicators are strength, ductility and grain size, as one would expect, and the work of Liao et al. (2009), showed that the Charpy impact energy could be increased from ~10 J (for an alloy with a grain size of 5–10 µm) to more than 25 J (for an alloy with a grain size of <3 µm). Magnesium alloys are very anisotropic but Tucker et al. (2009) also discovered that AZ31B-H24 has a strong strain-rate dependency (see Fig. 3.36); each test orientation exhibited a different degree of dependency. They also observed that the twin density and number of fractured particles also

Table 3.5 Grades, compositions and properties of Mg alloys

Grade	Alloying elements	Density (kg/m ³)	Yield strength (MPa)	Tensile strength (MPa)	Elastic modulus (GPa)	Elongation (%)	Development stage
AZ31B-H24 ^a	3% Al, 1% Zn	1780(b)	150	245		7	Approved to MIL- DTL- 323333
AZ31B-H24, hard rolled sheet ^f	Al 2.5–3.5, Ca ≤ 0.040, Cu ≤ 0.050, Fe ≤ 0.0050, Mn ≥ 0.20, Ni ≤ 0.0050, Si ≤ 0.10, Zn 0.60–1.4	1770	220	290	45	15	
ZK60A ^e	Zn 4.8–6.2%, Zr ≥ 0.45%	1830	305	365	44.8	11	
Elektron 675 ^b	4% Y, 3% rare earths, 0.4% Zr,	1900(b)					
Elektron 675 ^g		1950	310	407		9	
Elektron WE43-T5 ^c	4% Y, 3% rare earths, 0.4% Zr,	1840	287 (L) 225 (LT)	351 (L) 343 (LT)		4.2 (L) 8.6 (LT)	
Elektron 43 ^h – thickness 38.1 mm	3.7–4.3 Y, 2.3–3.5 rare earths, ≥0.20 Zr	1840	255	345	44	14	
AMX602 ^d	6% Al, 2% Ca, 0.5% Mn		310 (L) 240 (LT)	356 (L) 310 (LT)		19.9 (L) 10.8 (LT)	
ZAXE1711 ^d	7% Al, 1% Zn, 1% Ca, 1% La		270 (L) 242 (LT)	380 (L) 369 (LT)		18.1 (L) 16.9 (LT)	

^aJones et al., ASB24, New Orleans, 2008.

^bHazell et al., Acta Materialia 2012.

^cCho et al., ARL-RP-236, February 2009.

^dJones and Kondoh, ISB26, Miami, 2011.

^e<http://www.azom.com/article.aspx?ArticleID=6710>.

^f<http://www.matweb.com/search/datasheet.aspx?matguid=d1e286e1ac0742358544b953bbf3c2e9&ckck=1>.

^g<http://www.matweb.com/search/datasheet.aspx?matguid=1c5d941454cb405fbd6dae334ffd77>.

^h<http://www.matweb.com/search/datasheet.aspx?matguid=a3a15f442b4c4d41a8e6aaf13372bac1>.

Table 3.6 Selected minimum mechanical properties of magnesium alloy, AZ31B (Specification, 2007)

Alloy and temper	Thickness range (mm)	Tensile strength (MPa)	Yield strength (MPa)	Elongation (%)
AZ31B-O	12.5–50.0	221–275	NR	9
AZ31B-H24	12.5–25.0	248 min	152 min	7
AZ31B-H26	12.5–20.0	255 min	172 min	5

Note: Only some of the available thickness ranges have been included here, for ease of comparison between temper conditions.

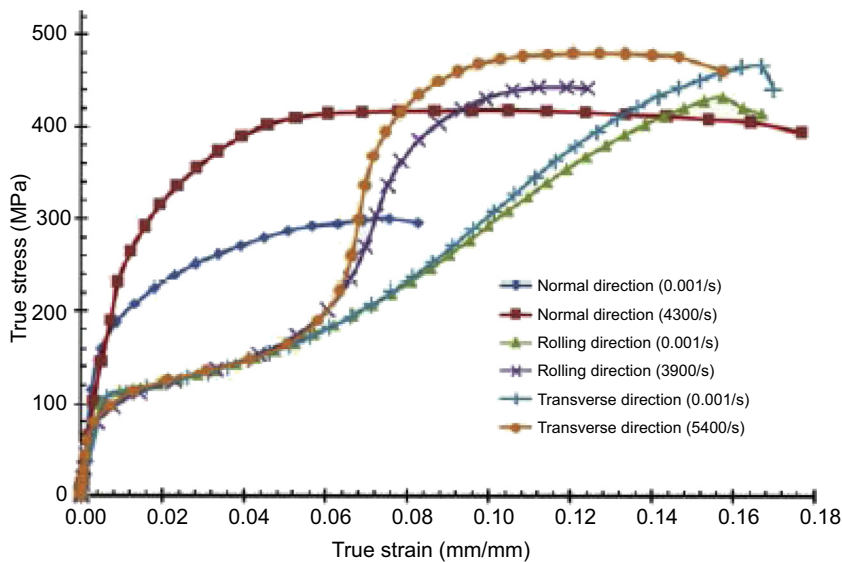


Figure 3.36 Compressive stress—strain curves for AZ31B-H24 showing the isotropic effects on the strain-rate dependence.

Reproduced from Tucker, M.T., et al., 2009. Anisotropic effects on the strain rate dependence of a wrought magnesium alloy. Scripta Materialia 60, 182–185.

increased as the strain rate was increased, in all three orientations. Interestingly, they calculated that more energy, per unit volume, was absorbed in the through-thickness (normal) direction, than in either of the in-plane orientations (rolling and transverse), with an increase in strain rate — a perfect scenario for an armour material, since most of the initial impact energy from a blunt projectile will be converted into through-thickness compression (see Chapter 1).

3.4.2 Research grades

3.4.2.1 Alloys with rare earth additions

This alloy variant includes rare earth additions from the Lanthanides group (see Periodic Table in Chapter 1), neodymium, erbium, dysprosium and gadolinium, which promote both solid solution hardening and precipitation hardening options when heat-treating. In a report by Tyrone Jones at ARL (Jones and Placzankis, 2011), having evaluated the ballistic and corrosion properties of Elektron E675, it was found that the E675 alloy had a higher ballistic protection limit (up to 28%) for single strikes, compared with both AZ31B and aluminium alloy 5083. However, as thickness increased, the performance gain was much reduced, due to the alloy's brittle nature and propensity to fail by discing (see Fig. 3.37). More significantly, they showed that E675 does not pass the corrosion requirements of MIL-DTL-32333, and point out that the use of rare earth additions is likely to increase the cost. With reference back to Table 2.6, one can see that magnesium alloys are very expensive and therefore not a very competitive armour material. Elektron 675 is normally supplied in the cast, extruded and heat-treated condition, T5.

Alloy WE43 is a conventional casting alloy but has been researched as a potential wrought armour grade (Cho et al., 2009), via a direct chill casting process, followed by selected thermo-forming treatments. Ballistic tests on such material (Cho et al., 2009) showed significant improvement over AZ31B but was only assessed up to $\sim 75 \text{ kg/m}^2$, with a V-50 well below that required for full protection against the 0.3 cal APM2 projectile. However, this does not negate its future use in thin sections.



Figure 3.37 Rear view of an Elektron E675-T5 plate, at 131 BHN, impacted with a 20 mm FSP. Reproduced from Jones, T., Placzankis, B., 2011. ARL-TR-5565, the Ballistic and Corrosion Evaluation of Magnesium Elektron E675 vs Baseline Magnesium Alloy AZ31B and Aluminium Alloy 5083 for Armor Applications.

3.4.2.2 Alloys with Al and Ca additions

These experimental grades, designated as AMX602 and ZAXE1711, contain higher percentages of aluminium than the standard production alloy, AZ31B: 6–7% aluminium as well as 1–2% of calcium. A US study looking at the effects of manufacturing route (Jones and Kondoh, 2009) found that AMX602 exhibited ~20% ballistic improvements over AZ31B. Both kinds of magnesium alloy, AMX602 and AZ31B, were manufactured by the spinning water atomisation process (SWAP) followed by spark plasma sintering (see Chapter 7) to aid metallurgical bonding. The experimental alloys were extruded into 5-mm thick bars and tested against the 1.1-g FSP. These were then compared with conventionally rolled plates of similar areal density.

As can be seen from Figs 3.38 and 3.39, the conventionally processed AZ31B-H24 Mg alloy plate, tested against the 1.1-g FSP, showed a minimal amount of spalling, around the periphery of the exit hole, compared with the experimental alloy. The experimentally processed alloy showed quite extensive spalling on the rear face, albeit at low ejection velocities (very little damage to witness screen). Their respective V-50 values (based upon Partial penetration/Complete penetration (PP/CP)) were reported to be ~275 m/s (against 1.1-g FSP) with very little difference between all processing variables. However, the ejection of spall from the experimental SWAP alloy, suggests that if spall could be suppressed in this alloy, then the V-50 would increase.

3.4.3 Future alloy developments

Even though there is a ground swell from within the R&D community for work on magnesium armour alloys, this light-alloy family is battling some inherent

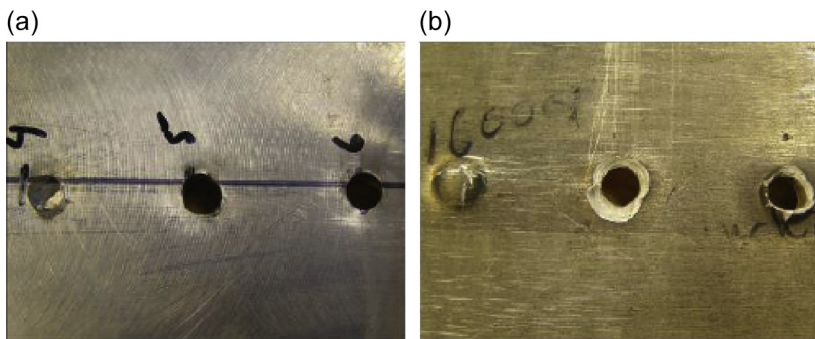


Figure 3.38 Front (a) and rear (b) views of impact damage from 1.1-g FSP impact against wrought plate, AZ31B-H24.

Reproduced from Jones, T., Kondoh, K., 2009. ARL-TR-4828, Initial Evaluation of Advanced Powder Metallurgy Magnesium Alloys for Armor Development.

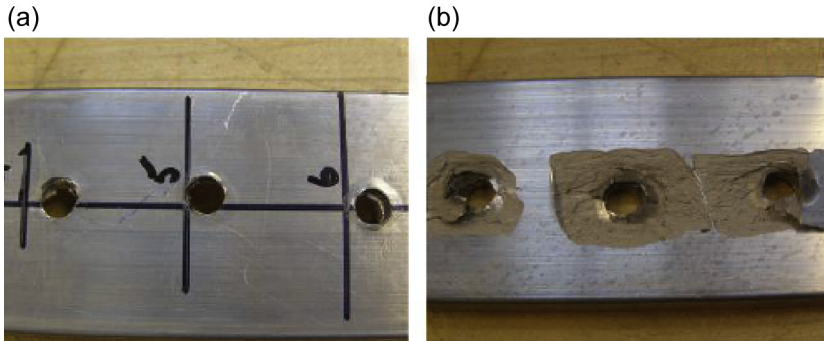


Figure 3.39 Front (a) and rear (b) views of impact damage from 1.1-g FSP impact against experimentally extruded alloy, AMX602, after SWAP, cold compaction and extrusion at 325°C.

Reproduced from Jones, T., Kondoh, K., 2009. ARL-TR-4828, Initial Evaluation of Advanced Powder Metallurgy Magnesium Alloys for Armor Development.

disadvantages: its inability to be cold-worked, extremely poor general corrosion resistance, severe challenges in welding, and most of all its low yield strength (specific or not!). Whilst welding issues might be overcome through use of new methods like FSW (see Section 3.2.4.3), its other inherent disadvantages will hold back any real applications.

Experimental approaches to alternative manufacturing processes must also remain scalable. From a production perspective, it is worthless carrying out R&D into plasma sintering, for example, if one is considering magnesium alloys for plate applications.

From an armour technologist's viewpoint, one approach does have some value: consideration of magnesium alloys as part of a laminated system ([Van de Voorde et al., 2005](#)). This will be discussed more deeply in Chapter 4, but the sensible drivers for this approach would be suppression of discing failures and use of the material's exceptionally low shock impedance values (due to its low density).

3.5 Light alloy specifications and standards

The following set of tables ([Tables 3.7–3.9](#)) summarises the status of most of the useful light alloy armour materials. The lay reader should realise that for a military standard to exist, a real need/requirement must have been created. It is therefore very worthwhile keeping a watching brief on the status of military specifications: both new ones and redundant ones – they reflect real-time usage of qualified armour materials and technologies.

3.5.1 Aluminium alloys

Table 3.7 Relevant military specifications of most aluminium alloys

Grade	Notes	Application	References	Military standard, date
2090-T83	Lithium-containing, R&D alloy	Experimental		
2139-T8	Good penetration resistance	Applique grade	Gooch et al. (2007) and Gasqueres and Nussbaum (2011)	MIL-DTL-32341, 31st March 2010
2195	Good penetration resistance	Applique grade		MIL-DTL-32341, 31st March 2010
2219-T851				MIL-DTL-46118E, 26th August 1998
2519-T87		Extrusions in AAAV, USA	Crum et al. (2012)	MIL-DTL-46192C, 7th February 2000
5059-H131	Good spalling resistance	MRAP	Anon (2015b)	MIL-A-46027K, 17th April 2013
5083-H131		M113 and many more		MIL-A-46027K, 17th April 2013
5456		M113 and many more		MIL-A-46027K, 17th April 2013
6061-T6	Marine grade	Extrusions and plate	Manes (2014)	MIL-DTL-32262, 31st July 2007
6082	Marine grade			
7017	Preceeded by RARDE 1318B	UK Scimitar		
7020-T651				
7039-T64		US Bradley; M551	Gooch et al. (2007)	MIL-DTL-46063H, 12th June 2000
7075-T651	Aircraft grade with potential		Crouch et al. (1987) and Demir et al. (2008)	
7085-T711		New applique grade		MIL-DTL-32375, 11th December 2012
7449-T6	Popular R&D grade			
8090	Aerospace grade only	Not considered for armour	Crouch et al. (1992)	

3.5.2 Titanium alloys

Table 3.8 Relevant military specifications of most titanium alloys

Grade	Notes	Application	References	Military standard, date
Ti-6Al-4V	Grade 5 to MIL-T-9046J	M1A2 Abrams MBT	Montgomery et al. (1997)	MIL-DTL-46077G, Sept 2006
Ti-4V-2.5V-1.5Fe	ATI-425	Experimental	Anon (2008)	
Ti-6Al-1.5Fe	Timet 62S	Experimental		

3.5.3 Magnesium alloys

Table 3.9 Relevant military specifications for magnesium alloys

Grade	Notes	Application	Reference	Military standard, date
AZ31B-H24	Tested by US Army labs	Hard-rolled sheet	Jones, ISB24 (2008)	MIL-DTL-32333
Elektron 675	Experimental	Extrusions only		
AMX602	Experimental			

Acknowledgements

The authors are indebted to Professor Ian Polmear, of Monash University, for peer-reviewing this chapter. We are also thankful to various colleagues at the Defence Science and Technology Group, and the Defence Materials Technology Centre for useful discussions.

References

- Anon., 2008. ATI 425 Military Titanium Alloy. Allegheny Technologies Brochure.
- Anon., 2015a. Aluminium — Hull Structures in Naval Applications. www.austal.com.
- Anon., 2015b. Data Sheet on Alustar. www.aleris.com.
- Anon., 2015c. <http://energy.ornl.gov/armor/materials/materials.cgi?nav=1>.
- Anon., 2015d. <http://www.army.gov.au/Our-work/Equipment-and-clothing/Vehicles/M113AS4>.

- ASM, 2000. Hand Book Vol. 2. Properties and Selection: Nonferrous Alloys and Special-Purpose Materials, tenth ed. USA.
- Benedyk, J.C., August 2010. International temper designation systems for wrought aluminium alloys: part II – thermally treated (T temper) alloys. *Light Metal Age* 16–22.
- Borvik, T., Hopperstad, O.S., Pedersen, K.O., 2010. Quasi-brittle fracture during structural impact of AA7075-T651 aluminium plates. *International Journal of Impact Engineering* 37 (5), 537–551. <http://dx.doi.org/10.1016/j.ijimpeng.2009.11.001>.
- Burkins, M.S., Hansen, J.S., Paige, J.I., Turner, P.C., 2000. ARL-MR-486, The Effect of Thermo-Mechanical Processing on the Ballistic Limit Velocity of Ti-6Al-4V ELI.
- Burkins, M.S., Love, W.W., Wood, J.R., 1997. ARL-MR-359, Effect of Annealing Temperature on the Ballistic Limit of Ti-6Al-4V ELI.
- Burkins, M.S., Wells, M., Fanning, J., Roopchand, B., 2001. ARL-MR-515, the Mechanical and Ballistic Properties of an Electron Beam Single Melt of Ti-6Al-4V Alloy Plate.
- Cheeseman, B., Gooch, W., Burkins, M.S., 2008. Ballistic evaluation of aluminium 2139-T8. In: Paper Presented at the International Symposium on Ballistics, New Orleans, LA.
- Chen, Y., et al., 2009. Stress-strain behaviour of aluminium alloys at a wide range of strain rates. *International Journal of Solids and Structures* 46, 3825–3835.
- Chin, E.S.C., Cappucci, M.R., Huie, R.M., Pasternak, R.E., 1989. MTL-TR-89-97 Evaluation of 2090-T8E48.
- Chinella, J.F., 2004. ARL-TR-3185: High Strength Al-Cu-Li and Al-Zn Alloys: Mechanical Properties and Statistical Analysis of Ballistic Performance. US Army Research Laboratory.
- Cho, K., et al., 2009. ARL-RP-236, Magnesium Technology and Manufacturing for Ultra Lightweight Armored Ground Vehicles.
- Crouch, I.G., 1987. Metallic Armour: from cast aluminium alloys to high strength steels. In: Paper Presented at the RMIT University Centenary Seminar on Inter-Material Competition, Melbourne, Australia.
- Crouch, I.G., 1992. Discing failures in both traditional and composite armour materials. In: Paper Presented at the International Symposium on Ballistics, Stockholm, Sweden.
- Crum, K.A., McMichael, J., Novak, M., February 2012. Advances in aluminum relative to ship survivability. In: Paper Presented at the American Society for Naval Engineers.
- Demir, T., Ubeyli, M., Yildirim, R.O., 2008. Investigation on the ballistic impact behavior of various alloys against 7.62 mm armor piercing projectile. *Materials and Design* 29, 2009–2016.
- Devletian, J.H., DeVincent, S.M., Gedeon, S.A., 1988. MTL-TR-88-47 Weldability of 2519-T87 Aluminium Alloy.
- Doherty, K., et al., 2012. Expanding the availability of lightweight aluminium alloy armor plate procured from detailed military specifications. In: Paper Presented at the 13th International Conference on Aluminium Alloys (ICAA13), June 2012, Pittsburgh, PA.
- Durson, T., Soutis, C., April 2014. Recent developments in advanced aircraft aluminium alloys. *Materials and Design* 56, 862–871.
- Edwards, D., 2014. Private Communication. DST Group, Australia.
- Fanning, J.C., 1999. Ballistic evaluation of TIMETAL 6-4 plate for protection against armor piercing projectiles. In: Paper Presented at the Titanium 99, Science and Technology, St. Petersburg, Russia.
- Ferraris, S., Volpone, L.M., 2005. Aluminium alloys in the third millenium shipbuilding: materials, technologies and perspectives. In: Paper Presented at the The 5th International Forum on Aluminium Ships, Tokyo.

- Flores-Johnson, E.A., Saleh, M., Edwards, L., 2011. Ballistic performance of multi-layered metallic plates impacted by a 7.62-mm APM2 projectile. *International Journal of Impact Engineering* 38 (12), 1022–1032.
- Forrestal, M.J., Borvik, T., Warren, T.L., 2010. Perforation of 7075-T651 aluminum armor plates with 7.62 mm APM2 bullets. *Experimental Mechanics* 50, 1245–1251.
- Fras, T., et al., December 2015. Thick AA7020-T651 plates under ballistic impact of fragment simulating projectiles. *International Journal of Impact Engineering* 86, 336–353.
- Gallardy, D., 2011. Ballistic evaluation of aluminium 7085-T7E01 and T7E02. In: Paper Presented at the International Symposium on Ballistics, Miami, FL.
- Gasqueres, C., Nussbaum, J., 2011. Ballistic performance and failure mode of high performance 2139-T8 and 7449-T6 aluminium alloys. In: Paper Presented at the International Symposium on Ballistics, Miami, FL.
- Gooch, W.A., 2012. Processing and fabrication technologies for current and potential titanium military applications. In: Paper Presented at the Titanium 2012, Atlanta, Georgia, USA.
- Gooch, W.A., Burkins, M., Squillacioti, R.J., 2007. Ballistic testing of commercial aluminium alloys and alternative processing techniques to increase the availability of aluminium armor. In: Paper Presented at the International Symposium on Ballistics, Tarragona, Spain.
- Grainger, L., March 2014. Novel metal powder production route for additive layer manufacturing via the metalysis process. In: Paper Presented at the Additive World Conference II, Eindhoven, Netherlands.
- Hammond, C., Nutting, J., October 1977. The physical metallurgy of superalloys and titanium alloys. *Metal Science* 474–490.
- Hatch, J.E. (Ed.), 1984. *Aluminum: Properties and Physical Metallurgy*. American Society for Metals.
- Higgins, R.A., 1968. *Engineering Metallurgy: Part I Applied Physical Metallurgy*, second ed. The English Universities Press Ltd, London.
- Holmen, J.K., et al., October 2015. Perforation of welded aluminium components: microstructure-based modelling and experimental validation. *International Journal of Impact Engineering* 84, 96–107.
- Holmes, T.M., et al., 1992. Evaluation of 8090 and Weldalite 049 Aluminium-Lithium Alloys. ARL report ADA258121, September 1992.
- Holt, W.H., et al., 1993. Reverse ballistic impact study of shear plug formation and displacement in Ti-6Al-4V alloy. *Journal of Applied Physics* 73 (8), 3733–3759.
- Hopperstad, O.S., Børvik, T., Fourmeau, M., Pedersen, K.O., Benallal, A., 2014. Quasi-static and dynamic fracture of high-strength aluminium alloy. *Procedia Materials Science* 3, 51–56.
- Jones, T., Delorne, R., Burkins, M., 2008. A comparison of the ballistic performance between rolled plate in AZ31B-H24 magnesium and 5083-H131 aluminium' paper presented at the 24th International Symposium on Ballistics.
- Jones, T., Kondoh, K., 2009. ARL-TR-4828, Initial Evaluation of Advanced Powder Metallurgy Magnesium Alloys for Armor Development.
- Jones, T., Placzankis, B., 2011. ARL-TR-5565, the Ballistic and Corrosion Evaluation of Magnesium Elektron E675 vs Baseline Magnesium Alloy AZ31B and Aluminium Alloy 5083 for Armor Applications.
- Kackley, M.C., Bethoney, W., 1986. Engineering and ballistic properties of a newly developed 2XXX series aluminum alloy armor. In: Paper Presented at the 9th International Symposium on Ballistics 29th May–1st April. Royal Military College of Science, Shrivenham, UK.

- Lewis, J.A., 1994. Titanium concepts in heavy vehicles. In: Paper Presented at the Workshop on Low Cost Titanium in Ground Vehicles. ARL.
- Liao, J., et al., 2009. Enhanced impact toughness of magnesium alloy by grain refinement. *Scripta Materialia* 61 (2), 208–211.
- Lloyd, D.J., 2004. Some aspects of the metallurgy of automotive Al alloys. *Materials Forum* 28, 107–119.
- Lumley, R.N. (Ed.), 2011. *Fundamentals of Aluminium Metallurgy*. Woodhead Publishing, Cambridge, UK.
- Ma, Z.Y., 2008. Friction stir welding technology — a review. *Metallurgical and Materials Transactions A* 39, 642.
- Mahoney, M.W., et al., 1998. Properties of friction stir welded 7075-T651 aluminium alloy. *Metallurgical and Materials Transactions A* 29, 1955.
- Manes, A., Serpellini, F., Pagani, M., Saponara, M., Giglio, M., 2014. Perforation and penetration of aluminium target plates by armour piercing bullets. *International Journal of Impact Engineering* 69, 39–54. <http://dx.doi.org/10.1016/j.ijimpeng.2014.02.010>.
- Mishra, R.S., Ma, Z.Y., 2005. Friction stir welding and processing. *Materials Science and Engineering: R: Reports* 50 (1–2), 1–78. Retrieved from: <http://www.sciencedirect.com/science/article/B6TXH-4GX0C6S-1/2/cd3adba839cb56524581ff3c074f3b45>.
- Montgomery, J.S., Wells, M., Roopchand, B., Ogilvy, J., 1997. Low-cost titanium armors for combat vehicles. *Journal of Materials* 49 (5), 45–47.
- Nickodemus, G.H., Kramer, L.S., Pickens, J.R., Burkins, M.S., February 2002. Aluminium alloys advances for ground vehicles. *Advanced Materials & Processes* 160.
- Nie, J.-F., 2012. Precipitation and hardening in magnesium alloys. *Metallurgical and Materials Transactions* 43, 3891.
- Ogorkiewicz, R., 2005. *Fundamentals of Armour Protection: Advances in Armoured Vehicle Survivability* 19th–22nd September. Cranfield University.
- Pedersen, K.O., Børvik, T., Hopperstad, O.S., 2011. Fracture mechanisms of aluminium alloy AA7075-T651 under various loading conditions. *Materials & Design* 32 (1), 97–107.
- Pekguleryuz, M.O., Kainer, K.U., Kaya, A.A., 2013. *Fundamentals of Magnesium Alloy Metallurgy*. Woodhead Publishing.
- Perez-Bergquist, S., Gray, G., Cerreta, E., Trujillo, C., Lopez, M., 2011. The Dynamic Constitutive Response of Three Aluminum Alloys: 5083, 7039, and 5059. Los Alamos National Laboratory. LA-UR-11-01302.
- Peters, M., et al., 2003. *Titanium and Titanium Alloys*. Wiley-VCH.
- Pickens, J., May 2004. Low cost titanium for ships and tanks. *Advanced Materials & Processes* 37.
- Polmear, I.J., 2006. *Light Alloys*, fourth ed. Butterworth-Heinemann.
- Ryan, S., Cimpoeu, S., 2015. An evaluation of the Forrestal Scaling Law for predicting the performance of targets perforated in Ductile Hole Formation. In: 3rd International Conference on Protective Structures (ICPS3), Newcastle, Australia.
- Sanders Jr., R.E., Hollinshead, P.A., Simiell, E.A., 2004. Industrial development of non-heat treatable aluminium alloys. In: Nie, J.F., Morton, A.J., Muddle, B.C. (Eds.), *Materials Forum*, vol. 28.
- Schlenker, B.R., 1970. *Introduction to Material Science*. John Wiley & Sons Australasia P/L, Sydney.
- Showalter, D.D., Placzankis, B.E., Burkins, M.S., 2008. Ballistic Performance Testing of Aluminum Alloy 5059-H131 and 5059-H136 for Armor Applications. ARL-TR-4427.
- Specification, 1992. Military Specification MIL-DTL-46063G Armor Plate, Aluminum Alloy 7039: AMSRL-WM-MA. US Army Research Laboratory.

- Specification, September 2006. MIL-DTL-46077G, Armor Plate, Titanium Alloy, Weldable.
- Specification, 2007. ASTM B 90/B 90M, Standard Specification for Magnesium Alloy Sheet and Plate.
- Specification, 2009. MIL-DTL-32333(MR), 2009, Armor Plate, Magnesium Alloy, AZ31B, Applique.
- Specification, 2012. MIL-DTL-32375(MR), December 2012, Armor Plate, Aluminium Alloy, 7085, Unweldable Applique.
- Sukumar, G., et al., April 2013. Ballistic impact behaviour of Beta-CEZ Ti alloy against 7.62 mm armour piercing projectiles. *International Journal of Impact Engineering* 54, 149–160.
- Tucker, M.T., et al., 2009. Anisotropic effects on the strain rate dependence of a wrought magnesium alloy. *Scripta Materialia* 60, 182–185.
- Van de Voorde, M.J., Diederan, A.M., Herlaar, K., 2005. Preliminary investigation of potential lightweight metallic armour plates. In: Paper Presented at the International Conference on Ballistics, Vancouver, Canada, November 2005.
- Van Horn, K.R., 1967. Aluminum Vol. I. Properties, Physical Metallurgy and Phase Diagrams. American Society for Metals, Metals Park, Ohio.
- Vega, F., 2014. Titanium additive manufacturing - a novel, game-changing technology. In: Paper Presented at the Titanium 2014, Chicago, IL, September 2014.
- Wasz, M.L., et al., 1996. Effect of oxygen and hydrogen on mechanical properties of commercial purity titanium. *International Materials Review* 41 (1), 1–12.
- Woodward, R.L., May 1979. Metallographic features associated with the penetration of titanium alloy targets. *Metallurgical and Materials Transactions A* 10A, 569–573.
- Zheng, C., et al., 2015. Failure mechanisms in ballistic performance of Ti-6Al-4V targets having equiaxed and lamellar microstructures. *International Journal of Impact Engineering* 85, 161–169.

Laminated materials and layered structures

4

I.G. Crouch

Armour Solutions Pty Ltd, Trentham, Victoria, Australia

4.1 General introduction

The most ballistically efficient armour materials and systems have a lamellar, laminated or layered structure. This is true whether it be through the use of anisotropy in specific metallic microstructures (see Chapters 2 and 3), through the use of individual plies of fibre-reinforced polymers (see Chapters 5 and 6), or through the development of a ceramic-composite armour system (see Chapter 7). Why is this? Is it simply because of the introduction of interfaces?

Just by having a layered structure does *not*, however, guarantee a beneficial outcome. Fig. 4.1(a) shows how the presence of a bible helped save the life of a WW1 digger, Lt. Elvas Jenkins (Aubusson, 2015). This was a remarkable event. However, having pondered the result I tried to reproduce it using a set of 'Yellow Pages'. After several attempts I managed to stop a 9 mm HG bullet, fired at full muzzle velocity, using not one but a pile of four, 27-mm thick 'Yellow Pages'. The stack had a bulk density of 550 kg/m^3 . So, with a DoP of $\sim 105 \text{ mm}$, the areal density works out to be $\sim 60 \text{ kg/m}^2$. This is more than 10 times the areal density of a typical soft armour insert (SAI); but why? Well, examining Fig. 4.1(b) more closely, one very important point emerged — the copper-jacketed round had not been deformed at all. Note: rule number one in the design of any armour system, of course, is to have the ability to change the shape of the penetrator, in some way or other (see Chapter 1). So, apart from

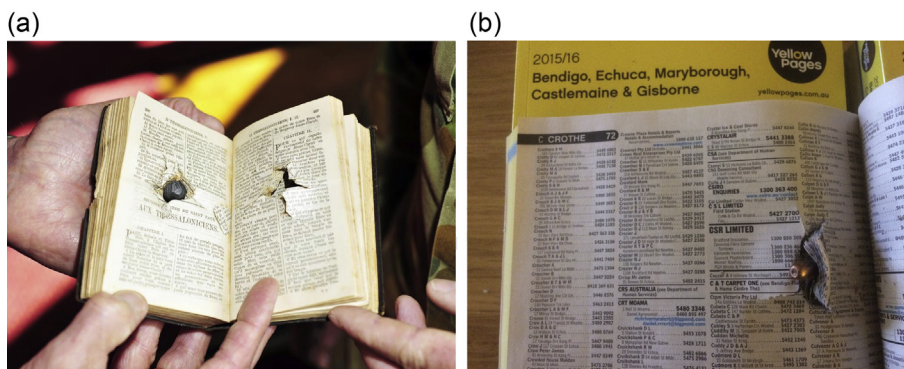


Figure 4.1 (a) 'Bible' armour from WW1 digger (www.images.defence.gov.au), and (b) a stack of 'Yellow Pages' armour.

discovering that a stack of laminated, telephone pages does *not* make a very good armour system, one serious point emerged: the digger should be extremely thankful that his bible was leather bound, for it was probably the leather cover that helped deform the lead-filled bullet and save his life.

4.1.1 Categories of laminated materials and layered structures

In 1986, I carried out my first review of armour materials (Crouch, 1986) — this work started my thinking on a number of composite materials for armour, including adhesively bonded aluminium laminates (see Section 4.4.2), metal-fibre-reinforced, squeeze-cast aluminium alloys, and fibre-reinforced polymers in general. Thirty years on, I can now see the bigger picture and appreciate the dominance of laminated materials.

At this point the reader should appreciate the extent of anisotropy within the world of materials and structures — anisotropy is extremely common — in fact, purely isotropic materials are quite rare. Most materials are, in fact, orthotropic, meaning that they have a different set of properties in the three orthogonal directions. The full range of lamellar, laminated materials and layered structures is listed in Table 4.1, which has been constructed to show the transition from wrought armour materials in the top example, through a whole series of laminated materials and layered systems, to a very complex, nonstructural, layered (spaced) system in the bottom example. Note how the numbers of materials (m) vary, as well as the number of layers (n). Pointing out the important characteristics and ballistic properties of all these categories of laminated or layered structures is the motivation behind writing this chapter.

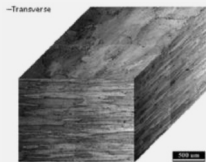
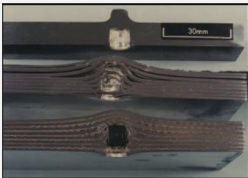
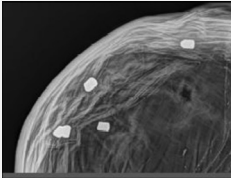
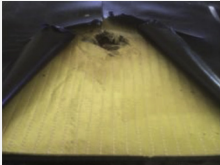
These groups of armour materials share many common features. However, apart from orthotropy, the one characteristic that defines all of them is their ability to delaminate, in one form or another. Whether the materials are continuous (as in the case of wrought solid metals), discontinuous materials (as in layers of soft fabrics), or simply separated by an interface (either a contact, spaced or bonded interface) the lamellar/laminated structure facilitates delamination (or further separation).

It is appreciated, at this stage, that classifying a heavily wrought homogeneous armour material like rolled homogeneous armour (RHA) (see Chapter 2) or a light alloy (see Chapter 3) might be stretching the analogy a little far as these materials, particularly RHA, do have a very strong resistance to delamination. However, as was described in Chapter 1, these materials do fail by delamination prior to discing failures. For example, Hamel carried out a parametric study of delamination in aluminium–lithium alloys and emphasised the influence that texturing has upon fracture toughness (Hamel, 2010) and the delamination process.

4.1.2 Design approaches, added value and creative thinking


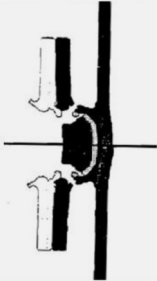
This is a transition chapter between Chapters 2 and 3, which described the conventional, traditional armour materials, and the more complex, ‘designer armours’ as covered in Chapters 5–7.

Table 4.1 A wide-ranging selection of laminated armour materials and systems, illustrating laminates with different numbers of layers, n , and different quantity of material types, m

Type of armour	Image	Detail
<p>1: Structural, homogeneous armour material/system with a lamellar structure</p> <p>$n = 1$ $m = 1$</p>		<p>Wrought, aluminium alloy 2099-T861, after Hamel (2010)</p> <p>Typical microstructure of rolled homogeneous armour, showing high degree of anisotropy</p>
<p>2: Structural, laminated armour materials (flat)</p> <p>$n = 2-10$ $m = 2-4$</p>		<p>Examples of adhesively bonded aluminium alloys, after Crouch (1986)</p> <p>Note the prevention of plugging in the laminates and the degree of delamination</p>
<p>3: Structural, laminated armour materials (curved)</p> <p>$n = 10-100$ $m = 2-4$</p>		<p>X-radiograph of a developmental combat helmet, constructed from multiple layers of Spectra SR3130, after Crouch (2013a)</p> <p>Note the ability to absorb numerous impacts from fragment simulating projectiles (FSPs) through delamination</p>
<p>4: Nonstructural, layered armour system</p> <p>$n = 20-40$ $m = 2-5$</p>		<p>Example of a soft armour insert showing multiple layers of aramid fabric, and a rear layer of foam, and a top and bottom layer of nylon fabric, after Crouch (2013b)</p>

Continued

Table 4.1 Continued

Type of armour	Image	Detail
5: Nonstructural, laminated armour system $n = 6-12$ $m = 6-12$		An example of a deconstructed hard armour plate consisting of hexagonal ceramic tiles, intermediate materials and aramid fabric, after Tencate
6: Complex spaced armour system consisting of: a nonstructural, laminated system; an air gap; a structural, homogeneous armour material/system $n = 10-20$ $m = 5-10$		<p>A numerical model of a complex armour system consisting of a ceramic armour appliqué system in front of a structural RHA armour, separated by an air gap; after Yaziv et al. (1996)</p> <p>Note how the damage from the ceramic system, caused by the impact of a high-velocity fragment, is impinging upon the front surface of the RHA rear plate</p>

The creation of a laminated material or layered system introduces added value. It provides choice for the armour engineer. It provides flexibility. Most of all, it opens up creative thinking — but in a focused way. The driver for an armour engineer is to defeat a threat whilst avoiding low-energy-absorbing failure mechanisms, as described in Chapter 1. In a purposeful manner, therefore, when designing a laminated armour the resultant performance should be better than that of the monolithic equivalent. However, there are many ways of achieving this goal, and this chapter is all about describing those different approaches.

The architecture of any laminate is engineered for a specific function and the functionality of each layer is not only related to its inherent properties but also to those of its nearest neighbours (adjacent layers). Consider the three categories listed in Table 4.2. A two-ply system has five principal variables; the types of material to be used, their thickness and the method of bonding them together. If they are not bonded, are they still classed as a laminate? In fact, when does a laminated material become a laminated structure?

A three-ply laminate introduces even more variables and a great deal more choice. If the third layer is considered to be an interlayer, a minor layer between the two principal layers, a number of other effects come into play based mainly around thin-film effects (see Section 4.2.2). If the interlayer material is fresh air, it transitions from

Table 4.2 Examples of laminated materials

Category	Schematic	Variables
Two-ply		<ul style="list-style-type: none"> • Material#1 • Material#2 • Thickness, t_1 • Thickness, t_2 • Bonding technique, if any
Three-ply		<ul style="list-style-type: none"> • Material#1 • Material#2 • Thickness, t_1 • Thickness, t_2 • Interlayer material • Interlayer thickness, x • Bonding technique, if any
Multi-ply		<ul style="list-style-type: none"> • Number of materials • Material#1,#2, etc • Thicknesses, t_1, t_2, etc • Number of plies per material • Orientation of plies • Ply sequence • Total thickness, T • Bonding technique, if any

being a laminated armour material into a spaced armour system. But, how wide should the space, x , be; the air gap between the two layers? (See [Section 4.2.6](#).)

Increasing the number of plies increases the complexity of the laminate. In fact, there are an infinite number of combinations and variables within a multi-ply laminate. In [Table 4.2](#), consider the multi-ply laminate to be a stack of aluminium alloy sheets, 1-mm thick (Material #1). If Material #2 is simply fresh air and the bond between the layers simply a contact surface, the laminate will have very little flexural strength (the bending of a pack of cards comes to mind). If, however, Material #2 is an adhesively bonded layer, the flexural properties will be governed by the interlaminar shear properties of the adhesive, which, in turn, will be affected by its thickness as well as its inherent set of mechanical properties. The family of adhesively bonded aluminium laminates (ABALs) is covered in [Sections 4.4.2 and 4.5.2](#).

As will be described in Chapter 7, bullet-proof glass traditionally consists of multi-ply laminates of glass, polycarbonate, as well as other interlayer materials, where n could be as high as 100. By way of example, the reader is directed to a paper by [Grujicic et al. \(2012\)](#), which provides design and material guidelines and strategies for transparent armour systems. It provides an excellent example of the adoption of a 'hierarchical ranking of influences' approach to designing multi-ply laminates ([Krell and Strassburger, 2008](#)).

As the number of material variables rise, in any multi-ply system, it is common to use numerical modelling to assist in investigating various effects. Chapter 9 provides a number of good examples of the penetration characteristics of laminated systems. [Yong et al. \(2010\)](#) also reported on the use of numerical computer codes to model and optimise the construction of hybrid, multilayered plates subject to ballistic impact.

4.2 Principles of laminates

There are many classical engineering textbooks that cover the mechanics of materials ([Jones, 1975](#); [Roylance, 1996](#)), and the design of composite materials and structures ([Barbero, 2010](#)), as well as standard publications, like [Nettles \(1994\)](#) from NASA. However, all of these treatments focus mainly upon the in-plane properties of relatively thin (2–10 mm) laminated structures, usually fibre-reinforced polymer composites for aerospace applications, where the benefits are well-recognised. For traditional engineering structures these are:

- Fracture toughness, through various orientation effects (see [Fig. 4.2](#));
- Fatigue behaviour, through crack arresting or splitting processes;
- Wear resistance, through modification of the subsurface;
- Corrosion resistance, through the application of hard coatings;
- Damping capacity, through the incorporation of low-modulus interlayers;
- Formability, through the use of multiple layers of thin material, rather than one thick-sectioned piece.

[Lesuer et al. \(1996\)](#) summarise these aspects extremely well in their review of metallic laminates. In this chapter, however, the same principles are applied to all

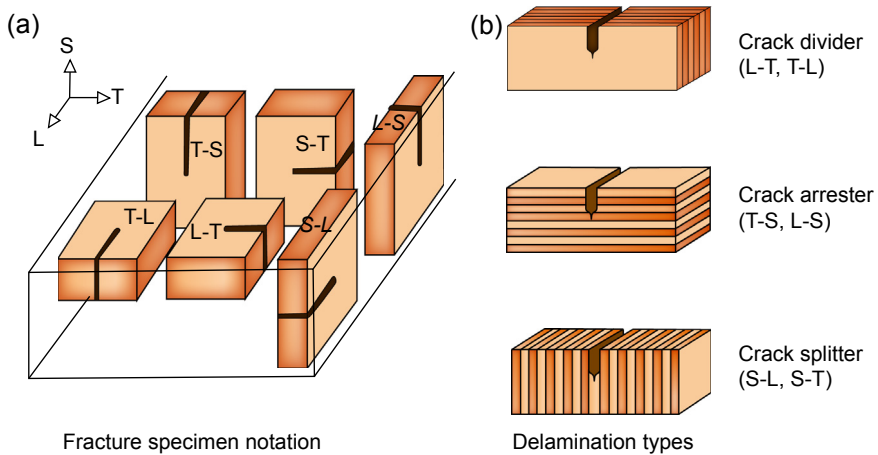


Figure 4.2 Notch orientations and delamination types associated with wrought and laminated materials.

laminates. Before considering these, it is essential to remind the reader of the nomenclature associated with laminated materials. Fig. 4.2 shows the classic way of describing the orientation of a notch or a crack relative to the rolling direction of a wrought product and/or the principal direction of a laminate. As was reported in Chapters 2 and 3, wrought products, which have a high degree of anisotropy, exhibit a much lower fracture toughness in the Short transverse - Longitudinal (S-L) and Short transverse - Transverse (S-T) orientation, this being the principal plane of delamination.

Fig. 4.2 also includes a definition of the three types of delamination:

1. Crack divider, in which the individual lamina fracture under plane stress conditions, rather than the whole laminate fracturing under plane strain conditions and, as a consequence, exhibit a much higher level of fracture toughness (see Fig. 4.3).
2. Crack arrestor, in which the principal crack is blunted or deflected at right angles through the presence of a layer at normal to its path. This is a very powerful means of retarding crack growth.
3. Crack splitter, which is the normal delamination mode. If one considers a bonded joint, for example, there is a plethora of data on peel strength or fracture toughness associated with this classical mode of delamination. However, this delamination mode is affected by the nature of the interlayer/interface and much can be gained by prudent material selection.

In Chapter 1, we learnt that the high-speed impact of a projectile, onto an armour material/system, produces a different set of loads and external forces compared to conventionally loaded composite structures. These dynamic impacts induce the following forces within the material/system:

1. Through-thickness compression;
2. Through-thickness shear (in the Transverse - Short transverse (T-S) and Longitudinal - Short transverse (L-S) orientation);
3. Three-dimensional (3D) bending of the target, creating membrane stretching (elastic and plastic).

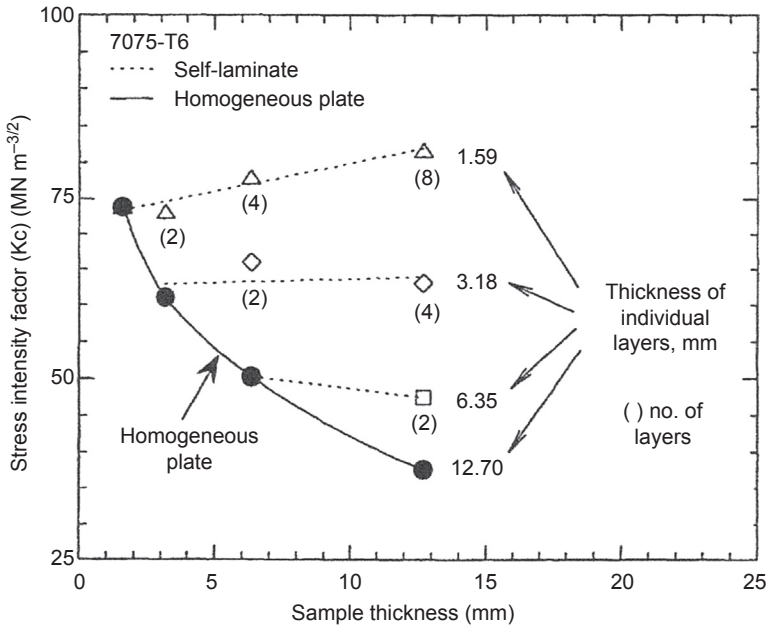


Figure 4.3 Fracture toughness of adhesively bonded layers of 7075-T6 as a function of sample thickness.

After Kaufman, J.G., September 1967. Fracture toughness of 7075-T6 and -T651 sheet, plate and multi-layered adhesive-bonded panels. *Journal of Basic Engineering* 503–507.

For a laminated material, as schematically shown in [Table 4.2](#), it is suggested that the through-thickness compressive strength can be treated using the standard rule of mixtures during elastic deformation and by the compressive flow properties of the lowest-strength component during plastic deformation. The through-thickness shear properties can be treated layer by layer. However, flexural properties need to be handled more astutely.

The maximum flexural stress, at the outer surface of a flexing beam, $\sigma_c = M \cdot c/I$, where M = the bending moment, c = distance from the neutral axis to the surface, and I = moment of inertia. For a rectangular beam, $I = w \cdot t^3/12$, where t = thickness of laminate or lamina, and w = width of the beam. In a laminated beam, however, a flexural load will produce interlaminar shear forces at the interfaces, or within the interlayer material, and these forces may dictate how the laminated beam fails. The salient point being that if the laminate, of total thickness, T , is not bonded at all, then the flexural properties of that laminate will be governed by the flexural properties of the individual lamina (of thickness t), since I is related to the third power of thickness. So, for example, in [Table 4.2](#), if the multiple laminate is a five-ply laminate where Material #1 is a metal sheet of thickness 1 mm, and Material #2 is a bonding medium of thickness 0.25 mm, then the total thickness will be 6 mm. If the bonding medium has a high interlaminar resistance, the moment of inertia of the laminate will be proportional

to $(6)^3$ up to the point of delamination, whereas with a very weak or nonexistent bonding medium, the moment of inertia of each ply will be proportional to $(1)^3$, about 1/200th of the bonded laminate. On the other hand, the section modulus of the bonded laminate will be 36 times greater than the unbonded laminate, since section modulus is proportional to t^2 .

Further consideration given by Woodward and Cimpoeru (1998) proposed a formula for the yield moment that accounts for the onset of plastic deformation in bending and is proportional to the thickness squared and number of layers, giving a ratio of 25 (for a 5-mm homogeneous plate) and 5 (for unbonded 1-mm plies). In other words, when subjected to plastic deformation, the homogeneous plate is five times stiffer than the laminate.

So, in both the elastic and plastic regimes, the existence and structural properties of the bond in a laminated panel is extremely important and will dictate how much energy the armour panel can absorb in flexure.

4.2.1 Layers and interfaces

For a given laminate, does the number of plies make a difference to how it might behave in a ballistic impact? Is a larger number of thin layers any different to a fewer number of thicker layers? In the previous section we learnt that the flexural properties of an unbonded laminate are substantially less than its monolithic equivalent. So, clearly, as far as energy absorption is concerned in an unbonded or weakly bonded laminate, a fewer number of thicker plies is beneficial. However, the opposite is true for the fracture toughness of bonded laminates, as seen in Fig. 4.3. In soft armours, as described in Chapter 6, a larger number of thinner plies is more effective against small-arms ammunition, although a fewer number of plies are preferred from a manufacturing point of view.

In laminates of two materials or more, the order in which those materials are laid-up is also important. Dual-hardness armours were briefly discussed in Chapter 2 and the concept of having a harder front layer is not new — it was, perhaps, the first design principle to be regularly adopted for laminated armours. Recently, however, some researchers have questioned this general principle, pointing out that it might be an advantage in some circumstances to have the softer layer in front. van de Voorde, Herlaar, and Broos (2007), for example, have pointed out that stripping of the jacket from a bullet may be advantageous in modifying the mode of penetration in some circumstances.

Having a multilayered armour is sometimes unavoidable. For example, most ceramics cannot be manufactured in thicknesses greater than 20–25 mm, without accepting a significant decrease in properties. So, when designing medium/heavy armour systems, multiple layers are required. Therefore, on occasions, there is a need to consider the interface between thick, rigid layers. Should these interfaces be simple contact of ground surfaces, or adhesively bonded layers or even brazed joints?

The existence of any dissimilar joint between materials, whether it is within a simple dual-hardness laminate or an interlayer between two adherends of similar materials, introduces a possible mismatch of physical and mechanical properties. Amongst the most significant are differences in coefficients of thermal expansion,

ductility and elastic moduli. Whilst the latter two properties are usually part of the decision-making design process, differences in thermal properties are often forgotten, even though typical service temperatures for most armour systems only range from -40°C to $+60^{\circ}\text{C}$. Thermal mismatch can lead to cyclical shear stresses developing at the interface.

In a recent study by Oberg et al. (2015), a series of small-scale experiments were performed to determine whether the fracture toughness of the bondline between a thin alumina tile (2 mm thick) and a carbon composite material (only 0.8 mm thick) affected the amount of energy being absorbed from a 50-J impact. The impactor was a hardened steel sphere, 8 mm in diameter and the impact velocities were ~ 220 m/s. They demonstrated that a bonded laminate, with a measured bondline toughness of ~ 620 J/m² absorbed more energy than a laminate with a measured bondline toughness of ~ 170 J/m², as one would expect. However, what they also calculated was, of all the energy-absorbing processes involved, the debonding process only absorbed ~ 5 J ($\sim 10\%$ of the impact energy). Fig. 4.4 shows very neatly the amount of energies being absorbed by the various defeat mechanisms — more calculations of this nature need to be carried out by other researchers — it keeps the line of research into perspective and enables researchers to focus their efforts upon the most important energy-absorbing processes.

4.2.2 Characteristics of interlayers

Consider a bonded three-ply laminate as shown in Table 4.2, where the adherends are relatively thick metal sheets. Adhesives work best not in tension but when placed in

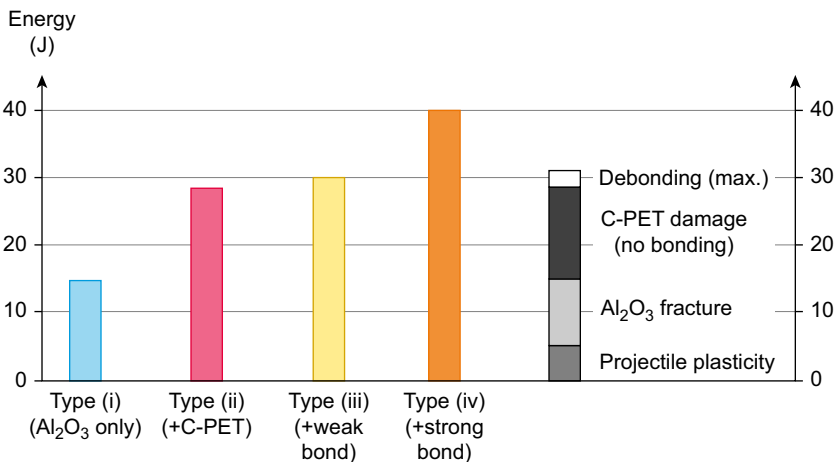


Figure 4.4 Schematic representation of the energies absorbed by four different targets (types i to iv). The right-hand bar illustrates the division of energy-absorption, by mechanism.

After Oberg, E.K., Dean, J., Clyne, T.W., 2015. Effect of inter-layer toughness in ballistic protection systems on absorption of projectile energy. *International Journal of Impact Engineering* 76, 75–82.

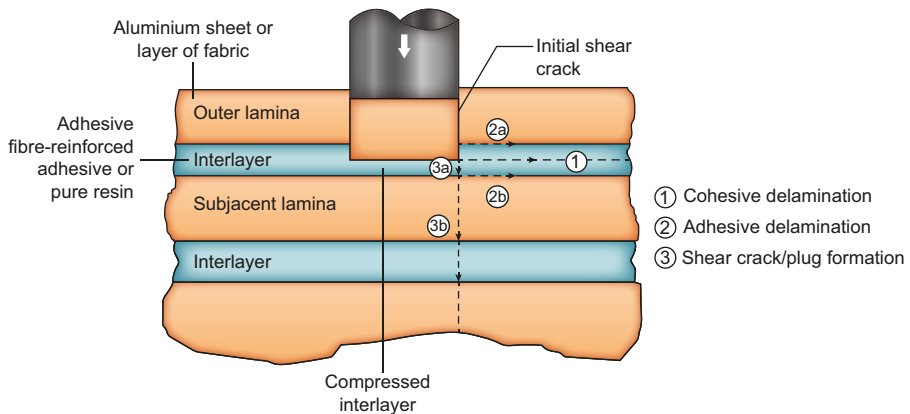


Figure 4.5 Schematic of alternative crack propagation paths in crack arrestor mode.

After Crouch, I.G., Greaves, L.J., Simmons, M.J., 1990. Compression failure in composite armour materials. Paper Presented at the 12th International Symposium on Ballistics, San Antonio, Texas, USA, October 1990.

shear as in a flexing plate. However, the physical nature of this interlayer material is important, especially its thickness and elastic modulus. The plasticity of an interlayer material and its crack tolerance also play a strong controlling role over the mode of delamination. Consider the alternative pathways for the through-thickness crack shown in Fig. 4.5. Path 1 is the preferred pathway, not only because it exercises the crack arrestor principle, but also because it creates cohesive delamination (ie, it occurs within the interlayer material). If this is typically a tough epoxy resin or a thin layer of ductile material, considerable energy can be absorbed during the internal fracturing of the interlayer material. Pathways 2a and 2b are least preferred because these represent failure at the adhesive/adherend interface and are invariably of low toughness (eg, due to poor preparation of the adherend's surface). In this impact scenario, pathway 3 is the least desirable — more about that in Section 4.3.2.

Cohesive delamination (ie, pathway 1 in Fig. 4.5) is also affected by plastic constraint. That is, the plastic zone ahead of the propagating crack can be limited in size because of the finite thickness of the interlayer (see Fig. 4.6). The thickness of the interlayer will have a strong influence over the crack propagation resistance of the joint and the overall performance of the laminate. From the work of Kruzic et al. (2004) the toughness of pure aluminium joints between alumina adherends increased by an order of magnitude when the interlayer thickness was increased from 5 to 100 μm . In adhesive joints, there is an optimal value for interlayer thickness of between 0.3 and 0.5 mm (Lees, 1988; Lopez-Puenta et al., 2005).

For ductile interlayers, one can observe a classical 'thin-film effect'. This was even measurable during through-thickness tensile testing performed on welded joints between thick plates of armour steel and an aluminium armour alloy (Crouch, 1981). The transition insert was an explosively welded joint between a low carbon steel and aluminium alloy 3003 having a yield strength of about 100 MPa. However,

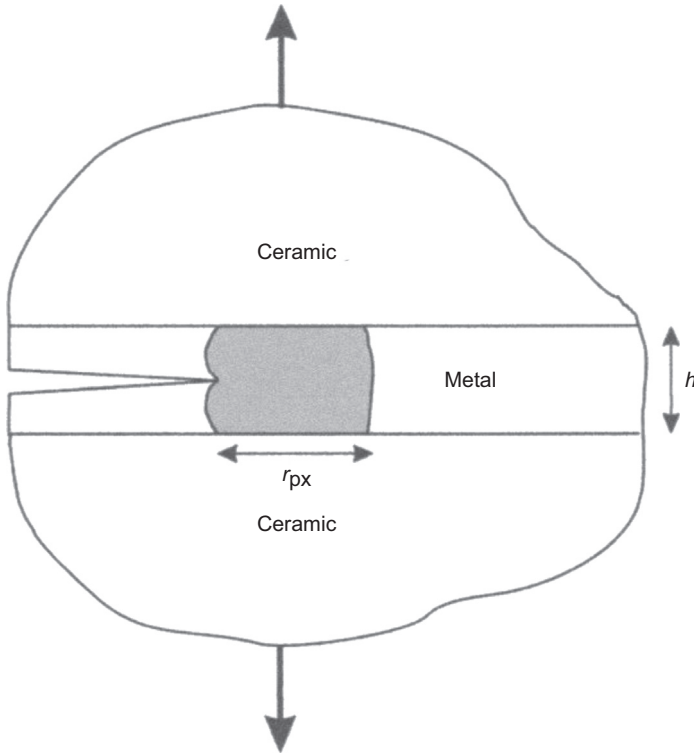


Figure 4.6 Schematic illustrating constraint of the plastic zone ahead of the crack tip which extends through the thickness of the metal layer bonded between two ceramic adherends. After Kruzic, J.J., McNaney, J.M., Cannon, R.M., Ritchie, R.O., 2004. Effects of plastic constraint on the cyclic and static fatigue behavior of metal/ceramic layered structures. *Mechanics of Materials* 36, 57–72.

what Crouch found was by reducing the thickness of the 3003 layer, which was effectively a weak interlayer within the joint, the in-plane tensile yield strength of the welded joint increased by a factor of two to three. The low-yielding material had been constrained from plastically deforming. This last example also illustrates another important point: boundary effects, such as size dependencies and difficulties in achieving uniform stress or strain fields, are more challenging in laminated materials than in monolithics — invariably mechanical property data are test size, or test method, specific.

The final example in this section refers to a classical armour-grade laminate between a ceramic supported by a composite material (see [Section 4.5.3](#) for more details). With reference to [Fig. 4.6](#), imagine the lower material as a composite material and the top layer as a ceramic. [Tasdemirci et al. \(2012\)](#) investigated the effects of widely different interlayer materials on the ballistic performance of such complex laminates. They considered three different material families, rubber, Teflon and an aluminium foam, and found that the presence of an interlayer altered the stress transmission between

the layers, as one would expect. They also discovered that the type of interlayer material affected the degree of delamination in the supporting composite and the breadth of the damage zone. Taking areal density into account, the Teflon interlayer, with a bulk density of only 760 kg/m^3 , and a thickness of 2 mm, worked most effectively. Chapter 9 contains a number of illustrative examples of the ballistic performance of different interlayer materials, including metal foams.

4.2.3 Surface effects and coatings

In this section, we need to consider the limitations and nature of the front material in a two-ply laminate. With reference to [Table 4.2](#), how thick does Material #1 need to be in order to make an effective strike face material? There are many traditional methods for improving the surface hardness or wear resistance of a metal: nitriding, carburising, hard-chrome plating, for example. However, whilst these methods work very favourably at increasing the hardness of the surface, either by enhancing the residual compressive stress within the surface or applying a thin hard facing material, neither method improves the ballistic performance of the base material. Why — because the surface coatings are just that — thin coatings. As was discussed in Chapter 1, the penetration resistance of an armour material is governed by through-thickness *bulk* properties and/or by the flexural behaviour of the armour panel. But what thickness is required? This depends upon the nature of the penetrator. It would appear from the work of [Ozsahin and Tolun \(2010\)](#) that the ballistic performance of high-strength aluminium alloys like 2024 and 6061 can be improved by applying a plasma coat only 0.76 mm thick when the threat is a 9-mm, lead-filled, handgun round. However, they did not report how ballistically efficient the coated system was compared with an uncoated plate of similar areal density. More recently, [Crouch, Appleby-Thomas, and Hazell \(2015\)](#) have shown that a minimum thickness of 3 mm is required for a boron carbide strike face to be effective against mild-steel-cored ammunition. For armour-piercing rounds, the minimum required thickness, to be ballistically efficient, would be even more.

There is a role, however, for thin coatings, less than 1 mm thick. Brittle materials, like ceramics and ultrahigh-hardness steels (UHHS) have exceptional compressive properties, which make them very attractive ballistic materials, but they do have a very low strain-to-failure in tension, and extremely low levels of fracture toughness: normally less than $5 \text{ MPa m}^{1/2}$. So, when flexing a brittle material and placing the underside in tension, the physical condition of the rear surface becomes very important: surface asperities, from grinding marks for example, can act as stress raisers and promote premature cracking. The importance of this will be realised when reading Chapter 7. The point being that the notch-sensitivity of a brittle material can be improved by applying a layer of adhesive to the distal face of a brittle target material. [Jaitlee \(2013\)](#) demonstrated this very recently with silicon carbide tiles and the DMTC have recently applied the same principles to UHHS. In the past, Crouch has detected differences in ballistic performance of high-hardness steels when impacting steel plates, which had only been ground on one side. In these cases, if the ground surface was put to the rear, the ballistic limit was reduced.

4.2.4 Disrupter-absorber principles

Some armour technologists have proposed two main categories for armour materials and systems (see Table 4.3), thus describing the constitution of a two-layered system.

1. Disrupters, which are placed on the impact side, are those materials or systems that disrupt the penetrator by some mechanism or another. For high-hardness, brittle materials, like the ultrahigh-hardness steels and ceramics, these disrupt the penetrator through plastic deformation, erosion or by initiating shatter. For glasses, it is often through comprehensive fracture and comminution. For armour systems, as described in Chapter 1, these work in various ways but largely by deflection of the penetrator.
2. Absorbers, which are placed on the distal side, as the name implies, absorb the residual energy of the penetrator after it has been disrupted. For materials, these are normally characterised by high ductility and an ability to absorb energy in flexure.

Whilst very top level, this classification does illustrate some classical disrupter/absorber combinations: UHHS and RHA as in dual-hardness armour (see Chapter 2); ceramics and fibre-reinforced plastics, as described in Chapters 5–7; and glasses and polymers, as in laminated, bullet-proof glass (see Chapter 7). All of the system disrupters are designed to work in front of the structural armours, like RHA and the aluminium armour alloys, as appliqué systems or as integrated, complex systems. The various system disrupters are briefly described in Chapter 1.

4.2.5 The air gap

Consider the three-ply laminate in Table 4.2 in which the interlayer material is fresh air. The interlayer thickness becomes an air gap with zero shear strength and the laminated armour material becomes a layered or spaced armour system. Layered, if it is in close contact with negligible air gap; spaced, if there is a significant air gap and one that has been ‘designed-in’.

Table 4.3 Top-level classification of armour materials and systems

	Disrupters	Absorbers
Materials	High-hardness steels Ultrahigh-hardness steels Ceramics Glasses Hard coatings (sometimes)	Low-carbon steels RHA Light alloys (Al, Ti and Mg) Metal laminates Fibre-reinforced plastics Polymers
Systems	Explosive reactive armours Non-explosive reactive armours Electric armour Bar armour Oblique plates Spaced plates	Structural armours, like RHA and weldable aluminium alloys

Why do this? What are the benefits of introducing an air gap, since clearly the armour is no longer structural? Perhaps the general answer is to allow Material #1, the disruptor, to maximise its ability to absorb energy without putting any dynamic or engineering loads on the absorber, Material #2. In absorbing impact energy, the strike face material may respond by forming a large bulge on its rear side – if this is the case, the gap should be large enough to accommodate this protrusion, without impinging on the front face of the absorber. If the gap is wide enough, and the angle of attack is oblique, then having a gap may allow the penetrator, exiting the front plate, to yaw and thereby strike the rear plate at an even more oblique angle. The case study described in Section 5.5.4.1 is an excellent example of this beneficial effect.

In 1996, one of Mike Iremonger's research students at RMCS, Shrivenham (Velentzas, 1996), carried out a neat, and informative, set of impact experiments on simple monolithic and spaced systems against small-arms ammunition. They used a set of five, 2-mm thick mild steel plates, and compared their performance to that of a monolithic 10-mm thick mild steel plate by varying the air gap between the plates. Their results are reproduced in Fig. 4.7 and show how effective larger spacings are at reducing the residual velocities of both the AK47 and SS109 rounds, fired at their respective muzzle velocities of 740 m/s and 915 m/s. From left to right, the results show the effect of increasing the air gap from zero, through 2 to 10 mm, and then onwards, through various combinations. It is clear that having a 10-mm gap between each plate significantly increased the target's penetration resistance.

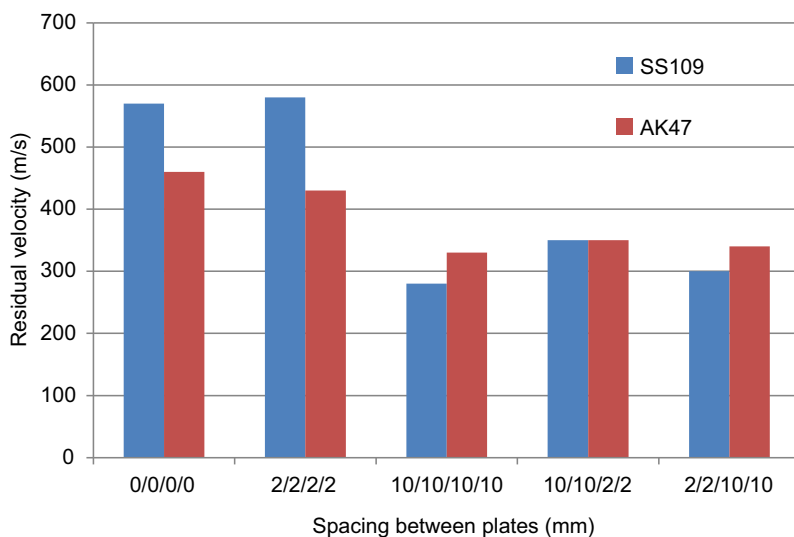


Figure 4.7 The effect of increasing the air gap between a set of five 2-mm thick mild steel plates on the residual velocity of small-arms ammunition.

After Velentzas, G.C., 1996. Spaced Armour Systems. 24 MVT M.Sc. Project Report, Royal Military College of Science, Shrivenham (Mike Iremonger, Supervisor).

This was reported to be due to increase yaw in the rounds, as they passed through each layer.

This example does bring to light two main disadvantages of using a spaced armour system: first, a reduction in space efficiency, because the system is now 50 mm thick rather than just 10 mm; second, a reduction in mass efficiency, since spaced plates need to be engineered onto a platform through the use of fixings and fixtures, all of which are parasitic in weight.

Whilst this might not be a real concern for lightweight systems, it certainly is for the heavier armour systems.

Finally, more details about the complex, spaced armour system shown in [Table 4.1](#), consisting of an alumina/aluminium appliqué armour system attached to, and spaced from, a plate of high-hardness steel armour ([Yaziv et al., 1996](#)). The system was impacted with a standard 20 mm FSP round travelling at 920–950 m/s. Both experimental and numerical experiments were carried out, by varying the air gap between the two elements (5, 15 or 25 mm) — a numerical simulation is reproduced in [Fig. 4.8](#), for different time steps between 30 and 150 μ s. The conclusion was very informative: there is an optimal value of air gap for the most effective penetration resistance. When the gap is small, or nonexistent, the aluminium backing layer is constrained in its ability to deform before it fails in plugging. When the gap is too large, the bulge at the rear of the aluminium plate perforates through ductile hole formation and results in a number of ductile petals. When the space is optimised, in this case at 15 mm, a bulge forms but without forming the petals — it simply gets compressed against the HHS rear plate — it was argued that the round will then have to deform more of the aluminium backing layer, thereby absorbing more impact energy (see [Fig. 4.8](#)). This sounds feasible. However, they forgot to mention that because of this confined deformation of the bulge, considerable force is placed on the HHS rear plate, necessitating heavier engineering solutions in order to develop a practical armour system.

4.3 Objectives in designing laminated armours

It would appear that many scientists have researched laminated or layered armours but seemingly without the appropriate motives — not quite ‘research for research sake’ but close on occasions, because it sounds, to the researcher, as though having a laminated armour should be fruitful! In fact, in a recent review of multilayered metal shields, [Ben Dor et al. \(2012\)](#), after cataloguing most published research on this topic since the late 1980s, only concluded that there are no clear trends and the ballistic performance of layered structures is difficult to predict. In some ways, this is a consequence of the infinite number of variables, as mentioned previously. However, very few published works report the response of real-world, laminated/layered targets to real threats, especially small-arms ammunition.

In the author’s view, the sole motive for designing a laminated, or layered, armour should be to overcome or prevent a failure mechanism or to enhance a well-recognised energy-absorbing mechanism. This is front, and central, to understanding the science of armour materials: designing an armour material or armour system to prevent a particular

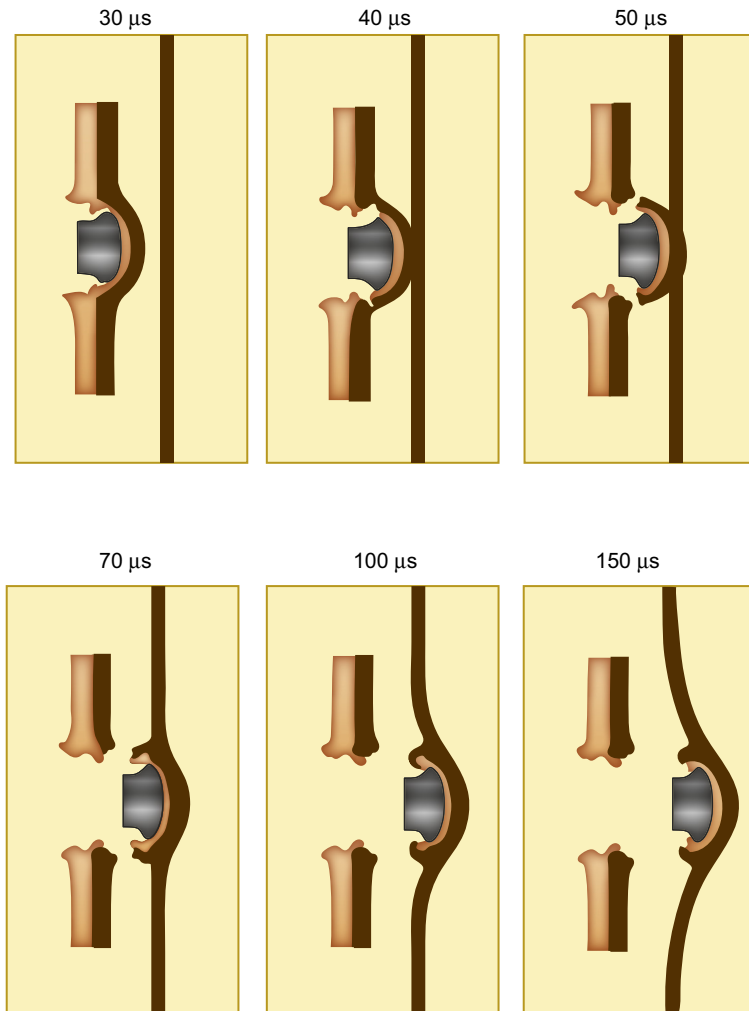


Figure 4.8 Numerical simulations, using the MSC/PISCES/2DELK hydrocode, of an alumina/aluminium appliqué armour in front of an HHS armour.

After Yaziv, D., Reifen, Y., Kivity, Y., 1996. Spacing effect on the performance of ceramic targets. Paper Presented at the 16th International Symposium on Ballistics, San Francisco, September 1996.

failure mechanism. The only palatable, alternative motive might be to reduce cost. At this point, the reader should familiarise themselves with the various penetration failure mechanisms described in great detail in Chapter 1, and be very mindful of the effect of nose shape (Gupta et al., 2008), since nose shape affects how the armour fails and therefore dictates what set of energy-absorbing mechanisms become operative. The nature of the threat can range from a single, intense point load (as in a knife or bullet) to an external blast event or internal stress wave scenario.

4.3.1 Managing stress waves

To my knowledge, [James \(1995\)](#) reported one of the earliest applications of stress wave management techniques to ceramic-composite armour systems. James pointed out that, by controlling acoustic impedance mismatching effects, the degree of collateral damage could be minimised and, therefore, multihit resistance could be improved. In essence this meant modifying the acoustic properties of the adhesive/sealant used in mosaic ceramic tile arrangements (see [Fig. 7.1](#)).

This effect was also recognised in the work of [Yadav and Ravichandran \(2003\)](#), who attributed the presence of polyurethane interlayers to the improved ballistic performance of laminated aluminium nitride ceramic tiles. Their results indicate that the wave propagation speed in the interlayer material can either be between its components or lower than both components, for best effects.

The application of elastomeric coatings to high-hardness steels has reportedly been beneficial in increasing V-50 values against fragmentation attack. In an elegant paper by [Roland et al. \(2010\)](#), they demonstrated that rubbers undergo an impact-induced transition to a glassy phase and, more importantly, that multiple bilayers were most effective. This was believed to be attributed to the break-up and attenuation of compressive waves by impedance mismatching within the laminated layers.

4.3.2 Preventing plugging

Plugging of monolithic armour materials is the least energy-absorbing mechanism of all. Preventing, or suppressing, its occurrence can bring immediate benefits in terms of ballistic penetration resistance. The crack arrestor principle is applied to greatest effect (see [Fig. 4.2](#)). This was the motivation behind the development, between 1984 and 1994, of the family of adhesively bonded aluminium laminates (ABALs) ([Crouch, 1986, 1988, 1993](#); [Crouch and Woodward, 1989](#); [Crouch et al., 1990, 1994](#); [Woodward and Crouch, 1989](#); [Woodward et al., 1991](#)). The change in set of failure mechanisms is clear from the images in [Fig. 4.9](#). However, its success, as a ballistic lamination, was not just about lamination (see [Sections 4.4.2 and 4.5.2](#) for detailed accounts).

One other simple way of avoiding plugging failure of the entire system is to adopt a simple, spaced, two-plate array, with a well-defined air gap. Simply having an air gap prevents the transverse shear crack from propagating all the way through the system. Instead, the rear plate undergoes a series of higher-order energy-absorbing mechanisms like plastic deformation and membrane stretching. However, the spacing is important in relation to the length of the projectile. In work by [Dey et al. \(2007\)](#), the performance of two 6-mm Weldox 700E plates, spaced off by 24 mm, performed a lot better than a single 12-mm plate of the same steel (see [Fig. 4.10](#)). The penetrator was a 200-g, 20-mm diameter, hardened steel projectile, 80–100 mm in length. It should be noted that this is longer than the air gap, so the projectile will not have had the opportunity to yaw. The benefit seen in [Fig. 4.10](#) would appear to arise because, even though a disc (small plug) of material was ejected from *both* layers,

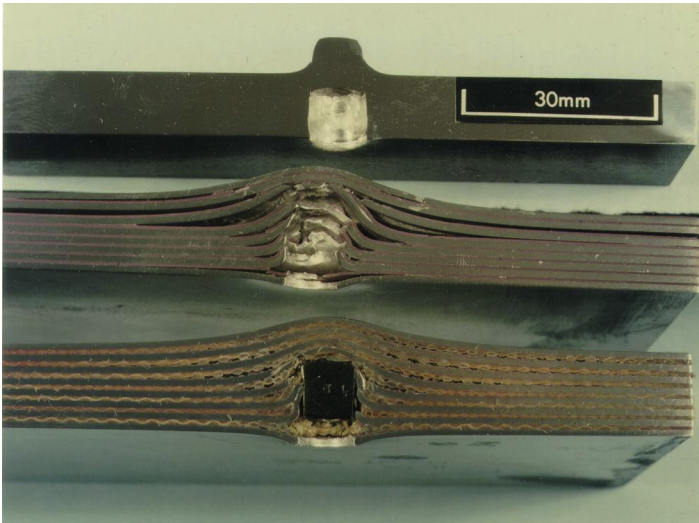


Figure 4.9 Examples of adhesively bonded aluminium laminates and a monolithic aluminium alloy impacted by a high-velocity fragmentation simulator projectile.
Crouch, I.G., 1986. A Review of Metallic Composite Materials for Armour. UK Government Internal Report, RARDE, Chertsey.

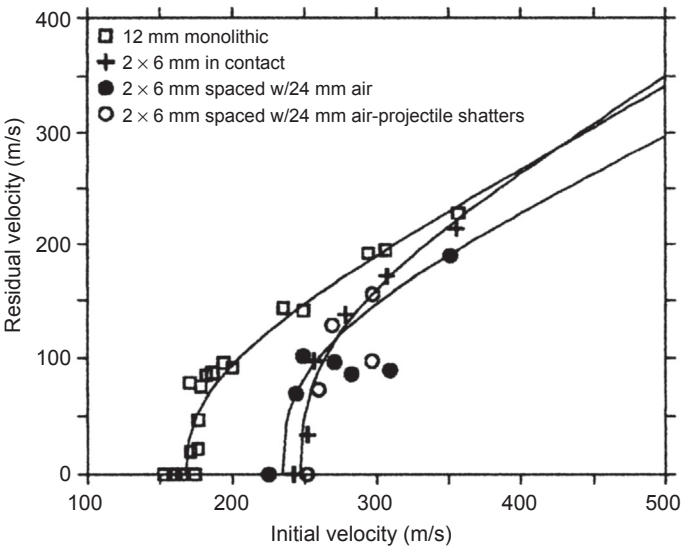


Figure 4.10 Residual velocity curves for different double-layered steel targets.
Dey, S., et al., 2007. On the ballistic resistance of double-layered steel plates: an experimental and numerical investigation. International Journal of Solids and Structures 44 (20), 6701–6723.

the impact on the second layer will have been much less intense, equivalent to the impact from a slightly hemispherical nose, making the shearing process more difficult. The Worked Example #1, in Chapter 9 gives an excellent description of the penetration of double-layered steel targets without an air gap.

4.3.3 Preventing discing

Discing failures are the Achilles heel of the family of armour-grade, light alloys, as covered in Chapter 3 and result in a reduction in the ballistic resistance of an armour material. Suppressing, or designing-out, discing failures should, therefore, reap due rewards, especially with heavily wrought materials possessing a strong degree of orthotropy.

Perhaps the most direct approach is to physically attach a second layer to the rear of the light-alloy plate. This approach was suggested by [Van de Voorde et al. \(2005\)](#) when recognising the discing weakness in thick sections of both magnesium and titanium alloys. They reported that a bimetallic laminate of a titanium alloy, backed by a plate of 7039 aluminium armour, worked very effectively when attacked with a 0.3" APM2 round.

However, lamination is not always the solution. During development of the family of ABALs, Crouch and others ([Woodward et al., 1991](#)) discovered that adhesively bonded laminates of Al–Li alloy sheets were also prone to discing, aptly demonstrating the requirement for a sufficiently ductile backing layer, thus maximising the work of membrane stretching, without premature failure. [Fig. 4.11](#) illustrates this point and [Crouch \(1992\)](#) provides both an explanation and a list of essential properties of a disc-free armour material/system.

4.3.4 Providing support for a brittle material

Brittle materials, like UHHS and ceramics, have excellent compressive properties but lack ductility in tension. They are very notch-sensitive materials and, when placed in bending, will fail prematurely. As will be learnt in Chapter 7, in order to maximise the effectiveness of having a hard strike face material, it needs to remain rigid for as long as possible. This can be exercised by having a supporting material placed behind the ceramic, as discussed earlier. Ceramics and glasses can *only* function, as an armour material, if they *are* supported. A two-ply laminate is therefore essential. The challenge is to provide maximum support to the strike face material by using a backing material that has a high modulus like steel (where $E = 208$ GPa) with the density of a polymer (where $\rho < 1$, preferably), whilst at the same time creating a sound metallurgical bond between the two elements (strike face and backing). This places great emphasis on the chosen bonding medium and the bondline thickness, already discussed in [Section 4.2.2](#) (see also [Lopez-Puerta et al., 2005](#)).

Placing an additional layer in front of the ceramic can also influence the ballistic performance of brittle materials. This is discussed more in Chapter 7 but, in brief, this is either through the use of a cladding layer ([Crouch, 2010, 2014](#)), or a buffer layer which might prestrip the jacket from small-arms ammunition ([Crouch et al., 2015](#)).

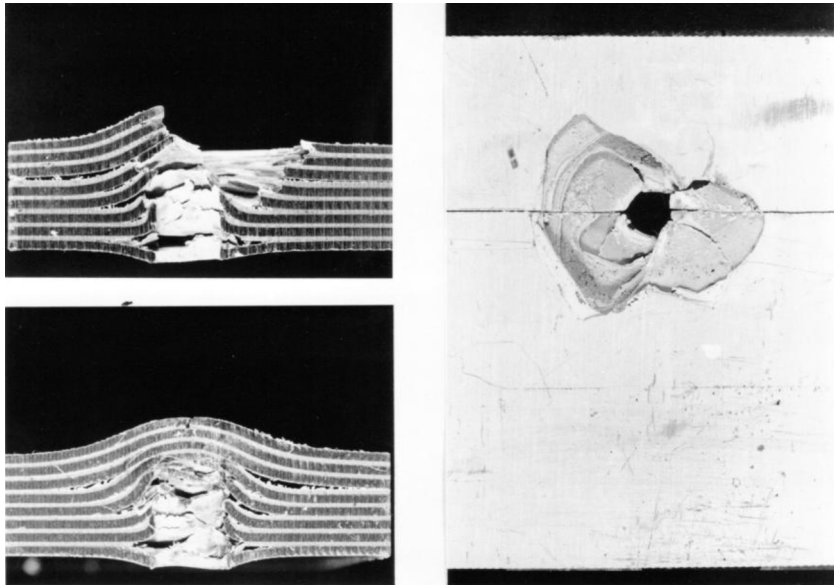


Figure 4.11 Left, sections through an eight-ply 8090 ABAL showing impacts just below and above the measured V-50 value and right, rear-face showing discing in rear laminae. Woodward, R.L., Tracey, S.R., Crouch, I.G., October 1991. The response of homogeneous and laminated metallic sheet material to ballistic impact. *Journal de Physique IV, Colloque C3*, 277–282.

With a well-designed cladding layer (eg, a 0.5-mm thick layer of aramid-fibre-reinforced epoxy) the multihit resistance of a ceramic-based armour system can be improved by minimising the crack opening displacement of radial cracks.

4.4 Research into laminated armours

4.4.1 Laminated steels

Laible (1980) covers the early development of dual-hardness, steel-based armours during the 1960s and 1970s, and Rosenberg and Dekel (2012), in their textbook on terminal ballistics, certainly extends this field to examples of layered and spaced armour systems. However, most of these latter studies have been against short and long rod penetrators. Very little work has actually been carried out and/or published against small-arms ammunition.

The design and performance of Japanese swords is legendary amongst both steel-makers and historians, and multiple layers of finely worked steel laminae have been crafted into very elegant and effective weapons, like the Damascus steel dagger (Lesuer et al., 1996), well before material scientists were able to measure physical and mechanical attributes like fracture toughness. Steels do have a number of natural benefits for manufacturing dual-hardness armours: (1) they have an ability to be

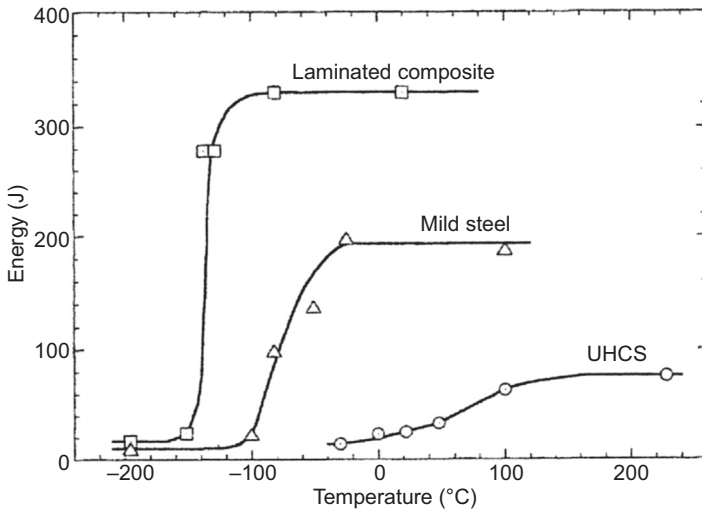


Figure 4.12 CVI and DBTT data for a 12-ply mild steel/ultrahigh carbon steel laminate, in the crack arrestor orientation.

Kum, D.W., Oyama, T., Wadsworth, J., Sherby, O.D., 1983. *Journal of Mechanics and Physics of Solids* 31, 173–186.

hardened to ~ 750 VHN, necessary to be an effective strike face material, and (2) they can be metallurgically bonded to themselves and create a near-perfect metallurgical bond with properties very similar to the base materials. In 1983, Kum et al. published some classical results for 12-ply mild steel/carbon steel laminates (Kum et al., 1983). One can see from Fig. 4.12, that synergistic improvements can be achieved in both Charpy V-notch impact (CVI) values and the ductile–brittle transition temperature (DBTT), in such laminates. CVI values in excess of 100 J are unheard of in typical armour steels of today.

Steels are also amenable to explosive welding and roll bonding and have been favoured approaches to produce experimental quantities of dual-hardness armours. There is even a US specification to facilitate purchase of such product, MIL-A-46099C, issued in 1987. Section 2.4.3 in Chapter 2 details this family of laminated armour materials. Work by Rolc et al. (1996) suggested that interfacial bond strengths were a key mechanism contributing to penetration resistance, eg, in roll-bonded laminates between tool steels (Hv ~ 750) and medium strength steels (Hv ~ 475). Measured bond strengths varied from 170 to 640 MPa. Explosively welded dual-hardness steels have also been considered for blast-resistant applications (Choi et al., 2014). It should be noted that explosive welding, as a method of producing dual-hardness armours, is a batch process and demands high-quality control practices to guarantee reproducibility. Roll-bonding is the most common production method, and is still being pursued as an effective method of producing Dual Hardness Armour (DHA), as indicated in recent patent action (Stefansson et al., 2012). It also enables multiple laminae to be used, rather than just creating a bimetallic laminate.

4.4.2 Laminated light alloys

Of all the material developments that have occurred over the past few decades, none, in my opinion, compare in success and influence with the creation, evolution and delivery of a family of bonded laminates often referred to as fibre metal laminates (FMLs). They consist of a small number of thin sheets (~ 0.3 mm thick) of a high-strength aluminium alloy, like 7075, bonded together with a fibre-reinforced polymeric inter-layer, also ~ 0.3 mm thick. The finished laminates are only 1–3 mm in thickness but have an exceptional set of mechanical properties. The impact resistance of this family has been reviewed twice in the last four years, indicative of its commercial importance, first by [Sadighi et al. \(2012\)](#), and then by [Chai and Manikandan \(2014\)](#) – both make recommended reading.

Developed in the Netherlands during the 1970s and 1980s, from original work carried out by Fokker Aviation ([Vermeeren, 2003](#)), this family of aluminium laminates epitomises all that is beneficial about a laminate: high specific strength (because of the chosen alloy), excellent fracture toughness (as illustrated by Kaufman back in the 1960s – see [Fig. 4.3](#)), excellent fatigue resistance (because of the fibre-bridging observed when the materials are loaded in the crack divider mode – see [Fig. 4.13](#)) and excellent blast performance (because of a high, out-of-plane, ductility). ARALL, an aramid-reinforced aluminium laminate, further refined and fully characterised by researchers at Delft University in the early 1980s, was the first to gain commercial acceptance for use in cargo doors on the C17 aircraft. However, the most successful variant has been GLARE, the glass fibre-reinforced variant, which is now the material of choice for Airbus Industries when building the upper fuselage skin of the A380

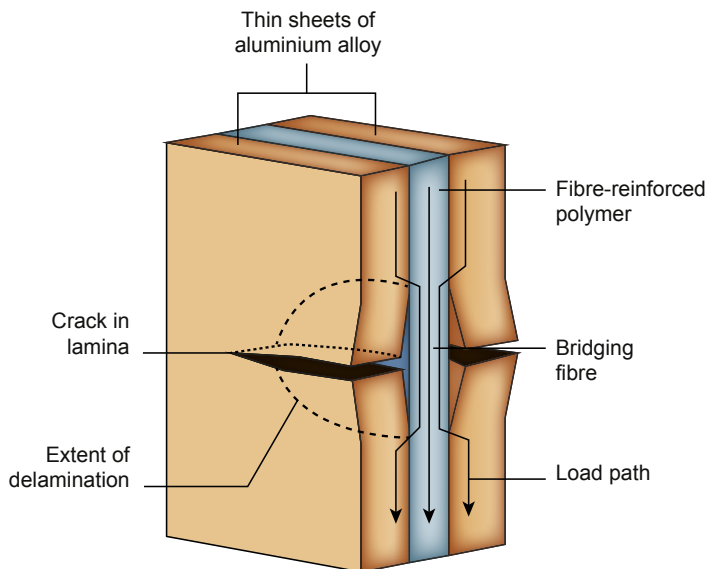


Figure 4.13 Illustration of fibre-bridging when FMLs are resisting crack propagation in the crack divider mode.

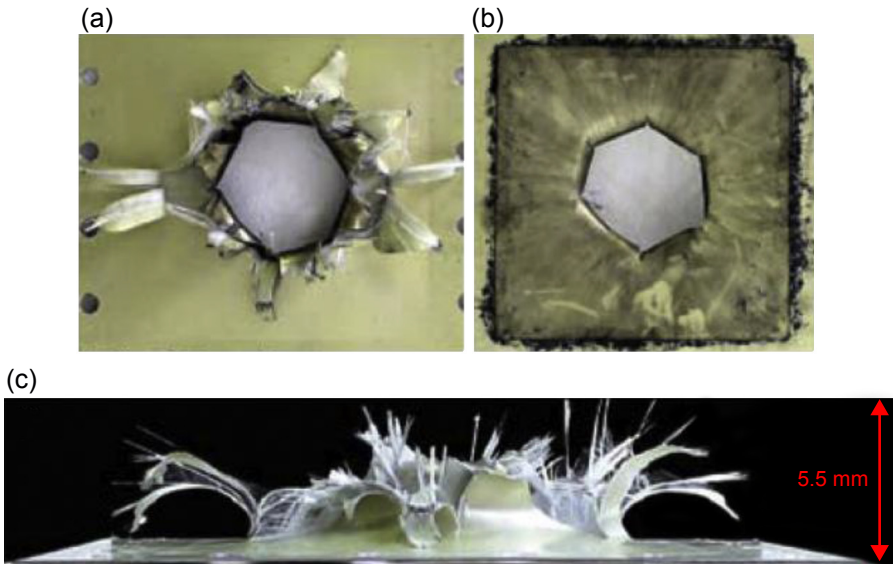


Figure 4.14 Images showing local blast damage in a GLARE panel. (a) Back face view, (b) Front face view, (c) Side view

After Langdon, G.S., et al., 2007. Behaviour of fibre metal laminates subjected to localised blast loading: part 1-experimental observations. *International Journal of Impact Engineering* 34, 1202–1222.

aircraft; 40 years after the laminate had been invented! In the post-Lockerbie era, GLARE has also been seriously considered in the construction of blast-resistant cargo containers (Anon, 2001), and Fig. 4.14 illustrates how GLARE behaves when locally blast-loaded: a multitude of plastically deformed metal shards and torn coated fibres are clearly evident in a well-contained damage zone.

This family of FMLs is really a subset of bonded aluminium laminates, as summarised in Table 4.4. The other, fibre-free variant, ABALs, was reviewed by Crouch in 1988, as an up-and-coming, energy-absorbing armour material (Crouch, 1988), and during the ensuing 5 years developed into a patentable material suitable for use in protecting structures from high-velocity fragments. Section 4.5.1 details that evolutionary story.

4.4.3 Hybrid laminates

With reference to Fig. 4.2, this section describes the benefits of having a two-ply laminate in which Material #1 and Material #2 are significantly different in both structure and properties: ceramic/metal, ceramic/composite, and steel/composite, for example. In each case, Material #1 is chosen to be a disrupter (a ceramic or high-hardness steel) and Material #2, the absorber (a ductile metal or a soft composite).

The classical use of ceramics as disrupter materials is covered, in detail, in Chapter 7. At this time, the reader is referred to papers by Yadav and Ravichandran (2003)

Table 4.4 Family of bonded aluminium laminates

Laminate	Interlayer	Lamina thickness (mm)	Laminate thickness (mm)	Uses/comments
ABAL	Polymer or adhesive only	1.0–3.0	5–25	Developmental product. Applications to lightweight armour systems, especially backing material
ARALL	Aramid fibre-reinforced polymer	0.2–0.4	1–3	Commercial product. Established use for impact-resistant aerospace structures
GLARE	Glass fibre-reinforced polymer	0.2–0.5	1–3	Commercial product. Established use as a commercial aero-structural fuselage material
CARALL	Carbon-aramid fibre-reinforced polymer	0.2–0.4	1–3	Commercial product. Niche applications

concerning simple aluminium nitride-based laminates, and [Pechoucek et al. \(2011\)](#) for more complex systems with areal densities as high as 300 kg/m^2 . This section will focus upon the benefits of using high-hardness steels as disrupters and composites as the absorber.

The use of spall liners to reduce the damaging effects from shaped-charge weapons and overmatching kinetic energy rounds will be described in Chapter 5. For this application, the spall liners are attached to the inside of the vehicle. But what conditions provide the best results? The armour technologists working at the Ernst Mach Institute in Germany during the late 1990s finally revealed the answers. [Strassburger et al. \(1998\)](#) carried out systematic studies on combinations of high-strength steels (7.5–13.5 mm in thickness) and fibre-reinforced polymers, consisting of 5–21 layers of an aramid fabric. The two materials were bonded together with a polyurethane adhesive. The projectiles were a range of blunt, steel cylinders with masses between 5 and 50 g, all with L/D ratios of 0.8, and fired at velocities up to 1800 m/s [Fig. 4.15](#), a plot of normalised areal density versus impact velocity, shows the overall results and the obvious benefits of using a composite backing material. When these results were converted into Em values, weight savings of up to 35% were reported for use of the thinner variants, especially at lower impact velocities of $\sim 800 \text{ m/s}$. Through the use of high-speed photography and round recovery techniques, they were also able to show that the spall cone was reduced because the composite retained the outer ring of target fragments, as shown schematically in [Fig. 4.16](#).

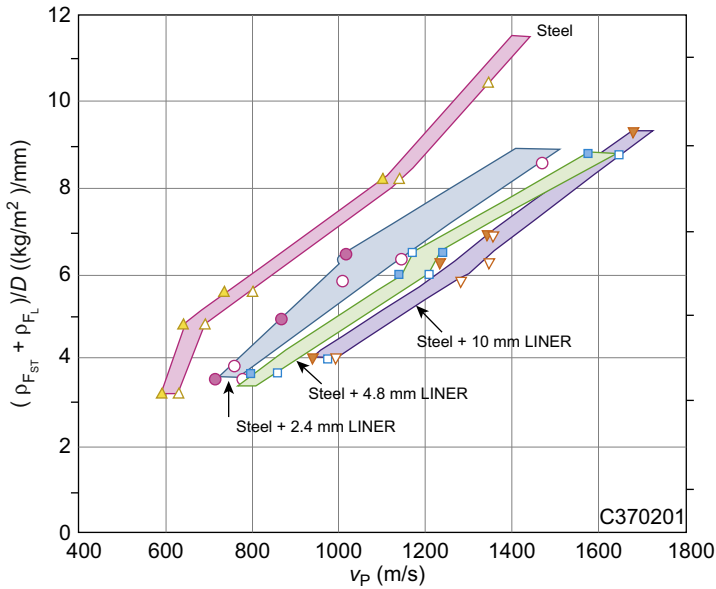


Figure 4.15 Normalised ballistic limit curves for various steel/composite laminates. After Strassburger, E., et al., 1998. The ballistic resistance of steel/aramid bi-layer armor against fragment impact. Paper Presented at the 17th International Symposium on Ballistics, South Africa.

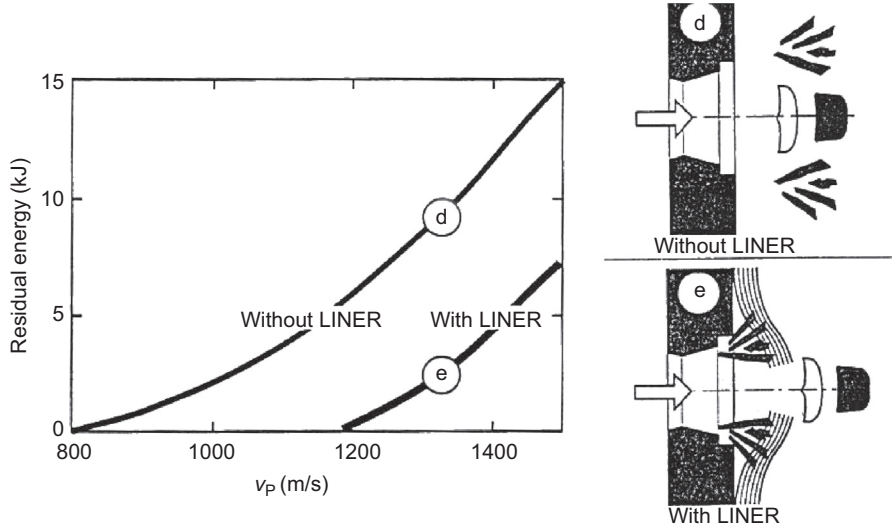


Figure 4.16 A plot of total residual energy, from all fragments and core, versus impact velocity for steel target and steel/composite laminate. Strassburger, E., et al., 1998. The ballistic resistance of steel/aramid bi-layer armor against fragment impact. Paper Presented at the 17th International Symposium on Ballistics, South Africa.

In a follow-up study, the same group published results for steel/composite laminates in which the composite was either an aramid-reinforced polymer, with a bulk density of $\sim 1100 \text{ kg/m}^3$ or a polyethylene-based laminate with a bulk density of only 950 kg/m^3 . In this case (Lexow et al., 1999), the threat was armour-piercing ammunition, including the AP M61 round (see Chapter 1). Strong synergistic effects were reported but only if the cores of the AP rounds were fragmented during impact. This is very poignant, as will be appreciated in Chapter 5: composites are excellent absorbers of blunt projectiles but not very effective against AP rounds.

In conclusion, the more recent paper by Rondot et al. (2013) has shown that an aluminium/composite laminate is more effective at resisting penetration from high-energy fragments than an armour steel with a hardness of $\sim 400 \text{ HB}$. Again, the efficacy of having a composite as an effective absorber was aptly demonstrated when designing armours against high-energy, blunt fragments.

4.5 Examples of laminated armours

Three examples have been chosen in order to demonstrate that the geometrical design of a laminated armour is just as important as the correct selection of the base materials. In the first, in Section 4.5.1, the ratio of the layers becomes significant; in the second, in Section 4.5.2, the ratio of the target thickness to calibre of the round was an important consideration; the third, in Section 4.5.3, revisits some classic work with ceramic armours that shows the importance of thickness ratio between the disrupter and the absorber.

4.5.1 Adhesively bonded aluminium laminates

Fig. 4.17 is a copy of the original schematic developed in 1984 to graphically illustrate the potential benefits of a ballistic laminate. It is as meaningful, and as powerful, today as it was 30 years ago! Against blunt projectiles, all research into laminated materials can be referred back to this diagram, especially the motivation: suppressing, or eliminating, low-energy-absorbing mechanisms.

The ABAL story can be traced through the following ABAL citations (Crouch, 1986, 1988, 1993; Crouch and Woodward, 1989; Crouch et al., 1990, 1994; Woodward and Crouch, 1989; Woodward et al., 1991). The key steps in that development are highlighted here:

- Applying the crack arrestor principle to prevent shear cracks developing in the armour and thus preventing premature failure by plugging (see illustration in Fig. 4.2);
- Recognising that, for this to occur, the shearing event had to be restricted to the outermost ply, as seen in Fig. 4.18(a);
- Recognising that the dynamic, through-thickness compression of the interlayer material, an epoxy adhesive, needed to be understood and well-characterised (see Crouch et al., 1994);
- Developing an ability to numerically model this impact event (see Fig. 4.18(b) and Section 9.6.6);

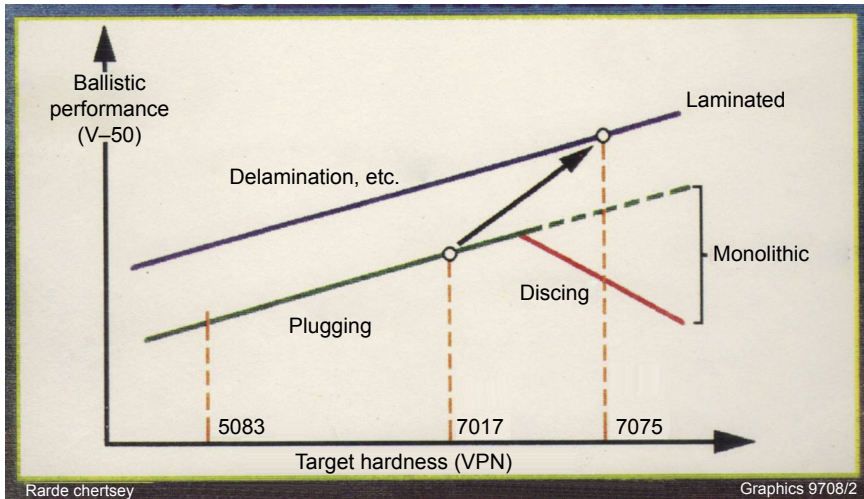


Figure 4.17 Copy of original schematic developed in 1984 to graphically illustrate the potential benefits of developing a ballistic laminate.

After Crouch, I.G., 1992. Discing failures in both traditional and composite armour materials. Paper Presented at the International Symposium on Ballistics, Stockholm, June 1992.

- Recognising that it was not only the thickness of the interlayer that was important but, crucially, the ratio of the thickness of the interlayer to the thickness of the ply (see Fig. 4.19).

So, when designing a ballistic laminate, it is not just about having a dry stack of laminae, nor just an adhesively bonded laminate, but one in which the laminae thickness to interlayer thickness is in the optimal ratio. Then, and only then, will plugging be suppressed and a ballistic advantage be gained. The more recent work of [Woodward and Cimpoeu \(1998\)](#) shows that simply stacking sheets of aluminium alloys together does not maximise penetration resistance against blunt projectiles.

Corollary: This beneficial mechanism only operates when the blunt impactor strikes the ABAL at normal. It does not operate when the nose shape of the penetrator is pointed, ogival or hemispherical. The trick is to organise your laminated armour such that the shearing crack always strikes the surface of the ABAL at normal, but how can that be achieved?

4.5.2 NewSentry armour; a steel-composite laminate

NewSentry armour is a commercial steel-composite ballistic laminate that has been applied to the walls and ceilings of the lookout towers of an Australian correctional centre. It is not only a good example of a poor-man's ceramic armour system but an excellent example of how to design a ballistic laminate with the optimal choice of disruptor and absorber materials.

In this instance, the threat was only 7.62 mm ball ammunition. However, against this threat, armour-grade steels are prone to fail by plugging because the thickness

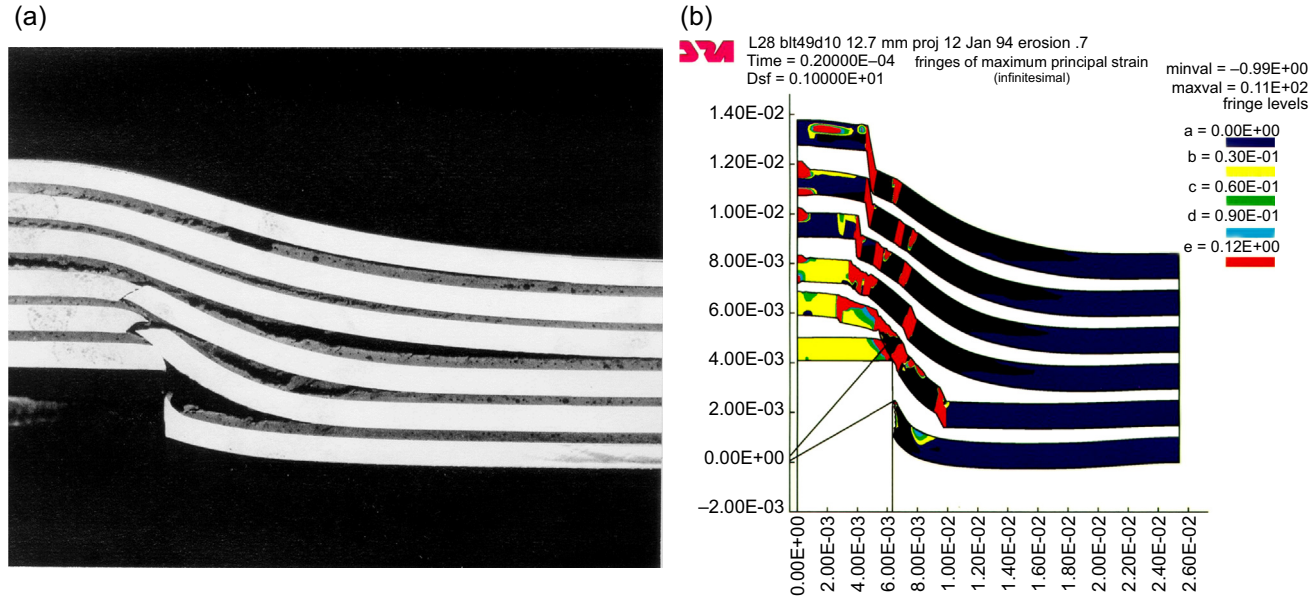


Figure 4.18 (a) Cross-section of a six-ply ABAL showing the shearing of the outermost ply, and (b) numerical simulation of the same. Crouch, I.G., Greaves, L.J., Ruiz, C., Harding, J., September 1994. Dynamic compression of toughened epoxy interlayers in adhesively bonded aluminium laminates. Supplement to Journal de Physique III, Colloque C8 4, 201–206.

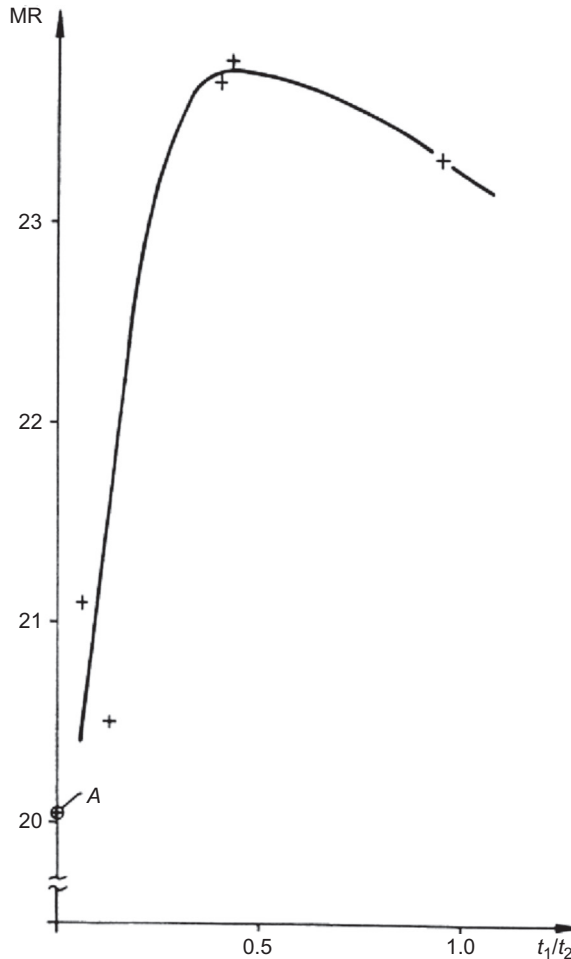


Figure 4.19 Extract from US patent illustrating the effect of ply thickness-to-adhesive thickness ratio on the ballistic properties of adhesively bonded aluminium laminates. Crouch, I.G., 1993. US Patent Number 5272954, Laminated Armour; Filed 28th September 1990; Granted 28th December 1993.

of steel required is approximately 7–9 mm. The t/D ratio is close to one, which often encourages plugging failure. In fact, at this thickness, high-hardness steels are particularly vulnerable to plugging against this threat.

The design philosophy was to reduce the thickness of the steel so as to reduce the t/D ratio and encourage ductile hole formation, and to support the steel with a cost-effective composite material. In this application there was no space restriction, nor any serious weight limitations – the project was driven by cost, as is normal in the construction industry.

The developed solution, certified to Level R2 in the AS/NZS 2343:1997 armour standard, consisted of:

- 5-mm thick, medium-strength steel, with a hardness of ~ 360 Hv;
- 0.5-mm thick bondline of Hysol adhesive 9309.3, a toughened epoxy adhesive;
- 19-mm thick, glass-fibre-reinforced, vinylester resin, with a volume fraction of glass fibres of $\sim 55\text{--}60\%$

The steel was chosen for its intermediate hardness — it was not a standard grade of armour steel. The absorber material, the GFRP, was selected for its high-volume fraction of fibres (see Chapter 5) and the adhesive was chosen because it was a proven, aerospace adhesive with a well-characterised dynamic behaviour (Crouch et al., 1994). Figs 5.1 and 5.6, in the next chapter, illustrate its ballistic performance and impact behaviour.

4.5.3 An alumina-aluminium laminated armour

In this final example, a classic body of work has been chosen to illustrate how the ratio of the thickness of the disrupter to the absorber is important in ceramic-based armour systems. The chosen work is that of John Hetherington who published data on a simple alumina/aluminium system back in 1992 (Hetherington, 1992). It is a classic example of the two-ply laminate schematically shown in Fig. 4.2. Consider the extreme limits of thickness for the two elements. Clearly, the alumina

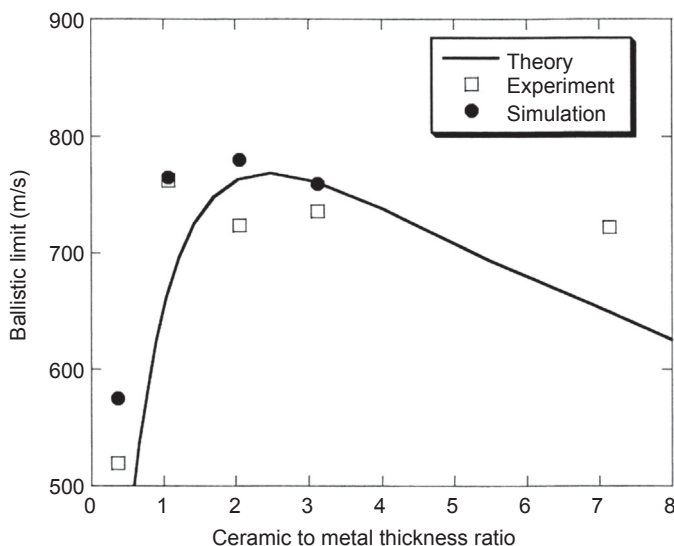


Figure 4.20 Ballistic limit velocities of alumina/aluminium targets of similar areal density but different ceramic-to-metal thickness ratios.

After Hetherington, J.G., 1992. The optimisation of two component composite armours. *International Journal of Impact Engineering* 12 (3), 409–414.

will not function without any support. Likewise, the relatively soft aluminium will not be as effective without a hard strike face in front of it. What Hetherington reported was a simple demonstration that there was an optimum thickness ratio for the most effective armour system. This is reproduced in Fig. 4.20 in which the optimum thickness ratio would appear to be $\sim 2:1$. On an areal density basis, this ratio becomes $\sim 3:1$. In other words, for optimum ballistic performance of a ceramic-based system, $\sim 75\%$, by weight, of that system should be ceramic. This has been one of the design rules for decades and has been confirmed in more recent numerical simulations by Lee and Yoo (2001). However, as Chapter 7 describes, there are ways to either refine or circumvent this general rule when designing cost-effective, light-weight, ceramic armour systems.

4.6 Conclusion

In conclusion, it is hoped that this transition chapter has not only stimulated some thought and design ideas, but has encouraged the reader to find out more about laminated armours and layered structures by reading Chapter 5 on polymers and fibre-reinforced plastics, Chapter 6 on fibres, textiles and protective apparel, and Chapter 7 on glasses and ceramics.

References

- Anon, 2001. Composite blastproofing systems move from R&D to the marketplace. *High-Performance Composites* 25–29 (January/February).
- Aubusson, K., 21 April 2015. Anzac Day 2015: The Bullet in the Bible that Led to Salvation. *Sydney Morning Herald*.
- Barbero, E.J., July 2010. *Introduction to Composite Material Design*, second ed. CRC Press, FL, USA.
- Ben Dor, G., Dubinsky, A., Elperin, T., 2012. Investigation and optimisation of protective properties of metal multi-layered shields - a review. *International Journal of Protective Structures* 3 (3), 275–291.
- Chai, G.B., Manikandan, P., 2014. Low velocity impact response of fibre-metal laminates - a review. *Composite Structures* 107, 363–381.
- Choi, C., Callaghan, M., van der Schaaf, P.L.H., Dixon, B., 2014. DSTO Technical Report, DSTO-TR-2960, Modification of the Gurney Equation for Explosive Bonding by Slanted Elevation Angle.
- Crouch, I.G., Woodward, R.L., 1989. The use of simulation techniques to study perforation mechanisms in laminated metallic composites. In: Paper Presented at the International Conference on Mechanical Properties and Materials at High Rates of Strain, Oxford, UK.
- Crouch, I.G., Greaves, L.J., Simmons, M.J., 1990. Compression failure in composite armour materials. In: Paper Presented at the 12th International Symposium on Ballistics, San Antonio, Texas, USA, October 1990.
- Crouch, I.G., Greaves, L.J., Ruiz, C., Harding, J., September 1994. Dynamic compression of toughened epoxy interlayers in adhesively bonded aluminium laminates. Supplement to *Journal de Physique III, Colloque C8*, 4, 201–206.

- Crouch, I.G., Appleby-Thomas, G., Hazell, P., 2015. A study of the penetration behaviour of mild-steel-cored ammunition against boron carbide ceramic armours. *International Journal of Impact Engineering* 80, 203–211.
- Crouch, I.G., 1981. Properties of Welded Transition Joints between Steels and Aluminium Alloys for Use in Structural Applications. Institution of Metallurgists. Course Volume (Series 3).
- Crouch, I.G., 1986. A Review of Metallic Composite Materials for Armour. RARDE, Chertsey. UK Government Internal Report.
- Crouch, I.G., 1988. Adhesively-bonded aluminium laminates - their future as energy-absorbing, structural materials. In: Paper Presented at the New Materials and Processes for Mechanical Design, Brisbane, Australia, May 1988.
- Crouch, I.G., 1992. Discing failures in both traditional and composite armour materials. In: Paper Presented at the International Symposium on Ballistics, Stockholm, June 1992.
- Crouch, I.G., 1993. Laminated Armour. US Patent Number 5272954. Filed 28th September 1990; Granted 28th December 1993.
- Crouch, I.G., 2010. A Comparative Study of Ceramic Coating Techniques, as a Means of Conferring Multi-hit Resistance on SAPI Ballistic Plates. Internal DMTC Report, May 2010.
- Crouch, I.G., 2013a. “Next Generation Combat Helmets”, 3rd DMTC Annual Conference, March 2013, Canberra, Australia.
- Crouch, I.G., 2013b. unpublished data from ADA.
- Crouch, I.G., 2014. Effects of cladding ceramic and its influence on ballistic performance. In: Paper Presented at the International Symposium on Ballistics, Atlanta, GA, USA, September 2014.
- Dey, S., et al., 2007. On the ballistic resistance of double-layered steel plates: an experimental and numerical investigation. *International Journal of Solids and Structures* 44 (20), 6701–6723.
- Grujicic, M., Bell, W.C., Pandurangan, B., 2012. Design and material selection guidelines and strategies for transparent armor systems. *Materials and Design* 34, 808–819.
- Gupta, N.K., Iqbal, M.A., Sekhon, G.S., 2008. Effect of projectile nose shape, impact velocity and target thickness on the deformation behavior of layered plates. *International Journal of Impact Engineering* 35, 37–60.
- Hamel, S.F., 2010. A Parametric Study of Delaminations in an Al-Li Alloy (M.Sc. thesis). University of Illinois, Urbana-Champaign, 2010.
- Hetherington, J.G., 1992. The optimisation of two component composite armours. *International Journal of Impact Engineering* 12 (3), 409–414.
- Jaitlee, R., 2013. Physical Protection: Inter-dependence between Hard and Soft Armours (Ph.D. thesis). RMIT University, Australia.
- James, B.J., 1995. Modification of ceramic failure in impact by stress wave management. In: Paper Presented at the Lightweight Armour Systems Symposium, Shrivenham, UK.
- Jones, R.M., 1975. *Mechanics of Composite Materials*. McGraw-Hill, New York.
- Kaufman, J.G., September 1967. Fracture toughness of 7075-T6 and -T651 sheet, plate and multi-layered adhesive-bonded panels. *Journal of Basic Engineering* 503–507.
- Krell, A., Strassburger, E., 2008. Hierarchy of key influences on the ballistic strength of opaque and transparent armor. *Ceramic Engineering and Science Proceedings* 20 (5), 45–55.
- Kruzic, J.J., McNaney, J.M., Cannon, R.M., Ritchie, R.O., 2004. Effects of plastic constraint on the cyclic and static fatigue behavior of metal/ceramic layered structures. *Mechanics of Materials* 36, 57–72.
- Kum, D.W., Oyama, T., Wadsworth, J., Sherby, O.D., 1983. *Journal of Mechanics and Physics of Solids* 31, 173–186.

- Laible, R., 1980. *Ballistic Materials and Penetration Mechanics*, Chapter 4 (Fibrous Armor). Elsevier.
- Langdon, G.S., et al., 2007. Behaviour of fibre metal laminates subjected to localised blast loading: part 1-experimental observations. *International Journal of Impact Engineering* 34, 1202–1222.
- Lee, M., Yoo, Y.H., 2001. Analysis of ceramic/metal armour systems. *International Journal of Impact Engineering* 25, 819–929.
- Lees, W.A., 1988. *Adhesives in Engineering Design*. Springer-Verlag, Berlin.
- Lesuer, D.R., et al., 1996. Mechanical behaviour of laminated metal composites. *International Materials Reviews* 41 (5), 169–197.
- Lexow, B., Strassburger, E., Senf, H., Rothenhausler, H., 1999. Ballistic resistance of steel/composite targets against 7.62 mm AP projectiles. In: Paper Presented at the 18th International Symposium on Ballistics, San Antonio, USA, November 1999.
- Lopez-Puenta, J., Arias, A., Zaera, R., Navarro, C., 2005. The effect of the thickness of the adhesive layer on the ballistic limit of ceramic/metal armours: an experimental and numerical study. *International Journal of Impact Engineering* 32, 321–336.
- Nettles, A.T., October 1994. *Basic Mechanics of Laminated Composite Plates*. NASA Publication 1351.
- Oberg, E.K., Dean, J., Clyne, T.W., 2015. Effect of inter-layer toughness in ballistic protection systems on absorption of projectile energy. *International Journal of Impact Engineering* 76, 75–82.
- Ozsahin, E., Tolun, S., 2010. On the comparison of the ballistic response of coated aluminium plates. *Materials and Design* 31 (7), 3188–3193.
- Pechoucek, P., Rolc, S., Buchar, J., 2011. Fragment simulating projectile penetration into layered targets. *Engineering MECHANICS* 18 (5/6), 353–361.
- Roland, C.M., Fragiadakis, D., Gamache, R.M., 2010. Elastomer-steel laminate armor. *Composite Structures* 92, 1059–1064.
- Rolc, S., Buchar, J., Obdrzalek, L., Hrebicek, J., 1996. On the penetration process in steel laminates. In: Paper Presented at the 16th International Symposium on Ballistics, San Francisco, September 1996.
- Rondot, F., et al., 2013. On the use of laminate protection against high velocity fragment impact. In: Paper Presented at the 27th International Symposium on Ballistics, Friburg, Germany, April 2013.
- Rosenberg, Z., Dekel, E., 2012. *Terminal Ballistics*. Springer-Verlag, Berlin.
- Roylance, D., 1996. *Mechanics of Materials*. Wiley & Sons, New York.
- Sadighi, M., Alderliesten, R.C., Benedictus, R., 2012. Impact resistance of fiber-metal laminates: a review. *International Journal of Impact Engineering* 49, 77–90.
- Stefansson, N., Bailey, R.E., Swiatek, G.J., 2012. PCT/US2011/066691, Entitled “Dual Hardness Steel Article and Method of Making”. Filed 22nd December 2011.
- Strassburger, E., et al., 1998. The ballistic resistance of steel/aramid bi-layer armor against fragment impact. In: Paper Presented at the 17th International Symposium on Ballistics, South Africa.
- Tasdemirci, A., Tunusoglu, G., Guden, M., June 2012. The effect of the interlayer on the ballistic performance of ceramic/composite armors: experimental and numerical study. *International Journal of Impact Engineering* 44, 1–9.
- van de Voorde, M.J., Diederan, A.M., Herlaar, K., 2005. Preliminary investigation of potential lightweight metallic armour plates. In: Paper Presented at the International Conference on Ballistics, Vancouver, Canada, November 2005.

- van de Voorde, M.J., Herlaar, K., Broos, J.P.F., 2007. Is a hard top layer always the right choice?. In: Paper Presented at the 23rd International Symposium on Ballistics, Tarragona, Spain, April 2007.
- Velentzas, G.C., 1996. Spaced Armour Systems, 24 MVT M.Sc. Project Report. Royal Military College of Science, Shrivenham (Mike Iremonger, Supervisor).
- Vermeeren, C.A.J.R., 2003. An historic overview of the development of fibre metal laminates. *Applied Composite Materials* 10, 189–205.
- Woodward, R.L., Cimpoeu, S.J., 1998. A study of the perforation of aluminium laminate targets. *International Journal of Impact Engineering* 21 (3), 117–131.
- Woodward, R.L., Crouch, I.G., 1989. MRL Research Report, MRL-RR-9–89, “A Computational Model of the Perforation of Multi-Layer Metallic Laminates”. DSTO Materials Research Laboratory.
- Woodward, R.L., Tracey, S.R., Crouch, I.G., October 1991. The response of homogeneous and laminated metallic sheet material to ballistic impact. *Journal de Physique IV, Colloque C3*, 277–282.
- Yadav, S., Ravichandran, G., 2003. Penetration resistance of laminated ceramic/polymer structures. *International Journal of Impact Engineering* 28, 557–574.
- Yaziv, D., Reifen, Y., Kivity, Y., 1996. Spacing effect on the performance of ceramic targets. In: Paper Presented at the 16th International Symposium on Ballistics, San Francisco, September 1996.
- Yong, M., Iannucci, L., Falzon, B.G., 2010. Efficient modelling and optimisation of hybrid multi-layered plates subject to ballistic impact. *International Journal of Impact Engineering* 37, 605–624.

Polymers and fibre-reinforced plastics

5

I.G. Crouch¹, J. Sandlin², S. Thomas³

¹Armour Solutions Pty Ltd, Trentham, Victoria, Australia; ²DMTC, Hawthorn, Victoria, Australia; ³Defendtex, Dandenong South, Victoria, Australia

5.1 General introduction

The phrase, ‘composite armour’ has, unfortunately, taken on a number of different meanings over the past few decades. From a systems point of view, it usually means the use of both a ceramic and a backing material to create a ‘composite’ armour system of two different material groups. However, to the material scientist, the word ‘composite’ usually refers to a fibre-reinforced plastic (FRP), such as carbon fibre reinforced epoxies which have become the material of choice in the aerospace industry. This chapter deals with both unreinforced polymers, like the polycarbonates, and fibre-reinforced polymers (or plastics), like fibreglass. Composite armour systems will be covered in other chapters including Chapter 7.

Composite materials, as detailed in Chapter 4, are laminated materials and, as such, introduce enormous choice in the basic materials that are used: type of resin (thermo-setting or thermoplastic); grade of resin (polyester, epoxy, etc.); type of reinforcement (glass, carbon or aramid fibres); nature of reinforcement (volume fraction, orientation, pretreatment, etc.). This chapter will discuss most of the fundamental choices available to the armour technologist and provide an insight into the ballistic performance of specific material systems. For example, Fig. 5.1 provides a comparison between the areal densities of a range of composite armours designed to defeat the 7.62 mm M80, lead-filled bullet. The heaviest system is Martial Armour (a proprietary blend of fibreglass and syntactic foam); the lightest is the composite armour represented by a silicon carbide ceramic, backed by an aramid-reinforced plastic. The green-highlighted data refer to a more cost-effective, composite armour system, NewSentry armour from Armour Solutions Pty Ltd (Australia): this is a simple laminate of high-hardness steel, backed by a glass fibre-reinforced vinylester resin (see Chapter 4). All other data in Fig. 5.1 refer to monolithic laminates of a particular fibre-reinforced plastic — this is the family of materials to be discussed in this chapter. It should be noted that these ‘ballistic’ laminates are typically 10–50 mm in thickness — the impact resistance and energy-absorbing mechanisms associated with thin (1–5-mm thick) aerospace composites are covered elsewhere, especially through the classical review of Cantwell and Morton (1991).

In general, fibre-reinforced plastics do not make very good bullet-resistant materials: at least, not on their own. As detailed by Crouch (2009a) they tend to work

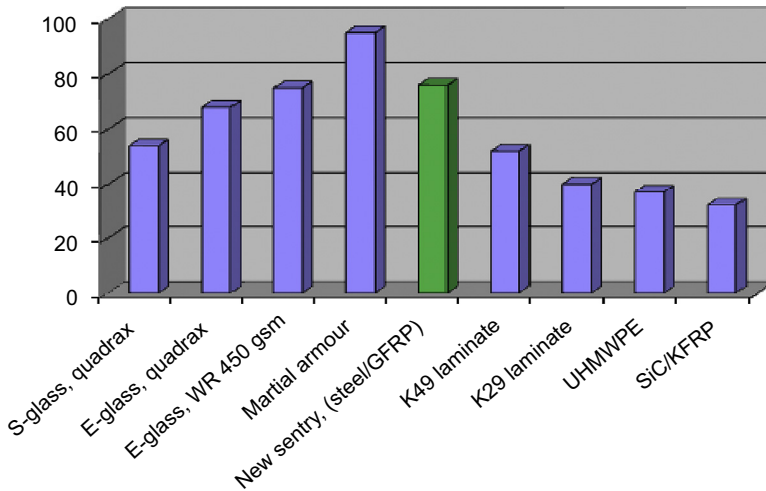


Figure 5.1 Comparative ballistic data for ‘composite’ armours against 7.62-mm ball ammunition. Reproduced from: Crouch, I.G., 2009a. Do composites make good armour. In: Composites Australia & the Composites CRC Annual Conference & Trade Show 2009. <http://www.compositesconference.com/>.

best in combination with other armour materials — but why is this? Fibre-reinforced plastics do, however, have very attractive structural properties and have been used in a semistructural manner in order to lighten the main structure of an armoured vehicle. They can also be formed a lot more easily than metals and have become very popular for armour products like helmets (see Section 5.5.2). As an energy-absorbing material, they are excellent at defeating blunt projectiles, like high-energy fragments, and have established a niche application as spall liners, since the 1970s. Since then, most armoured personnel carriers have included spall liners either as part of the main protection system or as part of an upgrade kit where these fibre-reinforced plastic laminates are retrofitted onto the inside of the main structural armour.

5.1.1 *Brief history: from spall liners to structural fibre-reinforced plastics (FRPs)*

The most prolific application for composites as an armour material is their use as spall liners. These are attached to the inside of the main structural armour, and are fitted in order to reduce the risk, and consequent effects, from rear-face spall. The main driver for their initial development was to overcome the issue of spall ejecting from the inside of thick-walled, lightweight, aluminium-based vehicles, especially when being overmatched by either Kinetic Energy (KE) or Chemical Energy (CE) weapons. As has been described in earlier chapters, especially Chapter 3, light alloys suffer from rear-face discing. In the case of shaped-charge weapons, the existence of spall liners also significantly reduces the cone angle of internal debris and thus the risk of serious injury to personnel.

These spall liners are typically laminates of glass fibre, or aramid fibre, reinforced thermosetting resin: normally a fire-retardant grade, such as a phenolic, since these materials lie inside the occupied space of an armoured personnel carrier (APC). Early forms were controlled through military specifications like MVEE 802 (c.1982), which have now evolved into defence standards (see [Section 5.6](#)) and such products were certainly used in British armoured fighting vehicles (AFVs) like the Warrior APC, as well as a number of US vehicles like the M113s, LSAC and the ASV ([Rush, 2007](#)). As will be appreciated later, these spall liners, irrespective of fibre type, are characterised by a high volume fraction of fibres.

Laminates of fibre-reinforced plastics have also been used ([Fig. 5.2](#)) in armoured vehicles where the polymer-based armour is utilised as an additional ballistic component with the steel, or aluminium alloy, still serving as both the primary armour and primary structure of the vehicle hull. The polymer-based materials augment ballistic performance within weight limitations. This can take the form of internal spall curtains (refer to [Section 5.6.2](#)) and even external coatings designed to mitigate blast response in the vehicle hull.

In the 1990s, a number of isolated examples appeared in which these approved ‘spall liner’ materials were used as building blocks for the protective cabs of light-weight land vehicles, such as the Land Rover (see [Fig. 5.2](#)). The UK CAV 100 vehicle, built from an S2-glass reinforced phenolic resin, was one of the very first and saw



Figure 5.2 Montage of vehicle applications for fibre-reinforced plastics.

Adapted from: Crouch, I.G., 2009a. Do composites make good armour. In: *Composites Australia & the Composites CRC Annual Conference & Trade Show 2009*. <http://www.compositesconference.com/>.

service within Northern Ireland during those troubled years. Weight savings were achieved but production was limited and reparability became an issue.

The most significant vehicle programme of the 1990s, however, was the UK's Advanced Composite Armoured Vehicle Platform. This project was built on the premise that spall liners simply added parasitic weight to the vehicle and provided no structural benefit. What the team at MVEE (Chobham) recognised, in the early 1990s, was the benefit of converting the spall liners into the structural armour elements, thereby enabling the main armour system to be attached to the outside of a permanent lightweight composite shell. Furthermore, if this could be achieved, then upgrading the main armour would be very easily carried out. Mark French's paper, entitled 'Composite materials and new modelling techniques for lighter AFVs', presented in Loen, Norway, in May 2001 ([French and Lewis, 1996](#)) gives a good overview of the composite vehicle programmes, c.2000, plus background data on ACAVP.

In the late 1990s, as confidence grew in the use of composites for armour applications, ADI (now Thales, Australia) investigated its application to turrets, mantlets and hatch covers: ie, those items which could be retrofitted with the aim of reducing overall weight. ADI selected the vacuum bagging resin infusion (VBRI) process (see [Section 5.4.2](#)) to manufacture a prototype hatch cover. A noncrimp fabric made of E-glass, was infused with a vinylester resin (Derakane 8084). [Fig. 5.3](#) shows the demonstration item: a one-piece, multicurved hatch cover with an integral window. Ballistic performance was excellent but, like a lot of early designs of standalone composite parts of its generation, it was shown to exhibit poor edge performance. The interface between a composite part and a metal structure needs careful design to eliminate 'ballistic windows' (pathways for bullets to bury their way through structural interfaces).

During the same period, Crouch and his team at ADI (c.1997), successfully developed a composite armour system for fitting to the Huon Class of RAN's Minehunters (see [Section 5.5.4.1](#)). Again, VBRI was the process of choice.

More recently, with the widespread adoption of aramid, glass, UHMWPE, and even carbon fibre polymer-based composites, these materials are being designed into

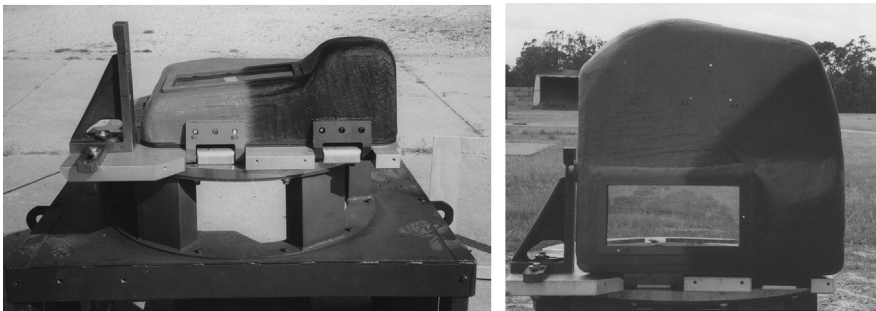


Figure 5.3 Images of the composite hatch cover fitted to an ASLAV during trials at Puckapunyal in 1998.

Source: ADI Limited (1998).

lightweight vehicles as both primary structure and primary armour. In this application they are starting to supplant the use of steel and aluminium. They do however remain more expensive than metallic materials and therefore their use as primary structure is limited to weight critical applications where the gross mass of the platform is paramount in deployment logistics (eg, airborne operations) or manoeuvrability.

Two examples of this are the General Dynamics Ocelot (Anon, 2014) and the Supacat SPV400 (Anon, 2015g), both of which are equipped with rear mission modules (crew pods), made from composite materials. In both cases the lightweight mission modules can be rapidly swapped out to reconfigure the vehicle and the gross unladen mass of the vehicle is in the range of 7–8 tons (Fig. 5.4).

While the use of polymer-based composites in personnel armour is now more widespread, there are reasons beyond cost which have slowed its adoption as the material of choice for the primary structure in vehicles. These include quasistatic stiffness particularly in the case of ultrahigh molecular weight polyethylene (UHMWPE), as discussed in Section 5.5.4 and more importantly changes in the mechanisms of ballistic response as the threat types are increased to land vehicle scales.

One long-standing success story has been the development of the UHMWPE materials. Invented in the 1970s, at DSM in the Netherlands, decades of evolution have now seen this ultra-lightweight material be regularly employed as up-armouring materials for saloon cars, energy-absorbing backing materials in body armour plates (see Section 5.6.2) and as a material of choice for combat helmets (see Section 5.6.3). Most recent works by Nguyen et al. (2015) and others have shown that this material absorbs an exceptional amount of impact energy and outperforms conventional predictions as previously laid out by Cunniff (1999).

5.1.2 Energy-absorbing mechanisms and failure modes

Conventional aerospace composites fail in a number of traditional ways involving matrix cracking, fibre pull-out, delamination, as well as fibre extension and fibre failure. These have been well documented (Cantwell and Morton, 1991) in the past. However, a



Figure 5.4 A Foxhound Light Protected Vehicle (LPV) being off-loaded in Afghanistan in 2012.

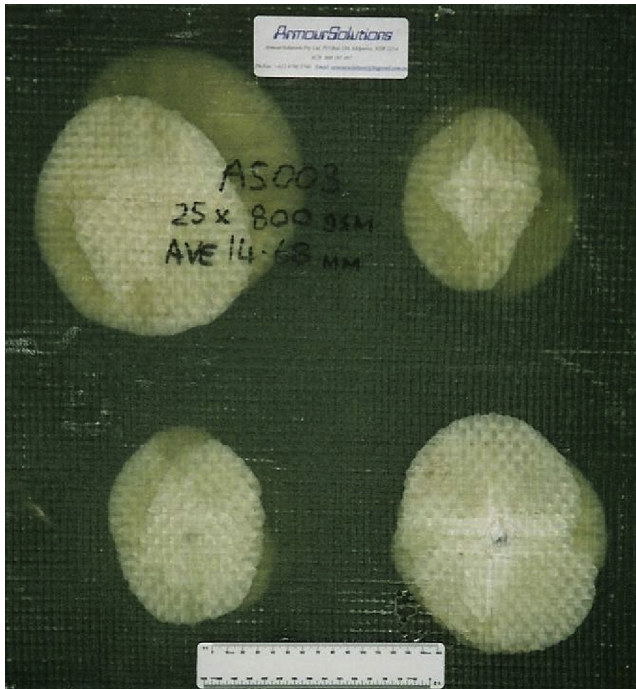


Figure 5.5 Rear surface of a NewSentry armour system showing extensive delamination of the glass fibre-reinforced resin backing material.

Source: Armour Solutions (1998).

ballistic impact event is quite different and considerable effort since the 1980s has been expended on identifying those mechanisms which are important in a ballistic penetration event, for composites between 15 and 50 mm in thickness. Delamination is, most certainly, involved, as can be seen from [Fig. 5.5](#). In fact, limiting/restricting the extent of this natural failure mode is one of the challenges when developing an acceptable composite armour material since multistrike performance is normally a prerequisite for any armour system. During the 1970s and early 1980s, it was conventional wisdom, from the work of Sierakowski and his team ([Cristescu et al., 1975](#)) at the University of Florida, Gainesville, USA, that delamination was the main failure mechanism and therefore absorbed most of the impact energy. However, this was not always supported by experimental evidence, which often showed that there was no difference in ballistic performance in glass–polyester systems between laminates constructed of many lightweight plies compared to those with a smaller number of heavier-weight plies ([Morrison and Bowyer, 1980](#)). These early researchers also suggested that delamination was only important because it enabled the individual plies to behave as if no resin were present. Nevertheless, delamination is an essential failure mode in ballistic composites even though it may not absorb most of the impact energy.

The earliest known work to try to identify the full range of energy-absorbing mechanisms emanated from international collaborative activities in the 1980s, especially

those between the USA (Gooch and Perciballi), Canada (Poursartip), Australia (Gellert) and the UK (Crouch), under an intergovernment collaborative scheme. Following a wide-ranging review by Crouch, in 1986 (Crouch, 1986), Greaves finally published work (see Fig. 5.6) which identified two main phases of penetration: Phase I involving, mainly, through-thickness compression; Phase II involving membrane stretching and delamination (Greaves, 1992).

In summary, and based upon earlier work of Rayner and Crouch (1984) on the development of metallic laminates, Fig. 5.7 shows an up-to-date summary of all of the known failure mechanisms that occur in a laminate, whether it be metallic or polymeric.

Fig. 5.7 shows a cross-section through a fibre metal laminate, which has been impacted by a 0.3" (7.6 mm) fragment simulating projectile travelling at about 900 m/s. The penetration process is divided into two phases: Phase I, involving extensive through-thickness compression, and Phase II, involving membrane stretching. Each of the failure mechanisms within the two principal phases has been attributed to a particular microscopic event:

1. Through-thickness compression;
2. Transverse shear;
3. Crushing and local shearing;
4. Delamination;
5. Membrane flexure; and
6. In-plane tensile failure.

Through-thickness compression (1) involves both an elastic and plastic response and culminates when the outer plies start to fail in transverse shear (2). This step involves both local shear and tensile failure of the reinforcing fibres and is an essential

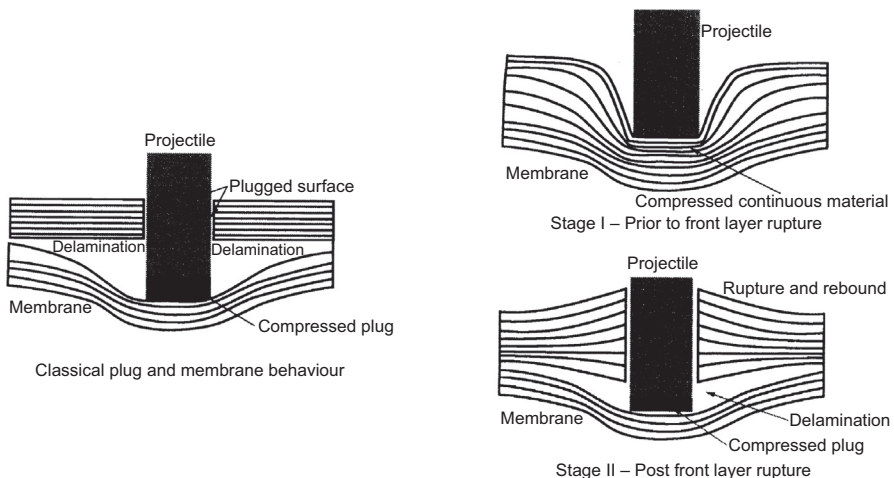


Figure 5.6 Illustration of two stages of failure.

After Greaves, L.J., 1992. Failure Mechanisms in Glass Fibre Reinforced Plastic Armour. MVEE, Chertsey, Internal Memorandum.

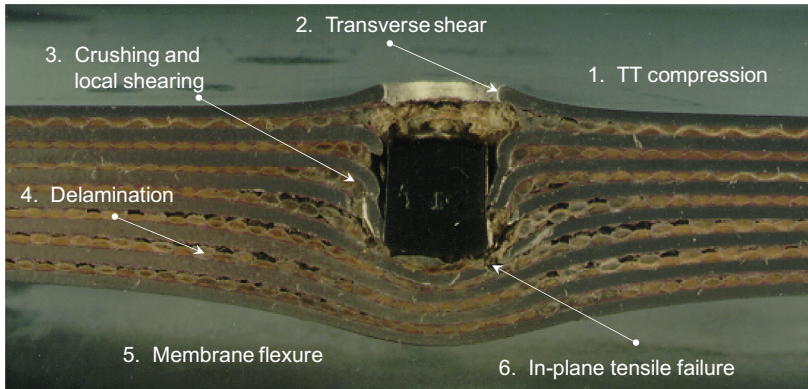


Figure 5.7 Illustration of the complete set of energy-absorbing processes within a laminated composite.

After Rayner, M.C., Crouch, I.G., August 1984. A Study of the Relationship between Hardness and the Ballistic Properties of Aluminium Alloys. MVEE, Chertsey, Technical Report.

step in high-performing laminated FRPs. This, in turn, is followed by extensive crushing (3) of a conglomeration of fibre and resin particles, which flow in all directions (depending upon the nose shape of the projectile), forcing undamaged material to move (by buckling, or through elastic/plastic strain). It is at this stage, that delamination (4) commences, and Phase II begins, since the relatively low interlaminar cracking resistance of the interply regions allows delaminating cracks to form quite easily. Propagation is then controlled by the resin's fracture toughness. As the rear sublaminate becomes delaminated from the front sublaminate, membrane stretching (5) occurs and impact energy is absorbed in flexure. In-plane tensile failure (6) of the fibres in the rear plies finally occurs if membrane strain exceeds the fibre's strain-to-failure.

Over the past three decades, specific mechanical tests, either quasistatic or dynamic, have been developed and/or identified as being useful methods for measuring each of these individual microscopic events. These were first summarised by Crouch at a European conference at Oxford University in 1993 (Crouch et al., 1993) and are reproduced here in Fig. 5.8. The Phase II mechanisms 'delamination' and 'membrane flexure' are based upon the earlier work of (Simmons et al., 1989).

This family of specialised testing techniques is covered more thoroughly within Chapter 10 but, by example, Fig. 5.9 shows a set of constrained compression test (CCT) curves for GFRPs of varying fibre volume fraction (V_f) — this shows quite clearly the increase in TT compressive strength as the V_f increases: as, indeed, does ballistic performance (Crouch et al., 1990). This set of data also shows that, for similar values of V_f (~67%), S2-glass-based composites are more effective than E-glass-based composites: both TT compressive modulus and peak loads are significantly higher.

The existence of Phase I was first demonstrated in some classical work published by (Bless and Hartman, 1989), as reproduced in Fig. 5.10. By using shadow x-radiography, and fiducial markers, they were able to show quite clearly the existence

Phase	Penetration mechanism	Microstructural events	Dedicated test procedures
I	1. Through-thickness compression	Elastic/quasi plastic response of matrix material Low modulus event Affected by V_f in an FRP	<ul style="list-style-type: none"> Simple compression test of a cylindrical sample Constrained compression test (CCT)
	2. Transverse shear	Transverse cutting of fibres or laminae	<ul style="list-style-type: none"> Constrained compression test (CCT) Stamping test, with variable punch diameter
	3. Crushing and local shearing	Local comminution of fibres, resin, etc. Flow of comminuted material	<ul style="list-style-type: none"> Conical indentation test, with variable cone angles
II	4. Delamination	Both intra- and interlaminar separation	<ul style="list-style-type: none"> Short beam shear test Central plunger delamination (CPD) test
	5. Membrane flexure	Matrix cracking Debonding of laminae	<ul style="list-style-type: none"> Two-dimensional (2D) four-point bend test 3D centrally loaded punch (CLP) test
	6. In-plane tensile failure	Fibre pull-out Tensile fracture of fibres or laminae	<ul style="list-style-type: none"> In-plane tensile test, with variable orientation (eg, LT or TL)

Figure 5.8 List of energy-absorbing mechanisms and associated microstructural event, as well as corresponding QS simulation test.

Adapted from: Crouch, I.G., 1993. Penetration and perforation mechanisms in composite armour materials. In: Paper Presented at the Euromech Colloquium 299, Oxford University, March 1993.

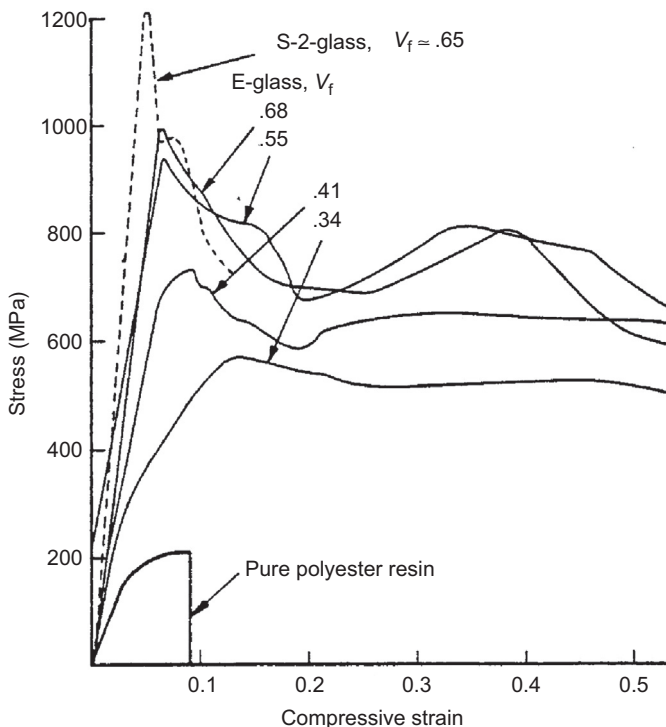


Figure 5.9 CCT data for a range of GFRP panels.

After Crouch, I.G., Greaves, L.J., Simmons, M.J., 1990. Compression failure in composite armour materials. In: Paper Presented at the 12th International Symposium on Ballistics, San Antonio, Texas, USA, October 1990.

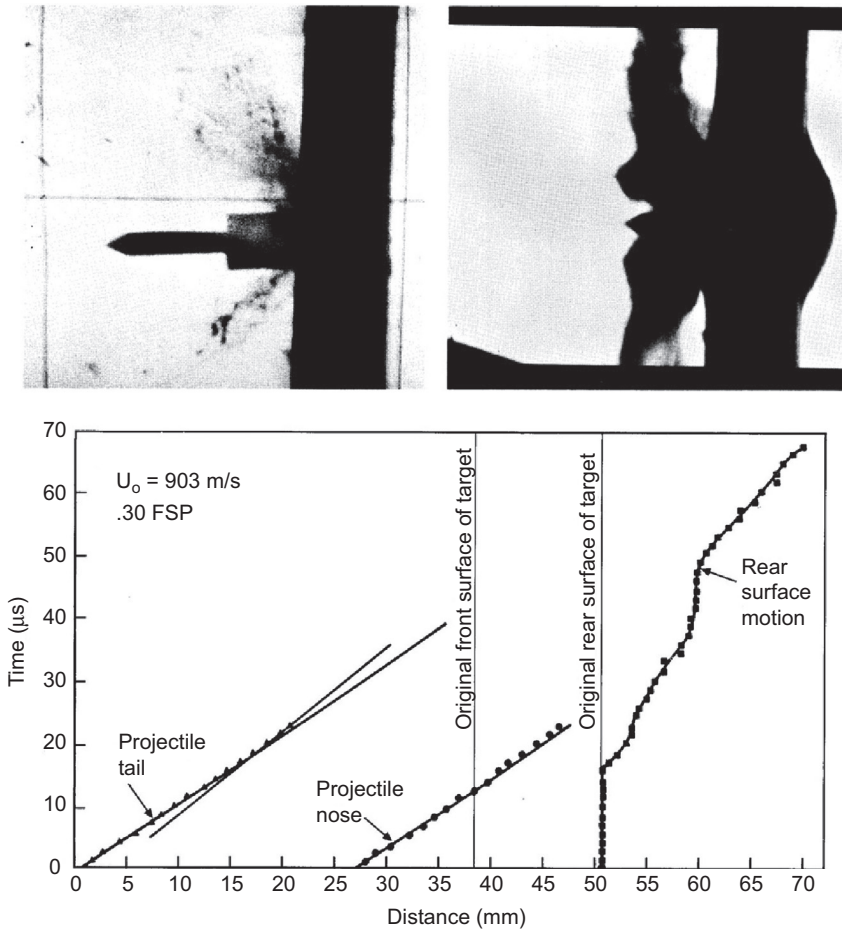


Figure 5.10 Evidence of through-thickness compression in Phase I failure mode. After Bless, S.J., Hartman, D.R., 1989. Ballistic penetration of S-2 glass laminates. In: Paper Presented at the 21st International SAMPE Conference, September 25–28, 1989.

of Phase I behaviour, the through-thickness compression of the GFRP material; in their case, it was an S2-phenolic laminate. As can be seen in Fig. 5.10, during the first 18 μs of impact, the rear surface of the target does not move. The impacting projectile is simply compressing the composite material in the through-thickness direction, within a naturally confining field of in-plane constraint.

But which phase is most important, Phase I or Phase II, and which phase absorbs most energy? It is common belief that the significant difference between a structural laminate and a ballistic laminate is that the latter delaminates more extensively and therefore leads to an increase in energy absorption, thereby enhancing penetration resistance. However, work carried out by Crouch, Greaves and Rutherford in the early 1990s (Crouch, 1993) showed this not to be the case (see Fig. 5.11): Phase I absorbs a

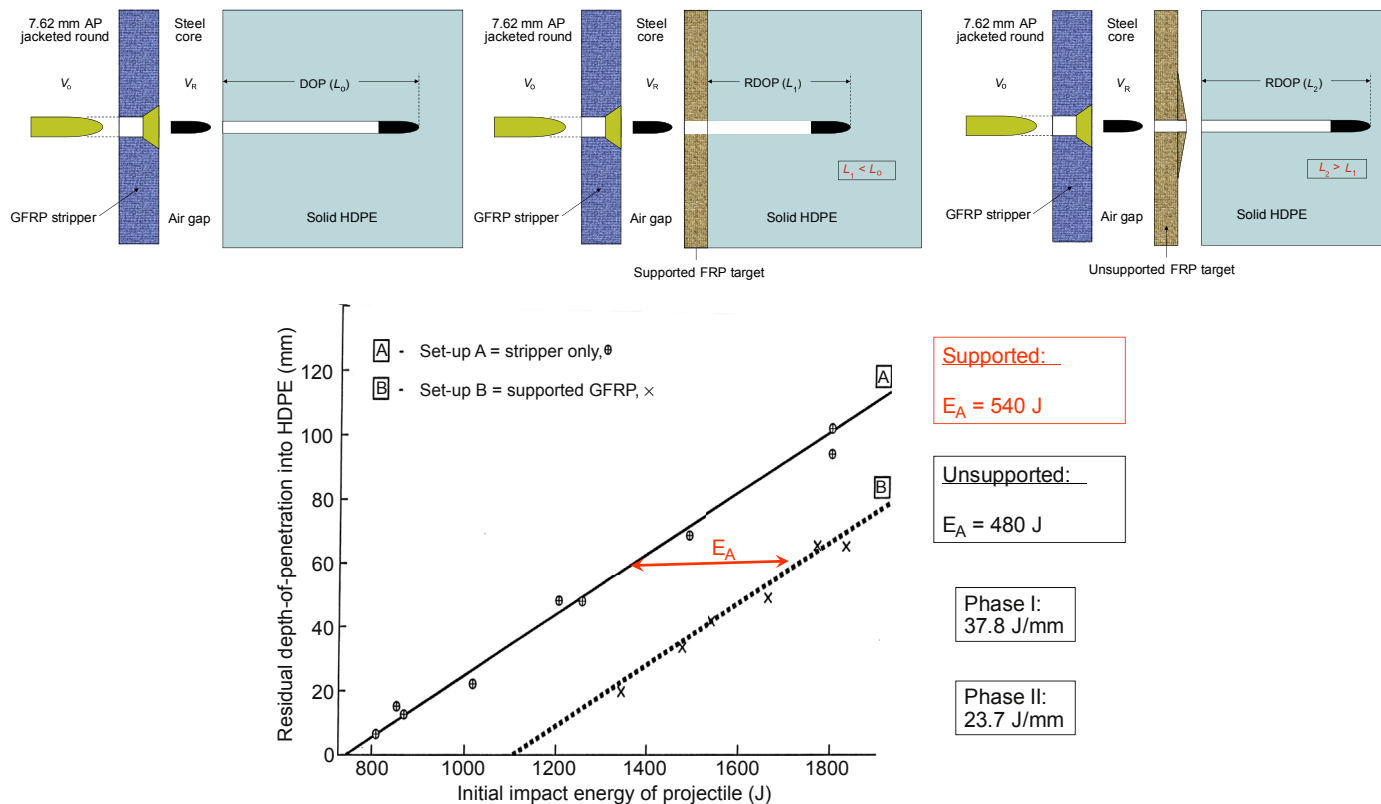


Figure 5.11 Schematic of residual depth of penetration (RDOP) for GFRP materials to determine energy absorption levels for Phase I and II modes of failure.

Reproduced from: Crouch, I.G., 1993. Penetration and perforation mechanisms in composite armour materials. In: Paper Presented at the Euromech Colloquium 299, Oxford University, March 1993.

lot more energy and is the main reason why FRPs are so good against blunt projectiles. In this well-designed series of experiments, involving a stripped steel core from a 0.3" APM2 bullet striking a composite armour material under different support conditions, Crouch was able to show that more than 60% of the impact energy was absorbed during Phase I. It should be noted that these experiments were performed with an ogival-shaped, rigid steel penetrator (the core of the APM2) — one would imagine that for blunt projectiles this fraction could be even greater.

Limiting, or totally suppressing, delamination does not, however, lead to the ultimate composite armour material. This has been demonstrated on numerous occasions through the use of different matrices (Gellert et al., 1998; Wong et al., 2001). In fact, Wong et al. showed quite clearly the trade-off required between having a tough or brittle matrix: their work showed the effect of adding 10% PVB additions to GFR phenolic resins to be beneficial and identified an inverse relationship between G_{Ic} and V-50 value.

In a similar way, work on three-dimensional (3D) composites was driven by the thought that the presence of Through-Thickness (TT) fibres would limit the extent of delamination and therefore improve ballistic performance. On the contrary, what James and Howlett (1997) found was that a 3D laminate absorbed only 85–90% of the 2D laminate and the performance against the 0.3" FSP actually decreased.

The ballistic performance of composite materials is also very dependent upon nose shape of the projectile and considerable work, over the decades, has tried to quantify this phenomenon. It can be explained in terms of a balance between TT compressive behaviour and in-plane compressive behaviour. Reid et al., in the early 1990s, used a number of dynamic indentation experiments, using conical indenters, to try to resolve this issue (Reid et al., 1995): they found that the in-plane compressive resistance did not vary with the rate of impact, whilst the TT resistance increased by an order of magnitude. More recent work of Jordan and Naito (2014) also illustrates this effect very clearly. They quantified the effect of eight different nose shapes impacting various glass/resin laminates, and compared the results with the analytical model of Wen (see Chapter 8). Fig. 5.12 reproduces the data. It is clear that FRPs perform better against the more blunt projectiles — as will now be appreciated, this is because more energy is absorbed in Phase I failure (TT compression).

One further effect recently brought to light (Crouch, 2013a), has been the effect of target curvature upon ballistic performance, especially blunt fragments, as in a typical helmet threat. Fig. 5.13 shows the schematic event in which the initial impact occurs against a more self-supporting structure and where the in-plane fibres have a vertical component to their penetration resistance. Phase I occurs under more lateral constraint, compared to a flat laminate, and Phase II occurs against higher, more resistive peeling forces. Phase II is delayed and becomes more reliant upon the plasticity (strain-to-failure) of the rear fibres/fabric plies. Under these conditions, one would expect the overall penetration resistance to be increased, as is observed with curved UHMWPE targets, but this is not the case for conventional glass fibre-reinforced phenolic resins (see Section 5.6.3.4).

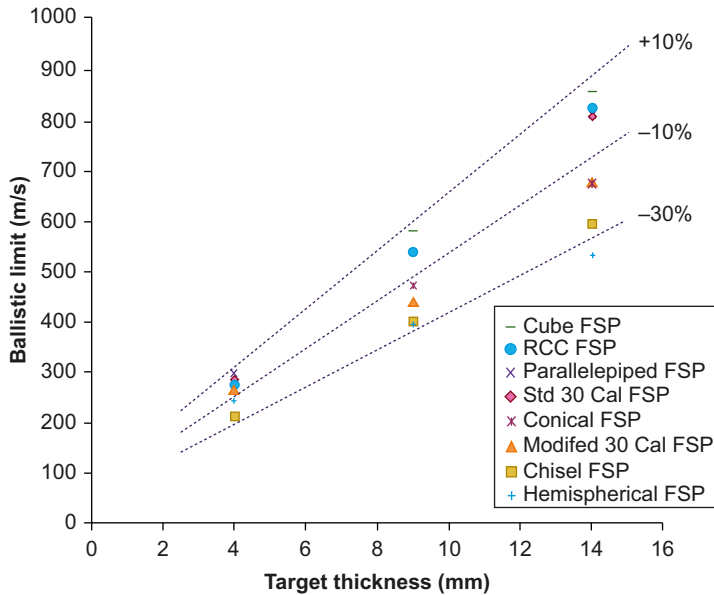


Figure 5.12 Effect of nose shape.

After Jordan, J.B., Naito, C.J., 2014. An experimental investigation of the effect of nose shape on fragments penetrating GFRP. *International Journal of Impact Engineering* 63, 63–71.

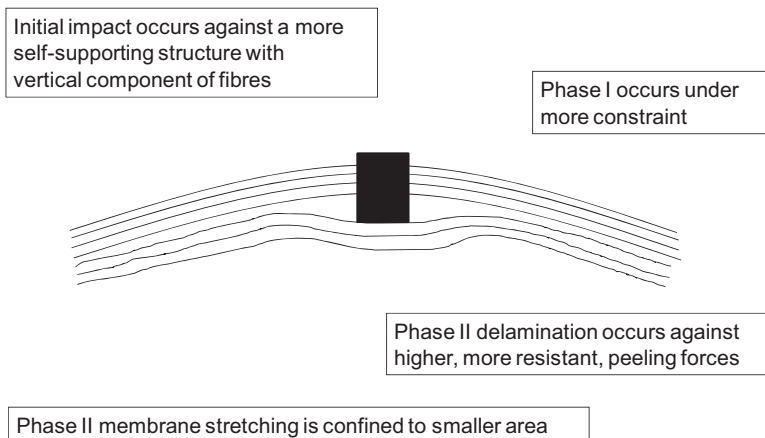


Figure 5.13 Schematic of failure mechanisms in curved targets against blunt objects.

After Crouch, I.G., 2013a. Next generation combat helmets. In: Paper Presented at the 3rd DMTC Annual Conference, March 2013, Canberra, Australia.

5.2 Polymers and resins

Unreinforced polymers, like their reinforced variants, do not make very good armour materials because of their very low tensile strength and high ductility. However, for

many other reasons, for example transparency, they do need to be used in applications that expose them to ballistic impact. These could be canopies for aircraft or laminated windows for armoured vehicles. They have also found niche applications such as spall covers [for hard armour plates (HAPs)] and eyewear (ballistic goggles) and will be introduced here, for completeness.

Table 5.1 lists essential mechanical properties for a range of thermoplastic polymers and thermosetting resins, whilst Fig. 5.14 shows a powerful schematic illustrating where these polymers sit on a spider map of physical properties. It should be noted that all of the engineering polymers, with attractive impact and ballistic properties, sit towards the very top of this chart.

5.2.1 Unreinforced polymers

The family of polyethylenes has been shown to be a very versatile group of armour materials with applications from catching materials (in RDOP tests), cover plates (on HAPs) and useful films for hot-stacking advanced laminates. Their properties vary widely depending upon polymer chain length (molecular weight) and morphology (degree of crystallinity), as can be seen in Fig. 5.15. For armour applications, the molecular weight normally exceeds 30,000 with the crystallinity at >50%.

They are classified into different grades by their bulk density values, as given in Table 5.2.

The LLDPE films, with a density $\sim 910 \text{ kg/m}^3$, have attractive forming characteristics (for hot-stacking), because of their low melt flow indices, and were used by Klintworth and Crouch (2002) to develop a unique manufacturing method for the

Table 5.1 List of mechanical properties of polymers

Polymer	Bulk density (kg/m^3)	Tensile strength (MPa)	Tensile modulus (GPa)	Elongation (in 50 mm) (%)
Acetals	1410	55–70	1.4–3.5	75–25
Acrylics	1190	40–75	1.4–3.5	50–5
Epoxies	1250	35–140	3.5–17	10–1
Nylon	1160	55–83	1.4–2.8	200–60
Phenolics	1135–2130	28–70	2.8–21	2–0
Polycarbonates	1200	55–70	2.3–3.0	125–10
Polyesters	1280	55–90	2–5	300–5
Polyethylenes	910–970	7–40	0.1–0.5	1000–15
Polyvinyl chloride	1330	7–55	0.014–4	450–40

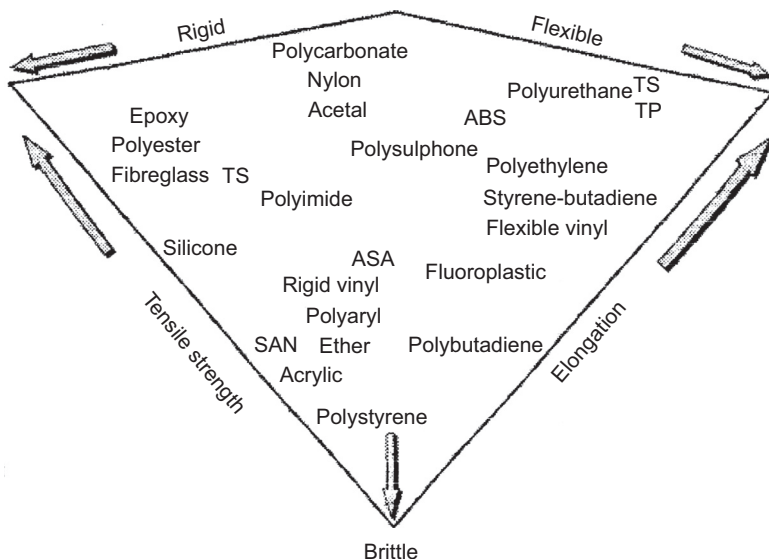


Figure 5.14 General classes of polymers.

From James, M., 2009. *Polymer Data Handbook*, second ed. Oxford University Press, Oxford, UK.

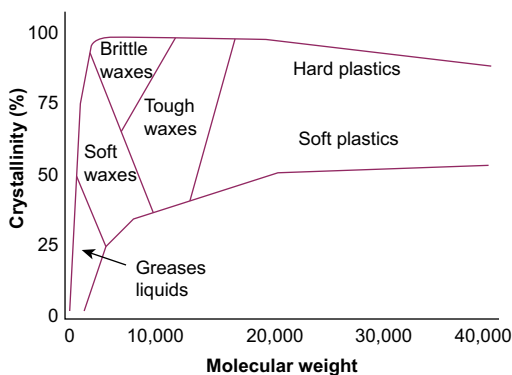


Figure 5.15 Classical phase diagram for polymorphs of polyethylene, showing dependence upon both crystallinity and molecular weight in determining physical state of this polymer. From James, M., 2009. *Polymer Data Handbook*, second ed. Oxford University Press, Oxford, UK.

backing laminates in HAPs (see Chapter 7). The LLDPE film, about 0.125-mm thick, was hot-stacked with a 308 gsm, K49 fabric, known as K900, under carefully controlled autoclave conditions, to prepare a very energy-absorbing backing layer for HAPs. Australian Defence Apparel (ADA) fully commercialised the process, during the 2000s, and sold many HAPs to international clients, using this proprietary process.

Table 5.2 Classification of the family of polyethylenes

Class of polyethylene	Abbreviated name	Bulk density (kg/m ³)
Linear low-density polyethylene	LLDPE	~ 910
Low-density polyethylene	LDPE	910–935
Medium-density polyethylene	MDPE	936–938
High-density polyethylene	HDPE	~ 950
Ultrahigh molecular weight polyethylene	UHMWPE	~ 970

HDPE has been used as an energy-absorbing catching layer in ballistic RDOP tests (Crouch, 1993) (see Fig. 5.11) and, of course, UHMWPE, with molecular weights in excess of 100,000, has been used to develop the ultrahigh-performing group of advanced fibres (see Chapter 6).

Wide ranges of other unreinforced polymers, principally thermoplastic polymers, are used in a number of niche applications, especially those requiring both transparency and impact resistance. These include the polycarbonates (PCs), polymethylmethacrylate (PMMA) and more recently modified nylons (Song et al., 2006). These materials have seen an extended period of use as transparent armours for windows, goggles and other applications where optical transparency and ballistic protection are required.

Historically, PMMA was recognised as a potential transparent armour in the 1940s as it was recognised as being tougher than most types of glass (Sands et al., 2004). In the 1960s, PC superseded PMMA, in many applications, owing to its much higher toughness, strength (nearly 300 times that of ‘single-strength’ glass) and ballistic efficacy. It also outperforms PMMA in thermal and flame resistance. Although PC is a superior ballistic material, it does have a number of drawbacks associated with its in-service use. Among these are its susceptibility to ultraviolet light (UV) and poor abrasion resistance. As such, hybrid systems are being developed based on PC/PMMA, PC/PMMA/glass, PC/PMMA/PU and newly modified transparent nylons (Sands et al., 2004; Hsieh et al., 2004; Song et al., 2006; Fountzoulas et al., 2009).

An added feature of these hybrid systems is their performance advantage over monolithic solutions on an areal density basis. For example, the work of Hsieh et al. (2004) notes that a PC-PMMA-PC laminate, tested against 0.22 cal FSP, of 22.6 kg/m² recorded a V-50 of 864 m/s, while a PC-only laminate of slightly higher areal density (23.5 kg/m²) yielded a ballistic limit of only 618 m/s. They report that the failure mechanism in the two materials differs, with PC demonstrating plugging behaviour, similar to that seen in metals, whilst PMMA exhibited ceramic-like, conoidal fracture which spreads the load transmitted to the back layer (Fig. 5.16).

In the case of torso and extended extremity protection applications (including helmets) the common PC and PMMA base materials are of particular interest because they are readily thermoformed into complex and high-tolerance geometries (Sands et al., 2004). Furthermore, their toughness (PC) combined with their ability to spread



Figure 5.16 Conoidal fracture behaviour observed in PMMA layer of PC-PMMA-PC laminate. Reproduced from: Sands, P., Patel, P., Dehmer, A., Hsich, M., October 2004. Protecting the future force: transparent materials safeguard the Army's vision. The AMPTIAC Quarterly, 8 (4).

the impact area through conoidal failure (PMMA) may be synergistic with ballistic fibre systems as an alternative strike face where geometries preclude the use of traditional ceramic solutions. This could be especially effective in promoting the defeat of high aspect ratio projectiles and fragments due to the amorphous structure of the plastics. In fact, recent modelling and experimental verification (Yong et al., 2010) suggest that a PC-PC-UHMWPE configuration presented a minimum weight solution for defeat of a specific threat (Fig. 5.17). This would suggest that plastic strike face configurations may be worth further exploration.

It is also worth noting that beyond the more common and traditional PC-, PMMA- and PU-based transparent plastic armours there are also some new transparent nylons available for ballistic applications (manufactured by Degussa). Work by Song et al. (2006) indicates that these materials have the potential to outperform both PC and PMMA on an areal density basis (Fig. 5.18). They are also noted to be suitable in hybrid applications and are therefore worthy of further investigation.

However, PCs are still the material of choice for ballistic goggles and, although PC has poor abrasion resistance, commercial lenses are coated with a scratch-resistant finish. The mechanical behaviour of polymers like PC at high strain rates and across a wide operating temperature regimen have been characterised by Siviour et al. (2005).

More recently, proprietary families of long-chain polymers, based upon polyurea and/or polyurethane, have been used as thick spray coatings for blast and spall resistance (Anon, 2015e). These highly ductile layers (up to several millimetres in thickness) can certainly enhance the blast-resistance of brick or concrete structures, and have also been applied to the underside of military vehicles (Anon, 2015a). However, when applied to the outer surface of HAPs, Crouch found that they were

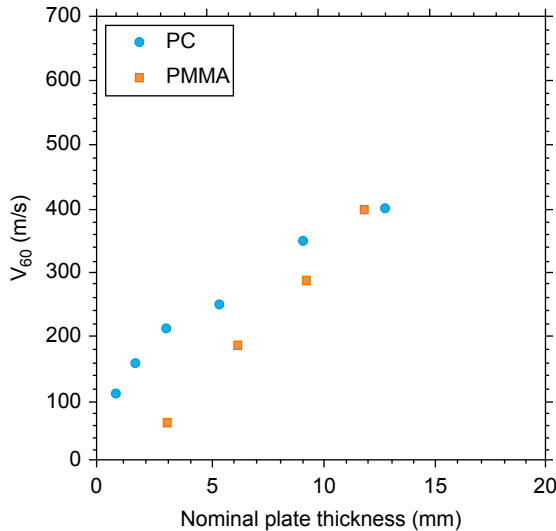


Figure 5.17 Extracts from the work of [Yong et al. \(2010\)](#) showing ballistic performance of PC and PMMA against 1.1 g FSPs.
Reproduced from: Yong, M., Iannucci, L., Falzon, B., 2010. Efficient modelling and optimisation of hybrid multilayered plates subject to ballistic impact. *International Journal of Impact Engineering*, 37 (6).

not ballistically efficient, compared with using fabric coatings, like ballistic nylon ([Crouch, 2013b](#)). They have, however, been reported to increase the multihit performance of ceramic-based systems, when sandwiching thin ceramic tiles (~ 3 -mm thick) in an envelope of a thick polymer film (also ~ 3 -mm thick) ([Ramsay, 2015](#)). At this stage, the authors are unsure of their true ballistic efficiency – nevertheless, such

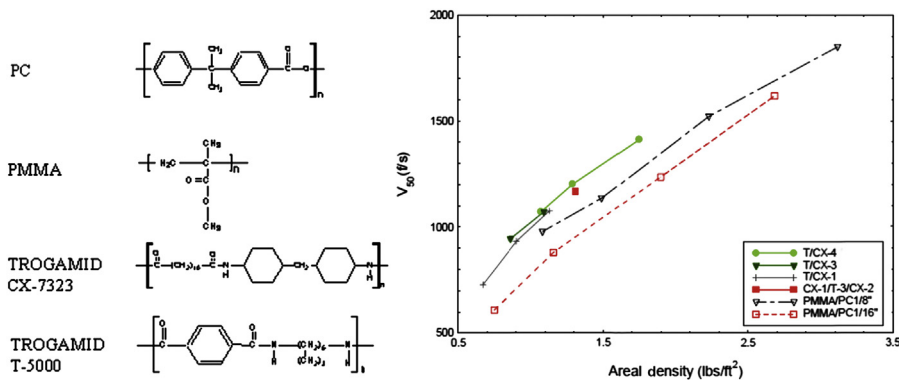


Figure 5.18 Chemical structure and V-50 versus AD data for transparent ballistic nylons.
After Song, J., Lofgren, J., Hart, K., Tsantinis, N., Paulson, R., Hatfield, J., November 2006. Aromatic Nylons for Transparent Armor Applications. U.S. Army Research Development and Engineering Command, Soldier Systems Center, Natick Soldier Center.

polymers are now available to the armour technologist, as part of possible blast mitigation strategies, though simply increasing the structural armour thickness is often more beneficial on a mass basis (Ackland et al., 2013).

5.2.2 Thermosetting resins

This group of polymers is traditionally used to manufacture the plethora of advanced composite materials used extensively in the marine, maritime, transport and aerospace markets. For armour applications, little attention has been given to their impact properties and/or high strain-rate behaviour and the choice of a particular grade is normally governed by other overriding, engineering requirements. Table 5.3 lists the general engineering properties of this range of thermosetting resins.

Both polyesters and phenolics have been used, worldwide, in the manufacture of spall liners, mainly the latter as it is inherently more fire-retardant. However, for structural armour applications and adhesively bonded laminates (ABALs; see Chapter 4), epoxy resins are more highly favoured.

In the early 1990s, Crouch, working with Harding and Ruiz at Oxford University, characterised the strain-rate dependency of Hysol 9309.3 (Crouch et al., 1994), a type of epoxy resin, approved for use within the aerospace industry (for secondary bonding) and in the armour field (for laminating and bonding). This set of data (see Fig. 5.19) was fitted to a Cowper–Symonds strength equation and used in numerical models to investigate critical failure modes associated with ABALs (see Chapters 4 and 9).

In unpublished work by Bourne, Howlett and Crouch (c.1993), Hugoniot curves for epoxy, glass and a polyester-based GFRP material (to MVEE 802) showed all to increase in stress with an increase in particle velocity, with results for the composite lying between that of glass and epoxy, as one would expect. The Hugoniot elastic limit (see Chapter 10) for the epoxy resin, Ciba–Geigy LY564, was also shown to be very similar to other advanced polymers like PMMA. In this same period, the polyester resin was found to have a shear wave speed of 1093 m/s and a longitudinal wave speed of 2302 m/s. More recently, the spall strength of GFRPs have been studied by Yuan et al. (2007) and, rather surprisingly, found that the spall strength for an E-glass composite was higher than for an S2-glass composite. They also reported that the longitudinal wave speed for an S2-glass polyester resin (Cycom 4102) was 3200 m/s.

5.3 Reinforcing fibres for hard armour

Chapter 6 addresses technical textiles for soft armour applications and, in so doing, covers many of the technical fibres (silk, nylon, aramid and polyethylene) and ballistic fabrics (weaves, knits and felts). Here, attention is given to those fibres (glass and carbon, as well as aramid and polyethylene) and fabrics that are laminated using either thermosetting or thermoplastic polymeric resins for hard armour applications. All such laminates are therefore constructed of layers, or plies, of fabric – a seemingly simple, but highly significant, feature.

Table 5.3 Brief summary of four main classes of thermosetting resins for armour applications

Resin type	Benefits	Drawbacks	Armour applications
Polyester	Low cost; easy to process; RT curing; moisture-resistant	Flammable; low mechanical properties; low operating temperature	Marine; spall liners; external fixtures
Vinylester	Medium cost; low viscosity; good mechanical properties; RT curing; chemical-resistant	Flammable; low operating temperature	Maritime; spall liners; laminated armours; VBRI components
Phenolic	Medium cost; nonflammable; good mechanical properties	Toxic ingredients; difficult to process; can be brittle	APC structures; spall liners; bulk heads; ablatives
Epoxy	Excellent mechanical properties; good chemical resistance; approved for structural use; high operating temperatures	Expensive; high processing temperatures	Structural composite armours; ABALs; adhesive layers

In [Section 5.1.2](#), penetration failure modes in laminated composites were discussed and the main energy-absorbing mechanisms identified (see [Fig. 5.8](#)). This leads to an understanding of the required properties of the solid laminate, or sublaminates. In turn, this dictates what type of microstructure is desirable for a penetration-resistant, laminated composite. [Table 5.4](#) summarises these requirements. From this new perspective, it becomes clear that fibre type, and fabric form, are the two most important selection criteria when developing a ballistic laminate. For a practical, multistrike laminate, which minimises the extent of delamination, it is also important to select a resin that provides a sufficiently strong resin-to-fibre interfacial bond. However, this can be an elusive balancing act.

In 1991, Pervorsek et al. first published a diagram showing the strong relationship between the specific tensile modulus of ballistic fibres and their tenacity. Crouch has recently updated this important relationship by including data for newly developed fibres (see [Fig. 5.20](#)). The upward trend for the ballistic fibres (glass, aramid and UHMWPE) is very clear and shows that the most recently developed variants of UHMWPE have now surpassed the values for Zylon, a PBO fibre claimed in the 2000s to be the ‘fibre of the future’. It is also clear from this new diagram that the more structural fibres, like K149, the steels and the carbon fibres (especially the HM variants) sit consistently above the trend line for the ballistic fibres. It also confirms that the ‘goal’ data, originally laid down for the development of the M5 fibre, were probably erroneously set! The data point for HT-700 carbon fibre suggests that

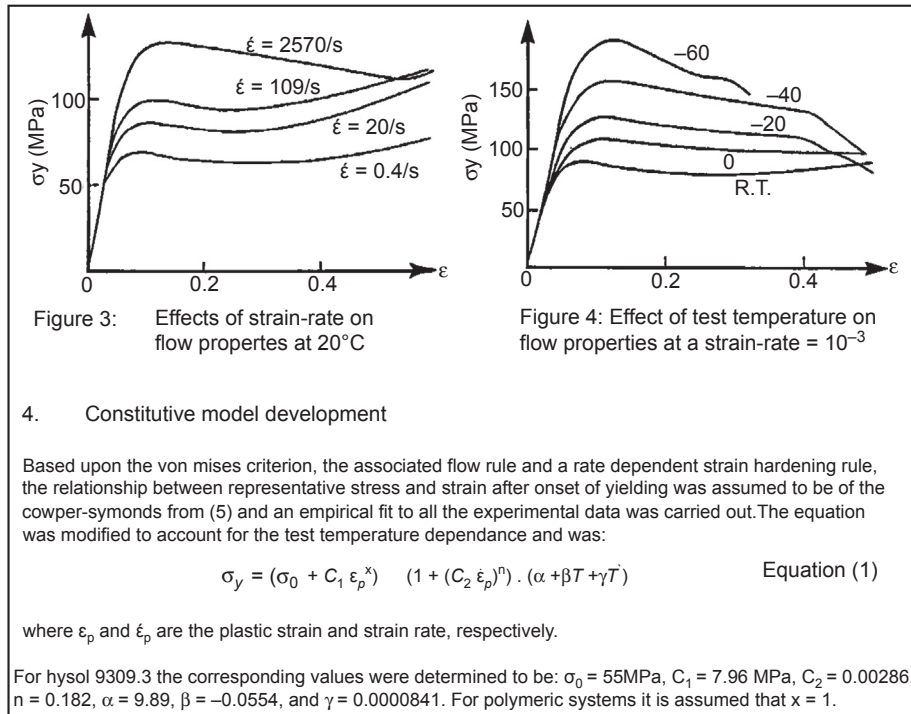


Figure 5.19 Extract from paper by [Crouch et al. \(1994\)](#), showing strain-rate characteristics of an epoxy material.

Reproduced from: Crouch, I.G., Greaves, L.J., Ruiz, C., Harding, J., September 1994. Dynamic compression of toughened epoxy interlayers in adhesively bonded aluminium laminates. Supplement to Journal de Physique III, Colloque C8 4, 201–206.

these HT variants might be the most suitable in hybrid laminates designed to cope with both structural loads and ballistic impacts.

During the US Army's programmes of the 1990s, like the Composite Armor Vehicle (CAV) and Future Combat Systems (FCS) programmes, various families of fibre-reinforced polymers were reviewed and considered as potential Composite Integral Armor (CAI) systems. At that time, glass fibres (in the form of an S2-glass reinforced vinylester resin) were considered to offer the best balance of weight, stiffness, and availability and, of course, cost. In the 1990s, UHMWPE fibres were not readily available in volume production and their mechanical properties were (and still are) considered to be far too low for structural vehicular applications. The following section discusses the advantages and disadvantages of each family of fibres.

5.3.1 Glass fibres

With a bulk density of $\sim 2620\text{ kg/m}^3$, E-glass fibres, manufactured from aluminoborosilicate, have been used for decades in traditional, nonaerospace markets such as transportation and marine/maritime. For example, many tonnes of a coarsely woven E-glass fabric, with low-volume fibre fraction, were used in every Huon class

Table 5.4 Required property against each of the six microstructural failure mechanisms (linked to Fig. 5.8)

#	Mechanism	Required property
1	Through-thickness compression of the entire laminate	<ul style="list-style-type: none"> • High fibre volume fraction • High transverse/flexural modulus for fibres
2	Transverse shear of front-face ply or plies	<ul style="list-style-type: none"> • High transverse shear strength for fibres
3	Crushing and local shearing of the comminuted fibre/resin mix	<ul style="list-style-type: none"> • High shear modulus of comminuted conglomerate of fibres and resin
4	Delamination along interlaminar planes	<ul style="list-style-type: none"> • High interlaminar shear strength, for the laminate (especially the interply regions)
5	Flexing of the rear plies, as individuals or as a sublaminate	<ul style="list-style-type: none"> • High flexural modulus of the rear sublaminate
6	Final, in-plane tensile failure of fibres in rear plies	<ul style="list-style-type: none"> • High strain-to-failure value for fibres in the rear sublaminate

Source: Crouch (2015).

minehunter built for the Royal Australian Navy (RAN) in the 1990s (see [Section 5.5.4.1](#)) but, for blast applications, their low modulus was very important for the monocoque structure to be adequately compliant. However, for ballistic applications, S-glass, manufactured from magnesium–aluminosilicate, is the preferred grade since both its strength and modulus values are much higher, as well as strain-to-failure (5.7% compared with 4.6%). The bulk density is also significantly lower, at 2480 kg/m³. Filament diameters are also much larger (~20 µm compared with ~7 µm). Owen–Corning’s S2-glass fibre became the material of choice in the 1990s for most armour applications, like small logistic vehicles and spall liners for APCs. Produced with a higher level of silica than standard glass fibre products, S-2 glass fibres offer enhanced physical properties including higher tensile and compressive strength, higher temperature resistance and improved impact resistance.

As of 2015, S-2 glass products are now made exclusively by Advanced Glassfiber Yarns (AGY) and are supplied in various grades to a wide variety of markets for applications such as helicopter blades, aircraft flooring and interiors, high-strength timing belts, as well as selected armour products. A lighter-weight variant, branded ‘Featherlight S-2 Glass’ ([Anon, 2010](#)) was introduced in 2008 and can provide weight savings of ~5% over standard S-2 glass-based solutions ([Anon, 2010](#)) (see [Fig. 5.21](#)). The fibres are certified and meet military specifications MIL-R-60346 (Type IV for rovings and MIL-Y-1140H for yarns). While S2-glass fibres are many times more expensive than E-glass fibres, they are still one of the least expensive ballistic materials.

AGY produces D450, G150 and G75 yarns with a starch/oil size system optimised for weaving processes where fabrics will be heat-cleaned and finished with fabric finishes. These yarns consist of numerous filaments twisted together to form single yarns. The chemistry of the sizing material used on the fibres protects the glass

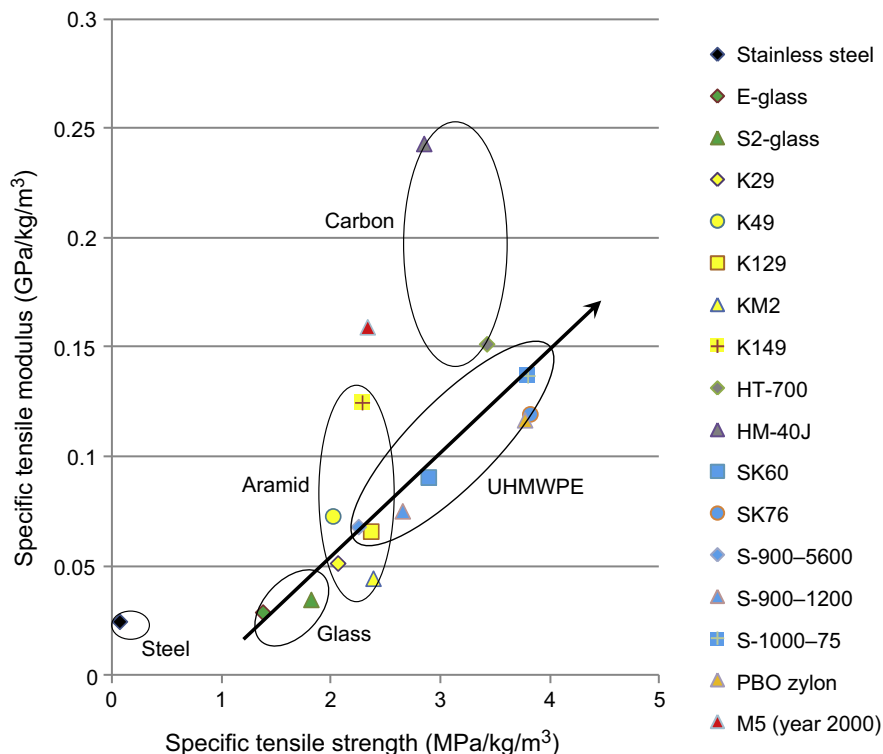


Figure 5.20 Relationship between tensile modulus and tenacity for a range of structural and ballistic fibres.

Source: Crouch (2015).

filaments from abrasion during processing and is typically removed after processing. Fabrics are available with a range of resin-compatible sizes/finishes.

The availability of glass fibres for both structural and/or ballistic applications has benefitted from the drive, since 2003, for lightweighting and cost reduction in military platforms. They do remain a very competitive armour material. The ballistic performance against the full suite of fragment simulating projectiles is shown in Fig. 5.22, comparing the 'Featherlight' variant against the standard S-2 glass fibre (Anon, 2010).

5.3.2 Carbon fibres

The very nature of carbon fibres makes them unsuitable for most armour applications: they have very high specific stiffness values and low strain-to-fail values. Nevertheless, they do find niche applications in armour systems, such as stiff supporting layers for a brittle ceramic (see Section 7.9), or as buffer or stripper layers in ceramic systems. A number of demonstration vehicle programmes, especially in the United States, have also investigated the feasibility of using carbon-based fabrics in hybrid structural solutions (Ogorkiewicz, 2015).

Since their invention in the early 1970s, at RAE (Farnborough) in the United Kingdom, numerous grades have evolved, based upon a raft of manufacturing techniques. These have been reviewed by Huang (2009), who concluded that

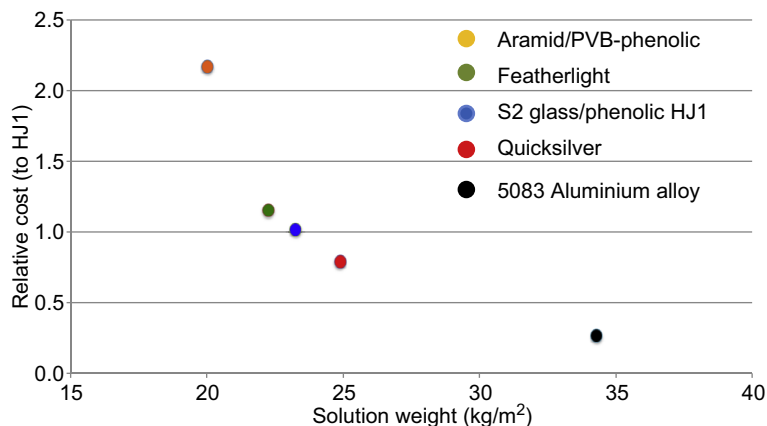


Figure 5.21 Relative cost and areal weight of three variants of glass fibre-based armour solutions against the 0.3" FSP threat with a V-50 value of 760 m/s.

Reproduced from: Anon., 2010. AGY Featherlight. AGY website. www.agy.com.

polyacrylonitrile and mesophase pitch are the most important carbon fibre precursors, and that cost reduction, amongst others, remain the major challenges, especially for applications outside of the aerospace industry. Manufacturing companies, such as ACP Composites now supply large-sized tows, up to 50K, available at much reduced prices (\$/kg) but uptake is still relatively slow. In Australia, Carbon Nexus, in Geelong, lead the R&D efforts to find commercialisation outlets in nonaerospace markets.

The strength and modulus values for a range of commercial PAN-based carbon fibres are summarised in Table 5.5, whilst Fig. 5.23 illustrates the wide range of products available.

Like all other composite materials, carbon fibre-reinforced plastics are very anisotropic and the properties of the finished laminate will depend upon a number of key parameters like:

1. Grade of carbon fibre and resin matrix;
2. Fibre volume fraction;
3. The form of the fibre: woven, nonwoven, etc.;
4. Fibre orientation and layup sequence;
5. The uniformity of fibre distribution.

As a potential armour material, factors like surface hardness, mode of failure and abrasion resistance should also be considered. Of course, their low bulk density ($\sim 1550 \text{ kg/m}^3$) is an advantage and, on occasions, their low coefficient of thermal expansion is attractive.

5.3.3 Aramid fibres

Section 6.2.5 gives a detailed account of the chemistry and physical properties of all the evolutionary grades of aramid fibres, and principally those used in the soft body armour market. Here, the focus is upon structural armours and laminated variants.

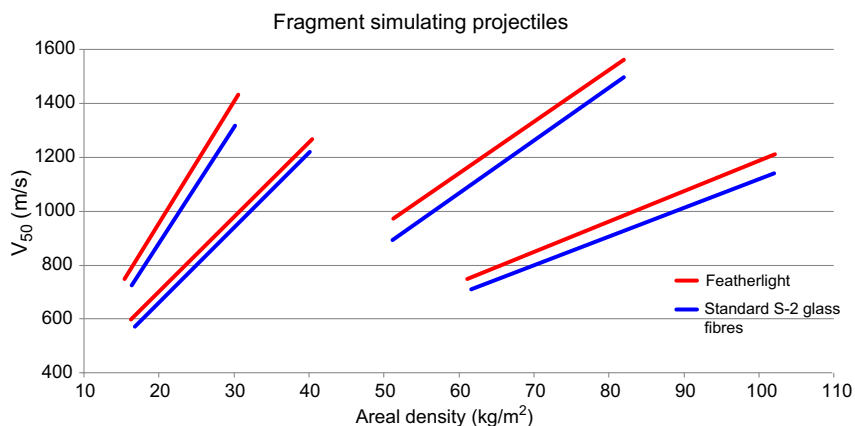


Figure 5.22 Ballistic performance of two grades of GFRP against, from right to left, 5.56, 7.62, 12.5 and 20 mm FSPs.

From Anon., 2010. AGY Featherlight. AGY website. www.agy.com.

For this purpose, the higher modulus grades are preferred, like the K49 fibre from DuPont. Because these fibres/fabrics need to be laminated, their surface finish is very important and, quite often, will be provided in the scoured condition. Typical properties of different fibres are shown in Table 5.6 (see also Table 6.2, in Chapter 6).

An ultrahigh modulus grade, K149, was introduced in the 1990s but never established itself as a commercial product. DuPont, and other suppliers, have preferred to develop new fibres for the body armour market rather than structural grades for hard armour applications. In the early 2000s, DuPont released a new type of aramid fibre, Kevlar KM2, which is now used extensively for body armour applications, especially in the United States. This fibre is a transversely isotropic material. Its tensile stress–strain response in the axial direction is linear-elastic until failure.

A new aramid product from DuPont, initially known as Kevlar XP500, and now commercially produced as S102 (Anon, 2015c), can consistently stop a .44 Magnum bullet in the first two to three layers of an 11-layer ballistic panel/vest. Developed primarily for the soft armour market, it is cost-competitive with solutions based upon conventional woven aramid fabrics. Hard armour applications are few and far between but Crouch and Jaitlee used it, in laminated form, when studying the interdependence between soft armour inserts and hard armour plates (Jaitlee, 2013).

Technora is another aramid, which is produced in Japan by Teijin; it has a slightly lower modulus than Kevlar 29 but a slightly higher resistance to flexural fatigue. The fibre's lower UV resistance is enhanced by dyeing the naturally gold fibre black. Technora is most often used as bias support (the cross-ply) in laminated sailcloth. Twaron is another aramid fabric which is produced in The Netherlands by Teijin. It is chemically and physically similar to DuPont's Kevlar. Twaron HM (High Modulus) has similar stretch properties to Kevlar 49, greater tensile strength and better UV resistance and Twaron SM is similar to Kevlar 29. Like Kevlar, the fibre is a bright gold colour.

Table 5.5 List of key mechanical properties for grades of carbon fibre

Grade	Tensile modulus (GPa)	Tensile strength (GPa)	Country of manufacture
HT – T300	230	3.53	France/Japan
HT – T700	235	5.3	Japan
HT – AS4	241	4.0	USA
HT – Panex 33	228	3.6	USA/Hungary
IM – T800	294	5.94	France/Japan
IM – IM6	303	5.10	USA
IM – T40	290	5.65	USA
HM – M40	392	2.74	Japan
HM – M40J	377	4.41	France/Japan
UHM – M46J	436	4.21	Japan
UHM – UHMS	441	3.45	USA

Anon., 2015d. Gurit Website. www.gurit.com.

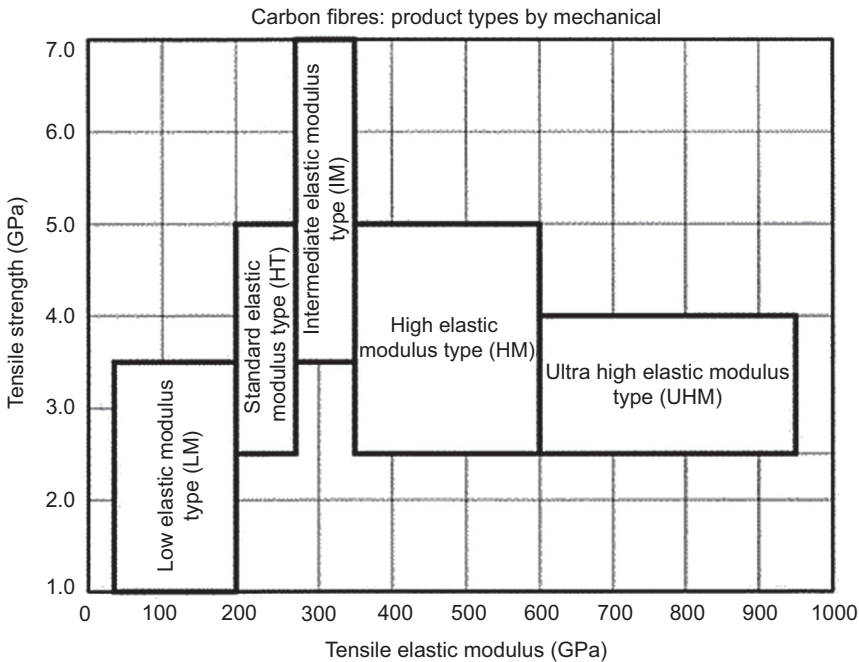


Figure 5.23 Graphical representation of variations in tensile modulus and strength values for carbon fibres, from Clearwater Composites.

Reproduced from: Anon., 2015b. Clearwater Composites Website. <https://www.clearwatercomposites.com/>.

5.3.4 Polyethylene fibres

Chapter 6 deals with these UHMWPE fibres, in detail, since they are now extremely popular as generic materials in soft armour inserts. However, whilst the range of fibres is the same, the matrices do differ depending upon their application, so only those relevant to hard armour technology are covered here. UHMWPE fibres are used in ballistic vests, ballistic helmets and ballistic vehicle protection, as well as bow strings, climbing equipment, fishing line, spear lines for spear-guns, high-performance sails, suspension lines on sport parachutes, rigging in yachting, kites, and kite lines for kite sports. Spectra is also used in a high-end Wakeboard line.

Dyneema is a registered trademark of DSM (the Netherlands) and was invented by DSM in 1979. It has been in commercial production since 1990 at a plant in Heerlen, the Netherlands. In the Far East, DSM has a cooperation agreement with Toyobo Co. for commercial production in Japan. In the United States, DSM has a production facility in Greenville, North Carolina, which is the largest production facility in the United States for UHMWPE fibre. Allied Signals, commercially licensed the technology in the United States back in the 1980s. Today, Honeywell continue to develop a whole range of UHMWPE fibres under the brand name of Spectra. Although the production details are somewhat different, the resulting materials are very comparable in properties. Other trade names for consolidated UHMWPE materials include TIVAR, by Quadrant EPP Inc., Polystone-M, by Röchling Engineering Plastics, Tensylon, by Integrated Textile Systems, and GARDUR by Garland Manufacturing.

Dyneema and Spectra are gel spun through a spinneret to form oriented-strand synthetic fibres of UHMWPE, which have yield strengths as high as 2.4 GPa and a bulk density as low as 970 kg/m³, like Dyneema SK75. High-strength steels have comparable yield strengths, and low carbon steels have yield strengths much lower (around 0.5 GPa). Since steels have a bulk density of approximately 7800 kg/m³, this gives strength/weight ratios for these materials 10–100 times higher than for steel. Strength to weight ratios for UHMWPE fibres are about 50% higher than for the aramid fibres.

Table 5.6 Typical properties of selected aramid fibres

Fibre grade	Bulk density (kg/m ³)	Elastic modulus (GPa)	Tensile strength (MPa)	Strain-to-failure (%)
Technora	1.39	74	3400	4.5
Twaron HM	1.45	110	3100	2.2
Kevlar 29	1.44	74	2965	3.5
Kevlar 129	1.44	95	3400	3.4
Kevlar 49	1.44	105	2900	2.5
Kevlar KM2	1.44	64	3430	4.3
Kevlar 149	1.49	186	3400	2.0

Unidirectional, biaxial and quadriaxial variants of fabrics are available using a range of different fibre grades and matrix resins. These are supplied in rolls of thin sheets, with typical weights between 100 and 300 gsm. Fabricators then use platen pressing (see [Section 5.5.1](#)) or compression moulding (see [Section 5.5.2](#)) to convert the fabrics into useable armour products, with fibre volume fractions normally in excess of 80% (see [Fig. 5.24](#)). These can range from flat panels (for up-armouring saloon cars) to deep-drawn helmet shells (see [Section 5.6.3](#)). [Nguyen et al. \(2015\)](#) have recently reported on the ballistic performance of UHMWPE laminates up to 100 mm in thickness and have shown how superior this family of ballistic materials is.

Since the late 1980s, Crouch has observed that products from the two main suppliers (Honeywell and DSM) have been very similar in structure, properties and ballistic performance, and he believes this is the same for today's products. Unfortunately, Crouch only has direct experience of Honeywell products from 2000 to 2013, during his time with Australian Defence Apparel, Melbourne, Australia. The following comments in this section are consequently based upon those grades, as supplied by Honeywell.

[Table 5.7](#) summarises the historical evolution of a range of products from both suppliers. Crouch also recollects there being a world shortage for this family of materials in the early 2000s when huge quantities were being used for personal body armour systems, especially those manufactured in the United States. Since then, supply has outpaced demand and, better still, the product has markedly improved, year-on-year, in terms of ballistic performance and mechanical properties,

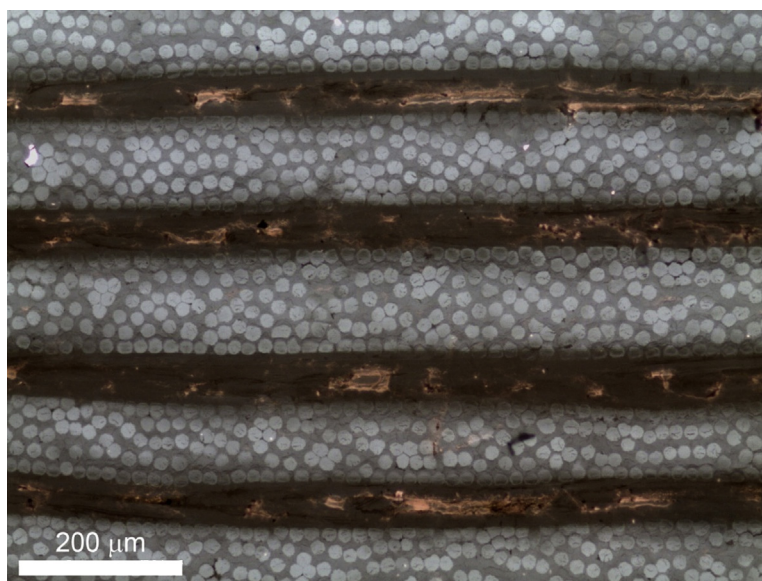


Figure 5.24 Cross-section through a UHMWPE laminate, based upon HB26 fabric from DSM. Reproduced from: Nguyen, L.H., Ryan, S., Cimpoeu, S.J., Mouritz, A.P., Orifici, A.C., 2015. The effect of target thickness on the ballistic performance of UHMW polyethylene composite, *International Journal of Impact Engineering*, 75, 174–183.

Table 5.7 Summary of different UHMWPE products from Honeywell and DSM

Supplier	Grade	Approximate date of supply	Weight of product (gsm)	Number of plies	Fibre grade	Resin matrix	Melting point (°C)	Recommended use	Comments
Honeywell	PCR Plus	2000	95	2	Spectra 1000	NK	NK	Hard armour backings	Low AD
Honeywell	PCRw	2000	250	4	Spectra 1000	NK	NK	Hard armour backings	
Honeywell	SR3124	2006	257	4	Spectra 3000	Kraton?	147	Backings, multistrike	Tacky, compliant product
Honeywell	SR3130	2008	257	4	Spectra 3000	PU-based	147	Backings, multistrike	See DMTC data
Honeywell	SR3136	2009	257	4	Spectra 3000	PU-based	150	Backings, single strikes	Firm, higher modulus product
Honeywell	SR3137	2009		4	Spectra 3000	PU-based	NK	Helmets, plus backings	Suitable for D4 process
Honeywell	SR4221	2013	257	4	Spectra 4000	NK	150	Multipurpose	Similar performance to SR3136

Continued

Table 5.7 Continued

Supplier	Grade	Approximate date of supply	Weight of product (gsm)	Number of plies	Fibre grade	Resin matrix	Melting point (°C)	Recommended use	Comments
Honeywell	SR5143	2014	163	4	NK	NK	NK	Hard armour backings	Compliant, Broad BFS
Honeywell	SR5231	2014	167	4	NK	NK	NK	‘Structural’ grade	High rigidity, low BFS
DuPont	Tensylon	2010	110	2	NK	PE adhesive on one side	147	Vehicle, HAPs, HAP backings	Excellent multihit performance
DSM	HB2	2004	NK	NK	NK	NK	NK	Ships, aircraft, vehicles, HAPs, backings	Early variant
DSM	HB26	2004	264	4	SK76	PU-based	155	Ships, aircraft, vehicles, helmets, HAPs, backings	Suitable for helmets
DSM	HB50	2010	233	4	NK	Rubber-based	150	Ships, helicopters, HAP’s	
DSM	HB80	2010	145	4	SK76	PU-based	151	Vehicles, ships, helmets	Developed US (Tokareva)
DSM	BT10 (tape)	2009	168	NK	NK	Self-reinforced (woven tape)	151	Structural armour applications, backings	Suitable for helmets

Disclaimer: information contained in this table is, to the authors’ knowledge, true and accurate. However, because data related to the grade of fibre and resin matrix are highly proprietary, the information is only of a general nature.

Source: Crouch and Thomas, DMTC (2015).

offset only by increased prices. Until c.2006, all of these grades were very unsuitable for structural applications of any sort, even helmets. In fact, Crouch can recall that he could carry out a four-point-bend test on first-generation UHMWPE laminates simply by using his fingers!

UHMWPE products do, however, make exceptionally good backing materials for ceramics in the construction of HAPs for body armour systems (BASs). Early products were only two-ply sheets (see PCR Plus, c.2000) and therefore numerous plies (approximately 100) were usually required for a backing laminate. Since then most products have been four-ply sheets of cross-ply UD fibres. Grade SR3124 was very popular for many HAPs produced for the Australian Defence Force in the 2000s. When processed in an autoclave, it produced very compliant laminates with a tacky surface finish. The grade was selected for its forgiving nature under multihit conditions. During the late 2000s, new grades became available which were manufactured using different proprietary matrix materials, based upon polyurethane: SR3130 and subsequently SR3136 were significant improvements over SR3124, especially for single-strike performance. The DMTC research team throughout 2009–2013 has determined a range of mechanical and physical property data. A quantum jump in mechanical properties came about with the evolution of SR3137, which has been specifically developed by Honeywell for use in construction of combat helmets. Most recently, c.2014, both fibres and matrices have been further developed and grades SR5143 and SR5231 are now commercially available. Honeywell recommend SR5231 be selected for solutions requiring reduced trauma, excellent multihit performance and a 20–25% increase in V-50 values (compared with SR3136) against high-velocity rifle rounds. SR5143 is recommended for the lightest solutions against M80 ball ammunition and high-energy fragments. Hybrid solutions of these two grades may also bring about a better balance of ballistic characteristics.

Details of comparable grades of DSM Dyneema fabrics are also shown in [Table 5.7](#): HB2, HB26, HB50 and HB80. These products are similarly used for hard armour applications. DSM also point out that their highly compressed laminates are capable of defeating mild steel-cored ammunition, as well as standard NIJ Level III ammunition without any ceramic facing. In fact, DSM place more emphasis on the effects of consolidation pressure upon ballistic performance and provide details of processing requirements ([Anon, 2004b](#)).

As a group, this family of ballistic materials is now being developed for combat helmet applications. Following many years of development (see [Section 5.6.3.3](#)) the DMTC have demonstrated a holistic capability to design, develop and manufacture, combat helmets using materials like SR3130, SR3136 and HB80 ([Cartwright et al., 2015](#)). UHMWPE in tape form, like BT10, is also becoming very popular, with a patent action from the United States ([Bhatnagar et al., 2015](#)).

5.4 Woven fabrics for hard armours

In polymeric composite terms, a fabric is defined as a manufactured assembly of long fibres to produce a flat sheet of one or more layers of fibres. These layers are held together

either by mechanical interlocking of the fibres themselves or with a secondary material to bind these fibres together and hold them in place, giving the assembly sufficient integrity to be handled. Fabric types are categorised by the orientation of the fibres used, and by the various construction methods used to hold the fibres together. The main fibre orientation categories are: unidirectional, 0/90 (woven, stitched or hybrid), multiaxial, and other/random. Fibres and woven fabrics are described in more detail in Chapter 6.

5.4.1 Fabric style

These can range from plain, tightly woven fabrics to noncrimp fabrics (NCFs). Woven fabrics are produced by the interlacing of warp (0°) tows and weft (90°) tows in a regular pattern or weave style. The fabric's integrity is maintained by the mechanical interlocking of the fibres. Drape (the ability of a fabric to conform to a complex surface), surface smoothness, and the stability of a fabric are all controlled primarily by the weave style. The areal weight, porosity and (to a lesser degree) wet out (the ability of a fluid to infiltrate the woven fabric) are determined by selecting the correct combination of tow size and the number of fibres/cm. Some of the more commonly found weave styles are described below.

- Plain weave
Each warp tow passes alternately under and over each weft tow as shown in Fig. 5.25. The fabric is symmetrical, with good stability and reasonable porosity. However, it is the most difficult of the weaves to drape, and the high level of fibre crimp imparts relatively low mechanical properties compared with the other weave styles. With large tow sizes (high tex) this weave style gives excessive crimp and therefore it tends not to be used for heavy fabrics.

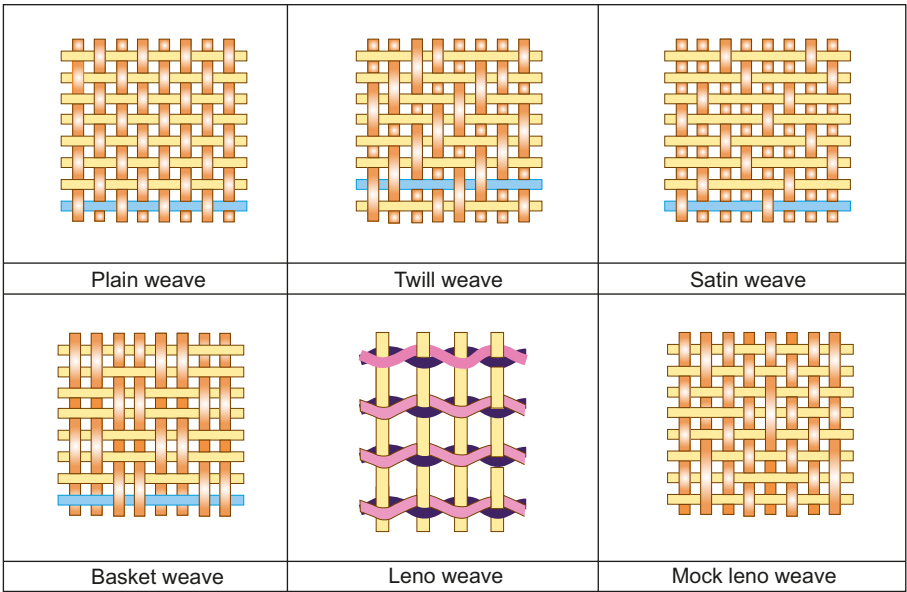


Figure 5.25 Schematic of common weave styles for both ballistic and structural laminates.

- **Twill weave**
One or more warp tows alternately weave over and under two or more weft tows in a regular repeated manner as per Fig. 5.25. This produces the visual effect of a straight or broken diagonal ‘rib’ to the fabric. Superior wet out and drape is seen in the twill weave over the plain weave with only a small reduction in stability. With reduced crimp, the fabric also has a smoother surface and slightly higher mechanical properties.
- **Satin weave**
Satin weaves are fundamentally twill weaves modified to produce fewer intersections of warp and weft as per Fig. 5.25. The ‘harness’ number used in the designation (typically 4, 5 and 8) is the total number of fibres crossed and passed under, before the fibre repeats the pattern. A ‘crowsfoot’ weave is a form of satin weave with a different stagger in the repeat pattern. Satin weaves are very flat, have good wet out and a high degree of drape. The low crimp gives good mechanical properties. Satin weaves allow fibres to be woven in the closest proximity and can produce fabrics with a close ‘tight’ weave. However, the style’s low stability and asymmetry needs to be considered. The asymmetry causes one face of the fabric to have fibre running predominantly in the warp direction, while the other face has fibres running predominantly in the weft direction. Care must be taken in assembling multiple layers of these fabrics to ensure that stresses are not built into the component through this asymmetric effect.
- **Basket weave**
Basket weave is fundamentally the same as plain weave except that two or more warp tows alternately interlace with two or more weft tows as per Fig. 5.25. An arrangement of two warps crossing two wefts is designated 2×2 basket, but the arrangement of fibre need not be symmetrical. Therefore it is possible to have 8×2 , 5×4 , etc. Basket weave is flatter, and, with less crimp, stronger than a plain weave, but less stable. It must be used on heavy-weight fabrics made with thick (high tex) fibres to avoid excessive crimping.
- **Leno weave**
Leno weave improves the stability in ‘open’ fabrics, which have a low fibre count as per Fig. 5.25. It is a form of plain weave in which adjacent warp fibres are twisted around consecutive weft fibres to form a spiral pair, effectively ‘locking’ each weft in place. Fabrics in leno weave are normally used in conjunction with other weave styles because if used alone their openness cannot produce an effective composite component.
- **Mock leno weave**
This is a version of plain weave in which occasional warp tows, at regular intervals but usually several tows apart, deviate from the alternate under–over interlacing and instead interlace every two or more tows as per Fig. 5.25. This happens with similar frequency in the weft direction, and the overall effect is a fabric with increased thickness, a rougher surface and additional porosity.

The general properties of these various weaves are compared in Table 5.8: the best-performing fabrics are those that have low crimp and low porosity, namely the satin weaves. Of these, a 5HS (Harness Satin) and an 8HS weave are particularly attractive for ballistic protection (Crouch, 2009b).

5.4.2 Three-dimensional fabrics

For completeness, the topic of 3D fabrics is covered here. They are not normally considered for soft vest applications because they are too stiff and restrict interply slippage. However, some researchers have looked at the various effects of z-stitches

Table 5.8 Comparative fabric properties of different weaves

Property	Plain	Twill	Satin	Basket	Leno	Mock leno
Stability	****	***	**	**	*****	***
Drape	**	****	*****	***	*	**
Low porosity	***	****	*****	**	*	***
Smoothness	**	***	*****	**	*	**
Balance	****	****	**	*****	**	****
Symmetrical	*****	***	*	***	*	****
Low crimp	**	***	*****	**	**/*****	**

Key: *, Poor; *****, Excellent.

in a composite armour laminate, as illustrated in Fig. 5.26. It has been shown that most forms of z-stitching reduce the extent of the delamination – however, the presence of z-stiches does limit the maximum volume fraction of in-plane fibres attainable, which, in turn, reduces the ballistic properties of the laminate (compared with normal 2D laminates).

5.4.3 Hybrid fabrics

The term hybrid refers to a fabric that has more than one type of structural fibre in its construction. In a multilayer laminate, if the properties of more than one type of fibre are

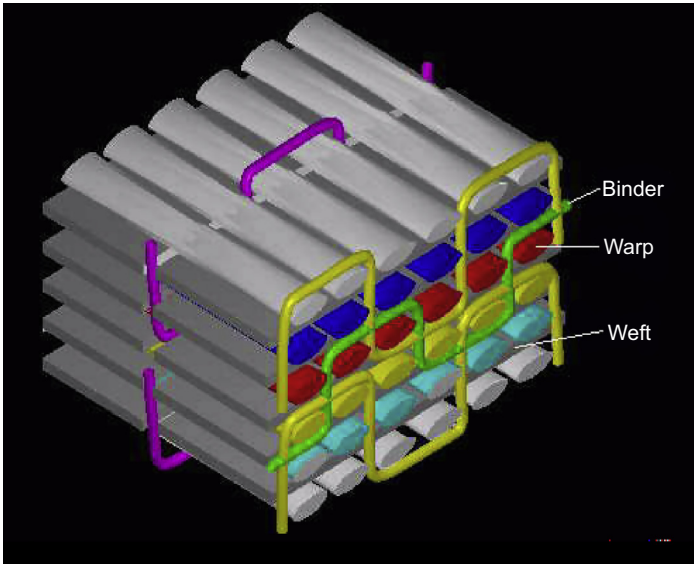


Figure 5.26 A multi-ply noncrimp fabric showing various z-stitching patterns. Source: Coman, RMIT, 2009.

required, then it would be possible to provide this with two fabrics, each containing the fibre type needed. However, if low weight or extremely thin laminates are required, a hybrid fabric will allow the two fibres to be presented in just one layer of fabric instead of two. It would be possible in a woven hybrid to have one fibre running in the weft direction and the second fibre running in the warp direction, but it is more common to find alternating threads of each fibre in each warp/weft direction. Although hybrids are most commonly found in 0/90 woven fabrics, the principle is also used in 0/90 stitched, unidirectional and multiaxial fabrics. The most common hybrid combinations are:

1. Carbon/aramid

The high impact resistance and tensile strength of the aramid fibre combines with the high compressive and tensile strength of carbon. Both fibres have low density but relatively high cost.

2. Aramid/glass

The low-density, high impact resistance and tensile strength of the aramid fibres are combined with the good compressive and tensile strength of glass, coupled with its lower cost.

3. Carbon/glass

Carbon fibre contributes high tensile compressive strength and stiffness and reduces the density, while glass reduces the cost.

Whilst most of these hybrid fabrics are well used in the boat-building industry and for sporting applications, they are not normally used in ballistic applications because the effectiveness of the high-performance fibres (ie, aramid) is simply diluted by the hybridising fibres (glass and carbon).

5.5 Processing routes: general introduction

The many methods of manufacturing conventional composite materials and structures are comprehensively covered elsewhere (Davê and Loos, 1999; Campbell, 2003; Baker et al., 2004). However, for armour products, it should be remembered that the main contributor to a mass-efficient, fibre-reinforced laminate is a high volume fraction of fibres. So, all of the following processes, covered in this section, are aimed at achieving high V_f values, in combination with an adequate fibre–resin bond, whilst meeting any overriding engineering requirements and cost-effective working practices.

Liquid moulding techniques, especially for large composite structures, have received specific attention since the 1990s as reported by Rudd et al. (1997), Summerscales and Searle (2005), and Kruckenberg and Paton (2012). In particular, John Summerscales' work at Plymouth University, UK, reviewed all relevant processes in 2005 and, amongst much else reported, the huge list of acronyms that reflect the endless variations of resin transfer moulding and vacuum-assisted variants: VARTM, CIRTM, RIFT, VARI, etc.

5.5.1 Platen pressing

This is the traditional way of producing commercial quantities of spall liners. Being flat and typically in panels about 1 m × 2 m in area, these precision products lend

themselves to platen pressing using a high-pressure (HP) hydraulic press. The fabrics are normally hand-laminated and then laid-up prior to transferring into the platen press. High pressures are then used to maximise fibre volume fraction (typically around 65%). The use of room temperature curing resins permits completion of the processing cycle within the press.

A variant of this process was developed by Crouch and his team at ADI (now Thales, Australia) during the mid-1990s, in which dry fabrics were impregnated with resin using the VBRI process (see [Section 5.5.4](#)). An external platen pressure was then applied to the vacuum-bagged part in order to achieve even greater V_f values. With the excess resin being retained within the bag, the whole process was a lot cleaner than conventional hand-lay-up techniques, and individual panels, once gelled, could be removed from the platen prior to final curing, thus shortening production cycle times.

Of course, heated platen presses can be used to produce a number of hot-stacked, fibre–resin–fibre combinations: not only hand laid-up parts but also laminates of pre-impregnated fabrics, with either thermosetting resins ('pre-pregs') or thermoplastic resins, like the UHMWPE-reinforced polymer films (eg, Spectra SR3124 and DSM's HB80). These platen presses are normally flat or of single curvature. For more complex curvatures, compression moulding (see [Section 5.5.5](#)) or diaphragm forming (see [Section 5.5.6](#)) is much preferred.

Another variant of this approach was invented by [Klintworth and Crouch \(2002\)](#) when faced with developing a cost-effective manufacturing route for HAPs. In this case, the ceramic breastplate tiles were used as individual tooling, the vacuum bagging process was used to preposition the laminated product, and a typical autoclave cycle used to apply the desirable time–temperature–pressure conditions. A fully cured, partially impregnated laminate was thus formed which perfectly matched the complex curvature of individual ceramic tiles, down to the last surface blemish – perfect replication facilitated perfect support at every location on the ceramic strike face, thus guaranteeing maximum ballistic performance across the entire product and without having to apply any nonuniform pressure to the brittle ceramic.

Of all the possible material combinations, it has become very popular in recent years (2005–2015) to use matched metal tooling, flat or not, for the manufacture of UHMWPE-based products, especially at elevated temperatures, typically around 140°C. Important engineering considerations in this manufacturing route include applied pressure, heat transfer (both into, and out of, the laminate), temperature control, resin type and fibre volume fraction.

Final consolidation of a ballistic laminate has a marked effect upon its impact behaviour. Poorly consolidated laminates will have poor mechanical stiffness and may debond during ballistic impact leading to severe back-face deformations. Therefore, higher pressures tend to lead to better consolidation and better ballistic performance for the intended application. In the case of aramid/thermoplastic laminates, increased pressure can improve the wetting of the fabric by the dry film adhesive. In the case of UD UHMWPE pre-pregs information published by a manufacturer indicates that for 165 bar, approximately doubling the consolidation pressure will only yield a 10% increase in V-50 ([Anon, 2004b](#)). It is the experience of the authors,

that adequate ballistic performance can be achieved at significantly lower consolidation pressures, especially when the UHMWPE laminate is only part of an armour system.

It should be noted that particularly in the case of UHMWPE pre-preg materials, it is advisable to vacuum, or pressure, debulk the laminate stack prior to hot-pressing. This is because the materials are not breathable, which can lead to air entrapment resulting in voids or disbonds in the final component. In the case of aramid thermoplastic laminates, this may also be useful for part-handling. However, this is not essential as these materials are gas-permeable.

Aramid and PE materials are poor heat conductors. The rate of heat conduction in and out of the laminate is, however, dependent upon the mass of the tooling and the press force. In a worst-case scenario, when processing a preheated preform with a cold tool, there is a high risk that the outer layers of the laminate will be below their minimum bonding temperature before full pressure is achieved. In spite of the rapid thermal conduction out of the laminates at high pressure, at atmospheric pressures heat transfer into the laminate is slow (Fig. 5.27). Therefore, care must be taken to ensure the laminate core reaches the process temperature prior to pressing.

Thermal energy is a required component in platen pressing. When using thermoplastics systems, the matrix/adhesive system must be preheated beyond its minimum

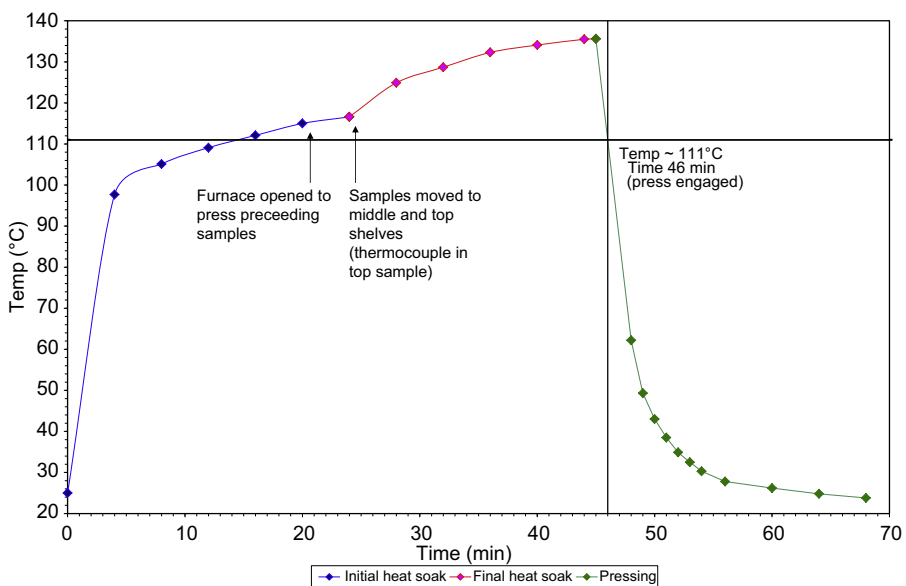


Figure 5.27 Time—temperature profile of Spectra Shield UHMWPE laminate, heated at atmospheric pressure and pressed in ambient ‘cold’ tooling. Note: rapid quench of material at high pressure ~ 12 MPa.

After Sandlin, J., November 2007. Trial Pressing of Spectra SR3124 Backing Plates, VCAMM report.

bond-line temperature. Where pre-pregs are not used (eg, aramid/thermoplastic composites), a variety of thermoplastic dry film adhesives are available. From one manufacturer alone, there are more than 40 different grades of adhesive film, all having slightly different chemistries for differing applications (Anon, 2004a). The advice of the adhesive manufacturer should therefore be sought when selecting a resin system. However, common thermoplastic dry films used in laminating aramid are typically derived from the polyethylene and polyurethane families of polymers. In these systems, once the critical bond-line temperature is reached, overshooting of the pressing temperature is not critical, as the temperatures at which the aramid fibres begin to degrade are far in excess of this point. When using UHMWPE pre-pregs, care must be taken as the minimum bond-line temperature of the matrix is within 20°C (or less) of the fibre's melting temperature. In the case of both thermoplastic pre-pregs and dry film adhesives the part must be sufficiently cooled prior to releasing the pressure or the bonding will not be sufficient to retain consolidation of the laminate.

5.5.2 High-pressure (HP) compression moulding

High-pressure moulding of curved ballistic laminates in a matched metal-heated press is a subset of platen pressing designed to achieve deeply curved components such as combat helmets. Traditional ballistic helmet shell manufacture (and more generally manufacture of items from low-extensibility fabrics) remains a labour- and capital-intensive, low-volume process. The majority of contemporary helmet shells for ballistic protection are made from aramid/phenolic composites — although in recent years helmet shells based on UHMWPE pre-pregs and materials hybrids have become available.

The manufacturing process consists of pre-pregs or dry fabrics being cut into various geometric sections (eg, 'pin-wheel' and 'petal' splice patterns) (see Fig. 5.28), and carefully laid-up such that the cut-lines do not overlap. The lay-up is then placed over a male matched metal tool with inbuilt heating and cooling jackets, in a driven press. If dry fabric has been used, a liquid resin is applied during lay-up on the tool. The upper female matched metal tool is driven into the laminate forcing it to conform to the tool profile, using very high pressure and moderate temperatures to consolidate and form the material whilst curing the resin.

After manufacture there is a significant amount of flash, due to the starting shape of the layers, which then must be trimmed to arrive at the final helmet shell. Trimming is typically done on a band-saw by a skilled operator. If designed to do so, the flash can also be trimmed through a cropping action within the tooling (see Fig. 5.29). Because splicing and high pressures (which can lead to fibre breakage, wrinkling and crimping) are used, the ballistic performance of the final article is often inhomogeneous near the spliced areas.

Furthermore, the process itself is slow and labour- and energy-intensive. Due to the rigid tooling the process can only accommodate a single thickness of article as any changes to areal density also require the manufacture of a new male or female tool (Sandlin and Kenyon, 2014). Another drawback of using solid, matched tooling in a uniaxial press is that a nonuniform consolidation force will be imparted to the helmet

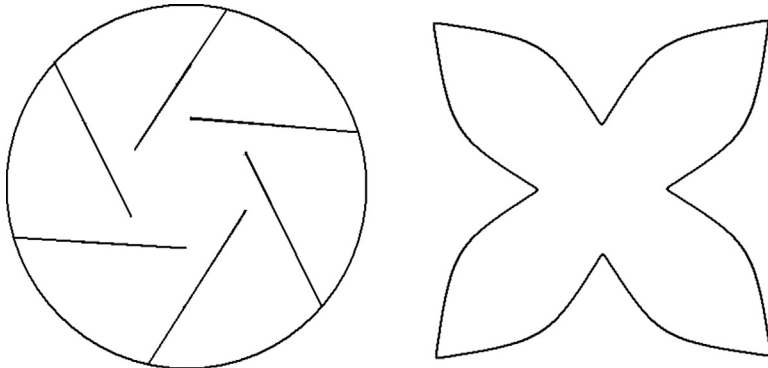


Figure 5.28 Pin-wheel (left) and petal splicing patterns used in contemporary manufacture of ballistic helmet shells.

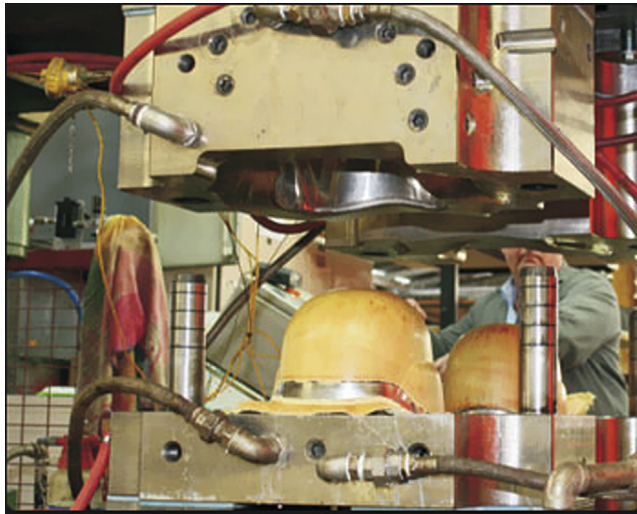


Figure 5.29 Heated and cooled matched metal HP compression press.

After Anon., 2015f. RBR Technology. <http://www.ccaprotect.com.au/rbr-armour-systems/aboutus.aspx> (last accessed 26.02.15.).

during curing. As the draft angle of a typical combat helmet approaches zero (at the ears) the vertical force component diminishes, decreasing the effective press force in these locations. This is likely to result in disproportionate consolidation in the ‘vertical’ regions of the helmet – ears, nape and brim in contrast to the relatively horizontal crown region – and a possible reduction in ballistic performance in these areas.

The use of thermoplastic pre-pregs in compression-moulded helmets can lead to a higher incidence of air entrapment due to the lack of breathability of these materials. This commonly occurs on the inside of the helmet, at the crown (Ling, 2013). To avoid this, careful vacuum debulking of the preform is required prior to the compression

cycle. It has been suggested (Sandlin et al., 2011) that inverting the male and female tools (ie, forming the helmet upside down) poses a simple geometric advantage to allow air to escape via the helmets annulus in situ.

5.5.3 Resin transfer moulding

This is a well-established manufacturing process for the production of high-quality, precision-engineered composite parts (Kruckenberg and Paton, 2012). It is a closed-mould, near-net-shaping process in which a set of preforms of dry fabrics are carefully placed into a die cavity prior to resin injection. The preforms are normally either stitched or tack-welded layers of the chosen fibres/fabrics. A thermosetting resin, of appropriate viscosity and curing chemistry, is forced into the die cavity and designed to flow through the preform in a controlled manner such that all of the reinforcement is duly wetted and completely filled with resin. A gating system, consisting of a number of inlets, outlets and venting gates, much like a metal casting process, aids lineal, in-plane flow through the preform. For armour applications requiring high fibre volume fractions, noncrimp fabrics, like quadriaxial fabrics, are normally used — these fabric architectures also aid uniform flow. The resin can be preheated, to reduce viscosity and thereby fill-times. Vacuum lines can also be added in order to draw the resin into the mould cavity, thus decreasing fill-time even further. This variant is referred to as vacuum-assisted resin transfer moulding (VARTM) (see Fig. 5.30).

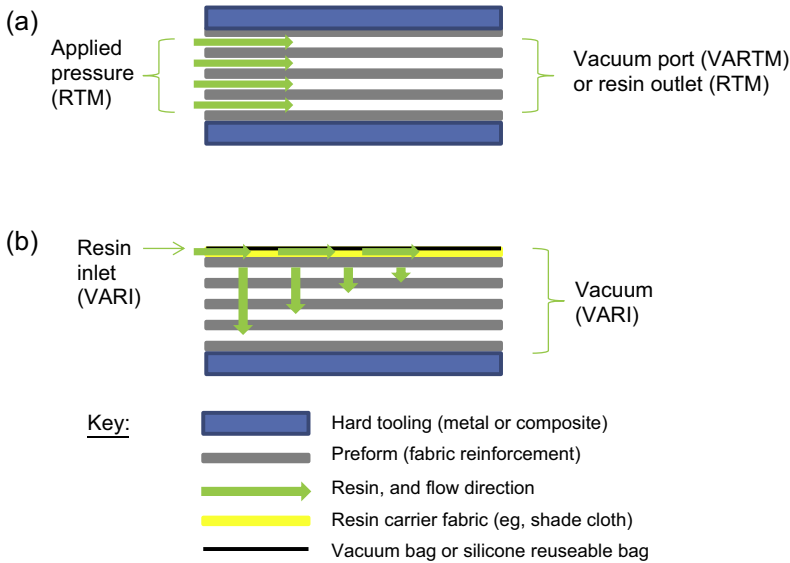


Figure 5.30 Schematic diagram of the principal differences between an RTM process (Polymer Data Handbook) and a vacuum-assisted resin infusion (VARI) process (b). After Summerscales, J., Searle, T.J., 2005. Low-pressure (vacuum infusion) techniques for moulding large composite structures. Proceedings of the Institution of Mechanical Engineers, Part L: Journal of Materials Design and Applications, 219.

Resin transfer moulding (RTM) was the process of choice when the UK embarked upon the ACAVP project in the early 1990s — early work carried out by Crouch (DRA, Chertsey) in conjunction with Summerscales (Plymouth University, UK), laid the foundations for the very first, monolithic, thick-section composite panels representative of an AFV. As reported by [Summerscales \(2015\)](#) this early work included a 1 m square, single curvature panel, with thicknesses increasing across the panel from 35 mm at one edge to 60 mm at the opposite side. The panels weighed almost 100 kg and were supplied to the DRA (Chertsey) for ballistic testing. Through such tests and other underpinning research and development, confidence was sufficiently high for the ACAVP project to proceed ([Ogorkiewicz, 1996](#)), as did similar work in the USA ([Ostberg et al., 1996](#)).

In 2000, Shelly reported that the armour on the ACAVP was attached using studs, which screwed into threaded inserts in threaded holes in the composite ([Shelley, 2000](#)). The reason for this approach was to allow the base vehicle to be transported by air, and one of the requirements of the design programme was that the vehicle could fit into a C130 transport aircraft. Cost was an issue right from the beginning, so it was decided to go for E-glass noncrimp fabric reinforcement, at about £3/kg, as opposed to more exotic substances such as S2-glass at £11/kg, ‘Kevlar’ aramid fibre at £20/kg or carbon. Hexcel Composites supplied the fabric. The matrix was Ciba’s ‘Araldite’ LY556 epoxy, which is chosen to be able to withstand engine bay temperatures of up to 130°C. In total, the composite hull weighed about five and a half tonnes. The bottom half was made as a single 3-tonne piece, 6.5 m long, with torsion bar suspension covers bonded and bolted on the inside. In the original concept, it would have been necessary to cure the moulding in a large autoclave, but one of the consequences of Shorts dropping out of the project was going to Vosper Thornycroft (VT), who already knew how to make large, thick, composite sections which only required curing in an oven. The component parts of the hull were therefore manufactured using VT’s vacuum infusion variant of RTM, namely SCRIMP, a patented process for which VT had a license at the time. See next section.

5.5.4 Vacuum-assisted resin infusion (VARI) processes

[Summerscales and Searle \(2005\)](#) has reviewed the many variations of this family of moulding processes. In essence, as shown in [Fig. 5.30](#), the VARI processes differ from the RTM processes in the way the resin flows and impregnates the fabric reinforcement: with RTM, the flow is in-plane; with VARI, the flow is through-thickness. The VARI approach significantly eases the filling operation by shortening the flow distances, which is especially advantageous with thick-sectioned parts for armour applications. Seemann Composites, founded in 1987 to develop a VARI process, and based upon Bill Seemann’s boat-building experience, were the first to commercialise and patent such a process, although there has been much conjecture as to the validity of the original IP, especially outside of the USA. SCRIMP, one of the many acronyms for very similar VARI processes stands for Seemann Composites Resin Infusion Manufacturing Process (see [Fig. 5.31](#)).

It has revolutionised the boat-building industry and since its adoption in the 1980s, especially by the US Navy, it has been used for many large-scale composite parts,

5.5.4.1 Case study: application of VARI in a composite armour system for the RAN

In 1997, ADI (now Thales, Australia) was in the middle of building Huon class Minehunters for the Royal Australian Navy, in a purpose-built, composite fabrication facility in Carrington, Newcastle, Australia, from advanced composite materials. Many tonnes of E-glass fibre-reinforced polyester resin were used for each vessel, and most of that was laid up, virtually by hand, with some assistance from a preimpregnating machine supplying fabric to the job from high above the workplace. The ship was designed, by Intermarine (Italy), as a monocoque structure, of varied thickness, with primary and secondary bulkheads laminated into position.

The ships were naturally designed to possess excellent blast resistance and this was achieved, in the main, by using compliant hull materials but, unfortunately, because the fibre volume fraction was relatively low its ballistic penetration resistance was not optimal and certain areas of the ship needed to be up-armoured.

A single plate of RHA would have been a simple solution but, being a mine hunter, no magnetic elements were permitted so Crouch, and his Advanced Composites team at ADI, had to search for a composite armour solution. Through clever design and with intimate knowledge of the penetration behaviour of composite materials, as compared with metals, a unique composite solution was developed.

The composite panels were designed using an approved thermosetting resin, reinforced with advanced glass-fibre fabrics to an optimal volume fraction of fibres. Each panel was manufactured using the VBRI process on site at ADI, Carrington. Selected areas of each of the Huon class minehunters was fitted-out with the composite armour system.

5.5.5 Diaphragm forming

Diaphragm forming, an extension of vacuum forming, is a process whereby vacuum force is used to mould a laminate to the shape of a tool. It is conventionally used in forming unreinforced polymers such as PE, PC and PMMA which have been covered in [Section 5.2.1](#) of this chapter. In limited cases it has been adapted to form fibre-reinforced polymers such as CFRP, GFRP, UHMWPE composites and aramid/thermoplastic composites (covered in [Sections 5.3 and 5.4](#)).

The process itself is straightforward and typically involves low-cost tooling. There are a number of variations to the process, which include single diaphragms, double diaphragms and positive or negative tooling. However, in its simplest form, vacuum forming is used with thermoplastic sheet polymers where the laminate itself can be used to seal the vacuum and is illustrated in [Fig. 5.33](#). The laminate is loaded into a frame and clamped at its edges so that it is fully sealed on its perimeter. Once the part is loaded, a heating array (typically a set of infrared lamps) is used to bring the material to forming temperature. At the forming temperature the perimeter frame is sealed against the tooling platen and vacuum is applied below the tool to evacuate the area between the tool and the laminate, causing the laminate to deform onto the tool profile.

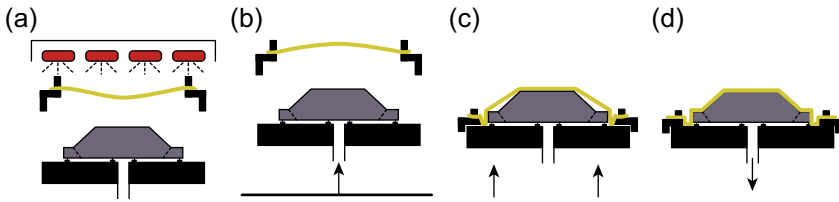


Figure 5.33 The basic vacuum forming process.
Reproduced from: Web.

If a particular surface finish is required on the nontool side of the part a single diaphragm can be included on this side of the laminate. This technique can also be utilised to increase the force applied, and minimise part material wasted as flash by extending the surface area of the vacuum diaphragm beyond the perimeter of the laminate to be formed. Because vacuum is fixed for a given area, increasing the area of the diaphragm increases the forming force.

The process is typically used for shaping of ductile polymers like the polycarbonates and polypropylenes. Aircraft canopies, ballistic shields, and visors are manufactured using this process and there are numerous technical guides to assist (Anon, 2005a,b).

5.5.6 Double diaphragm forming

An extension of the diaphragm forming technique is the double diaphragm forming (DDF) process. If the laminate to be formed is captured between two diaphragms, which are evacuated a number of additional parameters can be controlled. Surface finishes on both sides of the part can be modified. This setup also provides membrane tension in the laminate, which reduces wrinkling in the final part, and also allows multiple laminates to be used, in which case the evacuated diaphragm also provides some consolidation force. The further advantage of this process, if forming fabric systems, is that the ‘stretch’ in the diaphragm allows the edges of the fabric to move and accommodate the 3D shape required.

Commonly used diaphragm materials include latex and silicone (reusable) and high-ductility nylon and Teflon (disposable). When utilised with a fibre-based system, the process is compatible with both preimpregnated composites and dry fabrics. In the latter case, resin infusion is typically accomplished after the double diaphragm has been evacuated but prior to the tool vacuum being applied (ie, while the laminate is flat). There are however a number of intrinsic limitations to the process having to do with fibre geometry in the starting material (when using fibre-based laminates), tooling geometry, processing temperatures and heat transfer (Crouch and Sandlin, 2010).

In diaphragm forming of unreinforced polymers, mechanical constraints include starting laminate thickness which is typically ≤ 12.7 mm (above which a positive tool may be needed to assist forming), part cavity depths which may not exceed 75% of the cavity width, undercuts are not permissible, ribs and mounting bosses

cannot be made, and the wall thickness cannot be varied (Sabart and Gangel, 2010). For many of the applications discussed herein these limitations would not be an issue. In fact, with regards to the primary armour-grade, unreinforced plastics (PC and PMMA), there is a wealth of freely available literature on the processing parameters used in vacuum forming them (Anon, 2005a,b). Less widely available are the engineering considerations that must be taken into account when utilising DDF to manufacture parts from fibre-reinforced composites.

The DMTC have been studying these DDF parameters since 2005 because, for FRP parts, interply and intraply friction, fabric locking angle, and trellising all have a marked effect on fabric formability and, therefore, the product's ballistic performance.

5.5.6.1 Influence of fabric tow width and weave geometry on drapeability

Drapeability is the general term used to describe a fabric's ability to drape uniformly over a curved object. In forming terms, this ability is extremely important for the fabric or entire preform to form over a male tool, without wrinkling. The physical properties of the fabric that govern drapeability are fabric tow width and weave geometry. The manufacturing parameters to be considered include depth of draw (ie, aspect ratio of the tooling design) and radius of curvature.

Fig. 5.34 shows two hemispheres formed using 'square' or 'plain' woven aramid fabrics manufactured from 40 to 20 mm width aramid tape (tow width), respectively. Both hemispheres were made using double diaphragm forming, utilising identical forming pressures and temperatures. As can be seen, the 40-mm tow aramid shows a higher drapeability compared to the 20-mm tow aramid. During forming of preforms into double curvatures, like these hemispheres, the fibres will be rearranged due to in-plane shearing. In this case the smaller tow width results in increased intraply friction because there are four times the orthogonal intersections in the weave having a smaller tow. As such the more intricately woven, or 'tighter' woven, fabric requires more forming force to achieve the same draw of the 'looser' woven fabric with larger tows and fewer intersections. Therefore, it can be concluded that lower forming

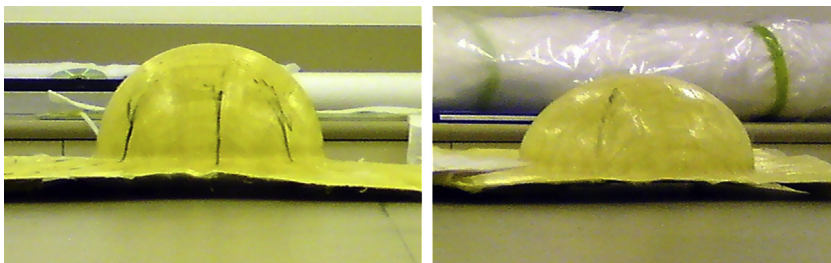


Figure 5.34 Tow width versus drapeability in double diaphragm formed plain woven aramid hemispheres: 40-mm tow (right) and 20-mm tow (left).

After Naebe, M., Sandlin, J.D., Crouch, I.G., Vella, J., July 2009. Next Generation Armour Technologies Program Advanced Manufacturing CRC, Technical Report.

pressures would be required in larger tow fabrics to overcome the frictional forces and compaction during the forming process, due to fewer intersections between the warp and weft tows in the deformed area.

To investigate and quantify process limits as they relate to the various tow widths, forming depth of hemispheres manufactured using the same processing conditions were measured using a vernier caliper. Forming depth of three aramid hemispheres are shown in Table 5.9. It should be noted that where larger radii were formed the narrower tow fabrics did not limit the forming depth. This is due to the same forming pressure being applied to a larger surface area, which results in more forming force being applied. However, when the areal density is increased to 12 kg/m², the forming depth, of the 40-mm tow aramid, dropped by ~6% to 97.24 mm. This is simply the result of increased interply and intraply friction as more laminates are formed, and is discussed further in the following section (Naebe et al., 2009).

5.5.6.2 Inter- and intra-laminate frictional constraints

Another factor affecting the ability of the system to achieve full deformation for a given set of forming conditions is the internal friction of the system. This frictional resistance of the system is proportional to (1) the number of laminates to be formed and (2) the coefficient of friction between adjacent plies following differing deformation paths. In the first case the variable is the number of plies whereas in the second instance there are a number of variables that can be influenced to encourage complete forming of the part.

In the aramid-based system, where an intermediate adhesive layer is necessary for consolidating the laminate, this thermoplastic or liquid thermosetting layer is fully liquid during forming. This reduces the fibre to fibre friction induced by the high degree of transverse constraint placed on the fibres by the diaphragm, in which they are contained. With UHMWPE systems, although a thermoplastic, the material which forms the matrix cannot be fully melted as its melting temperature is too close to the temperature at which the fibres lose molecular weight and thus ballistic performance

Table 5.9 Forming depth data of formed aramid helmets

	Areal density (kg/m ²)	Tool radius (hemisphere) (mm)	Forming depth (mm)	Forming pressure (MPa)
20-mm tow aramid	2.2	103.2	90.70	2.0
40-mm tow aramid	2.2	103.2	103.2	2.0
40-mm tow aramid	12.0	103.2	97.24	2.0
20-mm tow aramid	13.0	150.0	150.00	2.0

upon resolidification. Therefore the material is heated until the matrix becomes 'soft', which reduces the pressure required to induce interfibre sliding and rearrangement, however the fibres are still in contact with one another with no lubrication. The result is a greater rate of increasing interlaminar friction as the AD is increased in nonlubricated systems.

In the latter case, working with UHMWPE, intralaminar friction cannot be controlled. However, interlaminar friction conditions can be improved through the introduction of a thermoplastic layer between the plies. This can have an added positive influence on the dynamic back-face displayed by the laminate in ballistic applications. It is, however, a small change in the overall forming force of the system as typical fibre-based UHMWPE/TPU composites are composed of four intralayers of orthogonal fibres which make up one layer of fabric.

5.5.6.3 Locking angle and the trellis effect

It has been noted in the forming of woven fabrics that the primary limiting factor is a phenomenon known as the 'locking angle'. This is the angle of relative deformation at which adjacent fibres come together and lock, thus any deformation beyond this angle will create 'out of plane' wrinkling. To determine if this limiting constraint has been reached in a woven system, the following locking angle equation is used

$$\theta = \arcsin[t_2/(t_2 + l_2)]$$

where t_2 is the width of the weft tow and l_2 is the tow spacing (see Fig. 5.35).

In the case of plain woven systems, the tow widths in the warp and weft directions are equal and the tow spacing (l_2) is zero, as the weave is tight. Therefore, the locking angle of this system is 90° . This value holds true assuming the system is unconstrained (ie, the edges of the fabric are not fixed) as the individual tows within the weave can move linearly to assume whatever rotation is required by the deformation (Fig. 5.36).

In square woven systems without end constraint where the limiting factor in the deformation is not the locking angle, another phenomenon is responsible for the limitations in vacuum forming — the 'trellis effect' (Rozant et al., 2000; Miravette, 1993). The trellis effect is a result of the resolved forces acting on the material to induce tow rotation and shear, as the material assumes the geometry dictated by the process. At the start of the process the forces at play are acting orthogonally (out of plane) to the fibres and weave, and maximum moment is applied to the reorientation of the fibres. As deformation progresses the fibres become more and more in line with the forces acting on them. In low-extensibility fibre systems, like those utilised in armour (eg, aramid, glass and UHMWPE), as the forming process progresses, the forces at play are acting more longitudinally on the fibres than orthogonally. As a result, the applied force is attempting to stretch rather than reorient the fibres (Fig. 5.37). The only way to address this is to either change the direction of applied force, or increase the magnitude of the force to compensate for the decreased rotational and shear moments being applied (Naebe et al., 2009).

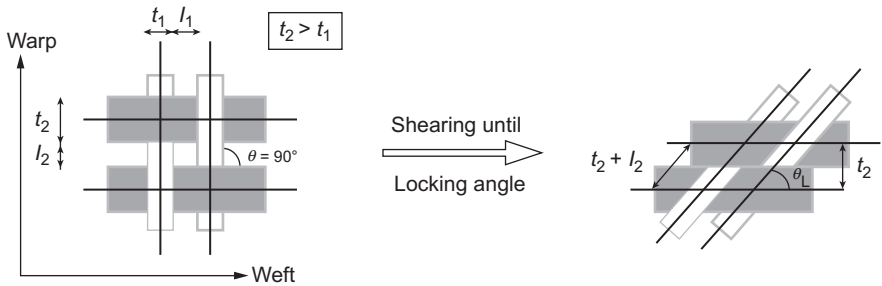


Figure 5.35 Locking angle and weave parameters.
After Rozant, O., Bourban, P.E., Manson, J.A., 2000. Drapability of dry textile fabrics for stampable thermoplastic preforms. *Composites Part A: Applied Science and Manufacturing* 31 (11), 1167–1177.

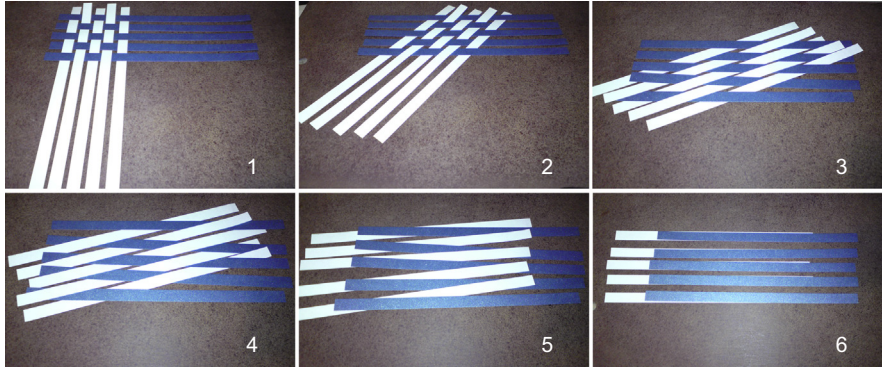


Figure 5.36 Ninety degree locking angle in square woven system with no end constraint.

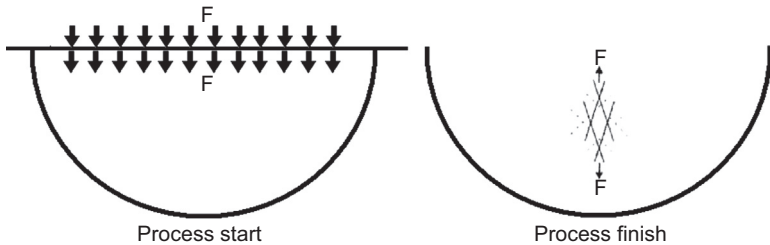


Figure 5.37 Alignment of fibres with applied force as deformation process progresses: the ‘trellis effect’.

In cases where the ‘locking angle’ is the limiting factor in formability, modifying the fabric weave can control the system. In systems where the ‘trellis effect’ limits formability the only option is to introduce additional forming force. For pure vacuum double diaphragm forming this can be done utilising larger diaphragms, thus increasing the area

over which vacuum pressure is applied to increase net force. Additional positive pressure can also be introduced to aid in forming. One such process utilising a combination of vacuum pressure and positive pressure is examined in [Section 5.5.7](#), which describes the evolution of the double diaphragm deep drawing (D4) process.

5.5.7 Double diaphragm deep drawing (D4) process

Following ground work by ADA, VCAMM and the Defence Science and Technology Organisation (during 2005–09), the Defence Materials Technology Centre developed a unique variant of the double diaphragm forming process, between 2009 and 2013, which culminated in a full-scale capability to produce lightweight spliceless combat helmet shells in 2014. Some detail on this work was recently published by the DMTC team (see [Cartwright et al., 2015](#)).

Invented by James Sandlin (then of VCAMM) the double diaphragm deep drawing (D4) process was developed at the request of the Australian Defence Department, via the Defence Science and Technology Group's (DST Group) Capability and Technology Demonstrator (CTD) programme. The aim of this work was to reduce the cost and complexity involved in shaping composite armour systems so that personnel armour coverage could be made more cost effectively with the potential to be extended to the soldier's extremities.

In order to draw an article with a high aspect ratio (eg, a helmet) some of the intrinsic limitations of ballistic textiles must be overcome. Firstly their high modulus and strength, combined with a lack of ductility results in a system that, for all practical purposes, does not deform plastically when force is applied. Secondly, and dependent upon weave geometry, most ballistic fabrics do not respond well to double curvatures of the depth and radius typical of human anatomy; they wrinkle up.

The project was therefore deliberately focused on combat helmets, with the aim of reducing the cost and complexity associated with the traditional methods (refer to [Section 5.5.2](#)). Development was supported within the DMTC by a collaborative team consisting of the inventor, James Sandlin, Stuart Thomas (then of VCAMM), and Madhusudan Suryanarayana, Minoo Naebe and John Vella (of Deakin University) and many others from various institutions. The team worked to develop a manufacturing route that for composites would be analogous to metal stamping. The goal was to arrive at a manufacturing methodology where splicing and hand layup of the materials was no longer required.

Based on the composites experience resident within Deakin University, double diaphragm forming was the first technique to be trialled (described in [Section 5.4.4](#)). It was initially thought that the vacuum applied between membranes would provide sufficient consolidation and constraint to induce sufficient levels of planar tension during the forming process, thus suppressing uncontrolled 'out of plane movement' (eg, wrinkling).

Two limitations were encountered. Firstly, the stiffness of the materials to be formed at the thicknesses required meant that the force available from tool vacuum alone was not sufficient to fully form the articles to the full depth of the tool. Secondly, the vacuum applied between the diaphragms was insufficient to suppress wrinkling in the parts.

The primary inventive steps taken in November 2006 to overcome these limitations and move from double diaphragm forming to the D4 process were application of external positive pressure (effecting full forming) and the addition of a mechanical method for application of planar tension within the laminate stack (suppressing wrinkling). Others have since adapted positive pressure and blank holders to composite forming. For example, a similar method was outlined by Dr. Jinhua Wang in his PhD thesis, *Predictive Modelling and Experimental Measurement of Composite Forming Behaviour*, submitted to the University of Nottingham in August 2008. It should be noted that whilst comparatively new in composite application both positive pressure and blank holder devices are common to deep drawing of sheet metal where a hydraulic ram (for positive force) and an annular blank holder (for planar tension) are used to control the flow of material into the tool (Fig. 5.38).

The D4 equipment was developed to include a number of features converting it into a rapid composite-forming capability. Following the construction of four laboratory-scale concept demonstrators, in October 2013, a turn-key pilot prototype was built (see Figs. 5.39 and 5.40), capable of pressing a ballistic helmet shell and curing the constituent materials in a 20-min cycle. Prior to the commissioning of the D4 Pilot Prototype, previous laboratory-scale equipment heated and cooled the laminates in situ. While the actual step of forming of composite components (ballistic helmets) only takes approximately 30 s, in situ heating takes approximately 45 min to achieve an isothermal state in the laminate (forming temperature $\sim 135^{\circ}\text{C}$). Without a method for forced cooling, following the heating and forming steps, $\sim 1\text{ h }15\text{ min}$ was required to cool the formed component to a suitable demoulding temperature ($\sim 40^{\circ}\text{C}$).

In order to achieve the reduced cycle time the pilot prototype operates with the ballistic laminates heated in an oven containing a full shift's complement of materials (materials for 24 helmets). The laminates are held isothermally, at forming temperature, under vacuum, and experiments have shown no degradation in the laminates over an 8-h period. The table top onto which the materials are loaded in the equipment

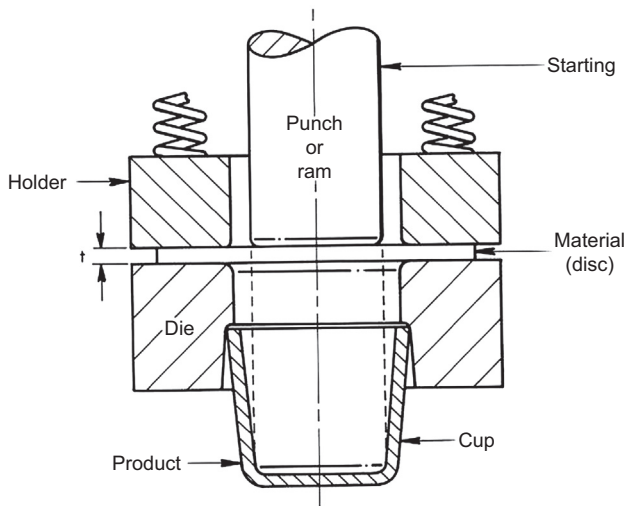


Figure 5.38 Deep drawing of metallic sheet schematic of tooling – typical.



Figure 5.39 DMTC D4 pilot prototype (c.2013).

Courtesy of Marand Precision Engineering.

is also heated to forming temperature and contains active cooling for cycling between forming and demoulding temperatures.

In practice this system reduces the cycle time to 20–25 min, when the preheated laminates are quickly moved to the D4 equipment and formed, then actively heated/cooled utilising the fluid jacket in the tool. Where thermoplastic materials are used, the material is loaded (1 min), formed (30 s), cooled (17 min 30 s) and demoulded (1 min). When combinations of thermoplastic and thermosetting material are used there is an addition of 5 min following the forming cycle where heated fluid is passed behind the tool to provide thermal energy for curing the thermoset.

Beyond achieving a commercially viable cycle time, understanding the effect of starting materials orientation on fibre deformation routes during forming is also a challenge in forming a wrinkle free part. The final materials used in the construction of prototype helmets manufactured using D4 consisted primarily of bidirectional and unidirectional fabrics (UHMWPE thermoplastic and carbon fibre epoxy thermoset composites, respectively). Understanding the relationship between the initial and final fibre orientations was crucial in manufacturing a helmet of uniform thickness, fibre

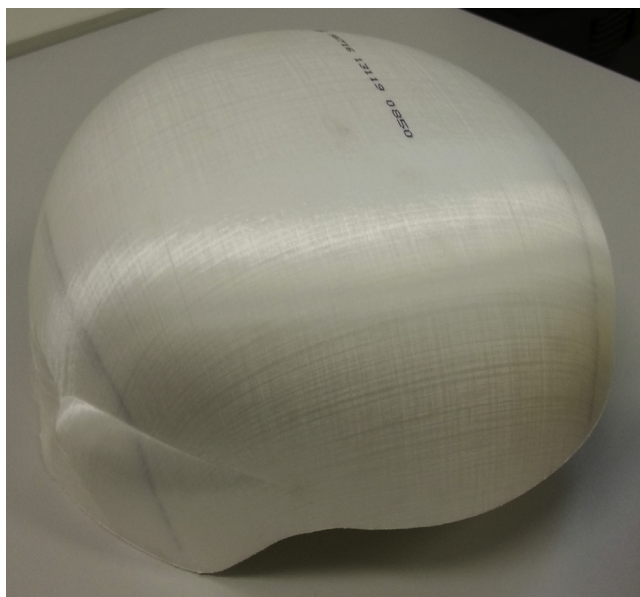


Figure 5.40 Spectra Shield SR-3136 helmet produced from the newly commissioned preproduction prototype D4 machine.

density, ballistic performance and structural behaviour. Analysis of the starting and finishing fibre orientations was initially performed empirically by James Sandlin and Minoo Naebe (see [Fig. 5.41](#)).

Fibre deformation routes and orientations were later confirmed through dynamic simulation of the process and manufactured components performed by Bruce Cartwright (Pacific ESI) (see [Fig. 5.42](#)). In the dynamic simulation a simplified nine-ply helmet was used. Further details of the simulation techniques have been reported elsewhere ([Cartwright et al., 2015](#)).

From both the empirical and simulation studies it can be seen that along the major fibre axes, the change in fibre orientation and fibre density (thickness) is minimal. However in the off-fibre axes (45°) the thickness has increased and the fibre angle has decreased from the 90° starting orientation to as little as 60° .

If the laminate had been constructed from plies having the same starting orientation the result would be a helmet shell or component of variable thickness and therefore variable ballistic performance. This challenge in spliceless helmet development is similar to the challenge in spliced articles where care must be taken to ensure splices do not overlap (refer to [Section 5.5.2](#)).

In summary, 7 years of discontinuous development activities have resulted in a process capable of starting with a flat, unprepared laminate of desired thickness and, in one step, forming that preform into a helmet or product of complex geometry. D4 is a scalable process with tooling provisions in the pilot prototype for parts of up to 750×750 mm with a 500-mm draw depth. Much larger sizes are possible with

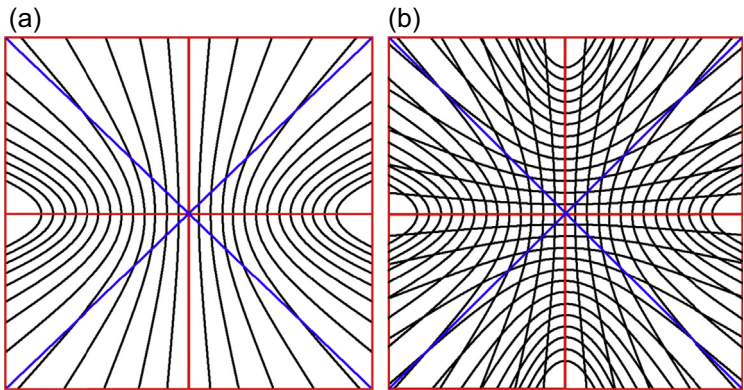


Figure 5.41 Conceptualised 2D representation of fibre paths after hemispherical deformation if projected on flat plane in unidirectional (a) and bidirectional (b) materials. Centre represents crown, with red lines on orthogonal axes and blue lines on 45° axes.

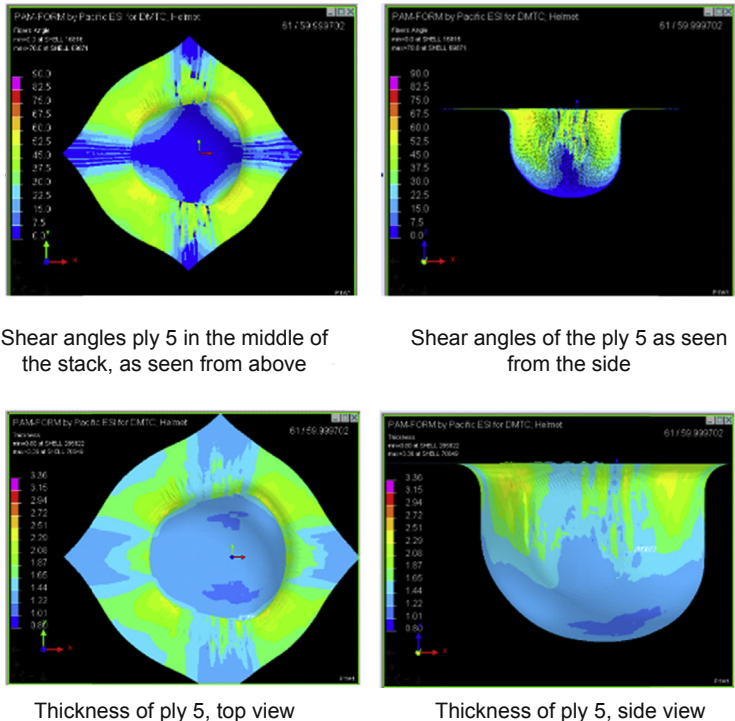


Figure 5.42 Change in fibre orientation and ply thickness after deformation of a biaxial composite using the D4 process.

increased equipment dimensions. With cycle times of 20–25 min (depending on thermoplastic or thermosetting starting materials, or a mixture of both) and resultant products with excellent ballistic properties and good structural properties, the D4 process compares very favourably with other internationally developed thermo-forming technologies. The DMTC has carried out a thorough review of all commercial processes for producing combat helmet shells (Sandlin and Kenyon, 2014). For the sake of brevity, Table 5.10 simply compares the pros and cons of using the D4 process compared with conventional HP compression moulding.

5.6 Armour products for personal protection

Most elements of a body armour system are constructed of soft fabrics (see Chapter 6) but a number of components are manufactured from rigid laminates of fibre-reinforced composites or solid thermoplastics, like polycarbonate.

5.6.1 Thermoformed shields and visors

Transparent accessories, like riot shields, are traditionally manufactured from thermoformed polycarbonate sheets with antifogging, abrasion-resistant coatings. The innovative Intruder G2 is the first ballistic shield of its kind to incorporate PROTECH's unique triangular, front and back overlapping viewport. The shield addresses an operator's need for increased vertical peripheral vision in a ballistic shield. It also offers added coverage and high-speed manoeuvrability and protects against Type IIIA rounds and velocities.

5.6.2 Hard armour plates (HAPs)

As described in Chapter 7, the majority of hard armour plates on the market is ceramic-based and will use a laminated, fibre-reinforced composite as its main energy-absorbing, trauma-reducing, backing material. In the very early years of development, when HAPs were moving away from solid ceramic elements, glass–fibre fabrics were used since these had been used to clad the original ceramic elements. However, after the invention of Kevlar in the 1960s, aramid fibre reinforcements became the material of choice for HAP backings. As has been referenced elsewhere, Australian Defence Apparel, in Bendigo, Australia, developed a proprietary process in which an aramid fibre-reinforced LLDPE laminate was preformed using the ceramic element as its forming tool. See European Patent Application, EP 1 319 917 A2, filed in 2002 (Klintonworth and Crouch, 2002) for more details.

Around 2005, UHMWPE fibres and fabrics had been developed to such a level of performance that solid laminates of the same became very popular. Using high-pressure, platen-pressing techniques, these products simplified HAP manufacture by eliminating the ceramic element. It is also well documented that the ballistic performance of solid, rigid laminates of both Dyneema-based and Spectra-based products vary depending upon the applied compression load. Measurements of V-50 values,

Table 5.10 Comparison of D4 and HP compression moulding processes for combat helmets (Sandlin and Kenyon, 2014)

	Cycle time	Advantages	Disadvantages
DMTC double diaphragm deep drawing (D4)	20 min	<ul style="list-style-type: none"> • Cycle time • Forming of spliceless laminates • The use of a negative rather than positive mould • A unique method for governing tension within the laminate • Combined use of vacuum and positive displacement pressure in the formation of the part • Use of positive pressure for curing • Comparatively low pressures and flexible tooling • Ability to co-cure thermosetting and thermoplastic materials 	<ul style="list-style-type: none"> • Precommercial TRL • Consolidation challenges • Poor thermal control in tool • Internal part wrinkling • Relies on pre-pregs
Compression moulding (matched metal pressing)	7–60 min	<ul style="list-style-type: none"> • Relies on existing technology • Technically simple • Can process pre-pregs and dry fabrics • Can process materials hybrids 	<ul style="list-style-type: none"> • Labour-intensive • Expensive capital equipment and tooling • Materials waste from splicing • Inhomogeneous article performance • Process variability • Inhomogeneous application of pressure • Positive tooling can result in gas inclusions

as well as both dynamic and permanent BFS values do fluctuate with applied pressure. Against handgun bullets, high-velocity fragments and the lead-filled variants of high-velocity rifle rounds (eg, the M80 round), solid UHMWPE plates perform very well. However, they remain noncompetitive against hard-cored rifle rounds — ceramic-based systems are far more mass- and space-efficient (ie, lighter and thinner). Solid UHMWPE do float, and therefore provide the combatant with some buoyancy, but

they are also very thick compared with an optimum ceramic-based system, and therefore not ideal for low-profile operations.

It should be noted that whilst it is recognised that the ballistic performance of UHMWPE laminates may increase with applied pressure, this does not always translate into improved ballistic properties of a multilayered armour system, like a complex HAP/SAI combination (see Chapter 7).

DSM provide processing data (Anon, 2004b) for manufacture of a 73-ply, HB2 compression moulding (see Fig. 5.43) which has a resultant areal density of 19 kg/m^2 , but is $\sim 20\text{-mm}$ thick — a comparable ceramic-based system would only be $\sim 14 \text{ mm}$ thick. This is a typical example of the trade-off between cost, robustness, weight and profile.

5.6.3 Combat helmets

‘Unfortunately, the human skull is not the same as its Neanderthal forebears: the top and sides of the cranium of Peking Man, for example, had thick, bony walls and a low, wide profile, designed to protect the brain, ears and eyes from impact. In contrast, we modern humans hold our enormous, easily-injured, semi-liquid brains in relatively thin-walled bony globes. We have to buy our bicycle helmets!’, (Boaz and Ciochon, 2004).

5.6.3.1 History and evolution of combat helmets

While the head and neck represents only 12% of the body area typically exposed in combat, this area receives 25% of all hits, and furthermore, head wounds account for almost half of all combat deaths (Carey et al., 2000). Thus, helmets designed to provide protection against high-velocity projectiles are important for reducing combat casualties. Carey et al. outlined the history of the modern military helmet and the factors underlying its design. Soldiers have used body armour, including helmets,

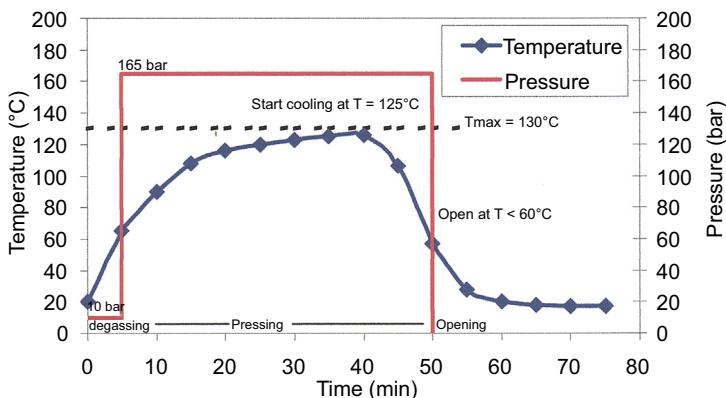


Figure 5.43 Recommended pressure cycle for production of a UHMWPE panel, constructed of 73 plies of Dyneema HB2 fabric.

Reproduced from: Anon., July 14, 2004b. Recommended Processing Data for HB2 and HB25 Dyneema Materials. DSM datasheet.

for thousands of years. While effective against swords and arrows, body armour eventually fell out of favour as the weight of armour required to provide protection against the balls fired by ever more powerful guns became excessive. At the start of the WW1 most soldiers had no personal armour of any kind. The military helmet was reintroduced during World War I to provide some degree of head protection, eg, the first steel calotte or cap provided to some French troops is credited with defeating 60% of shrapnel hits. Combatants between WW1 and the Vietnam War used various steel helmet designs. A Kevlar composite helmet was developed by the US military in the 1970s and became standard issue in the 1980s.

Designs and materials for combat helmets have changed over the years (see Fig. 5.44). The PASGT and the ACH helmets are made from ballistic aramid fabrics and a thermoset resin as the matrix. The evolution of ballistic helmets from steel to aramid provided the wearer with enhanced coverage and ballistic performance. As a result of improved ballistic performance aramid helmets are rapidly being replaced with helmets made primarily of unidirectional pre-pregs of ultrahigh molecular weight polyethylene (UHMWPE). An example of this, the Enhanced Combat Helmet, features these materials while offering the wearer a combination of reduced weight and enhanced performance. Typically these unidirectional pre-pregs are laminated in a thermoplastic matrix. This is a departure from the high modulus thermosetting pre-pregs utilised in earlier generations of helmets and has ballistic and process advantages at the expense of structural rigidity.

5.6.3.2 Design considerations

Cranial coverage, weight and ballistic performance are only a subset of the overall criteria against which a ballistic helmet must be designed. In addition to these

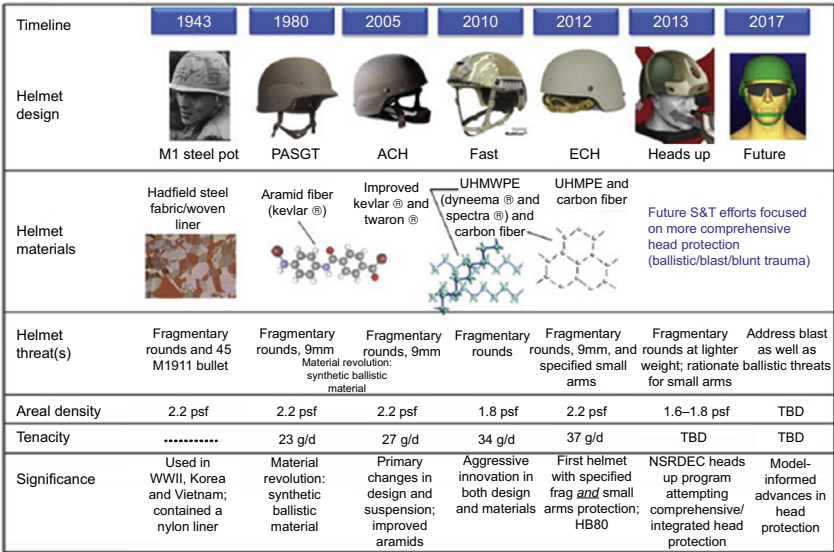


Figure 5.44 Historical perspective of US army helmet design and materials (Walsh et al., 2012).

requirements, manufacturing, structural, durability, in-service and system requirements play a large role in driving the design of a helmet (Utracki, 2010). Once ballistic performance is specified, and therefore the areal density of the material decided, the final weight of the shell will be singularly linked to cranial coverage.

Durability and manufacturing drivers are in part addressed through the materials suppliers and via the manufacturing method chosen, which are discussed in previous sections. In-service and systems requirements are typically driven by purchase specifications which have been developed by government procurement experts. Therefore, the most challenging engineering aspects of helmet design are meeting the structural and ballistic requirements, both of which are normally specified in procurement documentation.

Structural requirements

A significant number of injuries are caused by blunt impact (as opposed to ballistic trauma). These result from cranial impacts caused by a number of incidents including falling while dismounting vehicles and running into projecting structures. In addition, troops can be hard on their helmets, using them as ad hoc seats and dropping them onto hard surfaces. As a result of this, helmets are required to meet stringent structural requirements.

While helmets manufactured from woven aramid/thermoset systems have a high structural modulus, helmets manufactured from unidirectional UHMWPE/thermoplastic systems are challenged to meet the structural requirements at a reasonable shell thickness. This is due to the low modulus of the thermoplastic matrix and poor fibre matrix adhesion. As such, using these thermoplastic-based ballistic materials results in significant structural design challenges.

Solutions to this challenge have been proposed by a number of parties including PacificESI Australia (Mulcahy and Cartwright, 2011) and the United States Army Research Laboratories (Walsh, 2009). The proposed solutions centre on placing an internal or external chassis on the thermoplastic ballistic shell made from high modulus plastic or fibre-reinforced composites (eg, CFRP). Both internal and external approaches have advantages and disadvantages including the potential for reductions in ballistic efficiency with commensurate improvements in back-face signature (internal chassis) and the converse trade-off in the case of external reinforcement. One novel approach, employed by Ops-Core in manufacture of shells using the Diaphorm process is the use of an intermediate layer of CFRP at the ballistic neutral axis in combination with an external CFRP shell. This yields a mass-efficient solution without limiting the ballistic efficiency of the thermoplastic ballistic core, however back-face signature performance remains compromised.

The most stringent structural testing requirement of a combat helmet (at the time of writing) is outlined in the US ECH standard (Passagian, 2009) where the vertical and lateral loads are 1778 and 1330 N, respectively. Each load case is repeated for 25 cycles, and limited deformation posttest is allowed. Blunt impact testing required a 54 N m impact be adsorbed with minimal shell damage.

Ballistic requirements

In designing for ballistic requirements there are typically two key metrics that are measured against a series of threats and test conditions. These metrics are V-50

(the ballistic limit of the helmet) and back-face signature (a measure of the permanent or transient deformation of the rear face of the helmet shell). The test conditions can involve temperature, shot obliquity and a variety of projectiles including 5.56-mm FSP and RCC as well as a 9-mm handgun bullet.

The ballistic performances of a number of UHMWPE products, in the form of either flat panels or helmet shells, have been determined by the DMTC research team, led by [Sandlin and Kenyon \(2014\)](#). One clear, and reproducible aspect, was the apparent increase in V-50 of the curved UHMWPE helmet shells compared with the flat panels. In Crouch's experience, this is the exact opposite to similar experiments with aramid-reinforced phenolic laminates.

Limitations on BFS are naturally more important with cranial protection than with torso protection, and for helmet shells these BFS values can be as small as 15 mm of dynamic (transient) deflection ([Freitas et al., 2014](#)). This is quite a challenge for UHMWPE materials which have poor interlaminar shear, and through-thickness tensile strengths.

5.7 Specifications and ballistic standards

Specifications, for both civilian and military end-users are classified into three types:

1. Material, manufacturing or product specification (MS);
2. Testing procedures (TP);
3. Ballistic performance requirement (BPS).

[Table 5.11](#) includes examples of all three types. Category MS simply provides a prescriptive means of manufacturing an armour product, whereas TP just describes the actual test procedure to be followed. Category BPS, the most sensitive of all standards, defines the ballistic performance required with well-defined pass/fail criteria. Of course, for security reasons, all three types are not normally available for a single product. Manufacturing specifications are usually restricted to standard products or key elements like the FSPs. There is a definite trend towards having BPS, as well as TPs, and leaving suppliers the freedom, and the competition, to develop their own solutions. This is certainly the case with body armour systems.

In 2006, Bhatnagar provided an overview of standards and specifications for light-weight ballistic materials, including hard armour plates and helmets. In this section, we provide a brief synopsis of standard metrics pertaining to eyewear and spall liners. [Table 5.11](#) also provides a brief summary of the most common standards and their application.

5.7.1 Eyewear

Military specification MIL-PRF-31013 states that spectacles shall be capable of resisting an impact from a 0.15-in. diameter steel projectile at 640–660 feet per second with no failure of lens or frame. This is more than four times the impact velocity requirement for industrial safety glasses. For goggles, this requirement changes to

Table 5.11 A selection of the most common standards for polymers and FRP armour materials and products

Category	Specification	Country of origin	Test details	Comments
General	MIL-STD-662F	USA	Used for standard V-50 determination Uses AI witness plate to judge failure	General use for any armour materials
	STANAG 2920	NATO	General purpose use for ballistic testing methods	Adopted worldwide
	MIL-P-46593	USA	Manufacturing standard for fragment simulating projectiles	
	MIL-STD-8109	USA	Specifies environmental conditioning practices	
	DEF-STAN-00-35	UK	Specifies environmental conditioning practices	
Shields, doors, etc.	NIJ 0108.01	USA	Ballistic standard which covers threats up to 0.3" APM2	
Eyewear	MIL-DTL-43511D	USA	Used for testing goggles and visors	
	MIL-PRF-31013	USA	Used for safety spectacles	
FRP laminates	MIL-DTL-62474F	USA	Manufacturing specification for flat and moulded laminates	Provides extensive manufacturing details
	MIL-DTL-64154B	USA	Manufacturing specification for flat and moulded laminates	Provides extensive manufacturing details
	MIL-DTL-32378	USA	Manufacturing specification for flat and moulded cross-plyed, UD, para-aramid laminates	Provides extensive manufacturing details
	DEF STAN 93-111/1	UK	Production specification for spall liners. Refers to Def Stan 08-44 for ballistic standard and uses 0.3" and 0.5" FSPs	Previously MVEE 802 and RARDE 802, which included ballistic tables

Hard armour plates	NIJ 0101.04, level IV	USA	Ballistic standard for body armour. Uses RDOP into catching material as measure of penetration resistance	Most common, although not latest version
	NIJ 0101.06, level IV	USA	Ballistic standard for body armour, with smaller edge distances and vastly increased sample sizes compared to NIJ 0101.04	Latest version, with more stringent conditioning requirements
	HOSDB RF1, RF2	UK	Ballistic standard for UK police	Sets a smaller minimum for BFS of 25 mm (cf, 42 mm)
	DEF(AUST) 10946	Australia	Detailed test procedures based upon world's best practice	Most recent test procedure for body armour
Helmets	NIJ 0106.01	USA	Ballistic test standard. Uses head forms to record head accelerations. Covers threats up to 9 mm FMJ	
	MIL-H-44099A	USA	Manufacturing and performance specification for combat helmets	US PASGT helmet made to this specification

Source: Crouch and Eu (2015).

a 0.22 caliber steel sphere at 550–560 ft/s. These steel projectiles are launched using special plastic sabots. A polycarbonate lens between 2.2- and 2.8-mm thick normally defeats this threat.

5.7.2 Spall liners

Researchers at MVEE (Christchurch and Chertsey) were responsible for drafting the original manufacturing specification for spall liner materials, MVEE 802, in the early 1980s, based upon local UK production of platen-pressed E-glass laminates. This standard transitioned to RARDE 802, in December 1986, with a restructuring of the UK R&D establishments. This standard then formed the basis of DEF STAN 93-111/1, in March 2004 – it still defines some essential structural property requirements.

Singleton et al. (2011) reported at ISB26, the evolution of the US material specifications for different grades of spall liners from woven glass to UD aramid laminates, from 1992 to 2012. The latter system is based upon Honeywell's Gold Shield products, GV-2016 and GV-2018. Against the 0.3" FSP round, this more recent grade provides about a 6–8% increase in V-50 value compared with the original aramid-based specifications (MIL-L-62,474B) of 1992.

In conclusion, these same spall liner materials, with their high volume fraction of fibres, are often used as the backing panels for ceramic-based armour solutions (see Chapters 4 and 7).

References

- Ackland, K., Anderson, C., Ngo, T.D., 2013. Deformation of polyurea-coated steel plates under localised blast loading. *International Journal of Impact Engineering* 51 (2013), 13–22.
- Anon., March 2004a. Collano Xiro® Adhesive Films. Collano®, Product selection sheet.
- Anon., July 14, 2004b. Recommended Processing Data for HB2 and HB25 Dyneema Materials. DSM datasheet.
- Anon., 2005a. Lexan Sheet Processing Guide. GE Structured Products.
- Anon., 2005b. Workshop Handbook – Perspex From Lucite. Lucite International UK Ltd.
- Anon., 2010. AGY Featherlight. AGY website. www.agy.com.
- Anon., 2014. Ocelot Specifications, General Dynamics Specialty Vehicles. <http://www.gdls.com/index.php/products/other-vehicles/ocelot> (accessed 21.04.15.).
- Anon., 2015a. Armorthane Website. www.armorthane.com.
- Anon., 2015b. Clearwater Composites Website. <https://www.clearwatercomposites.com/>.
- Anon., 2015c. DuPont Datasheet for XP500 (S102) Non Crimp Fabric. DuPont website. http://www2.dupont.com/Kevlar/en_US/assets/downloads/DSP_Kevlar%20XPS102_datasheet_K23846.pdf.
- Anon., 2015d. Gurit Website. www.gurit.com.
- Anon., 2015e. PAXCON Website. www.safetydrape.com/products/paxcon.
- Anon., 2015f. RBR Technology. <http://www.ccaprotect.com.au/rbr-armour-systems/aboutus.aspx> (last accessed 26.02.15.).
- Anon., 2015g. Supacat, SPV400 Specifications. <http://www.supacat.com/files/pdf/Supacat-SPV400-specification.pdf> (accessed on 21.04.15.).

- Baker, A., Dutton, S., Kelly, D., 2004. *Composite Materials for Aircraft Structures*, second ed. Beehag, A., July 2015. End of an era for composites R&D. *Connections: The Official Magazine of Composites Australia*, Issue 39, 15–18.
- Bhatnagar, A., 2006. *Lightweight Ballistic Composites*. Woodhead Publishing, Cambridge, England.
- Bhatnagar, A., et al., 2015. High Performance Laminated Tapes and Related Products for Ballistic Application. US Patent Application 9,138,961. Filed October 2012.
- Bless, S.J., Hartman, D.R., 1989. Ballistic penetration of S-2 glass laminates. In: Paper Presented at the 21st International SAMPE Conference, September 25–28, 1989.
- Boaz, N.T., Ciochon, R.L., February 2004. Headstrong Hominids. *Natural History Magazine*.
- Campbell Jr., F.C., 2003. *Manufacturing Processes for Advanced Composites*. Elsevier Advanced Technology, Oxford.
- Cantwell, W.J., Morton, J., 1991. The impact resistance of composite materials — a review. *Composites* 22 (5), 347–362.
- Carey, M., Herz, M., Corner, B., McEntire, J., Malabarba, D., Paquette, S., Sampson, J.B., 2000. Ballistic helmets and aspects of their design. *Neurosurgery* 47, 678–689.
- Cartwright, B.K., Mulcahy, N.L., Chhor, A.O., Thomas, S.G.F., Suryanarayana, M., Sandlin, J.D., Crouch, I.G., Naebe, N., September 2015. Thermoforming and structural analysis of combat helmets. *Journal of Manufacturing Science and Engineering* 137 (5), 051011.
- Criscescu, N., Malvern, L.E., Sierakowski, R.L., 1975. Failure Mechanisms in Composite Plates Impacted by Blunt-Ended Penetrators. ASTM STP 568, Foreign Object Impact Damage to Composites, p. 159.
- Crouch, I.G., 1986. A Review of Metallic Composite Materials for Armour. Internal Report. RARDE, Chertsey.
- Crouch, I.G., 1993. Penetration and perforation mechanisms in composite armour materials. In: Paper Presented at the Euromech Colloquium 299, Oxford University, March 1993.
- Crouch, I.G., 2009a. Do composites make good armour. In: *Composites Australia & the Composites CRC Annual Conference & Trade Show 2009*. <http://www.compositesconference.com/>.
- Crouch, I.G., 2009b. Private Communication. Armour Solutions Pty Ltd.
- Crouch, I.G., 2013a. Next generation combat helmets. In: Paper Presented at the 3rd DMTC Annual Conference, March 2013, Canberra, Australia.
- Crouch, I.G., 2013b. Unpublished Data.
- Crouch, I.G., Sandlin, J.D., May 2010. Review of Alternative Materials for Next Generation Torso Armours. DMTC Technical Report, Project 6.1.2.
- Crouch, I.G., Greaves, L.J., Simmons, M.J., 1990. Compression failure in composite armour materials. In: Paper Presented at the 12th International Symposium on Ballistics, San Antonio, Texas, USA, October 1990.
- Crouch, I.G., Greaves, L.J., Ruiz, C., Harding, J., September 1994. Dynamic compression of toughened epoxy interlayers in adhesively bonded aluminium laminates. Supplement to *Journal de Physique III, Colloque C8 4*, 201–206.
- Crouch, I.G., Greaves, L.J., Simmons, M.J., Rutherford, K.L., 1993. Penetration and Perforation Mechanisms in Composite Armour Materials. *Euromech Colloquim*, Oxford, UK, p. 299.
- Cunniff, P.M., 1999. Dimensionless parameters for optimisation of textile-based body armor systems. In: Paper Presented at the 18th International Symposium on Ballistics, San Antonio, Texas.
- Davê, R.S., Loos, A.C., 1999. *Processing of Composites*. Hanser, Munich.

- Dutton, S.E., Crouch, I.G., St. John, N.A., 2000. Meeting requirements for a composite rail vehicle application. In: Paper Presented at the ACUN-2 on Composites in the Transportation Industry, UNSW, Sydney, Australia.
- Fountzoulas, C., Cheeseman, B., Dehmer, P., Sands, J., June 2009. A Computational Study of Laminate Transparent Armour Impacted by FSP. US Army Research Laboratory.
- Freitas, C.J., et al., 2014. Dynamic response due to behind helmet blunt trauma measured with a human head surrogate. *International Journal of Medical Sciences* 11.
- French, M., Lewis, M., 1996. The advanced composite armoured vehicle platform (ACAVP) programme. *Journal of Defence Science* 1 (3), 296–301.
- Gellert, E.P., Pattie, S.D., Woodward, R.L., 1998. Energy transfer in ballistic perforation of fibre reinforced composites. *Journal of Materials Science* 33, 1845–1850.
- Greaves, L.J., 1992. Failure Mechanisms in Glass Fibre Reinforced Plastic Armour. MVEE, Chertsey. Internal Memorandum.
- Hsieh, A., DeSchepper, D., May, P., Dehmer, P., February 2004. The Effects of PMMA on Ballistic Impact Performance of Hybrid Hard/Ductile All-plastic and Glass-Plastic Based Composite. ARL-TR-3155. Army Research Laboratory.
- Huang, X., 2009. Fabrication and properties of carbon fibres. *Materials* 2009 (2), 2369–2403.
- Jaitlee, R., 2013. Physical Protection: Inter-Dependence Between Hard and Soft Armours (Ph.D. thesis). RMIT University, Australia.
- James, B.J., Howlett, S.A., 1997. Enhancement of post-impact structural integrity of GFRP composite by through thickness reinforcement. In: Paper Presented at the 2nd European AFV Symposium, RMCS Shrivenham, May 1997.
- James, M., 2009. *Polymer Data Handbook*, second ed. Oxford University Press, Oxford, UK.
- Jordan, J.B., Naito, C.J., 2014. An experimental investigation of the effect of nose shape on fragments penetrating GFRP. *International Journal of Impact Engineering* 63, 63–71.
- Kalpakjian, S., Schmid, S.R. (Eds.), 2008. *Manufacturing Processes for Engineering Materials*, fifth ed.
- Klintworth, W.R., Crouch, I.G., 2002. European Patent, EP 1 319 917 A2, Filed 12.12.2002, Hard Armour Panel and Production Method Therefor.
- Kruckenbergt, T., Paton, R., 2012. *Resin Transfer Moulding for Aerospace Structures*. Springer.
- Ling, M., June 27, 2013. Private Communication DMTC to DSM Re Dyneema®. Asia Pacific Technical Centre, Singapore.
- Miravette, A., 1993. Composites design. In: Ninth International Conference on Composite Materials (ICCM/9). Madrid, July 1993. Woodhead Publishing.
- Morrison, C.E., Bowyer, W.H., 1980. Factors Affecting the Ballistic Impact Resistance of Kevlar Laminates. Fulmer Research Institute report, 1980.
- Mulcahy, L., Cartwright, B., 2011. Structural Analysis of Composite Helmets. DMTC Internal Report, Project 8.10, November 2011.
- Naebe, M., Sandlin, J.D., Crouch, I.G., Vella, J., July 2009. Next Generation Armour Technologies Program. Advanced Manufacturing CRC, Technical Report.
- Nguyen, L.H., Ryan, S., Cimpoeru, S.J., Mouritz, A.P., Orifici, A.C., 2015. The effect of target thickness on the ballistic performance of ultra high molecular weight polyethylene composite. *International Journal of Impact Engineering* 75, 174–183.
- Ogorkiewicz, R., 2015. *Tanks: 100 years of Evolution*. Osprey Publishing, Oxford, UK.
- Ogorkiewicz, R.M., 1996. High fibre diet for armour. *Janes International Defense Review* 1 (1996), 57.
- Ostberg, D.T., et al., 1996. Composite Armored Vehicle (CAV) advanced technology demonstrator. In: Paper Presented at the 14st International SMAPE Symposium, March, 1996.

- Passagian, A., 2009. Purchase Description for Enhanced Combat Helmet Revision 1.0. GL-PD-09–04. U.S. Department of Defense, U.S. Marine Core. April 2009.
- Pervorsek, D.C., Chin, H.B., Kwon, Y.D., Field, J.E., 1991. Strain rate effects in ultrastrong polyethylene fibres and composites. *Journal of Applied Polymer Science* 47, 45–66.
- Ramsay, J., 2015. Private Communication.
- Rayner, M.C., Crouch, I.G., 1984. A Study of the Relationship Between Hardness and the Ballistic Properties of Aluminium Alloys. MVEE, Chertsey. Technical Report.
- Reid, S.R., Reddy, T.Y., Ho, H.M., Crouch, I.G., Greaves, L.J., 1995. Dynamic indentation of thick fibre-reinforced composites. In: Paper Presented at the ASME Conference on High Strain Rate Behavior of Composites, San Francisco, November 1995.
- Rozant, O., Bourban, P.E., Manson, J.A., 2000. Drapability of dry textile fabrics for stampable thermoplastic preforms. *Composites Part A: Applied Science and Manufacturing* 31 (11), 1167–1177.
- Rudd, C.D., et al., 1997. *Liquid Moulding Technologies*. Woodhead Publishing, Cambridge, UK.
- Rush, S., January 2007. The art of armor development. *High Performance Composites*.
- Sandlin, J., November 2007. Trial Pressing of Spectra SR3124 Backing Plates. VCAMM report.
- Sabart, B., Gangel, J., 2010. Thermoforming for Prototype and Short-Run Applications. www.redeyeondemand.com (accessed 14.05.10.).
- Sandlin, J., Kenyon, M., 2014. Helmet Technologies Overview. DMTC Technical Report, Project 7.1.2.
- Sandlin, J., et al., 2011. Research, Development, Design and Manufacture of a New Combat Helmet. DMTC Technical Report, Milestone 2, Projects 6.1 & 3.7.
- Sands, P., Patel, P., Dehmer, A., Hsich, M., October 2004. Protecting the future force: transparent materials safeguard the Army's vision. *The AMPTIAC Quarterly* 8 (4).
- Shelley, T., 2000. Composite hull gives tank top performance. *Eureka Magazine*.
- Simmons, M.J., Smith, T.F., Crouch, I.G., 1989. Delamination of metallic composites subjected to ballistic impact. In: 11th International Conference on Ballistics, Brussels, Belgium, pp. 351–360.
- Singletary, J., Chang, K., Scott, B., Squillacioti, R., 2011. Properties of cross-plyed unidirectional aramid fiber laminates for a new detailed military specification: MIL-DTL-32378. In: Paper Presented at the 26th International Symposium on Ballistics, Miami, FL, USA.
- Siviour, C.R., Walley, S.M., Proud, W.G., Field, J.E., 2005. The high strain rate compressive behaviour of polycarbonate and polyvinylidene difluoride. *Polymer* 46 (2005), 12546–12555.
- Song, J., Lofgren, J., Hart, K., Tsantinis, N., Paulson, R., Hatfield, J., November 2006. Aromatic Nylons for Transparent Armor Applications. U.S. Army Research Development and Engineering Command, Soldier Systems Center, Natick Soldier Center.
- Summerscales, J., 2015. www.tech.plym.ac.uk/sme/acavp.htm.
- Summerscales, J., Searle, T.J., 2005. Low-pressure (vacuum infusion) techniques for moulding large composite structures. *Proceedings of the Institution of Mechanical Engineers, Part L: Journal of Materials Design and Applications* 219.
- Utracki, L.A., October 2010. CNRC-NRC Report, Rigid Ballistic Composites (Review of Literature). Canada.
- Walsh, S., 2009. Enhancing the Performance of Thermoplastic-Based Ballistic Helmets. Society of Photographic Instrumentation Engineers.
- Walsh, SM, Vargas-Gonzalez, LR, Scott, BR, Lee, D. Developing an Integrated Rationale for Future Head Protection in Materials and Design. U.S. Army Research Laboratory, Aberdeen Proving Ground; Md: 2012.

- Wong, W., et al., 2001. The effect of matrix type on the ballistic and mechanical performance of E-glass composite armour. In: Paper Presented at the International Symposium on Ballistics, Interlaken, Switzerland, May 2001.
- Yong, M., Iannucci, L., Falzon, B., 2010. Efficient modelling and optimisation of hybrid multilayered plates subject to ballistic impact. *International Journal of Impact Engineering* 37 (6).
- Yuan, F., et al., 2007. Spall strength of glass reinforced polymer composites. *International Journal of Solids and Structures* 44 (2007), 7731–7747.

Fibres, textiles and protective apparel

6

I.G. Crouch¹, L. Arnold¹, A. Pierlot², H. Billon³

¹RMIT University, Brunswick, Victoria, Australia; ²CSIRO, Waurn Ponds, Victoria, Australia;

³Defence Science and Technology Group, Fishermans Bend, Victoria, Australia

6.1 General introduction to protective apparel

6.1.1 Personal body armour

The words 'Kevlar vest' are synonymous with protective apparel for both civilians and military personnel and most people recognise that Kevlar has been universally used as the main bullet-resistant material, since the early 1980s. But, what is Kevlar? Who invented it? What sort of aramid fibre is it? How does it absorb so much impact energy, from a lead-filled, handgun bullet travelling at velocities of up to 450 m/s? Is it the only fibre for such an application, and are there even better fibres now available?

This chapter explains how and why technical fibres, in the form of fabrics, are still the material of choice for advanced, lightweight, protective apparel and, while stopping a bullet is not easy, preventing an ice-pick from perforating a prison officer's clothing can be even more challenging.

Before looking at these high-strength materials in more detail, we need to consider the actual impact event itself. Several common features are associated with the impact of a projectile against protective apparel, whether the projectile is a knife, a low-velocity handgun bullet or a high-velocity rifle round:

- The projectile imposes an intense, point-load on the body armour system (BAS).
- A medium-to-high-velocity impact event creates stress waves (or, under high enough impact pressures, even shock waves) in the armour material. These can be reflected from internal surfaces and create severe secondary effects like behind armour blunt trauma (BABT).
- The associated impact force is a nonuniform function of time, but has a finite amount of input energy.
- The impact event occurs over a short duration, typically lasting between 20 μ s for high-speed bullets and 0.2 s for knife attacks.
- The impact imposes large deformation strains on the armour which usually leads to localised failure.
- The armour material will respond differently under different impact conditions, compared to normal quasistatic loading, especially if any of its physical properties are strain-rate sensitive. Most polymeric materials, as well as some metals, are sensitive to changes in loading rate.



Figure 6.1 Typical example of personal body armour circa 2014.
From images.defence.gov.au

For personal body armour (PBA), a typical bulletproof vest will consist of many layers of fabric that are normally stitched together to form a coherent mass (commonly referred to as a pack). But how many layers are required? What sorts of fabrics are best? Which fibres should be used? What are their physical properties and how do they behave at high rates of strain? Each element plays its part. [Section 6.2](#) covers the fibres, [Section 6.3](#) the fabrics, [Section 6.4](#), the layering of the fabrics and, finally, [Section 6.5](#) treats the entire body armour system, holistically. [Fig. 6.1](#) shows such a body armour system as an integral part of the modern combatant's apparel.

Textiles, like armour materials in general, are primarily selected based upon their ballistic merit rating but, because armours need to function in a particular environment, the chosen materials also need to meet a range of engineering requirements, such as chemical, weather, and water resistance, as well as comfort, and any overriding occupational health and safety requirements. The general properties of textiles, particularly in terms of the processing options, have been well reviewed in [Bhatnagar \(2006\)](#). Here, we focus upon ballistic properties.

6.1.2 Energy-absorbing mechanisms and failure modes

Ballistic impact onto an armour material can be envisaged as an energy balance between the impacting projectile and the target. The impacting projectile possesses kinetic energy that is transferred to the target where the kinetic energy is converted

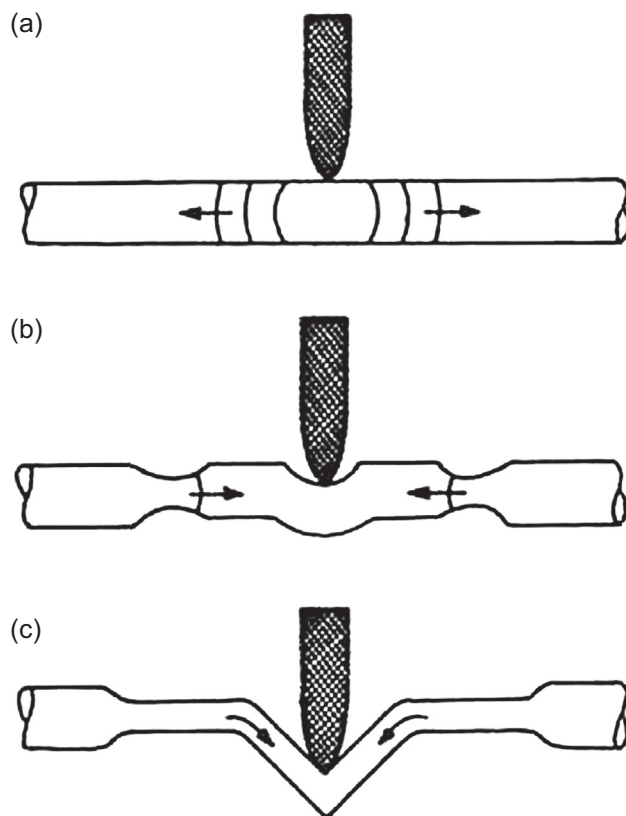


Figure 6.2 Transversal and longitudinal waves in a yarn impacted by a projectile.

into other forms of energy. For a textile-based target this will include the kinetic and potential energy of textile elements, such as yarns and fibres. Nonconservative forces play a major role in most ballistic events so that a significant percentage of the energy is dissipated. It is also possible for a projectile to undergo deformation during impact.

The simplest element of a ballistic fabric is usually a fibre or yarn. An understanding of yarn impact can lead to insights into the behaviour of more complex fabrics or fabric assemblies. A ballistic impact onto a yarn (Fig. 6.2) leads to deformation that is manifested as two types of wave that propagate away from the impact point. One type of wave is linked to the stretching of the yarn and is known as a longitudinal wave. This travels outward along the yarn at the speed of sound and is independent of the impact velocity of the projectile. This initiates the movement of the material within the yarn towards the impact point and is linked to the stretching of the yarn. The second type of wave is the transverse wave: it is slower and makes the yarn material move in the same direction as the projectile. Therefore, when a high-speed projectile impacts a fabric made up of woven yarns, it is deformed in a direction perpendicular to the fabric plane (see Fig. 6.3).

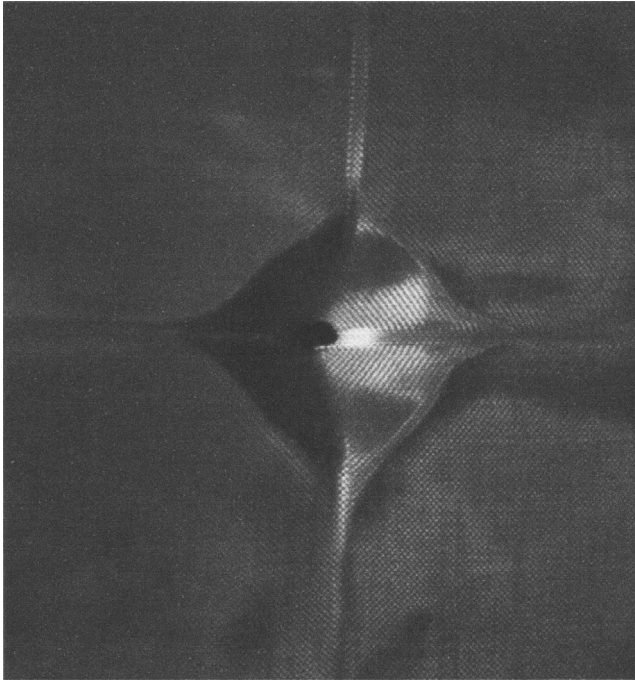


Figure 6.3 Deformation of a single layer of fabric by a fragment-simulating projectile. Sakaguchi, S., Carr, D., Horsfall, I., Girvan, L., 2012. Protecting the extremities of military personnel fragment protective performance of one- and two-layer ensembles. *Textile Research Journal* 82 (12), 1295–1303.

As Fig. 6.2 shows, there are three distinct zones in an impacted yarn:

1. Two undisturbed regions on either side that are yet to be influenced by the impact.
2. Two regions where polymer molecules within the yarn are only deflected horizontally — where necking of the yarn material occurs.
3. A central V-shaped zone where yarn is deflected in the direction of the impact.

Careful observations, and classical research by [Cunniff \(1992\)](#), amongst others, have confirmed the following facts:

- The yarn in the V-shaped region only possesses a transverse velocity component. All horizontal motion ceases as soon as yarn material enters this zone from the adjacent necked zones of horizontal deflection.
- All yarn material in the zones of horizontal deflection is strained to a value, ϵ , which is a function of the yarn's physical properties as well as the impact velocity, V_p . This strain may be assumed to be constant over the extent of the horizontal zones.
- All yarn material in the horizontal stretching zones move with the same speed.
- Provided the projectile velocity remains constant during the impact, the vertical component of the velocity of the yarn in the V-shaped zone is the same for all yarn material. This component equals the projectile impact velocity, V_p .

This last assumption is an excellent one for most impacts because the kinetic energy of, for example, a bullet at muzzle velocity, is a large overmatch for the very small amount of energy absorbed by the individual yarns.

The out-of-plane (transverse) deformation progresses outwards, away from the point of impact. In addition, the in-plane (longitudinal) strain waves propagate outward along the yarns at the speed of sound within the woven material. The higher the in-plane wave velocity, the greater the dissipation of strain away from the impact zone. It is very important, therefore, for the material to have a high wave velocity. This is proportional to the square root of the elastic modulus and inversely proportional to the square root of the density of the yarn. The wave velocity in the fabric is not necessarily the same as in the constituent yarn since the fabric structure introduces crimp at the cross-over points.

The velocity of impact is crucial in determining how the fabric responds. At a low impact velocity, coupled with a high wave velocity in the fabric, the stress level reached within the fabric may be below the critical value of yarn strength needed to rupture the yarns within the fabric, thus allowing the stress wave to propagate throughout the fabric. In this scenario, the energy transferred during the transverse deformation will be one of the main energy-absorbing mechanisms. The projectile may nevertheless penetrate the fabric by pulling yarns out of the fabric structure. This mechanism depends on interyarn friction within the fabric and projectile–yarn friction.

As the projectile penetrates a multilayered soft armour insert, it may experience different failure modes since the impacting bullet is both deforming and spinning. The copper jacket is also plastically deforming and failing and can, on occasions, be seen to cut its way through some plies (see [Fig. 6.4](#)).

If the impact velocity is high enough, the fabric may be perforated during the initial stress rise because it is unable to respond quickly enough to absorb the energy of the

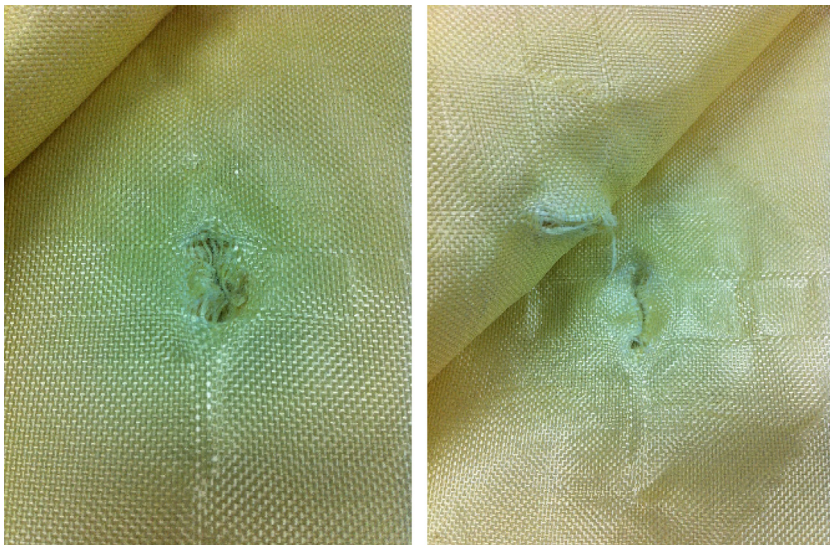


Figure 6.4 Typical perforation damage within a multilayered, aramid soft armour insert, showing different degrees of failure through different plies.

projectile before the breaking load of the yarn material is exceeded. This results from the limitations on stress relaxation due to the finite longitudinal wave velocity within the fabric. This reinforces the importance of the high strain-rate-dependent properties of the yarn material.

For textile armour therefore, the tenacity, elongation at rupture, and the wave velocity within the yarns are the most important properties. Thus, yarns used in modern armour systems are chosen because they exhibit a good combination of these properties, as indicated in [Section 6.2](#). In summary, these two energy-absorbing mechanisms can be described using just two equations:

$$V = (E/\rho)^{1/2} \quad (6.1)$$

where V = strain wave velocity, E = elastic modulus of the yarn and ρ is the bulk density of the yarn, and

$$E_S = \sigma \varepsilon / 2\rho \quad (6.2)$$

where E_S is the elastic stored energy in the fibre, σ is the stress and ε is the strain, up to the yield stress.

[Phillip Cunniff \(1999b\)](#) presented a keynote paper at the 18th International Symposium on Ballistics, in San Antonio, and proposed combining these two main factors into one unified, dimensionless factor $(U^*)^{1/3}$, where

$$(U^*)^{1/3} = V \cdot E_S \quad (6.3)$$

His analysis assumed that the elastic stored energy (E_S) and fibre strain velocity, V , were the only two key mechanical properties and that the impact area (surface area of the front of the projectile) and its mass were the only two key parameters of the impactor. This approach has produced a carpet plot for all fibre types (see [Fig. 6.5](#)) and appears to be universal. During the 2000s, it became a very popular way of providing a direction for further research. Cunniff and Auerbach ([Cunniff et al., 2002](#)), for example, used this approach, in 2002, to predict the properties of the PBO fibre (see [Section 6.2.7](#)). However, as pointed out recently by Cunniff himself at ISB2014, in Atlanta ([Cunniff, 2014](#)), the UHMWPE family of materials appears to be the exception to this universal rule and further work is required.

6.2 Technical fibres for ballistic fabrics

6.2.1 Brief history, from Kwolek to carbon nanotubes

Although fabrics, such as silk, nylon, and even paper ([Dekker, 2009](#)), have been used for ballistic protection, the modern era of ballistic protection from fibre-based textiles can be dated to the invention of Kevlar by Stephanie Kwolek and her team at DuPont.

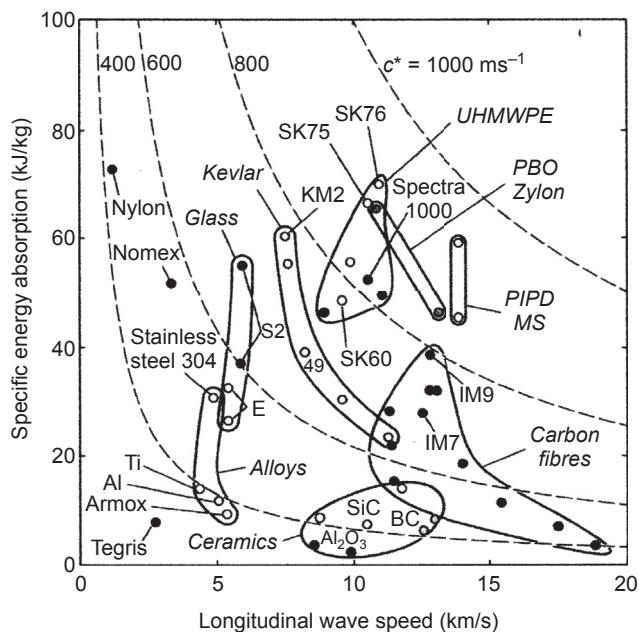


Figure 6.5 Families of typical armour materials, plotted as longitudinal wave speed and specific energy absorption, overlaid with contours of constant Cuniff factors.

Cunniff, P.M., 1999b. Dimensionless parameters for optimisation of textile-based body armor systems. Paper Presented at the 18th International Symposium on Ballistics, San Antonio, Texas.

Kwolek discovered that para-amino benzoic acid could be polymerised and solubilised. It was initially believed that this solution could not be spun into fibres. However, it was found that the solution formed liquid crystals that could be spun easily (Pramanik and Chakraborty, 2004). Kevlar (poly 1,4 phenyleneterephthalamide) consists of long-chain molecules in which the backbone aromatic rings connect to each other via para-bonds to give an extremely strong and inextensible rod-like structure. Closely related Nomex has the same chemical formula but its aromatic rings are interconnected via meta-bonds (Laible, 1980).

Another milestone was the development of ballistic fibres based upon ultrahigh molecular weight polyethylene (UHMWPE). UHMWPE consists of long-chain molecules, like Kevlar, but there are some important differences between the two materials. Kevlar has a much higher decomposition point at high temperatures, while UHMWPE molecules rely heavily on the molecular length for bonding strength. This is because the bonding between the UHMWPE molecules depends on relatively weak dispersion forces, not hydrogen bonding.

UHMWPE yarns or fibres may be found in a variety of fabric types. Yarns may be woven into simple weave fabrics or the individual filaments or fibres may be laid up in a 0/90 cross-ply configuration. UHMWPE fibres have also even been felted (see Section 6.3.5) and are available commercially as Fraglight.

A further recent advance in the ballistic protection field was the development by SRI and Toyobo of fabrics based upon poly *p*-phenylene-2,6-benzobisoxazole (PBO) fibres (known commercially as Zylon). PBO fibre has a much higher tensile strength and stiffness than Kevlar. However it was found to degrade rapidly when exposed to hot, wet environments and its ballistic properties were severely compromised. This led to incidents where law enforcement personnel protected by Zylon-based vests, manufactured by Second Chance Body Armor Inc., were killed or seriously injured when the vests failed unexpectedly while in use. This had a profound effect not only upon the material developers, and suppliers, but the law enforcement agencies and governing bodies — a new version of the NIJ0101 body armour standard was quickly developed ([National Institute of Justice, 2008](#)). This, in turn, placed even greater pressure upon suppliers, with far more stringent testing regimens, and some companies did not survive.

Attempts have also been made to develop biological materials, in particular spider silk for armour. Spider silk ([Bolduc and Lazaris, 2002](#)) is said to have the highest toughness of all ballistic fibres. Bolduc stated that spider dragline silk is three times tougher (toughness defined as area under the stress–strain curve) than aramid fibre and five times stronger than steel (ultimate strength relative to density). Since there are issues associated with the domestication of spiders for silk production (spiders are not social animals and the process of extracting silk is cumbersome) ([Cunniff et al., 1994](#)), some effort has been devoted to artificial manufacture methods.

Transgenic production of recombinant silk proteins and their secretion into the milk of mice and goats has been investigated ([Tokareva et al., 2013](#)). In the case of goats, Nexia Biotechnologies and the Lewis Group have done this. Over the past decade there has been progress in understanding genetic information related to spider silk and the cloning, expression and purification of spider silk has improved. A potential advantage of using a recombinant approach is that it might be possible to use the silk element to produce custom structures. Tokareva concluded that the major challenge is the scaling up of silk production.

Some effort has recently been devoted to the development of ballistic protective materials derived from, or incorporating, nanotechnology. This includes carbon nanotubes. For example, [Mylvaganam and Zhang \(2007\)](#) have conducted small-scale numerical studies using molecular dynamics to simulate a diamond projectile impact onto a carbon nanotube. They concluded that body armour of only 600- μm thickness could stop a bullet with a muzzle energy of 320 J. However, a number of challenges must be overcome before the molecular level properties of carbon nanotubes can be translated into practical ballistic protection.

[Du et al. \(2007\)](#) acknowledge the extremely high tensile strength (200 GPa) and elastic modulus (1–2 TPa) predicted for carbon nanotubes but also list a number of problems. These include a lack of consistency in structure, morphology, aspect ratio, crystallinity and mechanical properties. [Song et al. \(2011\)](#) describe the chemical vapour deposition (CVD) process commonly used to produce carbon nanotubes. They state that the quality of the nanotubes decreases with length and that tube nonuniformity and defects limit the lengths that can be spun into yarn.

6.2.2 Structure and properties of fibres

High-performance fibres for ballistic applications have high strength and stiffness (modulus) but low elongation ($<5\%$). In comparison, commodity fibres used in other textile applications (eg. polyester, nylon, silk and acrylic fibres) have lower strength and modulus values but higher elongation before rupture. Commodity fibres have crystallinity of around 30–65% with a crystalline orientation factor in the 0.9–0.98 range. In order to achieve high strength and stiffness, the molecules must be fully extended and well-orientated. Chain folding and off-axis orientation of molecular segments must be avoided. The higher strength and modulus of high-performance fibres are attributed to the higher degree of crystallinity (approaching 100%) and orientation factor (>0.99) with significantly fewer defects such as voids, chain ends and bends. Stress transfer between parallel chains is through intermolecular bonds and chain overlap. Where intermolecular bonding is strong, lower molecular weights are needed to achieve high strength. Fig. 6.6 shows the measured relationship between crystal modulus and fibre modulus. These data are from c.2000 — it would be expected that the fibre modulus for UHMWPE fibres, like Spectra, c.2015, will be approaching that of the crystal modulus of 220 GPa, although reported figures are still only 120–150 GPa.

The structure and morphology of the individual fibres will dictate how they fail, when ballistically tested, and therefore how much impact energy they might absorb.

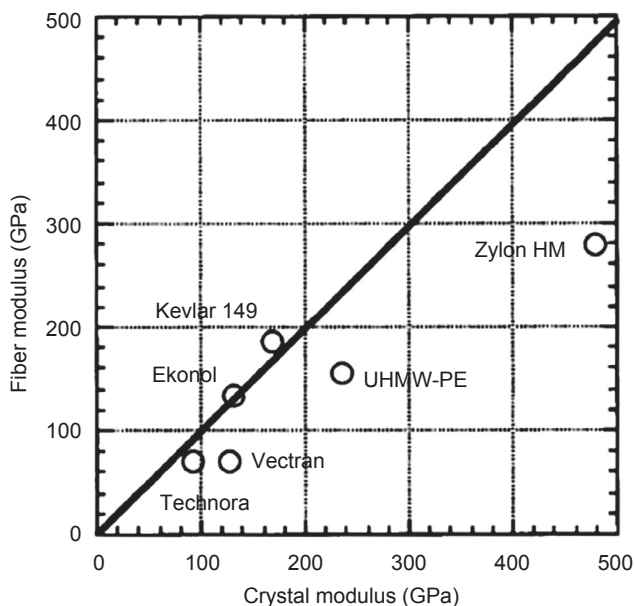


Figure 6.6 Comparison between fibre modulus and crystal modulus for ballistic fibres. Kitigawa, T., Ishitobi, M., Yabuki, K., 2000. *Journal of Polymer Science, Part B: Polymer Physics* 38, 1605.

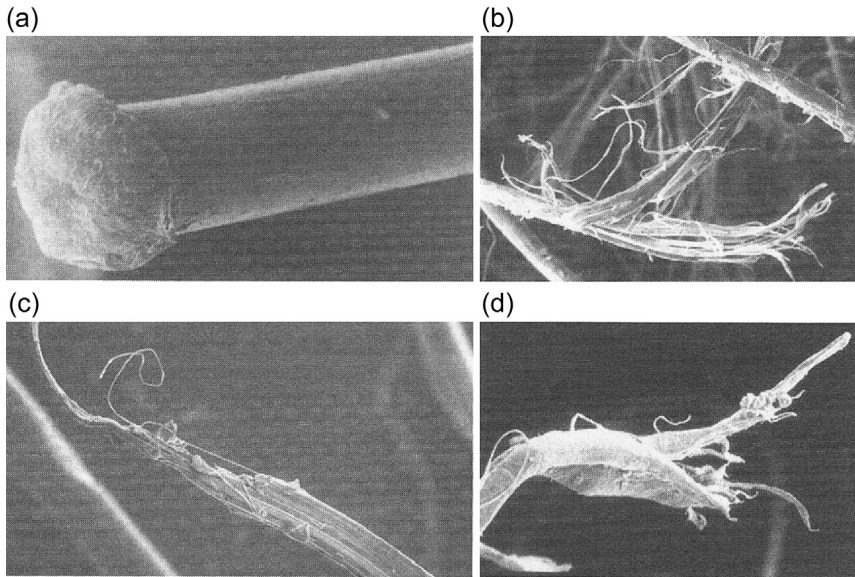


Figure 6.7 Failure of fibres: Nylon 66 (a), Kevlar 29 (b), Spectra UHMWPE (c) and Zylon (d). Bhatnagar, A., 2006. *Lightweight Ballistic Composites*. Woodhead Publishing, Cambridge, England.

Fig. 6.7 (after Bhatnagar, 2006) shows the different morphologies and failure modes of various ballistic fibres: considerable defibrillation is seen in the Kevlar and PBO fibres, with slightly more fibril straining and splitting in the Spectra fibre. In comparison, the nylon fibre shows clear evidence of melting, at its tip. It should be noted that these failure modes will vary depending upon location within the impact zone.

The most common fibres available for ballistic protection systems are based on UHMWPE, poly-*para*-phenylene terephthalamide (often abbreviated as PPTA, para-aramid or *p*-aramid) and polyamide (nylon). Silk was once used as a ballistic fibre but has now been replaced by synthetic fibres, except when used in underwear. Ballistic nylon is superior to silk but has significantly lower performance compared to UHMWPE or PPTA. These latter two groups of fibres currently dominate the market with a number of companies supplying these fibre types.

Apart from ballistic properties, other properties are also important in selecting a fibre for a particular protection application. Alternative commercial fibres exist because these additional performance attributes cannot be optimised in one particular fibre type. Although strong, UHMWPE has a low melting temperature and can burn and drip molten polymer so is avoided in applications where this may cause further injuries. PPTA is significantly degraded by even short-term ultraviolet (UV) exposure so is avoided when products are likely to be in direct sunlight unless they are protected from UV in some manner. Less common ballistic fibres include poly(*p*-phenylene-2,6-benzobisoxazole) (abbreviated to PBO), poly(*p*-phenylene benzobisthiazole) (abbreviated to PBT or PBZT), and poly{2,6-diimidazo[4,5-*b*:4',5'-*e*]

Table 6.1 Typical properties of first-generation fibres used in ballistic applications

Fibre type	Bulk density (kg/m ³)	Tensile strength (MPa)	Tensile modulus (GPa)	Tenacity (N/tex)	Elongation at rupture (%)	Wave velocity (m/s)	Cunniff factor, (U^*) ^{1/3} (m/s)
Silk ^a	1,250	740	10	0.6	10–30	2,800	550
Nylon 66	1,140	910	10	0.8	15–20	2,960	482
Kevlar 29	1,440	3,000	74	2.1	3.5	6,996	621
Kevlar 49	1,440	2,900	105	2.0	2.5	9,649	612
Spectra 1000	970	3,000	171	3.1	2.7	13,277	801
PBO	1,560	5,200	169	3.3	3.1	10,400	813
M5 (2001)	1,740	3,960	271	2.3	1.4	12,500	583

^a<http://nsrdec.natick.army.mil/LIBRARY/90-99/R94-30.pdf> for information.

pyridinylene-1,4-(2,5-dihydroxy) phenylene} (abbreviated to PIPD). Typical fibre properties are given in [Table 6.1](#).

During fibre production, treatment conditions, for example draw ratio and heating profile, are modified to produce fibres with properties optimised for specific applications. With extended drawing, the tenacity and modulus can be increased but typically at the expense of fiber elongation before break. Often these variations in fibre properties are marketed as ‘standard’, ‘high-modulii and ‘high-tenacity’ fibres. The diameter of individual filaments and the number combined to form a yarn may also be varied. In addition to producing fibres and yarns, companies also produce a number of woven and nonwoven fabrics (with the inclusion of fabric treatments) for ballistic applications.

6.2.3 Silk fibres

From the padded silk armours developed during the sixth and seventh centuries ([Fig. 6.8](#)) to the silk-quilted armours introduced into England in the 17th century, armour technologists have always had an interest in taking advantage of its attractive properties: lustre, comfort and environmental stability. In the 1950s ([Laible, 1980](#)), US researchers demonstrated that silk fabrics could achieve a ballistic performance, against 1.1-g FSPs, that was greater than nylon fabrics. Of greater interest, these same researchers also discovered that both the strength and modulus of the silk fibres increased significantly with strain rate. However, silk fibres were found to be susceptible to biological attack and low tensile strength when wet, and even though many others have investigated alternative varieties like spider silk ([Cunniff et al., 1994](#)) fibres, manufactured from farmed silkworms, have not been widely adopted as a modern, mainstream armour material.

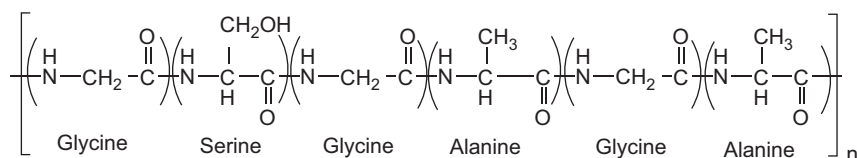
Silks are protein fibres produced by various animals, the most commonly available silk being from the cocoons of the mulberry silkworm (*Bombyx mori*) larvae. In its



Figure 6.8 Quilted silk armour circa seventh century.
Source: Crouch, Royal Armouries Museum, Leeds (2015).

raw state, *B. mori* silk consists of two proteins, sericin, a sticky material that is removed during processing, that surrounds the core structural protein, fibroin. The fibroin is composed of various amino acids that are linked together by amide bonds. The amino acids glycine (49%), alanine (30%) and serine (11%) make up 90 mol% of silk (fibroin) fibre. It is a large, complex polymer (see Fig. 6.9), consisting of recurrent sequences of these amino acids with spatial conformation permitting both intra- and intermolecular hydrogen bonding and the formation of layers of antiparallel beta pleated sheets. The fibre has a triangular cross-section with rounded corners giving silk its lustre.

Due to its improved comfort and moisture absorption properties compared to synthetic ballistic fibres, silk may be used in underwear to provide some protection



Bombyx mori silk

Figure 6.9 Predominant structural unit for *Bombyx mori* silk.

to the groin and femoral artery from small fragments generated from improvised explosive devices.

6.2.4 Polyamide (nylon) fibres

The invention of nylon is attributed to Carothers, while working at Du Pont in the early 1930s. Commercialisation was fairly rapid and, by WW2, aircrews were wearing flak jackets to prevent shrapnel wounds. The soft armour pack weighed 15.2 kg/m^2 , about three times the weight of today's packs! However, Nylon 6,6, commonly referred to as 'ballistic nylon', remained the material of choice throughout the 1940s and 1950s and [Vanderbie \(1957\)](#) reported the effectiveness of nylon flak jackets during the Korean War with chest injuries for US soldiers reduced by up to 60%. By this time, the typical areal density of these vests was down to around 6 kg/m^2 . The first military specification [MIL-C-12369F(GL)] was published in 1974, and has been modified several times since.

Nylon or polyamide fibres are polymers are fairly simple, straight polymer chains (see [Fig. 6.10](#)) with repeating units linked through amide bonds. Silk and wool are examples of natural polyamide fibres, while examples of synthetic polyamide fibres include nylon and aramid. Nylon is a thermoplastic polyamide formed through the condensation reaction of a diamine and a dicarboxylic acid. To be more specific when describing nylon (fibre), numerical suffixes are used to denote the number of carbon atoms in each monomer, the diamine first followed by the dicarboxylic acid, for example, Nylon 6,6 the most common form of nylon [also known as poly(hexamethylene adipamide)]. Nylon 6 is synthesised by ring opening polymerisation of caprolactam (azepan-2-one; six carbon atoms in ring).

6.2.5 Poly(*p*-phenylene terephthalamide) (PPTA) fibres

PPTA (commonly known as para-aramid) fibres are synthesised by polymerisation of benzene-1,4-diamine [also known as *p*-phenylenediamine (PPD)] and terephthaloyl dichloride (TCL) in a condensation reaction that eliminates hydrochloric acid as a

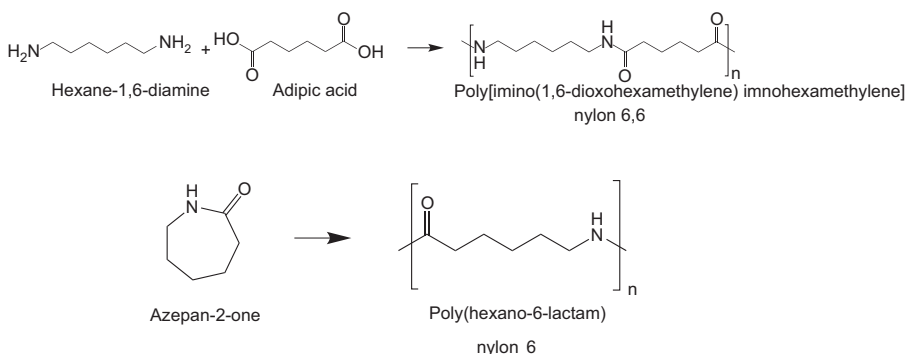


Figure 6.10 Chemical structure of Nylon 6,6 and Nylon 6.

Table 6.2 Examples of PPTA fibre types and properties

Fibre type	Tensile strength (MPa)	Tensile modulus (GPa)	Elongation at rupture (%)	Typical application
Kevlar 29 ^a	3000	74	3.5	Early soft armours
Kevlar 49	2900	105	2.5	Hard armours
Kevlar 129	3400	95	3.4	Most soft armours
Kevlar – KM2	3429	64	4.3	Recent US SAIs
Twaron standard ^b	2400–2500	60–80	3.0–4.4	Soft armours
Twaron high-modulus	3000–3600	100–120	2.2–3.0	Hard armours
Twaron high-tenacity	3400–3600	85–95	3.3–4.0	Soft armours
Twaron 2640 ultramicro	3700	100	3.5	R&D grades
Tecnora 1.39 g.cm ³	3400	74	4.5	Soft armours
AuTx-WE ^c	3600	100–140	2.6–3	Very advanced SAIs
AuTx-DWE	4300	100–140	2.6–3	Very advanced SAIs

^ahttp://www.dupont.com/Kevlar/en_US/assets/downloads/KEVLAR_Technical_Guide.pdf.

^bhttp://www.teijinaramid.com/wp-content/uploads/2012/02/1090308_Twaron-productbrochurefinal_051.pdf.

^c<http://alchemie-group.com/core-materials-technology/autx-aramid-fibre/compliance/>.

byproduct. The polymer in solution has liquid-crystalline behaviour and, on mechanical drawing, the polymer chains orient in the fibre direction and crystallise. Common trade names for PPTA are Kevlar (DuPont), Twaron (Tejin) and Heracron (Kolon). Examples of PPTA fibres and their properties are given Table 6.2.

The generic term ‘aramid’ is used to describe a fibre in which the fibre-forming substance is a long-chain synthetic polyamide in which at least 85% of the amide linkages are attached directly to two aromatic rings (see Fig. 6.11).

Terpolymer fibres (synthesised from three monomers) based on PPTA are also commercially available. Examples include Technora (Teijin) and fibres manufactured in Russia under the trade names of Rusar and Armos. Rather than polymerisation of TCL with 100% PPD, some PPD is replaced by an alternative diamine, 3-(4-aminophenoxy) aniline for Technora and 2-(4-aminophenyl)-1*H*-benzo[*d*]imidazol-5-amine for some Russian-produced fibres (Allen and Newton, 2013).

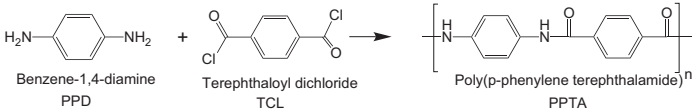


Figure 6.11 Reaction scheme and structure for PPTA.

Under a joint research program between Kamenskvloknokno and Alchemi, the fibre AuTx was developed based on Rusar fibre (from Kamenskvloknokno). This fibre is claimed to have improved toughness compared to PPTA and can be dyed and printed.

PPTA fibres have high crystallinity and strong intermolecular interactions providing the fibre with good organic chemical resistance, but hydrolytic degradation will occur when the fibre is exposed to conditions that are acidic or alkaline. PPTA fibres do not burn or melt but will begin to decompose when heated above 450°C. Prolonged exposure to temperatures above 150°C leads to degraded mechanical properties (strength, modulus and elongation). The mechanical properties of PPTA are significantly degraded by exposure to UV light, depending on wavelength, intensity and time. Fresh yarns will discolour after exposure to ordinary room light but this is normal and not indicative of degradation (Anon, 2015). External fibres in a yarn or fabric will shield (screen) interior fibres from degradation so higher count yarns retain a higher level of their original strength when exposed to UV light. In soft armour ballistic applications, a waterproof and UV-resistant material usually encases PPTA fabrics.

6.2.6 Polyethylene (UHMWPE) fibres

Developed during the late 1980s, these fibres started to make their mark in the field of armour materials during the 1990s and have been available from either DSM (the original inventor/supplier of UHMWPE fibres, under the trade name of Dyneema) or Honeywell (eg, Spectra fibres). Early work at the Cavendish Laboratory was published in 1991 and showed how advanced these fibres were. Using Spectra 1000 fibres in a matrix of Kraton D1107, Pervorsek et al. (1991) showed how damage-tolerant these fibres are, especially under ballistic impact.

UHMWPE is a thermoplastic polyolefin polymer formed from long molecular chains in excess of 100,000 monomer units. They are very simple, straight polymer chains, often referred to as 'rigid rod molecules', which reflects their needle-like characteristic. The high molecular mass is achieved through polymerisation of ethylene with a metallocene catalyst.

During fibre formation, drawing aligns the molecular chains allowing them to obtain a high degree of crystallinity (>80%). Interchain interactions are also important for strong fibres. Whereas hydrogen bonding dominates interchain interactions in PPTA fibres, these are not possible in (nonpolar) UHMWPE where interchain bonding is via much weaker dispersion forces. However, because the molecular chains are long, with high total intermolecular strength, the fibres are strong due to their ability to distribute the tensile load, via shear forces, between molecules. For high-strength PPTA fibres, relatively shorter chains are possible due to their stronger interchain forces. Common trade names for UHMWPE fibre are Dyneema (from DSM) and Spectra (from Honeywell) and examples of their properties are given Table 6.3.

It should be noted that there are no aromatic or other functional groups present in the UHMWPE chain, thus imparting excellent water and chemical resistance. Compare the simplicity of this molecular chain (Fig. 6.13) with that of the terpolymer molecules like the PPTA molecule (Fig. 6.12). However, while UHMWPE fibres are degraded by exposure to UV light over long periods of time, the rate of degradation is

Table 6.3 Examples of UHMWPE fibre types and properties

Fibre type	Tensile strength (MPa)	Tensile modulus (GPa)	Elongation at rupture (%)	Filament (dpf)
Dyneema SK60 ^a	2800	88	3.5	1–3
Dyneema SK76	3700	116	3.8	n/a
Spectra S-900-5600	2180	66	3.5	11.7
Spectra S-900-1200	2570	73	3.9	10.0
Spectra S-1000-2600	2910	97	3.5	5.4
Spectra S-1000-275	3080	113	3.1	4.6
Spectra S-1000-75	3680	133	2.9	1.9
Spectra 2000	3300	120	2.9	3.5

^aHearle (2001).

significantly lower than for PPTA fibres. UHMWPE does have a relatively low melting temperature of around 145–155°C and can only be used at operating temperatures up to 60–80°C. Being a thermoplastic fibre, when exposed to flame, UHMWPE melts, before decomposing, and the gases from this decomposition start burning, ie, the fibre is combustible.

Since the late 1990s, both Honeywell and DSM have continued to develop better and better fibres, with significantly improved properties. This has mainly come about through the ability to produce finer and finer fibres. As shown in Figs 6.14 and 6.15, both ultimate tensile strength (UTS) and elastic modulus of these UHMWPE fibres are strongly related to fibre diameter. However, as these improvements translate into superior ballistic properties, the market price for fabrics is escalating. For example, in 2014, a fourth-generation Honeywell fabric SA5143 was approximately twice the price of a third-generation fabric, like SA3118.

6.2.7 Research grade fibres

6.2.7.1 Polybenzazole fibres (PBO, PBT)

Two of the most common fibres of this type are abbreviated as PBO and PBZT. The latter is sometimes abbreviated to PBT and is often confused with poly(butylene terephthalate). These fibres are synthesised by the reaction of a dihydrogenchloride with benzene-1,4-dicarboxylic acid (terephthalic acid) in poly(phosphoric acid), which acts as the solvent, catalyst and dehydrating agent. Using the dihydrogenchloride, 2,5-diamino-1-3-benzenediol, the polymer poly[(benzo 1,2-*d*:5,4-*d'* bisoxazole-2,6-diyl)-1,4-phenylene] (PBO: poly(benzobisoxazole)) is formed. Alternatively, with 1,4-diamino-2,5-dithiobenzene, the polymer

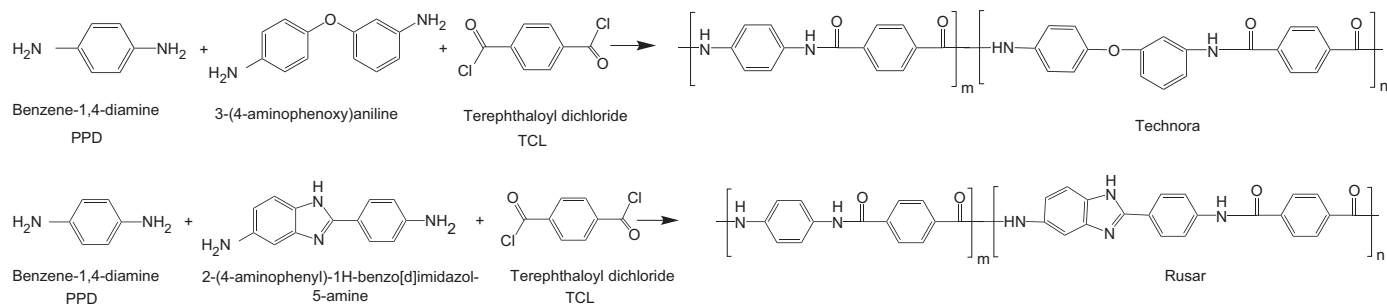


Figure 6.12 Reaction schemes and structures of terpolymers based on PPTA.

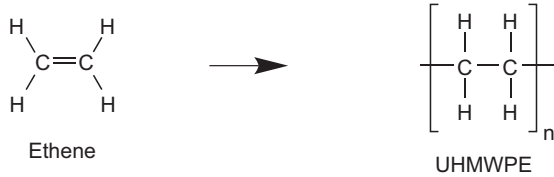


Figure 6.13 Reaction schemes and structures of ethane and UHMWPE.

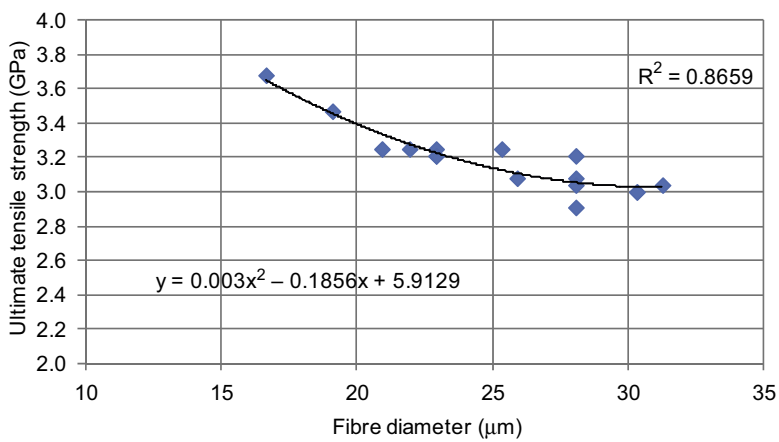


Figure 6.14 Plot of UTS of UHMWPE fibres as a function of fibre diameter.
Source: Crouch (2014).

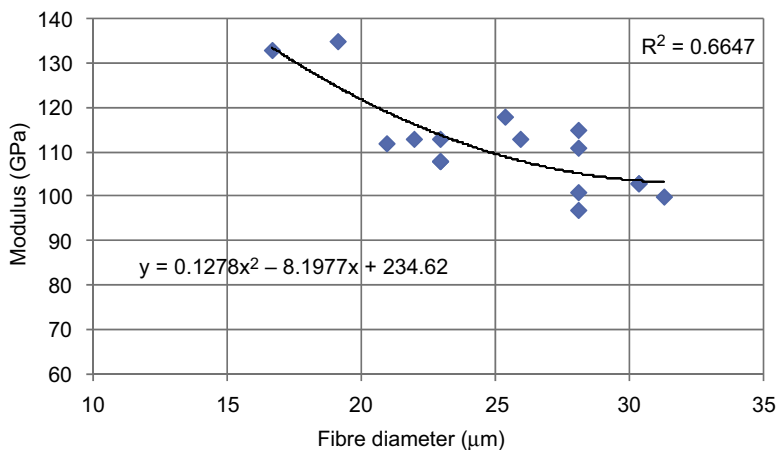


Figure 6.15 Plot of elastic modulus of UHMWPE fibres as a function of fibre diameter.
Source: Crouch (2014).

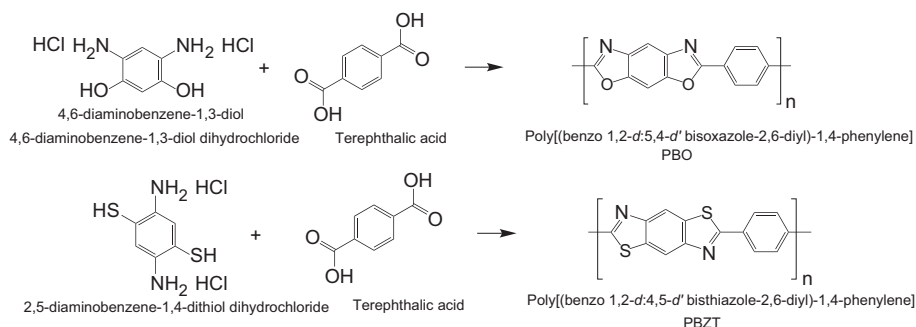


Figure 6.16 Reaction scheme and structure for PBO and PBZT.

Table 6.4 Properties of various PBO and PBZT fibres

Property	PBO ^a (Zylon) regular	PBO (Zylon) high Modulus	PBZT
Density (kg/m ³)	1540	1560	1580
Tenacity (MPa)	5800	5800	4100
Modulus (GPa)	180	270	325
Elongation at break (%)	3.5	2.5	1–2
Fibre diameter (μm)	12	12	NK

^a<http://www.toyobo-global.com/seihin/kc/pbo/>.

poly[(benzo 1,2-d:4,5-d' bisthiazole-2,6-diyl)-1,4-phenylene] (PBZT: poly(benzo-bisthiazole)) is formed (see Fig. 6.16). Both are very complex, large-diameter polymer chains.

The Toyobo Corporation currently manufactures PBO as Zylon. During the late 1990s this fibre was used for US police body armour but ceased when vests worn by two officers tragically failed. Subsequent studies indicated that hydrolysis of the fibre led to breakage of the oxazole-ring and rapid fibre degradation. The mechanical properties of PBO and PBZT are given in Table 6.4. PBO does not melt but decomposes in air at a temperature of 650°C. Its resistance to UV and visible light is very poor. PBZT fibre has similar but rather poorer properties to PBO, but PBO dominates due to lower production costs, even though the commercial uptake has been small.

6.2.7.2 Poly{diimidazo pyridinylene (dihydroxy) phenylene}; PIPD

A polymer can be produced from the reaction of 2,5-dihydroxyterephthalic acid and 2,3,5,6-tetraaminopyridine to produce a fibre abbreviated as PIPD with a trade name of M5. The chemical description of this fibre is poly[2,6-diimidazo-(4,5-b:4'5'-e)

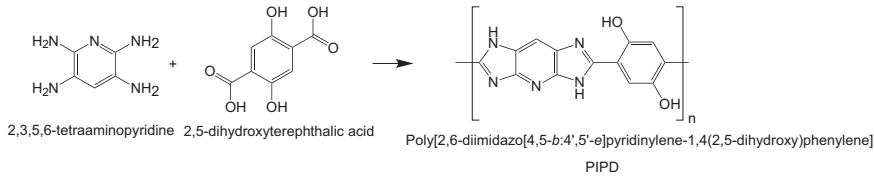


Figure 6.17 Reaction scheme and structure for PIPD.

Table 6.5 Properties of M5 fibres

Property	M5 (year 2000)	M5 goal
Tensile strength (MPa)	3960	9500
Tensile modulus (GPa)	271	450
Elongation at break (%)	1.4	2.0–2.5
Density (g/cm ³)	1.7	1.7

pyridinylene-1,4-(2,5-dihydroxy)phenylene. It is a very complex, large-diameter polymer chain (see Fig. 6.17), which is why the fibre exhibits good compressive strength.

This fibre has been under development for quite some time, and is being produced in the United States by Magellan Systems International in partnership with DuPont. It is believed to offer great potential based upon earlier theoretical modeling of its ideal structure and properties and experimental data. By 2000, properties were still low compared with the target values (see Table 6.5) but tensile strengths of up to 7200 MPa and tensile modulus values of 340 GPa were reported in the classic work by Cuniff and Auerbach (Cuniff et al., 2002), who assessed the potential of these fibres. More recently the Chinese have shown an active interest in researching this attractive fibre (Zhang, 2010). However, to date, this high-performance fibre has not been fully commercialised.

6.3 Technical textiles and ballistic fabrics

High-strength textiles can be designed to defeat a variety of threats from high-speed ballistic impacts, blast debris [eg, from improvised explosive devices (IEDs)], knives and spikes, and even hypodermic needles. Initial consideration is given to the almost infinite variety of single-layer fabrics that can be designed to reduce the effectiveness of a specific threat. The properties of a single layer may also be modified by surface treatments or enhanced by impregnation or coating. This section considers the structural and ballistic properties of single plies of fabric, but for a real body armour system, the final solution will involve a combination of such layers as discussed in Section 6.5.

6.3.1 Woven fabrics

For a woven fabric, the principal yarns are those that directly contact the nose of the impacting projectile. These are defined by the fabric sett (ends/cm in the warp and

Table 6.6 Typical fabric parameters for a range of DuPont pure Kevlar fabrics

Pure Kevlar	Units	D770, S745	D310	A363	S704
Yarn linear mass	tex	331.1	45.4	94.1	97.4
Sett — picks	p/cm	6.4	14.1	11.1	11.9
Sett — ends	e/cm	6.5	14.0	11.0	11.9
Fabric weight	g/m ²	426	128	219	232

picks/cm in the weft) relative to the size and shape of the projectile. The importance of these parameters can be assessed for a commercial Kevlar fabric such as DuPont's Type 363 in Table 6.6 that has ~ 11 yarns/cm in each direction (ie, it is square sett), each with a linear mass of ~ 94 tex. If the diameter of a high-speed projectile is 8 mm, then only seven or eight yarns in each direction can potentially interact as 'principle yarns'. This is reduced if some of them are forcibly displaced sideways by the penetration of the conical nose of the projectile.

The fibres that constitute each yarn, be they continuous filaments (eg, extruded synthetics) or short-length staple fibres (eg, natural, such as wool, or cut from continuous filaments), are selected for a variety of reasons — not necessarily just for their strength. Other selection criteria would include fibre extensibility, mass per unit length, surface friction, moisture management capabilities, UV tolerance, bending rigidity and brittleness, yarn cross-section, dyeability, flammability and melt performance. Filaments or fibres are thus selected, and perhaps blended, to provide desired yarn properties. Table 6.7 presents some of the important parameters that may determine the suitability of different yarns for incorporation in different ballistic fabric designs.

The internal structure of the yarns and their ultimate linear masses also determine the properties and final fabric mass per unit area. The energy absorbed by a single fabric layer is then determined by how the yarns stretch and break, via internal fibre interactions through friction, and their relative interactions within the fabric structure (eg, at yarn intersections).

The fibres constituting each yarn are selected to provide specific characteristics. Fibre extensibility is a vital parameter, particularly in terms of the stretch of the yarn, energy absorption and fabric recoil after impact. The surface friction of the constituent fibres is a significant property that determines the mode of tensile failure in yarns remote from the impact point and the yarn-pull mechanism in which principal yarns are dragged in toward the impact point and away from any unconstrained edges of the fabric layer.

In designing a woven fabric to defeat a specific threat, apart from yarn strength and fabric mass per unit area, most of the following points must also receive strong consideration.

A woven fabric can have a symmetric or asymmetric structure. Its penetration depends on the failures of two independent yarns (warp and weft) and these depend on how they are inserted within the fabric design. Many fabrics designed

Table 6.7 Sonic velocity, energy to rupture and tenacity of 100% high-strength fibre yarns

Fibre	Yarn count (dtex)	Sonic velocity (km/s)	Energy to rupture (kJ/kg)	Breaking force (N)	Extension at break (%)	Tenacity (N/tex)
Kevlar	220	8.03	33.4	55.1	2.8	2.50
	440	8.18	27.8	87.1	2.8	1.98
Twaron	550	7.54	28.2	111	2.9	2.01
	930	7.57	25.4	174	2.8	1.87
	1100	7.76	26.1	225	2.8	2.05
Spectra	240	9.07	42.6	71.7	2.7	2.99
	480	9.33	46.6	148	2.9	3.09
	720	9.04	40.3	182	3.0	2.53
Dyneema	220	10.5	65.9	85.0	3.1	3.00
	440	8.21	50.1	127	3.3	2.89
HT nylon	350	2.51	79.7	32.8	19	0.94
	470	2.47	63.0	42.8	16	0.91
	700	2.52	73.3	52.4	18	0.75
Silk	230	2.03	17.4	8.3	11	0.36

to defeat high-velocity impacts are square sett (symmetric) with the same yarns in warp and weft. Fabric asymmetry may be introduced by adjusting the end and pick densities and/or the relative tex of the warp and weft yarns. To prevent unequal lateral yarn separations in one direction that allow premature penetration, the warp and weft yarns should be broadly matched in strength. The design flexibility for yarns allows different blends and constituent properties to be inserted independently to achieve desired fabric properties (eg, bending rigidity, moisture management, or improved comfort). Introducing asymmetry into a fabric may solve some problems (eg, poor drape, moisture management improvement) but may compromise protective performance (Cunniff, 1992).

Fabric extensibilities in warp and weft primarily depend on those of the constituent fibres, with a secondary contribution from the yarn crimp (waviness) inserted by the weave structure. The design of the weave (eg, plain, twill), and the closeness (cover density) and cross-sectional profiles of adjacent yarns will largely determine the yarn crimp. In most ballistic applications, yarns should have low extensibility, as well as high strength. Since Kevlar typically has a breaking extensibility of 3–4% compared with 18–24% for ballistic nylon, this may be seen as the preferred strong-filament choice. Although Kevlar may also be stronger (by perhaps

30–50%) than ballistic nylon of the same tex, it suffers from significant UV degradation and rapid loss of strength — perhaps within days — unless it can be suitably shielded.

Simple twisted yarns have cross-sections that may have ‘circular’ (especially if highly twisted), ‘figure-of-eight’ (if two-folded) or oval shapes. Staple fibres must be twisted together to provide sufficient frictional interaction between the surfaces of adjacent fibres in order to give the yarns the necessary tensile strength. For the same fibre weight, a twisted bundle of staple fibres will be weaker than an equivalent yarn assembled from untwisted continuous filaments. Thus, most high-strength ballistic woven fabrics are made from continuous untwisted filament yarns (eg, ballistic nylon, aramids or UHMWPE) and these exhibit lenticular cross-sections.

Although the cross-sectional shapes of twisted yarns may be flattened somewhat at yarn intersections due to their mutual compression caused by crimp, high sett and lateral fabric tensions, the potential for holes to exist at each intersection is higher. The size of these holes must be minimised to try to eliminate easy entry points for sharp-nosed projectiles. In such events, adjacent yarns may be wedged apart rather than being forced to absorb energy via tensile failure. For commercial Kevlar fabrics such as Types 363 or 704 therefore, untwisted filament yarns are woven square sett and packed tightly together, so they flatten out into lenticular cross-sections so the hole sizes at intersections are minimised.

The minimisation of these holes, which also depends on the chosen weave, severely restricts the ability of the fabric to shear like a trellis and thus, to drape. Therefore the flexibility and comfort of the fabric in single-layer garments especially may be poor. One significant restriction on woven fabrics used for garments is that a layer can only bend in one direction without forming extraneous creases in other directions. To mould a woven fabric to cover a three-dimensional (3D) shape is impossible without sewing individual panels precut to precise pattern shapes. The strength of the resulting seams must then match that of the constituent fabric otherwise these lines of weakness will preferentially fail when impacted.

For most high-speed protective applications, the preferred design would be based on a square sett plain weave in which stability is maximised and there is minimal opportunity for holes to open up when the fabric is flexed. Where a yarn in one direction may interlace over/under several yarns in the transverse direction, twill weaves in their various forms are regarded as too flexible, with lower shear stability and an increased potential for holes to open up when the fabric is flexed.

The role of friction in the interaction between a high-strength fabric and an impacting threat cannot be underestimated. For high-velocity impacts, the frictional interactions within the fibre materials, between fibre surfaces, between yarns at intersections, within the impacting projectile (due to its internal distortion and mushrooming), and between the impacting bullet and the fabric, all absorb energy. If yarns have no twist, the interfacial friction between fibres may be significantly reduced unless the weave structure itself can force yarns or fibres into contact. Such interactions were considered in detail by [Briscoe and Motamedi \(1992\)](#), who investigated the ballistic performance of single layers of commercial aramid fabrics with different weaves, when the surface friction of the constituent yarns was modified by removing or adding lubricants.

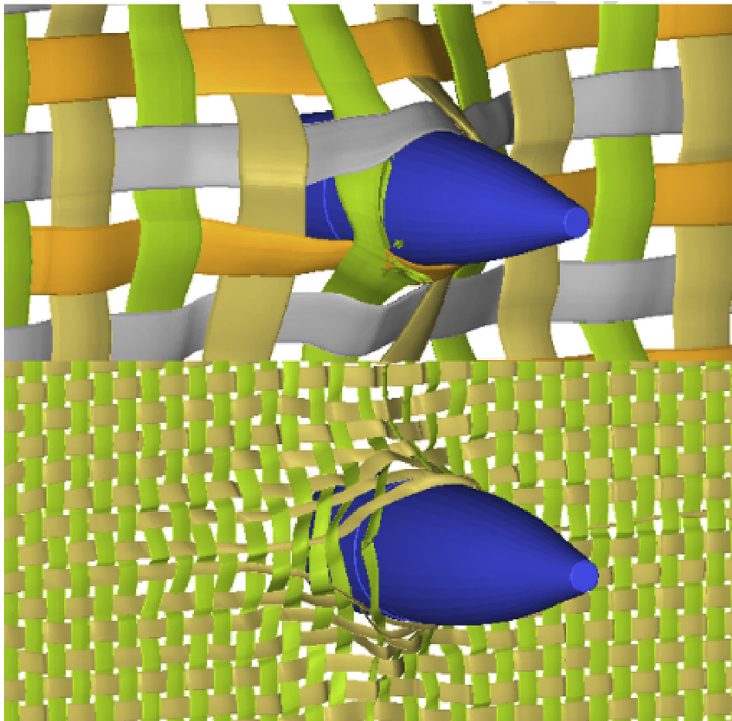


Figure 6.18 Numerical example of weave-parting (see Chapter 9).

They tested them under quasistatic penetrations and with ballistic impacts up to 200 m/s. They found that the ballistic performance improved when yarn frictions were higher, and identified that weave structures and yarn pretensioning within the weave were other important factors. The pretensioning of the yarns, their sett, and the weave structure would all be expected to influence the mutual compression between interlaced yarns at intersections. The addition of moisture that can lubricate yarn surfaces has been shown to significantly reduce the ballistic performance of fabrics (Kaharan et al., 2008).

Energy absorption via simple tensile failure of principal yarns is well understood and has been well covered by Erlich et al. (2003) and Cheeseman and Bogetti (2003), amongst others. The pyramidal extension of a layer in the direction of the impact initially causes the holes in the net structure merely to open up, with no relative slippage of the interlaced yarns at their intersections. As the projectile penetrates, however, some unbroken principal yarns, and secondary yarns in their close proximity, may be forced laterally aside, with an associated frictional dissipation at their intersections (see Fig. 6.18). The projectile may slip between these yarns without them rupturing, thus reducing the potential for energy dissipation and leaving a remnant hole smaller than the original projectile diameter. One consequent need is to design fabrics that minimise this lateral displacement and optimise energy dissipation via tensile breakage.

The importance of the frictional characteristics of yarns and fabrics, especially under wet conditions where surfaces and intersecting yarns may be lubricated, has caused attention to be given to improving the frictional interactions within yarns and woven structures to minimise yarn pull-in and to restrict lateral displacements of principal yarns.

Testing and modelling of energy dissipation via yarn pull-in mechanisms have been undertaken by researchers, such as [Bazhenov \(1997\)](#), who carried out yarn extraction tests from ballistic fabrics under a variety of conditions, and showed the detrimental effects when the fabric is wet. [Kirkwood et al. \(2004b\)](#) measured quasistatic extractions of yarns from laterally pretensioned fabrics and developed an explanatory model. Their observations were then related to ballistic impacts ([Kirkwood et al., 2004a](#)) with some success.

Yarn pull-in as an energy-absorbing mechanism is a two-stage process. Before an interlaced yarn can reach its breaking strain, it must be stretched and straightened to remove the weave crimp. Only then can the yarn be pulled in toward the impact point. The weave crimp affords the fabric some extra extensibility beyond that provided by the filaments themselves. Thus, for an impact at the centre of a large fabric sample, yarn pull-in occurs in both warp and weft to a degree depending upon the fabric structure and sett, type of yarns in warp and weft, their frictional properties and the size of the sample. If an impact occurs close to an unstabilised edge, yarns may preferentially be pulled in from that edge. They may then not fail in tension but merely cause the fabric to unravel so that energy dissipation is significantly reduced ([Kirkwood et al., 2004a](#)). The stabilisation of an edge by sewing, gluing or seam sealing, may significantly improve the ballistic performance for impacts in their close proximity.

When ballistic testing a single layer, or evaluating a multilayered panel, the boundary conditions — whether the layer edges are free to move or are constrained with or without tension — also have significant influence on the impact performance. [Cork and Foster \(2007\)](#) showed that the ballistic performance of narrow fabrics with selvedges could be improved relative to wider samples, but were sensitive to the weave and the boundary conditions applied.

Interest in the ballistic properties and performance of a single layer is not only driven by the need to understand the fundamental properties of layered structures (see [Section 6.5](#)) but also because of interest in the protection offered by conventional combat uniforms and lightweight covering fabrics over the extremities ([Sakaguchi et al., 2012](#)). These researchers measured V-50s between 105 and 145 m/s for single plies of aramid fabrics.

Suitably camouflaged single layers may be used in high-strength garments for combat soldiers, particularly where some form of injury mitigation against fragments and debris impact resulting from explosive devices is required. Fabric comfort, based on a range of attributes, would then assume higher importance, but perhaps at the expense of protective performance. The development of a spectrum of woven blend constructions which sought to achieve a balance between fragment protection and comfort for camouflaged outerwear for combat soldiers has been a prime objective of recent research ([Pierlot, 2012](#)). The basic characteristics of a selection of some of these fabrics are shown in [Table 6.8](#). In this DMTC research program, the provision

Table 6.8 Examples of blend-yarn constructions for debris-impact-resistant fabrics

Warp	Warp (tex)	Warp # filaments	Weft 1	Weft 1 (tex)	Weft # filaments	Weft 2	Weft 2 (tex)	e/cm	p/cm	Weave design	Fabric weight (g/m ²)
BN	94	140	BN	94	140	OEC	84	17.3	14.2	2 × 1	328
BN	94	140	BN	94	140	OEC	84	17.3	14.2	2 × 2	329
BN	94	140	BN	94	140	OEC	84	17.3	15.0	1 × 1	343
BN	94	140	BN	94	140	OEC	84	14.2	16.5	2 × 1	325
BN	94	140	BN	94	140	OEC	84	14.2	13.8	1 × 1	319
BN	94	140	BN	94	140	OEC	84	14.2	17.3	2 × 2	311
BN	47	140	BN	47	140	OEC	42	26.8	22.0	2 × 2	256
BN	47	140	BN	47	140	MOD ACR	2/20	26.8	22.0	2 × 2	259
BN	47	140	BN	47	140	WOOL FR/ VIS	2/25	26.8	22.0	2 × 2	266
HTPOLY	42	96	HT POLY	42	96	WOOL FR/ VIS	2/25	32.3	27.6	2 × 2	247
HTPOLY	42	96	ATY	45	128	WOOL FR/ VIS	2/25	32.3	27.6	2 × 2	256

HTPOLY	42	96	ATY	45	128	MOD ACR	2/20	32.3	27.6	2 × 2	246
HTPOLY	42	96	DTY	50	192	MOD ACR	2/20	32.3	27.6	2 × 2	267
SPECTRA	24	68	WOOL FR/VIS	2/25	—	WOOL FR/ VIS	2/25	26.8	27.6	1 × 4	215
SPECTRA	24	68	WOOL FR/VIS	2/25	—	WOOL FR/ VIS	2/25	26.8	26.8	2 × 3	205
SPECTRA	24	68	WOOL FR/VIS	2/25	—	WOOL FR/ VIS	2/25	26.8	27.6	2 × 3/ 1 × 2	210
PC	32	—	PC	54	—	—	—	38.6	17.7	3 × 1	235
BN	94	140	BN	94	140	—	—	17.3	13.4	2 × 1	310
BN	94	140	BN	94	140	—	—	17.3	12.2	1 × 1	299
BN	94	140	BN	94	140	—	—	17.3	13.8	2 × 2	312

ATP, Air-textured polyester; *BN*, ballistic nylon; *DTY*, drawn textured polyester; *FR/VIS*, flame-resistant viscose; *HTP*, high-tenacity polyester; *MOD ACR*, mod-acrylic; *OE*, open-ended cotton; *PC*, polyester cotton.

Source: DMTC (2014).

of high-velocity impact protection was the primary consideration, but comfort (mechanical, thermal and moisture management) was also an important consideration.

Duan et al. (2005) modelled the effects of friction and particularly considered the enhancement of frictional interactions at yarn intersections when different boundary conditions were applied to a plain weave sample subjected to the impact of a spherical impactor. Their models clearly replicated the observed lateral yarn separations that occur close to the point of impact when the coefficient of friction between yarns themselves, and the impactor, is reduced for a variety of boundary conditions. Modeling of such effects using a spherical impactor was also carried out by Rao et al. (2009) in their development of a fabric impact model.

In a counterintuitive approach to the problems of yarn pull and weave stabilisation, Sinnappoo et al. (2009) evaluated the effect of incorporating wool fibres into a square sett high-strength yarn (eg, Kevlar or ballistic nylon) fabric design. The weak wool was not intended to replace the high-strength yarns as the primary energy-absorbing fibre, but served to increase the frictional interactions between the filaments and yarns. Thus, lateral separation of principal yarns near the impact point could be reduced, so forcing more yarns to rupture. Yarn pull-in from fabric boundaries could be restricted because the weave was better stabilised and edge unraveling was prevented. Because of its high regain, wool also had the capacity to absorb up to 36% of its own dry weight in moisture if the fabric became wet, and so was able to mop up excess moisture that may have served to lubricate the high-strength filaments. In absorbing this moisture, the wool fibres also expanded in diameter by $\sim 16\%$, so further stabilising and tightening the weave.

Comparing the samples resulting from two yarn-pull experiments shown in Fig. 6.19 exemplifies such natural fibre stabilisation. The left sample was woven from ballistic nylon, while the right was woven with the same sett from a blend of ballistic nylon and wool. The improved stability achieved by the introduction of wool can be appreciated from the significantly reduced degree of unravelling apparent along the top edge.



Figure 6.19 A woven sample of pure ballistic nylon (left) has a less stable structure than an equivalent wool/ballistic nylon (right) sample when subjected to a planar yarn pull-out test. Sinnappoo, K., Arnold, L., Padhye, R., 2009. PCT/AU2010/000157, Ballistic Fabric.

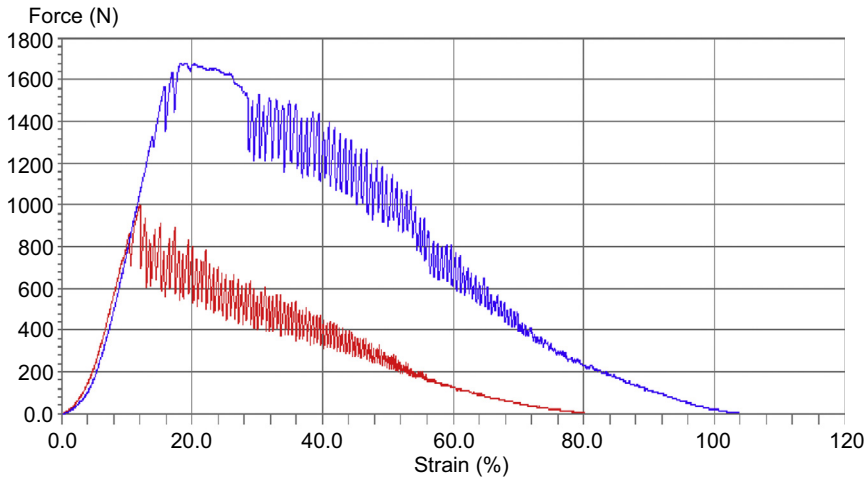


Figure 6.20 The energy absorbed when eight adjacent yarns are withdrawn from a woven wool/ballistic nylon fabric (blue) during a planar yarn-pull test is significantly greater than that from an equivalent pure ballistic nylon (Naik) fabric.

Sinnappoo, K., Arnold, L., Padhye, R., 2009. PCT/AU2010/000157, Ballistic Fabric.

Fig. 6.20 also shows the significant increase in energy absorbed during such a yarn-pull experiment as a result of the inclusion of the wool component. However, this did not result in an overall increase in ballistic performance.

While much of the past research on blended ballistic woven fabrics has concentrated on evaluating them for protection against high-speed blast-debris impact, recent work of [Duong et al. \(2010\)](#) has investigated the stab resistance (spike puncture and knife cut) of aramid/core-spun yarns woven with a range of weft setts. Their results confirmed that the fabric density significantly affected stab resistance and that an optimal density could be identified.

6.3.2 Nonwoven and noncrimp fabrics

Woven fabrics have been developed in order to meet the need for enhanced out-of-plane properties, higher impact resistance, low manufacturing cost and easy handling. However, the crimp of woven fibre yarns, while increasing the damage tolerance of the material, reduces the in-plane properties, leading to low energy-absorbing failures such as fibre kinking. To overcome this obstacle, and retain the enhancement of the in-plane properties, noncrimp fabric (NCF) composites have been developed. NCFs are obtained by stacking unidirectional yarns stitched together through their thickness.

Recent publications by [Nilakantan et al. \(2011\)](#) and [Sanborn and Weerasooriya \(2014\)](#) have drawn attention to a further benefit of using nonwoven high-strength fabrics. When high-strength yarns are subjected to the stresses of weaving

and finishing, and as a result are locked into a crimped profile, they may become sufficiently damaged that their protective performance is compromised. [Sanborn and Weerasooriya \(2014\)](#) studied the strength and extensibility, over a wide range of strain rates (0.001 to 1000 s^{-1}), of individual filaments taken from the warp and weft yarns of fully finished plain-woven Kevlar fabrics and compared them with pristine filaments that had not been subjected to such stresses. They reported that filaments taken from weft yarns were weakened by between 3% and 8%, and those taken from the warp were at least 20% weaker than equivalent unwoven filaments, at all loading rates.

[Nilakantan et al. \(2011\)](#) had reported similar weakening effects using yarns rather than individual filaments, but with even higher-strength reductions — by 16% for greige-state warp yarns and by as much as 30% for scoured warp yarns, compared with the unwoven controls. The observed yarn weakening and warp-to-weft differences were attributed to effects from warp pretensioning in the loom, crimp or twist, frictional interactions, and the effects of finishing or surface treatments.

Although not stated by them, an additional important weakening factor arises from any polymeric defects along the filaments that may be enhanced due to the high-speed cyclic application and release of warp tension, and associated frictional interactions with the healds, during weaving. Depending on the loom used, a general rule of thumb for weaving requires that warp yarns should ideally have an extensibility exceeding $\sim 10\%$ to allow the shed to open sufficiently to permit the insertion of each weft yarn. Kevlar yarns woven for ballistic application generally have no twist and their constituent filaments have a natural extensibility of only $\sim 4\%$. Thus, weaving such fabrics is difficult and high warp strains will be cyclically applied. Although the weft yarns will also be held in tension during weaving by the restraints applied to the selvages, such tensions are always lower than those in the warp. Once removed from the loom, the release of these tensions within the fabric will cause a crimp interchange as the inherent weaving stresses stabilise, leading to an asymmetry between warp and weft, even for a square-sett fabric design.

High-performance, soft armour vests/packs are commonly constructed of layers of NCFs. DuPont has recently made Kevlar XP available. This has excellent ballistic resistance when used as a soft vest material (see [Fig. 6.21](#)). In NCF materials, the fibre tows are very flat and almost form a continuous layer of UD fibres, except for the small amount of stitching as per [Fig. 6.27](#) ([Coman, 2009](#)).

Kevlar XP fabric avoids some of the problems posed by crimp in a woven construction because two perpendicular arrays of parallel Kevlar filaments, in the form of sheets, are mutually bonded together with a resin. Because the resin penetrates only a few of the surface filaments of each sheet, and not the full thickness, the whole array of fibres is stabilised during assembly by parallel lines of sewing 5 mm apart. These essentially define a ‘warp’ direction, with the perpendicular front and back filament layers angled at 45° to this direction. The resin contributes no ballistic benefits except to hold those filaments in their immediate vicinity in place until the sewing (by a nonaramid sewing thread) is completed. The resulting fabric is fairly stiff. Having no crimp, the filaments take full load immediately the fabric is



Figure 6.21 An aramid NCF fabric panel from DuPont (XP500) arresting a 9-mm handgun bullet.

impacted, thus eliminating the extra stretch normally associated with straightening out the yarn crimp. Only the filaments themselves thus define the extensibility of the fabric. NCFs have the following general qualities:

1. Very limited stretch and recovery.
2. Distortions to the structure tend to be permanent.
3. Can be formed as thick absorbent mats.
4. Very poor shape retention.
5. Difficult to bond – forming seams are a significant problem – with very limited strength.
6. Very poor drape, especially if thick.
7. Like a woven fabric, can only bend in one direction without forming creases.

The existence of quite extensive stitching acts as a constraint in some impact situations. Honeywell have overcome even this slight drawback in their NCF construction (eg, Spectra Shield), by developing 0/90 or 0/90/+45/–45 NCF materials that do not contain any stitching. Each individual ply (layer of UD fibres) is held within a thermoplastic matrix (like Kraton D1107, a styrene–butadiene–styrene block polymer) and the plies are bonded together to form the stable, multilayered NCF material. This maximises the number of fibres per ply and totally eliminates the need for stitching. Laminates manufactured using these materials maximise the volume fraction of fibres, thus maximising the number of fibres that get involved in an impact event. These constructions are used in the many advanced body armour systems around the world, especially for civilian police.

6.3.3 Coated fabrics

Dissipation of ballistic energy was discussed earlier in terms of the breakage of principal yarns and yarn pull-in. Attention was drawn to the problems of providing sufficient friction between yarns, and between fibres within yarns, to maximise yarn breakage as a means of energy dissipation. The forced lateral separation of principal yarns due to the projectile shape allows easier penetration because fewer principal yarns are broken. One way of holding the principal yarns in place and reducing their lateral separation is to form composite single layers by applying small amounts of resin, as done by [Lee et al. \(2003\)](#). [Zeinstra et al. \(2009\)](#) extended this idea by laminating semiconsolidated vinyl acetate foil layers on both sides of a plain-woven Twaron fabric. This limited lateral movement of principal yarns and increased in-plane shearing forces, as measured by picture-frame shearing tests. It also restricted the yarn-pull mechanism by increasing the frictional forces needed to stretch or remove yarns from the fabric, as measured by yarn-pull experiments. However, once the bonding between the foils and the yarns was broken, the yarn pull-out continued with little further influence from the foils. This contrasted with the increased friction achieved throughout the duration of the yarn extraction when wool was added to the weave ([Figs 6.19 and 6.20](#)). Nevertheless, the benefits of such impregnations or laminations in terms of ballistic performance have been well demonstrated. These coated, or laminated, products (eg, Argus from Barrday, Canada) are popular fabrics for use in stab and spike vests (see [Section 6.5.4.2](#)).

Adding resins or foils to form a single layer of semi-impregnated fabric composite causes the bending stiffness and shear rigidity to increase, so reducing its propensity to drape and form folds so the comfort of the fabric suffers. This is a significant problem where a single-layered composite fabric must be tailored into a garment where gas- or liquid-impermeable performance is required, as may be the case for combat outerwear where exposure to aerosol or gas chemical impacts may occur in a blast incident.

6.3.4 Knitted fabrics

For the simplest weft-knit single jersey fabrics, a single yarn holds the whole structure together by being looped back into itself to form a series of interlinked successive courses (e.g. [Fig. 6.22](#)). This single yarn may contain several components that are chosen to provide desired properties (eg, high strength, good recovery from extension, improved comfort). Altering loop placement and their interlacing within a knit design can enhance or introduce desired properties in the final fabric, so allowing the design of complex 3D structures.

Warp-knitted fabrics offer an alternative structure to the weft knit. In their simplest form, warp knits are based on an assembly of multiple parallel yarns that interlink with each other in such a way as to define a ribbed structure in the wale direction. Each yarn is formed into a continuous series of looped stitches that zigzag back and forth in the wale direction and interlink with equivalent loops from adjacent yarns on either side. The stable structure so formed is resistant to hole formation and has asymmetric tensile and stretch properties. The sequencing and positioning of each of the looping interlinks

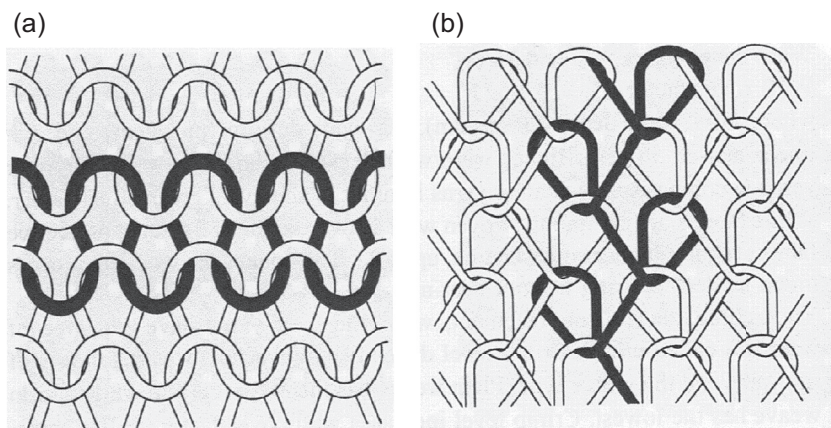


Figure 6.22 (a) Plain weft knitted structure — back side, and (b) warp knitting — half tricot — face side, from ‘Textiles for Protection’.

can be controlled to form complex designs that can fit 3D shapes. Because of their special structural properties and speed of production, warp knits can be used to produce industrial fabrics from high-strength yarns, such as carbon fibre, that may have poor bending properties. Structures can also be designed to allow the bonding of multiple layers made from dissimilar materials having individually unique properties. This form of material lamination is known as stitch bonding. An application of such warp knitting has been applied to the problems of stab resistance recently reported by [Miao et al. \(2012\)](#) and [Naebe et al. \(2013\)](#).

Unlike woven fabrics, weft knits can readily mould without creases to 3D shapes (within fairly broad limits), and this flexibility provides wearer comfort in a single layer. The penalty is, however, that when stretched excessively over a 3D shape, or distorted by the wearer, the holes within the structure open up, leaving larger access points for penetration.

In work carried out by [Dwivedi et al. \(2013\)](#) using 0.22 in. glass spheres, it became clear that knitted structures do not perform very well against high-energy fragments. On the other hand, felted fabrics perform very well (see [Section 6.3.5](#)).

6.3.5 Felts

Felted fabrics are needle-punched, nonwoven fabrics manufactured from short-length (~ 50 mm) fibres, such as, nylon, UHMWPE and the aramids. They have poor structural properties, very little drape characteristics, and are thick for their weight. Because of their open structure, they also absorb water, and other fluids, very easily. However, they are excellent at absorbing impact energy from small high-velocity fragments and blast debris. [Thomas \(2003\)](#) identified the benefits as limiting deflection into the body, reducing back face signatures and therefore trauma to the wearer.

A commercial product called ‘Fraglight’ from Dyneema, at an areal density of only 1.2 kg/m^2 , is claimed to stop 1.1-g FSPs at 450 m/s. In a recent assessment of this



Figure 6.23 Edge view of a three-ply FF520 SAI, often used for extremity protection.

material, [Chocron et al. \(2008\)](#) described the properties of these felts as ‘very peculiar’: they found the material to be very anisotropic with no dependence upon strain rate and properties that varied with size of test sample, since the material uses 5-cm long fibres. This type of felt is often used in between plies of other 2D fabrics, as part of a hybrid soft armour pack.

DuPont launched their own aramid-based product, known as FF520 ([Fig. 6.23](#)), in 2011 at the Milipol exhibition and conference, in Paris, and described it as an innovative felt reinforced by a ballistic fabric that offers intrinsic ballistic protection, enabling the user to wear a lightweight vest while still being protected against fragments, bullets and blunt impact. Kevlar FF520 uses a new felting technology that combines ballistic properties with softness, for a comfortable and flexible fit ([Fig. 6.24](#)). It offers a versatile and cost-effective solution to threats as it can be used alone as lightweight ballistic protection or with ballistic pack layers for increased protection. Ballistic woven fabric is actually incorporated into the structure, differentiating it from conventional fabric felt solutions. Kevlar FF520 vests can be used in combination with Kevlar XP material for a global solution capable of protecting against specific threats. Due to the combination of low flammability and protection against fragments, Kevlar FF520 can also be used in seats for armoured vehicles. Possible hybrid combinations are covered in a recent US patent application, the US army is apparently using felted fabrics for extremity protection and, most recently, in multithreat vests worn by the Scottish police force ([Anon \(2015\)](#)). DuPont website, www.dupont.com).

6.3.6 Fabrics coated with shear thickening fluid

Several workers have suggested that the ballistic performance of fabrics may be improved by impregnating the fabric with additives. One such material is a shear-thickening fluid (STF) that is expected to possess a low viscosity under strain

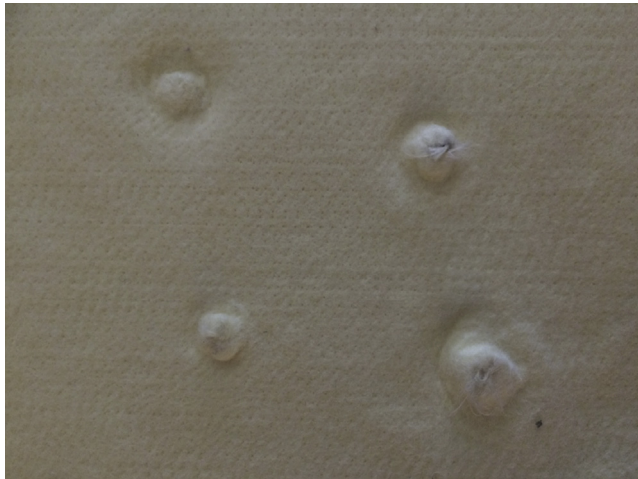


Figure 6.24 Rear view of three-ply FF520 SAI illustrating limited involvement of felted fabric beyond the point of impact (ie, unlike woven fabrics which pull-in lengths of fibres from outside the impact site).

rates associated with normal motion of the wearer but to stiffen rapidly under the high strain rates associated with a ballistic impact.

Shear-thickening fluids are also known as dilatant fluids. The properties of such fluids have been well-characterised for some time. In general, the behaviour of such fluids may be expressed in terms of the shear stress, τ , and the shear rate, $\dot{\gamma}$, when the fluid is tested in a viscometer. They may often be described by a power-law relationship,

$$\tau = k|\dot{\gamma}|^{n-1}\dot{\gamma} \quad (6.4)$$

where the index, n , is greater than one. Dilatant fluids were originally described by [Reynolds \(1885\)](#). The proposed mechanism was of a concentrated suspension with only sufficient fluid to fill voids within the suspension. If the suspension is sheared slowly there is sufficient fluid to lubricate the motion so that low τ values are the result. However, higher shear rates disturb the packing of the structure and there is insufficient liquid to flow and lubricate the new structure so that higher values of τ are the result.

In succeeding years the meaning of the term ‘dilatant’ has been expanded to encompass all fluids that exhibit increasing viscosity with increasing shear rate (including fluids that do not possess the mechanism described above). It should be noted that classical dilatant fluids are considered to be time-independent rheological fluids. This means that the shear stress at any point in the fluid only depends on the shear rate. This is obvious from [Eq. \(6.4\)](#), and this equation also implies a lack of dependence on shear history and time of application of shear. For these reasons, it is likely that it represents an idealisation that is only approached in practice. Certainly, time

dependence, for example in the form of thixotropy (Barnes, 1997) is very commonly encountered in particulate fluid suspensions.

From a practical viewpoint, pure dilatant behaviour may be exhibited by measuring τ for increasing and decreasing values of $\dot{\gamma}$. The flow curve for increasing $\dot{\gamma}$ should coincide with the flow curve for decreasing $\dot{\gamma}$ so that there is no hysteresis. It should be noted that, unless the experimenter is careful and thorough, dilatant effects may be confounded with time-dependent or thermal effects on the material under investigation. Another practical problem is that ballistic events are generally associated with high values of $\dot{\gamma}$. It may not be possible to achieve such strain rates in a conventional viscometer and this may lead the experimenter to extrapolate the material behaviour obtained at relatively low shear rates in a viscometer to explain its behaviour in a ballistic event. Another issue that may require consideration is that many viscometers measure behaviour under pure shear while a ballistic event may also require consideration of other types of strain, eg, compressive.

The ballistic performance of fabrics may be improved by impregnating them with shear-thickening fluids that possess low viscosity under low strain rates (as during normal wear), but may stiffen rapidly when these fabrics are subjected to the high strain rates associated with ballistic impacts. However, ballistic events are generally associated with very high values of $\dot{\gamma}$, often too high, for the shear-thickening effects to take place. At lower impact speeds, more associated with stab and spike events, the shear thickening may have time to occur.

For shear thickening to occur the particles must be either neutral or repel one another by virtue of electrostatic, steric or entropic interactions (Raghavan and Khan, 1997). The critical shear rate tends to zero (where no flow is possible) when the phase volume is around 60%. This represents the maximum packing fraction when the particles come into contact with each other. Particles between 100 nm and 5 μm will shear thicken and if the particle size is decreased, the critical shear rate increases. The critical shear rate for the onset of shear thickening is very high for moderately concentrated suspensions and decreases with increasing particle concentration. Broader particle size distributions of stabilised dispersions significantly reduce the viscosity, leading to higher shear rates when shear thickening sets in, so the increase in viscosity may not be high. In addition, in the case of particle size, particle shape and size distribution, the critical parameter is ϕ_m , which suggests that anything that changes ϕ_m modifies the form of shear thickening (including the influence of shape and particle interactions). Mixing of particle sizes can lead to a less severe shear thickening transition (Maranzano and Wagner, 2001). The severity of shear thickening depends on the particle concentration in proportion to the maximum packing fraction (Zupancic et al., 1997). Lee and Wagner (2003) investigated the viscous behaviour of 32-nm diameter charged stabilised silica nanoparticles in ethylene glycol to determine the lower limits of shear thickening. They observed reversible shear thickening, although only at very high shear rates.

The shear thickening phenomena have been utilised by several groups for impact protection. d3o is one such shear thickening material developed by the British company d3o lab (2008). This lightweight material is very flexible and malleable, until subjected to abrupt force, making it useful in protective clothing in situations where

the wearer may be exposed to blunt trauma. d3o is used as a low-profile and flexible impact protection in sports, motorcycle and industrial applications. Products such as football shin guards, motorcycle gloves, beanie 'helmets' and even ballet shoes have integrated the technology to enhance wearer protection.

A 3D spacer fabric 4.5-mm thick, and impregnated with STF (called Active Protection System), has been developed by Dow Corning to provide impact protection that is lightweight, breathable, flexible, washable, and can be stitched directly into garments (Budden, 2006). The silicone can readily absorb the impacting force through the spacer yarns in the direction of the force. The silicone polymer has transient bonding to a crosslinking component. Under a long-period deformation force, the crosslinks open and the material flows. When the force is removed, the bonds reform and the silicone returns to its original state. When the silicone is suddenly impacted the crosslinks have insufficient time to open so the material resists the force and appears as a solid. After the force has been dissipated, the silicone returns to being soft and flexible.

The introduction of shear thickening fluids (eg, silica particles) into fabrics to form composite materials that have improved energy-absorbing properties for ballistic impacts have been studied by Lee and Wagner (2003), Lee et al. (2003), Wetzel et al. (2004), Gadow and Von Niessen (2006) and Kordani and Vanini (2014) amongst others. Defense against knife and spike impacts has also been considered by various research groups (Decker et al., 2007). At low strain rates, the impregnated fabrics flex normally, however when high shear stresses are impulsively created, the nano-sized colloidal particles (eg, silica in ethylene glycol) lock together to give a significant increase in shear viscosity that in turn stiffens the fabric structure. Once the impulsive stress is relieved, the shear thickening ceases and the fabric relaxes to its prestressed flexible state. The 'liquid armour' prevents pointed weapons from penetrating between yarns in the fabric without compromising the fabric thickness or flexibility (Burton et al., 2007). The performance enhancement provided by the STF may be due to an increase in the yarn pull-out force upon transition of the STF to its rigid state.

In the corresponding patent they specify that the STF can be diluted to enable spreading of the STF and impregnation of the fabric. They used ethanol as the diluting solvent and evaporated it at 80°C after spreading out the STF. Shear thickening was observed with both ethylene glycol and polyethylene glycol but better results were obtained with ethylene glycol (Table 6.9). They also found that 30-nm silica particles performed similarly to 450-nm silica. Nonspherical particles consisting of elliptically shaped calcium carbonate particles in ethylene glycol show enhanced ballistic resistance comparable to the spherical particles (Wagner et al., 2005).

They obtained the silica as an aqueous suspension from Nissan Chemicals Japan. The silica was obtained by centrifugation of colloidal silica in water and resuspension. Another reported method uses successive transfer of the silica into *n*-propanol and then into 1,2-dichloroethane by azeotropic distillation to yield a stable organosol (Kasseh and Keh, 1998).

The breathability of a comparable series of ballistic fabrics and STF-treated ballistic fabrics has been evaluated. Breathability was characterised using measurements of water vapour transport rate through fabric samples. The results show that uncoated ballistic fabrics offer good breathability that is only slightly lower than conventional

Table 6.9 Performance of impregnated Kevlar fabrics

Four layers of Kevlar impregnated with:	Sample weight (g)	Impact velocity (m/s)	Penetration depth (cm)
Nothing else	1.9	247	2.12
2-ml STF (450-nm spherical silica in ethylene glycol)	4.8	243	1.23
2-ml STF (450-nm polymer stabilised spherical silica in ethylene glycol)	4.9	259	0.74
2-ml STF (450-nm spherical silica in polyethylene glycol)	4.9	246	1.80
2-ml STF (30-nm spherical silica in polyethylene glycol)	5.3	331	1.57
1.6-ml STF (anisotropic COCO_3 particles in ethylene glycol)	4.8	244	0.48

Wagner, N., Wetzel, E.D., Wagner, N.J., 2005. WO2004103231-A1; US2005266748-A1; EP1633293-A1; US2006234577-A1; US7226878-B2.

military outer garments. Ballistic fabrics treated with STF show a slight decrease in breathability, as compared with uncoated fabrics. Ballistic fabrics with continuous polymer coatings, however, exhibit very low water vapour transport rates. The fabrics treated with STF introduce no significant penalty in breathability relative to conventional, uncoated ballistic fabrics (Chin and Wetzel, 2008).

The same group investigated the effect of using softer polymethylmethacrylate (PMMA) particles in polyethylene glycol as the STF to see if the hardness of the particles made a difference to the STF effect (Kalman et al., 2007). They had observed that the silica particles had significantly abraded the Kevlar fibres in the damage zone (where the projectile strikes the fabric). They thought that this might be one enabling mechanism for stress transfer between the STF and the fabric. The PMMA particles were applied at a lower loading but gave a significantly poorer ballistic performance over the silica particles (V-50 145 m/s for 14% PMMA and V-50 248 m/s for 20% silica). In contrast to the silica STF, the PMMA STF was observed to shear thin in postshear thickening region at high shear rates. This is likely to be due to the softness of the particles.

In a recent paper by Park et al. (2014) a 35% saving in weight was reported: KM2-based soft armour insert (SAI) packs were impregnated with nano silica particles, via a polyethylene glycol/methanol carrier fluid, and their ballistic performance assessed at velocities in excess of 1000 m/s, using 120-mm squares of multilayered fabrics. The impregnated packs showed less distinctive cross patterns, at the impact site, indicating greater energy dissipation. The penetrated hole size was also smaller. More work of this nature should be encouraged.

6.4 Layered fabric structures

6.4.1 *Stitched structures*

It has been suggested that the incorporation of a stitched pattern into a fabric armour panel might lead to benefits in terms of protection against ballistic threats. This appears to have been confirmed by some studies but not others. Possible mechanisms that might account for these benefits would include increased frictional resistance to yarn motion and reduction in weave parting by the projectile. [Ahmad et al. \(2008\)](#) investigated the effect of stitching on multiple layers of Kevlar 29/natural rubber-coated Kevlar 29 fabric systems. The stitching was conducted using four-ply Kevlar thread at five stitches per inch and samples were stitched in 1-in. field diamond, 2-in. field diamond, diagonal or perimeter patterns. Their testing was conducted using 9-mm full metal jacket, round nose (FMJ RN) projectiles. They claim that some patterns might enhance ballistic performance and state that the 2-in. diamond, diagonal and perimeter stitched fabrics gave much higher ballistic performance, while the 1-in. diamond had a lower ballistic limit than the unstitched system. However, Ahmad et al. admit that their results are inconclusive and recommend further testing. They believe the mechanism behind the improved ballistic limit of some systems is not fully understood but suggest the stitching removes the gap between layers, resulting in better interlayer interaction so that the impact energy is transferred to each fabric layer much faster than in an unstitched system. On the other hand, they suggest that the 1-in. diamond system had stitching that was too close and the resulting stiffness made the system behave as a single body system rather than as a multiple-layer system.

[Kaharan et al. \(2008\)](#) studied the effect of different stitch patterns on Twaron CT 710. They used three stitching types:

1. Type A: Only sewn 2.5 cm in from the edges of the panel — parallel to the edges.
2. Type B: Sewn 2.5 cm in from the panel edges and also in a large diamond pattern across the panel.
3. Type C: Sewn 2.5 cm in from the panel edges and then with 5-cm intervals in a bias type.

They used 9-mm projectiles for their tests and their main findings are:

1. Increasing the ply number from 20 to 32 decreased trauma depth by 35.40% and trauma diameter by 12.7%.
2. Stitching type had a significant effect on ballistic properties. Type C stitching reduced trauma depth by 6.7% compared to Type A (with the same ply number).
3. Conditioning panels had a limited effect on trauma depth — only 3.6% difference was observed between dry and wet panels.
4. Energy absorption increased as the number of plies increased.
5. The type of stitching significantly influences energy transmitted to the back of the panel. The biggest difference was observed between Type A and Type C (11.5%). However, no significant difference was observed in energy absorbed.
6. Conditioning had a limited effect on energy transmitted to the back of the panel and no significant effect on absorbed energy.

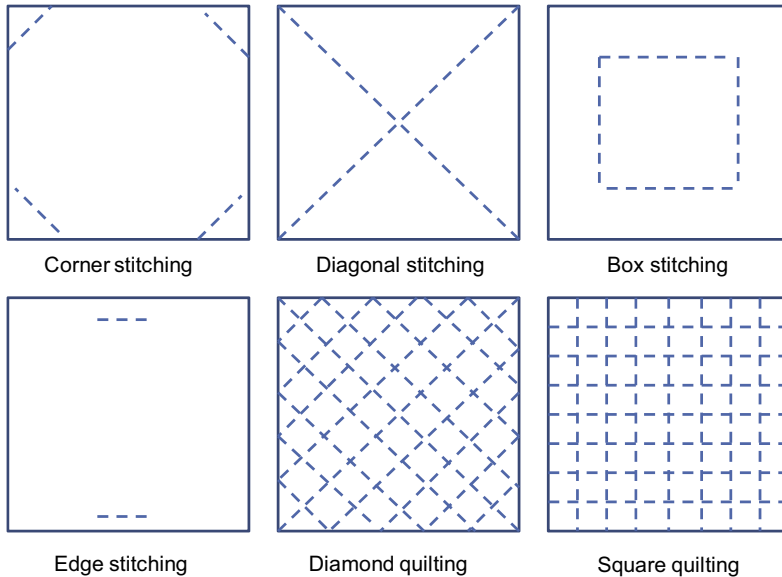


Figure 6.25 Different stitching and quilting patterns employed for SAIs.
Armour Solutions (2015) private communication.

[Bilisik and Turhan \(2009\)](#) investigated the effect of multidirectional stitching of ballistic fabrics. They tested stitched and unstitched fabrics against five types of ballistic threat (covering NIJ levels I to III). They found no significant energy absorption differences between stitched and unstitched structures. However, they also found that the stitched structures had low back-face signature compared to unstitched structures.

[Bilisik and Korkmaz \(2010\)](#) made an attempt to understand the energy absorption and failure modes of stitched structures by means of a yarn pull-out test. They found that the specific energy absorption was slightly better in the stitched structure compared with the unstitched structure and confirmed that stitched structures have low conical depth compared to unstitched structures. They concluded that the stitching generated frictional forces on each layer. An assessment was conducted of the effect of multilayered and multistitched ballistic structures on bending rigidity ([Bilisik, 2011](#)). This was done to measure the potential effect on wearer comfort. It was found that the bending rigidity depended on the number of fabric layers and stitching directions. Although multistitched structures had low conical depth compared to unstitched structures, they could not be easily formed and could decrease wearer comfort. Commonly used stitching and quilting patterns are shown in [Fig. 6.25](#).

6.4.2 Quilted structures

[Carr et al. \(2012\)](#) have investigated the effects of quilting on body armour. It was noted that earlier workers had provided anecdotal evidence that quilting could improve

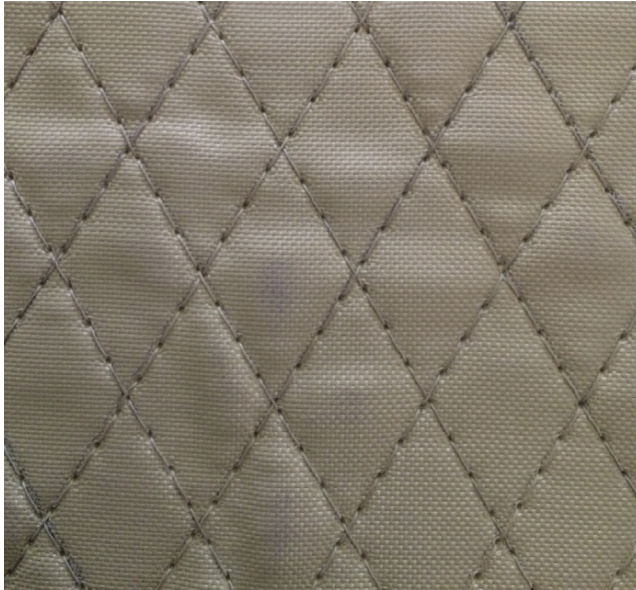


Figure 6.26 Example of diamond quilted SAI.
Armour Solutions (2014) private communication.

armour performance against fragments. Carr investigated the effects of diamond and square quilting on multiple fabric layers on ballistic performance against 5.5-mm diameter fragment-simulating projectiles (FSPs). The motivation was to lower the mass penalty and improve the ballistic performance of the original armour pack and the work was initiated in response to anecdotal evidence of improvements from other sources. It was found that the energy absorbed by a diamond quilted armour pack was between approximately 14% and 22% higher than for a nonquilted pack. A difference was found in the energy absorption as a function of impact velocity with fast impacts resulting in about 45% more energy absorption than slow impacts. Carr attributes this to a change in failure mechanism at higher-velocity impacts. Carr also suggests that yarn pull-out might contribute to the improved performance of quilted fabrics. An example of diamond quilting is shown in [Fig. 6.26](#).

6.4.3 Hybrid structures

Many manufacturers market ballistic protective concepts consisting of a combination of two or more different types of fabric. Motivations for this practice include cost reduction or expected improvement in ballistic performance. Although this approach can indeed lead to improvements in armour system performance, it is necessary to be aware of the underlying threat, impact and failure mechanisms in order to provide an optimal solution. ([Cunniff, 1992](#)) has investigated system effects arising from hybrid armour systems and the relationship to yarn and single-layer impact dynamics. Cunniff notes that the force acting on an impacting projectile is due to the tension

component in the direction of projectile velocity. This force is then transferred through the principal yarns and all the fabric layers.

The other layers also affect the transverse stress. If these stresses are large enough then adding further plies will have an adverse effect on performance. Cunniff also gives an example of a two-ply system consisting of one layer of Kevlar 29 and a layer of Spectra 1000. It was found that when the Kevlar was impacted first the ballistic limit of the system was 269 m/s but it was only 114 m/s when the Spectra was impacted first. Cunniff explains this result as a consequence of constraint on the transverse deflection of the Spectra layer when it is impacted first. This is due to the difference in material properties between the two materials. However, a similar experiment with Kevlar 29 and Kevlar 49 layers was less conclusive (Cunniff, 1992).

6.4.4 *Three-dimensional structures*

Considerable attention has been directed toward the development of 3D fabrics. The basic problem with single-layer 2D fabrics is that they are too thin, and thus to be effective against high-speed impacts or knife attack, they must be combined as multiple layers into a panel. Such panels lack flexibility, have poor drape, and are uncomfortable to wear due to poor thermal performance. For a vest protecting upper-body vital organs however, multiple layers of thin fabric thus was an accepted penalty. The performance of single layers may be improved by the incorporation of other materials within the fabric structure to form composites or laminates as discussed for example by Naik et al. (2006) and by Zeinstra et al. (2009), but the penalties in this case are the loss of fabric flexibility and the likely delamination of the fabric with a resultant loss of protective performance in the event of multiple impacts. Ha-Minh et al. (2012) referred to some of the recent work in developing 3D textiles with a view to increasing single-layer fabric thickness and therefore ballistic performance, with particular emphasis on improving the internal frictional interactions between the constituent yarns. One major difficulty in modelling the ballistic performance of such fabrics is the complexity of the weave structure.

For completeness, the topic of 3D fabrics is covered here (see Fig. 6.27). They are not normally considered for soft vest applications because they are too stiff and restrict interply slippage. However, some researchers have looked at the various effects of z-stitches in a composite armour laminate. It has been shown that most forms of z-stitching reduce the extent of the delamination — however, the presence of z-stitches does limit the maximum volume fraction of in-plane fibres attainable, which, in turn, reduces the ballistic properties of the laminate (compared with normal 2D laminates).

Work by Ko and Hartman (1986), as well as by James and Howlett (1997), aptly illustrates that while 3D composites do limit the degree of collateral damage (ie, reduce the amount of delamination) they are often less effective at absorbing kinetic energy. The poorer performance of the 3D fabrics can be attributed to their higher resin content and/or the suppression of the delamination process.

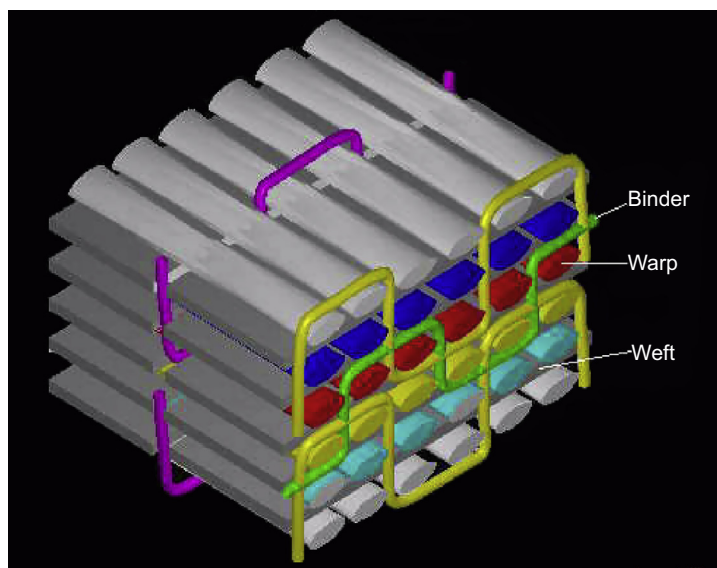


Figure 6.27 Computer graphic of a typical 3D woven structure, after Coman, 2009.

6.5 Soft armour inserts

6.5.1 Introduction and general approach

Soft armour inserts consist of multiple layers of fabrics, as described in [Section 6.4](#), and stitched or quilted together in a well-defined body shape. Body armour systems come in all shapes and sizes, as do humans! The traditional tradeoffs between coverage, protection, weight and mobility are paramount, of course (see [Section 6.7.2](#)), and there are excellent guides available to assist with selection criteria. For police service personnel, especially in the USA, NIJ standard 100-01 (November 2001) covers the threats as well as construction options and ballistic standards. However, for military personnel, the design and construction of these SAIs is very specific to the requirements of the end user (eg, the Australian Defence Force).

Form, fit and function are key attributes to an acceptable product, so most SAIs are tailor-made to satisfy a customer's very specific statement of requirement (see [Fig. 6.28](#)). Minimising wear and tear is also very important, so most SAIs are contained within a sealed, or stitched, nylon bag, in order to prevent water ingress and/or minimise exposure to UV radiation.

6.5.2 General properties: edge effects; multistrike effects

A significant factor in ballistic impact onto a target is the influence on the penetration process of proximity of the impact point to either a previous impact point or an edge of



Figure 6.28 Selection of soft armour inserts.

Source: ADA (2012).

the target. Several well-known ballistic standards recommend minimum values for these. A prior impact can have an influence on the behaviour of a subsequent one. This is because the yarns or fibres that make direct contact with the impacting projectile (the primary yarns) may be either damaged or displaced after the first impact. There will also be an influence on yarns other than the primary yarns. However, this is generally less significant than the influence on the primary yarns. Another factor is the distance between the initial and subsequent strikes with the influence of the first strike diminishing as the distance increases.

Usually the influence of a prior impact results in a reduction in ballistic performance. This is because damage or displacement of yarns or fibres in the fabric structure means a reduction in the capacity of the fabric to absorb impact energy during a subsequent strike. These considerations form the basis for the well-known test requirements to maintain a suitable distance between impacts or between an impact and the edge of the target. A good example is the National Institute of Justice ([Specification, 2008](#)) fair hit requirement for a minimum shot-to-shot distance of 51 mm. This standard also permits the manufacturer to define the minimum shot-to-edge distance but places upper limits of either 51 mm (lighter weight threat) or 76 mm (heavier weight threat) on it.

From a practical viewpoint it is often possible to visually examine an impacted target and determine the extent of the damage from prior impacts. However, account must be taken of the fact that what is viewed in an impacted target is the residual deformation which is of a lower magnitude than the transient deformation of the fabric during the impact event. It should also be recalled that the deformation of yarns will extend beyond the more easily observed transversely deformed region so that even areas of the target with no perceptible transverse deformation might include yarns that have been displaced laterally due to the action of the longitudinal wave (that precedes the transverse wave in the yarn).

A related issue is an impact that occurs near the edge of a target. For an impacted fabric it is easy to explain why an impact near an edge should result in lower ballistic performance. An impacting projectile is arrested by a fabric because, at each point in

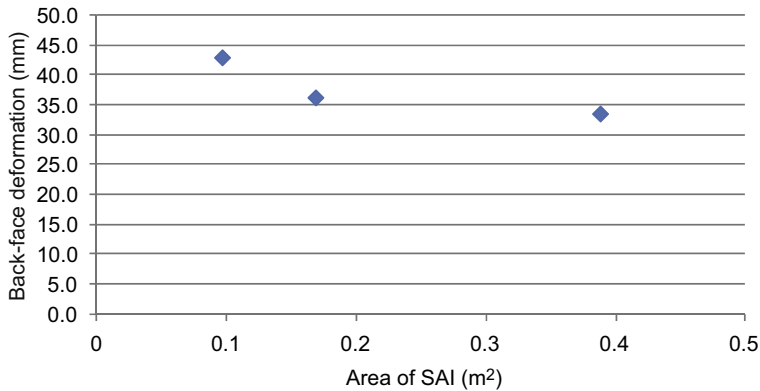


Figure 6.29 Effect of surface area of an SAI on back-face deformation for an experimental pack consisting of layers of XP S102 noncrimp fabric. The BFD values are means from at least six impacts per vest. ADA (2012).

time during the impact, some of the projectile's kinetic energy is transferred into kinetic energy of the fabric yarns (Cunniff, 1999a). For an impact far from an edge this energy can be transferred laterally in all directions around the projectile. However, if the impact occurs near an edge then this may no longer be the case. However, the rate at which energy is transferred from an impacting projectile is dependent on the longitudinal wave speed of fabric yarns or fibres and this is a property of the yarn material that usually cannot change significantly during the impact (Noori, 1999). Therefore, the combination of these two facts means that a smaller amount of energy is transferred from the impacting projectile per unit time than if there was no proximity to the edge. This, in turn, results in poorer ballistic performance by the fabric. This poorer performance can manifest itself in, eg, a lower V-50 near an edge. It may also manifest itself as larger back-face deformation. In fact, it is known that a phenomenon called 'pencil-ling' can occur for impacts near an edge. Pencilling is the back-face deformation from a nonperforating impact that results in a deep, narrow deformation of the fabric. Such a deformation can result in a laceration of the underlying flesh of the wearer even though the projectile has not perforated the armour. Lewis et al. (2004) present evidence for the occurrence of pencilling while studying impacts onto cadavers and pig tissue. They also present a case study where a nonperforating impact of body armour resulted in a laceration and protrusion of body armour into the victim's tissue.

More recently, Crouch determined that size and shape, especially total surface area, play a significant role in determining the specific performance of a particular SAI. For example, Fig. 6.29 shows a decrease in back-face signature (BFS) as the area of the SAI increases: it was suggested that this occurs because, with certain fabrics (especially the nonwoven varieties), a larger volume of fibres get pulled in towards the event site.

Furthermore, and as will be described in more detail in Chapter 7, the size of the SAI has a profound effect upon the ballistic performance of a hard armour plate,

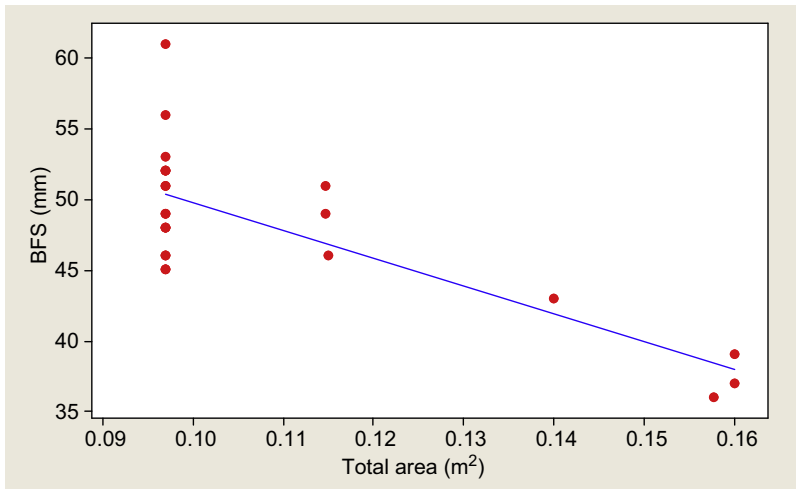


Figure 6.30 Effect of surface area of an SAI on back-face signature of an XP500-based SAI upon the performance of a lightweight HAP. All data corresponds to one specific shot location. ADA (2012).

especially the lighter weight variants. Fig. 6.30 illustrates how the surface area of an XP500 (now designated as S102, from DuPont) based SAI affects the overall performance of the system and, indeed, the scatter of the BFS results.

The BFS value is also very dependent upon the location of the impact. For example, the most recent ballistic test standard, NIJ 0101.06, dated July 2008 (see Chapter 11 for more details) describes the shot locations very precisely, in relation to the edge of the SAI. Fig. 6.31 illustrates the specified shot pattern. It should be noted that Shots 4 and 5 are shot at an angle of obliquity of 30° or 45°. What is interesting to note is that the BFS value of Shot 6, in a central location, is significantly less than the BFS values for Shots 1, 2 and 3, which are near the edge of the SAI. Fig. 6.32 shows this very clearly.

6.5.3 Soft armour inserts for handgun protection

Soft armour inserts (SAIs) for protection against handgun bullets would typically be manufactured from woven fabrics like Kevlar A802 or Kevlar A363F (see Fig. 6.33); both these plain-woven fabrics have a water-repellant finish. For example, 36 plies of A363 fabric, made from K129 aramid fibres (see Table 6.10 for specific details of the yarn), would normally be required to meet the ballistic requirements of the NIJ Standard for Level IIIA. This standard requires that the panel withstand (under dry and wet conditions) six shots in a set pattern from both the 9 mm FMJ RN at 436 m/s and the 44 Magnum SJHP also at 436 m/s.

However, popular alternative solutions now include SAIs based upon Kevlar XP S102, a 500 gsm, four-ply NCF, introduced by DuPont in 2008 (see Table 6.11)

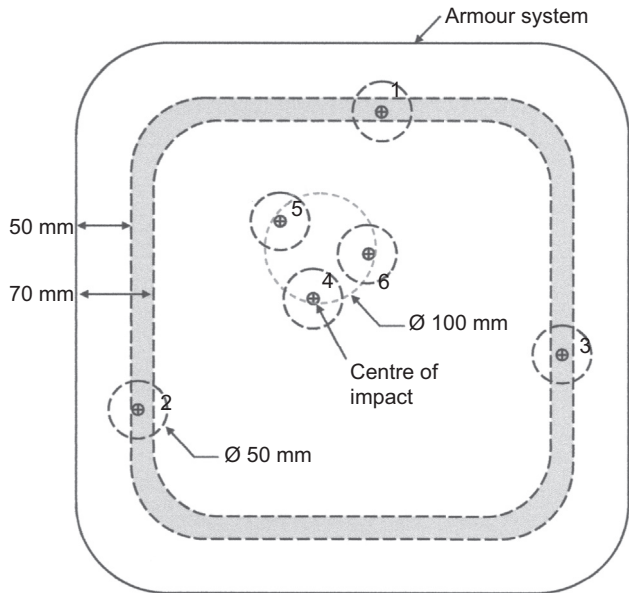


Figure 6.31 Shot pattern for handgun impacts.
According to National Institute of Justice, July 2008. NIJ 0101.06, Ballistic Resistance of Body Armor.

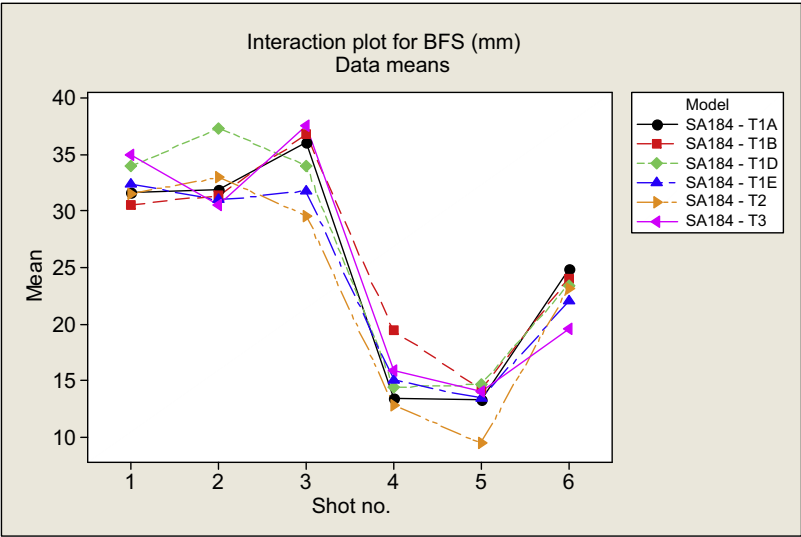


Figure 6.32 Variation of mean BFS values for UHMWPE-based SAIs, of different sizes, for the six shot locations shown in Fig. 6.36. The projectile was a 9 mmHg round.
Source: ADA (2013).

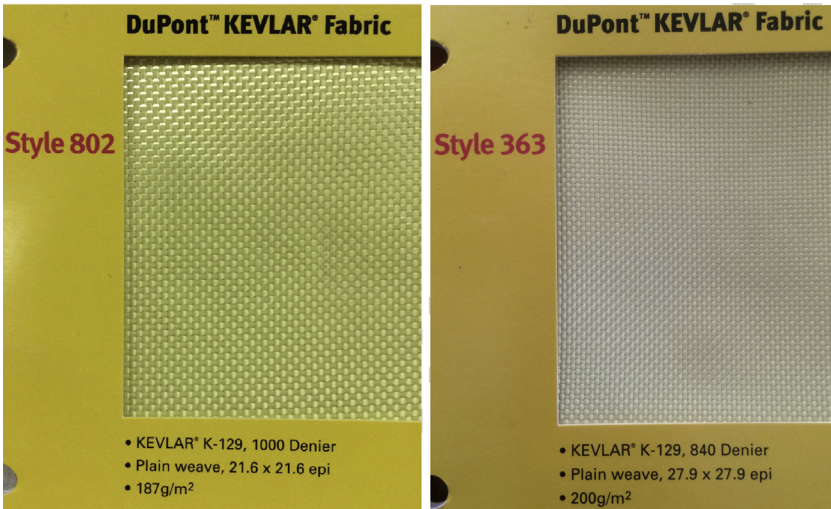


Figure 6.33 Images of swatches of DuPont style A802 and A363.

Table 6.10 Details of yarn as used in Kevlar Fabric A363

Property	Units	Value
Type of Kevlar		T964C Kevlar 129
Yarn weight	Tex	93
Breaking load	N	141
Breaking extension	%	2.6
Tenacity	cN/tex	152
Filament cross-sectional shape	—	Circular
Number of filaments in each yarn cross-section	—	570
Nominal weight of fabric	gsm	200
Coefficient of static friction	—	0.30
Coefficient of dynamic friction	—	0.28

and those based upon an UHMWPE fibre, like Spectra SA3118, a quadriaxial NCF, from Honeywell, weighing 180 gsm.

This last group, based upon the latest UHMWPE fabrics, represents one of the lightest SAI packs possible for protection against handgun ammunition. Even greater savings in weight may be possible using fourth-generation fabrics like Spectra SA5128 or SA5143 (commercially available from 2014 onwards). Commercial quantities of aramid fabrics, using AuTx fibres, are also claiming even further reductions in weight.

In summary, the ballistic performance of SAIs is assessed through a very strict procedure, normally governed by a test standard like NIJ 0101.06. Even though the test

Table 6.11 Ballistic performance of various commercial SAIs

Construction of SAI	Threat	AD (kg/m ²)	Typical V-50 (m/s)	Typical BFD (mm)
10 plies of XP S102 (no stitching) + 1 layer of 3 mm foam	0.44 Mag	5.10	513	35
10 plies of XP S102 (no stitching) + 1 layer of 3 mm foam	9 mm	5.10	517	24
11 plies of XP S102, with corner stitching	0.44 Mag	5.50	526	35
11 plies of XP S102, with corner stitching	9 mm	5.50	524	22
5 plies of XP S102 + 7plies of XP 307 (quilted) + 3 plies of XP S102, with corner stitching	0.44 Mag	5.13	518	35
26 plies of SA3118 (Honeywell data sheet, May 2009)	9 mm	4.59	560	n/a
26 plies of SA3118 (Honeywell data sheet, May 2009)	9 mm	3.71	530	n/a

DuPont and Honeywell datasheets.

standards are very rigorous, the actual V-50 value obtained will still depend upon the following non-exhaustive list of variables:

1. Areal weight of pack, irrespective of construction;
2. Construction of the pack, including interleaves, stitching, etc.;
3. Quality and homogeneity of the fabric plies, especially if few in number;
4. Size of vest, especially total length of fibres involved;
5. Shape of vest, especially if SAI has wings (essentially smaller panels) linked to above effect;
6. Location of impact, with respect to the edge of the fabric (see test standards);
7. Location of impact, with respect to a stitch line;
8. Intershot distance (see test standards);
9. Effect of prior damage (ie, if same rows of fibres are involved);
10. Flatness/smoothness of pack;
11. The precise temperature of the backing clay, and therefore its mouldability — see Chapter 11;
12. Homogeneity of clay (ie, whether it has been refilled correctly) — see Chapter 11;
13. Behaviour of bullet. Atypical round deformation should be classed as an unfair hit.

6.5.4 Soft armour inserts for stab and spike resistance

6.5.4.1 Very fine-woven fabrics

Woven aramid fabrics have proven their ability to provide excellent protection against bullets from typical handgun weapons; however, conventional ballistic aramid fabrics

offer little resistance to puncture and stab. However, a range of extremely fine-woven fabrics has been developed to overcome this limitation, which is a successful approach to arresting the tip of a blade or spike.

Such commercial products tend to offer spike resistance only. One example is commercially available under the trade name of Kevlar Correctional, as supplied by DuPont. The fabric is manufactured from superfine yarns, which allow it to be woven very tightly with a high packing density. When sharp instruments such as spikes or knives penetrate the fabric, the fibre readily absorbs and dissipates the energy of the puncture or penetration. These fabrics are so fine that the tip of the spike does not easily perforate the fabric but instead gets initially arrested by making direct contact with the tightly woven yarns. The typical failure mode of woven fabrics as a result of a spike threat is related to yarn mobility and depends on friction between and within yarns where the separation of filaments causes 'windowing'. On the other hand, failure due to yarn fracture is relative to yarn strength and will usually result from a knife threat (Gong, 2013).

Another similar example of a 'densified' weave is Microflex by Teijin Aramid. Soft body armour prepared using these fabrics can be more breathable, flexible, concealable and easily contoured with the body than alternatives, helping the wearer to achieve increased mobility and comfort and in turn enhancing their confidence and survivability during counter attacks. However, the fabric is expensive, difficult to manufacture because of its tight weave construction, and the fabric has limited protection against ballistic threats, so needs to be worn in conjunction with a ballistic armour to provide multithreat protection, becoming an increased burden. These structures are lightweight, but do not give effective knife protection and therefore are in need of further development.

Another aspect in using such fabrics is the choice of stitching pattern, where different stitch densities and stitch location may affect performance. A balance needs to be reached between, on the one hand, providing a stiff pack of fabrics, which provides greater energy absorption through flexure, and a loose pack of fabrics which provides a maximum amount of interply slippage, of which the latter has been historically preferred.

6.5.4.2 *Laminated fabrics*

Laminated fabrics, in particular thermoplastic impregnated woven aramids, have been shown to have improved stab, and particularly puncture, resistance due to reduced windowing of the fibres (Mayo et al., 2009), reduced yarn stretching and slippage.

Available commercial products are either based upon woven aramid fabrics or nonwoven, unidirectional UHMWPE fabrics and are most commonly laminated with a polymer resin. Most major suppliers of ballistic fabrics have a number of products of this type, such as the soft body armour (Larsen) range from DSM Dyneema, composed of cross-ply laminated unidirectional fabrics, and the Gold Shield range of resin-coated woven aramids from Honeywell. However, these products, although marketed as including stab protection, are designed to defeat ballistic threats and the level of stab resistance is unqualified. A popular laminated product providing stab

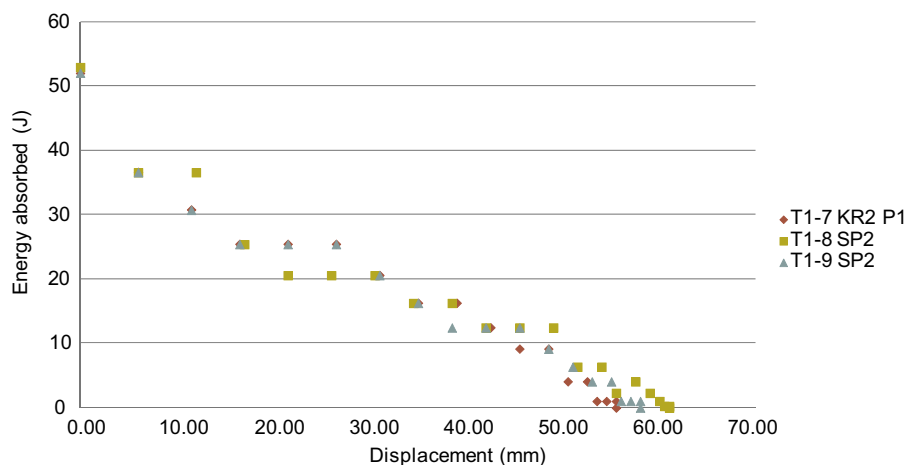


Figure 6.34 Energy absorbed, as a function of displacement of a knife and spike penetrating a pack of Argus fabrics: T1-7 is P1 KR2 data; T1-8 and T1-9 are SP2 data.

Source: DMTC (2015).

resistance is that supplied by Barrday under the trade name of Argus. This is supplied as sheets of aramid fabrics preimpregnated with a thermosetting resin. The individual sheets tend to have a stiff handle but the product has been shown to offer excellent cutting resistance from both knife and spike attacks (Crouch, 2013). The DMTC used standard Stab and Spike (S&S) upgrade packs consisting of 15 plies of Argus material, weighing 4.8 kg/m^2 , during a series of instrumented impact tests. These recorded the displacement of a P1 blade, as a function of time, as it penetrated the target. These data were used to generate absorbed energy versus displacement plots in order to better understand the energy-absorbing mechanisms involved in a stabbing event.

From these plots, in Fig. 6.34, it appears that we may have identified three phases in this penetration event:

1. Compression of the pack, ahead of the knife tip (0 to ~ 20 mm);
2. Intermediate arrest of the knife, as it starts to penetrate the pack (~ 20 to 25 mm);
3. Cutting of the fabric, and final arrest of the knife (~ 25 to 55 mm).

DuPont have developed their 'AS' (antistab) range of Kevlar woven fabrics using Kevlar fibres that have been laminated and cured with a film, offering single resin-coated and a double-face resin-coated option. DSM Dyneema also incorporate knife resistance with their SB range, including SB21 and SB31 composed of UHMWPE (Dyneema) composite laminates. Both products consist of single layers of unidirectional sheet, at cross-ply of 90° and are laminated with a rubber-based matrix and protective film. The SB21 consists of four layers and the SB31 of two layers, so having the lower areal density. Natural rubber latex-coated fabrics have also shown improved puncture resistance, energy absorption and elasticity (Hassim et al., 2012).

Kang et al. (2010) developed fumed silica/Kevlar composite fabrics for stab resistance material and investigated their mechanical and stab resistance properties.

Fumed silica suspension was used as an STF and Kevlar KM2 woven fabric was used as a matrix in the research. The STF, which showed the reversible liquid–solid transition at a certain shear rate, significantly improved the stab resistance of Kevlar fabrics against spike threat.

Li et al. (2013) prepared high-modulus puncture-resistant nonwoven fabrics by opening, mixing, carding, lapping needle punching as well as hot-pressing processes using blends of recycled Kevlar, Nylon 6 and bicomponent polyester fibres. The static puncture resistance, tensile strength and bursting strength of the fabrics were evaluated and the effect of fibre content, needle punching density and hot-pressing temperature on these properties assessed. It was observed that the tensile strength largely depended on the needle punching density and hot-pressing temperature. However, the bursting strength and static puncture resistance were dependent on all the three parameters. An increasing trend followed by a decreasing trend was observed for tensile strength, bursting strength and static puncture resistance with increase in the concerning parameters. In addition, it was observed that there is a linear dependence of static puncture resistance test on the bursting strength.

Gadow and Von Niessen (2006) observed increased energy absorption of aramid fabrics thermally sprayed with hard ceramic coatings during quasistatic stab testing. However the fabric weight was significantly increased. The combination of coating of high-performance hard material and high-tenacity fibre woven fabrics can improve the stab and slash protection. The impact resistivity of high-tenacity fibres is achieved due to the damping and dissipating the shock wave velocity. The use of ceramic coating increases the interfibre friction, which prevents wave distortion and delamination during stabbing. The coating of the hard material blunts the sharp metal blades by abrasive action, which prevents the cutting action of the knives and the high friction between the ceramic coating and the metal blade reduces/minimises the knife penetration.

Mayo et al. (2009) investigated the stab and puncture resistance of thermoplastic impregnated woven aramid fabric under dynamic and quasistatic test methods. The fabrics were laminated with polyethylene, Surlyn and coextruded polyethylene-Surlyn films of varying thickness. The stab and puncture behaviour of the laminated fabrics were compared with the neat fabrics of similar areal density and number of layers. The results established that the stab and puncture resistance of the fabrics increases with thermoplastic lamination due to a combined effect of increase in the cut resistance and reduced windowing. Although Surlyn lamination provided the best performance, all other films were effective. The thermoplastic film needs to be integrally bonded to the fabric to achieve synergistic improvement in the performance.

Hosur et al. (2008) prepared thermoplastic-Kevlar (TP-Kevlar) composites which were less bulky, more flexible and far more resistant to puncture. The Kevlar fabric was impregnated with thermoplastic film (polyethylene, Surlyn and coextruded-Surlyn) using a hot press to produce the composites. Static and dynamic puncture-resistant properties of the TP-Kevlar composites were investigated using NIJ Standard 0115.00 test method. The impregnation of TP films into the Kevlar fabric significantly increased the puncture resistance during quasistatic and dynamic testing with spikes.

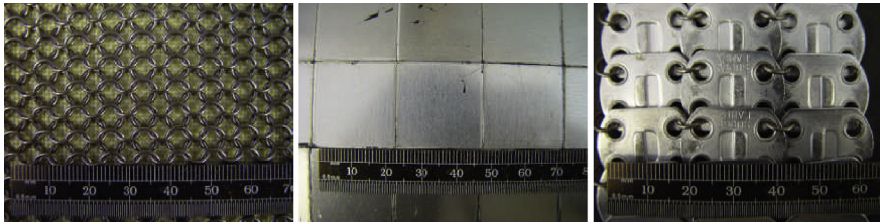


Figure 6.35 Examples of chain-mail.

Source: Internet.

6.5.4.3 Chain mail

Chain mail or metal ring mesh is commercially used for cut protection in meatpacking, which is often incorporated into stab-resistant vests (see Fig. 6.35). Because of its open structure, chain mail does not have very much puncture resistance. Chain mail is prepared from welded rings of material (Atkins, 2009) with the correct mechanical properties such as strength (resistance to tensile, compressive or shear force), hardness (resistance to abrasion deformation or indentation) and toughness (resistance to cracking, often used in the context of shock loading). Titanium and stainless steel are the key materials for preparing chain mail. Another material, titanium foil, can be used for both puncture and cut resistance. However, they are poor in ballistic resistance and comparatively heavy.

The mechanical properties of a chain-mail ring depend on its dimensions and the properties (such as yield strength, ductility and toughness) of the metal from which the armour was made. During a stab, when the point of a knife passes through the chain-mail and fractures one or more interwoven rings, it is easier for the knife to penetrate further. The actual mechanism by which a ring fractures or finally breaks will depend on constructional factors of the ring such as how the ring was made (riveting or welding or stamped out of the solid). The systematic analysis of the problem can help to optimise the chain-mail design.

The use of metal ring mesh, thermoplastic-coated fabrics, ceramic elements or flexible arrays of rigid metal can protect from knife stabbing. Similarly, slash protection can be achieved by using multiple layers of conventional woven ballistic fabrics or specially knitted fabrics with hardened metal wires. The use of hard materials such as ceramic, metal or composite plates for stab-resistant body armour has been reported. Although these hard materials can provide excellent stab resistance, they are inflexible, bulky and uncomfortable to wear. The preferred material for stab and puncture protection is the flexible body armour, which allows free body movement and provides a fair amount of comfort.

6.5.4.4 Turtleskin, a proprietary product

This is a commercially available product (see Fig. 6.36) from Warwick Mills in the United States, which offers complete protection against spike, knife and hypodermic needles when worn in conjunction with a ballistic armour panel. The product consists



Figure 6.36 A bespoke example of Turtleskin.

Source: Armour Solutions, 2014.

of a layer, or layers, of titanium or stainless steel, triangular-shaped, metal stampings, encapsulated in a polymeric-based, fabric-reinforced matrix. The items are fairly thin and flexible and each size and style of vest is individually designed. The product can be supplied in a number of grades to match the desired threat.

6.6 Protective garments/apparel

6.6.1 *Typical body armour systems*

For generations, armour technologists, whether they are legendary outlaws of the outback or professional designers, have always been inventive and cutting-edge when it comes to protecting the armed combatant (Crouch, 2009). Fig. 6.37 illustrates the Modular Combat Body Armour System, supplied to the Australian Defence Force in 2008–2011, for use in ground-based operations in Iraq, where the soldiers were patrolling the streets. For such operations, body armour systems (BASs) needed to offer full protection, including all extremities, as well as wrap-around torso SAIs.

Soft armour inserts (SAI), in the form of packs, are central to all body armour systems and provide the basic level of bullet protection. Of course, the SAI also forms the support structure for a hard armour plate (HAP), which is worn in conjunction with the SAI. As we will learn in Chapter 7, the construction



Figure 6.37 Body armour systems: past, present and future.

Crouch, I.G., 2009. Threat defeating mechanisms in body armour systems. Paper Presented at the Next Generation Body Armour, London, September 2009.

of the SAI also has a significant influence over the performance of the HAP. SAIs can also be enhanced with additional packs that provide additional protection against stab and spike threats and, like the HAPs, work in conjunction with the SAI.

In 2012, the ADF found themselves involved in the Afghanistan conflict with body armour systems that were not designed to suit a highly mobile fighting force. The MCBAS system was unsuitable, so a tiered body armour system (TBAS) needed to be developed which not only retained the modular concept adopted with MCBAS but also developed a wider range of elements with different levels of coverage and protection. [Fig. 6.38](#) shows the two systems, side-by-side, so that trade-offs can be appreciated.

6.6.2 Trade-offs: weight versus mobility versus protection

Tactics used in modern warfare often require mobility from the soldier. This is countered by a requirement to provide the soldier with the best possible protection. This is because this protection often carries with it the penalties of increased mass or bulk. In addition, there is the possibility that the armour solution may impose a thermal burden on the soldier.



MCBAS (2008)



TBAS (2012)

Figure 6.38 The MCBAS and TBAS systems, supplied to the Australian Defence Force by ADA.

The problem of striking a balance between armour bulk or mass and the protective and operational requirements of a soldier is not new. [Laible and Barron \(1980\)](#) indicate that such considerations have, to a greater or lesser extent, always played a role in armour selection. The ancients often used flexible options such as sewing together small scales to facilitate articulation. The Romans, Koreans and Chinese often used lighter materials such as thin metal scales, leather or cloth. The Normans used scale armour made from iron, bronze, leather and horn and some medieval armour contained metal components in combination with felt. There appears to have been relatively sporadic use of armour against firearms until the advent of WW1 and WW2. They claim the first use of body armour on a large scale was during WW2 with the necessity of protecting air crews.

The first attempt at such protection was to use steel plates. However, it was soon found that fibreglass laminated with polyester (eg, Doron) provided better protection for the same weight, leading to greater efficiency for the same burden on the soldier. However, this development by the Air Force was not entirely satisfactory to the foot soldier. This was primarily because of a perceived problem with armour weight and lack of flexibility. This led to the development of nylon vests. For ground troops a maximum areal density of 6 kg/m^2 with a total vest mass of 4 kg was selected. The Doron and nylon vests were first used in the Korean War (1950s). Physiological studies of the nylon vest indicated it could be used by the soldier without undue heat stress ([Laible and Barron, 1980](#)) although its protective ability was limited.

[Larsen et al. \(2011\)](#) have critically reviewed the effect of body armour on the performance of personnel conducting military-type tasks. It was found that the successful

performance of military tasks and protection against hazards are often conflicting requirements. There is also evidence that treadmill walking and high-intensity maximal efforts in an obstacle course were adversely affected. The addition of a full combat load might exacerbate these performance decrements. However, it is acknowledged that there is still a lack of knowledge in some areas such as intermittent or repeated high-intensity tasks and that the tension between increased protection and decreased performance is still to be resolved.

A study of the effects of wearing an armoured vest and/or extremity armour indicated a significant influence of body armour on conducting standard physical tasks. In particular it was found that performance on maximal effort tasks was poorer when extremity armour was worn compared with performance while wearing either no armour at all or only the vest (Hasselquist et al., 2008). This finding was confirmed by Adams (2010), who found a metabolic cost increase and an influence on gait kinematics.

Horn et al. (2011) conducted a study to determine approaches to lightening body armour. It was concluded that no simple material solution currently exists and that a 10% reduction in weight seems to be feasible but is not easy to accomplish while a 20% reduction is not realistic. The study also pointed to a synergy between material, nonmaterial and modular concepts and recommended a systems approach (ie, considering hard and soft armour together as one item).

The most recent example of this dilemma — this trade-off — has been the transition in BAS within the Australian Defence Force, as mentioned above, in Section 6.6.1. The TBAS is much lighter compared with MCBAS, as shown in Fig. 6.38. This was achieved not only through use of improved armour materials and products but also more realistic specification requirements and reduced coverage. It enabled the ground troops to be more mobile and to cope with conditions found in Afghanistan c.2013–15.

Acknowledgements

The authors are extremely grateful to their colleagues within the Defence Science and Technology Group (DST Group), and the Defence Materials Technology Centre, who have contributed to this chapter. In particular, we would like to thank Dr Bin Lee, Dr Jie Ding and Dr Ping Tan (from the DST Group) as well as Dr Menghe Miao (from CSIRO) for their valuable discussions and input.

References

- Adams, A., 2010. Effects of Extremity Armor on Metabolic Cost and Gait Biomechanics (M.Sc. thesis). Worcester Polytechnic Institute.
- Ahmad, M., Ahmad, W., Salleh, J., Samsuri, A., 2008. Effect of fabric stitching on ballistic impact resistance of natural rubber coated fabric systems. *Materials and Design* 29, 1353–1358.
- Allen, S.R., Newton, C.W., 2013. EP 2663679 A1, Production of, and Drying of, Polymer Fibres.

- Anon, 2015. DuPont Website: www.dupont.com.
- Atkins, A., 2009. The deformation and fracture of chain mail. In: Paper Presented at the Next Generation Body Armour, London, September 2009.
- Barnes, H., 1997. Thixotropy — a review. *Journal of Non-Newtonian Fluid Mechanics* 70, 1–33.
- Bazhenov, S., 1997. Dissipation of energy by bulletproof aramid fabric. *Journal of Materials Science* 32, 4167–4173.
- Bhatnagar, A., 2006. *Lightweight Ballistic Composites*. Woodhead Publishing, Cambridge, England.
- Bilisik, A., Turhan, Y., 2009. Multidirectional stitched layered aramid woven fabric structures and their experimental characterization of ballistic performance. *Textile Research Journal* 79 (14), 1331–1343.
- Bilisik, K., 2011. Bending behavior of multilayered and multidirectional stitched aramid woven fabric structures. *Textile Research Journal* 81 (17), 1748–1761.
- Bilisik, K., Korkmaz, M., 2010. Multilayered and multidirectionally-stitched aramid woven fabric structures: experimental characterization of ballistic performance by considering the yarn pull-out test. *Textile Research Journal* 80 (16), 1697–1720.
- Bolduc, M., Lazaris, A., 2002. Spider Silk-based Advanced Performance Fiber for Improved Personnel Ballistic Protection Systems. DRDC Valcartier Technical Memorandum TM 2002-222.
- Briscoe, B.J., Motamedi, F., 1992. The ballistic impact characteristics of aramid fabrics: the influence of interface friction. *Wear* 158, 229–247.
- Budden, G., 2006. Defense and Comfort: New Advancement in Impact-Protection Textiles. Technical Textile Technology. Retrieved from: <http://www.activeprotectionsystem.com/DowComing3.pdf>.
- Burton, C., University of Delaware, 2007. Shear Thickening Fluid (STF) Fabric Home. Retrieved from: <http://www.ccm.udel.edu/STF/index.html>.
- Carr, D., Lankester, C., Peare, A., Fabri, N., Gridley, N., 2012. Does quilting improve the fragment protective performance of body armour? *Textile Research Journal* 82 (9), 883–888.
- Cheeseman, B.A., Bogetti, T.A., 2003. Ballistic impact into fabric and compliant composite laminates. *Composite Structures* 61, 161–173.
- Chin, W.K., Wetzel, E.D., 2008. Breathability Characterization of Ballistic Fabrics, Including Shear Thickening Fluid-treated Fabrics.
- Chocron, S., et al., 2008. Lightweight polyethylene, non-woven felts for ballistic impact applications: material characterisation. *Composites Part B: Engineering* 39 (2008), 1240–1246.
- Coman, F., April 2009. Personnel Communication.
- Cork, C.R., Foster, P.W., 2007. The ballistic performance of narrow fabrics. *International Journal of Impact Engineering* 34, 495–508.
- Crouch, I.G., 2009. Threat defeating mechanisms in body armour systems. In: Paper Presented at the Next Generation Body Armour, London, September 2009.
- Crouch, I.G., 2014. Private Communication.
- Cunniff, P., 1992. An analysis of the system effects in woven fabrics under ballistic impact. *Textile Research Journal* 62 (9), 495–509.
- Cunniff, P., 1999a. Decoupled response of textile body armor. In: Paper Presented at the 18th International Symposium on Ballistics, pp. 814–821.
- Cunniff, P., Fossey, S., Auerbach, M., Song, J., Kaplan, D., Adams, W., Eby, R., Mahoney, D., Vezie, D., 1994. Mechanical and thermal properties of dragline silk from the spider *Nephila clavipes*. *Polymers for Advanced Technologies* 5, 401–410.

- Cunniff, P.M., 1999b. Dimensionless parameters for optimisation of textile-based body armor systems. In: Paper Presented at the 18th International Symposium on Ballistics, San Antonio, Texas.
- Cunniff, P.M., 2014. Keynote address: overview of impact on composites. In: Paper Presented at the 28th International Symposium on Ballistics, Atlanta, GE, September 2014.
- Cunniff, P.M., Auerbach, M.A., Vetter, E., Sikkema, D.J., 2002. High performance M5 fibre for ballistics/structural composites. In: Paper Presented at the 23rd Army Science Conference, Orlando, 2002.
- d3o lab, 2008. d3o. Retrieved from: www.d3o.com.
- Decker, M., Halbach, C., Nam, C., Wagner, N., Wetzel, E., 2007. Stab resistance of shear thickening fluid (STF)-treated fabrics. *Composites Science and Technology* 67 (3), 565–578.
- Dekker, P., 2009. Practically invulnerable. *Hand Papermaking* 24 (2), 10–13.
- Du, J., Bai, J., Cheng, H., 2007. The present status and key problems of carbon nanotube based polymer composites. *Express Polymer Letters* 1 (5), 253–273.
- Duan, Y., Keefe, M., Bogetti, T.A., Cheeseman, B.A., 2005. Modeling friction effects on the ballistic impact behavior of a single-ply high-strength fabric. *International Journal of Impact Engineering* 31, 996–1012.
- Duong, T.T., Jong, S.K., You, H., 2010. Stab-resistant property of the fabrics woven with the aramid/cotton core-spun yarns. *Fibers and Polymers* 11 (3), 500–506.
- Dwivedi, A., Dalzell, M.W., Long, L.R., Slusarski, K.A., Fossey, S.A., Perry, J., Wetzel, E.D., September 2013. Continuous filament knit aramids for ballistic protection. In: Paper Presented at the 28th Technical Conference of the American Society for Composites. Pennsylvania State University.
- Erlich, D.C., Shockey, D.A., Simons, J.W., 2003. Slow penetration of ballistic fabrics. *Textile Research Journal* 73 (2), 179–184.
- Gadow, R., Von Niessen, K., 2006. Lightweight ballistic with additional stab protection made of thermally sprayed ceramic and cermet coatings on aramide fabrics. *International Journal of Applied Ceramic Technology* 3 (4), 284–292.
- Gong, X., 2013. Study of knife stab and puncture-resistant performance for shear-thickening fluid enhanced fabric. *Journal of Composite Materials* 48, 641.
- Ha-Minh, C., Boussu, F., Kanit, T., Crépin, D., Imad, A., 2012. Effect of frictions on the ballistic performance of a 3D warp interlock fabric: numerical analysis. *Applied Composite Materials* 19 (3), 333–347.
- Hasselquist, L., Bense, C., Corner, B., Gregorczyk, J., 2008. Understanding the physiological, biomechanical, and performance effects of body armor use. In: Paper Presented at the 26th Army Science Conference, Orlando. Florida.
- Hassim, N., et al., 2012. Puncture resistance of natural rubber latex unidirectional coated fabrics. *Journal of Industrial Textiles* 42 (2), 118–131.
- Hearle, J.W.S., 2001. *High Performance Fibres*. Woodhead Publishing, Cambridge, UK.
- Horn, K., Biever, K., Burkman, K., DeLuca, P., Jamison, L., Kolb, M., Sheikh, A., 2011. *Lightening Body Armor*. Rand Arroyo Center Technical Report. U.S. Army Contract, W74V8H-06-C-0001.
- Hosur, M., et al., 2008. Studeis on the fabrication and stab resistance characterisation of novel thermoplastic-Kevlar composites. *Solid State Phenomona* 136, 83–92.
- James, B.J., Howlett, S.A., May 1997. Enhancement of post impact structural integrity of GFRP composites by through thickness reinforcement. In: Paper Presented at the Second European Armoured Fighting Vehicle Symposium, Shivenham, UK.

- Kaharan, M., Kus, A., Eren, R., 2008. An investigations into ballistic performance and energy absorption capabilities of woven aramid fabrics. *International Journal of Impact Engineering* 35, 499–510.
- Kalman, D.P., Schein, J.B., Houghton, J.M., Laufer, C.H.N., Wetzel, E.D., Wagner, N.J., 2007. Polymer dispersion based shear thickening fluid-fabrics for protective applications. In: Paper Presented at the SAMPE, Baltimore, MD.
- Kang, T.J., Hong, K.H., Yoo, M.R., 2010. Preparation and properties of fumed silica/Kevlar composite fabrics for application of stab resistant materials. *Fibres and Polymers* 11 (5), 719–724.
- Kasseh, A., Keh, E., 1998. Transfers of colloidal silica from water into organic solvents of intermediate polarities. *Journal of Colloid and Interface Science* 197 (2), 360–369.
- Kirkwood, J.E., Kirkwood, K.M., Lee, Y.S., Egres, R.G., Wagner, N.J., 2004a. Yarn pull-out as a mechanism for dissipating ballistic impact energy in Kevlar® KM-2 fabric. Part 2: predicting ballistic performance. *Textile Research Journal* 74 (11), 939–948.
- Kirkwood, K.M., Kirkwood, J.E., Lee, Y.S., Egres, R.G., Wagner, N.J., 2004b. Yarn pull-out as a mechanism for dissipating ballistic impact energy in Kevlar® KM-2 fabric. Part 1: quasi-static characterisation of yarn pull-out. *Textile Research Journal* 74 (10), 920–928.
- Kitigawa, T., Ishitobi, M., Yabuki, K., 2000. *Journal of Polymer Science, Part B: Polymer Physics* 38, 1605.
- Ko, F.K., Hartman, D., 1986. Impact behavior of 2D and 3D glass/epoxy composites. *SAMPE Journal* 11.
- Kordani, N., Vanini, A.S., 2014. Optimising the ethanol content of shear thickening fluid/fabric composites under impact loading. *Journal of Mechanical Science and Technology* 28 (2), 663–667.
- Laible, R., 1980. *Ballistic Materials and Penetration Mechanics, Chapter 4 (Fibrous Armor)*. Elsevier.
- Laible, R., Barron, E., 1980. *Ballistic Materials and Penetration Mechanics, Chapter 2, History of Armor*.
- Larsen, B., Netto, K., Aisbett, B., 2011. The effect of body armor on performance, thermal stress, and exertion: a critical review. *Military Medicine* 176, 1265–1273.
- Lee, Y.S., Wagner, N.J., 2003. Dynamic properties of shear thickening colloidal suspensions. *Rheologica Acta* 42 (3), 199–208. <http://dx.doi.org/10.1007/s00397-002-0290-7>.
- Lee, Y.S., Wetzel, E.D., Wagner, N.J., 2003. The ballistic impact characteristics of Kevlar® woven fabrics impregnated with a colloidal shear thickening fluid. *Journal of Materials Science* 38 (13), 2825–2833. Retrieved from ISI:000183835300006.
- Lewis, E., Johnson, P., Bleetman, A., Bir, C., Horsfall, I., Watson, C., Wilhelm, M., Sherman, D., Eck, J., Walilko, T., 2004. An investigation to confirm the existence of ‘pencil’ as a non-penetrating behind armour injury. In: Paper Presented at the PASS 2004, pp. 151–159.
- Li, T.T., et al., 2013. Evaluation of high modulus, puncture-resistant composite non-woven fabrics by response surface methodology. *Journal of Industrial Textiles* 43 (2), 247–263.
- Maranzano, B.J., Wagner, N.J., 2001. The effects of particle-size on reversible shear thickening of concentrated colloidal dispersions. *Journal of Chemical Physics* 114 (23), 10514–10527.
- Mayo, J., et al., 2009. Stab and puncture characterisation of thermoplastic-impregnated aramid fabrics. *International Journal of Impact Engineering* 36 (9), 1095–1105.
- Miao, X., Kong, X., Jiang, G., October 2012. The experimental research on the stab resistance of a warp-knitted spacer fabric. *Journal of Industrial Textiles* 43. <http://dx.doi.org/10.1177/1528083712464256>.
- Mylvaganam, K., Zhang, L., 2007. Ballistic resistance capacity of carbon nanotubes. *Nanotechnology* 18, 475701.

- Naebe, M., Lutz, V., McGregor, B.A., Tester, D., Wang, X., 2013. Effect of surface treatment and knit structure on comfort properties of wool fabrics. *Journal of The Textile Institute* 104 (6, Special Edition: Wool Research), 600–605.
- Naik, N.K., Shrirao, P., Reddy, B.C.K., 2006. Ballistic impact behaviour of woven fabric composites: Formulation. *International Journal of Impact Engineering* 32, 1521–1552.
- National Institute of Justice, 2008. NIJ 0101.06, Ballistic Resistance of Body Armor.
- Nilakantan, G., Obaid, A.A., Keefe, M., Gillespie, J.W., 2011. Experimental evaluation and statistical characterization of the strength and strain energy density distribution of Kevlar KM2 yarns: exploring length-scale and weaving effects. *Journal of Composite Materials* 45 (17), 1749–1769.
- Noori, A., 1999. A Numerical Investigation of Ballistic Impact on Textile Structures (M.Sc. thesis). University of British Columbia.
- Park, Y., Kim, Y., Baluch, A.H., Kim, C.-G., 2014. Empirical study of the high velocity impact energy absorption characteristics of shear thickening fluid (STF) impregnated Kevlar. *International Journal of Impact Engineering* 72 (2014), 67–74.
- Pervorsek, D.C., Chin, H.B., Kwon, Y.D., Field, J.E., 1991. Strain rate effects in ultrastrong polyethylene fibres and composites. *Journal of Applied Polymer Science* 47, 45–66.
- Pierlot, A., 2012. DMTC First Milestone Report for Project 7.3.1.
- Pramanik, P., Chakraborty, R., July 2004. The unique story of a high-tech polymer. *Resonance* 39–50.
- Raghavan, S.R., Khan, S.A., 1997. Shear-thickening response of fumed silica suspensions under steady and oscillatory shear. *Journal of Colloid and Interface Science* 185 (1), 57–67.
- Rao, M.P., Duan, Y., Keefe, M., Powers, B.M., Bogetti, T.A., 2009. Modeling the effects of yarn material properties and friction on the ballistic impact of a plain-weave fabric. *Composite Structures* 89, 556–566.
- Reynolds, O., 1885. On the dilatancy of media composed of rigid particles in contact with experimental illustrations. *Philosophical Magazine, Series 5* 20 (127), 469–481.
- Sakaguchi, S., Carr, D., Horsfall, I., Girvan, L., 2012. Protecting the extremities of military personnel fragment protective performance of one- and two-layer ensembles. *Textile Research Journal* 82 (12), 1295–1303.
- Sanborn, B., Weerasooriya, T., 2014. Quantifying damage at multiple loading rates to Kevlar KM2 fibers due to weaving, finishing, and pre-twist. *International Journal of Impact Engineering* 71, 50–59.
- Sinnappoo, K., Arnold, L., Padhye, R., 2009. PCT/AU2010/000157, Ballistic Fabric.
- Song, Y., Li, G., Kluener, J., Conroy, G., Simmons, K., Jones, J., Koenig, R., Shanov, V., Li, W., Cho, W., Jayasinghe, C., Abot, J., Dandino, C., Schulz, M., 2011. Carbon nanotube materials for smart composites. *Polymer Preprints* 52 (2), 115–116.
- Specification, 2008. NIJ 0101.06, Ballistic Resistance of Body Armor. National Institute of Justice.
- Thomas, H.L., July 2003. Needle-punched, non-woven fabric for fragmentation protection. In: Paper Presented at the 14th International Conference of Composite Materials SME.
- Tokareva, O., Lacerda, V., Rech, E., Kaplan, D., 2013. Recombinant DNA production of spider silk proteins. *Microbial Biotechnology* 6, 651–663.
- Vanderbie, J.H., 1957. Clothing Series Report No.2: Headquarters Quartermaster Research and Engineering Command, Natick, MA.
- Wagner, N., Wetzel, E.D., Wagner, N.J., 2005. WO2004103231-A1; US2005266748-A1; EP1633293-A1; US2006234577-A1; US7226878-B2.

- Wetzel, E.D., Lee, Y., Egres, R., Kirkwood, K., Kirkwood, J., Wagner, N., 2004. The effect of rheological parameters on the ballistic properties of shear thickening fluid (STF)-Kevlar composites. In: Paper Presented at the AIP Conference Proceedings.
- Zeinstra, M., Thije, R.H.W., Warnet, L., 2009. Low velocity impact on a single-ply aramid semipreg. *International Journal of Material Forming* 2 (Suppl. 1), 193–196.
- Zhang, T., 2010. Preparation and Properties of novel PIPD fibers. *Chinese Science Bulletin* 55, 4203–4407.
- Zupancic, A., Lapasin, R., Žumer, M., 1997. Rheological characterisation of shear thickening TiO_2 suspensions in low molecular polymer solution. *Progress in Organic Coatings* 30 (1–2), 67–78.

I.G. Crouch¹, G.V. Franks², C. Tallon³, S. Thomas⁴, M. Naebe⁵

¹Armour Solutions Pty Ltd, Trentham, Victoria, Australia; ²The University of Melbourne, Victoria, Australia; ³Virginia Tech, Blacksburg, VA, United States; ⁴Defendtex, Dandenong South, Victoria, Australia; ⁵Deakin University, Warrnambool, Victoria, Australia

7.1 General introduction

Glasses and ceramics are the most important class of armour materials. The opaque ceramics, both oxides and nonoxides, are the most advanced, applicable armour material available to the armour technologist because they make a very effective disruptor, as was highlighted in Chapter 4. The family includes both opaque and transparent materials, with the amorphous glasses making very suitable transparent armours. However, over the past three decades a number of transparent ceramic materials (eg, sapphire) have been advancing. Unlike metallic and composite armours, ceramics are usually isotropic, much to their advantage. However, they are brittle and contain pre-existing manufacturing flaws which give rise to some interesting bulk properties, as was described in Chapter 1.

Lightweight ceramic composite armours typically consist of a ceramic front plate bonded to a ductile backing plate as shown in Fig. 7.1. The function of the ceramic is to erode and break up an impacting projectile, whereas the role of the backing plate is twofold: it adds stiffness to the ceramic to delay the onset of tensile fracture, and it absorbs some of the kinetic energy of the impacting projectile through deformation.

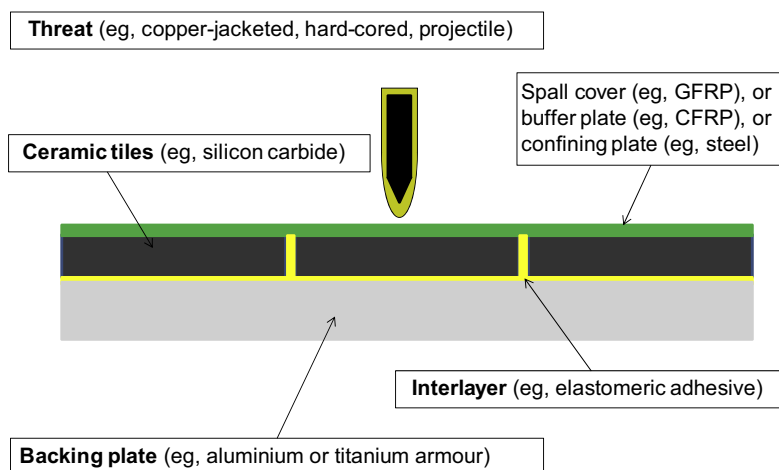


Figure 7.1 Schematic of a cross-section through a lightweight ceramic composite armour.

The foundation work of Mark Wilkins in the late 1960s and 1970s (Cline and Wilkins, 1969; Wilkins, 1978) did much to further the understanding of the mechanics of ceramic armour defeat by ballistic projectiles. His work helped identify the role of both the ceramic front plate and the rear support plate in the defeat of a projectile, and was crucial in identifying the timing of these events. Wilkins points out that for an aluminium-backed ceramic, the rigidity of the aluminium plate is important to the defeat mechanism (with increasing rigidity providing increased protection) since it offers more support and hence increases the time delay before the eventual break-up of the ceramic. On the other hand, a fibre-reinforced composite backing plate offers less support but undergoes greater deflection than an aluminium plate, and this is the primary defeat mechanism employed by this type of armour configuration.

A series of reports covered in the review by John Field and colleagues at the Cavendish Laboratory, Cambridge (Field et al., 2004) indicate that an increase in the toughness of an armour ceramic is unlikely to be beneficial to ballistic performance, while ceramics with a high hardness/density ratio are preferred, providing that their hardness is greater than that of the projectile.

A low-density front plate is not only desirable to reduce the weight of the total armour package but also because the distribution of the load applied to the support plate is dependent on the base area of the fracture conoid that is generated immediately following projectile impact, and this increases with increasing ceramic thickness. A lower-density ceramic will permit a greater thickness of ceramic for the same areal density of armour.

If a steel projectile impacts an alumina plate at 1000 m/s then an impact pressure of approximately $\sigma_m = 19.4$ GPa will be generated. This is well in excess of the compressive strength of the ceramic (typically $\sigma_c = 2\text{--}7$ GPa) but however is only maintained for a couple of microseconds at most as relief waves from the ceramic free surfaces drop this pressure to a quasisteady-state value about one-tenth of this peak value, ie, ~ 2 GPa. During this very short duration of high triaxial compressive stress, some of the ceramic directly beneath the projectile will fail in compression (while eroding the penetrator). However, since the quasisteady-state value is less than the compressive

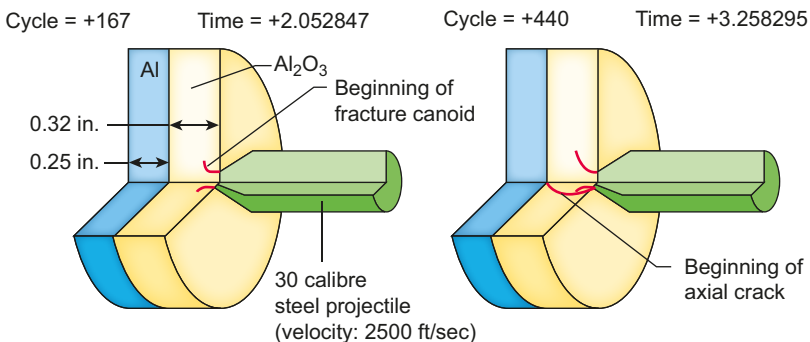


Figure 7.2 Computer simulation of projectile impact on a ceramic armour showing the early formation of a fracture conoid and subsequent initiation of axial tensile fractures.

Wilkins, M.L., 1978. Mechanics of penetration and perforation. *International Journal of Engineering Science* V16, Special Edition (Penetration Mechanics), 793–808.

strength of the ceramic no further compressive failure occurs. A fracture conoid is generated beneath the projectile (refer to Fig. 7.2) at the same time as the relief waves from the rear surface begin to generate a tensile stress field at the rear surface of the ceramic — which can be of magnitude 300–500 MPa — and is maintained as this relief field moves forward into the ceramic.

Since the tension field produced during ballistic impact is usually of greater magnitude than the fracture strength of the ceramic, even under purely hydrostatic conditions, axial cracking will be initiated in the ceramic at the rear surface.

Wilkins et al. (1969) noted that it is axial cracking which limits the performance of the ceramic front plate and since this initiates as the back-up plate begins to move, allowing the ceramic to move with it, this could be delayed by either a higher-modulus back-up plate or by improved tensile properties of the ceramic. They suggest that an additional strain tolerance of 0.2% in the ceramic would delay axial crack initiation by 17 μ s and so increase the ballistic limit by 80 m/s. They propose that the optimum ceramic should have a balance between high elastic impedance (ie, its incompressibility), high compressive yield strength (ie, the amount of compression before yield), low density and the ability to withstand tensile stresses before failure.

Several authors have attempted to pinpoint the mechanical properties of both the ceramic and the backing plates that improve their resistance to ballistic defeat, the most recent being the work of Medvedovski (2006b), although no satisfactory correlation between the quasistatic mechanical properties of a ceramic and its ballistic performance has been identified. This is not too surprising given the extreme pressures generated during an impact event and the complex stress states imposed beneath the projectile tip. Rosenberg and Yeshurin (1988) determined a good empirical relationship between ballistic efficiency and a normalised effective strength where the effective strength is defined as the average of the static and dynamic compressive yield strengths of the ceramic divided by the density of the tile. The dynamic strength of a ceramic tile is a measure of the compressive strength of the tile under uniaxial strain conditions, ie, the Hugoniot elastic limit (HEL), and is not a parameter that can be measured without specialist facilities (see Chapter 10). In general, a good indicator that a ceramic will offer reasonable ballistic performance is high hardness (greater than that of the impactor), low density and high strength in both tension and compression. However, selecting the most appropriate grade is always a balance between cost, mass and bulk, since the end user will always want all three minimised: low cost, low mass and low bulk!

In general, ceramics with high hardness values (>10 GPa), high elastic moduli (>300 GPa) and good flexural strength values (>350 MPa) make excellent opaque armour materials (Crouch et al., 2015b). However, they are normally very expensive (>\$10/kg) and difficult to shape. Therefore, in general tiles of relatively simple geometry (typically square or hexagonal) have been used in advanced armour systems for military vehicles. However, for body armour applications, there is a need to form a monolithic ceramic into a double-curved, or even multicurved, shape in order to better conform to the human torso. In a recent review (Leo et al., 2014) of the shaping techniques used for body armour components, carried out by the Defence Materials Technology Centre of Australia, uniaxial pressing of breastplates was still recognised to be the most feasible (and commercially available) process, even though other techniques, such as viscous

plastic processing (VPP) were becoming established. One particular variant of the dry-pressing route is known as reaction sintering, or reaction bonding, in which a prepressed, dry powder compact is infiltrated, at elevated temperature, with a liquid metal. However, the process is prone to the formation of a range of manufacturing defects, some of which are extremely deleterious to impact behaviour and ballistic performance of the finished product (Crouch et al., 2015b). These specialised processes are covered in future sections (eg, Section 7.6), especially a novel VPP-based process recently developed by the DMTC, and fully commercialised in 2012.

7.1.1 Key properties and drivers

Table 7.1 summarises the typical mechanical properties of a range of both glass and ceramic armour materials. Firstly, the range of hardness values presented is significant, since this intrinsic property will dictate how and where these materials are used, and how effective they are against particular threats. It is quite obvious even to the uninitiated that as the hardness increases the penetration resistance increases, just like all of the metals. What is also clear is that these materials are very brittle, and apart from glass which has a fracture toughness of less than $1 \text{ MPa m}^{1/2}$, all ceramics are equally poor, with values ranging from 3 to $7 \text{ MPa m}^{1/2}$. In comparison, a high-hardness, armour-grade, steel would have a toughness value $>20 \text{ MPa m}^{1/2}$, and most structural armours, $>40 \text{ MPa m}^{1/2}$. Their bulk densities are less than 50% that of steel and their specific moduli and strength values are more than seven times greater than the armour steels. Therefore, despite the losses in fracture toughness, on an areal density basis these ceramic armour systems will always outperform conventional steel and light alloy systems — refer back to Fig. 2.6 for comparable masses. However, they are difficult to manufacture, and therefore cost is not in its favour. The development of low-cost production processes and materials has become the biggest driver in recent ceramic development programmes.

Both Asenov et al. (2013) and Karandikar et al. have published recent reviews of armour-grade ceramics, in particular Karandikar who lists minor phases, grain size and amorphisation as influential factors in addition to hardness (Karandikar et al., 2010). Krell and Strassburger also included a hierarchy of key influences on the ballistic strength of both opaque and transparent armour in 2008, with emphasis on micro-structural effects (Krell and Strassburger, 2008).

In recent decades, the drivers for ceramic developments have been increased performance (suppress premature failure mechanisms), reduced costs and ease of shaping. By far the biggest driver has been to reduce the cost of such materials. In about 2005, according to Crouch (2005) the market price for aluminas was $\sim \$50/\text{kg}$, hot-pressed silicon carbide $\sim \$150/\text{kg}$ and hot pressed boron carbide $\sim \$400/\text{kg}$. During that period, ARL in conjunction with BAE, attempted to reduce the high cost of hot pressing (Campbell et al., 2008), while Crouch and Klintworth were developing a low-cost version of reaction sintered silicon carbide (RSSC) (Crouch and Klintworth, 2003). The latter process was used throughout the 2005–2012 period to produce body armour systems for the Australian Defence Force. At this same time, Crouch was leading efforts in Australia to develop a cost-effective version of boron carbide. Fig. 7.3

Table 7.1 Summary of important properties of a range of ceramic armour materials

Class of material	Source, grade (reference)	Density (kg/m^{-3})	Hardness (GPa)	Elastic modulus (GPa)	Flexural strength (MPa)	Fracture toughness ($\text{MPa/m}^{-1/2}$)
Float glass	Schott, Borofloat ^a	2230	1.6	62	25	<1
Glass ceramics	Silceram ^b	2900	7.0	122	180	NR
Alumina	CoorsTek, AD85 ^c	3420	9.4	221	296	3–4
Alumina	CoorsTek, AD998 ^c	3920	14.1	370	375	4–5
AlON	Surmet ^d	3695	18.5	323	380	~2
TiB ₂	CoorsTek, PAD ^c	4480	26.4	555	275	~7
SiC	CoorsTek, SiC-N, PAD ^c	3200	23.5	460	570	~5
SiC	MCC, RSSC ^e	3106	24.5	399	504	NR
B ₄ C	CoorsTek, PAD ^c	2500	25.5	460	410	4

^a<http://www.schott.com/borofloat/english/attribute/mechanical/index.html>.^bCarter et al. (1988).^chttp://www.coorstek.com/resource-library/library/8510-1364_ceramic_properties_mp.pdf.^d<http://www.surmet.com/products-and-applications/ALON-Transparent-Armour/>.^eMCC data sheet, 2009, as reported by Crouch et al. (2015b).

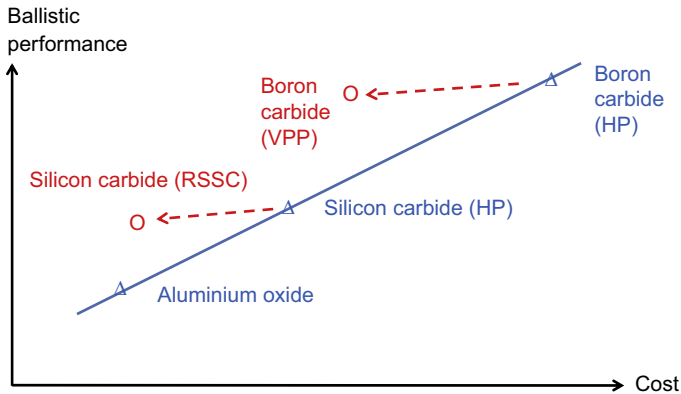


Figure 7.3 General relationship between cost and ballistic performance with indicative vectors representing direction of price points during the 2005–2015 period.

illustrates this decade-long effort to successfully reduce the manufacturing costs of these armour-grade ceramics.

7.1.2 Energy-absorbing mechanisms and failure modes

The failure modes associated with the penetration of glass and ceramic armours can be summarised schematically as illustrated in Fig. 7.4, the details of which are given in Chapter 1. Of these, comminution ahead of the projectile has been well observed (LeGallic et al., 1996), as have all other forms of cracking. However, not all of these modes absorb energy. For example, fracture of any kind was calculated to absorb less than 1% of the total impact energy (Woodward et al., 1989). In the same work, it was estimated that a large proportion of the total energy was removed from the impact site by ejecta (ceramic rubble ejected as front spall).

Fig. 7.4 shows the well-established steps in the penetration of a ceramic armour system which, in the main, consists of two layers: a ceramic element on the impact side, supported by a backing material on the distal side. This backing material is typically an aluminium alloy, steel or a fibre-reinforced polymer. The impacting bullet is partly eroded at the surface during a time-period known as the dwell, followed by the formation of Hertzian cracks on the surface of the ceramic, and final failure through conoidal fracture. The formation of the conoid increases the area of contact with the backing material which then bulges and absorbs energy principally through membrane stretching. This local failure is accompanied by the formation of radial cracks (see Fig. 7.5), which emanate from the point of impact (PoI), followed by circumferential cracking of the individual segments.

It is absolutely essential that armour-grade ceramics fail in this particular manner in order for their high level of ballistic performance to be maintained. It is therefore critically important to identify any material defect which may affect this mode of failure. Of greatest importance is the dynamic, through-thickness, compressive modulus of the

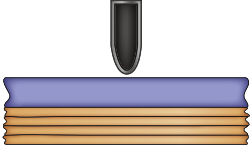
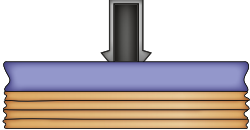
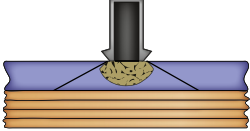


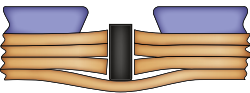
	<p>1. Starting position: Normal impact from hard-cored, copper-jacketed small arms bullet</p>
	<p>2. Dwell Period: Jacket starts to get stripped away from impact zone (and ignored) and tip of core gets eroded. The core loses mass and becomes more blunt.</p>
	<p>3. Cone Formation: Hertzian cracks initiate around Pol, and conoidal fracture follows</p>
	<p>4. Core penetrates rubble: Eroded core penetrates comminuted area and continues to erode. Backing material starts to bulge under pressure from cone.</p>
	<p>5. Through-thickness compression of backing material: The eroded, blunt core exerts TT compression in backing material which starts to delaminate.</p>
	<p>6. Ejection of fractured ceramic: As the shortened core comes to rest in the rear layers of the backing material, most of the fractured ceramic from the Pol gets ejected and removes energy from the impact site</p>

Figure 7.4 Schematic of typical sequence of physical events during the penetration of a ceramic armour system by an armour-piercing projectile.

material, immediately in front of the impacting projectile. This cylinder of material, similar in size to the core diameter of the bullet (about 6–8 mm), must be as rigid as possible and resist the initial impact. Therefore, the presence of porosity or otherwise poor-quality material in that cylindrical zone, or the existence of a crack or tear running through or near the cylindrical zone, may well reduce its compressive modulus and therefore its penetration resistance. For example, Crouch recently reported (Crouch et al., 2015b) that an impact immediately adjacent to a crack, with a

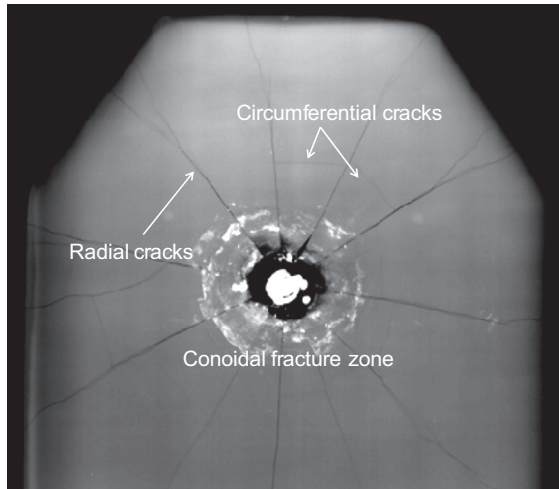


Figure 7.5 X-radiograph of an impacted hard armour plate showing impact damage from a 7.62-mm APM2 round. Note the central conoidal fracture zone, as well as radial cracks, extending to edge of product, and circumferential bending cracking (Crouch, 2014).

crack opening displacement (COD) of up to 1 mm, reduces the ballistic performance by up to 9%. On the other hand, the effects of either local porosity or poorly processed material in that cylindrical zone have been more difficult to quantify. However, common-sense, material science and engineering rules have been applied when considering the likely effects of such defects. The criticality of a range of manufacturing defects upon ballistic performance and behaviour is covered elsewhere (Crouch et al., 2015b).

Hard armour plates (HAPs) are precision-engineered components (Crouch, 2009) based upon the use of a ceramic tile which has a known bulk density, to within $\pm 10 \text{ kg/m}^3$, and a uniform thickness, to within $\pm 0.2 \text{ mm}$. This is essential because ballistic performance of an HAP is a function of the areal density of the finished product: areal density (kg/m^2) is the product of bulk density (kg/m^3) and thickness (m). The shape of the finished HAP is dictated by the shape of the ceramic tile. Since these products must exhibit a consistent level of ballistic performance across the entire surface area of the HAP, the microstructure, bulk density and thickness of the tile are critically important and must be as consistent as possible.

7.2 Conventional glasses

Conventional glasses are exceptionally brittle materials (see Table 7.1) and produce numerous shards when fracturing. So, unless they are used in laminated form, as described in Chapter 4, they do not make practical armours. They are also very soft materials and have little inherent penetration resistance to armour-piercing rounds. When used in ballistic windows in ground vehicles, the laminated glass system is

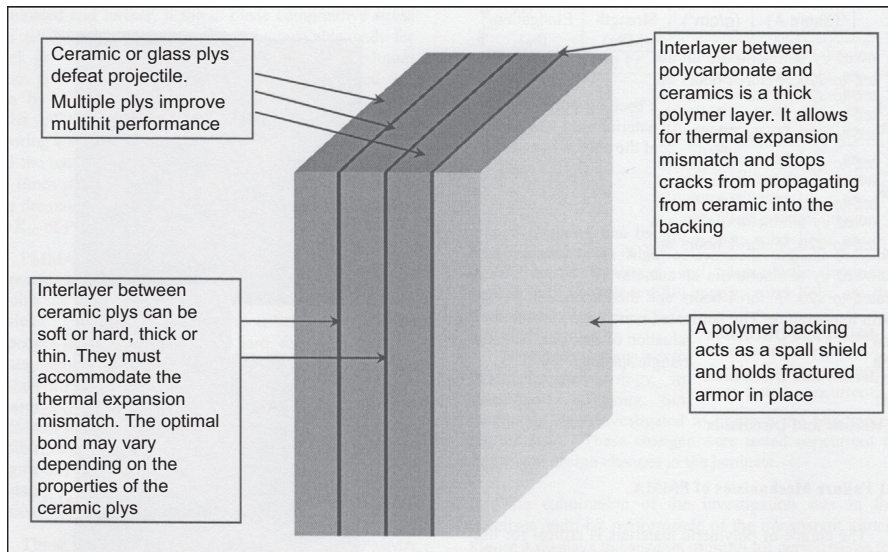


Figure 7.6 Typical structure of a laminated glass armour system.

After Patel, P.J., et al., 2000. Transparent armor. AMPTIAC Newsletter, 4 (3), Fall 2000.

therefore very thick (Fig. 7.6). Retaining transparency in thick sections is therefore the major challenge for designers of these systems. Patel and Gilde have recently provided an excellent overview of user requirements and applications, as well as R&D directions (Patel and Gilde, 2002; Patel et al., 2006).

Of course, selection of the most suitable constituents plays its part in determining the overall performance of the laminated system. Soda-lime glass and borosilicate glasses are very common, although their performance is limited. Kim et al. (2003) investigated the effects of back plate materials on the perfect cone formation in impact-loaded soda-lime glass, and compared different backing materials: polyurethane, PMMA as well as aluminium. Forde et al. (2009) studied the ballistic impact of a borosilicate glass by using mild steel rods against pyrex, while studying fracture patterns with high-speed photography.

Transparent armours are very popular with experimental physicists because the fracture processes are so visual (Field et al., 1988). More recently, Charles Anderson and his group at Southwest Research Institute (Anderson et al., 2014) have looked at the impact of a simulated armour-piercing threat against two simple bilaminates of borosilicate glass (Borofloat 33) and polycarbonate backings. As one would expect, they found that V-50 decreased with increasing number of impacts and decreasing intershot spacing. Interestingly, they also found that there was a threshold velocity below which projectile erosion occurred but above which none occurred — this gives designers the opportunity to place the glass elements at particular locations within a laminated system.

A typical bullet-proof glass, offering protection against handgun ammunition (eg, to G2 specification), with an areal density of $\sim 23 \text{ kg/m}^2$, would be constructed in the following manner (Ramsay, 2015). Two or three layers of float glass would be

Table 7.2 Armour solutions to meet European Standard EN1063 for ballistic glazing

Threat level	Ammunition	Velocity range (m/s)	Through-thickness composition	Total thickness (mm)	Areal density (kg/m ²)
BR4	0.44 Magnum	430–450	6 mm annealed glass 1 mm SentryGlas 6 mm annealed glass 5 mm SentryGlas 2.5 mm annealed glass 1.7 mm Spallshield	21.3	41.7
BR6	7.62 × 51 mm M80	820–840	8 mm annealed glass 0.76 mm Butacite 8 mm annealed glass 0.76 mm Butacite 8 mm annealed glass 0.76 mm Butacite 6 mm annealed glass 5 mm SentryGlas 2.5 mm annealed glass 1.7 mm Spallshield	39.5	85.9

Source: Kuraray. 2014. Kuraray Europe GmbH.

bonded together using interlayers of polyvinylbutene (PVB). This sublaminate would then be bonded to a polycarbonate (PC) backing layer (acting like a spall shield) using a polyurethane (PU) adhesive, since PVB does not bond to PC very well. This involves a two or three-step process in an autoclave. Such armour systems have a high areal density but have excellent transparency.

The choice of the most effective interlayer material is crucial in the design of glass-based transparent armours. Different radial cracking behaviours have been reported (Najim et al., 2007), and most recently, DuPont have released a new interlayer material called SentryGlas (DuPont, 2015), which uses a new elastomeric interlayer which shows far superior dynamic properties compared to conventional PVB interlayer materials, especially vastly increased values for elastic and shear moduli. Typical examples of practical armour solutions, as offered by Kuraray (2014) are given in Table 7.2. It is particularly instructive to look at the constructions: both solutions have a rear sublaminate of identical

laminae (emboldened), illustrating the usefulness of the high-modulus SentryGlas material at the rear of the laminate where out-of-plane bending will occur. In contrast, the front sublaminate of the BR6 solution is constructed of conventional materials, including the use of PVB interlayers. These solutions are $\sim 20\%$ lighter than conventional armoured glass consisting of Float Glass, PVB and PU (Ramsay, 2015), and potentially cheaper because they are laminated in a one-step autoclave process.

7.3 Glass ceramics

Glass ceramics are a class of crystalline, organic material with relatively poor mechanical properties (see Table 7.1) compared to other armour-grade ceramics. However, they are a glassy, low-density material, and can be formed at relatively low temperatures followed by a crystallisation heat treatment. Complex shapes are therefore possible and so body armour applications are favoured.

Following early pioneering work by Richard Shepherd in the early 1980s, at the then Stores and Clothing Research and Development Establishment in Colchester, Tracey and Crouch (1989) carried out an initial assessment of lithium-based glass ceramics, as patented (Jones, 1987) and provided by Richard Jones at Ceramic Developments (Midlands). Against 7.62-mm APM2 ammunition they found that it was unsuitable against this threat. Since that time, these crystalline materials have been limited in their application to soft-cored projectiles up to and including the 7.62-mm M80 round.

In 2001, Horsfall published his own findings (see Fig 7.7) on this same lithium zinc silicate material, designated LZ1 and supplied by CDM (Horsfall, 2001). In some well-designed experiments, he showed that the ballistic properties were strongly linked to

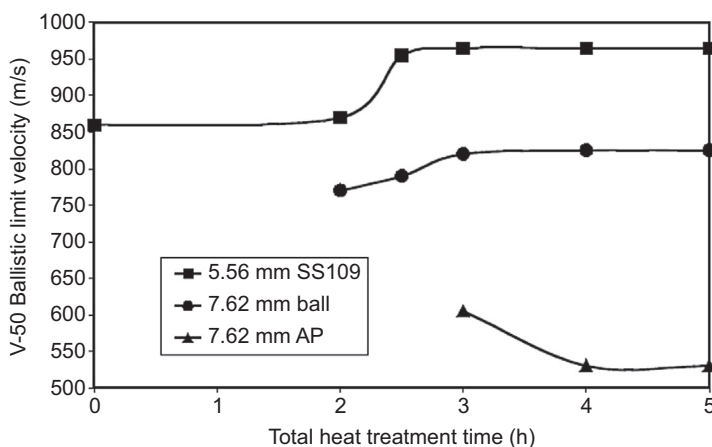


Figure 7.7 The effect of heat treatment cycle upon the ballistic properties of LZ1.

Horsfall, I., 2001. Glass ceramic armour systems for light armour applications. Paper Presented at the 19th International Symposium on Ballistics, Interlaken, Switzerland, May 2001.

Table 7.3 Data from Henson Ceramics Ltd

Grade	Type	Bulk density (kg/m ³)	Elastic modulus (GPa)	Modulus of rupture (MPa)
HCL2087	Lithium alumino-silicate	2400	83	350
HCL2088	Zinc alumino-silicate	3100	84	170
HCL2090	Lithia alumina silica	3100	84	n/a

the material's microstructure. During this heat treatment process, the compressive strength of the material increases from 733 to 1535 MPa, while the elastic modulus increases from 63 to 77 GPa. In comparison to standard 95.5% alumina, while the strengths are comparable, the modulus for the glass ceramic is only 22% of that for alumina. The density of the GC was 2780 kg/m³ and the tiles were 9 mm in thickness. The tiles were backed with 9.5 mm of glass fibre-reinforced plastic (GFRP) prior to testing. The increase in performance, at 2.5 h, corresponds to the formation of crystalline phases throughout the material. The research confirmed that this grade of material does not perform well against armour-piercing ammunition.

In 2010, an HAP designed by Crouch (then at ADA), weighing ~1.7 kg and based upon ~6 mm of HCL2087 (see [Table 7.3](#)) and a proprietary backing of aramid-reinforced polyethylene, was approved for use in the UK.

7.4 Transparent crystalline ceramics

Transparent armour refers to a group of materials assembled together to provide personal protection in the event of a blast or a multihit ballistic threat, while guaranteeing visibility and optical transparency throughout ([Grujicic et al., 2012](#)). The traditional field of application of these materials includes windows and windshields for ground armoured vehicles and aircraft, as well as face shields and visors ([Wang et al., 2013](#)). Transparent armour is also required for multimode weapon systems for use in extreme environments.

The basic requirements for transparent armour include high blast and single- and multihit ballistic resistance and transparency in the visible and infrared spectrum, but the key aspects in the selection of the constituting materials are strongly conditioned by the design and application. The most important requirements are as follows ([Grujicic et al., 2012](#); [Wang et al., 2013](#)):

- Distortion-free surfaces.
- Scratch and damage resistance and durability when exposed to extreme conditions which involve high-wear and low-velocity impact situations (eg, blowing sand, rock impact).
- Low weight and reduced areal density, which does not compromise vehicular and personal mobility and stability.

- Capability to be manufactured in large pieces with minimum thickness to aid the assembly within vehicle and other personal protective systems.
- Noninteraction in the infrared, UV and visible spectra with regards to imaging and communication equipment.
- High performance/cost ratio.

Transparent armours are normally constituted by three different optically transparent layers, each of them with a very specific function (Grujicic et al., 2012):

1. A hard strike face material, such as glass, glass ceramic or transparent ceramics, to blunt, erode and fragment the projectile;
2. An intermediate layer, such as glass or polymethylmethacrylate (PMMA), which is able to absorb the energy of the impact or blast, resist critical crack propagation in a multihit event, and also offers high bending stiffness to help support the strike face; and
3. A spall/backing layer able to contain the fragments and debris from the armour system, such as polycarbonate (PC). The adhesive interlayers used to join these materials also help mitigate possible differences in the thermal expansion coefficient of the layers of material.

The necessary thickness for each of these layers to protect against certain threats leads to very heavy designs which significantly affect the functionality of the vehicle or personal armour device, and also result in a severe reduction in the transparency and visibility throughout the component (Jones et al., 2006a). Transparent ceramic strike faces offer several advantages versus the other conventional transparent materials mentioned above (Grujicic et al., 2012; Jones et al., 2006a; Wang et al., 2013). Not only can they exhibit extraordinary hardness and compressive strength, therefore requiring much thinner sections to offer the same or improved ballistic protection than glass or glass ceramic-based systems, but also they offer high transparency in the visible and infrared spectrum, which is paramount for avoiding interactions with imaging and communication systems. In addition, they exceed in thermal and chemical stability, and resistance against ultraviolet light (UV) and erosion, minimising the cost associated with replacement of these parts.

The most suitable transparent ceramics for transparent armour strike faces are single-crystal sapphire, aluminium oxynitride and magnesium aluminate spinel (Grujicic et al., 2012; Johnson et al., 2012; Klement et al., 2008; Wang et al., 2013). They possess the perfect combination of strength, hardness, impact resistance (mechanical properties related to excellent ballistic and blast protection) and low density to outperform ballistic glasses and other materials. Table 7.4 summarizes the main properties of these three ceramics in comparison with other materials considered for transparent armour applications. Spinel has been identified by several authors as the best of the transparent ceramic strike faces based on its superb transparency up to 5-mm wavelength, becoming the preferred material for domes for infrared (IR) sensors on several defence systems operating under extreme environments (Grujicic et al., 2012; Wang et al., 2013). Sub-micrometre polycrystalline alumina (Johnson et al., 2012; Krell et al., 2009b; Stuer et al., 2010; Wang et al., 2013) has also been extensively investigated, as have other ceramics, such as ZnS (Johnson et al., 2012), yttrium garnet YAG ($\text{Y}_3\text{Al}_5\text{O}_{12}$), lead zinc niobate lead titanate (PZN-PT) (Wang et al., 2013), but their processing and properties require further optimisation if they are to become genuine candidate materials.

Table 7.4 Summary of important material properties of a range of transparent ceramics (Grujicic et al., 2012; Johnson et al., 2012; Klement et al., 2008; SAFirE Transparent Armor Solutions; Surmet)

Property	Units	Fused silica	Quartz	Glass ceramic	Float glass	Sapphire	AION	Spinel	Submicrometre-sized poly crystalline alumina
Density	kg/m ³	2210	2650	2400	2500	3970	3690	3590	3986
Areal density (1-in. thickness)	kg/m ²	55.85	67.31	60.96	63.5	100.97	93.89	90.86	101.24
Elastic modulus	GPa	70	76.5 G	65	72	344–386	315–334	260–277	390
Mean flexural strength	MPa	48	50	35	50	350–742	228–380	184–241	600
Fracture toughness	MPa m ^{1/2}	0.78	0.7	0.71	0.6–0.7	3–3.5	2.4	1.7	3.5
Knoop hardness	GPa	4.5	756 Pa	633 Pa	572 Pa	16–19	14–18	12–15	20–23
Refractive index	—	1.4585	1.4586	1.5263	1.5204	1.7681	1.7983	1.7162	1.7682
Transmission UV	%	1–90	53–91	1–29	1–87	1–75	1–82	50–87	60–85
Transmission VIS	%	80–90	91–92	29–88	82–92	75–82	82–85	76–82	40–70
Transmission NIR	%	40–90	83–93	70–88	72–82	82–85	85–87	84	—
Melting point	°C	1710	1670–1713	500–1650	1040	2040	2150	2135	2072

Source: Tallon (2015).

This section will primarily focus on the state-of-the-art related to the processing-microstructural-compositional aspects to control the grain size, properties and ballistic testing and performance of these three main ceramics used as strike faces for transparent armour: sapphire, AlON and spinel, as well as trends and recommendations to pursue in the future.

7.4.1 Microstructural and processing aspects

As discussed before, transparent ceramics for strike faces for armour applications are required to exhibit remarkable mechanical properties. In order to achieve this, an exhaustive control of each of the processing stages is crucial to ensure a defect-free fine-grained microstructure. Transparency is the physical property of materials that allows light to pass through it without being scattered (Krell et al., 2009a; Wang et al., 2013). This is referred to as in-line transmission (ILT), and for armour applications materials are required to be ‘highly transparent materials’, which in practice denotes an ILT value above 75% (materials with ILT between 50% and 75% are classified as ‘transparent’, and between 20% and 50%, the materials are classified as ‘translucent’; Goldstein, 2012). Therefore, any microstructural, compositional or surface features in the material, which result in light scattering, must be avoided during the processing and manufacturing of transparent ceramics. These features are the following.

7.4.1.1 Crystal structure

If the crystal structure of the ceramic is optically anisotropic, light scattering occurs at the grain boundaries. It is recommended to work with transparent ceramics with a cubic lattice structure (isotropic), such as the spinel structure (Krell et al., 2009a; Wang et al., 2013). In addition, it has been suggested that ceramic materials with band gap greater than 3.1 eV are the most suitable for transparent applications, since that minimises energy absorption from incident photons (Johnson et al., 2012).

7.4.1.2 Impurities

The presence of impurities and/or second phases inside grains or on grain boundaries, as well as differences in composition across the material, are one of the main reasons for opacity (Goldstein, 2012; Wang et al., 2013). The optical behavior of the grains and grain boundaries has to be as similar as possible. In order to achieve this, the composition needs to be precisely controlled using very high-purity precursors, raw materials and control over the processing steps to minimise and avoid contamination from grinding media, sintering furnace and sintering atmosphere.

7.4.1.3 Porosity

Pores in the microstructure (whether inside grains or on grain boundaries) are one of the major sources for light scattering, and therefore loss of transmission and transparency (Krell et al., 2009a). Residual porosity has to be almost completely eliminated and with any residual pores occupying a very narrow size distribution centred below

the wavelength at which transparency is required. It has been reported that the maximum porosity in a ceramic material to ensure its transparency is around 100 ppm (as a reference, 0.1–1.5% porosity is normally allowable for prosthetics or high-wear resistance parts; [Goldstein, 2012](#)). In order to reach such low values of porosity (or full densification), pressure-assisted sintering techniques, such as hot-pressing ([Karthikeyan et al., 2013](#)), hot isostatic pressing (HIP) or spark plasma sintering (SPS) can be used ([Wang et al., 2013](#)), or a combination thereof.

7.4.1.4 Grain size control

A fine-grained microstructure is necessary to ensure superb mechanical and thermal performance in any ceramic. A very high particle packing and green density will enhance densification and a narrow grain size distribution after sintering, even under pressureless conditions. In addition, to increase the driving force for densification and thus achieve that minimum level of porosity described beforehand, small powder particle sizes are preferred in the starting powders. The processing of transparent ceramics has therefore been focused on the usage of nanopowders and nanocomposites ([Goldstein, 2012](#); [Wang et al., 2013](#)) to ensure the final grain size will be in the order required.

7.4.1.5 Processing and sintering

The presence of loosely packed agglomerated clusters in the green body are detrimental for the processing of a transparent ceramic as the presence of such may limit green body density, and thus final sintered density resulting in a significant loss of transmission, and compromised mechanical and thermal performance due to defects in the final product ([Goldstein, 2012](#); [Wang et al., 2013](#)). A careful choice of the synthesis, shaping and sintering techniques is the key for success when manufacturing with this class of materials. The control of interparticle forces during the early stages of processing will ensure the minimisation of agglomerated clusters and defect formation in the shaping stages, and thus maximise the particle packing to favour sintering.

7.4.1.6 Surface finishing

The sample surface finishing must be as smooth as possible to avoid diffuse scattering owing to roughness of the surface ([Wang et al., 2013](#)).

7.4.1.7 Thickness

Increasing the thickness of the transparent ceramics normally results in a decrease in its transparency. Ideally, the material should reach a transparency which is independent of the thickness, at least within the practical thickness limit given areal density considerations. This is only possible when the material reaches its theoretical maximum in-line transmission ([Wang et al., 2013](#)).

The strategies discussed above are followed in the manufacturing of sapphire, AION and spinel strike faces. In the next sections, the general characteristics, properties and trends in their manufacturing are discussed for each of these materials.

7.4.2 Aluminium oxynitride

Aluminum oxynitride (AION) was first investigated during the 1960s–1970s, when the first Al_2O_3 –AlN equilibrium phase diagram was completed and the material was processed to nearly full density by reactive sintering, producing a translucent aluminium oxynitride spinel ceramic (McCauley, 1978; McCauley and Corbin, 1979; McCauley et al., 2009; Yamaguchi and Yanagida, 1959). Since then it has been widely used as a transparent ceramic in many applications, including transparent armour.

AION has a cubic spinel crystal structure, which is stabilised by additions of small amounts of nitrogen over a wide range of compositions (Johnson et al., 2012; Wang et al., 2013). Significant research is still ongoing to refine the phase diagram and the exact compositional range of the cubic phase, motivated by some discrepancies in the ballistic performance of AION components and the need for thermally-mechanically stable electromagnetic windows and domes (McCauley et al., 2009; Surmet). For example, the composition of the commercially available AION by Surmet has been reported to be 30.98 mol% AlN and 69.01 mol% Al_2O_3 (ie, 40.68% Al, 51.59% O, 7.72% N, average composition determined by EDS) (McCauley et al., 2009). It is stable up to $\sim 2050^\circ\text{C}$, at which point it melts incongruently.

Its isotropic optical properties (80% transparency over the region from near ultraviolet to visible and near-infrared wavelengths), combined with its remarkable hardness (see Table 7.4) makes AION the perfect candidate for this type of application (Johnson et al., 2012; Wang et al., 2013). It has been reported that submicrometre grain-sized AION materials outperform sapphire (Grujicic et al., 2012).

Normally, the manufacturing of AION components starts with the synthesis of the precursor powders, from the simple reaction between AlN and Al_2O_3 powders, via plasma arc synthesis, carbothermal reduction or self-propagating high-temperature synthesis (SHS) (Fukuyama et al., 1999; McCauley et al., 2009; Rafaniello and Cutler, 1981; Zientara et al., 2007). The synthesised powder is then shaped to form the green body and then sintered at high temperatures ($>1850^\circ\text{C}$) for extended periods under a nitrogen atmosphere (via pressureless sintering, hot pressing, hot isostatic pressing or reaction sintering; Wang et al., 2013). Section 7.6 covers the various manufacturing options in more detail. The use of transient liquid-phase sintering has also been investigated, shifting the material from the liquid/solid region into the solid solution region as the liquid reacts with and is incorporated within the AION phase as densification occurs (McCauley et al., 2009; Patel et al., 2003).

The company Raytheon was the first to produce commercially available highly transparent AION (McCauley et al., 2009). The technology was then transferred to Surmet Corporation, which is currently the main manufacturer of this material (Surmet). Fig. 7.8 shows an example of their commercial products and their typical microstructure. The AION materials exhibit grains in the 150–200- μm range. Current research trends are focused on developing materials on the nanoscale to improve their

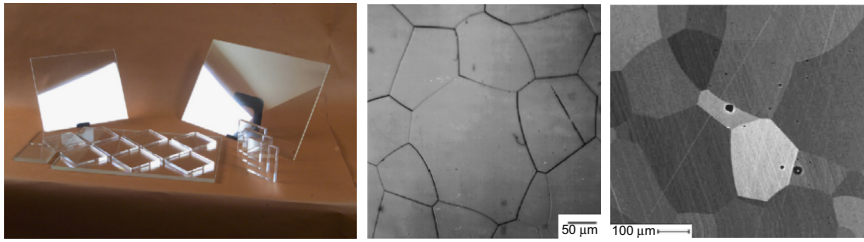


Figure 7.8 Examples of AlON components manufactured by Surmet, and microstructures typical of this material.

Images extracted from McCauley, J.W., Patel, P., Chen, M., Gilde, G., Strassburger, E., Paliwal, B., Dandekar, D.P., 2009. ALON: a brief history of its emergence and evolution. *Journal of the European Ceramic Society* 29, 223–236.

properties further. Due to its hardness there are still significant costs associated with the final machining and polishing of AlON products, especially for large components (Surmet), providing further incentive for good near-net shape control.

7.4.3 Magnesium aluminate spinel

Magnesium aluminate spinel (MgAl_2O_3), commonly (but wrongly) referred to simply as ‘spinel’, is a very attractive material for transparent armour applications for two main reasons:

1. It is much less expensive to produce than AlON and sapphire, since (i) there are good-quality, high-purity commercial powders available for bulk purchases, and (ii) it requires significantly lower temperatures for processing (from 1000 to 1900°C) (Goldstein, 2012; Grujicic et al., 2012; Wang et al., 2013). However, large transparent spinel panels are mostly available just for research applications (Grujicic et al., 2012).
2. Apart from its superb mechanical properties and wear and impact resistance and ballistic performance, this material also exhibits much better chemical and thermal stability in comparison with the other two materials, making it a candidate for a wider range of extreme applications (Johnson et al., 2012).

These have superior optical properties, with broadband transparency from mid IR up to the UV range (87% transmission in the range 0.2–5.5 mm). This transparency range is beyond those offered by AlON or sapphire. Therefore, this material could be used not only for transparent armour components due to excellent mechanical properties and wear and impact resistance when properly processed, but also for lenses, IR windows and missile domes (Goldstein, 2012; Grujicic et al., 2012; Johnson et al., 2012; Wang et al., 2013).

The research around this material started in the late 1960s, when moderately transparent spinel samples were produced. Within just 20 years, there was worldwide research into producing high-transmission parts (Goldstein, 2012). Spinel has a cubic crystal structure where the magnesium and oxygen atoms are tetrahedrally coordinated while the aluminium and oxygen atoms are octahedrally coordinated (Johnson et al., 2012) and it is optically isotropic (Wang et al., 2013). The MgO and Al_2O_3 phase

diagram shows the spinel ($\text{MgO} \cdot n\text{Al}_2\text{O}_3$) as the only compound. This phase forms as a solid solution with compositions ranging from $n = 0.8$ (Mg-rich) to $n = 3.5$ (Al_2O_3 -rich), with the stable range varying as a function of temperature, but it does not undergo polymorphic transformations. Although in theory all solid compositions would have the potential to be prepared as transparent single-phase ceramics, the Al_2O_3 -rich nonstoichiometric polycrystalline spinel has been suggested as the best candidate for its high optical transparency and fracture toughness (Wang et al., 2013).

In terms of processing, the preparation of transparent spinel materials normally requires pressure-assisted densification (ie, hot pressing, hot isostatic pressing or spark plasma sintering) to eliminate the trapped porosity between loose powder agglomerates and clusters and obtain high-transparency materials with a fine microstructure for mechanical properties. However, the most common manufacturing approach recommends the application of two-stage sintering, where initially the powder is compacted and densified to around 95–99% density by pressureless sintering, with just closed porosity and no open porosity, after which samples are hot-isostatically pressed to full density (Goldstein, 2012; Goldstein et al., 2009; Wang et al., 2013). LiF and B_2O_3 have been used as sintering aids to promote full densification and pore removal (Goldstein, 2012). It has been found that lattice defects and vacancies in the crystal structure could result in the diffusion of impurities arising at the sintering stage into the material structure, thus compromising the overall transparency and colour. For example, it has been found that carbon impurities from the residual CO atmosphere and graphite furnace furniture used in hot-pressing and SPS affect the transmission profiles and give the material grey/orange/yellow hues (Goldstein, 2012; Wang et al., 2013).

Although there are commercially available powders, there has been significant research into synthesising powder precursors to remove any impurities from the grain boundaries in the final material, which could lead to spots and prevent high transparency. The most common precursor routes to prepare ceramic powders have been explored and reported in the literature to produce this powder. A few examples are metal-ion exchange (Reimanis et al., 2004), flame spray pyrolysis (Goldstein et al., 2008), SHS (Ping et al., 2001) or chemical and mixtures methods (Mitchell, 1972). The main obstacle to be overcome after all the synthesis routes is still the presence of agglomerates which are difficult to break down, and become a source of opacity in the final compound (Goldstein, 2012; Wang et al., 2013).

Large plates with dimensions around 25 cm have been produced with submicrometre-sized grains, a Vickers hardness of 15 GPa and optical transmission close to the theoretical limit. However, when larger plates and dome-shaped parts were attempted (>0.5 m), the microstructure was coarser (with a lower hardness as a consequence), although such pieces still exhibit highly uniform optical properties (Goldstein, 2012). Other components with maximum dimensions up to 240 mm and thickness up to 20 mm have been manufactured from submicrometre range and nanosized powders (Wang et al., 2013). Large-scale production using such has already started (Goldstein, 2012).

The unique combination of properties of the spinel structure has led to its wide use in other nonarmour applications such as windows for barcode readers, pressure vessels, laser spark plugs, tuneable laser (Ti) hosts, high refractive index optics for ultra-violet microlithography, high-pressure arc lamps, watch casings and optical heat exchangers (Goldstein, 2012).

7.4.4 Single-crystal aluminium oxide (sapphire)

Single-crystal aluminium oxide, or sapphire, is the most commonly used transparent ceramic material for strike faces for armour applications due to its outstanding mechanical properties (flexural strength, fracture toughness, elastic modulus, hardness) and its exceptional optical properties (it transmits light from the ultraviolet through the visible into the mid-infrared region; [Grujicic et al., 2012](#); [Harris, May 2004](#); [Johnson et al., 2012](#); [Jones et al., 2006a](#)). Although the manufacturing technology is well matured, there is still an exorbitant cost and time associated with the manufacturing of large single crystals of sapphire, and in the machining, polishing and surface finishing of large-size components ([Grujicic et al., 2012](#); [Johnson et al., 2012](#); [Jones et al., 2006a](#)).

A possible solution to the high manufacturing cost and time while keeping the same mechanical properties would be the use of polycrystalline alumina. Although it can be processed to almost full densification with a very fine submicrometre-sized grain microstructure by a number of versatile shaping and sintering techniques and combinations ([Krell et al., 2009a](#); [Stuer et al., 2010](#); [Wang et al., 2013](#)), its noncubic crystallography leads to light-scattering losses, reducing their transparency significantly with increasing thickness (thicker sections become translucent). Even for components of only 1-mm thickness (not enough for ballistic protection), the transparency becomes only 70–75% ([Johnson et al., 2012](#)).

Sapphire is also resistant to abrasion, wear, temperature and chemical corrosion. It is also known as corundum, the natural crystal of aluminium oxide. Its melting temperature is 2050°C. Natural sapphire has a variety of colours, but pure corundum is clear and colourless ([Harris, 2004](#)). The manufacturing and processing of sapphire components can be via a range of crystal growth methods. The common industrial techniques are summarised below ([Fig. 7.9](#)):

1. *Czochralski method*. This method has been used for sapphire growth since the early 1960s ([Jones et al., 2006a](#)). Alumina is melted in an iridium crucible under a controlled atmosphere (98% N₂ and 2% O₂). A seed crystal is dipped into the molten liquid and withdrawn at a speed of 6–25 mm/h while being slowly rotated. During this withdrawal stage, the alumina from the melt pool crystallizes onto the seed. The size of the boule (synthetic single crystal) is controlled by the rate of withdrawal of the seed ([Harris, 2004](#)). The Kryopoluls method is very similar, but the crystal is formed deep under the surface of the molten melt pool and takes on the shape of the crucible as it gradually solidifies.
2. *Heat-exchanger method (Chen)*. This technique was initially developed in the late 1960s ([Jones et al., 2006a](#)). A molybdenum crucible is loaded with pure alumina crackle containing a sapphire seed crystal at the bottom. The furnace is evacuated and heated to melt the crackle (vacuum and heat help remove the vaporising impurities from the alumina) while keeping the seed crystal just below its melting point by circulating helium gas through the heat exchanger below the centre of the crucible. The seed partially melts, and the helium flow is increased to cool down the seed and start the crystallisation of the alumina onto the seed, and it is kept at a constant temperature until the crystal reaches the desired dimensions. Then, the temperature is decreased and the boule is annealed slowly in situ, eliminating defects and consequently higher transparency ([Harris, 2004](#)).

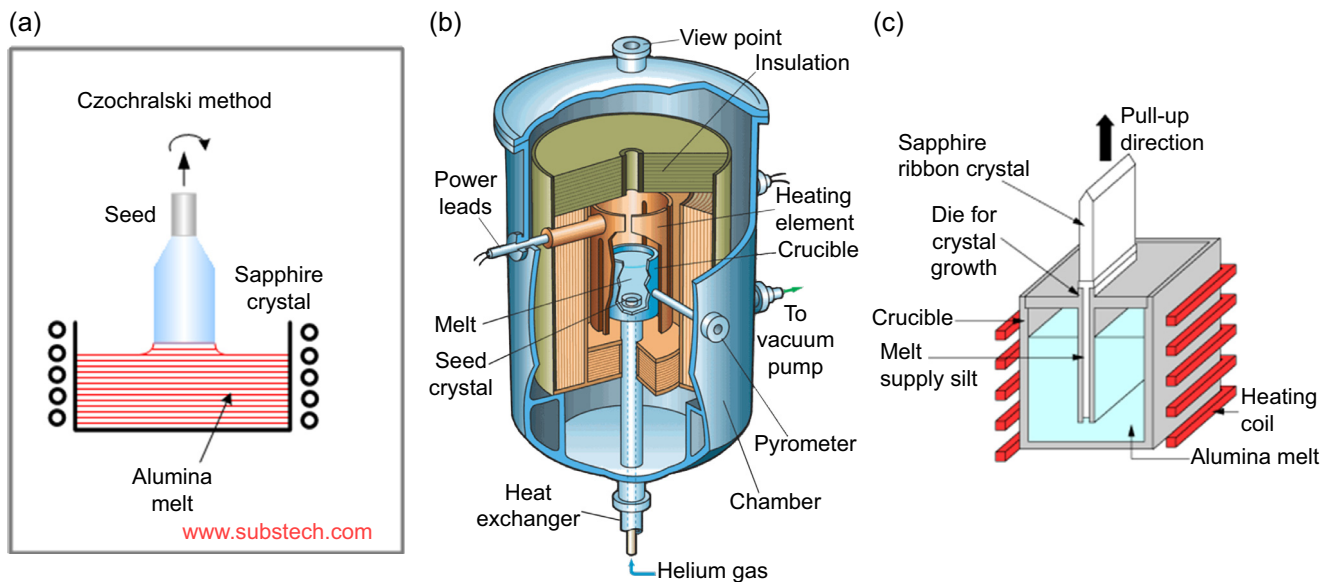


Figure 7.9 Schematic representations of the main techniques used to produce sapphire armour components: (a) Czochralski method; (b) heat exchanger method and (c) edge-defined film-fed growth.

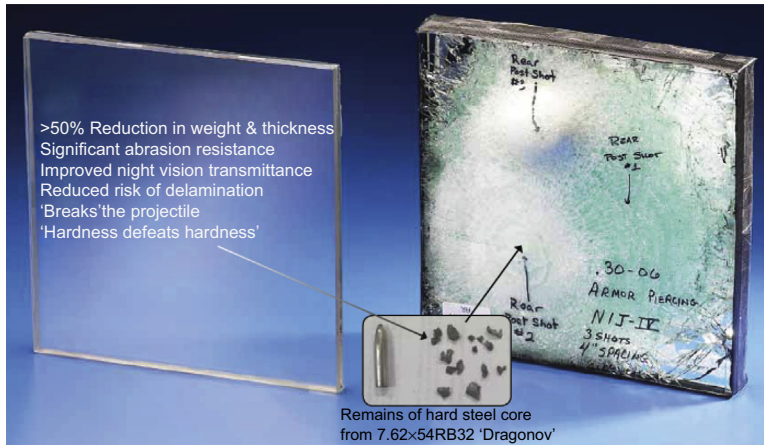


Figure 7.10 SAFirE components produced by Saint-Gobain.

SAFirE Transparent Armor Solutions, S.-G.C., http://www.crystals.saint-gobain.com/SAFirE_Transparent_Armor.aspx.

3. *Edge-defined film-fed growth (EFG)*. This can produce surface areas almost twice as large as other techniques (Jones et al., 2006a). The EFG method was developed in US and is related to the Stepanov method developed in the USSR in the late 1960s (Jones et al., 2006a). In this method, alumina is melted inside a crucible. This melt wets the surface of a die (tube, rod or ribbon) and is fed into it by capillary attraction. The sapphire seed is dipped into the melt on top of the die and drawn out. The melt will solidify into the sapphire following the shape of the die. The versatility of this method allows producing a wider range of shapes to be grown in particular crystallographic direction, as far as the dies can be created for that particular shape. The Stepanov method uses a combination of wettable and nonwettable aids to shape the crystal (Harris, 2004).

Transparent armour applications also include the manufacturing of domes for infrared-guided missiles. In order to make these highly curved components, a process called *scooping* is used, where the sapphire is rotated in one direction while the tool is rotated in the opposite direction (Harris, 2004). Domes have also been grown using the gradient solidification method developed at Rotem, which uses a very similar set up to the HEM but a gradient temperature is carefully created from the top to the bottom of the melt.

Saint-Gobain Crystals was a pioneer in the manufacturing of sapphire components for transparent armour components. They have produced SAFirE Transparent Armor Solutions by EFG (Fig. 7.10) and they have been able to reduce the weight and thickness by 50% while keeping the same ballistic protection as traditional glass components and offering protection versus a wider range of ballistic threats, as well as wear and chemical resistance (SAFirE Transparent Armor Solutions). This system also offers a 20% improvement in night vision transmittance when compared with glass. This material is currently being used in both ground vehicle and rotary wing platforms.

Using this technology, more than 1000 large-area sapphire components have been manufactured at dimensions of 305-mm wide, 775-mm long and 11-mm thick. There is a demand for even larger areas and it is expected that the technology will also allow for the production of such larger-sized components (Jones et al., 2006a). As per spinel, apart from its use in armour applications, sapphire is also used in other applications such as in barcode scanners, the scratch-proof crystal face of wristwatches and phones, and as a substrate for blue light-emitting diodes and diode lasers (Harris, 2004). Based on the information described in this section, the four main families for transparent ceramic applications can be evaluated in terms of potential processability and performance for armour applications as shown in Table 7.5.

Data collected over a 4-month period in Iraq (c.2007) found that $\sim 56\%$ of damage to windscreens occurred during combat and $\sim 36\%$ from rock strikes: none occurred from delamination and none due to sandstorms. In a cost–benefit study from 2010 (Franks, 2010), Lisa Franks identified a real need for improved transparent armour systems and suggested that a nanostructured spinel (compared with the normal commercial grade) may be worth pursuing. Fig. 7.11 shows the extent to which armoured glass is utilised in today's reconnaissance vehicles, and indicates how much vehicle weight could be saved with adoption of more ballistically efficient solutions.

7.4.5 Comparative ballistic properties

Patel et al. (2000) presented an excellent overview of transparent armour systems in 2000, which included reports of V-50 testing of a number of laminated systems against 1.1-g FSP rounds. They demonstrated that having a ceramic front face reduced the areal density of the system by as much as 65%. Table 7.6 summarises the data from this work.

Jones et al. (2006b) reported more detailed ballistic results for a series of single strikes against 150-mm square samples of sapphire, as supplied by Saint-Gobain. PC was used as the spall liner. They demonstrated that a laminate with an areal density of $\sim 52 \text{ kg/m}^2$ could resist impacts from a 7.62-mm M80 ball round at 850 m/s, as well as the $7.62 \times 39 \text{ mm}$ API-BZ round at velocities up to 750 m/s. However, against the armour-piercing M61 round, full protection was not achieved at this areal density. Nevertheless, these were impressive results compared with conventional glass/PC laminates.

More recently, in 2009, Elmer Strassburger from the Ernst Mach Institute in Germany, published an elegant paper on the ballistic testing of a range of transparent armour materials (Strassburger, 2009) against the $7.62 \times 51 \text{ mm}$ AP round, the P80, (see Chapter 1) impacting at velocities between 835 and 865 m/s. All targets consisted of a ceramic strike face, laminated to the front of a float-glass/polycarbonate backing. Fig. 7.12 shows the residual velocity plot for the various targets, including a range of different thicknesses of ceramic tiles, from 1.5 to 4.5 mm.

All transparent ceramics show significant weight savings compared to the standard glass/PC system (dashed line), and all show improved performance with an increase in

Table 7.5 Potential processability, and performance, of the main four transparent ceramic armour materials, for armour applications. [Evaluations between 1 (min) and 10 (max).]

Criteria	Sapphire	AlON	Spinel	Submicrometre-sized polycrystalline alumina
Mechanical performance	9	9	9	8
Optical performance	9	9	9	6
Demonstrated ballistic protection	9	9	9	7
Commercial availability	Yes SAFiRE Saint-Gobain	Yes SURMET	Predominantly at lab scale	Predominantly at lab scale
Manufacturing	Crystal growth	Powder processing and two-stage sintering	Powder processing and two-stage sintering	Powder processing and two-stage sintering
Production cost	10 ^a	9 ^b	9 ^b	7
Availability of high purity raw materials	8	8	6 ^c	8
Maturity of technology	Well established	Established phase diagram and microstructure properties relationship. Established processing	Well-known phase diagram and microstructure properties relationship. Well-known processing, continuous advancements	Established phase diagram and microstructure properties. Well-known processing, continuous advancements
Potential to be produced in a range of complex shapes and large sizes	8	10 ^d	10 ^d	10 ^d

^aAccess to equipment, high-temperature processing and surface finishing.

^bHigh sintering temperature and pressure required for sintering and surface finishing.

^cPowder synthesis required to achieve high-purity powders with the right stoichiometry.

^dWide range of shaping technologies available when combined with two-stage sintering (pressureless sintering and HIP).

Source: Tallon (2015).



Figure 7.11 Up-armoured HMMWV, M1114, ‘Iraq Pope Glass’.
Franks, L., 2010. Transparent Materials for Armor - A Cost Study. US Army RDECOM 20473RC, January 2010.

Table 7.6 Ballistic performance of various grades of transparent ceramics, tested against the 1.1-g FSP fragment

Laminated system	Total areal density (kg/m ²)	V-50 (m/s)
AlON/glass/PC	80	915
Spinel/PC	58	890
AlON/PC	51	850
Sapphire/PC	51	810
Al ₂ O ₃ /PC	51	780

Based upon results of Patel, P.J., et al., 2000. Transparent armor. AMPTIAC Newsletter, 4 (3), Fall 2000.

ceramic thickness (as one would expect). An areal density of $\sim 60 \text{ kg/m}^2$ was required to defeat the P80 round, compared with $\sim 170 \text{ kg/m}^2$ for glass/PC. Interestingly, increases in the thickness of ceramic beyond 4 mm did not improve ballistic efficiency (see Fig. 7.13).

All experimental evidence to date clearly shows that the integration of transparent ceramics into laminated glass systems has enormous benefits in terms of saving weight. The challenge remains to make them more cost-effective and to produce them in larger, shapeable quantities — this remains one of the most rewarding challenges for the armour technologist.

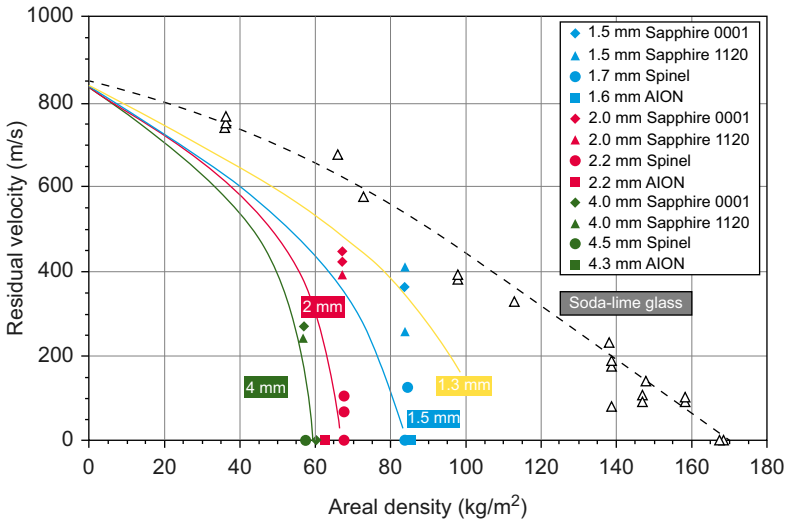


Figure 7.12 Residual velocity versus areal density for ceramic/glass/PC targets against 7.62 mm P80 round.
Strassburger, E., 2009. Ballistic testing of transparent armour materials. Journal of the European Ceramic Society 29, 267–273.

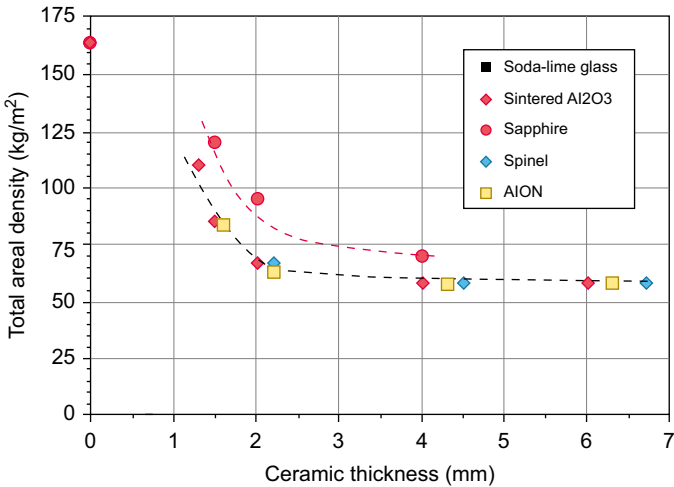


Figure 7.13 Areal density versus ceramic front layer thickness for different transparent ceramics against 7.62 mm P80 round.
Strassburger, E., 2009. Ballistic testing of transparent armour materials. Journal of the European Ceramic Society 29, 267–273.

7.5 Monolithic ceramics

7.5.1 Aluminium oxides

This family has been the well-established baseline for ceramic armour systems for well over 40 years, with grades like Sintox FA (coloured pink) and Hylox H (coloured brown) becoming legendary amongst the numerous grades of aluminas. AD85, with an alumina content of 85%, was the standard material in use for helicopter applications, as well as body armour plates, in the 1980s. Today, CoorsTek (Anon, 2015b), amongst others, supply the full range from AD85, with a density of 3420 kg/m^3 , to AD998, with a density of 3920 kg/m^3 . Against small arms ammunition, it became clear very early on that ballistic efficiency increased with purity of composition, and this was simply explained through an increase in baseline properties, especially hardness (see Table 7.1).

Very little research had been undertaken to determine the controlling properties of aluminas until the 1990s, when international teams in France and the UK began studying the effects of composition, grain size and porosity, as well as determining HEL and spall strength values (see Chapter 10). Bourne et al. (1994) published one of the first studies in this field, covering seven different compositions, and structures, with glass contents $\sim 2.5\text{--}4.5\%$, porosity levels $\sim 3.3\text{--}5.9\%$, and grain sizes $\sim 2\text{--}8 \mu\text{m}$. They identified that HEL was related to both grain size and porosity levels. In a follow-up study, James (1995) also showed that these materials exhibited thermal expansion anisotropy (Allain et al., 2004) and that the fracture energy associated with this TEA was calculated to be a function of grain size and showed good correlation with ballistic efficiencies. This body of work had two spin-offs: firstly, a European patent application for aluminas with small, controllable grain sizes and secondly, the first ever visual demonstration of comminution ahead of a projectile (LeGallie et al., 1996).

In the 2000s, Madhu et al. (2005) used the RDOP test to compare the ballistic efficiencies of AD95 and AD995 aluminas against both the 12.7 and 7.62 mm AP rounds, while keeping the ratio of projectile diameter to target thickness in a similar range between 0.8 and 1.0. Mosaics of ceramic tiles were supported by a 7017 aluminium alloy back plate (see Chapter 3), which represented a typical ceramic composite armour system of the day. While they confirmed that the AD995 had a superior ballistic efficiency (as had been expected), they also found that ballistic efficiencies varied with impact velocity and grade. As the tile thickness increased from 10 to 14 mm, the ballistic efficiency decreased for AD995, but increased for AD95.

More recently (2010–15), others have attempted to modify the composition of the base alumina through additions of 10% zirconia (Zhang and Li, 2010), and even carbon nanotubes (CNTs) (Bolduc et al., 2014) with varying levels of success. There is still much to do in lifting our fundamental understanding of the broad family of aluminas.

7.5.2 Silicon carbides

Silicon carbides have become the material of choice in many real ceramic armour systems throughout the world, especially the grade known as SiC-N as produced using pressure-assisted densification (Johnson et al., 2012) by CoorsTek (Anon, 2015b).

This is because it has a ballistic efficiency greater than the aluminas, mainly due to its higher hardness values, but also due to its consistent performance across the full range of small arms ammunition. [Table 7.1](#) provides the basic properties of two grades; a hot pressed version (SiC-N), and a reaction-bonded version (RSSC).

Silicon carbide is a solid with strong covalent bonds and exists in low temperature (β -SiC) and high temperature (α -SiC) forms. The transformation of β to α occurs at approximately 2100°C but seems to depend on impurities, gas atmosphere and pressure ([Somiya and Inomata, 1991](#)). β -SiC has a cubic (C) and α -SiC a hexagonal (H) crystal structure. Some of the α crystal structure formations found are polytypes, eg, the hexagonal 4H-SiC, the hexagonal 6H-SiC and the rhombohedral (R) 15R-SiC. 2H-SiC and 3C-SiC are formed below 1400°C and ~1600°C, respectively. 4H-SiC, 6H-SiC and others are formed at and above 2000°C. 6H is the most stable of these polytypes at temperatures between 2200 and 2600°C.

In general, β -SiC is obtained using the Chemical Vapour Deposition (CVD) process. The Acheson process technology produces mainly α -SiC and it involves a reaction between quartz sand and coke at temperature between 2000 and 2300°C. The same raw materials are used to prepare a ceramic body from the silicon carbide particles. For a long time it was thought that solids with strong covalent bonds could be densified by hot-pressing only, and even under these condition small amounts of metallic sintering aids had to be added. [Prochazka \(1976\)](#) succeeded in pressureless sintering of β -SiC to high densities by using a powder with a high specific surface area; boron and carbon were also used as sintering additives. In 1978, Coppola and McMurtry ([Coppola, 1978](#)) proved that the process was not limited to β -SiC and that α -SiC powders are equally good and can be used to produce dense silicon carbides as long as the specific surface area of the powders is in the range of 10–18 m²/g. Around the same time, Bourne, Millet and Pickup reported that the processing route affected both the HEL and the amount of shear strength lost ([Bourne et al., 1997](#)). Like the aluminas, a smaller grain size appears to be beneficial in terms of ballistic performance and, as can be seen in [Fig. 7.14](#), so does the final hardness values for the different products.

Since then, many researchers have produced silicon carbide using different additives, sintering aids and also different process controls such as atmosphere, powder bed composition and pretreatment of the powders. However, while the PAD SiC-N variant represents the highest-performing grade of silicon carbide, it is extremely expensive. In 2002, James Campbell (from ARL) and Richard Palicka (from BAE Systems) recognised this disadvantage and attempted to reduce the high costs associated with hot-pressing operations. At that time, a square tile of SiC-N cost ~60 USD/kg – the goal was to achieve a cost of ~16 USD/kg, the estimated cost of reaction sintered tiles c.2006. The use of dry-pressed powders, coupled with computer-controlled machining and semicontinuous furnace operation were tried, but the final outcome remains unreported.

On the other hand, armour-grade RSSC has become very popular because it is very cost-effective. Recently reviewed by [Crouch et al. \(2015b\)](#), RSSC materials were originally developed in the 1950s with a number of US patents following between the mid-1960s and mid-1970s ([Taylor, 1965](#); [Taylor and Palicka, 1973](#)). Russian technologists

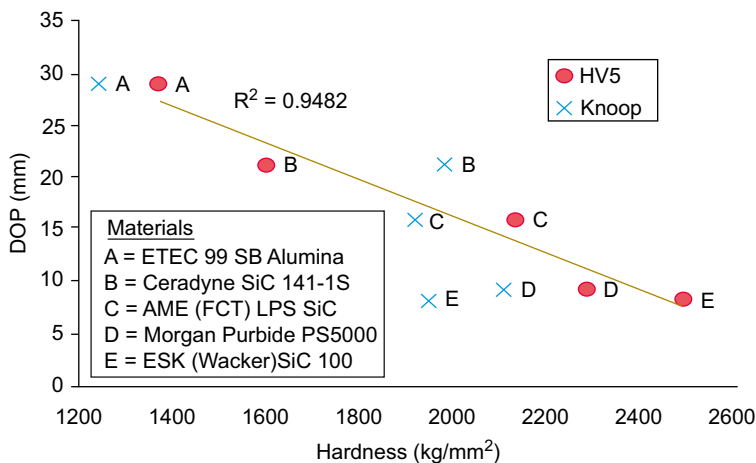


Figure 7.14 Apparent correlation between DOP and hardness for a range of SiC ceramics, manufactured by different routes, compared with alumina.

Roberson, C., et al., 2005. The effective hardness of hot pressed boron carbide with increasing shock stress. Paper Presented at the 29th International Conference on Advanced Ceramics and Composites, Cocoa Beach, FL, January 2005.

were also hard at work developing a similar process (Popov, 2003) but it was not until the late 1990s that full-scale production was commercially available in both the United States (Aghajanian et al., 2001) and Australia. More details are given elsewhere in a proprietary, technical memorandum issued by MCC in 2009 and written by Evgeniy Popov, founder of this particular variant of the RSSC process in 1998, Andrew Ruys (University of Sydney, Australia) and Ian Crouch (Managing Director, Armour Solutions Pty Ltd, Australia). The article was entitled ‘Quality of Reaction Sintered Silicon Carbide products’ (Popov et al., 2007). More details of the RSSC process are given in Section 7.6.

7.5.3 Boron carbides

Boron carbide is one of the hardest ceramic materials known (see Table 7.1), falling just short of diamond and cubic boron nitride. Because of its low density ($\sim 2520 \text{ kg/m}^3$), it has become the material of choice for body armour systems (Crouch, 2009). Its structure, properties and stability under stress have recently been reviewed in a highly recommended paper by Domnich et al. (2011).

For reference, Fig. 7.15 shows the boron-rich corner of the B–C phase diagram. Boron carbide is a covalently bonded solid with a high melting point (2427°C), outstanding hardness (Vickers: 3770 kg/mm^2), good mechanical properties and low specific gravity (2.52 g/cm^3), making it ideal for use in lightweight armours. The nominal boron carbide stoichiometric formula is B_4C ; however, it has a very wide phase stoichiometric range from B_4C up to $\text{B}_{10.5}\text{C}$. Boron carbide powder is produced commercially using either (1) fusion, which involves a reduction of boron anhydride (B_2O_3) with carbon (endothermic); or (2) magnesiothermy, in which

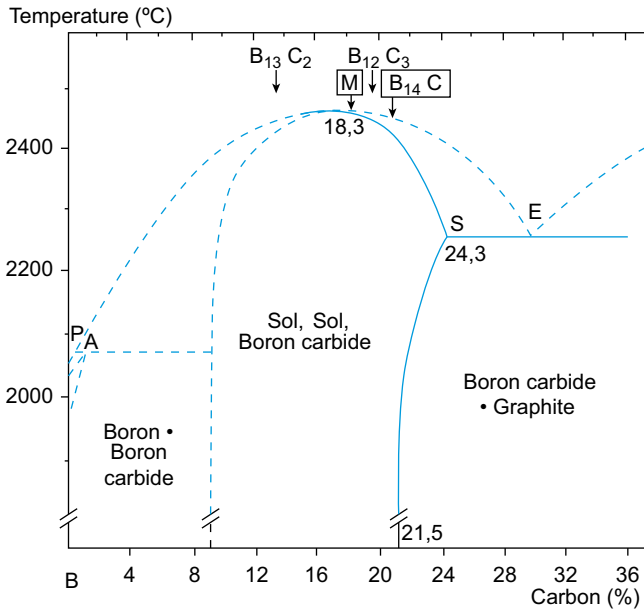


Figure 7.15 Boron-carbon (C–C) phase diagram.

boron anhydride reacts with magnesium in the presence of carbon black (exothermic). In the former case, the product forms into a large egg-shaped lump at the centre of the smelter. This egg is removed, crushed and milled to produce the grain size appropriate for its final use. In the latter case, stoichiometric carbide with low granularity (0.1–5 μm) is obtained directly, but it contains impurities including up to 2% graphite. Being a covalently bonded inorganic compound, boron carbide is difficult to sinter without the simultaneous application of heat and pressure. Therefore, it is preferable to hot press the boron carbide into dense shapes using fine and pure powders (<2 μm) under vacuum or inert atmosphere at high temperature (2100–2200°C). Boron carbide can also be produced using pressureless sintering at very high temperature close to the melting point of boron carbide (~ 2300 – 2400°C). Sintering aids such as alumina, Cr, Co, Ni and glass added to the powder mix help in reducing the temperature required for densification via pressureless sintering. The DMTC have used pressureless sintering, in combination with a VPP route, to develop a unique shaping process, details of which are given in [Section 7.6](#).

It is well known that boron carbide strike face materials behave in a more glass-like manner when impacted by high-velocity rounds, as compared with SiC and Al_2O_3 materials. However, this does not affect their excellent ballistic performance except against some specific threats where they under perform.

This underperformance appears to be due to shear localisation occurring within the material under shock loading. As reported by [Volger et al. \(2004\)](#), the shear strength of boron carbide in the shocked state decreases rapidly above the HEL,

indicating premature failure of the material as the shock stress reaches a threshold of ~ 20 GPa (see Fig. 7.16) — but why is this? What is occurring within the material?

Current understanding of this premature failure mechanism is favouring the notion of a phase transformation although the proposition that it might be related to catastrophic propagation of microcracks is still mooted. Chen et al. (2003) reported shock-induced localised amorphisation in boron carbide in 2003. This appears to be attributed to the presence of a particular polytype of boron carbide present within the material. Most recently, Taylor et al. (2011) noted that boron carbide contains several polytypes. Briefly, the B_4C crystal structure consists of 12-atom icosahedra linked by three-atom chains. Most pertinently, these can include B_{12} icosahedra linked by C—C—C chains and $B_{11}C$ icosahedra linked by C—B—C or B—C—C chains (either polar or equatorial icosahedral sites). Murray (2011) stated that the B—C—C chains are weaker than the B—C—B chains, leading to a reduced HEL, and that the B—C—C chains are more likely to collapse under impact. In-depth levels of research into this interesting phenomenon are continuing.

Boron carbide continues to be used with confidence in high-end, weight-driven armour applications, but it does have a number of natural drawbacks: cost of manufacture and shapeability. These aspects have been addressed in a number of ways through the adoption of liquid phase sintering and pressureless sintering (see Section 7.6) or by utilising the reaction bonding (or sintering) process as reported by Chhillar in 2008, and Karandikar in 2010. However, the most exciting developments in recent years have been those that couple a shaping process with a pressureless sintering operation. Researchers at the Georgia Institute of Technology, led by Robert Speyer, reported

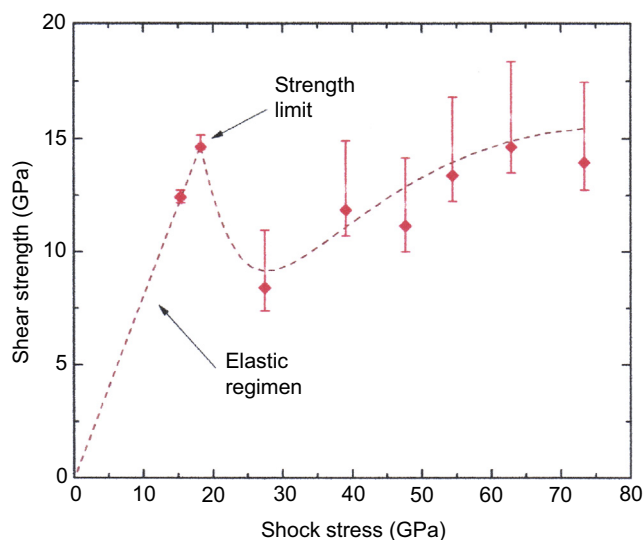


Figure 7.16 Shear strength of boron carbide as a function of shock stress.

Volger, T.J., Reinhart, W.D., Chhabildas, L.C., 2004. Dynamic behaviour of boron carbide. *Journal of Applied Physics* 95 (8), 4173–4183.

(Speyer, 2005) success with the use of preformulated, dry powders being forged into final shapes, followed by pressureless sintering, and the Israeli researchers from Haifa filed a patent in 2005 (Bar-Ziv et al., 2012), which relied upon similar technology. These works were followed by a relevant PhD thesis published in 2011, by Charles Wiley, entitled ‘Synergistic methods for production of high-strength and low cost boron carbide’ (Wiley, 2011). However, one of the most successful advances in this field has been led by the DMTC in the development and full-scale commercialisation of a unique shaping process, especially effective for thin boron carbide, armour-grade ceramics (see Section 7.6.1.5).

7.6 Manufacturing options and shaping methods

The manufacture of ceramic components typically occurs in two steps: (1) shape forming of the powder into a compact called a green body and (2) densification of the green body into the final component (see Fig. 7.17). There are a couple of instances where both steps are combined, as discussed below.

Finishing or machining may also be necessary. As such, near-net-shaping techniques are preferable as they minimize the expensive diamond grinding necessary to machine hard and dense ceramics (Leo et al., 2014). In addition, densification at lower temperature, and without the need to apply pressure to the powder compact, is desirable to minimise densification costs. The properties of the green body (particularly particle size, packing density and homogeneity) influence how easy (and costly) it is to densify the material. First the various options for shaping the green body are discussed (see right panel of Fig. 7.17); then the densification techniques are summarised before discussing the advantages and limitations of combining the different shaping methods with the densification strategies. As described in Chapter 1, it is important to minimise the introduction of flaws into the ceramic object during both steps of the processing to produce strong reliable ceramics.

Due to commercial and defence sensitivities, it is very difficult to determine the precise methods used and their relative abundance in the production of actual armour products. The most commonly used techniques for shaping ceramic components for armour applications include dry pressing, slip casting, VPP, gelcasting, injection moulding and freeze casting (Fig. 7.18). Each technique has its own advantages and disadvantages in terms of quality of product, cost, suitability to produce complex shapes and production rate.

7.6.1 Shaping

7.6.1.1 Dry pressing

Dry pressing (Fig. 7.18(a)) is simply the process of filling the ceramic powder into a die and uniaxially pressing a tile of uniform thickness. The micron-sized powders generally need to be agglomerated into approximately 100- μm sized granules in order to produce a free-flowing powder. Although it is generally used to make flat tiles, it can

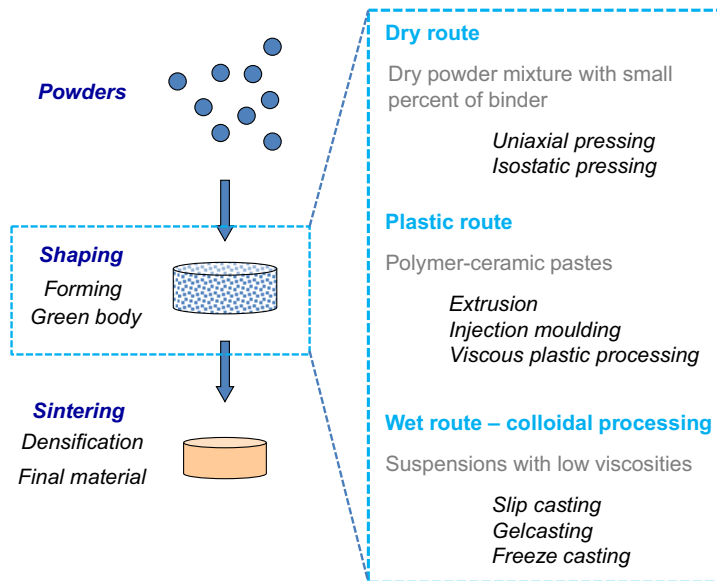


Figure 7.17 The steps in ceramic processing and the most commonly used shaping techniques for armour cagatorised as dry, plastic and wet routes.

be used to produce slightly curved tiles (such as breast plates) although the curvature presents difficulties in uniform mould filling. Dry pressing even in flat tiles is susceptible to nonuniform green density, which (as will be discussed in the next section) leads to problems with densification. Otherwise, dry pressing is a simple, commonly used and inexpensive method for producing simple shaped green tiles. The main limitation of dry pressing is the low and nonuniform green density which results from the adhesive friction between particles caused by van der Waals attraction. Typical green density is 45–50% of the theoretical density.

Dry pressing is not amenable to removing inclusions and agglomerates which may be present in the raw material (ie, incoming ceramic powder) or introduced during the processing (such as from abrasive wear of metal parts). For this reason, dry-pressed ceramics are typically less reliable [have lower Weibull modulus (see Chapter 1)] than those made by the wet, colloidal processing routes described next (Lange, 1989; Pujari et al., 1995).

7.6.1.2 Wet powder processing

Wet powder processing is an alternative to dry pressing which provides a mechanism to produce a denser and more uniform particle packing (Lange, 1989). By immersing the particles in liquid the van der Waals attraction is reduced and one has several options for producing repulsion between particles (ie, dispersion) which reduces the friction between particles and enables higher and more uniform particle packing in the green body. The higher and more uniform particle packing makes it easier to densify the ceramics during sintering, as will be made clear in the following discussion about densification. In addition, wet processing provides opportunities for removing flaws by

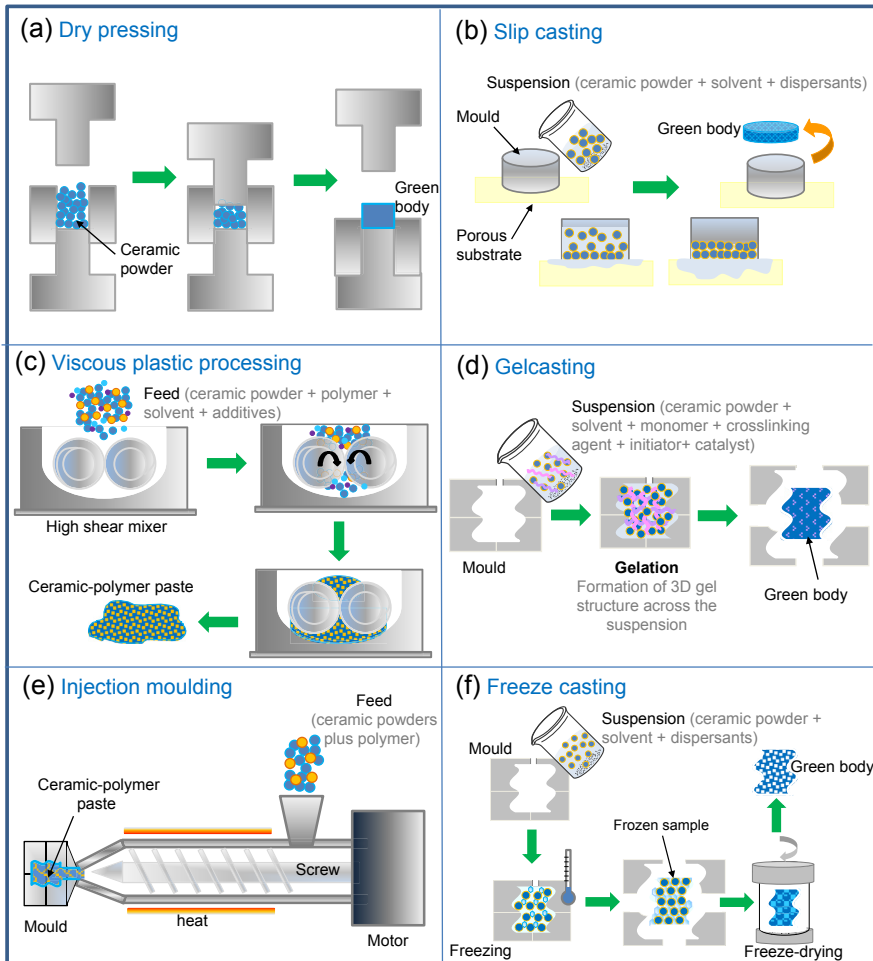


Figure 7.18 Schematics of the main ceramic shaping techniques used to produce armour plates.

breaking up and dispersing agglomerates and filtering or settling out large or dense inclusions. Reducing the size and number of flaws will improve the reliability of the ceramic objects, as described in Chapter 1 (Pujari et al., 1995).

7.6.1.3 Slip casting

Slip casting (Fig. 7.18(b)) is a shaping method that requires a dispersed or weakly flocculated suspension with solids content typically around 30–50 volume percent. Well-dispersed suspensions are preferred because they produce high-density uniform green bodies, but weakly flocculated suspensions may be used to increase the casting rate. The suspension is poured or injected into a plaster of Paris or porous polymer mould. The capillary suction of the micron-scale pores in the mould draw the liquid (usually water) into the mould leaving behind a layer of consolidated particles. The thickness of

the consolidated layer on the mould increases with time. The body is cast for a sufficient time to allow the body to reach the required thickness. The approach produces green bodies with high and uniform green density (when well-dispersed slurries are used). The shape of the object is usually limited to objects with uniform thickness. Objects thicker than a few millimetres can take hours to cast, making the process economically disadvantaged. Typical green densities achieved by this process range from 55 to 65% of the theoretical density.

7.6.1.4 Reaction bonding or reaction sintering

This process has recently been reviewed by [Crouch et al. \(2015b\)](#). In general, the process involves the infiltration of liquid silicon, through a prepressed compact of a mixture of SiC and carbon particles. The liquid silicon reacts with the carbon to form new-SiC. A residual amount of silicon remains when all of the carbon has reacted. Thus, in principle, there is no porosity; only isolated islands of metallic silicon in a matrix of original SiC and new SiC. However, the process relies upon the production of uniformly compacted and dispersed preforms of SiC, carbon and an appropriate binding agent, normally a phenolic resin. The resin is burnt off, and/or converted into carbon, during a preparatory pyrolysis process. The porous preform is then infiltrated with liquid silicon and this gives rise to another set of possible defects. Because the infiltration process involves flow of liquid silicon through the preform, a number of casting-like defects are possible, such as air-entrapment, cold shuts and incomplete filling (cold shuts are where two molten surfaces come into contact but do not metallurgically bond or fuse, forming a planar, crack-like defect). Nevertheless, Crouch and other industrial partners developed a strict set of acceptance criteria ([Crouch et al., 2015b](#)) and this process was used during the 2000s to supply hard armour plates to the Australian Defence Force.

7.6.1.5 Viscous plastic processing

Plastic processing routes are intermediate between dry pressing and colloidal processing. In these routes (see [Fig. 7.17](#)) the ceramic paste is typically slightly less than saturated with liquid in order that the paste can have plastic ‘clay-like’ mechanical flow properties. VPP ([Fig. 7.18\(c\)](#)) uses a plastic paste that is similar in rheological (flow) properties to that used in the extrusion, ram pressing or jiggering of clay-based products. The paste is made with the minimal amount of liquid required to produce an extrudable plastic dough (see [Fig. 7.19](#)). The plastic dough is then typically extruded into billets that are further processed into shape for objects such as tiles or breastplates. The low moisture content ensures a high green density. One of the advantages of VPP is that it affords the opportunity for secondary processing to produce shapes with high curvature and variable cross-section. Operations similar to forging (of metals) or ram pressing (of ceramics) can be utilised to produce components such as deltoids, knee or shin protection. In addition, the plastic nature of the paste allows for embossing or pressing patterns or shapes into the tile. It has been

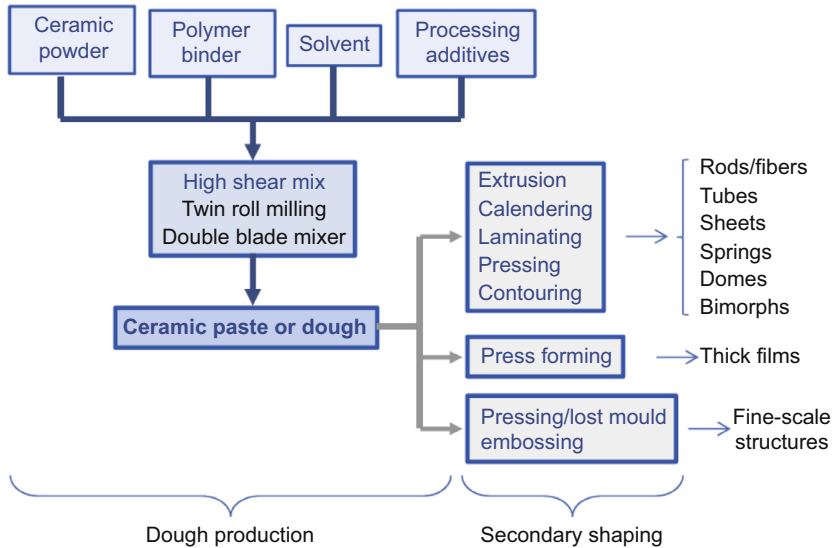


Figure 7.19 A schematic of the general VPP route for ceramics.

demonstrated that particular geometries are useful in managing the shock waves produced during impact (Martin et al., 2010).

After 5 years of development work, a variant of this processing route was commercialised, through the Defence Materials Technology Centre. As a result, many breast-plate tiles were manufactured by Australian Defence Apparel, and supplied to the ADF in the form of fully finished hard armour plates (see Section 7.10) in 2012. The DMTC has continued to develop the process and demonstrate its potential by producing a number of concept demonstrators, as seen in Fig. 7.20. More details can be found elsewhere (Leo et al., 2014; Crouch et al., 2016).

7.6.1.6 Gelcasting and related techniques

Gelcasting, injection moulding and freeze casting (Fig. 7.18(d–f)) have also been used to produce some ceramic armour components. The advantage of these techniques is that they can be used to produce very complex shapes, with varying cross-section, curved surfaces and intricate details. The techniques can be optimised to produce high- and uniform-density green bodies. Reducing the cost of such manufacturing processes is not always a simple and straightforward task. These techniques are useful to produce objects with shapes more complex than those generally required for armour components (which are typically relatively flat and of uniform cross-section) (Leo et al., 2014). In other studies Zhang et al. (2015) used dextrin as the carbon source and found that carbon content needed to be $>1\%$ for full densification.

After shape forming via colloidal (wet) processes, the wet green body must be dried. Care must be taken to remove the liquid at a slow enough rate as to not allow the air–water interface to penetrate the surface of the green body until the drying

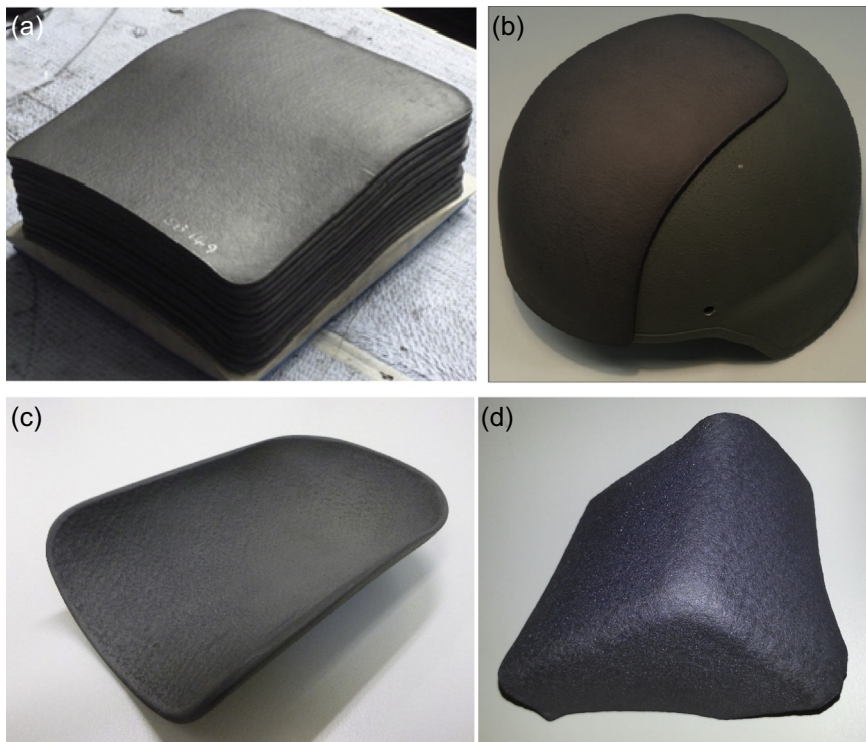


Figure 7.20 Examples of VPP boron carbide products: (a) multicurved breastplate tiles for HAPs, (b) up-armouring tile for combat helmets, (c) and (d) shaped demonstration items.

shrinkage is nearly complete, in order to avoid drying stresses and the possibility of cracking.

7.6.2 Densification

Densification of the green body is the second phase of ceramic processing. As shown in Fig. 7.21, densification can occur either with or without the assistance of pressure and/or electrical current. The dry powder compact is heated to about two-thirds to three-quarters of its absolute melting temperature in order to sinter (densify) the powder compact. During sintering, mass transfer, driven by reduction in surface area (reducing surface energy), causes the particles to first bond together then to eliminate the pores. The primary mass transfer mechanisms in solid state sintering are bulk, surface and grain boundary diffusion as well as evaporation/condensation and plastic flow. The sintering process should produce a nearly fully dense body ($>95\%$ of full theoretical density) with small isolated pores or better yet, a fully dense material without porosity since the ballistic performance improves with increased density. The ceramic material should have micron-scale grain size for best mechanical properties. Higher and more uniform green density in the green

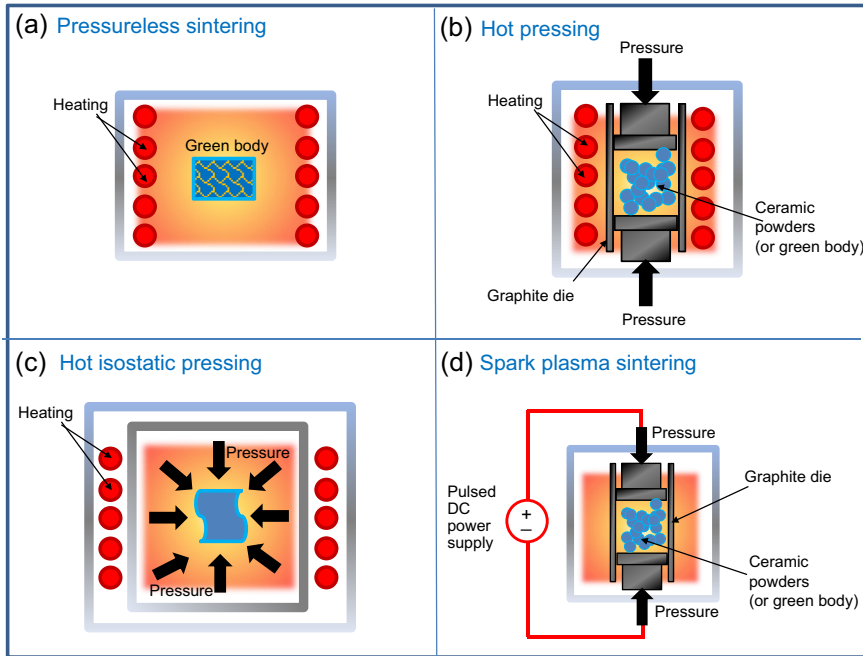


Figure 7.21 Sintering techniques used in the densification of ceramic armour components.

body make it easier to eliminate the porosity during sintering. Because the powder compact increases in density from the green value (typically 45–65% TD) to nearly full density, the object shrinks during densification. The greater the shrinkage the more difficult it becomes to control the dimensional tolerances of the final object. Serious problems can occur such as distortion, warping and cracking if the green density of the object is not uniform. In such cases, the shrinkage of the object varies from location to location and differential shrinkage leads to stresses resulting in loss of shape and cracking.

7.6.2.1 Pressureless sintering

Pressureless sintering (Fig. 7.21(a)) is conceptually the simplest and least costly densification process. The green body is simply heated in a chamber with an atmosphere suitable for the ceramic to be densified: air for oxides and typically argon or nitrogen for nonoxides. This technique can be used to densify green bodies of very complex shape, as the green body is not constrained by a die or mould in the furnace. The challenge of this technique is to reach sufficiently high density while keeping the temperature low enough to prevent grain growth. Careful control of the temperature profile as a function of time as well as the composition and pressure of the atmosphere in the furnace is important. Also a high and uniform green density has been shown to be a key factor in enabling high-density fine-grained ceramics to be produced.

7.6.2.2 Hot pressing

The majority of the ceramics used in armour applications are produced by hot pressing (Fig. 7.21(b)). In this densification technique, a graphite mould or die is filled with powder and plungers inserted (usually top and bottom). The filled die is placed in a furnace (usually an induction furnace) and heated to sufficient temperature to induce densification. Pressure (typically 10–40 MPa) is applied uniaxially to the plungers to aid in the densification process. Hot pressing is able to produce higher-density ceramics at lower temperatures than pressureless sintering – the major advantage of hot pressing is that the density is typically higher than can be obtained during pressureless sintering (unless particular care is taken in producing the green body for pressureless sintering). Another advantage of hot pressing is that green body formation is usually not required. Ceramic powder can simply be poured into the die then covered with a graphite spacer (typically a stack of tiles is produced) then the top plunger. However, care must be taken to uniformly fill the die with a uniform depth of powder to avoid density variations across the hot-pressed item. Granulation of the micron-sized particles into grains on the order of 100 μm in size helps with uniform mould filling. Some disadvantages of hot pressing are the limitation to shapes of uniform thickness and the lack of capability to produce complex shapes. These are not significant problems for the production of ceramic tiles and breast plates for ballistic protection as these components typically have uniform cross-section. However, the major issue with hot pressing is that the processing cost is higher due to the graphite dies and press required.

7.6.2.3 Hot isostatic pressing

Hot isostatic pressing (HIPing) (Fig. 7.21(c)) is a technique used to take advantage of the additional densification produced by pressure which also accommodates the ability to produce complex shapes. In HIPing, the pressure is applied isostatically by virtue of a gas in a pressure vessel containing the furnace. Green bodies with complex shapes can be produced as indicated in Section 7.6.1, then encapsulated within a molten glass (viscous liquid at densification temperature) which transmits the pressure to the ceramic component. Alternatively, a complex-shaped metal can is filled with the ceramic powder, then evacuated and sealed. The technique is generally expensive but can be useful for shapes with more complex geometry than is required for most armour applications.

7.6.2.4 Spark plasma sintering

Spark plasma sintering (SPS) (see Fig. 7.21(d)) is a densification approach whereby very rapid heating is produced by applying an electrical current (typically pulsed DC) across the ceramic powder contained within a uniaxially loaded conductive die, typically made from graphite. The electrical current produces rapid heating and enhanced densification at temperatures typically lower than those required for pressureless sintering. Also the densification is very rapid, with hold times typically in minutes rather than hours, which is of course an advantage with regards to total cycle

time, and minimises grain growth. The ability to retain fine-grained microstructures and metastable phases that would normally disappear during conventional sintering are the primary advantages of SPS, along with enhanced densification. Unfortunately, due to the requirement of the die, the shapes produced by SPS are limited by the same constraints as hot pressing. In addition, the application of the electrical current is not without cost, particularly where the product has a large cross-sectional area. Paris has recently reported work using SPS for manufacture of SiC and B₄C materials (Paris et al., 2010), and Hallam et al. (2015) include ballistic performance of a range of SPS-manufactured ceramic armours against AP threats.

7.7 Polymer ceramics

High values of specific compressive strength have made ceramics a widely used material for ballistic protection in armours, especially strike face materials (disruptors). Nevertheless, there are a number of drawbacks and challenges associated with monolithic ceramics used in armour systems, including limited formability and poor multihit capability.

Polymer ceramics is a new class of strike face material that demonstrates improved mechanical properties and enhanced impact energy dissipation. In an attempt to improve on current ceramic systems, various ceramic-based composites, reinforced with fibres, whiskers and particulates have been studied for application in hard armours (Arias et al., 2003; Colombo et al., 2006). In addition, polymer-infiltrated ceramic foam was prepared and examined for ballistic application. This armour system demonstrated some promising ballistic properties when compared to an armour system based on monolithic ceramic plates (Medvedovski, 2006a).

The polymer ceramics developed by the DMTC research team offer a number of economic and performance advantages including ease of formability, low-temperature processing and extreme multihit performance (Forrest et al., 2007; Naebe et al., 2013) (see Fig. 7.22). In broad terms, polymer ceramics consist of a hard ceramic particle phase bonded *in situ* by a rigid polymer phase. The hard ceramic phase constitutes a minimum 40% by weight of the total system, with the remainder comprising a polymer or a mixture of polymer and reinforcing filler. They function by taking advantage of the increased dynamic yield found during high strain rate compression which results in the material 'locking up' and behaving like a monolithic ceramic during the dwell phase of ballistic impact. Polymer ceramics have shown the potential to be developed to a performance level approaching those of traditional, high-temperature sintered ceramics.

There are a number of ceramics that are significantly harder than the commonly used silicon carbide. The strength of polymer ceramic armour materials lies in the flexibility of the choice of different ceramics of varying hardness. Only a small addition of a harder phase can offset the hardness reduction of the polymer phase. Other factors, such as cost, can be used in selecting an appropriate volume fraction of those ceramics used.

The polymer ceramic composite can be processed using conventional compression moulding equipment, via a powder-processing route. Dry resin is mixed with the

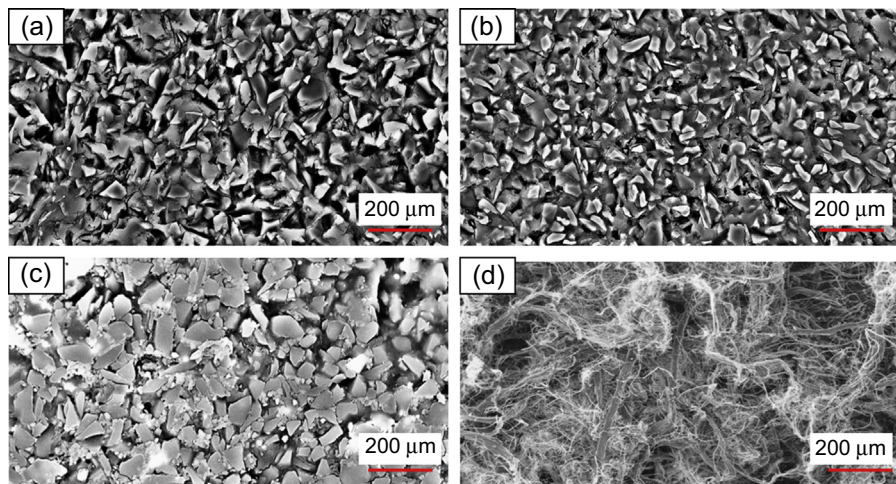


Figure 7.22 SEM images of mixes of phenolic resin and aramid pulp with (a) B_4C and (b) cBN and B_4C , and mixes of epoxy resin and aramid pulp with (c) B_4C . (d) shows an image of the aramid pulp.

Naebe, M., Sandlin, J., Crouch, I.G., Fox, B., 2011. Novel lightweight polymer ceramic composites for ballistic protection. Paper Presented at the ICCS 16, Porto, Portugal, 2011.

ceramic, processing aids and other additives before being highly compacted and cured by compression moulding. The moulding step itself has a very short cycle time (of the order of minutes), and unlike ceramics that typically require temperatures greater than $1500^{\circ}C$ for sintering, the required temperature is between 100 and $400^{\circ}C$. The saving in terms of both cycle time and energy cost is thus very significant. As an added benefit, the compression moulding method is highly reproducible, leading to very low (often nonexistent) scrap rates. The superior toughness of the new ceramic/polymer composite plate will also reduce general-handling breakages common in conventional ceramic processing, in addition to some improvement in projectile energy absorption.

7.7.1 Compositional effects and ballistic performance

Apart from formability at fairly low temperatures and that the tooling required is of relatively low cost, there is another characteristic that makes this new class of materials an interesting candidate for armour application, namely that the resultant plates may offer multihit capability (Naebe et al., 2013), a performance characteristic favoured in vehicle armour applications (Naebe et al., 2009). Fig. 7.23(a) shows an X-ray image of B_4C /phenolic strike face after ballistic impact from a 1.1-g FSP. As shown, there is limited radial and circumferential cracking given the relatively close distance of projectile impacts. For comparison, an X-ray image of an equivalent AD monolithic sintered B_4C tile (Fig. 7.23(b)), which shows extensive radial cracking and severe circumferential cracking particularly in the central upper impact site. We have noticed that polymer

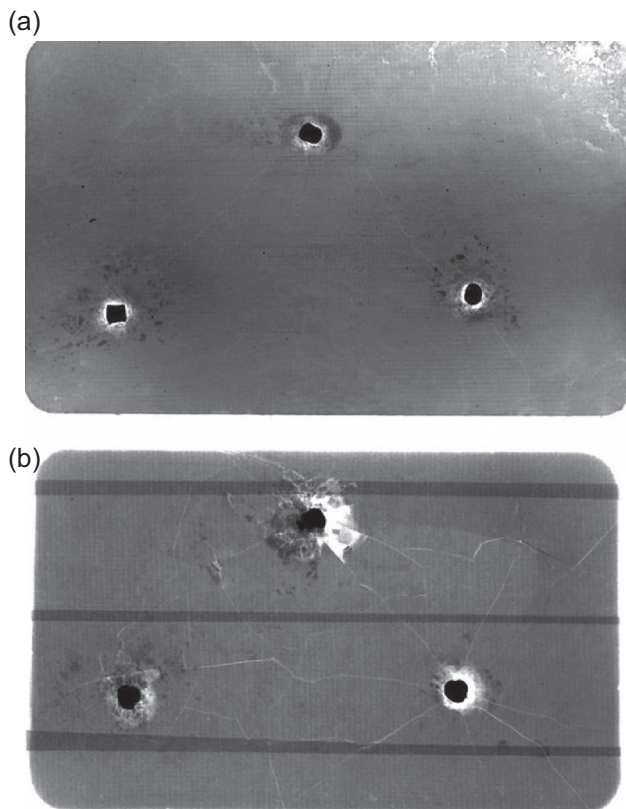


Figure 7.23 X-ray of (a) B4C based polymer ceramic (203 mm \times 123 mm) showing limited circumferential and radial cracking and (b) a monolithic sintered B4C tile of equivalent AD and dimension showing extensive radial and circumferential cracking. Note: horizontal lines in (b) are an X-ray artifact resulting from tape used to keep ceramic fragments in place. Naebe, M., Sandlin, J., Crouch, I., Fox, B., 2013. *Polymer Composites*, p. 180.

ceramic armours tend to sustain damage of 2–3 times the projectile diameter with occasional radial cracks extending between impact sites (Naebe et al., 2009). One of the advantages of this novel polymer ceramic material is that the armour is far more damage-tolerant than traditional sintered ceramic materials (Medvedovski, 2010).

Through a series of proof-of-concept and optimisation tests, it has been demonstrated that the early generation of polymer-ceramic composites with ~ 70 – 75% ceramic content and small volume fractions of reinforcing materials (~ 2 wt%) have a ballistic limit (V-50) within 15% of SiC monolithic strike faces when incorporated in a composite armour (ie, strike face and backing). Fig. 7.24 shows the V-50 and hardness values for various polymer ceramic variants. In the case of the materials studied, hardness proved to be a good indicator of ballistic performance, with relative V-50 values correlating with measured hardness values.

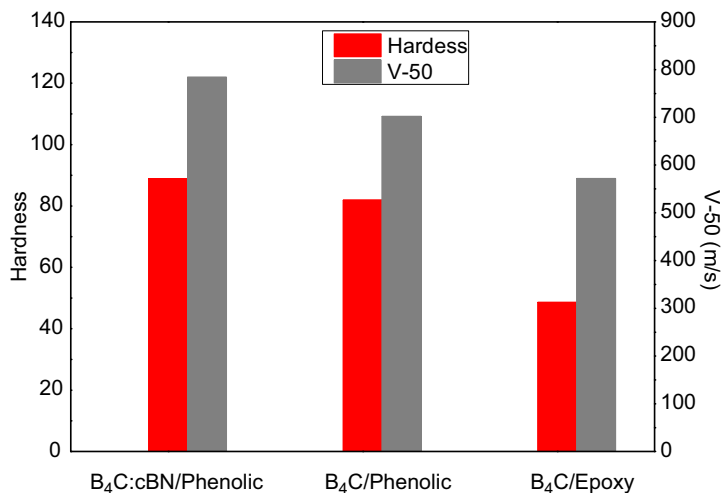


Figure 7.24 V-50 and hardness values for various polymer ceramic variants.

7.8 Application of transparent armours to vehicle platforms

All windows in military vehicles, whether they be logistic, reconnaissance or front-line vehicles, will benefit from being bullet- and blast-resistant (Fig. 7.25). However, there is often a trade-off between weight, thickness, transparency and requisite levels of protection. However, guaranteeing a complete solution as installed into a military platform can be more challenging for the armour engineer. It is outside the scope of this book to delve into proprietary, or sensitive, engineering solutions but several engineering pointers will be useful to the lay reader.

Firstly, it must be fully realised that laminated, bullet-resistant glass is both thick and heavy. The supporting structure needs to be substantial. The fitments need to be substantial. Flat screens are more easily integrated into the platform than curved windows. Since the windows are laminated using different materials with different physical and chemical properties, the armour engineer needs to be aware of the possibility of dissimilar joints. Differences in coefficients of expansion can be troublesome, necessitating good design of rebated joints. The use of flexible gaskets is normally preferred over the use of proprietary sealants, like Sikaflex, since these materials can attack polyurethane adhesives and cause delamination issues.

7.9 Application of opaque ceramics to vehicle platforms

Following realisation in 1998 by the US Army that the time had come to develop a capability to design materials for passive, kinetic energy, armour applications, a gathering of world experts at a conference in Maui, enabled a number of landmark papers



Figure 7.25 Bullet-resistant windscreen of the Bushmaster, demonstrating expanse and transparency.

Anon, 2015a. Australian Defence Force Photo Library.

to be presented and discussed (McCauley et al., 2002). Amongst these was a paper by Bill Gooch who presented an overview of significant US developments in ceramic armour applications over the 30-year period 1970–2000 (Gooch, 2001). The conference proceedings make highly recommended reading.

7.9.1 *System variables*

Ceramics are brittle materials such that cracks, once initiated, propagate to free surfaces. The robustness of the system is therefore paramount, and rugged designs a necessity, for design authorities to accept a ceramic-based armour system onto a long-serving, military platform. Multistrike behaviour under ballistic impact is a constant challenge and needs to be well defined by the end user. The armour technologist also needs to be able to design with brittle materials — this is not the same as designing a conventional, crack-tolerant structure in which fracture toughness and stress intensity factors might play a part.

The first top-level decision that needs to be made is whether the ceramic is to be added to an existing structure (eg, tiles simply bonded onto the front of an armour steel plate) or whether a balanced, optimised ceramic-based armour system is required as a standalone appliqué system. In the past, for example, the US up-armoured a demonstration version of the Bradley APC by adhesively bonding titanium diboride tiles to the outside of the aluminium armour (Gooch, 2001). Around the same era, even “hook-and-loop” pads were trialled. Simple as the approach was, it worked ballistically and functionally, and the tiles were easily replaced.

The form of the ceramic, as a strike face material, is critically important: its shape, surface finish and thickness will all affect overall performance. It is convention to adopt small tiles, either square or hexagonal, so that complete coverage is achieved via a mosaic

pattern, and collateral damage is minimised. Mosaic patterns can vary, although a typical brick pattern (see Fig. 7.26) is normal and certainly preferred over a square pattern: the number of nodes is reduced from quad-points to triple points. Tile size is most important and the industry guideline for many years has been that the length of the tile, l , should be greater than ~ 10 times the core of the small arms ammunition it is designed to defeat. This is essentially a reflection of edge performance: ie, how consistent the performance of a tile is from an edge through the centre to the opposite edge. Attempts to quantify this effect have been published by Hazell et al. (2008), in which 5.2-mm cored ammunition had a consistent level of performance at a distance greater than ~ 25 mm from an edge: ie, the minimum tile size needed to be >50 mm (~ 10 times the core diameter).

In earlier work, James (2001) reported that edge geometry (eg, a 45° chamfer) can markedly affect performance, and lead to weight savings of up to 30%. Critically, the width of the tile gap, x , and the properties of the interlayer material within it control the extent of collateral damage, since any impedance mismatch will cause shear stresses to occur at the interface (see Chapter 1). Epoxy resins, polysulphone adhesives, PVB rubbers, and metal-filled pastes have all been tried, and each has its own advantages and disadvantages, but no consistent solution has been determined. Practical engineering considerations normally prevail.

With reference back to Fig. 7.1, the ballistic performance of a free-standing, appliqué armour system will depend upon a number of other system variables, primarily the ratio of ceramic tile thickness, t_1 , to backing thickness, t_2 . This is normally expressed as a fraction of the areal density of the whole system:

$$\text{Ceramic content (\%)} = t_1 \cdot \rho_1 \cdot 100 / (t_1 \cdot \rho_1) + (t_2 \cdot \rho_2) \quad (7.1)$$

where ρ_1 and ρ_2 are the respective bulk densities of the ceramic and backing materials. Values of ceramic content between 65% and 75% appear to be optimal as far as ballistic performance is concerned, although other considerations like fabricability and the cost of materials can influence design considerations. Early work by Hetherington (1995) showed that a thickness ratio, t_1/t_2 , for an alumina/aluminium system was optimum at 1.5, although this changed to 1.0 at 30° obliquity. James (2001) has also

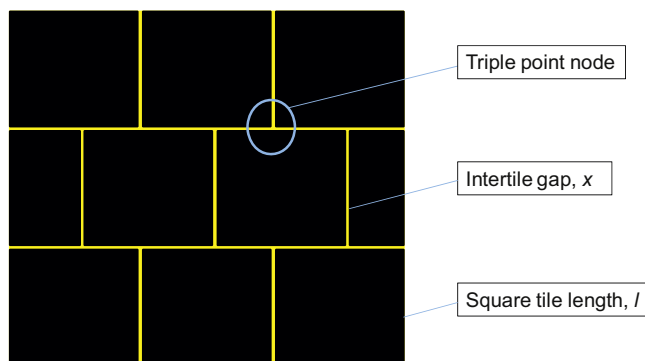


Figure 7.26 Schematic of typical brickwork mosaic of square ceramic tiles.

indicated that this optimum ratio changes with both impact velocity, V (m/s), and angle of attack (obliquity), θ , and suggested that a more useful equation, for optimal solutions, is:

$$t_1/t_2 = V \cdot (90 - \theta) / 60,000 \quad (7.2)$$

Significant improvements in ceramic armour systems can be achieved through using confinement techniques, either in plane [for example, by surrounding the entire mosaic structure within a steel frame (Savio et al., 2011)] or by placing a plate on the front of the target, so that the ceramic is sandwiched between the confining plate and the backing material. This confining plate prevents ceramic debris from being ejected early on in the penetration process, and allows the comminuted ceramic to retain more inherent compressive strength, thereby eroding/damaging the projectile for longer. However, these confining plates can become parasitic so optimum thicknesses are sought.

Crouch et al. (2015a) have also indicated that such material placed in front of the ceramic might also be beneficial in prestripping the jacket, allowing the bared core to impact undamaged ceramic and thereby experience more penetration resistance.

One final thought about systems: one other approach to increasing the multistrike performance of ceramic systems is to isolate individual ceramic elements. For example, spheres, cylinders or even small tiles could be embedded in a ductile matrix, thereby totally limiting collateral damage. While by design such systems do not have a continuous array of ceramic material, as a standard mosaic would do, they might prove beneficial at higher angles of obliquity. The proprietary nature of these unique systems prevents the authors from disclosing any details.

7.9.2 Material variables

The choice of ceramic grade is not always easy — it very much depends upon design drivers, the budget and user confidence. It is very clear now that the hardness of the ceramic armour controls its penetration resistance: even the latest research (c.2015) by the UK team led by Bryn James into advanced armour grades using advanced manufacturing processes (Hallam et al., 2015) came to this conclusion. In general, we know that penetration resistance — and therefore normally ballistic performance — increases with hardness (see Table 7.1). Therefore, apart from a few exceptions (see Section 7.5.3) the boron carbides have a higher ballistic efficiency than silicon carbides, which in turn have higher values than the aluminas. Fig. 7.3 therefore generally applies. It also holds true for the various blends, like the B_4C -SiC blends: an intermediate composition (between B_4C and SiC) will lead to intermediate hardness values which, in turn, will lead to intermediate levels of ballistic performances. The trade-off, of course, is cost.

Fig. 7.27 shows an excellent series of X-ray images of a 7.62-mm APM2 round penetrating ceramic armour. The various stages of the penetration process should be compared with the earlier schematic in Fig. 7.4. The works of Savio et al. (2011) and Sherman (2000) should also be considered. Understanding this complex

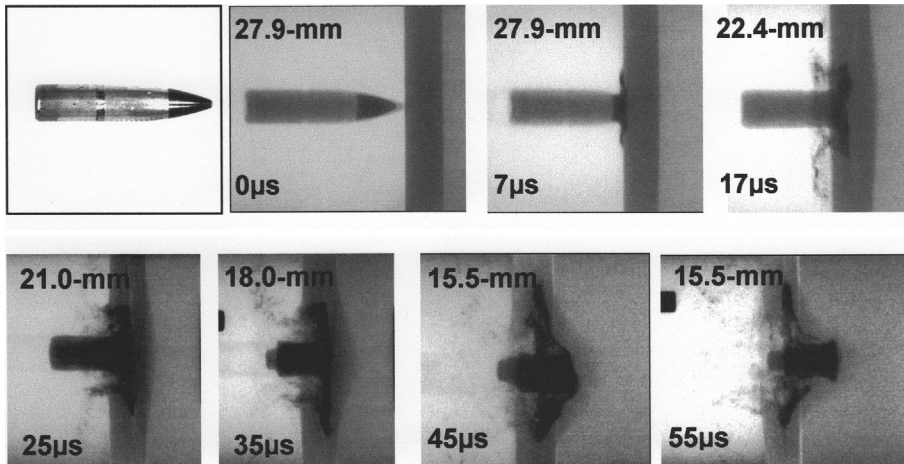


Figure 7.27 X-ray images of a 7.62-mm APM2 round, as a function of time, after first impact. Note the respective lengths of the core, and where most of the erosion is occurring.

Gooch, W.A., Burkins, M.S., 2002. Dynamic X-ray imaging of tungsten carbide projectiles penetrating boron carbide. Paper Presented at the 13th Annual Ground Vehicle Survivability Symposium, Monterey, CA, USA, April 2002.

penetration process, and the system variables which affect it, will lead to professional choices of which ceramic armours are best in a particular vehicular application.

An interesting set of corollaries to this section is the effects of surface finish, surface texture and surface geometry. While these are more of a geometrical effect than a material-related one, the reader should familiarize themselves with the work of Shukla (Shukla et al., 2003) and various patented ideas on the subject, like that by Roger Medwell (2008). Some interesting surface geometries are presented in Fig. 7.28, because while the principle is, at first, very attractive and thought-provoking, the effect of surface asperities upon ballistic efficiencies remain largely underresearched. With the advent of three-dimensional printing, of course, more interesting and effective surface profiles may now be feasible.

7.10 Application of opaque ceramics to body armour systems

7.10.1 Historical background

In a recent review (Crouch, 2010b), based upon 10 years of designing body armour systems and assessing market alternatives, Crouch presented an overview of the historical evolution of ceramic-based HAPs, as a function of protection level. The general trend in reduction of areal density of these HAPs over the past four decades was quite apparent, from the lightly wrapped alumina plates of the 1970s to the sophisticated, optimally designed boron carbide plates of the 2000s.

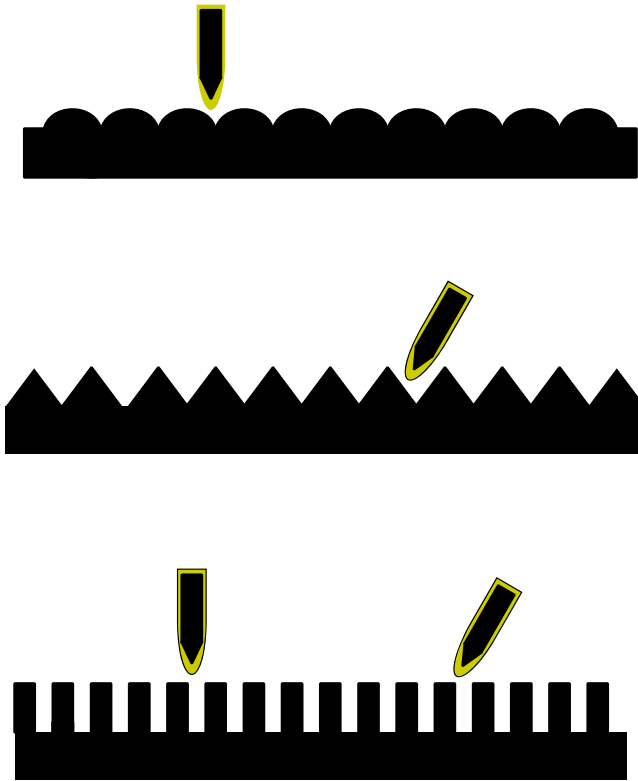


Figure 7.28 Schematics of possible surface profiles for ceramic tiles/armour.

The major outcome of this review was the fact that during the 2000s, the actual weight of these protective items rose sharply to match the rapid increase in perceived threat levels, due to operational conflicts at the time. However, in 2009, upon assessing the further weight increase that an XSAPI plate would have to bear, compared to an ESAPI plate, the US Congress delayed introduction of the XSAPI plates. An extra 0.5 lb was obviously ‘a step too far’ for an already overburdened foot soldier.

At the time of presenting these data in February 2010, Crouch forecast that most R&D should be focused upon lightening the lower-performing plates. The nature of conflicts was changing and the dismounted soldiers needed to be more agile. The total weight of body armour systems was finally on its way down!

7.10.2 Design principles

When designing ceramic-based hard armour plates ([Fig. 7.29](#)), the specific requirements as laid down by the end user play an enormous part in dictating the final weight of the product, especially the following key requirements:

- The number of required strikes;
- The minimum distance between strikes;

- The shot pattern, now well-defined by military customers;
- The edge performance: how close to the edge can 'full protection' be guaranteed?;
- Environmental preconditioning, prior to testing, to simulate 'worst' conditions in the field.

The most significant of these, in terms of adding necessary weight to the product, is the number of strikes required. This rose sharply in the 2000s, and as new military requirements were published, the number of strikes continued to rise. Fabricators were boasting as to how many shots their plates could take! What they did not consider at the time was that those boastful claims were simply adding weight to these systems! Conversely, the potential for actually *reducing* the weight of plates by simply *reducing* the number of required strikes was recognised. On a visit to ADA in 2009, Lt General John Caligari challenged the principle of dismounted soldiers wearing HAPs that were designed to withstand multiple shots, when most incidents in the field only involve one, or, at the most, two strikes.

The following sections describe the major design features that affect both weight and ballistic performance. Of these, the correct choice of the full range of materials for every element of the product is the most important.

7.10.3 Choice of materials

The principles behind material selection for every element of the hard armour plate as a ceramic-based system were first reported by [Crouch \(2009\)](#), who presented each element in turn.

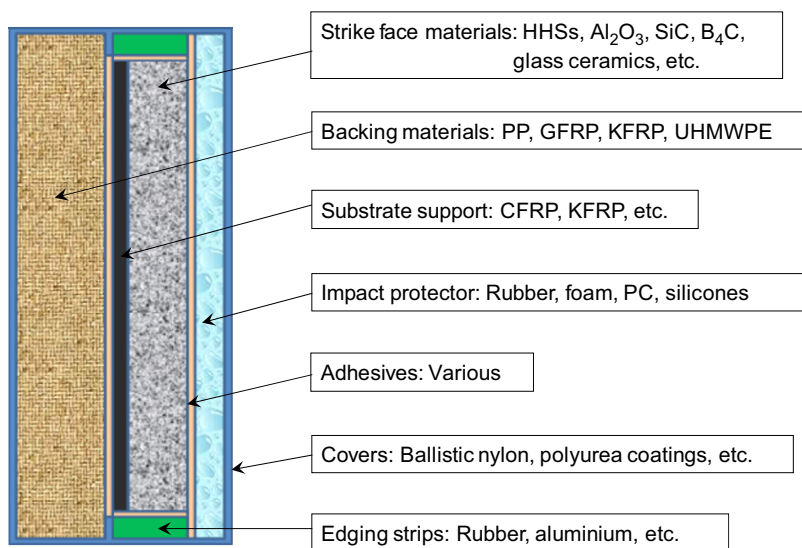


Figure 7.29 Schematic cross-section of a hard armour plate.

Crouch, I.G., 2009. Threat-defeating mechanisms in body armour systems. Paper Presented at the Next Generation Body Armour Conference, London, UK, September 2009.

7.10.3.1 Strike face material

Hard facing materials, from high-hardness steels (HHS) to glass ceramics, have been used. Choice will often be based upon cost, affected by availability, and dictated by the specified ballistic performance requirements. HHS elements are heavy, very readily available and of low cost: they are also thin (for the same weight) and therefore attractive for low-profile applications. On the other hand, most ceramics are expensive, but ballistically very efficient. The thickness of the ceramic element, and the ratio of ceramic to backing, requires detailed study and calculation. Eqs (7.1) and (7.2) are used, as well as fundamental information like that shown in Fig. 7.30 (Crouch et al., 2015a). Here, data from some relevant reverse ballistic experiments clearly indicate that the minimum thickness of ceramic required to commence deformation or erosion of the core is ~ 3 mm.

Some designers have chosen to use mosaics of small tiles, like those used for military platforms, to try to restrict collateral damage and thereby improve multihit performance. Unfortunately, a consistent level of ballistic performance across the entire product cannot be guaranteed, due to the presence of gaps between tiles, and quality assurance challenges in production have prevented this approach from being seriously adopted. Most of today's HAPs are either double- or multicurved, which introduces even more challenges for mosaic designs.

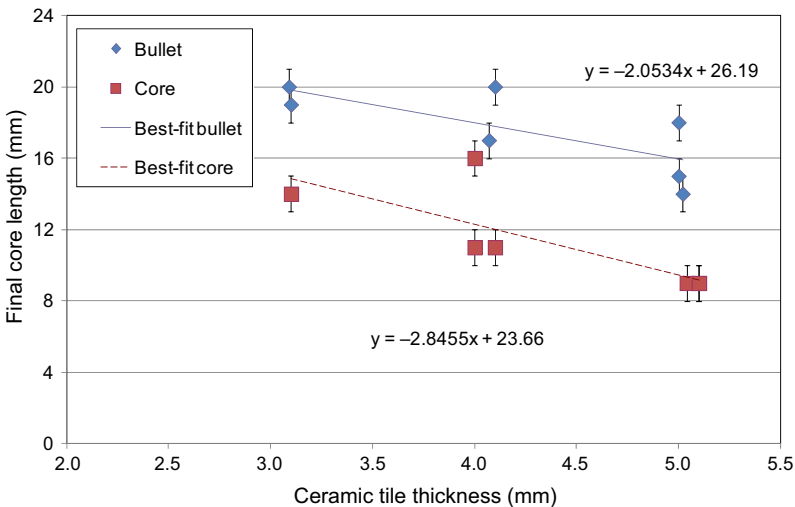


Figure 7.30 Experimental data, from reverse ballistic tests, on boron carbide ceramics of different thicknesses, using an AK47 round, with and without the steel jacket. The initial length of the mild steel core was 20 mm.

Crouch, I.G., Appleby-Thomas, G., Hazell, P., 2015a. A study of the penetration behaviour of mild-steel-cored ammunition against boron carbide ceramic armours. *International Journal of Impact Engineering* 80, 203–211.

7.10.3.2 Backing material

Ideally, backing materials for ceramics need to be as rigid as possible and therefore metal-based systems are attractive. Unfortunately, they cannot be shaped very easily. Hence, mouldable, fibre-reinforced plastics are the obvious choice. Functionally, they also need to be very effective at arresting blunt projectiles, since the ceramic strike face will blunt the core of any bullet. As we learnt in Chapters 5 and 6, FRPs are exceptionally good at absorbing energy in this way; so fibre-reinforced, polymeric laminates are ideal as backing materials. As a general rule, the most effective backing materials are those that have the greatest ballistic efficiency against FSPs. These are presently (2015) those based upon UHMWPE fibres, which is why many HAPs are manufactured using either Spectra or Dyneema products. They are expensive though, which is why the aramid-reinforced plastics, and even glass fibre-reinforced thermosets are still in use.

7.10.3.3 Substrate support

With reference to [Fig. 7.29](#), some fabricators use a stiff layer (eg, CFRP) directly below the ceramic in an attempt to provide the ceramic with a little more support, increasing dwell and thereby performance. However, it should be noted that there is no evidence to objectively assess this approach. On the other hand, one additional layer that has been shown to be effective is a cladding layer which is placed on both surfaces of the ceramic, prior to final construction. Crouch reported the benefits of cladding layers in 2014 ([Crouch, 2014](#)) (see [Fig. 7.31](#)). The presence of a number of different fibre-reinforced, polymeric, cladding layers was assessed, using BFS as a measure of the ballistic resistance of each of three strikes. The increase in BFS with each round is clear for all systems. However, the use of an aramid fibre-reinforced epoxy proved to be most beneficial in terms of multistrike performance. In a parallel study, [Jaitlee \(2013\)](#) suggested that these benefits might be further enhanced by applying tension to the cladding layer, during application. In earlier studies, both [Sarva et al. \(2007\)](#) and [Nunn et al. \(2008\)](#) had found efficiency gains against single strikes through placing a polymeric layer on the front of the ceramic plates. The underpinning reasons for these effects are still being researched ([Crouch et al., 2015a](#)).

7.10.3.4 Other elements

The most suitable materials for the other elements (covers, edging strips and impact protectors) are governed by nonballistic, overarching, engineering requirements of robustness and environmental resistance. For example, edging strips are occasionally used to protect the final product from edge and side impacts, and are often included in military statements of requirement.

7.10.4 Method of construction

Choice of construction methodology is driven by the need to bond the ceramic to the backing material and in providing a suitable finish to the product, in terms of wear and

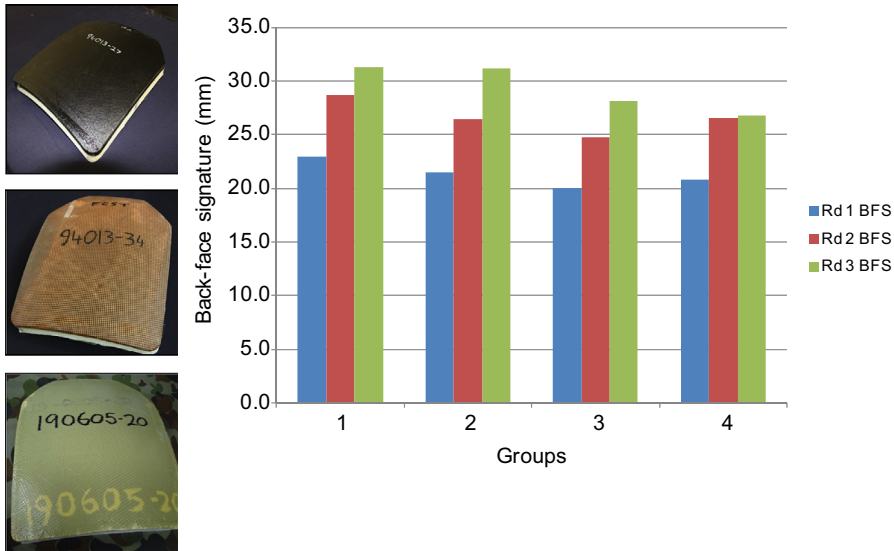


Figure 7.31 Back-face signature depths for three-strike HAPs, manufactured using three different cladding materials.

After Crouch, I.G., 2010a. A Comparative Study of Ceramic Coating Techniques, as a Means of Confering Multi-hit Resistance on SAPI Ballistic Plates. Internal DMTC Report, May 2010; Crouch, I.G., 2010b. Recent trends in personnel survivability. Paper Presented at the DMTC Annual Conference, Melbourne, Australia, February 2010.

tear. The decision is normally carried out at corporate level since both approaches involve capital investment. [Table 7.7](#) compares the two methods: the use of autoclaves/hydroclaves or compression moulding, and lists their respective advantages and disadvantages. In summary, compression moulding may produce a slightly higher-performing product, believed to be due to the possible benefit of higher compaction pressures (see Chapter 5), but from a quality assurance point of view the use of an autoclave or hydroclave is far superior, since up to 200 HAPs can be manufactured at any one time, in just one processing step, using a standard 1.5-m diameter autoclave (see [Fig. 7.32](#)). For high-performing HAPs, it is fundamental that the backing needs to be intimately bonded to the ceramic at every location, and for the bondline to be as small as possible, preferably less than 0.5 mm. The use of tough thermoplastic adhesives is also highly recommended.

7.10.5 Ballistic performance

7.10.5.1 V-50 determinations

In general, ballistic testing is covered in Chapter 11. However, ballistic testing of ceramic-based armour is fraught with erroneous approaches and data analysis, and needs special mention here. As an individual armour element, a ceramic-based hard armour

Table 7.7 A comparison between alternative manufacturing methods for HAPs

Alternative HAP production methods		
	Autoclave/hydroclave	Compression moulding
Advantages	<ul style="list-style-type: none">• Backing fits like a glove, and therefore backing provides guaranteed support to ceramic• One-step process, using vacuum bagging techniques• Hydrostatic pressure applied; therefore no danger of fracturing ceramic tile	<ul style="list-style-type: none">• Maximises applied pressure and takes advantage of any possible increase in ballistic performance• Flexibility of production steps
Disadvantages	<ul style="list-style-type: none">• Finite pressure maxima• Slightly reduced ballistic performance of backing material	<ul style="list-style-type: none">• Uniaxial pressure only• Each HAP bonded individually• Poor fit-up possible• Possibility of fracturing (thin) ceramic tile

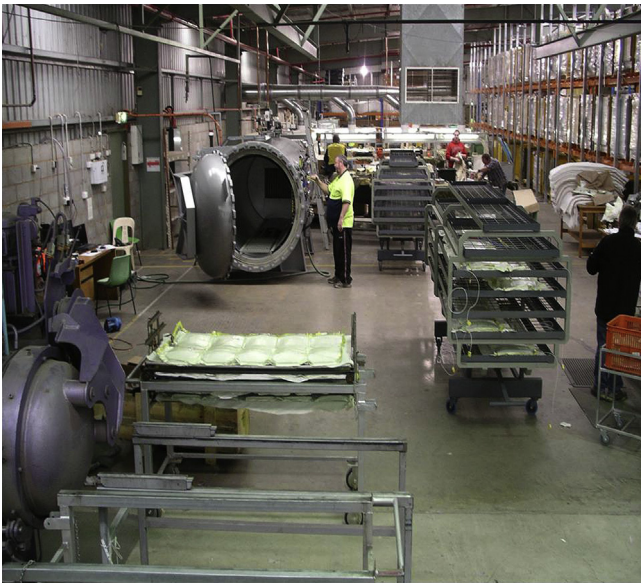


Figure 7.32 ADA's HAP production facility, c.2009.
Crouch, I.G., 2009. Threat-defeating mechanisms in body armour systems. Paper Presented at the Next Generation Body Armour Conference, London, UK, September 2009.

plate can be ballistically tested in a number of different ways. During product development, and final proofing of first articles against the prescribed threat, testing is very straightforward: the HAP, in combination with a soft armour insert (if specified), can be proof-tested. However, what approach should be adopted for quality assurance purposes, as part of check-production of HAPs? Until the mid-2000s, it was convention to determine a V-50 of the entire body armour system by assessing a representative set of HAPs, in conjunction with standard SAIs, of standard size (eg, 400-mm square). However, the resultant V-50 results are subject to large standard deviations since the entire system contains so many individual materials, and therefore material variables. To reduce the number of variables, HAPs can be tested as standalone items, and V-50s determined using up to four strikes per plate. Unfortunately, in carrying out this practice, Crouch discovered that the V-50 value correlated with the starting velocity (see Fig. 7.33), even though numerous V-50 tests, on many batches, were undertaken on separate occasions, with different starting velocities. From an engineering point of view, this is totally unacceptable: any measurement needs to be independent of the test method.

An example of an alternative approach would be to test a set of 12 HAPs, shot by shot, using a standard shot pattern, preferably a triangular pattern. The simple approach is to test each of the 12 plates, by firing all 'first rounds' into virgin plates. A series of 'second rounds' is then fired across the entire set of 12 plates, independently

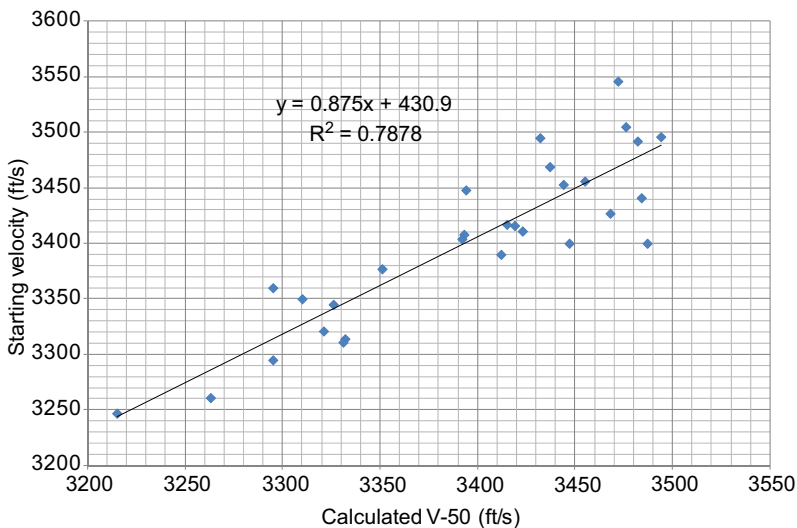


Figure 7.33 Correlation between V-50 determinations and the test starting velocity, for a series of HAPs.

Crouch, I.G., 2010a. A Comparative Study of Ceramic Coating Techniques, as a Means of Conferring Multi-hit Resistance on SAPI Ballistic Plates. Internal DMTC Report, May 2010; Crouch, I.G., 2010b. Recent trends in personnel survivability. Paper Presented at the DMTC Annual Conference, Melbourne, Australia, February 2010.

determining a V-50 value for second strike behaviour, and so on. In so doing, a V-50 value can be determined for all first round shots, and subsequent shots, as was reported by Crouch (2009, 2014), as shown in Fig. 7.34. Such an approach not only provides more accurate V-50 values, with reduced standard deviations, but it also records the level of degradation with each subsequent shot.

The degradation in ballistic performance with each subsequent impact, as shown in Fig. 7.34, is a strong indication that the presence of cracks does reduce the averaged penetration resistance of an HAP. The presence of cracks in HAPs is a natural concern of the end user but not as alarming as one might initially think. This reduction in ballistic performance has been investigated by both the Netherlands (Broos and Gunters, 2007) and by the UK (Watson et al., 2007): Watson et al. (2007) actually reported a 4–10% decrease in V-50 value for ‘cracked’ plates. More recently, Crouch (2012) showed that this decrease in V-50 value, by up to 9%, depends upon the distance between the POI and a pre-existing crack (see Fig. 7.35).

One final salient point about the ballistic performance of cracked plates: this need not be a serious issue, or any issue at all for that matter. A multistrike HAP will have been designed to cope with a number of impacts, by definition. All evidence shows that after the first strike, the plate contains many cracks, both radial and circumferential. Therefore, second and subsequent strikes are impacting damaged plates (ie, plates containing cracks) and they have still been shown to resist penetration. For example, using data shown in Fig. 7.34, the V-50 from a series of third strikes far exceeds the muzzle velocity of a standard 7.62 mm APM2 round. Therefore, the existence of cracks in an unused plate which has been properly designed to have multihit capacity like that shown in Fig. 7.34, would not be expected to provide less than the full level of protection.

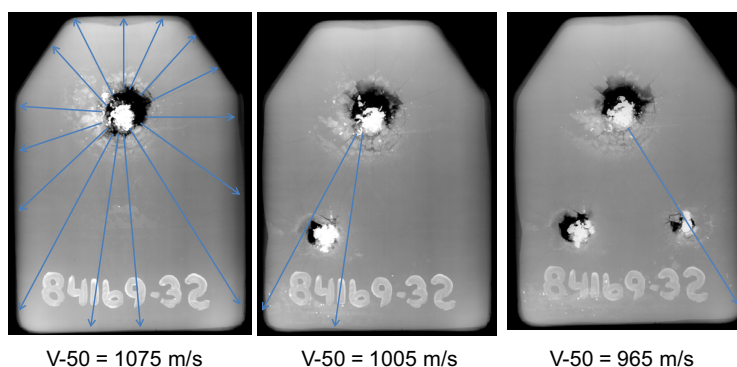


Figure 7.34 High-resolution, X-ray images of a single HAP, after each of three impacts, together with the respective V-50 values for first, second and third strikes (Crouch, 2009). The blue lines emphasise the radial cracks and the location of second and third strikes in relation to nearby radial cracks.

Crouch, I.G., 2014. Effects of cladding ceramic and its influence on ballistic performance. Paper Presented at the International Symposium on Ballistics, Atlanta, GA, USA, September 2014.

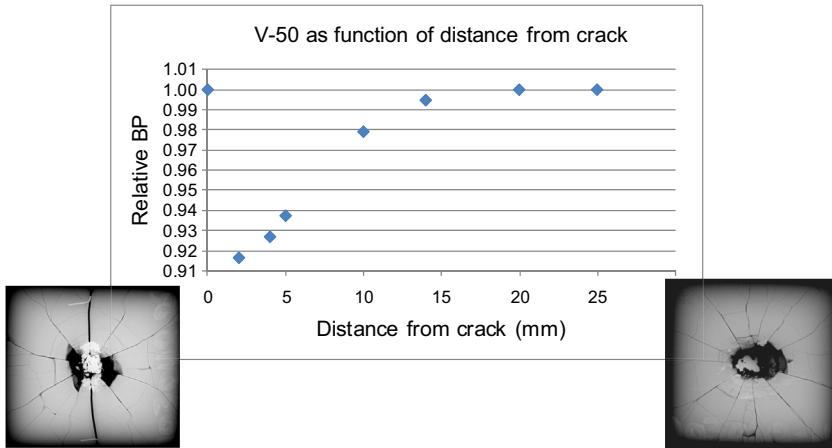


Figure 7.35 Plot of relative ballistic performance of a HAP test sample, as a function of distance from pre-existing crack.

Crouch, I.G., 2012. Advanced body armour systems. Paper Presented at the DMTC Annual Conference, Melbourne, Australia, March 2012.

7.10.5.2 Edge performance

For any free-standing armour system, whether it be a piece of aluminium armour plate, a section of laminated armour glass or even a soft armour vest (as was described in Chapter 6) the product will have a slightly lower ballistic performance towards the edge of the system. This is also true for hard armour plates.

Crouch and his colleagues at the DMTC (Sandlin and Crouch, 2010) discovered that the ballistic performance of HAPs was also governed by the size of the supporting soft armour insert and, in particular, the overlap length (OL) between the edge of the plate and the edge of the soft vest (see Fig. 7.36).

The trend was apparent for all types of plate but became extremely challenging with the lighter-weight body armour systems when trying to reduce the overall weight through not only optimising the ballistic performance of the HAP but also by reducing the size of the SAI.

7.10.6 Cost

A final word about cost, since this is not always appreciated by the end user: not only will the weight of a hard armour plate increase with threat level but, in general, so will the cost of the final product, simply through the need to use more material (eg, a thicker ceramic strike plate). Fig. 7.37 is a scatterplot of the areal density of a number of commercial HAPs as a function of the estimated cost of goods sold, expressed in Australian dollars (c.2015). The final cost will be affected by the required number of strikes, for example. In general, multi-strike plates will be more costly than single-strike plates. Enhancing edge-performance and/or decreasing shot-spacing may also, indirectly, add additional cost. It is therefore advisable that detailed specifications be reviewed in the light of probable cost.

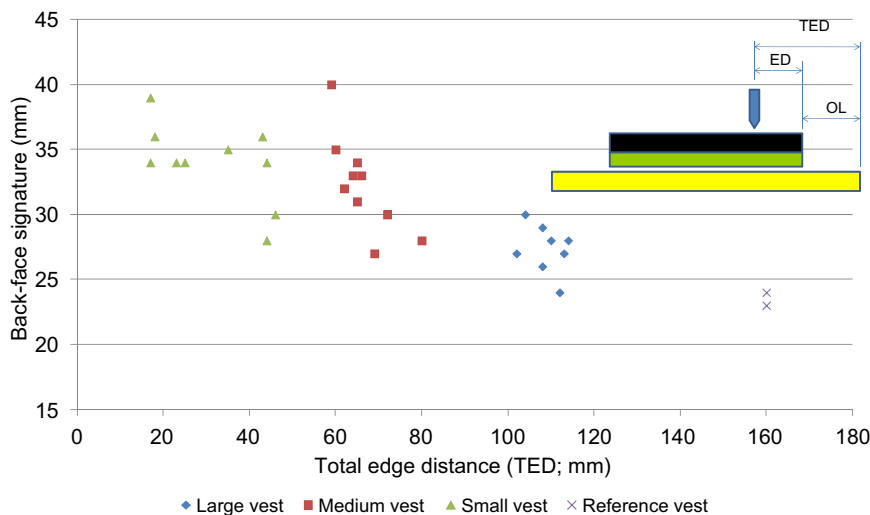


Figure 7.36 BFS values as a function of total edge distance (TED) for a series of impacts from a standard 7.62-mm APM2 round.

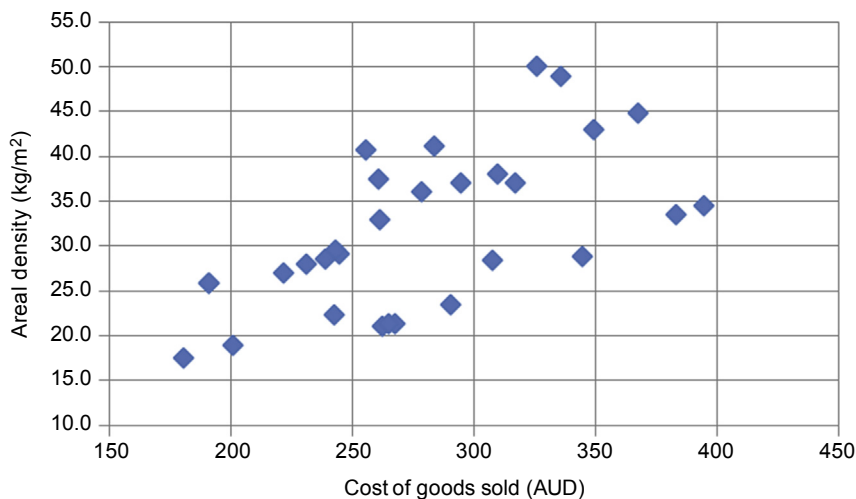


Figure 7.37 Estimated cost of goods sold for a range of HAPs as a function of areal density.

References

Aghajanian, M.K., et al., 2001. A new family of reaction bonded ceramics for armor applications. In: Paper Presented at the Pac Rim IV, Maui, Hawaii, November 2001.

Allain, S., Chateau, J.P., Dahmounb, D., Bouaziz, O., 2004. Modeling of mechanical twinning in a high manganese content austenitic steel. *Materials Science and Engineering A387–389*, 272–276.

- Anderson, C.E., et al., 2014. Investigation of impact performance of transparent armor. In: Paper Presented at the 28th International Symposium on Ballistics, Atlanta, GA, September 2014.
- Anon, 2015a. Australian Defence Force Photo Library.
- Anon, 2015b. Ceramic Properties Standard. CoorsTek. www.coorstek.com.
- Arias, A., Zaera, R., Lopez-Puente, J., Navarro, C., 2003. Composite Structures 61, 151.
- Asenov, S., Lakov, L., Toncheva, K., 2013. Promising ceramic materials for ballistic protection. Journal of Chemical Technology and Metallurgy 48 (2), 190–195.
- Bar-Ziv, S., et al., 2012. In: U.P. Office (Ed.), US 8 110 165 B2, Process for Manufacturing High Density Boron Carbide. Rafael - Armament Development, Haifa, Israel.
- Bolduc, M., et al., 2014. Towards better personal ballistic protection. In: Paper Presented at the Personal Armour Systems Symposium, Cambridge, UK, September 2014.
- Bourne, N., Rosenberg, Z., Crouch, I.G., Field, J.E., 1994. The effect of microstructural variations upon the dynamic compressive and tensile strengths of aluminas. Proceedings of the Royal Society of London A 446, 309–318.
- Bourne, N., Millet, J., Pickup, I., 1997. Delayed failure in shocked silicon carbide. Journal of Applied Physics 81 (9), 6019–6023.
- Broos, J.P.F., Gunters, R., 2007. Study of the ballistic performance of monolithic ceramic plates. In: Paper Presented at the 23rd International Symposium on Ballistics, Tarragona, Spain, April 2007.
- Campbell, J., et al., 2008. New low-cost manufacturing methods to produce SiC for lightweight armor systems. In: Paper Presented at the 26th Army Science Conference Orlando, FL, December 2008.
- Carter, S., Ponton, C.B., Rawlings, R.D., Rogers, P.S., 1988. Microstructure, chemistry, elastic properties and internal-friction of Silceram glass-ceramics. Journal of Materials Science 23 (1988), 2622–2630.
- Chen, M., McCauley, J.W., Hemker, K.J., 2003. Shock induced localized amorphization in boron carbide. Science 299 (5612), 1563–1566.
- Chhillar, P., et al., 2008. The effect of Si content on the properties of B₄C-SiC-Si composites. Advances in Ceramic Armor III, Ceramic Engineering and Science Proceedings 20 (5), 161–167.
- Cline, C.F., Wilkins, M.L., 1969. The Importance of Material Properties in Ceramic Armor. DCCIC Report, Part 1 (Ceramic Armor), pp. 13–18.
- Colombo, P., Zordan, F., Medvedovski, E., 2006. Advances in Applied Ceramics 105, 78.
- Coppola, A., 1978. US Patent 4124667.
- Crouch, I.G., Klintworth, W., 2003. Cost-effective lightweight armour systems. In: Paper Presented at the Land Warfare Conference, Adelaide, Australia, October 2003.
- Crouch, I.G., Appleby-Thomas, G., Hazell, P., 2015a. A study of the penetration behaviour of mild-steel-cored ammunition against boron carbide ceramic armours. International Journal of Impact Engineering 80, 203–211.
- Crouch, I.G., Kesharaju, M., Nagarajah, R., 2015b. Characterisation, significance and detection of defects in Reaction Sintered Silicon Carbide armour materials. Ceramics International 41, 11581–11591.
- Crouch, I.G., Sandlin, J., Thomas, S., Seeber, A., 2016. Material Science behind the development of a new, shapeable, boron carbide, armour material. In: Paper Presented at the 29th International Symposium on Ballistics, Edinburgh, May 2016.
- Crouch, I.G., 2005. Private Communication.
- Crouch, I.G., 2009. Threat-defeating mechanisms in body armour systems. In: Paper Presented at the Next Generation Body Armour Conference, London, UK, September 2009.

- Crouch, I.G., 2010a. A Comparative Study of Ceramic Coating Techniques, as a Means of Conferring Multi-hit Resistance on SAPI Ballistic Plates. Internal DMTC Report, May 2010.
- Crouch, I.G., 2010b. Recent trends in personnel survivability. In: Paper Presented at the DMTC Annual Conference, Melbourne, Australia, February 2010.
- Crouch, I.G., 2012. Advanced body armour systems. In: Paper Presented at the DMTC Annual Conference, Melbourne, Australia, March 2012.
- Crouch, I.G., 2014. Effects of cladding ceramic and its influence on ballistic performance. In: Paper Presented at the International Symposium on Ballistics, Atlanta, GA, USA, September 2014.
- Domnich, V., et al., 2011. Boron carbide: structure, properties and stability under stress. *Journal of the American Ceramic Society* 94 (11), 3605–3628.
- DuPont, 2015. www.sentryglas.com.
- Field, J.E., Townsend, D., Sun, Q., 1988. High speed photographic studies of the ballistic impact of ceramics. *Proceedings of SPIE* 1988 (1032), 672–679.
- Field, J.E., Walley, S.M., Proud, W.G., Goldrein, H.T., Siviour, C.R., 2004. Review of experimental techniques for high rate deformation and shock studies. *International Journal of Impact Engineering* 30 (7), 725–775. <http://dx.doi.org/10.1016/j.ijimpeng.2004.03.005>.
- Forde, L.C., et al., 2009. Ballistic impact studies of a borosilicate glass. *International Journal of Impact Engineering* 2009, 1–11.
- Forrest, M., Li, Y., Sandlin, J., 2007. Lightweight Composite Armour for Personnel Protection. Stage 3 Report: Final Technology Review.
- Franks, L., 2010. Transparent Materials for Armor - A Cost Study. US Army RDECOM 20473RC, January 2010.
- Fukuyama, H., Nakao, W., Susa, M., Nagata, K., 1999. New synthetic method of forming aluminum oxynitride by plasma arc melting. *Journal of the American Ceramic Society* 82 (6), 1381–1387.
- Goldstein, A., Goldenberg, A., Yeshurun, Y., Hefetz, M., 2008. Transparent MgAl_2O_4 spinel from a powder prepared by flame spray pyrolysis. *Journal of the American Ceramic Society* 91 (12), 4141–4144.
- Goldstein, A., Goldenberg, A., Hefetz, M., 2009. Transparent polycrystalline MgAl_2O_4 spinel with submicron grains, by low temperature sintering. *Journal of the Ceramic Society of Japan* 117 (1371), 1281–1283.
- Goldstein, A., 2012. Correlation between MgAl_2O_4 -spinel structure, processing factors and functional properties of transparent parts (progress review). *Journal of the European Ceramic Society* 32, 2869–2886.
- Gooch, W.A., Burkins, M.S., 2002. Dynamic X-ray imaging of tungsten carbide projectiles penetrating boron carbide. In: Paper Presented at the 13th Annual Ground Vehicle Survivability Symposium, Monterey, CA, USA, April 2002.
- Gooch, W.A., 2001. An overview of ceramic armor applications. In: Paper Presented at the PacRim IV International Conference on Advanced Ceramics and Glasses, Wailea, Maui, Hawaii, November 2001.
- Grujicic, M., Bell, W.C., Pandurangan, B., 2012. Design and material selection guidelines and strategies for transparent armor systems. *Materials and Design* 34, 808–819.
- Hallam, D., Heaton, A., James, B., Smith, P., Yeomans, J., 2015. The correlation of indentation behaviour with ballistic performance for spark plasma sintered armour ceramics. *Journal of the European Ceramic Society* 35 (2015), 2243–2252.
- Harris, D.C., May 2004. A century of sapphire crystal growth. In: Paper Presented at the Proceedings of the 10th DoD Electromagnetic Windows Symposium, Norfolk, Virginia.
- Hazell, P.J., Roberson, C.J., Moutinho, M., 2008. The design of mosaic armour: the influence of tile size on ballistic performance. *Materials and Design* 29 (2008), 1497–1503.

- Hetherington, J.G., 1995. Two component composite armours. In: Paper Presented at the Light Armour Systems Symposium (LASS), Shrivenham, UK.
- Horsfall, I., 2001. Glass ceramic armour systems for light armour applications. In: Paper Presented at the 19th International Symposium on Ballistics, Interlaken, Switzerland, May 2001.
- Jaitlee, R., 2013. Physical Protection: Inter-dependence between Hard and Soft Armours (Ph.D). RMIT University, Australia.
- James, B.J., 1995. The influence of the material properties of alumina on ballistic performance. In: Paper Presented at the 15th International Symposium on Ballistics, Jerusalem, May 1995.
- James, B.J., 2001. Practical issues in ceramic armour design. In: Paper Presented at the PacRim IV International Conference on Advanced Ceramics and Glasses, November 2001, Wailea, Maui, Hawaii.
- Johnson, R., Biswas, P., Ramavath, P., Kumar, R.S., Padmanabham, G., 2012. Transparent polycrystalline ceramics: an overview. *Transactions of the Indian Ceramic Society* 71 (2), 73–85.
- Jones, C.D., et al., March 2006a. Large-area sapphire for transparent armor. *American Ceramic Society Bulletin* 83 (3), 24–28.
- Jones, C.D., Rioux, J.B., Locher, J.W., Bates, H.E., Zanella, S.A., Pluen, V., Mandeartz, M., 2006b. Large-area sapphire for transparent armor. *American Ceramic Society Bulletin* 85 (3).
- Jones, R.W., 1987. Patent application, PCT/GB87/00801, “Armour Materials”, dated November 1987.
- Karandikar, P., et al., 2010. Optimization of reaction bonded B₄C for personnel armor. In: Paper Presented at the Personal Armour Systems Symposium, Quebec, Canada, September 2010.
- Karthikeyan, K., Russell, B.P., Fleck, N.A., Wadley, H.N.G., Deshpande, V.S., 2013. The effect of shear strength on the ballistic response of laminated composite plates. *European Journal of Mechanics A/Solids* 42 (2013), 35–53.
- Kim, M.-S., Shin, H.-S., Lee, H.-C., 2003. The effects of back plate materials on the perfect cone formation in impact-loaded soda-lime glass. *International Journal of Impact Engineering* 28 (2003), 281–290.
- Klement, R., Rolc, S., Mikulikova, R., Krestan, J., 2008. Transparent armour materials. *Journal of the European Ceramic Society* 28, 1091–1095.
- Krell, A., Strassburger, E., 2008. Hierarchy of key influences on the ballistic strength of opaque and transparent armor. *Ceramic Engineering and Science Proceedings* 20 (5), 45–55.
- Krell, A., Hutzler, T., Klimke, J., 2009a. Transmission physics and consequences for materials selection, manufacturing, and applications. *Journal of the European Ceramic Society* 29, 207–221.
- Krell, A., Klimke, J., Hutzler, T., 2009b. Advanced spinel and sub-mm Al₂O₃ for transparent armour applications. *Journal of the European Ceramic Society* 29, 275–281.
- Kuraray, 2014. Kuraray Europe GmbH.
- Lange, F.F., 1989. Powder processing science and technology for increased reliability. *Journal of the American Ceramic Society* 72 (1), 3–15.
- LeGallic, C., et al., 1996. A consideration of damage in the interaction between tungsten rod penetrators and ceramic materials. In: Paper Presented at the International Symposium on Ballistics, San Francisco, CA, September 1996.
- Leo, S., Tallon, C., Stone, N., Franks, G.V., 2014. Near-net-shaping methods for ceramic elements of (body) armor systems. *Journal of the American Ceramic Society* 97 (10), 3013–3033.
- Madhu, V., et al., 2005. An experimental study of penetration resistance of ceramic armour subjected to projectile impact. *International Journal of Impact Engineering* 32 (1–4), 337–350.

- Martin, et al., 2010. US patent 7685922, 30 March, 2010.
- McCauley, J.W., Corbin, N.D., 1979. Phase-relations and reaction sintering of transparent cubic aluminum oxynitride spinel (ALON). *Journal of the American Ceramic Society* 62 (9–10), 476–479.
- McCauley, J.W., Crowson, A., Gooch, W.A., Rajendran, A.M., Bless, S.J., Logan, K.V., Normandia, M., Wax, S. (Eds.), 2002. *Ceramic Armor Materials by Design*, from Proceedings of the PacRim IV Conference on Advanced Ceramics and Glasses, November 2001, The American Ceramic Society, Maui, Hawaii Ohio.
- McCauley, J.W., Patel, P., Chen, M., Gilde, G., Strassburger, E., Paliwal, B., Dandekar, D.P., 2009. ALON: a brief history of its emergence and evolution. *Journal of the European Ceramic Society* 29, 223–236.
- McCauley, J.W., 1978. A simple model for aluminum oxynitride spinels. *Journal of the American Ceramic Society* 61 (7–8), 372–373.
- Medvedovski, E., 2006a. Advances in Applied Ceramics 105, 241.
- Medvedovski, E., 2006b. Lightweight ceramic composite armour systems. *Advances in Applied Ceramics* 105 (5), 241–245.
- Medvedovski, E., 2010. *Ceramics International* 36, 2103.
- Medwell, R.T., 2008. EP 1 878 993 A2 Ceramic or Metal Tile Armour. European Patent Office.
- Mitchell, P.W., 1972. Chemical method for preparing MgAl_2O_4 spinel. *Journal of the American Ceramic Society* 55 (9), 484.
- Murray, P., 2011. Low Temperature Synthesis of Boron Carbide Using a Polymer Precursor Powder Route (M.Sc. thesis). University of Birmingham, UK.
- Naebe, M., Sandlin, J., Crouch, I., 2009. Next Generation Armour Technologies. Program Technical Report.
- Naebe, M., Sandlin, J., Crouch, I.G., Fox, B., 2011. Novel lightweight polymer ceramic composites for ballistic protection. In: Paper Presented at the ICCS 16, Porto, Portugal, 2011.
- Naebe, M., Sandlin, J., Crouch, I., Fox, B., 2013. *Polymer Composites* 180.
- Najim, F., Tawfique, H., Abbud, L., 2007. Behaviour forms of glass and other transparent material targets under high speed impact loading. *Mecanica Experimental* 14 (2007), 99–104.
- Nunn, S., et al., 2008. Improved ballistic performance by using polymer matrix composite facing on boron carbide armor tiles. In: Paper Presented at the 29th International Conference on Advanced Ceramics and Composites, Ceramic Engineering and Science Proceedings, Volume 26, Number 7, pp. 287–292, Cocoa Beach, Florida.
- Paris, V., et al., 2010. The spall strength of silicon carbide and boron carbide ceramics processed by Spark Plasma Sintering. *International Journal of Impact Engineering* 37 (2010), 1092–1099.
- Patel, P.J., Gilde, G.A., 2002. Transparent armor materials: needs and requirements. *Ceramic Transactions* 134, 573–586.
- Patel, P.J., et al., 2000. Transparent armor. *AMPTIAC Newsletter* 4 (3). Fall 2000.
- Patel, P.J., Gilde, G., McCauley, J.W., 2003. The role of gas pressure in transient liquid phase sintering of aluminum oxynitride (ALON). *Ceramic Engineering and Science Proceedings* 24 (3), 425–431.
- Patel, P.J., Hsieh, A.J., Gilde, G.A., 2006. Improved Low-cost Multi-hit Transparent Armor. ARL Technical Report, ADM002075, November 2006.
- Ping, L.R., Azad, A.M., Dung, T.W., 2001. Magnesium aluminate (MgAl_2O_4) spinel produced via self-heat-sustained (SHS) technique. *Materials Research Bulletin* 36 (7–8), 1417–1430.
- Popov, E., Ruys, A., Crouch, I.G., 2007. Quality of reaction sintered silicon carbide products. In: MCC Technical Memorandum, October 2007.

- Popov, E., 2003. Private Communication (with I.G. Crouch).
- Prochazka, A., 1976. US Patent 4004934.
- Pujari, V.K., et al., 1995. Reliable ceramics for advanced heat engines. *American Ceramic Society Bulletin* 74 (4), 86–90.
- Rafaniello, W., Cutler, I.B., 1981. Preparation of sinterable cubic aluminum oxynitride by the carbothermal nitridation of aluminum-oxide. *Journal of the American Ceramic Society* 64 (10), C128.
- Ramsay, J., 2015. Private Communication.
- Reimanis, I.E., Kleebe, H.J., Cook, R.L., DiGiovanni, A., May 20, 2004. Transparent Spinel Fabricated from Novel Powders: Synthesis, Microstructure and Optical Properties. Retrieved from: www.dtic.mil/cgi-bin/GetTRDoc?AD=ADA460575.
- Roberson, C., et al., 2005. The effective hardness of hot pressed boron carbide with increasing shock stress. In: Paper Presented at the 29th International Conference on Advanced Ceramics and Composites, Cocoa Beach, FL, January 2005.
- Rosenberg, Z., Yeshurun, Y., 1988. The relationship between the ballistic efficiency of ceramic tiles and their compressive strengths. *International Journal of Impact Engineering* 7 (1988), 357–362.
- SAFirE™ Transparent Armor Solutions, S.-G.C., http://www.crystals.saint-gobain.com/SAFirE_Transparent_Armor.aspx.
- Sandlin, J.D., Crouch, I.G., 2010. Edge Performance of Various Hard Armour Plates. DMTC Project 6.1.3 Technical Report.
- Sarva, S., et al., 2007. The effect of thin membrane restraint on the ballistic performance of armor grade ceramic tiles. *International Journal of Impact Engineering* 343 (2007), 277–302.
- Savio, S.G., et al., 2011. An experimental study on ballistic performance of boron carbide tiles. *International Journal of Impact Engineering* 38 (2011), 535–541.
- Sherman, D., 2000. Impact failure mechanisms in alumina tiles on finite thickness support and the effect of confinement. *International Journal of Impact Engineering* 24 (2000), 313–328.
- Shukla, A., Parameswaran, V., Kovolyan, E.J., 2003. Ballistic performance of surface modified ceramic body armor material. In: Paper Presented at the Society of Experimental Mechanics (SEM) Annual Conference on Experimental and Applied Mechanics, Charlotte, NC, June, 2003.
- Somiya, S., Inomata, Y. (Eds.), 1991. *Silicon Carbide Ceramics 1-Fundamentals and Solid Reaction*. Elsevier Science, Barking, UK.
- Speyer, R., 2005. Georgia Tech Newsletter. Atlanta, December 2005.
- Strassburger, E., 2009. Ballistic testing of transparent armour materials. *Journal of the European Ceramic Society* 29, 267–273.
- Stuer, M., Zhao, Z., Aschauer, U., Bowen, P., 2010. Transparent polycrystalline alumina using spark plasma sintering: effect of Mg, Y and La doping. *Journal of the European Ceramic Society* 30 (6), 1335–1343.
- Surmet, A. <http://www.surmet.com/technology/alon-optical-ceramics/index.php>.
- Taylor, K.M., Palicka, R.J., 1973. Dense Carbide Composite for Armor and Abrasives. US Patent No. 3765300.
- Taylor, D., Wright, T., McCauley, J., 2011. First Principles Calculation of Stress Induced Amorphization in Armor Ceramics. Army Research Laboratory Report ARL-MR-0779.
- Taylor, K.M., 1965. Cold Moulded Dense Silicon Carbide Articles and Methods of Making Same. US Patent No. 3275722.
- Tracey, S.R., Crouch, I.G., 1989. The Ballistic Performance of Glass Ceramics against Small Calibre, Armour-piercing Projectiles - an Initial Assessment. RARDE Divisional Note 8/89, September 1989.

- Volger, T.J., Reinhart, W.D., Chhabildas, L.C., 2004. Dynamic behaviour of boron carbide. *Journal of Applied Physics* 95 (8), 4173–4183.
- Wang, S.F., Zhang, J., Luo, D.W., Gua, F., Tang, D.Y., Dong, Z.L., Kong, L.B., 2013. Transparent ceramics: processing, materials and applications. *Progress in Solid State Chemistry* 41, 20–54.
- Watson, C., et al., 2007. The effect of cracks on the ballistic performance of controlled protective body armour plates. In: Paper Presented at the 23rd International Symposium on Ballistics, Tarragona, Spain, April 2007.
- Wiley, C.S., 2011. Synergistic Methods for the Production of High Strength and Low-cost Boron Carbide (Ph.D.). Georgia Institute of Technology.
- Wilkins, M.L., Cline, C.F., Honodel, C.A., 1969. UCRL report #50694. In: 4th Progress Report of Light Armor Program. Lawrence Livermore Laboratory, UCLA.
- Wilkins, M.L., 1978. Mechanics of penetration and perforation. *International Journal of Engineering Science* 16, 793–808. Special Edition (Penetration Mechanics).
- Woodward, R.L., O'Donnell, R.G., Baxter, B.J., Nicol, B., Pattie, S.D., 1989. Energy absorption in the failure of ceramic composite armours. *Materials Forum* 13, 174–181.
- Yamaguchi, G., Yanagida, H., 1959. Study on the reductive spinel—a new spinel formula $\text{AlN}-\text{Al}_2\text{O}_3$ instead of the previous one Al_3O_4 . *Bulletin of the Chemical Society of Japan* 32 (11), 1264–1265.
- Zhang, X.F., Li, Y.C., 2010. On the comparison of the ballistic performance of 10% zirconia toughened alumina and 95% alumina ceramic targets. *Materials and Design* 31 (4), 1945–1952.
- Zhang, J., et al., January 2015. Properties of silicon carbide ceramics from gel-casting and pressureless sintering. *Materials and Design* 65, 12–16.
- Zientara, D., Bucko, M.M., Lis, J., 2007. ALON-based materials prepared by SHS technique. *Journal of the European Ceramic Society* 27 (2–3), 775–779.

Analytical techniques and mathematical modelling

8

S. Ryan

Defence Science and Technology Group, Fishermans Bend, Victoria, Australia

8.1 Introduction

Predictive methods for evaluating the penetration of projectiles and fragments into armour are used to support experimental design, perform preliminary comparative studies between different armour solutions and perform deterministic vulnerability assessments of armoured platforms in threat environments. Although numerical codes are capable of delivering quantitatively accurate predictions of penetration events, they can require considerable resources, are sensitive to the skill of the analyst and are highly dependent on a priori experimental results. Furthermore, numerical models are unsuitable for vulnerability codes, which require embedded analytical or tabular solutions. Perhaps most critically, analytical models can provide an improved understanding of the penetration event and relevant failure mechanisms of the armour. This is not necessarily achieved in a numerical model. Ideally, analytical models are used in combination with numerical techniques and experimental studies to fully evaluate an armour system, as exemplified in recent work by [Walker et al. \(2013\)](#).

There is an extensive volume of literature on analytical penetration models, including a number of comprehensive reviews ([Backman and Goldsmith, 1978](#); [Ben-Dor et al., 2013](#); [Teland, 1999](#)). As such, any attempt to encompass all the relevant work within a single book chapter is impossible. Rather, we have attempted here to present a number of key models, as well as those developed at, or regularly applied within, the Defence Science and Technology Group (DST Group), Australia.

8.2 Analytical modelling of penetration into semi-infinite metallic targets

Targets can be considered semi-infinite when the thickness and lateral extension are such that the free boundaries do not influence the penetration process. By removing free surface effects, target response to a penetrating object is simplified to a one-dimensional problem if the projectile has axial symmetry.

8.2.1 Hydrodynamic jet penetration

In 1948, Birkhoff et al. applied hydrodynamic theory to develop an equation for the penetration depth of jets into semi-infinite targets. In this approach, it is assumed

that impact-generated pressures are sufficiently high that the materials behave hydrodynamically (ie, similar to fluids). By defining a moving coordinate system, located on the projectile–target interface (see Fig. 8.1), and assuming a steady state is reached instantaneously, Bernoulli's theorem can be used to determine the flow variables (ie, relevant to the projectile motion).

For incompressible flow, the pressure at the stagnation point in the projectile is calculated as:

$$p_s = \frac{1}{2} \rho_p (V - u)^2 \quad (8.1)$$

where p_s is the stagnation pressure (Pa); ρ_p is the projectile density (kg/m^3); V is the projectile velocity (m/s) and u is the interface velocity (m/s).

Similarly, for the target:

$$p_s = \frac{1}{2} \rho_t u^2 \quad (8.2)$$

where ρ_t is the target density (kg/m^3).

By equating Eqs (8.1) and (8.2), the interface velocity, u , can be determined:

$$\frac{u}{V - u} = \sqrt{\frac{\rho_p}{\rho_t}} \quad (8.3)$$

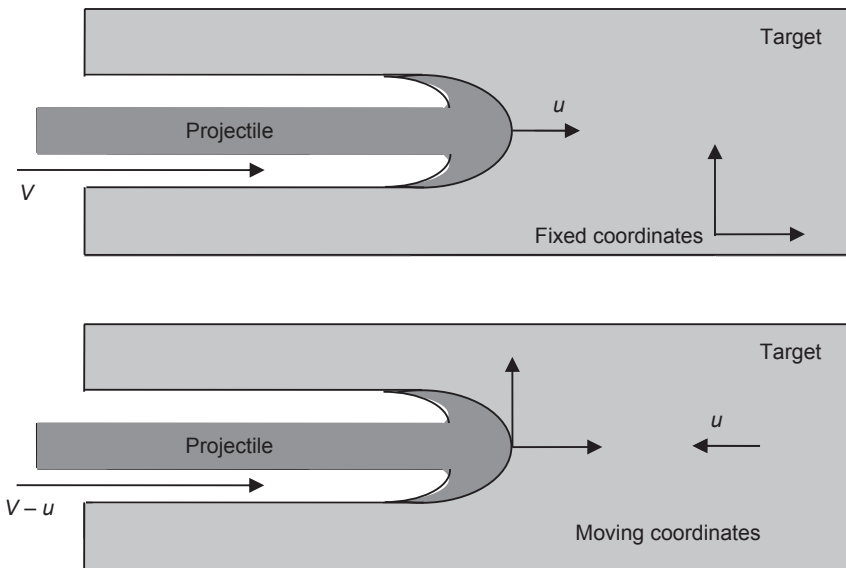


Figure 8.1 Idealised jet penetrating target material. Top: fixed coordinate system; bottom: moving coordinate system defining a stagnation point at the projectile–target interface.

or

$$u = \frac{V}{1 + (\rho_t / \rho_p)^{1/2}} \quad (8.4)$$

If it is assumed that penetration begins when the front surface of the projectile impacts the target and ends when the tail of the projectile reaches the projectile–target interface, then the duration of impact, t , is given by:

$$t = \frac{L}{V - u} \quad (8.5)$$

where L is the projectile length (m).

The depth of penetration, P_∞ , following the hydrodynamic assumption, is then simply calculated as the distance that the interface has moved into the target during time, t , ie:

$$P_\infty = ut = L \left(\frac{u}{V - u} \right) = L \sqrt{\frac{\rho_p}{\rho_t}} \quad (8.6)$$

A commonly noted aspect of Eq. (8.6) is the dependence of penetration depth on the length and density of the penetrator, but not its velocity. As such, hydrodynamic theory is commonly defined as the theoretical upper limit of penetration depth into semi-infinite targets, although experimental findings (Hohler and Stülp, 1977) show this assumption to be questionable.

The two primary assumptions of Birkhoff et al.'s work are that of hydrodynamic flow, and the instantaneous and prolonged steady-state condition at the projectile–target interface. Application of hydrodynamic theory is valid for impacts in which generated pressures are orders of magnitude greater than material strengths, such that fluid flow can be assumed. However, even for such impact events, material strengths play an important role at the limits of damage extension, and during the late-time penetration process when pressures have significantly decreased. The assumption of an instantaneous steady-state condition at the projectile–target interface fails to consider the initial transient shock phase, which occurs during the early stages of penetration and results in very high shock pressures at the interface. Since this phase is extremely short-lived it is commonly neglected in analytical procedures.

8.2.2 Four-phase penetration model

General Motors Defense Research Laboratories performed a series of rod impact experiments against aluminium targets, and found that for equal rod masses, crater depths increased with impact velocity and rod length-to-diameter ratio (Christman et al., 1964). Furthermore, the experimental crater depths from impacts at 5.0 km/s exceeded the theoretical predictions of Birkhoff et al.'s theory for all projectile

length-to-diameter ratios (L/D) tested. To justify this discrepancy, Christman and Gehring proposed the application of a penetration model for high velocity (Christman and Gehring, 1966) that incorporates four phases: transient; primary penetration; secondary penetration (ie, cavitation) and recovery, depicted in Fig. 8.2.

The first, or transient, phase lasts for the first few microseconds of the impact event and encompasses the formation and detachment of a shock wave from the projectile–target interface. During the primary, or steady-state, penetration phase the projectile–target interface velocity is constant, as is the pressure level behind the shock front. During the primary penetration phase, the projectile is eroded as it penetrates. As such, for long projectiles this phase can be relatively long and account for the majority of the total penetration depth, while for low aspect-ratio projectiles (ie, thin disks), it will be relatively short and contribute little to the crater depth. The secondary, or cavitation, penetration phase begins once the projectile has been completely deformed and essentially removed from the system as a source of energy (Christman and Gehring, 1966). In this phase, crater growth is driven by the still-expanding shock wave, until the wave strength decays below material strengths. Since the shock is associated with projectile diameter, and not length, they defined a simplistic modification of Eq. (8.6), valid for all L/D ratios:

$$P_{\infty} = L \sqrt{\frac{\rho_p}{\rho_t}} + \frac{D_c}{2} \quad (8.7)$$

where D_c is the crater diameter at the target surface (m).

Cavitation may actually occur simultaneously with the primary penetration phase for high aspect-ratio projectiles (ie, long rods) as the eroding projectile may be surrounded by a radially expanding crater that is in the cavitation phase (Christman et al., 1964). It should be noted that Birkhoff et al. (1948) identified residual cratering

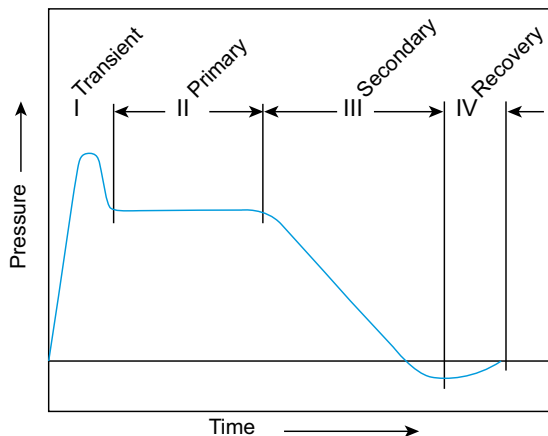


Figure 8.2 Four-phase penetration model.

From Christman, D.R., Gehring, J.W., 1966. Analysis of high-velocity projectile penetration mechanics. *Journal of Applied Physics* 37(4), 1579–1587.

for impact on ‘relatively soft target’ materials. However, rather than shock-wave-driven cavitation, they defined ‘secondary penetration’ due to residual momentum of the projectile.

The recovery phase defines the period in which contraction of the crater occurs, but may also include brittle fracture of the crater surface and recrystallisation and annealing beneath the crater surface (Christman and Gehring, 1966). As a result of this phase, the final crater size may actually be smaller than the maximum reached during the cavitation phase.

For hypervelocity impact of rocks with $L/D = 1$ on geological materials, craters are generally hemispherical, ie, $P_\infty = D_c/2$. In which case, Eq. (8.7) overpredicts penetration depth (ie, $L\sqrt{\rho_p/\rho_t} \neq 0$). As such, Christman and Gehring (1966) proposed a modification that summates the penetration depth of an $L/D = 1$ projectile and that of a rod with length equal to $L - D$, ie:

$$P_\infty = (L - D)\sqrt{\frac{\rho_p}{\rho_t}} + P_c \quad (8.8)$$

where P_c is the penetration depth of a cylinder with $L/D = 1$.

8.2.3 Empirical cratering relationships

Christman and Gehring also introduced the effect of target strength via P_c in Eq. (8.8), considering that the rapid decay of stress wave amplitude as it propagates from the impact location results in stress/pressure to strength ratios approaching 1.0 in the cavitation phase. Thus, for calculation of P_c , empirical cratering relationships should be applied, for example (Christman and Gehring, 1965):

$$P_c = 0.13 \left(\frac{\rho_p}{\rho_t} \right)^{1/3} \left(\frac{m_p V^2}{2B_{\max}} \right)^{1/3} \quad (8.9)$$

where m_p is the projectile mass (kg) and B_{\max} is the maximum target hardness (HB).

The maximum hardness term, B_{\max} , is intended to account for target strain hardening and can be measured on a sectioned target just below the bottom of a crater. Some examples from Christman and Gehring (1966) are reproduced in Table 8.1.

Although an improvement over pure hydrodynamic theory, the requirement for a postimpact measurement in a predictive model is clearly not ideal. Furthermore, a strength term is only included in Eq. (8.9) for the target material. As such, there is no mechanism to determine projectile deceleration during impact — an experimentally observed process that contradicts the hydrodynamic assumption (see Eq. (8.5)).

8.2.4 Modified hydrodynamic theory

Eichelberger (1956) and Allen and Rogers (1961) also proposed modifications to the hydrodynamic theory in order to include target strength. This was achieved through a

Table 8.1 Target hardness data for calculating penetration in the cavitation phase

Target material	Target hardness before impact, B_t (HB)	Maximum target hardness after impact, B_{\max} (HB)	Increase in hardness (%)
Al 1100-0	25	45	80
Al 2024-T3	125	155	24
C1015	110	156	50
AZ31B-F	57	72	26

Christman, D.R., Gehring, J.W., 1966. Analysis of high-velocity projectile penetration mechanics. *Journal of Applied Physics* 37(4), 1579–1587.

modification of the target stagnation pressure, calculated using Bernoulli's Eq. (8.2), where:

$$p_s = \frac{1}{2} \rho_t u^2 + \phi \quad (8.10)$$

where ϕ is the difference between the resistance of the target and projectile to the plastic deformation required by the penetration process (Pa).

Equating Eqs (8.10) and (8.1) and solving for interface velocity, the depth of penetration can be expressed (as per Eq. (8.6)) as:

$$P_\infty = L \frac{-\rho_p V + \left[\rho_p^2 V^2 - 2(\rho_p - \rho_t) \left(\frac{1}{2} \rho_p V^2 - \phi \right) \right]^{1/2}}{\rho_t V - \left[\rho_t^2 V^2 - 2(\rho_p - \rho_t) \left(\frac{1}{2} \rho_p V^2 - \phi \right) \right]^{1/2}} \quad (8.11)$$

As the impact velocity, V , increases, material strength effects become less significant, and Eq. (8.11) converges to the hydrodynamic solution (Eq. (8.6)) as shown in Fig. 8.3. Problems with the modified Bernoulli approach arise when defining the resistance parameter, ϕ . Allen and Rogers (1961) developed an empirical equation:

$$\phi = \phi_0 + bu + cu^2 \quad (8.12)$$

where ϕ_0 is the critical stagnation stress (Pa), calculated from $\phi_0 = \frac{1}{2} \rho_p V_0^2$; b is a constant, calculated from $b = -\rho_p V_0(1 - 1/a)$ ($\text{kg/m}^2\text{s}$); c is a constant, calculated from $c = \frac{1}{2} \left[\rho_p(1 - 1/a)^2 - \rho_t \right]$ (kg/m^3); V_0 is the threshold velocity required for steady-state penetration (m/s) and a is an adjustable parameter determined from experiment (no units).

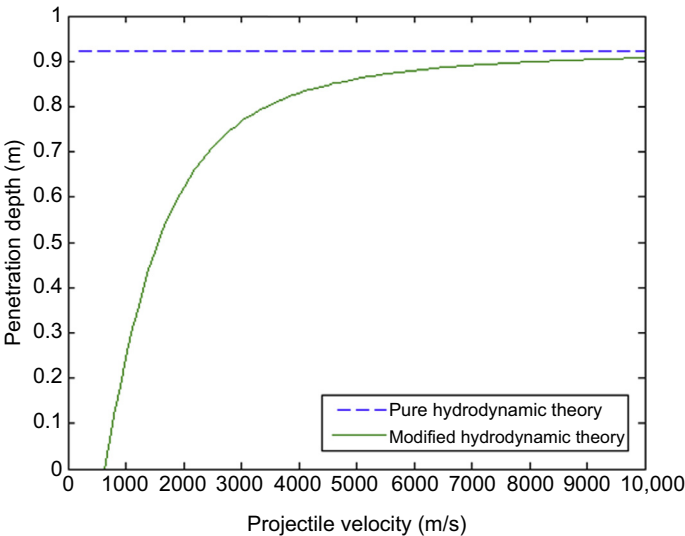


Figure 8.3 The effect of impact velocity on penetration depth of a 0.465-m long lead projectile on an Al7075-T6 target assuming a constant value for ϕ of 2.22 GPa. After Teland, J.A., 1999. A Review of Analytical Penetration Mechanics (FFI/RAPPORT-99/01264). Retrieved from: Kjeller.

Table 8.2 Adjustable parameters of some metals for calculating ϕ

Metal	Threshold velocity, V_0 (m/s)	Parameter a
Gold (Au)	479	0.90052
Lead (Pb)	583	0.81329
Copper (Cu)	672	0.81705
Tin (Sn)	675	0.76894
Aluminium (Al)	1170	0.68072
Magnesium (Mg)	1481	0.64308

From Allen, W.A., Rogers, J.W., 1961. Penetration of a rod into a semi-infinite target. Journal of the Franklin Institute 272(4), 275–284. [http://dx.doi.org/10.1016/0016-0032\(61\)90559-2](http://dx.doi.org/10.1016/0016-0032(61)90559-2).

Allen and Rogers (1961) provide a list of values for V_0 and a , reproduced in Table 8.2.

A general approach for determining the steady-state penetration threshold velocity, V_0 , is to extrapolate the depth of penetration curve defined by Eq. (8.11) to zero by empirically adjusting the dynamic strength parameter, ϕ .

From results of the six jet materials in Table 8.2 penetrating into an aluminium target, Allen and Rogers (1961) defined an average value of $\phi = 0.0222$ Mbar for

all metals. Although less accurate for calculating the penetration velocity, u , than Eq. (8.12), the complexity of the calculation is significantly decreased.

Alekseevskii (1966) and Tate (1966) independently introduced further strength effects to the hydrodynamic theory, based on the following assumptions:

- After an initial transient phase (see Fig. 8.2), the penetrator–target interface moves with a velocity u ;
- For an eroding penetrator, the rear end of the rigid portion moves with a velocity v , which corresponds to a rate of erosion of $u - v$;
- The projectile strength, Y_p , corresponds to the pressure at which the projectile behaviour transitions from that of a rigid body to that of a fluid. Thus, at pressures above Y_p , the projectile material behaves hydrodynamically;
- Similarly, the pressure in the target required to induce hydrodynamic flow, R_t , must be high enough that it may overcome the rigidity of the target material in the immediate locality of the impact, as well as the inertia of the surrounding material. Although Tate acknowledged that this pressure likely varies with factors such as penetration depth and impact velocity, it is assumed to be constant throughout the penetration process.

These assumptions can be represented by the following set of coupled differential equations, which are identical for both the Tate and Alekseevskii formulations:

$$\frac{dP}{dt} = u \quad (8.13)$$

$$\frac{dl}{dt} = -(v - u) \quad (8.14)$$

$$l\rho_p \frac{dv}{dt} = -Y_p \quad (8.15)$$

where l is the instantaneous projectile length (m) at time t (s) and P is the instantaneous penetration depth (m).

There are four unknowns (P , u , v , l) in the set of differential equations, and, as such, an additional equation is required to solve Eqs (8.13)–(8.15). Alekseevskii defines a force (or pressure) balance across the interface:

$$k_p \rho_p (v - u)^2 + \sigma_{SD} = k_t \rho_t u^2 + H_t \quad (8.16)$$

where σ_{SD} is the projectile dynamic yield point (Pa) and H_t is the dynamic hardness of the target (Pa), while Tate uses a modification of the Bernoulli stagnation pressure equality:

$$\frac{1}{2} \rho_p (v - u)^2 + Y_p = \frac{1}{2} \rho_t u^2 + R_t \quad (8.17)$$

where Y_p is the projectile strength (Pa) and R_t is the target strength (Pa).

Parameters Y_p and R_t from Tate are essentially equivalent to σ_{SD} and H_t from Alekseevskii, respectively. Thus, when the flow geometry variables k_p and k_t are constant and equal to 1/2 (see Alekseevskii, 1966), Eqs (8.16) and (8.17) are identical (albeit with different physical justification). As such, the approach is commonly referred to as the Alekseevskii–Tate model. For both approaches, the interface velocity, u , is calculated by rearranging Eq. (8.17), such that:

$$u = \frac{1}{1 - \mu^2} \left(v - \mu \sqrt{v^2 + A} \right) \quad (8.18)$$

where

$$\mu = \sqrt{\frac{\rho_t}{\rho_p}} \quad (8.19)$$

and

$$A = 2 \frac{(R_t - Y_p)(1 - \mu^2)}{\rho_t} \quad (8.20)$$

Penetration depth is calculated by integrating the interface velocity, u , over the duration of the penetration event, t :

$$P_\infty = \int_0^t u \, dt \quad (8.21)$$

The solution of Eq. (8.21) is considered by Tate for three different conditions: case 1 ($R_t > Y_p$); case 2 ($R_t < Y_p$) and case 3 ($R_t = Y_p$).

Case 1 ($R_t > Y_p$)

In penetration events in which the target strength is greater than that of the projectile, the jet always penetrates as a fluid, and therefore Eq. (8.21) is valid for the duration of the penetration process, which ceases when:

$$v = \sqrt{2(R_t - Y_p)/\rho_p} \quad (8.22)$$

Rearranging Eq. (8.15) and substituting into Eq. (8.21) give the penetration depth in terms of the velocity of the projectile tail, v :

$$P_\infty = \frac{\rho_p}{Y_p} \int_v^V u l \, dv \quad (8.23)$$

where V is the impact velocity (m/s).

The instantaneous length of the projectile, l , is calculated as:

$$\frac{l}{L} = \left[\frac{v + \sqrt{v^2 + A}}{V + \sqrt{V^2 + A}} \right]^{\left(\frac{R_t - Y_p}{\mu Y_p} \right)} \exp \left[\frac{\mu \rho_p}{2(1 - \mu^2) Y_p} \left((v \sqrt{v^2 + A} - \mu v^2) - (V \sqrt{V^2 + A} - \mu V^2) \right) \right] \quad (8.24)$$

Case 2 ($R_t < Y_p$)

For impact of projectiles stronger than the target material, ie, $R_t < Y_p$, the rod is penetrating and being consumed (ie, Eq. (8.23) is valid), until the velocity, v , is equal to $[2(Y_p - R_t)/\rho_t]^{1/2}$, beyond which the rod behaves as a rigid body until brought to rest. The extra penetration by the rigid body, P_e , can be calculated using:

$$P_e = \frac{l_s}{\mu^2} \ln \left(\frac{Y_p}{R_t} \right) \quad (8.25)$$

where the length of the rod during the rigid body penetration, l_s , is calculated by:

$$\frac{l_s}{L} = \left[\frac{\sqrt{A(\mu + 1)/(\mu - 1)}}{V + \sqrt{V^2 + A}} \right]^{\left(\frac{R_t - Y_p}{\mu Y_p} \right)} \exp \left[\frac{-\mu \rho_p}{2(1 - \mu^2) Y_p} (V \sqrt{V^2 + A} - \mu V^2) \right] \quad (8.26)$$

The total penetration is calculated as:

$$P_\infty = \frac{\rho_p}{Y_p} \int_{v_c}^V u l dv + \frac{l_s}{\mu^2} \ln \left(\frac{Y_p}{R_t} \right) \quad (8.27)$$

where $v_c = \sqrt{2(Y_p - R_t)/\rho_t}$

Case 3 ($R_t = Y_p$)

When projectile strength is equal to target strength, ie, $Y_p = R_t$, the rod behaves hydrodynamically throughout the penetration event, coming to rest when both v and u are zero. In this case, Eq. (8.23) can be integrated explicitly, to give:

$$\frac{P_\infty}{l} = \frac{1}{\mu} [1 - \exp(-B(V^2 - v^2))] \quad (8.28)$$

where

$$B = \frac{\mu \rho_p}{2(1 + \mu) Y_p} \quad (8.29)$$

The effect of Alekseevskii and Tate's extension of the modified hydrodynamic theory can be observed in Figs 8.4 and 8.5. For the case $R_t < Y_p$, the predicted penetration

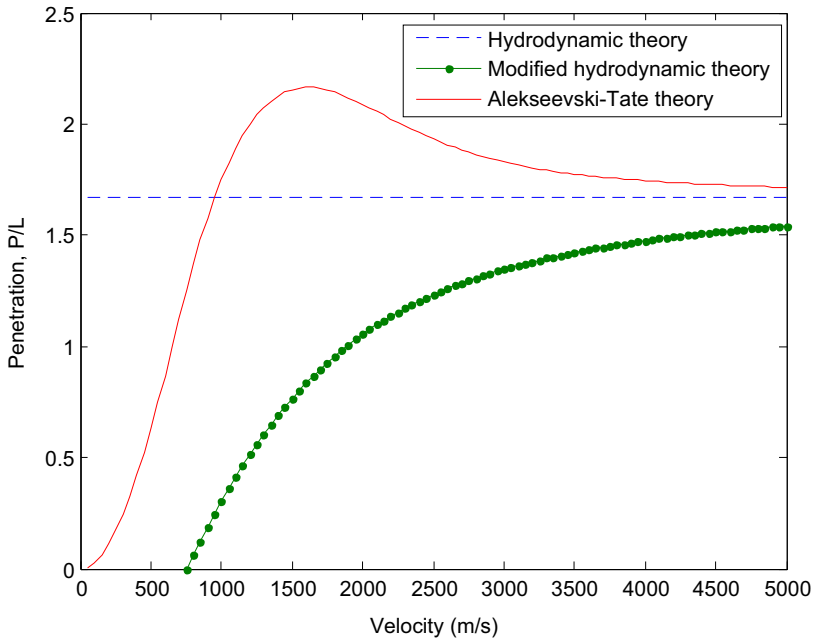


Figure 8.4 Comparison between Aleksseevskii–Tate predicted penetration with the hydrodynamic theories for the case $R_t < Y_p$. After Teland, J.A., 1999. A Review of Analytical Penetration Mechanics (FFI/RAPPORT-99/01264). Retrieved from: Kjeller.

does not monotonically increase with impact velocity, and is shown to reach a finite depth above the hydrodynamic limit. For the case $R_t = Y_p$, the predictions are seen to be much closer to the modified hydrodynamic theory, approaching the hydrodynamic limit at very high velocities.

Although widely employed, there remain a number of drawbacks to the Aleksseevskii–Tate equations. Similar to the strength term, ϕ , in the approach of Eichelberger (1956) and Allen and Rogers (1961) (see Eq. (8.11)), the definition of Tate’s projectile and target strength terms, Y_p and R_t , is widely debated. For metals, Tate (1967) recommends use of the Hugoniot elastic limit for the projectile material and $3.5 \times \text{HEL}$ for the target (with rod and target composed of the same material). For ceramic targets, the HEL multiplier is closer to 1.0 (Sternberg, 1989). In an update to the original model, Tate (1986) defined the strength parameters as a factor of the dynamic compressive yield strength, σ_{yp} :

$$Y_p = 1.7\sigma_{yp} \quad (8.30)$$

and

$$R_t = \sigma_{yt} \left[\frac{2}{3} + \ln \left(\frac{0.57E_t}{\sigma_{yt}} \right) \right] \quad (8.31)$$

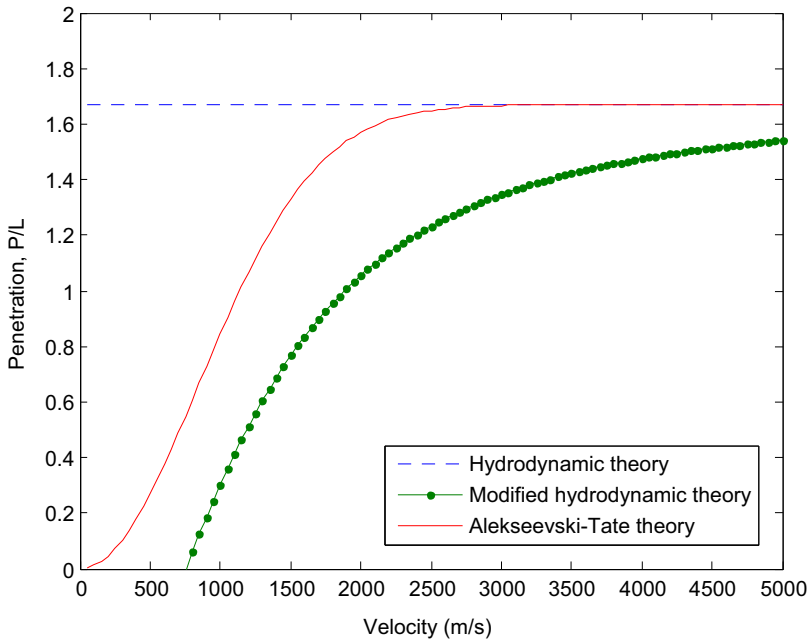


Figure 8.5 Comparison between Aleksievskii–Tate predicted penetration with the hydrodynamic theories for the case $Y_p = R_t$.

After Teland, J.A., 1999. A Review of Analytical Penetration Mechanics (FFI/RAPPORT-99/01264). Retrieved from: Kjeller.

where σ_{yp} and σ_{yt} refer to the dynamic compressive yield strength of the projectile and target material, respectively, and can be estimated from the Brinell hardness, where $\sigma_y = 3.92 \times \text{HB}$ (N/mm²) (from Recht, 1978); E_t is the Young's modulus of the target material.

Another common approach for the projectile strength term is to use the tensile strength property, as the loading state away from the projectile–target interface (ie, nonplastically deformed zone) is effectively in a state of uniaxial tension. For the target, however, the stress state is much more complex and does not correspond to any common characterisation test. Furthermore, material strengths are subject to strain-dependence, suggesting that the properties Y_p and R_t vary not only with impact velocity, but also during the penetration process.

Typically, the Aleksievskii–Tate model (ie, Eq. (8.21)) is solved numerically, or by using the exact solution developed by Walters and Segletes (1991). However, these approaches give penetration as an implicit function of time. Walters et al. (2006) developed an explicit, albeit approximate, solution to the Aleksievskii–Tate equations, which defines penetration, penetration velocity and residual rod length as a function of time.

A number of further modifications to the Aleksievskii–Tate model have been proposed. Tate (1969) evaluated the accuracy of the approach in predicting the penetration of steel rods into aluminium and lead targets. For the case $R_t < Y_p$, at

velocities below $[2(Y_p - R_t)/\rho_t]^{1/2}$ the rod behaves as a rigid body as previously discussed. This condition can lead to the prediction of decreased penetration depth with increased velocity, a phenomenon observed in impact of aluminium projectiles on lead targets (see Fig. 8.6(a)). However, for projectiles with densities much greater than that of the target material, eg, steel striking aluminium, this phenomenon was not observed (see Fig. 8.6(b)). Tate (1969) suggested that this may be

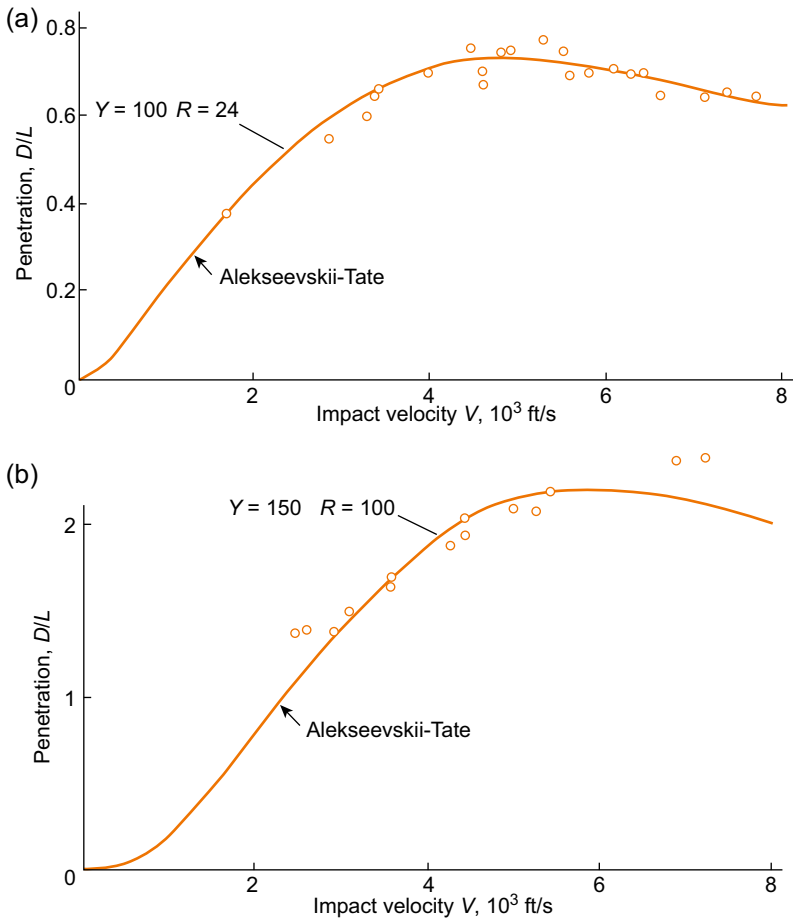


Figure 8.6 Alekseevskii–Tate prediction compared to test data for (a) impact of aluminium alloy projectiles striking lead targets and (b) Vibrac steel projectiles striking aluminium alloy targets (From Tate, A., 1969. Further results in the theory of long rod penetration. *Journal of the Mechanics and Physics of Solids* 17(3), 141–150. Retrieved from: <http://www.sciencedirect.com/science/article/B6TXB-46G2J79-5B/2/4e3a5422f14314720216082f36f73101>). For projectiles with densities much greater than that of the target the test data do not show any evidence of reduced penetration depth with increasing projectile velocity, unlike that observed for the case of strong, light projectiles into weak, dense targets. The Alekseevskii–Tate model fails to predict this continual increase in penetration depth for this class of target and projectile materials due to an inability to capture residual or secondary penetration (see Section 8.2.2).

due to an inability of the model to capture ‘residual’ or ‘secondary’ penetration, as discussed previously in [Section 8.2.2](#). As such, a possible means of improvement is the inclusion of the cavitation phase, proposed by [Christman et al. \(1964\)](#) (see [Eq. \(8.8\)](#)).

[Frank and Zook \(1987\)](#) proposed an alternate modification of the Alekseevskii–Tate model, based on separation of the penetration phases (ie, [Fig. 8.2](#)):

$$P_{\infty} = m_1 D S_{D1}(Z_0, Z_1) + (L - m_2 D) S_{L2}(Z_1, Z_2) + m D S_{D3}(Z_2, Z) \quad (8.32)$$

where $Z_0 > Z_1 > Z_2 > Z \geq 0$ are normalised velocities of the penetration phases; S_{D1} , S_{L2} and S_{D3} are characteristic functions; D is the rod diameter; m , m_1 and m_2 are adjustable parameters.

The first term in [Eq. \(8.32\)](#) describes the transient penetration in which m_1 diameters of the rod are eroded. The second term relates to penetration during the quasisteady state phase (ie, penetration as a rigid body), and the third term describes residual penetration by a constant mass penetrator (ie, shock-wave-driven crater expansion). A simplification of [Eq. \(8.32\)](#) is applied:

$$P = (L - mD) S_i + m D S_D \quad i = 1, 2, 3 \quad (8.33)$$

where m is typically between 1 and 2 (no units).

The diameter function, S_D , accounts for penetration of a nondeforming, constant mass projectile and attempts to describe both stages 1 and 3 of the Christman and Gehring curve (ie, transient and secondary penetration phases) (see [Fig. 8.2](#)). The function is defined as:

$$S_D(Z_0, Z) = \left(\frac{\rho_p}{\rho_t} + \frac{1}{3m} \right) \ln \left[\frac{1 + Z_0^2}{1 + Z^2} \right] \quad (8.34)$$

To account for stage 2 of the penetration process (ie, the primary penetration phase, in which the projectile is penetrating and eroding) [Frank and Zook \(1987\)](#) define a number of conditional functions, S_i , that can be related to the special conditions of the Alekseevskii–Tate relationship, ie: S_1 for $R_t > Y_p$; S_2 for $R_t = Y_p$; S_3 for $Y_p = R_t/(2 + \mu)$:

$$S_1(Z_0) = \begin{cases} \left(Z_0(Z_0^2 + 1 - \mu^2)^{1/2} - \mu \right) / (\mu(1 + Z_0^2)) & \text{for } Z_c < Z_0 \leq \infty \\ 0 & \text{for } 0 < Z_0 < Z_c = \mu \end{cases} \quad (8.35)$$

where $Z_0^2 = \frac{\rho_t V^2}{2R_t}$ and V is the impact velocity; $Z_c^2 = \frac{\rho_t v_c^2}{2R_t}$ and v_c is the cut-off velocity below which no penetration occurs; $\mu^2 = \rho_t / \rho_p$.

$$S_2(Z_0, Z) = \left(1 - e^{[(Z^2 - Z_0^2) / (\mu(1 + \mu))]} \right) / \mu \quad (8.36)$$

where $Z^2 = \frac{\rho_t v^2}{2R_t}$

$$S_3(Z_0, 0) = \begin{cases} [1 - (1 + \mu)/a + 1/a \exp(\mu - a)]/\mu & \text{for } a_c \leq a \leq \infty \\ 0 & \text{for } 0 \leq a \leq a_c \end{cases}$$

where $a = Z^2(2 + \mu)/(\mu(1 + \mu))$; $a_c = \mu$.

The fourth conditional function, S_4 , attempts to define the primary penetration phase for projectile/target combinations between the limit cases of S_2 (ie, $R_t = Y_p$) and S_D (ie, noneroding projectile, $Y_p/R_t \rightarrow \infty$). To achieve this, Frank and Zook apply the assumption that projectile erosion occurs at a constant rate during target penetration, ie:

$$-r \frac{dP}{dt} = \frac{dl}{dt} \quad \text{or} \quad \frac{v}{u} = \text{constant} \quad (8.37)$$

where l is the instantaneous length of the projectile (m) and r is a dimensionless constant defining the proportionality factor between projectile mass loss and penetration depth ($r = \frac{v}{u} - 1$).

The above assumption, identified as ‘radical, if not bizarre’ by the authors, is clearly questionable, yet enables a conditional function to be defined that is useful for (at the least) parametric studies in the range between S_D and S_2 :

$$S_4(Z_0, Z) = \frac{1+d}{r} \left(1 - \left(\frac{1+c^2 Z^2}{1+c^2 Z_0^2} \right)^b \right) \quad (8.38)$$

where

$$b = \frac{r(1+r)}{\mu^2 - r^2} > 0 \quad (8.39)$$

$$c^2 = \frac{\mu^2 - r^2}{\mu(1+r^2)} \quad \text{and} \quad 0 \leq c^2 < 1 \quad (8.40)$$

$$d = e/(1+r) \quad (8.41)$$

$$e = \mu^2/(3(f-m)) \quad (8.42)$$

and f is the projectile fineness ratio, $f = \frac{L}{D}$.

For the conditional statement, S_4 , as $r \rightarrow \mu$, $S_4 \rightarrow S_2$, and similarly, as $r \rightarrow 0$, $S_4 \rightarrow S_D$. The various conditional statements are plotted in Fig. 8.7.

The Frank–Zook penetration model is widely used in the ballistics fields, particularly within the US Army (eg, MUVES vulnerability estimate code). The approach has been modified for use on finite armour packages by, for example, adapting the Walker–Anderson momentum balance equation into the Frank–Zook framework (see

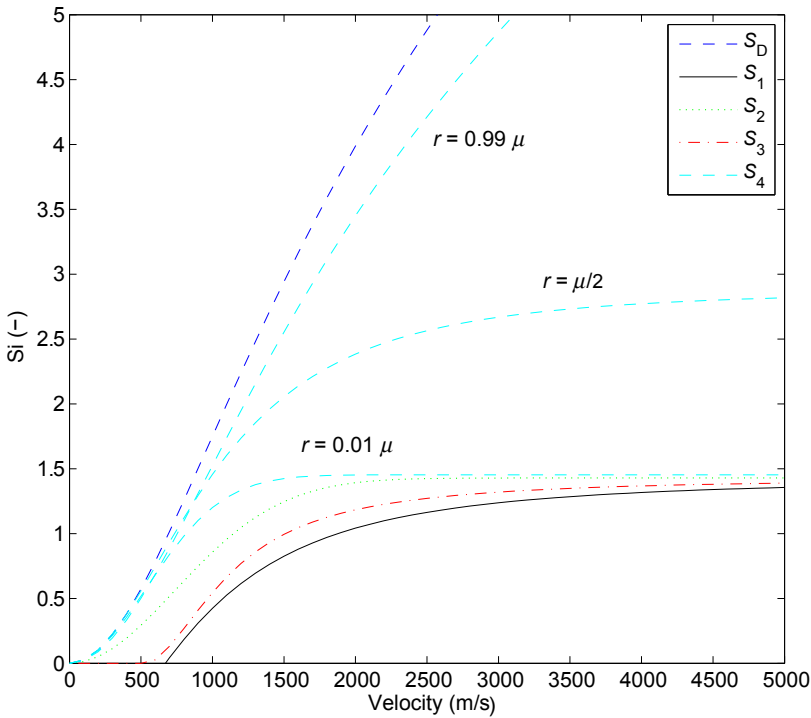


Figure 8.7 Frank–Zook characteristic ‘S’ functions related to penetrator length ($S_1 - S_4$) and diameter (S_D). The effect of proportionality factor, r , on S_4 is demonstrated.

Frank, K., Zook, J., 1987. Energy-efficient penetration and perforation of targets in the hypervelocity regime. *International Journal of Impact Engineering* 5(1–4), 277–284. [http://dx.doi.org/10.1016/0734-743x\(87\)90045-5](https://doi.org/10.1016/0734-743x(87)90045-5).

Segletes, 2000). A benefit of the Frank–Zook model over the original Alekseevskii–Tate model is its application on thin, multilayer armour packages by modification of the target effective strength term, R_t (originally H in Frank and Zook, 1991).

Galanov et al. (2001) present a modification of the Alekseevskii–Tate model suitable for penetration into plastic and brittle materials (eg, ceramics), as well as metals. The primary difference in the model is the replacement of the modified Bernoulli equivalency (Eq. (8.17)) with a system of two differential equations, which define the velocity of the contact surface and the dynamics of the cavity formation in the target during penetration, ie:

$$\frac{\rho_t}{2} \frac{d(au^*)}{dt} + \rho_t \frac{u^2}{2} + R_t = \frac{\rho_p(v-u)^2}{2} + Y_p \equiv p_c \quad (8.43)$$

$$\rho_t a \frac{d^2 a}{dt^2} + \frac{3}{2} \rho_t \left(\frac{da}{dt} \right)^2 + R_t = \frac{\rho_p(v-u)^2}{2} + Y_p \quad (8.44)$$

where $u^* = u - da/dt$ and p_c is the pressure on the contact surface (Pa); and a is the cavity radius (m).

The term $\frac{d(au^*)}{dt}$ in Eq. (8.43) takes into account the change in cavity radius during penetration. At $\frac{d(au^*)}{dt} = 0$, the equation becomes the Alekseevskii–Tate relationship. Eq. (8.44) equates the dynamic expansion of the spherical cavity in a metallic target to the pressure of the penetrator, p_c . The Galanov approach divides penetration into two phases: the elastic penetration phase and the elastic–plastic penetration phase. For impact on metal targets, these phases are differentiated by the target strength term, R_t , which is calculated as:

$$R_t = \begin{cases} \frac{4E}{9} \left(1 - \frac{a_0^3}{a^3}\right), & a_0 \leq a < a_1 = a_0 \left(1 + \frac{3}{2} \frac{Y_p}{E}\right)^{1/3}, \quad 0 \leq t \leq t_1 \\ \frac{2}{3} Y_p \left(1 + \log \left(\frac{2E}{3Y_p}\right)\right) + \frac{2}{3} Y_p \left(1 - \frac{a_0^3}{a^3}\right), & a \geq a_1, \quad t > t_1 \end{cases} \quad (8.45)$$

where values of $a \in [a_0, a_1]$ correspond to the elastic penetration phase, and the values $a > a_1$ correspond to the elastic–plastic penetration phase.

For use with elastic-brittle targets, the penetration phases are referred to as elastic and fracture, and are differentiated by an alternate governing equation, as well as a strength term, R_t . Eq. (8.44) becomes time-dependent, and is calculated for the different penetration phases as:

$$\rho_t a \frac{d^2 a}{dt^2} + \frac{3}{2} \rho_t \left(\frac{da}{dt}\right)^2 + R_t = \frac{\rho_p (v - u)^2}{2} + Y_p, \quad (0 \leq t \leq t_1) \quad (8.46)$$

$$\frac{\rho_t \gamma_1}{1 - 2\alpha} a \frac{d^2 a}{dt^2} + \left(\frac{2\rho_t \gamma_1}{1 - 2\alpha} - \frac{\rho_t \gamma_2}{2 - \alpha}\right) \left(\frac{da}{dt}\right)^2 + R_t = \frac{\rho_p (v - u)^2}{2} + Y_p, \quad (t > t_1) \quad (8.47)$$

where

$$\gamma_1 = 1 - \left(\frac{b}{a}\right)^{2\alpha-1}; \quad \gamma_2 = 1 - \left(\frac{b}{a}\right)^{2\alpha-4}; \quad a = \frac{6m}{3 + 4m}; \quad m = \frac{3\mu}{3 - 4\mu};$$

and

$$R_t = \begin{cases} \frac{4E}{9} \left(1 - \frac{a_0^3}{a^3}\right), & a_0 \leq a < a_1 \\ Y_p \left(\frac{b}{a}\right)^{2\alpha}, & a \geq a_1 \end{cases}$$

and the ratio b/a (for $a \geq a_1$, $t \geq t_1$), dependent on time, is defined by the equation:

$$\frac{1}{3} \left(\frac{a}{b} \right)^3 = \frac{(1+\nu)}{\sqrt{2E}} \sqrt{\sigma_f Y} \exp - \left(\frac{C_c(t-t_1)}{b} \right) - \frac{Y}{E} \left[\exp - \left(\frac{C_c(t-t_1)}{b} \right) - 1 \right],$$

$$a \geq a_1 \quad (8.48)$$

where σ_f is the target static tensile strength (Pa), C_c is the longitudinal wave velocity in the cracked region (m/s), Y is the yield strength (elastic–plastic target) or static strength at uniaxial compression (elastic–brittle target) (Pa), b is the radius of the pulverised region (m), t_1 is the time for transition from elastic penetration to penetration into the plastic or fractured medium (s) and ν is the velocity of the solid part of the rod (m/s).

8.2.5 Centreline momentum balance

Walker and Anderson (1995) compared the performance of the Tate model with numerical predictions of a tungsten-alloy projectile penetrating an armour steel target. Although the model was found to provide qualitatively and quantitatively comparable results, a number of discrepancies were identified, namely: an inability to account for the transient phase at the beginning of the penetration event (ie, initial formation and detachment of the shock wave, see Section 8.2.2); underestimating deceleration at the rear of the projectile late in the penetration event and overestimating projectile erosion. Recognising the difficulty in defining the projectile and target strength terms (ie, R_t and Y_p), Walker and Anderson proposed an alternative approach based on a momentum balance along the impact centreline using the coordinate system defined in Fig. 8.8.

The momentum balance along the z -axis, defined in Eulerian coordinates and with axial symmetry, is written as:

$$\rho \frac{\partial u_z}{\partial t} + \frac{1}{2} \rho \frac{\partial (u_z)^2}{\partial z} - \frac{\partial \sigma_{zz}}{\partial z} - 2 \frac{\partial \sigma_{xz}}{\partial x} = 0 \quad (8.49)$$

where ρ is the relative density term depending on location (ie, projectile or target) and σ_{ij} denotes directional components of a stress tensor.

Based on hydrocode simulations, Walker and Anderson defined three assumptions which enabled the axial momentum (Eq. (8.49)) to be integrated and an equation of motion for the interface location to be determined. An equation for the deceleration of the rear of the projectile can also be determined. The assumptions are provided as:

1. A velocity profile along the centreline in both projectile and target is specified;
2. The back end of the projectile is decelerated by elastic waves, with a magnitude proportional to the flow stress of the projectile;
3. Shear stress profile along the target centreline (in terms of the gradients of the velocity field) is specified.

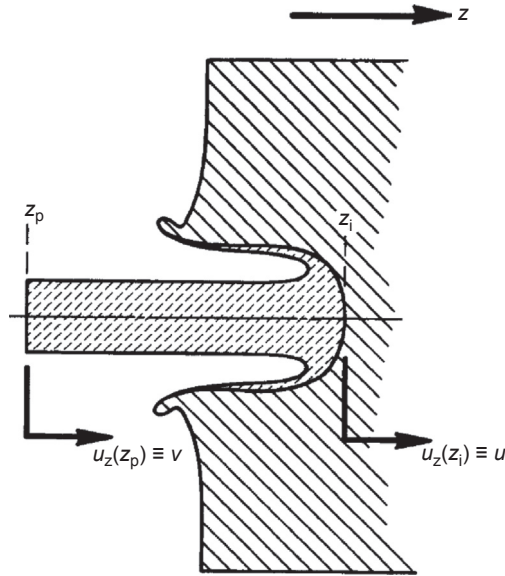


Figure 8.8 Schematic of projectile and target with coordinate notation for Walker–Anderson centreline momentum balance model.

After Walker, J.D., Anderson, C.E., 1995. A time-dependent model for long-rod penetration. *International Journal of Impact Engineering* 16(1), 19–48. Retrieved from: <http://www.sciencedirect.com/science/article/B6V3K-3Y5FP72-1F/2/ff023a977ec6a5e3f443e2cae2d1cb56>.

An in-depth discussion of the assumptions is made in [Walker and Anderson \(1995\)](#). With expressions for velocity profile along the centreline, and the assumed stress behaviour in the target, the momentum balance, [Eq. \(8.49\)](#), becomes:

$$\begin{aligned} \rho_p \dot{v}(L-s) + \dot{u} \left(\rho_p s + \rho_t R \frac{\alpha-1}{\alpha+1} \right) + \rho_p \left(\frac{v-u}{s} \right) \frac{s^2}{2} + \rho_t \dot{\alpha} \frac{2Ru}{(\alpha+1)^2} \\ = \frac{1}{2} \rho_p (v-u)^2 - \left[\frac{1}{2} \rho_t u^2 + \frac{7}{3} \log(\alpha) Y_t \right] \end{aligned} \quad (8.50)$$

where s is the extent of the plastic flow field in the projectile over which the velocity varies (with constant slope) (m); α is the dimensionless extent of the plastic flow field within the target (along the centreline) (no units); R is the crater radius in the target (m); \dot{v} is the deceleration of the projectile tail (m/s²) and \dot{u} is derivative of the interface velocity with respect to time (m/s²).

The deceleration of the projectile tail, \dot{v} , is given as:

$$\dot{v} = - \frac{\sigma_p}{\rho_p(L-s)} \left(1 + \frac{v-u}{c} + \frac{\dot{s}}{c} \right) \quad (8.51)$$

where σ_p is the magnitude of the stress wave in the projectile (negative sign corresponds to a compressive wave) (Pa); c is the elastic bar wave speed, $c = \sqrt{E/\rho}$; \dot{s} is the derivative of the extent of the plastic zone along the axis over which the velocity

changes with respect to time (m/s) and the rate of change of projectile length, \dot{L} , is the difference between the penetration velocity, u , and the speed of the tail, v , ie:

$$\dot{L} = -(v - u) \quad (8.52)$$

If the two measures of spatial extent, s and R , are set to zero, and the Young's modulus is made very large such that $c \rightarrow \infty$, Eqs (8.50)–(8.52) become:

$$-\rho_p \dot{v}L + \frac{1}{2}\rho_p(v - u)^2 = \frac{1}{2}\rho_t u^2 + \frac{7}{3}\log(\alpha)Y_t \quad (8.53)$$

$$\dot{v} = -\sigma_p/\rho_p L \quad (8.54)$$

$$\dot{L} = -(v - u) \quad (8.55)$$

which correspond to Tate's original model where:

$$Y_p = \sigma_p, \text{ ie, flow stress of the projectile} \quad (8.56)$$

$$R_t = \frac{7}{3}\log(\alpha)Y_t \quad (8.57)$$

As such, the Walker–Anderson model defines a target resistance, R_t , that varies with the extent of plastic flow zone and the flow stress, Y_t , of the target. Alternatively, the second, third and fourth terms of Eq. (8.50), along with the term $(7/3)\log(\alpha)Y_t$ define a R_t that varies with time, as suggested by Anderson et al. (1992). Initial conditions for the model require an initial interface velocity (particle velocity in the Rankine–Hugoniot relations), and a relationship between crater radius and impact velocity.

The model is shown in Walker and Anderson (1995) to provide excellent agreement with rigid-body penetration of steel projectiles into aluminium targets, penetration of eroding tungsten rods into steel targets, and penetration of tungsten alloy and steel projectiles into steel targets. Discrepancies in initial predictions were overcome by including velocity dependence in definition of the plastic flow field extension within the target, α , ie:

$$\left(1 + \frac{\rho_t u^2}{Y_t}\right) \sqrt{K_t - \rho_t \alpha^2 u^2} = \left(1 + \frac{\rho_t \alpha^2 u^2}{2G_t}\right) \sqrt{K_t - \rho_t u^2} \quad (8.58)$$

where G_t is the shear modulus of the target and K_t is the bulk modulus of the target.

The penetration of an $L/D = 10$ tungsten alloy projectile into armour steel at 1.5 km/s, predicted by the Walker–Anderson and Alekseevskii–Tate models, is compared to a numerical prediction in Fig. 8.9. Although both models provide a reasonable reproduction of the numerical data, the initial penetration of the projectile nose and final deceleration of the tail are more accurately reproduced by the Walker–Anderson model. Additional improvements are made in the prediction of residual projectile length compared to that of the Alekseevskii–Tate model (see Walker and Anderson, 1995).

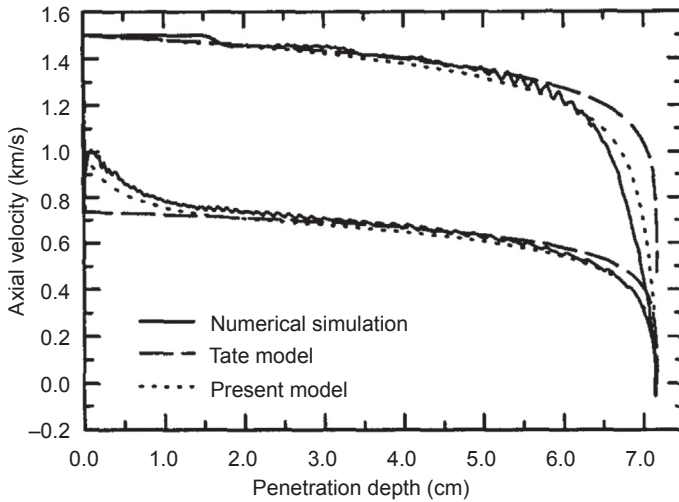


Figure 8.9 Penetration measured at the nose (lower curves) and tail (upper curves) of an $L/D = 10$ tungsten alloy projectile into armour steel at 1.5 km/s predicted by the Walker–Anderson centrelime momentum balance model and the Alekseevskii–Tate model (see Section 8.2.4) compared to numerical simulation.

Walker, J.D., Anderson, C.E., 1995. A time-dependent model for long-rod penetration. *International Journal of Impact Engineering* 16(1), 19–48. Retrieved from: <http://www.sciencedirect.com/science/article/B6V3K-3Y5FP72-1F/2/ff023a977ec6a5e3f443e2cae2d1cb56>.

8.2.6 One-dimensional finite difference discretisation

Woodward (1982) developed a model, which considered the projectile and target as impacting cylinders. The surrogate cylinders mushroom upon impact, with lateral extension of the target restricted by a constraint factor to account for the surrounding material. The portion of the projectile, which enters the target, is also subject to a lateral constraint. In Woodward's model, the impacting cylinders are discretised into a number of elements (see Figs 8.10 and 8.11), for which the equations of motion are given as:

$$N_{i+1,j} - N_{i,j} - T_{i,j} - m_i \ddot{u}_{i,j} = 0, \quad \text{for projectile elements} \quad (8.59)$$

$$N_{i,j} - N_{i-1,j} - T_{i,j} - m_i \ddot{u}_{i,j} = 0, \quad \text{for target elements} \quad (8.60)$$

where m_i is the mass of element i at time j ; $N_{i,j}$, $N_{i+1,j}$, $N_{i-1,j}$ describes the forces in the i th, $(i+1)$ th and $(i-1)$ th elements, respectively, at time j ; $T_{i,j}$ is the shear force on element i at time j ; $\ddot{u}_{i,j}$ is the acceleration of element i at time j .

The relation between the acceleration of each individual element, $\ddot{u}_{i,j}$, and its position, u_i , is obtained using the central difference equation:

$$u_{i,j+1} = \ddot{u}_{i,j}(\delta t)^2 + 2u_{i,j} - u_{i,j-1} \quad (8.61)$$

where δt is the time increment, $\delta t = t_{j+1} - t_j$.

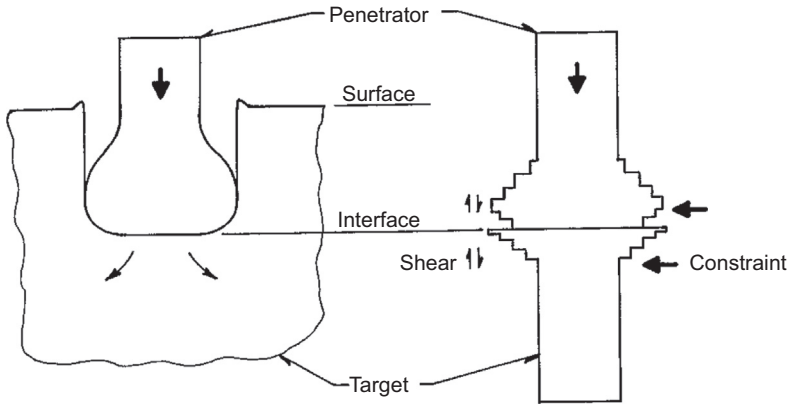


Figure 8.10 Schematic of the correspondence between the geometry of penetration (left) and the model using impacting cylinders.

Woodward, R., 1981. Modelling Penetration by Slender High Kinetic Energy Projectiles (MRL-R-811). Retrieved from: Ascot Vale.

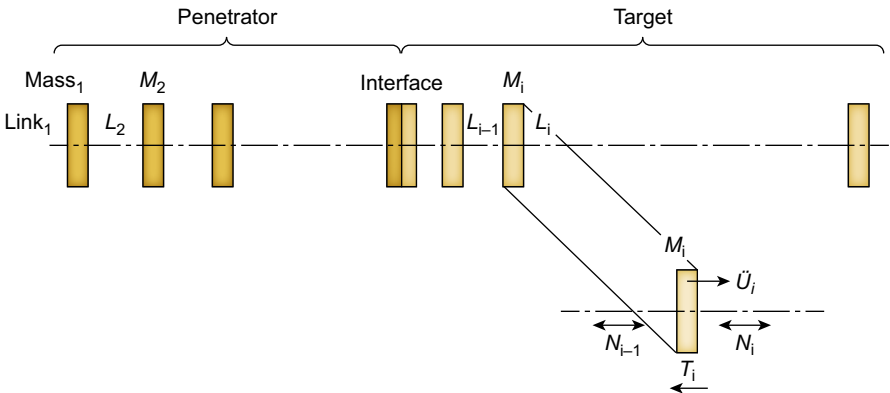


Figure 8.11 Division of the penetrator and target into a series of elements, each containing a point mass and a mass less link.

Woodward, R., 1981. Modelling Penetration by Slender High Kinetic Energy Projectiles (MRL-R-811). Retrieved from: Ascot Vale.

The magnitude of the shear force, $T_{i,j}$, on an element of material is given by:

$$|T_{i,j}| = \frac{\pi}{\sqrt{3}} D_{ij} h_{ij} \sigma_0^*, \quad \text{for projectile elements} \quad (8.62)$$

$$|T_{i,j}| = \frac{\pi}{\sqrt{3}} D_{20,j} h_{ij} \sigma_{0t}, \quad \text{for target elements (assuming 20 projectile elements)} \quad (8.63)$$

where D_i is the diameter of element i ($D_{20,j}$ is used for all target elements as all target elements are taken to have a diameter equal to the projectile interface diameter) (m);

h_i is the element height (m); σ_{0p} is the stress constant for the projectile material (Pa); σ_{0t} is the stress constant for the target material (Pa); σ_0^* is the lesser of σ_{0p} or σ_{0t} (Pa) and σ_0 refers to a stress constant fit to a uniaxial true stress—true strain curve such that $\sigma = \sigma_0 \epsilon^n$.

The sign of the shear force depends on the direction of deformed element movement and is such that the shear force retards the movement. The normal force, N_i , on an element is given by:

$$N_i = (\sigma_i + \sigma_{ri})(A_i + A_{i-1})/2, \text{ for projectile elements} \quad (8.64)$$

$$N_i = (\sigma_i + \sigma_{ri})(A_i + A_{i+1})/2, \text{ for target elements} \quad (8.65)$$

where σ_i is the compressive flow stress of the material (Pa); A_i is the area of element i (constant element volume assumed) (m^2); σ_{ri} is an increment in stress due to radial inertia (Pa), calculated as:

$$\sigma_{ri} = \frac{3}{64} \rho_p \left(\frac{D_i}{h_i} \right)^2 (\dot{u}_i - \dot{u}_{i-1})^2, \text{ for projectile elements} \quad (8.66)$$

and

$$\sigma_{ri} = \frac{3}{64} \rho_t \left(\frac{D_i}{h_i} \right)^2 (\dot{u}_{i+1} - \dot{u}_i)^2, \text{ for target elements} \quad (8.67)$$

Shock wave formation and propagation is not accounted for in Woodward's model, as these processes are assumed to occur within a few microseconds post-impact, compared to the deformation process, which occurs over an order of magnitude longer time.

8.3 Analytical modelling of the perforation of finite metallic armour targets

The perforation of finite armour targets is a more difficult process to analytically model than penetration into semi-infinite plates due to the increased complexity of the stress state between the projectile and rear surface of the armour target. Depending on the geometry of the projectile and target, material of the projectile and target and impact conditions (ie, velocity and incidence), the armour can be perforated in a wide variety of mechanisms. Typically, analytical models will be developed from, and applied to, a single perforation mode (eg, ductile hole formation).

8.3.1 Cavity expansion theory

The perforation of armoured plates by nondeforming projectiles in ductile hole formation is amongst the simplest ballistic conditions, and as such is readily modelled

by analytical methods. The work done in expanding a cylindrical hole in a thin plastic sheet from zero initial radius, assuming a plane stress condition, is determined by:

$$W_{\text{DHF}} = \pi r^2 h_0 C Y \quad (8.68)$$

where r is the final radius of the hole, equal to the calibre of the projectile; h_0 is the initial thickness of the target; Y is the yield stress of the target and C is a constant alternatively reported as, for example: 2.0 (Bethe, 1941), 1.33 (Taylor, 1948) and 1.92 (Hill, 1949).

The ballistic limit, V_{bl} , is then determined by equating the work done in cavity expansion to the kinetic energy of the projectile (note that in the following discussions the V_{50} [a statistical parameter representing a median velocity] may sometimes be used interchangeably with the V_{bl}),

$$\frac{1}{2} m_p V_{\text{bl}}^2 = \pi r^2 h_0 C Y \quad (8.69)$$

where m_p is the mass of the projectile and thus,

$$V_{\text{bl}} = \sqrt{\frac{2\pi r^2 h_0 C Y}{m_p}} \quad (8.70)$$

Woodward (1978) reviewed the accuracy of the cavity expansion theory (Eq. (8.69)) with Hill's value of $C = 1.92$ and determined that for a range of conditions the work performed, and thus ballistic limit, was underestimated, particularly for materials with high levels of work hardening. The flow stress at a true strain of 1.0, σ_0 , was proposed in place of the yield strength in Eq. (8.68).

Forrestal et al. (1990) and Piekutowski et al. (1996) proposed a similar application of cavity expansion theory for predicting the ballistic limit of plates perforated through ductile hole formation. Rather than the yield stress, Y , proposed by Taylor (1948) or flow stress, σ_0 , proposed by Woodward (1978), they define the stress required to expand the cylindrical cavity, σ_s , as:

$$\sigma_s = \frac{Y}{\sqrt{3}} \left(1 + \left(\frac{E}{\sqrt{3}Y} \right)^n \int_0^b f(x) dx \right) \quad (8.71)$$

where

$$f(x) = \frac{(-\ln(x))^n}{1-x}, \quad 0 < n < 1 \quad (8.72)$$

$$b = 1 - \frac{2(1+\nu)Y}{\sqrt{3}E} \quad (8.73)$$

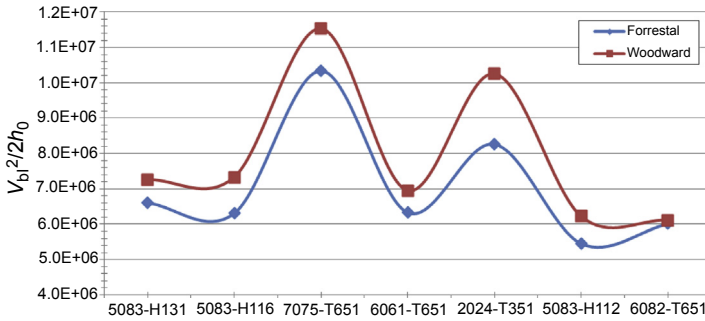


Figure 8.12 Comparison between the Forrestral and Warren (2009) and Woodward (1978) cavity expansion models for a range of aluminium alloys against 7.62 mm APM2 projectiles.

and Y is the target yield strength; E is the target elastic modulus and n is the strain-hardening exponent used to fit the stress–strain curve, from:

$$\sigma = \begin{cases} E\varepsilon, & \sigma < Y \\ Y(E\varepsilon/Y)^n, & \sigma \geq Y \end{cases} \quad (8.74)$$

For a given projectile, Forrestral and co-workers simplify Eq. (8.70) according to Forrestral et al. (2013):

$$V_{bl} = K\sqrt{\sigma_s h_0} \quad (8.75)$$

where K is a constant that can be empirically fit to ballistic test results.

In Fig. 8.12 the difference between the Woodward analytical model and Forrestral et al. scaling law is plotted in terms of $V_{bl}^2/2h_0$ for a range of aluminium alloys against the 7.62 mm APM2 projectile. Clearly, for this projectile and this range of target materials there is minimal difference in the two approaches, however the Woodward model would predict a higher V_{50} in all instances. Interestingly, for a fixed projectile diameter, Woodward accounts for the difference in penetration capability for different projectiles through the mass, while Forrestral considers the explicit geometry (in terms of projectile nose shape, shank and nose length).

8.3.2 Plasticity theory

Woodward and Cimpoeu (1998) and Cimpoeu (2002) define a two-stage model for predicting the ballistic limits of rigid, perfectly plastic homogeneous and laminate metal plates. The model treats perforation as a process of projectile indentation into the target armour (stage one), and either shear, dishing, or ductile hole formation failure of the target rear side (stage two). Assuming simplified projectile–target equilibrium, shown in Fig. 8.13, if the force required to indent the target is less than the resistance of the target plug to move forward by shear, then indentation and compression of the target material will occur.

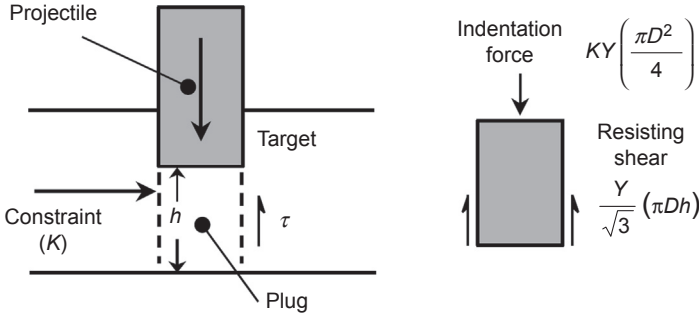


Figure 8.13 Simple force equilibrium used in Woodward and Cimpoeu (1998). If the indentation force is greater than the shear resistance of the plug, the target material is first indented and compressed.

The indentation force, F_1 , is equal to the cross-sectional area of the projectile multiplied by the flow stress and a constraint factor, K , which accounts for the lateral confinement of the target plug by the surrounding target material, ie:

$$F_1 = KY \left(\frac{\pi D^2}{4} \right) \quad (8.76)$$

where Y is the target flow stress (Pa); K is the constraint factor = 2.7 from Woodward and Cimpoeu (1998) (no units) and D is the projectile diameter (m).

The resistance of the target to forward movement by shear of a cylindrical plug in front of the projectile, F_S , is equal to the plug cross-sectional area by the shear flow stress, ie:

$$F_S = \frac{Y}{\sqrt{3}} (\pi D h) \quad (8.77)$$

where h is the target thickness ahead of the projectile (m).

Eqs (8.76) and (8.77), the force to achieve forward movement of the target plug is less than the force to indent the target when the remaining target thickness is $\sqrt{3}/4K$ times the projectile diameter, at which point it becomes easier for a plug to shear from the target (see Fig. 8.14).

For targets thinner than $\sqrt{3}/4K$ times the projectile diameter, stage one of the model can be ignored and failure is assumed to occur by either dishing (for $h < D/2$) or ductile hole formation (for $D/2 < h < \sqrt{3}/4KD$). The dishing failure mechanism involves both stretching and bending deformation. A modification of the solutions of Taylor (1948) and Thompson (1995), which includes plate bending with radial and tangential curvature, was developed (Woodward and Cimpoeu, 1998).

For dishing, the work done (in joules) is:

$$W_D = \pi D Y h_0 (D + 2\pi h_0) / 8 \quad (8.78)$$

where h_0 is the initial thickness of the target (m).

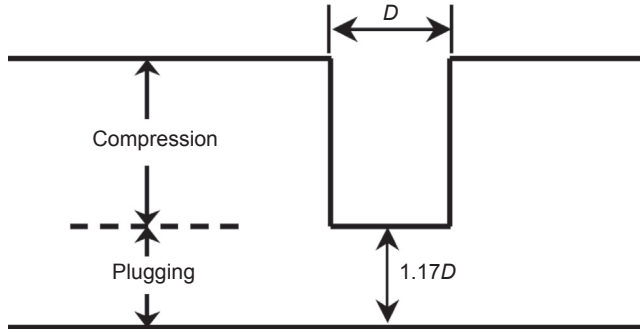


Figure 8.14 Schematic of target and crater geometry at the limit of projectile indentation and onset of target plugging in the Woodward plasticity model.

From Woodward, R.L., Cimpoeu, S.J., 1998. A study of the perforation of aluminium laminate targets. *International Journal of Impact Engineering* 21 (3), 117–131.

The first term in Eq. (8.78) refers to the work done in stretching, while the second refers to that done in bending.

For ductile hole formation (after Woodward, 1978):

$$W_{\text{DHF}} = \pi D^2 h_0 Y / 2 \quad (8.79)$$

For targets thicker than $\sqrt{3}/4K$ times the projectile diameter, failure is assumed to occur as a result of ductile shear plugging. In this case, work done in perforating the target is summed from that done in indenting the target, W_I , and shearing the target plug, W_S , ie:

$$W_{\text{I,S}} = W_I + W_S \quad (8.80)$$

where

$$W_I = \pi D^2 KY (h_0 - 1.17D) / 4 \quad (8.81)$$

and

$$W_S = \pi h^2 DY / 2\sqrt{3} \quad (8.82)$$

For conically tipped projectiles, additional work is assumed to be done in forming a conical indentation in the impact side of the target plug:

$$W_C = \frac{\pi}{24} D^3 KY \cot \frac{\Phi}{2} \quad (8.83)$$

where Φ is the angle of the conical tip of the projectile.

The ballistic limit velocity, V_{bl} , is calculated from a work–energy balance, assuming the projectile is brought to rest, ie:

$$W = \frac{1}{2} m V_{bl}^2 \quad (8.84)$$

where W is the work done in perforating the target by dishing (W_D , from Eq. (8.78)), ductile hole formation (W_{DHF} , from Eq. (8.79)), indentation and shear plugging (W_{LS} , from Eq. (8.80)) or other appropriate failure mechanisms; and m is the projectile mass (kg).

Although very simple, the Woodward plasticity model is shown in Woodward and Cimpoeu (1998) and Cimpoeu (2002) to provide a reasonable level of accuracy in predicting the ballistic limits of a wide range of homogeneous and metal laminate plate combinations. For impacts in which the projectile undergoes significant deformation, erosion or fracture, simple plasticity-based approaches such as this are invalid.

8.3.3 Ravid–Bodner multistage model

Ravid and Bodner (1983) developed a 2D analytical model for dynamic perforation of viscoelastic plates by rigid projectiles, later extended to consider eroding projectiles (Ravid et al., 1994). In their model, the perforation process is separated into a five-phase sequence, namely: (1) dynamic plastic penetration; (2) bulge formation; (3) bulge advancement; (4) plug formation and exit and (5) projectile exit.

In stage 1 of the perforation process, a simplified plastic flow field is developed about the projectile using three rectangular zones (ie, regions I through III in Fig. 8.15).

Within the rectangular flow zones, velocities normal to a zone boundary are required to be continuous, while discontinuities in the tangential direction lead to shear energy dissipation. Material ejected from the front surface of the flow field leads to formation of a crater lip, maintaining zero volume change. A plastic zone develops ahead of the projectile, extending a distance αR into the target, with radius ηR , where α and η are obtained by minimising the nondimensionalised function for work rate in the target, \dot{W}'_T , at each increment of penetration, Δx , where:

$$\dot{W}'_T = \dot{W}'_V + \dot{W}'_s + \dot{W}'_f + \dot{W}'_k \quad (8.85)$$

where \dot{W}'_V is the nondimensional plastic work rate in a volume, V ; \dot{W}'_s is the nondimensional shear strain energy rate; \dot{W}'_f is the nondimensional frictional energy rate and \dot{W}'_k is the nondimensional convective inertial energy rate.

In stage 2 of the model, the front of the plastic zone described in stage 1 reaches the rear surface of the target, leading to the formation of a spherical bulge, as shown in Fig. 8.16. Growth of the crater lip ceases in this stage, and bulge growth is driven by the conical section between the projectile tip and target rear surface, according to:

$$\pi \eta_b^3 R^3 \frac{(1 - \cos \beta)^2 (2 + \cos \beta)}{3 \sin^3 \beta} = \pi R^2 (x - x_0) \quad (8.86)$$

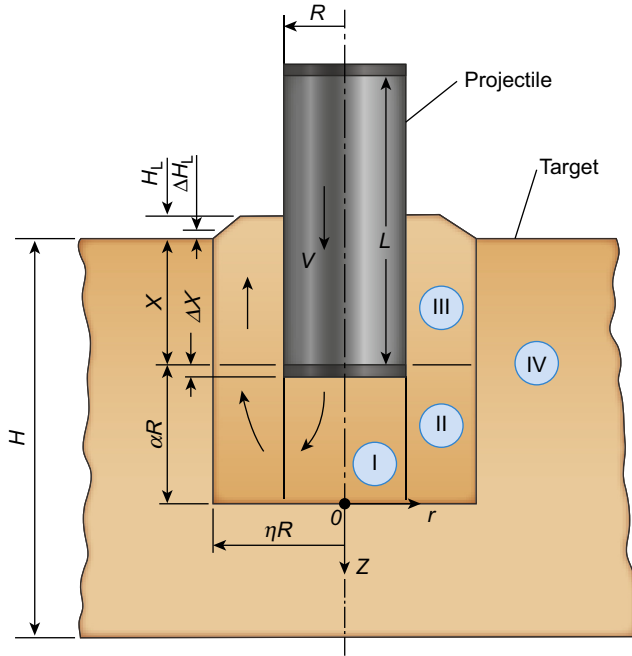


Figure 8.15 Plastic flow field for stage 1.

From Ravid, M., Bodner, S.R., 1983. Dynamic perforation of viscoplastic plates by rigid projectiles. *International Journal of Engineering Science* 21(6), 577–591. [http://dx.doi.org/10.1016/0020-7225\(83\)90105-2](http://dx.doi.org/10.1016/0020-7225(83)90105-2).

where $\eta_b R$ is the radial extent of the bulge; $x - x_0$ is the displacement of the projectile from the end of stage 1; β is the semicone angle of the conical section driving bulge growth.

During stage 2 of the penetration, material in zone I is moving uniformly with the projectile velocity, v , such that a tangential velocity discontinuity exists on the interface between zones I and II. The flow field in zone II includes strain rate components in the radial, $\dot{\epsilon}_{rr}$, and angular, $\dot{\epsilon}_{\theta\theta}$, directions of a polar coordinate system established at the point '0' (see Fig. 8.16), as well as a shear strain component, $\dot{\epsilon}_{r\theta}$, where:

$$\dot{\epsilon}_{rr} = -2v \left(\frac{r_1^2}{r^3} \right) \cos \theta \quad (8.87)$$

$$\dot{\epsilon}_{\theta\theta} = \dot{\epsilon}_{\phi\phi} = v \left(\frac{r_1^2}{r^3} \right) \cos \theta \quad (8.88)$$

$$\dot{\epsilon}_{r\theta} = -\frac{1}{2} v \left(\frac{r_1^2}{r^3} \right) \sin \theta \quad (8.89)$$

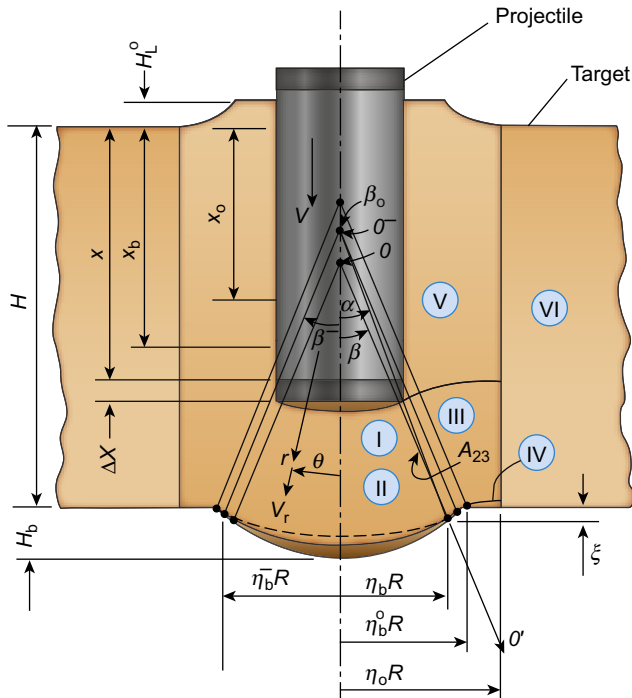


Figure 8.17 Plastic flow field for stage 3.

From Ravid, M., Bodner, S.R., 1983. Dynamic perforation of viscoplastic plates by rigid projectiles. *International Journal of Engineering Science* 21(6), 577–591. [http://dx.doi.org/10.1016/0020-7225\(83\)90105-2](http://dx.doi.org/10.1016/0020-7225(83)90105-2).

where α is the radial angle from the origin at the previous location, 0^- , to the new boundary limit $\eta_b R$ and the bulge height, H_b , is calculated as $H_b = \xi + (\eta_b R / \sin \beta) (1 - \cos \beta)$.

Ravid and Bodner consider three levels of energy resistance to ballistic impact, which are defined by the target failure mode. Adiabatic shearing and brittle failure are considered ‘low-energy’ modes of plugging failure, and may occur during stage 2 or 3 of the perforation process. In the case of adiabatic shearing, formation of shear bands along the A_{23} surface (see Fig. 8.17) would lead to a slip interface, thereby separating zone III from the developing plug consisting of zone I and II material. Adiabatic shear failure will occur when:

$$\gamma = \sqrt{3\varepsilon} \quad (8.91)$$

Stage 4 of the perforation model refers to the terminal phase, during which the target is perforated and material is ejected into the protected volume. For failure by plugging, a straightforward extension of stage 3 is made, where the material in zone

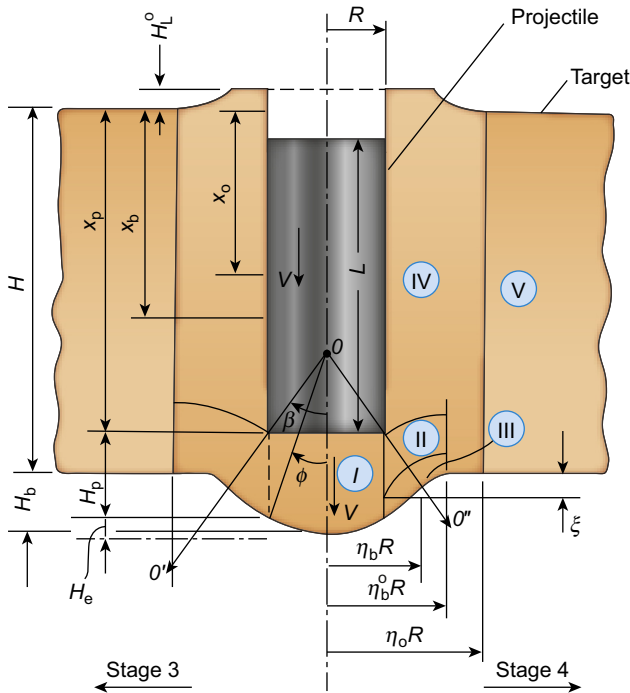


Figure 8.18 Plastic flow field for stage 4.

From Ravid, M., Bodner, S.R., 1983. Dynamic perforation of viscoplastic plates by rigid projectiles. *International Journal of Engineering Science* 21(6), 577–591. [http://dx.doi.org/10.1016/0020-7225\(83\)90105-2](http://dx.doi.org/10.1016/0020-7225(83)90105-2).

I is assumed to move at the projectile velocity, v , and is restrained by shear stresses in zone II (refer to Fig. 8.18).

The bulge will continue to advance until the ultimate shear strain in zone II is exceeded, upon which the cylindrical plug (zone I) will detach. The plug length, H_p , is calculated from:

$$H_p = R(\cot \phi - \cot \beta_p) \quad (8.92)$$

where ϕ is the radial angle from the origin, 0, to the limit of the detached material measured on the bulge surface; β_p is the sector angle for the flow field of stage 2 or 3 at the onset of plug formation, $x = x_p$.

In the event that the ultimate shear strain in zone II is not exceeded, bulge growth will continue until ductile failure of the target occurs. In this case, a spherical cap with radius larger than the projectile and consisting of material from both zones I and II will form on the front of the projectile.

The possibility of adiabatic shearing and brittle failure during stage 2 or 3 is also addressed in Ravid and Bodner (1983). These ‘low-energy’ modes of plugging failure

lead to ejection of zone I and (possibly) zone II from the target plate, the velocity of which can be approximated using momentum balances.

8.3.4 Breakout (Walker–Anderson)

The Walker–Anderson momentum balance model (Walker and Anderson, 1995) is applicable for penetration up to a depth at which the target rear surface affects the penetration process. From this point onwards, modifications are required in order to model plate perforation.

Walker (1999) extended the Walker–Anderson model flow field to include bulging at the back of a finite target. The velocity field is a blend of the original deep penetration field, with that of pure shear deformation — weighted by an empirical blending parameter, λ . Additionally, the velocity flow field at the outer edge of the plastic region is no longer zero (as in the original model), but is inversely proportional to the square of the radial offset, r . Chocron et al. (1999) supplement Walker's extension with a simplistic failure criterion based on equivalent plastic strain at the target rear surface. However, for target plates which commonly fail through brittle shear (eg, thin, high-hardness materials), the Chocron et al. model can overpredict perforation limits. The 'Breakout' program for terminal ballistics developed by Southwest Research Institute is a visualisation of the Walker–Anderson model incorporating both extensions. Screenshots from the program are provided in Fig. 8.19.

Ravid et al. (1998) proposed a unification of the Walker–Anderson model with their failure modes. In this unified model, the momentum balance equation is used to determine the penetration velocity of the projectile and extension of the plastic

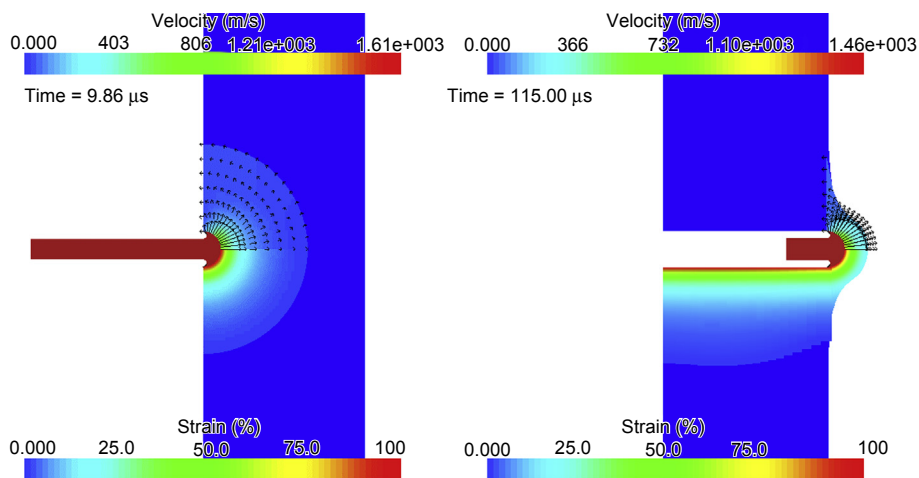


Figure 8.19 Screen shots from the Breakout program visualising penetration predicted by the Walker–Anderson–Chocron analytical model.

Shearn, M., 2000. Breakout Ballistic Simulation Program V1.1.

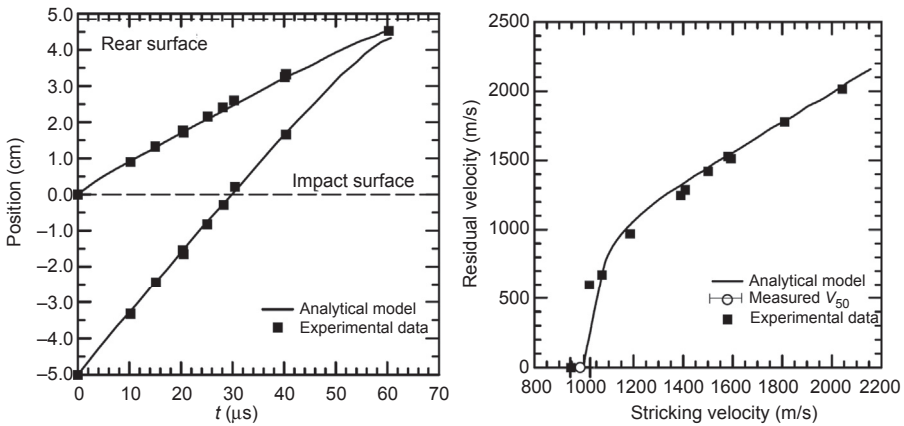


Figure 8.20 Predictions of a long-rod tungsten alloy projectile penetrating a thick steel target (HB = 415). Left: comparison of projectile motion (nose and tail locations); right: residual projectile velocity.

From Chocron, S., Anderson, C.E., Walker, J.D., Ravid, M., 2003. A unified model for long-rod penetration in multiple metallic plates. *International Journal of Impact Engineering* 28(4), 391–411. Retrieved from: <http://www.sciencedirect.com/science/article/B6V3K-473FV4K-1/2/f684ae5a3baeadd3369e036ca2a87d85>.

boundary. Once the plastic flow field reaches the rear target surface, bulge formation, advancement and target failure are adapted to the failure modes proposed in [Ravid and Bodner \(1983\)](#).

[Chocron et al. \(2003\)](#) extended the unified model of [Ravid et al. \(1998\)](#) for application on multiplate target configurations. Upon failure of a target plate, Chocron et al.'s model assumes the projectile faces no further resistance to penetration until impact with consecutive armour plates. Continued erosion of the projectile following perforation, due to residual stresses in the plastic zone, is included in the model, providing the initial conditions (along with velocity) for impact upon backup armour plates. The Ravid and Bodner model defines seven modes of target failure: ductile exit, early brittle shear failure (two modes), brittle shear failure (three modes) and fragmentation. Although a number of these failure modes define 'plugging' failure, in which a truncated conical section of target material is ejected at velocities close to that of the penetration velocity, any impact of target material on backup armour plates is not included in Chocron et al.'s model. Nonetheless, the model is shown in [Chocron et al. \(2003\)](#) to provide excellent agreement with experiments and numerical simulations of, for example, long-rod tungsten-alloy projectiles against a variety of hard steel targets (see [Fig. 8.20](#)).

8.3.5 Penetration/perforation of laminated materials/targets

[Woodward and Crouch \(1988\)](#) were responsible for the development of one of the early analytical models to estimate the critical perforation velocity of a blunt

projectile striking a laminated target consisting of a number of structurally bonded layers of metal (eg, adhesively bonded aluminium laminates [ABALs] — see Chapter 4). The analytical model, LAMP, a simple FORTRAN program, divided the perforation process into two: a plug formation and acceleration stage, followed by dishing of the rear part of the target. It also accounted for the effects of interlaminar shear. More significantly, the input parameters for each stage in the model were derived from simple, simulating mechanical tests, especially the constrained compression test (CCT) (see Chapter 10). LAMP was successfully used to predict the perforation resistance of a number of different metal laminates against blunt projectiles (Woodward and Crouch, 1988).

Scott (2011) extended this approach by modifying the detail of stage 1 to include a membrane stretching component since, for some polymeric laminates, the front plies were observed to stretch and deform prior to shearing. Scott also used the CCT to illustrate the applicability of this analytical approach to the high performance ultrahigh molecular weight polyethylene (UHMWPE) laminates (see Chapter 5).

More recently, Moriniere et al. (2014) reviewed modelling methods developed for fibre metal laminates (FMLs) — this review included a broad examination of the various analytical models by Reid and Wen (2000), Abdullah and Cantwell (2006) and Hoo Fatt et al. (2003) for high-velocity impacts against a range of FMLs including GLARE. Key aspects of the impact modelling included aluminium ply deformation, stiffness degradation, projectile nose shape, target size, and strain rate, as well as material characteristics like alloy grade, fibre pretreatment, quality of adhesion and delamination resistance. They concluded that classical laminate theory integrated into an energy-balance model appears to be the most promising approach due to its generic nature. Of course, because of the multiplicity of material and target parameters, in a multimaterial, multilayered system, this task is not trivial. Furthermore, very little work has been performed on curved surfaces (rather than flat) or using multiple impacts, so there are many decades of work left for the analytical modeller!

8.3.5.1 Case study 1: predicting the performance of an Al alloy against armour piercing projectiles

Forrestal et al.'s scaling model (Eq. (8.75)) requires empirical determination of a constant, K , related to the projectile material and geometry. Once defined for a particular projectile, the scaling constant can be applied to any target which is perforated in ductile hole formation to provide an estimate of the V_{50} ballistic limit.

Consider the ballistic data presented in Table 8.3 and the mechanical properties presented in Table 8.4 for a range of aluminium alloys. The ballistic data are plotted in Fig. 8.21 in terms of plate thickness and $(\sigma_s h_0)^{1/2}$ from Eq. (8.75). Using a least squares fit the constant, K , can easily be determined.

Consider now Al2139-T8, which was developed in order to meet a requirement for a high-strength, high-fracture toughness 2XXX series alloy for damage-tolerant applications. The material showed promising performance when subject to mechanical

Table 8.3 Compiled ballistic limit data for impact of 7.62 mm APM2 on aluminium alloy plates

Alloy	Thickness (mm)	V ₅₀ (m/s)	Source
2024-T351	26	651.7	Ryan et al. (2015a)
2024-T351	30	715.4	
2024-T351	34	773.9	
2024-T351	38	830.6	
5083-H112	20	474.3	
5083-H112	30	588.6	Borvik et al. (2010)
5083-H112	40	697.7	
5083-H116	20	492	
5083-H116	40*	722	
5083-H116	60**	912	
5083-H131	26	588	Forrestal et al. (2014)
5083-H131	37.8	712	
5083-H131	38	738.5	Ryan et al. (2015a)
5083-H131	50.9	876	Forrestal et al. (2014)
5083-H131	54.7	890	
5083-H131	57.2	927	
6061-T651	25	578.3	Ryan et al. (2015a)
6061-T651	25.7	596	Gooch et al. (2007a)
6061-T651	26	583	
6061-T651	38.8	754	
6061-T651	50	896.2	Ryan et al. (2015a)
6061-T651	51.2	883	Gooch et al. (2007a)
6082-T651	20	501.0	Forrestal et al. (2014)
7075-T651	20	628	Forrestal et al. (2010)
7075-T651	26	718.4	Ryan et al. (2015a)
7075-T651	30	784.3	
7075-T651	32	817.5	
7075-T651	38	909.5	Forrestal et al. (2010)
7075-T651	40*	909	

*2 × 20 mm thick plates.

**3 × 20 mm thick plates.

Table 8.4 Compiled mechanical properties and power-fit stress–strain relationships for a range of aluminium alloys

Alloy	E (GPa)	Y (MPa)	n (–)	Source
2024-T351	73.1	290	0.170	Ryan et al. (2015a)
5083-H112	70.3	225	0.110	
5083-H116	70.3	240	0.108	Borvik et al. (2010)
5083-H131	70.3	276	0.100	Ryan et al. (2015a)
6061-T651	69	262	0.085	Piekutowski et al. (1996)
6082-T651	69	265	0.060	Forrestal et al. (2014)
7075-T651	71.1	520	0.060	Forrestal et al. (2010)

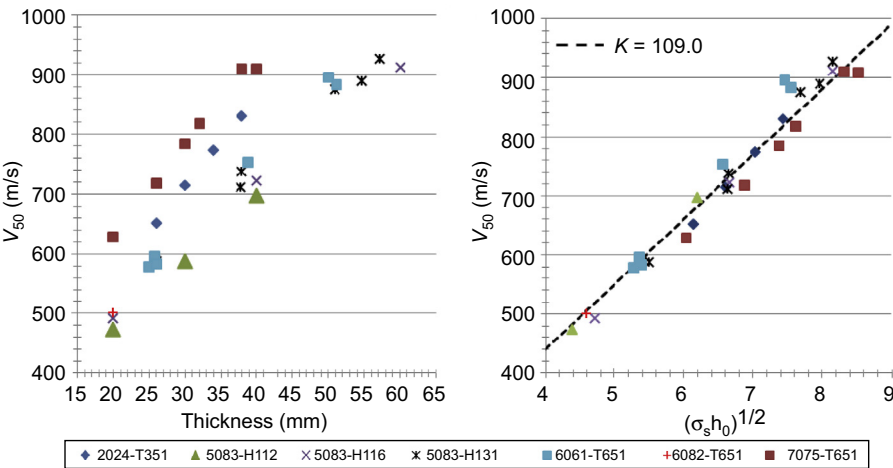


Figure 8.21 Ballistic limit of aluminium alloys impacted by 7.62 mm APM2 projectiles. Left: in terms of target thickness; right: in terms of Forrestal et al.’s scaling law.

(Cho and Bes, 2006) and ballistic (Cheeseman et al., 2008) testing. To provide a prediction of the ballistic performance using the Forrestal scaling law, knowledge of the material stress–strain behaviour is required. Casem and Dandekar (2012) performed an extensive characterisation of 2139-T8, including quasistatic compression tests to which the power-law fit can be applied: $E = 73.1$ GPa; $Y = 430$ MPa; $n = 0.085$ (see Fig. 8.22).

The scaling law is compared to ballistic data from Cheeseman et al. (2008) in Fig. 8.23, and the accuracy of the resulting predictions is assessed in Table 8.5. For the four plate thicknesses tested, the scaling law predicts the V_{50} to within 5%, in all instances overpredicting the experimental measurement.

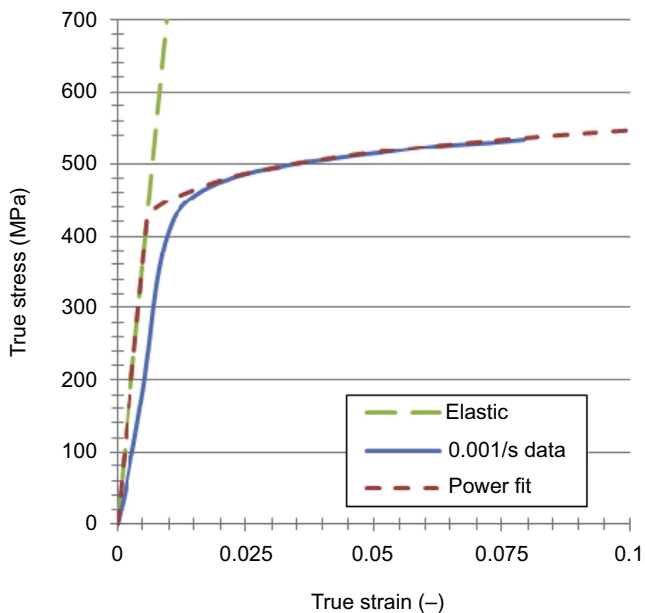


Figure 8.22 Quasistatic compressive stress–strain behaviour of Al2139-T8 from [Casem and Dandekar, 2012](#) and power-law fit.

Casem, D.T., Dandekar, D.P., 2012. Shock and mechanical response of 2139-T8 aluminum. *Journal of Applied Physics* 111.

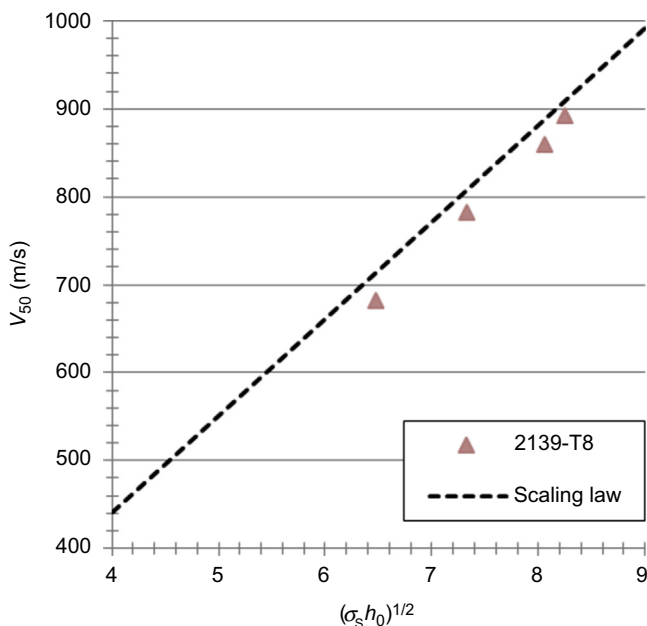


Figure 8.23 Comparison between the Forrestal scaling law prediction and ballistic test data for Al2139-T8.

From Cheeseman, B., Gooch Jr, W.A., Burkins, M.S., 2008. Ballistic evaluation of aluminum 2139-T8. In: Paper Presented at the 24th International Symposium on Ballistics, New Orleans.

Table 8.5 Predicting the ballistic limit of Al2139-T8 plates impacted by 7.62 mm APM2 projectiles using the Forrestal scaling law for ductile hole formation

Projectile	Target	Thickness (mm)	V ₅₀ (m/s)		Variance	
			Predicted	Measured	(m/s)	%
7.62 mm APM2	2139-T8	25.2	705.0	682.1	30.5	4.5
7.62 mm APM2	2139-T8	32.3	798.4	782.7	24.4	3.1
7.62 mm APM2	2139-T8	39.0	877.1	860.1	26.5	3.1
7.62 mm APM2	2139-T8	40.9	898.3	892.5	15.6	1.8

8.4 Analytical modelling for penetration/perforation of nonmetallic armour

The most common types of nonmetallic armour are ceramics and composites. These materials can provide highly effective armour performance, however their response under ballistic loading rates is very complex. As such, analytical models for these types of materials are typically more complex, or incorporate higher levels of empiricism or broader simplifying assumptions.

8.4.1 Penetration/perforation of fabric armour

Classical yarn theory (Smith et al., 1958) describes the response of a single yarn to transverse impact in terms of the velocity at which the impact-induced transverse wave propagates through the fibre, U , and the so-called critical velocity, V_{crit} , at which the strain that develops in the fibre upon impact exceeds the failure strain. The transverse wave speed is given by:

$$U = c \left(\sqrt{\varepsilon(1 + \varepsilon)} - \varepsilon \right) \quad (8.93)$$

where c is the speed of sound in the yarn, $c = \sqrt{\frac{E}{\rho}}$, equal to the propagation speed of the longitudinal wave; ε is the strain in the yarn.

The strain in the yarn, ε , is related to the impact velocity, V , by:

$$V = c \sqrt{\varepsilon \left(2\sqrt{\varepsilon(1 + \varepsilon)} - \varepsilon \right)} \quad (8.94)$$

To determine the critical impact velocity, V_{crit} , the strain in Eq. (8.94) is simply set to the failure strain of the yarn, ε_f , ie:

$$V_{\text{crit}} = c \sqrt{\varepsilon_f \left(2 \sqrt{\varepsilon_f (1 + \varepsilon_f)} - \varepsilon_f \right)} \quad (8.95)$$

A number of investigations have experimentally observed lower breaking speeds for a range of fibre yarns, including Kevlar (Bazhenov et al., 2001), nylon (Wilde et al., 1970) and UHMW polyethylene (Walker and Chocron, 2011). Walker and Chocron (2011) demonstrated that for impact of a flat-nosed penetrator, the yarn bounces off the projectile upon impact, inducing higher acceleration loads in the yarn which, in turn, leads to failure below the critical value predicted by Eq. (8.95). Accounting for this effect, the modified critical impact velocity is bounded by two expressions:

$$V_{\text{crit}} = 1.19c \varepsilon_f^{3/4} \quad (8.96)$$

$$V_{\text{crit}} = 2^{-3/4} c \varepsilon_f^{3/4} \sqrt{2 - \sqrt{\varepsilon_f/2}} \quad (8.97)$$

Eq. (8.96) defines the condition when the yarn does not bounce off the projectile and Eq. (8.97) refers to the worst-case condition in which the yarn is accelerated to a velocity double that of the impact velocity. A comparison between the critical velocities predicted by classical theory (Eq. (8.97)) with the modified relationships proposed in Walker and Chocron (2011) for impact of flat-nosed projectiles is made in Fig. 8.24.

Cunniff (1999) defined a set of dimensionless parameters for characterising the performance of fabric armour systems against steel or tungsten projectiles with length-to-diameter ratios of approximately one. For this system, the dimensional ratios (ie, Pi groups) were defined as:

$$\Phi \left(\frac{V_{50}}{(U^*)^{1/3}}, \frac{AD_t A_p}{m_p} \right) = 0 \quad (8.98)$$

where AD_t is the areal density of the target system; A_p is the presented area of projectile; m_p is the mass of the projectile and U^* is the product of fibre specific toughness and strain wave velocity,

$$U^* = \frac{\sigma \varepsilon}{2\rho} \sqrt{\frac{E}{\rho}} \quad (8.99)$$

where σ is the ultimate axial tensile strength of the fibre; ε is the ultimate tensile strain of the fibre; E is the elastic modulus of the fibre and ρ is the fibre density.

According to Eq. (8.98), the ballistic limit of a fabric armour system is thus directly proportional to $(U^*)^{1/3}$. This property provides a useful guide in comparative analysis

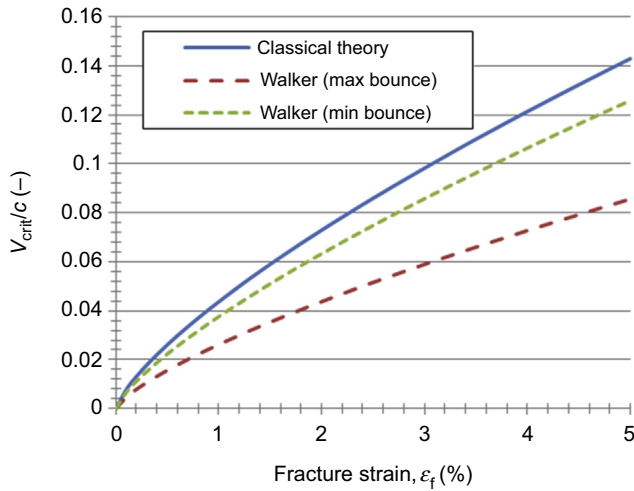


Figure 8.24 Comparison of critical velocity versus failure strain predicted by classical yarn theory and the Walker and Chocron model incorporating yarn bounce from the nose of a flat projectile.

Walker, J.D., Chocron, S., 2011. Why impacted yarns break at lower speed than classical theory predicts. *Journal of Applied Mechanics* 78(5), 051021–051021. <http://dx.doi.org/10.1115/1.4004328>.

between fabric armour types, and can be used to drive performance improvements in fabric developments. Cunniff proposed an empirical relationship for defining the V_{50} of fabric armour as a function of the areal density P_i group in Eq. (8.98), ie:

$$V_{50} = f\left(\frac{AD_t A_p}{m_p}\right) \quad (8.100)$$

An analytical model was developed in Phoenix and Porwal (2003) to provide a full analytical description in order to replace the empirical fit of Eq. (8.100) applied by Cunniff. Phoenix and Porwal proposed:

$$\frac{V_{50}}{(U^*)^{1/3}} = 2^{1/3} \epsilon_{y \max}^{1/12} \frac{(1 + \theta^2 \Gamma_0)}{K_{\max}^{3/4}} \quad (8.101)$$

where Γ_0 is Cunniff's nondimensional P_i group, $\Gamma_0 = \frac{AD_t A_p}{m_p}$; $\epsilon_{y \max}$ is the failure strain of the yarn; θ is an adjustable parameter used to define an effective diameter of impact, typically equal to 1.25–1.35, which represents a response area of the target material larger than the projectile diameter (or presented area) as a result of wrap-around and spreading of the impact energy; K_{\max} is the maximum strain amplification factor in the membrane at the edge of the projectile following impact,

$$K_{\max} \approx \exp \left\{ -\frac{4\theta^2 \Gamma_0}{3(1 + \theta^2 \Gamma_0)} (\psi_{\max}^2 - 1) \right\} \\ \times \psi_{\max}^{1/3} \left[\frac{\sqrt{\psi_{\max}/\varepsilon_{\max}} (\psi_{\max} - 1)}{\ln \left\{ 1 + \sqrt{\psi_{\max}/\varepsilon_{\max}} (\psi_{\max} - 1) \right\}} \right]^{2/3}$$

$$\text{and } \psi_{\max} \approx \sqrt{(1 + \theta^2 \Gamma_0)/(2\theta^2 \Gamma_0)}.$$

For very thick targets, or short, large-calibre fragments such that $\Gamma_0 \geq 1$, $K_{\max} = 1$. As the nondimensional areal density term decreases, K_{\max} increases to account for the larger effect of strain concentration about the projectile edge.

Billon and Robinson (2001) provided a further means to assess the performance of fabric armours incorporating layers of multiple fabric materials. The ballistic limit of a single fabric layer is determined by:

$$V_{\text{bl}} = \left(\frac{2}{m_p \rho} \right)^{1/2} \left[\int_0^A f(a) da \right]^{1/2} \quad (8.102)$$

where a is the areal density of the penetrated layers, $a = \rho x$; x is the penetrated depth; A is the areal density of the fabric layer and

$$\int_0^{AD_i} f(a) da = \alpha A \quad (8.103)$$

where α is an empirical constant.

The empirical constant α is determined by substituting Eq. (8.103) into Eq. (8.102),

$$\alpha = \frac{V_{\text{bl}}^2 m_p \rho}{2A} \quad (8.104)$$

and requires a description of the fabric layer V_{bl} in terms of a power fit, namely:

$$V_{\text{bl}} = a(A)^b \quad (8.105)$$

where a , b are empirically fit to test data.

Billon and Robinson define $b = 0.5$ for tests on nylon, UHMWPE, and aramid fabrics with 25.4-mm diameter circular boundaries. Lee et al. (1994) characterised the ballistic performance of square clamped UHMWPE composites with a 200-mm diameter circular aperture according to Eq. (8.105), where $b = 0.65$. Similar values were reported by Song and Egglestone (1987) for aramid and S-2 glass fabrics, where $b = 0.56$ and 0.64 , respectively. It should be noted that the performance

of fabrics under ballistic impact is highly dependent on their span and method of restraint. The values reported in [Billon and Robinson \(2001\)](#) for 25.4 mm circular test sections vary from those that can be derived for tests on a 203 mm \times 203 mm square section.

Once the performance of a fabric layer is described as per [Eq. \(8.105\)](#), assuming a constant rate of change in projectile kinetic energy with penetration depth, the ballistic limit of fabric armour (including hybrid layups) can be determined using:

$$V_{bl} = \left(\frac{2}{m_p} \right)^{1/2} \left[\sum_{i=1}^N \frac{\alpha_i A_i}{\rho_i} \right]^{1/2} \quad (8.106)$$

where N is the total number of fabric layers in the armour system.

It should be noted that [Eq. \(8.106\)](#) is only valid for the special case in which interference effects between fabrics are not present, or are negligible (ie, the penetration of the individual layers occurs as though they are isolated incidents). The hybrid configurations tested in [Billon and Robinson \(2001\)](#) were designed such that impact occurred on layers with increasing sonic velocities in order to minimise the interference effects. For hybrid fabric armours which are not impedance-optimised, the performance can be significantly degraded through interference effects (see, eg, [Cunniff, 1992](#)), in which case [Eq. \(8.106\)](#) would overpredict armour performance.

8.4.2 Penetration/perforation of composite armour

[Gellert et al. \(2000\)](#) investigated the performance of glass fibre-reinforced plastic (GFRP) laminates using blunt- and conical-nosed penetrators. For thin targets, penetration of the laminates occurred through a dishing mechanism where a conical section of target material delaminates and bends away from the projectile in the direction of projectile motion (see [Fig. 8.25](#)). The initiation of dishing is related to the bending resistance of the target. For thin targets, the resistance is insufficient to prevent delamination, separation of the plies and subsequent dishing. For sufficiently thick targets, the resistance to bending is sufficient to prevent dishing during the initial stages of penetration. As a result, penetration of such thick targets can be considered to occur in two phases: an initial indentation phase and a secondary dishing phase.

[Fig. 8.26](#) shows that the differences between experimental measurements for thin (dished) and thick (indented and dished) targets are well captured by a bilinear fit.

The ballistic limit of GFRP panels is calculated by equating the kinetic energy of the projective with the work required to fail the target in dishing (for thin targets), or indentation and dishing (for thick targets),

$$KE = \frac{1}{2} m_p V_{50}^2 = \begin{cases} W_D, & \text{for thin targets} \\ W_I + W_D, & \text{for thick targets} \end{cases} \quad (8.107)$$

where W_D is the work done in dishing; W_I is the work done in indentation.

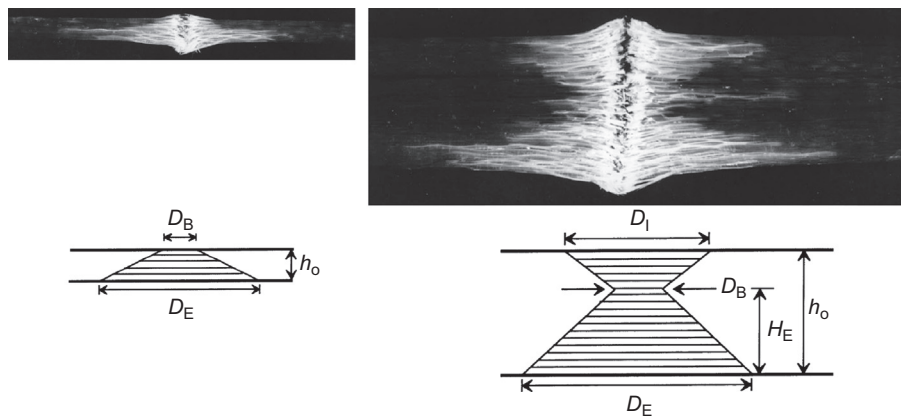


Figure 8.25 Characteristic patterns of damage or delamination in GFRP laminates subject to ballistic impact by blunt and conical nose penetrators. Left: thin target failing in a single-phase dishing mode; right: thick target failing in a two-phase indentation and dishing process. The projectile is travelling from the top to the bottom of the page.
Gellert, E. P., Cimpoeu, S. J., Woodward, R. L., 2000. A study of the effect of target thickness on the ballistic perforation of glass-fibre-reinforced plastic composites. *International Journal of Impact Engineering* 24(5), 445–456. [http://dx.doi.org/10.1016/S0734-743X\(99\)00175-X](http://dx.doi.org/10.1016/S0734-743X(99)00175-X).

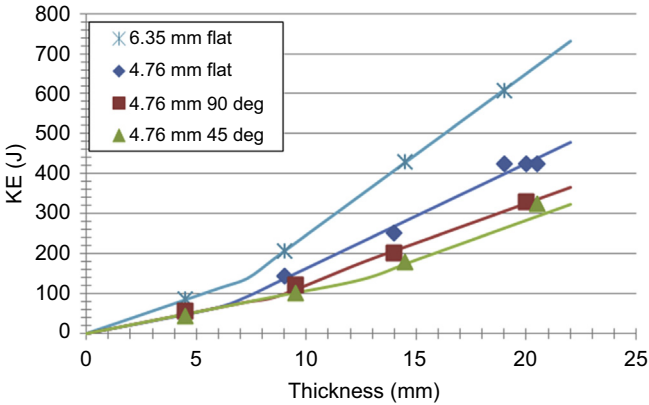


Figure 8.26 Kinetic energy at ballistic limit versus target thickness for a range of projectile types against glass fibre reinforced plastic composite. The bilinear fit corresponds to a two-stage penetration process, within initial indentation followed by dishing.
After Gellert, E. P., Cimpoeu, S. J., Woodward, R. L., 2000. A study of the effect of target thickness on the ballistic perforation of glass-fibre-reinforced plastic composites. *International Journal of Impact Engineering* 24(5), 445–456. doi:[10.1016/S0734-743X\(99\)00175-X](http://dx.doi.org/10.1016/S0734-743X(99)00175-X).

The work done in dishing is determined from:

$$W_D \approx W_T + W_F = L^2 h_0 (C_1 \sigma_m^2 / E + C_2 G_C) \tag{8.108}$$

where W_D is the work done in dishing; W_T is the work done in tensile stretching of the material; W_F is the work done in fracturing the matrix phase (ie, delamination); L is the diameter of the delaminated conical dish at the rear surface of the target; h_0 is the target thickness; σ_m is the mean tensile strength of the composite; E is the tensile modulus of the composite; G_C is the fracture toughness of the composite and C_1 and C_2 are empirical constants.

The work done in indentation is determined from:

$$W_I = C_4 D^2 \sigma_C (h_0 - \phi) \quad (8.109)$$

where C_4 is an empirical constant accounting for the effect of confinement on the material flow stress; D is the projectile diameter; σ_C is the through-thickness compressive strength of the composite and ϕ is the thickness of target that fails in dishing.

Although providing a mechanistic justification of the bilinear penetration model, Eqs (8.108) and (8.109) are not used in Gellert et al. (2000) to determine the ballistic limit relationship. Rather they manually fit the bilinear curve to test data. Similarly, the thickness of the target that fails in dishing, ϕ , used in the model does not correspond to the thickness H_E , measured from the recovered target samples. Again, as per the work calculation, it is determined from a manual fit to the test data.

Nguyen et al. (2015a) observed two-phase perforation of thick UHMWPE composite panels by fragment-simulating projectiles: initial penetration by shear plugging (indentation followed by a bulging stage where the panel behaves like a membrane failing in tension). The representative fibre fracture morphology is shown in Fig. 8.27, demonstrating predominantly fibre cutting or shearing during the initial phase (likely as a result of the sharp edges of the penetrators) and transitioning to failure primarily in tension towards the rear of the laminate. Unlike the clean fracture surface exhibited by fibres failing in shear, fibres failing in tension undergo significant elongation and reduction in diameter.

As per Gellert et al., the two-phase perforation model of Nguyen et al. (2015a) was formulated in terms of energy and momentum laws, where the ballistic limit is assumed to be equal to the total energy absorbed (or work done, in the nomenclature of Gellert et al. (2000)) during penetration,

$$KE = \frac{1}{2} m_p V_{50}^2 = E_S + E_B \quad (8.110)$$

where m_p is the mass of the projectile; E_S is the energy absorbed in the shear plugging stage; E_B is the energy absorbed in the bulging stage.

The energy absorbed in the shear plugging stage, E_S , is equal to the work required to produce a shear plug, where the shear area is the circumference of the projectile multiplied by the thickness of the material in the shear plugging stage,

$$E_S = \int_0^{t_S} \tau_{\max} (2\pi r_p) t dt = \tau_{\max} \pi r_p t_S^2 \quad (8.111)$$

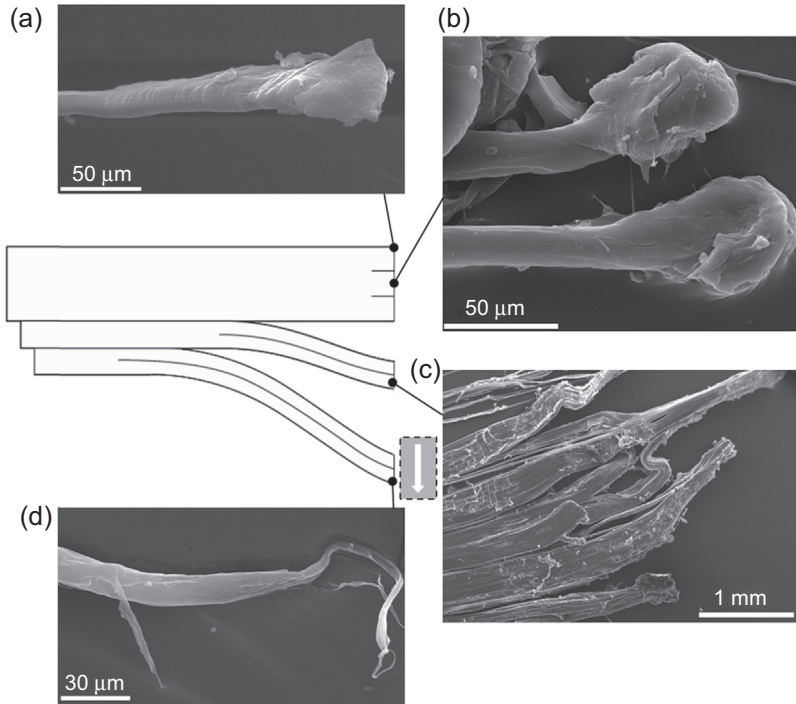


Figure 8.27 Fibre fracture morphology from a 35-mm thick Dyneema HB26 laminate impacted by a 12.7 mm fragment simulating projectile at 1346 m/s. Images taken (a) at the front face of the composite laminate, (b) within the shear plugging phase, (c) within the bulging phase and (d) at the back face.

Nguyen, L.H., Ryan, S., Cimpoeu, S.J., Mouritz, A.P., Orifici, A.C., 2015a. The effect of target thickness on the ballistic performance of ultra high molecular weight polyethylene composite. *International Journal of Impact Engineering* 75(0), 174–183. <http://dx.doi.org/10.1016/j.ijimpeng.2014.07.008>; Nguyen, L.H., Ryan, S., Cimpoeu, S.J., Mouritz, A.P., Orifici, A.C., 2015b. The efficiency of ultra-high molecular weight polyethylene composite against fragment impact. *Experimental Mechanics*. <http://dx.doi.org/10.1007/s11340-015-0051-z>.

where t is the thickness of the composite panel; t_s is the thickness of the panel failed in shear plugging; τ_{\max} is the effective through-thickness shear strength of the laminate and r_p is the projectile radius.

The energy absorbed in the bulging stage, E_B , can be determined by the respective change in momentum of the projectile,

$$E_B = \frac{1}{2} m_p V_B^2 \quad (8.112)$$

where V_B is the projectile velocity at the onset of the bulging phase, determined from

$$m_p V_B = (m_p + m_B) V_{pB} \quad (8.113)$$

where m_B is the mass of the target in the bulging stage initially involved in the momentum transfer and V_{pB} is the velocity of the combined projectile and target mass at the onset of the bulging phase.

The projectile velocity at the onset of the bulging phase, V_B , can be related to the response of a fabric membrane impacted by a projectile (Phoenix and Porwal, 2003), assuming no strain concentration about the projectile as a result of deformation, and substituting the failure strain, ϵ_{\max} :

$$V_B = \left(1 + \beta^2 \frac{t_B \rho A_p}{m_p}\right) \sqrt{\frac{E_f}{\rho}} \sqrt{\frac{v_f}{2}} \sqrt{2\epsilon_{\max} \sqrt{\epsilon_{\max} + \epsilon_{\max}^2} - \epsilon_{\max}^2} \quad (8.114)$$

where t_B is the thickness of the panel failed in the bulging stage; A_p is the presented area of the projectile; ρ is the fibre density; E_f is the fibre elastic modulus in tension; v_f is the fibre volume fraction and β is a nondimensional parameter that accounts for the response of the target in bulging occurring over a larger area than that of the penetrator, from Phoenix and Porwal (2003) and Walker (1999) (see Fig. 8.28).

Substituting Eq. (8.114) into Eq. (8.112) gives:

$$E_B = \frac{1}{2} m_p V_B^2 = \frac{1}{2} m_p \left(1 + \beta^2 \frac{t_B \rho A_p}{m_p}\right)^2 \frac{E_f}{\rho} \frac{v_f}{2} \left(2\epsilon_{\max} \sqrt{\epsilon_{\max} + \epsilon_{\max}^2} - \epsilon_{\max}^2\right) \quad (8.115)$$

The ratio of panel thickness failing by shear plugging to membrane tension, k , can be empirically determined by measuring recovered target panels. A separation plane

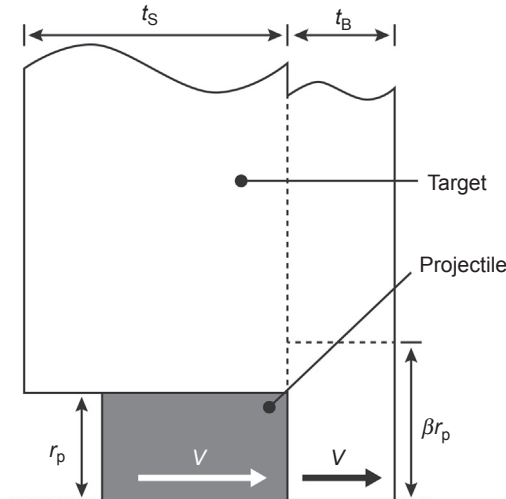


Figure 8.28 Momentum exchange at the separation plane demonstrating a larger area of target response than that of the projectile presented area.

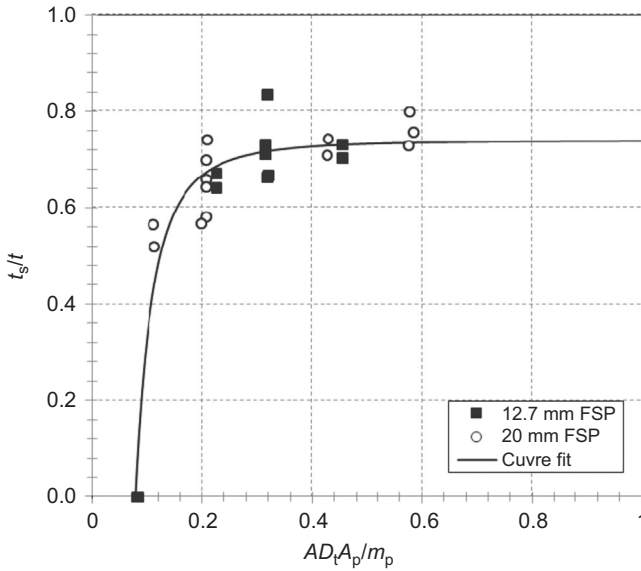


Figure 8.29 Ratio of composite panel thickness failed in shear plugging to the total panel thickness in terms of Cunniff's nondimensionalised areal density parameter. Experimental data points shown are within $\pm 5\%$ of the panel ballistic limit (V_{50}).

Nguyen, L.H., Ryan, S., Cimpoeu, S.J., Mouritz, A.P., Orifici, A.C., 2015a. The effect of target thickness on the ballistic performance of ultra high molecular weight polyethylene composite. *International Journal of Impact Engineering* 75(0), 174–183. <http://dx.doi.org/10.1016/j.ijimpeng.2014.07.008>; Nguyen, L.H., Ryan, S., Cimpoeu, S.J., Mouritz, A.P., Orifici, A.C., 2015b. The efficiency of ultra-high molecular weight polyethylene composite against fragment impact. *Experimental Mechanics*. <http://dx.doi.org/10.1007/s11340-015-0051-z>.

forms in the composite, beyond which the panel begins to bulge and the failure mechanism transitions from shear plugging to membrane tension. Fig. 8.29 plots the thickness of panel failed in shear plugging to total thickness, t_s/t ($=k$), and defines the empirical trend as a power fit in terms of Cunniff's nondimensional parameter.

$$k = \frac{t_s}{t} = C_1 \left(\frac{AD_t A_p}{m_p} \right)^{C_2} + C_3 \quad \frac{AD_t A_p}{m_p} \geq C_T \quad (8.116)$$

where C_1 , C_2 and C_3 are curve fit parameters equal to -0.0013 , -2.5 and 0.74 , respectively; C_T is the Cunniff parameter that defines the transition between thin and thick targets, equal to 0.08 .

Finally, the V_{50} ballistic limit is calculated as:

$$V_{50} = \sqrt{\frac{2}{m_p \rho^2} \tau_{\max} \pi r_p k^2 AD_t^2 + \left(1 + \beta^2 (1 - k) \frac{AD_t A_p}{m_p} \right)^2 \frac{E_f}{\rho} \frac{v_f}{2} \left(2 \varepsilon_{\max} \sqrt{\varepsilon_{\max} + \varepsilon_{\max}^2} - \varepsilon_{\max}^2 \right)} \quad (8.117)$$

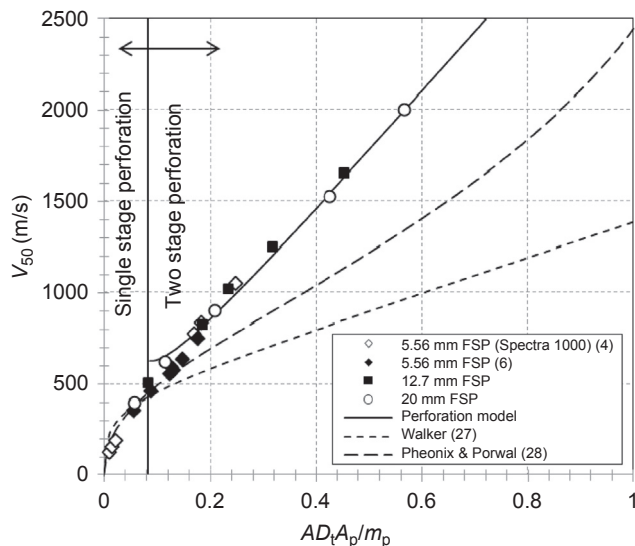


Figure 8.30 Comparison of the two-stage penetration model and single-stage membrane tension models of Walker (1999) and Phoenix and Porwal (2003) with ballistic limit data of UHMWPE against different-calibre fragment-simulating projectiles.

Nguyen, L.H., Ryan, S., Cimpoeu, S.J., Mouritz, A.P., Orifici, A.C., 2015a. The effect of target thickness on the ballistic performance of ultra high molecular weight polyethylene composite. *International Journal of Impact Engineering* 75(0), 174–183. <http://dx.doi.org/10.1016/j.ijimpeng.2014.07.008>; Nguyen, L.H., Ryan, S., Cimpoeu, S.J., Mouritz, A.P., Orifici, A.C., 2015b. The efficiency of ultra-high molecular weight polyethylene composite against fragment impact. *Experimental Mechanics*. <http://dx.doi.org/10.1007/s11340-015-0051-z>.

Fig. 8.30 compares the predictions of Eq. (8.117) with V_{50} data on UHMWPE composite for three different-calibre fragment-simulating projectiles (FSPs). The two-stage model provides very good agreement with the experimental results for configurations with nondimensional areal density values over ~ 0.175 . For 20 and 12.7 mm calibre MIL-STD-662F fragment-simulating projectiles, this corresponds to target thicknesses of ~ 30 mm and ~ 20 mm, respectively. For thinner targets, or lower nondimensionalised areal density values, perforation is considered to occur through membrane tension without an initial shear plugging phase. For interactions with nondimensionalised areal densities of $< \sim 0.08$, fabric models based on membrane tension from Phoenix and Porwal (2003) or Walker (1999) are shown to provide a high level of agreement with the test data. Between $\sim 0.08 < AD_t A_p / m_p < \sim 0.175$ a transitioning to two-stage penetration is expected to occur in which the target response is still dominated by membrane action in bulging. An increasing degree of projectile deformation in this transition zone results in a reduction of strain concentration effects which are incorporated in the models of Walker and that of Phoenix and Porwal but not in Eq. (8.115). In Fig. 8.31 the degree of projectile deformation in recovered FSPs is shown for impact velocities between 365 and 1966 m/s, which led to increased relaxation of strain concentrations in the UHMWPE target material.



Figure 8.31 Deformation in FSPs from ballistic limit tests resulting in partial penetration of UHMWPE targets. Impact velocity (from left to right): 365, 615, 911, 1410, and 1966 m/s. Nguyen, L.H., Ryan, S., Cimpoeu, S.J., Mouritz, A.P., Orifici, A.C., 2015a. The effect of target thickness on the ballistic performance of ultra high molecular weight polyethylene composite. *International Journal of Impact Engineering* 75(0), 174–183. <http://dx.doi.org/10.1016/j.ijimpeng.2014.07.008>; Nguyen, L.H., Ryan, S., Cimpoeu, S.J., Mouritz, A.P., Orifici, A.C., 2015b. The efficiency of ultra-high molecular weight polyethylene composite against fragment impact. *Experimental Mechanics*. <http://dx.doi.org/10.1007/s11340-015-0051-z>.

8.4.3 Penetration/perforation of ceramic armour

Ceramics have the ability to provide highly efficient protection, both in terms of weight and space requirement, against ballistic threats. Traditionally, ceramic armours were developed for protection against armour-piercing projectiles. The performance of ceramic armour is highly variable, depending on the geometry of the armour, the configuration of the armour system (eg, backing plate, cover plate, etc.), the stress state in the ceramic during the impact event, as well as typical material variables such as purity and porosity. Additionally, depending on the application and design of the armour system, ceramic armours can be designed to exploit specific defeat mechanisms such as dwell or interface defeat, in which the impacting projectile is completely eroded on the face of the ceramic armour.

Carlucci and Jacobson (2007) define the progression of damage within a ceramic under ballistic impact. Initially, tensile cracks appear on the strike face of the ceramic, forming circular rings and progressing along the principal stress planes (typically $25\text{--}75^\circ$ from the surface normal). Once the cracks reach the rear face of the ceramic, they coalesce into conical form. If the plate is backed, as is typical for ceramic armours, the stress is redistributed circumferentially and radial cracks appear. Finally, lateral cracks form in the plane of the impact surface. This process is depicted in Fig. 8.32.

Woodward (1989) proposed a model which defined the resistance of ceramic armour with a thin backing plate in terms of the inertia of the ceramic and backing bounded by the conical crack and the dishing deformation of the backing. A simplified velocity distribution within the armour was proposed (see Fig. 8.33) defined by a 68° cone angle based on quasistatic observations of simple systems. The system can be simplified to a lumped mass model for determining the inertial resistance of the armour.

Two failure modes are considered: ductile instability of the backing plate leads to failure of the armour system with ceramic still separating the projectile and backing plate, and complete penetration of the ceramic by an intact projectile, leading to perforation of

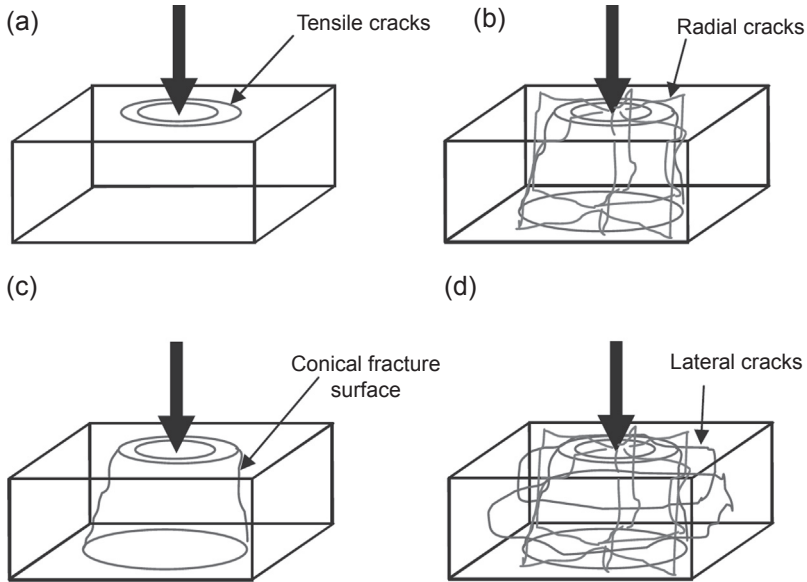


Figure 8.32 The progression of damage within ceramic armour with backing: (a) tensile cracks forming circular rings about the impact site; (b) the progression of radial cracks through the ceramic thickness; (c) coalescence of the radial and tensile cracks into a conical fracture zone and (d) lateral crack formation in the plane of the impact surface. From Carlucci, D.E., Jacobson, S.S., 2007. *Penetration Theories Ballistics: Theory and Design of Guns and Ammunition*. CRC Press.

backing plate via ductile hole formation. In the first instance, the failure threshold is determined by calculating the work done to dish the backing plate, W_D , assuming ideally plastic response of the backing plate hinged about the point defined in Fig. 8.33, ie,

$$W_D = \pi b h Y \left(\frac{2}{3} b + \frac{1}{2} h \right) \quad (8.118)$$

where b is the thickness of the backing plate; h is the displacement of the backing plate and Y is the flow stress of the backing plate material.

Complete penetration of the ceramic followed by perforation of the backing plate by ductile hole formation is evaluated by:

$$\frac{1}{2} m_{p,II} (V_{b,II} - V_{p,II})^2 = \frac{\pi}{2} D_p^2 b Y \quad (8.119)$$

where V_b and V_p are the velocities of the backing plate and projectile and the subscript II refers to the system state at the beginning of stage II (ie, following complete penetration of the ceramic). The right-hand side of Eq. (8.119) can be recognised from Woodward's expression for work done in ductile hole formation (see Section 8.3.1).

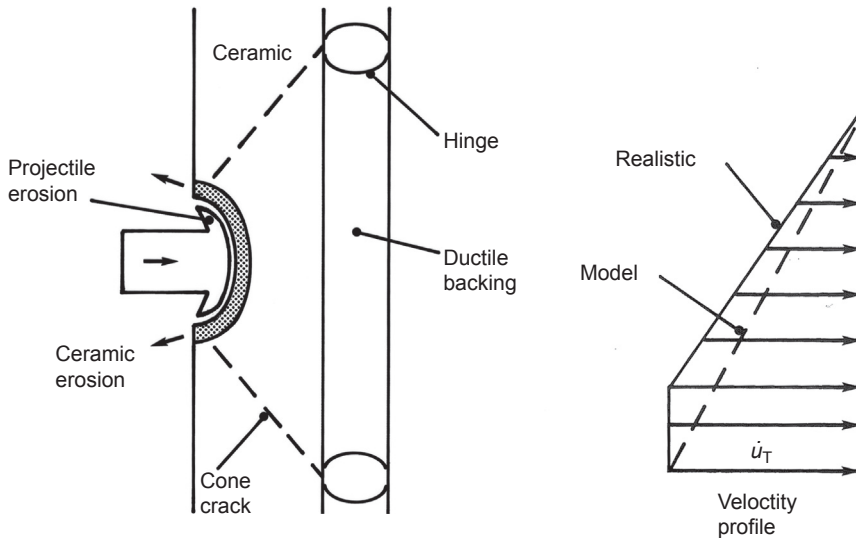


Figure 8.33 Simplification of ceramic armour with thin backing under ballistic impact. Left: definition of a 68° conical section providing resistance to projectile penetration; right: simplification of the velocity field.

Woodward, R.L., 1989. A Basis for Modelling Ceramic Composite Armour Defeat. Maribyrnong, Vic: DSTO Materials Research Laboratory.

Erosion of the projectile and target material occur in the event that the force at the interface exceeds the strength of the target or projectile, where strength is some measure of uniaxial flow stress, hardness, etc. The acceleration of the target backing plate and deceleration of the projectile during the ceramic penetration stage are approximated according to basic equations of motion defined for a simplified lumped mass model. An example of the projectile erosion and deceleration, together with acceleration of the backing plate during penetration of the ceramic material (ie, stage I) is shown in Fig. 8.34 for the projectile and target combination defined in Woodward (1989).

Woodward provides an extension to the ceramic model to account for the presence of a thick backing plate. For this case the two failure modes for the thin-backed ceramic model are simplified to a single model which assumes:

1. No acceleration of the backing plate during penetration of the ceramic target, and;
2. The dishing failure mode of the backing plate is replaced by a plugging model, where the plug is defined by the residual projectile mass at the end of stage I penetration (ie, $m_{p,II}$ from Eq. (8.119)).

Plugging of the thick backing material can be calculated using the plasticity model described in Section 8.3.2, after Woodward and Cimpoeu (1998).

A key mechanism in the application of ceramic armour is that of dwell — the process by which a projectile is eroded on the front surface of the ceramic with minimal penetration (see Chapter 7 for additional discussion). Sustainment of dwell through complete erosion of the projectile is known as interface defeat.

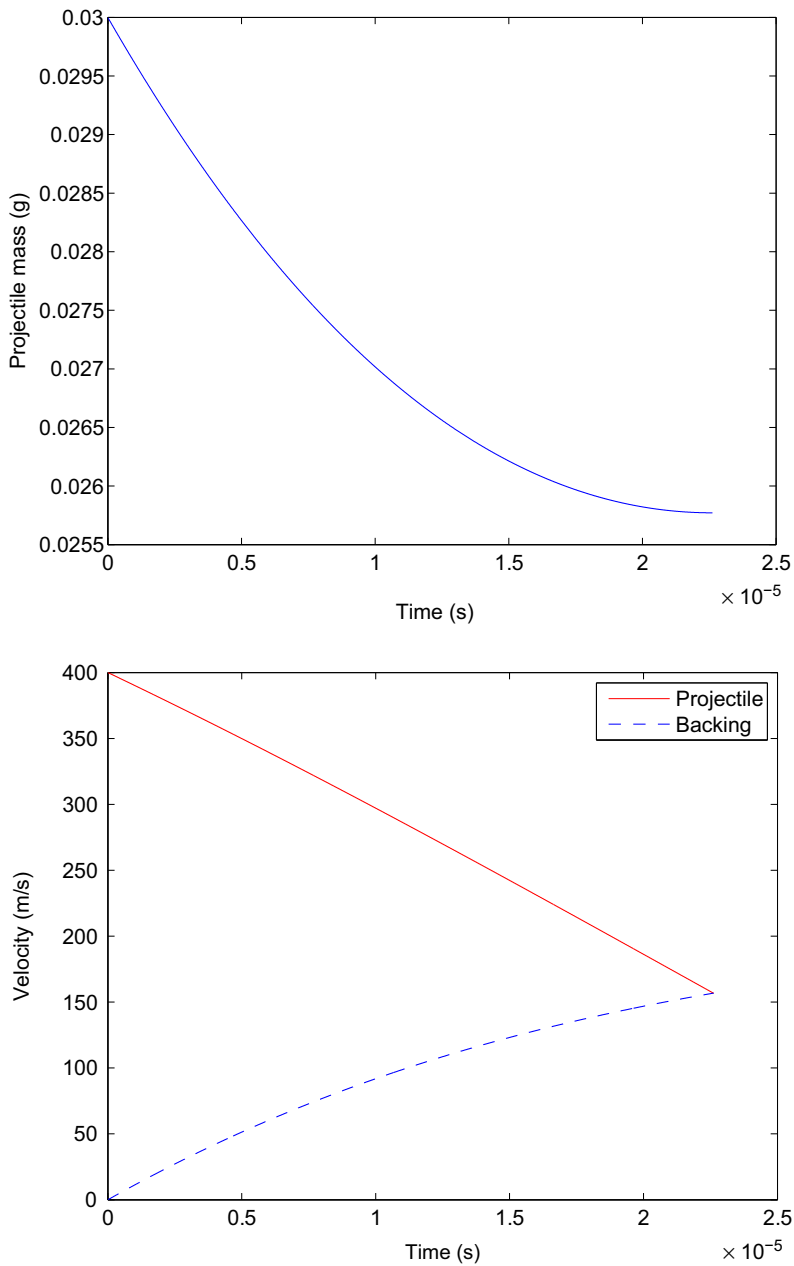


Figure 8.34 Example calculations of projectile erosion and deceleration during ceramic penetration, calculated for impact of a 30-g flat-nose cylindrical penetrator against an 8.8-GPa hardness ceramic target as per [Woodward \(1989\)](#). Woodward, R.L., 1989. A Basis for Modelling Ceramic Composite Armour Defeat. Maribymong, Vic: DSTO Materials Research Laboratory.

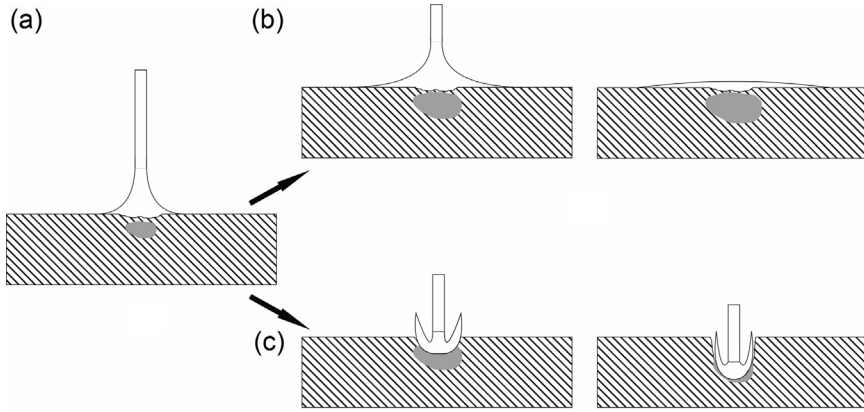


Figure 8.35 Following initial projectile impact and the beginning of dwell (a), a projectile can either be entirely eroded upon the surface of the ceramic, known as interface defeat (b), or can transition to penetration if the conditions for dwell cannot be sustained (c).

Thus, analytical models for ceramic armour should ideally address two conditions: an initial period of dwell followed by either penetration of the ceramic by the residual projectile, or sustainment of dwell through interface defeat (Fig. 8.35). The Woodward model presented previously does not account for the presence of dwell, rather projectile erosion occurs during penetration of the ceramic armour. Thus, for configurations with extended dwell periods, models such as Woodward's can be expected to underestimate armour performance.

There are a number of analytical models which can be applied to investigate interface defeat, although none provides a complete means of analysis. Taylor's seminal work on the impact of a flat-ended cylinder on a rigid target can be considered analogous to a simplified dwell condition – assuming a stationary interface and idealised response of the ceramic. Once the stresses at the interface exceed the elastic limit of the projectile material, plastic flow of the projectile occurs radially along the rigid interface, decreasing the length of the projectile (Anderson and Walker, 2005). The dwell time, t_D , can be approximated from Taylor's theory by:

$$t_D = \frac{L}{V_0} \frac{\epsilon_1}{\sqrt{1-\epsilon}} \int_{\epsilon}^{\epsilon_1} \frac{x}{L} \frac{(1-\frac{x}{L})}{(1-\epsilon)^{3/2}} d\epsilon \quad (8.120)$$

where L is the initial length of the projectile; V_0 is the impact velocity; ϵ is the longitudinal compressive strain in the projectile; ϵ_1 is the final strain in the projectile and x is the length of the projectile which has not yet experienced plastic strain, from:

$$\ln\left(\frac{x}{L}\right)^2 = \frac{1}{1-\epsilon} - \ln(1-\epsilon) - \frac{1}{1-\epsilon_1} + \ln(1-\epsilon_1) \quad (8.121)$$

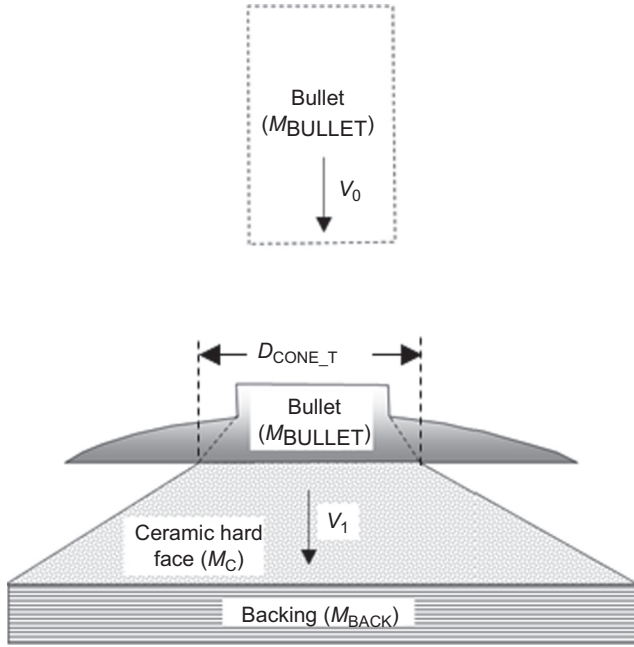


Figure 8.36 Impact of a projectile upon a ceramic armour with backing.

From Elder, D., 2010. DMTC KBE Tool Extension — Revision B. Retrieved from: Hawthorn.

Elder (2010) extended application of Taylor's theory to account for a nonzero velocity at the end of the dwell phase. From Fig. 8.36, an impacting projectile with initial velocity V_0 and diameter D_0 is deformed upon impact with a ceramic armour. During an initial dwell phase, the bullet is deformed and a conical area of the ceramic is fractured. Per conservation of momentum, the final velocity of the bullet, fractured ceramic, and backing material at the conclusion of the dwell phase, V_1 , is determined by:

$$V_1 = \frac{V_0 m_p}{m_p + m_c + m_b} \quad (8.122)$$

where m_p is the initial mass of the projectile; m_c is the mass of the fractured ceramic and m_b is the mass of the backing plate.

The force required to accelerate the cone of fractured ceramic and backing material, F , is determined from:

$$F = (m_c + m_b) \times a_{c,b} \quad (8.123)$$

where $a_{c,b}$ is the acceleration of the cone of fractured ceramic and backing plate, from

$$V_1 = a_{c,b} \times t_D \quad (8.124)$$

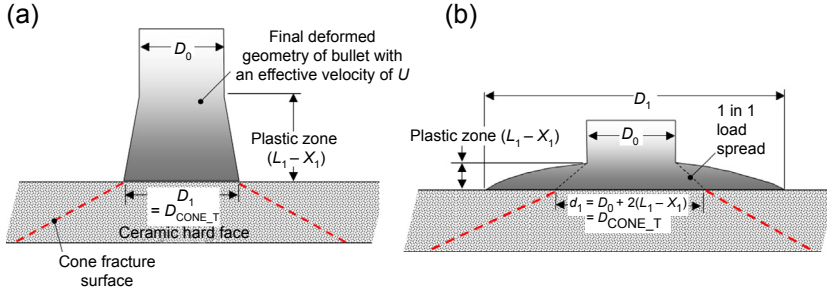


Figure 8.37 Definition of the conical fracture zone in the ceramic target for a low deformation case (left) and high deformation case (right).

From Elder, D., 2010. DMTC KBE Tool Extension – Revision B. Retrieved from: Hawthorn.

Rearranging Eq. (8.123),

$$F = \frac{(m_c + m_b) V_1}{t_D} \quad (8.125)$$

Two cases are presented: a high deformation case and a low deformation case (see Fig. 8.37). The cone fracture surface is defined by its diameter at the interface, D_1 and d_1 for the low deformation and high deformation cases, respectively.

The effective velocity of the projectile relative to the ceramic, U , is defined as:

$$U = V_0 - V_1 \quad (8.126)$$

The dynamic yield strength, S , of the projectile is estimated from the Johnson and Cook constitutive strength model (Johnson and Cook, 1983), where:

$$S = [A + B\epsilon^n] \left[1 + C \ln \left(\frac{\dot{\epsilon}}{\dot{\epsilon}_0} \right) \right] \left[1 - \left(\frac{(T - T_{\text{ref}})}{(T_m - T_{\text{ref}})} \right)^m \right] \quad (8.127)$$

where A is the static yield strength; ϵ is the strain, in this instance determined from the Taylor analysis,

$$\epsilon = \epsilon_1/2 \quad (8.128)$$

$\dot{\epsilon}$ is the strain rate, determined from the Taylor analysis,

$$\dot{\epsilon} = U/(2(L_0 - X_1)) \quad (8.129)$$

U is the effective projectile velocity, Eq. (8.126); $\dot{\epsilon}_0$ is the reference strain rate; T is the material temperature (K); T_m is the melting temperature of the material (K); T_{ref} is the reference temperature, typically 293 K; B , n , C and m are empirical constants fit to characterisation data.

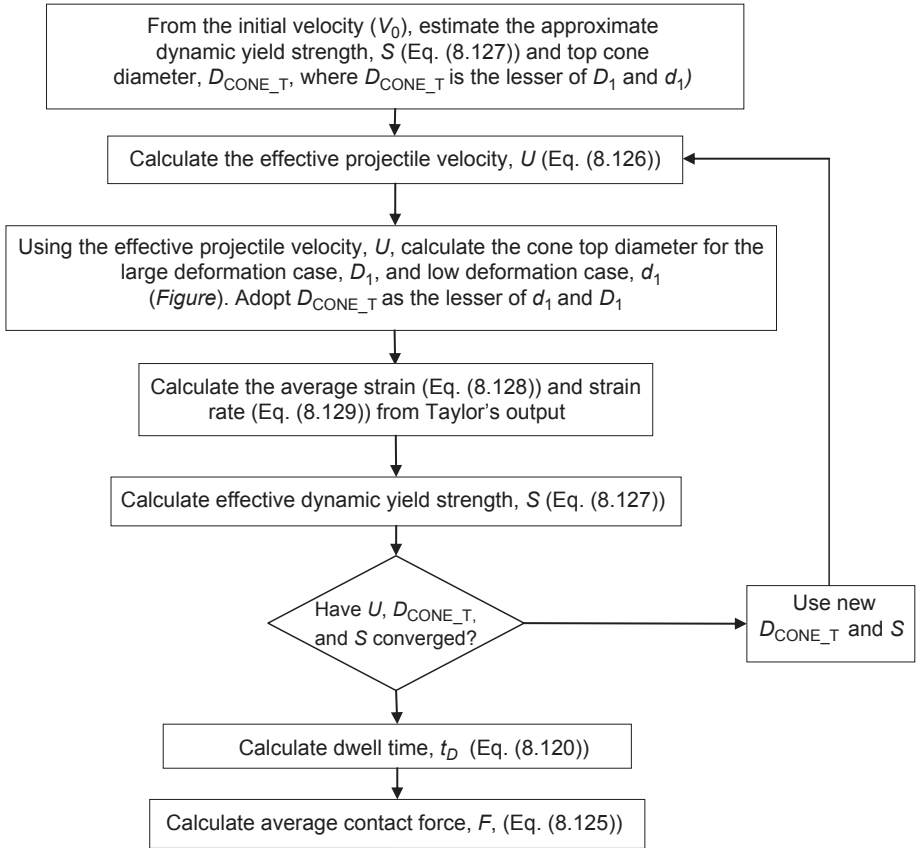


Figure 8.38 Flow chart for projectile impact on nonrigid ceramic armour with backing. From Elder, D., 2010. DMTC KBE Tool Extension – Revision B. Retrieved from: Hawthorn.

Elder presents an iterative flowchart to calculate the dwell time and average contact force, shown in Fig. 8.38.

Anderson and Walker (2005) provide a simple analytical model based on centreline momentum balance (as per the Alekseevskii–Tate modified hydrodynamic theory, see Section 8.2.4):

$$\frac{1}{2} \rho_p (u - v)^2 + Y_p = \frac{1}{2} \rho_t u^2 + R_t \quad (8.130)$$

$$\rho_p l \frac{dv}{dt} = -Y_p \quad (8.131)$$

$$\frac{dl}{dt} = -(v - u) \quad (8.132)$$

During dwell the interface velocity, u , is zero. For this condition Eq. (8.132) is thus simplified and Eq. (8.130) is no longer valid. Now Eqs (8.131) and (8.132) can be solved simultaneously, and, $dv/dt = vdv/dx$, can be explicitly integrated such that:

$$\frac{1}{2}\rho_p(v^2 - v_0^2) = Y_p \ln\left(\frac{l}{l_0}\right) \quad (8.133)$$

where l is the remaining projectile length; l_0 is the initial projectile length; v is the remaining projectile velocity and v_0 is the initial projectile velocity.

With minimal inputs (ie, projectile length, density and target flow stress), the model is shown in Anderson and Walker (2005) to provide an excellent level of agreement with experimental measurement of an armour-piercing projectile and long-rod projectile against ceramic armours. Clearly, the limitation of the model is that it is only valid for the case when the interface velocity, u , is approximately zero (ie, dwell is sustained). The model does not provide a means of determining when those conditions are no longer met, such that dwell will transition to penetration.

Lundberg et al. (2000) define a model, which, rather than predict projectile response during a dwell phase, can be used to determine the conditions for interface defeat. They consider that under the high strain rates and stresses of impact, inertial effects, rather than strength and compressibility, dominate projectile behaviour at the interface. As such, the projectile can be considered to experience radial hydrodynamic flow during the dwell phase across a rigid and frictionless surface. Considering the dwell phase as a steady state (ie, ignoring transient shock effects), the surface load at the centreline, p_0 is defined as:

$$p_0 \approx q_p \left(1 + \frac{1}{2\alpha} + 3.27\beta \right) \quad (8.134)$$

where $\alpha = \frac{K_p}{q_p}$ $\beta = \frac{\sigma_{yp}}{q_p}$ $q_p = \frac{1}{2}\rho_p v_p^2$ and K_p is the bulk modulus of the projectile material; q_p is the stagnation pressure of an ideal fluid with density ρ_p and velocity v_p ; σ_{yp} is the yield strength of the projectile material; and α and β are dimensionless parameters that relate elastic and plastic effects, respectively, to the effect of inertia ($\alpha \gg 1$, $\beta \ll 1$).

The transition from interface defeat to normal penetration is bounded by two limits corresponding to shear failure of the ceramic as a result of surface pressure (Eq. (8.135)) and shear failure through indentation (Eq. (8.136)), ie:

$$p_0^{\text{lower}} = (2.601 + 2.056 \nu) \tau_y \quad (8.135)$$

$$p_0^{\text{upper}} = 5.70 \tau_y \quad (8.136)$$

where ν is the Poisson's ratio of the ceramic; τ_y is the ceramic shear strength and τ_y is related to the ceramic yield strength, σ_y , by Tresca's criterion: $\sigma_y = 2\tau_y$.

Thus, the transition velocity is defined within the boundaries:

$$v_t^{\text{lower}} = \sqrt{\left(\frac{2K_p}{\rho_p}\right) \left[-1 + \sqrt{1 + 2 \left(\frac{(1.30 + 1.03 \nu) \sigma_y - 3.27 \sigma_{yp}}{K_p} \right)} \right]} \quad (8.137)$$

$$v_t^{\text{upper}} = \sqrt{\left(\frac{2K_p}{\rho_p}\right) \left[-1 + \sqrt{1 + 2 \left(\frac{2.85 \sigma_y - 3.27 \sigma_{yp}}{K_p} \right)} \right]} \quad (8.138)$$

A number of projectile and target combinations were tested in Lundberg et al. (2000), the results of which are reproduced in Fig. 8.39.

The assumption of a quasistatic loading on the ceramic until the point of either interface defeat or penetration ignores damage caused by the initial transient shock, reflected impact shock waves (Zukas et al., 1982), and the effect of strain rate on ceramic yield strength (Nemat-Nasser and Deng, 1994). To minimise the effect of the initial impact shock, experimental coupons in Lundberg et al. (2000) incorporated a steel buffer to reduce the amplitude of the impact shock and provide a more gradual loading profile on the ceramic. Techniques exist to disperse the reflected shock, and thus delay its interaction with the assumed steady-state stress condition at the interface (eg, Hauver et al. (2005)), however they were not applied.

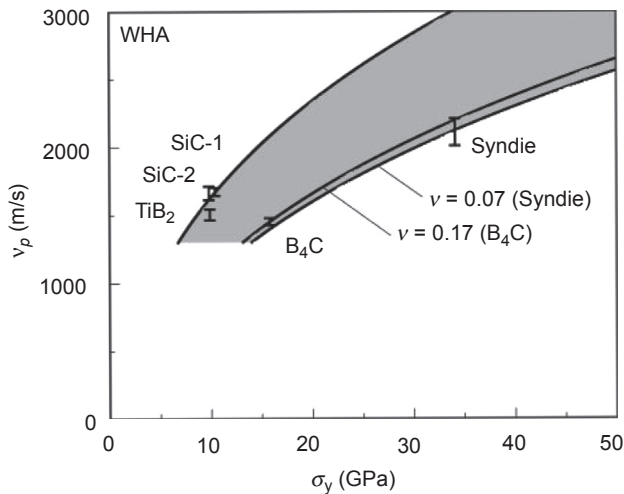


Figure 8.39 Interface defeat transition velocity bounds plotted in terms of projectile impact velocity, v_p , and target yield strength, σ_y , from Lundberg et al. (2000). The experimentally measured transition velocities are shown to approximately lie on either the upper or lower analytical bounds.

Lundberg, P., Renström, R., Lundberg, B., 2000. Impact of metallic projectiles on ceramic targets: transition between interface defeat and penetration. *International Journal of Impact Engineering* 24(3), 259–275. [http://dx.doi.org/10.1016/S0734-743X\(99\)00152-9](http://dx.doi.org/10.1016/S0734-743X(99)00152-9).

Although applying a number of potentially significant assumptions, the results in Fig. 8.39 suggest the model proposed by Lundberg et al. has quantitative merit. The location of experimentally determined transition velocities on either the upper or lower bound for all combinations of materials implies the model reproduces the physical phenomenon and failure mechanisms that determine penetration accurately, although it offers no explanation for which material will be located on which boundary.

LaSalvia et al. (2000) considered that the yielding criteria used in Lundberg et al. (2000) to establish the lower bound for critical pressure (Eq. (8.137)), were not supported by their observations. Rather than bulk material yield under excessive shear, they proposed that penetration was initiated once the comminuted region extended to the free surface and became unconstrained, or due to a shock-induced damage region extending into the material from the surface. The critical pressure, p_0^* , required to expand the comminuted region to the interface is calculated by:

$$\left(\frac{p_0}{\tau_y}\right)^* = \frac{2\sqrt{2}\pi\Delta\sqrt{\frac{l_t}{c}}}{1 - 2\nu - (3 + 2\nu)\mu - \sqrt{2}\pi(1 + 2\nu)\left(\frac{l_t}{c}\right)} \quad (8.139)$$

where l_t is the length of tensile ‘wing’ cracks, typical for brittle materials (eg, c is the length of typical microcracks in the ceramic, where $2c$ is taken as the average grain size); μ is the coefficient of friction that opposes relative movement of the crack edges and Δ is a ductility parameter that determines the dominant behaviour of the wing cracks (based on the model developed in Horii and Nemat-Nasser (1986)),

$$\Delta = \frac{K_{IC}}{\tau_y\sqrt{\pi c}} \quad (8.140)$$

where K_{IC} is the mode I fracture toughness.

Above a critical value for Δ , crack behaviour is affected by plastic relaxation around the crack tips, suppressing propagation. As Δ is decreased the material becomes more brittle and, as such, less plastic relaxation is possible. This leads to advanced crack formation and earlier (lower-impact velocity) penetration. The critical transition velocity is determined from Eq. (8.139) as:

$$v_t^{\text{lower}} = \sqrt{\left(\frac{2K_p}{\rho_p}\right) \left[-1 + \sqrt{1 + 2\left(\frac{p_0^* - 3.27\sigma_{yp}}{K_p}\right)} \right]} \quad (8.141)$$

The transition velocity bound calculated by Eq. (8.141) is shown in LaSalvia et al. (2000) to be highly sensitive to parameters τ_y , Δ , μ , ν and l_t/c , where Δ and l_t/c are not independent variables. The friction coefficient, μ , for example, is poorly defined. The authors define $\mu = 0.4$ based on the original work of Horii and Nemat-Nasser, which provides no conditions for its derivation or justification for selecting this value.

Bruchey and Horwath (1998) presented a methodology to design a ceramic armour system capable of achieving interface defeat. In assessing the performance of an encapsulated ceramic, they consider failure via compression under the projectile, or tensile failure at the back of the ceramic as a result of flexure.

The maximum deflection required to cause tensile fracture at the rear surface of the ceramic, δ_{cer} , is determined through a three-point bending test, where:

$$\delta_{\text{cer}} = \frac{P}{8KL_e^2} \quad (8.142)$$

$$L_e^2 = \frac{E_c t_c^3}{(12K(1 - \nu^2))^{0.25}} \quad P = \frac{2\sigma_{\text{rup}} \pi t_c^2}{3(1 + \nu) \left[\ln \left(\frac{L_e}{r_{\text{pen}}} \right) + 0.6159 \right]}$$

with

$$K = \frac{(w/A_1)}{\delta} \quad w = \frac{\delta E_b t_b^3}{0.1267b^2}$$

where K is the modulus of the entire configuration, relating applied load to linear deformation; w is the load required to produce a deflection δ at the rear of the backing plate; A_1 is the cross-sectional area of the projectile presented to the ceramic during dwell; t_c and t_b are the thickness of the ceramic and backing plate, respectively; E_c and E_b are the Young's modulus of the ceramic and backing plate, respectively; b is the radius of the mushroomed projectile; δ is the deflection of the backing plate measured under load w ; P is the surface load causing rupture at the rear surface of the ceramic; σ_{rup} is the rupture stress of the ceramic measured in three-point bending tests and r_{pen} is the initial projectile radius.

Thus if the load, P , is such that the maximum deflection is exceeded, failure at the ceramic rear surface will occur and interface defeat cannot be achieved. The load P is calculated as:

$$P = P_1 A_1 \quad (8.143)$$

where P_1 is the pressure at the interface, calculated based on the Rankine–Hugoniot shock jump condition, where:

$$P_1 = \rho_p C_p (V_0 - u_{p,c}) + \rho_p S_p (V_0 - u_{p,c})^2 \quad (8.144)$$

and $u_{p,c}$ is the particle velocity in the ceramic, determined by solving:

$$u_{p,c}^2 (\rho_c S_c - \rho_p S_p) + u_{p,c} (\rho_c c_c + \rho_p c_p + 2\rho_p S_p V_0) - \rho_p (c_p V_0 + S_p V_0^2) = 0 \quad (8.145)$$

ρ_p and ρ_c are the density of the projectile and ceramic, respectively; c_p and c_c are the bulk sound speed of the projectile and ceramic, respectively; S_p and S_c are the slope of

the $u_p - U_S$ curve for the projectile and ceramic, respectively; $u_{p,p}$ and $u_{p,c}$ are the particle velocities in the projectile and ceramic, respectively and V_0 is the impact velocity.

For bulk compressive failure, Bruchey and Horwath simply compare the pressure determined by Eq. (8.143) to an estimate of the dynamic strength of the material. They apply Tate's estimate, where the dynamic strength is a function of the Hugoniot elastic limit, HEL, and Poisson's ratio, ν :

$$R_t = \text{HEL} \left(\frac{1 - 2\nu}{1 - \nu} \right) \quad (8.146)$$

The interesting thing about Bruchey and Horwath's model is that it is, in effect, a modular approach. As such, the failure criteria could easily be updated with those from, for example, LaSalvia et al. (2000) and Lundberg et al. (2000). The approach first checks that the conditions for interface defeat are valid, ie, the ceramic will not fail in compression or through flexure-induced tension, and then scales the performance in terms of the ceramic mass efficiency, ie:

$$e_{mf} = e_m \left(\frac{R_t}{P_1} \right) \left(\frac{\delta_{cer}}{\Delta_{cer}} \right) \text{ for } P_1 \geq R_t \text{ or } \Delta_{cer} \geq \delta_{cer} \quad (8.147)$$

where Δ_{cer} is the deflection of the target under the impact load P_1 ; e_m is the initial mass efficiency of the undamaged target (ballistically measured) and e_{mf} is the mass efficiency of the fractured ceramic.

Thus, for impact conditions in which the ceramic does not fail in bulk compression or tensile failure at the rear surface, the mass efficiency is equal to that of the undamaged target. For conditions which exceed either of the failure criteria, the mass efficiency is degraded.

The approach was shown in Bruchey and Horwath (1998) to provide a very good level of agreement with experiments for a number of hot isostatically pressed ceramics, predicting mass efficiencies and rolled homogeneous armour (RHA) equivalent values for a number of target configurations and projectile materials to within 10% of the experimentally derived values. While it does not calculate transition velocity directly, a lower bound can be estimated by back-calculating from final efficiency values.

8.4.4 Predicting collateral damage in ceramic targets

Many modellers have developed mathematical treatments to mirror the complex, through-thickness damage and penetration mechanisms associated with a high-velocity impact, as described in previous sections. However, what is equally important is an ability to predict the extent of collateral damage, especially the radial cracking which emanates from the point of impact. In brittle, ceramic-based systems, like hard armour plates (HAPs) (see Chapter 7), these radial cracks propagate to the very edge of the target and can seriously affect the target's multistrike performance. Predicting

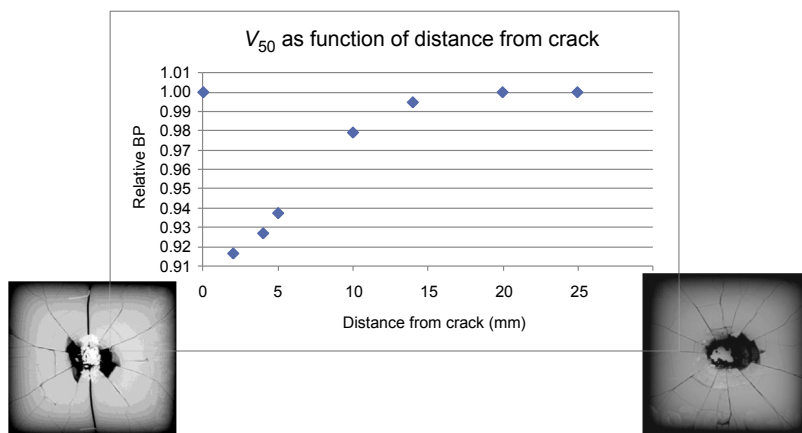


Figure 8.40 Ballistic performance of a cracked silicon carbide-based armour system showing how performance varies with distance from main crack.

Crouch, I.G., 2014. Effects of cladding and its influence on ballistic performance. In: Paper Presented at the 28th International Symposium on Ballistics, Atlanta.

the ballistic performance of a second, and subsequent, strike is therefore very important when designing HAPs (see Chapter 7). During the period 2009–2012, the DMTC (Defence Materials Technology Centre) began to develop a knowledge-based engineering-based, 2D analytical model, under the leadership of Crouch and Elder. This took account of the degradation in the performance of the ceramic as a function of distance from the edge of the target, as well as distance from a crack (see Fig. 8.40). Empirical relationships were embedded into iterative calculations, which determined a damage index after the first strike. The output was based upon strike location (see Fig. 8.41). On-going activities at the DMTC are looking to progress this work.

In a recent paper (Crouch, 2014), the effect of cladding upon the extent of radial cracking was aired. The following thesis was proposed: many radial cracks form when an HAP is impacted but only a finite number of cracks propagate based upon the tensile hoop stress developed in the rear of the target, as the ceramic bends. The number of cracks would appear to be related to the magnitude of this circumferential hoop stress field – the cracks propagate catastrophically to relieve this hoop stress. See Chapter 7 for more details.

8.4.4.1 Case study 2: predicting the performance of composite armour against fragments

Nguyen et al. (2015b) found that the V_{50} of typical ballistic composites and fabrics scaled linearly with the second dimensionless parameter in Eq. (8.98) (see Fig. 8.42). Furthermore, the use of the dimensionless parameter was successful in collapsing ballistic limit data with different-calibre projectiles on to the same curve. Thus, these relationships can be used to both define the ballistic efficiency of

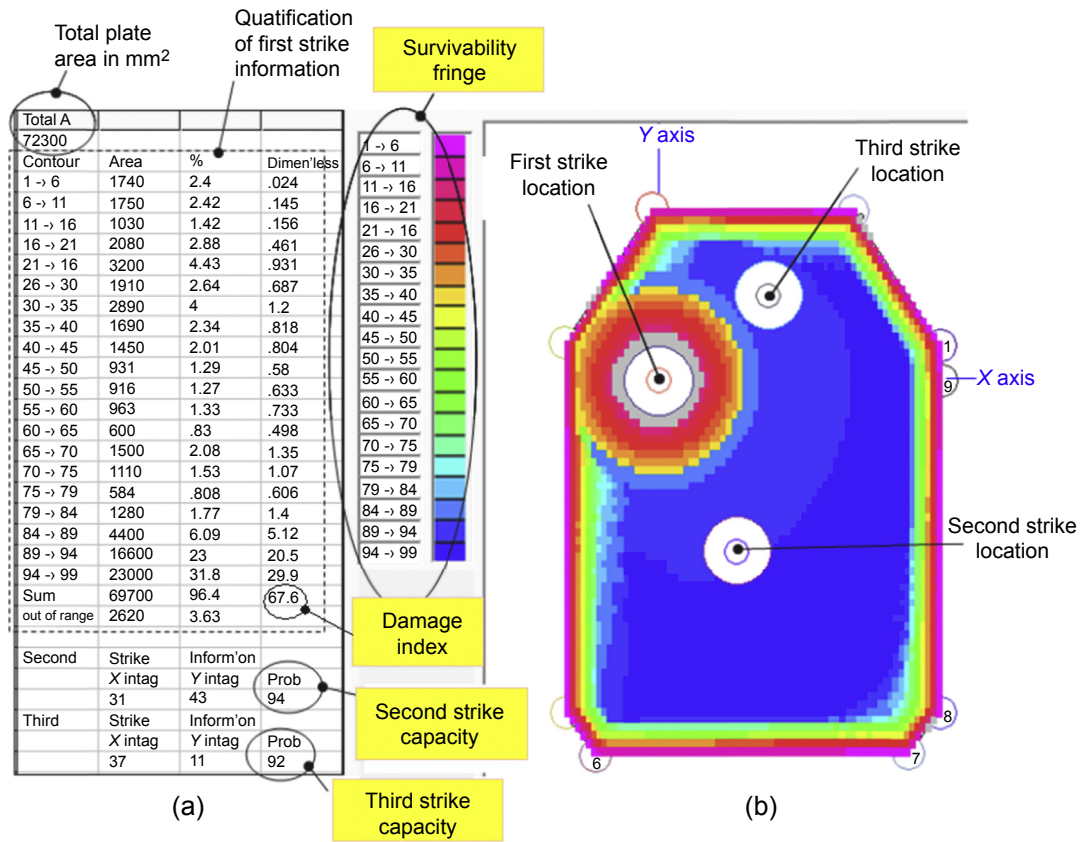


Figure 8.41 Extract from work of Elder and Crouch.
 Elder, D., 2010. DMTC KBE Tool Extension — Revision B. Retrieved from: Hawthorn.

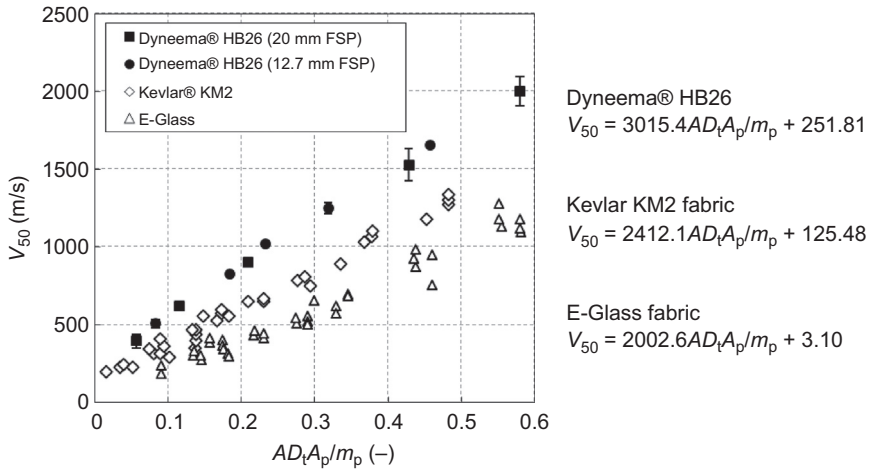


Figure 8.42 The performance of various composite and fabric materials against blunt steel and tungsten projectiles with length to diameter ratios of ~ 1.0 . Performance is plotted in terms of Cunniff's nondimensional parameter (Cunniff, 1999).

Dyneema data from Nguyen, L.H., Ryan, S., Cimpoeu, S.J., Mouritz, A.P., Orifici, A.C., 2015a. The effect of target thickness on the ballistic performance of ultra high molecular weight polyethylene composite. *International Journal of Impact Engineering* 75(0), 174–183. <http://dx.doi.org/10.1016/j.ijimpeng.2014.07.008>; Nguyen, L.H., Ryan, S., Cimpoeu, S.J., Mouritz, A.P., Orifici, A.C., 2015b. The efficiency of ultra-high molecular weight polyethylene composite against fragment impact. *Experimental Mechanics*. <http://dx.doi.org/10.1007/s11340-015-0051-z>, Kevlar and E-glass data from Cunniff, P.M., 1999. Dimensionless parameters for optimization of textile-based body armor systems. In: Paper Presented at the 19th International Symposium on Ballistics, San Antonio.

composite and fabric armours against blunt penetrators as well as design armour systems to defeat specified threats.

From Fig. 8.42, UHMWPE, Kevlar and GFRP armours can all be designed for a particular fragment threat. The efficiency of an armour system is typically described in terms of the mass and space required to defeat a specific threat, relative to the mass and space required by a baseline armour to provide the same level of protection, RHA is defined as the baseline. The mass and space efficiency of an armour, E_m and E_s , respectively, is determined by:

$$E_m = \frac{t_{\text{ref}} \times \rho_{\text{ref}}}{t \times \rho} \quad (8.148)$$

$$E_s = \frac{t_{\text{ref}}}{t} \quad (8.149)$$

where t is the armour thickness required to defeat the threat, ρ is the density of the armour material and the subscript *ref* refers to the reference condition (eg, RHA).

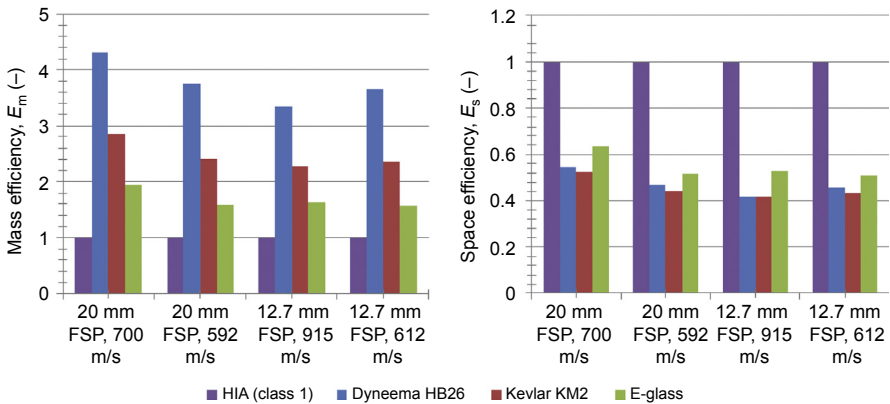


Figure 8.43 Mass efficiency (left) and space efficiency (right) of UHMWPE, aramid and glass fibre-reinforced composites for protecting against 12.7 and 20 mm fragment-simulating projectiles.

The product of the two efficiency terms is known as the *quality factor*, q^2 . Values of q^2 represent armours or materials that are thinner and/or lighter than the baseline armour, thus providing superior performance (Gooch et al., 2004).

The calculated space and mass efficiency values are plotted in Fig. 8.43. All three composite armour materials are shown to provide improved mass efficiency at a cost of space efficiency, compared to the baseline RHA surrogate material. In other words, the composite armours can provide a comparable level of protection with less weight, but requiring a larger space claim than the baseline steel material. The armour quality values in Table 8.6 show that Dyneema provides the best armour solution against the presented threat conditions, while the Kevlar and E-glass materials are comparable with the baseline steel. Although useful for direct comparison, the armour quality factor q^2 is rarely used in practice as mass and space claims are rarely equal. Rather the armour design will be more sensitive to, and thus driven by, one variable over the other.

8.5 Computational packages for the perforation of finite-thickness armour targets

Although capable of providing a high level of accuracy, the application of many of the analytical models discussed is limited to impacts between certain classes of projectiles or targets, or combinations of the two which produce a consistent failure mechanism in the armour plate (eg, ductile hole formation). A number of computational packages have been developed which aim to provide a wider range of application for vulnerability assessments of armoured vehicles, either by including the means for application on a larger range of targets and projectiles (typically through increased empiricism), or by the use of a decision-tree concept which first classifies an impact and then identifies the appropriate algorithm for application.

Table 8.6 Example design calculations for typical composite and fabric armour materials to protect against 20 and 12.7 mm calibre fragment-simulating projectiles

Projectile	Material	Velocity (m/s)	Required thickness (mm)	AD (g/cm ²)	E_m (—)	E_s (—)	q^2 (—)
20 mm FSP	RHA*	595	10.3	80.8	1.0	1.0	1.0
	Dyneema HB26	595	21.9	21.5	3.8	0.5	1.8
	Kevlar KM2	595	23.2	33.4	2.4	0.4	1.1
	E-glass	595	19.9	50.8	1.6	0.5	0.8
20 mm FSP	RHA*	700	15.0	117.0	1.0	1.0	1.0
	Dyneema HB26	700	27.6	27.1	4.3	0.5	2.3
	Kevlar KM2	700	28.6	41.1	2.8	0.5	1.5
	E-glass	700	23.6	60.1	2.0	0.6	1.2
12.7 mm FSP	RHA*	610	6.6	51.6	1.0	1.0	1.0
	Dyneema HB26	610	14.4	14.1	3.7	0.5	1.7
	Kevlar KM2	610	15.1	21.8	2.4	0.4	1.0
	E-glass	610	12.9	32.9	1.6	0.5	0.8
12.7 mm FSP	RHA*	915	10.2	80.1	1.0	1.0	1.0
	Dyneema HB26	915	24.4	23.9	3.3	0.4	1.4
	Kevlar KM2	915	24.6	35.4	2.3	0.4	0.9
	E-glass	915	19.3	49.2	1.6	0.5	0.9

*Bisalloy HIA (class 1) used as a surrogate for RHA.

These computational packages are typically classified, or have a limited distribution. Additionally, they provide a varying range of automation — for instance older packages such as ConWep provide documentation which can be followed to identify the classification process and interrogate which penetration algorithm is applied in which case. Newer, more complex packages, such as FATEPEN, operate as a de facto black-box, providing limited information on which penetration algorithm is used in which instance. Additionally, for projectile—target interactions which do not fit within the validity range of a particular algorithm these packages can apply some level of interpolation or extrapolation between models — a process which is not clearly traceable.

As such, these packages are an invaluable tool to the defence community, however to apply them correctly a level of knowledge about the underlying algorithms and their validity bounds is always required.

8.5.1 THOR

Project THOR was an intermediate-range ballistic missile programme performed in the United States during the 1950s. As part of the programme, a substantial number of tests were performed using short cylinder and cube-on-cylinder fragments with length to diameter (L/D) ratios close to 1 to evaluate the penetration resistance of metallic and nonmetallic targets (Anon., 1961, 1963).

Two sets of empirical formulae were developed from the test data, which, when used together, can provide information on impact conditions for which the impacting fragment disintegrates without perforation. The equation sets relate the fragment residual velocity and weight to the impact parameters, target geometry, material properties, etc. The THOR equation for residual fragment velocity, V_r , is defined as:

$$V_r = V_s - 10^C (TA)^\alpha W_f^\beta (\sec \theta)^\gamma V_s^\lambda \quad (8.150)$$

where V_s is the fragment striking velocity (fps); T is the target thickness (in); A is the average fragment impact area (in²); W_f is the fragment weight (grains); θ is the impact obliquity measured normal to the target surface (deg) and C , α , β , γ , λ are empirical constants.

Alternatively, Eq. (8.150) can be rearranged and solved for V_s , when $V_r = 0$ to provide an estimate of protection velocity (denoted as V_0 rather than V_s), ie:

$$V_0 = 10^{C_1} (TA)^{\alpha_1} W_f^{\beta_1} (\sec \theta)^{\gamma_1} \quad (8.151)$$

where $C_1 = C/(1 - \lambda)$ $\alpha_1 = \alpha/(1 - \lambda)$ $\beta_1 = \beta/(1 - \lambda)$ $\gamma_1 = \gamma/(1 - \lambda)$

It should be noted that protection velocity, V_0 , is different to the V_{50} ballistic limit velocity, as it defines the velocity above which perforation is predicted to not occur, rather than the point at which the projectile has a 50% probability of perforating the target. In the case of perforation, the residual weight of the fragment, W_r , can be calculated using:

$$W_f - W_r = 10^C (TA)^\alpha W_f^\beta (\sec \theta)^\gamma V_s^\lambda \quad (8.152)$$

A simplification of Eqs (8.150)–(8.152) is provided in Anon. (1961) for fragments with a length to diameter ratio of ~ 1.0 for which the average presented area is nearly directly proportional to two-thirds the power of the mass, and is accounted for in the modified constants C^* and β^* , ie:

$$V_r = V_s - 10^{C^*} T^\alpha W_f^{\beta^*} (\sec \theta)^\gamma V_s^\lambda \quad (8.153)$$

$$V_0 = 10^{C_1^*} T^{\alpha_1} W_f^{\beta^*} (\sec \theta)^{\gamma_1} \quad (8.154)$$

$$W_f - W_r = 10^{C^*} T^{\alpha} W_f^{\beta^*} (\sec \theta)^{\gamma} V_s^{\lambda} \quad (8.155)$$

For fragments that have length to diameter ratios above 3, the accuracy of the generalised THOR equations (Eqs (8.150)–(8.152)) is questionable.

The THOR 47 report (Anon., 1961) contains empirical constants for magnesium, Al2024-T3, titanium alloy (type unspecified), cast iron, face-hardened steel, mild homogeneous steel, hard homogeneous steel, copper, lead and depleted uranium (referred to as Tuballoy). An additional set of empirical constants is provided in the THOR 51 report (Anon., 1963) for application of the equations to nonmetallic targets, including bonded and unbonded nylon, Lexan (polycarbonate), Plexiglas (both as cast and stretched), Doron plate (fibreglass/plastic composite) and bullet-resistant glass. For application of the THOR equations to other, nonspecified target materials, the standard approach is to select the closest THOR material, and modify the thickness by the density ratio of the two materials.

The empirical constants in Eqs (8.150)–(8.155) were derived for impact of compact steel fragments, which did not deform or breakup during testing. Thus, although the equations have been applied with other projectile materials (eg, depleted uranium), their predictions have not been validated and should be used with care (particularly for projectile materials which are expected to breakup upon impact). The equations have been shown to provide reasonable agreements for projectiles with L/D ratios up to 3. However, for extrapolation to fragments with larger L/D ratios, their accuracy is unknown and should be approached with scepticism.

The primary concern with application of the THOR equations relates to the use of mild steel SAE 1020 as a projectile material. FSP standards, such as STANAG 2920 or MIL-P-46593B, require type 4337H/4340H steel, which have substantially higher hardness/strength than SAE 1020 (eg, 286 versus 134 HB).

8.5.2 JTCG/ME penetration handbook

The Joint Technical Coordinating Group for Munitions Effectiveness (JTCG/ME) Anti-Air built upon the work published in THOR in their handbook of penetration equations for both projectiles and fragments (Anon., 1985).

For projectiles, differentiation is made between penetrators likely to perforate a target by ductile hole formation (ie, piercing or sharp attack) and those likely to perforate a target by plugging (ie, blunt attack) (see Fig. 8.44).

Penetration by sharp projectiles is assumed by the JTCG/ME equations to occur as a two-step process: initially, the tip of the projectile induces intense deformations in the target, creating an opening; the body of the projectile then expands this opening, pushing aside target material as it penetrates. This description corresponds to cavity expansion theory (see Section 8.3.1), however in the case of the JTCG/ME equations a higher level of empiricism is incorporated.

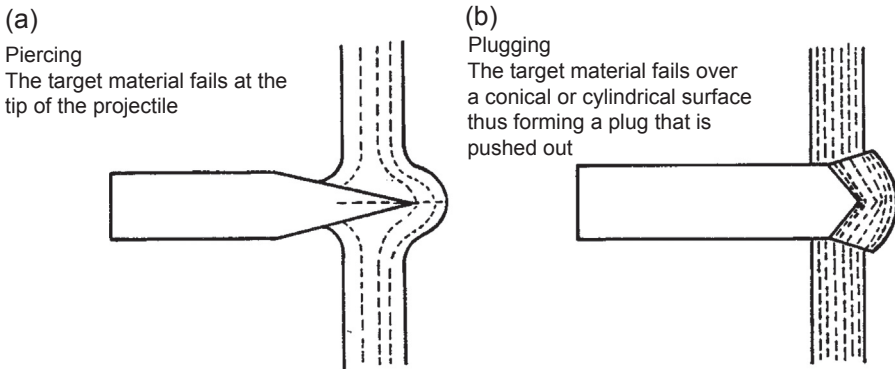


Figure 8.44 Failure mechanisms for plates penetrated by (a) sharp and (b) blunt projectiles within the JTCG/ME penetration handbook.

Anon., 1985. Penetration Equations Handbook for Kinetic-Energy Penetrators (61 JTCG/ME-77-16 (revision 1)). Retrieved from: Aberdeen.

For impact of blunt projectiles and fragments, the equations are based on nondimensional forms of those presented in [Anon. \(1961\)](#). An empirically defined fragmentation threshold, derived for the impact of steel fragments on steel plates and based on equality of impact pressure ([Yatteau et al., 2005](#)), enables application of the JTCG/ME equations for projectiles that breakup during the impact event, unlike the THOR equations.

Material constants to be used with the JTCG/ME penetration equations are provided in [Anon. \(1985\)](#) for a range of common materials in aerospace and defence applications. For metals and alloys for which constants are not provided, scaling equations are provided based on material strength and ductility properties.

8.5.3 ConWep

ConWep is a collection of conventional weapons effects calculations from the equations presented in [Hyde \(1986\)](#). It provides the capability to evaluate the impact of fragments, projectiles, fire, incendiary, chemical agents and blast on structures based on empirical characterisation of test data.

ConWep defines a standard fragment shape based on casing fragments of an explosive-loaded munition (ie, mild steel). Although considered less critical than sharper edged fragments, the standard fragment, shown in [Fig. 8.45](#), is assumed to be statistically representative.

The base equations for ConWep, both for application with fragments and small-calibre projectiles, are highly empirical. Equations are provided for impact on mild steel targets, from which scaling relationships are applied. For fragment impact, these scaling laws are based on target hardness alone, and as such are applicable on a limited range of targets.

The CONWEP equations assume that the impact of a fragment at normal incidence (ie, normal to the target surface) is the worst-case scenario, and should be used for the design condition. As such, the equations are not applicable for oblique impacts.

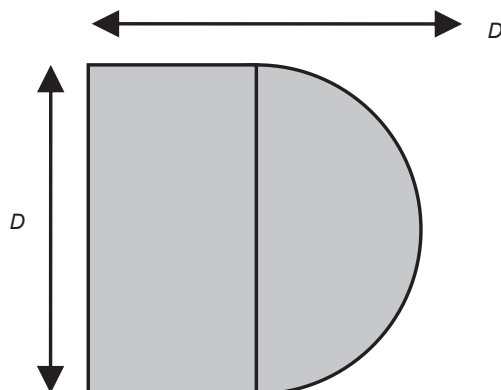


Figure 8.45 ConWeb primary fragment shape and descriptors.

8.5.4 FATEPEN

The Fast Air Target Encounter Penetration (FATEPEN) package is a software program maintained by Applied Research Associates on behalf of the US Naval Surface Warfare Center (Dahlgren Division) that is a modern extension of the THOR and JTCG/ME empirical ballistic penetration equations (Yatteau et al., 2005). The program uses a sequence of empirical models (ballistic penetration, fragment cloud formation, etc.) to predict the effectiveness of weapons against lightly armoured and multiwall targets. FATEPEN allows for the definition of multiple impactor shapes, including: spheres, parallelepiped and cylinders (with round, tapered or truncated noses). However, projectile shape is only taken into account for distinguishing between differences in fracture characteristics, and in presented area. For the majority of calculation steps, projectiles are represented by mass equivalent right circular cylinders.

A number of different approaches are incorporated in FATEPEN for calculating the ballistic limit of a target (V_{50}), depending on the target and fragment material. The ballistic limit equations in FATEPEN are a combination of analytical techniques and empirical curve fits sourced from over 2000 penetration experiments (Yatteau et al., 2005), primarily involving cylindrical steel FSPs. Specific empirical equations are provided for target/projectile combinations for which ballistic limit data exist (ie, tungsten alloy on steel), while other projectiles are replaced with weight-equivalent steel FSPs. Target materials are grouped into 'metallic (or harder)' and 'nonmetallic (or softer)', for which differing ballistic limit relationships are applied. The target thickness to effective projectile diameter ratio is also used to categorise impact geometries in which target flexural response is significant, and alternative failure modes (such as shear plugging or perforation without fragment deformation or flexural plate response) are considered.

8.5.5 Future techniques

Methods such as THOR/ConWep/JTCG, etc. attempt to simplify a highly complex interaction through varying levels of empiricism. They typically retain some level of

analytical foundation, for example through the inclusion of projectile or target material parameters. For these types of approaches, increasing levels of empiricism, although often decreasing the complexity of the algorithm and improving accuracy for a particular application, limit the conditions for which the technique can be applied. Outside of the empirical data set from which the algorithm has been derived, such techniques can be wildly inaccurate.

Machine learning techniques are well suited to solve problems in classification, regression and novelty detection — particularly in high-dimension problem spaces such as dynamic impact events. The application of such fully empirical techniques enables impact events to be characterised without any limitation on the dimensionality of the problem (ie, number of input variables), rather than a partial limitation as employed by techniques such as THOR.

The aptitude of machine learning techniques, specifically artificial neural networks (ANN) and support vector machines, has been investigated in [Ryan and Thaler \(2013\)](#) and [Ryan et al., \(2015b\)](#) for predicting the outcome of hypervelocity impact events on spaced aluminium armour. The techniques were found to provide comparable or improved levels of accuracy in classifying the result of an impact event (perforated/ not perforated). Additionally, the qualitative output of the techniques was compared to traditional semiempirical methods, and found to show improved sensitivity in capturing behaviour related to projectile fragmentation, melt and vaporisation (see [Fig. 8.46](#)).

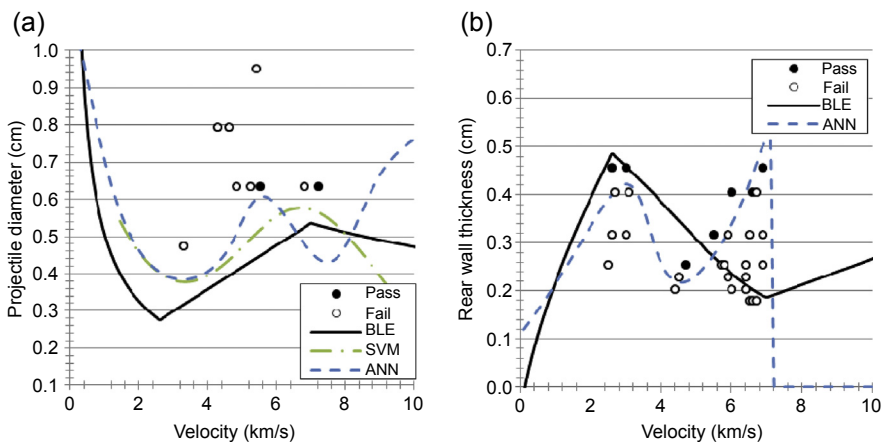


Figure 8.46 Ballistic limit curves for hypervelocity impact of spherical aluminium projectiles on a spaced aluminium armour (ie, Whipple shield). Left: Plotted in terms of critical projectile diameter versus impact velocity, the curves define the threshold above which the rear element of the armour will be perforated. Right: plotted in terms of critical rear wall thickness versus impact velocity, the curves define the required thickness of the rear element of the armour required to defeat a 0.3175 cm diameter Al2017-T4 spherical projectile.

Ryan, S., Kandanaarachchi, S., Smith-Miles, K., 2015b. Support vector machines for characterising whipple shield performance. *Procedia Engineering* 56, 61–70.

There are three main limitations to the application of full empirical, machine learning approaches:

- They require a large database of test data;
- That database should be self-consistent and provide a comprehensive and even sampling of the parameter space and;
- They are a ‘black-box’ approach that yields limited information about the computational steps undergone to generate the output.

Although large databases of ballistic test data exist, the data are typically clustered about projectiles and armour materials of interest, geometries representative of fielded systems, and impact conditions likely to be encountered (eg, impact velocities based on muzzle velocities and typical encounter range). Also, given the costs associated with ballistic testing, data are typically generated as proof of adherence to a standard (ie, repeated testing at a specific velocity), or to determine the ballistic limit. Optimally, the training database for a machine learning approach would include:

- A wide distribution of armour materials and geometries;
- A wide range of projectile types, calibres, and impact conditions (eg, angles, velocities, etc.); and
- An even distribution of test results, not just about the ballistic limit, but across a range from well below the ballistic limit to well above the ballistic limit.

Although relevant to a different problem space, the database compiled in [Ryan and Thaler \(2013\)](#) is representative of the difficulties in the application of machine learning tools to characterise ballistic performance. In [Fig. 8.47](#) the database is evaluated in terms of impact velocity, a nondimensional geometry parameter, and the ratio of projectile diameter to critical projectile diameter defined by the state-of-the-art empirical expression. Additionally, the distribution of the database population density is also shown in [Fig. 8.47](#) in terms of impact velocity and nondimensional geometry parameter. Clearly the database does not provide a homogeneous sampling of the problem space. Rather, the data are clustered about geometries of interest (eg, corresponding to flight hardware), experimentally accessible conditions (eg, 7 km/s), and as-close-as-possible to perforation thresholds. In [Fig. 8.47](#), t_b refers to the thickness of the front armour component (ie, bumper), t_w is the thickness of the rear armour component, S is the spacing between armour components, d_c is the projectile diameter above which the armour will be perforated and d_p is the projectile diameter.

In general, for problems with inhomogeneous sampling of the parameter space, machine learning methods have difficulty interpolating through sparsely populated regions (ie, between clusters), depicted in [Fig. 8.48](#). Thus, in order to generate the ballistic limit curves in [Fig. 8.47](#), the training data were likely sparse at the velocity limits (ie, <2 km/s and >7 km/s) and more densely populated at velocities between 2 and 7 km/s.

A method is proposed in [Ryan et al. \(2016\)](#) for remediating the effects of a poorly sampled parameter space with a minimum number of additional experiments. Using an autoassociative neural net trained in conjunction with a hetero-associative multilayer perceptron (referred to as a creativity machine), an optimisation procedure can be conducted to, for example, design armour optimised to defeat a given impact condition.

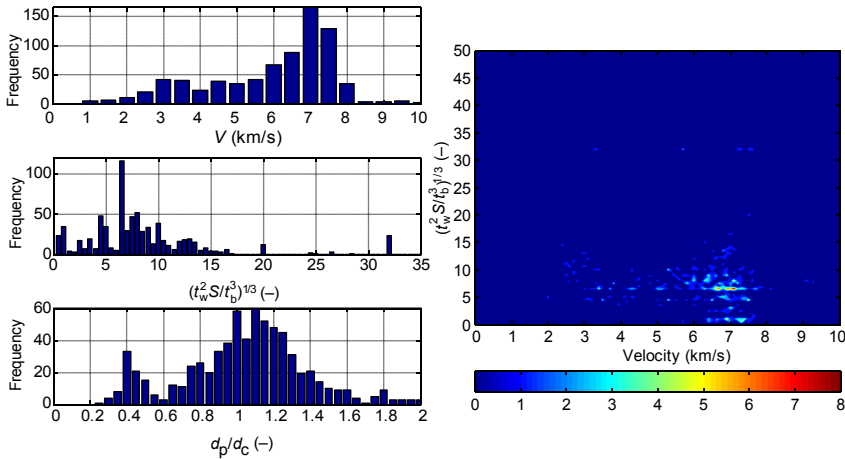


Figure 8.47 Statistical evaluation of the impact test database compiled in [Ryan and Thaler \(2013\)](#). Data are clustered about an impact velocity of 7 km/s and a nondimensional geometry parameter $(t_w^2 S / t_b^3)$ of 6.5. Additionally, the bulk of test data occur for conditions near the ballistic limit, displayed here in terms of the ratio of projectile diameter to critical projectile diameter predicted by the JSC Whipple shield ballistic limit equation.

Ryan, S., Thaler, S.L., 2013. Artificial neural networks for characterising Whipple shield performance. *International Journal of Impact Engineering* 56, 61–70.

When applied to sparse datasets, this optimisation procedure can provide erroneous designs that are associated with poorly sampled regions in the parameter space, often as a result of mistaken correlations identified by the ANN. By constructing such erroneous designs, subjecting them to testing, and retraining the dual-net machine, these problematic regions can be mediated within the problem space defined by the training data. Referred to as ‘bootstrapping’ and shown in [Fig. 8.49](#), this iterative process shows great promise in enabling the application of machine learning techniques on terminal ballistics problems which are inherently poorly sampled due to the cost and difficulty associated with experimentation.

8.5.6 Case study 3: predicting the performance of a range of steel grades against fragments and armour-piercing projectiles

A large number of penetration algorithms have been presented which can be applied to predict the ballistic limit of finite steel plates impacted by common projectiles or fragment threats. The algorithms encompass a range of analytical foundations, simplifying assumptions, empirical adjustments, etc. So, the question arises — which algorithm should be applied, and when?

In [Fig. 8.50](#), the predictions of a number of models are plotted for the impact of 7.62 mm APM2 projectiles against RHA steel. The Forrestal, Woodward, Walker–Anderson (+breakout), Conwep, and JTCG/ME models are compared to the required

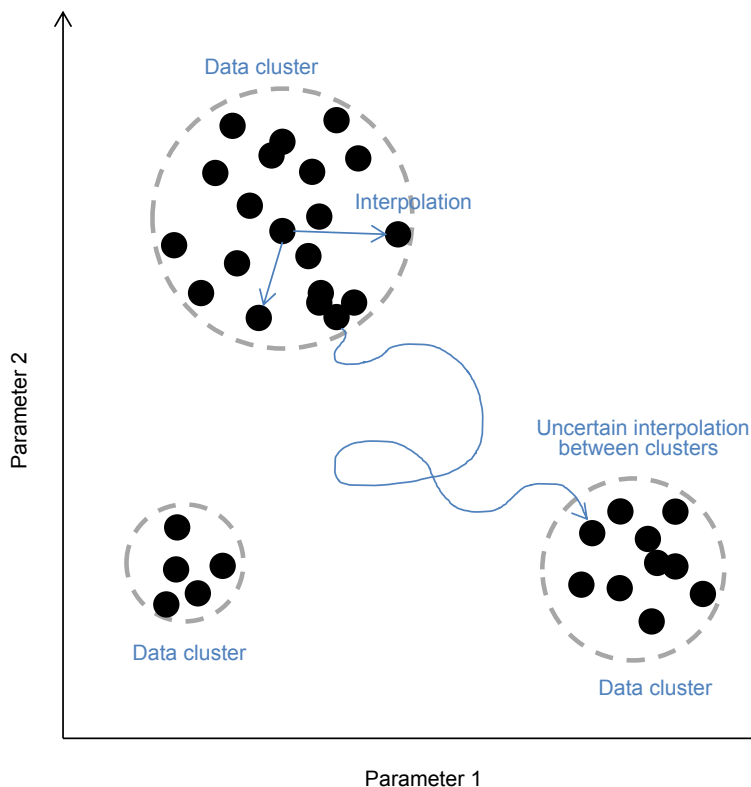


Figure 8.48 Machine learning methods such as ANNs are ideally trained on a uniform sampling of the problem's parameter space. Test data for ballistic or hypervelocity impact are typically clustered around areas of interest (eg, geometry corresponding to fielded systems), experimentally accessible conditions, and as-close-as-possible to perforation thresholds. As a result of the inhomogeneous sampling of the parameter space, machine learning methods have difficulty interpolating through sparsely populated regions of the parameter space (right). High levels of predictive accuracy can be expected in regions of high sampling rates, outside of these regions the networks may be inaccurate.

performance of RHA, as per MIL-A-12560. The performance requirement listed in the MIL-spec would typically relate to the two sigma velocity, V_{05} , which is defined as two standard deviations below the V_{50} .

The JTCG/ME and Forrestal models are shown to provide an excellent level of agreement with the RHA required performance. The Walker–Anderson/Breakout model is shown to overpredict the armour performance, likely due to the use of a hemispherical projectile nose, which is less effective than a pointed ogive typical of armour-piercing projectiles. The ConWep model also overpredicts the performance of the armour, which may be due to the use of constants derived for application with hard homogeneous armour (360–440 HB) compared to that of the softer MIL-spec RHA (290–390 HB) — particularly for thicker sections. The

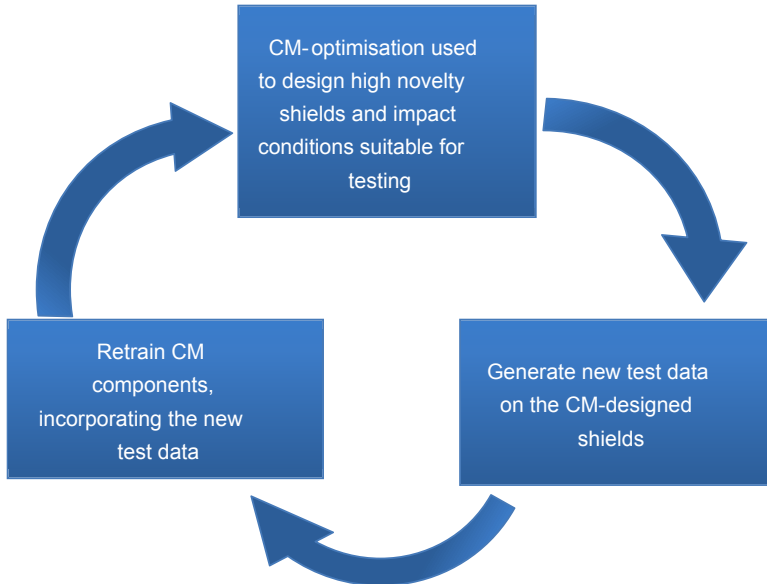


Figure 8.49 An iterative procedure (‘bootstrapping’) for improving the predictions of an artificial neural network trained on data that does not provide a sound sampling of the parameter space, as might typically be expected in many engineering applications, particularly those requiring high cost or difficult experimentation.

Woodward model initially underpredicts performance for thin plates (dished or ductile hole formation failure), but for thicker sections the performance becomes less conservative. The effect of the projectile diameter to thickness ratio on the Woodward model, resulting in the application of different failure mechanisms, is clearly identifiable.

In [Fig. 8.50](#), five models are also applied to predict the performance of RHA against 12.7 mm calibre FSPs at normal incidence, including two forms of the THOR model corresponding to different fragment shape assumptions (see [Section 8.5.1](#)). The JTCG/ME, ConWep, and the THOR expression for fragments of no particular shape (*THOR standard*) provide nearly identical predictions, but all underestimate the armour performance. Frank-Zook and the compact fragment form of THOR provide the highest level of agreement with the test data. The predictions of the Woodward model are the most conservative, particularly for thicker plates (ie, those failing under indentation and shear plugging mode). The Woodward model is based on simple plasticity and assumes rigid projectile behaviour during penetration. For impact of FSPs on RHA, significant projectile deformation would be expected, resulting in an increased projectile presented area and thus requiring more work to indent the target plate. Thus, the underprediction of armour performance by the Woodward model in this instance is expected. In [Table 8.7](#), the FSP test data are listed, together with the predictions of the analytical/empirical models and the variation from the experimental measurement.

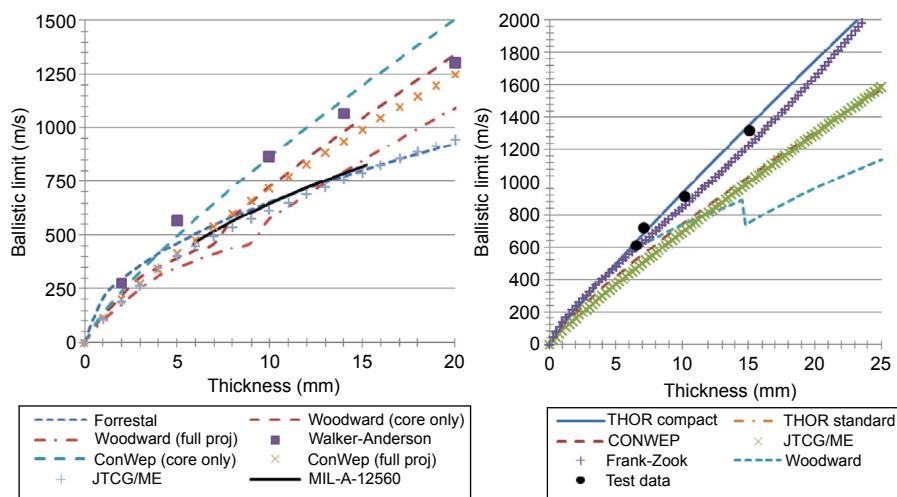


Figure 8.50 The effect of thickness on the predicted ballistic limit of rolled homogeneous armour steel (350 HB) impacted by 7.62 mm APM2 projectiles (left) and 12.7 mm FSPs (right) at normal incidence.

Test data for FSP impact on RHA are from Nguyen, L.H., Ryan, S., Cimpoeu, S.J., Mouritz, A.P., Orifici, A.C., 2015a. The effect of target thickness on the ballistic performance of ultra high molecular weight polyethylene composite. *International Journal of Impact Engineering* 75(0), 174–183. <http://dx.doi.org/10.1016/j.ijimpeng.2014.07.008>; Nguyen, L.H., Ryan, S., Cimpoeu, S.J., Mouritz, A.P., Orifici, A.C., 2015b. The efficiency of ultra-high molecular weight polyethylene composite against fragment impact. *Experimental Mechanics*. <http://dx.doi.org/10.1007/s11340-015-0051-z>.

The improved ballistic performance of steels with increasing hardness is well established (eg, Rapacki et al., 1995). Gooch et al. (2007b) found increasing performance against 7.62 mm AP M2 projectiles with increasing steel hardness, plateauing for plate hardness above 400 HB. On the other hand, Rapacki et al. (1995) did not observe such a plateauing for depth of penetration tests with tungsten alloy projectiles, finding increased performance up to Brinell hardness values of 600. In Fig. 8.50 the results from Gooch et al. (2007b) are supplemented with additional test data on 600 HB steel. The results are consistent with Rapacki et al.'s findings, and suggest continual improvements in armour-piercing (AP) performance with increasing hardness of steel armour. It is interesting to note that tests with steel core AP projectiles at normal incidence against steel armours with Brinell hardness values between 400 and 500 are typically affected by shatter gap issues (see, eg, Chang and Bodt, 1997). For tests on the 600 HB steel no shatter gap was identified — for this material all tests resulted in shatter of the projectile core (extending to impact velocities as much as 300 m/s below the measured V_{50}).

A direct evaluation of the model predictions in terms of hardness is difficult, given the different application ranges. For instance, JTCG/ME provides constants for steel target hardness value between 100 and 350 HB only. The projectile equation for

Table 8.7 Comparison of FSP test data with predictions from a number of analytical models for a range of steel target thicknesses

Thickness (mm)	Exp. V_{50} (m/s)	THOR comp.		THOR stan.		ConWep		JTCG/ME		Woodward		Frank-Zook	
		V_{50} (m/s)	Error (%)	V_{50} (m/s)	Error (%)	V_{50} (m/s)	Error (%)	V_{50} (m/s)	Error (%)	V_{50} (m/s)	Error (%)	V_{50} (m/s)	Error (%)
6.57	612	633	−3.4	468	23.6	521	14.9	469	23.4	591	3.5	595	2.8
7.11	718	677	5.7	500	30.3	554	22.9	501	30.2	627	12.7	618	14.0
10.2	913	935	−2.4	691	24.3	742	18.8	692	24.2	845	7.5	738	19.1
15.07	1320	1350	−2.3	998	24.4	1034	21.7	1000	24.2	1225	7.2	750	43.2

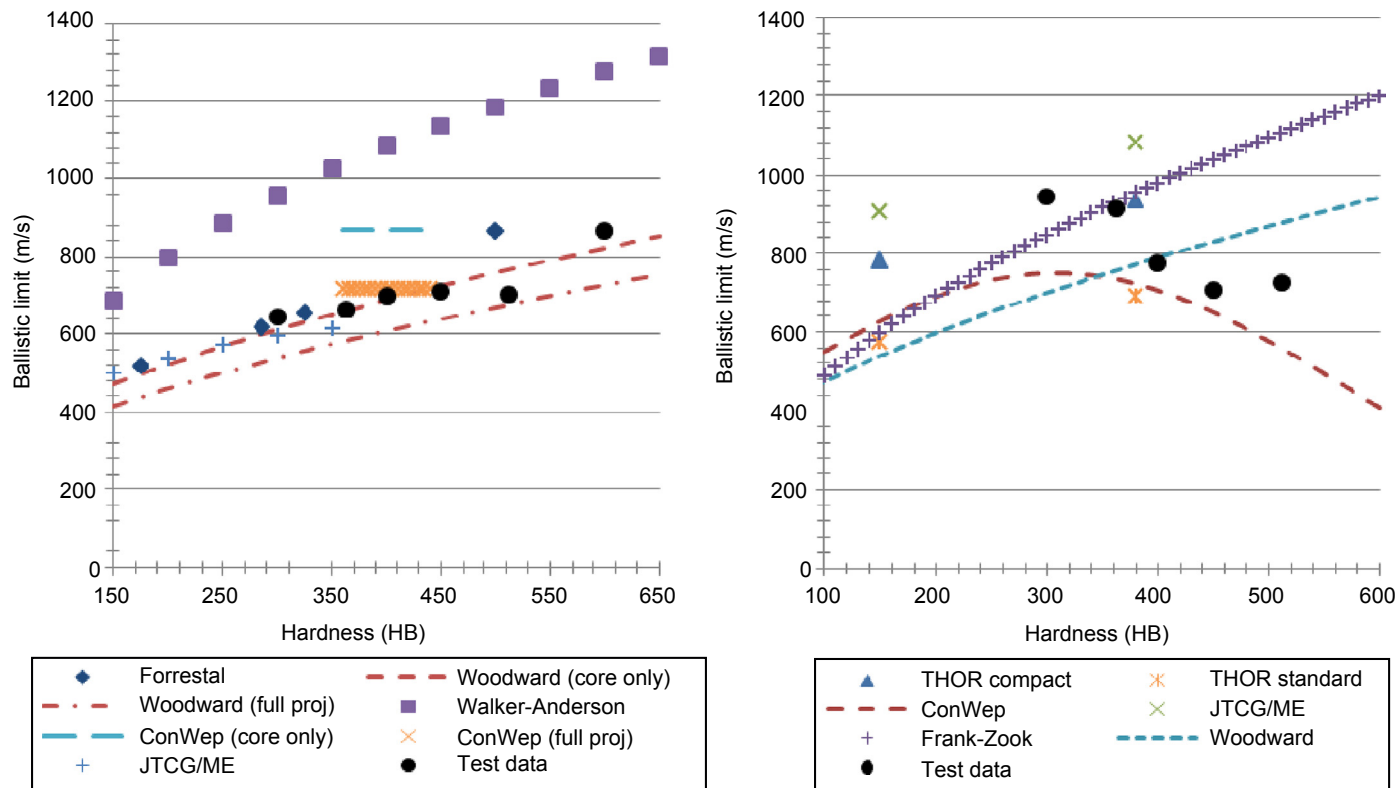


Figure 8.51 The effect of hardness on the ballistic performance of nominal 10-mm thick steel plates impacted by 7.62 mm APM2 projectiles (left) and 12.7 mm calibre FSPs (right).

Table 8.8 Comparison of FSP test data with predictions from a number of analytical models for a range of steel target hardnesses

Hardness (HB)	Exp. V_{50} (m/s)	THOR		ConWep		JTCG/ME		Frank-Zook		Woodward	
		V_{50} (m/s)	Error (%)	V_{50} (m/s)	Error (%)	V_{50} (m/s)	Error (%)	V_{50} (m/s)	Error (%)	V_{50} (m/s)	Error (%)
300	945	—	n/a	751	−20.6	—	n/a	848	−10.2	700	−26.1
363	913	935*	2.4*	736	−19.3	1084*	18.8*	929	1.8	758	−17.3
400	774	935*	20.8*	707	−8.7	1084*	40.1*	980	26.6	789	1.7
450	708	—	n/a	650	−8.2	—	n/a	1039	46.7	829	17.1
512	726	—	n/a	560	−22.8	—	n/a	1106	52.4	877	20.6

* Based on empirical constants for hard homogenous steel (HB = 380).

ConWep is only valid in a range of target hardness values between 360 and 440 HB. The Forrestal model can be applied to any target hardness provided target failure occurs through ductile hole formation, but requires knowledge of the target material stress–strain behaviour. The Walker–Anderson model, although theoretically applicable to any hardness target, is only applicable for hemispherical projectiles, which do not fracture during impact. The Woodward model assumes a rigid, nondeformable projectile. As such, there are limitations and complications surrounding the application of nearly any analytical penetration model. For the techniques applied in Fig. 8.51, the Woodward model (core-only) shows the best level of agreement with the test data. The JTCG/ME, ConWep (full projectile), Woodward (full projectile) and Forrestal model also show a good level of agreement for the most part. The Walker–Anderson model is shown to significantly overestimate the ballistic limit, however, as discussed previously this is considered in part due to a less penetrating projectile nose shape. Additionally, the Walker–Anderson model defines the projectile in terms of density, diameter and length (ie, projectile weight is not a direct input value). As such, the core-only parameters were used for this analysis. It is unclear however, how much the lead filler and copper jacket of the 7.62 mm APM2 projectile influences the penetration performance. Investigations on the performance of the 7.62 mm APM2 projectile against aluminium alloy targets (eg, Borvik et al. (2010)), demonstrate a ca. 10% variation in the measured ballistic limit between the full projectile and the core-only.

Gooch et al. (2007b) also investigated the effect of increasing hardness on the performance of steel targets against 12.7 mm FSPs. The performance was found to decrease with increasing hardness due to an increased susceptibility to adiabatic shear plugging, plateauing for plate hardness above 400 HB. Interestingly, the models considered demonstrate different qualitative relationships with hardness, shown in Fig. 8.51. The THOR, Woodward, Frank-Zook and JTCG/ME models all show predicted increases in performance with increasing target hardness. ConWep, however, shows an initial increase in performance with hardness, peaking at ca. 300 HB, and then decreasing with further increases in hardness. Although none of the models provides a high degree of quantitative agreement (see Table 8.8), the ConWep prediction shows the best qualitative agreement with the test data.

Acknowledgements

The author is extremely grateful to Dr Stephen Cimpoeu, of the Defence Science and Technology Group, Australia, for his guidance and technical input, in compiling this chapter.

References

- Abdullah, M.R., Cantwell, W.J., 2006. The impact resistance of polypropylene-based fibre-metal-laminates. *Composite Science and Technology* 66 (1112), 1682–1693.
- Alekseevskii, V.P., 1966. Penetration of a rod into a target at high velocity. *Combustion, Explosion, and Shock Waves* 2 (2), 63–66. Retrieved from: <http://dx.doi.org/10.1007/BF00749237>.

- Allen, W.A., Rogers, J.W., 1961. Penetration of a rod into a semi-infinite target. *Journal of the Franklin Institute* 272 (4), 275–284. [http://dx.doi.org/10.1016/0016-0032\(61\)90559-2](http://dx.doi.org/10.1016/0016-0032(61)90559-2).
- Anderson Jr., C.E., Walker, J.D., 2005. An analytical model for dwell and interface defeat. *International Journal of Impact Engineering* 31 (9), 1119–1132. Retrieved from: <http://www.sciencedirect.com/science/article/B6V3K-4DHXDGB-1/2/a1a08db698d24efb83a1a6139a468604>.
- Anderson Jr., C.E., Walker, J.D., Hauver, G.E., 1992. Target resistance for long-rod penetration into semi-infinite targets. *Nuclear Engineering and Design* 138 (1), 93–104. [http://dx.doi.org/10.1016/0029-5493\(92\)90281-y](http://dx.doi.org/10.1016/0029-5493(92)90281-y).
- Anon, 1961. The Resistance of Various Metallic Materials to Perforation by Steel Fragments, Empirical Relationships for Fragment Residual Velocity and Residual Weight (AD322781). Retrieved from: Aberdeen.
- Anon, 1963. The Resistance of Various Non-Metallic Materials to Perforation by Steel Fragments; Empirical Relationships for Fragment Residual Velocity and Residual Weight (AD336461). Retrieved from: Aberdeen.
- Anon, 1985. Penetration Equations Handbook for Kinetic-Energy Penetrators (61 JTCG/ME-77–16 (revision 1)). Retrieved from: Aberdeen.
- Backman, M.E., Goldsmith, W., 1978. The mechanics of penetration of projectiles into targets. *International Journal of Engineering Science* 16 (1), 1–99. [http://dx.doi.org/10.1016/0020-7225\(78\)90002-2](http://dx.doi.org/10.1016/0020-7225(78)90002-2).
- Bazhenov, S.L., Dukhovskii, I.A., Kovalev, P.I., Rozhkov, A.N., 2001. The fracture of SVM Aramid fibers upon a high-velocity transverse impact. *Polymer Science Series A* 1, 61–71.
- Ben-Dor, G., Dubinsky, A., Elperin, T., 2013. *High-Speed Penetration Dynamics*. World Scientific, Singapore.
- Bethe, H.A., 1941. An Attempt at a Theory of Armor Penetration (R-492). Retrieved from: Frankford Arsenal.
- Billon, H.H., Robinson, D.J., 2001. Models for the ballistic impact of fabric armour. *International Journal of Impact Engineering* 25 (4), 411–422. [http://dx.doi.org/10.1016/S0734-743X\(00\)00049-X](http://dx.doi.org/10.1016/S0734-743X(00)00049-X).
- Birkhoff, G., MacDougall, D.P., Pugh, E.M., Taylor, G., 1948. Explosives with lined cavities. *Journal of Applied Physics* 19 (6), 563–582.
- Borvik, T., Forrestal, M.J., Warren, T.L., 2010. Perforation of 5083-H116 aluminum armor plates with ogive-nose rods and 7.62 mm APM2 bullets. *Experimental Mechanics* 50, 969–978.
- Bruchey, W.J., Horwath, E.J., 1998. System considerations concerning the development of high-efficiency ceramic armors. In: Paper Presented at the 17th International Symposium on Ballistics, Midrand, South Africa.
- Carlucci, D.E., Jacobson, S.S., 2007. *Penetration Theories Ballistics: Theory and Design of Guns and Ammunition*. CRC Press.
- Casem, D.T., Dandekar, D.P., 2012. Shock and mechanical response of 2139-T8 aluminum. *Journal of Applied Physics* 111.
- Chang, A.L., Bodt, B.A., 1997. JTCG/AS Interlaboratory Ballistic Test Program – Final Report (ARL-tr-1577). Retrieved from: Aberdeen Proving Ground.
- Cheeseman, B., Gooch Jr., W.A., Burkins, M.S., 2008. Ballistic evaluation of aluminum 2139-T8. In: Paper Presented at the 24th International Symposium on Ballistics, New Orleans.
- Cho, A., Bes, B., 2006. Damage tolerance capability of an Al-Cu-Mg-Ag alloy (2139). *Materials Science Forum* 519-521, 269–301.

- Chocron, S., Anderson, C.E., Walker, J.D., Ravid, M., 2003. A unified model for long-rod penetration in multiple metallic plates. *International Journal of Impact Engineering* 28 (4), 391–411. Retrieved from: <http://www.sciencedirect.com/science/article/B6V3K-473FV4K-1/2/f684ae5a3baeadd3369e036ca2a87d85>.
- Chocron, S., Anderson Jr., C.E., Walker, J., 1999. A consistent plastic flow approach to model penetration and failure of finite-thickness metallic targets. In: Paper Presented at the 18th International Symposium on Ballistics, San Antonio.
- Christman, D.R., Gehring, J.W., 1965. Penetration Mechanisms of High Velocity Projectiles (TR 65–50).
- Christman, D.R., Gehring, J.W., 1966. Analysis of high-velocity projectile penetration mechanics. *Journal of Applied Physics* 37 (4), 1579–1587.
- Christman, D.R., Wenzel, A.B., Gehring, J.W., 1964. Penetration mechanisms of high-velocity rods. In: Paper Presented at the Seventh Hypervelocity Impact Symposium, Tampa.
- Cimpoeru, S.J., 2002. Analytical modelling of the perforation of multi-layer metallic targets by fragment simulating projectiles. In: Paper Presented at the 20th International Symposium on Ballistics, Orlando.
- Crouch, I.G., 2014. Effects of cladding and its influence on ballistic performance. In: Paper Presented at the 28th International Symposium on Ballistics, Atlanta.
- Cunniff, P.M., 1992. An analysis of the system effects in woven fabrics under ballistic impact. *Textile Research Journal* 62 (9), 495–509.
- Cunniff, P.M., 1999. Dimensionless parameters for optimization of textile-based body armor systems. In: Paper Presented at the 19th International Symposium on Ballistics, San Antonio.
- Eichelberger, R.J., 1956. Experimental test of the theory of penetration by metallic jets. *Journal of Applied Physics* 27 (1), 63–68. Retrieved from: <http://www.scopus.com/inward/record.url?eid=2-s2.0-0009412051&partnerID=40&md5=c6d0679654e0f73efd7f8f99865d1529>.
- Elder, D., 2010. DMTC KBE Tool Extension – Revision B. Retrieved from: Hawthorn.
- Forrestal, M.J., Borvik, T., Warren, T.L., 2010. Perforation of 7075-T651 aluminum armor plates with 7.62 mm APM2 bullets. *Experimental Mechanics* 50, 1245–1251.
- Forrestal, M.J., Borvik, T., Warren, T.L., Chen, W., 2014. Perforation of 6082-T651 aluminum plates with 7.62 mm APM2 bullets at normal and oblique impacts. *Experimental Mechanics* 54, 471–481.
- Forrestal, M.J., Luk, V.K., Brar, N.S., 1990. Perforation of aluminum armor plates with conical-nose projectiles. *Mechanics of Materials* 10 (1–2), 97–105. [http://dx.doi.org/10.1016/0167-6636\(90\)90020-G](http://dx.doi.org/10.1016/0167-6636(90)90020-G).
- Forrestal, M.J., Warren, T.L., 2009. Perforation equations for conical and ogival nose rigid projectiles into aluminum target plates. *International Journal of Impact Engineering* 36 (2), 220–225. <http://dx.doi.org/10.1016/j.ijimpeng.2008.04.005>.
- Forrestal, M.J., Warren, T.L., Borvik, T., 2013. A scaling law for APM2 bullets and aluminum armor. In: Paper Presented at the Annual Conference on Experimental and Applied Mechanics, Lombard.
- Frank, K., Zook, J., 1987. Energy-efficient penetration and perforation of targets in the hypervelocity regime. *International Journal of Impact Engineering* 5 (1–4), 277–284. [http://dx.doi.org/10.1016/0734-743x\(87\)90045-5](http://dx.doi.org/10.1016/0734-743x(87)90045-5).
- Frank, K., Zook, J., 1991. Energy-Efficient Penetration of Targets (BRL-MR-3885). Retrieved from: Aberdeen.
- Galanov, B.A., Ivanov, S.M., Kartuzov, V.V., 2001. On one new modification of Alekseevskii-Tate model for nonstationary penetration of long rods into targets. *International Journal of Impact Engineering* 26 (1–10), 201–210. Retrieved from: <http://www.sciencedirect.com/science/article/B6V3K-46K5SKJ-S/2/5fc47e71c487cda7483fddec02408382>.

- Gellert, E.P., Cimpoeru, S.J., Woodward, R.L., 2000. A study of the effect of target thickness on the ballistic perforation of glass-fibre-reinforced plastic composites. *International Journal of Impact Engineering* 24 (5), 445–456. [http://dx.doi.org/10.1016/S0734-743X\(99\)00175-X](http://dx.doi.org/10.1016/S0734-743X(99)00175-X).
- Gooch Jr., W.A., Burkins, M.S., Palicka, R., 2004. Ballistic development of U.S. High density tungsten carbide ceramics. In: Society, T.A.C. (Ed.), *Progress in Ceramic Armor*. John Wiley & Sons.
- Gooch Jr., W.A., Burkins, M.S., Squillacioti, R., 2007a. Ballistic testing of commercial aluminum alloys and alternate processing techniques to increase the availability of aluminum armor. In: Paper Presented at the 23rd International Symposium on Ballistics, Tarragona.
- Gooch Jr., W.A., Showalter, D.D., Burkins, M.S., Thorn, V., Cimpoeru, S.J., Barnett, R., 2007b. Ballistic testing of Australian Bisalloy steel for armour applications. In: Paper Presented at the 23rd International Symposium on Ballistics, Tarragona.
- Hauver, G.E., Rapacki Jr., E.J., Netherwood, P.H., Benck, R.F., 2005. Interface Defeat of Long-rod Projectiles by Ceramic Armor (ARL-TR-3590). Retrieved from: Aberdeen Proving Ground.
- Hill, R., 1949. Plastic distortion of non-uniform sheets. *Philosophical Magazine* 40 (309), 971–983.
- Hohler, V., Stilp, A.J., 1977. Penetration of steel and high density rods in semi-infinite steel targets. In: Paper Presented at the Third International Symposium on Ballistics, Karlsruhe.
- Hoo Fatt, M.S., Lin, C., Revilock Jr., D.M., Hopkins, D.A., 2003. Ballistic impact of GLARE fibre-metal-laminates. *Composite Structures* 61 (1–2), 73–88.
- Hori, H., Nemat-Nasser, S., 1986. Brittle failure in compression: splitting, faulting and brittle-ductile transition. *Philosophical Transactions A* 319, 337–374.
- Hyde, D.W., 1986. *Fundamentals of Protective Design for Conventional Weapons* (TM 5-855-1). Retrieved from: Washington, DC.
- Johnson, G.R., Cook, W.H., 1983. A constitutive model and data for metals subject to large strains, high strain rates and high temperatures. In: Paper Presented at the 7th International Symposium on Ballistics, the Hague.
- LaSalvia, J.C., Horwath, E.J., Rapacki, E.J., Shih, C.J., Meyers, M.A., 2000. Microstructural and micromechanical aspects of ceramic/long-rod projectile interactions: dwell/penetration transitions. In: Paper Presented at the Explomet, Albuquerque.
- Lee, B.L., Song, J.W., Ward, J.E., 1994. Failure of spectra polyethylene fiber-reinforced composites under ballistic impact loading. *Journal of Composite Materials* 28 (13), 1202–1226.
- Lundberg, P., Renström, R., Lundberg, B., 2000. Impact of metallic projectiles on ceramic targets: transition between interface defeat and penetration. *International Journal of Impact Engineering* 24 (3), 259–275. [http://dx.doi.org/10.1016/S0734-743X\(99\)00152-9](http://dx.doi.org/10.1016/S0734-743X(99)00152-9).
- Moriniere, F.D., Alderliesten, R.C., Benedictus, R., 2014. Modelling of impact damage and dynamics in fibre-metal-laminates – a review. *International Journal of Impact Engineering* 67 (2014), 27–38.
- Nemat-Nasser, S., Deng, H., 1994. Strain-rate effect on brittle failure in compression. *Acta Metallurgica et Materialia* 42 (3), 1013–1024.
- Nguyen, L.H., Ryan, S., Cimpoeru, S.J., Mouritz, A.P., Orifici, A.C., 2015a. The effect of target thickness on the ballistic performance of ultra high molecular weight polyethylene composite. *International Journal of Impact Engineering* 75, 174–183. <http://dx.doi.org/10.1016/j.ijimpeng.2014.07.008>.
- Nguyen, L.H., Ryan, S., Cimpoeru, S.J., Mouritz, A.P., Orifici, A.C., 2015b. The efficiency of ultra-high molecular weight polyethylene composite against fragment impact. *Experimental Mechanics*. <http://dx.doi.org/10.1007/s11340-015-0051-z>.

- Phoenix, L.S., Porwal, P.K., 2003. A new membrane model for the ballistic impact response and V50 performance of multi-ply fibrous systems. *International Journal of Solids and Structures* 40 (24), 6723–6765. [http://dx.doi.org/10.1016/S0020-7683\(03\)00329-9](http://dx.doi.org/10.1016/S0020-7683(03)00329-9).
- Piekutowski, A.J., Forrestal, M.J., Poormon, K.L., Warren, T.L., 1996. Perforation of aluminum plates with ogive-nose steel rods at normal and oblique impacts. *International Journal of Impact Engineering* 18 (7–8), 877–887. [http://dx.doi.org/10.1016/S0734-743X\(96\)00011-5](http://dx.doi.org/10.1016/S0734-743X(96)00011-5).
- Rapacki Jr., E.J., Frank, K., Leavy, B., Keele, M., Prifti, J., 1995. Armor steel hardness influence on kinetic energy penetration. In: Paper Presented at the 15th International Symposium on Ballistics, Jerusalem.
- Ravid, M., Bodner, S.R., 1983. Dynamic perforation of viscoplastic plates by rigid projectiles. *International Journal of Engineering Science* 21 (6), 577–591. [http://dx.doi.org/10.1016/0020-7225\(83\)90105-2](http://dx.doi.org/10.1016/0020-7225(83)90105-2).
- Ravid, M., Bodner, S.R., Holcman, I., 1994. A two-dimensional analysis of penetration by an eroding projectile. *International Journal of Impact Engineering* 15 (5), 587–603. [http://dx.doi.org/10.1016/0734-743x\(94\)90111-w](http://dx.doi.org/10.1016/0734-743x(94)90111-w).
- Ravid, M., Bodner, S.R., Walker, J., Chocron, S., Anderson Jr., C.E., Riegel, P.J., 1998. Modification of the Walker-Anderson penetration model to include exit failure modes and fragmentation. In: Paper Presented at the 17th International Symposium on Ballistics, Midrand.
- Recht, R.F., 1978. Taylor ballistic impact modelling applied to deformation and mass loss determinations. *International Journal of Engineering Science* 16 (11), 809–827. [http://dx.doi.org/10.1016/0020-7225\(78\)90067-8](http://dx.doi.org/10.1016/0020-7225(78)90067-8).
- Reid, S.R., Wen, H.M., 2000. Perforation of FRP laminates and sandwich panels subjected to missile impact. In: Reid, S.R., Zhou, G. (Eds.), *Impact Behaviour of Fibre-Reinforced Composite Materials and Structures*. Woodhead Publishers, Loughborough, UK, pp. 239–279.
- Ryan, S., Cimpoeu, S.J., 2015a. An evaluation of scaling laws for predicting the performance of targets perforated in ductile hole formation. In: 3rd International Conference on Protective Structures. Newcastle.
- Ryan, S., Kandanaarachchi, S., Smith-Miles, K., 2015b. Support vector machines for characterising whipple shield performance. *Procedia Engineering* 56, 61–70.
- Ryan, S., Thaler, S.L., 2013. Artificial neural networks for characterising Whipple shield performance. *International Journal of Impact Engineering* 56, 61–70.
- Ryan, S., Thaler, S., Kandanaarachchi, S., 2016. Machine learning methods for predicting the outcome of hypervelocity impact events. *Expert Systems with Applications* 45, 23–39. Retrieved from: <http://dx.doi.org/10.1016/j.eswa.2015.09.038>.
- Scott, B.R., 2011. Unusual transverse compression response of non-woven laminates. In: 26th International Symposium on Ballistics, Miami.
- Segletes, S.B., 2000. An Adaptation of Walker-Anderson Model Elements into the Frank-Zook Penetration Model for Use in MUVES (ARL-TR-2336). Retrieved from: Aberdeen.
- Shearn, M., 2000. Breakout Ballistic Simulation Program V1.1.
- Smith, J.C., McCrackin, F.L., Schiefer, H.F., 1958. Stress-strain relationships in yarns subjected to rapid impact loading — Part V: wave propagation in long textile yarns impacted transversely. *Textile Research Journal* 28 (4), 288–302.
- Song, B.L., Egglestone, G.T., 1987. Investigation of the PVB/PF ratios on the crosslinking and ballistic properties in glass and aramid fiber laminate systems. In: 19th SAMPE International Technical Conference, Crystal City.

- Sternberg, J., 1989. Material properties determining the resistance of ceramics to high velocity penetration. *Journal of Applied Physics* 65 (9), 3417–3424. <http://dx.doi.org/10.1063/1.342659>.
- Tate, A., 1967. A theory for the deceleration of long rods after impact. *Journal of the Mechanics and Physics of Solids* 15 (6), 387–399. Retrieved from: <http://www.sciencedirect.com/science/article/B6TXB-46G4YJ3-6V/2/4096e3a29c50f69f4df1e60147f75b54>.
- Tate, A., 1969. Further results in the theory of long rod penetration. *Journal of the Mechanics and Physics of Solids* 17 (3), 141–150. Retrieved from: <http://www.sciencedirect.com/science/article/B6TXB-46G2J79-5B/2/4e3a5422f14314720216082f36f73101>.
- Tate, A., 1986. Long rod penetration models—Part II. Extensions to the hydrodynamic theory of penetration. *International Journal of Mechanical Sciences* 28 (9), 599–612. Retrieved from: <http://www.sciencedirect.com/science/article/B6V49-47YSCPK-PS/2/4a2579b4a9aacc40d19963e8587e32e1>.
- Taylor, G., 1948. The formation and enlargement of a circular hole in a thin plastic sheet. *The Quarterly Journal of Mechanics and Applied Mathematics* 1 (1), 103–124.
- Teland, J.A., 1999. A Review of Analytical Penetration Mechanics (FFI/RAPPORT-99/01264). Retrieved from: Kjeller.
- Thompson, W.T., 1995. An approximate theory of armor penetration. *Journal of Applied Physics* 26, 80–82.
- Walker, J.D., 1999. Constitutive model for fabrics with explicit static solution and ballistic limit. In: 18th International Symposium on Ballistics, San Antonio.
- Walker, J.D., Anderson, C.E., 1995. A time-dependent model for long-rod penetration. *International Journal of Impact Engineering* 16 (1), 19–48. Retrieved from: <http://www.sciencedirect.com/science/article/B6V3K-3Y5FP72-1F/2/ff023a977ec6a5e3f443e2cae2d1cb56>.
- Walker, J.D., Chocron, I.S., Anderson Jr., C.E., Riegel, J.P., Riha, D.S., McFarland, J.M., Abbott, B., 2013. Survivability modeling in DARPA's Adaptive Vehicle Make (AVM) program. In: Paper Presented at the 27th International Symposium on Ballistics, Freiburg.
- Walker, J.D., Chocron, S., 2011. Why impacted yarns break at lower speed than classical theory predicts. *Journal of Applied Mechanics* 78 (5), 051021. <http://dx.doi.org/10.1115/1.4004328>.
- Walters, W., Williams, C., Normandia, M., 2006. An explicit solution of the Alekseevski-Tate penetration equations. *International Journal of Impact Engineering* 33 (1–12), 837–846. <http://dx.doi.org/10.1016/j.ijimpeng.2006.09.057>.
- Walters, W.P., Segletes, S.B., 1991. An exact solution of the long rod penetration equations. *International Journal of Impact Engineering* 11 (2), 225–231. [http://dx.doi.org/10.1016/0734-743x\(91\)90008-4](http://dx.doi.org/10.1016/0734-743x(91)90008-4).
- Wilde, A.E., Ricca, J.J., Cole, L.M., Rogers, J.M., 1970. Dynamic Response of a Constrained Fibrous System Subject to Transverse Impact Part I – Transient Responses and Breaking Energies of Nylon Yarns (AMMRC TR 70–32). Retrieved from: Watertown.
- Woodward, R., 1981. Modelling Penetration by Slender High Kinetic Energy Projectiles (MRL-R-811). Retrieved from: Ascot Vale.
- Woodward, R., Crouch, I.G., 1988. Analysis of the Perforation of Monolithic and Simple Laminate Aluminium Targets as a Test of Analytical Deformation Models (MRL-R-1111). Retrieved from: Ascot Vale.
- Woodward, R.L., 1978. The penetration of metal targets by conical projectiles. *International Journal of Mechanical Sciences* 20 (6), 349–359. [http://dx.doi.org/10.1016/0020-7403\(78\)90038-3](http://dx.doi.org/10.1016/0020-7403(78)90038-3).

- Woodward, R.L., 1982. Penetration of semi-infinite metal targets by deforming projectiles. Retrieved from: *International Journal of Mechanical Sciences* 24 (2), 73–87 <http://www.sciencedirect.com/science/article/B6V49-4814GFC-FF/2/2eb250ea8472921029ab1b73516729d0>.
- Woodward, R.L., 1989. A Basis for Modelling Ceramic Composite Armour Defeat. DSTO Materials Research Laboratory, Maribyrnong, Vic.
- Woodward, R.L., Cimperu, S.J., 1998. A study of the perforation of aluminium laminate targets. *International Journal of Impact Engineering* 21 (3), 117–131. [http://dx.doi.org/10.1016/s0734-743x\(97\)00034-1](http://dx.doi.org/10.1016/s0734-743x(97)00034-1).
- Yatteau, J., Zernow, R., Recht, G., Edquist, K., 2005. FATEPEN Volume 1-Analyst's Manual (Version 3.0.0) (Retrieved from: Littleton).
- Zukas, J., Nicholas, T., Swift, H., Greszczuk, L., Curran, D., 1982. *Impact Dynamics*. John Wiley & Sons, Inc, New York.

Numerical modelling and computer simulations

9

M. Saleh¹, L. Edwards¹, I.G. Crouch²

¹ANSTO, Lucas Heights, NSW, Australia; ²Armour Solutions Pty Ltd, Trentham, Victoria, Australia

The development of armour materials and systems is a very expensive business, especially when it involves lengthy ballistic trials. Penetration and perforation events are also highly complex and involve competition between alternative failure mechanisms. The physical conditions within an impact zone also vary, with location, in temperature, strain rate, strain, stress state and pressure. This is true across all threats — here, though, we shall focus exclusively upon the interaction between small arms ammunition and, to a less extent, blast loadings, upon lightweight armour materials and structures.

Numerical modelling has rapidly evolved, within both the armour and antiarmour communities, in order to better understand, and model, these complex, and sometimes unpredictable, dynamic events, with the benefit of reduced costs, increased speed and attention to detail. In a numerical model, the material response is calculated in an iterative, step-wise fashion where incremental elements of strain lead to changes in stress via a material constitutive equation. But which equations are best to use? The modeller also has the choice of using 2-D or 3-D, finite element or finite difference methods, and linear or nonlinear material behaviour.

Table 9.1 outlines the structure and content of this chapter by covering the range of computer codes available, the types of processors used, and the breadth of both yield strength models and damage criteria which are employed to describe how an armour material flows, fractures and fails. At the end of the chapter, four worked examples illustrate the choices available when modelling armour/antiarmour interactions.

9.1 Introduction to numerical modelling

The central motivation for this chapter is to highlight the use of computational material science in the analysis of impact phenomena, with particular reference to recent bodies of work in this area that cover most of the ballistic scenarios discussed (Anderson 1987; Anderson and Bodner, 1988; Børvik et al., 2001, 2009; Deshpande and Fleck, 2000a; Holmquist and Johnson, 2008; Nilakantan and Gillespie 2012; Nilakantan et al., 2010b; Tabiei and Nilakantan, 2008; Zukas, 2004; Zukas and Scheffler, 2000; Johnson and Anderson 1987). There is a plethora of online resources that cover the spectrum of impact scenarios; rather, the intent here is to highlight the particular role of numerical modelling in capturing the physical attributes of impact and explosive events.

Table 9.1 Breakdown of fundamental parts of any numerical model

Aspect	Example	Comment
Software system	Autodyn, LS-Dyna	Now ANSYS (via LEAP Australia)
Solvers	Lagrangian, Eulerian, ALE, SPH	Select, as appropriate
Equations of state	Linear, bulk, shock, etc	Conservation of energy and momentum
Constitutive equations (strength models)	<ul style="list-style-type: none"> • Modified Zerelli—Armstrong • Johnson—Holmquist • Cowper—Symonds 	<ul style="list-style-type: none"> • Numerous models • Requires determination of constants • Requires high strain rate material characterisation data • Use anisotropic values, if available
Damage criteria	Johnson—Cook parameters	Requires another set of input data
Contact algorithms	Coulomb friction	How to treat interfaces
Cell erosion	Critical strain	How to attribute energy when cells become too distorted

The chasm between numerical simulation and experimental results has certainly lessened over the last three decades with the advent of faster computing and more robust software, often encompassing new contact algorithms, element formulations, continuum treatments and material models. To gauge the issues that affect hydrocodes, Zukas (Zukas, 1993, 2004; Scheffler and Zukas, 2000) has sought to identify the discrepancies that arise between experimental and numerical results in the light of the inherent nonlinear behaviour of these highly transient problems.

The Finite Element (FE) practitioner is ultimately motivated to resolve two basic notions: wave propagation through the impacting bodies, and the strain-rate dependence of the material's response (Zukas, 1993). Often the combined use of experiments and calculations, specifically material characterisation at high strain rates, reduces the development cost and time, with a commensurate increase in information when compared to experiments or calculations alone. Herein lies the usefulness of hydrocodes, a class of wave-propagation codes, which were first developed in the 1950s to simulate the effects of weapons (Orphal, 2006) by means of a fluid dynamics-like approach. A comprehensive summary of these early developments can be found in Johnson and Anderson (1987). These codes were grounded in the conservation equations of energy, momentum and mass which will be discussed in later sections. An excellent introduction to the formulations and use of hydrocodes can be found in Benson (1992), Zukas (2004), Anderson (1987) and Anderson and Bodner (1988). Fig. 9.1 shows a typical integration scheme utilised in a hydrocode

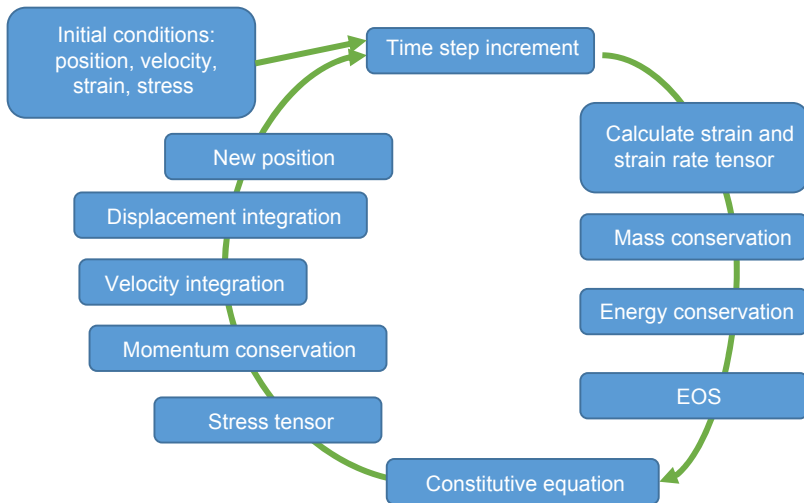


Figure 9.1 Typical integration scheme utilised in a hydrocode.

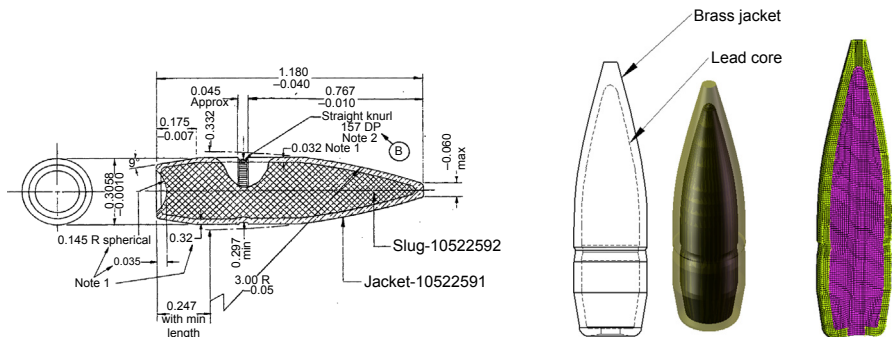


Figure 9.2 Idealisation of the 7.62 mm NATO ball and the discretisation of the computational domain.

and Fig. 9.2 illustrates how small arms ammunition, like the commonly used, 7.62 mm M80 round (see Chapter 1) is described within the computational space.

Most engineering evaluations of ballistic and blast events venture far beyond the confines of most undergraduate assumptions of elastic material behaviour, suffice to say the computational scientist and engineer must be well versed in the various plasticity models currently in use (Dunne and Petrinic, 2005; Meyers, 1994; Meyers and Murr, 1981; Johnson, 2011). Major achievements in hydrocode development were based on the early work of Los Alamos National Laboratory (LANL) and the Lawrence Livermore National Laboratory (LLNL) and these works influence almost all commercial hydrocodes currently available. Their initial problems investigated the hydrodynamic behaviour of hypervelocity impact of steel and aluminium targets. The material strength models that nowadays describe the deviatoric stress were not present in the early simulations; rather, the hydrostatic pressures were the major

contributor to material deformation. As the scope of applications for detonation and impact-induced shock-wave simulations widened so has the need for deviatoric stress components to be identified. Over the preceding decades more physical phenomena and material models have found implementation into hydrocodes. For example, Johnson–Cook (JC), Zerilli–Armstrong (ZA) and the mechanical threshold stress (MTS) models are notable amongst the many used to describe plasticity in metals. The number of hydrocodes has also increased manifold with the original LANL implementations seeing commercialisation through the AUTODYN and the LS-DYNA software. Other notable packages include CTH, ABAQUS and Altair’s RADIOSS solvers, which have wide military and commercial uses. The ever-pertinent question that remains is what necessitates a successful simulation? Is it accurate geometry and boundary conditions or is it the applicable constitutive models that ultimately govern armour performance? This chapter will ultimately equip the computational engineer to gauge the fundamental issues that arise in the successful simulation of ballistic and blast events.

A final word, as the reader consults the following pages; you should heed the words of [Jean Lemaître and Rodrigue Desmorat \(2005\)](#), below, and reflect at various stages, upon the uniqueness of your solution and the sensitivity of the numerical models in representing the correct physics.

Very accurate calculations are too often made with very poor accuracy of the material parameters.

Lemaître and Desmorat (2005)

9.2 A short review of software packages

The underlying calculations common to all hydrocodes for armour penetration mechanics analysis are computing a solution for the conservation equations of energy, mass and momentum. This is done through spatial and time discretisation. The former is achieved through the finite elements, finite differences, finite volumes or mesh-free methods. Most hydrocodes utilise explicit and implicit schemes to resolve the time-dependent response of the basic conservation equations. Both implicit and explicit methods are applicable to modelling structural contact, with the implicit methods being capable of larger time steps at the same, or higher, accuracy as those of the explicit method. In practice, most dynamic processes in terminal ballistics and blast modelling, use an explicit integration scheme to better resolve the wave propagation effects over micro- or nanoseconds and to better model the nonlinearity of these problems. Additionally, most codes utilise formulations for nonlinear equations of state that account for shock-wave formation and propagation. For example, an artificial bulk viscosity is often used to capture the discontinuous nature of shock waves by smearing the pressure across a number of elements.

Decoupled treatments of the stress tensor are commonplace and the material behaviour is computed in terms of hydrostatic and deviatoric stress components: the former

being described by an equation of state (EOS) and the latter by constitutive equations for the flow stress that account for a range of behaviours: elastic and inelastic strain, rate-dependent material behaviour including damage, failure and postfailure behaviour. Some of the most widely used codes are highlighted next with a breakdown of the capabilities of each given in [Table 9.2](#) along with contact details.

LS-DYNA is a general-purpose, vectorised, finite-element code used to analyse the nonlinear response of structures, specifically large deformations using an explicit integration scheme. The software DYNA3D ([Whirley and Engelmann, 1993](#)) was a predecessor to LS-DYNA and is where many of the more than 130 material models originate from. Contact-impact algorithms utilise both constraint and penalty-based methods to satisfy many contact conditions, which allows for difficult contact problems to be analysed, e.g. element erosion for ballistic impact, single surface contact for thin sheet buckling, heat transfer across interfaces and adaptive remeshing for severely deformed elements. Preprocessing is largely defined by its keyword interface using LS-PREPOST or a text editor with the user needing a sound knowledge of all the required input cards for their respective simulation.

LS-DYNA contains a large library of 1-D, 2-D and 3-D element types. These can be used alongside lumped masses and discrete elements (e.g. springs and dampers) to provide model simplification. Continuum treatments are available for Lagrangian, Eulerian, smooth particle hydrodynamics (SPH) and arbitrary Lagrangian Eulerian (ALE) methods for most material models. Owing to its vectorised code structure, the solver is largely optimised for massively parallel processor (MPP) computing. The latest release of LS-DYNA, version 980 R8.0, includes a Computational Fluid Dynamics (CFD) module for compressible flow solver based upon the conservation element/solution element and an incompressible flow solver that is fully coupled with the solid mechanics solver.

AUTODYN is an explicit code used for nonlinear dynamics of solids, fluids and gases. With similar capabilities to LS-DYNA, the code additionally integrates with the ANSYS workbench environment and utilises the embedded material libraries. In mixed domain, multiphysics modelling is possible through variations of the solvers called:

1. Finite element solvers for structural dynamics;
2. Finite volume solvers for transient CFD (Eulerian, ALE);
3. Mesh-free particle solvers for high velocities, large deformation and fragmentation (SPH); and
4. SMP/MPP solvers for both shared and distributed memory.

Early development of the code precipitated from the work of Lawrence Livermore Laboratory physicists who developed AUTODYN's predecessor, PISCES. Naury Birnbaum, from the PISCES team, joined Malcolm Cowler, from the United Kingdom Atomic Authority, and they released the first fully integrated coupled Euler-Lagrange explicit code, AUTODYN 1.0, in 1985. Prior to 2005 AUTODYN was developed by Century Dynamics Inc., with AUTODYN becoming part of the ANSYS work environment thereafter. ANSYS-AUTODYN has a very user-friendly interface with limited user input requirements and a large library of inbuilt material data. It is an attractive software package for most modelling practitioners.

Table 9.2 Breakdown of selected hydrocodes and their relevant formulations

Software available	Processors	Equations of state	Strength models	Damage criteria	Contact
ANSYS AutoDyn	Lagrangian ALE Eulerian SPH CFD	Polynomial Shock Two-phase liquid–vapor Ideal gas Jones–Wilkins–Lee Porous SESAME Tabular multiphase	Piecewise Johnson–Cook Johnson–Cook Zerilli–Armstrong Steinberg–Guinan High explosive (HE) Mooney–Rivlin Ceramic/glass (Johnson–Holmquist)	Maximum stress/strain Effective stress/strain Shear damage Orthotropic damage Johnson–Holmquist Johnson–Cook Orthotropic stress/ strain Tsai–Wu, Tsai–Hil Crack softening Stochastic	LEAP Australia http://www.leapaust.com.au
LSTC/ANSYS LS-DYNA	Lagrangian ALE Eulerian SPH CFD	Mie–Grueneisen JWL Ideal gas Polynomial	Steinberg Johnson–Cook Zerilli–Armstrong Johnson–Holmquist Ceramics Gurson Modified piecewise linear plasticity Rate-sensitive composite fabric	Johnson–Cook Composite damage with change failure Composite damage with Tsai–Wu failure Brittle damage Johnson–Holmquist Gurson	LEAP Australia http://www.leapaust.com.au LSTC http://www.lstc.com/

Dassault Systemes ABAQUS	Lagrangian ALE Eulerian SPH CFD	Ideal gas Jones—Wilkins—Lee Linear U_s-U_p	Modified crushable foam Semianalytical model for polymers — 1 (SAMP) Rate-sensitive composite fabric Johnson—Cook Crushable-Foam Rate-dependent elastic- plastic	Ductile Shear Johnson—Cook Hashin damage for FR composites	Dassault systemes www. simuserv.com
Altair RADIOSS	Lagrangian Eulerian SPH CFD	JWL Lee—Tarver Mie—Grueneisen Incompressible fluid Multiphase + explosive Ideal gas	Johnson—Cook, Zerilli—Armstrong Ductile damage for porous materials, Gurson Closed cell foams Steinberg—Guinan Johnson—Holmquist	Johnson—Cook Spalling Traction (strain failure) Hashin Model Bao—Xue—Wierzbicki ductile failure Chang—Chang composite failure	Altair Hyperworks http:// www.hyperworks-anz.com/

ABAQUS is based on the finite element method and is classified as a general hydrocode applicable to both linear analyses and nonlinear simulations of single- or multiphase problems. Material models are formulated for metals, composites, rubber, polymers, reinforced concrete, crushable foams and soils/rock. Mechanical, coupled mechanical–thermal and CFD simulations are possible in *ABAQUS*. In both linear and nonlinear simulations limited user input is required largely through the input of the engineering data (structure geometry, material behaviour, boundary conditions and applied loads) and *ABAQUS* automatically chooses appropriate load increments to maintain tractability of the solution which ensures convergence for standard solutions and stability for explicit simulations. *ABAQUS* runs on a variety of desktop workstations and clusters and has a user-friendly interface through *ABAQUS/CAE*.

RADIOSS is a transient explicit and implicit finite element solver technology that simulates mechanical, structural, fluid and fluid–structure interaction (FSI) phenomena, taking into account nonlinear material, for quasistatic and dynamic loading events. *RADIOSS* allows simulation of impact events, automotive safety assessment, metal stamping and forming, structural wave propagation, rigid-body motion and FSIs. *RADIOSS* is part of the Altair HyperWorks package which allows for the solutions for linear, nonlinear, fluid and FSI problems.

9.3 An overview of the various solvers

9.3.1 Lagrangian methods

The fundamental theory relies upon the discretisation of the continuum to solve for the dynamic stress wave propagation which are ever-present in ballistic and blast simulations (Benson, 1992). The solid body is divided into ‘*N*’ elements. The meshing procedure is usually performed using a graphical user interface-based preprocessor. This is especially true for complex geometries. In a Lagrangian computation the material is embedded within the mesh. The motion of the material is thus inferred from the distortion, rotation and the displacement of the mesh itself. The boundaries of the target are represented by the outer boundary elements of the mesh as shown in Fig. 9.3. The mesh resolutions will govern the accuracy of the solution as coarser meshes act to filter out high-frequency components of the dynamic waves. Using a fine mesh will improve the solution accuracy at the expense of computational efficiency with a prohibitively sharp rise in the calculation times (Zienkiewicz et al. (2005)).

Fig. 9.4 shows an example of a Lagrangian simulation of the 5.56 mm NATO ball against the armour steel, Weldox 500E (see Chapter 2). Note the severe deformation and distortion of the elements. The consequence of this is a severe reduction in the computational time step and localised stress concentration. Comparisons with the SPH simulation show similar deformation profiles albeit with no element distortion or deletion in the latter. This method will be further discussed in a later section.

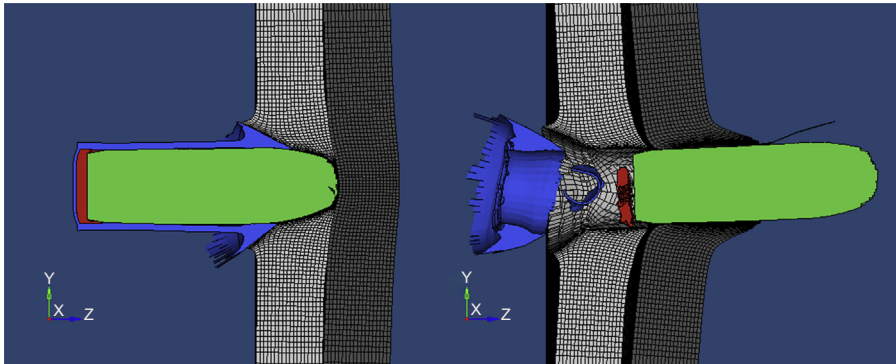


Figure 9.3 Lagrangian simulation of APM2, 7.62 mm round impacting ARMOX 560T armour.

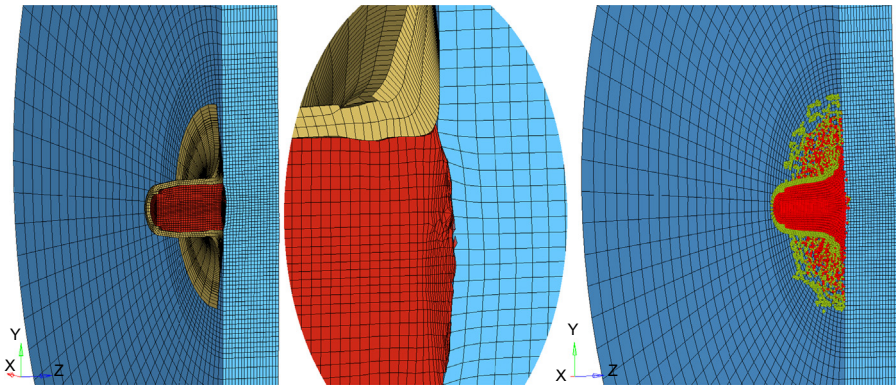


Figure 9.4 A comparison of Lagrangian and SPH methods for the analysis of the 5.56 mm NATO ball against Weldom 500E. It demonstrates the response of the projectile, the severe element distortion and the elongation which is apparent in the Lagrangian formulation.

9.3.2 Eulerian and arbitrary Lagrangian Eulerian (ALE) methods

In traditional Lagrangian-based analysis, the spatial and material domains deform in unison, hence no material flow is allowed across the discretised elements. Conversely, the Eulerian description is based upon fixed grid points and cells which occupy the spatial domain. Their positions and volume, respectively, are invariant in time, thus allowing material to flow across element boundaries. The ALE formulation introduces a third domain (Hughes et al., 1981), an arbitrary displacement of the reference domain. The ALE formulation uses both a Lagrangian and Eulerian formulation and this allows for the analysis of FSI. This method has the added complexity and benefit of computing the moving boundaries, free surfaces and large deformations using an advection step (Alia and Souli, 2006; Souli et al., 2000). The inherent strength of the ALE formulation is the ability to model events where large element distortions would otherwise give erroneous results. The errors in the Lagrangian formulations generally precipitate out of (1)

highly distorted elements degrading accuracy and (2) severe reduction of the time step since explicit FEA uses the Courant–Friedrich–Levy condition, which is based on element length and wave speed through the medium of interest. The major applications of ALE are in blast simulations, hypervelocity impact and FSI, e.g. fuel sloshing, with the common trend being rapid advection of fluids driven by high-pressure gradients over short time periods (μs – ms).

The ALE formulation allows for multimaterial treatment and FSI by using a two-step process to solve the Navier–Stokes equation for fluid flow. The Lagrangian step is computed whereby the mesh moves with the fluid allowing for the calculation of the changes in velocity and internal energy. This is followed by an advection step in which changes in mass, momentum and energy are calculated across the element boundaries. The Eulerian method is effectively a subset of the ALE method whereby the spatial coordinate system is fixed. The amount of material being advected is greater in the Eulerian method compared with the ALE method. The formulae governing the ALE and Eulerian conservation equations are shown in Table 9.3, where ρ is the density, v is the material velocity vector, w is the coordinate velocity vector, σ is the Cauchy stress tensor, b the specific body force and E is the internal energy.

The Eulerian method does contain some shortcomings in the form of a large computational penalty due to the advection and coupling required. Since the ALE method does not solve the Navier–Stokes equation fully it cannot account for boundary layer effects such as drag. The method also exhibits a loss of fidelity, mesh biasing and some ill-prescribed treatments of contact interfaces as evident by the ‘leakage’ phenomena exhibited in some FSI simulations (Chafi et al., 2009; Zhu et al., 2009; Saleh and Edwards, 2015).

The advection process in ALE is dissipative and will underpredict energy for first-order advection schemes; though this can be reduced through the use of second-order advection schemes and the refinement of the mesh to reduce the amount of advection within each time step. These remedies do have a significant computational cost and should be borne in mind.

Figs 9.5 and 9.6 demonstrate the use of the ALE method for the analysis of an internal blast. In this instance, the Lagrangian shipping container is placed within a large Eulerian domain that simulates the surrounding fluid. A small spherical charge

Table 9.3 Conservation equations for ALE and Eulerian methods

Property	ALE	Eulerian (where $w = 0$)
Mass	$\frac{\partial \rho}{\partial t} \Big _x + (v - w) \cdot \nabla \rho = -\rho \nabla \cdot v$	$\frac{\partial \rho}{\partial t} \Big _x + v \cdot \nabla \rho = -\rho \nabla \cdot v$
Momentum	$\rho \left(\frac{\partial v}{\partial t} \Big _x + ((v - w) \cdot \nabla) v \right) = \nabla \cdot \sigma + \rho b$	$\rho \left(\frac{\partial v}{\partial t} \Big _x + (v \cdot \nabla) v \right) = \nabla \cdot \sigma + \rho b$
Energy	$\rho \left(\frac{\partial E}{\partial t} \Big _x + ((v - w) \cdot \nabla) E \right) = \nabla \cdot (\sigma \cdot v) + v \cdot \rho b$	$\rho \left(\frac{\partial E}{\partial t} \Big _x + (v \cdot \nabla) E \right) = \nabla \cdot (\sigma \cdot v) + v \cdot \rho b$

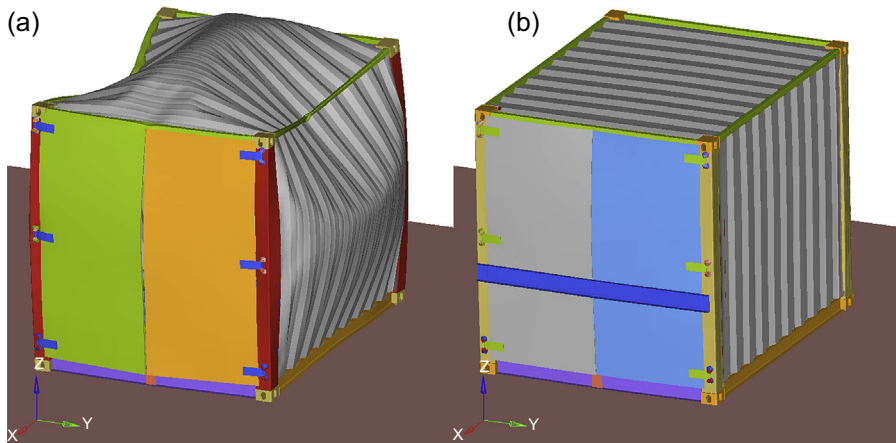


Figure 9.5 Evaluation of an internal blast of (a) standard shipping container, (b) up-armoured shipping container utilising an ALE analysis method.

is placed within the structure. The blast products are fluid-like; hence a conventional choice of Lagrangian formulation for the charge would have resulted in large distorted elements, a severe reduction in the time step, and the possibility of a negative Jacobian due to the presence of inverted elements. Ultimately, these would render the simulation unstable and lead to premature termination. Conversely, the ALE method accounts for the advected fluid without any element distortion and resolves the complex wave interaction and reflections of the incident shockwave, which causes pinching of the fluid in the corners of the container. The coupling between the blast products and the shipping container is achieved through a penalty method akin to the widely used penalty-based contact algorithms. This method initially computes the penetration distance of the ALE material across the Lagrangian parts. When a penetration is found a force proportional to the penetration depth is applied, this acts to resist the penetration and ultimately eliminate it. The iso-surface plot of the explosive gases, shown in Fig. 9.6, is of the volume fraction of the blast products and exhibits a characteristic pinching effect resulting from the reflection of shock waves from the container's edge interacting with the blast products.

9.3.3 Mesh-free methods: smooth particle hydrodynamics

There are three main groups to the mesh-free methods (Liu et al., 2004):

1. Methods based on strong formulations: these are computationally efficient, but often unstable and less accurate;
2. Methods based on weak formulations [element free Galerkin, meshless local Petrov–Galerkin, point interpolation method], which are accurate but slow with particular applications in fracture mechanics and manufacturing simulations; and
3. Particle methods [molecular dynamics (MD), Monte Carlo, SPH], which are based on weak formulations but are efficiently stable for arbitrary distributed nodes and can cope with large deformation. These are also more suited to impact/penetration events.

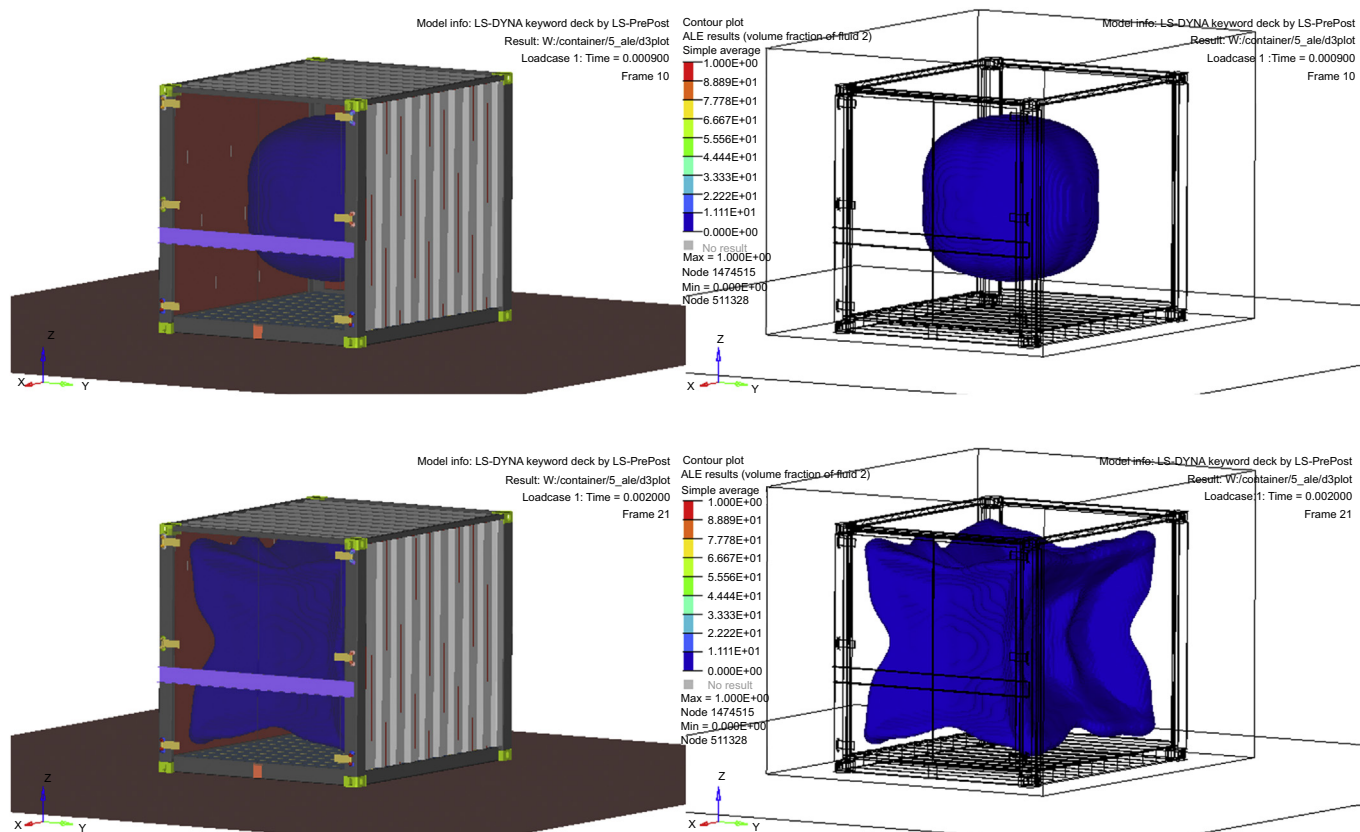


Figure 9.6 The rapid advection of blast products (visible as blue iso-surface) and complex reflections, at 0.9 ms and 2 ms, respectively, necessitates the use of ALE formulations where severe element distortions would ultimately cause errors. The automatic handling of material flow and the creation of material interfaces allows for easier visualisation.

The SPH method is the most widely used in ballistics simulations and largely grew from the astrophysical community based on the work of [Lucy \(1977\)](#) and [Gingold and Monaghan \(1977\)](#) in order to solve large gas-dynamics problems. Most of the developments of the SPH method were thus carried out within this field of study since its inception. Increasingly other researchers have sought to apply the SPH method to other areas such as fluid dynamics, high-velocity impact and metal cutting. There are a number of advantages of the SPH method that qualify it for application to ballistic analyses, namely:

1. Advection of the material that is handled well since there is no material movement across any elements as is the case of Euler or ALE formulations.
2. There is no need to explicitly track the contact interfaces, as in the case of the Lagrangian formulations.
3. The discretised particle domain allows for the computational solution of largely deformed structures without the associated problems of severely deformed elements, reduced time steps in the explicit codes, and the need to rezone and remesh in Lagrangian formulations.
4. SPH can also handle complex geometries which reduces the requirements for partitioning.
5. The mass conservation properties of the SPH method also ensure that both the energy and the momentum of the simulation are conserved, although volume may not be conserved.

The discrete nature of the SPH formulation lends itself to rapid scaling, which is an advantage when modelling small features or geometries. The SPH method is based on a collective movement of the particles in a similar fashion to fluids and it can be thought of as a Newtonian fluid with the associated conservation equations. An excellent treatment of the subject can be found in [Liu et al. \(2004\)](#). The SPH method is comprised of two important constituents: (1) the kernel approximation of the field functions and (2) the particle approximation. The kernel approximation gives an integral representation of the field functions, which can be any history variable of interest such as pressure or density.

The neighbour particle search ([Fig. 9.7](#)) is an important aspect to consider when using the SPH technique. A radius equal to $2h$ defines the sphere of influence around each particle, where h is the smoothing length. The purpose of the search is to compute the interaction between each particle at each time step. The search for neighbouring particles for a random set of M particles would result in $M(M - 1)$ neighbour searches. This is often a limiting factor to consider when meshing since large numbers of elements would quickly overwhelm the numerical computation. The SPH search algorithm in most hydrocodes utilises a system analogous to that of the bucket sort algorithms to find neighbouring particles. The analysis domain is discretised into boxes each containing a number of SPH elements. The boxes are smaller than the sphere of influence, hence the neighbour search only looks for neighbouring particles within the immediate box and then within neighbouring boxes which fall within the $2h$ radius limit. This method helps alleviate the problems associated with unbounded searches with the number of distance computations reducing significantly.

The use of a constant smoothing length has been noted to be problematic ([Benz, 1990](#)) for both large compressive and tensile forces. In the compressive case, the large number of particles within the $2h$ influence spheres would effectively make any large simulations ineffective as the number of neighbouring particles, and consequently the

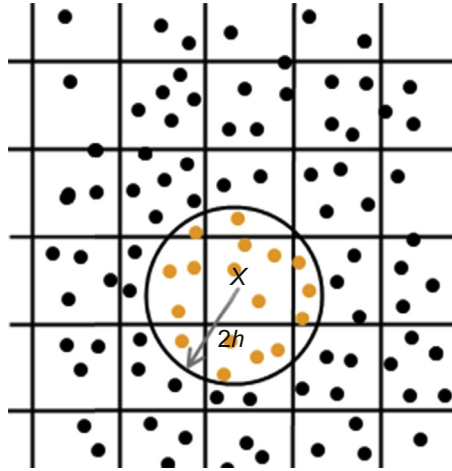


Figure 9.7 Neighbour particle search scheme for SPH.

number of neighbour searches, increases rapidly. With large tensile stresses the distance becomes too large, reducing the number of neighbouring particles and making the simulation more prone to instabilities and inaccuracies. It is thus advantageous to maintain a relatively consistent number of neighbouring particles by using a variable smoothing length, as given by the time derivative used by [Benz \(1990\)](#), where t is time and ρ is the density:

$$\frac{dh}{dt} = -\frac{h}{3\rho} \frac{d\rho}{dt}$$

This formulation works well if the density is continually updated. The drawback of the SPH method is the large computational cost associated with the requirement of large numbers of particles and the neighbour search algorithms. The work of [Swegle et al. \(1994\)](#) highlighted the propensity of the SPH to exhibit tensile instabilities. They observed that particles under tension exhibit unstable motion and this numerical instability may result in unrealistic fracture and particle clustering in an SPH simulation. Another recognised weakness of the SPH technique is the treatment of boundary elements and the incorrect results precipitating out of the SPH particle approximation method at those boundaries. This is especially true where contact, and by default the interface, between different materials is of concern. The work by [Randles and Libersky \(1996\)](#) looked to address the issue of boundary particles through the use of renormalisation schemes. Worked Example #4 demonstrates the successful use of the SPH method in ballistic simulations of soft-cored projectiles.

In traditional mesh-based ballistic simulations highly distorted Lagrangian elements will reduce the computational time step or cause inaccuracies within the simulation. Element erosion is utilised to remove these elements from the calculation, while providing the user with the option of retaining the newly freed nodes as this conserves the mass of the simulation. A considerable drawback of this method is the rapid loss of

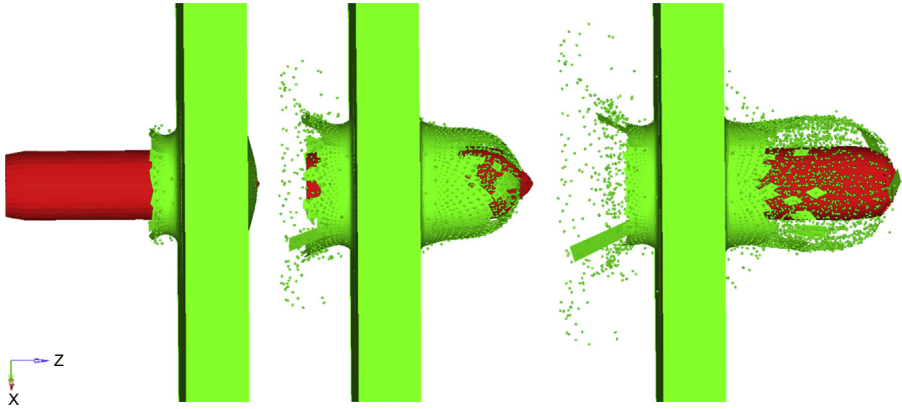


Figure 9.8 Hybrid Lagrangian–SPH formulation with deleted elements being converted to SPH particles and allowed to further interact with the structure using a subsequent node-to-surface contact.

contact in segment-based formulations. Whilst element erosion is widely used, the hybrid formulation shown in Fig. 9.8 allows for the transformation of deleted solid elements into SPH elements with these newly formed elements being capable of further contact, thus allowing for the analysis of fragmentation, spalling and the visualisation of debris clouds. These methods do not conserve volume but do conserve momentum.

9.4 Equations of state

9.4.1 Mie–Grueneisen EOS

The hydrostatic stress (pressure) within a material in dynamic analysis is often expressed in terms of density/volume and temperature (energy) terms. The Mie–Grueneisen EOS originated from statistical mechanics where atoms were considered as quantised harmonic oscillators. The Mie–Grueneisen EOS is based on the Rankine–Hugoniot descriptions of the shock-wave behaviour in solids, through 1-D analysis of the Euler equation for the conservation of mass, momentum and energy. The importance of the EOS is often dependent on the nature of the analysis. For strain rates typical for ballistic or blast simulations, a linear EOS is generally sufficient (Zukas, 1982). Thus the pressure term is computed as a function of volumetric strain and bulk modulus. The Mie–Grueneisen relation is used to extrapolate for the pressure and temperature of materials at different thermodynamic states by utilising Hugoniot shock data, the adiabatic curve or the 0K isotherm. In its algebraic form the relation appears as follows:

$$\gamma(\nu) = \nu \left(\frac{\partial p}{\partial e} \right)_\nu, \quad \gamma(\nu) = \frac{\gamma_0 + a\mu}{1 + \mu}$$

where γ = Grueneisen parameter, p is pressure, γ_0 is the initial Grueneisen parameter, e is the internal energy, v is the specific volume $\mu = \frac{\rho}{\rho_0} - 1$ is the relative volume change (ρ is the current density and ρ_0 is the initial density) and lastly a is the first-order volume correction for γ_0 .

The pressure can thus be expressed in terms of Hugoniot pressure and the Grueneisen parameter.

$$P = f(\rho, e) = P_h \left(1 - \frac{\gamma}{2} \mu \right) + \rho \gamma e$$

where P_h is the Hugoniot pressure.

The Mie–Grueneisen EOS, in a number of hydrocodes defines pressure, as a cubic function for the shock velocity (U_s) and particle velocity (U_p) relationship, as:

$$p = \frac{\rho_0 C_{sp}^2 \mu \left[1 + \left(1 - \frac{\gamma_0}{2} \right) \mu - \frac{a}{2} \mu^2 \right]}{\left[1 - (S_1 - 1) \mu - S_2 \frac{\mu^2}{\mu + 1} - S_3 \frac{\mu^3}{(\mu + 1)^2} \right]} + (\gamma_0 + a \mu) e$$

This relation holds true for compressed materials. For expanded materials the relation is as follows:

$$p = \rho_0 C_{sp}^2 \mu + (\gamma_0 + a \mu) e$$

The parameters S_1 , S_2 , S_3 are the coefficients of the slope of U_s versus U_p . C_{sp} corresponds to the bulk sound speed and is evaluated from the vertical axis intercept.

It should be noted that the shock Hugoniots of steels are nonlinear in their relationships. This is due to a documented phase transition from alpha phase to sigma phase in the steel (Franz and Robitaille, 1979; Kerley, 1993). The transition from alpha phase to sigma phase in the steel occurs in the 13 GPa pressure range. The cubic function, while successful in generally approximating the slope, fails to accurately account for the rapid decrease in wave velocity associated with the phase transition. The cubic function also fails to account for a precursor elastic phase which is also observed. In this phase shock velocity remains static with increasing particle velocity. A user subroutine for the multiphase EOS may be required to accurately model the transition. A tabulated EOS may also be used with reasonable accuracy.

The largest drawback of this EOS is the fact that it does not account for any phase transitions and the resultant overcalculation of pressure response in hypervelocity impact, e.g. shaped charges. The EOS in this strain-rate regimen treats the material as a superheated solid. Other useful forms of the EOS that allow for the treatment of phase transition are the GRAY, three-phase equation for metals (Royce, 1971) and the tabular input of the SESAME EOS library which will be discussed in the following section.

9.4.2 SESAME EOS

The SESAME EOS is a library of thermodynamic properties for a large number of materials (about 170) and is presented in a tabulated form (Lyons and Johnson, 1992; Holian, 1984). EOS parameters are presented for: simple elements, compounds, metals, minerals, polymers and mixtures. The thermodynamic data stored in the library include tables of pressure P and internal energy E (additionally the Helmholtz free energy for many materials is also included). These dependent variables are expressed as functions of density ρ and temperature T in the range of $0\text{--}10^5$ g/cc and $0\text{--}10^9$ K, respectively (Johnson, 1994). The common form of the SESAME EOS can be expressed as:

$$P(\rho, T) = P_c(\rho) + P_N(\rho, T) + P_e(\rho, T)$$

where $P_c(\rho)$ is the cold curve (defining the contribution from cohesive and repulsive force at $T = 0$), $P_N(\rho, T)$ is the nuclear motion contribution and $P_e(\rho, T)$ is the thermal electronic term. The different components of the EOS are derived through experimental tests; empirical observations; the Thomas–Fermi–Dirac statistical theorems for high-density materials; the shock Hugoniot with Mie–Grueneisen assumption for the EOS of shocked solids; MD simulation of pseudopotentials and melting in metals; Einstein, Debye, Cowan, Chart-D and generalised Chart-D models for lattice vibrations in solids; along with a multitude of other theoretical model for the phase transitions, e.g. Maxwell construction for first-order phase transition. The breadth of materials covered by the SESAME EOS data precludes any detailed discussion of the theoretical basis but the reader should consult the aforementioned LANL reports for further clarifications.

A distinct advantage of the SESAME library is the ability to compute the properties of multiphase mediums. This allows for the description of all the states of the materials: solid, liquid, gas, plasma and their transitions. The SESAME EOS tables are available in the CTH code and limited access through the AUTODYN code. The example given in Fig. 9.9 shows a representative $P(\rho, T)$ data set for material 3541 (tungsten-carbide) (Holian, 1984).

9.5 Strength models and failure criteria for metals

In simple mathematical treatments of the response of a material to an external force, a solid body can be described as perfectly rigid (in which all movement is restricted), linear elastic (without any yield value being required), linear elastic-perfectly plastic (with a well-defined, singular value of yield strength) or linear elastic – work hardening (in which both a yield strength value and a work hardening exponent are required). In some modelling cases, these simple solid mechanics relationships are still used. However, over the past four decades or so, mathematical modellers have wanted to describe the flow of a material in far greater detail in order to cover the infinite range of conditions experienced in a dynamic penetration event. The following sections

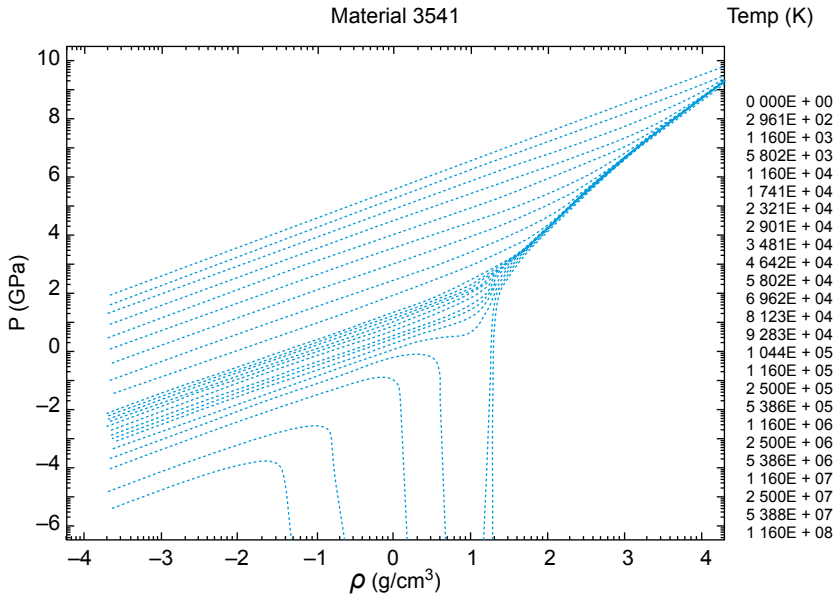


Figure 9.9 EOS data of material 3541 (tungsten-carbide).

Holian, K.S., 1984. T-4 Handbook of Material Properties Data Bases Vol. Ic: Equations of State. Los Alamos National Laboratory, USA.

describe some of the most popular strength models and damage criteria. Please note that nomenclature for the Johnson–Cook, Zerilli–Armstrong and other models are given in [Appendix 9A](#).

9.5.1 Johnson–Cook strength model

The Johnson–Cook strength model ([Johnson and Cook, 1983](#)) is a phenomenological model that is ubiquitous with impact problems, having being firstly presented in the 7th International Symposium on Ballistics, and is often used to compute the strength behaviour of materials under high strain-rate deformation. The model does not stem from first principle in mechanics, rather it is a flow stress relation that stems from experimental observation of metals under impact and penetration. As such the scope of the relation encompasses three prominent parameters:

- Equivalent plastic strain and the associated strain hardening;
- Strain rate and the associated dislocation sensitivity resulting in strain-rate hardening;
- Temperature and the effects of thermal softening due to adiabatic temperature rise.

The original material parameters were derived from three test procedures:

- A torsional test for strain rates ranging from quasi static to 400/s;
- Split Hopkinson pressure bar (SHPB) tensile tests at varying temperatures;
- Quasi-static tensile tests.

Upon publication the authors justified the simplicity of the model by identifying the need for a versatile model that can provide reasonable accuracy when imbedded in numerical codes. The three parameters of the Johnson–Cook model are combined multiplicatively with no additional weight criterion:

$$\sigma_{eq} = [A + B\varepsilon^n][1 + C \ln \dot{\varepsilon}^*][1 - (T^*)^m]$$

The first bracketed term accounts for the increase in yield stress due to strain hardening. The required shear stress, to produce continuous slip within the metal, increases continually with increasing shear strain. Strain hardening is a material response to the interaction of dislocations with each other and with barriers within the crystal structures, which impede their movement. Dislocation pile-up at grain boundaries or slip planes within the crystal is one of the better-understood mechanisms by which materials strain harden. The resultant back-stresses produced due to this pile-up oppose the applied stress on the slip planes, thus requiring additional stress to induce further slip. The second bracketed term models the increase in yield stress with increased strain rate. This is evident in a number of strain-rate sensitivity studies (Last et al., 1996; Lee and Yeh, 1997; Boyce and Dilmore, 2009; Meyers, 1994; Meyers and Murr, 1981; Zukas, 1980; Johnson and Cook, 1983). The authors (Boyce and Dilmore, 2009) carried out a number of strain-rate sensitivity studies for a number of high-strength steels, namely AerMet 100, 4340M based on AISI 4340 steel (similar to the steel evaluated in the original JC paper), HP9-4-20M and ES-1c. In evaluating the strain-rate sensitivity of these high-strength steels they observed an increase in both yield strength and tensile strength with increasing strain rate (Fig. 9.10).

The last term in the JC model is that of the homologous temperature T^* . This temperature-dependent expression accounts for the thermal softening of the material due to thermal-plastic instability. The last term is essentially a thermal softening fraction, which allows for the evaluation of the ratio of flow stress at elevated temperature to that of the flow stress at room temperature. The temperature increase is assumed adiabatic owing to the highly transient nature of the testing procedure. The temperature increment increase due to this heating is:

$$\Delta T = \int_0^\varepsilon \chi \frac{\sigma_{eq} d\varepsilon}{\rho C_p}$$

The Taylor–Quinney coefficient, χ is normally taken to be 0.9 as shown by Børvik et al. (2009) in the investigation of armour-piercing rounds against Armox and Weldox steels. It is important to note that at high strain rates the bulk of the plastic work is converted to adiabatic heating of the specimen; hence it is of particular importance to evaluate the adiabatic heating to the highest possible temperature to better the accuracy of the exponent's prediction.

Further to the strain hardening effect of dislocation pile-up, the authors in Boyce and Dilmore (2009) and Kapoor and Nemat-Nasser (2000) outline additional dislocation phenomena and implore the need for careful identification of the flow stress

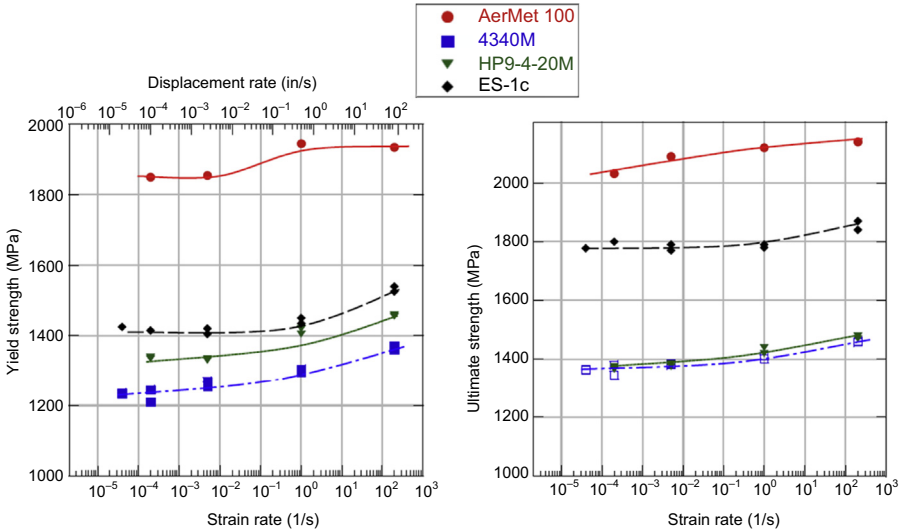


Figure 9.10 Effect of strain rate on yield and tensile strength of steels.

Boyce, B.L., Dillmore, M.F., 2009. The dynamic tensile behavior of tough, ultrahigh-strength steels at strain-rates from 0.0002 to 200 s⁻¹. *International Journal of Impact Engineering* 36, 263–271.

regimen. Amongst the distinctions made is the nature of the obstacle encountered by the dislocation. The obstacles are categorised as either thermal (short-range) or athermal (long-range) based on whether dislocations can overcome these obstacles with the aid of thermal energy or not. The athermal barriers are dependent upon the microstructural properties of the specimen and these may or may not evolve with the deformation of the specimen. For example, the amount of precipitates or solutes does not evolve with deformation whilst the dislocation density and grain size will evolve with material deformation. Similarly, the thermal barriers are a time-dependent, diffusion-limited mechanism; these are therefore coupled to the strain rate and temperature. An example of a thermal barrier is the mechanism for dislocation climb, whereby the incident dislocation will ‘sense’ the increase in the stress field around an obstacle and transfer to an adjacent plane to continue its diffusion.

The resistance to deformation can be evaluated in terms of athermal, thermal and viscous-drag shear resistance (Kapoor and Nemat-Nasser, 2000):

$$\tau = \tau_a + \tau^* + \tau_d$$

This relation can be extended to an evaluation of the flow stress in terms of the athermal, thermal and viscous drag stresses:

$$\sigma = \sigma_{a1}(\rho) + \sigma_{a2} + \hat{\sigma}^* \left[1 - \left(\frac{kT}{F_0} \ln \frac{\dot{\epsilon}_0}{\dot{\epsilon}} \right)^{1/q} \right]^{1/p} + \sigma_{\text{drag}}$$

The authors in Boyce and Dillmore (2009), Kapoor and Nemat-Nasser (2000), Campbell and Ferguson (1970) and Meyers (1994) were able to outline the likely prevalent mechanisms for high strain rate and low-temperature material deformation. With increasing strain rate the prevalent mechanisms are those that correlate to the thermally induced short-range barriers, this is more common since short-range obstacles are usually weaker and these become the controlling mechanism in the highly transient events. The corresponding increase in strength is observed as a direct consequence of the reduction in diffusion-limited dislocation mechanisms.

At lower strain rates and high temperatures the controlling mechanisms are the athermal long-range obstacles. Conceivably these are accompanied by higher energy requirements and are thus categorised as athermal, as mechanical work is a greater driver. Long-range obstacles are largely strain rate insensitive and are thus more pronounced where dislocation diffusion is likely at grain boundaries or slip planes. The JC model does not recognise this dual mechanism (thermal and athermal), this is evident in other constitutive models, such as the Rusinek–Klepaczko (Klepaczko et al., 2009) and Zerilli–Armstrong models (Zerilli and Armstrong, 1987; Armstrong and Zerilli, 1994), the latter is discussed in section 9.5.4.

It is necessary to stress that temperature softening has microstructural underpinning, which is coupled to the athermal barriers. Furthermore the viscous drag component plays a greater role at higher temperature. It is noted in Mawaja and Stumpf (2006) that viscous drag will increase the flow stress with increasing strain. Though this ceases to increase at a certain strain rate and will remain constant thereafter. The JC model does not account for any viscous drag effects. The major mechanisms for the thermal softening are the reduced pathway obstacles to dislocation movement, diffusion of interstitial atoms, phase transformation and the accompanying formation of new grains, dynamic recrystallisation (Andrade et al., 1994), with reduced dislocation densities.

9.5.1.1 Limitations of the Johnson–Cook strength model

The Johnson–Cook model, being the most widely used strength model, has come under heavy scrutiny from a large user base, more so than most other models. The model couples the three aforementioned parameters through a multiplicative process. This has been found to be deficient by Meyers (1994) as it fails to observe the discrete coupling of certain mechanisms and the influence of both strain and temperature histories. Secondly, due to the phenomenological nature of the JC relation, it is important to note that no account is taken of the aforementioned athermal, thermal and viscous drag components, which are fundamental constituents of the Zerilli–Armstrong model. Furthermore, the strain hardening component (n) is evaluated as a constant which is contrary to many studies outlined in Klepaczko et al. (2009).

The reference strain ($\dot{\epsilon}_0$) was noted as equal to 1.0/s in the original JC paper. This has been reproduced in many other studies without a clear understanding of its role. Some papers have assumed the inclusion of a reference strain was an intermediate step to render the second term nondimensional, thus a strain rate of 1.0/s is used. The reference strain is indeed used for that purpose, but the plastic strain rate employed

must be the quasistatic strain rate used in the tests to determine the (A), (B) and (n) constants in the first term of the JC relation. If a strain rate of 1/s is used and this is higher than the actual reference strain rate, the JC model will under predict the low strain-rate response. The work by Schwer (2007) contains additional discussion of this topic.

The third term of the JC relation, the standard homologous temperature term, becomes redundant if the temperature is below that of the room or reference temperature. It is thus useful to evaluate temperature softening in a realistic temperature range. The report in Gray et al. (1994) has used a stricter definition of the homologues where the relation becomes a direct ratio between the current temperature and the absolute melting temperature, $T^* = \frac{T}{T_{\text{melt}}}$. They employed this method for temperatures below the reference temperature. At temperature extremes the authors (Gray et al., 1994) further concluded that the JC relation fails to adequately describe the material behaviour, this is likely to precipitate out of the model's simplicity.

In the original JC paper the strains evaluated ranged from quasistatic to 400/s. A number of authors (Meyers, 1994; Klepaczko et al., 2009; Gray et al., 1994; Sasso et al., 2008) identified the inaccuracy of the JC model at elevated strain rates. They concluded that the JC model is not entirely appropriate for strain rates greater than 10²/s, strain rates higher than this order of magnitude may require modifications to the model or the employment of other constitutive models. Variations of the JC strength model are often implemented as user-defined material subroutines, which allow for additional mechanisms to be considered.

The JC relation is not appropriate for metals (e.g. tantalum) where the work hardening remains constant or decreases with increasing strain rates (Liang and Khan, 1999). Although the phenomenological nature of the JC strength model neglects the nuances of other mechanistic models, it has seen wide use in many ballistic and blast applications by virtue of its consistent and accurate results for varying strain rate regimens. The smearing of different mechanisms results in a generalised behaviour that is captured well through the model. While the physical underpinning of a specific mechanism poses an interesting question, from a material science perspective, for a ballistics or simulation engineer a conservative result that correlates well, quantitatively and qualitatively is paramount. The JC strength model successfully captures the most pronounced components of these responses. The reader can consult Appendix 9B for a list of material parameters for the JC strength model with associated references.

9.5.2 Johnson–Cook damage criteria

Analogous to the J–C strength model, Johnson and Cook (1985) developed a fracture model built on the work of Mackenzie et al. (1977). The main variable identified in the Mackenzie study is the fracture of ductile materials due to stress triaxiality sensitivity. The increasing hydrostatic pressure inevitably leads to increased nucleation and void growth; this is directly proportional to a decrease in ductility and a reduction in the fracture strain. Johnson and Cook identified the additional effects of temperature,

strain rate and strain path dependency on the damage through phenomenological observations. The resulting J–C fracture model can be written as:

$$D = \sum \frac{\Delta \bar{\epsilon}_p}{\epsilon_f}$$

The sum of the incremental strain accumulated is used to define complete fracture when $D = 1$. Hence the material will fail when $\Sigma \Delta \bar{\epsilon}_p = \epsilon_f$. The failure strain is computed from a multiplicative relation that expresses the stress triaxiality, strain-rate dependence and the homologous temperature:

$$\epsilon_f = (D_1 + D_2 \exp(D_3 \sigma^*)) (1 + D_4 \ln(\dot{\epsilon}^*)) (1 + D_5 T^*)$$

The stress triaxiality property, first bracketed term, has been investigated by a number of authors (Bonora et al., 2005; Brünig et al., 2008; Bao and Wierzbicki, 2005; Mirone, 2007; Hopperstad et al., 2003) and the most prevalent method for quantifying the stress triaxiality is through testing of notched specimens of varied notch geometries. The second bracketed term is representative of the strain-rate effect on the fracture strain. The model computes a decrease in the fracture strain with increasing strain rate. This is due to the slight observed decrease in ductility with increasing strain rate (Johnson and Cook, 1985). The last term accounts for the increase in the fracture strain with increased temperature. It was observed that increasing the temperature increased the ductility. Dey et al. (2006) observed that with increasing temperature Weldox 460E exhibited a decrease in the yield strength, the flow stress though exhibited a maximum value at temperatures of 200–300°C, and this was attributed to the blue brittle region as defined by Dieter (1984). At this temperature the steel shows minimum strain-rate sensitivity and maximum strain ageing. It is noted that the ductility of the material decreases in this region as dislocations are arrested by newly liberated secondary solutes.

We shall now consider the following scenario for a multi-hit simulation on two ARMOX 500T plates positioned as shown in Fig. 9.11 to illustrate the interplay between material properties and geometric variations. The initial velocities of each APM2 round are identical with the spatial and temporal separation between each bullet corresponding to an idealised firing rate. From a qualitative point of view the top configuration with two parallel plates allows for both kinetic energy (KE) threats to penetrate. The spatial separation between the two rounds is greatly diminished as they perforate the plates. This is likely a product of the complex wave interaction in the plates, prior damage caused by the first KE impactor leading to a larger dwell period of the first round in comparison to the second. A more quantitative study of multilayered plate configuration can be found in the work of Flores-Johnson et al. (2011), where it was found that multilayered targets using different metallic materials could improve the ballistic properties of armour with a commensurate reduction in areal density.

Observing the model with an inclined and spaced first plate, the second impactor has partially penetrated the back plate but has remained lodged within it. The degree

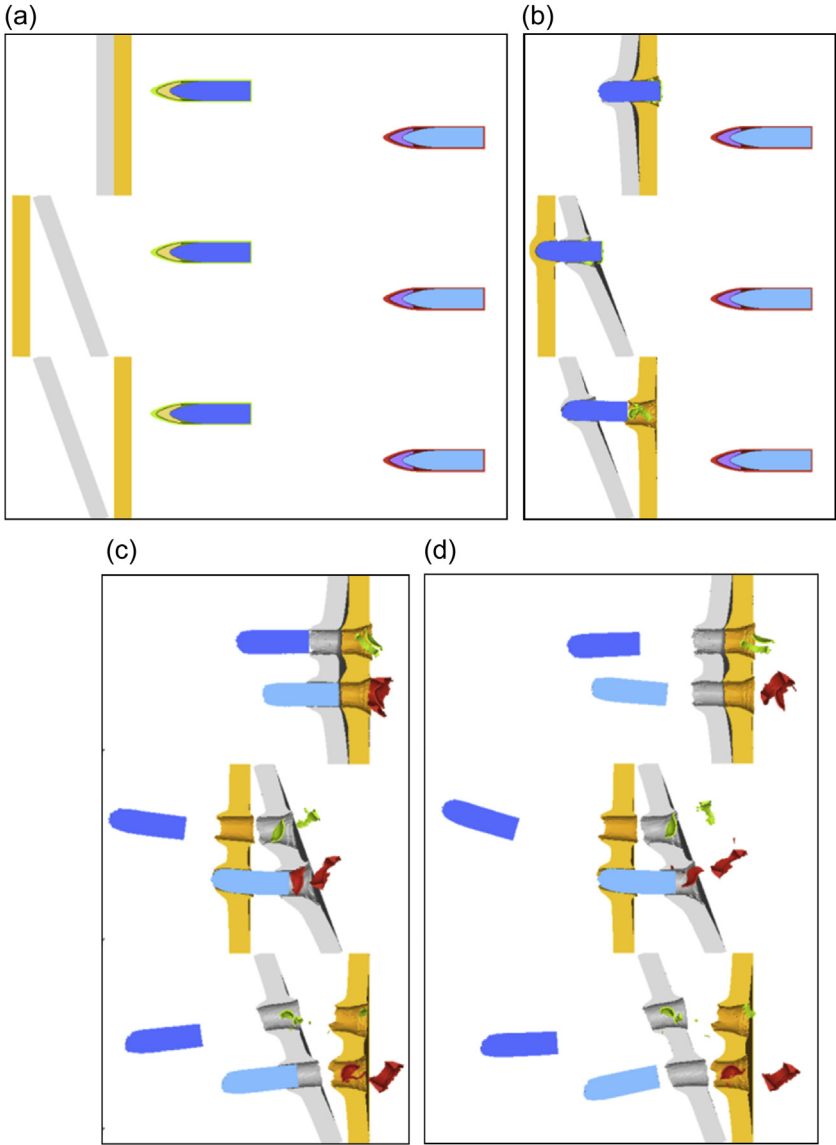


Figure 9.11 Multihit simulation with variation of armour inclination, spatial and temporal spacing.

of obliquity affects the effective through thickness that the impactor interacts with, the resultant rotation is induced by the asymmetric confinement of the projectile (and thus asymmetric stress field in the plate) at the surface of the target. This tumbling behaviour can greatly diminish the effectiveness of armour-piercing rounds (Zukas, 1990).

9.5.3 Cockcroft–Latham damage criteria

The Cockcroft–Latham (C–L) fracture criterion outlined in [Cockcroft and Latham \(1968\)](#) is based on an evaluation of the stresses and strains within metallic materials. The theory underlying their model is that plastic work per unit volume at the fracture point can be computed via the relation:

$$W = \int_0^{\varepsilon_f} \sigma d\varepsilon_p$$

A more appropriate notation is given in terms of the peak stress or maximum principal stress, and the effective plastic strain:

$$W = \int_0^{\bar{\varepsilon}_f} \langle \sigma \rangle d\bar{\varepsilon}_p$$

The inclusion of the Macauley bracket ensures the stress is positive for tension and zero for compression, ie, $\langle \sigma \rangle = \sigma_1$ when $\sigma_1 > 0$ and $\langle \sigma \rangle = 0$ when $\sigma_1 \leq 0$. It is thus appropriate to conclude that the fracture of the material can only occur where tensile stresses are present. The damage indicator is seen to have the property of energy density. This fracture criterion has been used extensively in bulk-forming and metal-cutting simulations but to a lesser extent in perforation analysis as noted by [Teng and Wierzbicki \(2006\)](#). The Cockcroft–Latham model had been employed and compared with the Johnson–Cook model by [Dey et al. \(2006\)](#). The accuracy of each model was deemed to be within the range of the experimental fracture strain values for experimental tests on Weldox 460E, Weldox 700E and Weldox 900E.

The C–L damage criterion, whilst not explicitly stating the role triaxiality plays in the fracture of the material, has, implicitly, accounted for this through the restrictions on the applicable stresses, i.e. only tensile stresses cause failure. The model does not explicitly account for any temperature or strain-rate effects but remains accurate in describing the general behaviours observed, namely:

- Increase in ductility and reduction in strength with increasing temperature;
- Increase in strength and reduction in ductility with increasing strain rate.

The C–L damage criterion predicts the ductile failure of the metal as a function of both the stress and the strain. The damage parameter is thus computed as

$$D = \frac{W}{W_{cr}} = \frac{1}{W_{cr}} \int_0^{\bar{\varepsilon}_f} \langle \sigma \rangle d\bar{\varepsilon}_p$$

The computation of the Cockcroft–Latham critical plastic work term, W_{cr} , involves measuring the strain up to the point of fracture (ie, $\varepsilon_{eq} = \varepsilon_f$). The ‘plastic work’ is evaluated as the area under the curve of the true stress versus true strain curve. The simplicity of this model makes it attractive as only a quasistatic tensile test is required to calibrate it. However, this criterion may not successfully capture the complex physical loading in

all ballistic simulations. In a similar vein to the Johnson–Cook fracture model, complete fracture of the model is computed when the scalar damage parameter, $D = 1$.

If we reconsider the problem in Fig. 9.3, and the results illustrated in Fig. 9.12, we see the implementation of the Johnson–Cook strength model along with the C–L

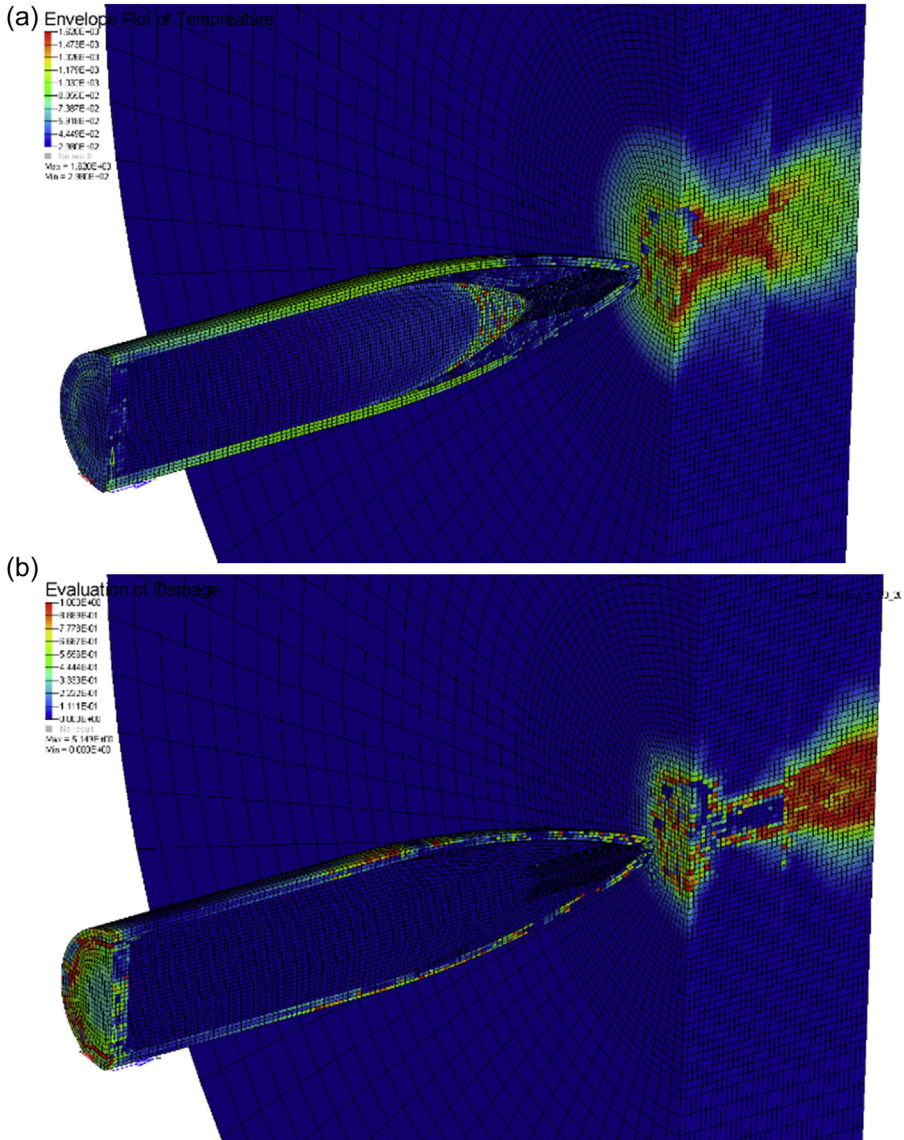


Figure 9.12 Envelope plot of the (a) thermal and (b) damage response during the ballistic impact of 7.62 mm APM2 with two, spaced, 6 mm Armox 500T plates. Refer to Worked Example #1 for further discussion.

damage model. The erosion criterion is two pronged in this simulation. Element deletion is based on the damage progression as per C–L and is also driven by large adiabatic heating to a threshold equal to 90% of the melting temperature. Fig. 9.12 shows an envelope plot of these two criteria, i.e. the maximum values experienced by all the elements throughout the simulation. The red-coloured elements in each figure correspond to elements that have ultimately reached the aforementioned thresholds and have been deleted. A third group of elements has been deleted due to an additive decomposition of the two failure modes, e.g. the tip of the projectile experiences large adiabatic heating in addition to some plastic deformation with neither threshold solely reached. It is apparent that the comparatively thin layer of elements in the first plate is more influenced by the adiabatic temperature rise, which in turn leads to thermal softening and more pronounced ductile hole growth [Fig. 9.12(a)], with limited plastic straining and more radial displacement. Conversely the second plate has severe element erosion as a result of the damage accumulated as per the Cockcroft–Latham damage model [Fig. 9.12(b)]. It should be apparent to the reader that while the resultant penetration event is characterised by ductile hole growth the mechanisms that lead to material flow, plasticity and failure vary across the two plates. The large bending stresses cause damage at the free surface of the back plate. These bending stresses are largely supported in the front plate by the back plate, hence similar damage is not apparent.

9.5.4 Zerilli–Armstrong (Z–A) strength model

The Z–A model (Zerilli and Armstrong, 1987; Armstrong and Zerilli, 1994) is not phenomenological in nature rather it is a more mechanistic model with a physical underpinning rooted in dislocation analysis. The relation is governed by Arrhenius' definition of the activation state whereby a species occupies an intermediate state between products and reactants. The reaction rate can thus be thought of as constant, governing the reactions in the form of:

$$k' = A * e^{\left(\frac{-\Delta E_a}{kT}\right)}$$

The movements of dislocation can, analogously, be linked to a movement through a transition or activated state by way of thermal energy as outlined earlier in the section on the Johnson–Cook constitutive model. This relation is linked to statistical mechanics, specifically the Boltzmann law governing energy distribution which is discussed in Meyers et al. (2002). The Z–A relation was derived for both body-centered cubic (BCC) and face-centred cubic (FCC) metals. Unlike the J–C model, the Z–A model is an additive relation and cannot be easily decoupled. Furthermore, the Z–A relation distinguishes between the rate-controlling mechanisms for the deformations of FCC and BCC metals. It was found that the controlling mechanism for FCC metals is the intersection of dislocations, while for BCC overcoming the Peierls–Nabarro barriers is the controlling step. These controlling mechanisms are the result of material response observations. It was observed that plastic yield stress in BCC metals was more sensitive to temperature and strain rate, compared to FCC.

For FCC metals the Z–A relation is expressed as:

$$\sigma = \Delta\sigma' + c_2\epsilon^{\frac{1}{2}} \exp(-c_3T + c_4T \ln\dot{\epsilon}) + kl^{-\frac{1}{2}}$$

For BCC metals:

$$\sigma = \Delta\sigma' + c_1 \exp(-c_3T + c_4T \ln\dot{\epsilon}) + c_5\epsilon^n + kl^{-\frac{1}{2}}$$

As mentioned previously in the discussion of the Johnson–Cook model, the Zerilli–Armstrong model takes account of both the thermal and athermal components. The above relation can thus be written as:

$$\sigma = \sigma_{\text{thermal}} + \sigma_{\text{athermal}} + kl^{-\frac{1}{2}}$$

The last term, $kl^{-\frac{1}{2}}$, accounts for the slip-band stress concentration that is required to transmit the flow between polycrystals. It is a product of the microstructural stress intensity (k), and the inverse square root of the average grain diameter. This incrementally increases the flow stress even at low temperatures. The ($\Delta\sigma'$) term is the athermal stress, which relates to the initial presence of solutes and the initial dislocation density. When combined with the slip-band concentration term, the resultant flow stress formula is the Hall–Petch (Tresvyatskii, 1971) relation, which describes the linear dependence of the yield stress on the inverse square root of the grain diameter.

$$\sigma_{\text{HP}} = \sigma_{\text{athermal}} + kl^{-\frac{1}{2}}$$

The thermal part of the Z–A relation is

$$\sigma_{\text{thermal-fcc}} = c_2\epsilon^{\frac{1}{2}} \exp(-c_3T + c_4T \ln\dot{\epsilon})$$

$$\sigma_{\text{thermal-bcc}} = c_1 \exp(-c_3T + c_4T \ln\dot{\epsilon})$$

The thermal portion of the Z–A relation is seen to be a power-law fitting of a number of constants based on temperature, strain rate and strain. The strain-rate hardening and the thermal softening show greater dependence on the strain hardening factor in FCC metals. Conversely, strain-rate hardening and thermal softening have a lesser dependence on the strain than in BCC metals. As such, a strain-hardening term is decoupled from the strain-rate hardening and thermal softening component in BCC metals. Having demonstrated the different components that comprise the Z–A relation, the reader can see that Z–A combined an exponential function, which is very similar to the multiplicative J–C relation, with the Hall–Petch relation. Hence similar phenomenological considerations underpin both models. These theories are the cornerstone of dislocation-based analysis but are in most cases very difficult to quantify let alone measure accurately or in situ. The Z–A model relates these physical

principles by way of secondary macroscopic physical attributes, which are measurable and useable to the current application.

The most obvious shortcoming of the original Z–A model is the sole application to BCC and FCC metals without any considerations of hexagonal close-packed (HCP) materials such as Ti-6Al-4V (Meyer, 2006). Later permutations of the Z–A model have included treatments of HCP materials (Zerilli and Armstrong, 1996). A number of authors have found that the invariant constants of the Z–A model do not reflect the experimental results and have instead considered the time-integrated effects of the temperature, strain rate and deforming processes (Lin and Chen, 2011). A common criticism of the model pertains to its consistency at high temperatures as outlined by He et al. (2014) and Abed and Voyiadjis (2005), the assumption of the Z–A model is that thermal stress is ever present up until $T \rightarrow \infty$, this assumption is untrue at critical temperature, where the plastic flow stress is wholly reliant on the athermal component.

9.5.5 Mechanical threshold stress (MTS) strength model

The MTS model was developed by Follansbee and Gray (1989) and Follansbee and Kocks (1988) and is a physically based model that can be used to simulate material response at high temperatures and high strain rates. The model adopts the same approach for the thermally activated dislocation motion as the Z–A model, whilst precluding solute diffusion effects. This approach takes dislocations motion into account through an internal state variable, called the mechanical threshold stress (MTS). Shown below is an abbreviated breakdown of the model. The yield stress is given by:

$$\sigma_y(\epsilon_p, \dot{\epsilon}_p, T) = \sigma_a + (S_i \sigma_i + S_e \sigma_e) \frac{\mu(p, T)}{\mu_0}$$

where σ_a is the athermal component of mechanical threshold stress, σ_i is the flow stress component due to intrinsic barriers to thermally activated dislocation motion and dislocation–dislocation interactions, σ_e is the component of the flow stress due to microstructural evolution with increasing deformation (strain hardening), S_i and S_e are temperature- and strain-rate-dependent scaling factors, and μ_0 is the shear modulus at 0K and ambient pressure. The Arrhenius form of the scaling factors is expressed as (Banerjee, 2005):

$$S_i = \left[1 - \left(\frac{k_b T}{g_{0i} b^3 \mu(p, T)} \ln \frac{\dot{\epsilon}_{p0i}}{\dot{\epsilon}_p} \right)^{\frac{1}{q_i}} \right]^{\frac{1}{p_i}}$$

$$S_e = \left[1 - \left(\frac{k_b T}{g_{0e} b^3 \mu(p, T)} \ln \frac{\dot{\epsilon}_{p0e}}{\dot{\epsilon}_p} \right)^{\frac{1}{q_e}} \right]^{\frac{1}{p_e}}$$

where k_b is the Boltzmann constant, b is the magnitude of the Burgers' vector, g_{0i} , g_{0e} are normalised activation energies, $\dot{\epsilon}_{p0i}$, $\dot{\epsilon}_{p0e}$ are constant reference strain rates and

(q_i, p_i, q_e, p_e) are material constants, $0 \leq p \leq 1$ and $1 \leq q \leq 2$. The σ_e term describes the strain-hardening component of the mechanical threshold stress and is given by a modified Voce hardening law:

$$\frac{d\sigma_e}{d\varepsilon_p} = \theta(\sigma_e)$$

where

$$\theta(\sigma_e) = \theta_0[1 - F(\sigma_e)] + \theta_{IV}F(\sigma_e)$$

$$\theta_0 = a_0 + a_1 \ln \dot{\varepsilon}_p + a_2 \sqrt{\dot{\varepsilon}_p} - a_3 T$$

$$F(\sigma_e) = \frac{\tanh\left(\alpha \frac{\sigma_e}{\sigma_{es}}\right)}{\tanh(\alpha)}$$

$$\ln\left(\frac{\sigma_{es}}{\sigma_{0es}}\right) = \left(\frac{kT}{g_{0es}b^3\mu(p, T)}\right) \ln\left(\frac{\dot{\varepsilon}_p}{\dot{\varepsilon}_{p0es}}\right)$$

θ_0 is the hardening due to dislocation accumulation, θ_{IV} is the contribution due to stage IV hardening, $(a_0, a_1, a_2, a_3, \alpha)$ are constants, σ_{es} is the stress at zero strain-hardening rate, σ_{0es} is the saturation threshold stress for deformation at 0K, g_{0es} is a constant and $\dot{\varepsilon}_{p0es}$ is the maximum strain rate. The maximum applicable strain rate using this model is limited to approximately $10^7/s$.

One of the big drawbacks of the MTS model is the larger number of constants required and the difficulty of repeated testing to fixed strains and very low temperatures that is required to fit the model (Meyers, 1994). The original MTS model does not account for the effect of viscous drag at high strain rates as noted by Banerjee and Bhawalkar (2008). The MTS model will also capture a small increase in the flow stress with increasing strain rate for $1 \leq q \leq 2$, this may prove erroneous for material with strong strain-rate dependence.

9.5.6 Steinberg–Cochran–Guinan–Lund (SCGL) strength model

The SCGL model is a semiempirical model that was initially developed by Steinberg et al. (1980) for high strain-rate situations and later extended to low strain-rate regimens and BCC crystal structures by Steinberg and Lund (1989). The original model made the assumption that above a critical strain rate ($10^5/s$) strain-rate effects reached a saturation point, and material strength becomes independent of strain rate. The rapid decrease of rate-dependent effects with increasing dynamic stress was explained by the increase in temperature with increasing stress. This holds true for FCC materials but is inaccurate for BCC materials (Scapin et al., 2011). The flow stress in the SCGL model is given by:

$$\sigma_y(\varepsilon_p, \dot{\varepsilon}_p, T) = [\sigma_a f(\varepsilon_p) + \sigma_t(\dot{\varepsilon}_p, T)] \frac{G(p, T)}{G_0}$$

where $\sigma_a f(\epsilon_p) \leq \sigma_{\max}$, the product of the athermal stress component σ_a , ϵ_p is the plastic strain, $\dot{\epsilon}_p$ is the plastic strain rate, T is the temperature, G_0 is the shear modulus at the reference state and the strain hardening function, $f(\epsilon_p)$ cannot exceed the saturation value of the athermal stress, σ_{\max} . The thermally activated stress cannot exceed the Peierls–Nabarro stress, $\sigma_t \leq \sigma_p$. The pressure and temperature dependence of the shear modulus $G(p, T)$ is accounted for through the relation:

$$G(p, T) = G_0 \left[1 + \left(\frac{G'_p}{G_0} \right) \frac{P}{\eta^{1/3}} + \left(\frac{G'_T}{G_0} \right) (T - 300) \right]$$

where $\eta = v_0/v = \rho/\rho_0$ is compression defined as the fraction of the initial specific volume divided by the specific volume at the reference state ($T_{m0} = 300\text{K}$, $P = 1$, $\epsilon = 0$). The hardening function is expressed as:

$$f(\epsilon_p) = [1 + \beta(\epsilon_p + \epsilon_{pi})]^n$$

where β and n are work-hardening parameters, and ϵ_{pi} is the initial equivalent plastic strain which is usually taken as zero. Steinberg et al. recognised that for BCC materials the thermal component is large σ_t and highly dependent on the plastic strain rate $\dot{\epsilon}_p$ and they used the work of [Hoge and Mukherjee \(1977\)](#) to better formulate the resultant behaviour in terms of:

$$\dot{\epsilon}_p = \left\{ \frac{1}{C_1} \exp \left[\frac{2U_k}{kT} \left(1 - \frac{\sigma_T}{\sigma_P} \right)^2 \right] + \frac{C_2}{\sigma_T} \right\}$$

where $2U_k$ is the energy to form a pair of kinks in a dislocation segment of length L , and k is the Boltzmann constant. The constants C_1 and C_2 are given by:

$$C_1 = \frac{\rho Lab^2 v}{2w^2}$$

$$C_2 = \frac{D}{\rho_d b^2}$$

where ρ_d is the dislocation density, a is the distance between Peierls–Nabarro valleys, b is the Burger's vector, v is the Debye frequency, w is the width of a kink loop and D is the drag coefficient. The temperature evolution in the SCGL model is formulated in terms of the difference between the total energy and the energy along the zero Kelvin isotherm, $E_c(\eta)$ divided by the specific heat, C_m .

$$T = \frac{E - E_c(\eta)}{C_m}$$

where

$$E_c(\eta) = \int_1^\eta P(\eta) \frac{dn}{\eta^2} - C_m T_{m0} \exp \left[a \left(1 - \frac{1}{\eta} \right) \right] \eta^{\gamma_0 - a}$$

where $C_m = \frac{3R\rho_0}{A}$, R is the gas constant, ρ_0 is the initial density and A is the atomic weight, T_{m0} is the melt temperature at $\eta = 1$, γ_0 is the Grueneisen gamma with a correction factor, a .

One of the major shortcomings of the original 1980 model was the treatment of the flow stress as independent of strain rate. The original SG model was only applicable to high strain rates but was later corrected to account for strain-rate dependence through the SCGL model. Work by [Zocher and Maudlin \(2000\)](#) has shown that the SCGL model trails the MTS model in terms of accuracy in predicting the deformation of the Taylor cylinder impact test but produces better results than the JC model.

9.6 Strength models for nonmetals

9.6.1 Johnson–Holmquist ceramics model

The constitutive behaviour of ceramics and the computational framework for the analysis of these armour systems is less developed than those of their metallic counterparts. The work of [Johnson and Holmquist \(1992\)](#) established the original JH1 phenomenological model for the analysis of brittle materials under high strain rate. The model captured the pressure-dependent strength of the intact and failed materials, damage-induced dilation, and the strain-rate-dependent strength of armour ceramics. An iteration of their earlier work resulted in the JH2 model ([Johnson and Holmquist, 1994](#)). The model included additional terms to describe the gradual softening of the ceramic from ‘intact’ to ‘failed’ and a gradual increase in the bulking pressure until full damage. The JH2 formulation expresses the equivalent stress as a function of the static resistance, fracture strength, strain, strain rate, pressure and the scalar damage variable ($0 \leq D \leq 1$). The third iteration of the model JHB ([Johnson et al., 2003](#)) sought to better describe the ceramic strength and failure using analytical descriptions. The model also included the effects of high-pressure phase transformation seen in some ceramics as shown in [Fig. 9.13](#).

The term of the equivalent stress, JH2 model, is given by:

$$\sigma^* = \sigma_i^* - D(\sigma_i^* - \sigma_f^*)$$

where σ_i^* and σ_f^* are the undamaged and damaged strength, respectively, and are given by:

$$\sigma_i^* = A(P^* + T^*)^n (1 + C \ln \dot{\epsilon}^*)$$

$$\sigma_f^* = B(P^*)^m (1 + C \ln \dot{\epsilon}^*) \leq \text{SFMAX}$$

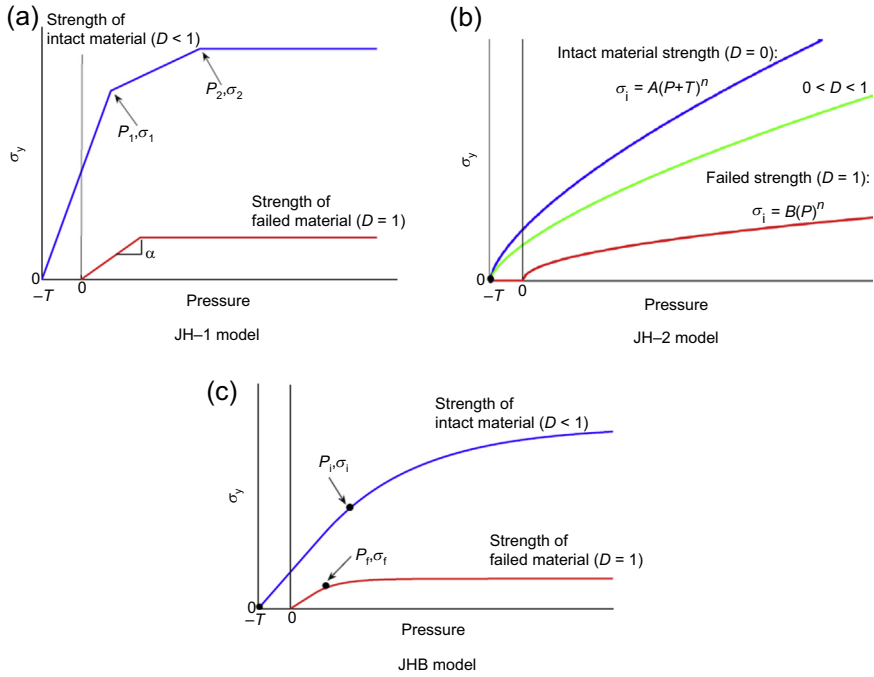


Figure 9.13 Description of the various Johnson–Holmquist models.

Lamberts, A.P.T.M.J., 2007. Numerical Simulation of Ballistic Impacts on Ceramic Material (Masters thesis). Eindhoven University of Technology.

where $P^* = P/P_{\text{HEL}}$ is the normalised pressure term at the Hugoniot elastic limit. Pressure, P_{HEL} , and $T^* = T/P_{\text{HEL}}$ is the normalised tensile fracture strength, $\dot{\epsilon}^* = \frac{\dot{\epsilon}}{\dot{\epsilon}_0}$ is the normalised strain rate, SFMAX is the maximum normalised fracture strength. A , B , C , M and N are all material constants. The accumulated scalar damage variable is expressed as the accumulation of incremental plastic strain, $\Delta \epsilon^P$, akin to the model by Johnson and Cook (1985), where

$$D = \sum \frac{\Delta \epsilon^P}{\epsilon_f^P}$$

$$\epsilon_f^P = D_1 (P^* + T^*)^{D_2}$$

and D_1 and D_2 are material constants.

The hydrostatic behaviour of the undamaged ceramic compression and tension is described by an EOS given by:

$$P_{\text{com}} = K_1 \mu + K_2 \mu^2 + K_3 \mu^3 + \Delta P$$

$$P_{\text{ten}} = K_1 \mu$$

where K_1 is the bulk modulus, K_2, K_3 are constant, $\mu = \left(\frac{\rho}{\rho_0}\right) - 1$ where ρ_0 is the initial density and ρ is the current density. The ΔP is added when damage begins to accumulate and represents the increase in potential energy due to the material softening and a reduction in the deviatoric stress component.

9.6.2 Kayenta ceramic model

The Kayenta model (Brannon et al., 2009) is a generalised plasticity model used to describe ceramics at the macroscopic continuum level. The model is not implemented into any commercial hydrocodes, but is implemented in some restricted access research codes, e.g., ALEGRA. The model strikes a balance between first-principles micromechanics and phenomenological, homogenised and semi-empirical modelling strategies (Leavy et al., 2010). The model allows for the smooth transition of the prescribed ceramic damage from principal stress dominated failure at low pressure, Drucker–Prager behaviour at intermediate pressures and cap plasticity at extremely high pressure. The smooth yield surface is defined by the function:

$$f(\sigma, \alpha, \kappa) = \Gamma^2(\Theta)J_2 - [F_f(I_1) - N]F_c^2(I_1, \kappa)$$

where I_1, J_2 and Θ are three invariants of the stress tensor σ and its deviator s :

$$I_1 = \text{tr } \sigma, \quad J_2 = \frac{1}{2} \text{tr } s^2, \quad J_3 = \frac{1}{3} \text{tr } s^3, \quad \sin 3\Theta = -\frac{J_3}{J_2} \left(\frac{3}{J_2}\right)^{3/2}$$

The material response is assumed to be elastic for $f < 0$, and the material is considered to yield when $f = 0$. The function F_f governs the behaviour in shear-dominated loading where the material softens due to microcracking. The N parameter defines the shift of the yield surface due to kinematic hardening and the resultant shifted stress tensor, $\xi = S - \alpha$, where S is the stress deviator and α is the back stress, as illustrated in Fig. 9.14.

The function, F_c , governs the strength reduction of the porous materials under hydrostatically dominated loading. The function $\Gamma(\Theta)$ governs the material strength difference between triaxial extension and compression for the shifted stress with a Lode angle, Θ . The internal state variable κ governs the hydrostatic elastic limit. Unlike the JH models, which have a fixed failure strain, Kayenta allows for scale-dependent time to failure which regulates the energy of failure. Kayenta uses a spatially variable probability function, and a Weibull distribution, which incorporate uncertainty in flaw size and orientation of the macroscopically homogeneous media. By means of internal scaling the inelastic and failure behaviour is captured in the fuzzy failure boundary theory, which incorporates length scales, while at the same time mitigating mesh dependence (Fig. 9.15). This allows for damage to propagate at the same speed, regardless of element size.

The Kayenta model is very powerful but is quite complex with experimental and nonlinear regression fitting of the parameters requiring a thorough understanding of

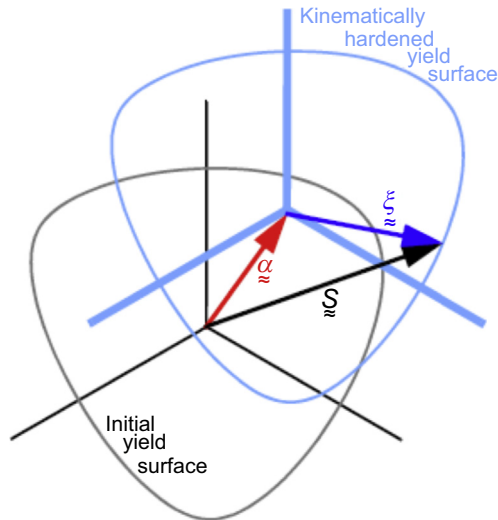


Figure 9.14 Back stress and shifted stress.

Brannon, R., Fossum, A. Strack, E., 2009. *Kayenta: Theory and User's Guide*. Sandia National Laboratories, Albuquerque, NM.

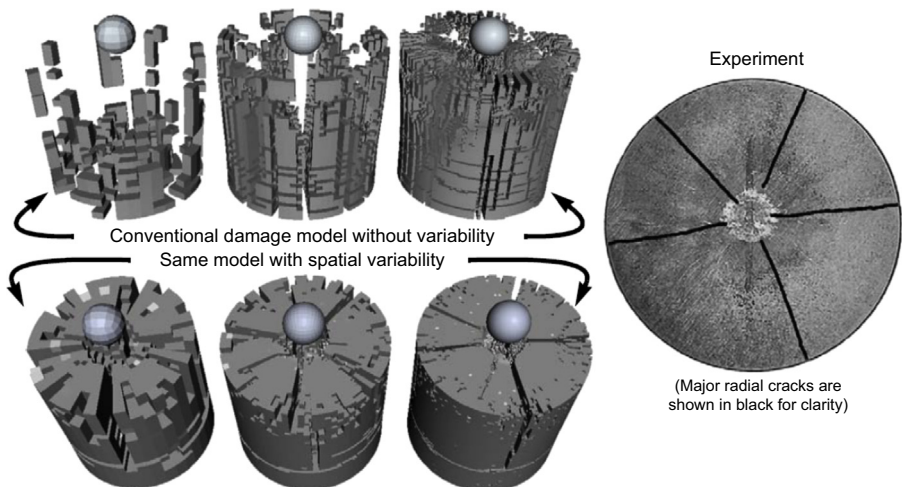


Figure 9.15 Reduction of mesh dependence of the Kayenta failure model.

Brannon, R., Fossum, A. Strack, E., 2009. *Kayenta: Theory and User's Guide*. Sandia National Laboratories, Albuquerque, NM.

the model's nuances. Depending on the user inputs and the intent of the simulation the model can potentially be used for (Fuller et al., 2013):

- Linear and nonlinear thermoelasticity;
- Von Mises and Tresca thermoplasticity;
- Linear and nonlinear, associative and nonassociative Drucker–Prager, Mohr–Coulomb and Willam–Warnke plasticity;

- Rate-independent or strain-rate sensitive yield;
- Damage through the loss of stiffness and strength;
- Evolution of porosity;
- Pressure- and shear-dependent compaction.

9.6.3 Strength models for polymeric materials

Over the decades, very little research has been carried out on the dynamic properties of adhesives and adhesive layers. However, with the evolution of the family of adhesively bonded aluminium laminates (ABALs) in the 1990s (see Chapter 4), for lightweight armour materials and containment systems, [Crouch \(1994\)](#) recognised the need to develop appropriate-strength equations for adhesive layers. They duly recognised the adhesive's strain-rate sensitivity, as indicated by the set of data shown in [Fig. 9.16](#), for the toughened epoxy system, Hysol 9309.3 (NA). This adhesive has been approved for use in the aerospace industry to carry out secondary bonding procedures and has been employed in many ceramic-based, body armour systems ([Crouch, 2009](#)), as well as laminated armours.

This work led to full characterisation of the epoxy adhesive and development of a new strength model, based upon a Cowper–Symonds equation ([Jones, 1989](#)):

$$\sigma_y = [\sigma_0 + C_1 \cdot \epsilon_p^x] \cdot [1 + (C_2 \cdot \dot{\epsilon}_p)^n] \cdot [\alpha + \beta T + \gamma T^2]$$

where the first term describes the strain dependency, the second term describes the strain-rate dependency, and the third term accounts for the temperature dependence. ϵ_p and $\dot{\epsilon}_p$ are the plastic strain and strain rate, respectively, and T is the absolute temperature. For polymeric systems, it is assumed that $x = 1$.

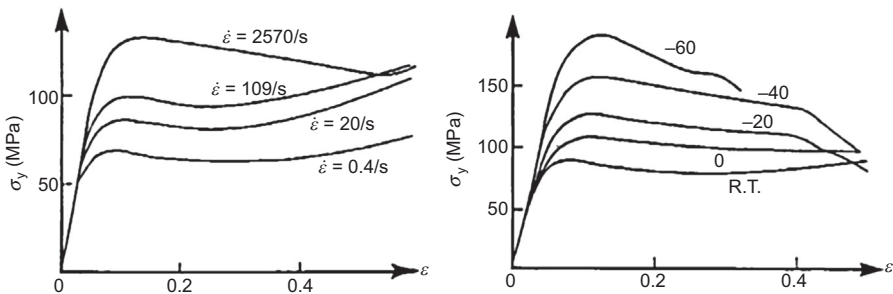


Figure 9.16 Characterisation of epoxy-based adhesive, Hysol 9309.3(NA) showing effect of strain rate upon flow properties at 20°C (left) and the effect of temperature at a strain rate of 10^{-3} .

Crouch, I.G., Greaves, L.J., Ruiz, C., Harding, J., 1994. Dynamic compression of toughened epoxy interlayers in adhesively bonded aluminium laminates. Supplement to Journal de Physique III, Colloque C8 4, 201–206.

For Hysol 9309.3, the following parametric values were determined to be $\sigma_0 = 55$ MPa, $C_1 = 7.96$ MPa, $C_2 = 0.00286$, $n = 0.182$, $\alpha = 9.89$, $\beta = -0.0554$, and $\gamma = 0.0000841$ (Crouch, 1994).

9.6.4 Strength models for rubbers and elastomers

Materials, such as rubbers, are best described using constitutive relations that rely upon the theories of hyperelasticity to capture the large deformation behaviour. Unlike other constitutive stress flow models where the small strain calculation is used to derive stress, hyperelastic material stresses are derived from the concept of virtual work using a strain energy potential function, W . This is expressed using the principal invariants, I_1 , I_2 and I_3 , of the right Cauchy–Green deformation tensor, $W = W(I_1, I_2, I_3)$ where:

$$I_1 = \lambda_1^2 + \lambda_2^2 + \lambda_3^2$$

$$I_2 = (\lambda_1 \lambda_2)^2 + (\lambda_2 \lambda_3)^2 + (\lambda_3 \lambda_1)^2$$

$$I_3 = (\lambda_1 \lambda_2 \lambda_3)^2$$

For isotropic materials the stretch ratios λ_i are utilised and for incompressible materials $I_3 = 1$. The most commonly used energy potentials for incompressible material are polynomial and reduced polynomial forms expressed as

$$W = \sum_{i,j=0}^N C_{ij}(I_1 - 3)^i(I_2 - 3)^j + \sum_{k=1}^q D_k(I_3 - 1)^{2k}$$

where C_{ij} is a material constant that governs the distortional response, N is the polynomial rank and D_k is the material constant related to the volumetric response. The last term is nullified for incompressible materials as previously mentioned. The most commonly used strain energy models (Fig. 9.17) are all based on this concept:

Neo-Hookean: $W = C_{10}(I_1 - 3)$

Mooney–Rivlin (Rivlin, 1948; Mooney, 1940) ($N = 1$, first-order polynomial):

$W = C_{10}(I_1 - 3) + C_{01}(I_2 - 3)$

Mooney–Rivlin ($N = 2$, second-order polynomial): $W = C_{10}(I_1 - 3) + C_{01}(I_2 - 3) + C_{11}(I_1 - 3)(I_2 - 3) + C_{20}(I_1 - 3)^2 + C_{02}(I_2 - 3)^2$

Varga: $W = 2\mu(\lambda_1 + \lambda_2 + \lambda_3 - 3)$

Ogden (1972): $2\mu \frac{\lambda_1^\alpha + \lambda_2^\alpha + \lambda_3^\alpha - 3}{\alpha}$

where μ , C_{ij} , α are positive constants with the aforementioned constraint of incompressibility.

More recently the work by Mohotti et al. (2014) has developed a strain-rate-dependent constitutive material model to predict the high strain-rate behaviour of polyurea. Using the nine-parameter Mooney–Rivlin constitutive model they derived

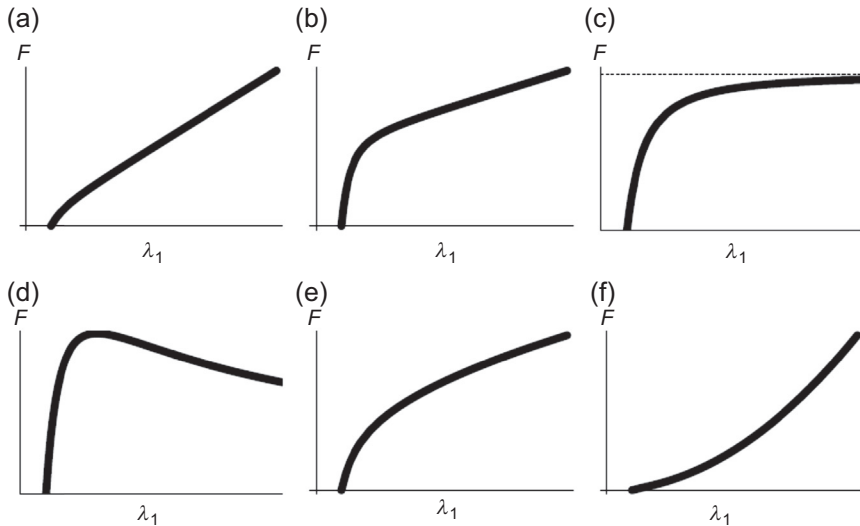


Figure 9.17 Typical force—strain graphs for materials described using the strain energy density concept: (a) neo-Hookean, (b) Mooney—Rivlin, (c) Varga, (d) Ogden ($\alpha < 1$), (e) Ogden ($1 < \alpha < 2$), (f) Ogden ($\alpha > 2$).

Howell, P., Kozyreff, G. Ockendon, J., 2009. Applied Solid Mechanics, Cambridge University Press.

an additional rate-dependent term which was validated using high strain material data. They identified that the original Mooney—Rivlin model can predict the behaviour of polyurea at different strain rates, albeit with unique material constant for each strain rate of interest. Their modifications allow for the strain-rate dependence to be incorporated into the model, thus providing better correlation with the experimental data.

9.6.5 Constitutive equations for textiles and fibre-reinforced polymers

In an armour system, woven textile fabrics can be used in two forms: either as a dry stack of woven layers (see Chapter 6) or as a layered product laminated together using either a thermosetting resin or a thermoplastic matrix (see Chapter 5). In either form, they present a very specific set of challenges for the numerical modeller. By far the greatest of these relates to the scale of the unit material. Does one model the fibres, the fabric itself, a stack of individual plies or simply the finished product?

The hierarchal nature of fabric and compliant composite laminate materials and the scale at which such materials are modelled is broken down into eight subcategories which [Grujicic et al. \(2011\)](#) detail. These subcategories are presented in [Fig. 9.18](#).

Due to the complex nature of these materials the model applied must first address the material response required, and secondly assess the required scale to be modelled to observe the desired physical phenomena. The model scale often determines the computational efficiency at which the analysis will be performed, as the complexity of

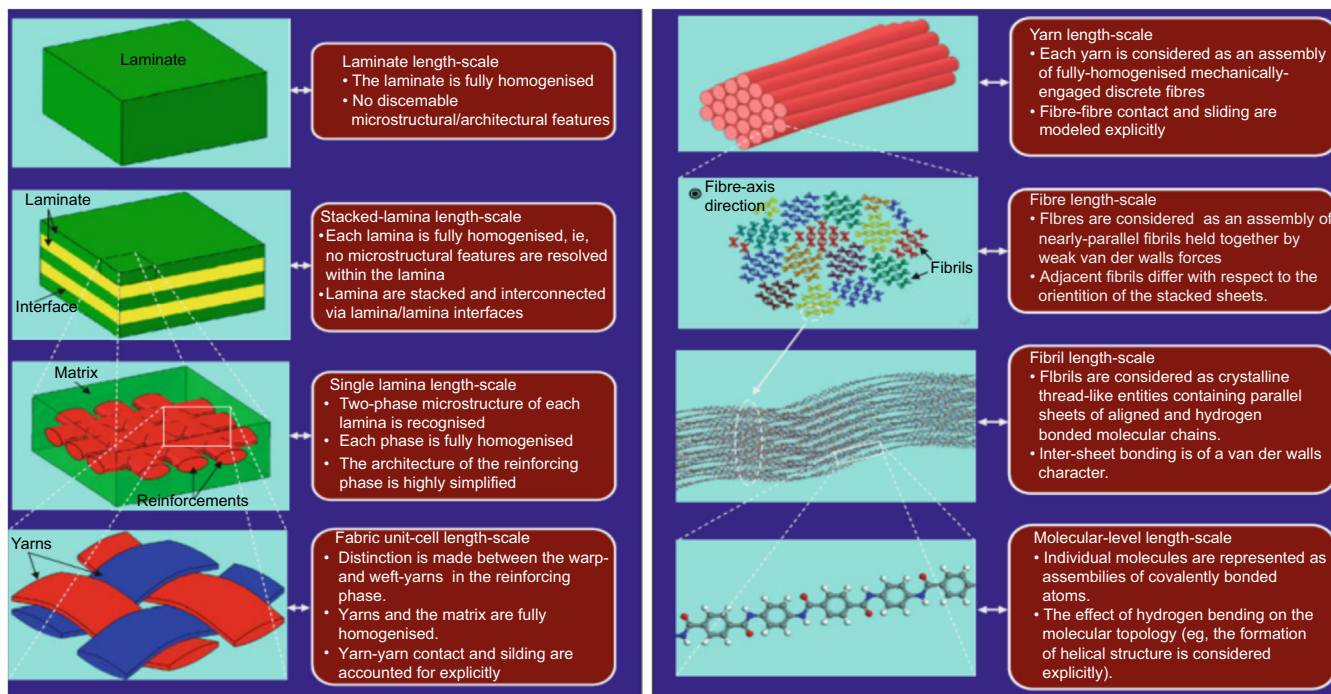


Figure 9.18 Hierarchical order for a fibre-reinforced, polymeric composite armour based on length scale, as represented from macroscale to mesoscale, and microscale to atomic scale.

After Grujicic, M., Arakere, G., He, T., Bell, W.C., Glomski, P.S., Cheeseman, B.A., 2009a. Multi-scale ballistic material modeling of cross-plyed compliant composites. *Composites Part B: Engineering* 40, 468–482.

mechanics increases with a decreasing scale. For example, small-length scales required to model high-resolution intralamina mechanisms and damage/failure nucleation are highly computationally expensive and thus may be unsuited to large structural or component-level simulation. However, the higher length scale models, while offering higher computational efficiency, are accompanied by a reduced resolution of the complex damage mechanisms and intermaterial response due to oversimplified assumptions. These may lead to inaccuracies as noted by (Grujicic et al., 2010; Nilakantan et al., 2010b).

The fibres within a yarn are not modelled individually for the mesoscale models. The yarns are bundled together and a solid volume is generated to represent the bounds of the fibres. The reason for this approximation is the ease by which bundle behaviour can be computed from experiments and fit to standardised material models. Secondly, the computational penalty for analysis of textile properties at the single yarn level would be prohibitive. Fig. 9.19 shows an example of FE models of both a 2-D and 3-D woven fabric.

The work by Grujicic et al. (2008a,b) provides the simplest approach to modelling these composites using homogenised structures to increase the computational efficiency. The deformation and failure of single yarns and the localised interaction between fabric and KE threat in the impact zone can only be studied using mesoscale simulations that capture orthotropic or anisotropic behaviour in the narrow impact area. A number of authors (Chocron et al., 2010; Grujicic et al., 2009b; Hou et al., 2013; Nilakantan and Gillespie 2012; Tabiei and Ivanov, 2001; Tabiei and Nilakantan, 2008) have adopted the mesoscale approach with viscoelastic constitutive models used to model: (1) breakage of bonds, (2) local yarn rupture, (3) remote yarn failure, (4) yarn pull-out, (5) fibrillation and (6) bowing. A more sophisticated approach involves modelling the yarn using woven shell elements of constant thickness which are tied to solid elements in the impact zone, using kinematic constraints that model the translational and rotational degrees of freedom. This provides a more robust modelling approach as it allows for larger domains to be analysed using computationally inexpensive shell elements. The evaluation of the wave speed, which is a critical factor for the

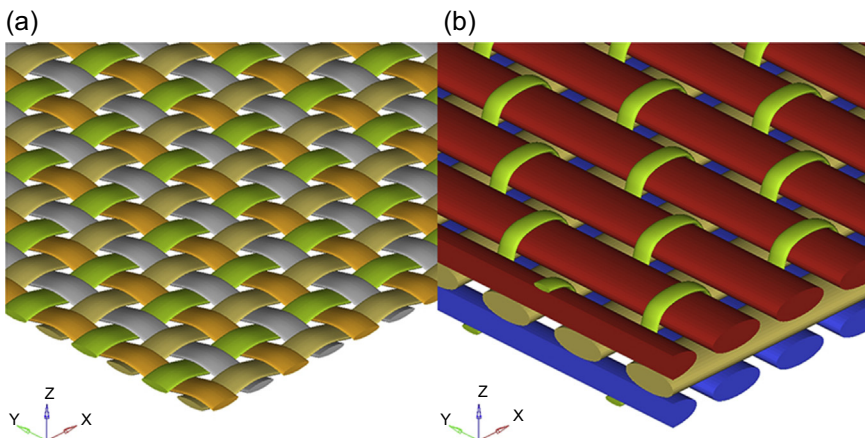


Figure 9.19 Finite element model of woven fabric: (a) plain weave, (b) 3-D cross-stitched fibre bundles.

fabric to dissipate the imparted kinetic energy, is also more adequately handled using 3-D elements with discrete handling of contact and friction, hence the user must resolve the impedance mismatch between the two element formulations.

Continuum approaches to modelling fibres and resin vary greatly with a plethora of failure models having been developed over the last four decades by different research groups. The study by [Orifici et al. \(2008\)](#) provides a relatively recent overview of failure models that have applicability to ballistic simulations. The broader framework for numerical analysis looks to model the loading response in particular fibre directions through anisotropic material definitions, within the generalised frame work of Hookes' law for elastic behaviour. In the general three-dimensional case, there are six components of the normal and shear stresses: $\sigma_x, \sigma_y, \sigma_z, \tau_{xy}, \tau_{yz}, \tau_{zx}$. Alongside these are the six corresponding components of strain: $\varepsilon_x, \varepsilon_y, \varepsilon_z, \gamma_{xy}, \gamma_{yz}, \gamma_{zx}$. The general anisotropic form is given by the following six equations written in the matrix configuration below:

$$\begin{Bmatrix} \varepsilon_x \\ \varepsilon_y \\ \varepsilon_z \\ \gamma_{xy} \\ \gamma_{yz} \\ \gamma_{zx} \end{Bmatrix} = \begin{bmatrix} S_{11} & S_{12} & S_{13} & S_{14} & S_{15} & S_{16} \\ S_{21} & S_{22} & S_{23} & S_{24} & S_{25} & S_{26} \\ S_{31} & S_{32} & S_{33} & S_{34} & S_{35} & S_{36} \\ S_{41} & S_{42} & S_{43} & S_{44} & S_{45} & S_{46} \\ S_{51} & S_{52} & S_{53} & S_{54} & S_{55} & S_{56} \\ S_{61} & S_{62} & S_{63} & S_{64} & S_{65} & S_{66} \end{bmatrix} \begin{Bmatrix} \sigma_x \\ \sigma_y \\ \sigma_z \\ \tau_{xy} \\ \tau_{yz} \\ \tau_{zx} \end{Bmatrix}$$

where S_{ij} is called the compliance matrix. Orthotropic materials have symmetry about three orthogonal planes. Hence a sparser matrix can be constructed to establish the linear relationship between stresses and strains through nine elastic constants:

$$\begin{Bmatrix} \varepsilon_x \\ \varepsilon_y \\ \varepsilon_z \\ \gamma_{xy} \\ \gamma_{yz} \\ \gamma_{zx} \end{Bmatrix} = \begin{bmatrix} \frac{1}{E_{xx}} & \frac{-\nu_{yx}}{E_{yy}} & \frac{-\nu_{zx}}{E_{zz}} & 0 & 0 & 0 \\ \frac{-\nu_{xy}}{E_{xx}} & \frac{1}{E_{yy}} & \frac{-\nu_{zy}}{E_{zz}} & 0 & 0 & 0 \\ \frac{-\nu_{xz}}{E_{xx}} & \frac{-\nu_{yz}}{E_{yy}} & \frac{1}{E_{zz}} & 0 & 0 & 0 \\ 0 & 0 & 0 & \frac{1}{G_{yz}} & 0 & 0 \\ 0 & 0 & 0 & 0 & \frac{1}{G_{xz}} & 0 \\ 0 & 0 & 0 & 0 & 0 & \frac{1}{G_{xy}} \end{bmatrix} \begin{Bmatrix} \sigma_x \\ \sigma_y \\ \sigma_z \\ \tau_{xy} \\ \tau_{yz} \\ \tau_{zx} \end{Bmatrix}$$

where E , G and ν are the elastic modulus, shear modulus and Poisson's ratio, respectively. In the work of [Wicklein et al. \(2008\)](#) the plastic response of composites was evaluated using a quadratic yield function proposed by [Chen et al. \(1997\)](#) in which the flow stress is described by nine plasticity coefficients a_{ij} , and an isotropic hardening parameter, k , which define the shape and size and are expressed as:

$$\begin{aligned} f(\sigma_{ij}) &= a_{11}\sigma_{xx}^2 + a_{22}\sigma_{yy}^2 + a_{33}\sigma_{zz}^2 + 2a_{12}\sigma_{xx}\sigma_{yy} + 2a_{23}\sigma_{yy}\sigma_{zz} + 2a_{13}\sigma_{xx}\sigma_{zz} \\ &\quad + 2a_{44}\sigma_{yz}^2 + 2a_{55}\sigma_{zx}^2 + 2a_{66}\sigma_{xy}^2 \\ &= k. \end{aligned}$$

The work of [Nguyen et al. \(2016\)](#) and [Lässig et al. \(2015\)](#) applied the above models, implemented in the AUTODYN Hydrocode, to the analysis of ultrahigh molecular weight polyethylene and found good correlation between their modelling results and ballistic experiments. Their study utilised a Mie-Gruneisen EOS to describe the shock response and invoked material failure based on the modified Hasin failure criterion, with two additional terms to accounts for in-plane and out-of-plane shear, where e_{ij} defines the three failure surfaces for the three orientation planes:

$$e_{ij}^2 = \left(\frac{\sigma_{ii}}{SF_{ii}(1 - D_{ii})} \right)^2 + \left(\frac{\sigma_{ij}}{SF_{ij}(1 - D_{ij})} \right)^2 + \left(\frac{\sigma_{ki}}{SF_{ki}(1 - D_{ki})} \right)^2$$

where SF is the failure stress, and D is the damage parameter, which reduces the effective strength of the material. The material is deemed to have softened when the value of e_{ij} reaches unity. Their results demonstrated the model's applicability with realistic perforation predictions up to hypervelocity scenarios but, the associated mechanical testing required for the model input is very rigorous and requires highly specialised equipment to ascertain.

9.6.6 Modelling metallic laminates

The modelling of metallic laminates is a much simpler challenge than modelling the impact behaviour of fibre-reinforced polymeric laminates or technical textiles, since their constitutive materials can be simulated using conventional material-strength models. The simplest form is a very basic, fibre-free ABAL, which consists of two material types of material: a high-strength aluminium alloy sheet (between 0.5 and 2.5 mm thick) and an adhesive layer (between 0.2 and 0.8 mm thick). This is an example of the 'stacked lamina, length scale' approach shown in [Fig. 9.18](#). In the following example, Crouch and Greaves ([Crouch et al., 1994](#)) carried out a number of early DRA-DYNA simulations of a number of ABALs with different adhesive bondline thicknesses to investigate the critical defeat mechanism in laminated armours: the independent shearing of the external lamina (see Chapter 4). The strength model derived from detailed characterisation of the adhesive interlayer material, Hysol

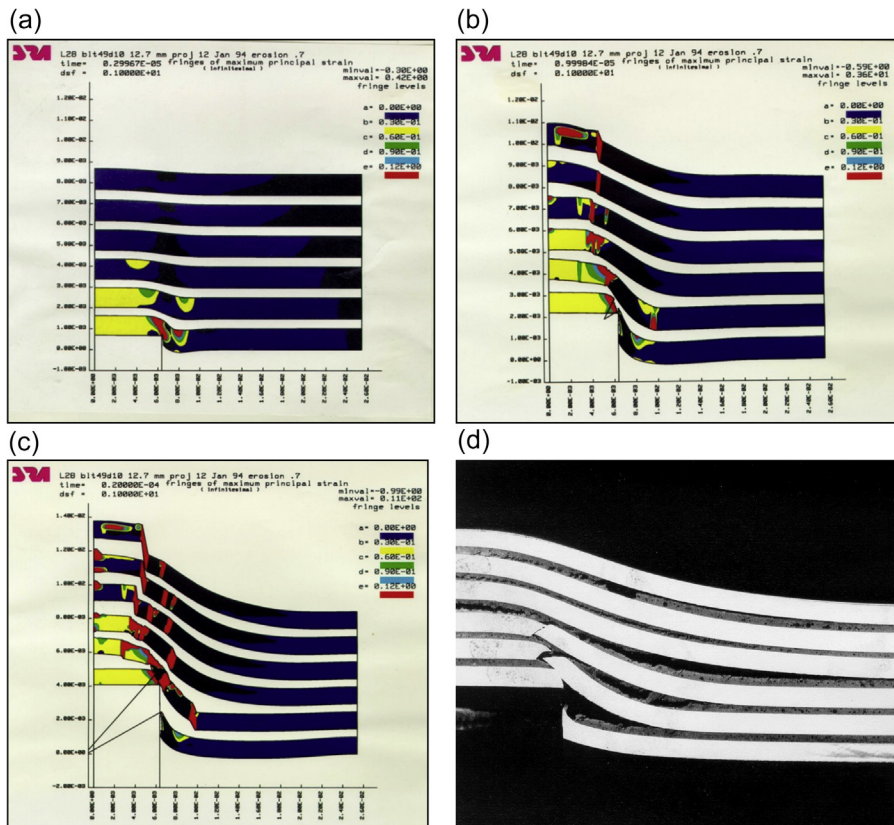


Figure 9.20 Modelling the impact of a blunt projectile against an ABAL using DRA-DYNA, c.1992, showing simulated penetration after (a) 3 μ s, (b) 10 μ s and (c) 20 μ s, compared with a section taken through an experimental target of the same ABAL. Note how in both (c) and (d), the first ply has been sheared — this an essential defeat mechanism in an ABAL.

Crouch, I.G., Greaves, L.J., Ruiz, C., Harding, J., 1994. Dynamic compression of toughened epoxy interlayers in adhesively bonded aluminium laminates. Supplement to Journal de Physique III, Colloque C8 4, 201–206.

9309.3(NA), as described in [Section 9.6.3](#) above, was used in these computer simulations. [Fig. 9.20](#) shows the impact of a blunt projectile at three different time steps (3, 10 and 20 μ s) and compares the final output with a metallographic section of an ABAL showing local shearing of the first ply. This is an excellent illustration of how computer analysis can best be used in the design of armour materials and systems.

9.6.7 Modelling cellular materials

The family of metallic foams are a good example of a cellular material. Their mechanical behaviour can be characterised by three major phenomena: (a) a small elastic

Table 9.4 Review of closed cell foam strain-rate sensitivity

Brand	Material	Relative density	Processing method	Strain-rate effects	References
ALPORAS	Al (Ca, Ti, Fe)	0.08–0.1	Batch casting	Sensitive	Paul and Ramamutry (2000)
ALPORAS	Al (Ca, Ti, Fe)	0.106/0.155	Batch casting	Sensitive	Mukai et al. (2006)
ALPORAS	Al (Ca, Ti, Fe)	0.074/0.15	Batch casting	Sensitive	Dannemann and Lankford (2000)
ALULIGHT	Al (Mn, Si)	0.16–0.31	Powder metallurgy	Insensitive	Deshpande and Fleck (2000)
SCHUNK	Al (CaO ₂)	0.07–0.28	Powder metallurgy	Sensitive	Montanini (2005)
IFAM	6061 Al (Ti)	0.23	Powder metallurgy	Sensitive	Zhao et al. (2005)
—	6061 Al (Ti)	0.1–0.3	Powder metallurgy	Insensitive	Hall et al. (2000)
CYMAT	Al-SiC	0.09	Melt gas injection	Insensitive	Zhao et al. (2005)
CYMAT	Al-SiC	0.1–0.24	Melt gas injection	Insensitive	Montanini (2005)

Liu, Y.D., Yu, J.L., Zheng, Z.J., Li, J.R., 2009. A numerical study on the rate sensitivity of cellular metals. *International Journal of Solids and Structures* 46, 3988–3998.

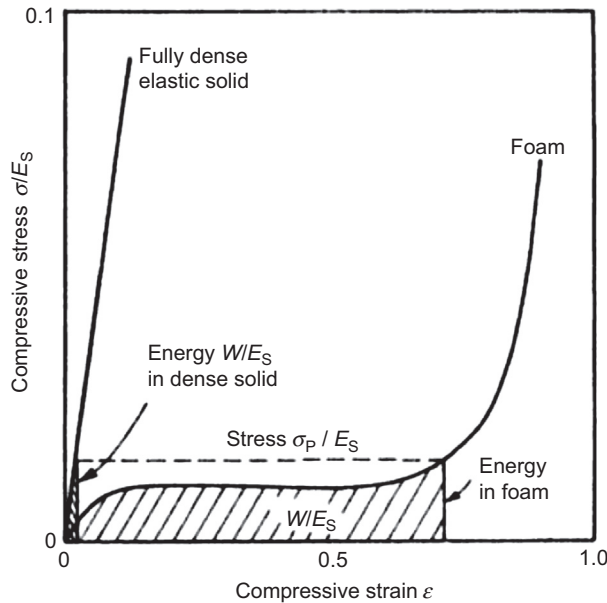


Figure 9.21 Comparison of elastic solid material and a foam sample under compressive load. Gibson, L.J., Ashby, M.F., 1999. *Cellular Solids: Structure and Properties*, Cambridge University Press.

regimen, followed by (b) a long plateau region in the stress–strain that precipitates from the collapse of the closed or open cells walls, plastic yielding and crushing and lastly (c) the densification of the foam and the rapid rise of peak stress with a commensurate small increase in strain as shown in Fig. 9.21. A more comprehensive treatment of cellular materials and metallic foams can be found in Lefebvre et al. (2008), Gibson and Ashby (1999), Gibson et al. (2000), Ashby et al. (2000) and Ashby (2006).

At higher strain rates sensitive materials will exhibit an increase in the yield point before the plateauing region. Early work by Hall et al. (2000) and Deshpande and Fleck (2000a) indicated that some aluminium foams, e.g. Alulight and Duocel, exhibited little strain-rate hardening at high strain rate, while the work of Zhao et al. (2005) highlighted four main pertinent points to describe the observed hardening of behaviour of IFAM foams with the most pertinent being the micro inertia effect in the successive folding process which resulted in a 15% strength enhancement of IFAM foam. Studies by Xu et al. (2014) have highlighted significant strain hardening which was attributed to an increase in the pressure of the entrapped air in their honeycomb structure during the dynamic out-of-plane compression. Furthermore, their study attempted to link the strain-rate hardening with the pile-up of the cell walls under compression, causing localised densification regions and strain hardening. They also observed lateral inertial effects under dynamic loading with deformation bands having higher nominal strain rates than the bulk nominal strain rate providing additional

hardening. The work by [Liu et al. \(2009\)](#) (Table 9.4) further highlights the state of research in the strain-rate sensitivity of cellular foams with the complexity of the materials, the variation in sample densities and testing procedures all proving problematic in nailing down all of the physical attributes of cellular foams. Of note in Liu's research are the inhomogeneous deformation and the observation of the rapid increase in the plateau stress on the impact surface for a critical velocity, i.e., the transition velocity from homogeneous mode to transition mode. They concluded that the nominal stress–strain curve loses its physical meaning and size effects become a greater driver of deformation response.

9.6.7.1 Continuum models for cellular materials

Cellular materials such as metallic foams often utilise the 'self-similar yield surface model' of [Deshpande and Fleck \(2000a\)](#), which provides a theoretical basis for the constitutive model with the yield strength of the foam defined by a yield function Φ :

$$\Phi = \hat{\sigma} - \sigma_c \leq 0$$

where σ_c is the yield strength of the core, and the equivalent stress, $\hat{\sigma}$, is given by:

$$\hat{\sigma}^2 = \frac{[\sigma_e^2 + \alpha^2 \sigma_m^2]}{1 + (\alpha/3)^2}$$

where σ_e is the von-Mises stress, $\sigma_e \equiv \sqrt{3/2 \sigma'_{ij} \sigma'_{ij}}$ and σ_m is the mean stress. The hydrostatic yield strength is given by:

$$|\sigma_m| = \sqrt{\frac{1 + (\alpha/3)^2}{\alpha^2}} \sigma_c$$

where parameter α is used to define the aspect ratio between the hydrostatic and von-Mises effective stress when plotted in (σ_m, σ_e) space. The resultant elliptical yield surface is representative of the experimental test provided an appropriate value of α is chosen ([Deshpande and Fleck, 2000b](#)). The equivalent plastic strain rate, $\dot{\epsilon}_{ij}^p$ is expressed as:

$$\dot{\epsilon}_{ij}^p = \frac{\dot{\hat{\sigma}}}{H} \left[\frac{\partial \Phi}{\partial \sigma_{ij}} \right]$$

where H is the hardening modulus. It can be seen that the model by Deshpande and Fleck does not contain a damage criterion to characterise foam failure through core shear. The material model is implemented in most hydrocodes.

The example below ([Saleh et al., 2015](#)) is of ALULIGHT and ALPORAS sandwich panels, with AA 3104-H19 face sheet, modelled in ABAQUS, with a

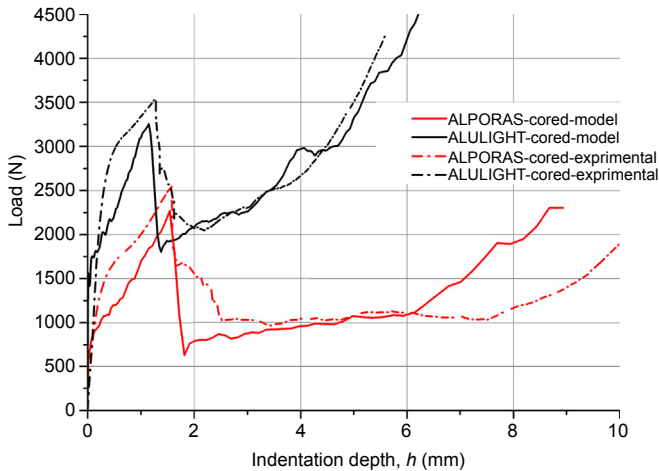


Figure 9.22 Experimental and simulation load-indentation depth curves of ALPORAS- and ALULIGHT-cored sandwich panels locally damaged by an indenter of 20 mm diameter. Saleh, M., Luzin, V., Toppler, K., Kabir, K., 2015. Response of thin-skinned sandwich panels to contact loading with flat-ended cylindrical punches: experiments, numerical simulations and neutron diffraction measurements. *Composites Part B: Engineering* 78, 415–430.

rate hardening rule based on the yield ratio as a function of plastic strain rate

$$\text{where } \dot{\epsilon}^{\text{pl}} = \sqrt{\frac{2}{3}} \dot{\epsilon}_{\text{axial}}^{\text{pl}}$$

If we consider the results shown in Fig. 9.22 they indicate that both models, regardless of foam composition, underestimate the peak load by a similar value of 250 N but the subsequent skin failure is predicted in close proximity to the experimentally deduced values. The results shown in Fig. 9.23 show that peak plastic strains in the ALPORAS panels are located beneath the indenter, while the ALULIGHT panels exhibit greater plastic strain at the periphery of the indenter. The former is characteristic of severe plastic deformation in the crush zone with more pronounced brittle tearing of cell walls. Conversely, the ALULIGHT panels, with a higher cell wall yield stress, have reduced incidents of cell wall tearing during indentation. This can be attributed to the significantly higher densities of the ALULIGHT foams that support the notion that, at higher strains, dislocation slip is the more pronounced deformation mode in the FCC structure. The results show that the use of the forming limit curve in conjunction with Deshpande and Fleck model, for sandwich panels, can produce viable results that correlate well with experiments. The reliance on a uniaxial compression test to gauge the strength of aluminium foams may underestimate the propensity for some of the foams to harden further and faster under hydrostatic compression (Ashby et al., 2000). The experimentally observed peak loads are believed to be influenced, marginally, by the fibre-impregnated adhesive used on both samples, which is often neglected from high strain rate models to simplify the simulations. The adhesive, while brittle, does exhibit a small load-bearing capacity

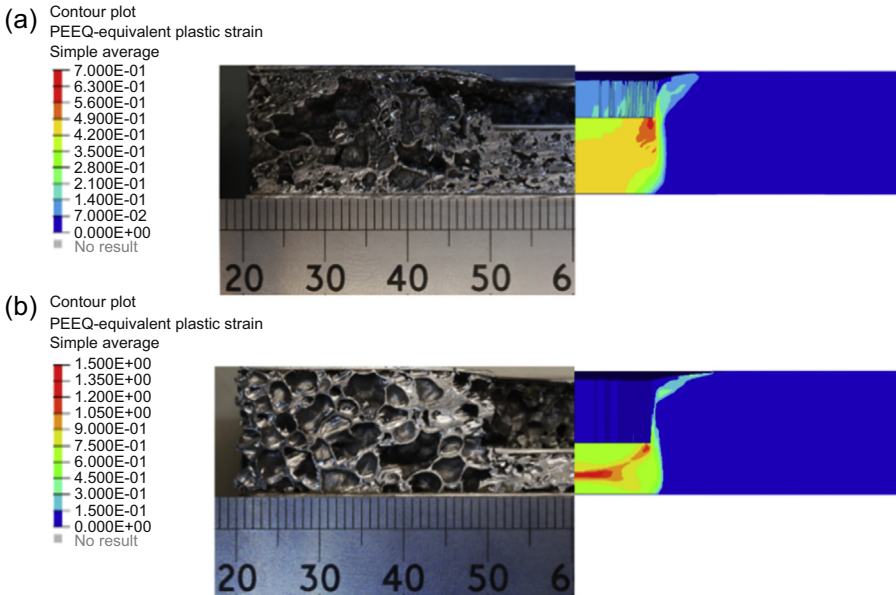


Figure 9.23 Comparison of the final deformed state of the experimental and simulated panels with the corresponding equivalent plastic strain of (a) ALULIGHT and (b) ALPORAS. Saleh, M., Luzin, V., Toppler, K., Kabir, K., 2015. Response of thin-skinned sandwich panels to contact loading with flat-ended cylindrical punches: experiments, numerical simulations and neutron diffraction measurements. *Composites Part B: Engineering* 78, 415–430.

and this may partially account for the slight underestimation of load in the elastic–plastic transition zone in addition to the peak load. Studies by [Burton and Noor \(1997\)](#) also show that the modest shear strength of the adhesive in their study made a small contribution to the increase in strain energy of 11%. Another issue of significant importance is the size effects often exhibited in metallic foams and outlined by [Chen and Fleck \(2002\)](#), in which the yield strength gradually increases as the foam thickness decreases. This is attributed to the overconstraining effects of the face sheets in sandwich construction.

A comprehensive study by [Hanssen et al. \(2002\)](#) looked at nine constitutive models, five of which were implemented in the ABAQUS and LS-DYNA packages. Their study comprised (1) foam material calibration tests, (2) foam material validation tests and (3) structural interaction tests where the foam interacts with aluminium extrusions. Their comparison between the Deshpande and Fleck model, the Miller model ([Miller, 2000](#)) and the Schreyer model ([Schreyer et al., 1994](#)), in addition to the others, highlighted the inability of the models to represent all load configurations with convincing accuracy. The cited inadequacy stems from the treatment of foam fracture where the localised effects are not accounted for in the formulations and where global failure mechanism and the interplay between global and the local failure is yet to be fully elucidated.

9.6.7.2 Micromechanical models for cellular materials

To combat the shortcoming of the continuum models, some researchers opt to model the exact geometry of cellular materials by utilising repeating patterns as per the work of [Fleck and Deshpande \(2004\)](#) shown in [Fig. 9.24](#). Sandwich panels with pyramidal cores, diamond-celled lattice materials, metal foams, hexagonal honeycombs and square honeycombs are common geometries and can be idealised as elastic, perfectly plastic homogeneous materials with a von-Mises type relation to model the flow stresses and yield. Some models utilise kinematic hardening, but conceivably any relevant constitutive model can be used to model the material's flow stress regimen along with local failure criterion. The explicit simulation of the morphology of repeating patterns has been successful in the works of [Khoshravan and Najafi Pour \(2014\)](#), [Li et al. \(2014\)](#) and [Zhu et al. \(2009\)](#) in evaluating blast and compressive performance of sandwich panels. The computational cost of such schemes is perhaps application-dependent with a large number of elements required to study the cell wall buckling. The walls of the cellular structures are often constructed using shell elements with tied constraints to the face sheet, to approximate the adhesion of the two parts.

Another method that has found increasing use is the Voronoi and Laguerre–Voronoi tessellation technique ([Redenbach et al., 2012](#); [Siegkas et al., 2014](#); [Wejrzanowski et al., 2013](#)), shown in [Fig. 9.25](#), in which a random foam cellular structure is created. By utilising a set of seeds randomly distributed in the simulation domain, the user can develop a 2-D or 3-D Voronoi diagram. The formation of the diagram is essentially a bubble growth model with the following assumptions ([Sotomayor and Tippur, 2014](#)): (1) the bubbles nucleate simultaneously, (2) bubble positions are fixed during the growth phase, (3) constant growth rate is assumed in all directions and (4) growth stops when a bubble touches an adjacent bubble. The tessellation structure is fully determined by the initial locations of the seeds, thus using regularly positioned seeds produces a regular Voronoi diagram with a repeating

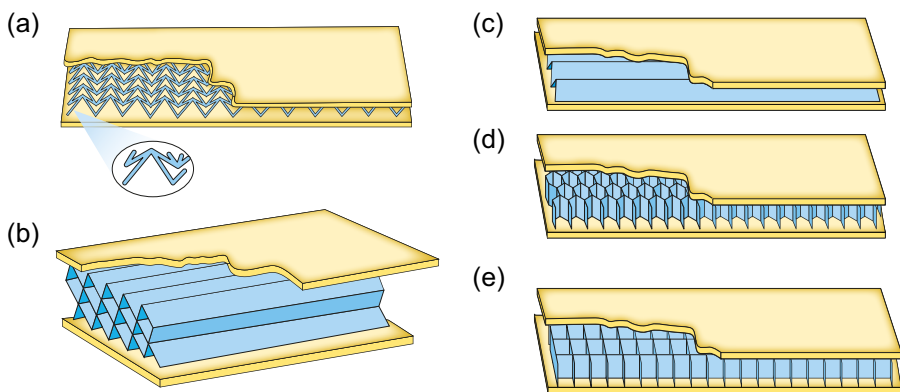


Figure 9.24 Cellular composite panels as per Fleck and Deshpande.

Fleck, N.A., Deshpande, V.S., 2004. The resistance of clamped sandwich beams to shock loading. *Journal of Applied Mechanics* 71, 386–401.

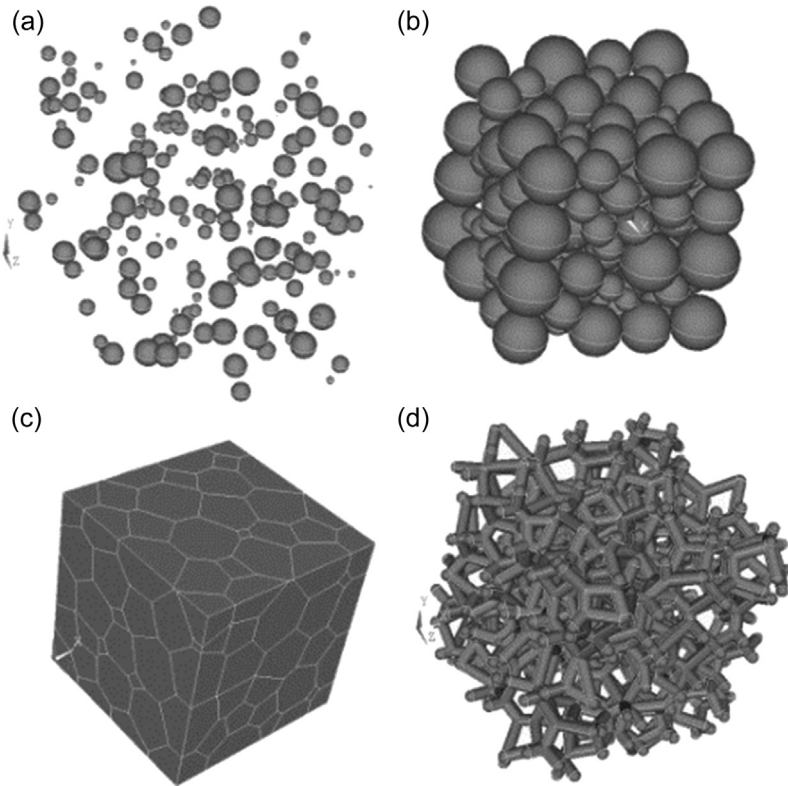


Figure 9.25 Schematic illustration of the algorithm for foam structure generation using the Laguerre–Voronoi tessellation.

Wejrzanowski, T., Skibinski, J., Szumbariski, J., Kurzydowski, K.J., 2013. Structure of foams modeled by Laguerre–Voronoi tessellations. *Computational Materials Science* 67, 216–221.

structure. These models often utilise elastoplastic relation to describe the cell wall behaviour with bilinear relationships for the isotropic hardening response.

The last method, and perhaps the most geometrically accurate, is the use of X-ray tomography and micro-computed tomography to extract the morphology of the cellular structures (Fig. 9.26). The early work of [Bart-Smith et al. \(1998\)](#) looked at the surface strains in metallic foams, evaluating the deformation modes and the cell morphologies that govern the onset of yielding. In the preceding years a number of authors ([Youssef et al., 2005](#); [Maire et al., 2003](#); [Jeon et al., 2010](#)) utilised the method to investigate various aspects of the deformation process. The results of [Jeon et al. \(2010\)](#), for example, show that the formation of localised plastic strain bands in the cell walls causes the plastic collapse of the foam material. The initiation of cell wall collapse is by means of plastic hinges that form in these plastic strain bands. The FE results for their computed stress–strain curves were very different from their experimental results. This was attributed to the volumetric error in the FE models along with deviation in the material properties utilised for the simulation away from the actual

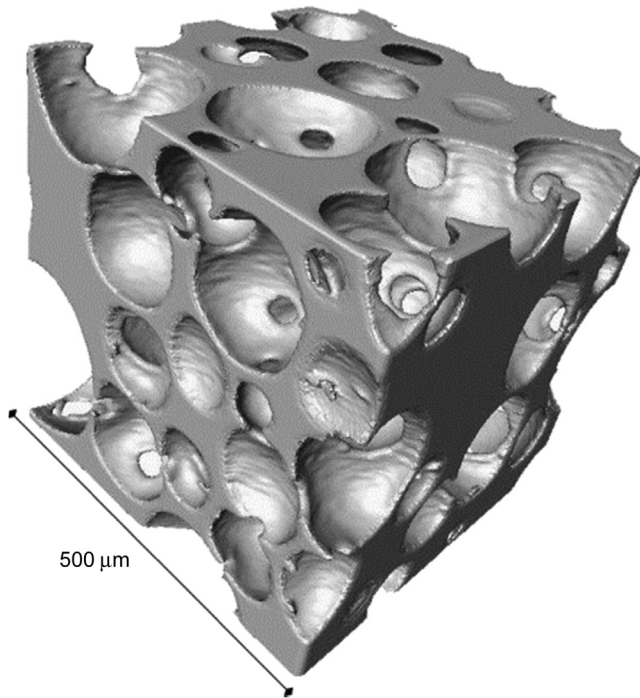


Figure 9.26 Results of 3-D tomography of polyurethane foam.

Youssef, S., Maire, E., Gaertner, R., 2005. Finite element modelling of the actual structure of cellular materials determined by X-ray tomography. *Acta Materialia* 53, 719–730.

material performance of the foam's constituent metal. While this method is very powerful in capturing the minute details of the foams, it has limited ability for scaling to larger structures due to the significant computational penalty associated with the large number of elements required. Additionally, as the scale of the computational domain reduces so does the need to evaluate the anisotropic behaviour precipitating from the microstructure, with particular regard to: grain orientation, the role of alloying elements in precipitation hardening, void coalescence and crack propagation, etc., all of which pose a significant hurdle to accurate synergistic modelling.

9.7 Threat definitions

It is perhaps counterproductive to stipulate specific threat geometries to analyse as these can vary considerably between countries and the battle space. Nonetheless, various standards set out a number of threats which have wide application in the qualification of different armour materials in light-armoured platforms. Additionally, the US Department of Justice sets out a widely used standard for the qualification of body armour, for example [Doj \(2008\)](#).

Chapter 1 provides detailed descriptions of most of the small arms ammunition of interest to the armour technologist. This following section describes how the numerical modeller sets out to model these various threats.

9.7.1 Modelling KE impactors

In modelling various ballistic threats the FE engineer/scientist must take care to achieve a numerical balance to reproduce accurate simulations. The complexity or simplicity of the terminal ballistic problems will wholly rely on the fidelity of the model in terms of mass of the materials, bullet velocity, projectile nose shapes, overall dimensions, contact formulation and material behaviour. The geometries shown in Fig. 9.27 demonstrate the importance of capturing both the external and internal details of the ballistic threats. The interaction of various bullet components, as in the jacket of a mild steel-cored bullet, will affect the experimental tests (Crouch, 2015). Experimentally the jacket serves three functions: (1) contacts the rifling of the gun barrel upon firing, (2) for the case of hardened cores the case protects the barrel and lastly (3) the in-flight performance is improved through the use of the jackets. None of these are explicitly modelled in terminal ballistics; rather the jacket serves as containment for the lead and steel cores upon impact. It also contributes to the inertia of the bullet and provides for lubrication when used in conjunction with frictionally governed contact algorithms.

Small features are routinely discarded such as bullet knurl, small filleted or chamfered edges and the driving bands on the bullet jacket. Features such as these serve to

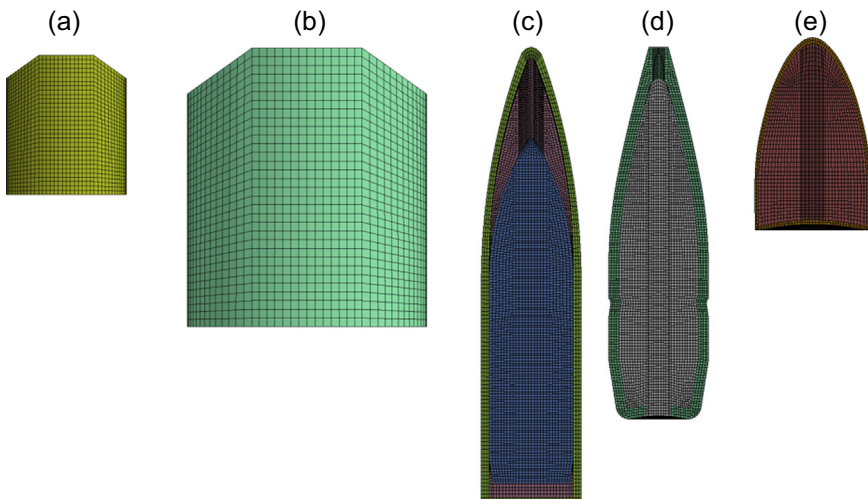


Figure 9.27 KE impactors models L-R (a) 1.1 g FSP (b) 20mm FSP (c) 7.62 mm APM2 (d) 7.62 mm NATO Ball (e) HG 9 mm.

aerodynamically stabilise the projectile in experimental tests but are of little importance in modelling the impact phenomena. Specific yaw, spin or oblique characteristics are implemented as initial condition and these are automatically propagated through the time steps pursuant to the resultant interaction. Meshing techniques for Lagrangian models vary considerably but most models employ CAD-based Boolean operations to partition the varying components (Fig. 9.27), with care taken during the meshing step to avoid initial penetrations. Initial penetrations will result in artificial stresses within the projectile. Most hydrocodes will attempt to resolve initial penetration by moving the slave node to the surface of the master component; these methods are prone to large stress oscillation and distorted mesh geometry during initialisation.

For the case of Eulerian-type simulations, the volume fraction of the filled elements is often defined using shell containers with the shell or segment normal direction dictating the fill direction. Native geometries of various hydrocode can also be used, e.g. cylinders, cubes, etc. to initialise the container shape and to fill the elements within the geometry. In ALE and Eulerian simulations a fine mesh is needed to reduce the advection errors previously discussed.

Adequate mesh resolution is essential for contact and for the stress evaluation in the penetrators, the mesh skewness and the aspect ratio of the mesh are also important to consider. Very small or highly distorted elements will ultimately reduce the time step. Hexahedral elements with single-point integration and hour-glassing control are widely accepted for ballistic assessment. Tetrahedral elements are also widely used in AUTODYN as the default element formulation, while fully integrated hexahedral elements have a large computational cost and are not widely used for ballistic simulations.

The explicit assignment of master–slave contact will often be too computationally costly and may fail in instances of self-contact or with newly formed surfaces in eroding contact. Care should thus be taken in their designation. The material assignment of most armour-piercing bullets will comprise three major materials, a brass jacket, a lead filler and a steel core (Table 9.5). A large number of researchers assume rigid penetrators as these provide a conservative solution. Where the material strength plays a secondary role and the inertial effects are more paramount the user can prescribe the material strength using an EOS only to describe the hydrostatic stress state. Instances where projectile defeat, as in the case of ceramic armour, is the primary interaction of interest, a more nuanced assessment of the projectile strength is required and this will be discussed in Worked Example #3.

Table 9.5 JC parameters for 7.62 mm APM2

Material	A (MPa)	B (MPa)	n	C	m	$\dot{\epsilon}_0(\text{s}^{-1})$
Bullet cores	1200	50,000	1.0	0.0	1.0	5E-4
Lead bullet cap	24	300	1.0	0.1	1.0	5E-4
Brass jacket	206	505	0.42	0.01	1.68	5E-4

9.7.2 Modelling high-explosive (HE) events

It is perhaps pertinent to provide a brief introduction to blast threats as these do pose significant risk to armour materials. An explosion will give rise to a shock wave in the surrounding medium of the rapidly expanding gas. This wave is inherently in a discontinuous condition where pressure, density, temperatures, etc. increase. The shock-induced compression of the surrounding fluid leads to an increase in fluid temperature behind the shock front. The Rankine–Hugoniot jump equation describes the conservation equations for mass, momentum and energy ahead of and behind the shock wave. The shock wave is characterised by a distinct pressure spike, overpressure and an exponential decay beyond the atmospheric pressure (Fig. 9.28).

The Friedlander formulation is generally used to describe a simplified blast wave pressure–time history:

$$P_s(t) = P_{so} \left(1 - \frac{t - t_a}{t_0} \right) \cdot e^{(-B \frac{t - t_a}{t_0})}$$

where P_{so} = peak incident pressure; t_0 = positive phase duration; t_a = arrival time; B = decay coefficient.

The impulse can be calculated as follows:

$$I_{\max} = \frac{(t - t_a)P_{so}}{B^2} [B + e^{-B} - 1] = \int_{t_a}^{t_a+t_0} P_s(t) dt$$

The parameters for this model are computed from the data published by Kingery and Bulmash and the US Army standard Tm-5-855-1 (US Army, 1986, Kingery

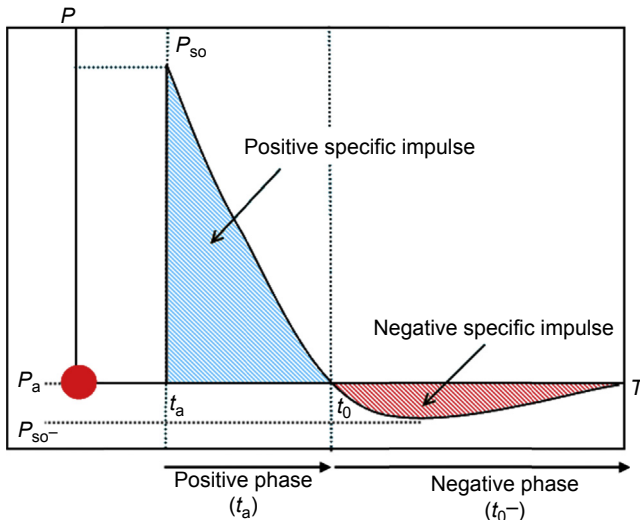


Figure 9.28 Pressure–time history for an ideal blast wave.

et al., 1984). The Friedlander formulation generally fails to accurately represent the static overpressure for distances less than 10 charge radii. As such, its application for detonics, or near-field blast regimens, is limited. The incident pressures, upon encountering a fixed or deformable structure, will experience a sudden decrease in shock-wave velocity and particle velocity. This will lead to the development of a reflected pressure wave, P_r , of magnitude (Smith and Hetherington, 1994) which will drive the structural response of the impacted target:

$$P_r = C_R P_{so}, \quad 2 \leq C_R \leq 8$$

This relationship is shown to be valid for air blast, but can extend beyond the higher ratio as show in Fig. 9.29.

This method of applying the blast loads is numerically implemented into most hydrocodes as in the ConWep method (see Chapter 8). The implementation of the ConWep air blast model in LS-DYNA was done by Randers-Pehrson and Bannister (1997) as hemispherical or spherical type blasts. It was previously found (Saleh and Edwards, 2011, 2015) that for the case of landmine detonation the CONWEP model fails to account for charge shape, shadowing, soil composition or confinement effects.

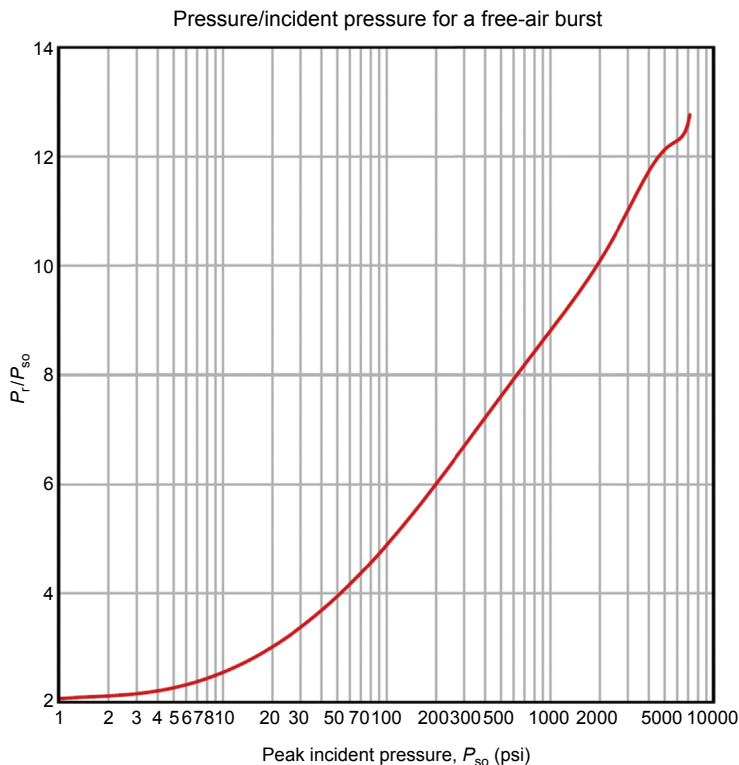


Figure 9.29 Ratio of $\frac{P_r}{P_{so}}$ as a function of P_{so} .
Department of Defence, 2008. Structures to Resist the Effects of Accidental Explosions.

The model also largely fails to accurately predict both peak pressures and impulse for near-field blast regimens.

A blast in soil, which is a common analysis scenario, cannot generally be characterised in the same fashion as air, rather, three distinct phases are generally recognised:

1. The detonation transforms the stored chemical energy of the solid explosive into a gaseous product. At very small standoff distances the soil is crushed by the enveloping shock wave. This process is largely independent of the physical properties of the soil. Beyond this initial rupture zone the second zone is characterised by irreversible plastic deformation through crushing and pore collapse. The last significant response of the soil is in a third zone which is elastically loaded by the shock wave with the process being largely reversible.
2. As the gas expands the confinement of the soil forces the gas to expand upwards towards the surface. The soil cap at this point is ejected in a hemispherical fashion; this correlates to the depth of the charge from the surface. As the compressive waves travel through the soil towards the surface they are partially transmitted into the air as a shock wave but largely reflected back into soil as tensile waves. This is due to the large impedance difference between the soil and the air.
3. The final phase sees the soil ejected and in an inverse cone shape forming an annulus of ejecta surrounding the detonation products. Generally, the angle of the soil ejecta is between 60° and 90° depending on the depth of burial and the moisture content of the soil. It is during this phase that the soil impacts neighbouring structures causing localised material deformation and possible breach of these structures. The expansion of the explosive gases and the impact of entrapped soil and debris provide additional loading on nearby structures and these must be explicitly modelled to ascertain their effects at the short stand-off distances encountered in the battle arena.

As previously mentioned ALE simulations can account for confinement effects, charge shape and orientation, shadowing and fluid expansion but do require the use of an EOS to describe the explosive products. The John Wilkins and Lee (JWL) EOS is widely used in conjunction with the ALE or Eulerian method to explicitly model the charge and the surrounding fluid. There are a number of resources (Souers et al., 1996; Dobratz, 1981; Lee et al., 1973), for JWL data with the most widely used versions being those of Dobratz (Zukas and Walters, 2013). Of note is the variability in the EOS data from the three different sources. This largely stems from the test methodology employed but the reader is encouraged to form an informed view about the applicability of each data set to their problem.

The pressure term for explosives is given by:

$$P = A \left(1 - \frac{\omega}{R_1 V} \right) e^{-R_1 V} + B \left(1 - \frac{\omega}{R_2 V} \right) e^{-R_2 V} + \frac{\omega E}{V}$$

where A , B , R_1 , R_2 , ω are material constants usually derived from cylindrical explosive testing or thermos-chemical kinetic simulations. V is relative volume and E is energy per initial unit volume. The first term of the JWL is the high-pressure term where the relative volume is close to 1. The second intermediate pressure term applies when V is close to 2. As V becomes larger in the expanded state the EOS

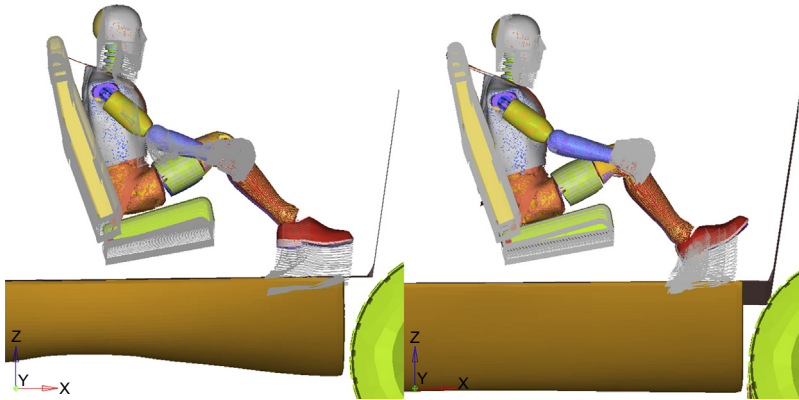


Figure 9.30 H-III dummy displacement during the simulation.

reduces to the last term, $\frac{\omega E}{V}$ (Zukas and Walters, 1998). The example below (Saleh et al., 2014) incorporated a multiphysics blast FE simulation in the LS-DYNA code to investigate the interaction of soil blast with an idealised V-hull vehicle. The author's used the Hybrid III Anthropomorphic Test Devices model, a JC material model for the deformable hull, a JWL EOS for the explosive and a modified Mohr–Coulomb material model for the soil. The authors evaluated the dynamic response index and the head injury criterion along with the acceleration and forces of the vehicle's underbody. For example, Figs 9.30–9.32 show the increased complexity that can be achieved through the coupling of different modelling

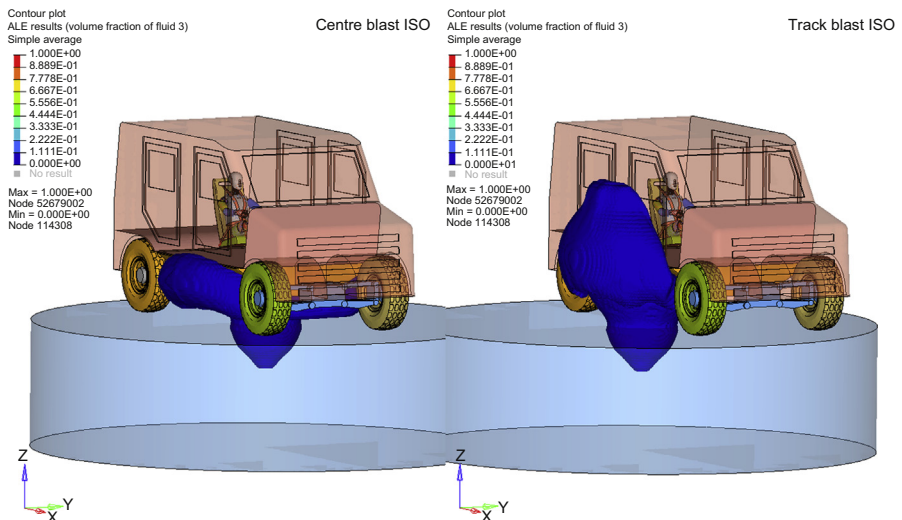


Figure 9.31 FSI between the blast products and the vehicle showing the expansion of the blast products.

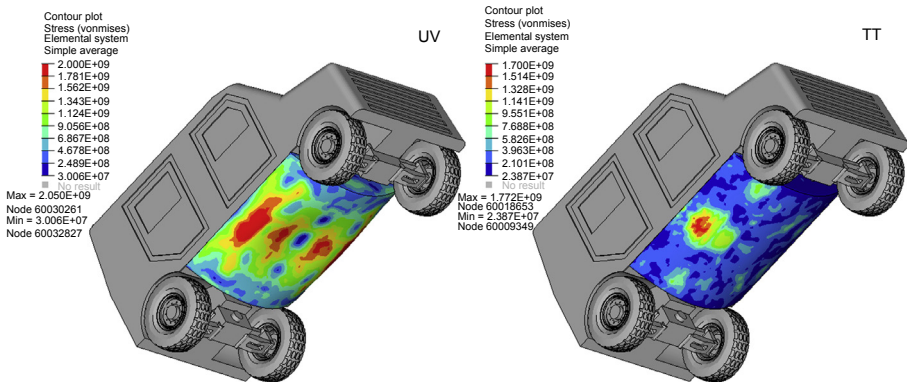


Figure 9.32 Contours of the von-Mises stress for the different blast scenarios.

strategies and different material models to gain a better understanding of the blast interaction with armour materials.

9.7.2.1 Worked Example #1: modelling of multilayered armour (Lagrangian)

This worked example is based on a benchmarking study against the work of [Børvik et al. \(2009\)](#), who investigated the ballistic performance of a double layer of armour steels of grade ARMOX 560T, as supplied by Swedish steelmaker SSAB, against the 7.62 mm APM2 steel-cored bullet. Such layered configurations are sometimes desirable as they allow for the provision of add-on armour: different layouts can be investigated and a potentially higher ballistic limit determined, compared to a monolithic plate configuration.

The model is implemented in the LS-DYNA code with the following broad features: penalty-based eroding contact, with segment-based slave–master designation, and self-contact applied. Due to the nature of the multicomponent bullet, assigning master and slave nodes for the highly distorted elements is problematic and can cause instabilities. Instead, a segment-based contact is used, as it is stable for materials with varied stiffness and mesh densities. Since the bullet jacket has a propensity for rolling onto itself this was found to be more robust. The modified Johnson–Cook model was implemented ([Børvik et al., 2009](#)) to describe the flow stress with a single-parameter Cockcroft–Latham failure criterion. Whilst element erosion is not a real physical phenomenon it ‘mimics’ the material fracture when the user employs a fracture/damage-based erosion criterion. Since material failure cannot occur at the seams of neighbouring elements, the freed vertices of the deleted elements are free to act as point masses.

Underintegrated, single-point, solid, hexahedral elements were used with stiffness-based hour-glassing control. The major disadvantage of the constant stress elements (i.e. single integration point) is the appearance of zero-energy modes that can, unbounded, grow exponentially to severely distort the elements. A study of the hour-glassing controls showed that a direct correlation between the hour-

glassing energies and the ballistic behaviour of the armour in the FEA analysis exists, with the elements becoming overly stiff when calibrated using default values (Saleh and Edwards, 2010).

A one-half reflective symmetry 3-D model was built with the aim of capturing the prevailing physical attributes of the penetration event. The model was calibrated against an initial round velocity of 920 m/s. This was conveniently chosen as comprehensive descriptions of the impact and post-impact behaviour were provided in the published study allowing for greater comparison. The modified Johnson–Cook material parameters and the Cockcroft–Latham fracture criteria for the ARMOX 560T steel are shown in Table 9.6.

Fig. 9.33 shows the penetration process with the brass jacket stripped from the bullet. The lead filler atop the steel core is largely eroded due to adiabatic heating as a result of the plastic work, previously discussed in Fig. 9.12. The collapsing brass jacket damages the lead filler to the rear of the bullet. This damage is induced by the complex contact, which creates disparities in the bullet component velocities. The penetration of the first plate is generally characterised by piercing and ductile hole growth, i.e. radial expansion of the hole. This is evident by the increasing mesh densities at the periphery of the steel core. The bulk of the bullet tip erosion occurs during the impact with the first plate and arises from the adiabatic heating of the metal, which exceeds the thermal threshold specified, $T_{\text{threshold}} = 0.9T_{\text{melt}}$. As the model does not compute the rate of heat transfer between varying components the

Table 9.6 Material data for ARMOX 560T

		ARMOX 560T
Strain hardening parameters	A (MPa)	2030
	B (MPa)	568
	n	1
Strain-rate hardening	C	0.001
Reference strain rate	$\dot{\epsilon}_0$ (s ⁻¹)	5.00E-04
Thermal softening parameter	m	1
Melting temperature	T_m (K)	1800
Specific heat	C_p (J/kg K)	452
Expansion coefficient	α (K ⁻¹)	1.20E-05
Taylor–Quinney coefficient	χ	0.9
Reference temperature	T_0 (K)	298
Element temperature threshold	T_{del}	$0.9T_{\text{melt}}$
Cockcroft–Latham fracture criteria	W_{cr} (MPa)	2310

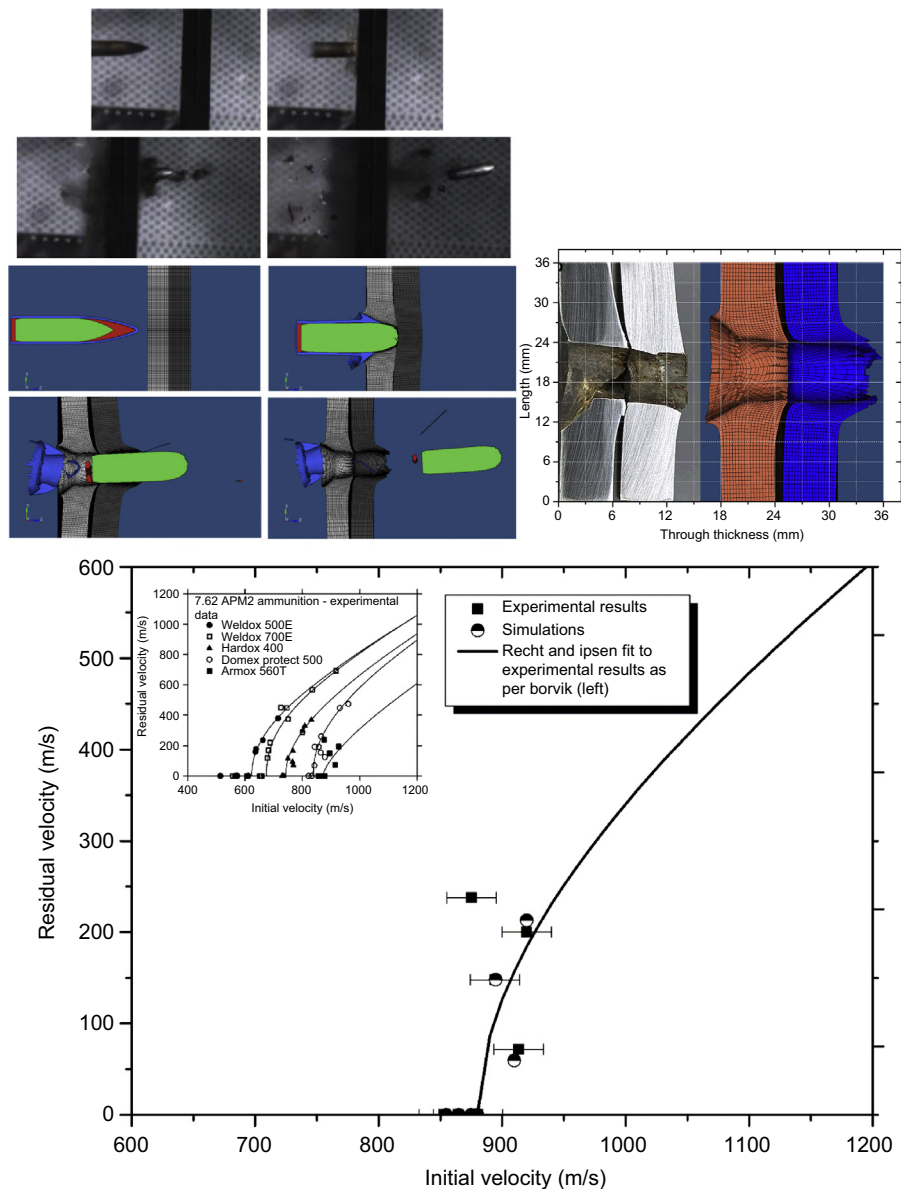


Figure 9.33 Quantitative and qualitative measure of the ballistic response shows good agreement.

temperature rise in each part is wholly attributable to the plastic work and the adiabatic heating.

The reduction of the bullet velocity after the impact with the first plate ensures that subsequent heating of the bullet tip is below the thermal threshold and no

additional erosion is apparent. The resultant bulging of the second plate is evidence of increasing bending stresses induced by the passage of the bullet. The flattened shape of the core nose changes the nature of the impact problem; as it passes into the second plate it creates a more blunt type of impact. Contact forces associated with the second plate generate a high strain-rate zone. Of note is the rotation of the bullet, which was initially thought to be a byproduct of the numerical solution but later it was deemed to be the consequence of asymmetric confinement, resulting from minute asymmetric plate deformations.

The evaluation of the ballistic response of the armour is often done through an incident velocities versus residual velocities, V_i-V_r , diagram plotted against a Recht–Ipson fit (Recht and Ipson, 1963). It should be noted that some discrepancies are apparent between the simulation and the experimental results. Thus it was pertinent to evaluate the correlation between the data points using some common regression analysis tools, analysis of variance (ANOVA), to validate the accuracy of the simulations. In the first instance the correlation is carried out for all seven experimental and simulation data points. The R^2 value, square of the correlation coefficient, for the linear regression of the two sets of data shows that the correlation is poor with an R^2 value of 0.304 (Fig. 9.34). Further analysis was carried out to determine the 95% confidence interval. The analysis shows that a single experimental point falls outside the 95% confidence interval, and was deemed to be an outlier that most likely falls outside the Gaussian data set, in Fig. 9.35 and with the outlier omission, the R^2 value improves to 0.994.

9.7.2.2 Worked Example #2: failure of unconfined and confined SiC impacted by 7.62 mm APM2

In this worked example, the ballistic performance of unconfined SiC impacted by a 7.62 mm APM2 round is evaluated and the evolution of damage studied. The

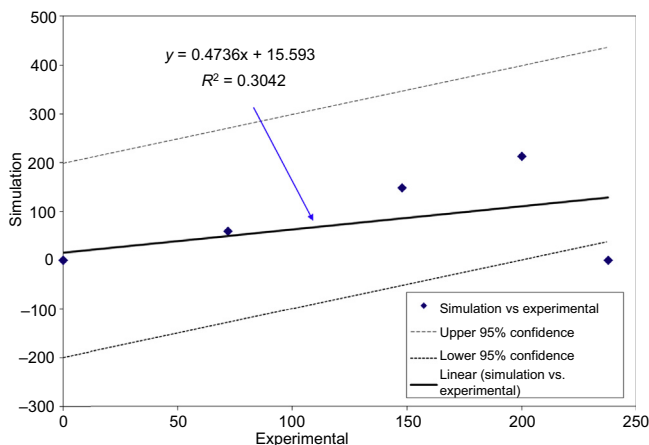


Figure 9.34 ANOVA analysis of residual velocity with outlier.

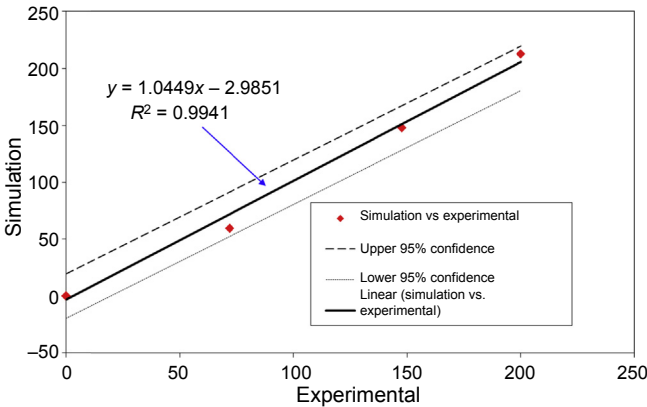


Figure 9.35 ANOVA analysis of residual velocity without outlier.

numerical code was LS-DYNA and the strength model used was the JH2. A penalty-based eroding contact was used with segment-based contact. The material data were sourced from [Cronin et al. \(2003\)](#) and are reproduced in [Table 9.7](#).

A one-half reflective symmetry 3-D model was used as per the previous case study in order to simulate the impact of the APM2 round, with an initial velocity of 900 m/s, onto a 12-mm thick SiC plate. In observing the results the fracture conoid is apparent and the penetrator will begin to erode due to the aforementioned comminution zone as seen in [Fig. 9.36](#). The brass jacket and the lead filling are mostly eroded away with the steel core developing a blunt face profile due to material erosion. Also apparent in the simulation results is the rapid propagation of radial and circumferential cracks in the ceramic plate. The resultant conoid zone fails locally and a large bulge forms with the ceramic being ejected from the back face. The material erosion correlates with a linear reduction of the projectile velocity with a corresponding 2% mass loss of the ceramics due to erosion. Comparison between the previous case study and this shows considerable variations in the bullet's response to the armour, with greater erosion shown in the current case.

Table 9.7 Material data for SiC

ρ_0 , Density (kg/m ³)	3163	$\dot{\epsilon}_0$	1.0	D_1	0.48
G , shear modulus (GPa)	183	T (GPa)	0.37	D_2	0.48
A	0.96	SFMAX	0.8	K_1 (GPa)	204.785
B	0.35	HEL (GPa)	14.567	K_2 (GPa)	0
C	0.0	HEL pressure (GPa)	5.9	K_3 (GAP)	0
M	1.0	HEL vol. strain		β	1.0
N	0.65	HEL strength (GPa)	13.0	F_s	3.0

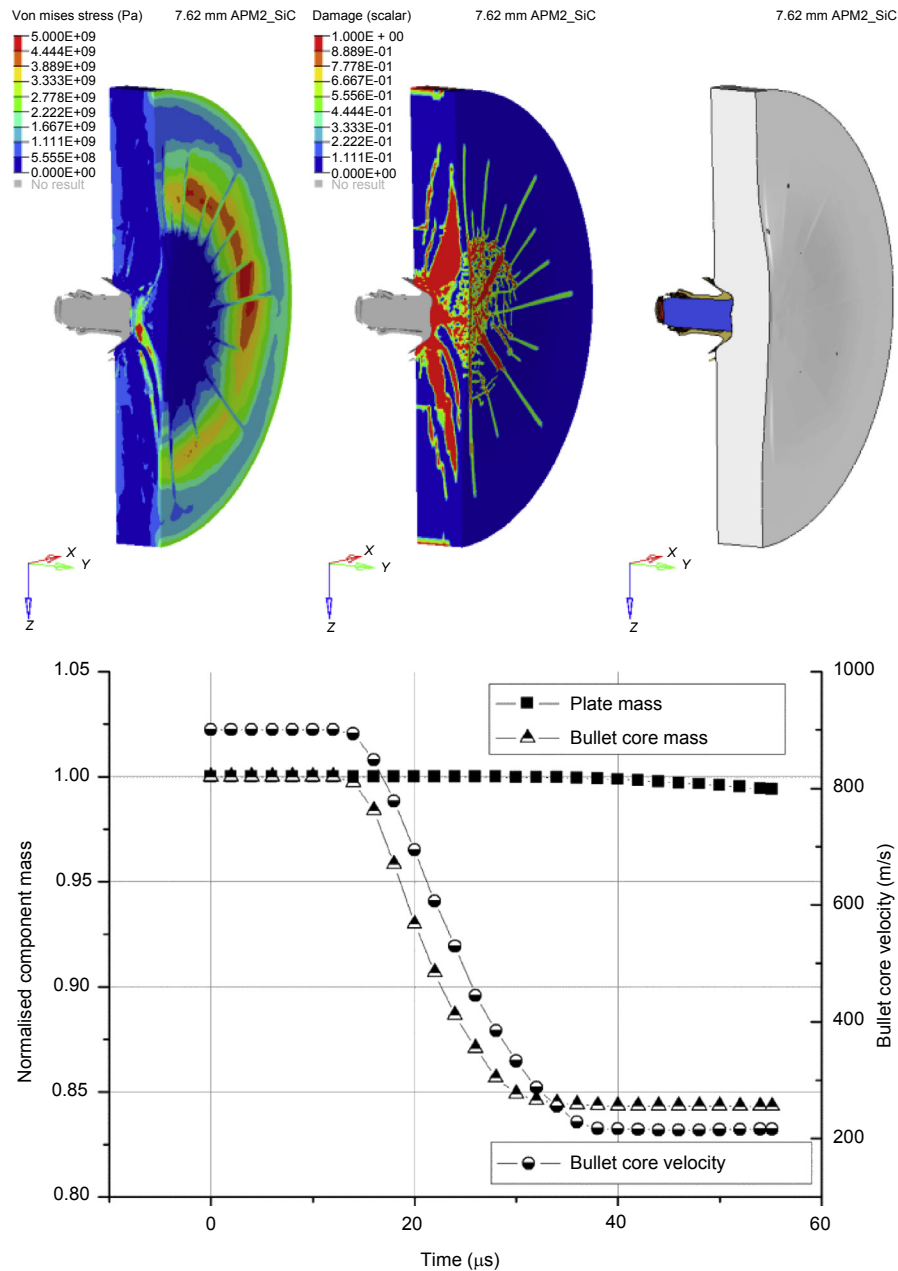


Figure 9.36 Impact of APM2 with SiC at $t = 50 \mu\text{s}$ and temporal variation of bullet and plate mass loss and velocity profile of the impacting bullet.

Having established a broad qualitative performance of the ceramic with the available data a second iteration looks to assess the performance of ceramic plates by means of DOP (depth of penetration) simulations based on the work by [Moynihan et al. \(2000\)](#), in which 3.75 mm ceramic plates bonded and backed by 75 mm AA5083-H131 backed were impacted by 7.62 mm APM2 rounds at a velocity of 841 m/s. The resultant DOP was used to assess the armour's efficiency through an analytical relationship in the experimental study. The current simulation will look to capture the bullet–ceramic–metal interaction and assess the accuracy of the model.

Previous work by [McIntosh \(1998\)](#) has highlighted the discrepancies between the experimental and modelling results for DOP experiments. He attributed this to the rate at which the material moves from the undamaged to the damaged state and the strength of the weakened material. As these are not directly measurable they cannot be established with great confidence and the simulation in turn requires greater levels of calibration to achieve the required experimental correlation. The lack of a sophisticated element erosion criterion is problematic for the JH-2 model. The wide use of the failure strain, F_s , requires a more nuanced approach as noted by [McIntosh \(1998\)](#) due to the interplay between it and other material variables, specifically the ' b ' value which governs the strength of the damaged material. To pursue this sensitivity of the JH-2 model, three further models were run, in addition to the base line data, with varying b and F_s , D_1 and D_2 combinations: (1) $b = 0.6$, $F_s = 3$, $D_1 = 0.4$, $D_2 = 0.48$; (2) $b = 0.6$, $F_s = 3$, $D_1 = 0.2$, $D_2 = 0.48$ and (3) $b = 0.6$, $F_s = 3$, $D_1 = 0.2$, $D_2 = 0.2$. The base line material model data for SiC are shown in [Table 9.7](#), while the AA5083 is modelled using the Johnson–Cook strength and fracture models as per the study by [Clausen et al. \(2004\)](#). The quarter model realised is shown in [Fig. 9.37](#) and the results are shown in [Figs 9.38 and 9.39](#).

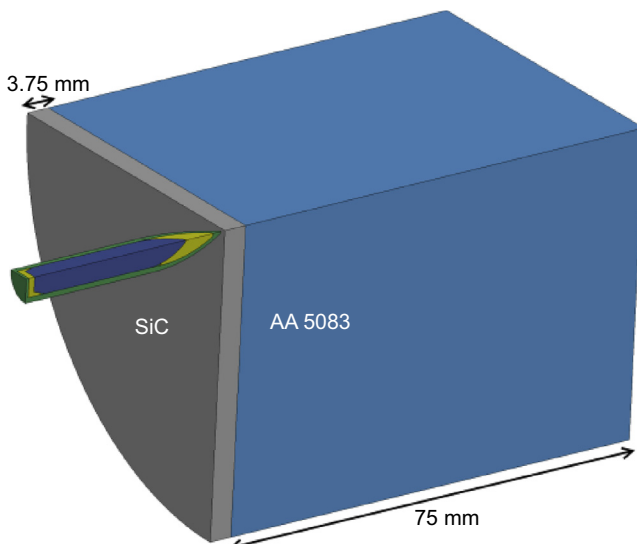


Figure 9.37 Setup of DOP simulation on SiC-AA5083 targets.

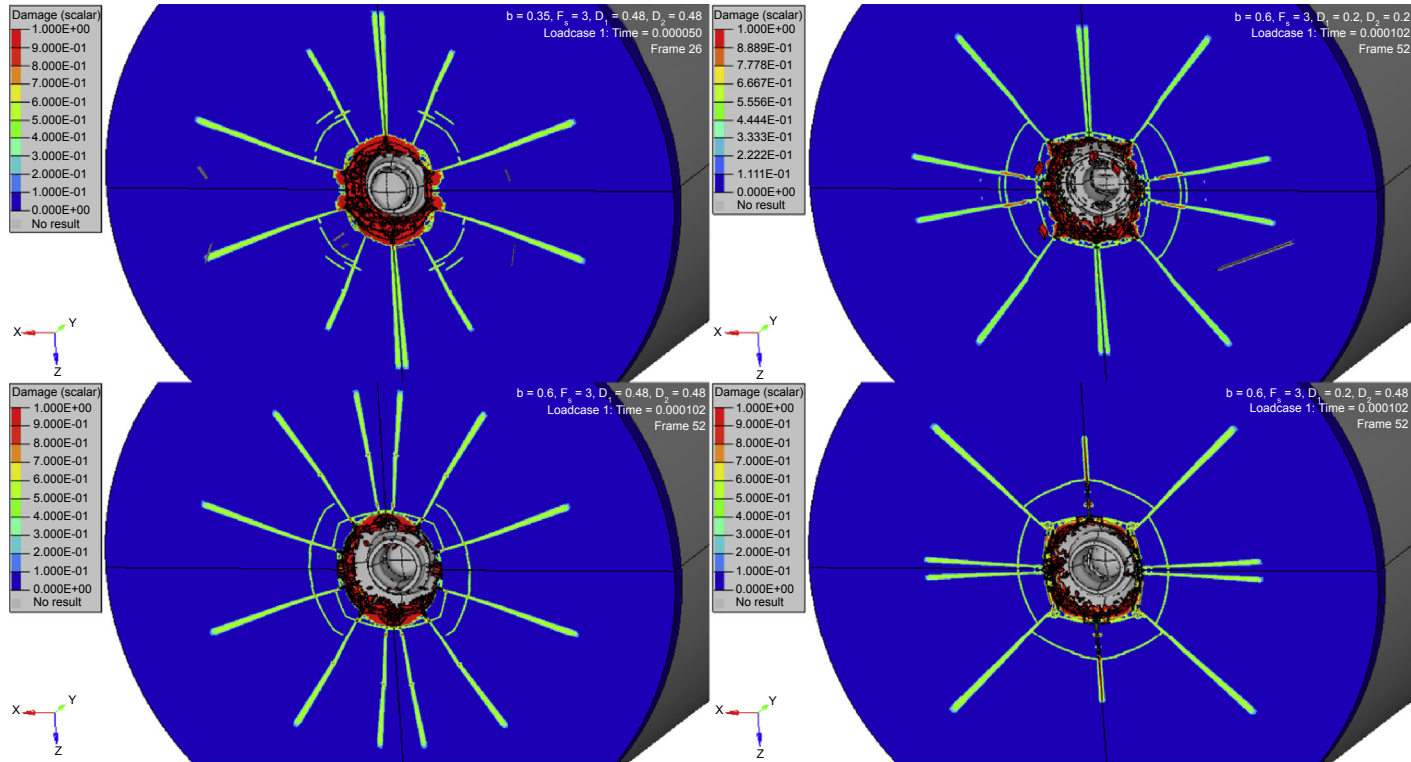


Figure 9.38 JH-2 scalar damage parameters for the four cases (note the use of the x - y and y - z plane reflection for presentation clarity).

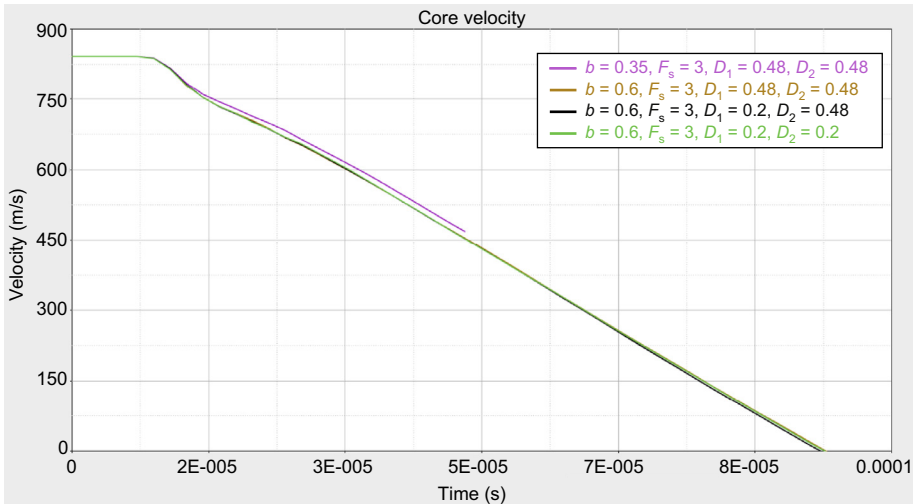


Figure 9.39 Core velocity for the four models.

The base model has the highest residual velocity of the four models. By increasing the b term to $b = 0.6$ we achieve greater reduction in the residual velocity of the APM2 core and a reduction in penetration depths (Fig. 9.39). The models all achieved greater residual penetration compared to the experimental results. These difference may have arisen from the variation of the ceramic material strength compared to the literature-sourced data, greater undocumented ceramic confinement, the influence of the adhesive on damping and confinement (not modelled), or the variation between the high strain-rate performance of AA5083 used in the ballistic experiment and the literature sourced JC data. The resultant smallest DOP was for case (3) at 22 mm compared to the 6.7 mm DOP for the experimental study. The model thus requires greater calibration to achieve better correlation. In the author's experience the small variations in bullet velocity with changes in the J–H II model indicated that the response of the bullet is perhaps not being captured correctly, with overprediction of the bullet strength leading to greater penetration.

In examining the post-deformation profiles of the bullets Moynihan et al. noted that with increasing ceramic thickness, the SiC-B plates cause severe damage to the bullet core with pronounced erosion and fracture, leading to a rapid decrease in penetration depth. For the case of the 3.75-mm thick plate, the recovered bullets were characterised as having body fractured [Fig. 9.40(d)]. This was not replicated accurately in the above models, the authors thus elected to use the SiC parameters from case (3) combined with a new data set for the bullet core, shown in Table 9.8.

The results of the DOP simulation show far greater material erosion (Fig. 9.41) in the bullet core, in line with the experimentally observed fracture seen in Fig. 9.40. The DOP measurements show a steep reduction of the depth from 22 mm for case (3) to 10.64 mm in the new case with the updated bullet core data. This case study highlights the importance of identifying the model's sensitivities and identifying the largest

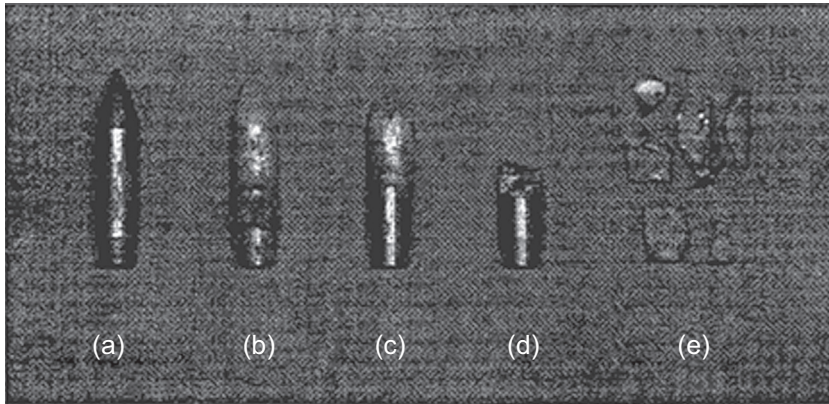


Figure 9.40 Bullet deformation post impact.

Moynihan, T.J., Chou, S.-C., Mihalcin, A.L., 2000. Application of the Depth-of-Penetration Test Methodology to Characterize Ceramics for Personnel Protection. Army Research Lab, Aberdeen Proving Ground, MD.

Table 9.8 J–C data for bullet core

		Bullet core
Strain-hardening parameters	A (GPa)	2.79
	B (GPa)	0.211
	n	0.065
Strain-rate hardening	C	0.005
Reference strain rate	$\dot{\epsilon}_0$ (s ⁻¹)	1.00E-04
Thermal softening parameter	m	1.17
Melting temperature	T_m (K)	1800
Specific heat	C_p (J/kg K)	452
J–C fracture	D_1	0.4
	$D_2 = D_3 = D_4 = D_5$	0

sources of variations, ultimately for the analysis of ceramic armour where the bullet defeat is through material erosion, greater emphasis must be placed on more accurate characterisation of the threat.

9.7.2.3 Worked Example #3: soft fabric armour

This numerical case study seeks to identify the variations of fabric response to a 7.62 mm NATO ball, treated as a rigid body, and a deformable 9 mm handgun bullet. Two models with a single layer of plain weave Kelvar tows are initially used with

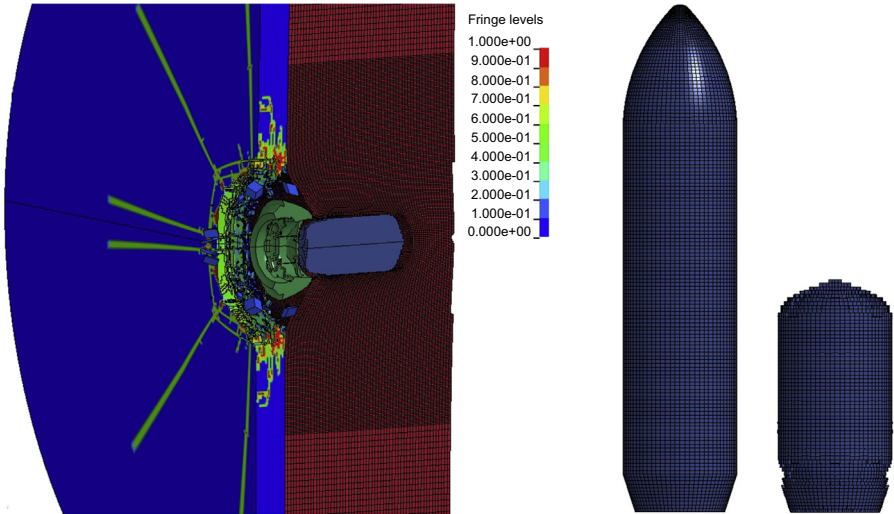


Figure 9.41 Simulation results with updated bullet core data showing the scalar damage and the bullet erosion at the conclusion of the simulation.

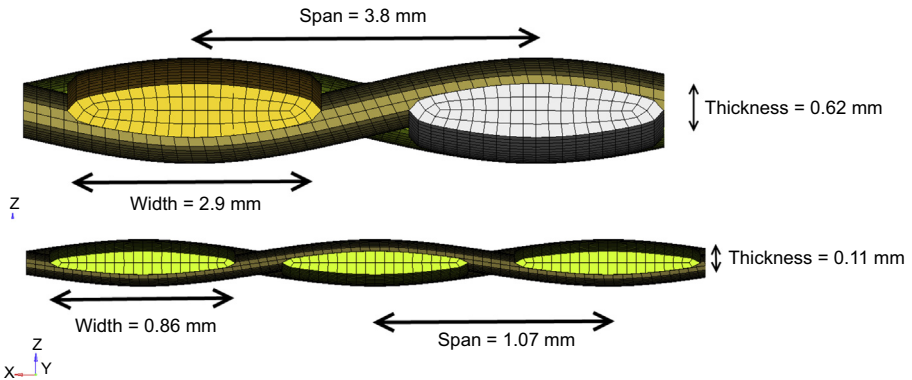


Figure 9.42 Dimensions of the single-layer fabric yarn simulation with element discretisation.

bullet velocities of 150 m/s. The geometries are shown in Fig. 9.42. A second model setup involves a four-layered configuration of the larger weave with a 9 mm bullet with velocities of 250 and 150 m/s to observe the response of multilayered configurations. The models are constructed using a representative volume approach and then replicated to a size equal to 20 times the diameter of the KE impactors.

The fabrics are modelled using 3-D solid elements to discretise the yarn bundles. The element formulations chosen should ideally capture yarn bending, uncrimping, eroding and contact, as well as frictional sliding. Furthermore, the anisotropy of the fabric bundles can be implemented using anisotropic material models. The work by Nilakantan et al. (2010a) provides the orthotropic material data for Kelvar (see Table 9.9) and is used herein with an orthotropic elastic material model in

Table 9.9 Material data for Kelvar

Material data	Warp yarns	Fill yarns
E_{xx}	62 GPa	620 MPa
E_{yy}	620 MPa	62 GPa
E_{zz}	620 MPa	620 MPa
G	3.28 GPa	3.28 GPa
$\sigma_{failure}$	3.4 GPa	3.4 GPa

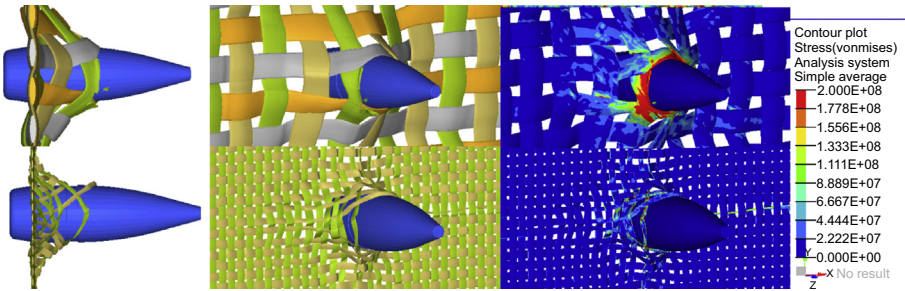


Figure 9.43 Response of a single-layer, plain weave, dry fabric configuration with the stress development.

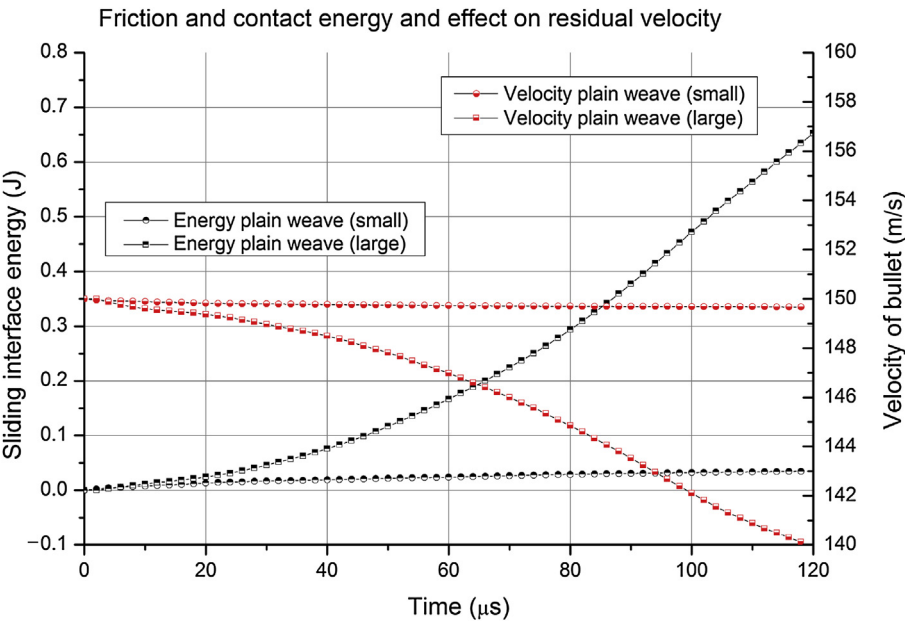


Figure 9.44 Kevlar fibre simulation results for interface energy and residual velocity.

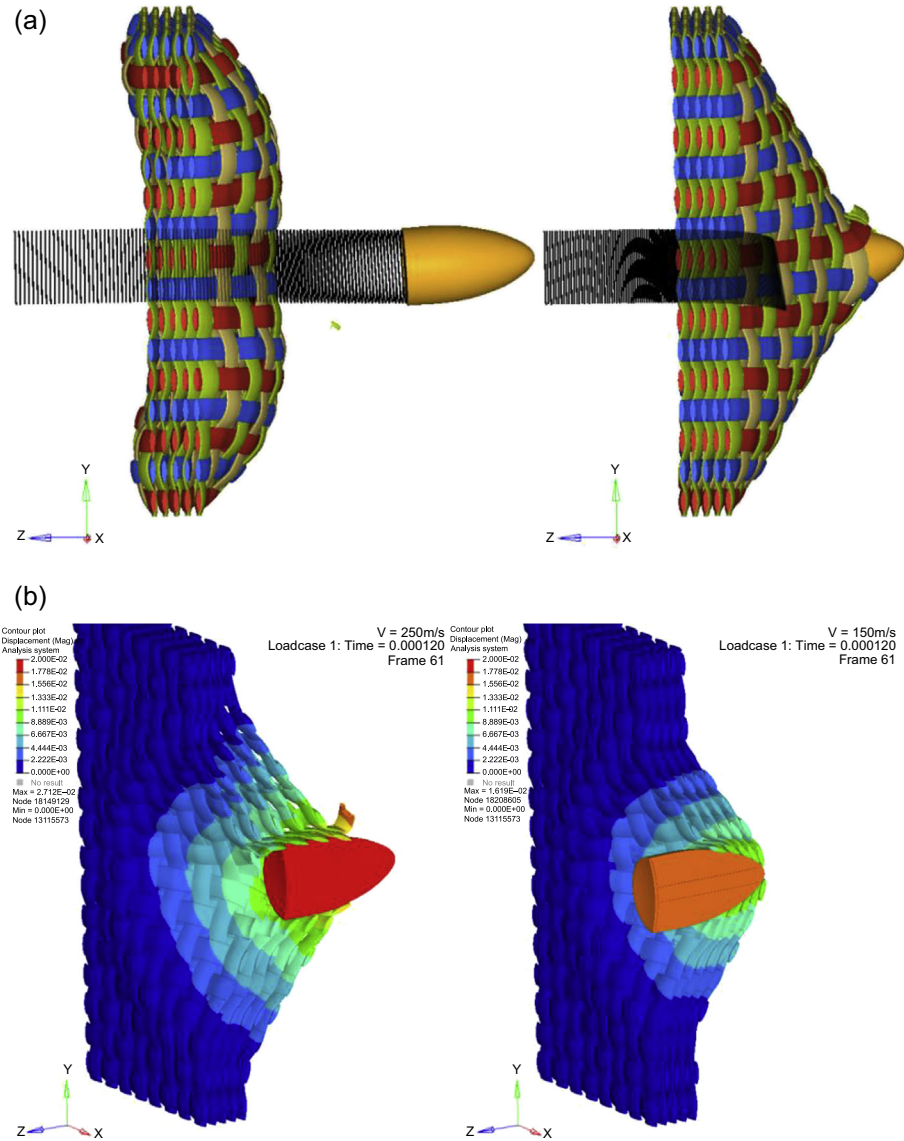


Figure 9.45 Response of a four-ply, plain weave Kevlar fabric to two velocities ($L = 250$ m/s, $R = 150$ m/s): (a) deformed shape at the end of the simulation, (b) displacement at $t = 120 \mu\text{s}$ and (c) von-Mises stress contours at $t = 120 \mu\text{s}$.

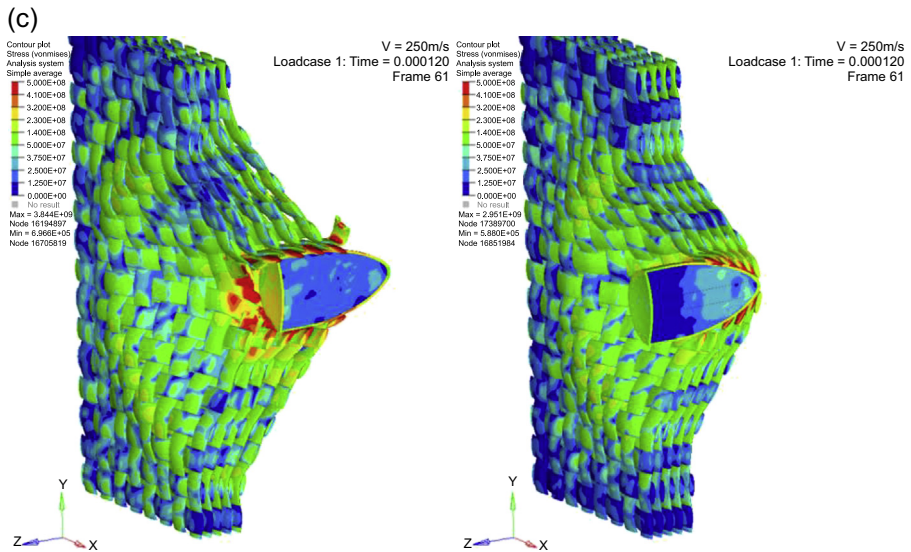


Figure 9.45 Continued

LS-DYNA and erosion criteria based upon the principal stress at failure, provided by the same study.

Analysis of the sliding interface energy in the first model, which accounts for the contact energy and the frictional energy, shows that the larger surface area present in the large 2-D weave model, and prolonged contact, demonstratively reduces the residual velocity, when compared to the small plain weave configuration by way of increased frictional dissipation and strain energy gain in the fabric (see [Figs 9.43 and 9.44](#)).

Simulation of the multilayered configurations provides greater capacity for energy absorption through interlayer interaction. The impact event in the second set of simulations ([Fig. 9.45](#)) can be subdivided into three stages. The primary contact induces longitudinal compressive and shear stress waves that travel along the thickness direction. The fibre bundles undergo compression directly below the projectile. The elongation of the fibres in stage two produces tension along the in-plane direction in the surrounding region. In stage three, the bundles begin to fail under tension as the induced strains and stresses exceed the corresponding failure thresholds. During this stage, there is in-plane friction between the warp and fill yarns.

The multilayered simulation is characterised by a mismatched deceleration profile for the core and the jacket with the stress propagation, temporal variation in bullet fibre contact and the eroding fibres, all of which contribute to a fluctuating profile. Both simulations show a pyramidal deformation profile with a strong ripple, apparent on contact, propagating through the layers. There is evidence of spatial separation of the layers upon full penetration through layer recoil, as in

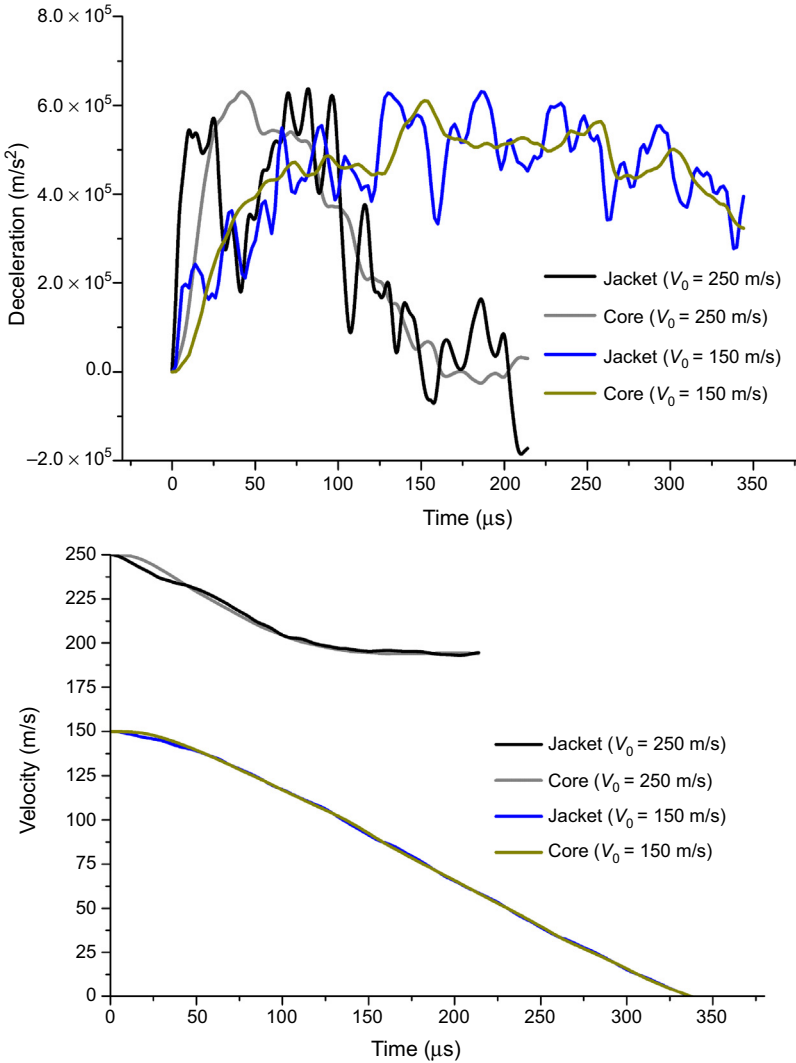


Figure 9.46 Kevlar fibre simulation results for deceleration and residual velocity.

Case 1 at 250 m/s. In the second case the bullet protrudes through the more tightly packed fibre layers but is effectively stopped as shown in the velocity profile in Fig. 9.46.

Recent and similar studies by Yang et al. (2015a) have shown that for multilayer fabrics, the ballistic resistance performances are less influenced by the weaving architecture. Their single-layer study looked at the plain, 2/2 basket, 2/2 twill and four-harness satin weaves and the energy absorption was found to be greatest for plain weave and lowest for the twill weave (Fig. 9.47). In the five-layered study

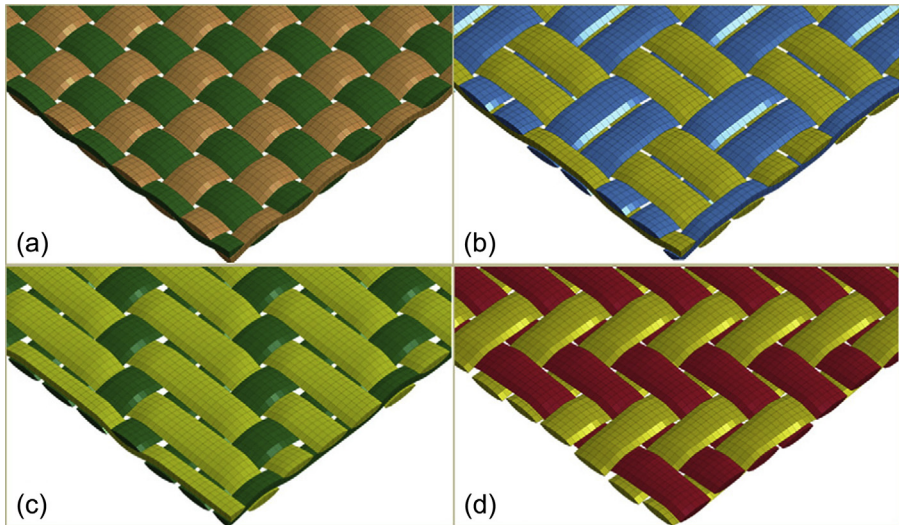


Figure 9.47 Geometry of (a) plain, (b) 2/2 basket, (c) four-harness satin, (d) 2/2 twill weave models (Yang et al., 2015a).

they found less variance in performance due to the diminishing gaps between the yarns. The use of multilayer fabrics was found to smear out the individual characteristics of the weaving architecture, in its place the interlayer behaviour becomes more pronounced.

The work of Yang et al. (2015b) and Tran et al. (2013) identified two main common impact resistance mechanisms: energy absorption through deformation and energy dissipation through frictional energy dissipation, they also observed the process of yarn breaking precipitating from transverse shear loading, which can only be captured accurately using mesoscale model with solid elements, hence the large computational penalty associated with fabric simulations. The simulation of the 2/2 basket in (Tran et al., 2013) weave demonstrated similar ballistic resistance compared to the knitted fabrics but provided greater flexibility compared to the more rigid plain weave fibres. Surprisingly they found the kinetic energy components did not contribute greatly to the energy dissipation, rather it was the strain and friction energy that provided the bulk of the energy dissipation.

In this small worked example, it can be appreciated that during a ballistic impact event against soft armour packs, the impact energy is dissipated through a number of mechanisms: (1) strain energy gained by the fabric; (2) kinetic energy of the fabric yarns and (3) frictional dissipation due to sliding. However, what is not apparent in these simulations is the deformation of the 9 mm HG bullet, which accounts for much of the impact energy absorption in real impacts. For this to be achieved in a numerical simulation, 20–30 plies of fabric would be required (see Chapter 6) which is currently beyond the computing power available to the authors. Hopefully in 5–10 years time, such detailed simulations will be possible.

9.7.2.4 Worked Example #4: modelling of metallic appliqué armour (Lagrangian and SPH)

In this worked example an initial analysis of the 7.62 mm NATO ball against a high-hardness steel plate is carried out using Lagrangian methods in LS-DYNA as per [Børvik et al. \(2009\)](#). The simulation is then modified to use the SPH method to highlight the strength of the formulation for the same problem. The study is based on the analysis of a single 6-mm Weldox 500E plate ([Børvik et al., 2009](#)) using a modified Johnson–Cook strength model ([Børvik et al., 2001](#)), which assumes the EOS can be, by default, described using the bulk modulus and is not explicitly input by the user in contrast to the original Johnson–Cook model which requires a user-input EOS. The modified Johnson–Cook material parameters and the Cockcroft–Latham fracture criteria for the Weldox 500E steel are shown in [Table 9.10](#).

The numerical model for the 7.62 mm NATO ball projectile was based upon the geometry provided by THALES, Land Systems, Australia. The increased detail, such as the position of the cannellure and the fillet radii around the bullet, ensures greater accuracy of the projectile mass, and might have captured geometric sites where failure instabilities of the bullet may arise. Though this comes at a considerable computational cost and such details were discarded where appropriate.

Major attributes of this model centred on the lead bullet core and an eroding surface-to-surface penalty method was used with segment-based contact. The large deformations encountered in the lead bullet led to a number of segment contact violations; hence the contact algorithm was changed from the previous simulation, in

Table 9.10 J–C strength model parameters for WELDOX 500E

		WELDOX 500E
Strain hardening parameters	A (MPa)	605
	B (MPa)	409
	n	0.5
Strain-rate hardening	C	0.0166
Reference strain rate	$\dot{\epsilon}_0$ (s ⁻¹)	5.00E-04
Thermal softening parameter	m	1
Melting temperature	T_m (K)	1800
Specific heat	C_p (J/kg K)	452
Expansion coefficient	α (K ⁻¹)	1.20E-05
Taylor–Quinney coefficient	χ	0.9
Reference temperature	T_R (K)	298
Cockcroft–Latham fracture criteria	W_{cr} (MPa)	1516

Worked Example #1, to better account for the master and slave contact surfaces. The segment-based contact is beneficial as it is stable for materials with varied stiffness and mesh densities.

Published data for lead-antimony derived from Børvik et al. (2009) were a best-fit estimate derived by Børvik. This strength estimate did not influence the APM2 simulation markedly due to the comparatively low volume of lead in the bullet. Conversely, the 7.62 mm NATO ball is comprised largely of the lead antimony and this was of greater concern. Because of this, an SPH simulation was set up for the lead with an elastic–plastic material model and a shock EOS. The SPH formulation did not contain an erosion criterion but accounts for fluid-like material behaviour where inertial effects are of greater concern. The SPH form IFORM = 2 were implemented in LS-DYNA for comparison.

The 7.62 mm NATO ball full 3-D model was evaluated against a single 6-mm plate. Of note was a discrepancy between the perforation event between the 7.62 mm NATO ball and the 7.62 mm APM2. In the Lagrangian formulation the NATO ball is characterised by non-distinct modes of failure. The severe erosion, while nonrealistic, exhibited moderate effects on the residual velocity calculation as shown in Fig. 9.48(b), as the nodal masses continue to participate in the simulation. For velocities below the ballistic limit the core's erosion is severe but the model accurately calculates the nonperforation events. At higher velocities the erosion of the bullet is still apparent but the perforation is modelled correctly with a reasonable prediction of the residual velocity. The author would like to stress that whilst the elements are eroded the nodes continue to take part in the simulation to ensure conservation of the kinetic energy.

Predictably the stripping of the bullet jacket is apparent in these simulations but a great deal of material is imparted backwards upon collision. These observations were also noted in the published literature.

The published benchmarking study (Børvik et al., 2009) attempted to carry out a Lagrangian simulation of the 2D 7.62 mm NATO ball. They noted that complete erosion occurred and the results were not feasible. The current full 3-D model, while lengthy in its run time, can predict the perforation events in a reasonable manner with limited erosion. Ductile hole growth was seen in the early stages of the perforation but this transitioned into a bulk fracture bending of the steel. The behaviour of the lead core ceased to act like an ogival-nosed projectile with the ongoing erosion, rather a highly deformed lumped mass was ejected after perforation, exhibiting severe fragmentation and dispersal as seen in Fig. 9.48. The WELDOX 500 exhibits high ductility and underwent greater plastic deformation prior to failure, the resultant V_i - V_r diagram for the bullet can be seen in Fig. 9.48(b).

There are a number of SPH particle approximation theories present within LS-DYNA and their application to the momentum equation is shown below:

$$\frac{Dv_i^\alpha}{Dt} = - \sum_{j=1}^N m_j \left(\frac{\sigma_i}{\rho_i^2} A_{ij} - \frac{\sigma_j}{\rho_j^2} A_{ij} \right) \quad \text{IFORM} = 0 \text{ (the default option)}$$

7.62 mm ball, F4 ANSTO (08/04/2010) wel
time = 7.0644e-005

7.62 mm ball, F4 ANSTO (08/04/2010) wel
time = 7.0644e-005

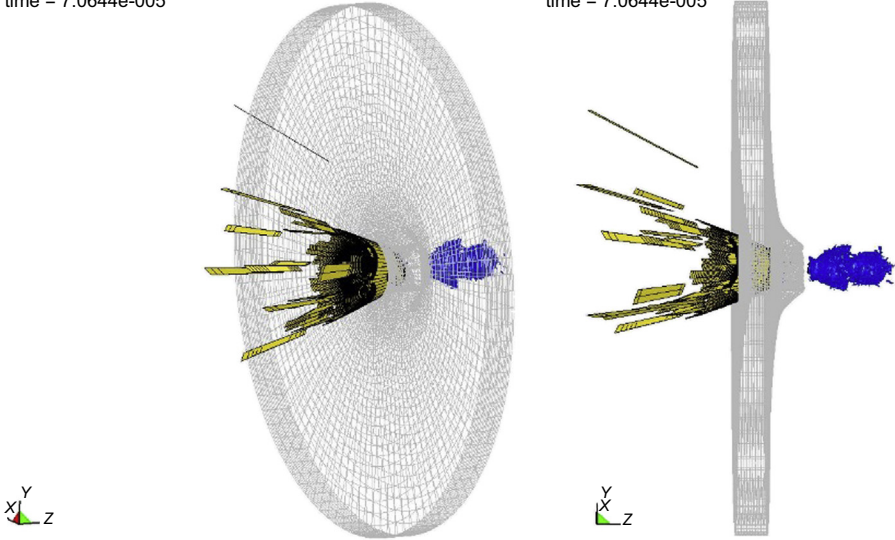


Figure 9.48 (a) Lagrangian simulation of 7.62 mm NATO ball against Weldox 500 plate (b) V_i - V_r plot for the Lagrangian simulation. .

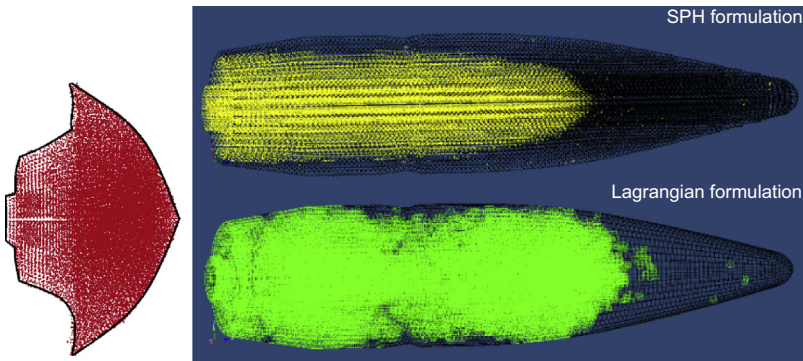
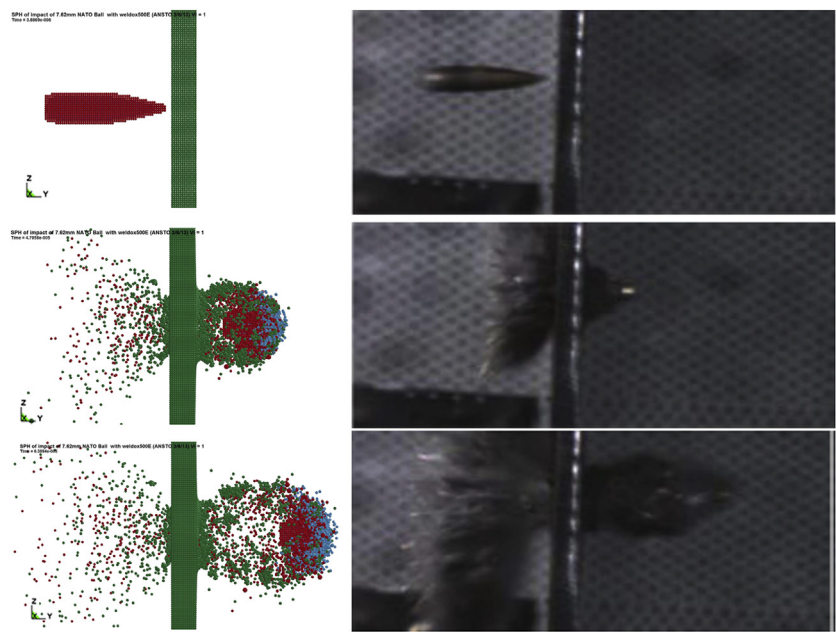


Figure 9.49 Evaluation of uneroded elements and comparison to the SPH elements remaining intact.

$$\frac{Dv_i^\alpha}{Dt} = - \sum_{j=1}^N m_j \left(\frac{\sigma_i^{\alpha\beta}}{\rho_i^2} + \frac{\sigma_j^{\alpha\beta}}{\rho_j^2} \right) \nabla W_{ij} \quad \text{IFORM} = 2 \quad \text{symmetric formulation}$$

The second form, the symmetric formulation, was found to be the most appropriate as it is mathematically tractable (Liu et al., 2004) and exhibited less tensile



7.62 mm NATO ball velocity plot

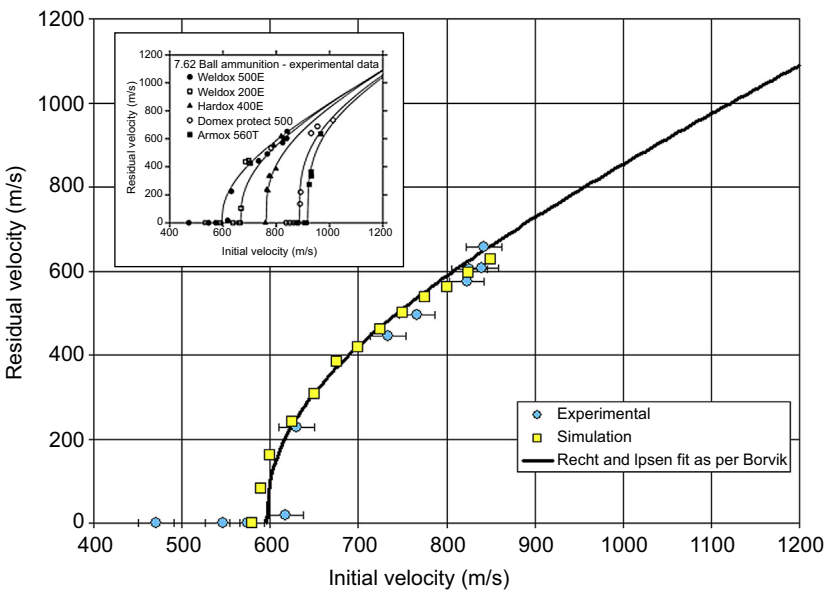


Figure 9.50 Qualitative and quantitative benchmarking of the NATO ball SPH simulation using IFROM = 2.

instabilities compared to the default formulation, $IFORM = 0$. One recognised weakness of the SPH technique is the treatment of boundary elements and the incorrect results precipitating out of the SPH particle approximation method at those boundaries. This is especially true where contact, and by default the interface, between different materials is of concern. The SPH search algorithm within LS-DYNA uses a system analogous to that of the bucket sort algorithms used in the contact card within LS-DYNA, as previously discussed.

The method used to generate the V_i-V_r diagram was to create a set representing the lumped mass of the bullet behind the armour. By averaging the nodal velocities within that mass a more accurate residual velocity can be achieved. Similarities between the uneroded Lagrangian parts and the intact SPH element set (both highlighted in Fig. 9.49) show close agreements in the mass distribution of the bullet. The corrected residual velocities from the SPH simulations are plotted in Fig. 9.50 and compared with the experimental values of Borvik.

The analysis of soft bullet material against steel armour becomes less dependent on the material strength of the bullet and far more dependent on the inertial properties of the projectile. Large distortions associated with these impacts require the use of more robust element formulations. The advantage of the SPH formulation is the ability to model particular parts using this method. The SPH formulation does not exhibit mesh entanglement or the severe distortion characteristic of a Lagrangian mesh. For impacts involving lead-filled rounds, like the M80 and the 9 mm handgun bullets, SPH is the recommended formulation.

Acknowledgements

The authors would like to thank Dr Shannon Ryan of the Defence Science and Technology Group, Australia, for his comprehensive review of this chapter and significant technical direction.

The authors would also like to acknowledge various colleagues whose help, ideas, and problems, provided the impetus for the development of these modelling capabilities: Richard Smith and Dinesh Shanmugam (THALES), Vladimir Luzin, Karl Toppler, Daniel Gleeson, Greg Doherty (ANSTO), James Sandlin (DMTC), Mark Callaghan (University of Manchester formerly at University of Wollongong), Huijun Li (University of Wollongong), Dong Ruan (Swinburne University of Technology), Kaveh Kabir (Macquarie University formerly at UNSW).

References

- Abed, F.H., Voyiadjis, G.Z., 2005. A consistent modified Zerilli-Armstrong flow stress model for BCC and FCC metals for elevated temperatures. *Acta Mechanica* 175, 1–18.
- Alia, A., Souli, M., 2006. High explosive simulation using multi-material formulations. *Applied Thermal Engineering* 26, 1032–1042.
- Anderson Jr., C.E., Bodner, S.R., 1988. Ballistic impact: the status of analytical and numerical modeling. *International Journal of Impact Engineering* 7, 9–35.

- Anderson Jr., C.E., 1987. An overview of the theory of hydrocodes. *International Journal of Impact Engineering* 5, 33–59.
- Andrade, U., Meyers, M.A., Vecchio, K.S., Chokshi, A.H., 1994. Dynamic recrystallization in high-strain, high-strain-rate plastic deformation of copper. *Acta Metallurgica et Materialia* 42, 3183–3195.
- Armstrong, R.W., Zerilli, F.J., 1994. Dislocation mechanics aspects of plastic instability and shear banding. *Mechanics of Materials* 17, 319–327.
- Ashby, M.F., Evans, A.G., Fleck, N.A., Gibson, L.J., Hutchinson, J.W., Wadley, H.N.G., 2000. *Metal Foams: A Design Guide*. Butterworth-Heinemann, Boston, Oxford.
- Ashby, M., 2006. The properties of foams and lattices. *Philosophical Transactions of the Royal Society A* 364, 15–30.
- Banerjee, B., Bhawalkar, A., 2008. An extended mechanical threshold stress plasticity model: modeling 6061-T6 aluminum alloy. *Journal of Mechanics of Materials and Structures* 3, 391–424.
- Banerjee, B., 2005. An Evaluation of Plastic Flow Stress Models for the Simulation of High-temperature and High-strain-rate Deformation of Metals.
- Bao, Y., Wierzbicki, T., 2005. On the cut-off value of negative triaxiality for fracture. *Engineering Fracture Mechanics* 72, 1049–1069.
- Bart-Smith, H., Bastawros, A.F., Mumm, D.R., Evans, A.G., Sypeck, D.J., Wadley, H.N.G., 1998. Compressive deformation and yielding mechanisms in cellular Al alloys determined using X-ray tomography and surface strain mapping. *Acta Materialia* 46, 3583–3592.
- Benson, D.J., 1992. Computational methods in Lagrangian and Eulerian hydrocodes. *Computer Methods in Applied Mechanics and Engineering* 99, 235–394.
- Benz, W., 1990. Smooth particle hydrodynamics: a review. In: Buchler, J.R. (Ed.), *The Numerical Modelling of Nonlinear Stellar Pulsations*. Springer, Netherlands.
- Bonora, N., Gentile, D., Pironi, A., Newaz, G., 2005. Ductile damage evolution under triaxial state of stress: theory and experiments. *International Journal of Plasticity* 21, 981–1007.
- Børvik, T., Hopperstad, O.S., Berstad, T., Langseth, M., 2001. A computational model of viscoplasticity and ductile damage for impact and penetration. *European Journal of Mechanics – A/Solids* 20, 685–712.
- Børvik, T., Hopperstad, O.S., Berstad, T., Langseth, M., 2002. Perforation of 12 mm thick steel plates by 20 mm diameter projectiles with flat, hemispherical and conical noses. Part II: numerical simulations. *International Journal of Impact Engineering* 27, 37–64.
- Børvik, T., Dey, S., Clausen, A.H., 2009. Perforation resistance of five different high-strength steel plates subjected to small-arms projectiles. *International Journal of Impact Engineering* 36, 948–964.
- Boyce, B.L., Dilmore, M.F., 2009. The dynamic tensile behavior of tough, ultrahigh-strength steels at strain-rates from 0.0002 to 200 s^{-1} . *International Journal of Impact Engineering* 36, 263–271.
- Brannon, R., Fossum, A., Strack, E., 2009. *Kayenta: Theory and User's Guide*. Sandia National Laboratories, Albuquerque, NM.
- Brünig, M., Chyra, O., Albrecht, D., Driemeier, L., Alves, M., 2008. A ductile damage criterion at various stress triaxialities. *International Journal of Plasticity* 24, 1731–1755.
- Buchar, J., Voldřich, J., Rold, S., Lisy, J., 2002. Ballistic performance of the dual hardness armour. In: *20th International Symposium on Ballistics* Orlando, FL.
- Burton, W.S., Noor, A.K., 1997. Structural analysis of the adhesive bond in a honeycomb core sandwich panel. *Finite Elements in Analysis and Design* 26, 213–227.

- Campbell, J.D., Ferguson, W.G., 1970. The temperature and strain-rate dependence of the shear strength of mild steel. *Philosophical Magazine* 21, 63–82.
- Chafi, M.S., Karami, G., Ziejewski, M., 2009. Numerical analysis of blast-induced wave propagation using FSI and ALE multi-material formulations. *International Journal of Impact Engineering* 36, 1269–1275.
- Chen, C., Fleck, N.A., 2002. Size effects in the constrained deformation of metallic foams. *Journal of the Mechanics and Physics of Solids* 50, 955–977.
- Chen, S.R., Gray III, G.T., Bingert, S.R., 1996. Mechanical Properties and Constitutive Relations for Tantalum and Tantalum Alloys Under High-Rate Deformation. Material Science and Technology Division, Los Alamos National Laboratory.
- Chen, J.K., Allahdadi, F.A., Sun, C.T., 1997. A quadratic yield function for fiber-reinforced composites. *Journal of Composite Materials* 31, 788–811.
- Chen, X.W., Chen, G., Zhang, F.J., 2008. Deformation and failure modes of soft steel projectiles impacting harder steel targets at increasing velocity. *Experimental Mechanics* 48, 335–354.
- Chocron, S., Figueroa, E., King, N., Kirchdoerfer, T., Nicholls, A.E., Sagebiel, E., Weiss, C., Freitas, C.J., 2010. Modeling and validation of full fabric targets under ballistic impact. *Composites Science and Technology* 70, 2012–2022.
- Clausen, A.H., Børvik, T., Hopperstad, O.S., Benallal, A., 2004. Flow and fracture characteristics of aluminium alloy AA5083–H116 as function of strain rate, temperature and triaxiality. *Materials Science and Engineering: A* 364, 260–272.
- Cockcroft, Latham, D.J., 1968. Ductility and workability of metals. *Journal of the Institute of Metals* 96, 33–39.
- Cronin, D.S., Bui, K., Kaufmann, C., Mcintosh, G., Berstad, T., 2003. Implementation and validation of the Johnson–Holmquist ceramic material model in LS-Dyna. In: 4th European LS-DYNA Users Conference, Ulm, Germany.
- Crouch, I.G., Greaves, L.J., Ruiz, C., Harding, J., 1994. Dynamic compression of toughened epoxy interlayers in adhesively bonded aluminium laminates. *Supplement to Journal de Physique III, Colloque C8 4*, 201–206.
- Crouch, I.G., Appleby-Thomas, G., Hazell, P., 2015. A study of the penetration behaviour of mild-steel-cored ammunition against boron carbide ceramic armours. *International Journal of Impact Engineering* 80, 203–211.
- Crouch, I.G., 2009. Threat-defeating mechanisms in body armour systems. In: Next Generation Body Armour Conference, London, UK, September 2009.
- Dabboussi, W., Nemes, J.A., 2005. Modeling of ductile fracture using the dynamic punch test. *International Journal of Mechanical Sciences* 47, 1282–1299.
- Dannemann, K.A., Lankford, J., 2000. High strain rate compression of closed-cell aluminium foams. *Materials Science and Engineering A* 293, 157–164.
- Daridon, L., Oussouaddi, O., Ahzi, S., 2004. Influence of the material constitutive models on the adiabatic shear band spacing: MTS, power law and Johnson–Cook models. *International Journal of Solids and Structures* 41, 3109–3124.
- Department of Defence, 2008. Structures to Resist the Effects of Accidental Explosions.
- Deshpande, V.S., Fleck, N.A., 2000a. High strain rate compressive behaviour of aluminium alloy foams. *International Journal of Impact Engineering* 24, 277–298.
- Deshpande, V.S., Fleck, N.A., 2000b. Isotropic constitutive models for metallic foams. *Journal of the Mechanics and Physics of Solids* 48, 1253–1283.

- Dey, S., Børvik, T., Hopperstad, O.S., Leinum, J.R., Langseth, M., 2004. The effect of target strength on the perforation of steel plates using three different projectile nose shapes. *International Journal of Impact Engineering* 30, 1005–1038.
- Dey, S., Børvik, T., Hopperstad, O.S., Langseth, M., 2006. On the influence of fracture criterion in projectile impact of steel plates. *Computational Materials Science* 38, 176–191.
- Dieter, G.E., 1984. *Mechanical Metallurgy*. McGraw-Hill, Japan.
- Dobratz, B.M., 1981. *LLNL Explosives Handbook: Properties of Chemical Explosives and Explosives and Explosive Simulants*.
- Doj, U., 2008. *Ballistic Resistance of Body Armor*. NIJ Standard-0101.06. National Institute of Justice, USA.
- Dunne, F., Petrinic, N., 2005. *Introduction to Computational Plasticity*. Oxford University Press, USA.
- Fleck, N.A., Deshpande, V.S., 2004. The resistance of clamped sandwich beams to shock loading. *Journal of Applied Mechanics* 71, 386–401.
- Flores-Johnson, E.A., Saleh, M., Edwards, L., 2011. Ballistic performance of multi-layered metallic plates impacted by a 7.62-mm APM2 projectile. *International Journal of Impact Engineering* 38, 1022–1032.
- Follansbee, P.S., Gray, G.T., 1989. An analysis of the low temperature, low and high strain-rate deformation of Ti–6Al–4V. *Metallurgical Transactions A* 20, 863–874.
- Follansbee, P.S., Kocks, U.F., 1988. A constitutive description of the deformation of copper based on the use of the mechanical threshold stress as an internal state variable. *Acta Metallurgica* 36, 81–93.
- Franz, R., Robitaille, J.L., 1979. The Hugoniot of 4340 Steel RC 54-55. US Army Armament Research And Development Command (Ballistic Research Laboratory).
- Fuller, T.J., Dewers, T.A., Swan, M.S., 2013. Development and Deployment of Constitutive Softening Routines in Eulerian Hydrocodes.
- Gibson, L.J., Ashby, M.F., 1999. *Cellular Solids: Structure and Properties*. Cambridge University Press.
- Gibson, L.J., Kelly, A., Carl, Z., 2000. Properties and applications of metallic foams. In: *Comprehensive Composite Materials*. Pergamon, Oxford.
- Gingold, R.A., Monaghan, J.J., 1977. Smoothed particle hydrodynamics: theory and application to non-spherical stars. *Monthly Notices of the Royal Astronomical Society* 181, 375.
- Gray III, G.T., Chen, S.R., Wright, W., Lopez, M.F., 1994. *Constitutive Equations for Annealed Metals Under Compression at High Strain Rates and High Temperatures*. Los Alamos National Laboratory.
- Grujicic, M., Arakere, G., He, T., Bell, W.C., Cheeseman, B.A., Yen, C.F., Scott, B., 2008a. A ballistic material model for cross-plyed unidirectional ultra-high molecular-weight polyethylene fiber-reinforced armor-grade composites. *Materials Science and Engineering A* 498, 231–241.
- Grujicic, M., Bell, W.C., He, T., Cheeseman, B.A., 2008b. Development and verification of a meso-scale based dynamic material model for plain-woven single-ply ballistic fabric. *Journal of Materials Science* 43, 6301–6323.
- Grujicic, M., Arakere, G., He, T., Bell, W.C., Glomski, P.S., Cheeseman, B.A., 2009a. Multi-scale ballistic material modeling of cross-plyed compliant composites. *Composites Part B: Engineering* 40, 468–482.

- Grujicic, M., Bell, W.C., Arakere, G., He, T., Cheeseman, B.A., 2009b. A meso-scale unit-cell based material model for the single-ply flexible-fabric armor. *Materials and Design* 30, 3690–3704.
- Grujicic, M., He, T., Marvi, H., Cheeseman, B.A., Yen, C.F., 2010. A comparative investigation of the use of laminate-level meso-scale and fracture-mechanics-enriched meso-scale composite-material models in ballistic-resistance analyses. *Journal of Materials Science* 45, 3136–3150.
- Grujicic, M., Bell, W., Glomski, P., Pandurangan, B., Yen, C.F., Cheeseman, B., 2011. Filament-level modeling of aramid-based high-performance structural materials. *Journal of Materials Engineering and Performance* 20, 1401–1413.
- Hall, I.W., Guden, M., Yu, C.J., 2000. Crushing of aluminum closed cell foams: density and strain rate effects. *Scripta Materialia* 43, 515–521.
- Hanssen, A.G., Hopperstad, O.S., Langseth, M., Ilstad, H., 2002. Validation of constitutive models applicable to aluminium foams. *International Journal of Mechanical Sciences* 44, 359–406.
- He, A., Xie, G., Zhang, H., Wang, X., 2014. A modified Zerilli–Armstrong constitutive model to predict hot deformation behavior of 20CrMo alloy steel. *Materials and Design* 56, 122–127.
- Hoge, K.G., Mukherjee, A.K., 1977. The temperature and strain rate dependence of the flow stress of tantalum. *Journal of Materials Science* 12, 1666–1672.
- Holian, K.S., 1984. T-4 Handbook of Material Properties Data Bases Vol. Ic: Equations of State. Los Alamos National Laboratory, USA.
- Holmquist, T.J., Johnson, G.R., 1991. Determination of constants and comparison of results for various constitutive models. *Journal of Physics IV France* 01, C3-C853-C3-860.
- Holmquist, T.J., Johnson, G.R., 2008. The failed strength of ceramics subjected to high-velocity impact. *Journal of Applied Physics* 104, 013533.
- Hopperstad, O.S., Børvik, T., Langseth, M., Labibes, K., Albertini, C., 2003. On the influence of stress triaxiality and strain rate on the behaviour of a structural steel. Part I. Experiments. *European Journal of Mechanics – A/Solids* 22, 1–13.
- Hou, Y., Jiang, L., Sun, B., Gu, B., 2013. Strain rate effects of tensile behaviors of 3-D orthogonal woven fabric: experimental and finite element analyses. *Textile Research Journal* 83, 337–354.
- Howell, P., Kozyreff, G., Ockendon, J., 2009. *Applied Solid Mechanics*. Cambridge University Press.
- Hughes, T.J.R., Liu, W.K., Zimmermann, T.K., 1981. Lagrangian-Eulerian finite element formulation for incompressible viscous flows. *Computer Methods in Applied Mechanics and Engineering* 29, 329–349.
- Jeon, I., Asahina, T., Kang, K.-J., Im, S., Lu, T.J., 2010. Finite element simulation of the plastic collapse of closed-cell aluminum foams with X-ray computed tomography. *Mechanics of Materials* 42, 227–236.
- Johnson, W.E., Anderson Jr., C.E., 1987. History and application of hydrocodes in hypervelocity impact. *International Journal of Impact Engineering* 5, 423–439.
- Johnson, G.R., Cook, W.H., 1983. A constitutive model and data for metals subjected to large strains, high strain rates and high temperatures. In: *Proceedings of 7th International Symposium on Ballistics*, The Netherlands, pp. 541–547.
- Johnson, G.R., Cook, W.H., 1985. Fracture characteristics of three metals subjected to various strains, strain rates, temperatures and pressures. *Engineering Fracture Mechanics* 21, 31–48.

- Johnson, G.R., Holmquist, T.J.A., 1992. Computational constitutive model for brittle materials subjected to large strains, high strain rates, and high pressures. In: Meyers, M.A., Murr, L.E., Staudhammer, K.P. (Eds.), *Shock Waves and High-Strain Rate Phenomena in Materials*. Marcel Decker, pp. 1070–1077.
- Johnson, G.R., Holmquist, T.J., 1994. An improved computational constitutive model for brittle materials. *AIP Conference Proceedings* 309, 981–984.
- Johnson, G.R., Holmquist, T.J., Beissel, S.R., 2003. Response of aluminum nitride (including a phase change) to large strains, high strain rates, and high pressures. *Journal of Applied Physics* 94, 1639–1646.
- Johnson, J.D.E., 1994. The SESAME Database. Los Alamos National Laboratory.
- Johnson, G.R., 2011. Numerical algorithms and material models for high-velocity impact computations. *International Journal of Impact Engineering* 38, 456–472.
- Jones, N., 1989. *Structural Impact*. Cambridge University Press.
- Kapoor, R., Nemat-Nasser, S., 2000. Comparison between high and low strain-rate deformation of tantalum. *Metallurgical and Materials Transactions A* 31, 815–823.
- Kerley, G., 1993. Multiphase Equation of State for Iron. Sandia National Laboratories.
- Khoshnavan, M.R., Najafi Pour, M., 2014. Numerical and experimental analyses of the effect of different geometrical modelings on predicting compressive strength of honeycomb core. *Thin-Walled Structures* 84, 423–431.
- Kingery, C.N., Bulmash, G., U.S. Army Ballistic Research Laboratory, 1984. Air Blast Parameters from TNT Spherical Air Burst and Hemispherical Surface Burst. Ballistic Research Laboratories, Aberdeen Proving Ground, MD.
- Klepaczko, J.R., Rusinek, A., Rodríguez-Martínez, J.A., Pecherski, R.B., Arias, A., 2009. Modelling of thermo-viscoplastic behaviour of DH-36 and Weldox 460-E structural steels at wide ranges of strain rates and temperatures, comparison of constitutive relations for impact problems. *Mechanics of Materials* 41, 599–621.
- Lamberts, A.P.T.M.J., 2007. Numerical Simulation of Ballistic Impacts on Ceramic Material (Masters thesis). Eindhoven University of Technology.
- Lässig, T., Nguyen, L., May, M., Riedel, W., Heisserer, U., Van der Werff, H., Hiermaier, S., 2015. A non-linear orthotropic hydrocode model for ultra-high molecular weight polyethylene in impact simulations. *International Journal of Impact Engineering* 75, 110–122.
- Last, H.R., Garrett, R.K., Rajendran, A.M., 1996. A comparative study of high strain rate behavior of three martensitic steels. *AIP Conference Proceedings* 370, 631–634.
- Leavy, R.B., Brannon, R.M., Strack, O.E., 2010. The use of sphere indentation experiments to characterize ceramic damage models. *International Journal of Applied Ceramic Technology* 7, 606–615.
- Lee, W.-S., Yeh, G.-W., 1997. The plastic deformation behaviour of AISI 4340 alloy steel subjected to high temperature and high strain rate loading conditions. *Journal of Materials Processing Technology* 71, 224–234.
- Lee, E., Finger, M., Collins, W., 1973. JWL Equation of State Coefficients for High Explosives. Lawrence Livermore Laboratory.
- Lefebvre, L.P., Banhart, J., Dunand, D.C., 2008. Porous metals and metallic foams: current status and recent developments. *Advanced Engineering Materials* 10, 775–787.
- Lemaitre, J., Desmorat, R., 2005. *Engineering Damage Mechanics: Ductile, Creep, Fatigue and Brittle Failures*. Springer-Verlag, Netherlands.
- Leuser, D., 1999. Experimental Investigations of Material Models for Ti-6Al-4V and 2024-T3. Lawrence Livermore National Laboratory.

- Li, X., Zhang, P., Wang, Z., Wu, G., Zhao, L., 2014. Dynamic behavior of aluminum honeycomb sandwich panels under air blast: experiment and numerical analysis. *Composite Structures* 108, 1001–1008.
- Liang, R., Khan, A.S., 1999. A critical review of experimental results and constitutive models for BCC and FCC metals over a wide range of strain rates and temperatures. *International Journal of Plasticity* 15, 963–980.
- Lin, Y.C., Chen, X.-M., 2011. A critical review of experimental results and constitutive descriptions for metals and alloys in hot working. *Materials & Design* 32, 1733–1759.
- Liu, G.R., Liu, M.B., Li, S., 2004. Smoothed particle hydrodynamics — a meshfree method. *Computational Mechanics* 33, 491.
- Liu, Y.D., Yu, J.L., Zheng, Z.J., Li, J.R., 2009. A numerical study on the rate sensitivity of cellular metals. *International Journal of Solids and Structures* 46, 3988–3998.
- Lucey, L.B., 1977. A numerical approach to the testing of the fission hypothesis. *Astronomical Journal* 82, 1013–1024.
- Lyon, S.P., Johnson, J.D.E., 1992. SESAME: The Los Alamos National Laboratory Equation of State Database. Los Alamos National Laboratory.
- Macdougall, D., Harding, J., 1997. Materials testing for constitutive relations. *Journal of Physics IV France* 07, C3-C103–C3-108.
- Mackenzie, A.C., Hancock, J.W., Brown, D.K., 1977. On the influence of state of stress on ductile failure initiation in high strength steels. *Engineering Fracture Mechanics* 9, 167–188.
- Maire, E., Fazekas, A., Salvo, L., Dendievel, R., Youssef, S., Cloetens, P., Letang, J.M., 2003. X-ray tomography applied to the characterization of cellular materials. Related finite element modeling problems. *Composites Science and Technology* 63, 2431–2443.
- Marsh, S.P., 1980. LASL Shock Hugoniot Data (USA).
- Maweja, K., Stumpf, W., 2006. Fracture and ballistic-induced phase transformation in tempered martensitic low-carbon armour steels. *Materials Science and Engineering: A* 432, 158–169.
- Mcintosh, G., 1998. The Johnson-Holmquist Ceramic Model as Used in LS-DYNA2D. Defence Research Establishment Valcartier, QUEBEC.
- Meyer Jr., H.W., Kleponis, D.S., 2001. Modeling the high strain rate behavior of titanium undergoing ballistic impact and penetration. *International Journal of Impact Engineering* 26, 509–521.
- Meyer, J.H.W., 2006. A Modified Zerilli-Armstrong Constitutive Model Describing the Strength and Localizing Behavior of Ti-6Al-4V. Weapons and Materials Research Directorate, ARL.
- Meyers, M.A., Murr, L.E., 1981. *Shock Waves and High-Strain-Rate Phenomena in Metals: Concepts and Applications*. Plenum Press, New York, USA.
- Meyers, M.A., Benson, D.J., Vöhringer, O., Kad, B.K., Xue, Q., Fu, H.H., 2002. Constitutive description of dynamic deformation: physically-based mechanisms. *Materials Science and Engineering: A* 322, 194–216.
- Meyers, M.A., 1994. *Dynamic Behaviour of Materials*. John Wiley & Sons, Inc.
- Miller, R.E., 2000. A continuum plasticity model for the constitutive and indentation behaviour of foamed metals. *International Journal of Mechanical Sciences* 42, 729–754.
- Mirone, G., 2007. Role of stress triaxiality in elastoplastic characterization and ductile failure prediction. *Engineering Fracture Mechanics* 74, 1203–1221.
- Mohotti, D., Ali, M., Ngo, T., Lu, J., Mendis, P., 2014. Strain rate dependent constitutive model for predicting the material behaviour of polyurea under high strain rate tensile loading. *Materials & Design* 53, 830–837.
- Montanini, R., 2005. Measurement of strain rate sensitivity of aluminium foams for energy dissipation. *International Journal of Mechanical Sciences* 47, 26–42.

- Mooney, M., 1940. A theory of large elastic deformation. *Journal of Applied Physics* 11, 582–592.
- Moynihan, T.J., Chou, S.-C., Mihalcin, A.L., 2000. Application of the Depth-of-Penetration Test Methodology to Characterize Ceramics for Personnel Protection. Army Research Lab, Aberdeen Proving Ground, MD.
- Mukai, T., Miyoshi, T., Nakano, S., Somekawa, K. H., 2006. Higashi Compressive response of a closed-cell aluminum foam at high strain rate *Scripta Materialia* 54, 533–537.
- Nguyen, L.H., Lässig, T.R., Ryan, S., Riedel, W., Mouritz, A.P., Orifici, A.C., 2016. A methodology for hydrocode analysis of ultra-high molecular weight polyethylene composite under ballistic impact, *Composites Part A: Applied Science and Manufacturing*, 84, 224–235.
- Nilakantan, G., Gillespie Jr., J.W., 2012. Ballistic impact modeling of woven fabrics considering yarn strength, friction, projectile impact location, and fabric boundary condition effects. *Composite Structures* 94, 3624–3634.
- Nilakantan, G., Keefe, M., Bogetti, T.A., Adkinson, R., Gillespie Jr., J.W., 2010a. On the finite element analysis of woven fabric impact using multiscale modeling techniques. *International Journal of Solids and Structures* 47, 2300–2315.
- Nilakantan, G., Keefe, M., Bogetti, T.A., Gillespie Jr., J.W., 2010b. Multiscale modeling of the impact of textile fabrics based on hybrid element analysis. *International Journal of Impact Engineering* 37, 1056–1071.
- Ogden, R., 1972. Large deformation isotropic elasticity-on the correlation of theory and experiment for incompressible rubberlike solids. *Proceedings of the Royal Society of London A. Mathematical and Physical Sciences* 326, 565–584.
- Orifici, A.C., Herszberg, I., Thomson, R.S., 2008. Review of methodologies for composite material modelling incorporating failure. *Composite Structures* 86, 194–210.
- Orphal, D.L., 2006. Explosions and impacts. *International Journal of Impact Engineering* 33, 496–545.
- Özel, T., Karpat, Y., 2007. Identification of constitutive material model parameters for high-strain rate metal cutting conditions using evolutionary computational algorithms. *Materials and Manufacturing Processes* 22, 659–667.
- Paul, A., Ramamutry, U., 2000. Strain rate sensitivity of a closed-cell aluminum foam *Materials Science and Engineering A* 281, 1–7.
- Randers-Pehrson, G., Bannister, K.A., 1997. Airblast Loading Model for DYNA2D and DYNA3D. Army Research Laboratory.
- Randles, P.W., Libersky, L.D., 1996. Smoothed particle hydrodynamics: some recent improvements and applications. *Computer Methods in Applied Mechanics and Engineering* 139, 375–408.
- Recht, R.F., Ipson, T.W., 1963. Ballistic perforation dynamics. *Journal of Applied Mechanics* 30, 384–390.
- Redenbach, C., Shklyar, I., Andrä, H., 2012. Laguerre tessellations for elastic stiffness simulations of closed foams with strongly varying cell sizes. *International Journal of Engineering Science* 50, 70–78.
- Rivlin, R.S., 1948. Large elastic deformations of isotropic materials. IV. Further developments of the general theory. *Philosophical Transactions of the Royal Society of London A: Mathematical, Physical and Engineering Sciences* 241, 379–397.
- Royce, E.B., 1971. Gray, a Three-Phase Equation of State for Metals. Lawrence Livermore Laboratory.
- SAFIRE™ Transparent Armor Solutions, S.-G.C., http://www.crystals.saint-gobain.com/SAFIRE_Transparent_Armor.aspx.

- Saleh, M., Edwards, L., 2010. Evaluation of a hydrocode in modelling NATO threats against steel armour. In: 25th International Symposium on Ballistics, Beijing, China.
- Saleh, M., Edwards, L., 2011. Application of a soil model in the numerical analysis of landmine interaction with protective structures. In: 26th International Symposium. DEStech Publications, Inc., USA, pp. 265–276.
- Saleh, M., Edwards, L., 2015. Evaluation of soil and fluid structure interaction in blast modelling of the flying plate test. *Computers & Structures* 151, 96–114.
- Saleh, M., Smith, R., Shanmugam, D.K., Edwards, L., 2014. Numerical FE modelling of occupant injury in soil-vehicle blast interaction. In: 28th International Symposium on Ballistics, USA.
- Saleh, M., Luzin, V., Toppler, K., Kabir, K., 2015. Response of thin-skinned sandwich panels to contact loading with flat-ended cylindrical punches: experiments, numerical simulations and neutron diffraction measurements. *Composites Part B: Engineering* 78, 415–430.
- Sasso, M., Newaz, G., Amodio, D., 2008. Material characterization at high strain rate by Hopkinson bar tests and finite element optimization. *Materials Science and Engineering: A* 487, 289–300.
- Scapin, M., Peroni, L., Dallochio, A., Bertarelli, A., 2011. Shock Loads Induced on Metal Structures by LHC Proton Beams: Modelling of Thermo-Mechanical Effects. *Applied Mechanics and Materials* 82, 338–343.
- Scheffler, D.R., Zukas, J.A., 2000. Practical aspects of numerical simulation of dynamic events: material interfaces. *International Journal of Impact Engineering* 24, 821–842.
- Schreyer, H., Zuo, Q., Maji, A., 1994. Anisotropic plasticity model for foams and honeycombs. *Journal of Engineering Mechanics* 120, 1913–1930.
- Schwer, L., 2007. Optional strain-rate forms of the Johnson Cook constitutive model and the role of the parameter ϵ_0 . In: 6th European LS-DYNA Users' Conference, Gothenburg.
- Sieggas, P., Tagarielli, V., Petrinic, N., 2014. Modelling stochastic foam geometries for FE simulations using 3D Voronoi cells. *Procedia Materials Science* 4, 221–226.
- Smith, P.D., Hetherington, J.G., 1994. *Blast and Ballistic Loading of Structures*. Butterworth-Heinemann.
- Sotomayor, O.E., Tippur, H.V., 2014. Role of cell regularity and relative density on elastoplastic compression response of 3-D open-cell foam core sandwich structure generated using Voronoi diagrams. *Acta Materialia* 78, 301–313.
- Souers, P.C., Wu, B., Haselman, L.C.J., 1996. Detonation Equation of State at LLNL, 1995. Revision 3. Other Information: PBD: 1 Feb 1996.
- Souli, M., Ouahsine, A., Lewin, L., 2000. ALE formulation for fluid–structure interaction problems. *Computer Methods in Applied Mechanics and Engineering* 190, 659–675.
- Steinberg, D.J., Lund, C.M., 1989. A constitutive model for strain rates from 10^{-4} to 10^6 s^{-1} . *Journal of Applied Physics* 65, 1528–1533.
- Steinberg, D.J., Cochran, S.G., Guinan, M.W., 1980. A constitutive model for metals applicable at high-strain rate. *Journal of Applied Physics* 51, 1498–1504.
- Steinberg, D.J., 1996. *Equation of State and Strength Properties of Selected Materials*. Lawrence Livermore National Laboratory.
- Swegle, J.W., Attaway, S.W., Heinstein, M.W., Mello, F.J., Hicks, D.L., 1994. *An Analysis of Smoothed Particle Hydrodynamics* (Sandia Report).
- Tabiei, A., Ivanov, I., 2001. Computational micro-mechanical model of composite flexible woven fabric with fiber reorientation. In: 2001 ASME International Mechanical Engineering Congress and Exposition, November 11, 2001–November 16, 2001. American Society of Mechanical Engineers, New York, NY, United States, pp. 333–350.

- Tabiei, A., Nilakantan, G., 2008. Ballistic impact of dry woven fabric composites: a review. *Applied Mechanics Reviews* 61, 0108011–01080113.
- Teng, X., Wierzbicki, T., 2006. Evaluation of six fracture models in high velocity perforation. *Engineering Fracture Mechanics* 73, 1653–1678.
- Tran, P., Ngo, T., Yang, E., Mendis, P., Humphries, W., 2013. Effects of architecture on ballistic resistance of textile fabrics: numerical study. *International Journal of Damage Mechanics* 23 (3), 359–376.
- Trana, E., Zecheru, T., Bugaru, M., Chereches, T., 2007. Johnson-Cook constitutive model for OL 37 steel. In: 6th WSEAS International Conference on System Science and Simulation in Engineering, Venice, Italy.
- Tresvyatskii, S.G., 1971. Dependence of the yield stress of metals on grain size. *Strength of Materials* 11, 1320–1323.
- US Army, 1986. Fundamentals of Protective Design for Conventional Weapons. US Army Waterways Experimental Station.
- Wejrzanowski, T., Skibinski, J., Szumbariski, J., Kurzydowski, K.J., 2013. Structure of foams modeled by Laguerre–Voronoi tessellations. *Computational Materials Science* 67, 216–221.
- Whirley, R.G., Engelmann, B.E., 1993. DYNA3D: A Nonlinear, Explicit, Three-dimensional Finite Element Code for Solid and Structural Mechanics User Manual.
- Wicklein, M., Ryan, S., White, D.M., Clegg, R.A., 2008. Hypervelocity impact on CFRP: testing, material modelling, and numerical simulation. *International Journal of Impact Engineering* 35, 1861–1869.
- Xu, S., Ruan, D., Lu, G., 2014. Strength enhancement of aluminium foams and honeycombs by entrapped air under dynamic loadings. *International Journal of Impact Engineering* 74, 120–125.
- Yang, C.-C., Ngo, T., Tran, P., 2015a. Influences of weaving architectures on the impact resistance of multi-layer fabrics. *Materials & Design* 85, 282–295.
- Yang, E., Ngo, T., Ruan, D., Tran, P., 2015b. Impact resistance and failure analysis of plain woven curtains. *International Journal of Protective Structures* 6, 113–136.
- Youssef, S., Maire, E., Gaertner, R., 2005. Finite element modelling of the actual structure of cellular materials determined by X-ray tomography. *Acta Materialia* 53, 719–730.
- Zerilli, F.J., Armstrong, R.W., 1987. Dislocation-mechanics-based constitutive relations for material dynamics calculations. *Journal of Applied Physics* 61, 1816–1825.
- Zerilli, F.J., Armstrong, R.W., 1990. Description of tantalum deformation behavior by dislocation mechanics based constitutive relations. *Journal of Applied Physics* 68, 1580–1591.
- Zerilli, F.J., Armstrong, R.W., 1996. Constitutive relations for titanium and Ti-6Al-4V. *AIP Conference Proceedings* 370, 315–318.
- Zhao, H., Elnasri, I., Abdennadher, S., 2005. An experimental study on the behaviour under impact loading of metallic cellular materials. *International Journal of Mechanical Sciences* 47, 757–774.
- Zhu, F., Zhao, L., Lu, G., Gad, E., 2009. A numerical simulation of the blast impact of square metallic sandwich panels. *International Journal of Impact Engineering* 36, 687–699.
- Zienkiewicz, O.C., Taylor, R.L., Zgue, J.Z., 2005. *The Finite Element Method Set*, sixth ed. Butterworth-Heinemann, Oxford.
- Zocher, M.A., Maudlin, P.J., 2000. An Evaluation of Several Hardening Models Using Taylor Cylinder Impact Data.

Zukas, J.A., Scheffler, D.R., 2000. Practical aspects of numerical simulations of dynamic events: effects of meshing. *International Journal of Impact Engineering* 24, 925–945.

Zukas, J.A., Walters, W.P., 1998. *Explosive Effects and Applications*. Springer-Verlag, New York.

Zukas, J.A., Walters, W., 2013. *Explosive Effects and Applications*. Springer, New York.

Zukas, J.A., 1980. *Impact Dynamics: Theory and Experiment*. US Army Armament Research and Development Command Ballistic Research Laboratory, Aberdeen Proving Ground, MD.

Zukas, J.A., 1982. *Impact Dynamics*. Wiley.

Zukas, J.A., 1990. *High Velocity Impact Dynamics*. Wiley.

Zukas, J.A., 1993. Some common problems in the numerical modeling of impact phenomena. *Computing Systems in Engineering* 4, 43–58.

Zukas, J.A., 2004. *Introduction to Hydrocodes*. Elsevier.

Appendices

Appendix 9A

Nomenclature applies to J–C, Z–A and Cockcroft–Latham models

A, B, n, m, C	Johnson–Cook material constants
σ_{eq}	JC flow stress
ε	Equivalent plastic strain
$\dot{\varepsilon}$	Strain rate
$\dot{\varepsilon}_0$	Reference strain rate
$\dot{\varepsilon}^* = \dot{\varepsilon}/\dot{\varepsilon}_0$	JC dimensionless plastic strain rate
T	Temperature of test specimen
T_{melt}	Temperature at melting point in JC model
T_0	Temperature t reference conditions in JC model
$T^* = \frac{T-T_0}{T_{melt}-T_0}$	JC homologues temperature
	Note $T^* = 0$ for $T < T_0$. $T^* = 1$ for $T > T_{melt}$
τ	Shear resistance to deformation
τ_a	Athermal shear resistance
τ^*	Thermal shear resistance
τ_d	Viscous drag shear resistance
σ	Flow stress
$\sigma_{a1}(\rho)$	Athermal stress (evolving with deformation)
σ_{a2}	Athermal stress (not evolving deformation)

$\widehat{\sigma}^*$	Thermal stress
σ_{drag}	Viscous drag stress
σ^{exp}	Experimentally deduced stress
k	Boltzman constant = 1.38E-23 J/K
F_0	Free energy required to overcome obstacle for $\tau^* = 0$
p	Material constant $0 < p \leq 1$
q	Material constant $0 \leq q \leq 2$
χ	Taylor–Quinney coefficient representing portion of plastic work converted to heat = 0.9
C_p	Specific heat of test specimen
k'	Arrhenius rate constant
A^*	Arrhenius frequency factor
ΔE_e	Arrhenius activation energy
T'	Arrhenius reaction temperature
E_{state}	Energy of the system in any given state
T_{state}	Absolute temperature of system
E_i	Energy levels in dislocation distribution
n_i	Number of dislocations
β, J	Boltzmann distribution parameters for dislocations
S	Entropy
E_{internal}	Internal energy
ΔH	Enthalpy
ΔG	Gibbs energy (not in the strict thermodynamic sense)
θ	$\Delta S/k$
R	Phenomenological constant
m'	Phenomenological exponent constant
b	Burgers vector
ρ'	Dislocation length per unit volume (density)
Δl	Distance between dislocation barriers
M	Orientation parameter
v_s	Speed of sound through crystal grain
τ_{line}	Dislocation glide resistance
$\widehat{\tau}$	Maximum glide resistance

Continued

$\dot{\gamma}$	Glide plane shear strain rate
$\dot{\gamma}_0$	Constant in phenomenological relation
ν_0	Vibrational frequency of dislocation
γ	Shear strain produced due to dislocation glide
$C_0, C_1, C_2, C_3, C_4, C_5$	Zerilli–Armstrong (ZA) material constants
D	Scalar damage variable
δS	Cross-sectional area of plane cutting RVE
δS_D	Cross-sectional area of voids lying on RVE plane
$\Delta \bar{\epsilon}_p$	Increment of accumulated plastic strain
$\bar{\epsilon}_p$	Plastic strain
ϵ_f	Fracture strain
D_1, D_2, D_3, D_4, D_5	JC fracture strain model constants
W	Cockcroft–Latham plastic work term
W_{cr}	Cockcroft–Latham critical plastic work term at which material fails

Appendix 9B

The following armour materials data are provided ‘as-is’ to aid the FE scientist/engineer, to find and select the most appropriate input data to use in their numerical models. Whilst the authors have made all reasonable efforts to source the data correctly, they shall not be held liable for omissions or mistakes in the data given in [Tables 9B1–9B8](#). Users should also ascertain the accuracy of the data independently.

Table 9B1 Johnson–Cook material data

Material	A (MPa)	B (MPa)	n	C	m	$\dot{\epsilon}_0$ (s ^{−1})	Sources
6061-T6 (Al)	355	85	0.11	0.012	1.0	1	Dabboussi and Nemes (2005)
Ti-6Al-4V	1050	955	0.63	0.011	1.0	1	
Nitronic33 (SS)	446	2075	0.84	0.05	1.0	1	
Weldox 500E	605	409	0.5	0.0166	1.0	5E-4	Børvik et al. (2009)
Weldox 700E	819	308	0.64	0.0098	1.0	5E-4	

Table 9B1 Continued

Material	A (MPa)	B (MPa)	<i>n</i>	<i>C</i>	<i>m</i>	$\dot{\epsilon}_0(\text{s}^{-1})$	Sources
Hardox 400	1350	362	1.0	0.0108	1.0	5E-4	Børvik et al. (2002) Meyer and Kleponis (2001) Klepaczko et al. (2009) Gray et al. (1994)
Domex Protect 500	2030	504	1.0	0.001	1.0	5E-4	
Armox 560T	2030	568	1.0	0.001	1.0	5E-4	
Bullet cores	1200	50,000	1.0	0.0	1.0	5E-4	
Lead bullet cap	24	300	1.0	0.1	1.0	5E-4	
Brass jacket	206	505	0.42	0.01	1.68	5E-4	
Weldox 460 E	490	807	0.73	0.0114	0.94	5E-4	
Ti-6Al-4V	862.5	331.2	0.34	0.012	0.8	1.0	
DH-36 steel	1020	1530	0.4	0.015	0.32	0.1	
4340 tempered martensite	2100	1750	0.65	0.0028	0.75	NA	
RHA steel	1832	1685	0.754	0.00435	0.8	NA	
RHA steel	1400	1800	0.768	0.0049	1.17	NA	
RHA steel	1225	1575	0.768	0.049	1.09	NA	
RHA steel	900	1305	0.9	0.0575	1.075	NA	
Al-7039	475	550	0.275	0.0125	1	NA	
Al-7039	260	650	0.225	0.02875	1.17	NA	
Al-7039	515	810	0.2775	0.01575	0.705	NA	
AL-7039	180	510	0.22	0.0265	0.875	NA	
Al-7039	390	945	0.235	0.0295	0.62	NA	
Al-5083	210	620	0.375	0.0125	1.525	NA	
Al-5083	200	600	0.38	0.02	1.5	NA	
Al-5083	275	545	0.475	0.01225	1.65	NA	
Al-5083	270	470	0.6	0.0105	1.2	NA	
Al-5083	205	500	0.405	0.028	1.7	NA	

Continued

Table 9B1 Continued

Material	<i>A</i> (MPa)	<i>B</i> (MPa)	<i>n</i>	<i>C</i>	<i>m</i>	$\dot{\epsilon}_0(\text{s}^{-1})$	Sources
Al-5083	170	425	0.42	0.0335	1.225	NA	Trana et al. (2007)
OL 37 steel	220	620	0.12	0.01	1.0	NA	
AISI 1018 CR steel	520	269	0.282	0.0476	0.553	NA	
Weldox 460E	499	382	0.458	0.0079	0.893	1.0	Dey et al. (2004)
Weldox700E	859	329	0.579	0.0115	1.071	1.0	
Weldox900E	992	364	0.568	0.0087	1.131	1.0	
OFHC copper	65	356	0.37	0.013	1.05	0.002	Holmquist and Johnson (1991)
ARMCO iron	233	468	0.42	0.047	0.42	0.002	
OFHC copper	90	292	0.31	0.025	1.09	1.0	
Cartridge brass	112	505	0.42	0.009	1.68	1.0	Johnson and Cook (1983)
ARMCO iron	175	380	0.32	0.06	0.55	1.0	
1006 steel	350	275	0.36	0.022	1.0	1.0	
2024-T351 Al	265	426	0.34	0.015	1.0	1.0	
7039 Al	337	343	0.41	0.01	1.0	1.0	
4340 steel	792	510	0.26	0.014	1.03	1.0	
S-7 tool steel	1539	477	0.18	0.012	1.0	1.0	
Tungsten alloy	1506	177	0.12	0.016	1.0	1.0	
TENAX tool steel	1440	492	0.011	0.24	1.03	NA	
AREMA iron	175	376	0.06	0.32	0.55	NA	Buchar et al. (2002)
2P armour	1210	773	0.014	0.26	1.03	NA	
Steel projectile	1650	807	0.008	0.1	1.0	NA	
Ti-6Al-4V	1098	1092	0.93	0.014	1.1	1E-4	Leuser (1999)
2024-T3 Al	369	684	0.73	0.0083	1.7	1E-4	
45 steel	506	320	0.28	0.064	1.06	NA	
A3 steel	410	20	0.08	0.1	0.55	NA	Chen et al. (2008)

Table 9B2 Zerilli–Armstrong material data

Material	C_0 (MPa)	C_1 (MPa)	C_2 (K ⁻¹)	C_3 (K ⁻¹)	C_4 (K ⁻¹)	C (MPa)	n	Sources
OFHC copper	60	—	656	0.00198	0.000060	—	0.37	Holmquist and Johnson (1991)
ARMCO iron	65	3214	—	0.00973	0.000321	332	0.42	
AISI 1045 steel	159.2	1533.7	—	0.00609	0.00018	742.6	0.171	
AISI 4340 steel	89.8	2073.6	—	0.0015	0.0000485	1029.4	0.531	
6082-T6 Al	0	—	3551.4	0.00341	0.000057	—	—	Özel and Karpaz (2007)
Ti6Al4V	740	—	240	0.00240	0.00043	656	0.5	
Ta	25	1040	—	0.00525	0.0003	480	0.575	
Ta (large ϵ)	5	1200	—	0.0065	0.00035	390	0.3	
4340 Tempered martensite	89.8	2073.6	—	0.0015	0.0000485	1029.4	0.531	Gray et al. (1994)
RHA steel	50	1800	—	0.0015	0.000045	1200	0.62	Chen et al. (1996)
Tantalum	75	1000	—	0.005	0.00025	700	0.5	
Copper	11	—	1350	0.0011	0.000025	—	0.7025	
Al-7039	17	—	1090	0.00155	0.000052	—	0.135	
Al-5083	23	—	970	0.00185	0.00008	—	0.225	Macdougall and Harding (1997)
Ti6Al4V	778	1465	—	0.00864	0.000546	508	0.3529	
OFHC copper	65	—	890	0.0028	0.00015	—	—	
ARMCO iron	65	1033	—	0.00698	0.000415	266	0.289	
Ta	30	1125	—	0.00535	0.000327	310	0.44	Zerilli and Armstrong (1990)

Table 9B3 Steinberg—Cochran—Guinan—Lund (SCGL)

	AA (6061-T6)	Cu	Mg	Ni	SS 304	Ti
$G_0(\text{GPa})$	27.6	47.7	16.5	85.5	77	43.4
$\sigma_a \text{ (GPa)}$	0.29	0.12	0.19	0.14	0.34	0.71
$\sigma_p \text{ (GPa)}$	0.68	0.64	0.48	1.2	2.5	1.45
β	125	36	1100	46	43	780
N	0.1	0.45	0.12	0.53	0.35	0.065
$\frac{G'_p}{G_0}(\text{TPa}^{-1})(\text{kK}^{-1})$	65	28	103	16	26	11.5
$\frac{G'_T}{G_0}(\text{TPa}^{-1})(\text{kK}^{-1})$	0.62	0.38	0.51	0.33	0.45	0.62
$T_{m0} \text{ (K)}$	1220	1790	1150	2330	2380	2260
γ_0	1.97	2.02	1.54	1.96	1.93	1.23
a	1.5	1.5	1.2	1.5	1.4	1.0

Table 9B4 MTS model

Metal specimen	HY-100	Ti-6Al-4V
Source	Daridon et al. (2004)	
$\tau_a \text{ (MPa)}$	23.55	58
$\widehat{\tau}_i \text{ (MPa)}$	779.65	872
$\mu_0 \text{ (GPa)}$	71.46	49.02
$D \text{ (MPa)}$	2910	
$T_0 \text{ (K)}$	204	
$k \text{ (J/K)}$	1.38E-23	
$b \text{ (m)}$	2.48E-10	2.55E-10
$\dot{\gamma}_{0i} \text{ (s}^{-1}\text{)}$	1E13	1E10
g_{0i}	1.161	0.264
q_i	1.5	2
p_i	0.5	1
$\dot{\gamma}_{0e} \text{ (s}^{-1}\text{)}$	1E7	1E7
g_{0e}	1.6	1.6
q_e	1	1
p_e	2/3	2/3
g_{0es}	0.112	

Table 9B4 Continued

Metal specimen	HY-100	Ti-6Al-4V
g_{0s}		0.8
$\hat{\tau}_{\epsilon s}$ (MPa)		310.62
$\hat{\tau}_s$ (MPa)		486.6
$\dot{\gamma}_{0s}$		1E10
q_s		2
p_s		1
θ_0 (MPa)		
$\dot{\gamma}_{0\epsilon s}$	1E7	

Table 9B5 Johnson–Cook damage model

Material	D_1	D_2	D_3	D_4	D_5	Sources
Ti-6Al-4V	−0.09	0.25	−0.50	0.014	3.87	Leuser (1999)
2024-T3	0.13	0.13	−1.5	0.0011	0.0	
Weldox 460E	0.0705	1.732	−0.54	−0.015	0.0	(Børvik et al. (2001)
OFHC copper	0.54	4.89	−3.03	0.014	1.12	
ARMCO iron	−2.2	5.43	−0.47	0.016	0.63	Johnson and Cook (1985)
4340 steel	0.05	3.44	−2.12	0.002	0.61	
6061-T6	−0.77	1.45	−0.47	0.0	1.60	Özel and Karpaz (2007)

Table 9B6 Cockcroft–Latham damage model

Material	ϵ_f	W_{cr} (MPa)
Source	Børvik et al. (2009)	
Weldox 500E	1.46	1516
Weldox 700E	1.31	1486
Hardox 400	1.16	2013
Domex Protect 500	0.67	1484
Armox 560T	0.92	2310
Lead bullet cap	—	175
Brass jacket	—	914

Table 9B7 EOS (Mie–Grueneisen)

Metal specimen	S_1	γ_0	ρ_0 (kg/m ³)	C_{sp}	Hugoniot Relation	Sources
Brass	1.43	1.78	8520	3740	Linear ($S_2 = S_3 = 0$)	Marsh (1980)
Lead	1.47	2.8	10,660	2030	Linear ($S_2 = S_3 = 0$)	
Copper	1.489	2.02	8930	3940	Linear ($S_2 = S_3 = 0$)	Steinberg (1996)
Aluminium 2024	1.338	2.00	2785	5328	Linear ($S_2 = S_3 = 0$)	
Aluminium 6061	1.4	1.97	2703	5240	Linear ($S_2 = S_3 = 0$)	
Tungsten carbide	1.16	1.5	14,900	5190	Linear ($S_2 = S_3 = 0$)	
Graphite	2.16	0.24	2200	3900	($S_2 = 1.54, S_3 = -9.43$)	
Ti-6-4	1.028	1.23	4419	5130	Linear ($S_2 = S_3 = 0$)	
Polycarbonate	3.49	0.61	1196	1933	($S_2 = -0.82, S_3 = 9.6$)	
Vasomax 250	1.58	1.6	8129	3980	Linear ($S_2 = S_3 = 0$)	
Steel (4340 RC 38) Core and plate	1.33	1.67	7810	4578	Linear ($S_2 = S_3 = 0$)	

Table 9B8 Johnson—Holmquist JH-2 model

Variable	B ₄ C	SiC	AlN	Al ₂ O ₃	Silica float glass
Source: Cronin et al. (2003)					
ρ_0 (kg/m ³)	2510	3163	3226	3700	2530
G shear modulus (GPa)	197	183	127	90.16	30.4
A	0.927	0.96	0.85	0.93	0.93
B	0.7	0.35	0.31	0.31	0.088
C	0.005	0.0	0.013	0.0	0.003
M	0.85	1.0	0.21	0.6	0.35
N	0.67	0.65	0.29	0.6	0.77
$\dot{\epsilon}_0$	1.0	1.0	1.0	1.0	1.0
T (GPa)	0.26	0.37	0.32	0.2	0.15
SFMAX	0.2	0.8			0.5
HEL (GPa)	19	14.567	9	2.79	5.95
HEL pressure (GPa)	8.71	5.9	5	1.46	2.92
HEL vol. strain	0.0408		0.0242	0.01117	
HEL strength (GPa)	15.4	13.0	6.0	2.0	4.5
D_1	0.001	0.48	0.02	0.005	0.053
D_2	0.5	0.48	1.85	1.0	0.85
K_1 (GPa)	233	204.785	201	130.95	45.4
K_2 (GPa)	−593	0	260	0	−138
K_3 (GPa)	2800	0	0	0	290
β	1.0	1.0	1.0	1.0	1.0

High strain rate and specialised testing

10

D. Ruan¹, M.A. Kariem², I.G. Crouch³

¹Swinburne University of Technology, Hawthorn, Victoria, Australia; ²Bandung Institute of Technology, Bandung, West Java, Indonesia; ³Armour Solutions Pty Ltd, Trentham, Victoria, Australia

10.1 General introduction

Armour materials and armoured structures are required to perform under a variety of dynamic conditions, from local penetration events to global blast loadings, and understanding how these structures behave during an impact event is an important aspect for military engineers to consider. Many well-known authorities in this field have published widely on the subject, Zukas (1982), Meyers (1994), Stronge (2000), Field et al. (2004) and Ramesh (2008), to name but a few. However, when it comes to developing new armour materials or designing real armour systems, there is a unique subset of tests that armour technologists use. These range from purely observational, drop-weight tests onto real components (to check structural integrity and explosion bulge tests to prove that a welded panel can withstand a particular blast load) to very sophisticated tests that help characterise a material's response to a stress wave or a shock wave, and which go to the very heart of understanding armour physics. The plate impact (PI) test, described in Section 10.5, is one such method. However, by far the most important set of material characterisation tests are those that derive material parameters for strength models and fracture criteria, used as critical input data for numerical modelling of armour/antiarmour events, as described in Chapter 9. Section 10.6 is devoted to this group of test methods, based on the Split Hopkinson Pressure Bar (SHPB) test; Section 10.7 then provides a number of examples of applications and data manipulation.

Overlaid on these dynamic tests is a range of specialised, quasistatic test methods, which have evolved to simulate and quantify particular energy-absorbing mechanisms in lightweight armour materials. Even though these tests are carried out at quasistatic rates, using conventional test equipment, they do provide a means of either ranking potential armour materials or providing input data for analytical models, as covered in Chapter 8. During the 1980s and 1990s, Raymond Woodward of DSTO (Australia) was a pioneer of this approach — carrying out simple, carefully selected, mechanical tests to measure a relevant material property for an analytical model. For example, an early paper by Crouch and Woodward (1989) illustrated this useful approach.

One must also remember that there are numerous (more than 10,000) standard material characterisation tests as listed by ASTM International, and the International Standards Organisation (ISO) — these are not covered here but are duly referenced wherever possible.

10.1.1 Specialised quasistatic (QS) testing

When seeking to understand the behaviour of lightweight armour materials, there is often a need to simulate a particular aspect or feature of an impact event, whether it is the initial indentation of a pointed projectile into a ductile target or the latter-stage process of delamination in laminated armour. With this objective in mind, a number of specialised test methods, carried out at near-QS rates, have evolved (see Table 10.1). For the purpose of these tests, any strain-rate effects that might exist are ignored, since these data usually form input parameters for fairly coarse analytical models: the difference between a QS result and a dynamic one is, depending on material family, often within the estimating errors associated with analytical modelling.

Table 10.1 List of specialised test procedures for each energy-absorbing mechanism in a monolithic, laminated or FRP armour material

Phase	Penetration mechanism	Microstructural events	Dedicated test procedures
I	1. Through-thickness compression	Elastic/quasiplastic response of matrix material Low modulus event Affected by V_f in a fibre-reinforced polymer (FRP)	<ul style="list-style-type: none"> • Simple compression test of a cylindrical sample • Constrained Compression Test, CCT
	2. Transverse shear	Transverse cutting of fibres or laminae	<ul style="list-style-type: none"> • CCT • Stamping test, with variable punch diameter
	3. Crushing and local shearing	Local comminution of fibres, resin, etc. Flow of comminuted material	<ul style="list-style-type: none"> • Conical indentation test, with variable cone angles
II	4. Delamination	Both intra- and interlaminar separation	<ul style="list-style-type: none"> • Short beam shear test • Central plunger delamination (CPD) test
	5. Membrane flexure	Matrix cracking Debonding of laminae	<ul style="list-style-type: none"> • 2D four-point bend test • 3D centrally loaded plate (CLP) test
	6. In-plane tensile failure	Fibre pull-out Tensile fracture of fibres or laminae	<ul style="list-style-type: none"> • In-plane tensile test, with variable orientation (eg, LT or TL)

LT, Longitudinal Transverse; *TL*, Transverse Longitudinal.
 After Crouch, I.G., March 1993. Penetration and Perforation Mechanisms in Composite Armour Materials, Euromech Colloquium 299. Oxford University.

These QS test methods are described in detail in [Section 10.2](#). For example, the constrained compression test (CCT), described in [Section 10.2.2](#), is now a well-established test when studying the early penetration mechanisms associated with Phase I mode of failure (see [Table 10.1](#)).

10.1.2 High strain rate testing

In earlier chapters, we learnt that some key properties (strength, ductility and fracture toughness) of most materials vary significantly with strain, strain rate and temperature. For example, the yield strength of mild steel, under dynamic loading conditions, could be double that under quasistatic loading. It is preferable, therefore, to measure key mechanical properties of armour materials under some form of dynamic loading.

One measurement of loading velocity is strain rate, $\dot{\epsilon}$, which is defined as the ratio of the incremental change of strain, $d\epsilon$, to the incremental change of time, dt ([ASM International, 2003](#)),

$$\dot{\epsilon} = \frac{d\epsilon}{dt}$$

If engineering strain is employed, where $d\epsilon = dL/L_0$, then

$$\dot{\epsilon} = \frac{d\epsilon}{dt} = \frac{\frac{dL}{L_0}}{dt} = \frac{dL}{dt} \frac{1}{L_0} = \frac{v}{L_0}$$

where L_0 is the original length of a specimen, dL is the incremental change of specimen length and v is the loading velocity.

[Meyers \(1994\)](#) classified strain rates into five different regions as follows:

1. Creep and stress-relaxation regime (for strain rates less than 10^{-5} s^{-1});
2. Quasistatic regime (for strain rates from 10^{-5} s^{-1} to 5 s^{-1});
3. Dynamic-low regime (for strain rates from 5 s^{-1} to 10^3 s^{-1});
4. Dynamic-high regime (for strain rates from 10^3 s^{-1} to c. 10^5 s^{-1});
5. High-velocity impact regime (for strain rates from 10^5 s^{-1} to 10^7 s^{-1}).

The associated testing methods at various strain rates are listed in [Table 10.2](#). Although several testing methods can be used at the same strain rate, there are differences in those testing methods/machines. For example, both high-speed hydraulic machines and drop-weight testing devices can be used at strain rates between 1 and 10^2 s^{-1} (dynamic-low range). Constant strain rate can be achieved in tests conducted by a high-speed hydraulic machine. However, when a drop-weight test method is employed, the strain rate varies from the initial velocity at the beginning of the tests to zero at the end of the test. Similarly in the dynamic-high range (eg, 10^3 s^{-1}), a constant strain rate can be achieved in tests conducted using a SPHB. However, in a single Taylor test (comprising of the impact of a flat-ended cylindrical rod onto a stationary anvil), the strain rate in a specimen varies from quasistatic at the distal end to the dynamic shock at the impact end of the specimen. Therefore, it is important to choose the most

Table 10.2 Testing methods at various strain rates

Strain rate (s ⁻¹)	Common testing methods	Dynamic considerations
10 ⁷ —	High velocity impact <ul style="list-style-type: none"> • Explosive • Normal plate impact • Pulsed laser • Exploding foil • Incl. plate impact (pressure shear) 	Shock-wave propagation
10 ⁶ —		
10 ⁵ —		Shear-wave propagation
10 ⁴ —		
10 ³ —	Dynamic high <ul style="list-style-type: none"> • Taylor anvil tests • Hopkinson bar • Expanding ring 	Plastic-wave propagation
10 ² —		
10 ¹ —		
10 ⁰ —	Dynamic low <ul style="list-style-type: none"> • High-velocity hydraulic or pneumatic machines • Cam plastometer • Drop-weight test 	Mechanical resonance in specimen and machine is important
10 ⁻¹ —		
10 ⁻² —		
10 ⁻³ —	Quasi-static <ul style="list-style-type: none"> • Hydraulic, servo-hydraulic or screw-driven test machines 	Tests with constant cross-head velocity and stress the same throughout length of specimen
10 ⁻⁴ —		
10 ⁻⁵ —		
10 ⁻⁶ —		
10 ⁻⁷ —		
10 ⁻⁸ —		
10 ⁻⁹ —	Creep and stress-relaxation <ul style="list-style-type: none"> • Conventional machines • Creep testers 	Visco-plastic response of materials

Meyers, M.A., 1994. *Dynamic Behavior of Materials*. John Wiley & Sons, Inc., New York.

appropriate test method/machine according to the accuracy requirement of material properties to be measured.

[Section 10.3](#) describes a series of impact tests, and [Section 10.4](#) captures some of the salient fracture test methods, [Sections 10.5 and 10.6](#) report the latest developments in high strain rate material characterisation tests.

10.2 Specialised testing techniques

10.2.1 Indentation tests

It should not be a surprise by now to know that an indentation test is at the heart (well, at the very forefront) of understanding penetration mechanics associated with armour materials. An indentation hardness test is an excellent simulation of

the very early stage of a penetration event, especially one involving a rigid, pointed projectile and a plastically deforming metal. It is a simple test but an extremely powerful and meaningful one.

Hardness testing indenters come in a whole range of shapes and sizes and correct selection is essential. For example, it is fairly common when measuring the hardness of an armour casting to use a Brinell hardness test because the indenter is a ball. Remember that the surface of a casting can be fairly irregular and the substrate is likely to be heterogeneous in nature. Likewise, when measuring the micro-hardness of a ceramic, using the correct indenter diameter to grain-size ratio is very important.

Classical understanding was published by [David Tabor \(1951\)](#), the godfather of the science of indentation hardness. His outstanding contribution to this field was captured in a tribute article by [Ian Hutchings \(2009\)](#). Since the 1950s, the indentation test has been adopted to study the Hertzian fracture phenomena in glasses and ceramics ([Lawn and Wilshaw, 1975](#)), as well as the dynamic ‘flow’ properties of glass fibre-reinforced polymers in the work of [Reid et al. \(1995\)](#). [Fig. 10.1](#) illustrates the principle behind this conical indentation test: by varying the included angle of the cone, the respective in-plane, R_{IP} , and through-thickness, R_{TT} , resistive forces can be measured and the effects of anisotropy in composite armour materials studied. More recently, [Gama et al. \(2004a,b\)](#) used a similar QS punch shear loading test to study ballistic damage mechanisms in thick, S-2 glass-reinforced resin, and perform numerical simulations of the same.

The hardness test continues to be used because, more than any other singular material parameter, hardness consistently correlates very well with ballistic performance. This is why careful selection of the most appropriate hardness test from an established range of methods is so important. ISO/TC 164/SC 3 – Hardness Testing, is a useful guide.

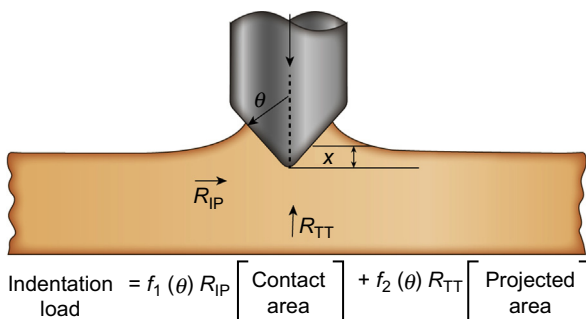


Figure 10.1 Illustration of conical indentation of FRP armour material and calculations to decouple through-thickness and in-plane ‘flow’ of comminuted material.

After Reid, S.R., Reddy, T.Y., Ho, H.M., Crouch, I.G., Greaves, L.J., 1995. Dynamic indentation of thick fibre-reinforced composites. In: ASME Conference on High Strain Rate Behavior of Composites, San Francisco, November 1995.

10.2.2 Through-thickness compression tests

Through-thickness (TT) compression has been identified as one of the key energy-absorbing mechanisms in both monolithic and laminated armour materials, especially against blunt projectiles (see Chapters 4 and 5). When measuring this property it would be conventional practice to test the compressive resistance of simple cylinders of material. However, an armour material concurrently undergoes TT penetration as well as TT compression and so a CCT is far more representative and realistic. As shown in Fig. 10.2, it is a simple test involving the TT compression of a planar test sample by using a pair of opposing, matching and high-strength punches, contained within a rigid, self-supporting frame. The ‘cylinder’ of material under test is residing in a field of plastic constraint, limiting lateral flow, as would happen in a ballistic penetration test. The diameter of the punches is chosen to represent the core of the projectile: the test sample thickness closely resembles the proposed armour thickness.

Fig. 10.3 shows a typical stress–strain plot for both a constrained and uniaxial test for aluminium alloy 2024-T351. The effect of the constraint is quite evident. If such data are curve-fitted to an expression of the form, $\sigma = K \sigma_0 \epsilon^n$, the constraint factor, K , can be determined and for this aluminium alloy, K was calculated to be ~ 2.7 .

The test itself has its historical roots in the early work of Woodward and De Morton (1976) who used the test to generate data for a simple plugging model (see Chapter 8). Woodward and Crouch (1988) extended the usefulness of this test by utilising CCT data as input data for the analytical model, LAMP, to predict the penetration behaviour of laminated armours. More recently, Scott (2011) has applied a variation of this same model to the penetration of ultrahigh molecular weight polyethylene (UHMWPE) targets

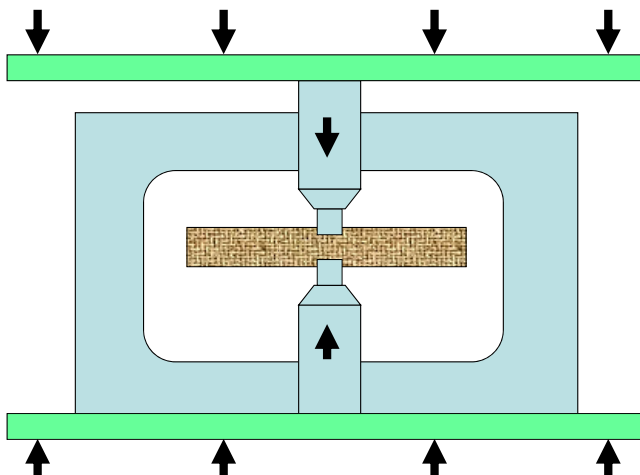


Figure 10.2 Schematic of the constrained compression test (CCT) rig.

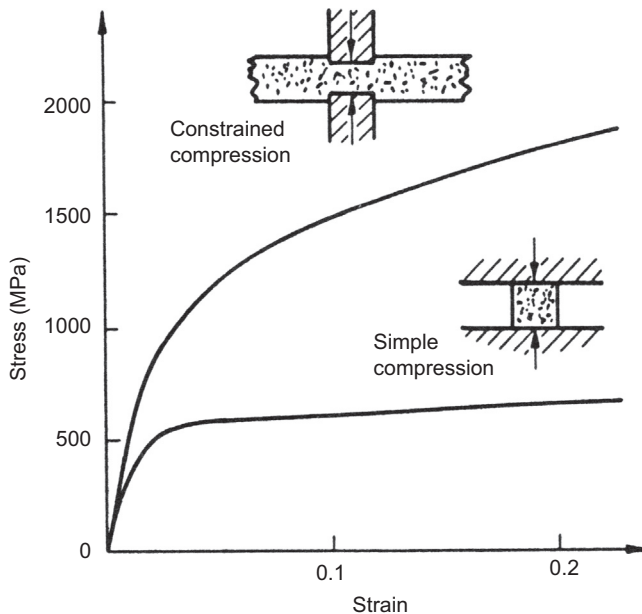


Figure 10.3 Typical example of a CCT curve, for 2024-T351 aluminium, compared with a conventional, simple compression test curve.

Woodward, R.L., De Morton, M.E., 1976. *International Journal of Mechanical Sciences* 18, 119–127.

and used the CCT test to generate the input data. Very recently [Thomas and Crouch \(2015\)](#) compared potential buffer materials using this test procedure. [Fig. 10.4](#) shows a range of CCT data for Carbon Fibre Reinforced Polymer (CFRP), Kevlar Fibre Reinforced Polymer (KFRP) as well as UHMWPE materials; the effective TT elastic moduli of the different materials were estimated and compared with in-plane properties.

10.2.3 Delamination tests

Delamination of laminated targets, whether they are fibre metal laminates (FMLs) or fibre-reinforced polymers (FRPs), is an important failure mechanism in composite armour materials. The delamination process itself embraces interlaminar shearing and interlaminar fracture (with the creation of new fracture surfaces), as well as peeling forces (normally measured in 2D) and membrane stretching (caused by out-of-plane displacement). It is a complex event and these individual components need to be uncoupled and each individually measured if any sensible development or analysis is to occur.

Conventional tests are well established, as covered by [Davies et al. \(1998\)](#) and [Sridharan \(2008\)](#), and evolving all the time, especially for advanced composite materials used in aircraft structures (eg, [Wood et al., 2007](#)). What is covered here is a specialised

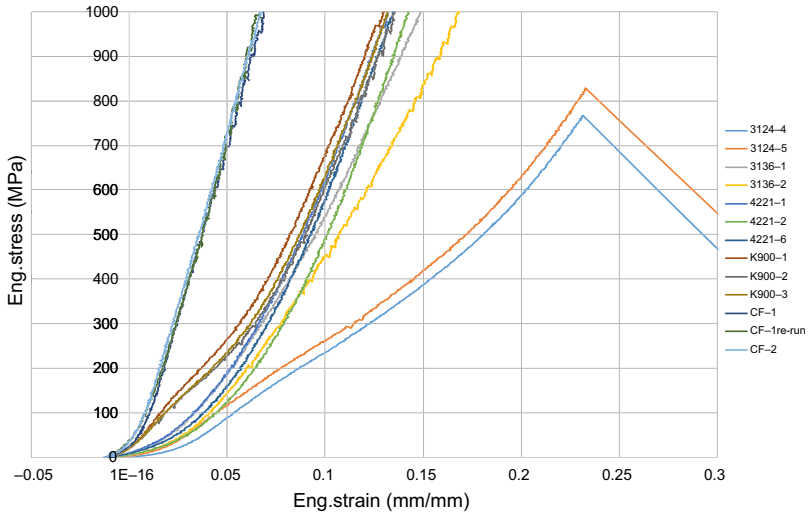


Figure 10.4 A series of CCT curves for different composite materials: a carbon fibre-reinforced epoxy (CF-1 and CF-2) an aramid fibre-reinforced epoxy (K900) and various grades of UHMWPE (SR3124, SR3136 and SR4221 from Honeywell).
After Thomas, S., Crouch, I.G., 2015.

technique for measuring adhesive peel strengths, and for estimating the energy absorbed in the delamination process, for fibre-metal laminates, in particular (see Chapter 4).

The CPD test, as described by [Simmons et al. \(1989\)](#), is an axisymmetric peel test of a bondline, where one plate (the flexing plate) is peeled away from another (the static plate) by a central force applied by a plunger through a hole in the static plate (see [Fig. 10.5](#)). The CPD test consists of two principal energy-absorbing processes: (1) the elastic and plastic deformation of the flexing plate and (2) the delamination of

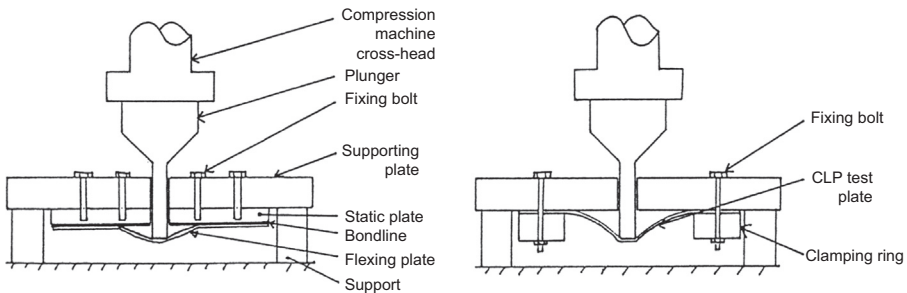


Figure 10.5 Specialised testing techniques: the CPD test (left) and CLP test (right) for studying the delamination process in FMLs.
After Simmons, M.J., Smith, T.F., Crouch, I.G., 1989. Delamination of metallic composites subjected to ballistic impact. In: 11th International Symposium on Ballistics, Brussels, Belgium, May 1989.

the bond. In order to isolate these two contributing factors a second test can be used. This is a simple dishing test, called a centrally loaded plate (CLP) test. Here, a plate is clamped at a particular radius and loaded centrally by a plunger. Force–displacement histories can be recorded from both the CPD and CLP tests and, through a simple subtraction process, the energy absorbed due to the 3D peeling process can be calculated. Using this methodology, it was estimated that between 15% and 70% of the impact energy could be absorbed by the delamination process, depending upon the impact conditions.

10.3 Impact tests

10.3.1 Drop-weight tests

The drop-weight test is a very common tool in a mechanical engineering laboratory because of its versatility in studying the impact behaviour of structures. Reviewed by [Lu and Yu \(2003\)](#), the test method is essential when studying the energy-absorption of both materials and structures. In recent decades, end-on crushing of tubes (both metal and composite) has become very popular in the development of energy-absorbing, crash-resistant structures. Such systems are also very usefully employed in armour engineering, especially of heavy systems.

[Fig. 10.6\(a\)](#) is a sketch of a drop-weight device and its accessories, which include a fixture to support or hold specimens, a load cell, which is placed under the fixture, and a laser device. A high-speed camera is also normally employed to capture the deformation of specimens in such dynamic tests.

When conducting a drop-weight test, a mass is lifted up to a certain height and drops freely to crush a specimen. The impact force history is recorded by the load cell and the displacement history of the drop mass or indenter is recorded by the laser device. A force–displacement curve can then be generated and the total energy absorbed by the specimen can be calculated accordingly, which is the area under the force–displacement curve. In such a drop-weight test, the total input energy is constant, which is mgh , where m is the drop mass, g is the gravitational acceleration (9.8 m/s/s) and h is the drop height. The velocity of the drop mass or indenter varies throughout the impact process. A typical setting in a drop-weight test at Swinburne University of Technology is shown in [Fig. 10.7\(a\)](#). A specially designed and manufactured fixture was employed to support the pipe-like specimens ([Fig. 10.7\(b\)](#)). Such a test method is also used when studying the behaviour of soft armours against stab and spike attack (see Chapter 6).

10.3.2 Taylor impact test

In 1946, Taylor proposed a direct impact test to determine the dynamic yield strength of a material at high strain rates ([Fig. 10.8](#)). When conducting such a test, a cylindrical specimen was accelerated by a device (such as a gas gun) towards a rigid target. The specimen impacts the rigid target at a certain velocity. Plastic deformation develops at the impact

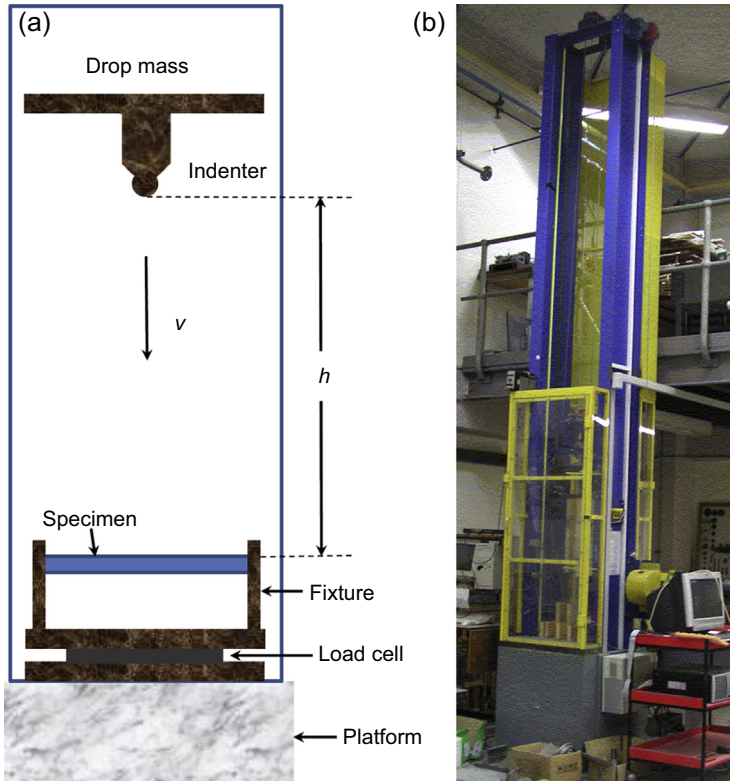


Figure 10.6 (a) Schematic of a typical drop-weight device, and accessories, and (b) drop-weight device at Swinburne University of Technology, Australia. The drop mass varies from 25 to 150 kg and the maximum drop height is 3 m.

end of the specimen and propagates to the distal end in the specimen. The shape of the specimen at the impact end after impact changes due to plastic deformation, while the far end remains the same (ie, no plastic deformation). After the impact, the length of the specimen decreases from L_0 (original length of the specimen before the impact) to L_f (the final total length of the specimen after the impact). The length of the deformed portion of the specimen is assumed to be L_p . By measuring these dimensions (L_0 , L_f and L_p), the dynamic yield strength of the specimen material can be calculated as

$$\sigma_Y = \frac{(L_0 - L_p)\rho v^2}{2(L_0 - L_f)\ln(L_0/L_p)}$$

where ρ is the density of the specimen.

The Taylor anvil test is relatively easy to conduct. However, to precisely determine the boundary of elastic and plastic deformation zones (ie, the magnitude of L_p) is challenging and L_p is normally determined by hardness test (Hiermaier, 2008).

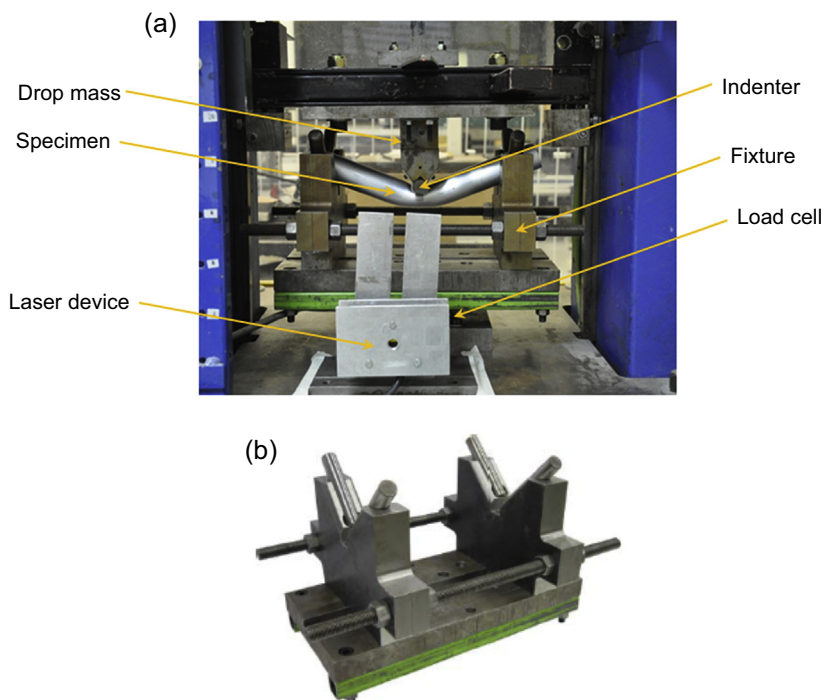


Figure 10.7 A photograph of: (a) the setting on the platform of the drop-weight equipment: load cell, laser device, fixture, specimen, indenter and drop mass. (Rathnaweera, G., 2014. Thesis. Swinburne University of Technology, Melbourne, Australia.); (b) the specially designed and manufactured fixture. (Kinoshita, S., 2011. Thesis. Swinburne University of Technology, Melbourne, Australia.)

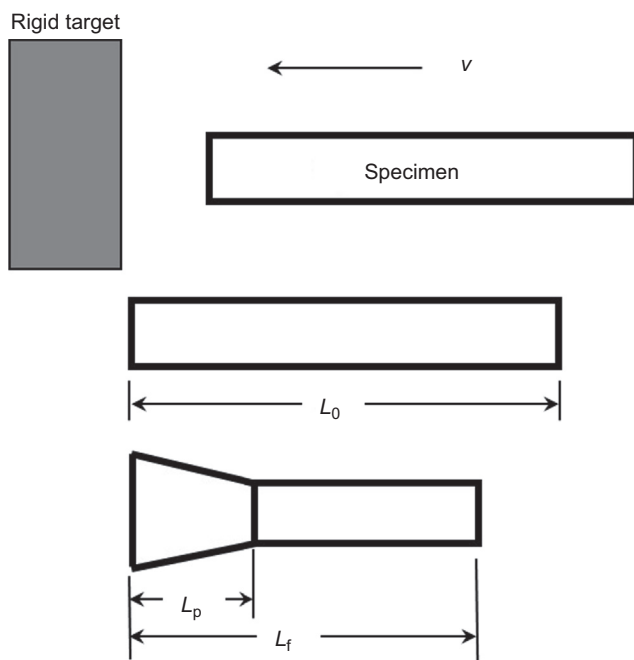


Figure 10.8 Schematic of Taylor impact test.

10.3.3 Gas gun impact experiments

As recently stated by [Rosenberg and Dekel \(2012\)](#), most experimental work in terminal ballistics is carried out using laboratory-based gas guns, in which a single- or two-stage gas gun is used to propel a projectile along the barrel to impact upon a target specimen. Typical barrels range in diameter from 5 to 50 mm with impact velocities as high as 10,000 m/s. [Stilp and Hohler \(1990\)](#) describe the engineering details of the different types of gas gun and [Fig. 10.9\(a\)](#) shows a typical experimental set-up for a single-stage gun ([Hou et al., 2010](#)). The gas pressure developed in the charge chamber controls the velocity of the projectile. In this case, the impact velocity is measured by a laser velocity meter, before the penetration event, and by a high-speed camera during and/or after the penetration event. The total energy absorbed by the target specimen can be calculated according to the difference between the two measured velocities. Projectiles can be self-designed and manufactured ([Fig. 10.9\(b\)](#)) or sourced commercially.

Critical structures may be subjected to the impact from deformable objects, similar to what happened with the Columbia Space Shuttle in 2003, where a piece of foam hit a wing panel, with tragic consequences. In such events, deformation happens to both the structure and impacting object, with the impact energy being dissipated by both the structure and the deformable object. With a rigid penetrator, only the structure will deform, and the impact energy is dissipated by the structure only. The former case is, of course, the most complex to resolve and understand. In the past decade or so, Fleck and his co-workers pioneered the study of the ballistic resistance of beams and panels subjected to the impact of deformable aluminium foam projectiles ([Radford et al., 2005, 2006; Rathbun et al., 2006; McShane et al., 2006; Tagarielli et al., 2007, 2010; Rubino et al., 2009; Russell et al., 2012](#)). A sketch of the experimental set-up used by [Rathbun et al. \(2006\)](#) is shown in [Fig. 10.10](#).

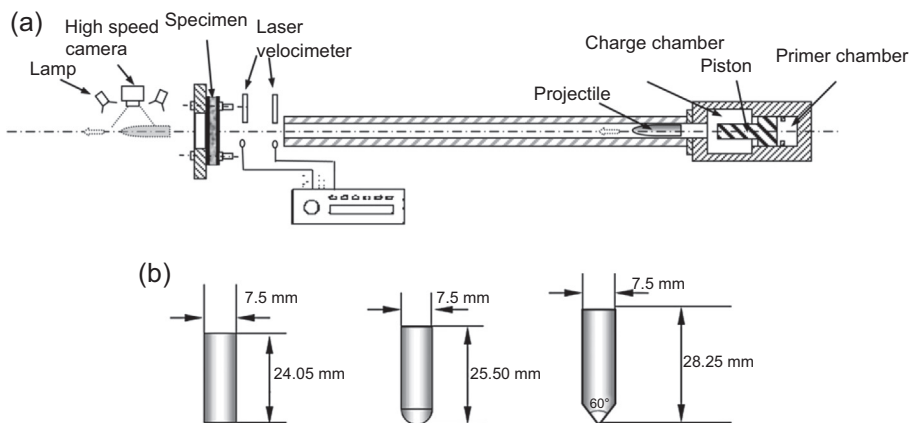


Figure 10.9 (a) Experimental set-up of ballistic test; (b) three types of projectiles used: flat-ended, hemispherical-nosed and conical-nosed.

Hou, W., Zhu, F., Lu, G., Fang, D.-N., 2010. *International Journal of Impact Engineering* 37, 1045–1055.

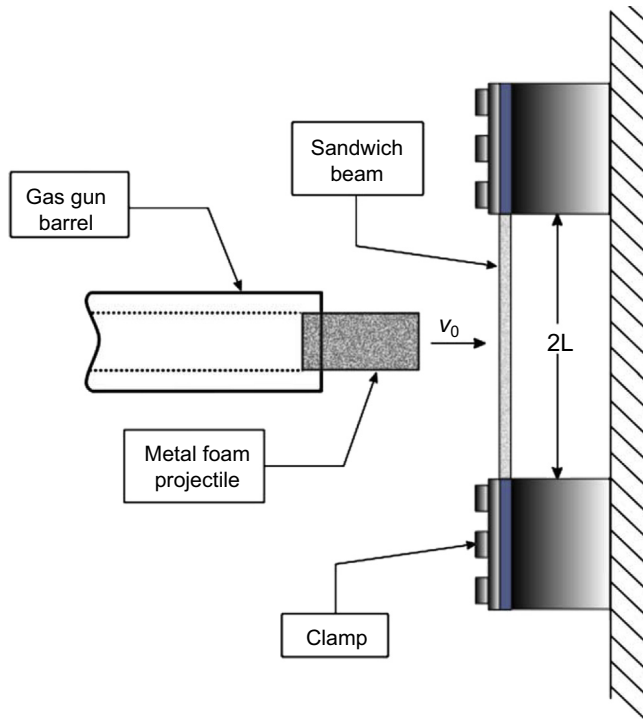


Figure 10.10 The experimental set-up of Rathbun et al. (2006).

Rathbun, H.J., Radford, D.D., Xue, Z., He, M.Y., Yang, J., Deshpande, V., Fleck, N.A., Hutchinson, J.W., Zok, F.W., Evans, A.G., 2006. *International Journal of Solids and Structures* 43, 1746–1763.

A similar experimental set-up together with a gas gun is shown in Fig. 10.11 (Yahaya et al., 2015). The photographs of foam projectiles and sandwich panels after the impact tests are shown in Figs. 10.12 and 10.13, respectively. The main objective of this work was to study the resistance of sandwich panels with different aluminium honeycomb cores, air sandwich panels (no core between the two face sheets) and monolithic plates of equivalent mass subjected to impact from foam projectiles. Sandwich panels had 1-mm thick aluminium face sheets and HEXCEL honeycomb cores. Cylindrical ALPORAS aluminium foam projectiles with a relative density between 9% and 11% were fired at several hundred meters per second towards the centre of the panels and plates using a gas gun. The deflection histories of the back-face were measured using a laser displacement sensor. For sandwich panels, it was found that the stronger the honeycomb core the less the deformation of the panel. It was also found that the honeycomb sandwich panels outperformed both the air sandwich panels and the monolithic plates within an impulse range of $2.25\text{--}4.70\text{ kNsm}^{-2}$. Outside this operational range, the advantages associated with employing the honeycomb sandwich panels as a protective structure upon impact of foam projectiles diminished.

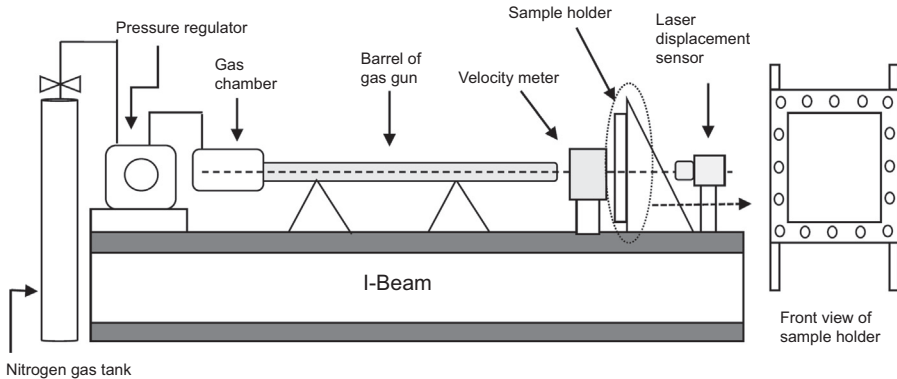


Figure 10.11 A sketch of the experimental set-up of [Yahaya et al. \(2015\)](#) – the diameter of the gas gun barrel was 37 mm.

Yahaya, M.A., Ruan, D., Lu, G., Dargusch, M.S., 2015. *International Journal of Impact Engineering* 75, 100–109.

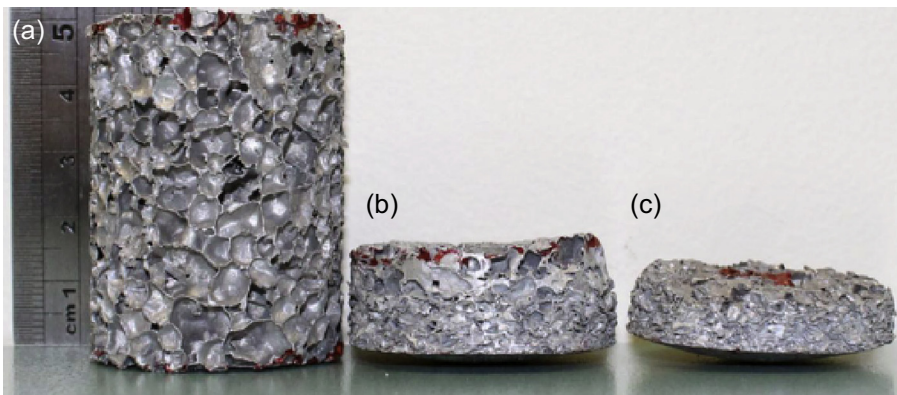


Figure 10.12 Photographs of aluminium foam projectiles: (a) initial shape; (b) after impacting a sandwich panel at 189 m/s; (c) after impacting a sandwich panel at 333 m/s.

Yahaya, M.A., Ruan, D., Lu, G., Dargusch, M.S., 2015. *International Journal of Impact Engineering* 75, 100–109.

10.4 Dynamic fracture tests

Cracks propagate differently under quasistatic and dynamic conditions – the major differences being as follows.

1. In quasistatic fracture, a single crack nucleates at a single site and propagates either along a grain boundary (causing intergranular fracture) or across the grains (causing transgranular fracture). However, under a dynamic load, numerous cracks nucleate at various independent sites and all propagate independently ([Meyers, 1994](#)).
2. There is an upper bound for the velocity of crack propagation in dynamic fracture, which is normally taken as the Rayleigh wave velocity, though experimentally measured crack

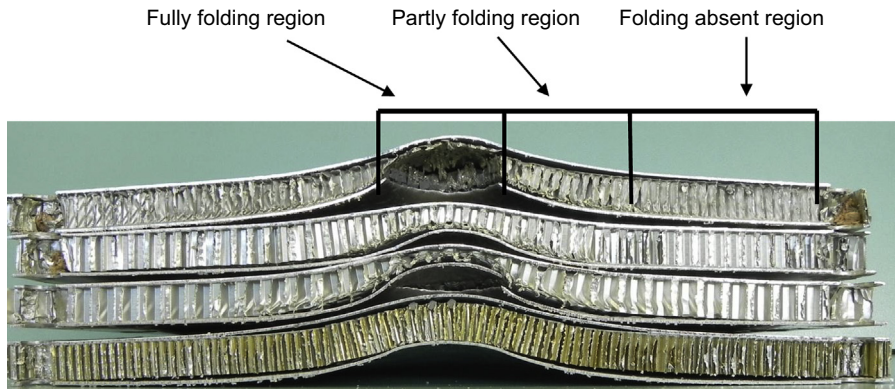


Figure 10.13 The comparison of deformed sandwich panels after impact by aluminium foam projectiles. The types of HEXCEL aluminium honeycomb cores from the top to bottom are: 3.1-1/8-0.0007, 6.1-1/8-0.0015, 4.4-3/16-0.0015 and 12-1/8-0.003.

Yahaya, M.A., Ruan, D., Lu, G., Dargusch, M.S., 2015. *International Journal of Impact Engineering* 75, 100–109.

velocities are always less (Meyers, 1994). Rayleigh wave velocities depend upon the properties of the material in which they propagate. In metals, it is between 2 and 5 km/s.

3. Quasistatic fracture toughness of a material is defined as:

$$K_{IC} = k\sigma\sqrt{\pi a}$$

where k is a parameter, σ is the stress of the material and a is the crack length. Fracture toughness values, determined at quasistatic rates, range from ~ 100 MPa m for tough steels to ~ 3 MPa m for brittle ceramics. However, it is more challenging to determine the dynamic fracture toughness, K_{Id} , although methods are available – see [Section 10.6.5](#).

10.4.1 Charpy and Izod impact tests

These are standard, metallurgical tests for ‘toughness’ – they are rather crude, comparative tests but very important as a critical component of an armour material specification, especially for steels which undergo a ductile–brittle transition. For this purpose, energy-absorption values are normally requested at both ambient and -40°C .

Both the Izod and Charpy impact tests are dynamic tests, which measure the impact energy absorbed by a V-notched or U-notched specimen. [Figs. 10.14\(a\) and \(b\)](#) are sketches of the Izod and Charpy impact test device. Both Izod and Charpy impact tests can be conducted using the same machine with different fixture to hold specimens. In an Izod impact test ([Fig. 10.14\(a\)](#)), the V-notched specimen is firmly held by a test rig; in a Charpy impact test, the V-notched specimen is simply supported at both ends. In either test, a pendulum is released at a certain height, h_1 , to impact the specimen and break it into two pieces. The pendulum will continue to rotate to a height of h_2 , after the

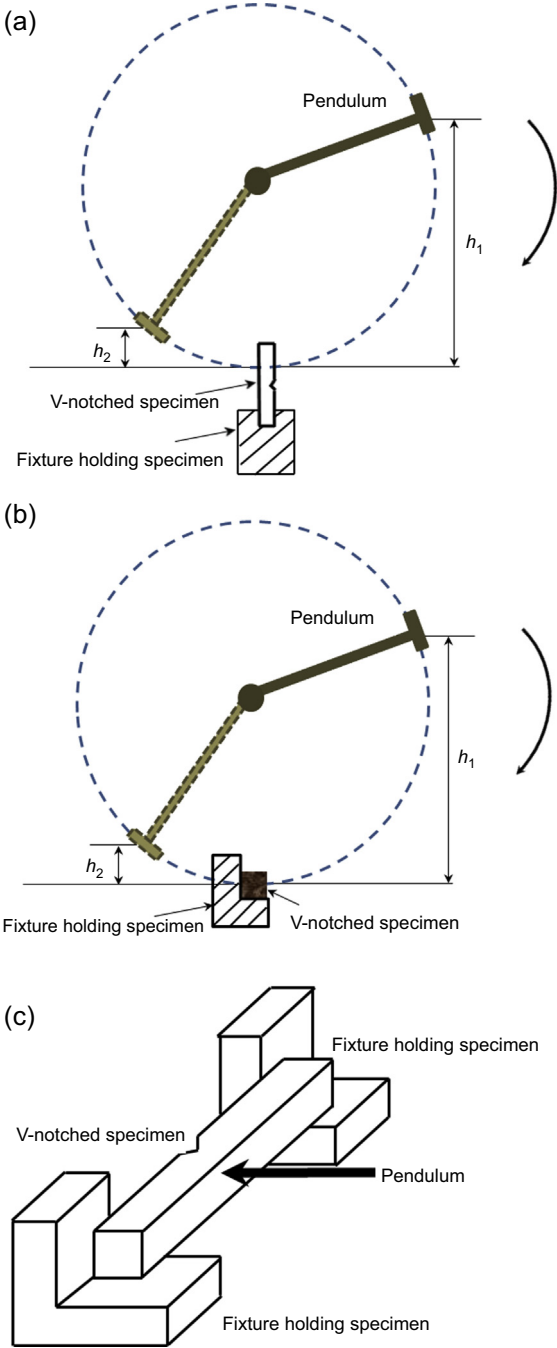


Figure 10.14 (a) A sketch of the Izod impact tests; (b) a sketch of a Charpy impact test; (c) enlarged view of the specimen layout in a Charpy test.

impact. By measuring h_1 and h_2 , the energy dissipated to break the specimen can be calculated as $mg(h_1 - h_2)$.

Three major differences between the Izod and Charpy impact tests are as follows.

1. In an Izod impact test, the specimen is placed vertical with notch facing the pendulum (Fig. 10.14(a)), while in a Charpy impact test, the specimen is placed horizontally with the notch facing away from the pendulum (Figs. 10.14(b) and (c)).
2. In an Izod impact test, the specimen is held in a cantilever beam configuration, whilst, in the Charpy impact test, the specimen is held in a three-point bending configuration.
3. Generally speaking, the Izod impact test is used to test plastics, while the Charpy impact test is normally employed to test metals, but it can be used for other materials such as polymers. The ASTM international standards for Izod and Charpy impact tests are ASTM D256 for plastics and ASTM E23 for metallic materials, respectively.

10.4.2 Fragmentation tests

Understanding fragmentation of brittle materials, like cast irons, is not only important when designing fragmenting munitions, like hand grenades, but also in setting standards for protection against the penetration of high-velocity fragments, where size, shape and individual velocities are critical in determining lethality.

When a metal ring is subjected to a quasistatic load, it may break into two pieces. However, if it is subjected to a dynamic load, it may break into several pieces (Meyers, 1994), which is due to the stress wave developed in the hoop direction of the ring (see Fig. 10.15) (Grady and Olsen, 2003). Mott (1947) pioneered the work to study the fragmentation in rings and proposed a statistics-based theoretical model. The model was compared with the experimental results obtained by Grady and Olsen (2003), who conducted tests on rings of U6N (uranium-6%-niobium).

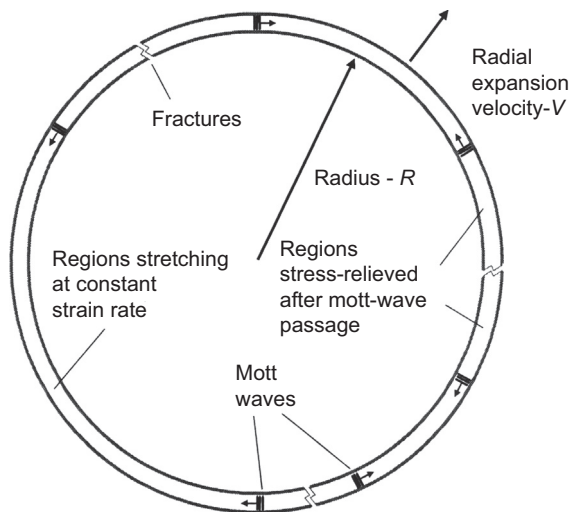


Figure 10.15 A sketch of Mott's fragmentation ring.

Grady, D.E., Olsen, M.L., 2003. *International Journal of Impact Engineering* 29, 293–306.

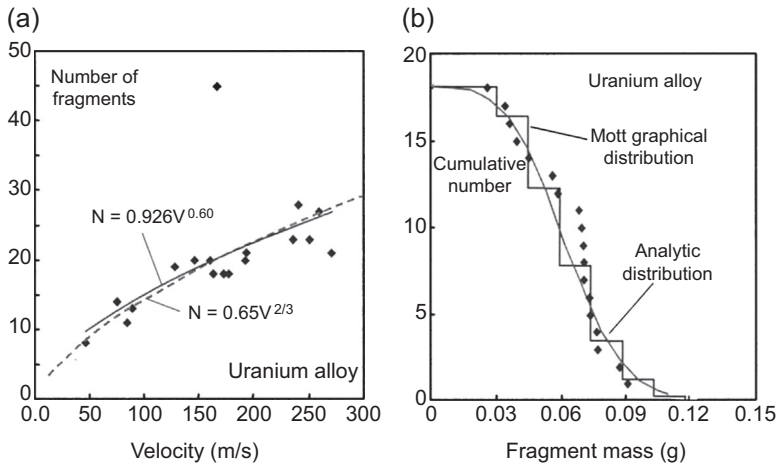


Figure 10.16 Comparison of experimental and Mott's theory in terms of: (a) fragment number; (b) fragment distribution.

Grady, D.E., Olsen, M.L., 2003. *International Journal of Impact Engineering* 29, 293–306.

The rings (diameter = 30 mm) were accelerated by a pulsed magnetic field to radial velocity of 50–300 m/s. Fragmentation happened at an expansion of up to approximately 30% and rings broke into several pieces. The number and distribution of fragments matched well with Mott's theory, as can be seen from Fig. 10.16.

By definition, a fragmentation event converts a monolithic material into a number of small fragments of material. The number, size and fracture pattern associated with this event are very dependent upon the nature of the impact. Chapter 1 introduced this type of failure mechanism, whilst Chapter 7 described the fragmentation of monolithic ceramic breastplate tiles into many segmented pieces, with the number of segments correlating with both target geometry and support conditions. Predicting the number of radial cracks emanating from a point of strike is still, however, poorly understood but very impact velocity-dependent.

10.4.3 Spallation tests

The failure mechanism known as spallation was described in Chapter 1. It occurs in materials when the interaction of stress waves causes the localised stress to exceed the material's spall strength. Spallation is a serious issue with body armour systems, for example, when high-energy spall is ejected from the impacted surface of a ceramic-based hard armour plate, and becomes a dangerous projectile to surrounding troops and equipment. Rear-surface spall, as described in Chapter 3, is also a common failure mechanism in aluminium armour alloys. Spall liners, manufactured from fibre-reinforced plastics, as described in Chapter 5, are designed to capture such spall. The spall strengths for a number of different metallic materials are given in Fig. 10.17.

Spallation tests can be conducted using an SHPB to determine the dynamic tensile strength of materials (Govender et al., 2011) (see Fig. 10.18). In spalling tests,

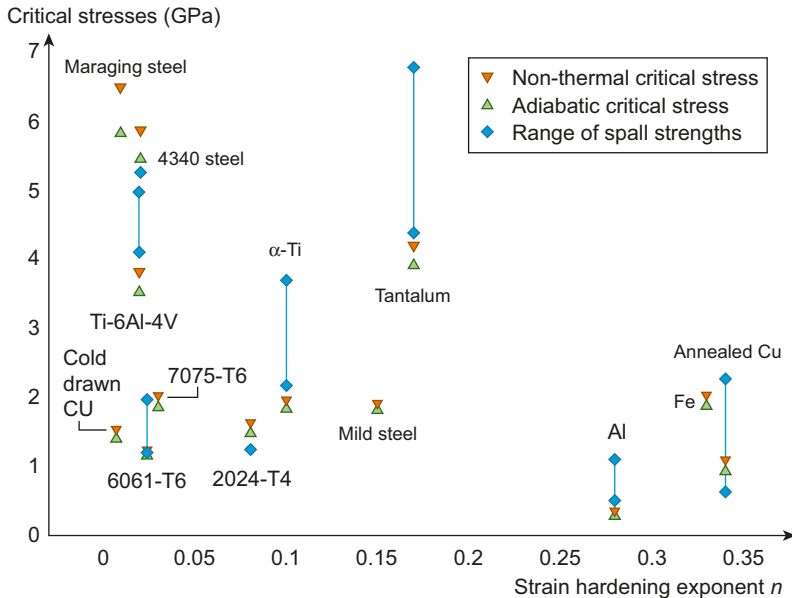


Figure 10.17 Spall strength values for a number of metals, as a function of strain hardening exponent.

After Wu, X.Y., Ramesh, K.T., Wright, T.W., 2003. *International Journal of Solids and Structures* 40, 4461–4478.

one end of the specimen is attached to the incident bar and the other end is free (ie, the transmitted bar is not required). When a striker bar impacts the incident bar, a compressive wave is generated in the incident bar and transmitted to the specimen. Since the other end of the specimen is free, the stress reflects as a tensile wave, which travels in the opposite direction of the initial compressive wave. The reflected tensile wave superimposes on the compressive wave. When the resultant wave is a tensile wave and the magnitude exceeds the tensile strength of the specimen material, spalling happens.

Spalling tests can be conducted on materials whose compressive strength is much larger than their tensile strength and whose behaviour is linear up to failure, such as ceramic, concrete and fibre-reinforced polymer. Otherwise, the initial compressive wave will cause failure in the material. Detailed quantitative spalling models and microstructural effects can be found in Meyer's book (Meyers, 1994).

10.4.4 Explosion bulge test

Until relatively recently, the main threat to an armoured vehicle, and its occupants, has been from small arms ammunition and high-velocity fragmentation. However, with the advent of improvised explosive devices as well as more sophisticated landmines, there has been an increased need to learn more about how armour plate, especially welded steel belly plates, behave when explosively loaded. Furthermore,

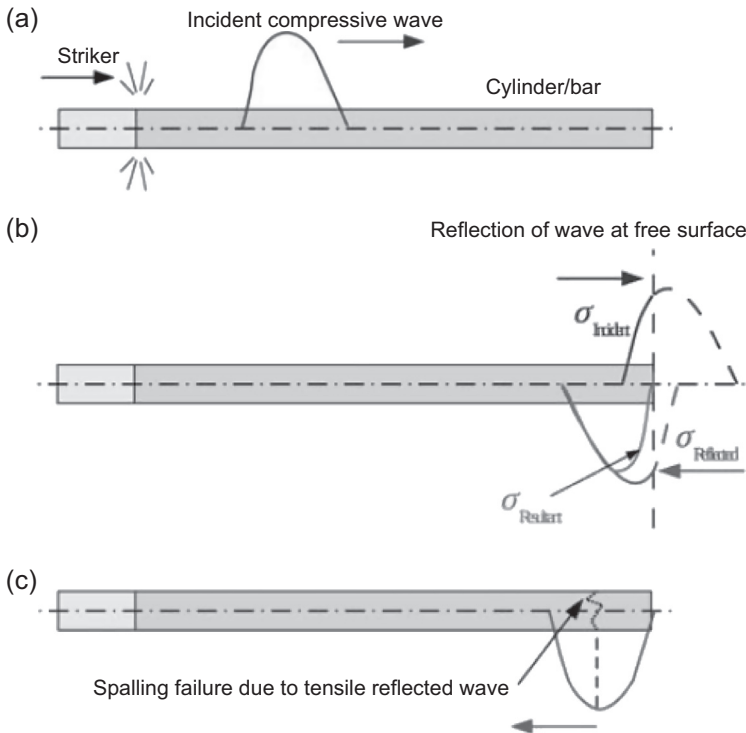


Figure 10.18 A sketch of the wave propagation in a spalling test using a Hopkinson pressure bar.

it is also imperative to limit the extent of elastic and plastic deformation and protect the occupants of a military vehicle from upward/inward explosive loadings. This is analogous to a crumple zone in a civilian car. The explosion bulge test (EBT) has been developed to help quantify the effects of explosive loadings, based upon the early requirements to test ship and submarine structures. The test plates are usually a representative panel of armour material, a weldment between two half-plates or a plate containing a weld bead. US DoD specification, MIL-STD-2149A(SH) ([Specification, 1990](#)) provides more detail.

[Fig. 10.19](#) illustrates the experimental set-up of an EBT. It comprises of a donut-shaped die block on which the test plate is placed. A standard stand-off of 320 mm is specified and a disposable item (like a cardboard box) is used as a spacer between the explosive charge and the test plate. A 2.3 kg explosive charge is placed in position directly over the centre of the plate. Thermocouples are attached to the sample, to check for correct temperature of the test, which is often subzero (eg, -40°C). After detonation of the explosive, the test plate is physically examined and the extent of plastic deformation recorded. Welds would normally be inspected, using an Non Destructive Inspection (NDI) technique, for any evidence of cracking.

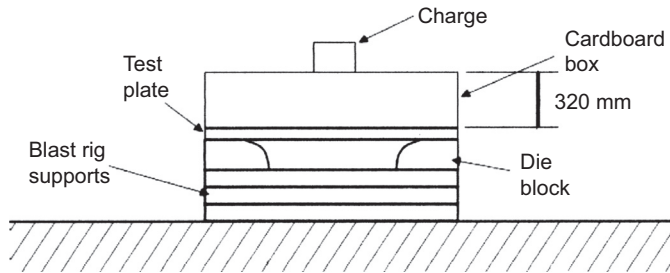


Figure 10.19 Schematic of the experimental set-up for an explosive bulge test.

10.4.5 Blast tests of panels (flat and curved) and tubes

The drive for lighter-weight military structures is always on-going and the use of light-weight, composite panels or tubular structures is increasing in popularity. However, these lightweight structures can be susceptible to impact damage from low-level blast events. This section considers the research currently underway in assessing and improving the blast behaviour of these lightweight structures. Hybrid structures, such as sandwich panels (a core sandwiched between two face sheets) or sandwich tubes (a tubular core sandwiched between two thin-walled tubes), are considered in which the core materials could be honeycomb structures, foams, lattice structures and even unique 3-D printed arrays.

The experimental facilities and test procedures for recording the deformation/damage modes of blast-tested specimens, supporting theoretical models, and numerical simulations were reviewed and summarised by [Jones \(1989a,b\)](#), [Nurick and Martin \(1989a,b\)](#) and, more recently, by [Zhu and Lu \(2007\)](#). A pendulum system is normally employed to measure the impulse generated by air blast explosions and imparted to a specimen ([Nurick and Martin, 1989a,b](#); [Hanssen et al., 2002](#); [Enstock and Smith, 2007](#); [Zhu et al., 2008a,b](#)). When an explosive charge detonates in front of a specimen, which is usually attached to the pendulum, a blast pressure is applied to the specimen and causes the pendulum to rotate or translate. A laser displacement measurement device normally measures the movement of the centre of the pendulum and the generated impulse can be calculate accordingly. [Figs. 10.20\(a\)–\(b\)](#) are photographs of two types of pendulum used by [Enstock and Smith \(2007\)](#), Nurick's research group in the University of Cape Town in South Africa, and [Zhu et al. \(2009a,b\)](#) respectively. [Fig. 10.21](#) shows a typical set-up for this type of experiment, in which a free-moving pendulum records the impulse from an air blast.

Pendulum systems can also be used in air blast tests on curved sandwich panels ([Shen et al., 2010, 2011](#)). In this case, the movement of the curved panel is detected by a laser transducer (Micro-Epsilon LD1625-200), placed on the supporting plate, behind the impacted panel, and recorded by an oscilloscope. [Fig. 10.22](#) shows the experimental set-up for a curved panel with a radius of 300 mm ([Shen et al., 2011](#)).

The air blast tests were also conducted on sandwich tubes with aluminium foam cores ([Shen et al., 2013](#)). The sketch of the experimental set-up is shown in

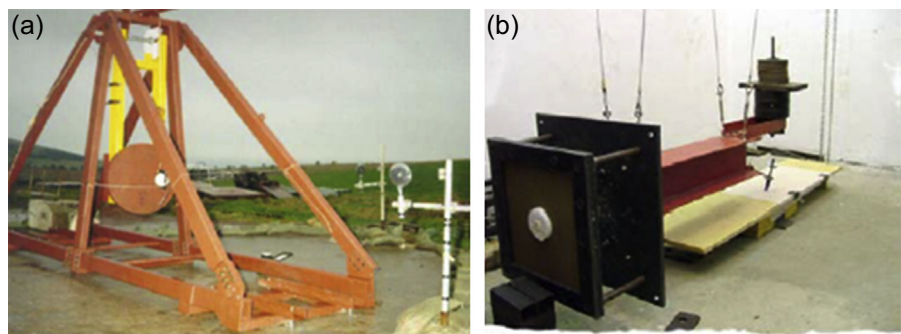


Figure 10.20 Photographs of: (a) a two-cable pendulum (Enstock and Smith, 2007); (b) a four-cable pendulum (http://www.bisru.uct.ac.za/bisru/facilities/lab equip/conv_bar_pend, viewed on 11 December 2014).

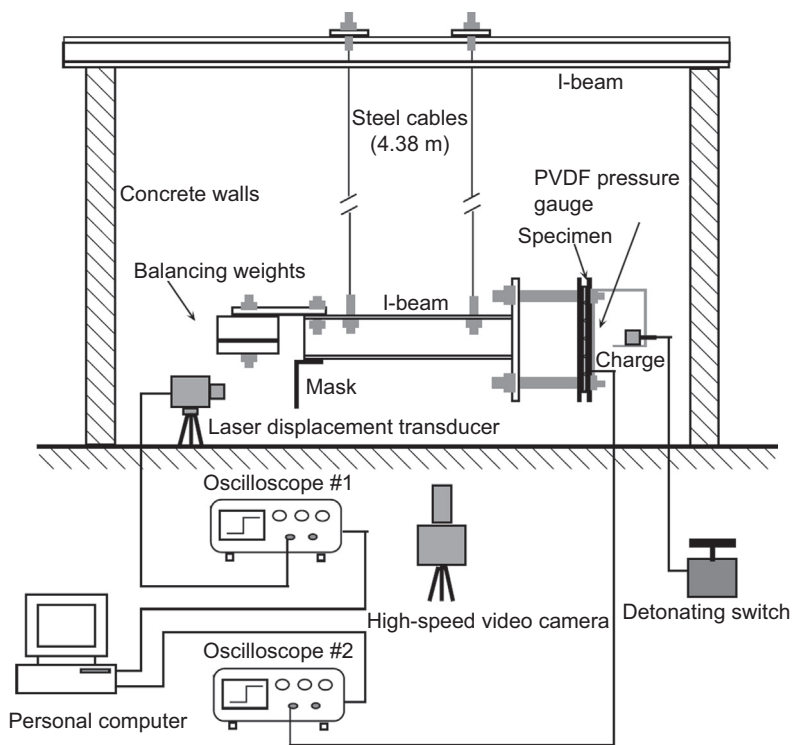


Figure 10.21 A sketch of blast test set-up (Zhu et al., 2009a).
Zhu, F., Longmao, Z., Guoxing, L., Emad, G., 2009a. International Journal of Impact Engineering 36, 687–699.



Figure 10.22 Pendulum with a curved sandwich panel ($R = 300$ mm).

Shen, J., Lu, G., Zhao, L., Qu, Z., 2011. *Journal of Performance of Constructed Facilities* 25, 382–393.

Fig. 10.23. A cylindrical Trinitrotoluene (TNT) charge with a diameter of 20 mm was placed in the centre of a 6×10 m blast chamber without a roof. No deformation history was recorded in these tests. The final deformation of specimens were observed and analysed after the tests.

10.5 Plate impact tests

Understanding the physics behind the creation, development and interaction of stress waves and shock waves is an important aspect of armour, especially hypervelocity impacts against heavy armour systems. However, whilst their role within the penetration of lightweight armour systems is quite small, if not negligible, the tracking of such stress waves through a material can reveal some fundamental properties. In a ballistic impact, the triaxial strain state created lies somewhere between uniaxial strain and uniaxial stress: uniaxial stress tests, based upon the SHPB test, will be described in [Section 10.6](#). Here, a uniaxial strain test, the Plate Impact (PI) test, is described as it forms a unique method of determining not only equation of state data, but also important measurements of the Hugoniot elastic limit (HEL), dynamic compressive strength and spall strength.

[Fig. 10.24](#) shows a schematic of the test equipment, whilst a paper by Field and co-workers at the Cavendish Laboratory, Cambridge ([Field et al., 1994](#)) records the establishment of the UK Plate Impact facility in 1993, and provides comprehensive tables of associated experimental techniques. The paper also gives an excellent overview of the history of high strain rate testing, and was the precursor to a well-cited review a decade later ([Field et al., 2004](#)).

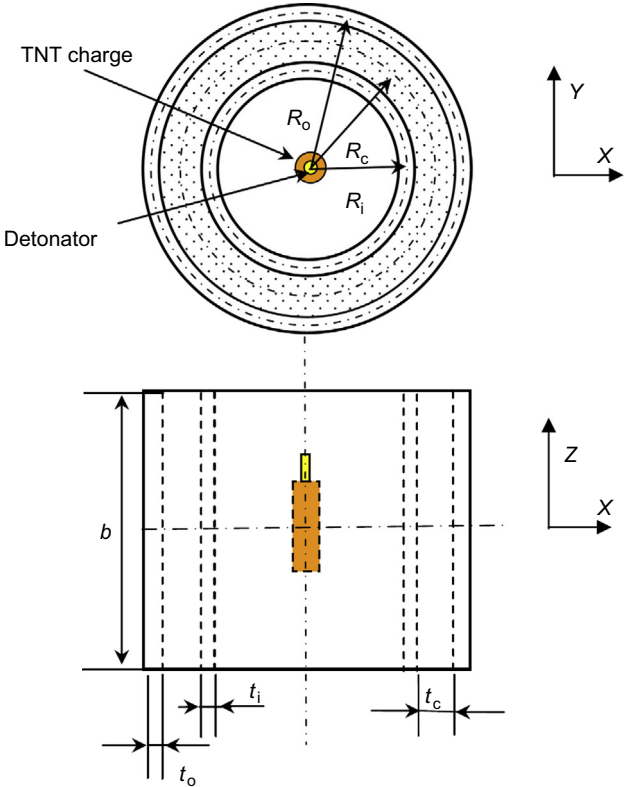


Figure 10.23 Sketch of sandwich tubes subjected to blast loading using TNT charge (Shen et al., 2013).

Shen, J., Lu, G., Zhao, L., Qu, Z., 2011. Journal of Performance of Constructed Facilities 25, 382–393.

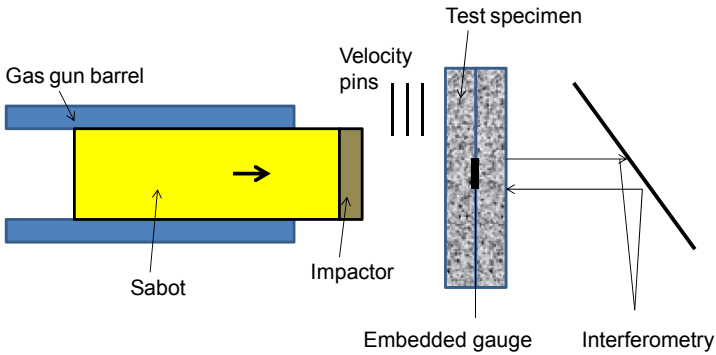


Figure 10.24 Schematic of the plate impact test.

The impactor (or flyer plate) attached to the front of a sabot, is propelled down a gas gun barrel towards the test specimen (or target plate), which is well aligned to give a perfectly planar impact. The impact velocity is measured by a set of velocity pins placed immediately in front of the specimen. The impact generates a stress (or shock) wave within the test specimen, the intensity of which, and associated transit times, being recorded by an embedded gauge, like a Manganin or polyvinylidene difluoride (PVDF) transducer. The rear surface particle velocity is normally measured by interferometry. For a particular flyer plate/target plate combination, as the impact velocity increases, the waves change their nature from being purely elastic at low velocities, to both elastic and plastic, at intermediate velocities, to shock waves at very high velocities.

10.5.1 EOS measurements

The three conservation equations covering mass, momentum and energy are fundamental relationships at the heart of impact physics and any numerical analysis of an impact event (see Chapter 9). These equations of state (EOS) relate the density of a shocked material to the pressures and temperatures generated within the solid material.

The method required to measure these fundamental relationships is clearly described by [Rosenberg and Dekel \(2012\)](#), with more general background provided by [Ramesh \(2008\)](#). If both the flyer plate and the target plate are the same material, then the particle velocity, u_p , will be equal to half of the impact velocity, V . Determining the relationship between shock pressure, U_S , and particle velocity, provides the Hugoniot curve for any solid. The curves can be described as follows, $U_S = C_0 + S u_p$, where C_0 is close to the bulk sound speed within the material and S is the gradient of the slope. According to Rosenberg and Dekel, S lies between 1 and 1.5 for most solids. However, values for C_0 and S are listed in the databases of numerical codes (see Chapter 9). Performing a series of PI experiments at different velocities can generate these curves.

10.5.2 HEL measurements

The Hugoniot elastic limit (HEL) is the point at which plastic yielding starts to occur within a material loaded under uniaxial strain conditions ([Fig. 10.25](#)). It can be derived by performing PI experiments over a wide range of impact velocities to determine the full extent of the Hugoniot curve, as shown in [Fig. 10.26](#).

The dynamic yield strength of the material, Y_d , can then be calculated using the following equation

$$Y_d = (\text{HEL}) \cdot (1 - 2\nu) / (1 - \nu)$$

where ν is Poisson's ratio. A table of measured HEL values for selected armour materials is shown in [Table 10.3](#).

The following published works illustrate the methodologies described in this section: [Dandekar \(1999\)](#) for soda lime glass; [Bourne et al. \(1994\)](#) for the aluminas;

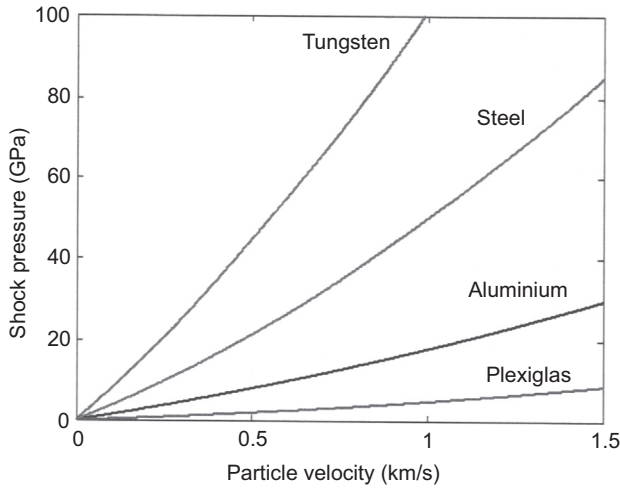


Figure 10.25 Typical Hugoniot curves for some armour materials.

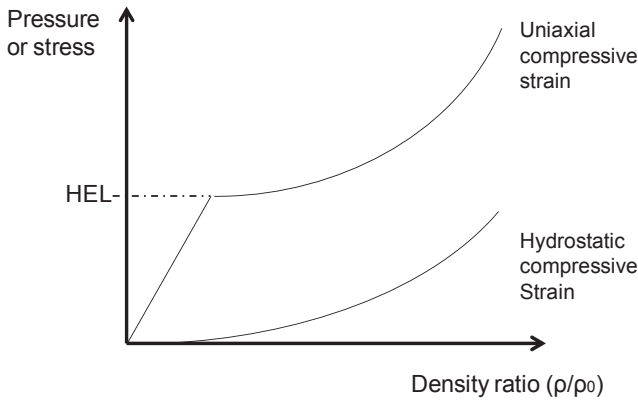


Figure 10.26 Schematic of strength curves under uniaxial and hydrostatic conditions.

[Bourne et al. \(1997\)](#) for the silicon carbides; [Paris et al. \(2010\)](#) for both silicon carbide and boron carbide processed via spark plasma sintering.

10.6 Split Hopkinson pressure bar tests

The split Hopkinson pressure bar (SHPB) technique has been commonly used for the dynamic characterisation of materials. The historical background of the SHPB technique has been reviewed in several references ([Gama et al., 2004a,b](#); [Forde et al., 2008](#); [Edwards, 2006](#); [Gray, 2003](#); [Nemat-Nasser et al., 1991](#); [Field](#)

Table 10.3 Examples of HEL values, extracted from the literature

Material	HEL (GPa)	Density (kg/m ³)	References
Magnesium alloy, Elektron 675-T5	0.37 ± 0.04	1903	Hazell et al. (2012)
Aluminium alloy 5083-H131	0.57 ± 0.04	2668	Boteler and Dandekar (2006)
Aluminium alloy 5083-H32	0.40 ± 0.03	2668	Boteler and Dandekar (2006)
Armour steel (Mars 190)	1.2–2.0	7840	Nahme and Lach (1997)
Armour steel (Mars 300)	1.6–2.2	7840	Nahme and Lach (1997)
Soda lime glass	6.0	2490	Bourne et al. (1998)
Alumina (95%)	7.7	3800	Bourne et al. (1998)
Silicon carbide (HP)	13.5	3160	Bourne et al. (1998)
Boron carbide (HP)	19.5	2500	Zhang et al. (2006)

[et al., 2004](#); [Al-Mousawi et al., 1997](#); [Chen and Song, 2011](#)). The technique is named after the Hopkinson family (John and Bertram Hopkinson) ([Hopkinson, 1872, 1905, 1914](#)) for their pioneering and major contribution to the research of high strain rate testing.

Several major developments have taken place, such as modifications of the Hopkinson bar for dynamic tension testing ([Harding et al., 1960](#); [Lindholm and Yeakley, 1968](#)), dynamic torsion testing ([Baker and Yew, 1966](#)), a miniaturised direct-impact Hopkinson bar ([Gorham et al., 1992](#)), development of large SHPB for structures and concrete testing ([Albertini et al., 1985](#)), and so on. [Table 10.4](#) provides an up-to-date summary of Hopkinson bar applications. This technique can be used for wide dynamic characterisation of materials such as brittle (eg, ceramic, concrete and rock), ductile (eg, metals) and soft materials (eg, rubber, poly(methyl methacrylate) (PMMA) and biological tissues). This technique can also be conducted in several load directions such as compression, tension, torsion, shearing and triaxial tests. It also can be used for conducting impact bending to determine the dynamic fracture toughness of materials.

The standard configuration for the SHPB set-up is in the compression mode, as illustrated in [Fig. 10.27](#). The cylindrical sample is simply placed between the input and output bars. According to [Gray \(2003\)](#) there are five components which are commonly used in a compressive SHPB test apparatus:

1. Two long symmetrical pressure bars with a uniform cross-section and usually made from the same materials;
2. A bearing and alignment fixture to allow the bars to move freely while retaining precise axial alignment;
3. A compressed gas launcher/gun tube or alternative propulsion device ([Silva et al., 2009](#));

Table 10.4 A brief summary of the Hopkinson bar tests ([Kariem et al., 2012](#))

Bar diameter, D (mm)	L/D ratio	Type of test	Strain rate, ($\times 10^3 \text{ s}^{-1}$)	Bar specimen	Specimen material	References
1.5	117	Direct impact	250	Tungsten	Cu	Kamler et al. (1995)
3	50	Direct impact	10–100	Ti-6Al-4V, W alloy, and W-C	W, W alloy, Ti-6Al-4V, Cu	Gorham et al. (1992)
3.2	114	Compressive	10–450	Maraging steel	6061-T651 Al	Jia and Ramesh (2004)
5	80	Shear	26–29	High-strength steel	Ti-6Al-4V	Guo and Li (2012)
5.2	47	Direct impact	20–45	Maraging steel	34 GS construction steel	Malinowski et al. (2007)
6.4	40	Tensile	0.6–1.75	Alloy	Mo, RR77 Al alloy, super-purity iron	Harding et al. (1960)
8		Tensile	0.1	PMMA	Lincoln wool fibres	Ruan et al. (2009)
8.1	*	Direct impact	4–120	Ti-6Al-4V	High-purity Al	Dharan and Hauser (1970)
9.2	133	Compressive	1.0–7.0	Maraging steel	Brass, Oxygen Free Electronic (OFE) Cu, Ir	Follansbee and Frantz (1983)
12	83	Compressive	*	PMMA	Dental composites (Filtek): Z100, Z250, P60, Flow and Supreme	Tanimoto et al. (2006)
12.7	69	Compressive	1.5–2.0	Maraging steel	6061-T6 Al, Cu, brass	Lifshitz and Leber (1994)
12.7	240	Triaxial	0.150–0.35	Maraging steel	Indiana limestone	Frew et al. (2010)
12.7	39	Compressive	3.2	AISI 4340	1045 Al	Wulf and Richardson (1974)

12.7	66	Compressive	1.2–3.2	PMMA	Duocel foam	Deshpande and Fleck (2000)
12.7	66	Compressive	1.9–3.6	Maraging steel	Alulight foam	Deshpande and Fleck (2000)
12.7	78	Compressive	0.04–4	Magnesium alloy	Silicon rubber and pig skin	Shergold et al. (2006)
13	78	Compressive	1.75	AISI 4140	AA 6060 T5	Kariem et al. (2010)
16.7	120	Three-point bending	N.A.	Polycarbonate	Glass fibre-reinforced polypropylene (CFPP)	Govender et al. (2013)
19	95	Compressive ^a	7.96	High-strength Al alloy	RTV630 silicone rubber	Chen et al. (1999)
19	96	Compressive	1.30	Maraging steel	AISI 1046	Chen et al. (2003)
19	193	Compressive ^a	–3.0	7075-T6 Al	Liver tissue	Pervin et al. (2010)
19	*	Compressive	1.0	HSS drill rod	Pb, Al, Cu	Lindholt (1964)
20	151	Tensile	0.9	4140 alloy steel	TRIP780 steel	Dunand et al. (2013)
22.2	*	Torsional	64	7075-T6 Al	1100 Al	Gilat and Cheng (2000)
25	60	Compressive	0.029–0.177	7075-T6 Al	Silicon foam rubber	Chen et al. (2009a)
25	60	Semicircular bending	N.A.	Maraging steel	Laurentian granite	Chen et al. (2009b)
25	*	Shear	0.1–10	Maraging steel	XES steel	Klepaczko et al. (1999)
25	144	Tensile	0.180–0.440	Maraging steel	XES low-carbon steel and 2024-T3 Al	Haugou et al. (2006)
25.4	72	Compressive	*	Silver steel	Polythene, rubbers, PMMA, Cu and Pb	Kolsky (1949)
25.4	*	Torsional ^a	0.80–9		DuPont-20 LDPE	Hu and Feng (2004)

Continued

Table 10.4 Continued

Bar diameter, D (mm)	L/D ratio	Type of test	Strain rate, ($\times 10^3 \text{ s}^{-1}$)	Bar specimen	Specimen material	References
31.8	115	Four-point impact bending	N.A.	7075-T6 Al (IB), 6061-T6 Al (OB)		
				7075-T6 Al	SiC-N	Weerasooriya et al. (2006)
37	48	Compressive-shear	0.35–0.5	7075 Al	Polymer-bonded explosives (PBXs)	Zhao et al. (2012)
40	75	Compressive	0.025–0.250	Nylon	Foams	Zhao (1997)
40	75	Compressive	N.A.	Nylon	Al honeycombs	Zhao and Gary (1998)
76.2	40	Compressive	*	*	Concrete	Gong et al. (1990)
80	125	Direct impact	N.A.	Steel	Brass square tube	Zhao et al. (2006)
100	*	Compressive	0.036–0.120	48CrMoA	Basalt fibre-Reinforced geo-polymeric concrete	Li and Xu (2009)

Note: *, data not available; a, output bar is hollow tube; N.A., not applicable.

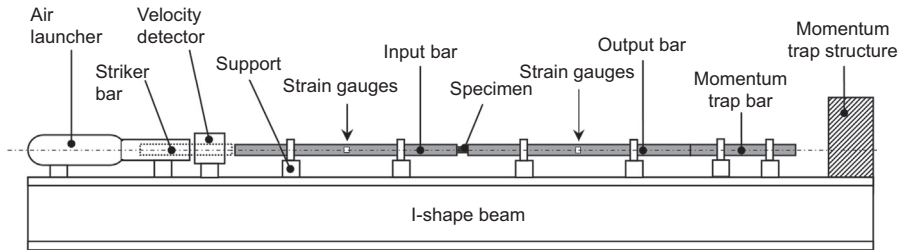


Figure 10.27 Typical schematic of the split Hopkinson pressure bar.

4. A pair of strain gauges mounted on each of the input and output bars; and
5. Associated instrumentation and data acquisition system to control, record and analyse the strain wave data (Gray, 1999).

The bars are usually made from the same material (Gray, 2003), eg, maraging steel (with a Young's modulus of 190–210 GPa) (Follansbee and Frantz, 1983; Lifshitz and Leber, 1994), AISI-SAE 4140 steel (190–210 GPa) (Kariem et al., 2010), titanium (110 GPa) (Gorham et al., 1992), aluminium (70 GPa) (Huh et al., 2002; Yew and Chen, 1978; Pervin et al., 2010), magnesium (45 GPa) (Gray, 2003; Gray et al., 1998) or polymeric materials (<20 GPa) (Zhao and Gary, 1995, 1997). The selection of the bar material depends on the sample material to be tested. The general rule for selecting the bar is that the bar should remain elastic during the entire experiment (ie, the yield strength of the bar is higher than the maximum compressive strength of specimen for the corresponding strain rate). Another consideration is the wave impedance properties, which are related to the bar sensitivity for the strain measurement. Bars manufactured from magnesium or PMMA might be preferred for dynamic characterisation of soft materials.

More recently Brown et al. (2016) have used the SHPB compression test method to observe the effects of radial confinement provided by the jacket of a 7.62 mm AK47 bullet, when impacting a boron carbide ceramic target. Sections of actual bullets, with and without the jacket material, were tested. The following sections describe the SHPB variants that have been established over the past 20 years or so.

10.6.1 SHPB for dynamic tensile experiments

The basic principle of a tensile SHPB is similar to the compressive SHPB. Please note that the negative sign is for a tensile pulse and vice versa. The main differences between these two techniques are the method for generating the pulse, specimen design and method for attaching the specimen (Gray, 2003). The following three methods of tensile SHPBs have been developed:

1. *Method 1.* In this method, developed by Lindholm and Yeakley (1968), the input bar is solid, while the output bar is a hollow tube. The specimen is of complex 'top-hat' geometry. During

the test, the specimen experiences a tensile load through four parallel bars that have similar geometry. The complex specimen geometry is the disadvantage of this method. However, this method can be conducted in a similar way to compressive SHPB, which implies that they use identical data analysis. Moreover, a hollowed tube of the output bar allows a rigid match with the input bars.

2. *Method 2.* This method involves a direct tensile loading of the input bar (Harding et al., 1960; Albertini and Montagnani, 1974). There are three different specimen geometries that are usually used: threaded axisymmetric circular, dumbbell-shaped and flat geometry. A hollow striker bar can be accelerated using a compressed gas breech or from a falling weight (in a vertical configuration of the apparatus).
3. *Method 3.* The third method (Nicholas, 1980) also uses a threaded circular specimen but the reflection wave is used as a tensile loading. A circular collar is applied to protect the specimen from the first compressive wave; however, it is unable to support any tensile loads because it is not fastened to the bars. The basic principle is similar with the SHPB for compressive test. When the end of the input bar receives a compressive pulse from the striker bar, it propagates along the bar and travels through the collar as if the specimen is not present (ideal condition). The pulse continues to travel until it reaches the free end of the input bars, and then it reflects and propagates back as a tensile pulse. The output bar acts like an input bar which gives the tensile pulse, ϵ_I , to the specimen. The tensile pulse is partially transmitted through the specimen, ϵ_T , and partially reflected back, ϵ_R , into the output bar.

As with any uniaxial tensile testing, necking occurs in the specimen. Thus, special data analysis has to be conducted because the average true stress cannot be calculated using standard SHPB analytical equations. High-speed photography may be applied to provide the dimensional change of the specimen, especially at the necking area. Thus, the analysis of the effective stress and strain can be obtained.

10.6.2 SHPB for dynamic torsion experiments

Baker and Yew (1966) introduced the torsional Kolsky bar in 1966. It was originally developed to eliminate two erroneous effects in experiments with the compressive Kolsky bar, which are the radial inertia effect in the specimen, and bars, and the radial traction between the specimen and the bars (if friction is not eliminated). The torsional Kolsky bar has proven to be very reliable in the strain rate range of 10^2 to 10^4 s^{-1} (Hartley et al., 1985). Higher strain rates have been conducted by Gilat and Cheng (2000, 2002). During the early 1970s, several modifications of the method to generate the torsional pulse were developed by investigators (Duffy et al., 1972; Nicholas and Lawson, 1972; Lewis and Campbell, 1972).

A torsional wave is generated in the input bar by the release of a stored torque (Nicholas and Lawson, 1972; Lewis and Campbell, 1972) or by an explosive detonation (Duffy et al., 1972). For the stored torque method, there were two designs of a clamping system that have been invented by Duffy (Hartley et al., 1985) and Gilat (Gilat and Cheng, 2000). In these cases, the specimen is held in position between the input and output bars either by using epoxy cement or by mechanical means.

10.6.3 SHPB for dynamic shear experiments

In the application of high-speed metal-forming operations, a high strain rate is expected. Therefore, the capability of the split Hopkinson pressure bar test has been extended to conduct (ISO/IEC 17025: 2005): double-notch shear test (Ferguson et al., 1967; Campbell and Ferguson, 1970; Gorham, 1979; ISO/IEC 17025: 2005), punch-test (Dowling et al., 1970) and (ASTM E83) shear test, by using a hat-shaped specimen (Hartmann et al., 1981; Beatty et al., 1992).

In the first technique, using a hollow tube to accommodate a double-notch shear specimen modifies the output bar. The effective gauge length in this specimen is 0.84 mm in which a shear strain rate of $40,000 \text{ s}^{-1}$ can be reached (Ferguson et al., 1967; Campbell and Ferguson, 1970).

Similar to the first technique, a hollow tube has also been used for the output bar of a punch-test using an SHPB. A flat-solid-circular shape is used for the specimen. In this design, the effective gauge length is determined by the gap between the outside diameter of the input bar and the inside diameter of the output bar. Dowling et al. (1970) used a clearance of 0.025 mm. However, it was found that the actual effective gauge length was considerably greater than this value. A shear strain rate of 10^4 s^{-1} has been reported.

The third technique uses a hat-shaped specimen which is sandwiched between the input and output bars of a standard compressive SHPB. A pulse shaper using a lead or copper disc of 3–5 mm (0.12–0.20 in.) in diameter and 0.25–0.5 mm (0.01–0.02 in.) thickness has been used to increase the rise time of the incident signal – this will reduce the ringing effect in the shear testing (Meyer and Schrödter, 1999; Beatty et al., 1992). High-speed photography has been used to record the deformation of specimen. The force–time ($F-t$) signal is constructed from the recorded transmitted strain, while the displacement–time ($s-t$) signal is constructed from the corresponding record of the high-speed photography. The shear stress–strain curve is then constructed from these two graphs.

In the study of shear band formation, it is desired to stop the shear displacement at a certain stage; therefore, a spacer ring can be used to stop the displacement at any target shear level (Andrade et al., 1994). The possible shear displacement (Δs) can be predetermined before the test by selecting an appropriate spacer ring length. One of the drawbacks of hat-shaped specimen experiments is the high-cost of specimen production due to high accuracy requirements.

10.6.4 SHPB for dynamic triaxial experiments

Brittle materials such as concrete or ceramics may require a triaxial loading condition in order to investigate their compressive properties and failure modes. This is due to the fact that their compressive properties and failure modes are dramatically affected by stress triaxiality. However, a modified SHPB can be used to conduct simultaneous axial and lateral loading to a specimen. The lateral compression may be applied through a pneumatic pressure vessel, as used by Christensen et al. (1972), Lindholm et al. (1974) and (Frew et al., 2010), or a dynamic load cell, as used by Rome et al. (2004).

In the early 1970s, Christensen et al. (1972) and Lindholm et al. (1974) developed a triaxial SHPB experiment by adding a pressure vessel to the test section of a standard

SHPB. The confining pressures of their devices were 207 and 690 MPa, respectively. A recent improvement of the triaxial experiment, which uses two chambers instead of one, has been conducted by [Frew et al. \(2010\)](#). The first chamber was used to employ a hydrostatic pressure on the specimen. This pressure would separate the interfaces. Thus, the second chamber was employed at the far end of the output bar to maintain the contact between input bar, specimen and output bar.

10.6.5 SHPB for dynamic fracture experiments

The SHPB technique has also been extended to the determination of the dynamic fracture toughness of notched specimens, K_{Id} . According to the way the force is applied to the crack, three groups can be classified: dynamic compressive loading, dynamic tensile loading and dynamic wedging. For dynamic compressive loading, several techniques have been developed such as one-point bending ([Homma et al., 1991](#)), three-point bending ([Jiang et al., 2004](#); [Mines and Ruiz, 1985](#); [Tanaka and Kagatsume, 1980](#); [Yokoyama and Kishida, 1989](#)), four-point bending ([Weerasooriya et al., 2006](#)), compact compression specimen ([Rittel et al., 1992](#)) and the Brazilian disc ([Zhou et al., 2006](#)). Dynamic tensile loading was employed by [Stroppe et al. \(1992\)](#) and [Owen et al. \(1998\)](#). Dynamic wedging was employed by [Klepaczko \(1982\)](#), who proposed using a wedge-loaded compact tension (WLCT) specimen in the conventional SHPB configuration.

[Figs. 10.28–10.37](#) show schematics of these various SHPB test set-ups.

Each technique has its own advantages and disadvantages. No standard method or even a well-agreed common approach for such experiments has been found yet ([Jiang and Vecchio, 2009](#)). However, the general rules among all of the above techniques are as follows:

1. Fundamental assumptions of the conventional SHPB technique should be maintained such as the system of the bars is linear and dispersion-free. This assumption implies that the one-dimensional stress wave analysis can be employed.
2. In most cases (except in the single loading bar), the stress equilibrium condition should be checked by comparing the one-wave and two-wave analyses. For a valid test, the stress equilibrium should be achieved prior to crack initiation.
3. Pulse shaping technique is strongly recommended in the SHPB for fracture testing. This technique increases the rise time and filters out the high-frequency oscillations.
4. In the WLCT configuration, the friction between the wedge and the specimen is a significant factor that is required to be included in the analysis.

10.7 Application of SHPB data

10.7.1 General implementation

The data generated by the above-mentioned SHPB tests are used, in the main, to refine the strength equations employed in numerical modelling of dynamic events. Chapter 9

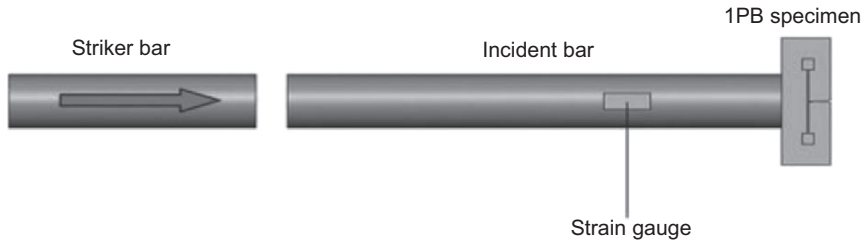


Figure 10.28 Schematic of the SHPB tension bar used to determine the dynamic fracture initiation toughness: one-point bending developed by [Homma et al. \(1991\)](#).

Homma, H., Kanto, Y., Tanaka, K., 1991. *Journal de Physique IV* 01, 589–596.

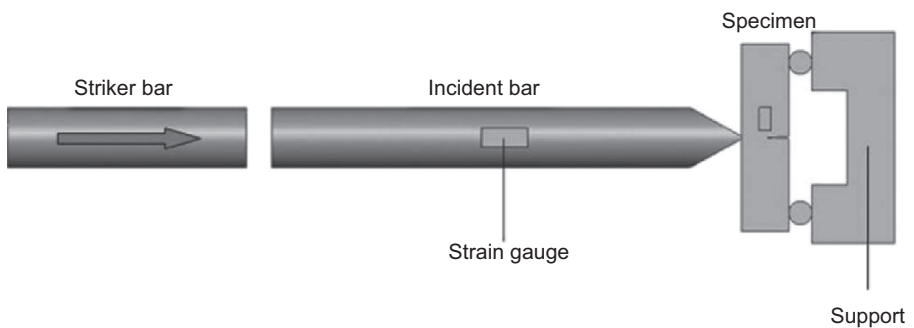


Figure 10.29 Schematic of the split Hopkinson tension bar used to determine the dynamic fracture initiation toughness: dynamic three-point bending developed by [Mines and Ruiz \(1985\)](#).

Mines, R.A.W., Ruiz, C., 1985. *Journal de Physique* 46, 187–196.

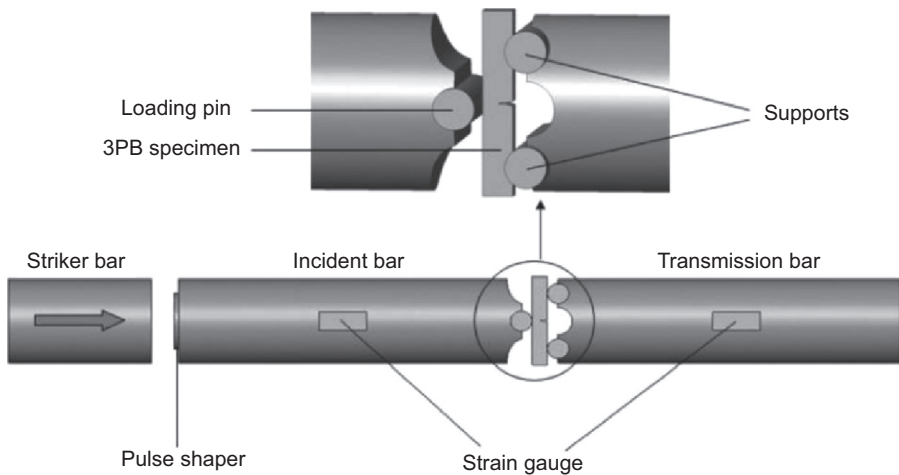


Figure 10.30 Schematic of the split Hopkinson tension bar used to determine the dynamic fracture initiation toughness: dynamic three-point bending developed by [Jiang et al. \(2004\)](#).

Jiang, F., Vecchio, K.S., 2009. *Applied Mechanics Reviews* 62, 060802–060839.

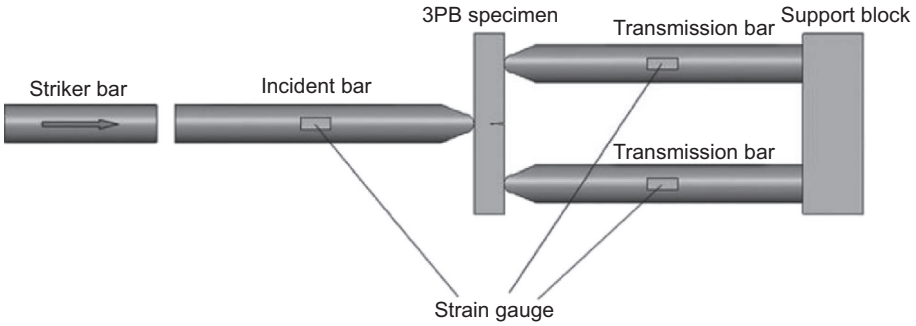


Figure 10.31 Schematic of the split Hopkinson tension bar used to determine the dynamic fracture initiation toughness: dynamic three-point bending developed by Yokoyama and Kishida (1989).

Yokoyama, T., Kishida, K., 1989. *Experimental Mechanics* 29, 188–194.

described, at length, the common strength models available (eg, Zerilli–Armstrong). Mathematical tools such as MatLab, are used to curve fit these data to the various strength models.

For example, the Cowper–Symonds strength model is one of the most popular phenomenological equations applied in impact problems (Lu and Yu, 2003). It explicitly represents the strength enhancement under dynamic loadings, using the following equation:

$$\frac{\sigma_d}{\sigma_Y} = 1 + \left(\frac{\dot{\epsilon}}{B} \right)^{1/q}$$

where σ_d and σ_Y are dynamic and quasistatic yield stresses respectively, B and q are material parameters. Typical values of B and q for some popular engineering materials are listed in Table 10.5.

The Johnson–Cook strength model is another widely used material model, which describes the flow stress of metals in terms of strain, strain rate and temperature (Johnson and Cook, 1985), using the following equation:

$$\sigma = \left(A + B \epsilon_p^n \right) (1 + C \ln \dot{\epsilon}^*) (1 - T^{*m})$$

where σ is the flow stress of the material, A is the yield stress, B is hardening modulus, ϵ_p is the equivalent plastic strain, n is hardening exponent, C is the strain rate coefficient, $\dot{\epsilon}^* = \dot{\epsilon}/\dot{\epsilon}_0$ is the dimensionless plastic strain rate for $\dot{\epsilon}_0 = 1.0 \text{ s}^{-1}$, m is a material constant, T^* is the homologous temperature and equal to:

$$T^* = \frac{T - T_0}{T_m - T_0}$$

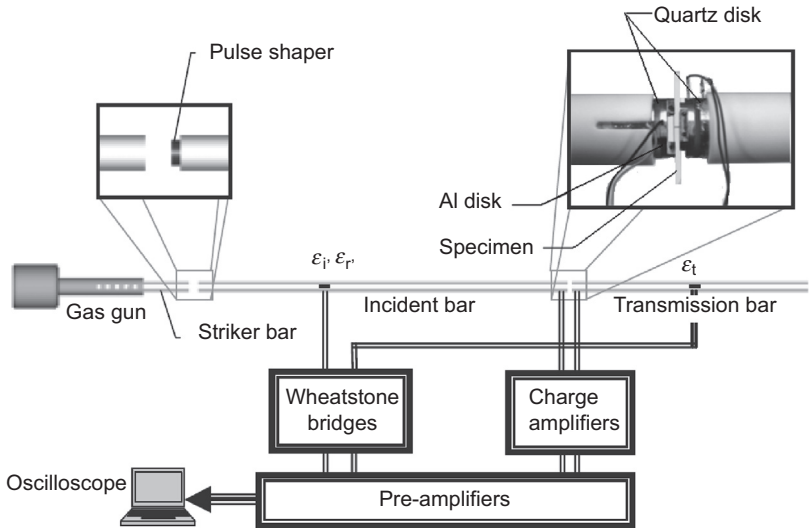


Figure 10.32 Schematic of the split Hopkinson tension bar used to determine the dynamic fracture initiation toughness: dynamic four-point bending developed by [Weerasooriya et al. \(2006\)](#).
Weerasooriya, T., Moy, P., Casem, D., Cheng, M., Chen, W., 2006. Journal of the American Ceramic Society 89, 990–995.

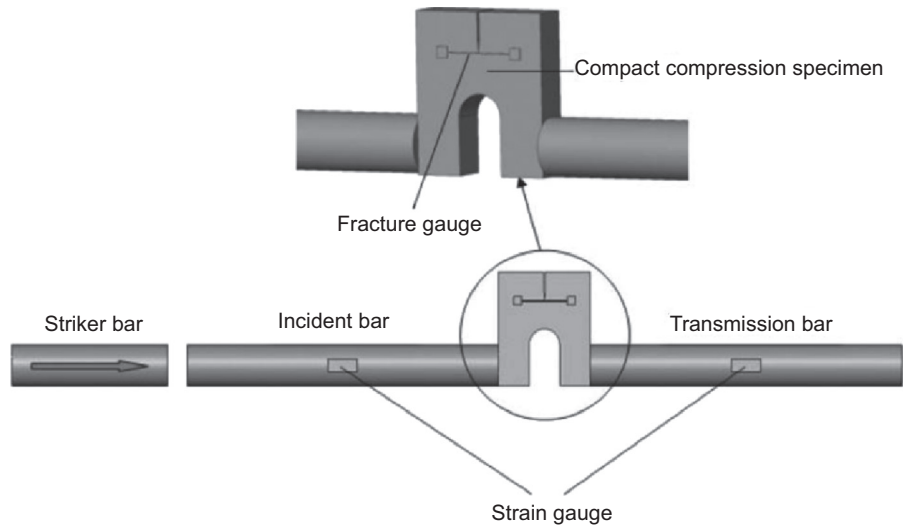


Figure 10.33 Schematic of the split Hopkinson tension bar used to determine the dynamic fracture initiation toughness: compact compression specimen set-up developed by [Rittel et al. \(1992\)](#).
Rittel, D., Maigre, H., Bui, H.D., 1992. Scripta Metallurgica et Materialia 26, 1593–1598.

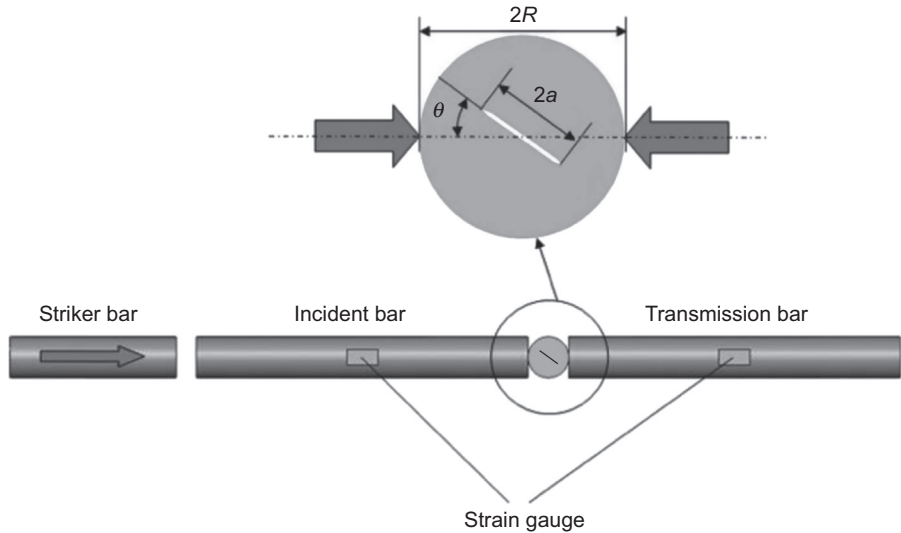


Figure 10.34 Schematic of the split Hopkinson tension bar used to determine the dynamic fracture initiation toughness: compact compression specimen set-up developed by Zhou et al. (2006).

Zhou, J., Wang, Y., Xia, Y., 2006. Journal of Materials Science 41, 8363–8366.

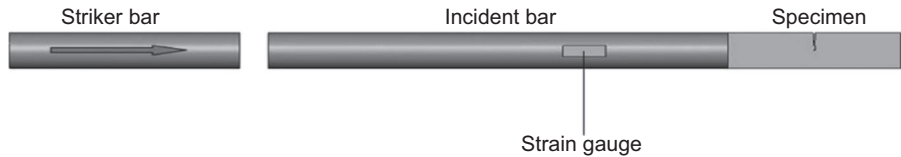


Figure 10.35 Schematic of the split Hopkinson tension bar used to determine the dynamic fracture initiation toughness: tensile fracture test developed by Stroppe et al. (1992). When the striker bar impacts the incident bar, a compressive wave is generated, propagates in the incident bar and transmits to the precracked specimen. When the compressive wave reaches the free end of the specimen, it reflects into a tensile wave and causes the crack growth or complete fracture of the specimen.

Stroppe, H., Clos, R., Schreppel, U., 1992. Nuclear Engineering and Design 137, 315–321.

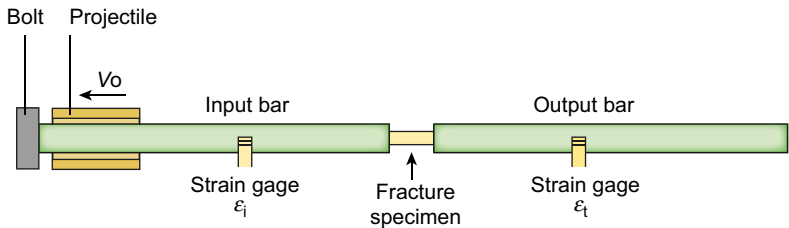


Figure 10.36 Schematic of the split Hopkinson tension bar used to determine the dynamic fracture initiation toughness: tensile fracture test developed by Owen et al. (1998).

Owen, D.M., Zhuang, S., Rosakis, A.J., Ravichandran, G., 1998. International Journal of Fracture 90, 153–174.

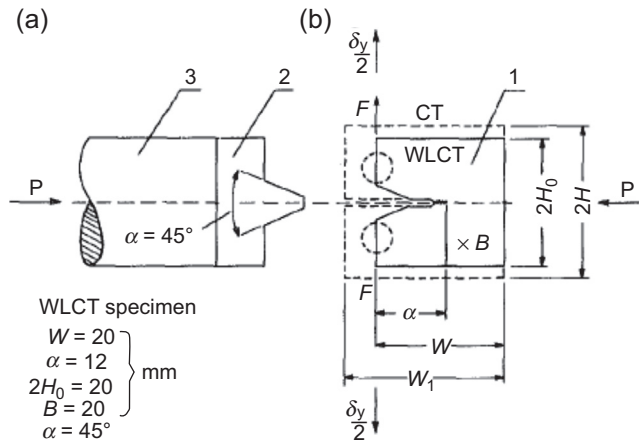


Figure 10.37 (a) Schematic of the split Hopkinson tension bar used to determine the dynamic fracture initiation toughness: WLCT and (b) the application of WLCT enables a tensile force F to be applied to the crack tip.

Klepaczko, J.R., 1982. *Journal of Engineering Materials and Technology* 104, 29–35.

Table 10.5 Typical values of B and q in Cowper–Symonds model for some popular engineering materials

Materials	B (s $^{-1}$)	q	References
Mild steel	40	5	Forrestal and Wesenberg (1977)
Stainless steel	100	10	Forrestal and Wesenberg (1978)
Titanium	120	9	Stronge and Yu (1993)
Aluminium 6061-T6	1.7×10^6	4	Symonds (1965)
Aluminium 3003-H14	0.27×10^6	8	Bodner and Speirs (1963)

Lu, G., Yu, T.X., 2003. Energy Absorption of Structures and Materials. Woodhead Publishing Limited, Cambridge, UK.

T_0 is the reference temperature and T_m is the melting temperature of the material.

Chapter 9 contains additional details of these strength models and provides comprehensive lists of the input material parameters for the full range of mathematical models. The following sections simply provide examples of the measured dynamic properties of various material families.

10.7.2 Armour steels

ARMOX 500T is a high-strength steel with excellent ballistic resistance. For its applications in armour, it is essential to understand its dynamic properties at high strain rates

and elevated temperature. By way of example, dynamic compressive tests of ARMOX 500T at high strain rates, from room temperature to 600°C, were conducted at Swinburne University of Technology by using a 14.5-mm diameter SHPB. The results are shown in Figs. 10.38–10.40, and demonstrate:

1. There was no evidence of strain hardening observed for the true flow stress of this steel.
2. The flow stress is not sensitive to strain rate from 1000 s^{-1} to 3000 s^{-1} .
3. The flow stress keeps almost constant at temperature below 150°C, while it decreases significantly at temperature beyond 300°C.

The above comprehensive test data can be used as the input of the material properties in computer simulation. They can also be used to derive the parameters in the relevant material models such as the Johnson–Cook model.

10.7.3 Metallic honeycombs and foams

Aluminium honeycombs and foams are cellular materials. They have high strength to weight ratio and attractive acoustic damping properties. They can undergo large deformation at almost constant force/stress to absorb a large amount of energy. Their mechanical properties were experimentally investigated by using a traditional MTS or Instron machine, a high-speed Instron machine and SHPBs at low strain rate (10^{-3} s^{-1}), moderate strain rate (10^2 s^{-1}) and high strain rate (10^3 s^{-1}), respectively. Zhao et al. (2005) conducted both quasistatic and dynamic tests on aluminium honeycombs and foams. The properties of the honeycomb cores are given in Table 10.6, and those of the metallic foams are given in Table 10.7 (Figs. 10.41 and 10.42). Strength

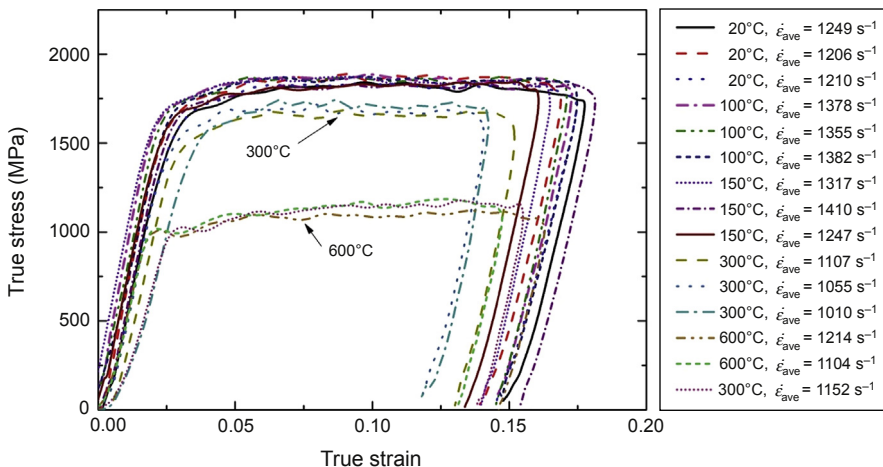


Figure 10.38 True stress–strain curves of high-strength steel (ARMOX 500T) at high strain rate (approximately 1000 s^{-1}) at 20°C, 100°C, 150°C, 300°C and 600°C.

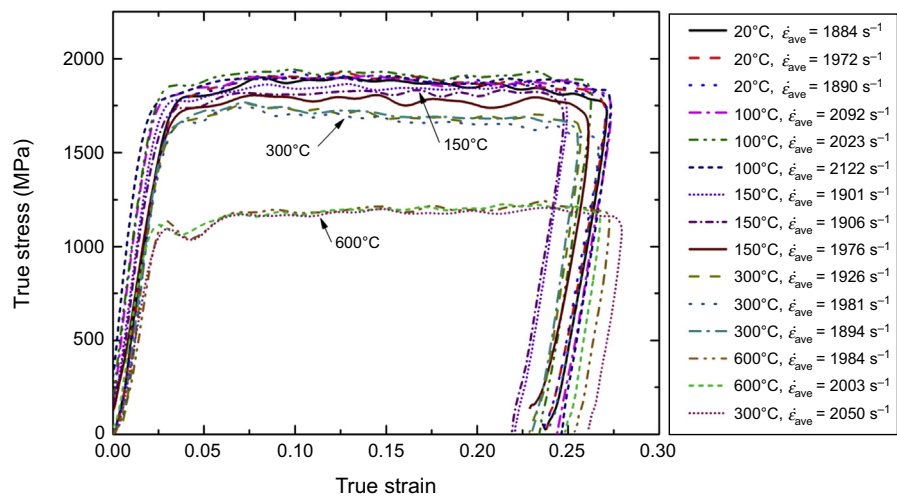


Figure 10.39 True stress—strain curves of high-strength steel (ARMOX 500T) at high strain rate (approximately 2000 s⁻¹) at 20°C, 100°C, 150°C, 300°C and 600°C.

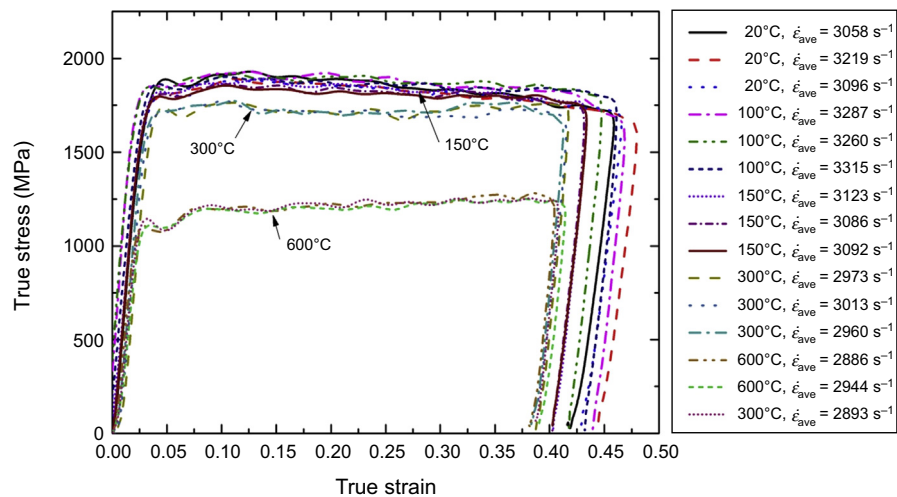


Figure 10.40 True stress—strain curves of high strength steel (ARMOX 500T) at high strain rate (approximately 3000 s⁻¹) at 20°C, 100°C, 150°C, 300°C and 600°C.

Table 10.6 Properties of honeycombs

Materials	h/S (mm/mm)	Density (kg/m^3)	Quasistatic (MPa)	Dynamic (MPa)	Difference (%)
5052	0.076/4.76	130	5.1	5.7	+12
5052	0.076/6.35	76	3	3.5	+17
5052	0.076/9.52	49	1.7	2	+15
5056	0.055/3	130	5.2	6	+15
5056	0.058/6	69	2.5	3	+20
5056	0.08/9.5	59	1.6	2	+25
5056	0.05/7	37	0.65	0.8	+12

Note: h and S are cell wall thickness and size of honeycombs, respectively.

Zhao, H., Elnasri, I., Abdennadher, S., 2005. International Journal of Mechanical Sciences 47, 757–774.

Table 10.7 Properties of IFAM and CYMAT foams

Foams	Cell size (mm)	Density (kg/m^3)	Quasistatic stress (MPa)	Dynamic stress (MPa)	Difference (%)
IFAM	5	600	13	15	+18
CYMAT	8	250	3	3	0

Zhao, H., Elnasri, I., Abdennadher, S., 2005. International Journal of Mechanical Sciences 47, 757–774.

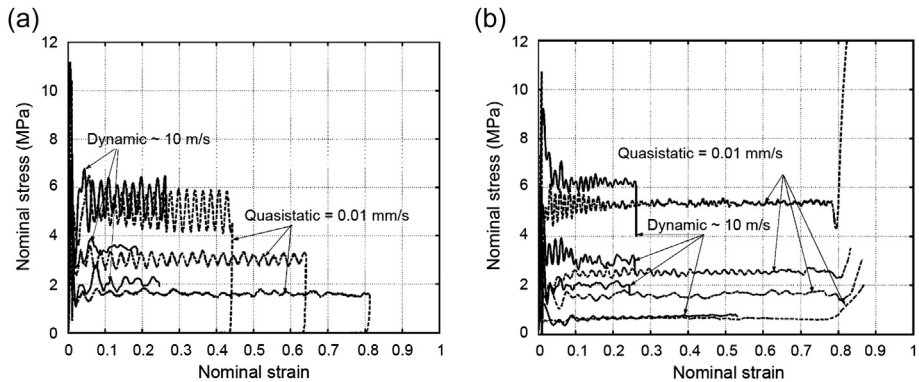


Figure 10.41 Out-of plane quasistatic and dynamic stress–strain curves for aluminium honeycombs: (a) 5052 (Abbasi-Bani, A., Zarei-Hanzaki, A., Pishbin, M.H., Haghdadi, N., 2014. *Mechanics of Materials* 71, 52–61.); (b) 5056 (Zhao, H., Elnasri, I., Abdennadher, S., 2005. *International Journal of Mechanical Sciences* 47, 757–774.).

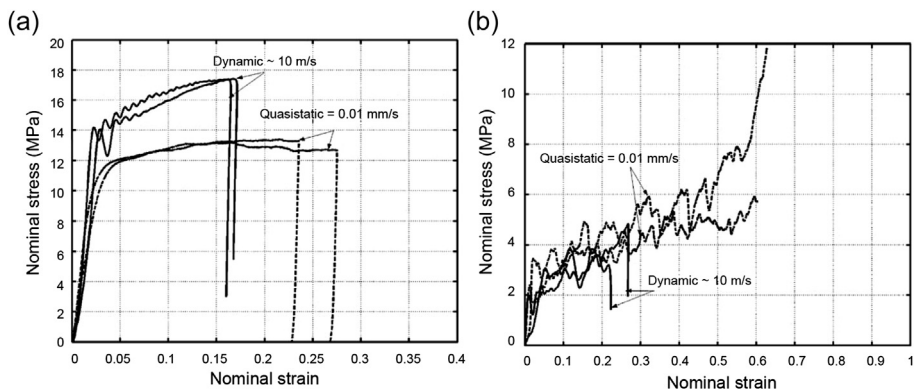


Figure 10.42 Out-of plane quasistatic and dynamic stress–strain curves for aluminium foams: (a) IFAM foam; (b) CYMAT foam. Zhao, H., Elnasri, I., Abdennadher, S., 2005. *International Journal of Mechanical Sciences* 47, 757–774.

enhancement with loading velocity was found in honeycombs and IFAM foam, but not in CYMAT foam.

In other work, [Shen et al. \(2010a\)](#) used the high-speed Instron at Swinburne University of Technology to conduct compressive tests on ALPORAS aluminium foam ([Fig. 10.43](#))

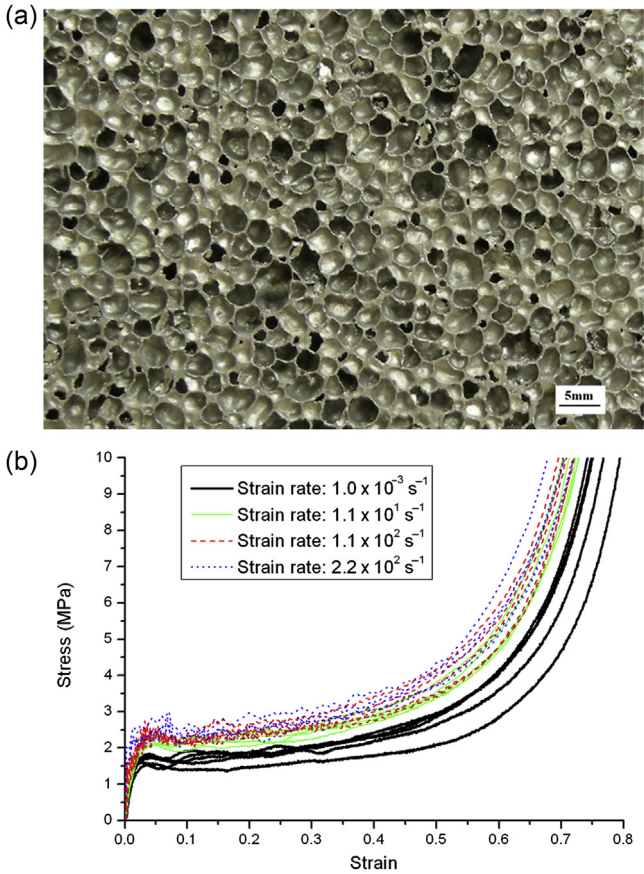


Figure 10.43 ALPORAS aluminium foam with a density of 240 kg/m^3 : (a) a photograph of the microstructure; (b) measured stress–strain curves at various strain rates.
Shen, J., Lu, G., Ruan, D., 2010a. Composites Part B: Engineering 41, 678–685.

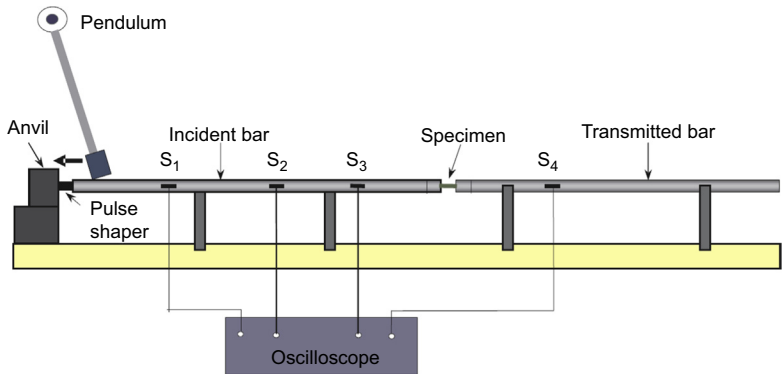


Figure 10.44 Sketch of the mini split Hopkinson tensile bar (mSHTB).
Ruan, D., Leung, M., Lu, G., Yu, T., Cao, J., Blicblau, A., 2009. Textile Research Journal 79, 444–452.

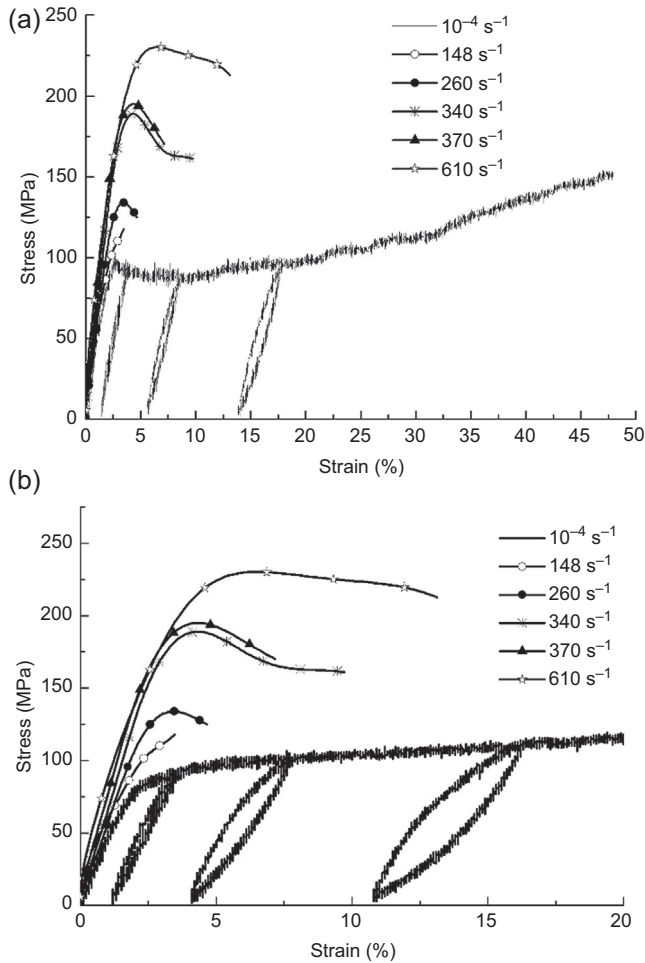


Figure 10.45 Measured stress–strain curves of Lincoln wool: (a) the whole graph; (b) an enlarged view with strain varying from 0% to 20%.

Ruan, D., Leung, M., Lu, G., Yu, T., Cao, J., Blicblau, A., 2009. Textile Research Journal 79, 444–452.

with a normal density of 9% (of solid aluminium) at strain rates of $1.1 \times 10^2 \text{ s}^{-1}$ and $1.1 \times 10^2 \text{ s}^{-1}$. Strength enhancement was observed (Fig. 10.43(b)) and could be expressed as follows:

$$\frac{\sigma_d}{\sigma_s} = 1 + 0.14\dot{\epsilon}^{0.17}$$

where σ_d , σ_s and $\dot{\epsilon}$ are dynamic stress, quasistatic stress and strain rate, respectively.

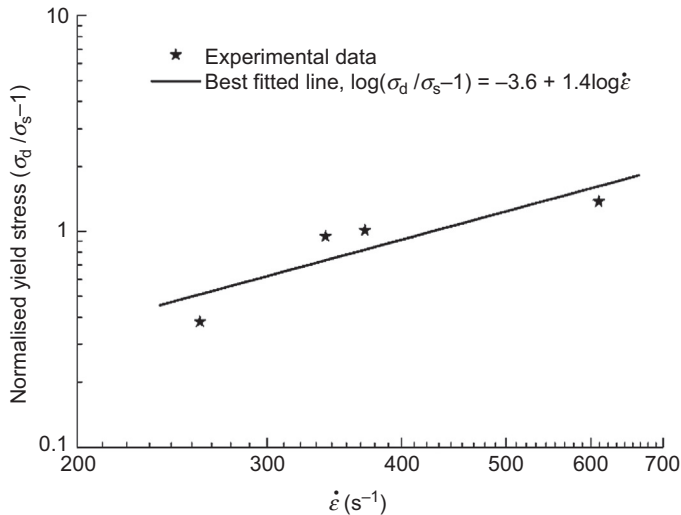


Figure 10.46 The relationship between yield stresses and strain rates for Lincoln wool fibres Ruan, D., Leung, M., Lu, G., Yu, T., Cao, J., Blicblau, A., 2009. Textile Research Journal 79, 4447–452.

10.7.4 Wool and aramid fibres

The mechanical properties of woollen fibres have been a subject of extensive research since the 1920s because wool fibres experience both static and dynamic loadings during their manufacturing processes and applications. Their tensile behaviour, under quasistatic loads, has been thoroughly studied, both experimentally and analytically, but only a few reports can be found in the open literature describing their impact response. Ruan et al. (2009) introduced a mini split Hopkinson tensile bar, mSHTB, as shown in Fig. 10.44, to obtain stress–strain curves of Lincoln wool fibres subjected to impact loadings at strain rates in the order of 10^2 s^{-1} .

The resultant impact stress–strain curves at various strain rates from mSHTB, together with the quasistatic stress–strain curve, are shown in Fig. 10.45, and the relationship between yield stress and strain rate is plotted in Fig. 10.46.

In contrast to the low-strength woollen fibres work, above, Tapie et al. (2015) published high strain rate testing results for aramid yarns, such as Twaron, which have applications in lightweight bullet vests and vehicle armour reinforcement. Virgin T1040 Twaron yarns and yarns extracted from plain-woven T717 Twaron fabric were tested using the tensile SHPB – Fig. 10.47 shows that the tensile strength of both types of fibre tensile split Hopkinson tensile bar increased with strain rate.

The reader is referred to Chapter 6 for more details of the high-strength/high-modulus fibres that are used in body armour systems.

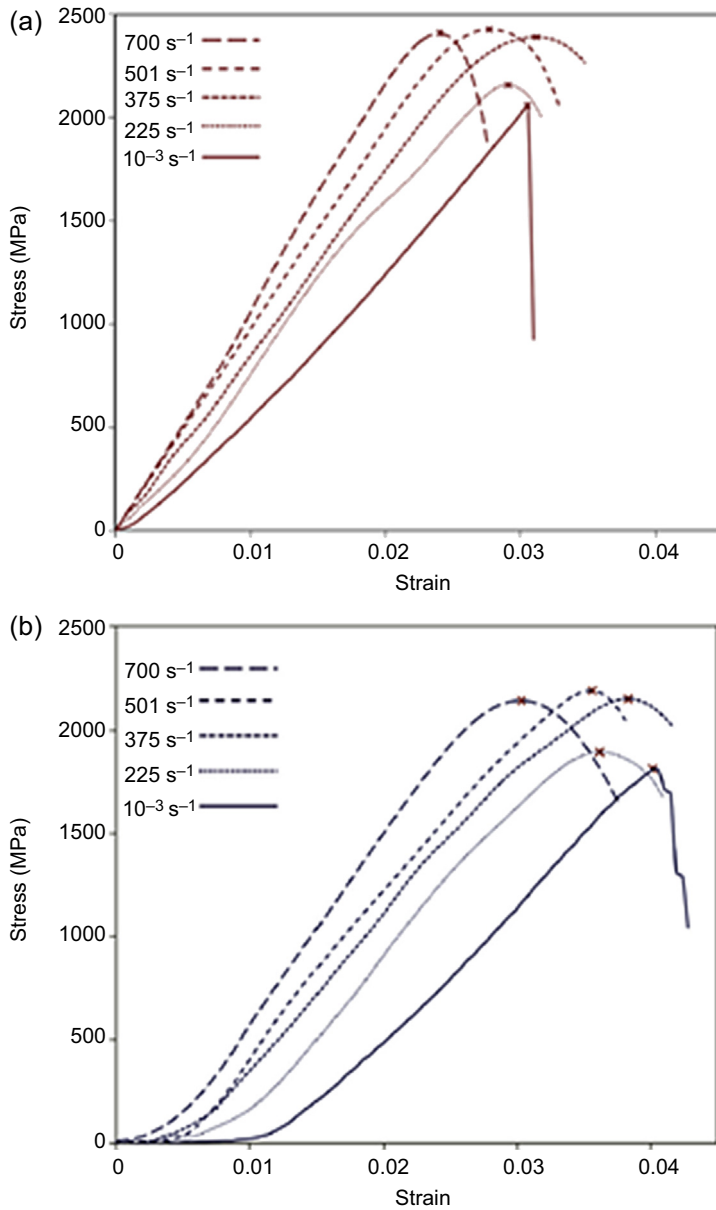


Figure 10.47 Tensile stress–strain curves of (a) virgin yarns and (b) woven yarns at various strain rates.

Tapie, E., Shim, V.P.W., Guo, Y.B., 2015. International Journal of Impact Engineering 80, 1–12.

10.7.5 Fibre-reinforced polymer composites

Fibre-reinforced polymers (FRPs) such as glass/vinyl ester and carbon/epoxy laminates can be applied in composite armour, as shown in Fig. 10.48 (Gama et al., 2001). The dynamic tests were conducted on plain-weave S-2 glass/vinyl ester composites using SHPB at strain rates between 200 and 1600 s⁻¹ by Gama et al. (2001). Specimens with rectangular cross-sections were used. It was found that dynamic maximum/ultimate stress increased with strain rate up to 675 s⁻¹, while it was kept constant at strain rates beyond 675 s⁻¹, as shown in Fig. 10.49.

The dynamic strength enhancement of S2-glass/epoxy fibre-reinforced composite was also measured by Vural and Ravichandran (2004) using an SHPB. On this occasion, the transverse strength was found to increase with strain rate and confining pressure, as shown in Fig. 10.50.

The dynamic through-thickness properties of one FRP (E-glass 24 oz woven roving in a vinyl ester, Derakane 8084 matrix) was also studied by Govender et al. (2011) using SHPB. The compressive strength was found to increase from 417 MPa at quasi-static to 462 MPa at strain rate of 510 s⁻¹ (see Fig. 10.51).

In very recent work by Woo and Kim (2014), a woven aramid composite showed a very strong rate-dependence, as shown in Fig. 10.52. This high dependence is probably due to the presence of the polymeric resin. This most recent work shows how low the TT properties of ballistic laminates can be, emphasising how vulnerable these laminates are to delamination, even though their TT properties improve at higher strain

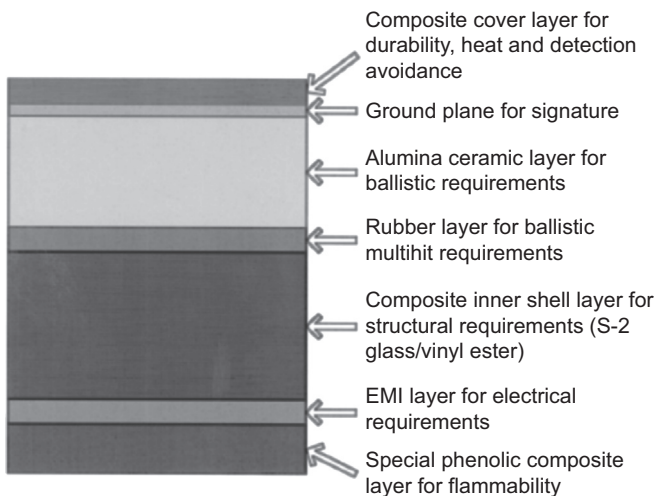


Figure 10.48 A range of material components of a multifunctional armour system, as proposed by Gama et al. (2001).

Gama, B.A., Gillespie Jr., J.W., Mahfuz, H., Raines, R.P., Haque, A., Jeelani, S., Bogetti, T.A., Fink, B.K., 2001. *Journal of Composite Materials* 35, 1201–1228.

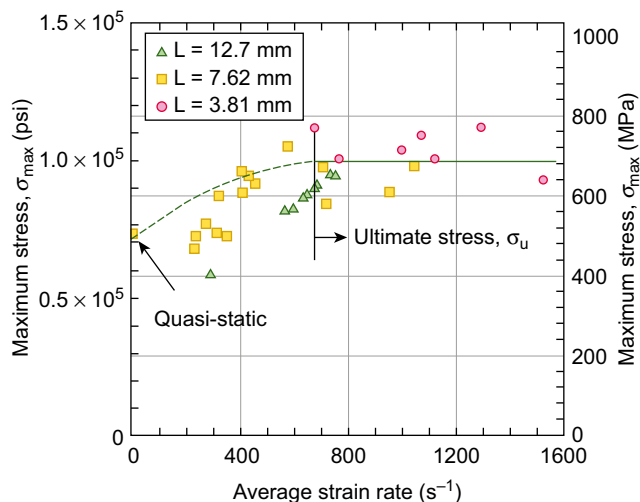


Figure 10.49 The effect of strain rate on the maximum/ultimate stress of S-2 glass/vinyl ester in the through-thickness direction. L is the thickness of the specimen.

Gama, B.A., Gillespie Jr., J.W., Mahfuz, H., Raines, R.P., Haque, A., Jeelani, S., Bogetti, T.A., Fink, B.K., 2001. *Journal of Composite Materials* 35, 1201–1228.

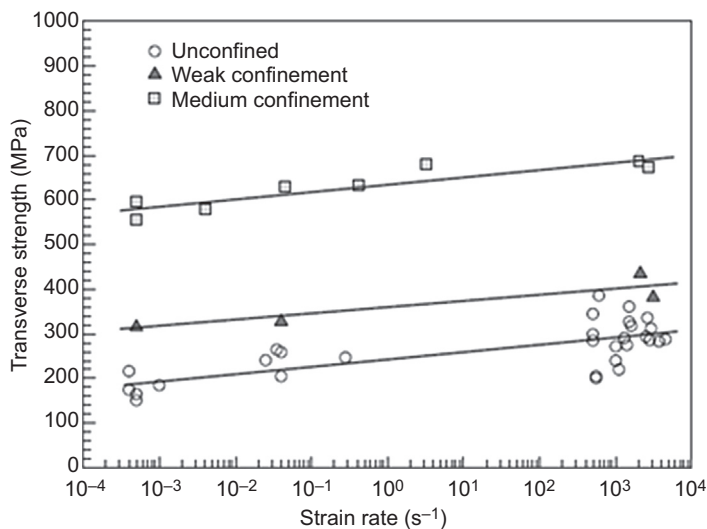


Figure 10.50 The effects of strain rate and degree of confinement on the transverse compressive strength of unidirectional S2-glass/epoxy fibre-reinforced composite.

Vural, M., Ravichandran, G., 2004. *Journal of Composite Materials* 38, 609–623.

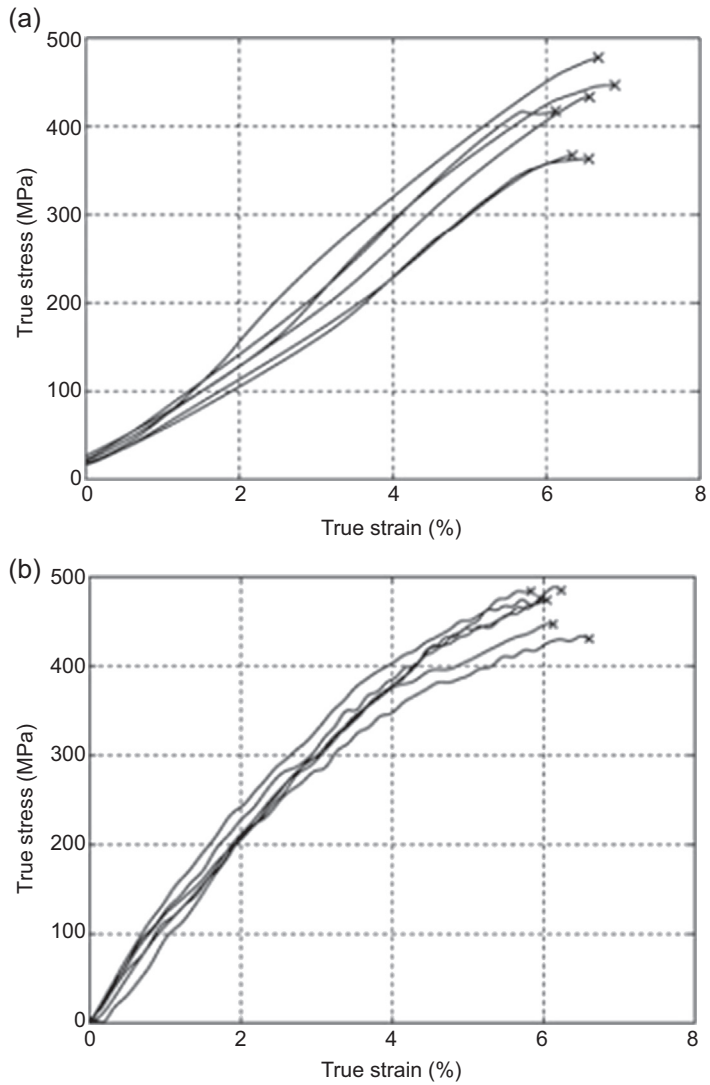


Figure 10.51 True stress–strain curves of FRP: (a) quasistatic; (b) dynamic at a strain rate of 510 s⁻¹.

Govender, R.A., Louca, L.A., Pullen, A., Fallah, A.S., Nurick, G.N., 2011. *Journal of Composite Materials* 46, 1219–1228.

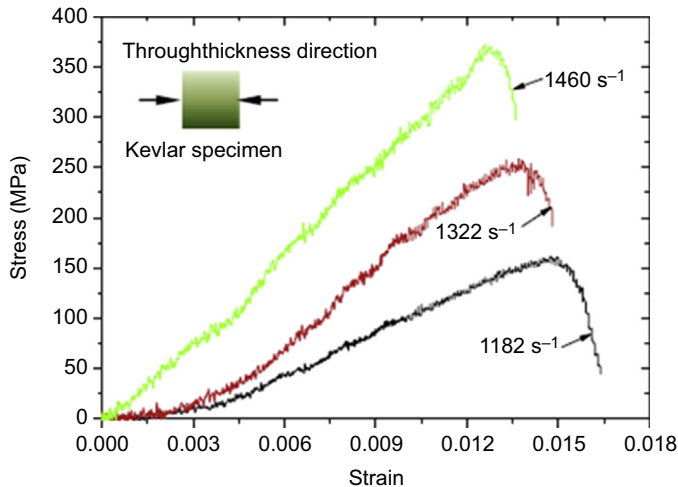


Figure 10.52 True stress—strain curves of FRP: (a) quasistatic; (b) dynamic at a strain rate of 510 s^{-1} .

Govender, R.A., Louca, L.A., Pullen, A., Fallah, A.S., Nurick, G.N., 2011. *Journal of Composite Materials* 46, 1219–1228.

rates. The reader is referred to Chapter 5 for more details of the fibre-reinforced polymers that are used in armour applications.

References

- Abbasi-Bani, A., Zarei-Hanzaki, A., Pishbin, M.H., Haghdadi, N., 2014. *Mechanics of Materials* 71, 52–61.
- Al-Mousawi, M.M., Reid, S.R., Deans, W.F., 1997. *Proceedings of the Institution of Mechanical Engineers – Part C – Journal of Mechanical Engineering Science* 211, 273–292.
- Albertini, C., Boone, P.M., Montagnani, M., 1985. *Le Journal de Physique Colloques* 46, 499–503.
- Albertini, C., Montagnani, M., 1974. *Testing Techniques Based on the Split Hopkinson Bar*.
- Anderson, S.P., 2006. *Journal of Sound and Vibration* 290, 290–308.
- Andrade, U., Meyers, M.A., Vecchio, K.S., Chokshi, A.H., 1994. *Acta Metallurgica et Materialia* 42, 3183–3195.
- ASM International, 2003. *ASM Handbooks Online*. ASM International, Materials Park, Ohio.
- ASTM E83 Standard Practice for Verification and Classification of Extensometer Systems.
- Baker, W.W., Yew, C.H., 1966. *Journal of Applied Mechanics* 33, 917–923.
- Beatty, J.H., Meyer, L.W., Meyers, M.A., Nemat-Nasser, S., 1992. In: Meyers, M.A., Murr, L.E., Staudhammer, K.P. (Eds.), *Shock Wave and High-Strain-Rate Phenomena in Materials*. Marcel Dekker, New York, pp. 645–656.
- Bodner, S.R., Speirs, W.G., 1963. *Journal of the Mechanics and Physics of Solids* 11, 65–77.
- Boteler, J.M., Dandekar, D.P., 2006. *Journal of Applied Physics* 100.

- Bourne, N., Millet, J., Pickup, I., 1997. *Journal of Applied Physics* 81.
- Bourne, N., Millet, J., Rosenberg, Z., Murray, N., 1998. *Journal of Mechanics and Physics of Solids* 46.
- Bourne, N., Rosenberg, Z., Crouch, I.G., Field, J.E., 1994. *Proceedings of the Royal Society of London A* 446, 309–318.
- Brown, L.B., Hazell, P.J., Crouch, I.G., Escobedo, J.P., Brown, A.D., Appleby-Thomas, G.J., 2016. Jacket effects during bullet penetration. In: *International Symposium on Ballistics*, Edinburgh, May 2016.
- Campbell, J.D., Ferguson, W.G., 1970. *Philosophical Magazine* 21, 63–82.
- Chen, R., Huang, S., Xia, K., Lu, F., 2009a. *Review of Scientific Instruments* 80, 076108–076113.
- Chen, R., Xia, K., Dai, F., Lu, F., Luo, S.N., 2009b. *Engineering Fracture Mechanics* 76, 1268–1276.
- Chen, W., Song, B., 2011. *Split Hopkinson (Kolsky) Bar: Design, Testing, Applications*. Springer, New York.
- Chen, W., Song, B., Frew, D., Forrestal, M., 2003. *Experimental Mechanics* 43, 20–23.
- Chen, W., Zhang, B., Forrestal, M., 1999. *Experimental Mechanics* 39, 81–85.
- Christensen, R., Swanson, S., Brown, W., 1972. *Experimental Mechanics* 12, 508–513.
- Crouch, I.G., March 1993. *Penetration and Perforation Mechanisms in Composite Armour Materials*, Euromech Colloquium 299. Oxford University.
- Crouch, I.G., Woodward, R.L., 1989. *International Conference on Mechanical Properties of Materials at High Rates of Strain*, Oxford, UK.
- Dandekar, D.P., 1998. *Journal of Applied Physics* 84, 6614–6622.
- Davies, P., Blackman, B.R.K., Brunner, A.J., 1998. *Applied Composite Materials* 5, 345–364.
- Deshpande, V.S., Fleck, N.A., 2000. *International Journal of Impact Engineering* 24, 277–298.
- Dharan, C., Hauser, F., 1970. *Experimental Mechanics* 10, 370–376.
- Dowling, A.R., Harding, J., Campbell, J.D., 1970. *Journal Institute of Metals* 98, 215–224.
- Duffy, J., Campbell, J.D., Hawley, R.H., 1972. *Journal of Applied Mechanics* 38, 83–91.
- Dunand, M., Gary, G., Mohr, D., 2013. *Experimental Mechanics* 53, 1177–1188.
- Edwards, M., 2006. *Journal of Materials Science and Technology* 22, 453–462.
- Enstock, L.K., Smith, P.D., 2007. *International Journal of Impact Engineering* 34, 487–494.
- Ferguson, W.G., Hauser, J.E., Dorn, J.E., 1967. *British Journal of Applied Physics* 18, 411–417.
- Field, J.E., Walley, S.M., Proud, W.G., Goldrein, H.T., Siviour, C.R., 2004. *International Journal of Impact Engineering* 30, 725–775.
- Field, J.E., Walley, S.M., Bourne, N.K., Huntley, J.M., September 1994. *Journal de Physique IV Colloque C8, supplement au Journal de Physique III* 4.
- Follansbee, P.S., Frantz, C., 1983. *Journal of Engineering and Materials Technology* 105, 61–66.
- Forde, L.C., Proud, W.G., Walley, S.M., 2008. Symmetrical Taylor impact studies of copper. *Proceedings of the Royal Society A: Mathematical. Physical and Engineering Sciences*. Retrieved from citeulike-article-id:3717650. <http://dx.doi.org/10.1098/rspa.2008.0205>.
- Forrestal, M.J., Wesenberg, D.L., 1977. *ASME Journal of Applied Mechanics* 44, 779–780.
- Forrestal, M.J., Wesenberg, D.L., 1978. *ASME Journal of Applied Mechanics* 45, 685–687.
- Frew, D.J., Akers, S.A., Chen, W., Green, M.L., 2010. *Measurement Science and Technology* 21, 105704.
- Gama, B.A., Gillespie Jr., J.W., Mahfuz, H., Raines, R.P., Haque, A., Jeelani, S., Bogetti, T.A., Fink, B.K., 2001. *Journal of Composite Materials* 35, 1201–1228.

- Gama, B.A., Lopatnikov, S.L., Gillespie Jr., J.W., 2004a. *Applied Mechanics Reviews* 57, 223–250.
- Gama, B.A., Xiao, J.-R., Haque, J., Gillespie, J.W., February 2004b. Army Research Laboratory Report, ARL-cr-534.
- Gilat, A., Cheng, C.-S., 2002. *International Journal of Plasticity* 18, 787–799.
- Gilat, A., Cheng, C., 2000. *Experimental Mechanics* 40, 54–59.
- Gong, J.C., Malvern, L.E., Jenkins, D.A., 1990. *Journal of Engineering Materials and Technology* 112, 309–314.
- Gorham, D.A., 1979. In: Harding, J. (Ed.), *Mechanical Properties at High Rates of Strain*. The Institute of Physics, Bristol, pp. 16–24.
- Gorham, D.A., Pope, P.H., Field, J.E., 1992. *Proceedings of the Royal Society of London Series A: Mathematical and Physical Sciences* 438, 153–170.
- Govender, R.A., Langdon, G.S., Nurick, G.N., Cloete, T.J., 2013. *Engineering Fracture Mechanics* 101, 80–90.
- Govender, R.A., Louca, L.A., Pullen, A., Fallah, A.S., Nurick, G.N., 2011. *Journal of Composite Materials* 46, 1219–1228.
- Grady, D.E., Olsen, M.L., 2003. *International Journal of Impact Engineering* 29, 293–306.
- Gray III, G.T., 2003. Classic split-Hopkinson pressure bar testing. In: Kuhn, H. (Ed.), *Mechanical Testing and Evaluation*, ASM Handbook, vol. 8. ASM International, Materials Parks, Ohio.
- Gray III, G.T., 1999. In: Kaufmann, E. (Ed.), *Methods in Materials Research*. John Wiley Press.
- Gray III, G.T., Idar, D.J., Blumenthal, W.R., Cady, C.M., Peterson, P.D., 1998. In: 11th International Detonation Symposium, Snowmass Village, CO, pp. 1–9.
- Guo, Y., Li, Y., 2012. *Acta Mechanica Solida Sinica* 25, 299–311.
- Hanssen, A.G., Enstock, L., Langseth, M., 2002. *International Journal of Impact Engineering* 27, 593–618.
- Harding, J., Wood, E.O., Campbell, J.D., 1960. *Journal of Mechanical Engineering Science* 2, 88–96.
- Hartley, K.A., Duffy, J., Hawley, R.H., 1985. In: Newby, J.R. (Ed.), *Mechanical Testing, Metals Handbook*, vol. 8. American Society for Metals, Metal Parks, Ohio, pp. 218–230.
- Hartmann, K.-H., Kunze, H.D., Meyer, L.W., 1981. In: Meyers, M.A., Murr, L.E. (Eds.), *Shock Wave and High-strain-rate Phenomena in Metals*. Plenum Press, New York, pp. 325–337.
- Haugou, G., Markiewicz, E., Fabis, J., 2006. *International Journal of Impact Engineering* 32, 778–798.
- Hazell, P.J., Appleby-Thomas, G.J., Wielewski, E., Stennett, C., Siviour, C., 2012. *Acta Materialia* 60, 6042–6050.
- Hiermaier, S., 2008. *Structures Under Crash and Impact: Continuum Mechanics, Discretization and Experimental Characterization*. Springer, New York.
- Homma, H., Kanto, Y., Tanaka, K., 1991. *Journal de Physique IV* 01, 589–596.
- Hopkinson, B., 1905. *Proceedings of the Royal Society* 498–507.
- Hopkinson, B., 1914. *Philosophical Transactions of the Royal Society of London Series A, Containing Papers of a Mathematical or Physical Character* 213, 437–456.
- Hopkinson, J., 1872. *Proceedings of the Manchester Literary and Philosophical Society* 40–45.
- Hou, W., Zhu, F., Lu, G., Fang, D.-N., 2010. *International Journal of Impact Engineering* 37, 1045–1055.
- Hu, Y., Feng, R., 2004. *Journal of Applied Mechanics* 71, 441–449.
- Huh, H., Kang, W., Han, S., 2002. *Experimental Mechanics* 42, 8–17.
- Hutchings, I.M., 2009. *Journal of Materials Research* 24, 581–589.

- ISO/IEC 17025: 2005, 2005. General Requirements for the Competence of Testing and Calibration Laboratories. International Organization for Standardization (ISO), Switzerland, p. 34.
- Jia, D., Ramesh, K.T., 2004. *Experimental Mechanics* 44, 445–454.
- Jiang, F., Rohatgi, A., Vecchio, K., Cheney, J., 2004. *International Journal of Fracture* 127, 147–165.
- Jiang, F., Vecchio, K.S., 2009. *Applied Mechanics Reviews* 62, 060802–060839.
- Johnson, G.R., Cook, W.H., 1985. *Engineering Fracture Mechanics* 21, 34–48.
- Jones, N., 1989a. *Structural Impact*. Cambridge University Press, UK.
- Jones, N., 1989b. *Applied Mechanics Review* 42, 95–115.
- Kamler, F., Niessen, P., Pick, R.J., 1995. *Canadian Journal of Physics* 73, 295–303.
- Kariem, M.A., Beynon, J.H., Ruan, D., 2010. Numerical simulation of double specimens in split Hopkinson pressure bar testing. In: *PRICM 7*, vol. 654–656. Trans Tech Publications, Cairns, Australia, pp. 2483–2486.
- Kariem, M.A., Beynon, J.H., Ruan, D., 2012. *International Journal of Impact Engineering* 47, 60–70.
- Kinoshita, S., 2011. Thesis. Swinburne University of Technology, Melbourne, Australia.
- Klepaczko, J.R., 1982. *Journal of Engineering Materials and Technology* 104, 29–35.
- Klepaczko, J.R., Nguyen, H.V., Nowacki, W.K., 1999. *European Journal of Mechanics – A/Solids* 18, 271–289.
- Kolsky, H., 1949. *Proceedings of the Physical Society Section B* 62B, 676–700.
- Lawn, B., Wilshaw, R., 1975. *Journal of Materials Science* 10, 1049–1081.
- Lewis, J., Campbell, J., 1972. *Experimental Mechanics* 12, 520–524.
- Li, W., Xu, J., 2009. *Materials Science and Engineering: A* 513–514, 145–153.
- Lifshitz, J.M., Leber, H., 1994. *International Journal of Impact Engineering* 15, 723–733.
- Lindholm, U., Yeakley, L., 1968. *Experimental Mechanics* 8, 1–9.
- Lindholm, U.S., 1964. *Journal of the Mechanics and Physics of Solids* 12, 317–335.
- Lindholm, U.S., Yeakley, L.M., Nagy, A., 1974. *International Journal of Rock Mechanics and Mining Sciences and Geomechanics Abstracts* 11, 181–191.
- Lu, G., Yu, T.X., 2003. *Energy Absorption of Structures and Materials*. Woodhead Publishing Limited, Cambridge, UK.
- Malinowski, J., Klepaczko, J., Kowalewski, Z., 2007. *Experimental Mechanics* 47, 451–463.
- McShane, G.J., Radford, D.D., Deshpande, V.S., Fleck, N.A., 2006. *European Journal of Mechanics – A/Solids* 25, 215–229.
- Meyer, L.W., Schrödter, A., 1999. ACAM. Canberra.
- Meyers, M.A., 1994. *Dynamic Behavior of Materials*. John Wiley & Sons, Inc., New York.
- Mines, R.A.W., Ruiz, C., 1985. *Journal de Physique* 46, 187–196.
- Mott, N.F., 1947. *Proceedings of the Royal Society* 6, 300–308.
- Nahme, H., Lach, E., 1997. *Journal de Physique IV JP 7 (C3)*, 373–378.
- Nemat-Nasser, S., Isaacs, J., Starrett, J., 1991. *Proceedings of the Royal Society of London Series A: Mathematical and Physical Sciences* 435, 371–391.
- Nicholas, T., 1980. *Experimental Mechanics* 21, 177–185.
- Nicholas, T., Lawson, J.E., 1972. *Journal of the Mechanics and Physics of Solids* 20, 57–64.
- Nurick, G.N., Martin, J.B., 1989a. *International Journal of Impact Engineering* 8, 171–186.
- Nurick, G.N., Martin, J.B., 1989b. *International Journal of Impact Engineering* 8, 159–170.
- Owen, D.M., Zhuang, S., Rosakis, A.J., Ravichandran, G., 1998. *International Journal of Fracture* 90, 153–174.

- Paris, V., Frage, N., Dariel, M.P., Zaretsky, E., 2010. *International Journal of Impact Engineering* 37, 1092–1099.
- Pervin, F., Chen, W.W., Weerasooriya, T., 2010. *Journal of the Mechanical Behavior of Biomedical Materials* 4, 76–84.
- Radford, D.D., Deshpande, V.S., Fleck, N.A., 2005. *International Journal of Impact Engineering* 31, 1152–1171.
- Radford, D.D., Fleck, N.A., Deshpande, V.S., 2006. *International Journal of Impact Engineering* 32, 968–987.
- Ramesh, K.T., 2008. In: Sharpe (Ed.), *Handbook of Experimental Solid Mechanics*. Springer.
- Rathbun, H.J., Radford, D.D., Xue, Z., He, M.Y., Yang, J., Deshpande, V., Fleck, N.A., Hutchinson, J.W., Zok, F.W., Evans, A.G., 2006. *International Journal of Solids and Structures* 43, 1746–1763.
- Rathnaweera, G., 2014. Thesis. Swinburne University of Technology, Melbourne, Australia.
- Reid, S.R., Reddy, T.Y., Ho, H.M., Crouch, I.G., Greaves, L.J., 1995. Dynamic indentation of thick fibre-reinforced composites. In: *ASME Conference on High Strain Rate Behavior of Composites*, San Francisco, November 1995.
- Rittel, D., Maigre, H., Bui, H.D., 1992. *Scripta Metallurgica et Materialia* 26, 1593–1598.
- Rome, J., Isaacs, J., Nemat-Nasser, S., 2004. In: Gdoutos, E.E. (Ed.), *Recent Advances in Experimental Mechanics*. Springer, Netherlands, pp. 3–12.
- Rosenberg, Z., Dekel, E., 2012. *Terminal Ballistics*. Springer-Verlag, Berlin.
- Ruan, D., Leung, M., Lu, G., Yu, T., Cao, J., Blichblau, A., 2009. *Textile Research Journal* 79, 444–452.
- Rubino, V., Deshpande, V.S., Fleck, N.A., 2009. *European Journal of Mechanics – A/Solids* 28, 14–24.
- Russell, B.P., Liu, T., Fleck, N.A., Deshpande, V.S., 2012. *International Journal of Impact Engineering* 48, 65–81.
- Scott, B.R., 2011. In: *26th International Symposium on Ballistics*, Miami, FL, USA, September 2011.
- Shen, J., Lu, G., Ruan, D., 2010a. *Composites Part B: Engineering* 41, 678–685.
- Shen, J., Lu, G., Wang, Z., Zhao, L., 2010b. *International Journal of Impact Engineering* 37, 960–970.
- Shen, J., Lu, G., Zhao, L., Qu, Z., 2011. *Journal of Performance of Constructed Facilities* 25, 382–393.
- Shen, J., Lu, G., Zhao, L., Zhang, Q., 2013. *Engineering Structures* 55, 56–65.
- Shergold, O.A., Fleck, N.A., Radford, D., 2006. *International Journal of Impact Engineering* 32, 1384–1402.
- Silva, C., Rosa, P., Martins, P., 2009. *International Journal of Mechanics and Materials in Design* 5, 281–288.
- Simmons, M.J., Smith, T.F., Crouch, I.G., 1989. Delamination of metallic composites subjected to ballistic impact. In: *11th International Symposium on Ballistics*, Brussels, Belgium, May 1989.
- Specification. MIL-STD-2149A(SH). Standard procedures for explosion testing ferrous and non-ferrous metallic materials and weldments, dated 2nd February 1990.
- Sridharan, S.E., 2008. *Delamination Behaviour of Composites*. Woodhead Publishing, Cambridge, UK.
- Stilp, A.J., Hohler, V., 1990. In: Zukas, J.A. (Ed.), *Impact Dynamics*. Wiley and Sons, New York, pp. 515–592.
- Stronge, W.J., 2000. In: *Impact Mechanics*. Cambridge University Press, Cambridge, UK.

- Stronge, W.J., Yu, T.X., 1993. *Dynamic Models for Structural Plasticity*. Springer-Verlag, London, UK.
- Stroppe, H., Clos, R., Schreppel, U., 1992. *Nuclear Engineering and Design* 137, 315–321.
- Symonds, P.S., 1965. *Behavior of Materials Under Dynamic Loading* 106–124.
- Tabor, D., 1951. *The Hardness of Metals*. Clarendon Press, Oxford, UK.
- Tagarielli, V.L., Deshpande, V.S., Fleck, N.A., 2007. *International Journal of Solids and Structures* 44, 2442–2457.
- Tagarielli, V.L., Deshpande, V.S., Fleck, N.A., 2010. *International Journal of Impact Engineering* 37, 854–864.
- Tanaka, K., Kagatsume, T., 1980. *Bulletin of the Japan Society Mechanical Engineering* 23, 1736–1744.
- Tanimoto, Y., Nishiwaki, T., Nemoto, K., 2006. *Dental Materials Journal* 25, 234–240.
- Tapie, E., Shim, V.P.W., Guo, Y.B., 2015. *International Journal of Impact Engineering* 80, 1–12.
- Taylor, G.I., 1946. *Journal of the Institute of Civil Engineers* 26, 486–518.
- Thomas, S., Crouch, I.G., 2015. DMTC unpublished data.
- Vural, M., Ravichandran, G., 2004. *Journal of Composite Materials* 38, 609–623.
- Weerasooriya, T., Moy, P., Casem, D., Cheng, M., Chen, W., 2006. *Journal of the American Ceramic Society* 89, 990–995.
- Woo, S.-C., Kim, T.-W., 2014. *Composites: Part B* 60, 125–136.
- Wood, M.D.K., et al., 2007. *Journal of Composite Materials* 41, 1743–1772.
- Woodward, R., Crouch, I.G., 1988. Report MRL-r-1111. Materials Research Laboratory.
- Woodward, R.L., De Morton, M.E., 1976. *International Journal of Mechanical Sciences* 18, 119–127.
- Wu, X.Y., Ramesh, K.T., Wright, T.W., 2003. *International Journal of Solids and Structures* 40, 4461–4478.
- Wulf, G.I., Richardson, G.T., 1974. *Journal of Physics E: Scientific Instruments* 7, 167–169.
- Xu, S., Shen, J., Beynon, J.H., Ruan, D., Lu, G., 2011. In: *Fragmeni, Venkatesan, Lam, Setunge (Eds.), pp. 727–732*.
- Yahaya, M.A., Ruan, D., Lu, G., Dargusch, M.S., 2015. *International Journal of Impact Engineering* 75, 100–109.
- Yew, E.H., Chen, C.S., 1978. *Journal of Applied Mechanics and Transactions of the ASME* 45, 940–942.
- Yokoyama, T., Kishida, K., 1989. *Experimental Mechanics* 29, 188–194.
- Zhang, Y., et al., 2006. *Journal of Applied Physics* 100, 113536.
- Zhao, H., 1997. *Polymer Testing* 16, 507–516.
- Zhao, H., Abdennadher, S., Othman, R., 2006. *International Journal of Impact Engineering* 32, 1174–1189.
- Zhao, H., Elnasri, I., Abdennadher, S., 2005. *International Journal of Mechanical Sciences* 47, 757–774.
- Zhao, H., Gary, G., 1995. *Journal of the Mechanics and Physics of Solids* 43, 1335–1348.
- Zhao, H., Gary, G., 1997. *Journal of the Mechanics and Physics of Solids* 45, 1185–1202.
- Zhao, H., Gary, G., 1998. *International Journal of Impact Engineering* 21, 827–836.
- Zhao, P.D., Lu, F.Y., Lin, Y.L., Chen, R., Li, J.L., Lu, L., 2012. *Experimental Mechanics* 52, 205–213.
- Zhou, J., Wang, Y., Xia, Y., 2006. *Journal of Materials Science* 41, 8363–8366.
- Zhu, F., Longmao, Z., Guoxing, L., Emad, G., 2009a. *International Journal of Impact Engineering* 36, 687–699.

- Zhu, F., Lu, G., 2007. *Electronic Journal of Structural Engineering* 7, 92–101.
- Zhu, F., Zhao, L., Lu, G., Wang, Z., 2008a. *International Journal of Impact Engineering* 35, 937–951.
- Zhu, F., Zhao, L., Lu, G., Wang, Z., 2008b. *Advances in Structural Engineering* 11, 525–536.
- Zhu, F., Zhihua, W., Guoxing, L., Dong, R., 2009b. *International Materials Engineering Innovation* 1, 133–153.
- Zukas, J.A., 1982. *Impact Dynamics*. Wiley, NY.

Ballistic testing methodologies

11

I.G. Crouch¹, B. Eu²

¹Armour Solutions Pty Ltd, Trentham, Victoria, Australia; ²Ballistic and Mechanical Testing, Port Melbourne, Victoria, Australia

11.1 General introduction

When attempting to understand armour materials and systems, or develop new ones, there is naturally no better place to start than with an actual ballistic impact test from a real-life projectile. However, the chaotic environment of today's battlefields makes it extremely difficult to obtain an up-to-date assessment of the current threat (albeit a very essential step of course) and then to set out a prescribed threat spectrum against which the armour technologists and engineers must develop an appropriate armour system. Specifying the threat spectrum is the most difficult, and most responsible, task: developing an armour system to defeat those specified threats is, in comparison, a relatively simple, albeit challenging task. Armour designers and engineers have, however, developed a set of design aids and test methods that facilitate this process — the simplest, of course, being the ballistic impact test itself. This chapter will be devoted to providing the reader, not with standard procedures (which can be found elsewhere — see references), but with various testing options, the philosophies behind them and their role in understanding the science of armour materials. If the reader requires a visual overview of the entire process, from designing an armour system through to ballistic testing, they should visit the episode of the TV series 'How do they do it', July 2014, called 'Beekeeping, Trikes and Body Armour' (Anon, 2014), with the punch line of '*two centimetres of pure science — saving lives on the front-line*'. The short documentary features the authors and shows off the facilities of Ballistic and Mechanical Testing (BMT), Melbourne, Australia.

11.1.1 The testing environment

A ballistic testing laboratory must never lose sight of the fact that the products it tests are designed to protect and save lives.

In order to conduct a fair test there are several levels of independent accreditation that a test house can use to demonstrate compliance. At the top level, in Australia, there is the National Association of Testing Authorities (NATA), which can ensure that a documented quality system is in place and that full traceability of the test data can be managed in strict accordance with internationally recognised test standards. One such standard is ISO/IEC 17,025:2005 — General Requirements for the Competence of Testing and Calibration Laboratories which governs laboratory quality management.

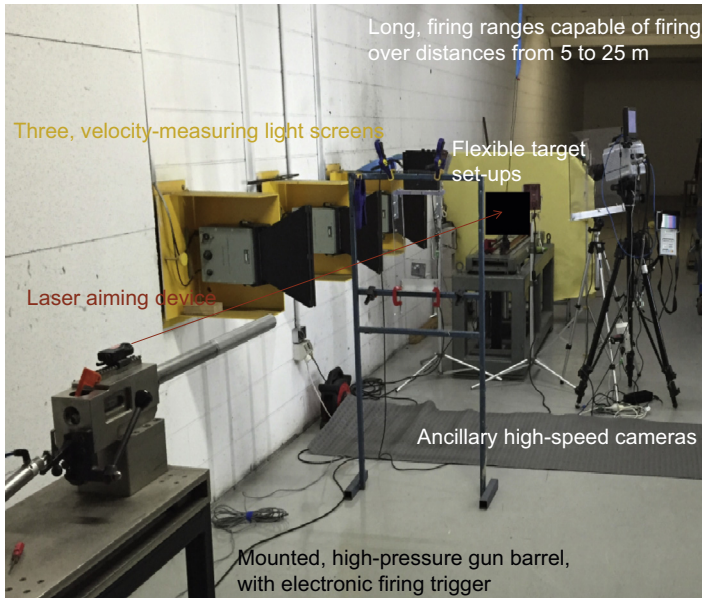


Figure 11.1 Typical ballistic testing arrangement for lightweight armour products.

In addition, further independent accreditation must be in place for each test standard that the laboratory conducts; once again, as assurance that competence has been demonstrated and assessed independently. A typical ballistic testing range set-up is shown in [Fig. 11.1](#).

These independent accreditations demonstrate that the ballistic testing laboratory can meet its objectives to provide test conditions that are fair, reproducible, reportable and auditable:

- An ability to perform any ballistic test to any test standard.
- A controlled environment within a climatic range (typically $21^{\circ}\text{C} \pm 5^{\circ}\text{C}$ and $\text{RH } 50\% \pm 20\%$).
- All testing equipment is calibrated within the required measurement uncertainty.
- The correct threat ammunition types are being used.
- The correct launching equipment is being used and stable bullet flight is being achieved and monitored.
- A well-defined set of charge weight/velocity relationships, thus enabling the range officer to provide any impact velocity, from a range of projectiles, including those that exceed the normal muzzle velocity that would typically be achieved when a projectile is fired from a conventional firearm.
- Highly accurate impact velocity measuring equipment capable of detecting a wide range of projectiles, including fragment-simulating projectiles, fired across a broad range of velocities.
- A well-established set of gun-to-target distances for delivery of yaw-free projectiles at a point of impact within $\pm 5 \text{ mm}$ (typically) and within a required strike angle of incidence range.
- A range of preconditioning chambers for armour types so that various environmental conditions can be simulated for controlled laboratory evaluation of armour performance in a range of situations: including high temperatures, subzero temperatures, varying humidity, low

pressure, deep water immersion, solar radiation, transport, drop/rough handling and combinations of these.

The use of projectiles as specified in the test standard is mandatory. Almost all ballistic test standards will specify a range of protection levels and corresponding test projectiles that are to be used. The use of substitute or surrogate ammunition is not an acceptable practice in the ballistic testing laboratory. An armour system will be designed to defeat and therefore protect against a specified threat – if the armour is not being tested with said threat there can be no guarantee of compliance. This requirement extends further to the materials which test bullets are constructed of. For example, NIJ (National Institute of Justice) Standard 0101.04 requires a 7.62-mm M80 bullet with a steel jacket. NIJ Standard 0101.06 goes further and specifies the bullet manufacturer and actual part number.

Controlling bullet velocity across the entire inventory of test bullets is another area of skill that is required of the laboratory range operators. The reliable function of factory-loaded ammunition can be affected by factors such as age, environmental exposure and manufacturing quality, all of which affect achievement of the required test velocity or the correct velocity spread tolerance. To overcome this, some laboratories will temperature condition the factory-loaded ammunition in an attempt to control the velocity. BMT's preferred method is to dismantle the factory-loaded round and hand-load it using best-practice techniques to achieve a low standard deviation across a series of shots. This level of velocity control affords the armour designer the flexibility to specify and work within a velocity range while developing an armour solution. Another key reason for a high level of velocity control is to reduce the need for repeated strikes and therefore minimise the likelihood of an unfair strike during the test. An armour sample may degrade slightly after each impact so, while permitted by some test standards, placing more than the required number of impacts onto a single target can be unrealistic and could result in an unfair assessment of the armour's performance.

Through the course of armour development, the ballistic testing laboratory will invariably be required to explore the upper protection limits of the armour system against the test bullet. This requires the laboratory to achieve velocities well in excess of those achieved when firing the factory-loaded ammunition from a conventional firearm. This may also be the case during ballistic limit testing. Pushing a bullet beyond the muzzle velocity that it was designed for can lead to instability in flight or excessive yaw, often called 'tumbling'.

Delivering a yaw-free bullet to the test sample is vital and cannot be emphasised enough. A bullet impacting off axis (yawing) has significantly reduced performance against armour, especially with armour-piercing bullets. The reality is that reduced bullet performance due to yaw will give a 'false-high' result in the ballistic test leading to a very dangerous and undesirable situation.

To give an anecdotal example of this, BMT had a client who was testing in the United Kingdom while developing an armour solution to protect against the Bofors 7.62 mm × 51 mm FFV (Försvarets Fabriksverk), an armour-piercing round with a tungsten carbide core. The armour solution was consistently and comfortably defeating the round. Towards the end of the testing the laboratory checked and found that the



Figure 11.2 An example of a yaw card with a number of different perforations.

bullets had been yawing which required rejection of the test data and a wasteful use of time and resources.

Yaw, or the absence of yaw, can be detected in several ways, most commonly either by high-speed filming of the bullet in flight referenced against a graticule, or through the use of ‘yaw cards’. A yaw card is a very thin, flat piece of material that is placed in front of the armour and the bullet fired through it. The material used for the yaw card must be carefully selected so that the bullet cuts a clean hole, allowing careful analysis of the perforation. Fig. 11.2 illustrates the extreme range of possible yaw. Some methods for measuring yaw are to simply measure the ovality of the hole in the yaw card. The authors’ preferred method is to make a simple go/no-go gauge from shim material and hold it over the hole to determine if yaw is present. Most ballistic test standards specify an acceptable upper level of yaw, typically about 3–5 degrees. Controlling bullet stability, within acceptable limits, is predominantly achieved by correct barrel rifling twist rate and/or distance of the test sample from the muzzle of the launcher.

11.1.2 Test procedures and terminologies

Of all the test variants that are available, the V-50 test is the most useful, the most practical, and the most relevant — this is why it has been used for decades. Fig. 11.3 shows a typical set of probability curves for the defeat of armour materials and systems. As the velocity is slowly increased from zero upwards, the number of rounds observed to defeat the target progressively increases, until a velocity is reached where all rounds penetrate the target. The probability of defeat can be usually fit to a normal distribution with a spread of probabilities described by a standard deviation, σ . The zone of mixed results (ZMR) covers the range from V-01, at -3σ , to V-99, at $+3\sigma$. The population median (ie, V-50) also coincides with the mean for a normal distribution.

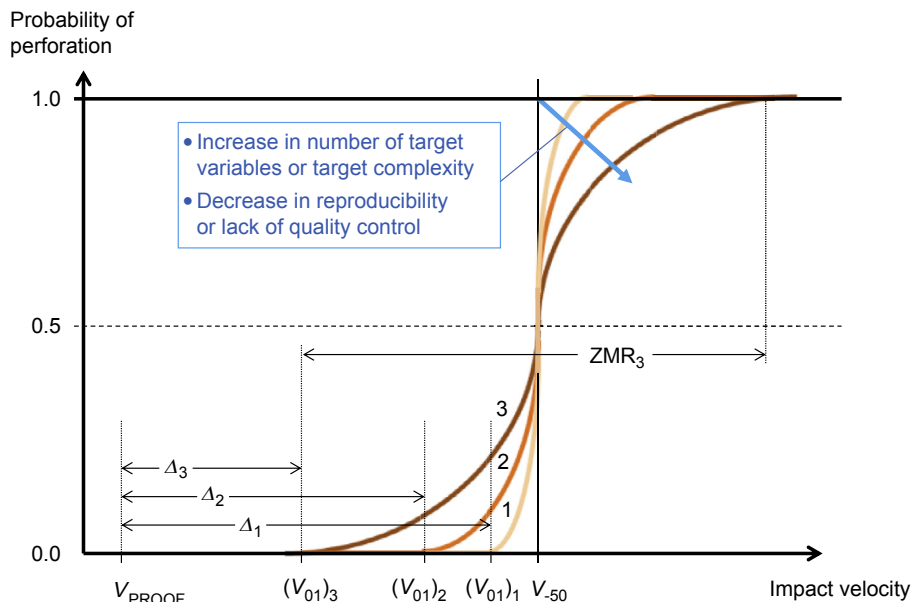


Figure 11.3 A set of probability curves for the defeat of armour materials and systems.

The many definitions of defeat (failure) will be described in [Section 11.1.3](#). Here, the derivation, and interpretation, of these V-50 curves will be covered in some detail because of their importance to the armour designer (see Chapter 1).

[Fig. 11.3](#) shows three different probability curves for three different imaginary armours: Curve #1 might be for an armour steel, Curve #2 might be for a soft armour insert (SAI), and Curve #3 might be for a body armour system (BAS), consisting of a hard armour plate (HAP) in conjunction with an SAI. The first thing to realise is that the magnitude of σ varies for a number of different, and highly significant, reasons: either because the number of target variables is increasing and/or because the material parameters are more varied, due to lack of (or poor) quality control. In the simplest of cases, that of a single piece of homogeneous armour steel, against a standard 7.62-mm APM2 round at normal incidence, the probability curve would be close to a 'step function' (ie, σ approaching zero, like Curve #1). However, in a multilayered, SAI, with slight variations in fabric weight and/or fibre strengths, σ will be larger, as in Curve #2. Furthermore, in a complex system, like a body armour system (including both an HAP and an SAI), the number of materials in the system increases to greater than 10, and each material will possess its own degree of variability. Hence, for a BAS, σ might be even larger, as in Curve #3, unless extreme measures are taken to maintain tight control over the variability of key material properties.

[Fig. 11.3](#) also shows the effect that an increase in σ has on the safety margin (Δ) of the armour system. Section 1.6 described how an armour system is designed. From a testing perspective, V_{PROOF} , the velocity used to prove the armour's total resistance to penetration, is the same as V_D , the design velocity, as shown in [Fig. 1.35](#). For the same value of V-50, as σ increases, V-01 decreases, and the safety margin (Δ) is reduced.

At this point it is worth debating V-0, the highest velocity at which zero penetrations should always be guaranteed. Statisticians will tell you that there is no such thing and that ‘the more tests you do, the more likely you are to observe a failure’ — however, terminal ballisticians know that there is a physical limit, since a pencil thrown at a pane of glass will not penetrate (an old Chinese proverb!). So, which value should one use for V-0? When designing an armour system, with good quality control of material variables, a value of 4σ might be conservatively used, with confidence, coupled with an appropriate level of safety margin, Δ .

There are a number of methods used to develop these probability curves. Accurate measurement of V_i , the impact velocity, is absolutely essential of course, and, in general, a V-50 calculation should involve as many shots as is practically feasible: four would be an absolute minimum, six to eight shots are more usual and up to 12 rounds very desirable — the more the better in terms of measuring an accurate, truly representative, value of V-50. The probit method involves 10 shots per velocity value, over the entire range of velocities between V-01 and V-50. The percentage of failures at each increment of velocity then provides a point on the probability curve. In theory, this provides a very accurate curve but consumes a large number of rounds and extensive range time.

A simpler approach, known as the Bruceton method or, more commonly, the up-and-down method, has been universally adopted and is described using the example given in Fig. 11.4. In this example, a starting velocity is selected and is assumed to result in a ‘failure’. The velocity for the second round is decreased by a guesstimated amount and, in this example, results in a ‘pass’. From this point onwards, the sequential velocities are ‘halved’, meaning subsequent velocities are halfway between the two previous rounds. This process continues, and is supplemented by repeat shots and by reassurance shots, until one has three passes and three failures within a specified velocity range. In

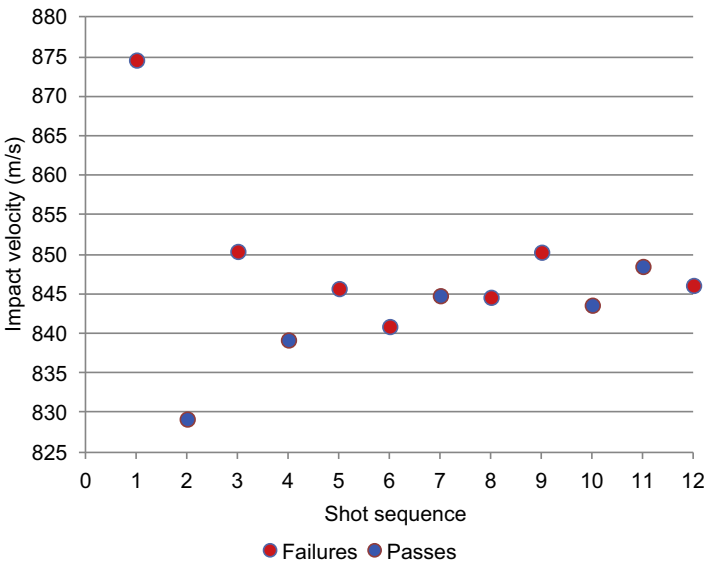


Figure 11.4 Example of firing sequence for the Bruceton method of determining a V-50 value.

this example, the V-50 is calculated from the last six shots and generates a value of 846.3 m/s with a standard deviation, σ , of 2.4 m/s. This gives a 3σ value of 7.1 m/s and therefore a 6σ value (the width of the ZMR) of 14.2 m/s. Acceptable ZMR widths, specified by certification authorities, are normally set at 15, 25 or 50 m/s. From this procedure, and assuming that $V-0 = V-50 - 4\sigma$, V-0 is calculated to be 836.8 m/s.

In performing such a V-50 assessment, the trick is to know where to start (ie, the velocity of Shot #1) but then also knowing how to change the velocity for Shot #2, and so on. It should also be noted that ‘every round counts’, irrespective of where it sits in the assessment and subsequent analysis. Hint: judging how far to change the velocity from Shot #1 to Shot #2 can only come from experience, and actually being present during a ballistic test!

Because a V-50 determination uses the assumption that the target is homogeneous and not affected by damage from a previous impact, the method is not normally used to assess the ballistic resistance of an armoured structure, nor for some elements of a body armour system, like hard armour plates. Instead, the V_{PROOF} method is normally adopted.

On occasions, V_r , the residual velocity of the round, after perforation, is measured in order to see how badly the target has failed. This can be qualitatively measured by using a catching material, like HDPE (high-density polyethylene), or a number of soft armour inserts, and judging how far the penetrating projectile has burrowed into the catching medium. A more precise measurement may also be obtained using high-speed photography. Alternatively, V_r/V_i curves can be developed, as detailed in [Section 11.2.1](#).






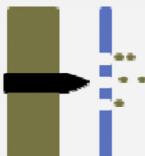
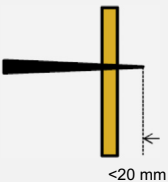
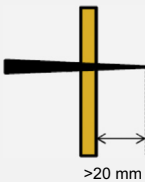

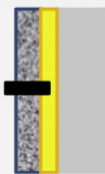


V_{PROOF} in [Fig. 11.3](#) is the same as V_D , the design velocity, in [Fig. 1.35](#), in Chapter 1. It is the velocity that will have been specified by the testing authority, acting on behalf of the User. V_{PROOF} is often the muzzle velocity of the selected threat: for example, 847 m/s for the 7.62-mm M80 bullet, as specified in test standards ([National Institute of Justice, 2008](#)). It can also be the velocity of a threat at a particular distance [eg, 7.62-mm API (armour piercing incendiary) X54R round at 300 m] which is ~ 655 m/s — see Table 1 in MIL-STD-662F for ballistic coefficients of various bullets ([Department of Defense, 1997](#)).

V_{PROOF} is the test velocity that the range officer will use as part of a ballistic assessment. It is also the velocity that the armour designer starts with: he would add a 3–4 σ value from his selected armour system, as well as a margin of safety (eg, Δ_1 , in [Fig. 11.3](#)) and then calculate the necessary V-50 value that his system needs to possess in order to comfortably pass the V_{PROOF} test. At the design stage, due consideration is also given to any preconditioning requirements that may reduce the ballistic performance of the system — see [Section 11.5](#). MIL-STD-662F ([Department of Defense, 1997](#)), issued by the US DoD (Department of Defense) in 1997, provides more details of the procedures required to perform a V-50 assessment of an armour system, and AS/NZS 2343 provides similar guidance for bullet-resistant panels and elements.

11.1.3 Definitions of ‘failure’

When carrying out a ballistic test to determine a ballistic limit or a V-50 value, it is essential to understand the pass–fail criteria since these are very different across the

Table 11.1 Different pass/fail criteria for armour materials and systems

Pass	Fail	Description
		Army ballistic limit: formation of a cracked bulge which allows light to pass through. Used for structural armours that need to maintain air-tightness on a battlefield. Classic ballistic limit for steel structures: see Table 1.7. Limit criteria between D damage and E damage
		Navy ballistic limit: entire projectile has penetrated the armour. Used for naval structures and large projectiles which, if fully penetrated, might cause lethal damage inside a vessel. Not normally used for small arms ammunition
		Protection ballistic limit: perforation of a witness panel placed behind the armour. Commonly used when the penetration of any ballistic debris (from projectile or armour) can enter a vessel and cause damage to occupants and/or internal equipment
		Critical depth of intrusion: where the penetrator (eg, a knife) has penetrated to an unacceptable depth. Commonly used to define failure criteria in knife and spike attacks. The unacceptable depth will depend upon the standard used for the impact energy of the penetrator
		Hard armour plate arrest: this is a nonintrusive criterion, in which the projectile must be arrested by the hard armour plate with zero intrusion into the soft armour insert. Used in conservative designs when the SAI needs to maintain integrity, for further use after initial impact damage
		Back-face signature: this is a nonintrusive criterion, in which the projectile must be arrested by the system (typically a body armour system). The maximum permissible depth for the BPS is normally 44 mm, for body armour systems, and can be as low as 15 mm for combat helmets

different fields of operation and types of threat. [Table 11.1](#) illustrates the different criteria.

For many years, especially during WW1 and WW2, it was common practice for the ballistic limit to be described by the Army Ballistic Limit when testing steel plate to be used in the construction of military vehicles. This was at a time when armoured vehicles needed to remain airtight on the battlefield. The pass/fail criteria corresponded to the borderline between a 'D' and an 'E' — see [Table 1.7](#) in [Chapter 1](#): D is code for a cracked bulge on the rear surface of a steel plate; E is the code for a cracked bulge, with light shining through, representing the start of perforation.

In a similar vein, sea systems engineers have used the Navy Ballistic Limit in which a failure is classified as an impact event resulting in the complete penetration of the projectile, thereby gaining access to the inside of the vessel. This is a very understandable criterion for exploding munitions and warheads like the Exocet missiles, which had such devastating effects during the Falklands War; however, the criterion is not normally used for small arms ammunition.

Far more commonly, the protection ballistic limit is used for armoured structures and military platforms. This makes use of a witness card that is placed behind the target. The witness card is normally a 0.5-mm thick sheet of an aluminium alloy like 2024-T3 and the stand-off distance is normally 150 mm. Failure is defined by the perforation of the witness card, as evidenced by the passage of light. Such perforations can originate from the bullet itself, and/or the target, in the form of spall. This criterion is employed when it is critical to protect personnel and/or equipment inside, or behind, an armoured structure.

The fourth criterion illustrated in [Table 11.1](#), represents an invasive criterion and is normally used to describe the pass/fail criterion for knife and spike attacks. These are fully described elsewhere ([National Institute of Justice, 2000](#)) but are set to represent lethal depths of penetrations and it is duly recognised that small, but limited intrusions, are acceptable.

For other elements of body armour systems, like the SAIs, a noninvasive criterion is adopted. When body armour is tested it is normally supported by a thick block of Plastillina (a nonhardening, temperature-controlled clay). In this instance, a failure is defined by the depth of the impact well, formed in the clay, from a nonpenetrating impact. The transient depth of deformation into the clay is described as the back-face signature (BFS) and the US National Institute of Justice (NIJ) has set the maximum acceptable depth at 44 mm. In some standards, for example, [UK Home Office \(2007a\)](#), this can be as low as 25 mm. In contrast, the back-face deformation (BFD) is defined as the permanent deformation, and is the measured bulge height at the rear of the armour (postimpact) — it is always less than the BFS value. Setting a maximum BFS criterion is also understandably used when testing combat helmets (see [Section 11.3.2](#)): in this situation, the maximum BFS is normally 15 mm or less.

One further criterion can also be applied to the testing of body armour systems that involve an HAP tested in conjunction with an SAI. Some military customers set an overriding pass/fail criterion, which stipulates that the projectile must be arrested within the HAP, rather than the system as a whole. This is a very conservative approach, on behalf of the user, and leads to overdesign of the HAP. Nevertheless, it does have the advantage

of preventing the SAI being damaged and being available for further use. It also provides some room for specification ‘stretch’ when the design threat requires to be raised.

The following sections describe the many techniques that are available to the armour technologist. [Section 11.2](#) details the range of experimental techniques available for evaluating armour systems and armour materials, as well as specific defeat mechanisms. [Section 11.3](#) covers standard methods, used to proof and certify armour systems, whilst [Section 11.4](#) introduces the topic of check production methodologies.

11.2 Experimental techniques used during armour development

‘Seeing is believing’, the old adage says. Well, in ballistic testing, ‘Witnessing is understanding’, if the armour technologist wishes to really understand and develop armour materials and systems — this has been the editor’s mantra for 30 years. It is not good enough, just to read a ballistic test report or to recognise a singular result, like a V-50 value. Armour materials, and especially the way they fail, need to be studied first hand, and the following basic test procedures illustrate the different techniques that are available.

Independent certification of an armour type is typically the final step in the development process and must be conducted in strict accordance with a test standard by an accredited test house. During the development phase, it is useful if the test house, like BMT, works with the armour technologist to establish in-house test methods which are tailored to the specific requirements of the customer. Using a recognised test standard as the framework for the developmental testing is very important so that the armour’s performance is measured against the criterion used in final certification. So, whilst the testing staff can be very flexible with bullet selection, impact velocity, impact angle, pretest conditioning of the armour, witness material selection, impact locations, and so on, they normally have very rigid views about stable bullet flight, target mounting, range configuration and pass/fail criteria.

As a footnote, numerical simulations of armour/anti-armour interactions through computer modelling or mathematical analysis, as covered in Chapters 8 and 9, are extremely valuable tools, and play a supporting role in the design process. However, there is no substitute for a comprehensive and in-depth ballistic testing programme, since actual ballistic testing can produce unpredictable results and unexpected failures are seen from time to time.

11.2.1 For evaluating armour systems

11.2.1.1 Through V-50, σ and BFS measurements

As described above, a V-50 test is the most common way of quantifying the ballistic performance of a system. However, for complex armour systems, in which the material is not homogeneous, a V-50 test is not always applicable. In this case, a V_{PROOF} test is more appropriate. However, in itself, this test gives no indication of the quality or

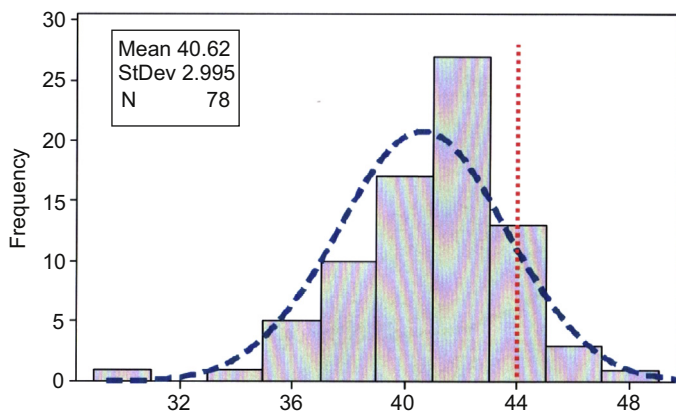


Figure 11.5 Statistical variability of BFS values (in mm) from a typical soft armour insert.

After Chiou, M., Schiffelbein, P., Fackler, J., 2007. NIST Workshop, October 3, 2007.

reproducibility of the armoured structure. This would have to be gained by observing the rear-face damage and grading it accordingly.

For body armour systems, the variation in ballistic performance can be determined by carrying out a large number of impacts at nominally the same velocity. Fig. 11.5, from DuPont's own data bank, provides an example of the statistical variability of BFS values for a soft armour insert tested against a 0.357 in. Magnum handgun round, and fired at 435 ± 10 m/s. The spread of results is huge, by anyone's standard, ranging from 30 to 48 mm, and, even though the mean value of 40.62 (from 78 impacts) is less than the acceptable maximum value of 44 mm, the armour will have been judged to have failed because of those impacts resulting in a BFS greater than 44 mm. In this case, σ is about 3 mm and the probability of failing a standard NIJ test, involving far fewer rounds, was estimated to be about 10% (Chiou et al., 2007). In this case, and in order to reduce the mean BFS value by about 8 mm, the areal density of the pack will have needed to be significantly increased. This is why it is imperative, in a body armour system, to exercise maximum control over quality and reproducibility of the product; otherwise overdesigned, and therefore overweight, products have to be fielded.

11.2.1.2 Through residual velocity curves

An alternative method for determining the ballistic limit of an armour system is to measure the residual velocity, V_r , of a series of penetrating rounds, with increasing impact velocities, V_i , and then plot a V_r/V_i curve, as given in Fig. 11.6, after the work of Borvik et al. (2003), when using blunt-nosed fragments against a range of armours with different thicknesses. Curve-fitting the data to either an existing mathematical model or equation can then determine a V-0 value. In 2007, Horace Billon, of the DST Group, Australia, reported a direct method of calculating V-0 from such a data set (Billon, 2007).

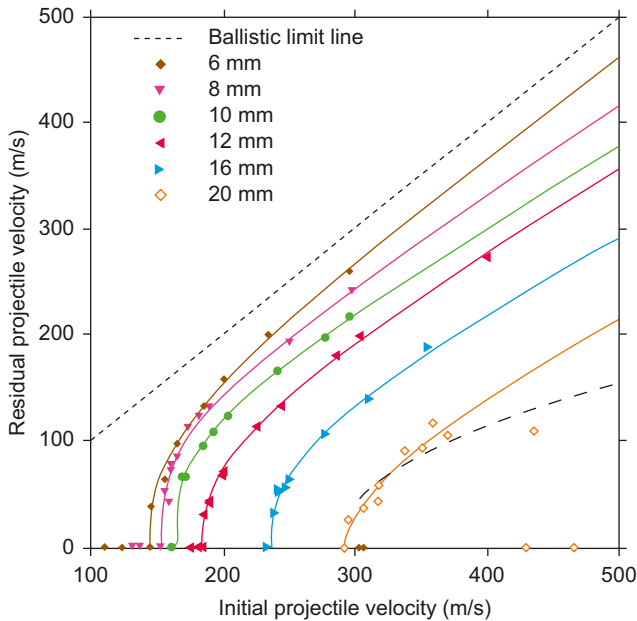


Figure 11.6 Residual velocity as a function of impact velocity.

After Borvik, T., et al., 2003. *International Journal of Impact Engineering* 28, 413–464.

11.2.2 For evaluating armour materials

11.2.2.1 Through a study of 'single strikes'

A great deal of qualitative information can be gleaned from studying the behaviour of candidate armour from just one impact from a representative projectile. In fact, if a series of armour materials are to be assessed and compared, then, as long as they are of similar areal density, they could be ranked by judging how well they behave against similar single strikes. For example, by taking some measure of back-face deformation. Whilst this is a quick and dirty approach, it takes advantage of the wealth of information that can be revealed from a single impact. For example, in [Fig. 11.7](#), if one was comparing targets A, B and C at a single velocity of, say, 650 m/s and you observed the results shown for that single value of velocity, then you could deduce that Target B *might* have the lowest V-50 value.

11.2.2.2 Through estimated V-50 tests

One could extend this comparison at a number of impact velocities, as shown in [Fig. 11.7](#). As long as the range of areal density values for the three targets is not too great (say, within 5%), then a reasonable comparison can be made from estimated V-50 values. In [Fig. 11.7](#), from the wider assessment across the four velocity levels, one would be fairly confident that the V-50 for target A is >675 m/s, that of target

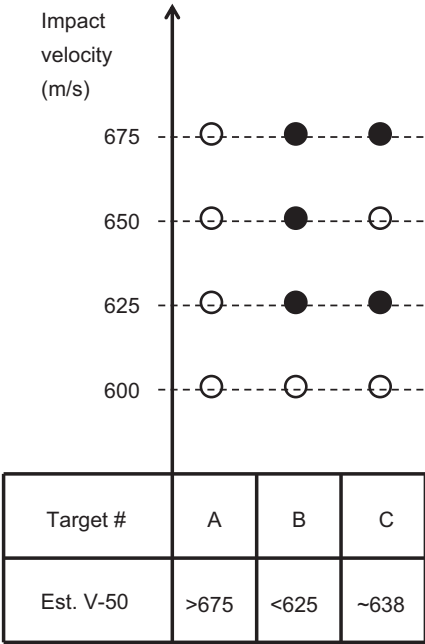


Figure 11.7 Simple test matrix for comparing targets A, B and C, against a well-defined set of impact velocities and observing failure mode (closed circles represent failures; open circles represent passes).

B <625 m/s and that of target C ~638 m/s. In other words, from this crude assessment, target A outperformed target C, and target B was probably the worst. This approach, whilst very qualitative, can be used in a simple downselection process for a number of candidate grades of armour materials, prior to carrying out a full, conventional V-50 assessment. Such a technique can, of course, be used in conjunction with any of the pass/failure criteria shown in [Table 11.1](#).

11.2.2.3 Through depth of penetration (DOP) tests

The penetrating power of a particular projectile is sometimes quoted as being able to penetrate a certain depth of rolled homogeneous armour (RHA): eg, 55 mm of RHA (see Fig. 1.6). This same approach could be used to assess the penetration resistance of armour materials, especially ductile ones, like the light alloys (see Chapter 3). However, such a technique, using semi-infinite targets as shown in [Fig. 11.8](#), does not account for any deleterious back-face behaviour or the effects that structural support conditions have upon targets of finite thickness, as in the real world. Nevertheless, the technique has been used in studies of thick-sectioned ultrahigh molecular weight polyethylene (UHMWPE) targets ([Nguyen et al., 2015](#)), and proved very informative in observing the various failure mechanisms involved in deep-impact experiments.

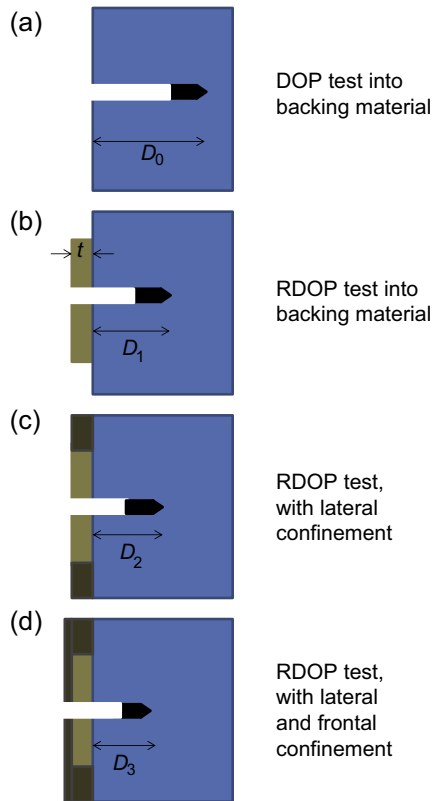


Figure 11.8 Schematic of DOP and RDOP tests, with variants.

11.2.2.4 Through residual depth of penetration tests

One variation of this DOP test has established itself as a standard method for assessing the ballistic performance of hard strike face materials, like ceramics. In 1987, Zvi Rosenberg, put forward a technique that enabled a merit rating to be calculated for any strike face material (Rosenberg et al., 1987). This test, called the residual depth of penetration (RDOP) test, was developed to determine the ballistic efficiency of armour-grade ceramic tiles. Fig. 11.8 illustrates how simple, but effective, this method is, especially for determining the most effective ceramic for absorbing most energy during the initial stages of a conventional impact scenario (see Fig. 7.4). This point illustrates its one limitation: it does not truly represent the support conditions experienced by a ceramic tile in a ceramic armour system of finite thickness. However, it does provide the best conditions under which a ceramic can function at its very best, as an armour material: in the fully supported condition.

The RDOP test method is self-explanatory: the selected penetrator is fired, at identical impact velocities, into a semi-infinite block of material, typically a very thick plate of an aluminium alloy, like 6082-T651, with and without a tile of the candidate strike-face material. Depths D_0 and D_1 (see Fig. 11.8) can be compared.

The ‘ballistic efficiency’ of the candidate tile can be calculated, and expressed as the differential tile efficiency, Δ_{Tile} , by the following equation:

$$\Delta_{\text{Tile}} = (D_0 - D_1) \cdot \rho_{\text{Backing}} / (t_{\text{Tile}} \cdot \rho_{\text{Tile}})$$

In addition, the mass effectiveness, E_m , of the candidate tile material can also be calculated by the following equation, but remember that this merit rating does not represent a ceramic in a real armour system, just the RDOP test:

$$E_m = (D_0 \cdot \rho_{\text{Backing}}) / (t_{\text{Tile}} \cdot \rho_{\text{Tile}} + D_1 \cdot \rho_{\text{Backing}})$$

A database of values for either E_m or Δ_{Tile} can be found in [Holmquist et al. \(1999\)](#) and a later work by [Hazell \(2006\)](#). The RDOP test can also be used to assess the effectiveness of various forms of confinement, as shown in [Fig. 11.8\(c\) and \(d\)](#). In both cases the parasitic weight of the confining plates would need to be accounted for in any calculation of mass effectiveness or differential tile efficiency. This RDOP test has also been used to estimate the minimum thickness of strike face material required to be most effective in a real armour system. This is a matter of carrying out a series of RDOP tests using tiles of different thicknesses and then plotting the various D_1 values against tile thickness. An example of this approach was reported by [Savio et al. \(2011\)](#) who studied the penetration resistance of boron carbide tiles, with and without confinement, against 7.62-mm AP rounds.

More recently, [Carton and Rosebroeks \(2014\)](#) challenged the validity of the RDOP technique and modified (and complicated) the approach by adding high-speed cameras (to measure V_i and V_f), as well as using standalone ceramic tiles. Although this has complicated the test, it removes the influence of fragment shape, etc., as well as the need for a massive backing layer. The validity of this variation, however, can also be challenged since they propose that the ceramic has no rear support at all: this is a long way from reality in which the ceramic tiles will always be backed by supporting materials of finite thickness. However, coupled with round recovery and final core length measurements, valuable information can be obtained from this modified technique, including estimates of dwell times.

11.2.2.5 Through spall tests

It is normal during a ballistic impact test to take account of the rear spall. For example, this is certainly included in a PBL determination (see [Table 11.1](#)). However, some ballistic test requirements stipulate that the extent of frontal spall be quantified. This is especially important with ceramic-based body armour systems that might create frontal spall and endanger fellow ground troops in the near vicinity as well as causing serious injury to the armour wearer’s body parts that are forward of the armour plate, ie, chin/face and arms.

Such a test involves enveloping the target in a five-side, aluminium box with a hole in it, through which the projectile can travel. As shown in [Fig. 11.9](#), the frontal spall box will get peppered by any stray spall and become a witness to the extent of

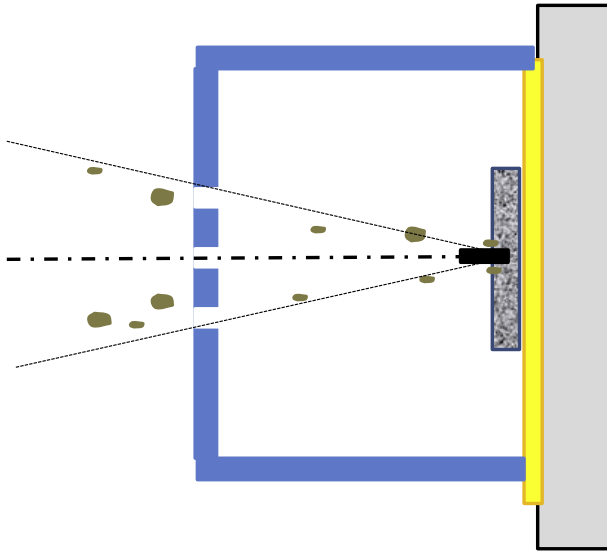


Figure 11.9 Front spall test for typical body armour system.

Australian Government, 2012a. DEF(AUST) 10946, ADF Personal Armour Test Standard, Part 1: Body Armour.

that spalling event. The number and size of perforations can be easily analysed and the maximum spall cone angle calculated from the geometry of the set-up. A maximum cone angle and/or maximum number of perforations will be set as the pass/fail criterion.

11.2.3 For studying defeat mechanisms

11.2.3.1 Through forensic examination of the impact site

There is much that can be gained from a metallographic study of the impact site and it is commonplace for the armour technologist to carry out a forensic examination to discover how the projectile has penetrated the armour, and to identify the failure mechanisms involved. Such discoveries will strongly indicate whether the target is absorbing energy in an efficient manner and/or whether it is failing through some low-energy absorbing mechanism. For example, adiabatic shear bands are indicative of the latter (see Chapters 2 and 3). If delamination has occurred, how broad is the delamination area? Has the impact involved any material not directly affected by the impact at the point of strike (PoS), as in an SAI (see Chapter 6)? Has the target simply been pierced by an overmatching round creating a fairly clean hole, with minimal collateral damage? How many radial cracks have emanated from the PoS, indicating how brittle the material might be or how close the impact velocity was to the V-50? There is much that can be gleaned from a single impact.

11.2.3.2 *Through stand-off RDOP tests*

With laminated armour materials, the amount of energy being absorbed in the two principal modes of failure, mode I (through-thickness compression) and mode II (delamination) failures, can be estimated from a variant of the RDOP test. Developed by Ian Crouch in the early 1990s, it involves stripping the jacket from an AP round, like the APM2, and then impacting the candidate laminate with or without a supporting medium. Fig. 11.10 shows the experimental set-up used by Crouch (1993) to demonstrate that mode I absorbs more energy than mode II. However, in general, it is a test that can be used for any laminated material to better understand the balance between modes I and II and to calculate associated energy-absorption values. If HDPE blocks are used as the supporting media, x-radiography can be used to indirectly measure the respective RDOP values.

11.2.3.3 *Through reverse ballistics tests*

Reverse ballistics is exactly what it sounds like: projecting a target at a stationary bullet! But why should this be useful, and how do you do it? The attractive advantages of this technique, compared with conventional forward ballistics, are illustrated in Fig. 11.11 and can be summarised as:

- Precise location, and alignment, of the point of impact can be achieved;
- Unwanted yaw or spin of the projectile can be avoided;
- A larger range of impact velocities (and consistency) can be achieved using a gas gun;
- Flash x-radiography can be more easily integrated into the experimental impact, with synchronisation, and multiplicity.

A typical test set-up is shown in Fig. 11.12 in which a 50-mm two-stage gas gun has been used to propel the target at the stationary bullet. The sabot target is a perfectly flat disc, slightly less than 50 mm in diameter — this is the one disadvantage of the technique: size of target, which can be limiting, especially for thick targets. Nevertheless, the technique has been well used over the past decade or so to study the early stages of interaction between a projectile and a target: for example, dwell. Combined with core recovery techniques, the erosion rates of steel-cored rounds can also be quantified (see Fig. 11.13). In this instance, the mild steel core of an AK47 bullet is seen to erode at a constant rate, within the ceramic material, once the jacket has been removed.

11.2.4 *Experimental diagnostic tools*

11.2.4.1 *High-speed digital video*

High-speed cinematography is an extremely valuable tool — it supports the editor's war cry of 'Witnessing is understanding'. A stab or spike impact test, for example, is ideal for such work, where impact velocities are not too high and where the impactor is usually nondeforming — its progress through a soft target can be tracked easily, and accurately. A typical set-up procedure is shown in Fig. 11.14, whilst an example of generated data is presented in Fig. 11.15. In this plot of energy absorbed (in Joules)

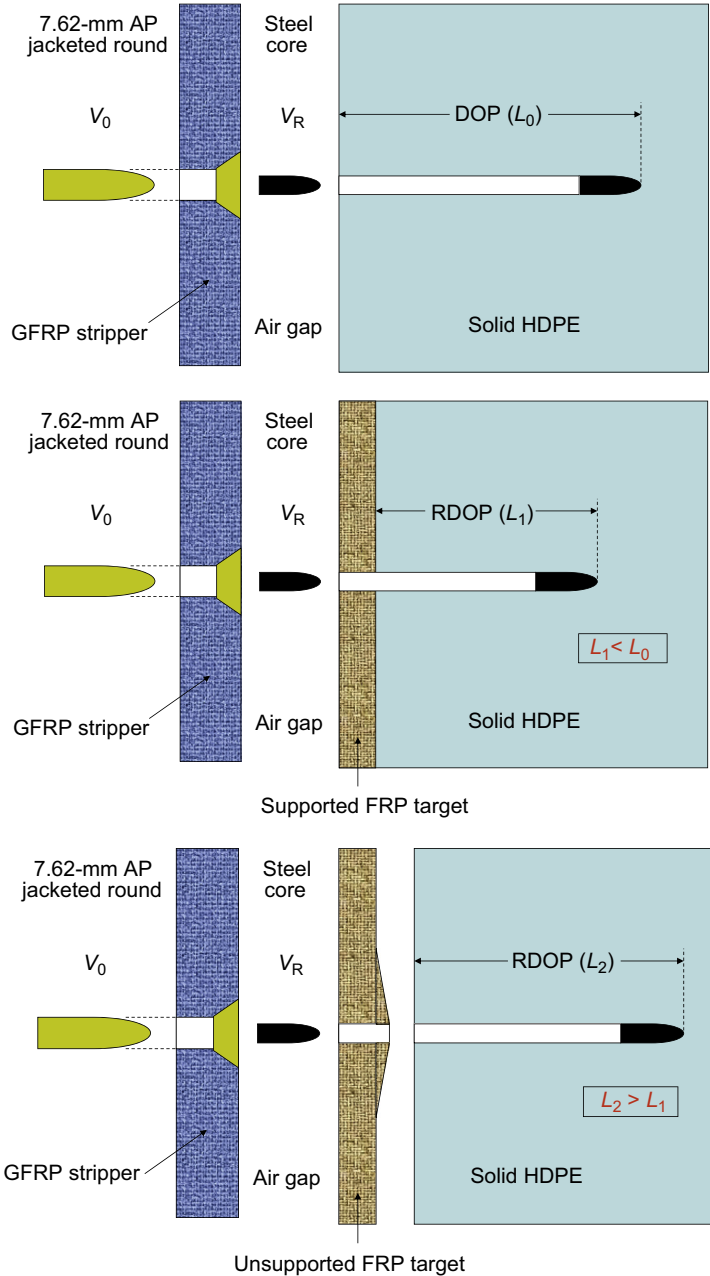
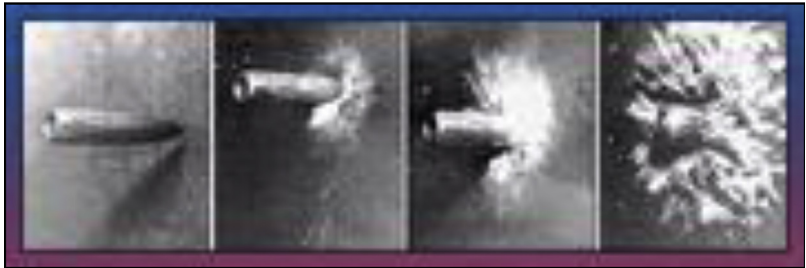


Figure 11.10 Variation of RDOP test for determining the relative contributions of mode I and mode II energy-absorbing mechanisms in laminated armour materials. Crouch, I.G., 1993. Penetration and Perforation Mechanisms in Composite Armour Materials, Euromech Colloquium 299. Oxford University, March 1993.

Forward ballistics icw HS video, at angle



Reverse ballistics icw flash x-ray, at normal

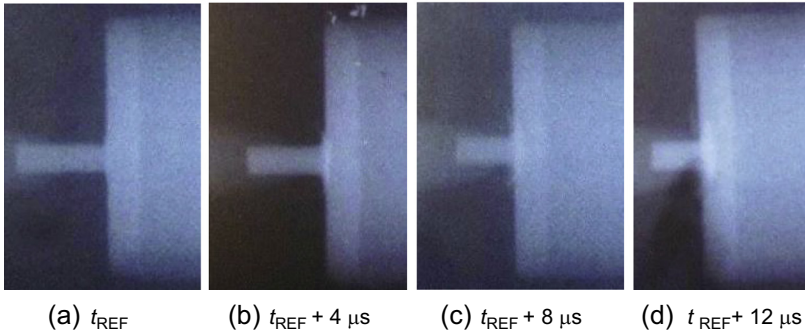


Figure 11.11 Comparison of forward ballistics and reverse ballistics visualisations. Crouch, March 2015. DMTC Conference.

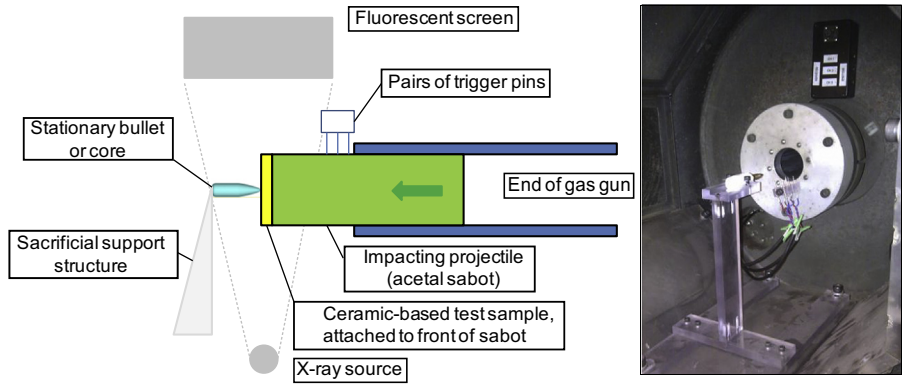


Figure 11.12 Experimental set-up for a reverse ballistics experiment. After Crouch, I.G., Appleby-Thomas, G., Hazell, P.J., 2015a. International Journal of Impact Engineering 80, 203–211.

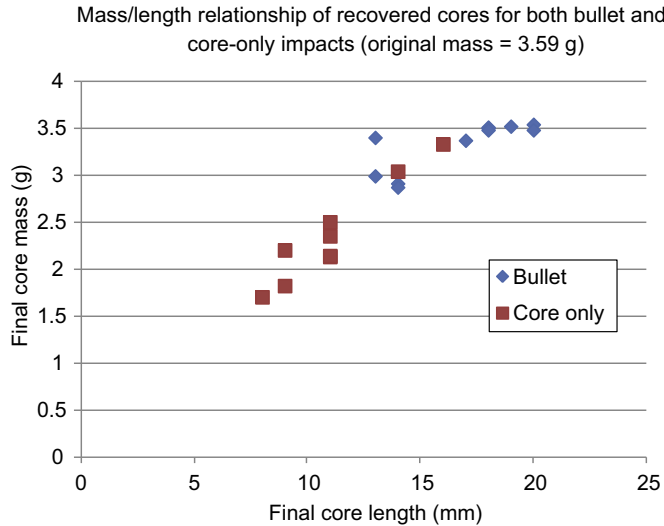


Figure 11.13 Erosion rates for the mild steel core of an AK47 bullet against a boron carbide target.

After Crouch, I.G., Appleby-Thomas, G., Hazell, P.J., 2015a. International Journal of Impact Engineering 80, 203–211.

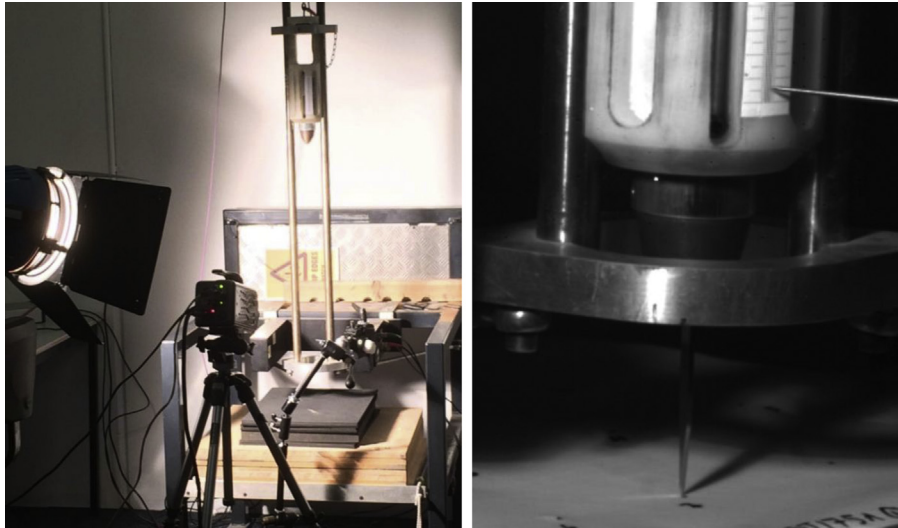


Figure 11.14 Experimental set-up for capturing knife or spike impact against a SAI pack. DMTC (2014).

versus displacement of the penetrator, two distinct phases of perforation are detected, whether the weapon is a knife (eg, KR2/P1) or a spike (eg, SP2) – the first phase from 50 to ~ 25 J corresponds to through-thickness compression of the soft fabric; the second phase, from ~ 25 J to zero corresponds to perforation of the fabric pack.

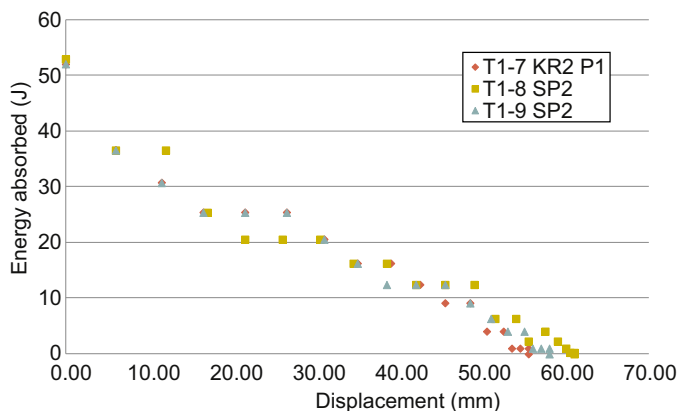


Figure 11.15 High-speed video set-up and experimental results for stab and spike impact studies at the DMTC (2014), showing generated curves of energy absorbed, as a function of time.

11.2.4.2 Flash x-radiography

High-intensity, flash radiography has been used by designers of armour systems for many decades since much information is revealed about the nature and disturbance of penetrators. In certain situations, it has also been used to great effect when studying impacts from small arms ammunition. Recent work by [Barbillon et al. \(2014b\)](#) is an excellent example of capturing essential, dynamic information that would have been lost simply by carrying out postimpact, forensic examination. [Figs 11.16 and 11.17](#) illustrate the dynamic effects of lead-filled, 7.62 mm rounds impacting UHMWPE helmet shells. The series of flash radiographs show the sequence of perforation whilst the data in [Fig. 11.17](#) reveal the significant differences between back-face signature

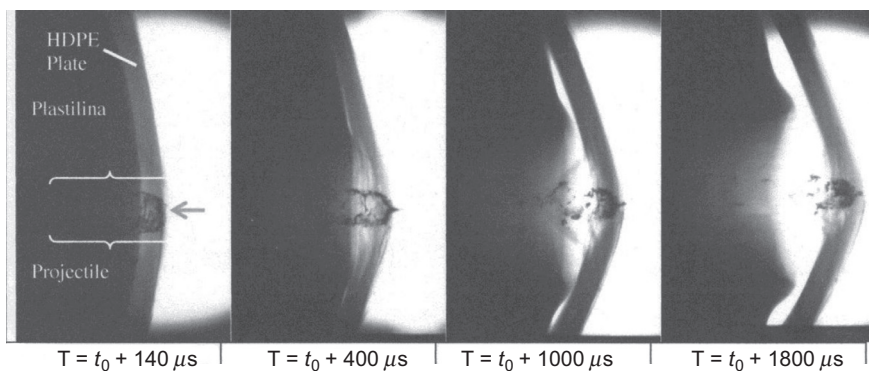


Figure 11.16 A series of flash x-rays of a lead-filled 7.62 mm bullet impacting an UHMWPE helmet shell.

Barbillon, F., Auchere, R., Vuillemot, V., Simonetti, J.M., 2014b. “Shatter-gap effects” on HDPE plates with a lead-core steel jacketed 7.62-mm calibre ammunition. Personal Armour Systems Symposium, PASS 2014, Cambridge, UK, September 2014.

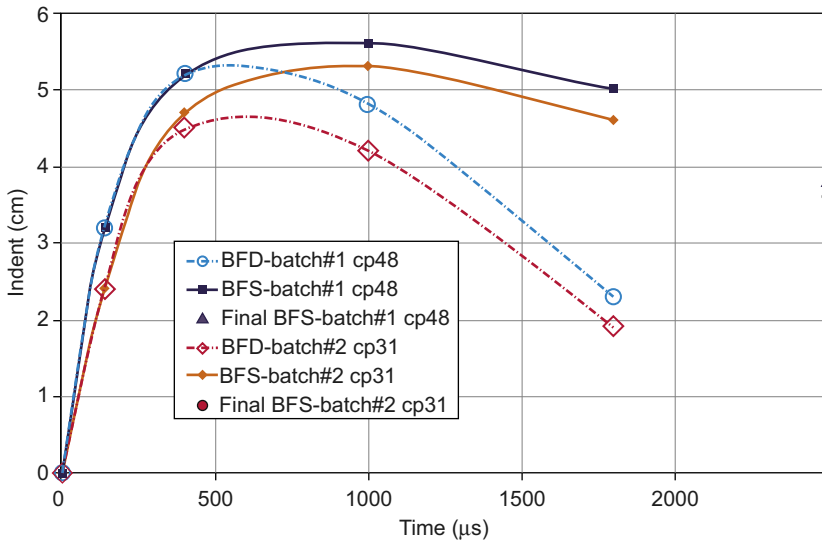


Figure 11.17 Back-face signature (BFS) and back-face deformation (BFD) measurements as a function of time for lead-filled 7.62 mm bullet against an UHMWPE helmet shell.

Barbillon, F., Auchere, R., Vuillemot, V., Simonetti, J.M., 2014b. “Shatter-gap effects” on HDPE plates with a lead-core steel jacketed 7.62 mm calibre ammunition. Personal Armour Systems Symposium, PASS 2014, Cambridge, UK, September 2014.

(as recorded by the flash x-rays) compared to the back-face deformation values (as measured, postimpact). Note that the indent depth in Fig. 11.17 is measured in centimetres so in this case the maximum BFS value exceeds 50 mm — an unacceptable depth by current standards.

11.2.4.3 High-resolution digital x-radiography [two-dimensional (2D)]

Postimpact analysis of armour materials and systems is vitally important to the armour technologist, especially when designing ceramic-based armour systems, as in HAPs. Using digital versions of x-radiography, with resolutions less than 100 μm, in which the 2D x-ray images can be postprocessed, in order to provide maximum information, is especially attractive.

Two-dimensional, digital, x-radiography of ceramic armour plates, for example, also allows for:

- Forensic analysis of fracture pattern, leading to possible cause of cracking/failure from durability/rough handling/drop testing/environmental conditioning, as well as ballistic impact, as seen in Fig. 11.18;
- Determinations that crack mitigation or arresting techniques are functioning correctly. For example, as in the effectiveness of padding to reduce damage from parachute drops or damage during transit;
- Precise records to be made of shot placement, as in Fig. 11.18, or simply studying the regularity of a mosaic of ceramic tiles (see Fig. 11.19).

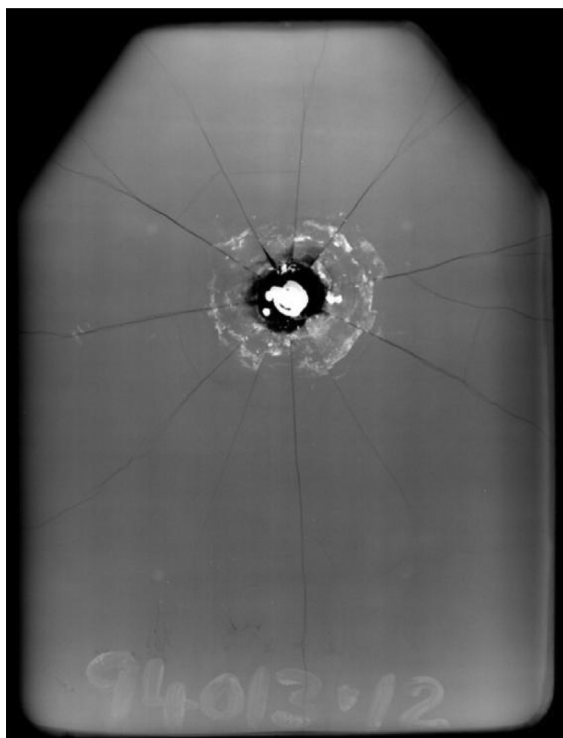


Figure 11.18 High resolution of an HAP which has been impacted with a 7.62-mm APM2 round which has been arrested within the HAP. The radiograph not only shows details of the impact site but also fine detail of the extent of radial cracking, emanating from the PoS. BMT (2009).

Of equal significance is the ability to detect and understand the significance of defects within an armour material, like a brittle ceramic. The authors have worked cooperatively over many years to develop a set of accept/reject criteria for silicon carbide breastplate tiles, manufactured using the reaction sintering technique (see Chapter 7). [Crouch et al. \(2015b\)](#) provide a detailed table of these criteria. Defects such as inhomogeneity, variable thickness and shrinkage cracks may indicate quality management issues in the manufacturing process which allow the armour technologist to reject ceramic products of poor quality before acceptance into the manufacturing process. In addition, this information can assist ceramic tile manufacturers to improve their process or guide designers of ceramic armour systems.

[Fig. 11.19](#) is an x-ray of an experimental ceramic armour system, made up of a mosaic of individual ceramic tiles, embedded within a composite structure on both front and rear surfaces. Therefore, during postimpact analysis, the ceramic tiles could not be visually inspected. Through analysis of the x-ray, however, shot placement can be checked, the uniformity of gaps between neighbouring tiles can be measured, and the morphology of the impact damage analysed. In this case, most of the impact damage has been confined to the central tile, near the PoS. However, the high-resolution imaging

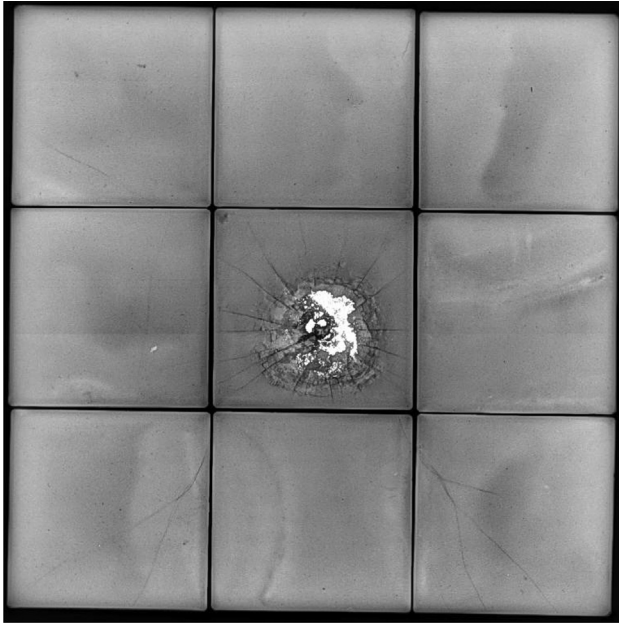


Figure 11.19 A digital, high-resolution x-radiograph of a standard 3×3 array of silicon carbide tiles, backed by a KFRP (Kevlar fibre-reinforced plastic) layer and placed directly in front of a 6-mm HHS (high-hardness steel) plate, having been impacted by a 7.62-mm round at ~ 700 m/s. The round was arrested by the system. The x-ray shows detail of the impact site as well as minor peripheral damage to adjoining tiles. BMT (2015).

allows detection of hairline cracks in some of the neighbouring tiles. As recently reported by [Crouch \(2014\)](#), the width of such cracks, as measured by crack opening displacement (COD) will affect subsequent penetration from small arms attack, but not as much as the general community might think.

11.2.4.4 High-resolution digital x-radiography (3D)

BMT continues to be at the forefront of armour systems nondestructive testing (NDT) and after several years of research are beginning to adopt computed tomography (CT) or 3D x-ray. The advantage of CT is that all materials within a complex armour system, like an HAP or a combat helmet, can be inspected, not just the ceramic elements.

Developed in the late 1990s ([Wells et al., 2001](#)), CT technology can be used to determine the health of critical areas within a composite structure ([Fig. 11.20](#)). BMT's research has demonstrated that key regions of interest within an HAP, or helmet, can only be inspected in detail using CT, such as:

- The interface between the ceramic tile and the backing material (as in an HAP);
- The layered/laminated backing material (as in an HAP);
- The entire high curvature structures (as in a helmet).

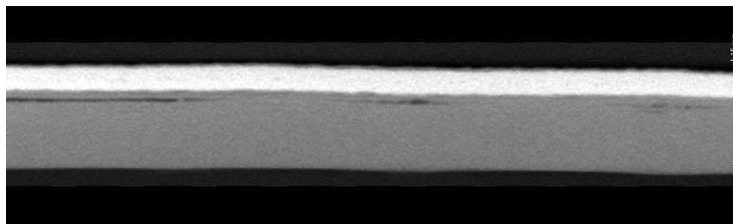


Figure 11.20 CT scan of a hard armour plate showing delamination in the subjacent layers of the backing material.
BMT (2015).

Delamination in these areas may affect the ballistic performance of an HAP or helmet, or may reduce the service life of such products. Delamination within a combat helmet, for example, will certainly affect its ability to withstand an ear-to-ear compression load. Monitoring the integrity of these structures over time can provide both the armour technologist and the end users with invaluable information regarding product integrity. By understanding the inner health of these structures it is now possible to better understand not only initial manufacturing procedures but also possible degradation of such products in service.

11.3 Standard techniques (for proving armour systems)

It is not the objective of this chapter to describe, in any detail, the standard test methods and ballistic performance specifications, which exist throughout the world. But the lay reader certainly needs to know that every armour system deployed will be tested against a rigid set of codes. Here, it is sufficient for the reader to be aware that different types of small arms ammunition are used across the various standards (see [Table 11.2](#)) — this should be helpful when deciding which ballistic test to carry out during the experimental, development and production phases of an armour design.

11.3.1 Body armour systems

The compliance and certification testing of body armour systems is probably the most extensively exercised ballistic test worldwide, and the most common standards have been those published by the National Institute of Justice (NIJ) in the United States. NIJ 0101, originally issued in 1987, is still widely adopted, with the issue of a July 2008 version. It is based upon a perforation — back-face signature (P-BFS) test method, as in the V_{PROOF} test mentioned previously - see [Section 11.2.1](#). The standard covers assessment of both soft and hard armour systems and is very comprehensive in its procedures and specifies shot patterns, angles of attack, minimum acceptable shot-to-edge distances, and much else, in great detail. Other standards, popular with civilians, are those of the UK Home Office's Centre for Applied Science and Technology (CAST) and STANAG 2920 (Edition 2) issued in 2003.

Table 11.2 Summary of ballistic test standards as a function of ammunition type

Threat ammunition	Ballistic standard										
	EN 1522	EN 1063	NIJ 0108.00	NIJ 0101.04	NIJ 0101.06	HOSDB 2007	GOST	STANAG 2920	VPAM	UL752	AS/ NZS 2343
Fragment-simulating projectiles											
0.22-in. 1.1 g FSP								Yes			
0.30"								Yes			
12.7 mm FSP								Yes			
20 mm FSP								Yes			
Shotgun											
12 gauge 00 buck shot						SG1	Class 2a			Spl	S0
12 gauge rifled slug		SG1&2								Spl	S1
Handgun											
5.45 mm × 18 mm PSM							Class 2				
22 long rifle	FB1	BR1	I	I					Level 1		
7.62 mm × 25 mm Tokarev							Class 2				
7.62 mm × 39 mm Nagant							Class 1				
357 SIG			IIa/II		IIIa						
9 mm × 18 mm makarov							Class 1				
9 mm × 19 mm (9 mm Luger) FMJ	FB2	BR2	Ia/II/IIIa;	Ia/II/IIIa;	IIa & II	HG1&2			Level 2&3	Level 1&6	G0
357 magnum	FB3&4	BR3	II	II	II	HG1&2				Level 2	G1
40 Smith & Wesson				IIa	IIa						
44 Rem. Magnum SJHP	FB4		IIIa	IIIa	IIIa						
44 Rem. Magnum SJSP		BR4							Level 4		G2
44 Rem. Magnum LSWGC			IIIa							Level 3	

Rifle										
5.45 mm × 39 mm ball							Class 3&4			
5.56 mm × 45 mm M193	FB5&6	BR5							Level 7	R1
5.56 mm × 45 mm SS109 (M855)									Level 7	
5.56 mm × 45 mm Tac Bonded						HG3				
5.56 mm × 45 mm APHC										
7.62 mm × 39 mm M43 MSC							Class 3		Level 6	
7.62 mm × 39 mm API-BZ							Class 5		Level 8	
7.62 mm × 51 mm Spitzer										Level 4
7.62 mm × 51 mm F4										R2
7.62 mm × 51 mm L2A2 ball						RF1				
7.62 mm × 51 mm M80	FB6	BR6	III	III	III				Level 7	
7.62 mm × 51 mm L40A1						RF2				
7.62 mm × 51 mm P80	FB7	BR7							Level 9	
7.62 mm × 51 mm WC core FFV									Level 11	
7.62 mm × 51 mm WC core Swiss AP									Level 12	
7.62 × 54R LPS										
7.62 × 54R API B32							Class 6		Level 10	
30-06 Springfield M2 ball										
30-06 Springfield M2 AP			IV	IV	IV					Level 9

In 2008, NIJ issued a new standard, NIJ 0101.06, following the tragic events that followed the introduction of police vests manufactured from PBO (poly [*p*-phenylene-2,6-benzobisoxazole]) fibres (see Chapter 6). The mechanical properties of these PBO-based vests were found to degrade after exposure to warm/humid weathering conditions, leading to substandard ballistic performance and tragic loss of life. The NIJ reacted by quickly introducing a new standard with far stricter preconditioning requirements, increased test sample sizes and reduced edge distances. Unfortunately, whilst the motivation for the new standard was well founded, the standard has resulted in many soft armour vest companies going out of business because of the burdensome cost of certification.

Two features of these well-accepted test methods require mention: strapping and remounting of soft armour vests and the measurement techniques for BFS. Various strapping methods are acceptable but they are very prescriptive (see standard) and when remounting the vest, between impacts, a certain amount of smoothing and repositioning of the vest is permitted. This can be quite subjective and should be carefully monitored. Over the years, BFS measurements have also been quite subjective and since these critical values need to be recorded to the nearest millimetre, the measurement technique needs to be well rehearsed. This is an area that has been made more rigorous with the issue of NIJ 0101.06 — Fig. 11.21 shows an excellent schematic of the BFS measurements to be made — making those measurements, though, is up to the range officer and a standardised method has not been adopted, which is why it is still an area of concern.

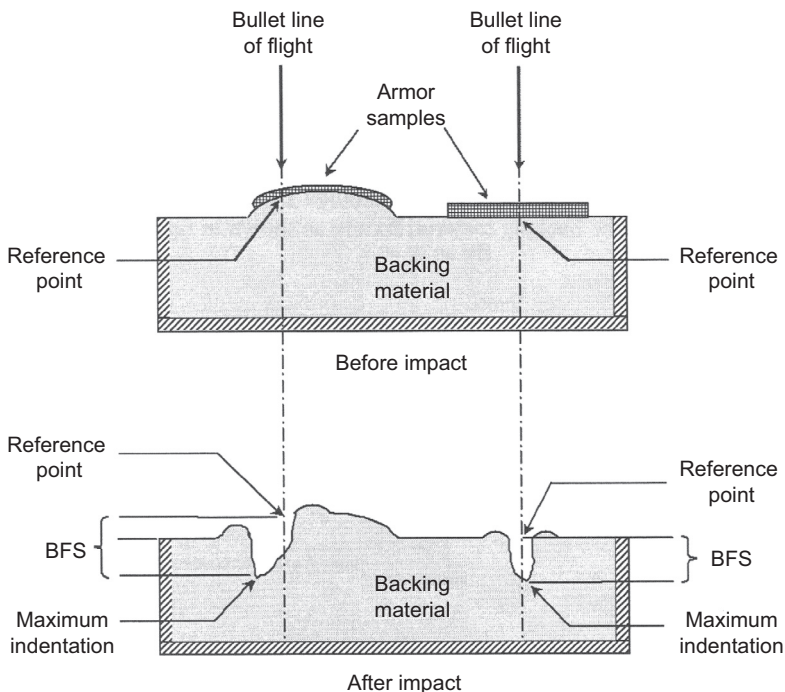


Figure 11.21 Definition of BFS measurement in NIJ 0101.06 test standard.

It should also be noted that military customers are now preferring to develop their own, in-country testing standards and ballistic specifications, for body armour systems, rather than just making due reference to the NIJ standards which were originally intended for law enforcement situations which differ significantly from military theatres. The Australian Department of Defence, for example, issued their own testing standard (Australian Government, 2012a), prior to a recent body armour tender in 2013 after a comprehensive review of test requirements and industry engagement.

In conclusion, Phil Gotts' paper from the Personal Armour Systems Symposium in 2014 (Gotts, 2014), makes excellent reading and critically reviews many important issues around the testing of body armour systems. It also makes due mention of a more detailed approach taken by 'The Met' (the London Metropolitan Police) in extending the assessment of body armours to a V-50 test coupled with critical perforation analysis (Quelch et al., 2002). In addition, Barbillon et al. (2014a) recently highlighted the measurable differences in results depending upon the specific ammunition used, especially the different jacket materials with the 7.62-mm ball rounds. The current authors, Crouch and Eu, have observed similar differences in the performance levels of different 9-mm handgun rounds.

11.3.2 *Combat helmets*

Typically, combat helmets are tested either to the USA law enforcement standard NIJ0106.01 for penetration and impact attenuation, the USA military standard MIL-H-44099A for fragment V-50 or STANAG 2920 (NATO, 2003). As with body armour, the Australian Department of Defence has issued its own test standard specifically written to assess the performance of combat helmets intended for military use and the specifics of such environments (Australian Government, 2012b).

The testing of combat helmets requires other performance measures to be assessed in addition to ballistic resistance. Secondary to the ballistic impact, serious injury may result to the head from the G-force of the impact and/or release of retention system components inside the helmet shell.

The release of retention system components inside the helmet shell is referred to as 'secondary fragmentation'. Secondary fragmentation usually occurs when a projectile impacts, either directly or in close proximity to, a harness retaining fixture, NVG mounting bracket or similar fixture mounted to the helmet, resulting in the release of part of the fixture inside the helmet and causing injury to the head of the wearer. In the design of a helmet, if through bolts or screws have been used, it is vitally important that secondary fragmentation tests be conducted.

A ballistic testing laboratory that conducts testing on helmets is required to have a broad knowledge base around the launching of FSPs across a wide range of sizes and shapes. As mentioned earlier in Section 11.1.1, when discussing the objectives of a ballistic testing laboratory, areas such as stable flight with acceptable yaw is of particular significance here. One of the most commonly required FSPs in helmet testing is a right circular cylinder (RCC), a steel cylinder with flat ends. Any yaw (within a certain angular range) at impact with an RCC changes the penetration mode from a normal, blunt impact to a cutting mode when yawing occurs. Differences of this nature can lead to varying results which are highly undesirable, particularly when comparing results from different laboratories or between different batch tests.

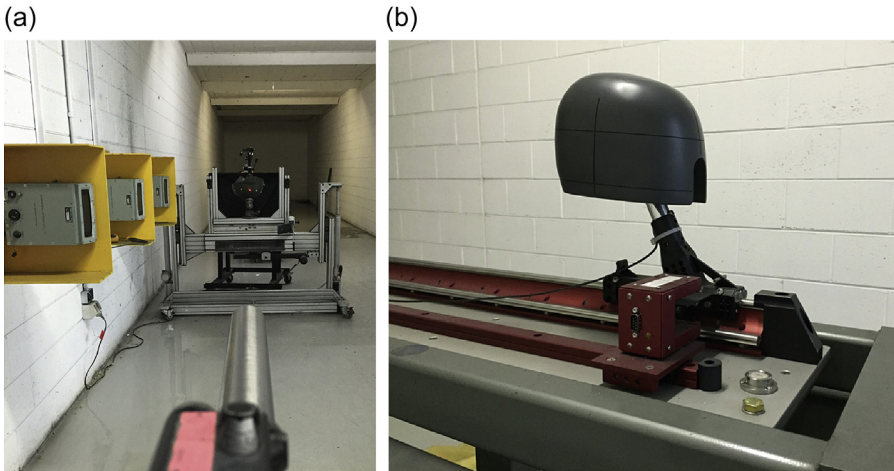


Figure 11.22 (a) One of BMT's ranges set up for testing of combat helmets and (b) BMT's helmet attenuation rig.

When conducting attenuation tests on helmets, in order to measure the acceleration experienced by the head, a head-form fitted with an accelerometer, is attached to a sliding stage [see Fig. 11.22(b)]. When the helmet is impacted by the bullet the sliding assembly is pushed back along the line of flight and the acceleration measured. Relevant standards set limits on the acceptable levels of acceleration.

11.3.3 *Stab and spike vests*

The constitution of these vests is covered in Chapter 6. They normally take the form of an additional pack which is placed in front of a standard SAI, or they could be integrated as part of a multithreat vest. Stab and spike threats are generally most often experienced by individuals in law enforcement and correctional roles although, more recently, military body armour is also tested against these types of threat.

Two industry standards for stab and spike resistance are the UK HOSDB ([UK Home Office, 2007b](#)) and the USA standard ([National Institute of Justice, 2000](#)). The most challenging aspect of stab and spike testing is the inconsistency found when testing blades and spikes from different suppliers. While all notionally comply with the requirements of the standards, insofar as the dimensions, hardness and surface finish are concerned, BMT has observed that there is a huge difference in their performance against real armour systems: those manufactured in the United States tend to be significantly more lethal than those manufactured in the United Kingdom, for example: to the point that a tested pack might pass with one and fail with the other!

11.3.4 *Bullet-resistant glass and transparent armours*

Virtually all ballistic testing standards that relate to buildings and/or vehicles will have a section relating to the testing of transparent armours. However, the mounting of the

transparent armour sample into the test fixture is vitally important to achieving a consistent and fair outcome. The test standard to which the armour sample is being tested will clearly define the mounting requirements and these must be strictly adhered to by the laboratory.

Environmental conditioning prior to ballistic testing is often required by the laboratory when testing laminated glass samples since operational factors from different climates, such as high/low temperature and thermal shock, can significantly affect the performance of the laminated glass. Vehicles can be expected to operate in a range of climates and it is common for them to experience long periods of time in direct sunlight during the day and low temperatures at night. Simulation of these conditions, through environmental preconditioning, has become very common.

Spall films are often used in the construction of transparent armours (see Chapter 7) and are designed to arrest small fragments of glass that may be released from the inside surface of the laminate behind the impact site. Being polymer-based, spall liner materials like polycarbonate can become very flexible when heated but very rigid and brittle when at subzero temperatures.

As described in Chapter 7, these surface layers, and interlayer materials, as well as the glass components, will invariably have different thermal expansion coefficients and therefore the laminated structure will be prone to delamination when heated or cooled. This is another reason why environmental conditioning prior to ballistic testing has become a vital part of any thorough ballistic testing program (see [Section 11.5](#)).

11.4 Check-production techniques

During a production run of armour products, whether it is a suite of body armour products, individual components like turret castings or even a set of RHA plate which is required in the construction of armoured vehicles, ballistic tests need to be carried out at a particular sampling rate. This is normally spelt out in the Statement of Requirements within the relevant procurement contract. For body armour components like HAPs, this could be 25 plates in every 1000 produced, with every one of the 25 plates being tested to particular ballistic standards. For cast steel turrets, this could be one in every 25 turrets. During such tests, as in the testing of a complete lightweight military vehicle, it is often a requirement to test the armoured structure's resistance to overmatching rounds. In the case of HAPs, this could involve the use of 20-mm FSPs. In the case of a turret casting, this could involve the use of a monolithic 17-pounder round, as used in WW2. These overmatching impacts are designed to give the component a really heavy shock loading, to test for structural integrity (eg, extensive secondary cracking) or unusual impact behaviour [eg, unacceptable generation of spall (see [Fig. 1.32](#))].

11.5 Preconditioning tests

Environmental conditioning of armour samples prior to ballistic testing is a very important part of any acceptance testing of any type of armour material or system. The user is



Figure 11.23 BMT's CL29 water.

very interested in gaining sufficient confidence that the armour will perform under a broad range of operational and climatic conditions. Any engineering weaknesses or material failings can be duly recognised and appropriately rectified, if need be.

There are two very similar test standards which are commonly used for environmental conditioning: the UK Def Stan 00-35 and the USA MIL-STD-810G, Environmental Engineering Considerations for Laboratory Testing. In addition, some of the more prominent body armour test standards have very specific pretest conditioning requirements. The USA body armour standards NIJ0101.03 and NIJ0101.04 feature a water spray condition while the latest version, NIJ0101.06, now has a requirement for water submersion, a drop weight durability test for hard armour and an entire section dedicated to environmental conditioning designed to stress the armour. The conditioning chamber for this test has strict internal conditions of $65^{\circ}\text{C} \pm 2^{\circ}\text{C}$ with $80\%\text{RH} \pm 5\%\text{RH}$ and is internally fitted with drums into which the armour is placed. The drums rotate at 5 ± 1 rpm.

Some of the more commonly requested environmental conditions the laboratory will be required to simulate are:

- Drop tests for HAPs, to simulate rough handling, transit drop, parachute drop and toppling. These tests are usually followed by x-ray imaging of the product;

- Water immersion — both salt and fresh water to various depths — to simulate use down to ~ 30 m of water, for example;
- A water spray technique, to test a material's ballistic response when slightly damp;
- Both high and low temperature, to cover the relevant diurnal range;
- Thermal shock, to simulate sudden change in operational temperatures;
- Exposure to solar radiation, to determine whether UV (ultraviolet) or IR (infrared) components cause damaging degradation in an armour product;
- The effects of low atmospheric pressure, to simulate conditions during air transport;
- The effects of vibration, to simulate tracked and wheeled vehicle transport;
- The effects of salt fog on possible corrosion;
- Contamination by fuels and chemicals;
- Any deleterious effects from fungal growth;
- The effects of humidity, particularly important with nonmetallic components.

The above list is by no means exhaustive and does not only apply to all armour products but the list *does* emphasise that armour materials, first and foremost, need to be sound engineering materials. It is therefore very essential that test houses, like BMT, are fitted out with a whole gamut of environmental conditioning chambers, fitted with appropriate data logging equipment so that accurate monitoring and reporting can be achieved. It is also good practice for the laboratory to log data from several locations



Figure 11.24 BMT's subzero conditioning immersion chamber room.



Figure 11.25 BMT's environmental conditioning bay.

within the chamber to monitor spatial variation and ensure that the samples are uniformly conditioned. [Figs 11.23–11.25](#) illustrate the range at the BMT facilities.

Acknowledgements

The authors are grateful to Horace Billon of the Defence Science and Technology Group, Department of Defence, Australia, for reviewing this chapter and to all of the staff at BMT, especially James Sutherland, who have contributed over the years to this essential suite of testing methodologies.

References

- Anon, 2014. Beekeeping, Trikes and Body Armour, TV Series: How Do They Do It? Released in USA on 17th July 2014.
- Australian Government, 2012a. DEF(AUST) 10946, ADF Personal Armour Test Standard, Part 1: Body Armour.
- Australian Government, 2012b. DEF(AUST) 10946, ADF Personal Armour Test Standard, Part 2: Combat Helmets.
- Barbillon, F., Auchere, R., Vuillemot, V., Simonetti, J.M., 2014a. Personal Armour Systems Symposium, Cambridge, UK.
- Barbillon, F., Auchere, R., Vuillemot, V., Simonetti, J.M., 2014b. "Shatter-gap effects" on HDPE plates with a lead-core steel jacketed 7.62 mm calibre ammunition. In: Personal Armour Systems Symposium, PASS 2014, Cambridge, UK, September 2014.
- Billon, H., 2007. DSTO-TN-0791.
- Borvik, T., et al., 2003. International Journal of Impact Engineering 28, 413–464.
- Carton, E., Rosebroeks, G., 2014. Testing method for ceramic armor and bare ceramic tiles. In: 38th International Conference on Advanced Ceramics and Composites: Armor Ceramic Symposium, Daytona Beach, USA, January 2014.
- Chiou, M., Schifflbein, P., Fackler, J., 2007. NIST Workshop, October 3, 2007.
- Crouch, I.G., March 1993. Penetration and Perforation Mechanisms in Composite Armour Materials, Euromech Colloquium 299. Oxford University.
- Crouch, I.G., 2014. Effects of cladding ceramic and its influence on ballistic performance. In: International Symposium on Ballistics, Atlanta, GA, USA, September 2014.

- Crouch, I.G., Appleby-Thomas, G., Hazell, P.J., 2015a. *International Journal of Impact Engineering* 80, 203–211.
- Crouch, I.G., Kesharaju, M., Nagarajah, R., 2015b. *Ceramics International* 41, 11581–11591.
- Department of Defence, 1997. AS/NZS 2343:1997, Bullet-Resistant Panels and Elements.
- Department of Defense, USA, 1997. DoD Test Method Standard MIL-std-662F, V-50 Ballistic Test for Armor.
- Gotts, P.L., 2014. Personal Armour Systems Symposium. Cambridge, UK.
- Hazell, P.J., 2006. *Ceramic Armour: Design and Defeat Mechanisms*. Argos Press, Canberra.
- Holmquist, T.J., Rajendran, A.M., Templeton, D.W., Bishnoi, K.D., 1999. Tardec TR 13754, Warren, MI, USA, January 1999.
- National Institute of Justice, USA, 2000. NIJ Standard 0115.00, Stab Resistance of Personal Body Armor, September 2000.
- National Institute of Justice, USA, 2008. NIJ Standard 0101.06, Ballistic Resistance of Body Armor.
- NATO, 2003. STANAG 2920 (Edition 2): Ballistic Test Method for Personal Armour Materials and Combat Clothing.
- Nguyen, L.H., Ryan, S., Cimpoeru, S.J., Mouritz, A.P., Orifici, A.C., 2015. *International Journal of Impact Engineering* 75, 174–183.
- Quelch, L.J., et al., 2002. Personal Armour Systems Symposium. The Hague, Netherlands, November 2002.
- Rosenberg, Z., et al., 1987. A new definition of ballistic efficiency of brittle materials based on the use of thick-walled backing plates. In: *Impact Loading and Dynamic Behaviour of Materials*, pp. 491–496 (Bremen).
- Savio, S.G., et al., 2011. *International Journal of Impact Engineering* 38, 535–541.
- UK Home Office, 2007a. HOSDB Body Armour Standards for UK Police (2007); Part 2-Ballistic Resistance.
- UK Home Office, 2007b. HOSDB Body Armour Standards for UK Police (2007); Part 3-Knife and Spike Resistance.
- Wells, M.W., Green, W.H., Rupert, N.L., 2001. Pre-impact damage assessment using x-ray tomography of SiC tiles encapsulated in discontinuously reinforced aluminium metal matrix composite. In: *Technology Convergence in Composites Applications*, UNSW, Sydney, Australia, February 2001.

The future of armour materials

12

I.G. Crouch

Armour Solutions Pty Ltd, Trentham, Victoria, Australia

The views and opinions expressed in this chapter belong entirely to the author, unless otherwise referenced, and the information given only applies to the future of armour materials for the following threats: small arms ammunition up to 14.5 mm armour-piercing (AP) rounds, high-velocity fragments, stab and spike threats, as well as all forms of blast, not just underbelly blasts.

12.1 General reflections

If the reader has managed to successfully navigate their way through the technical chapters of this book, they should now have a clear appreciation of what constitutes the ‘perfect’ armour material: a low bulk density, a high dynamic flow stress especially in the through-thickness direction, a high specific elastic modulus, high elongation to fracture, and excellent fracture toughness, whilst totally suppressing failure through plugging, discing, delamination and spallation. Of course, such a perfect armour does not exist. However, the ‘near-perfect’ solutions, as were discussed in Chapter 4, are those involving laminated materials and/or structures that contain layers of armour materials which have been specifically developed, tailored or selected for their functional properties. Because of this realisation, improvements in joining, bonding and laminating techniques are intrinsically important. For example, one could consider focusing the perceived benefits of graphene and carbon nanotubes (CNTs) by including them within polymeric films used to bond armour elements together, or even interleaving technical textiles with functional graphene-filled films. The beneficial effects of adding nanoparticles, of any kind, to enhance armour materials will be discussed throughout this chapter.

With a broad perspective, consider the individual families of armour materials, as discussed in Chapters 2–7. Have any of them reached their full potential in terms of ballistic performance and/or commercialisation? This is a serious question raised by many R&D managers and sponsors in the armour technology field when considering which particular technology to invest in, especially when budgets are limited. Fig. 12.1 provides a snapshot of my own top-level assessments. There are no firm technical bases for these views — just 35 years of active experience in the field, and 2 years of writing and editing this book. The ‘traffic light system’ of colours has been deliberately chosen to indicate where development work should stop, slow down, get ready or go, go, go. Red represents the oldest group of armour materials, the steels, which have been very close to reaching their full potential for a few decades now. Yellow identifies those groups where their physics and/or chemistry seriously limit further

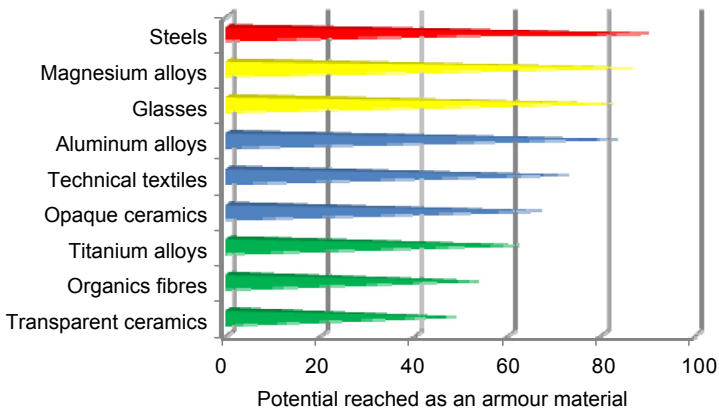


Figure 12.1 Potential reached as an armour material, as function of material groups.

development: both magnesium alloys and the conventional glasses are generically too soft to play any significant part in the future. The blue group offers some further scope through alloying and nanoparticle additions, whilst the green group is considered to have most development potential and an exciting future within the R&D community: armour-grade, titanium alloys have still not been fully commercialised; the organic fibres have much more to offer, as recent developments in ultrahigh molecular weight polyethylene (UHMWPE) fibre technologies have demonstrated; and the transparent ceramics have, in my view, perhaps the most still to gain. The US has spent many millions of dollars on this material group already over the past decade, and Surmet has recently supplied 200 ship sets of helicopter armour. However, panel sizes are still limited to 450 mm by 900 mm. Across all material groups, researchers please beware though — the industry does not need any more ‘PBO stories’ (see Chapter 6) so please remember: engineering properties first, ballistic performance second.

12.2 Trends in the threat spectra

New and increased levels of threat continue to challenge the armour technologist and applying the science of armour materials will be an on-going task for decades to come, with many careers-worth of research still left to do. Look at the evidence:

- A seemingly endless series of conflicts around the globe, especially in the Middle East, Eastern Europe and many other cross-border territories;
- Increased numbers of mass shootings, especially in the US ([Barrett, 2014](#));
- Increased numbers of domestic knife attacks, generally. A number of Australian hospitals now protect some of their employees with spike-resistant armour, as should most ‘first responders’, it is believed;
- Metal Storm technology, reborn under Defendtex ([Reddy, 2015](#)), is looking to further commercialise electronic weapon technologies that enable rapid fire of stacked projectiles. Minimum time between rounds means a greater likelihood of multiple strikes on, or near,

the same impact point. If this objective is realised, it will become a huge challenge for the armour technologist, especially when designing the ceramic-based armours with high E_m values, since these systems normally have relatively poor multihit performance;

- Improvised explosive devices are, by their nature, continually changing depending upon the availability of various materials around the battlefield. This is not likely to subside in the foreseeable future.

12.3 Trends in armour materials

12.3.1 Steels

As was reported in Chapter 2, steels are a very versatile armour material: available, structural, weldable, repairable and low cost. But they have been researched for more than a century and experienced rapid development during the birth of real material science in the 1950s and 1960s. Early in my own career, c.1984, I was asked to carry out a review of armour steels and a senior colleague and I came to the same conclusion then that steels were close to their natural asymptote.

However, three positive attributes remain unfulfilled, I believe:

- A high space efficiency;
- The bases of effective perforated armours or other geometrical/material combinations;
- The potential to increase the toughness of ultrahigh-strength variants through the production of roll-bonded, multi-ply laminates of high-hardness steels and mild steels (see Fig. 4.12, after [Kum et al., 1983](#)) to the author's knowledge this has never been fully explored for armour. One can imagine that underbelly armours could benefit quite significantly, if this idea materialised.

Finally, as will be discussed later, perhaps the biggest potential lies in *increasing* its cost, through more added-value. Perforated armours are one such example.

12.3.2 Light alloys

As was reported in Chapter 3, the light alloys are a mixed group of armour materials. The aluminum alloys were a child of the new science of strong materials in the 1960s and still offer considerable weight savings when used for construction of lightweight armoured vehicles. However, the need for grades that are stress corrosion-resistant, as well as weldable and AP-resistant is still a major objective. Of all the light alloys, titanium armour is a standout in terms of AP resistance but finding a low-cost manufacturing route is still elusive and limits the extent of its application. Suppressing discing failures, through laminating titanium with aluminum alloys is on the increase and has been a major success story for laminated armours. On the other hand, magnesium alloys, whilst fashionable within the research sector, offer little real potential and I believe that the majority of R&D in this narrow armour area should cease.

Throughout this book, very little has been said about metal matrix composites (MMCs). There is a good reason for this. MMCs do not make very good armour

materials because the addition of discrete organic particles or fibres into a ductile matrix does little to enhance the balance of properties required of an armour material: in general, MMCs have poor transverse properties, reduced ductility, and reduced toughness, with an increased propensity to discing and spalling. Very recent work by [McWilliams et al. \(2015\)](#) from the US Army Materials Laboratory demonstrates these undesirable aspects perfectly.

12.3.3 *Fibres and fibre-reinforced plastics*

As discussed in Chapters 5 and 6, the ongoing developments in high-performance fibres are exciting, with the properties and performance of both UHMWPE and aramid fibres and fabrics increasing year-on-year. However, are there limits to these developments and what might the downsides be?

Both polyethylene and aramid-based fibres are now available with very high tensile moduli, upwards of 140 GPa, and tensile strengths of up to 4.3 GPa, from fibres that have bulk densities between 950 and 1450 kg/m³. Fibre diameters are getting smaller and approaching 15 µm (see Figs 6.14 and 6.15). However, costs continue to rise. In fact, the AuTx fibres, manufactured using Ukrainian technology, have seemingly priced themselves out of many segments of the body armour market. Whilst I believe that the ceiling on properties is still way above current levels, prices may not be — there is as much work to do here as there is in continually improving mechanical properties.

I do have to add one cautionary note. The ageing of polymeric fibres is always a concern — the natural voids within a processed polymer control, to a large extent, the rate and degree of ageing ([Gladysz, 2014](#)). UHMWPE fibres, and fabrics, continue to be processed at higher and higher applied pressures, in an attempt to increase ballistic performance. However, this has two downsides: cost of materials and the cost of an effective method of production. UHMWPE laminates produced under extreme forming pressures are likely to retain a high level of residual stress which may, in turn, lead to higher levels of environmental degradation. I hope not. Rather than focus exclusively upon development of fibres that benefit from higher and higher forming pressures, I believe that new UHMWPE fabrics (ie, both fibre and matrix materials) should also be developed for processing via the autoclave route, since this is a far more preferable method of producing safe, reliable, reproducible quantities of Hard Armour Plate (HAPs) (see Chapter 5).

One other interesting application is worthy of some attention — the use of transparent Glass Fibre Reinforced Plastic (GFRP) interlayers ([Zhu, 2016](#)), within a transparent armour system. It is well known that glass fibre-reinforced epoxies, even in large section sizes of up to 60 mm, can have a high degree of transparency. The thought of utilising this principle by creating a stronger, tougher interlayer material, for laminated glass products, is intriguing. It also raises the possibility of making full use of sheets of graphene or carbon nanotubes to enhance the properties of thin polymeric interlayers.

Having mentioned CNTs, what about their potential as an armour material? To answer this, a landmark paper by [Mylvaganam \(2007\)](#) needs contextualising I think. Their work was totally based upon computer simulations and the fact that, unlike

metals which are significantly weaker when in the normal polycrystalline form, compared to their single-crystalline state, the length or size of CNTs does not involve atomic structural changes. Therefore their mechanical and physical properties should scale. However, after 15 years of laboratory-scale developments, I think it has become quite clear that manufacturing an armour element, based upon CNTs, of sufficient thickness and areal size, is extremely difficult, highly unlikely and probably cost-inhibited. The theoreticians have forgotten one thing about the science of armour materials — bulk properties, especially through-thickness properties, govern ballistic performance, not thin film effects per se (see Chapter 4). I hope the ‘graphene’ story can be more successfully applied to armour materials.

12.3.4 *Textiles*

The properties of textiles are naturally very dependent upon the fibres from which they are manufactured (see Chapter 6). Nevertheless, improvements in fibres which are targeted towards soft armour solutions continue to be made and represent some of the most innovative armour solutions. Two recent examples come to mind: Dyneema’s Diamond technology (DSM, 2015), and DuPont’s work on ceramic-coated Kevlar (Atanasov, 2014). Both these advancements are focused upon necessary improvements in stab and spike resistance. Dyneema’s Diamond technology involves the addition of ‘microparticles’ to very fine-diameter UHMWPE fibres and it is claimed (Anon, 2015) that a 25% reduction in the weight of a multitreat vest, resulting in an areal density of only 5.6 kg/m², is possible using such new fibres. In a similar manner, DuPont’s most recently published work has reported that researchers at North Carolina State University have developed a means of coating Poly-phenylene-terephthalamide (PPTA) (Kevlar) with a bilayer of TiO₂/Al₂O₃ using an atomic layer deposition method, leading to improvements in cutting resistance. Time will tell whether the process is scaleable and cost-effective.

One final thought. Most of the current UHMWPE-based fabrics tend to be nonwoven. However, tight and closely woven, fabrics still remain advantageous for stab and spike resistance, like DuPont’s Correctional fabric (see Chapter 6). Continual improvements in weaving technology, enabling finer and finer fabrics to be woven, is a technology worthy of parallel development, I believe.

12.3.5 *Glasses and ceramics*

Chapter 7 introduced the wide range of armour-quality glasses and ceramics and it is a field that has justifiably received an increased amount of attention over the past two decades. The well-attended series of the ‘Daytona Beach’ annual conferences on ‘Advances in Ceramic Armors’ is testament to this fact (Franks, 2007). Furthermore, in 2012, ARL established a program called ‘Enterprise for Multiscale Research of Materials (EMRM)’ (De Guire, 2013), which adopts a cohesive, materials-by-design approach to all basic science research into armour and electronic materials.

One of the first beneficiaries of this approach has been a comprehensive overview of the state-of-the-art in boron carbide, as reproduced in Fig. 12.2, recognising that some

State-of-the-art for ceramics (boron carbide)						
Scale or technical core element	Primary mechanism	Advanced experimental technique	Modelling & simulation	Bridging the scales	Material characterisation & properties	Synthesis & processing
Atomic	Electronic structure, thermal motion of nuclei, bond rupture	Spectroscopy, shock hugoniot	Quantum mechanics, density functional theory, energy of states	Coarse-grained DFT, potentials	Moduli, bandgap	Chemistry
Crystal	Cleavage, amorphisation, twinning, dislocation motion, stacking fault nucleation, twin-induced cracking	HREM, TEM, dynamic TEM, Kolsky bar, microcompression, nanoindentation, DAC	Molecular dynamics, discrete dislocation dynamics, discrete twinning dynamics, crystal plasticity	Coarse-grained DFT, hot QC, hyperdynamics	Anisotropic moduli, cleavage and twinning planes, intrinsic toughness	Powder production and control
Mesoscale	Triple-junction crack nucleation, grain-boundary failure, defect-activated cracks, intergranular vs transgranular fracture, crack interactions, anisotropic elastic effects on residual stresses and cracking	HREM, TEM, dynamic TEM, Kolsky bar, X-ray microdiffraction, instrumented indentation, phase contrast, in situ microcompression for GB strength, acoustic spectroscopy	Crystal plasticity, gradient terms, microstructure-resolved finite element method and optimal transportation meshfree	Defect dynamics, probabilistic models	Grain size distribution, grain morphology, texture, damage characterisation	Grain size control, grain boundary control, microstructural design, advanced processing techniques
Macroscale	Fast crack growth, effective plasticity, anisotropic damage growth, short vs long cracks, texture, fragmentation	Shock expts, Kolsky bar, spall experiments, in situ visualisation of damage	Viscoplasticity, FEM OTM, uncertainty quantification	Enhanced continua, nonlocal models, defect dynamics	High-strain-rate and high-pressure response, non-proportional loading, damage characterisation	Sintering, hot-pressing, advanced processing techniques
Generally identified, understood or implemented		Sometimes identified, some understanding, some implementation	Weak identification understanding, or implementation	Poorly identified, poorly understood, or early implementation	Not identified, not understood or not implemented	

Figure 12.2 A summary of views of relevant mechanisms, techniques, models and phenomena. Reproduced from De Guire, E., 2013. American Ceramic Society Bulletin 92, 26–31.

core elements are not well identified or understood, regardless of scale. This is an excellent and very commendable approach, especially for the US where expenditure on defence is still extremely high. The rest of the world needs to be a little more selective and targeted, perhaps. Certainly solving the amorphisation issue, associated with some of the B₄C polytypes, needs addressing as soon as possible for it is the Achilles heel of boron carbide.

The poor toughness of ceramics is usually perceived to be a real disadvantage as far as armour is concerned. However, I, for one, have become a keen advocate of designing with brittle materials since there are many ways of either suppressing or utilising brittle fracture behaviour. As reported in Chapter 7, a ceramic’s hardness is its most attractive feature as an armour material. So, even though recent researchers (Liu, 2015) have used the addition of ~1.5 volume% of reduced graphene oxide (rGO) to significantly increase the toughness of boron carbide to ~9 MPa m^{-1/2}, this was achieved by sacrificing both hardness and elastic modulus values. On the other hand, Belmonte (2016) recently published similar effects for rGO additions in SiC but, surprisingly, reported a 60% increase in strength. So, it appears that there are some exciting developments ahead in the use of rGO-reinforced ceramics.

One further way of increasing hardness still further would be to use cubic boron nitride powders, from commercial suppliers, or in nanotube form, as indicated by Bolduc (2014). However, both these forms are in very short supply and, whilst boron nitride nanotubes

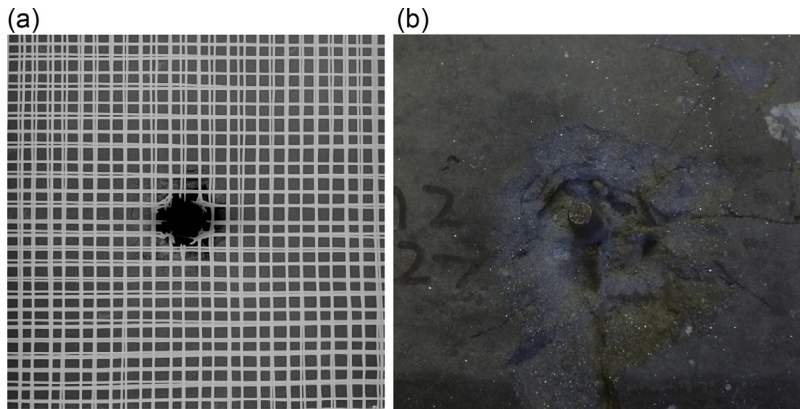


Figure 12.3 (a) A high-definition X-ray image of a SiC-based AusShield tile impacted by a 7.62 mm APM2 round, and (b) the core of an APM2 bullet that has simply embedded itself in the surface of a thick, unsupported tile of AusShield ceramic, showing minimal radial cracking (Crouch, 2010).

show great potential, the enabling technologies do not yet exist. Cubic boron nitride is the second hardest material, behind diamond.

On reflection, I also see a need to further explore more nonconventional approaches like that of Professor Andrew Ruys, who invented AusShield in the 1990s (Crouch, 2010) (see Fig. 12.3). This is a unique material consisting of 10 volume% steel fibres, in the form of a mesh (with or without z-pinning), reinforcing a zero-porosity ceramic component comprising about 85 volume% silicon carbide (or boron carbide or alumina) particles in about 15 volume% glass matrix. The thermal expansion mismatch of ceramic and steel fibres renders the ceramic in residual lateral tensile constraint in the order of 20 tonnes/m², in the case of a 12-mm thick tile. This means that considerable energy is required for crack propagation through the ceramic. However, such developments need to be achieved without disrupting cone formation, an essential failure mode in ceramic armours (Crouch, 2015).

As mentioned in Section 12.1, of all the types of glasses and ceramics, it is the transparent ceramics, based upon materials like the aluminium oxynitrides that have greatest untapped potential. Even though the market for transparent armours is much smaller than opaque armours, and considered quite a niche, there appears much still to do in terms of scaling the manufacturing processes. Of course, shaping techniques for both thin ceramics and thick transparent ceramics are still very desirable and remain a technology driver.

12.3.6 Microtruss materials

I have deliberately not referenced this class of material so far, in any of the chapters — this is because microtruss materials do not make very good, standalone, armour materials, especially when it comes to arresting small arms ammunition and high-velocity fragments. Nevertheless, as a limitless class of new materials they appear to have some

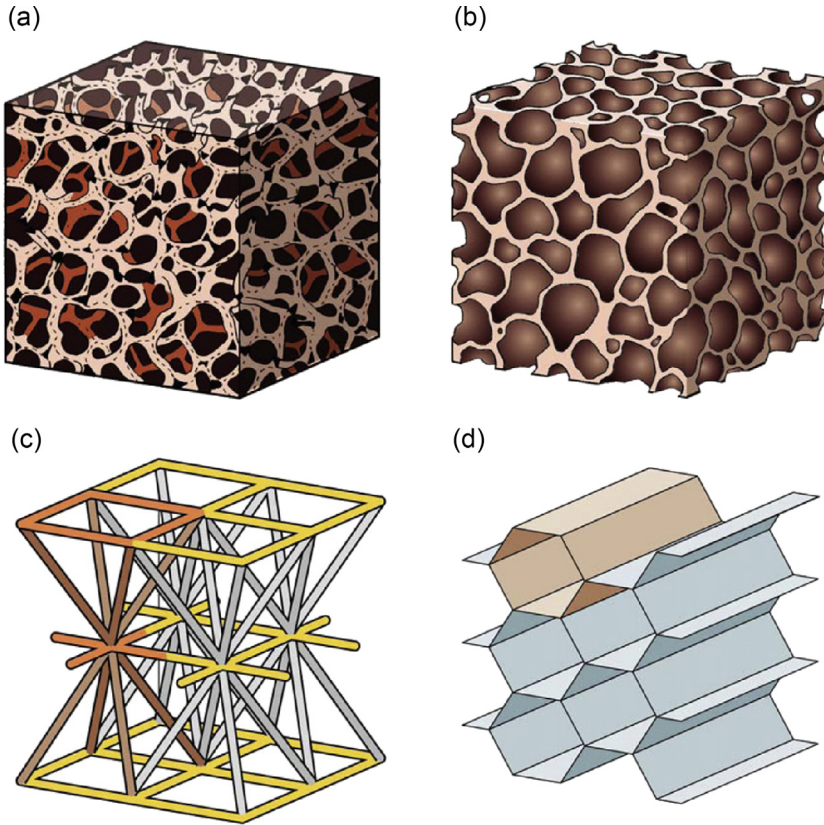


Figure 12.4 Examples of cellular materials that could be used for blast mitigation: (a) an open cell foam, (b) a closed cell foam, (c) a multilayered lattice structure and (d) a prismatic corrugated core.

After Wadley, H., et al., 2008. *International Journal of Impact Engineering*.

real potential when it comes to absorbing energy from blast; not necessarily underbelly blast but air blast.

Microtruss materials represent an infinitely wide range of engineered materials that provide a highly tailored set of mechanical properties. An example is shown in Fig. 12.4(c), compared with other classes of porous materials. Unlike metal foams, however, which are typically both cellular and irregular in structure, microtruss structures are engineered, repetitive, microbeams arranged into a ‘truss’ on a scale similar to the pores seen in typical metal foams. When investigated as shock wave mitigators, the literature reports individual ‘beam’ lengths in the trusses ranging from 6 to 20 mm (Bele, 2009; Wadley, 2008; McKown, 2007). When compression loaded in the through-thickness direction, they behave much like metal foams and display a stress plateau until the amount of strain collapses the microtruss structure, at which point they display generally monolithic compressive behaviour (Wadley, 2008).

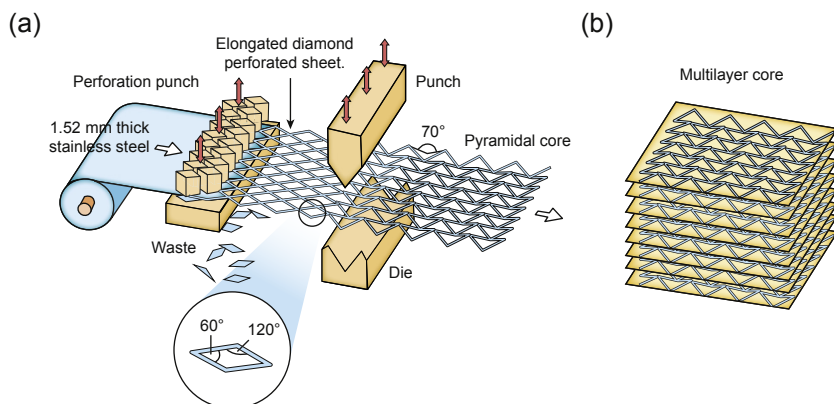


Figure 12.5 Sheet blanking method (a) for production of a microtruss structure as seen in (b). Reproduced from Wadley, H., et al., 2008. *International Journal of Impact Engineering*.

They therefore fall into line with other porous, energy-absorbing materials like the metallic foams, the honeycomb structures, as well as the numerous examples of fibre-reinforced, polymeric, end-crushing, tubes. However, there is one huge difference: coupled with rapidly expanding 3-D printing technologies, these structures can be tailormade with a uniform set of microproperties. [Rashed \(2016\)](#) has very recently reviewed the many different methods of manufacture, a coarse example of which is shown in [Fig. 12.5](#). These materials certainly spark the imagination but this calls for even greater selectivity when it comes to R&D programmes focused upon the development of new armour materials.

Finally, as a footnote to this section, and on a much smaller scale, metal-organic-frameworks are also receiving some attention, especially when associated with development of graphene-based nanostructures (see recent review by [Ahmed and Jung, 2014](#)). Like the microtruss materials, they can also be tailormade and ‘grown-to-order’.

12.4 Trends in armour systems

If there is one trend in armour systems it is that there is no trend in armour systems — they simply get more complex and more innovative, year-on-year, as the threats continue to evolve. Over the decades, I have not met many people, professional or otherwise, who do not have the ‘best’ idea for a ‘bullet-proof’ material or armour system. Ideas are seemingly limitless, thankfully, and the patenting community is increasingly active. The reader should take time to read the excellent paper by Haque, Kearney and Gillespie, from the University of Delaware ([Haque, 2012](#)) — it is a comprehensive review of the patent literature, as well as the history, of protective armours for both personnel and vehicles, and includes a very expansive catalogue of patented ideas.

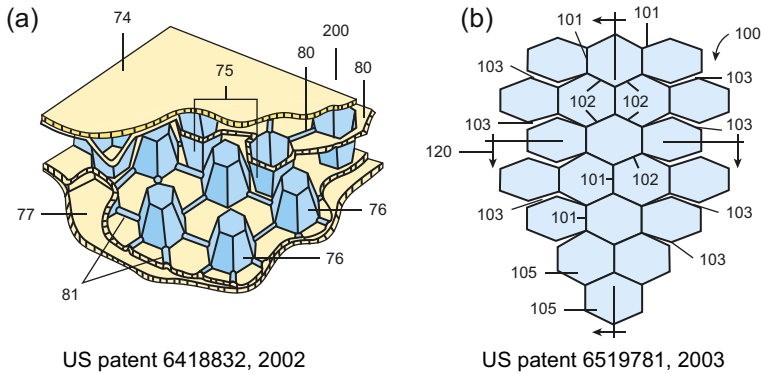


Figure 12.6 Extracts from just two of the plethora of patents related to body armour systems.

With all of these bright ideas, one very significant point appears to have been overlooked, by some of the inventors — it is important, when designing lightweight armour systems, that the ballistic performance of a proposed system is consistent at all possible points of impact. When viewing the selection of patented ideas in [Figs 12.6 and 12.8](#), consider how variable the ballistic performance might be from point to point. If the armour does not have a uniform, through-thickness structure, it will not display a uniform level of ballistic performance. For a nonuniform structure to become a real armour system, it would need to be designed around its weakest point, and therefore the final system will be overengineered, and therefore overly heavy. This is why ceramic systems using a mosaic of individual tiles are heavier than monolithic ones (see Chapter 7).

One other important point to note about the plethora of patented ideas — by definition, these publically available ideas will not represent, in any way, the classified nature of real armour systems employed by the military. However, the ever-increasing number of these patented ideas does reflect the commercial value placed on possible applications — the body armour market, in particular, is not getting any smaller, and the nonmilitary market is far larger than the military one.

12.4.1 Body armour systems

The market for personal protection systems continues unabated according to a number of publically available market surveys ([Visiongain, 2009](#)), with market size estimated to be worth about US\$1.4 billion by 2021. Many countries have military projects that are focusing upon development of the next generation of body armour systems: US Army's Soldier Protection Systems, the UK's Future Infantry Soldier Technology programme, France's FELIN programme and the Israelis' Advanced Soldier. Police militarisation also adds to the increasing demand for advanced body armour systems, on top of an already burgeoning police body armour market. In the US, [Horn et al. \(2012\)](#) carried out a strategic study of different approaches to lightening body armour systems for the US Department of Defense (DoD) and concluded that there was no 'silver bullet'

material solution and that future weight reductions would have to come through changes to the stated levels of ballistic performance or different design concepts. Interestingly, the report even suggested removing the Berry amendment so that 'US servicemen were ensured of wearing the best, most durable, and most protective, armor available in the world'. The Berry Amendment (USC, Title 10, Section 2533a), in place since 1941, requires the US DoD to give preference in procurement to domestically produced, manufactured, or homegrown products. In my view, the US DoD, and therefore its servicemen, are indeed missing out on some of the world's best practice and products, and would benefit from relinquishing this restrictive trading practice.

There is strong evidence to suggest that commercial suppliers of body armour systems are converging towards similar technical solutions as information becomes more public and designs become closer to ultimate solutions (Crouch, 2016). The major differentials are now cost (both acquisition costs and refurbishment costs) as well as responsiveness (meaning an ability to quickly provide a change in product, as the demand changes). A strategy of 'adaptive acquisition', as adopted by the Australian Defence Department in the early 2010s, now enables the user to take full advantage of the latest technological improvements. This acquisition policy is in strict contrast with traditional strategies of purchasing entire stocks of body armour systems, on an irregular basis, for the entire fleet. The Australian Army now has both modular systems, like Modular Combat Body Armour System (MCBAS), and tiered systems, like Tiered Body Armour System (TBAS) (see Chapter 6).

How can body armour systems be further lightened? I believe there are two additional approaches that could be taken: one, through a change in strategy, the other through a more holistic approach to design. In terms of strategy, I believe the time might have come for the user to review the reality of the operating environment and adopt a more pragmatic view without increasing the risk to the lives of the dismounted soldier. Reducing the number of strikes has already occurred (Crouch, 2016). However, further reductions in system weight could be achieved if oblique attacks were considered the norm and protection levels were reduced were re-evaluated in terms of distance from target. I am not advocating blind adoption of such an approach — just recognition that further weight savings are possible if the ballistic requirements were softened slightly. Food for thought, I hope.

In terms of a holistic approach to design, the users should now be aware that technologies, and a suite of armour materials, now exist that enable the user to seriously consider body armour systems that offer a range of protection levels, within a multirole, single-product, armour system. By way of example, Fig. 12.7 shows two general schemes developed by the author back in 2010. Scheme 1 is now possible with shapeable ceramics like the Viscous Plastic Processing (VPP) boron carbide described in Chapter 7, and Scheme 2 is quite feasible through adoption of newly developed UHMWPE soft and hard armour materials.

During the Afghanistan conflict, an adaptive acquisition strategy was adopted by both defence and industry in order to reduce the acquisition time and improve technology uptake. It is the much-preferred model for innovation, and prevents technology

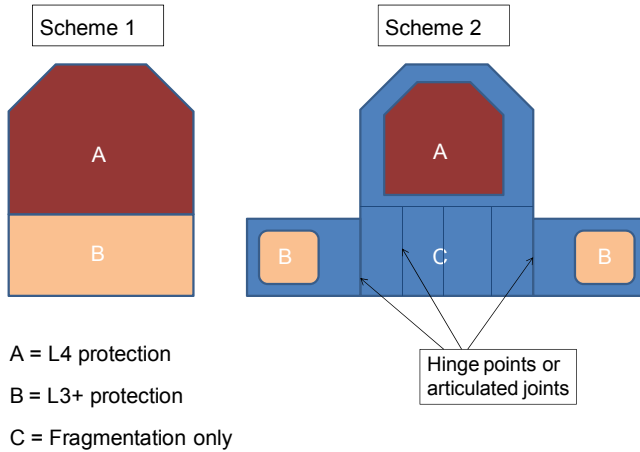


Figure 12.7 Generic examples of lightweighting Body Armour System (BAS) through grading protection levels across the product (Crouch and Sandlin, 2010).

disruption. I only hope that this system and procurement culture continues because it certainly maximises the value of limited R&D funding in the personal survivability space.

12.4.2 Vehicle armours

The market for military vehicles, including both upgrades and retrofitting programmes, continues unabated, with market sizes of around US\$2.4 billion per annum, based upon 2012 figures (Visiorgain, 2010). Fig. 12.8 shows a small sample of the plethora of patented ideas for new vehicular armours. Of course, increasing threat spectra will continue to drive the design of real systems and it would be impossible here to review all cases. I think it is sufficient to provide the reader with a few general observations and highlights.

When it comes to durable ceramic-based systems, it has become quite popular, I believe, to consider pelletised solutions as described in Wang (2013) and as shown in Fig. 12.8(c). These may be less efficient, ballistically, than monolithic solutions, but they are extremely robust (an important requirement in military applications) and the impact damage can be much localised.

Space efficiency is often overlooked as an attractive requirement. Nevertheless, I believe there is a need for new armour materials which are both space-efficient and mass-efficient. This can only be achieved, of course, by investigating the benefits of very hard, dense materials, like those of interest to the developers of long-rod penetrators. It is not a new idea: work on tungsten carbide ceramics was published by Gooch, Burkins and Palicka, 15 years ago (Gooch, 2000).

Chapter 2 included a section on the benefits of bolted structures over welded ones. From an armour technologist's point of view, this option is extremely attractive since bolted structures of modular designs are generically free of structural heterogeneities

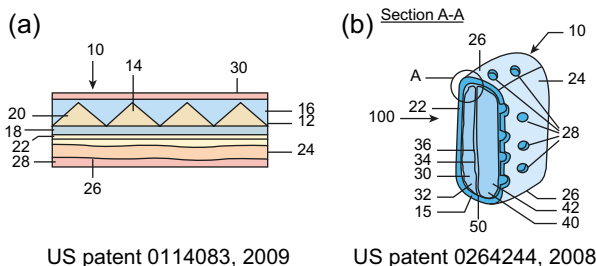


Figure 12.8 Extracts from just two of the plethora of patents related to vehicular armour systems.

associated with the welding process; they are easier to repair; the armour materials can be interchangeable and upgradeable, and armour materials with much higher ballistic efficiencies can be better utilised.

Finally, I believe that, as microengineered materials become a reality, more use will be made of blast-resistant armours — it is not just about geometry, when it comes to protecting underbellies, and the occupants, of military vehicles.

12.5 Final thoughts and suggestions

The design drivers for any armour system still need to be a reduction in processing costs (as well as raw material costs), as much as an increase in performance. This is what has driven me over the past 15 years to develop a cost-effective reaction sintered silicon carbide (Crouch, 2015), and why the Defence Materials Technology Centre (DMTC) has been driven to develop an alternative process to the hot-pressing of boron carbide, and develop the VPP process (see Chapter 7). The relationship between cost and ballistic performance is explored more deeply in this final section.

Consider the data set compiled for the 7.62 mm APM2 threat, as shown in Table 12.1. Of course, such a table of data should, and is, developed for any threat and the following analyses can be similarly applied to any threat scenario. The areal density data have been sourced from a number of references and include those well-established performance figures published in 1991 (Anon, 1991). The Em data have been generated in the conventional manner by normalising with respect to standard RHA. The cost data, on the other hand, have been compiled by the author through various means, and are at best, educated guesstimates of the cost of supplying medium-scale quantities of the materials into the Australian market c.2015. They are also expressed in Australian dollars, with currency conversion figures given in the footnote.

This set of data becomes very illuminating when plotted out, as shown in Fig. 12.9. As can be seen, there is a great deal of scatter in the data, as one would expect, but there is also a natural upward trend, again, as one would expect. I have used this plot to illustrate how a designer might select a particular armour system: first, one would set a minimum acceptable level of ballistic performance — in this case, I have selected an Em

Table 12.1 Em and Cost data, in AU\$/kg, for a range of armour materials

Armour material/system	Source for AD	AD (kg/m ²)	Em	Cost (\$/kg)
RHA	IDR (1991)	114	1.00	4
HHS	IDR (1991)	98	1.16	4
DHA	IDR (1991)	64	1.78	7
5083	IDR (1991)	128	0.89	9
5059-H131	Showalter et al. (2008)	128	0.89	10
6061-T651	Ryan (2015)	135	0.84	9
7039	IDR (1991)	106	1.08	15
7075-T651	Ryan (2015)	107	1.07	18
2519	IDR (1991)	100	1.14	12
Ti-6Al-4V	Timet (2015)	86	1.33	113
Mg alloy ZK60A	Van de Voorde (2005)	135	0.84	120
E-glass FRP	IDR (1991)	115	0.99	24
S2-glass FRP	IDR (1991)	93	1.23	30
Soda lime glass	Strassburger (2009)	170	0.67	24
AlON/PC/Glass/PC	Strassburger (2009)	65	1.75	150
Alumina/5083	IDR (1991)	50	2.28	35
Alumina/7020	IDR (1991)	42	2.71	38
Alumina/KFRP	IDR (1991)	38	3.00	150
B4C/6061	IDR (1991)	35	3.26	200
B4C/UHMWPE	Crouch (2014)		3.56	220

(1) Sources of Areal Density data: Anon (1991), Showalter et al. (2008), Ryan (2015), Timet (2015), Van de Voorde (2005), Strassburger (2009) and Crouch, (2014).

(2) Source of estimated cost data: Crouch (2015).

(3) Currency exchange rates used: 1 AU\$ = 0.70 US\$ and £0.50.

value of one. Then, on a case-by-case basis, a line of affordability could be drawn, the slope of which is equivalent to a cost–benefit line. The crucial question is ‘how much value does the user place on saving weight?’ So the slope of this line will depend whether one is designing a weight-sensitive item like a body armour system, or a weight-insensitive application, like a concrete bunker.

What this plot also provides is a very useful, pictorial overview of where improvements to either cost and/or performance should be focused. The four triangular zones are proposed areas of future development. The titanium alloys (light green triangle), the aluminium oxynitrides (blue triangle) and the boron carbides

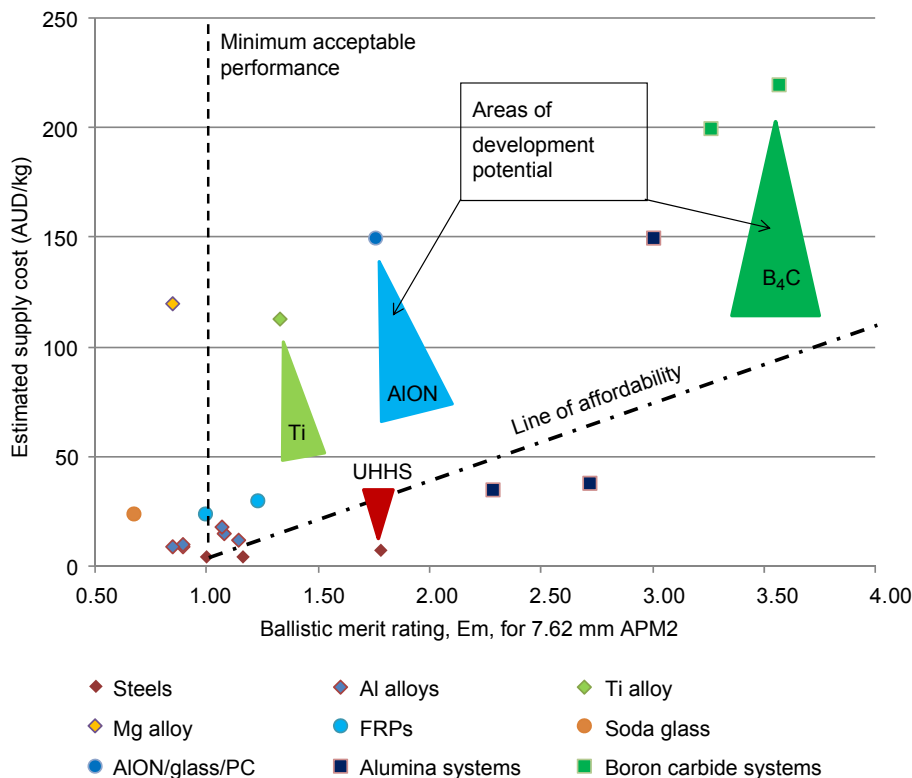


Figure 12.9 A plot of E_m versus estimated supply cost for most families of armour materials. Note that the E_m values have been calculated for the 7.62 mm APM2 round.

(dark green triangle) could certainly benefit, commercially, from a reduction in cost. It is suggested that this should be achieved without a reduction in ballistic performance, except in the case of boron carbide, perhaps, which already has a high E_m value. It is this latter example, corresponding to the dark green boron carbide triangular area, where the DMTC has focused most of its attention over the past 5 years.

An interesting, and unexpected, point came out of this exercise. The armour steels (brown development triangle) are the only family that sits below the line of affordability. The opportunity exists, therefore, for the ultrahigh-hardness steels to increase in cost, and still remain attractive to the armour engineer. Such an increase could come through some form of added-value perhaps.

Keeping R&D focused upon the needs of the end user is paramount, of course, as with any service provider. The technologies need to be scalable and commercialisation paths well prepared. The armour technologist should also be sufficiently broad-minded to take full advantage of parallel developments in other fields and, at this present time, this means additive manufacturing, 3-D printing, faster computing and better graphics (Wang, 2015). Crucially, though, it is about having a clear pathway to the end user.

The Australian model and system of acquisition is very efficient and very current: short supply chains and an adaptive acquisition strategy, facilitated by organisations like Diggerworks and the DMTC. I only hope that this approach continues in peacetime, as it did during recent conflicts, for it has been a very rewarding, as well as fruitful, experience to have been an active player during these last 10 years.

12.6 Final words

I have always enjoyed the works of Professor James Gordon (1968, 1978) and have unknowingly adopted a similar writing style: interesting and engaging (hopefully), as well as personal, rather than purely factual. It was Professor Gordon who pointed out that it is normal evolutionary behaviour for new engineering materials to be introduced via military applications/requirements: steels for swords, aluminium alloys for helmets and polyethylene for use in radar systems, and that these new introductory materials are always accompanied by higher acquisition costs, at least initially.

Gordon (1968) also wrote the following prophetic words in conclusion to his first work on *The New Science of Strong Materials*: ‘It is not possible to acquire a catholic knowledge of materials entirely by reading books; one must use direct observation and experience. Just as the real knub of learning photography, or drawing, or painting, lies in learning to see, so one has to cultivate the habit of noticing and observing the structures and materials around one — even the commonest of them — with a seeing eye’.

Here, in *The Science of Armour Materials*, ‘witnessing is understanding’, as has been stated on many occasions, and understanding how armour materials fail is the secret to the development of new armour materials, which brings me back to where this book started, with Kipling’s poem ‘Hymn of Breaking Strain’ (see the Preface). This was an offering to final year undergraduates, just before their ‘finals’ by Dr Chris Hammond, Lecturer in Metallurgy, University of Leeds in the 1970s. Thanks, Chris!

Acknowledgements

I would like to thank Deepak Ganga, from the Defence Materials Technology Centre, Australia, for reviewing this chapter and providing further insightful information about the Australian procurement system.

References

- Ahmed, I., Jhung, S.H., 2014. *Materials Today* 17, 136–146.
- Anon., 1991. *International Defence Review* 1991, 349.
- Anon., December 2015. www.dyneema.com.

- Atanasov, S.E., et al., 2014. Improved cut-resistance of kevlar using controlled interface reactions during atomic layer deposition of ultrathin, *Journal of Materials Chemistry A*.
- Barrett, D., September 25, 2014. *The Wall Street Journal* A3. Thursday.
- Bele, E., Bouwhuis, B., Hibbard, G., 2009. Failure mechanisms in metal/metal hybrid nanocrystalline micro-truss materials, *Acta Materialia*.
- Belmonte, M., et al., 2016. *Scripta Materialia* 113, 127–130.
- Bolduc, M., et al., 2014. Toward Better Personal Ballistic Protection. *PASS 2014*, Cambridge, UK.
- Crouch, I.G., Sandlin, J.D., 2010. DMTC Technical Report.
- Crouch, I.G., Kesharaju, M., Nagarajah, R., 2015. *Ceramics International* 41, 11581–11591.
- Crouch, I.G., Sandlin, J.D., Thomas, S., Seeber, A., 2016. Material science behind the development of a new, shapeable, boron carbide, armour material. In: 29th International Symposium on Ballistics, Edinburgh, UK, May 2016.
- Crouch, I.G., March 2010. *Materials World* 26–27.
- Crouch, I.G., 2014. Private Communication.
- De Guire, E., 2013. *American Ceramic Society Bulletin* 92, 26–31.
- DSM, 2015. www.dyneema.com.
- Franks, L.P., 2007. *Advances in Ceramic Armor III*. Wiley, New Jersey.
- Gladysz, G., Chawla, K., 2014. *Voids in Materials: From Unavoidable Defects to Designed Cellular Materials*. Elsevier.
- Gooch, W.A., Burkins, M.S., Palicka, R., 2000. *Journal de Physique IV* 10, 741–746.
- Gordon, J.E., 1968. *The New Science of Strong Materials*. Penguin Books, Middlesex, England.
- Gordon, J.E., 1978. *Structures*. Penguin Books, Middlesex, England.
- Haque, B.Z., Kearney, M.M., Gillespie, J.W., 2012. Recent Patents on Materials Science 2015, 103–134.
- Horn, K., et al., 2012. Lightening Body Armor – Arroyo Support to the Army Response to Section 125 of the National Defense Authorization Act for Fiscal Year 2011. RAND Corporation.
- Kum, D.W., Oyama, T., Wadsworth, J., Sherby, O.D., 1983. *Journal of the Mechanics and Physics of Solids* 31, 173–186.
- Liu, L., et al., 2015. *Journal of the American Ceramic Society* 2015, 1–8.
- McKown, S., et al., 2007. *International Journal of Impact Engineering* 35, 795–810.
- McWilliams, B., Yu, J., Pankow, M., Yen, C.-F., 2015. *International Journal of Impact Engineering* 86, 57–66.
- Mylvaganam, K., Zhang, L.C., 2007. *Nanotechnology* 18, 475701.
- Rashed, M.G., et al., 2016. Metallic microlattice materials: a current state of the art on manufacturing, mechanical properties and applications. *Materials and Design*. <http://dx.doi.org/10.1016/j.matdes.2016.01.146>.
- Reddy, T., 2015. www.defendtex.com.
- Ryan, S., Cimpoeu, S., 2015. An evaluation of the Forrestal Scaling Law for predicting the performance of targets perforated in Ductile Hole Formation. In: 3rd International Conference on Protective Structures (ICPS3), Newcastle, Australia.
- Showalter, D.D., Placzankis, B.E., Burkins, M.S., 2008. ARL-TR-4427.
- Strassburger, E., 2009. *Journal of the European Ceramic Society* 29, 267–273.
- Timet, 2015. www.timet.com.
- Van de Voorde, M.J., Diederan, A.M., Herlaar, K., 2005. Preliminary investigation of potential lightweight metallic armour plates. In: International Conference on Ballistics, Vancouver, Canada, November 2005.
- Visiongain, 2009. www.visiongain.com.
- Visiongain, 2010. www.visiongain.com.

- Wadley, H., et al., 2008. Compressive response of multilayered pyramidal lattices during underwater shock loading, *International, Journal of Impact Engineering*.
- Wang, Q., Chen, Z., Chen, Z., 2013. *Materials and Design* 46, 634–639.
- Wang, K., et al., 2015. *Materials and Design* 67, 159–164.
- Zhu, H., Khanna, S.K., 2016. *International Journal of Impact Engineering* 89, 14–24.

Index

‘*Note:* Page numbers followed by “f” indicate figures, “t” indicate tables.’

A

- AAAV. *See* Advanced Amphibious Assault Vehicle (AAAV)
- ABALs. *See* Adhesively bonded aluminium laminates (ABALs)
- ABAQUS, 485–486, 490, 528–530
- Absorbers, 180
- Active Protection System, 305
- ADA. *See* Australian Defence Apparel (ADA)
- Adaptive acquisition, 685
- ADF. *See* Australian Defence Force (ADF)
- Adhesively bonded aluminium laminates (ABALs), 172, 184, 193–194, 221, 428–429
- Adiabatic shear, 82–85
 ranking of material properties, 86t
- Adiabatic shear bands (ASBs), 62, 123
- Advanced Amphibious Assault Vehicle (AAAV), 121
- Advanced Glassfiber Yarns (AGY), 224
- AFVs. *See* Armoured fighting vehicles (AFVs)
- Age-hardening grades, 130–134
- Ageing process, 130–131
- AGY. *See* Advanced Glassfiber Yarns (AGY)
- Air blast
 loading, 15–17
 tests, 601–603
- Air gap, 180–182, 245
- AK47 bullet, 655
- Al-Li alloys. *See* Aluminium-lithium alloys (Al-Li alloys)
- Alcoa’s Al-2090 alloy, 136
- ALE methods. *See* Arbitrary Lagrangian Eulerian methods (ALE methods)
- ALEGRA, 516
- Alekseevskii–Tate equations, 405–406
- model, 403, 406, 408
 prediction, 407f
 relationship, 408–409
- Alloy 2139, 136
- Alloy WE43, 158
- AlON. *See* Aluminium oxynitride (AlON)
- ALPORAS, 528–530, 530f
- Al–Silicon 4xxxx series alloys, 127
- ALULIGHT, 528–530, 530f
- Alumina-aluminium laminated armour, 197–198
- Aluminium
 armours, 122
 naval vessels, 121
 oxides, 357
 plate, 332
- Aluminium alloys, 2, 117–118, 121–122, 125, 128t, 677
 age-hardening grades, 130–134
 against armour piercing projectiles, 429–431
 ballistic properties of different grades, 134–139
 designation system, 126t
 temper designations, 126t
 work-hardening grades, 127–129
- Aluminium oxynitride (AlON), 343
 processability and performance, 354t
- Aluminium-lithium alloys (Al-Li alloys), 137–139
- Aluminium–zinc–magnesium alloy, 119
- Analysis of variance (ANOVA), 543, 543f–544f
- Analytical modelling. *See also* Numerical modelling
 computational packages for finite-thickness armour targets perforation, 460–475

- Analytical modelling (*Continued*)
 penetration into semi-infinite metallic targets, 395
 centreline momentum balance, 412–414
 empirical cratering relationships, 399
 four-phase penetration model, 397–399, 398f
 hydrodynamic jet penetration, 395–397
 idealised jet penetrating target material, 396f
 modified hydrodynamic theory, 399–412
 one-dimensional finite difference discretisation, 415–417
 for penetration/perforation of nonmetallic armour, 433–460
 perforation of finite metallic armour targets, 417
 Breakout program, 427–428, 427f
 cavity expansion theory, 417–419
 penetration/perforation of laminated materials/targets, 428–431
 plasticity theory, 419–422
 Ravid–Bodner multistage model, 422–427
- ANN. *See* Artificial neural networks (ANN)
- ANOVA. *See* Analysis of variance (ANOVA)
- ANSYS-AUTODYN, 487
- Antistab (AS), 319
- AP. *See* Armour-piercing (AP)
- APCs. *See* Armoured personnel carriers (APCs)
- Aramid, 237, 282
 aramid-based fibres, 678
 aramid-based system, 248–249
 fibres, 226–227, 229t
 yarns, 626
- Arbitrary Lagrangian Eulerian methods (ALE methods), 487, 491–493
 conservation equations, 492t
- ARL. *See* US Army Research Laboratory (ARL)
- Armour development, experimental techniques during, 648
 for evaluating armour materials, 650–654
 for evaluating armour systems, 648–649
 for studying defeat mechanisms, 654–655
- Armour materials, 1
 in active service, 2f
 armour steels, 689
 armour systems design, 39–47
 defeat mechanisms, 21–23
 Em and vost data for range, 688t
 essential materials science, 47–51
 evaluation
 through DOP tests, 651
 through estimated V-50 tests, 650–651
 through residual depth of penetration tests, 652–653
 through spall tests, 653–654
 through study of single strikes, 650–654
 operational environment, 1–4
 penetration mechanics and failure modes, 23–39
 reflections, 675–676
 strain-rate events categories, 22t
 terminal ballistics, impact dynamics and armour physics, 19–21
 threat, 4–19
 trends
 in armour materials, 677–683
 in armour systems, 683–687
 in threat spectra, 676–677
- Armour materials, trends in
 fibres and fibre-reinforced plastics, 678–679
 glasses and ceramics, 679–681
 light alloys, 677–678
 microtruss materials, 681–683
 steels, 677
 textiles, 679
- Armour physics, 19–21
- Armour piercing projectiles, Al alloy against, 429–431
- Armour products for personal protection, 256
 combat helmets, 258–261
 HAPs, 256–258
 thermoformed shields and visors, 256
- Armour response, 19
- Armour steels, 60f, 619–620. *See also* Laminated armours
 alloying additions, 63t
 beneficial properties
 cost and availability, 80–82
 fabricability, 76–80

- hardness, strength and toughness, 67–70
- high strain rate effects, 70–75
- microstructural aspects, 64–67
- tensile quasistatic true stress–strain, 74f
- compositional ranges, and minimum properties, 93t
- failure mechanisms and modes, 82–92
- Fe–C phase diagram, 61f
- ferrous alloys, 59–63
- grades of armour steels, 92–104
- hardenability curve, 64f
- from ‘Little Willie’ to ‘Bushmaster’, 55–59
- specifications and standards, 104–111
- true stress–strain curves, 621f, 623f
- Armour systems, 663
 - BAS, 663–667
 - bullet-resistant glass and transparent armours, 668–669
 - combat helmets, 667–668
 - design, 39
 - categories of armour systems and materials, 45t
 - design process, design drivers and mathematical modelling, 42–44
 - for different applications, 44–47
 - Milne-de-Marre graph, 46f
 - multilayered systems design, 42
 - one-plate armour system, 40f
 - process, 43f
 - of simple, elemental systems, 40–42
 - evaluation
 - through residual velocity curves, 649
 - through V-50, σ and BFS measurements, 648–649, 649f
 - stab and spike vests, 668
 - trends in, 683–687
 - body armour systems, 684–686
 - vehicle armours, 686–687
- Armour-grade ceramics, 334
 - failure modes, 336–338
- Armour-piercing (AP), 127–129, 471, 675
 - rounds, 8–10
- Armoured fighting vehicles (AFVs), 205
- Armoured personnel carriers (APCs), 1, 58, 118, 205
- ARMOX 500T, 619–620
- Army Ballistic Limit, 647
- Artificial neural networks (ANN), 466
- AS. *See* Antistab (AS)
- ASBs. *See* Adiabatic shear bands (ASBs)
- Austenite, retained, 67
- Australian Defence Apparel (ADA), 216–217
- Australian Defence Force (ADF), 1, 58
- Australian Defence Standard 8030, 105
- Autoclave route, 678
- AUTODYN
 - Hydrocode, 524
 - software, 485–487
- AuTx fibres, 283, 678
- Axial cracking, 333
- Azepan-2-one. *See* Nylon 6
- B**
- B₂O₃. *See* Boron anhydride (B₂O₃)
- BABT. *See* Behind armour blunt trauma (BABT)
- Back stress, 516, 517f
- Back-face signature (BFS), 313–314, 647, 660f
- Back-face deformation (BFD), 647, 660f
- Backing material, 381
- Ballistic and Mechanical Testing (BMT), 639, 641, 662
 - CL29 water, 670f
 - environmental conditioning bay, 672f
 - subzero conditioning immersion chamber room, 671f
- Ballistic testing methodologies, 639
 - check–production techniques, 669
 - experimental techniques during armour development, 648–663
 - failure definitions, 645–648
 - pass/fail criteria for armour materials and systems, 646t
 - preconditioning tests, 669–672
 - standard techniques, 663–669
 - test procedures and terminologies, 642–645
 - firing sequence for Bruceton method, 644f
 - probability curves for defeat of armour materials and systems, 643f
 - testing environment, 639–642
 - arrangement for lightweight armour products, 640f
 - NIJ, 641
 - yaw card with number of different perforations, 642f

- Ballistic(s), 19
 fabrics
 element, 271
 technical fibres for, 274–288
 technical textiles and, 288–306
 grades, 127
 laminates, 203
 nylon, 281
 performance, 206
 edge performance, 386
 V-50 determinations, 382–385, 384f–385f
 properties
 of different grades, 134–139
 and specific failure modes, 122–125
 windows, 140–141
 BAS. *See* Body armour system (BAS)
 Basket weave, 235
 BCC. *See* Body-centred cubic (BCC)
 Behind armour blunt trauma (BABT), 269
 Benzene-1,4-diamine, 281–282
 Bernoulli's theorem, 396
 Beta-phase Mg_2Al_3 , 140
 BFD. *See* Back-face deformation (BFD)
 BFS. *See* Back-face signature (BFS)
 Blast events and loadings, 15
 air blast loading, 15–17
 armour response, 19
 underbelly blast loading, 17–19
 Blast tests of panels and tubes, 601–603
 blast test set-up, 603f
 pendulum with a curved sandwich panel, 604f
 two-cable pendulum, 602f
 Blast wave pressure–time history, 536, 536f
 BMT. *See* Ballistic and Mechanical Testing (BMT)
 Body armour system (BAS), 2, 3f, 233, 269, 322–323, 323f, 325, 643, 649, 663, 684–686
 BFS measurement in NIJ, 666f
 CAST, 663
 critical perforation analysis, 667
 lightweighting, 686f
 PBO, 666
 Body-centred cubic (BCC), 48
Bombyx mori. *See* Mulberry silkworm (*Bombyx mori*)
Bombyx mori silk, 279–280
 predominant structural unit, 280f
 Bootstrapping, 467–468, 470f
 Boron anhydride (B_2O_3), 359–360
 Boron carbides, 359–362
 shear strength, 361f
 VPP, 367f
 Boron-carbon phase diagram (C–C phase diagram), 359–360, 360f
 Borosilicate glasses, 339
 Breakout program, 414, 427–428, 427f, 469–475
 Breathability, 305–306
 Brinell hardness test, 585
 Brittle failure, 85–89
 Brittle materials, 186–187, 613
 Bruceton method, 644–645, 644f
 Bullet-proof glass, 339–340
 Bullet-resistant glass, 373, 374f, 668–669
 Burger's vector, 512–514
 from 'Little Willie' to 'Bushmaster', 55–59
 V-hull, 103f
 C
 CAI systems. *See* Composite Integral Armor systems (CAI systems)
 Capability and Technology Demonstrator programme (CTD programme), 251
 Carbides size and distribution, 65
 Carbon equivalent (CE), 57–58
 Carbon fibre-reinforced epoxies (CFRPs), 203
 Carbon fibres, 225–226
 Carbon nanotubes (CNTs), 357, 675
 Carbon/aramid, 237
 Carbon/glass, 237
 Carr attributes, 308–309
 CAST. *See* Centre for Applied Science and Technology (CAST)
 Cast irons, mild steels to, 59–63
 Cast steel armours, 94–95, 105–109
 Cauchy–Green deformation tensor, 519
 CAV. *See* Composite Armor Vehicle (CAV)
 Cavity expansion theory, 417–419
 C–C phase diagram. *See* Boron-carbon phase diagram (C–C phase diagram)
 CCT. *See* Constrained compression test (CCT)
 CE. *See* Carbon equivalent (CE)
 Cellular materials, 528

- continuum models for, 528–530
- micromechanical models for, 531–533
- Central plunger delamination test (CPD test), 588–589, 588f
- Centrally loaded plate test (CLP test), 588–589
- Centre for Applied Science and Technology (CAST), 663
- Centrelined momentum balance, 412–414
- Ceramic armour materials
 - properties, 334, 335t
 - sequence of physical events, 337f
- Ceramic armour penetration/perforation, 444–456
 - interface defeat transition velocity bounds, 453f
 - with thin backing, 446f
- Ceramic targets, predicting collateral damage in, 456–457
 - extract from work of Elder and Crouch, 458f
 - performance of composite armour, 457–460
- Ceramics, 49, 186, 331, 333–334, 679–681. *See also* Transparent crystalline ceramics
 - energy-absorbing mechanisms, 336–338
 - failure modes, 336–338
 - glass, 341–342
 - key properties and drivers, 334–336
 - manufacturing options, 362–370
 - monolithic, 357–362
 - opaque ceramics application to body armour systems, 373–377
 - polymer, 370–372
 - compositional effects and ballistic performance, 371–372
 - relationship between cost and ballistic performance, 336f
 - shaping, 362–367
 - SiC-based AusShield, 681f
 - steps in ceramic processing, 363f
 - vehicle platforms
 - opaque ceramics application, 373–377
 - transparent armour application, 373
 - views of relevant mechanisms, 680f
- Ceramics, 679–681
- CFRPs. *See* Carbon fibre-reinforced epoxies (CFRPs)
- Chain mail, 321
- Charpy impact testing, 88, 595–597
- Charpy transition temperature, 88
- Charpy V-notch impact (CVI), 187–188
- Check–production techniques, 669
- Chemical vapour deposition (CVD), 276
- Chobham Armour, 57
- Churchill, Winston, 55–56
- Circumferential cracking, 34–36
- C–L damage criteria.
 - See* Cockcroft–Latham damage criteria (C–L damage criteria)
- Classical yarn theory, 433
- Closed cell foam strain-rate sensitivity, 525–527, 526t
- CLP test. *See* Centrally loaded plate test (CLP test)
- CNTs. *See* Carbon nanotubes (CNTs)
- CoA. *See* Commonwealth of Australia (CoA)
- Coated fabrics, 300
- Cockcroft–Latham damage criteria (C–L damage criteria), 507–509, 576t
- Cockcroft–Latham model, 570–572
- COD. *See* Crack opening displacement (COD)
- Cold-rolling effects, 76–77
 - electron backscatter diffraction, 78f
 - scanning electron microscopy, 77f
- Combat helmets, 258, 667–668
 - design considerations, 259–261
 - history and evolution, 258–259
 - US army helmet design and materials, 259f
- Combat vehicle reconnaissance tracked (CVRT), 119
- Commercialisation, 281
- Comminuted material, 32–33
- Comminution, 32–33
- Comparative ballistic properties, 353–355
 - areal density vs. ceramic front layer thickness, 356f
 - residual velocity vs. areal density, 356f
 - up-armoured HMMWV, 355f
- Compliance matrix, 523–524
- Composite Armor Vehicle (CAV), 223
- Composite armour, 203. *See also* Laminated armours
 - penetration/perforation, 437–443

- Composite armour (*Continued*)
 characteristic patterns of damage in GFRP, 438f
 deformation in FSPs, 444f
 fibre fracture morphology, 440f
 system, 203
- Composite Integral Armor systems (CAI systems), 223
- Computed tomography (CT), 661–662
- Computer simulation, 524–525. *See also* Numerical modelling
- Cone fracture surface, 450
- Conoidal fracture, 29–32, 32f
- Constitutive equations for textiles and fibre-reinforced polymers, 520–524
- Constrained compression test (CCT), 210, 428–429, 581, 586
- Construction method, 381–382
- Continuum models for cellular materials, 528–530
- Conventional glasses, 338–341
 armour solutions, 340t
- ConWep
 model, 469–470, 537–538
 package, 464, 465f
- Corundum. *See* Single-crystal aluminium oxide
- Courant–Friedrich–Levy condition, 491–492
- Cowper–Symonds equation, 518
 Cowper strength model, 616
 strength equation, 221
- CPD test. *See* Central plunger delamination test (CPD test)
- Crack arrestor, 173
 principle, 184
- Crack divider, 173
- Crack opening displacement (COD), 336–338, 661–662
- Crack splitter, 173
- Cracking with welding, 90
- Creativity machine, 467–468
- Critical parameter, 304
- Critical velocity, 433
- Crowsfoot weave, 235
- Crystal structure of transparent ceramics, 345
- CT. *See* Computed tomography (CT)
- CTD programme. *See* Capability and Technology Demonstrator programme (CTD programme)
- Cubic boron nitride, 680–681
- Cutting effects, 79–80
- CVD. *See* Chemical vapour deposition (CVD)
- CVI. *See* Charpy V-notch impact (CVI)
- CVRT. *See* Combat vehicle reconnaissance tracked (CVRT)
- Cycom 4102, 221
- Czochralski method, 350
- D**
- D4 process. *See* Double diaphragm deep drawing process (D4 process)
- DBTT. *See* Ductile–brittle transition temperature (DBTT)
- DDF process. *See* Double diaphragm forming process (DDF process)
- Debye frequency, 512–514
- Defeat mechanisms, 21–23
 through forensic examination of impact site, 654
 through reverse ballistics tests, 655
 through stand-off RDOP tests, 655
- Defence Materials Technology Centre (DMTC), 5, 110–111, 456–457
 D4 pilot prototype, 253f
 high-velocity impact protection, 296
 research team, 233
 studying these DDF parameters, 96–97
- Defence Materiel Organisation, 118
- Defence Science and Technology Group (DST Group), 251, 395
- Defence Science and Technology Laboratory (DSTL), 99
- Defence Standard (DEF STAN 95–25), 94
- Deformation of single layer of fabric, 271, 272f
- Delamination, 27, 207–208
 tests, 587–589
 CPD test and CLP test, 588f
 types, 173
- Delayed cracking, 91–92
- Densification, 367–370
 HIPing, 369
 hot pressing, 369

- pressureless sintering, 368, 368f
 - SPS, 369–370
 - Department of Defence, 245
 - Depth of penetration (DOP), 546, 548–549, 651
 - Deshpande and Fleck model, 529–530, 531f
 - DHF. *See* Ductile hole formation (DHF)
 - DI. *See* Hardenability index (DI)
 - Diaphorm process, 260
 - Digger-works, 5
 - Dilatant fluids, 303
 - Dimensionless factor, 274
 - Discing, 27–29, 123
 - prevention, 186
 - Disrupter-absorber principles, 180
 - Disrupters, 180
 - DMTC. *See* Defence Materials Technology Centre (DMTC)
 - DoD. *See* US Department of Defense (DoD)
 - Domes, 352
 - DOP. *See* Depth of penetration (DOP)
 - Double diaphragm deep drawing process (D4 process), 251–256
 - D4 and HP compression moulding comparison, 257t
 - DMTC D4 pilot prototype, 253f
 - metallic sheet schematic of tooling, 252f
 - Spectra Shield SR-3136 helmet, 254f
 - 2D representation of fibre paths, 255f
 - Double diaphragm forming process (DDF process), 246
 - fabric tow width and weave geometry, 247–248
 - inter-and intralaminar frictional constraints, 248–249
 - locking angle, 249–251, 250f
 - trellis effect, 249–251
 - Downselection process, 650–651
 - Drapeability, 50
 - fabric tow width and weave geometry on, 247–248
 - Drop-weight tests, 589
 - setting on platform of drop-weight equipment, 591f
 - typical drop-weight device, and accessories, 590f
 - Dry pressing, 362–363, 364f
 - DST Group. *See* Defence Science and Technology Group (DST Group)
 - DSTL. *See* Defence Science and Technology Laboratory (DSTL)
 - Dual-hardness grades, 95–97
 - Ductile hole formation (DHF), 24–25, 25f, 67–68
 - Ductile–brittle transition temperature (DBTT), 187–188
 - DuPont
 - AS, 319
 - aramid NCF fabric panel from, 299f
 - Correctional fabric, 679
 - Kevlar FF520, 302
 - DuPont pure Kevlar fabrics, 288–289, 289t
 - Durable ceramic-based system, 686
 - Dwell period, 23, 336
 - Dwell time, 448
 - DYNA3D software, 487
 - Dynamic fracture experiments, SHPB for, 614
 - SHPB tension bar, 615f
 - split Hopkinson tension bar, 615f, 617f–618f
 - Dynamic fracture tests, 594–603
 - blast tests of panels and tubes, 601–603
 - Charpy and Izod impact tests, 595–597
 - EBT, 599–600, 601f
 - fragmentation tests, 597–598
 - spallation tests, 598–599, 600f
 - Dynamic loading, 72–73
 - Dynamic pressure, 17
 - Dynamic shear experiments, SHPB for, 613
 - Dynamic tensile experiments, SHPB for, 611–612
 - Dynamic torsion experiments, SHPB for, 612
 - Dynamic triaxial experiments, SHPB for, 613–614
 - Dynamic wedging, 614
 - Dynamic yield strength, 450
 - Dyneema, 229
 - Diamond technology, 679
- E**
- EBCHM. *See* Electron beam cold hearth melting (EBCHM)
 - EBT. *See* Explosion bulge test (EBT)
 - ED value. *See* Edge distance value (ED value)
 - Edge distance value (ED value), 386

- Edge performance, 386
 Edge-defined film-fed growth (EFG), 352
 Elastic stored energy, 274
 Elastomers, strength models for, 519–520
 Electron beam cold hearth melting (EBCHM), 150
 Electron beam melting, 143–144
 Electroslog refining (ESR), 66, 96
 grades, 98–99
 ELI. *See* Extra low interstitial grades (ELI)
 Empirical cratering relationships, 399
 EMRM. *See* Enterprise for Multiscale Research of Materials (EMRM)
 Energy-absorbing mechanisms, 207–214, 336–338
 armour materials, 275f
 deformation of single layer of fabric, 272f
 and failure modes, 270–274
 perforation damage, 273f
 transversal and longitudinal waves, 271f
 Enhanced Combat Helmet, 259
 Enterprise for Multiscale Research of Materials (EMRM), 679
 Equations of state (EOS), 486–487, 577t, 605
 measurements, 605
 Mie–Grueneisen, 497–498
 SESAME, 499
 ESR. *See* Electroslog refining (ESR)
 Essential materials science, 47
 ceramics, 49
 fibres, 49–50
 golden triangle, 51f
 metals, 48–49
 periodic table of elements, 48f
 polymers, 49
 stress–strain curves, 48f
 structure–property–performance relationships, 50–51
 textiles, 49–50
 Ethane, 286f
 Eulerian method, 491–493
 conservation equations, 492t
 Eulerian-type simulations, 535
 Experimental diagnostic tools, 655–663
 flash x-radiography, 659–660
 high-resolution digital x-radiography
 2D, 660–662
 3D, 662–663
 high-speed digital video, 655–658
 Explosion bulge test (EBT), 599–600, 601f
 Explosive bonding, 96–97
 External ballistics, 19
 Extra low interstitial grades (ELI), 144–145
- F**
 Fabric(s), 274–275
 armour penetration/perforation, 433–437
 asymmetry, 289–290
 comfort, 293–296
 deformation of single layer, 271, 272f
 tow width and weave geometry, 247–248
 Fabricability, 76
 cold-rolling effects, 76–77
 cutting effects, 79–80
 hot-rolling effects, 76–77
 welded and bolted structures comparison, 81t
 welding effects, 77–79
 Fabrics coated with shear thickening fluid, 302–306
 Face-centred cubic metals (FCC metals), 48, 509–510
 Failure
 definitions, 645–648
 mechanism, 598
 adiabatic shear, 82–85
 brittle failure, 85–89
 structural engineering failures, 89–92
 modes, 207–214, 336–338
 pass/fail criteria for armour materials and systems, 646t
 Fast Air Target Encounter Penetration package (FATEPEN package), 465
 Fatigue cracking, 91
 FATs. *See* First article tests (FATs)
 FBA. *See* Flash bainitic armour (FBA)
 FCC metals. *See* Face-centred cubic metals (FCC metals)
 FCS. *See* Future Combat Systems (FCS)
 Featherlight S-2 Glass, 224
 Felts, 301–302
 FeTiO₂. *See* Ilmenite (FeTiO₂)
 FFV. *See* Försvarets Fabriksverk (FFV)
 Fibre metal laminates (FMLs), 189, 429, 587
 Fibre-reinforced plastics (FRPs), 27, 203–204, 678–679
 composites, 628–631

- material components of multifunctional armour system, 629f
 - true stress–strain curves of, 631f
 - energy-absorbing mechanisms, 207–214
 - failure modes, 207–214
 - hard armour
 - reinforcing fibres for, 221–233
 - woven fabrics for, 233–237
 - nose shape effect, 215f
 - processing routes, 237–256
 - RDOP for GFRP materials, 213f
 - from spall liners to structural, 204–207
 - specifications and ballistic standards, 261–264
 - standards for, 262t–263t
 - Fibre-reinforced polymers (FRPs), 587, 628
 - constitutive equations for, 520–524
 - Fibre(s), 49–50, 271, 678–679
 - extensibility, 289–291
 - PPTA, 281–283, 282t
 - research grade, 284–288
 - silk, 279–281
 - strain velocity, 274
 - structure and properties, 277–279
 - failure of fibres, 278f
 - fibre modulus and crystal modulus comparison, 277f
 - properties of first-generation fibres, 279t
 - UHMWPE, 283–284, 284t
 - Fin Stabilised Armour Piercing Discarding Sabot rounds (FSAPDS rounds), 57
 - Fine-woven fabrics, 317–318
 - Finite element model of woven fabric, 522, 522f
 - Finite metallic armour targets, analytical modelling perforation of, 417. *See also* Semi-infinite metallic targets, analytical modelling penetration into breakout program, 427–428, 427f
 - cavity expansion theory, 417–419
 - penetration/perforation of laminated materials/targets, 428–431
 - plasticity theory, 419–422
 - Ravid–Bodner multistage model, 422–427
 - Finite-thickness armour targets perforation, computational packages for, 460
 - comparison of FSP test data, 472t, 474t
 - ConWep package, 464, 465f
 - FATEPEN package, 465
 - future techniques, 465–468
 - JTCG/ME penetration handbook, 463–464
 - machine learning methods, 469f
 - predicting performance of range of steel grades, 468–475
 - THOR Project, 462–463
 - First article tests (FATs), 42–44
 - Flash bainitic
 - process, 100
 - steels, 100
 - Flash bainitic armour (FBA), 100
 - Flash processing technique, 101f
 - Flash x-radiography, 659–660
 - Fluid–structure interaction (FSI), 490
 - FMLs. *See* Fibre metal laminates (FMLs)
 - Forensic examination of impact site, 654
 - Försvarets Fabriksverk (FFV), 641–642
 - '44 Magnum' bullet, 6–7
 - Fraglight, 301–302
 - Fragment-simulating projectiles (FSPs), 12, 13f, 69, 308–309, 443, 640
 - Fragmentation, 38–39
 - tests, 597–598
 - France's FELIN programme, 684–685
 - Frank–Zook penetration model, 409–410, 410f
 - Friction stir welding (FSW), 141
 - Friedlander formulation, 536–537
 - FRPs. *See* Fibre-reinforced plastics (FRPs); Fibre-reinforced polymers (FRPs)
 - FSAPDS rounds. *See* Fin Stabilised Armour Piercing Discarding Sabot rounds (FSAPDS rounds)
 - FSI. *See* Fluid–structure interaction (FSI)
 - FSPs. *See* Fragment-simulating projectiles (FSPs)
 - FSW. *See* Friction stir welding (FSW)
 - Future Combat Systems (FCS), 223
- ## G
- Gas gun impact experiments, 592–593
 - aluminium foam projectiles, 594f
 - deformed sandwich panels, 595f
 - set-up of ballistic test, 592f
 - Gating system, 242
 - Gelcasting, 364f, 366–367
 - General Motors Defense Research Laboratories, 397–398

- GFRP. *See* Glass fibre-reinforced plastic (GFRP)
- Glass armour materials
laminated, 339f
properties, 334, 335t
- Glass ceramics, 341–342
- Glass fibre-reinforced plastic (GFRP), 205, 341–342. *See also* Fibre-reinforced plastics (FRPs)
laminates, 437
- Glass fibre–reinforced epoxies, 678
- Glass(es), 186, 331, 679–681
ceramics, 341–342
and ceramics, 679–681
conventional, 338–341
fibres, 223–225
high-definition X-ray image of SiC-based AusShield, 681f
- Grades of armour steels
cast steel armours, 94–95
dual-hardness grades, 95–97
ESR grades, 98–99
research grades, 99–104
wrought homogeneous armours, 92–94
- Grain size
control of transparent ceramics, 346
and shape, 64–65
- H**
- HACC. *See* Hydrogen-assisted cold cracking (HACC)
- Hall–Petch relationship, 48, 127, 510–511
- Handgun
bullets, 6–7
protection SAIs for, 314–317
ballistic performance, 317t
shot pattern for handgun impacts, 315f
swatches of DuPont style A802 and A363, 316f
yarn as used in Kevlar Fabric A363, 316t
- HAP. *See* Hard armour plate (HAP)
- Hard armour. *See also* Laminated armours;
Nonmetallic armour
reinforcing fibres for, 221
aramid fibres, 226–227, 229t
carbon fibres, 225–226
glass fibres, 223–225
microstructural failure mechanisms, 224t
polyethylene fibres, 229–233
UHMWPE products, 231t–232t
woven fabrics for, 233–234
fabric style, 234–235
hybrid fabrics, 236–237
three-dimensional fabrics, 235–236
- Hard armour plate (HAP), 2–3, 215–216, 256–258, 322–323, 338, 379f, 643
ADA's HAP production facility, 383f
back-face signature depths, 382f
ceramic-based, 377
comparison between alternative manufacturing methods, 383t
cost of goods, 387f
high-resolution, X-ray images, 385f
presence of cracks, 385
- Hard-plugging, 67–68
- Hardenability, 62–63
curve, 64f
- Hardenability index (DI), 63
- Hardening function, 512–514
- Hat-shaped specimen, 613
- HAZs. *See* Heat-affected zones (HAZs)
- HCP. *See* Hexagonal close packed (HCP)
- HDPE. *See* High-density polyethylene (HDPE)
- HE events. *See* High-explosive events (HE events)
- Heat-affected zones (HAZs), 77–78, 140–141
- Heat-exchanger method, 350
- Heat-treatable
aerospace alloys, 133–134
aluminium alloys, 130–131
- Heat-treatment process, 99
- HEL. *See* Hugoniot elastic limit (HEL)
- Helmet shell, 667
- Hexagonal close packed (HCP), 48
- HHa grades. *See* High-hardness armour grades (HHa grades)
- High hardness steel (HHS), 40
plate, 57, 380
- High Modulus (HM), 227
- High strain rate. *See also* Specialized testing effects, 70–75
testing, 583–584
methods at various strain rates, 584t
- High-alloy, high-carbon steels, 103–104
- High-density polyethylene (HDPE), 645
- High-explosive events (HE events), 536

- blast in soil, 538
 - failure of unconfined and confined SiC, 543–549
 - four-ply, plain weave Kevlar fabric, 552f
 - H-III dummy displacement, 539f
 - impulse, 536
 - JH-2 scalar damage parameters, 547f
 - Kevlar fibre simulation results, 551f
 - Lagrangian simulation, 558f
 - material data for ARMOX 560T, 541t
 - material data for Kelvar, 551t
 - metallic appliqué armour modelling, 556–560
 - multilayered armour modelling, 540–543
 - soft fabric armour, 549–555
 - High-hardness armour grades (HHA grades), 69
 - High-performance fibres, 277
 - High-pressure (HP), 237–238
 - compression moulding, 240–242
 - D4 vs. HP, 257t
 - High-rate uniaxial compression testing, 72–73
 - High-resolution digital x-radiography
 - 3D, 662–663
 - CT scan of HAP, 663f
 - 2D, 660–662
 - high resolution of HAP, 661f
 - standard 3 x 3 array, 662f
 - High-speed cinematography, 655–658
 - High-speed digital video, 655–658
 - experimental set-up for capturing knife, 658f
 - set-up and experimental results, 659f
 - High-strength Al-5059 alloy, 129
 - High-strength low-alloy steels (HSLA steels), 85
 - High-strength textiles, 288
 - High-strength titanium alloy, 122
 - High-velocity
 - cored rounds, 8
 - fragmentation, 12
 - lead-filled rounds, 7
 - Highly transparent materials, 345
 - HIPing. *See* Hot isostatic pressing (HIPing)
 - HM. *See* High Modulus (HM)
 - Hollow tube, 611–612
 - Homogeneous Ni–Cr–Mo steels, 97
 - Hot isostatic pressing (HIPing), 369
 - Hot pressing, 369
 - Hot-rolling effects, 76–77
 - electron backscatter diffraction, 78f
 - scanning electron microscopy, 77f
 - HP. *See* High-pressure (HP)
 - HSLA steels. *See* High-strength low-alloy steels (HSLA steels)
 - Hugoniot elastic limit (HEL), 333, 456, 603, 605
 - measurements, 605–606
 - HEL values, extracted from literature, 607t
 - Hugoniot curves for some armour materials, 606f
 - Hybrid fabrics, 236–237
 - Hybrid Lagrangian–SPH formulation, 496–497, 497f
 - Hybrid laminates, 190–193
 - Hybrid structures, 309–310, 601
 - Hydrocodes, 484–485, 485f, 488t–489t
 - Hydrodynamic
 - jet penetration, 395–397
 - regime, 5–6
 - Hydrodynamic theory, 397
 - Hydrogen-assisted cold cracking (HACC), 78–79
 - Hylox H, 357
- I**
- IEDs. *See* Improvised explosive devices (IEDs)
 - Ilmenite (FeTiO₂), 143–144
 - ILT. *See* In-line transmission (ILT)
 - Impact dynamics, 19–21
 - Impact energy, 307
 - Impact tests
 - drop-weight tests, 589
 - gas gun impact experiments, 592–593
 - Taylor anvil test, 589–590
 - Impact velocity, 273
 - Impactor, 605
 - Improvised explosive devices (IEDs), 1, 18f, 288
 - Impurities of transparent ceramics, 345
 - In-line transmission (ILT), 345
 - Indentation tests, 584–585
 - Infrared (IR), 671
 - Inter- and intralaminar frictional constraints, 248–249

Interface defeat, 448f
 Interlayers characteristics, 176–179
 Internal ballistics, 19
 International Standards Organisation (ISO), 581
 IR. *See* Infrared (IR)
 ISO. *See* International Standards Organisation (ISO)
 ISO/IEC 17, 025:2005 standard, 639
 Israelis' Advanced Soldier, 684–685
 Izod impact test, 595–597

J

J–C model. *See* Johnson–Cook model (J–C model)
 JH ceramics model.
 See Johnson–Holmquist ceramics model (JH ceramics model)
 John Wilkins and Lee data (JWL data), 538
 Johnson–Cook model (J–C model), 75, 485–486, 570–572
 constitutive strength model, 450
 damage model, 577t
 material data, 572t–574t
 strength model, 500–504, 616
 JC damage criteria, 504–506
 limitations, 503–504
 Johnson–Holmquist ceramics model (JH ceramics model), 514–516, 515f
 Johnson–Holmquist JH-2 model, 579t
 Joint Technical Coordinating Group for Munitions Effectiveness (JTCG/ME), 463–464
 JTCG/ME. *See* Joint Technical Coordinating Group for Munitions Effectiveness (JTCG/ME)
 JWL data. *See* John Wilkins and Lee data (JWL data)

K

Kayenta ceramic model, 516–518
 KE. *See* Kinetic energy (KE)
 Kevlar, 274–275
 Correctional, 318
 FF520, 302
 performance of impregnated Kevlar fabrics, 306t
 XP500, 227
 Kevlar vest. *See* Protective apparel

Kinetic energy (KE), 437
 modelling impactors, 534–535
 penetrator models, 534f
 Knitted fabrics, 300–301, 301f
 Kraton D1107, 299

L

L/D ratios. *See* Length to diameter ratios (*L/D* ratios)
 Lagrangian methods, 490, 491f, 540–543, 556–560
 Laguerre–Voronoi tessellation technique, 531–532
 Laminated armours. *See also* Hard armour; Nonmetallic armour
 examples, 193–198
 family of bonded aluminium laminates, 191t
 hybrid laminates, 190–193
 laminated light alloys, 189–190
 laminated steels, 187–188
 objectives in designing, 182
 preventing discing, 186
 preventing plugging, 184–186
 stress waves management, 184
 support for brittle material, 186–187
 Laminated fabrics, 318–320
 Laminated light alloys, 189–190
 Laminated materials and layered structures, 171t
 armour materials and systems, 167
 categories, 168
 design approaches, added value and creative thinking, 168–172
 principles of laminates, 172–182
 wide-ranging selection of laminated armour materials, 169t–170t
 Laminated steels, 187–188
 Laminates, 299
 air gap, 180–182
 armour materials and systems classification, 180t
 characteristics of interlayers, 176–179
 constraint of plastic zone, 178f
 disrupter-absorber principles, 180
 layers and interfaces, 175–176
 maximum flexural stress, 174–175

- notch orientations and delamination types, 173f
- principles, 172
- surface effects and coatings, 179
- LANL. *See* Los Alamos National Laboratory (LANL)
- LAVs. *See* Light armoured vehicles (LAVs)
- Lawrence Livermore National Laboratory, 485–486
- Layered fabric structures. *See also* Soft armour inserts (SAIs); Protective apparel; Technical fibres for ballistic fabrics
 - hybrid structures, 309–310
 - quilted structures, 308–309
 - stitched structures, 307–308
 - three-dimensional structures, 310, 311f
- Layers and interfaces, 175–176
- Lead zinc niobate lead titanate (PZN-PT), 343
- Length to diameter ratios (*L/D* ratios), 397–398, 462
- Leno weave, 235
- Light alloys, 117–118, 677–678
 - aluminium alloys, 125–142
 - military specifications, 161t
 - Australian troops storming, 118f
 - ballistic properties and specific failure modes, 122–125
 - engineering issues, 139–142
 - palliative treatments for, 140
 - weldability, 140–142
 - magnesium alloys, 154–160
 - naval ships, 122f
 - specifications and standards, 160–162
 - titanium alloys, 139–142
 - UK Scimitar fighting reconnaissance vehicle CVRT, 120f
 - UK warrior variants, 120f
 - US Cavalry M3A1 Bradley fighting vehicle, 119f
 - US version of M113, c.1975, 117f
- Light armoured vehicles (LAVs), 79
- Lighter-weight military structures, 601
- Lightweight ceramic composite armours, 331, 331f
 - projectile impact, 332f
- Liquid armour, 305
- Liquid moulding techniques, 237
- Little Willie, 55f
 - to Bushmaster, 55–59
- Livermore Software Technology Corp. (LSTC), 487
- Locking angle, 249–251, 250f
- Longitudinal wave, 271, 271f
- Los Alamos National Laboratory (LANL), 485–486
- LS-DYNA software, 485–487, 530
- LSTC. *See* Livermore Software Technology Corp. (LSTC)
- M**
- M1A2 Abrams tank, 144
- M80 NATO ball round, 7
- Macauley bracket, 507
- Magnesium alloys (Mg alloys), 154
 - future alloy developments, 159–160
 - grades, compositions and properties, 156t
 - light-alloy properties compared with 4340 steel, 155f
 - Mg-3Al-1Zn alloys, 155–157
 - military specifications, 162t
 - research grades, 158–159
 - alloys with Al and Ca additions, 159
- Magnesium aluminate spinel, 343
 - processability and performance, 354t
- Main battle tank (MBT), 56, 205
 - challenger Mk II MBT, 57f
- Manganese sulphide stringers (MnS stringers), 66
 - size and shape, 66
- Martensite characteristics, 66–67
- Martensitic armour steels, 99
- Massively parallel processor (MPP), 487
- Material variables, 376–377
- MBT. *See* Main battle tank (MBT)
- MCBAS system, 323, 324f, 325
- MD. *See* Molecular dynamics (MD)
- Mechanical threshold stress models (MTS models), 485–486, 511–512, 576t–577t
- Membrane stretching, 27
- Mescall zone, 32–33
- Mesh-free methods, 493–497
- Metal matrix composites (MMCs), 677–678
- Metal ring, 597–598
- Metal Storm technology, 676–677

- Metallic honeycombs and foams, 620–625
 ALPORAS aluminium foam, 624f
 out-of plane quasistatic and dynamic
 stress-strain curves for aluminium,
 623f
 properties, 622t
 properties of IFAM and CYMAT foams,
 622t
- Metals, 48–49
- Mg–3Al–1Zn alloys, 155–157
 compressive stress-strain curves for
 AZ31B–H24, 157f
 mechanical properties of magnesium alloy,
 AZ31B, 157t
- MgAl₂O₃. *See* Magnesium aluminate spinel
- Microcomputed tomography, 532–533
- Micromechanical models for cellular
 materials, 531–533
- Microsegregation of alloying elements, 65
- Microstructure, 64, 131
 carbides size and distribution, 65
 grain size and shape, 64–65
 martensite characteristics, 66–67
 microsegregation of alloying elements, 65
 MnS stringers size and shape, 66
 retained austenite, 67
- Microtruss, 682–683
 materials, 681–683
 cellular materials, 682f
 sheet blanking method, 683f
- Mie–Grueneisen EOS, 497–498
- Mild steels to cast irons, 59–63
- mini split Hopkinson tensile bar (mSHTB),
 626
- MMCs. *See* Metal matrix composites
 (MMCs)
- MnS stringers. *See* Manganese sulphide
 stringers (MnS stringers)
- Mock leno weave, 235
- Modelling cellular materials, 525–533
- Modelling metallic laminates, 524–525
- Modified hydrodynamic theory, 399–412
- Modified Johnson–Cook model, 540
 strength model, 556
- Molecular dynamics (MD), 493
- Monolithic ceramic(s). *See also* Polymer
 ceramics; Transparent crystalline
 ceramics
 aluminium oxides, 357
 boron carbides, 359–362
 silicon carbides, 357–359
 tiles, 33–34
- Monomers, 49
- Mosaic patterns, 374–375
- MPP. *See* Massively parallel processor (MPP)
- mSHTB. *See* mini split Hopkinson tensile
 bar (mSHTB)
- MTS models. *See* Mechanical threshold
 stress models (MTS models)
- Mulberry silkworm (*Bombyx mori*),
 279–280
- Multilayered systems design, 42
- N**
- Naiver–Stokes equation, 492
- National Association of Testing Authorities
 (NATA), 639
- National Institute of Justice (NIJ), 312, 641,
 647, 663
- Navy Ballistic Limit, 647
- NCFs. *See* Noncrimp fabrics (NCFs)
- NDT. *See* Nondestructive testing (NDT)
- Near-field blast conditions, 19
- Neighbour particle search, 495, 496f
- NewSentry armour, 194–197
- NIJ. *See* National Institute of Justice (NIJ)
- Ni–Mo–Cr dual-hardness armour steels, 97
- Nonarmour grade alloys, 127
- Noncrimp fabrics (NCFs), 234–235,
 297–299
- Nondestructive testing (NDT), 662
- Nonheat-treatable alloys, 127, 140
- Nonmetallic armour. *See also* Hard armour;
 Laminated armours
 analytical modelling for penetration/
 perforation, 433
 ceramic armour penetration/perforation,
 444–456
 composite armour penetration/
 perforation, 437–443
 fabric armour penetration/perforation,
 433–437
 predicting collateral damage in ceramic
 targets, 456–460
- Nonwoven fabrics, 297–299
- Numerical modelling, 483–486, 484t. *See
 also* Analytical modelling
 EOS, 497–499

- software packages, 486–490
- solvers, 490–497
- strength models
 - and failure criteria for metals, 499–514
 - for nonmetals, 514–533
- threat definitions, 533–560
- Nylon, 278, 281
- Nylon 6, 281, 281f
- Nylon 6,6, 281, 281f
- O**
- OL. *See* Overlap length (OL)
- One-dimensional finite difference discretisation, 415–417
- Opaque ceramics application
 - to body armour systems
 - ballistic performance, 382–386
 - construction method, 381–382
 - cost, 386
 - design principles, 378–379
 - historical background, 377–378
 - material choice, 379–381
 - to vehicle platforms, 373–374
 - material variables, 376–377
 - surface profiles for ceramic tiles/armour, 378f
 - system variables, 374–376
- Operational environment, 1–4
- Out-of-plane deformation, 273
- Overlap length (OL), 386
- P**
- Pack, 270
- Para-aramid (*p*-aramid). *See* Poly-*para*-phenylene terephthalamide (PPTA)
- PBA. *See* Personal body armour (PBA)
- P–BFS. *See* Perforation–back–face signature (P–BFS)
- PBO fibres. *See* Poly *p*-phenylene-2,6-benzobisoxazole fibres (PBO fibres)
- PBT. *See* Poly(*p*-phenylene benzobisthiazole) (PBZT)
- PBZT. *See* Poly(*p*-phenylene benzobisthiazole) (PBZT)
- PCs. *See* Polycarbonates (PCs)
- pdr. *See* Pounders (pdr)
- Peierls–Nabarro barriers, 509
- Peierls–Nabarro stress, 512–514
- Pencilling, 312–313
- Pendulum systems, 601
- Penetration
 - analytical modelling into semi-infinite metallic targets, 395
 - centreline momentum balance, 412–414
 - empirical cratering relationships, 399
 - four-phase penetration model, 397–399, 398f
 - hydrodynamic jet penetration, 395–397
 - idealised jet penetrating target material, 396f
 - modified hydrodynamic theory, 399–412
 - one-dimensional finite difference discretisation, 415–417
- events, 483
- laminated materials/targets, 428–429
 - compiled ballistic limit data, 430t
 - predicting performance of Al alloy, 429–431
- laminated materials/targets, 428–431
- nonmetallic armour, 433–460
- phases, 411
- process, 209
- residual depth of tests, 652–653
- Penetration mechanics and failure modes, 23
 - circumferential cracking, 34–36
 - comminution, 32–33
 - conoidal fracture, 29–32, 32f
 - delamination, 27
 - DHF, 24–25, 25f
 - discing, 27–29
 - fragmentation, 38–39
 - plug thickness, 28f
 - plugging, 26–27, 26f
 - radial cracking, 33–34
 - spallation, 37
 - step-wise formation of radial cracks, 35f
- Perforation
 - analytical modelling of finite metallic armour targets, 417
 - breakout program, 427–428, 427f
 - cavity expansion theory, 417–419
 - plasticity theory, 419–422
 - Ravid–Bodner multistage model, 422–427
- events, 483
- laminated materials/targets, 428–431
- nonmetallic armour, 433–460
- perforated steel armours, 109–111

- Perforation—back—face signature (P—BFS), 663
- Personal body armour (PBA), 269–270, 270f
- p*-Phenylenediamine (PPD). *See* Benzene-1,4-diamine
- PI test. *See* Plate impact test (PI test)
- PIPD. *See* Poly{2,6-diimidazo[4,5-*b*:40,50-*e*]pyridinylene-1,4-(2,5-dihydroxy)phenylene} (PIPD)
- PISCES, 487
- Plain weave, 234
- Plasma beam melting, 143–144
- Plasticity theory, 419–422
- Plate impact test (PI test), 581, 603. *See also* Impact tests
EOS measurements, 605
HEL measurements, 605–606
Hugoniot curves for some armour materials, 606f
impactor, 605
- Plug thickness, 28f
- Plugging, 26–27, 26f
failures, 67–68
preventing, 184–186
- PMMA. *See* Poly(methyl methacrylate) (PMMA); Polymethylmethacrylate (PMMA)
- PoI. *See* Point of impact (PoI)
- Point of dtrike strike (PoS), 654
- Point of impact (PoI), 336
- Poisson's ratio, 32, 456
- Poly 1,4 phenyleneterephthalamide.
See Kevlar
- Poly *p*-phenylene-2, 6-benzobisoxazole fibres (PBO fibres), 276, 278–279, 284–287, 666
properties, 287t
reaction scheme and structure, 287f
- Poly-*para*-phenylene terephthalamide (PPTA), 278
fibres, 281–283, 282t
reaction scheme and structure, 282f
- Poly(hexamethylene adipamide), 6.
See Nylon 6
- Poly(methyl methacrylate) (PMMA), 607
- Poly(*p*-phenylene benzobisthiazole) (PBZT), 278–279, 284–287
properties, 287t
reaction scheme and structure, 287f
- Poly{2,6-diimidazo[4,5-*b*:40,50-*e*]pyridinylene-1,4-(2,5-dihydroxy)phenylene} (PIPD), 278–279, 287–288
- Polyamide fibres. *See* Nylon
- Polycarbonates (PCs), 218
- Polyethylene fibres, 229–233, 678
- Polymer ceramics, 370–372. *See also* Monolithic ceramics; Transparent crystalline ceramics
compositional effects and ballistic performance, 371–372
- Polymeric materials, strength models for, 518–519
- Polymers, 49. *See also* Fibre-reinforced plastics (FRPs)
classes, 217f
classification of family of polyethylenes, 218t
mechanical properties, 216t
and resins, 215–216
standards for, 262t–263t
thermosetting resins, 221, 222t
unreinforced polymers, 216–221
- Polymethylmethacrylate (PMMA), 218
particles, 306
- Porosity of transparent ceramics, 345–346
- PoS. *See* Point of dtrike strike (PoS)
- Pounders (pdr), 92–93
- PPTA. *See* Poly-*para*-phenylene terephthalamide (PPTA)
- Preconditioning tests, 669–672
- Pressureless sintering, 368, 368f
- 'Principle yarns', 288–289
- Processing routes, 237
D4 process, 251–256
DDF process, 246–251
diaphragm forming, 245–246
HP compression moulding, 240–242
platen pressing, 237–240
resin transfer moulding, 242–243
vacuum forming process, 246f
VARI processes, 243–245
- Projectiles, 641
- Proof testing, 42–44
- Propagation, 209–210
- Protective apparel. *See also* Soft armour inserts (SAIs); Layered fabric structures
BASs, 322–323, 323f

- energy-absorbing mechanisms and failure modes, 270–274
- personal body armour, 269–270, 270f
- weight vs. mobility vs. protection, 323–325
- Protective garments. *See* Protective apparel
- PZN-PT. *See* Lead zinc niobate lead tintonate (PZN-PT)
- Q**
- QS test. *See* Quasistatic test (QS test)
- Quality factor (q^2), 460
- Quasistatic test (QS test), 581
- Quenched martensitic steel, 104–105
- Quilted structures, 308–309
 - diamond quilted SAI, 309f
- R**
- Radial cracking, 33–34
- RADIOSS, 490
 - solvers, 485–486
- RAN. *See* Royal Australian Navy (RAN)
- Rankine–Hugoniot jump equation, 536
- Ravid–Bodner multistage model, 422–427
- Raytheon, 347–348
- RCC. *See* Right circular cylinder (RCC)
- RDOP. *See* Residual depth of penetration (RDOP)
- Reaction bonding. *See* Reaction sintering
- Reaction sintered silicon carbide (RSSC), 334–336
- Reaction sintering, 333–334, 364f, 365
- Reaction-bonded version (RSSC), 357–359
- Recombinant silk proteins, 276
- Recrystallisation, 76–77
- reduced Graphene oxide (rGO), 680
- Reinforcing fibres for hard armour, 221
 - aramid fibres, 226–227, 229t
 - carbon fibres, 225–226
 - glass fibres, 223–225
 - microstructural failure mechanisms, 224t
 - polyethylene fibres, 229–233
 - UHMWPE products, 231t–232t
- Remounting methods, 666
- Research grade fibres
 - PIPD, 287–288
 - polybenzazole fibres, 284–287
- Research grades, 99
 - alloys with Al and Ca additions, 159
 - alloys with rare earth additions, 158
 - Elektron E765-T5 plate, 158f
 - flash bainitic steels, 100
 - flash processing technique, 101f
 - high-alloy, high-carbon steels, 103–104
 - super bainitic steels, 99–100
 - transformation-induced plasticity steels, 102–103
 - twinning-induced plasticity steels, 101–102
- Residual depth of penetration (RDOP), 213f, 652
- Residual velocity curves, 649
- Resin transfer moulding (RTM), 243
- Resins
 - classes, 217f
 - classification of family of polyethylenes, 218t
 - mechanical properties, 216t
 - polymers and, 215–216
 - thermosetting resins, 221, 222t
 - unreinforced polymers, 216–221
- Reverse ballistics tests, 655
- Reverse ballistics tests, 655
- rGO. *See* reduced Graphene oxide (rGO)
- RHA. *See* Rolled homogeneous armour (RHA)
- Rifle bullets
 - armour-piercing rounds, 8–10
 - high-velocity, cored rounds, 8
 - high-velocity, lead-filled rounds, 7
- Right circular cylinder (RCC), 667
- Rigid rod molecules. *See* Ultrahigh molecular weight polyethylene (UHMWPE)
- Roll-bonding, 188
- Rolled homogeneous armour (RHA), 57–58, 118–119, 168, 456, 459, 651
- Royal Australian Navy (RAN), 223–224
 - VBRI in spaced composite armour system for, 245
- RSSC. *See* Reaction sintered silicon carbide (RSSC); Reaction-bonded version (RSSC)
- RTM. *See* Resin transfer moulding (RTM)
- Rubbers, strength models for, 519–520
- Rutile (TiO₂), 143–144

S

- Saboted target, 655
- Saint-Gobain Crystals, 352
- SAIs. *See* Soft armour inserts (SAIs)
- Sandwich tubes, 601
- Sapphire. *See* Single-crystal aluminium oxide
- Satin weave, 235
- Scabbing, 37
- SCC. *See* Stress corrosion cracking (SCC)
- SCGL strength model.
 - See* Steinberg–Cochran–Guinan–Lund strength model (SCGL strength model)
- Scooping, 352
- SCRIMP process, 244f
- Secondary fragmentation. *See* Helmet shell
- Semi-infinite metallic targets, analytical
 - modelling penetration into, 395. *See also* Finite metallic armour targets, analytical modelling perforation of
 - centreline momentum balance, 412–414
 - empirical cratering relationships, 399
 - four-phase penetration model, 397–399, 398f
 - hydrodynamic jet penetration, 395–397
 - idealised jet penetrating target material, 396f
 - modified hydrodynamic theory, 399–412
 - one-dimensional finite difference discretisation, 415–417
- SentryGlas, 340–341
- SESAME EOS, 499
- 7xxx series alloys, 131–133
- SFMAX, 514–515
- Shaping, ceramics
 - densification, 367–370
 - dry pressing, 362–363, 364f
 - gelcasting, 364f, 366–367
 - reaction bonding, 364f, 365
 - slip casting, 364–365, 364f
 - viscous plastic processing, 364f, 365–366, 366f
 - wet powder processing, 363–364
- Shear bands, 150
- Shear thickening fluids, 302–306
- Shifted stress, 516, 517f
- Shock physics, 21
- Shock wave(s), 536, 603
- Short-transverse (ST), 123
 - direction, 65
- SHPB test. *See* Split Hopkinson pressure bar test (SHPB test)
- α -SiC, 358
- β -SiC, 358
- Silicon carbides (SiC–N), 357–359
- Silk, 278–281
 - fibres, 279–281
 - natural polyamide fibres, 281
 - quilted silk armour, 280f
- ‘Single strikes’ study, 650–654
- Single Taylor test, 583–584
- Single-crystal
 - aluminium oxide, 350–353
 - processability and performance, 354t
 - sapphire, 343
- Sintering of transparent ceramics, 346
- Sintox FA, 357
- Slip casting, 364–365, 364f
- Small arms ammunition, 6, 483
 - handgun bullets, 6–7
 - rifle bullets, 7–10
- Smooth particle hydrodynamics method (SPH method), 487, 493–497, 556–560
 - drawback, 496
 - neighbour particle search, 495, 496f
- Soda-lime glass, 339
- Soft armour inserts (SAIs), 306, 311, 643.
 - See also* Layered fabric structures; Protective apparel
 - diamond quilted, 309f
 - edge effects, 311–314
 - for handgun protection, 314–317
 - multistrike effects, 311–314
 - selection, 312f
 - for stab and spike resistance, 317–322
 - stitching and quilting patterns, 308f
 - surface area effect, 313f–314f
- Software packages, 486–490
- Solvers
 - ALE methods, 491–493
 - Eulerian method, 491–493
 - Lagrangian methods, 490, 491f
 - mesh-free methods, 493–497
 - rapid advection of blast products, 494f

- SoRs. *See* Statements of Requirements (SoRs)
- Spaced composite armour system, VBRI in, 245
- Spall
films, 669
liners to structural FRPs, 204–207
tests, 653–654
- Spallation, 37. *See also* Failure mechanism tests, 598–599
wave propagation in test, 600f
- Spark plasma sintering (SPS), 369–370
- Specialized testing, 581
delamination tests, 587–589
dynamic fracture tests, 594–603
impact tests, 589–593
indentation tests, 584–585
plate impact tests, 603–606
procedures for energy-absorbing mechanism, 582t
SHPB tests, 606–614
data application, 614–631
specialised quasistatic testing, 582–583
TT compression tests, 586–587
- Specifications
armour, 104–105
armour class in DEF STAN 8030, 108t
cast steel armours, 105–109
Charpy toughness of armour steels, 107t
hardness of armour steel grades, 106t
perforated steel armours, 109–111
wrought armour steels, 105
and ballistic standards, 261
eyewear, 261–264
spall liners, 264
light alloys, 160–162
aluminium alloys, military specifications, 161t
magnesium alloys, military specifications for, 162t
titanium alloys, military specifications, 162t
- Spectra, 229, 310
fibres, 283
spectra-based products, 256–258
trends in threat, 676–677
- Spectra Shield SR-3136 helmet, 254f
- SPH method. *See* Smooth particle hydrodynamics method (SPH method)
- Spider silk, 276
- Spike impact test, 655–658
- Spike threats, 12–15
- Spike vests, 668
- Spinel. *See* Magnesium aluminate spinel
- Split Hopkinson pressure bar test (SHPB test), 581, 606–607, 615f
data application, 614–631
armour steels, 619–620
fibre-reinforced polymer composites, 628–631
general implementation, 614–619
metallic honeycombs and foams, 620–625
wool and aramid fibres, 626
dynamic
fracture experiments, 614
shear experiments, 613
tensile experiments, 611–612
torsion experiments, 612
triaxial experiments, 613–614
Hopkinson bar tests, 608t–610t
- SPS. *See* Spark plasma sintering (SPS)
- Squeeze-cast alloys, 135–136
- Squeeze-casting process, 120
- ST. *See* Short-transverse (ST)
- Stab
impact test, 655–658
threats, 12–15
vests, 668
- Stand-off RDOP tests, 655
- Standard Jominy EndeQuench test method, 63
- Standard techniques, 663
ballistic test standards of ammunition type, 664t–665t
BAS, 663–667
bullet-resistant glass and transparent armours, 668–669
combat helmets, 667–668
stab and spike vests, 668
- Standards
armour, 104–105
armour class in DEF STAN 8030, 108t
cast steel armours, 105–109
Charpy toughness of armour steels, 107t

Standards (*Continued*)

- hardness of armour steel grades, 106t
- perforated steel armours, 109–111
- wrought armour steels, 105
- ballistic standards, 261
 - eyewear, 261–264
 - spall liners, 264
- light alloys, 160–162
 - aluminium alloys, military specifications, 161t
 - magnesium alloys, military specifications, 162t
 - titanium alloys, military specifications, 162t
- Staple fibres, 291
- Statements of Requirements (SoRs), 5
- Static pressure, 16
- Steel(s), 334, 336, 677
 - projectile, 332–333
- Steinberg–Cochran–Guinan–Lund
 - strength model (SCGL strength model), 512–514, 576t
- Step-wise formation of radial cracks, 35f
- Stitched structures, 307–308
 - stitching and quilting patterns, 308f
- Strain hardening processes, 125, 141, 501
- Strain rate, 583
 - effect, 72–73
 - hardening, 72–73
- Strapping methods, 666
- Strength models
 - and failure criteria for metals, 499–514
 - for nonmetals, 514–533
- Stress corrosion cracking (SCC), 91, 121, 139
 - palliative treatments for, 140
- Stress triaxiality property, 505
- Stress wave(s), 603
 - management, 21, 184
- Strike face material, 380
- Structural engineering failures, 89
 - cracking with welding, 90
 - delayed cracking, 91–92
 - fatigue cracking, 91
 - stress corrosion cracking, 91
 - weld defects and discontinuities, 90f
- Structure—property—performance relationships, 50–51

Styrene–butadiene–styrene block polymer.

See Kraton D1107

Substrate support, 381

Super bainitic steels, 99–100

Surface effects and coatings, 179

Surface finishing of transparent ceramics, 346

Surmet Corporation, 347–348

System variables, 374–376

T

Taylor anvil test, 589–590

Taylor impact test, 591f

Taylor's theory, 448–449

Taylor–Quinney coefficient, 501

TBAS. *See* Tiered body armour system (TBAS)

TCL. *See* Terephthaloyl dichloride (TCL)

Technical fibres for ballistic fabrics. *See also* Layered fabric structures
history from Kwolek to carbon nanotubes, 274–276

nylon, 281

PPTA fibres, 281–283, 282t

research grade fibres, 284–288

silk fibres, 279–281

structure and properties of fibres, 277–279

failure of fibres, 278f

fibre modulus and crystal modulus comparison, 277f

properties of first-generation fibres, 279t

UHMWPE fibres, 283–284, 284t

Technical textiles and ballistic fabrics, 288.

See also Protective apparel; Layered fabric structures

coated fabrics, 300

fabrics coated with shear thickening fluid, 302–306

felts, 301–302

knitted fabrics, 300–301, 301f

nonwoven and noncrimp fabrics, 297–299

woven fabrics, 288–297

Technora (Teijin), 227, 282

Tempered martensitic steel, 104–105

Tenacity, 50

Terephthaloyl dichloride (TCL), 281–282

Terminal ballistics, 19–21, 32

Terpolymer fibres, 282

reaction schemes and structures, 285f

- Testing procedures (TP), 261
- Textiles, 49–50, 270, 679. *See also*
 Technical textiles and ballistic fabrics
 constitutive equations for, 520–524
- Thermal energy, 239–240
- Thermoformed shields and visors, 256
- Thermoplastic-Kevlar composites (TP-Kevlar composites), 320
- Thermosetting resins, 221, 222t
- Thickness of transparent ceramics, 346–347
- Thin-film effect, 177–178
- Thomas–Fermi–Dirac statistical theorems, 499
- THOR Project, 462–463
- Threat, 4–5, 533
 blast events and loadings, 15–19
 cored, high-velocity ammunition, 11t
 HE events modelling, 536–560
 high-velocity fragmentation, 12
 hydrodynamic regime, 5–6
 modelling KE impactors, 534–535
 small arms ammunition, 6–10
 spectrum, 639
 trends in, 676–677
 spike threats, 12–15
 stab threats, 12–15
- Three-dimensional fabrics, 235–236
- Three-dimensional structures, 310, 311f
- Three-ply FF520 SAI, 302f
- Through-thickness (TT), 586
 CCT curve, for 2024-T351 aluminium, 587f
 compression tests, 586–587
- Through-thickness compression, 209–210
- Ti-6Al-4V grades, 144–153
 adiabatic shear crack deflection, 148f
 ballistic data for low-cost titanium alloy, 153f
 ballistic limit velocity for, 148f
 ballistic performance, 151f
 β -CEZ alloy plates, 150
 ELI, 144–145
 microstructural changes in, 149f
 microstructures, 147f
 specification data for, 146t
- Ti-6Al-4V alloy, 149f
 annealed, 147f
 AP projectiles against, 152f
- Tiered body armour system (TBAS), 323, 324f
- TiO₂. *See* Rutile (TiO₂)
- Titanium alloys, 143
 alloying elements, 144f
 future titanium alloy armours, 153–154
 M1A2 Abrams and M777A1 field howitzer, 145f
 military specifications, 162t
 relative bulk densities of metallic alloys, 143f
 Ti-6Al-4V grades, 144–153
- Titanium armour, 677
- Toughness, 87, 276
- TP. *See* Testing procedures (TP)
- TP-Kevlar composites. *See* Thermoplastic-Kevlar composites (TP-Kevlar composites)
- Traditional Hall–Petch equation, 64–65
- Traffic light system, 675–676
- Transformation-induced plasticity steels (TRIP steels), 66–67, 102–103
- Transition velocity, 453
- Transparent armour(s), 339, 342
 applications, 352
 to vehicle platforms, 373
- Transparent armours, 668–669
- Transparent crystalline ceramics, 342–355.
 See also Monolithic ceramics;
 Polymer ceramics
 AlON, 347–348, 348f, 354t
 ballistic performance, 355t
 comparative ballistic properties, 353–355
 magnesium aluminate spinel, 348–349, 354t
 material properties, 342–355
 microstructural and processing aspects, 345–347
 single-crystal aluminium oxide, 350–353, 354t
- Transparent GFRP interlayers, 678
- β -Transus temperature, 143
- Transverse wave, 271, 271f
- Trellis effect, 249–251
- TRIP steels. *See* Transformation-induced plasticity steels (TRIP steels)
- TT. *See* Through-thickness (TT)
- Tuballoy, 463
- Turtleskin, 321–322, 322f

- Twaron, 227, 626
 Twill weave, 234–235
 Twinning, 102
 Twinning-induced plasticity steels (TWIP steels), 99, 101–102
 TWIP steels. *See* Twinning-induced plasticity steels (TWIP steels)
 Twisted yarns, 291
- U**
 U6N. *See* Uranium–6%–niobium (U6N)
 UHHA. *See* Ultra-high-hardness armour (UHHA)
 UHHS. *See* Ultrahigh-hardness steels (UHHS)
 UHMWPE. *See* Ultrahigh molecular weight polyethylene (UHMWPE)
 UK Def Stan 00–35, 670
 Future Infantry Soldier Technology programme, 684–685
 Ultra-high-hardness armour (UHHA), 69
 Ultrahigh molecular weight polyethylene (UHMWPE), 207, 259, 275, 278–279, 429, 586–587, 651
 elastic modulus, 286f
 fabrics, 316
 fibres, 223, 229, 283–284, 284t, 381, 675–676, 678
 mass efficiency and space efficiency, 460f
 pre-preg materials, 239
 reaction scheme and structure, 286f
 UTS, 286f
 Ultrahigh-hardness steels (UHHS), 179
 armours, 59
 Ultraviolet (UV), 671
 exposure, 278–279
 light, 218
 Underhead cracking, 90
 Underbelly blast loading, 17–19
 Uniaxial tensile test, 85–86
 Unreinforced polymers, 215–216
 Uranium–6%–niobium (U6N), 597–598
 US Army Research Laboratory (ARL), 129
 US Army's Soldier Protection Systems, 684–685
 US Department of Defense (DoD), 645, 684–685
 USA body armour standards NIJ0101.03, 670
 USA body armour standards NIJ0101.04, 670
 USA MIL-STD-810G, 670
 UV. *See* Ultraviolet (UV)
- V**
 V-50 test, 642, 648–649
 determinations, 382–385, 384f–385f
 estimation, 650–651
 σ and BFS measurements, 648–649
 statistical variability of BFS values, 649f
 V-shaped zone, 272
 Vacuum bagging resin infusion process (VBRI process), 206, 238, 243
 SCRIMP process, 244f
 in spaced composite armour system for RAN, 245
 Vacuum-assisted resin transfer moulding (VARTM), 242
 VBRI process. *See* Vacuum bagging resin infusion process (VBRI process)
 Vehicle armours, 686–687, 687f
 Vehicle platforms
 opaque ceramics application, 373–377
 transparent armour application, 373
 Velocity field, 427
 Viscous plastic processing (VPP), 333–334, 364f, 365–366, 366f
 boron carbide, 367f
 Volume fraction (V_f), 210
 von-Mises stress, 528
 Vosper Thorneycroft (VT), 243
 VPP. *See* Viscous plastic processing (VPP)
 V_{PROOF} test, 645, 648–649
 VT. *See* Vosper Thorneycroft (VT)
- W**
 Walker–Anderson model. *See* Breakout program
 Warp-knitted fabrics, 300–301
 'Warp' direction, 298–299
 Water-jet process, 79–80
 Wave propagation, 484–485
 Wave speed evaluation, 522–523
 Weave-parting, 291, 292f
 Wedge-loaded compact tension (WLCT), 614
 Weibull modulus, 49
 Weld-toe cracking, 90

- Weldability, 140–142
friction stir welding process, 142f
microstructural zones in FSP aluminium alloy, 142f
- Welding
cracking with welding, 90
effects, 77–79
- Weldment hardness profile, 78f
- Wet powder processing, 363–364
- Whilst approach, 650
- WLCT. *See* Wedge-loaded compact tension (WLCT)
- Woodward model, 469–470
- Wool and aramid fibres, 626
- Work-hardening grades, 127–129
- Woven aramid fabrics, 317–318
- Woven fabric(s), 288–297
blend-yarn constructions for debris-impact-resistant fabrics, 294t–295t
finite element model, 522, 522f
for hard armour, 233–234
fabric style, 234–235
hybrid fabrics, 236–237
three-dimensional fabrics, 235–236
woven sample of pure ballistic nylon, 296f
- Wrought armour steels, 105
- Wrought homogeneous armours, 92–94
- X**
X-radiography, 654
X-ray tomography, 532–533, 533f
- Y**
 $Y_3Al_5O_{12}$. *See* Yttrium garnet YAG ($Y_3Al_5O_{12}$)
Yarn, 271, 274
pull-in, 293, 296
sonic velocity, energy to rupture and tenacity, 290t
as used in Kevlar Fabric A363, 316t
Yaw card, 642
Yaw-free projectiles, 640
Yield function, 528
Yttrium garnet YAG ($Y_3Al_5O_{12}$), 343
- Z**
Zerilli–Armstrong model (Z–A model), 75, 485–486, 570–572
material data, 575t
strength model, 509–511
Zero Kelvin isotherm, 512–514
Zone of mixed results (ZMR), 642
Zylon. *See* Poly *p*-phenylene-2,6-benzobisoxazole fibres (PBO fibres)